NASA/TM–2012-217781

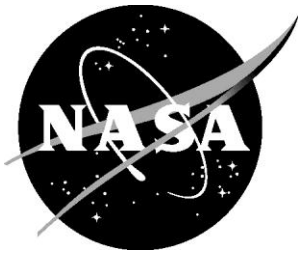

14- by 22-Foot Subsonic Tunnel Laser Velocimeter Upgrade

James F. Meyers
Analytical Services & Materials, Inc., Hampton, Virginia

Joseph W. Lee
Langley Research Center, Hampton, Virginia

Angelo A. Cavone
ATK Aerospace Systems Group, Hampton, Virginia

Mark T. Fletcher
Langley Research Center, Hampton, Virginia

November 2012

NASA STI Program . . . in Profile

Since its founding, NASA has been dedicated to the advancement of aeronautics and space science. The NASA scientific and technical information (STI) program plays a key part in helping NASA maintain this important role.

The NASA STI program operates under the auspices of the Agency Chief Information Officer. It collects, organizes, provides for archiving, and disseminates NASA's STI. The NASA STI program provides access to the NASA Aeronautics and Space Database and its public interface, the NASA Technical Report Server, thus providing one of the largest collections of aeronautical and space science STI in the world. Results are published in both non-NASA channels and by NASA in the NASA STI Report Series, which includes the following report types:

- TECHNICAL PUBLICATION. Reports of completed research or a major significant phase of research that present the results of NASA Programs and include extensive data or theoretical analysis. Includes compilations of significant scientific and technical data and information deemed to be of continuing reference value. NASA counterpart of peer-reviewed formal professional papers, but having less stringent limitations on manuscript length and extent of graphic presentations.

- TECHNICAL MEMORANDUM. Scientific and technical findings that are preliminary or of specialized interest, e.g., quick release reports, working papers, and bibliographies that contain minimal annotation. Does not contain extensive analysis.

- CONTRACTOR REPORT. Scientific and technical findings by NASA-sponsored contractors and grantees.

- CONFERENCE PUBLICATION. Collected papers from scientific and technical conferences, symposia, seminars, or other meetings sponsored or co-sponsored by NASA.

- SPECIAL PUBLICATION. Scientific, technical, or historical information from NASA programs, projects, and missions, often concerned with subjects having substantial public interest.

- TECHNICAL TRANSLATION. English-language translations of foreign scientific and technical material pertinent to NASA's mission.

Specialized services also include organizing and publishing research results, distributing specialized research announcements and feeds, providing information desk and personal search support, and enabling data exchange services.

For more information about the NASA STI program, see the following:

- Access the NASA STI program home page at *http://www.sti.nasa.gov*

- E-mail your question to help@sti.nasa.gov

- Fax your question to the NASA STI Information Desk at 443-757-5803

- Phone the NASA STI Information Desk at 443-757-5802

- Write to:
  STI Information Desk
  NASA Center for AeroSpace Information
  7115 Standard Drive
  Hanover, MD 21076-1320

NASA/TM–2012-217781

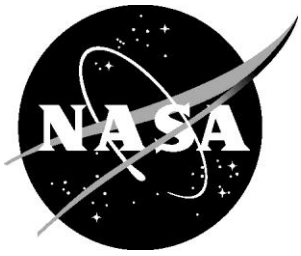

14- by 22-Foot Subsonic Tunnel Laser Velocimeter Upgrade

James F. Meyers
Analytical Services & Materials, Inc., Hampton, Virginia

Joseph W. Lee
Langley Research Center, Hampton, Virginia

Angelo A. Cavone
ATK Aerospace Systems Group, Hampton, Virginia

Mark T. Fletcher
Langley Research Center, Hampton, Virginia

National Aeronautics and
Space Administration

Langley Research Center
Hampton, Virginia 23681-2199

November 2012

Available from:

NASA Center for AeroSpace Information
7115 Standard Drive
Hanover, MD 21076-1320
443-757-5802

Table of Contents

Appendices

14-by 22-Foot Subsonic Tunnel
Laser Velocimeter Upgrade

Objectives

The primary objectives of the upgrade of the 14-by 22-Foot Subsonic Tunnel laser velocimeter were to remove as many optical components as possible from the harsh environment in the plenum surrounding the test section and replace the dedicated signal processing electronics with systems that can be supported in the future. The resulting system must have at least the same measurement capabilities and accuracies as the current system. This goal was specified to yield measurements that were accurate to ±1.5 m/s in both the U- and V-component velocity measurements. In order to meet these objectives the entire optics system, with the exception of the final zoom lens and pan/tilt mirror, would be replaced with more robust hardware that could be remotely controlled from outside of the plenum. Additionally the signal processing hardware would be replaced with high-speed analog-to-digital converters to capture signal bursts with processing performed by software. This would require the development of data acquisition, signal processing, and data processing software that would yield comparable, or better, real-time feedback capabilities than the original system. Further, inter-arrival time measurements and conditional sampling capabilities must be maintained. The overall goal was to develop a system that could be used by test engineers without the degree of training required utilize the original system, yet have safeguards in place to maintain the ability to obtain accurate velocity measurements.

Historical Background

In 1975 Richard Margason, Head of the Subsonic Aerodynamics Branch that operated the NASA Langley V/STOL Wind Tunnel (14-by 22-Foot Subsonic Tunnel), requested that the Gas Parameter Measurements Section (GPMS) of the Instrument Research Division (IRD) would design, construct and validate a laser velocimeter system capable of measuring two components of velocity in the V/STOL Wind Tunnel. As a first step, a proof-of-concept test was conducted using the two-component laboratory system developed by GPMS. The system was configured for coaxial-backscatter operation using a negative-positive zoom lens (final lens diameter of 150-mm) to obtain a focal distance of 3.87-m (tunnel centerline). A 15-W Argon ion laser was used in single line mode yielding approximately 4-W at 514.5 nm. The laser beam was split into three parallel beams configured in a 45-45 degree right triangle with the hypotenuse on the bottom parallel with the upstream / downstream flow of the tunnel centerline. The left beam was set to vertical polarization, the right beam set to horizontal polarization, and the central beam polarization set to 45-degrees. Thus polarization separation could be used to measure two velocity components that are ±45-degrees to free stream. Signals from the interference of the two beams at the extremes of the triangle would be eliminated by the polarizing beam splitter, and thus not affect measurement fidelity. This configuration was successfully used in an investigation of the flow field above a NACA 0012 airfoil in the Langley 7-x 10-foot High

Speed Tunnel, (Young, *et al* (1977), Figures I.1-I.3). However this original configuration did not provide the directionality capability required to fully define the flow above the airfoil at high angles-of-attack where the flow reversed. Thus the system was reconfigured by placing a single 40-MHz Bragg cell in the central beam to provide measurement directionality to both components to eliminate this deficiency. Unfortunately once in the tunnel, it was found that the Bragg effect destroyed the linear polarization of the central beam preventing polarization separation of the two components. Thus the velocity components were measured sequentially by using a remote controlled beam blocker to first block the left beam to allow the acquisition from the -45-degree component, then block the right beam to allow the acquisition of the +45-degree component. The optics system is shown in Figure I.4.

Bragg shifted signal bursts generated by the photomultiplier as a particle passed through the measurement volume, were down-mixed to 5-MHz using a double-balanced mixer and processed with a high-speed burst counter. The digital output from the counter was acquired by a prototype Laser Velocimeter Auto-covariance Buffer Interface (LVABI), a custom interface built by Jim Clemmons of GPMS (Meyers and Clemmons (1978), Clemmons (1983)). This prototype LVABI was capable of acquiring/buffering up to 4000 velocity measurements which were subsequently transferred to a minicomputer for processing.

The proof-of-concept investigation was essentially a repeat of the test conducted in the 7-x 10-foot High-Speed Wind Tunnel described above, except the model, tunnel and focal distances were far larger. The test was expanded to include 0.6-, 4.75-, and 19.4-degree angles of attack of the NACA 0012 airfoil model, Figure I.5, to provide a variety of flow fields for investigation. Seeding was provided by a vaporization/condensation generator using kerosene as the medium. The particle size distribution was measured by an optical particle size analyzer and found to be an exponentially shaped distribution extending to 4-microns, Figure I.6a. The sensitivity of the LV system was determined by a Monte Carlo simulation (Meyers and Walsh (1974), Meyers *et al* (1975)) that produced the probability distribution shown in Figure I.6b, which when multiplied by the particle distribution yielded the expected measurable particle range from 2- to 4-microns, Figure I.6c. The measured velocity maps for the three angles-of-attack are shown in Figures I.7-I.9, respectively. This extensive investigation resulted in several aerodynamic and instrumentation papers: Two NASA Technical Notes (Hoad *et al* (1978), Young *et al* (1978)), One invited journal article (Meyers (1979)), One referenceable NASA Technical Memorandum (Hoad *et al* (1978)), and three conference papers (Young *et al* (1977), Hoad *et al* (1978), and Meyers and Hoad (1979)).

With the completion of the proof-of-concept investigation, the specifications for the dedicated system could be developed realistically based on the practical experiences of using a system in the facility. The system was to measure two components of velocity at focal distances from 2.4- to 7.6-m. A mechanical traversing mechanism was to be developed that would move the measurement volume ± 1.0-m in the streamwise and vertical directions. Additionally a pan/tilt mirror was to be employed to align the optical

axis along angles within ±30-degrees to the tunnel centerline and ±10-degrees about the horizontal plane. The measurement volume was to have a diameter of 200 microns with a length of 1.0 cm at tunnel centerline.

A second proof-of-concept test was conducted to determine if the planned approach for the dedicated LV system would provide similar measurement quality as the previous system while expanding its capabilities. The primary modifications to the system were the implementation of the two-color approach to provide multiple measurement components and upgrades to the LVABI to record the inter-arrival times between particle passages through the measurement volume and the capability of conditional sampling (Clemmons (1983)). Again the 150-mm diameter zoom lens and burst counters were used. The optical system, shown in Figure I.10, was used to measure the wake flow downstream of a large NACA 0012 semi-span model. The data was lost to history primarily because this test was designed as a performance test of the LV and not an aerodynamic test, thus the data was considered unimportant. The results, however, were positive and the construction of the dedicated system proceeded.

The construction and testing of the system utilized the talents of several people from IRD and SAB. Dave Rhodes (OPMS, IRD) and Steve Jones (OPMS, IRD) performed the initial design of the optical system. Jim Meyers (GPMS, IRD) had the overall responsibility of the laser velocimeter and contributed to the final optical design along with the development of the signal processing and data acquisition systems, and the instrument control, data processing, and data display software. Tim Hepner (GPMS, Army) had the responsibility for the final design and construction of the LV system and developing techniques and procedures for its alignment. Jim Clemmons (GPMS, IRD) had the responsibility for the development of the advanced data acquisition hardware (LVABI). Dan Hoad (SAB, Army) had the responsibility for the design and construction of the LV traversing mechanism and the seeding system. The final system is shown installed in the V/STOL tunnel in Figure I.11 with Tim Hepner aligning the input optics. The key to the system was turned over to Dan Hoad representing the Subsonic Aerodynamic Branch and the U.S. Army in April 1982, Figure I.12. The representatives, from left to right, were: Dave Rhodes (OPMS, IRD), Tim Hepner (GPMS, Army), Jim Meyers (GPMS, IRD), Jim Clemmons (GPMS, IRD), Dan Hoad (SAB, Army), Bill Hunter (Head GPMS, IRD), Joe Elliott (SAB, Army), Bill Sellers (SAB), and Steve Jones (OPMS, IRD).

The first wind tunnel test conducted with the laser velocimeter was an investigation of the effects of helicopter fuselage widths and shapes and rotor-fuselage separations on time-average and detailed time-dependent rotor wake velocity characteristics (Hoad *et al* (1983)). Unfortunately the results of the investigation were ambiguous in that no apparent time-dependent velocity characteristics were observed. It appeared that the time-dependency was washed out in the open-throat tunnel configuration. But this did not explain the lack of time-dependency in the closed test section configuration. Although these were the findings reported by Hoad *et al* (1983), they most likely were not correct. The determination of time-dependency was obtained from the LVABI and its samples of the 72-per rev rotor shaft encoder. If there was time jitter in the readings, e.g. ±1 count of the

shaft encoder, the time-dependency would be lost even if the LVABI was accurate. Even this was questionable given that the LVABI was a prototype and conditional sampling was limited to one revolution or less.

The measurement problems that were found in the 1983 rotor-craft investigation led to several research programs to improve measurement accuracy and conditional sampling fidelity. The first area to be investigated was the effect particle seeding had on the LV signal-to-noise ratio. The 1983 test used vaporization/condensation generators with kerosene as the seed material. This approach yielded a polydisperse particle size distribution from approximately 0.4-microns to over 5.0-microns (based on measurements from an optical particle size analyzer with a range from 0.4-microns to 10.0 microns), Young *et al* (1978), Figure I.6. The sensitivity of the laser velocimeter was theoretically calculated using the Monte Carlo simulation by Meyers and Walsh (1974) to determine the probability of measurement as a function of particle size, Figure I.6b, yielding the combined probability of measurement shown in Figure I.6c. Scattered light from the other particle sizes produced only system noise which degraded the velocity measurement accuracy.

An investigation of the capabilities of laser velocimetry to measure turbulence intensity by Meyers and Wilkinson (1982) used polystyrene latex (PSL) particles for the seed material. These particles, 0.35-to 0.55-micron diameter spheres that form the basis of latex paint, were small enough to follow the turbulent flow in the 2-inch pipe used in the investigation yet scattered sufficient light to produce acceptable signals for a short focal length LV system, Figure I.13. A gallon of this material, without color or binding agents, was obtained from the manufacturer for evaluation. The material, 50-percent PSL by weight, was water suspended and could be injected into the flow with a standard paint sprayer. This process injected too many particles into the 2-inch pipe flow and the carrier water did not evaporate. A custom air-jet atomizer was developed that provided better control on the amount of liquid injected into the 2-inch pipe than the piston driven paint sprayer. The amount of PSL injected was reduced by diluting the base material. Through testing, the carrier with the greatest evaporation rate was determined to be a 50/50 mixture of ethanol and water. These changes produced LV signal bursts with very high signal-to-noise ratios with no noise between particle arrivals. Comparisons with simultaneous hot-wire measurements showed excellent LV measurement accuracies (Meyers and Wilkinson (1982)).

While these particles yielded excellent results with short focal length LV systems, they were too small to generate the scattering efficiency needed for long focal length systems. Larger PSL particles were available commercially, but at a prohibitive cost. With the help and guidance of the Chemical Engineering Department of Case Western Reserve University, a development program was undertaken at LaRC to manufacture PSL particles of a size applicable to long focal length systems. This effort led to the process developed by Nichols (1987) which was capable of producing monodisperse particles within a range from 0.5-microns to 2.4-microns. Aerodynamic and laser velocimetry simulations indicated that particles of 1.7-microns would scatter sufficient light energy to yield good signal-to-noise

ratios yet be small enough to faithfully follow all subsonic flows expected in the wind tunnel. The process produced a gallon of particles (10-percent by weight) in 24-hours, a sufficient production rate for wind tunnel investigations. The effectiveness of these particles in laser velocimeter applications was reported by Meyers (1991), Figure I.14. The seeding system in the V/STOL Tunnel (now renamed the 14-x 22-foot Low Speed Wind Tunnel), was rebuilt to provide remote scan capability that allowed the user to place the array of agricultural spray nozzles in the appropriate position to align the plume of PSL particles at the desired LV measurement location within the test section, Figure I.15.

The prototype LVABI was replaced by a commercial unit (manufactured by Macrodyne, Inc. under license from NASA-LaRC, Cavone *et al* (1987)). This unit was capable of acquiring up to six channels of laser velocimetry data, along with measuring the inter-arrival times for each channel. In addition up to 10 channels of analog and/or digital data could be acquired simultaneously with any LV channel or the multiple LV channel coincidence signal. The LVABI could acquire data, LV and/or 16-bit digital, up to 650k/s or 12-bit analog data up to 500k/s. Inter-arrival times were measured for each velocity component to a resolution of 0.1-microseconds up to a maximum time of 0.65 seconds (resolution drops to 1.0 μsec after 6.5 msec and 10 μsec after 65.5 msec). Each channel had a separate on-board memory of 16,384 16-bit words. Upon completion of a data acquisition sequence, the data was transferred via 16-bit data bus with Direct Memory Access (DMA) to the Hewlett-Packard model 1000 minicomputer for processing and real-time display of the statistics and velocity histograms.

The capabilities of the upgraded systems were determined with the investigation of the inlet flow to a helicopter rotor (Hoad *et al* (1988), Elliott *et al* (1988), Meyers (1988)). Maps of the entire velocity field were to be obtained at various rotor azimuth angles. Thus conditional sampling was required along with inter-arrival time measurements to determine if successive measurements occurred during the same revolution or a subsequent revolution. Sampling bias considerations required that only one measurement should be made at a given rotor azimuth per revolution. Thus redundant measurements were eliminated. The remaining measurements in each 3.0-degree azimuth angle wedge were thus independent and were statistically analyzed to yield the velocity maps. Example velocity maps of the inlet flow are shown in Figure I.16. The results obtained in this investigation demonstrated the capabilities of the laser velocimeter and proved that the system was ready for use as a flow diagnostic tool in the 14-by 22-Foot Low Speed Wind Tunnel, Figure I.17.

The advances in micro-electronics during the 1980's led to the possibility of replacing the high-speed burst counters with frequency domain signal processing systems. The increase in measurement accuracy was demonstrated by Meyers and Clemmons (1987) and Meyers and Stoughton (1988). This research led to a United States patent (Meyers *et al* (1988)) and the development of a commercially built frequency domain signal processor (manufactured by Macrodyne, Inc. under license from NASA-LaRC, Meyers and Murphy (1990)). The theoretical predictions that frequency domain processing would be more accurate than high-speed burst counters were proven experimentally by Hepner (1994).

During the early 1990's three frequency domain signal processors were obtained from Macrodyne and incorporated into the laser velocimeter system, replacing the high-speed burst counters. Also during this time period a third optical component was added and located below the test section floor, Figure I.18. The system could be operated in either the two- or three-component configuration depending on the requirements of the flow field investigations. The system remained in this configuration until the current effort began.

Laser Velocimetry – Its Development

The Laser Doppler Velocimeter (LDV), also known as the Laser Doppler Anemometer (LDA) was first developed in 1964 by Yeh and Cummins (1964). They used the principles found in RADAR where Doppler shifted scattered radiation from a moving target was combined with a reference signal and passed to a square-law detector where the two signals heterodyned. The output signal from the detector contained the original two frequencies, their sum and difference. Low pass filtering yielded the difference (Doppler) frequency that could be measured using a frequency discriminator. Since RADAR systems were normally used in a coaxial backscatter configuration, multiplying the measured Doppler frequency by the wavelength of the transmitted radiation yielded the velocity of the target along the axis of the transmitted radiation. Yeh and Cummins (1964) passed a He-Ne laser beam through a water flow in a glass pipe using the optical configuration shown in Figure I.19. As shown in the figure, a portion of the forward scattered light was collected and passed toward a photomultiplier along with a portion of the transmitted laser beam. The photomultiplier served as both the square-law detector and low-pass filter (200 MHz) to yield an electronic signal with the Doppler frequency biased by a DC level. This reference-beam configuration produced the first flow velocity measurements using laser light.

This development at Columbia University, funded by a grant from NASA – Marshall Space Flight Center, had the goal of developing a method that could be expanded to measure three component velocities in a supersonic wind tunnel. The technology was transferred to NASA where it was entrusted to Brown Engineering to develop further. This research led to the first ever LDV measurements of an air flow (Foreman *et al* (1965)). However, the effort also showed the necessity to maintain absolute optical alignment in order to obtain successful measurements. Thus the technology was transferred to Raytheon where hardened single-component and three-component systems were developed (Fridman *et al* (1969), Huffaker *et al* (1969), and Huffaker (1970)). Signal processors based on RADAR and FM radio technology were developed by Raytheon to operate in the expected Doppler frequency range (Fridman *et al* (1969)). A schematic of the optical system is shown in Figure I.20 and a photograph of the system being used to measure the flow in a high-speed jet is shown in Figure I.21.

After seeing the problems involved in maintaining the optical alignment, Goldstein and Kreid (1967) from the University of Minnesota reasoned that if the laser beam was split into two parallel beams that were crossed by a lens, one with 99-percent of the optical energy and the second with 1-percent, light scattered by particles passing through the

common volume would have a portion that would be aligned with the other beam. Thus by placing the photomultiplier along the axis of the low energy beam, scattered light from the high-energy beam would be automatically aligned and the problems with optical alignment sensitivity would be solved. A schematic of the configuration is shown in Figure I.22.

The breakthrough by Goldstein and Kreid led to the nearly simultaneous development of the dual-scatter configuration in Germany (Lehmann (1968)), France (vom Stein and Pfeifer (1969)), England (Rudd (1969)), and the United States (Brayton (1969), Brayton & Goethert (1970)). Instead of a 99:1 split of laser energy, a 50:50 division evolved in these systems and was used with the scattered light collecting optics placed between the two laser beams. The scattered light obtained from both beams heterodyned on the photocathode surface of the photomultiplier with the cross-beam angle maintained in the scattering geometry (Meyers (1971)), so the Doppler shift was constant regardless of the width of the collecting lens or its location in space. A schematic of the configuration is shown in Figure I.23, and the relationship between the Doppler frequency and the particle velocity is given by:

$$V = \frac{\lambda f_D}{2\sin(\frac{\theta}{2})} \tag{1}$$

where V is the particle velocity, λ is the wavelength of the laser light, f_D is the Doppler frequency, and θ is the angle between the two crossing laser beams.

Through experimentation researchers later reasoned that because laser light is coherent, the crossing of the two laser beams would produce interference fringes (Lennert *et al* (1970)), Durst and Whitelaw (1971)). The spacing between adjacent fringes can be determined from:

$$l_f = \frac{\lambda}{2\sin(\frac{\theta}{2})} \tag{2}$$

where l_f is the fringe spacing, λ is the wavelength of the laser light, and θ is the angle between the two crossing laser beams. A schematic of the interference fringes and their physical dimensions is shown in Figure I.24, and a photograph of the cross section of the fringes is shown in Figure I.25. A schematic of this cross section is shown in Figure I.26 along with representative signals obtained by particles passing through the fringes at various trajectories. The frequency of the scattered light could then be multiplied by l_f to obtain the velocity of the particle – the same relationship as the Doppler model, equation (1).

Later improvements to the optical configuration included techniques to measure two velocity components using polarization (Lennert *et al* (1970, 1972)) and color (Grant and Orloff (1973)). The inability of the technique to measure velocity directionality was

overcome by Mazumder (1970) through application of a rotating diffraction grating to shift the optical frequency of the two focusing laser beams in opposite directions. This approach artificially introduces an apparent velocity in the Doppler model by adding a fixed frequency bias in the frequency f_D, equation (1). Subtracting the value of this bias eliminates the directional ambiguity, provided all Doppler frequencies are less than the bias frequency. In the fringe model, the addition on the bias frequency results in moving fringes. Again subtracting the bias frequency will eliminate the directional ambiguity. Mazumder (1970) was also attempting to use a crystal Bragg cell to perform the same function as the rotating grading. This work led to the current use of Bragg cells in all LDV (or fringe-type laser velocimeters – if the optical interference model is preferred) optical systems. The final component that led to the current state-of-the-art optical systems was the use of polarization preserving fibers to separate the laser from the transmission optics (Dyott (1978), Sasaki *et al* (1980), and Knuhtsen *et al* (1982)).

Although all of the developments described above are used in the current state-of-the-art LDV optical systems, their configuration is far different than the earlier systems. The two primary changes were the placement of the Bragg cell(s) and the polarization preserving optical fibers. Originally a Bragg cell was placed in one of the two laser beams defining a given measurement component to offset the Doppler frequency of that component. However, Rhodes (1976), and Gartrell and Jordan (1977) used a two-dimensional water Bragg cell to divide a single laser beam into four beams forming a square. The left two beams were shifted 15 MHz from the right two beams, and the upper beams were shifted 25 MHz from the lower beams. Thus the Bragg cell not only split the input laser beam into the needed four beams for two-component measurements, but Bragg shifted each pair by a different amount so that the acquired signal frequencies obtained from a single photomultiplier could be separated by band-pass filters. Although there is no apparent traceability to this earlier development, current LDV optical systems use a single crystal Bragg cell to split the input all-lines Argon ion laser beam into multiple beams separated by color and the Bragg effect. The colors can be separated since the Bragg scattering angle is dependent on the wavelength of the incoming light. The cell orientation and RF drive power is set to equalize the energies of the zero and first order diffracted beams. Mirrors are then used to select the desired beams and direct them to optics that will pass the light to its respective polarization preserving fiber. The polarization preserving fibers are now used to transmit each of the four laser beams respectively, to the focusing optics instead of being used to transmit light energy between the laser and the splitting optics.

Signal processing technology translated from general purpose instrumentation to specifically designed instrumentation is now back to general purpose instrumentation. The original signal processor was an analog scanning spectrum analyzer and acquisition consisted of visual observations. The first real signal processor was a frequency tracker developed by Raytheon (Fridman *et al* (1969)). This modified RADAR frequency tracker was basically an FM radio with an analog feedback loop to hold the intermediate frequency (IF) constant during periods of signal dropout. After a user-selected period of time, the tracker will begin a search in an attempt to reacquire the signal frequency. Since the minimum duty cycle (fraction of time a signal MUST be present) was 15-percent, a very

high seeding density was necessary and since the occurrence of particles in the measurement volume is random, the technique was not practical for gas flows. This problem was addressed at the first ever conference on laser Doppler velocimetry held in March 1972 at Purdue University. A lively continuing discussion of the virtues of processing in the time domain versus the frequency domain extended over the course of the entire meeting. The characteristics of frequency domain signal processing were addressed by Milt Huffaker (NASA – Marshall) and Jim Meyers (NASA – Langley). The advantages included available hardware (frequency tracker) and continuous signals whose amplitudes were proportional to velocity – provided the duty cycle was high. The primary disadvantages were the high signal-to-noise ratio required and signal dropout not clearly defined in the output. There was also a concern that time-of-flight broadening (short burst lengths leading to a broadening of the frequency peak) produced measurement inaccuracies. The characteristics of time domain signal processing were addressed by Andy Lennert, Don Brayton and Les Crosswy (USAF – AEDC), Jeff Asher (General Electric), and Hans Pfeifer (ISL – France). The advantages of time domain processing were the ability to measure the Doppler frequency from a single particle passage through the measurement volume, and lower signal-to-noise requirements. Roy Pike (Royal Radar Establishment – England) proposed using photon correlation to determine the Doppler frequency from very low signal levels, down to photon resolved. While the technique was a time domain approach, it required contributions from many signal bursts in order to build up the correlogram. The disadvantages of the time domain approach included the development of multiple approaches with no clearly superior method, and the limited sampling clock frequencies and processing speed of the then state-of-the-art analog-to-digital converters and digital electronics, respectively.

During the next several years LDV signal processing aligned to a single direction. In the frequency domain, only four Raytheon frequency trackers were built (three for NASA – Marshall and one for NASA – Langley) because the capabilities did not justify the high cost. Later DISA Electronics (now Dantec) constructed a commercial unit using similar technology for liquid flow applications with lower signal frequency limits that reduced the cost to reasonable levels. Thermo Systems (now TSI) constructed a commercial unit using a digital feedback loop which reduced the minimum duty cycle to 1-percent. While a major improvement, it was still used mainly for liquid flow applications. In the time domain, photon correlation (Pike (1972)) was used when signals were photon resolved because of long focal length, limited laser power, and/or small collecting lenses. The correlators were custom built by Malvern Instruments in England. Unfortunately they used antiquated RTL circuits and the units were quite expensive. Their approach was to use AND gates to compute a single-bit correlation. This provided relatively high-speed processing, but the number of components involved resulted in limiting the correlogram to only 99 delay times. While the approach allowed the measurement of reasonably high Doppler frequencies, it required more signal bursts to reach a stable correlation than multi-bit correlation – thus only average velocity measurements were possible.

The time domain technique that had the greatest promise was the high-speed burst counter. In order to measure the relatively high Doppler frequencies obtained from air

flows there were several approaches used. The counter developed at the USAF Arnold Engineering and Development Center (AEDC) used pulse stretching techniques to allow more reference clock pulses to be counted within the data burst (Brayton *et al* (1972)). At Brown Boveri in Switzerland an analog/digital counter was developed to measure the zero crossing time of the central cycle (Iten and Mastner (1974)). The counter developed at General Electric was another analog/digital counter, but used the entire signal burst to make the measurement (Asher (1972)). The GE developed technology was later transferred to Macrodyne who then constructed a counter for NASA – Langley. Macrodyne redesigned the GE counter to be pure digital using TTL logic with a 125 MHz clock and a maximum signal frequency of 25 MHz. These circuits were upgraded to ECL logic in the second generation counters, available in the mid 1970s. A pure digital counter was also constructed at the Institute Saint Louis in France using two counters to measure the time for two different number of signal cycles simultaneously (vom Stein and Pfeifer (1972)). By the end of the 1970's both DISA (now Dantec) and TSI were also making pure digital counters and digital counters remained the standard until the early 1990's when digital circuits became fast enough to perform FFTs of a single burst in the frequency domain (Meyers and Stoughton (1988) and Meyers and Murphy (1990)). Currently frequency domain processors performing FFTs in hardware are available from several sources, notably Dantec. Time domain processing using high-speed digital circuitry to employ correlation techniques is available from TSI. Both systems have similar measurement accuracies and costs.

Although not fully appreciated at the time, even by the presenter, a presentation at the 1975 Minnesota Symposium on Laser Anemometry opened the door to the future (Griskey *et al* (1975)). Griskey was primarily presenting a method to automatically scan the LDV measurement volume throughout a water flow in a 2-inch pipe, when he gave a glimpse into the future by stating that his data was acquired by capturing each signal burst in its entirety using a “high-speed” (5.0 MHz) 8-bit waveform recorder with a register length of 2048 samples. These signal traces were transferred to a minicomputer for processing using FFT techniques. He stated that it took a long time to process a data ensemble, but the results were very good. Only a few attendees grasped the significance of this revelation, and even those did not pursue the technology, and Griskey's work was lost to history. It was another 15 years before FFT-based instrumentation was developed and shown to be superior to high-speed burst counters. And only now, some 35 years after Griskey's revelation, the integration of modern electronics with software algorithms will facilitate the application of his concepts to production testing.

Further detail on the laser Doppler velocimetry technique can be found in **Laser Doppler and Phase Doppler Measurement Techniques** by Albrecht, H. E.; Borys, M.; Damaschke, N.; and, Tropea, C. (2003), and the **Springer Handbook of Experimental Fluid Mechanics**, Tropea, C.; Yarin, A. L.; and Foss, J. F. (Eds), (2007).

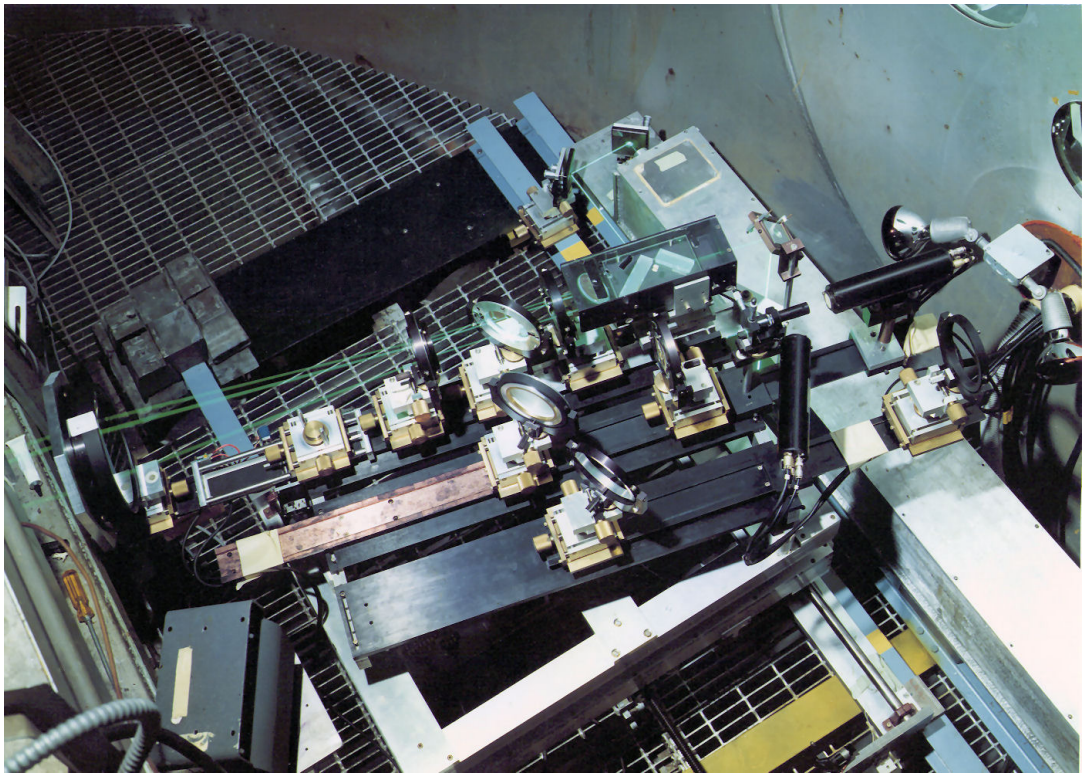

Figure I.1.- Two component laser velocimeter installed in the 7-x 10-foot High-Speed Wind Tunnel.

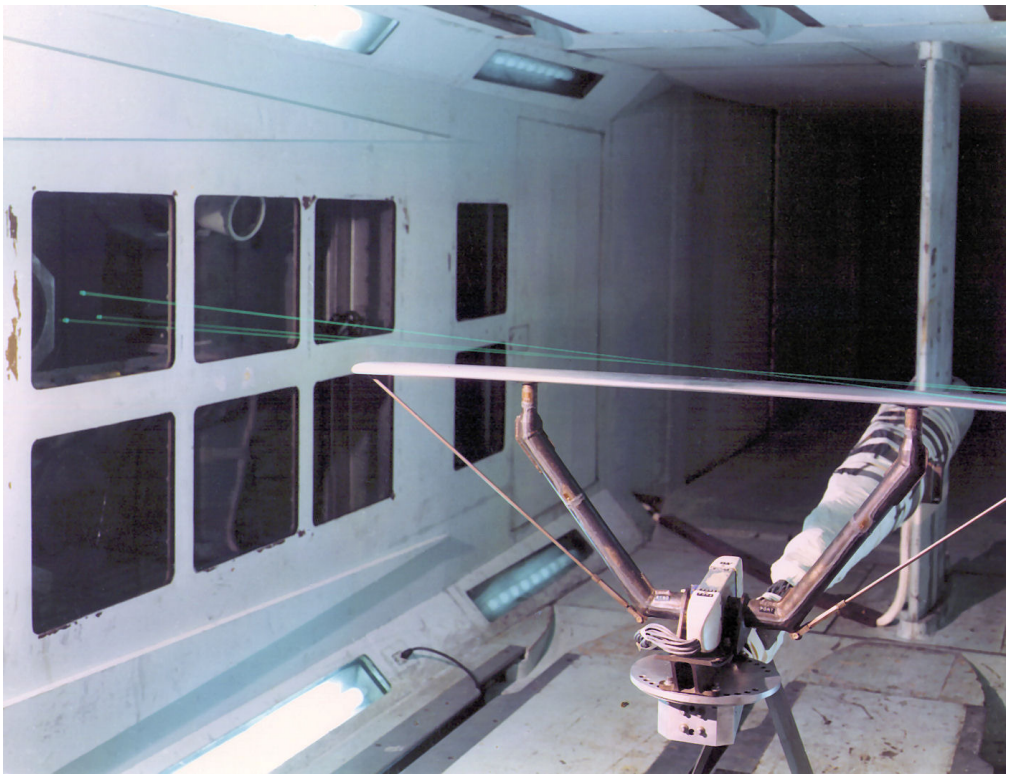

Figure I.2.- NACA 0012 airfoil installed in the 7-x 10-foot High-Speed Wind Tunnel.

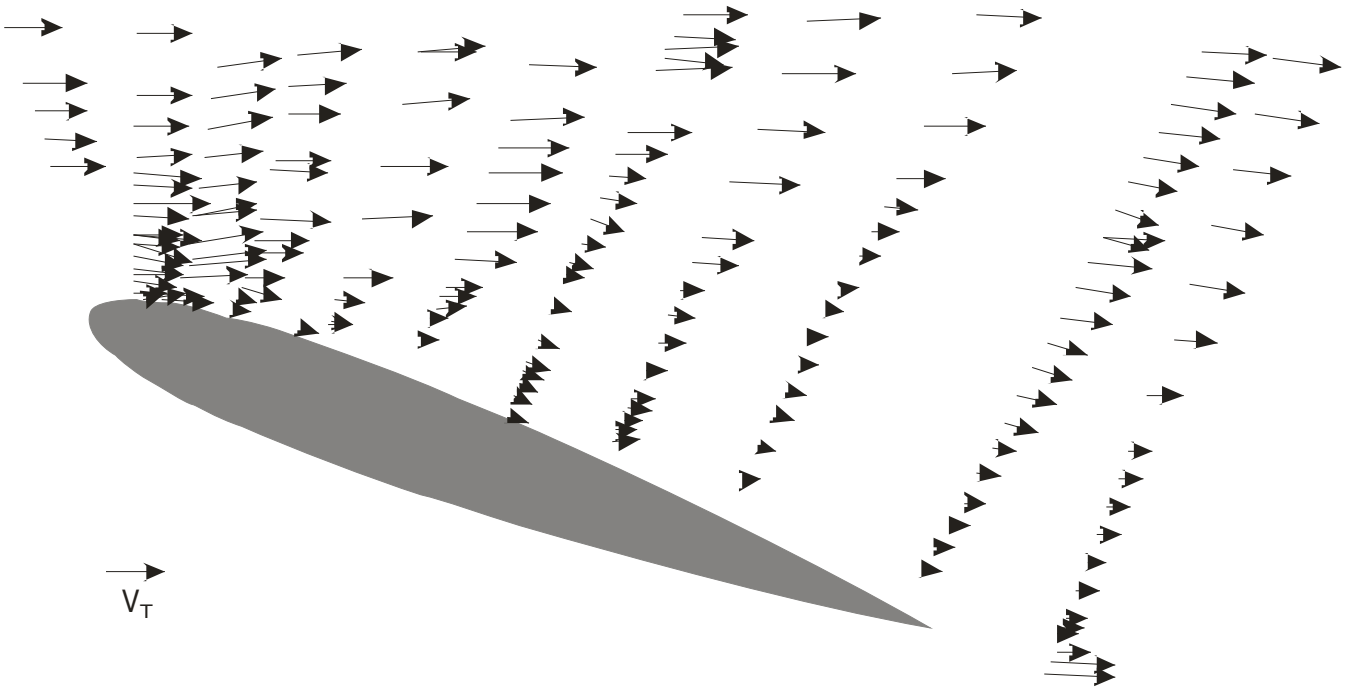

Figure I.3.- Laser velocimeter measurements of the flow above a NACA 0012 airfoil at 19.4-degrees angle-of-attack.

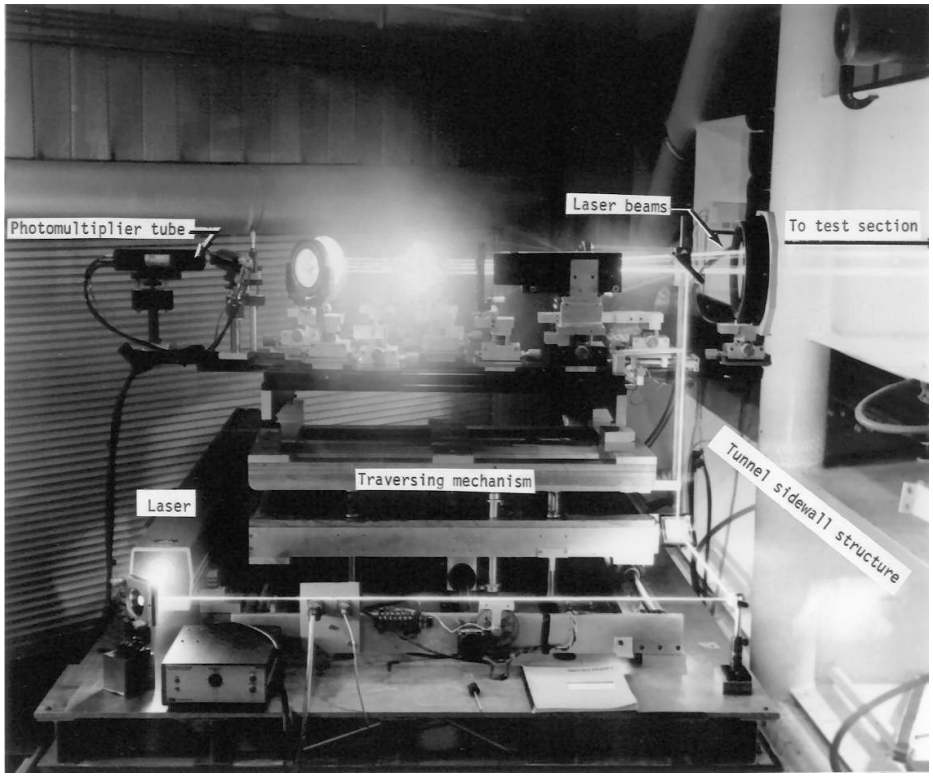

Figure I.4.- Two-component laser velocimeter installed in the V/STOL Wind Tunnel.

Figure I.5.- NACA 0012 airfoil installed in the V/STOL Wind Tunnel.

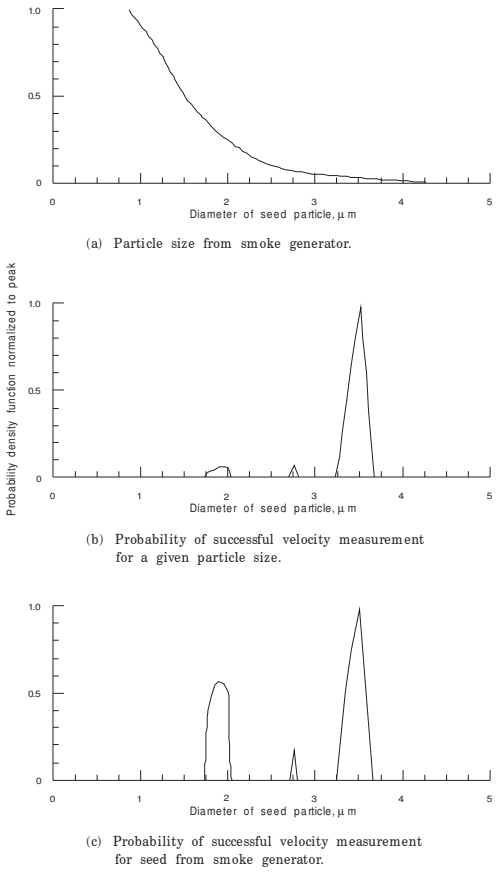

Figure I.6.- Probability of a successful measurement as a function of particle size.

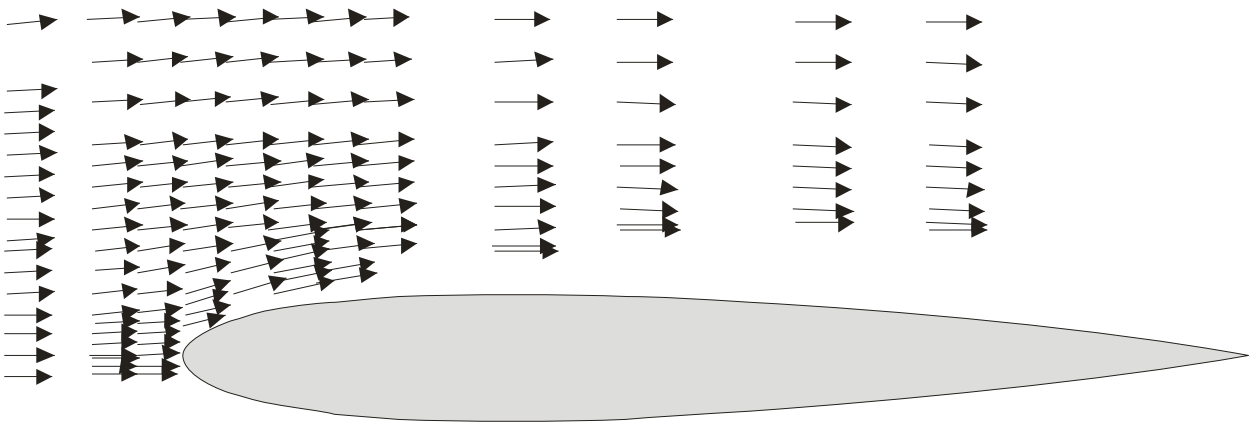

Figure I.7.- Laser velocimeter measurements of the flow above a NACA 0012 airfoil at 0.6-degrees angle-of-attack.

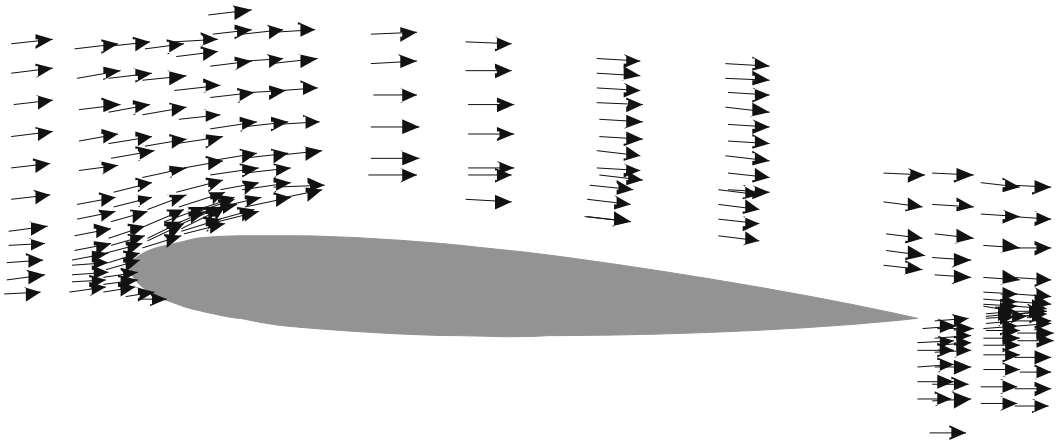

Figure I.8.- Laser velocimeter measurements of the flow above a NACA 0012 airfoil at 4.75degrees angle-of-attack.

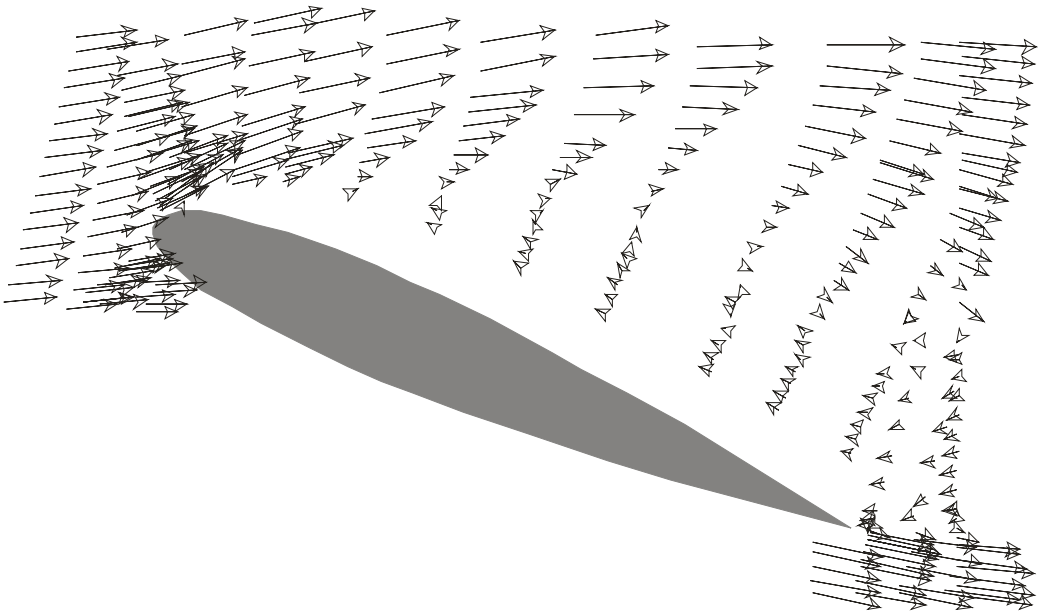

Figure I.9.- Laser velocimeter measurements of the flow above a NACA 0012 airfoil at 19.4-degrees angle-of-attack.

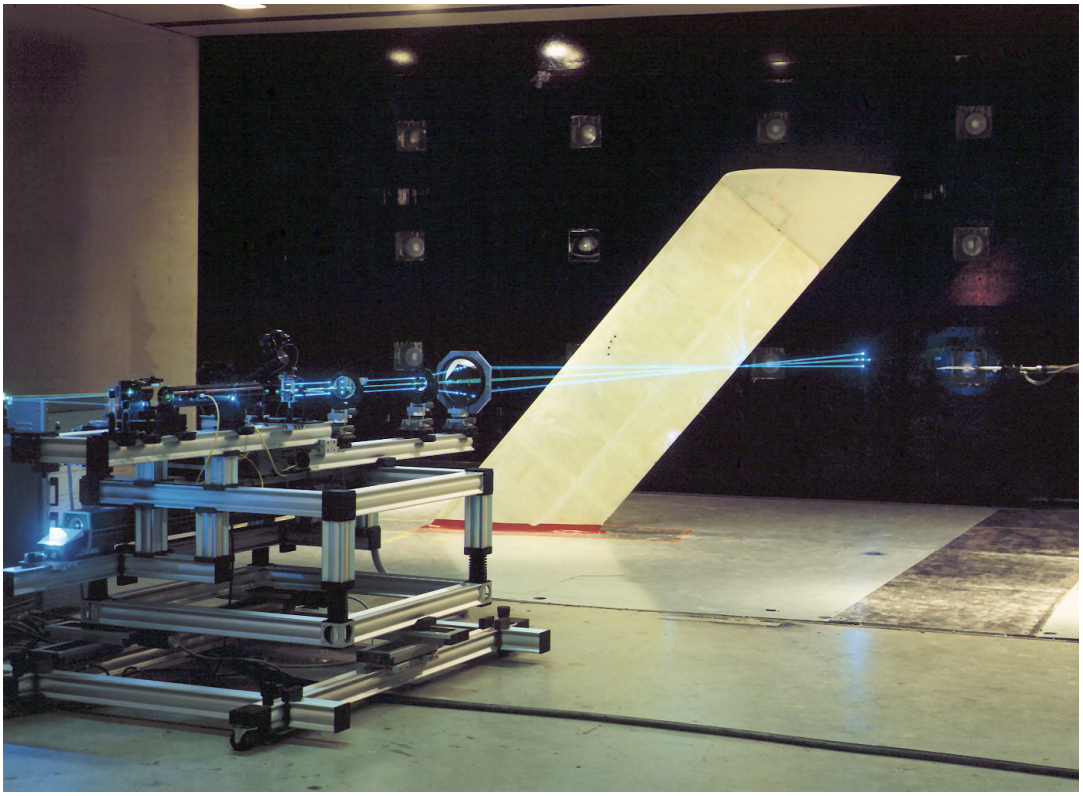

Figure I.10.- Upgraded proof-of-concept laser velocimeter.

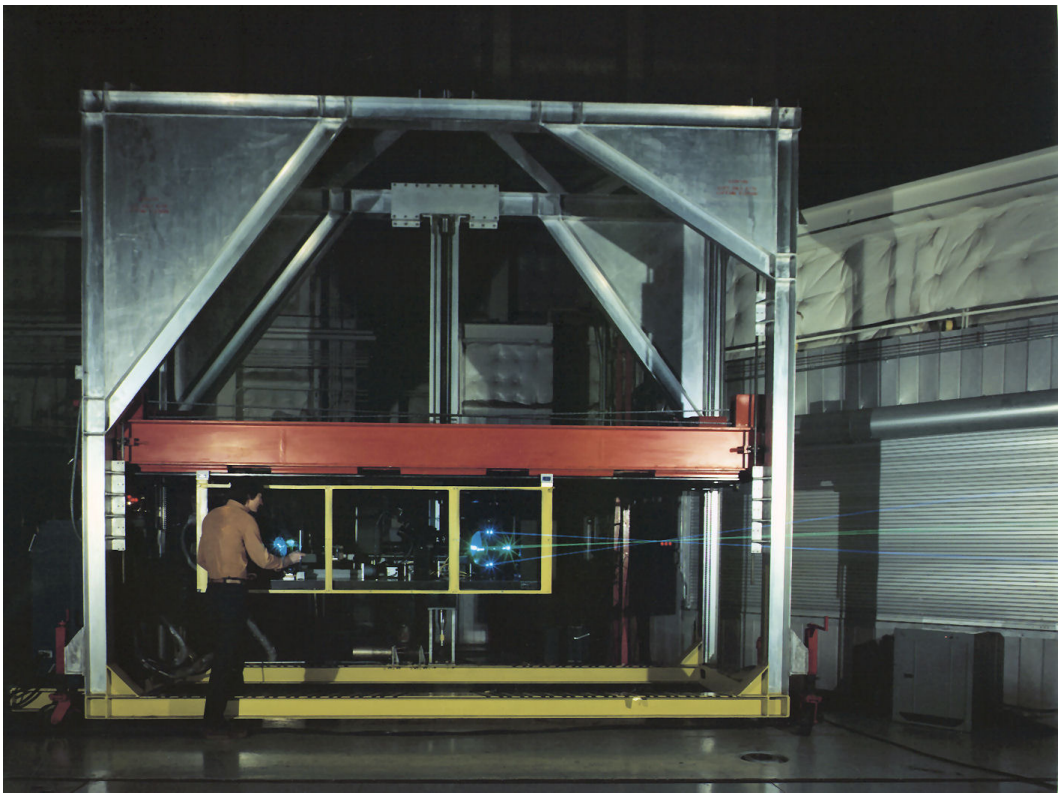

Figure I.11.- Completed laser velocimeter being aligned by Tim Hepner (GPMS, Army).

Figure I.12.- “Official” turn-over of the laser velocimeter to the Subsonic Aerodynamics Branch.

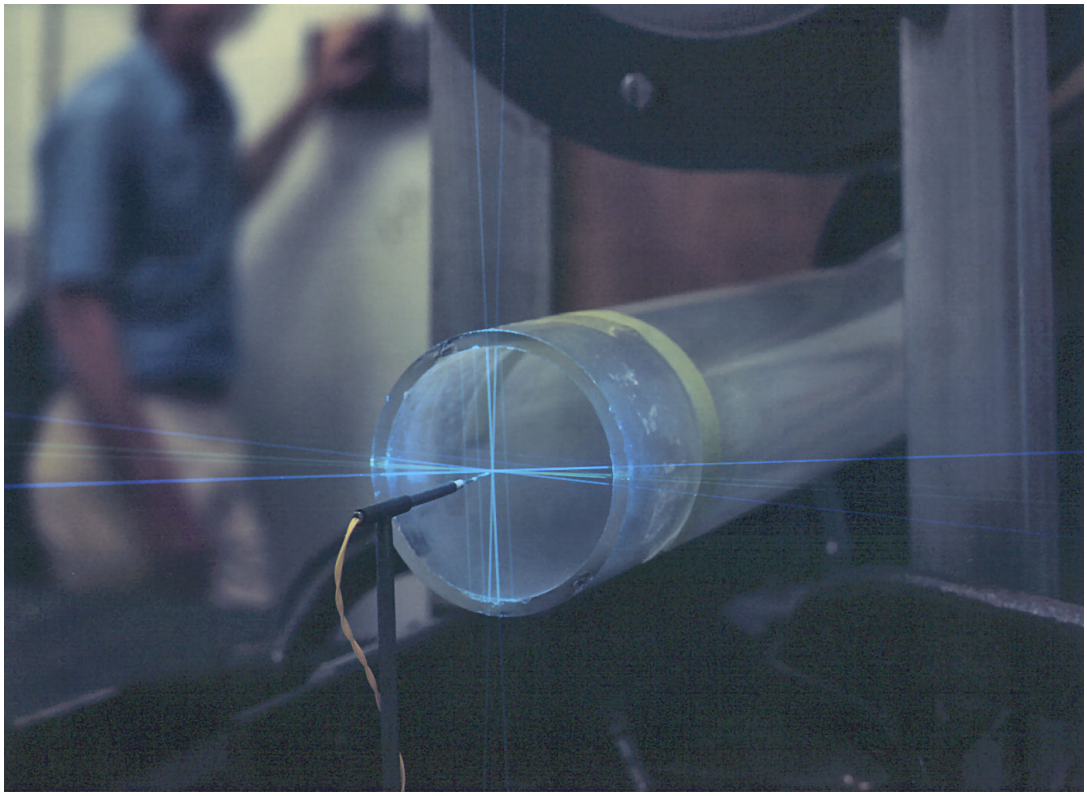

Figure I.13.- Polystyrene latex (PSL) seeding in the jet exiting a 2-inch pipe.

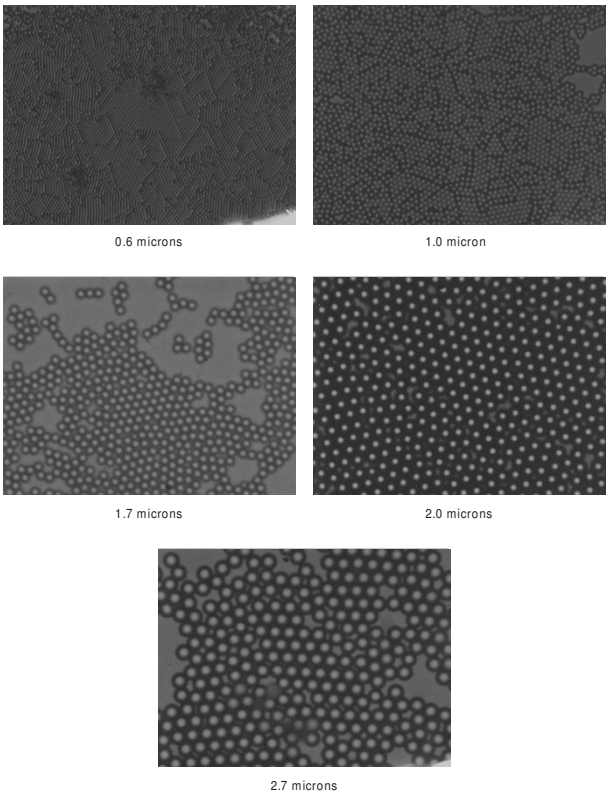

Figure I.14.- Microscope photographs of PSL microspheres, 2000x.

Figure I.15.- PSL particle generator traversing mechanism in the V/STOL settling chamber.

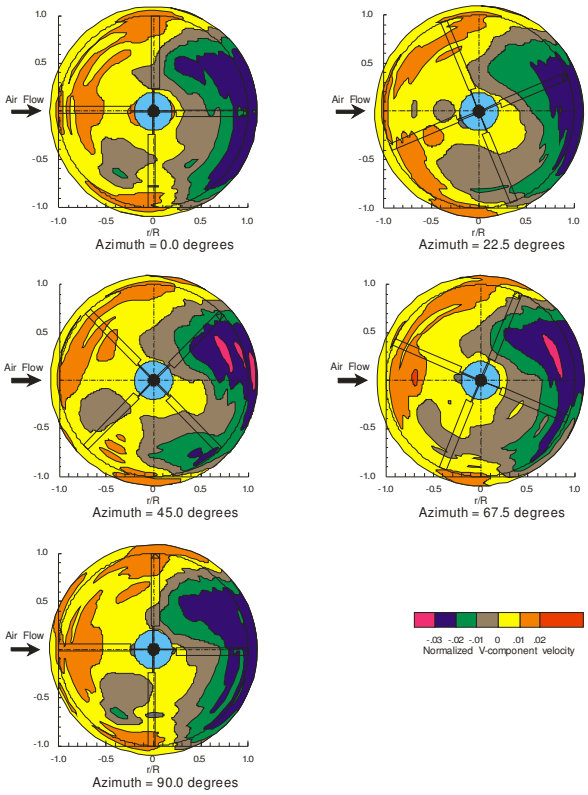

Figure I.16.- Freestream removed vertical-component of velocity 1.0 chord above the rotor disk.

Figure I.17.- Laser velocimeter during routine rotorcraft testing.

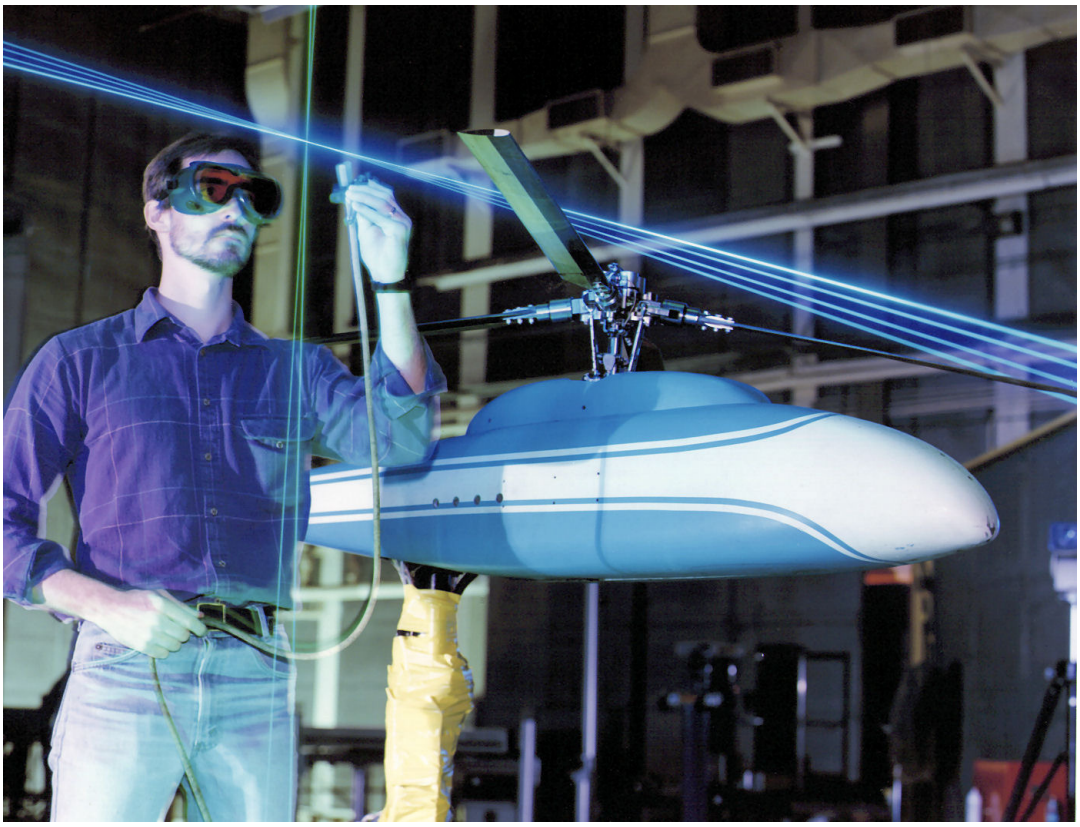

Figure I.18.- Laser velocimeter expanded to three-components.

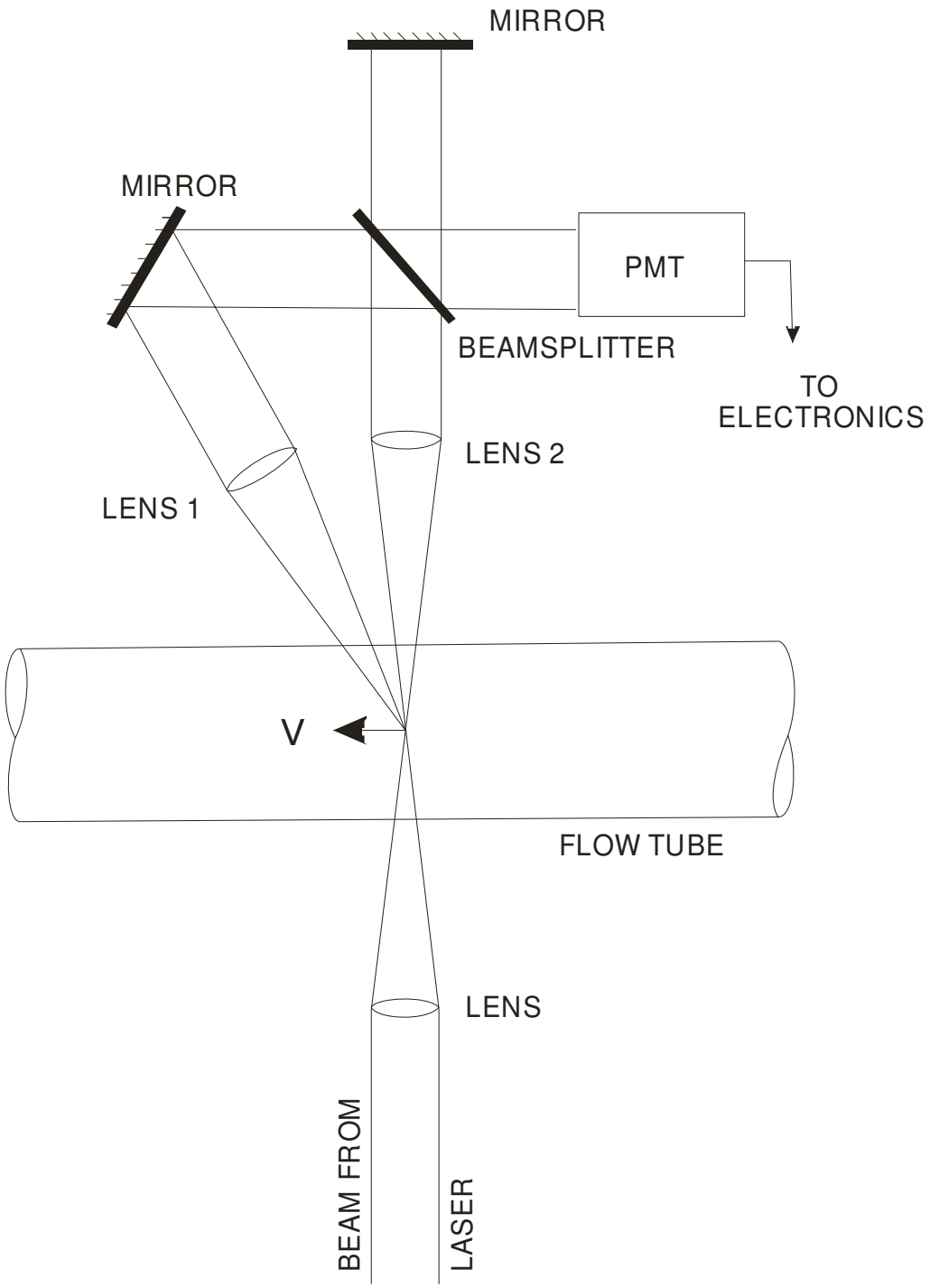

Figure I.19.- Laser Doppler velocimeter (reference beam) developed by Yeh and Cummins in 1964.

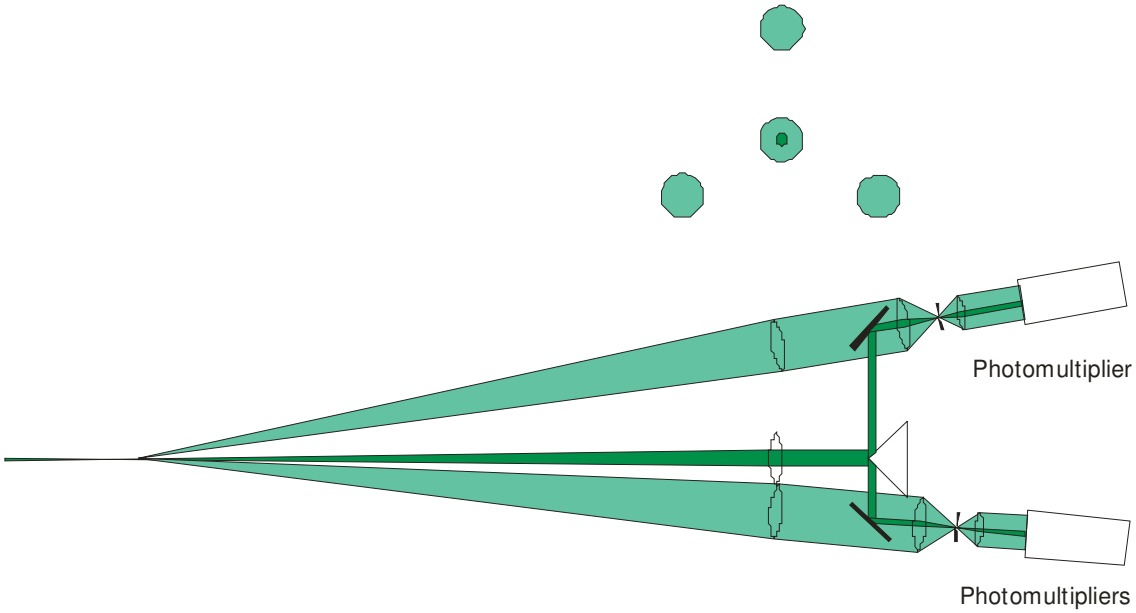

Figure I.20.- Three-component LDV (reference beam) developed by Fridman *et al* for NASA - Marshall.

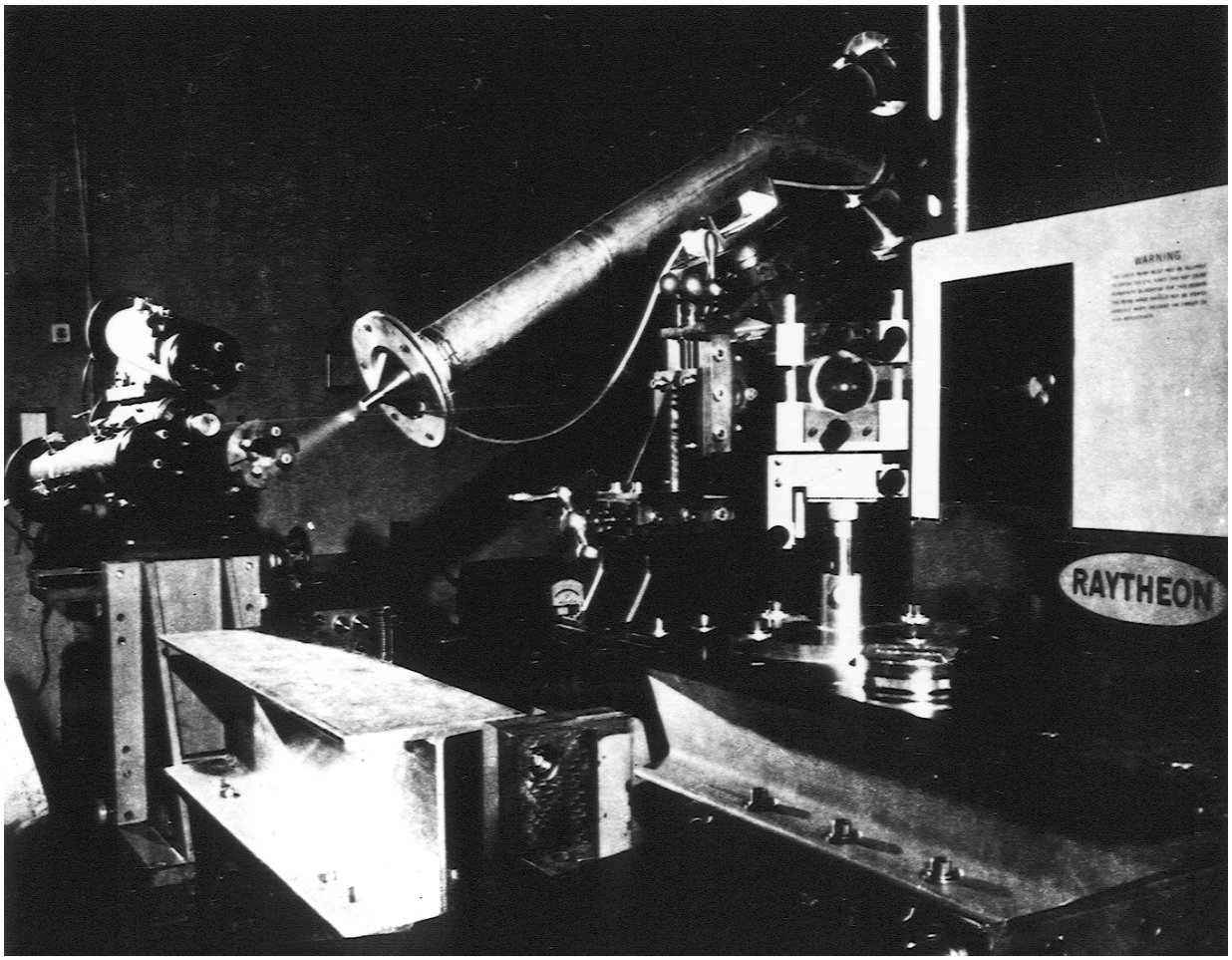

Figure I.21.- Three-component LDV (reference beam) measuring the flow in a supersonic jet.

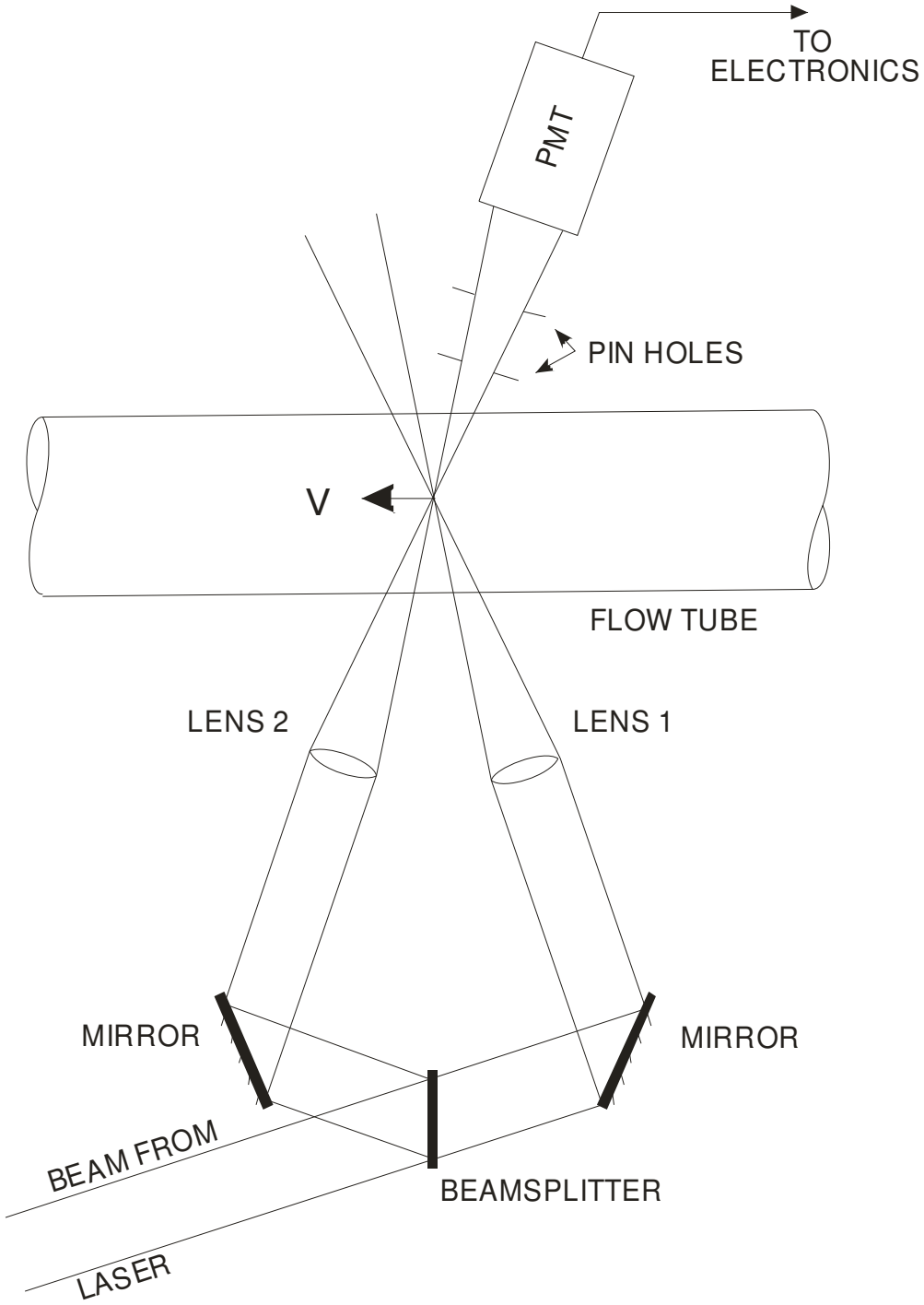

Figure I.22.- Cross-beam, reference-beam LDV developed by Goldstein and Kreid (1967).

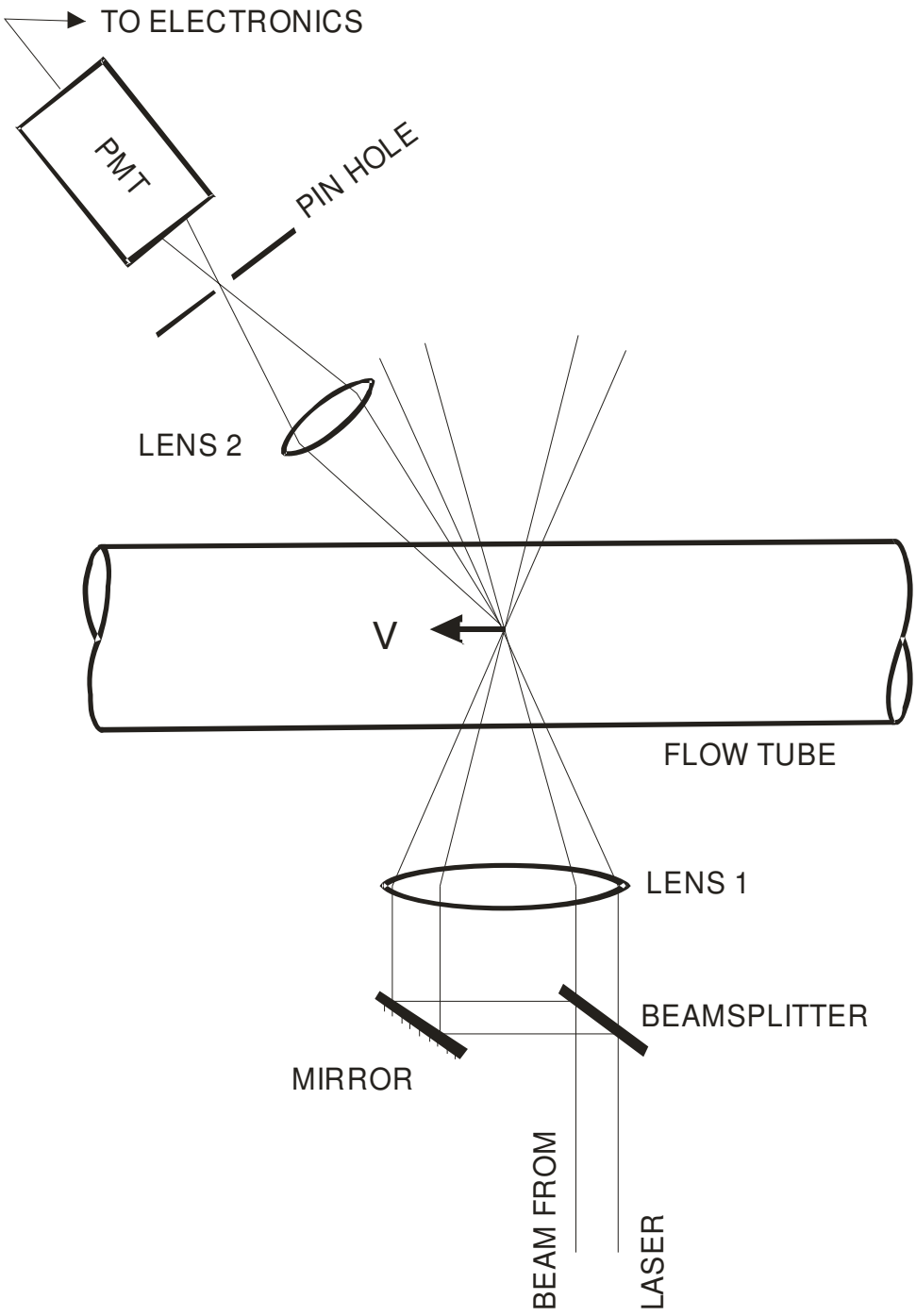

Figure I.23.- Cross-beam, dual-scatter LDV developed by multiple researchers (1968-1970).

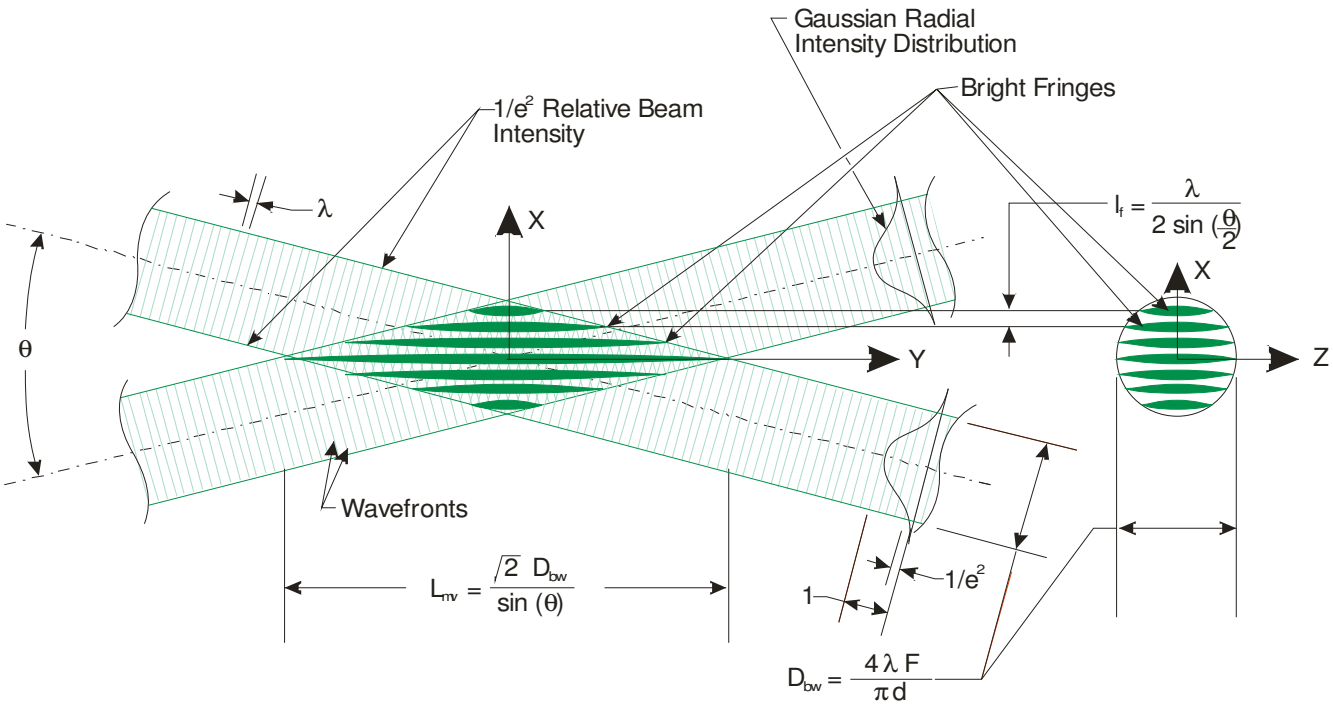

Figure I.24.- Schematic of the interference fringes produced by a cross-beam LDV.

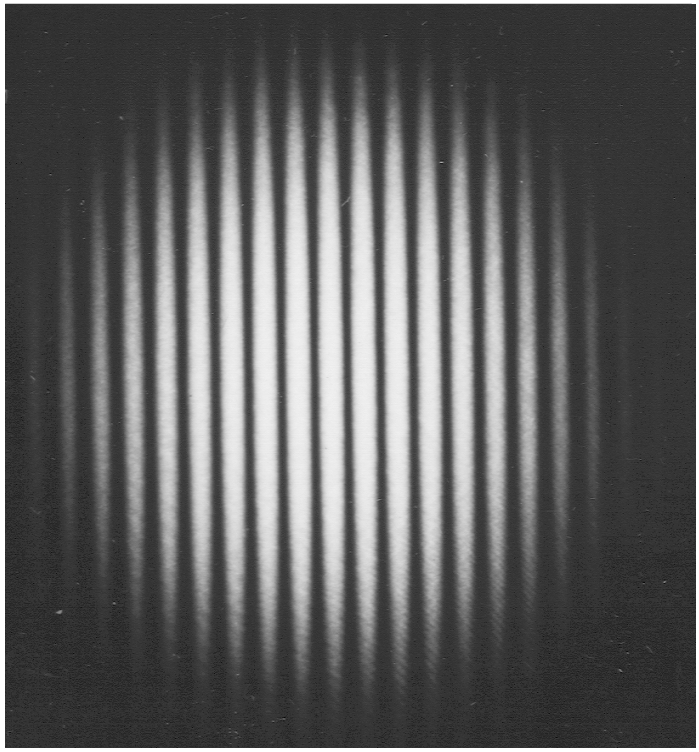

Figure I.25.- Photograph of the cross section of the interference fringes produced by a cross-beam LDV.

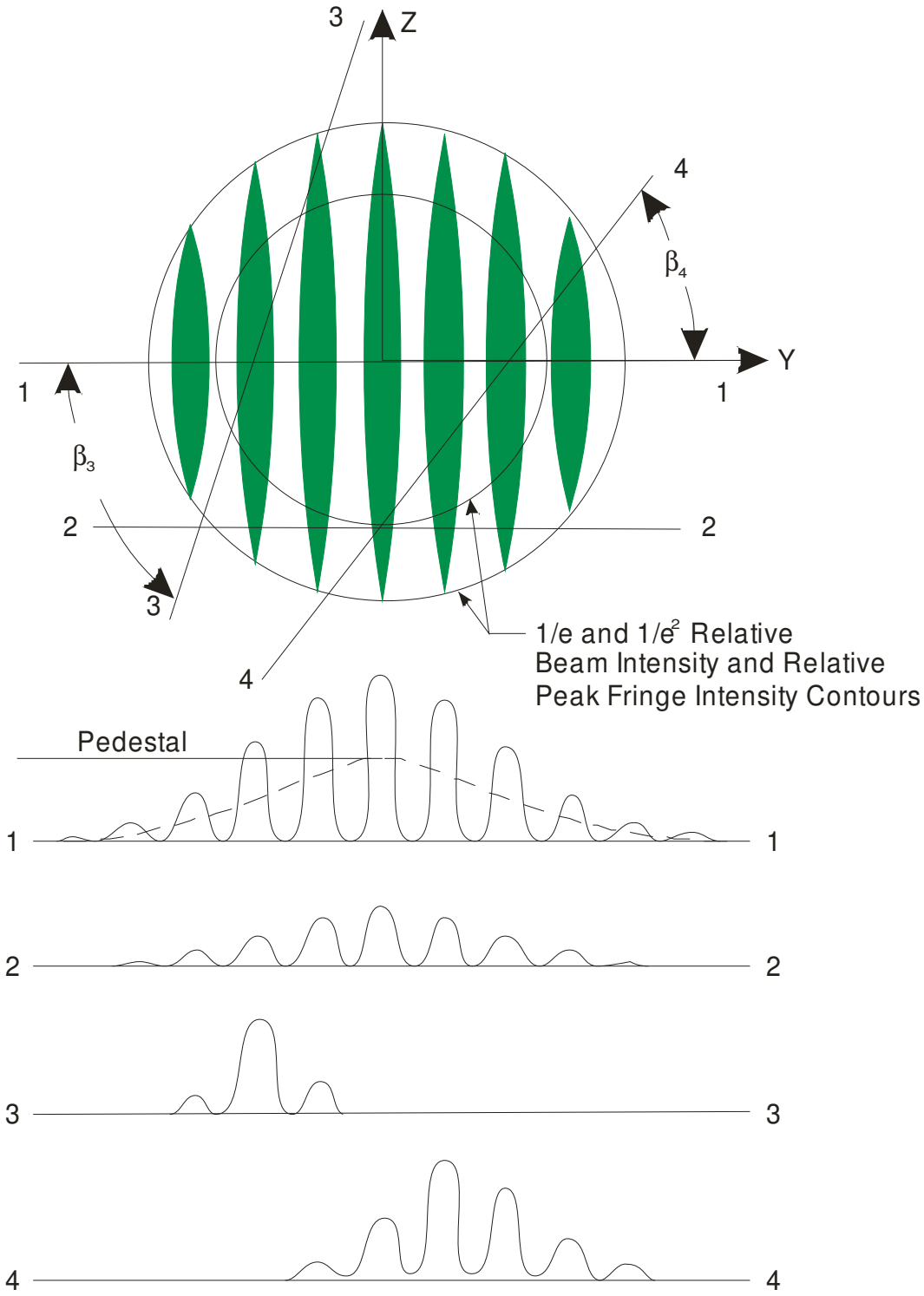

Figure I.26.- Schematic of signals that would be generated by various particle trajectories through the interference fringes in the cross-beam LDV.

Optical System Upgrades

The primary concerns with the current laser velocimeter optical system were focused on the influences that changes in temperature, flow buffeting, and tunnel vibration had on optical alignment, and also on the difficulty in aligning the system to obtain the maximum possible data rate. The objective was to remove as many of the optical components from the plenum area as possible and place them in a more environmentally friendly location that was offered by the stability typical of a laboratory environment.

Advances in polarization preserving single-mode optical fibers have increased optical transmission efficiency and reduced the losses that result from Brillouin scattering, a time dependent relative change in index of refraction caused by the transmitted laser beam. These modern fibers offer the ability to transmit higher optical powers over greater distances than their predecessors making their use a viable alternative to a free-space LV optical configuration. Manufacturers of laser velocimetry hardware have developed systems that utilize these new optical fibers to transmit the conditioned and frequency shifted output beams to the focusing lens using a pair of polarization preserving fibers for each velocity component. Additionally they have developed an optical system that uses a single Bragg cell to separate the colors in the all-line input laser beam, split each color to obtain the pair of beams needed for each measurement component, and impose a 40 MHz Bragg shift on one beam of each pair. This degree of integration greatly reduces the complexity of the transmission optics making the system more robust and easier to adjust in order to obtain and maintain the needed alignment tolerances. The scattered light collected from the particles passing through the measurement volume is transmitted to the color separation optics and photomultipliers via a multi-mode optical fiber. These new systems have reduced the need for sophisticated traversing mechanisms designed to move heavy optical systems including the laser. Additionally, these systems allow the primary optical components along with the laser to be separated from the test environment.

An updated LV system was designed based on this new technology that replaces all of the current optical components except for the large zoom lens and the pan/tilt mirror. The optical components along with some custom electronics were obtained from TSI, Inc. Once the various components were procured and delivered, laboratory testing was conducted to answer the primary questions:

1) Could the new transmission optics be used at the laser power levels needed for long-focal length applications?
2) Were the transmission efficiencies of the optical fibers sufficient to yield the needed laser power at the distal end of 15-meter long fibers?
3) Were the signal-to-noise ratios and signal levels sufficient to yield accurate measurements from 1.7-micron PSL particles at a focal length of 4-meters?

To answer these questions a laboratory investigation was conducted using the new optical system coupled to the zoom lens from the current 14-by 22-Foot ST laser velocimeter. The

laser was set to an all-lines output power of 5.0 W. An etalon was not used in the laser. The optical power exiting the polarization preserving fibers was 300 mW in each green beam (514.5 nm) and 280 mW in each blue beam (488.0 nm). The Monte Carlo simulation (Chapter III and Appendix A) predicted that these optical powers would yield acceptable signals from 1.7-micron PSL particles at the 4.0 m focal distance needed to reach the center-line of the 14-by 22-Foot Subsonic Tunnel. The first test used a Royco particle generator to provide a low-speed flow containing 2.0-micron PSL particles to determine the signal strength and quality at various injection points and flow angles with respect to the measurement volume. The signal levels and qualities were comparable to predictions and were sufficient to yield accurate velocity measurements. As expected reducing the particle size to 1.7-microns yielded signals that were still acceptable. A wind tunnel test was then simulated by using the LV to measure the flow at several locations within the jet exiting a 2-inch pipe. A six-nozzle atomizer was used to inject 1.7-micron particles into the inlet of the blower that provided a 50-m/s flow exiting the 2-inch pipe. The acquired signal levels were identical to those obtained from the Royco test using the same particles. Data rates and measured flow statistics were as expected based on previous measurements using Doppler global velocimetry (DGV) and point Doppler velocimetry (pDv).

The laser input side of the Fiberoptic LDV system, Figure II.1, is to be located in the environmentally controlled laser laboratory adjacent to the test section of the 14-by 22-Foot Subsonic Tunnel. Thus this portion of the LDV is isolated from the effects of tunnel buffeting, environmental temperature and pressure changes, and vibration. It consists of the laser, turning mirrors, the TSI *Fiberlight* and optical fiber couplers. The

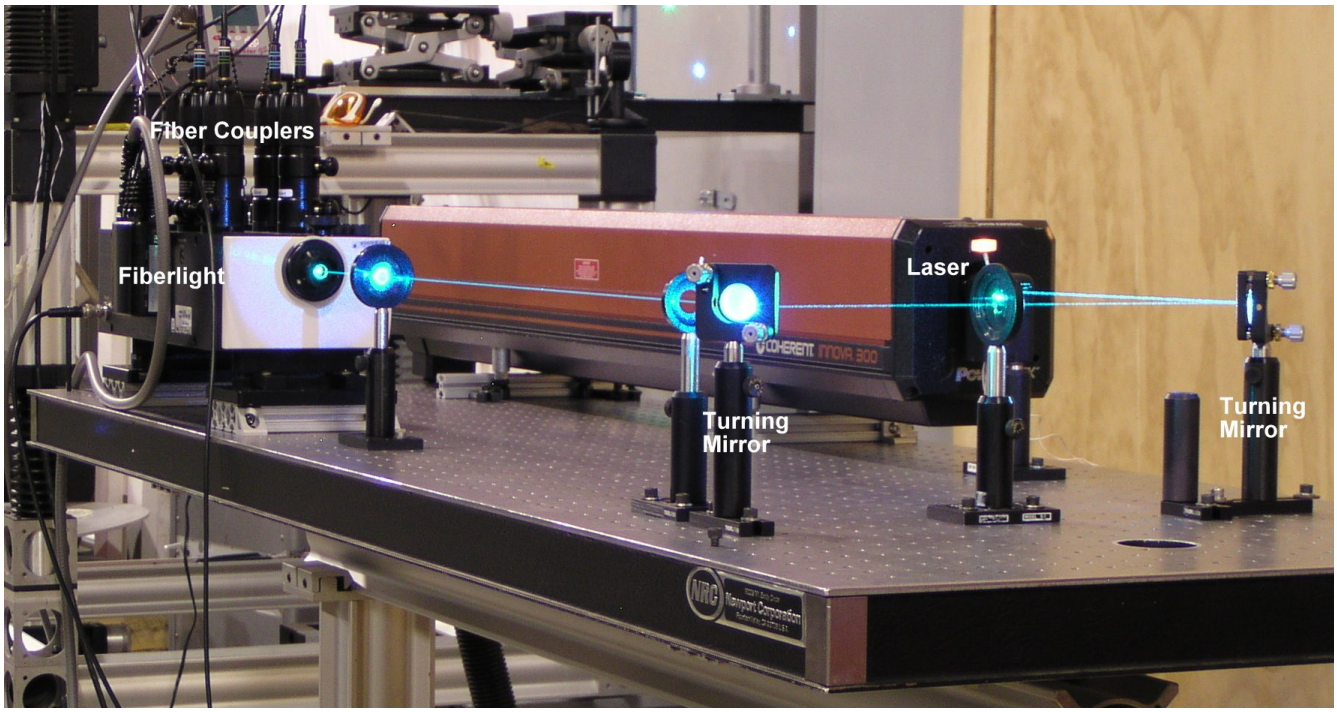

Figure II.1.- Laser and optical fiber coupler system – to be installed in the laser laboratory adjacent to the 14-by 22-Foot Subsonic Tunnel test section.

multi-wavelength input laser beam passes through the *Fiberlight* and is separated into two pairs of laser beams (488.0 nm and 514.5 nm) with each pair consisting of an unshifted beam and frequency shifted beam. The four beams are directed into individual optical fiber couplers where each beam is focused onto the end of a single mode, polarization preserving fiber and delivered to the transmit/receive fiber optic probe located in the plenum area about the test section of the 14-by 22-Foot Subsonic Tunnel.

Once the laser beams are delivered to the transmit/receive probe located within the tunnel plenum area, the four individual laser beams exit the fiber optic cables where they are re-collimated into parallel 2.5 mm-diameter beams within the probe. The four beams exiting the probe are arranged in an orthogonal pattern with the 488.0 nm beams located in the horizontal plane and the 514.5 nm beams located in the vertical plane. These laser beams are directed via turning mirrors to the two element zoom lens where they are focused at a desired location within the wind tunnel test section, Figure II.2. The characteristics of the zoom lens and the resulting measurement volume, where the four beams cross, are determined in Chapter VII.

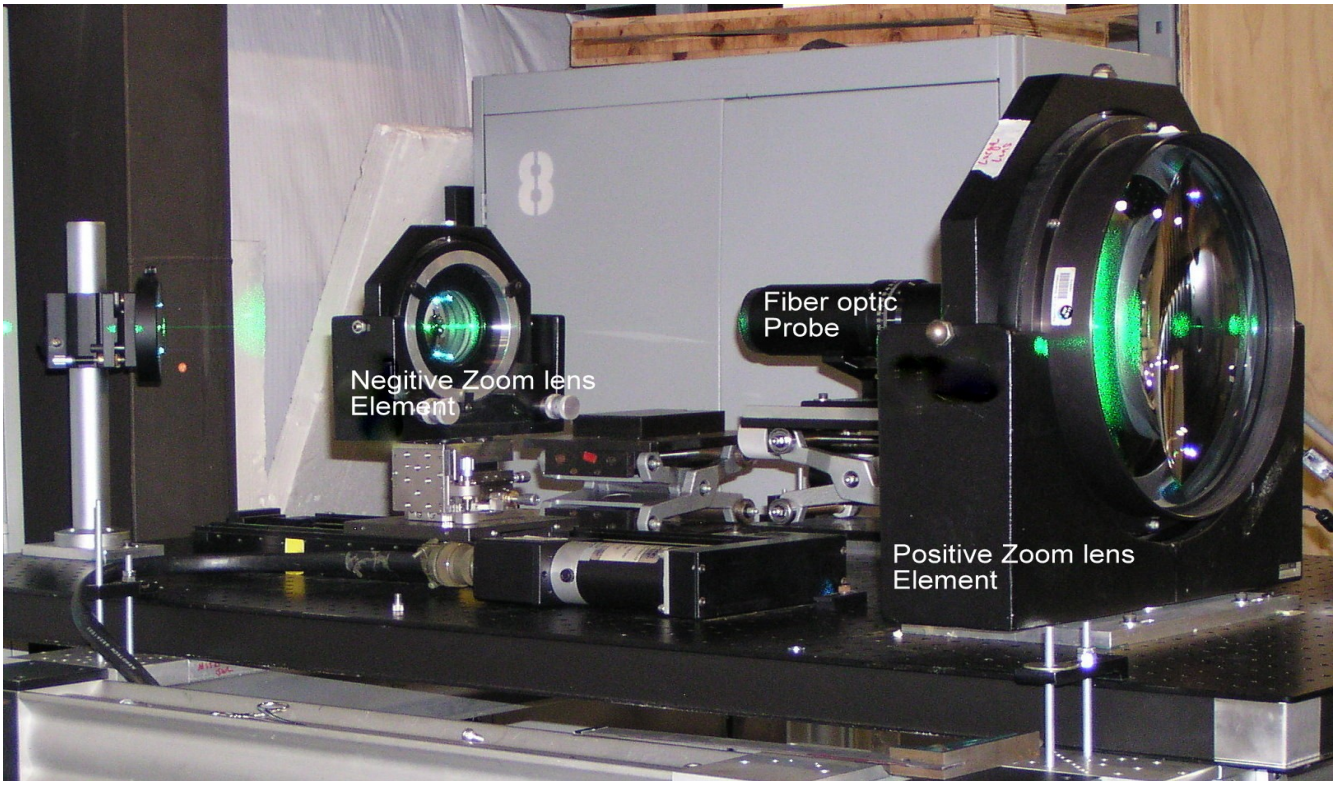

Figure II.2.- Transmit / Receive Optical System – to be installed within the plenum area about the 14-by 22-Foot Subsonic Tunnel test section.

When particles pass through the measurement volume, a portion of the light scattered from those particles is collected in the backscatter direction by the zoom lens. Since the laser beams entering the zoom lens are collimated and parallel, the collected scattered light exiting the negative lens is collimated. It is then directed via the turning mirrors to the

transmit/receive probe. The collecting lens on the probe focuses the collected scattered light onto a multi-mode optical fiber located at the rear of the probe. This fiber directs the light to the photo detector module located in the laser laboratory, Figure II.1. This module chromatically separates the collected scattered light, directing each wavelength to its respective photomultiplier to obtain the U- and V-component signal bursts which are then transmitted via coaxial cable to the data acquisition electronics.

The details for configuring and aligning the optics system are given in Appendix B.

Laser Velocimeter Data Acquisition System
Conceptual Design

The concern that the Frequency Domain Signal Processors utilized electronic components that were no longer available with no potential replacements would put wind tunnel testing at risk necessitated the replacement of the signal processors with something that could be supported. There were two potential approaches to their replacement. The obvious approach would be to replace the signal processors with devices affording similar functionality at a cost of approximately $40-50k per component. This approach would also require the re-engineering of the LVABI to utilize supported electronic components to provide the needed measurement capabilities, e.g., inter-arrival time measurements and conditional sampling.

An alternative option would be to use modern electronics and computers to implement the method first used by Griskey et al (1975) where he used a Biomation 805 waveform recorder to capture the signal bursts from a fringe-type laser velocimeter. After each signal burst was captured, the waveform was transferred to a minicomputer where it was analyzed using FFT techniques to determine the signal frequency, and thus the velocity of the particle that generated the signal burst. The technique proved to be very accurate because it used more information from the signal burst than the start/stop point of the then state-of-the-art signal processors – the high-speed burst counters. However because of the limited capability of electronics and computer technology in 1975, the approach was only useful for stable liquid flows because of the limited sampling frequency (5.0 MHz) of the waveform recorder and the time required to process each signal burst.

In the last 35 years high-speed electronics and computer technology have improved to the point where Griskey's method may now be a viable alternative for laser velocimetry data acquisition and signal processing, even for production testing in a wind tunnel. Additionally, the costs of implementing this approach using Commercial Off The Shelf (COTS) hardware are so low that the entire data acquisition system is cheaper than a single custom signal processor available from today's laser velocimetry system manufacturers, and could produce measurements with better precision. The challenge was to develop a system that maintained the capabilities of the current system, yet hopefully have additional capabilities and produce better measurement precision. Thus the design specifications include the following requirements:

1) Acquire and process signal bursts from two velocity components at rates that exceed the seeding arrival rates in the facility (with an option for the addition of the third velocity component);
2) Develop and implement a scheme which eliminates spurious signals or signal bursts with poor signal-to-noise ratios or inconsistent signal frequencies within the burst;
3) Provide the capability to enforce coincidence on the two velocity components;
4) Measurement precision of 0.2-percent of reading, e.g., 1.0 m/s for a velocity of

100.0 m/s and a Bragg shift of 40 MHz at tunnel centerline;
5) Measure the times between successive signal bursts (interarrival time);
6) Measure the rotor azimuth angle when each signal burst is acquired (conditional sampling);
7) Measure other selected parameters when each signal burst is acquired (conditional sampling);
8) Provide real time storage for at least 1000 signal frequency / velocity measurements per acquired ensemble; and,
9) Provide near real time display of ensemble statistics and velocity distributions.

The advantages of this approach were lower cost, flexible processing (since the processing would be done in software), easier to update and support, and potentially provide more accurate measurements. The primary disadvantage was whether acceptable data acquisition rates could be obtained.

In order to determine if the COTS / software approach would support the required capabilities, Monte Carlo simulation technology (Meyers and Walsh (1974)) was used to model the optical system and generate realistic signals that could be used to test and evaluate various data processing schemes. If a data processing scheme could be developed with accuracies equal to or better than hardware solutions with acceptable data processing times, the COTS / software approach would be a viable solution worth pursuing. The simulated signals could also be converted to electronic signal bursts using an arbitrary waveform generator. These electronic signals would be photon resolved with known signal frequencies that could be used to test and evaluate the data acquisition hardware and its influence on data processing time and measurement accuracy. The Monte Carlo simulation could also provide evaluation and optimization of the proposed upgraded optical system prior to laboratory testing.

System Design Using Monte Carlo Simulation

Monte Carlo simulation provides a direct path from selected flow field characteristics to particle selection and its trajectory through the measurement volume to the generation of the resulting signal burst. The simulation provides a dynamic range from photon resolved signals to full photomultiplier saturation while maintaining the Poisson statistics of the collected scattered photons from a particle passing through the laser velocimeter measurement volume as defined by the input optical system characteristics. The signal burst could then be processed by candidate techniques and algorithms and the result evaluated based on the known velocity of the particle that generated the signal. Although the specifics of the Monte Carlo simulation are presented in Appendix A, the applicability of this technology is easier understood by following an example particle from selection to the presentation of the resulting signal burst to the signal processing algorithms. Along with the text below, the logical path of the process may also be followed with the flow diagram presented in Appendix A.

The Simulator

Once started, the simulator requests the user to input the characteristics for a two-component, two-color laser velocimeter optical system. These user inputs include: (examples from the Basic Aerodynamic Research Tunnel (BART) configuration, Figure III.1, presented in the units needed by the program)

Transmission optics:

Focal distance of the transmitting lens in meters
Focal distance: 4.36 m

Diameter of the laser beam at the focusing lens in meters
Diameter: 0.02 m

X and Y location of each of the four transmitted laser beams about the center of the transmitting lens in meters
Beam 1: X = -0.135 m, Y = 0.0 m
Beam 2: X = 0.135 m, Y = 0.0 m
Beam 3: X = 0.0 m, Y = 0.135 m
Beam 4: X = 0.0 m, Y = -0.135 m

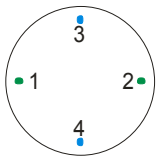

Transmission fraction of each of the four transmitted laser beams (power in each beam divided by the total input power for that component, e.g., input power is 2.0 W for the horizontal component, output power in Beam 1 is 0.8 W → 0.8/2.0=0.4)
Beam 1: 0.356
Beam 2: 0.280
Beam 3: 0.356
Beam 4: 0.280

Polarization of each of the four transmitted beams in degrees: 0.0 is horizontal in degrees
Beam 1: 84 degrees
Beam 2: 89 degrees
Beam 3: 0 degrees
Beam 4: 0 degrees

Laser wavelength of each of the beam pairs that make up a velocity component in micro-meters
Beams 1 & 2: 0.5145 μm
Beams 3 & 4: 0.4880 μm

Input laser power for each of the beam pairs that make up a velocity component in Watts
Input to beams 1 & 2: 1.0 W
Input to beams 3 & 4: 1.0 W

Bragg frequency for each of the two velocity components in mega-Hertz
Beam 2: 40 MHz
Beam 4: 40 MHz

Receiver optics:

Focal distance of the receiving lens in meters

Focal distance: 4.36 m

Vertical (phi) and horizontal (theta) angles in degrees of the receiver lens with respect to the optical axis of the transmission optics centered at the measurement volume

Phi: 0.0 degrees

Theta: 180.0 degrees

Effective lens diameter in meters: Diameter of receiver lens collecting light that passes through the spatial filter to the photomultipliers, e.g., a zoom lens is configured such that at a given focal length only the central 0.2 m diameter portion of the 0.3 m diameter lens collects light that passes through the spatial filter, thus the effective lens diameter is 0.2 m.

Effective lens diameter: 0.3 m

Transmission fraction of the receiver optical system for each component (the scattered light power impinging on the photomultiplier divided by the collected scattered light power within the effective lens diameter, e.g., the power impinging the photomultiplier is 0.1 μW and the scattered light power collected within the effective lens diameter is 0.2 μW → a transfer fraction of 0.1/0.2=0.5)

Horizontal component: 0.65

Vertical component: 0.65

Photomultiplier quantum efficiency as a fraction, e.g., a 21-percent quantum efficiency would be entered as 0.21

Quantum efficiency: 0.15

Photomultiplier gain in millions

Gain: 1.0 M

Electronic gain in dB

Electronic gain: 10 dB

The simulator applies the user characteristics of the transmission optical system and, assuming diffraction limited optics, determine the location and size of the measurement volumes. Optics corrected for chromatic aberrations and collimated laser beams are assumed so that the beam waist for all four laser beams is located at the common cross-over point. The optical power distribution of each laser beam is assumed to be Gaussian along any diameter. The starting point for each particle will be in a vertical plane defined to extend to the $1/e^3$ power limits as defined by the laser power at the center of the measurement volume for the horizontal velocity component. This plane is located upstream from the measurement volume at the $1/e^3$ power point in the plane defined by the horizontal velocity component, i.e., beams 1 & 2. The particle is tracked through the measurement volume based on its original trajectory until it passes through the exit plane, the $1/e^3$ power point downstream of the measurement volume.

Now that the characteristics of the laser velocimeter optical system have been defined, the input flow field must be established. The flow field is assumed to have Gaussian distributions of velocity magnitude and the two flow angles alpha (vertical plane) and beta (horizontal plane). The user defines the desired flow field by inputting the mean and standard deviation of velocity magnitude in meters per second. Then the user defines the desired flow angles by inputting the means and standard deviations for the two flow angles in degrees. The velocity magnitude and the two flow angles are assumed to be independent variables, e.g., no cross coupling among the selection of the respective random numbers.

The user then inputs the index of refraction (real and imaginary) of the seeding particles and the desired particle size distribution from the following:

single size	size in microns selected by the user
Gaussian	lower and upper standard deviation bounds selected by the user (Calculated inclusive to three standard deviation limits, e.g., 2 microns ±0.2 microns would be entered as 1.8 microns to 2.2 microns and calculated from 1.4- to 2.6-microns)
uniform	minimum and maximum sizes in microns selected by the user, and a uniform distribution in between
$1/r^3$ (Junge (1955))	minimum and maximum sizes in microns selected by the user (NOTE: The form of this distribution is automatically adjusted to map the selected limits to the distribution limits set to 0.4- to 1.0-microns (actual distribution in the atmosphere extends from 0.1- to 10.0-microns (Junge (1955))

The example particle size (0.1-micron resolution) is obtained from a random number generator configured to the characteristics of the selected particle size distribution. The velocity magnitude and two flow angles are obtained from their respective Gaussian random number generators. The starting point within the entrance plane is determined from two uniform random number generators that identify the vertical and on-axis locations respectively.

As the particle passes through the measurement volume along the randomly selected trajectory, an ideal signal based on Mie scattering theory as modified by Adrian and Earley (1975) is computed. The modified theory describes the scattering characteristics of a particle passing through two crossing coherent laser beams with a portion of the scattered light being collected within a given solid angle along a given direction. The theoretical amplitude of the collected light in watts is computed at spatial locations along the particle trajectory corresponding to a sample rate of 1.0 GHz until the particle passes through the exit plane. However, the scattered light amplitude is so low that it must be simulated as the arrival of single photons, (Mayo (1975)). This can be accomplished by integrating the

sampled ideal signal to yield a plot of acquired light energy as a function of time. The first sample step of the integrated ideal signal represents the energy acquired during the first nanosecond that the particle was within the measurement volume. Knowing that photon arrivals obey Poisson statistics, a Poisson random number generator was used to generate the number of photon equivalent energies to match or exceed the ideal energy of the first step. The integrated energy of the first and second steps then sets the equivalent total photon energies needed for the Poisson random number generator to produce for the second step. This process continues at each step until the particle has left the measurement volume at the exit plane. The number of random counts needed to reach the integrated energy of the ideal waveform by the Poisson random number generator is the simulated number of integrated photon arrivals. Differentiating this integral yields the simulated signal burst generated by the particle as it passed through the measurement volume with a temporal resolution of 1.0 ns.

The approach used in the current simulation is a bit simpler and more direct. The amplitude of the ideal signal at each time step represents the "instantaneous" collected scattered optical power at that point. At a given step, the ideal amplitude establishes the average number of photons per second scattered by the particle at that point in time. Inverting this rate yields the mean time between photon arrivals. Using this mean time as the mean of the Poisson distribution governing the random number generator, photons are generated at this rate until the arrival time exceeds the ideal time for that step. The photon that was acquired beyond the ideal time becomes the first photon and arrival time for the next step. This approach increases the fidelity of the photon arrivals because the assumption that the "last" photon always increases the energy above the ideal level is not needed. Additionally, this model provides the temporal spacings of the photons within the step sample times, i.e., temporal resolutions less than 1.0 ns.

The resulting impulse train is then interrogated by the model of the photomultiplier quantum efficiency. Quantum efficiency is defined as the amount of light energy actually converted to photo-electrons within the photomultiplier. In an analog sense, 1.0 micro Joule of energy would be multiplied by the quantum efficiency, e.g., 15-percent, to yield the amount of energy, e.g., 0.15 micro Joules being converted to photo-electrons or current in the analog sense. A Monte Carlo simulation of this process would be a uniform random number generator yielding numbers from 0 to 1. An amplitude threshold would be established representing the quantum efficiency, e.g., 0.15, where random numbers less than or equal to 0.15 would allow the impulse to pass to the photomultiplier, and numbers greater than 0.15 would block that impulse. Thus for every impulse in the photon train a uniform random number is generated. If the random number allows passage, the impulse remains along with its arrival time, otherwise it is excluded. Each remaining impulse representing a single accepted photon is converted to a photo electron by replacing the impulse by the photomultiplier response function, assumed to be a triangle function with a 2.5 ns rise time and a 2.5 ns fall time (Appendix A and Figure A.12). If there is any overlap among successive triangles, their amplitudes are added together to yield an analog, albeit noisy signal that has the characteristics of photon pile-up. This signal is then multiplied

by the gain of the photomultiplier to yield the simulated signal exiting the photomultiplier. It is noted that electron gain is a Gaussian random process with the number of electrons multiplying at each dynode obeying Gaussian statistics. This is not simulated as this noise is far less that the noise imposed by the photon arrival process, and is thus considered negligible. Example signals from particles with velocities nominally 100 m/s passing through various trajectories at points along the optical axis in the plane of the horizontal component laser beams are shown in Appendix A, Figures A.13-A.19.

The final step in the signal generation process is to apply the characteristics of the system electronics and, if selected, down-mix the signal to lower the effective signal frequency. The TSI *Fiberlight* Laser Velocimeter contains circuitry that filters the pedestal from the signal burst. The simulator must perform this task with a high-pass filter whose value is user selected to match the *Fiberlight* system characteristics. The *Fiberlight* also allows the user to select a low-pass filter to reduce high frequency noise. This function is also included in the simulator with a user selected low-pass filter setting. If down-mixing is desired, the user selects the reference frequency to produce a signal matching the desired frequency difference using a model of a double-balanced mixer. The reference signal is a sine wave at the selected frequency which is mixed with the photon-resolved signal burst resulting in a burst containing the difference frequency being output from the mixer.

Now that an equivalent signal burst to that produced by the *Fiberlight* system has been simulated, a simulation of the data acquisition electronics can be performed. The input signal is digitized using a high-speed analog-to-digital converter (ADC) with the user defined sample rate that can be up to a maximum rate of 1.0 GHz. The ADC bit depth is set to 8-bits to match typical acquisition boards. If the ADC is used normally with triggering set to some fixed level, signal processing would be required to determine if the trigger setting was satisfactory to obtain signal bursts with good signal-to-noise ratios. This process was considered too time consuming for production testing. An alternative approach would employ a digital oscilloscope to monitor the signals in real time. In this way the researcher could adjust the trigger level until acceptable signals were viewed. As the oscilloscope generates an external trigger pulse each time a signal burst is acquired, this signal could be used to trigger the ADC to capture the same signal burst viewed on the oscilloscope.

Normally when viewing signal bursts of the type produced by a laser velocimeter, the threshold is set to a fairly low amplitude so that the majority of the signal burst may be inspected. This approach also allows signals with low signal levels and signal-to-noise ratios to trigger the scope near the middle of the burst. This has two disadvantages. First the noise contained in these low level signals will increase the measurement standard deviation and potentially affect the other statistical quantities. And secondly, the measurement volume is increased because the majority of the low signal levels are produced by particles passing through the edges of the measurement volume. The problem becomes even worse if poly-disperse particles are used for flow seeding. However the use of an ADC with pretriggering capabilities would allow one to trigger the oscilloscope at higher

amplitudes thus viewing only signal bursts with good signal-to-noise ratios. Setting the pretrigger timing so that the circular storage registers on the ADC board would maintain the captured signal for a time that approximates half of the signal burst length to yield symmetric signal bursts. Applying the pretriggering capabilities available in the digital oscilloscope, the entire signal burst can be displayed even though triggering is set at amplitude levels near the center of the burst, which provides a display of the signals captured by the ADC. Thus only high signal-to-noise ratio signals generated by particles passing through the central portion of the measurement volume can be captured. Although the data rate would be reduced, the resulting measurements would be more accurate.

An additional benefit of viewing the signal bursts on the oscilloscope is that it also provides a measure of the signal amplitude. This feedback allows the input amplifier for the ADC to be adjusted to produce the desired amplitude resolution for the captured signals. A capture length of 10,000 samples would provide the processing software with the opportunity to interrogate the trace and optimize the selection of the portion to be Fourier transformed up to a length of 8192 samples.

The data acquisition capability of the simulator models the operation described above. The 1.0 GHz sampled floating point array containing the pedestal-removed signal burst generated by the model of the photomultiplier is filtered to simulate any in-line filters, and if selected, down-mixed to provide a signal for the model of the analog-to-digital converter. The signal burst is re-sampled at the user-selected rate and the amplitudes converted from floating point to an 8-bit integer array based on the user-selected ADC range. The integer array is then interrogated to determine if it triggers a burst capture based on the user-selected trigger level. With center (high-level) triggering and pretrigger capabilities selected, a successful capture will store a 10,000 element array with half of the elements occurring before the trigger.

Signal Processing

Now that the signal burst has been captured in the simulator or by the data acquisition hardware, signal processing can begin. The first step is to interrogate the signal trace and locate the peak voltage. This location is assumed to be at the center of the burst with the extent of the burst being defined at a cycle peak equal to $1/e^2$ times the peak voltage. A Bartlett (triangle) window is centered at the peak voltage location with its width set to the length of the burst. The remainder of the array containing the Bartlett window is set to the value of zero. Multiplying the captured signal trace by the Bartlett window will produce a symmetric signal burst without discontinuities. The resulting array is shifted to move the first non-zero value to the first array location and fast Fourier transformed with a length of the smallest power of 2 (from 7 (128 samples) to 13 (8,192 samples)) that would encompass the entire burst.

The array containing the frequency domain representation of the signal burst is then transferred to the signal processing subroutine under investigation. Frequency domain processing was selected because higher measurement accuracies can be obtained with less computational resources than equivalent time-domain approaches. The following six frequency domain processing schemes were written, verified and evaluated:

Peak Location	The highest peak is found and its frequency value returned
Gaussian Fit	A Gaussian fit is applied to the highest peak ±1 frequency step – the calculated frequency at the peak of the fit is returned
Histogram Fit (3)	The highest peak, ±1 frequency step, is processed as if it was a histogram where the weighted average frequency is returned
Histogram Fit (5)	The highest peak, ±2 frequency steps, is processed as if it was a histogram where the weighted average frequency is returned
Half Power	The amplitude of the highest peak is used to determine the frequency steps that lie within the half power limits – weighted average frequency is returned
True Half Power	Same as Half Power except the true locations of the half power points are determined using linear interpolation to find the weights and frequencies at the half power points – weighted average frequency is returned.

Example Particles

The primary advantage of the Monte Carlo simulation approach to investigate the characteristics of the system being designed is the ability to track a single particle and its resultant signal through the entire optical, electronic, and processing path. This can be easily followed by selecting example parameters that represent the upgraded laser velocimeter and sending a particle through the measurement volume at a random trajectory to generate a signal burst. This signal burst can then be processed to yield the measured component velocities from each of the six processing schemes and determine the exact error from each method. Although all of the random number generators will be used in this example, seven example particle trajectories will be selected that pass through the vertical center of the measurement volume at the 1/e, $1/e^2$, and $1/e^3$ locations along the optical axis. The particles selected are 1.7-micron diameter PSL particles thus matching those currently used in the 14-by 22-Foot Subsonic Tunnel. The resultant signals, Figures A.13-A.19 in Appendix A, illustrate the variations in signal characteristics based on particle trajectory, and the morphing of the signal from theory, to the Poisson statistics of the photomultiplier output, to the effects of pedestal removal and digitizing by the ADC.

The example laser velocimeter parameters are set to match the upgraded laser velocimeter with a focal distance to place the measurement volume at the tunnel centerline:

Transmission optics:

4.877	Focal distance of the transmitting lens, m
0.0175	Diameter of the laser beam at the focusing lens, m
-0.1294, 0.0	U-component, Beam 1 Location (X, Y), m
0.1294, 0.0	U-component, Beam 2 Location (X, Y), m
0.0, -0.1294	V-component, Beam 1 Location (X, Y), m
0.0, 0.1294	V-component, Beam 2 Location (X, Y), m
0.31	U-component, Beam 1 transmission fraction
0.28	U-component, Beam 2 transmission fraction
0.31	V-component, Beam 1 transmission fraction
0.28	V-component, Beam 2 transmission fraction
84.0	U-component, Beam 1 polarization, degrees (90 = vertical)
89.0	U-component, Beam 2 polarization, degrees (90 = vertical)
0.0	V-component, Beam 1 polarization, degrees
0.0	V-component, Beam 2 polarization, degrees
0.5145	U-component wavelength, microns
0.4880	V-component wavelength, microns
1.0	U-component power, W
1.0	V-component power, W
40.0	U-component Bragg frequency, MHz
40.0	V-component Bragg frequency, MHz

Receiver optics:

4.877	Focal distance of the receiving lens, m
0.0	Vertical (phi) angle of the receiver lens, degrees
180.0	Horizontal (theta) angle of the receiver lens, degrees
0.275	Effective receiving lens diameter, m
0.65	U-component transmission factor
0.65	V-component transmission factor
0.15	Photomultiplier quantum efficiency, fraction
1.0	Photomultiplier gain, M
10.0	Electronic gain, dB
2.0	U-component high-pass filter, MHz
2.0	V-component high-pass filter, MHz
100.0	U-component low-pass filter, MHz
100.0	V-component low-pass filter, MHz

Particle characteristics:

1.59, 0.0	Index of refraction, real, imaginary
1.7	Particle size

Flow characteristics:

100.0, 3.0	Mean velocity magnitude, standard deviation, m/s
0.0,4.0	Mean vertical flow angle, standard deviation, degrees
0.0,0.0	Mean horizontal flow angle, standard deviation, degrees

ADC characteristics:

0.05	Triggering threshold, V
1.0	±Full-scale ADC voltage, V
1000.0	Sample rate, MHz

The comparison of the six signal processing techniques applied to the seven example particle trajectories provides insight into the capabilities of the techniques, Table III.1. The two histogram techniques provided measurements from all of the particles whereas the remaining techniques only yielded five measurements each, all from the vertical center of the measurement volume. The True Half Power scheme yielded the greatest accuracy for the U-component measurement (0.04 m/s ±0.14 m/s), whereas the Histogram (5) scheme yielded the greatest accuracy for the V-component measurement (0.06 m/s ±0.12 m/s). The worst case among these two processing schemes was 0.15 m/s ±0.21 m/s, well within the required specifications.

Statistical Comparisons

In order to determine how the performance of True Half Power and Histogram (5) processing schemes would translate to the real world, a wind tunnel test simulation was conducted. An ensemble of 10,000 particles was launched through the entrance plane in the simulator based on a mean velocity magnitude of 100.0 m/s with a standard deviation of 3.0 m/s, and a vertical flow angle of 0.0 degrees with a standard deviation of 4.0 degrees. Histograms of particle position at the entrance plane, Figure III.2, indicate that the particles were uniformly distributed within the plane except at the extents of the measurement volume. The vertical distributions in the exit plane show the effects of the 4.0-degree standard deviation in flow angle. The statistics of the injection position ensembles are compared with the requested characteristics in Table III.2. The statistics of the randomly selected particle velocity magnitude and flow angle are also in Table III.2 and have an average velocity magnitude of 99.98 m/s with a standard deviation of 2.96 m/s, versus 100.0 m/s and 3.0 m/s requested. The vertical flow angle was found to have a mean of 0.01 degrees with a standard deviation of 4.02 degrees, versus 0.0 degrees and 4.0 degrees requested. This produced a U-component mean of 99.74 m/s with a standard deviation of 2.98 m/s, and a V-component mean of 0.02 m/s with a standard deviation of 7.0 m/s. Of the 9382 particles that triggered data capture, the U-component mean was 99.72 m/s with a standard deviation of 2.98 m/s, and a V-component mean of -0.01 m/s with a standard deviation of 6.97. The distributions of velocity and flow angle are shown in Figure III.3 for the randomly selected particles, and in Figure III.4 for the triggering particles. The statistics and distributions indicate that the simulator matched the desired particle characteristics with good fidelity. And as expected, with the relatively small

standard deviations in velocity magnitude and flow angle, the distributions for the U- and V-components were nearly Gaussian.

The ability of the simulator to record the actual velocity and trajectory for each particle along with the measured results provides the information needed to separate measurement precision from measurement accuracy. For example, from Table III.3 the effects of reducing the number of potential measurements to only those with signal levels sufficient to trigger the oscilloscope (9382 bursts) are found by a slight decrease in measurement accuracy and a relatively small change in their distributions, Figure III.4. The trend of reduced accuracy continues when the signal processing technique excludes signal bursts that have insufficient signal-to-noise ratios or other exclusions inherent with the processing technique. For example from Table III.3, the Peak processing technique reduces the accepted number of signal bursts to 6040.

From experience it is known that laser velocimeter signal processors of any type will allow spurious measurements to be made. This was particularly true with the high-speed burst counters developed in the 1970s. In the late 1980's researchers began to investigate causes of measurement uncertainty in laser velocimetry measurements and to develop methods to correct or eliminate those uncertainties (Edwards (1987)). The common practice of eliminating measurements that were found to be outside the limits of three standard deviations of the measurement ensemble was found to be ineffective. This was due to the nature of the spurious measurements in that they could occur far from the actual distribution. The inclusion of these outliers in the calculation of standard deviation would artificially increase its value, even to the point of including outliers within the allowed three standard deviation window. Meyers and Hepner (1988) reasoned that these spurious measurements were randomly distributed and typically well away from the true velocity measurements. Thus instead of assuming that the velocity distribution was Gaussian in form and thus followed Gaussian statistics, they developed a method to determine the limits of the distribution regardless of its form or underlying statistics. They reasoned that if the measurement ensemble contained sufficient data points, the velocity histogram of the ensemble would be contiguous until the limits were reached. The limits were determined by developing an amplitude threshold based on 5-percent of the value of the peak histogram bin, or the value of 3 whichever is larger. This level would correspond to the amplitude of a Gaussian distribution at the three standard deviation location. The envelope of the histogram would be followed from the peak toward the right (higher velocities) until the envelope went below the threshold for three consecutive bins. The limit of the histogram was then located at the last bin before the envelope went below the threshold. All data to the right of this location was considered spurious and eliminated along with corresponding data obtained from the other measurement components if the data was acquired in coincidence. As each spurious datum was removed from the component ensemble, the neighboring interarrival times were adjusted to maintain the integrity of measurement time. The process was then repeated on the left side of the histogram. This method has been incorporated in the current data processing schemes. Application of this technique to the results from the Peak processing technique, reduced

the number of acceptable signals to 4264. Although the errors, (mean and standard deviation of the velocity differences based on measured versus actual particle velocity on particle-by-particle computations and thus measurement precision), shown in Table III.3 have increased, they are still within the acceptable range. However, when the histograms are inspected, Figure III.5, one finds that the distribution of particle velocity has deviated from a Gaussian form (overlay), especially in the V-component. These distributions are further distorted by the Peak processing technique, resulting in measurements that should be considered unacceptable.

Replacing the Peak processing technique with the other techniques produced measurements of increased accuracy in both the statistics and in the distributions. The Gaussian processing technique accepted the same number of signal bursts as the Peak processing technique, but had fewer outliers, Table III.3. The increased number of accepted bursts (5909) improved the fidelity of the particle velocity histograms when compared to the theoretical Gaussian distributions. The measurement statistics and histograms also improved, but not to the point of acceptability, Figure III.6. The two Histogram processing techniques improved measurement fidelity in two ways, increased number of accepted signal bursts (7633) and distributions that closely matched the theoretical Gaussian distributions. Although the Histogram (3) approach yielded slightly better precision, Table III.3, the Histogram (5) approach produced far better distributions and thus should be considered the superior method, Figures III.7-III.8. Finally the two Half Power processing techniques also yielded acceptable measurement errors and nearly matching the theoretical Gaussian distributions, Figures III.9-III.10, but only 6040 signal bursts were accepted which may be the cause of the decrease in fidelity in the distributions. All techniques required approximately the same amount of time to process the data ensemble, thus there is no clear advantage of one over the rest. It is also noted that in this simulation investigation neither the Histogram or Half Power methods had outliers. Therefore, based on the simulation results, it appears that the Histogram (5) method is the superior approach based on measurement precision and the fidelity of the measured histograms when compared with the particle velocity histograms.

The characteristics of the six signal processing schemes found in the velocity magnitude and flow angle measurements continued with the U- and V-component measurements, Table III.3 and Figures III.11-III.16. Therefore the selected signal processing scheme was the Histogram (5) approach, which was then incorporated into the data processing software for the final system. A summary of all ensemble characteristics is given in Table III.2.

Analyzing the Statistical Results

The previous section indicated that the Histogram (5) approach yielded the best measurement accuracy of the six techniques. Yet one of the contributors to its superior performance was the larger number of signal bursts accepted, leading to better fidelity of the statistical stationarity of the particle velocity and, because of its better measurement

precision, increased measurement accuracy of the velocity distributions. Thus the measurement accuracy was improved and found superior to the other techniques. However, if the characteristics of the original distribution are unknown, e.g, flow field measurements in a wind tunnel, there is no current method to determine when the measurement distribution actually reflects the true distribution with acceptable fidelity. From classic statistical analysis it is known that the uncertainty in the measure of the ensemble mean and its standard deviation is dependent on the number of measurements in the ensemble (Yule and Kendall (1940)):

$$\text{Uncertainty in the mean} = \frac{2\sigma}{\sqrt{N}} \tag{3}$$

$$\text{Uncertainty in standard deviation} = \sigma \sqrt{\frac{2}{N}\left(1+\frac{E}{2}\right)} \tag{4}$$

where σ is the ensemble standard deviation, N is the number of independent data points in the ensemble and E is the statistical excess (kurtosis -3) of the ensemble. Excess provides an adjustment to the uncertainty in standard deviation to account for non-Gaussian distributions. Since the characteristics of the "flow field" are known with the simulation, the statistical uncertainties can be computed for a series of partial ensembles derived from the original measurement ensembles. For example, the mean and standard deviation would be calculated along with their respective measurement uncertainties for the first 100 measurements. Then the next 100 measurements are included in the first ensemble and the statistics calculated again. The process would continue until the entire measurement ensemble was included. This was performed on the measurement ensembles obtained from the six data processing schemes. The calculations of the statistical mean velocity magnitude as a function of ensemble size are shown in Figure III.17. The results from the Peak processing technique never reach the true mean of the velocity magnitude, which reinforces the earlier conclusion that this technique was unacceptable. While the Gaussian processing technique stabilizes at approximately 2000 measurements and the true mean is within the statistical uncertainty region, it is still marginally acceptable because of the poor representation of the velocity distribution. The two Histogram processing techniques stabilize at approximately 700 measurements with a small positive velocity bias. The two Half Power processing techniques stabilize at approximately 2000 measurements, also with a small positive velocity bias. Tracking the standard deviation measurements in Figure III.18 indicate similar trends, an underestimation with Peak processing, marginal underestimation with the Gaussian processing and virtually no error with the other methods. Tracking the skew measurements in Figure III.19 indicate marginally better performance by the Histogram methods over the Half Power methods with the Peak and Gaussian unacceptable. The results for excess, Figure III.20, indicate that the Half Power method was virtually perfect, the True Half Power and Histogram methods slightly worse and the Peak and Gaussian methods unacceptable. These trends continued with the flow angle (Figures III.21-III.24), U-component velocity (Figures III.25-III.28), and V-component velocity (Figures III.29-III.32).

This exercise has shown that tracking the measurement statistics as a function of ensemble size yields an asymptotic approach to the true statistics of the flow field. This may provide an indicator during the acquisition process that could be used in a feedback sense to determine when sufficient data points have been acquired. Since it was found in the previous section that histograms of the measurement distributions did not necessarily match the particle velocity histograms even though the means and standard deviations were fairly accurate, is tracking the means and standard deviations as a function of ensemble size sufficient to predict measurement fidelity? Although the statistical measures of skew and excess (kurtosis – 3) require larger ensembles than the means and standard deviations, they do converge to the true values for the Histogram and Half-Power methods, Figures III.19 and III.20. They also track the skew and excess statistics from the true particle velocity ensembles with good fidelity.

The overlay of the measurement statistics on the particle statistics appears to show that measurement precision is independent of measurement accuracy. To test whether this is true, the errors between the particle velocity/flow angle and the measured velocity/flow angle were computed on a particle-by-particle basis and the resulting error ensembles processed in the same manner as the convergence tests above. As shown in Figures III.33-III.36, the convergence of the error statistics occurs in the neighborhood of 500 particles. This indicates that sparse data sets within narrow error distributions is the cause of any convergence, not a dependency on the processing. As a comparison, these errors were well within the statistical uncertainties of the velocity/flow angle measurements.

In summary, a Monte Carlo simulator was used to model the upgraded 14-by 22-Foot Subsonic Tunnel laser velocimeter system. The simulator produced signal bursts from a simulated flow with a mean velocity magnitude of 100.0 m/s with a standard deviation of 3.0 m/s, and a mean vertical flow angle of 0.0 degrees with a standard deviation of 4.0 degrees. The horizontal flow angle was held at 0.0 degrees with no standard deviation as the laser velocimeter was incapable of measuring the on-axis component, and the inclusion of this angle could potentially modify the velocity distributions in the U- and V-components from being nominally Gaussian. The particles were injected within a plane defined by the $1/e^3$ power locations in the on-axis and vertical directions based on the optical power at the center of the measurement volume. This plane was located upstream at the $1/e^3$ power location. The simulator generated 10,000 1.7-micron PSL particles that entered this injection plane in a random manner with uniform statistics, Figure III.2, following the selected velocity magnitude and flow angle characteristics to generate random velocity magnitudes and flow angles with Gaussian statistics. The selection of velocity and flow angle was independent for each particle, thus no cross-dependence occurred between the two parameters. Of the 10,000 particles generated, 9382 passed through the measurement volume with sufficient signal strength to trigger the data acquisition system. Of these 9382 triggered signal bursts, only between 4264 to 7633 were processed depending on the signal/data processing scheme applied.

All six signal/data processing schemes under investigation processed the signal bursts in the frequency domain. The simplest was to detect the highest peak in the frequency spectra and output its location. This method processed the fewest signal bursts, with the worst measurement precision and measurement accuracy of the six schemes. The Gaussian approach detected the highest peak in the frequency spectra and curve fit the peak level ±1 frequency step with a Gaussian fit and then determined the location of the peak of the curve. This method was an improvement on the Peak method, but only slightly. Two Histogram approaches were evaluated with the highest peak location in the frequency spectra being the central element of a 3-bin and a 5-bin histogram. The signal frequency was determined by the weighted statistics of the histogram. These methods accepted the greatest number of signal bursts and thus, along with excellent measurement precision, yielded good measurement accuracy. The 5-bin method produced the best fidelity of any method when the measurement velocity histograms were compared to the particle velocity histograms. The final two approaches were similar to the histogram approaches in that the frequency spectra was processed as a histogram. The difference was that only bins yielding counts within the half-power of the peak level were included. One method used just the bins with levels greater than the half-power value, whereas the other interpolated the bin levels to obtain the exact locations of the half-power points, thus extending the width of the histogram by fractions of a bin. These methods accepted fewer signal bursts than the histogram methods, but measurement precision was the best except the velocity distributions did not have the fidelity of the Histogram (5) method. All methods showed strong convergence trends to their final values as the ensemble size was increased providing a method to determine when measurement and flow statistical stationarity was reached. Of the statistical quantities examined, standard deviation appears to provide the least deviation from the true particle velocity characteristics yet maintained the most stable convergence to the true value.

The following conclusions can be drawn from this simulation:

1) Measurement precision and measurement accuracy could be determined independently;
2) Measurement precision was virtually constant regardless of ensemble size;
3) Measurement accuracy depends on ensemble size with an asymptotic approach to the true value;
4) The measurement statistics track the particle statistics through the ensemble size range;
5) The true velocity/flow angle means and standard deviations fall within the statistical uncertainty calculations of mean and standard deviation of the particle and measurement ensembles;
6) Peak and Gaussian signal processing schemes are unacceptable;
7) The two Histogram methods and the Half-Power methods yield acceptable statistical results;
8) The two Histogram methods accept the greatest number of signal bursts;
9) The Histogram (5) method best replicates the true distributions and thus is

selected as the prime signal/data processing method even though its statistical results were slightly less accurate than the Half-Power methods;

10) Measurement accuracy can be defined in different ways. If the true mean velocity magnitude and flow angle was 100.0 m/s and 0.0 degrees, respectively, the errors in the corresponding means were 0.07 m/s and 0.01 degrees for both the Histogram (5) and True Half Power methods. The true standard deviations were 3.0 m/s and 4.0 degrees with measurement errors of 0.01 m/s and 0.03 degrees for the Histogram (5) method and 0.04 m/s and 0.05 degrees for the True Half Power method. However, the true mean velocity and flow angle for the particle ensemble that was actually measured was 99.95 m/s and -0.03 degrees with standard deviations of 2.97 m/s and 4.03 degrees for the Histogram (5) set and 2.96 m/s and 4.05 degrees for the True Half Power set. In this case both the Histogram (5) and True Half Power methods would have errors in the mean of 0.12 m/s and 0.04 degrees with the only error in standard deviation being 0.02 m/s by the Histogram (5) method.
11) On a particle-by-particle basis, both the Histogram (5) and True Half Power methods have an error in the mean of 0.12 m/s and 0.05 degrees which match the measurement accuracies for the ensembles of signal bursts actually measured. The standard deviation of the particle-by-particle errors are much larger than the accuracy results, 0.40 m/s and 0.23 degrees for the Histogram (5) method and 0.28 m/s and 0.14 degrees for the True Half Power.
12) It appears that the instrument precision in the means account for all of the errors in the mean measurements when considering the ensemble of signal bursts actually measured. It also appears that the standard deviation portion of the instrument precision must average out and makes no contribution to measurement error in standard deviation.
13) The above statistical results were obtained once the standard deviation had converged to the statistically stationary value.

Therefore, based on the results from the Monte Carlo simulation, the required measurement accuracy of ± 1.5 m/s can be theoretically satisfied. Additionally, a method to track measurement statistics as a function of ensemble size is necessary to insure that the flow measurements faithfully represent the characteristics of the actual flow field before termination of data acquisition at a selected measurement location. Otherwise no matter how precise the laser velocimetry measurements were, there can be no assurance that the flow measurements would be accurate. Even after convergence, there would still be no guarantee that the signal bursts being processed will accurately represent the true flow with statistical stationarity.

Beam Waist	182.6 microns	(Meyers (1971))
Sample Volume Length	4.868 mm	

Particle	Vertical distance Y/Beam Waist Radius		On axis distance 2*Z/Sample volume length		Particle Vectors Vel-mag	Alpha	Beta
	Start	End	Start	End	(m/s)	(degrees)	(degrees)
1	0.011	0.342	-1.483	-1.483	103.29	6.31	0.00
2	0.012	0.392	-1.006	-1.006	99.18	7.22	0.00
3	0.02	-0.319	-0.503	-0.503	100.57	-6.44	0.00
4	-0.009	0.266	-0.006	-0.006	105.32	5.23	0.00
5	0.01	-0.156	0.491	0.491	98.05	-3.18	0.00
6	0.022	-0.055	0.994	0.994	100.05	-1.46	0.00
7	0.009	0.161	1.499	1.499	97.46	2.9	0.00

U-Component (m/s)

	Actual	Peak Location	Gaussian Fit	Histogram (3)	Histogram (5)	Half Power	Half Power True
1	102.666			102.27	102.8		
2	98.398	97.58	97.93	98.26	98.47	98.69	98.65
3	99.936	99.95	99.97	100.01	100.25	99.98	99.99
4	104.885	104.68	104.77	104.93	104.99	104.87	104.87
5	97.896	97.58	97.67	97.79	97.79	97.76	97.76
6	100.02	99.95	100.01	100.12	100.54	100.04	100.07
7	97.337			97.32	97.34		

U-Component Error (m/s)

1			-0.4	0.14		
2	-0.82	-0.47	-0.14	0.07	0.29	0.25
3	0.01	0.03	0.07	0.32	0.04	0.05
4	-0.2	-0.12	0.04	0.11	-0.01	-0.01
5	-0.32	-0.22	-0.1	-0.11	-0.13	-0.13
6	-0.07	-0.01	0.1	0.52	0.02	0.05
7			-0.02	0.01		
Average:	-0.28	-0.16	-0.06	0.15	0.04	0.04
Sigma:	0.33	0.20	0.17	0.21	0.15	0.14

V-Component (m/s)

	Actual	Peak Location	Gaussian Fit	Histogram (3)	Histogram (5)	Half Power	Half Power True
1	11.358			11.49	11.36		
2	12.462	11.68	11.93	12.33	12.62	12.72	12.69
3	-11.279	-10.78	-10.9	-11.09	-11.35	-10.98	-11.03
4	9.601	9.44	9.49	9.58	9.58	9.55	9.55
5	-5.437	-6.29	-6.06	-5.64	-5.31	-5.24	-5.24
6	-2.555	-1.8	-2.01	-2.31	-2.58	-2.79	-2.73
7	4.931			5.15	5.18		

V-Component Error (m/s)

1			0.13	0		
2	-0.78	-0.53	-0.13	0.16	0.26	0.22
3	0.5	0.38	0.19	-0.07	0.3	0.25
4	-0.17	-0.11	-0.02	-0.02	-0.05	-0.05
5	-0.85	-0.63	-0.2	0.13	0.19	0.19
6	0.76	0.55	0.24	-0.02	-0.23	-0.18
7			0.21	0.25		
Average:	-0.11	-0.07	0.06	0.06	0.09	0.09
Sigma:	0.73	0.53	0.18	0.12	0.23	0.19

Table III.1.a.- Laser velocimeter Monte Carlo simulation results – Single particle passage.

Particle	Vertical distance Y/Beam Waist Radius		On axis distance 2*Z/Sample volume length		U-component			V-component		
	Start	End	Start	End	Actual m/s	Measured m/s	Error m/s	Actual m/s	Measured m/s	Error m/s
Peak Location										
1	0.011	0.342	-1.483	-1.483	102.666			11.358		
2	0.012	0.392	-1.006	-1.006	98.398	97.58	-0.82	12.462	11.68	-0.78
3	0.02	-0.319	-0.503	-0.503	99.936	99.95	0.01	-11.279	-10.78	0.5
4	-0.009	0.266	-0.006	-0.006	104.885	104.68	-0.2	9.601	9.44	-0.17
5	0.01	-0.156	0.491	0.491	97.896	97.58	-0.32	-5.437	-6.29	-0.85
6	0.022	-0.055	0.994	0.994	100.02	99.95	-0.07	-2.555	-1.8	0.76
7	0.009	0.161	1.499	1.499	97.337			4.931		
Gaussian Fit										
1	0.011	0.342	-1.483	-1.483	102.666			11.358		
2	0.012	0.392	-1.006	-1.006	98.398	97.93	-0.47	12.462	11.93	-0.53
3	0.02	-0.319	-0.503	-0.503	99.936	99.97	0.03	-11.279	-10.9	0.38
4	-0.009	0.266	-0.006	-0.006	104.885	104.77	-0.12	9.601	9.49	-0.11
5	0.01	-0.156	0.491	0.491	97.896	97.67	-0.22	-5.437	-6.06	-0.63
6	0.022	-0.055	0.994	0.994	100.02	100.01	-0.01	-2.555	-2.01	0.55
7	0.009	0.161	1.499	1.499	97.337			4.931		
Histogram (3)										
1	0.011	0.342	-1.483	-1.483	102.666	102.27	-0.4	11.358	11.49	0.13
2	0.012	0.392	-1.006	-1.006	98.398	98.26	-0.14	12.462	12.33	-0.13
3	0.02	-0.319	-0.503	-0.503	99.936	100.01	0.07	-11.279	-11.09	0.19
4	-0.009	0.266	-0.006	-0.006	104.885	104.93	0.04	9.601	9.58	-0.02
5	0.01	-0.156	0.491	0.491	97.896	97.79	-0.1	-5.437	-5.64	-0.2
6	0.022	-0.055	0.994	0.994	100.02	100.12	0.1	-2.555	-2.31	0.24
7	0.009	0.161	1.499	1.499	97.337	97.32	-0.02	4.931	5.15	0.21
Histogram (5)										
1	0.011	0.342	-1.483	-1.483	102.666	102.8	0.14	11.358	11.36	0
2	0.012	0.392	-1.006	-1.006	98.398	98.47	0.07	12.462	12.62	0.16
3	0.02	-0.319	-0.503	-0.503	99.936	100.25	0.32	-11.279	-11.35	-0.07
4	-0.009	0.266	-0.006	-0.006	104.885	104.99	0.11	9.601	9.58	-0.02
5	0.01	-0.156	0.491	0.491	97.896	97.79	-0.11	-5.437	-5.31	0.13
6	0.022	-0.055	0.994	0.994	100.02	100.54	0.52	-2.555	-2.58	-0.02
7	0.009	0.161	1.499	1.499	97.337	97.34	0.01	4.931	5.18	0.25
Half Power										
1	0.011	0.342	-1.483	-1.483	102.666			11.358		
2	0.012	0.392	-1.006	-1.006	98.398	98.69	0.29	12.462	12.72	0.26
3	0.02	-0.319	-0.503	-0.503	99.936	99.98	0.04	-11.279	-10.98	0.3
4	-0.009	0.266	-0.006	-0.006	104.885	104.87	-0.01	9.601	9.55	-0.05
5	0.01	-0.156	0.491	0.491	97.896	97.76	-0.13	-5.437	-5.24	0.19
6	0.022	-0.055	0.994	0.994	100.02	100.04	0.02	-2.555	-2.79	-0.23
7	0.009	0.161	1.499	1.499	97.337			4.931		
Half Power True										
1	0.011	0.342	-1.483	-1.483	102.666			11.358		
2	0.012	0.392	-1.006	-1.006	98.398	98.65	12.69	12.462	0.25	0.22
3	0.02	-0.319	-0.503	-0.503	99.936	99.99	-11.03	-11.279	0.05	0.25
4	-0.009	0.266	-0.006	-0.006	104.885	104.87	9.55	9.601	-0.01	-0.05
5	0.01	-0.156	0.491	0.491	97.896	97.76	-5.24	-5.437	-0.13	0.19
6	0.022	-0.055	0.994	0.994	100.02	100.07	-2.73	-2.555	0.05	-0.18
7	0.009	0.161	1.499	1.499	97.337			4.931		

Table III.1.b.- Calculated results for the selected particles based on six signal processing algorithms based on FFT processing.

Particle Injection Location

	Theoretical		Simulation			
	Y-start (*1/e^2)	Z-start (*1/e^2)	Y-start (*1/e^2)	Z-start (*1/e^2)	Y-end (*1/e^2)	Z-end (*1/e^2)
Number			10000	10000	10000	10000
Maximum	1.50	1.50	1.50	1.50	2.04	1.50
Minimum	-1.50	-1.50	-1.50	-1.50	-2.11	-1.50
Mean	0.00	0.00	0.01	0.00	0.01	0.00
Standard Dev	0.91	0.91	0.87	0.87	0.89	0.87
Skew	0.00	0.00	-0.03	0.01	-0.01	0.01
Excess	-1.20	-1.20	-1.21	-1.19	-1.07	-1.19

	Selected from Ideal Distribution				Triggered	
	Vel-mag (m/s)	Alpha (degree)	U-in (m/s)	V-in (m/s)	U-select (m/s)	V-select (m/s)
Number	10000	10000	10000	10000	9382	9382
Maximum	110.31	15.97	110.10	27.32	110.10	27.32
Minimum	89.23	-15.34	88.86	-26.45	88.86	-26.45
Mean	99.98	0.01	99.74	0.02	99.72	-0.01
Standard Dev	2.96	4.02	2.98	7.00	2.98	6.97
Skew	-0.03	0.00	-0.03	0.00	-0.02	0.00
Excess	0.00	-0.01	-0.01	-0.02	-0.02	-0.01
? Mean	0.06	0.08	0.06	0.14	0.06	0.14
? Standard Dev	0.04	0.06	0.04	0.10	0.04	0.10

(Signal bursts have triggered the oscilloscope, satisfied signal-to-noise thresholds for the processing algorithm, and outliers removed)

Peak Signal Processing Algorithm

	Vel-mag (m/s)	Alpha (degree)	Mag-meas (m/s)	Alpha-meas (degree)	Error-Mag (m/s)	Error-Alpha (degree)	U-select (m/s)	V-select (m/s)	U-meas (m/s)	V-meas (m/s)	Error U (m/s)	Error V (m/s)
Number	4264	4264	4264	4264	4264	4264	4264	4264	4264	4264	4264	4264
Maximum	106.03	3.59	105.03	3.05	1.92	0.93	105.95	6.13	104.68	4.94	1.93	1.55
Minimum	89.95	-5.83	90.48	-5.39	-1.78	-0.73	89.83	-9.97	90.47	-8.54	-1.75	-1.29
Mean	99.73	-0.69	99.83	-0.65	0.09	0.04	99.64	-1.19	99.73	-1.12	0.09	0.07
Standard Dev	2.76	2.42	2.83	2.41	0.70	0.38	2.77	4.21	2.83	4.19	0.70	0.66
Skew	-0.21	-0.19	-0.23	-0.20	0.05	0.03	-0.21	-0.19	-0.23	-0.19	0.05	0.03
Excess	-0.21	-1.02	-0.28	-1.06	-1.08	-1.14	-0.22	-1.03	-0.29	-1.07	-1.09	-1.15
? Mean	0.08	0.07	0.09	0.07	0.02	0.01	0.08	0.13	0.09	0.13	0.02	0.02
? Standard Dev	0.06	0.04	0.06	0.04	0.01	0.01	0.06	0.06	0.06	0.06	0.01	0.01

Gaussian Signal Processing Algorithm

	Vel-mag (m/s)	Alpha (degree)	Mag-meas (m/s)	Alpha-meas (degree)	Error-Mag (m/s)	Error-Alpha (degree)	U-select (m/s)	V-select (m/s)	U-meas (m/s)	V-meas (m/s)	Error U (m/s)	Error V (m/s)
Number	5909	5909	5909	5909	5909	5909	5909	5909	5909	5909	5909	5909
Maximum	108.21	8.91	108.08	8.76	1.61	0.77	108.12	15.19	107.31	14.23	1.70	1.33
Minimum	89.23	-11.93	88.64	-11.77	-1.42	-0.62	88.86	-20.88	88.35	-20.06	-1.39	-1.08
Mean	99.90	-0.18	100.01	-0.13	0.11	0.04	99.68	-0.31	99.78	-0.23	0.11	0.08
Standard Dev	2.91	3.83	2.96	3.83	0.51	0.28	2.93	6.66	2.97	6.67	0.51	0.48
Skew	-0.07	-0.17	-0.07	-0.18	0.04	0.02	-0.07	-0.17	-0.07	-0.18	0.04	0.01
Excess	-0.07	-0.34	-0.09	-0.34	-0.97	-1.07	-0.08	-0.35	-0.08	-0.35	-0.97	-1.08
? Mean	0.08	0.10	0.08	0.10	0.01	0.01	0.08	0.17	0.08	0.17	0.01	0.01
? Standard Dev	0.05	0.06	0.05	0.06	0.01	0.00	0.05	0.11	0.05	0.11	0.01	0.01

Table III.2.a.- Laser Velocimeter Results: Theory, Simulated, Selected and Signal Processing – Peak and Gaussian.

Histogram (3) Signal Processing Algorithm

	Vel-mag (m/s)	Alpha (degree)	Mag-meas (m/s)	Alpha-meas (degree)	Error-Mag (m/s)	Error-Alpha (degree)	U-select (m/s)	V-select (m/s)	U-meas (m/s)	V-meas (m/s)	Error U (m/s)	Error V (m/s)
Number	7633	7633	7633	7633	7633	7633	7633	7633	7633	7633	7633	7633
Maximum	110.31	13.96	110.59	14.06	1.85	1.02	110.10	25.12	109.89	25.20	1.85	1.71
Minimum	89.23	-15.34	88.96	-15.20	-1.53	-1.14	88.86	-26.45	88.40	-26.36	-1.56	-1.97
Mean	99.95	-0.03	100.06	0.01	0.11	0.05	99.70	-0.06	99.81	0.02	0.11	0.08
Standard Dev	2.97	4.03	2.98	4.03	0.31	0.18	2.98	7.01	3.00	7.02	0.31	0.31
Skew	-0.01	-0.01	0.00	-0.01	0.10	-0.07	-0.01	-0.01	0.00	-0.01	0.07	-0.10
Excess	0.01	0.00	0.03	0.01	1.46	2.66	0.00	-0.01	0.02	0.00	1.47	2.54
? Mean	0.07	0.09	0.07	0.09	0.01	0.00	0.07	0.16	0.07	0.16	0.01	0.01
? Standard Dev	0.05	0.07	0.05	0.07	0.01	0.00	0.05	0.11	0.05	0.11	0.01	0.01

Histogram (5) Signal Processing Algorithm

	Vel-mag (m/s)	Alpha (degree)	Mag-meas (m/s)	Alpha-meas (degree)	Error-Mag (m/s)	Error-Alpha (degree)	U-select (m/s)	V-select (m/s)	U-meas (m/s)	V-meas (m/s)	Error U (m/s)	Error V (m/s)
Number	7633	7633	7633	7633	7633	7633	7633	7633	7633	7633	7633	7633
Maximum	110.31	13.96	110.75	14.02	2.84	1.41	110.10	25.12	110.49	25.23	2.85	2.36
Minimum	89.23	-15.34	88.44	-15.24	-2.33	-1.33	88.86	-26.45	87.85	-26.35	-2.61	-2.31
Mean	99.95	-0.03	100.07	0.01	0.12	0.05	99.70	-0.06	99.82	0.02	0.12	0.08
Standard Dev	2.97	4.03	2.99	4.03	0.40	0.23	2.98	7.01	3.01	7.03	0.41	0.40
Skew	-0.01	-0.01	0.00	-0.01	-0.05	-0.18	-0.01	-0.01	-0.01	-0.01	-0.09	-0.19
Excess	0.01	0.00	0.04	0.00	2.85	4.83	0.00	-0.01	0.03	-0.01	2.93	4.74
? Mean	0.07	0.09	0.07	0.09	0.01	0.01	0.07	0.16	0.07	0.16	0.01	0.01
? Standard Dev	0.05	0.07	0.05	0.07	0.01	0.01	0.05	0.11	0.05	0.11	0.01	0.01

Half Power Signal Processing Algorithm

	Vel-mag (m/s)	Alpha (degree)	Mag-meas (m/s)	Alpha-meas (degree)	Error-Mag (m/s)	Error-Alpha (degree)	U-select (m/s)	V-select (m/s)	U-meas (m/s)	V-meas (m/s)	Error U (m/s)	Error V (m/s)
Number	6040	6040	6040	6040	6040	6040	6040	6040	6040	6040	6040	6040
Maximum	110.31	13.96	110.68	13.99	1.64	0.64	110.10	25.12	110.42	25.18	1.66	1.08
Minimum	89.23	-15.34	89.40	-15.29	-1.30	-0.71	88.86	-26.45	89.07	-26.41	-1.40	-1.12
Mean	99.94	-0.02	100.07	0.02	0.12	0.05	99.69	-0.04	99.82	0.04	0.12	0.08
Standard Dev	2.96	4.05	2.96	4.06	0.33	0.16	2.97	7.06	2.98	7.07	0.33	0.28
Skew	0.00	-0.01	0.01	-0.01	-0.03	-0.03	0.00	-0.01	0.01	-0.01	-0.03	-0.03
Excess	0.05	0.01	0.09	0.01	-0.04	-0.12	0.04	0.00	0.07	0.01	-0.01	-0.14
? Mean	0.08	0.10	0.08	0.10	0.01	0.00	0.08	0.18	0.08	0.18	0.01	0.01
? Standard Dev	0.05	0.07	0.06	0.07	0.01	0.00	0.05	0.13	0.06	0.13	0.01	0.00

True Half Power Signal Processing Algorithm

	Vel-mag (m/s)	Alpha (degree)	Mag-meas (m/s)	Alpha-meas (degree)	Error-Mag (m/s)	Error-Alpha (degree)	U-select (m/s)	V-select (m/s)	U-meas (m/s)	V-meas (m/s)	Error U (m/s)	Error V (m/s)
Number	6040	6040	6040	6040	6040	6040	6040	6040	6040	6040	6040	6040
Maximum	110.31	13.96	110.62	13.99	1.53	0.56	110.10	25.12	110.39	25.19	1.55	1.02
Minimum	89.23	-15.34	89.39	-15.27	-1.21	-0.64	88.86	-26.45	88.97	-26.39	-1.28	-1.01
Mean	99.94	-0.02	100.07	0.02	0.12	0.05	99.69	-0.04	99.82	0.04	0.12	0.08
Standard Dev	2.96	4.05	2.96	4.05	0.28	0.14	2.97	7.06	2.97	7.07	0.28	0.24
Skew	0.00	-0.01	0.01	-0.01	-0.02	-0.06	0.00	-0.01	0.01	-0.01	-0.02	-0.05
Excess	0.05	0.01	0.09	0.01	0.22	0.15	0.04	0.00	0.06	0.01	0.26	0.15
? Mean	0.08	0.10	0.08	0.10	0.01	0.00	0.08	0.18	0.08	0.18	0.01	0.01
? Standard Dev	0.05	0.07	0.06	0.07	0.01	0.00	0.05	0.13	0.05	0.13	0.01	0.00

Table III.2.a. (cont'd) - Laser Velocimeter Results: Signal Processing – Histogram (3), Histogram (5), Half Power, and True Half Power.

	Vel-mag	Alpha	Y-start	Y-end	Z-start	Z-end	U-in	V-in	U-select	V-select
Number	10000	10000	10000	10000	10000	10000	10000	10000	9382	9382
Maximum	110.31	15.97	1.50	2.04	1.50	1.50	110.10	27.32	110.10	27.32
Minimum	89.23	-15.34	-1.50	-2.11	-1.50	-1.50	88.86	-26.45	88.86	-26.45
Mean	99.98	0.01	0.01	0.01	0.00	0.00	99.74	0.02	99.72	-0.01
Standard Dev	2.96	4.02	0.87	0.89	0.87	0.87	2.98	7.00	2.98	6.97
Skew	-0.03	0.00	-0.03	-0.01	0.01	0.01	-0.03	0.00	-0.02	0.00
Excess	0.00	-0.01	-1.21	-1.07	-1.19	-1.19	-0.01	-0.02	-0.02	-0.01
? Mean	0.06	0.08	0.02	0.02	0.02	0.02	0.06	0.14	0.06	0.14
? Standard Dev	0.04	0.06	0.01	0.01	0.01	0.01	0.04	0.10	0.04	0.10

Particle	Vel-mag	Alpha	Y-start	Y-end	Z-start	Z-end	U-in	V-in	U-select	V-select
1	102.56	7.56	-1.49	-1.09	-1.47	-1.47	101.67	13.50	101.67	13.50
2	101.80	-4.64	0.81	0.57	-1.03	-1.03	101.47	-8.24	101.47	-8.24
3	101.39	5.00	0.74	1.00	1.49	1.49	101.00	8.83	101.00	8.83
4	101.44	0.86	1.03	1.07	-0.40	-0.40	101.43	1.52	101.43	1.52
5	101.90	-0.86	-1.19	-1.24	1.01	1.01	101.89	-1.53	101.89	-1.53
6	98.63	4.11	-1.25	-1.04	0.30	0.30	98.37	7.07	98.37	7.07
7	102.65	3.79	0.61	0.81	0.37	0.37	102.42	6.78	102.42	6.78
8	100.28	4.13	1.38	1.60	0.98	0.98	100.02	7.22		
9	96.60	-4.50	-0.31	-0.55	-0.94	-0.94	96.30	-7.58	96.30	-7.58
10	99.52	3.46	-1.05	-0.87	0.37	0.37	99.34	6.00	99.34	6.00
11	96.54	-3.54	0.57	0.38	-0.75	-0.75	96.36	-5.96	96.36	-5.96
12	104.99	3.63	1.36	1.55	0.24	0.24	104.78	6.64	104.78	6.64
13	98.51	1.36	1.01	1.08	-1.43	-1.43	98.48	2.34	98.48	2.34
14	97.87	2.76	-0.85	-0.71	0.80	0.80	97.76	4.71	97.76	4.71
15	98.23	-1.36	-0.18	-0.25	-0.94	-0.94	98.20	-2.34	98.20	-2.34
16	100.63	3.41	1.10	1.28	-1.22	-1.22	100.45	5.98	100.45	5.98
17	97.20	4.19	-0.36	-0.14	-1.43	-1.43	96.94	7.10	96.94	7.10
18	102.15	0.50	0.62	0.65	-0.68	-0.68	102.15	0.89	102.15	0.89
19	99.59	-9.05	0.44	-0.04	1.34	1.34	98.35	-15.66	98.35	-15.66
20	100.34	-6.08	-0.11	-0.43	0.04	0.04	99.78	-10.63	99.78	-10.63
21	98.96	-1.04	1.01	0.96	0.60	0.60	98.95	-1.79	98.95	-1.79
22	97.89	-4.40	0.63	0.40	-0.24	-0.24	97.61	-7.52	97.61	-7.52
23	99.15	1.35	0.28	0.35	0.06	0.06	99.12	2.34	99.12	2.34
24	105.90	-0.42	0.43	0.41	-0.25	-0.25	105.89	-0.78	105.89	-0.78
25	102.59	-0.69	-0.75	-0.79	-0.31	-0.31	102.58	-1.24	102.58	-1.24
26	102.14	0.06	0.22	0.22	1.28	1.28	102.14	0.12	102.14	0.12
27	99.33	-2.96	-0.78	-0.93	1.05	1.05	99.20	-5.13	99.20	-5.13
28	100.95	-4.65	1.16	0.92	-0.84	-0.84	100.62	-8.18	100.62	-8.18
29	97.03	6.65	-0.43	-0.09	-0.76	-0.76	96.38	11.24	96.38	11.24
30	101.83	-0.50	-0.28	-0.31	0.18	0.18	101.83	-0.89	101.83	-0.89
31	99.30	-2.89	-1.48	-1.64	0.33	0.33	99.18	-5.01		
32	101.79	-6.21	-0.97	-1.29	0.56	0.56	101.19	-11.01	101.19	-11.01
33	95.98	9.34	1.34	1.84	-0.08	-0.08	94.71	15.57	94.71	15.57
34	99.96	4.87	0.87	1.12	-0.39	-0.39	99.60	8.48	99.60	8.48
35	104.13	-5.26	0.65	0.37	-1.15	-1.15	103.70	-9.54	103.70	-9.54
36	103.87	-1.06	-0.53	-0.58	-1.36	-1.36	103.85	-1.93	103.85	-1.93
37	104.94	-2.36	0.82	0.70	1.12	1.12	104.85	-4.31	104.85	-4.31
38	99.12	-1.10	0.82	0.77	0.55	0.55	99.10	-1.91	99.10	-1.91
39	100.92	7.91	1.30	1.72	-0.56	-0.56	99.96	13.90		
40	93.67	-2.37	-0.97	-1.09	1.01	1.01	93.59	-3.88	93.59	-3.88
41	102.58	-4.01	-0.87	-1.08	1.33	1.33	102.33	-7.17	102.33	-7.17
42	104.88	5.32	-0.61	-0.33	1.09	1.09	104.43	9.73	104.43	9.73
43	96.87	8.06	0.32	0.74	0.41	0.41	95.92	13.58	95.92	13.58
44	102.20	2.07	0.91	1.01	0.04	0.04	102.13	3.69	102.13	3.69
45	101.06	3.18	1.07	1.23	-0.28	-0.28	100.91	5.60	100.91	5.60
46	102.35	1.98	0.63	0.73	-0.62	-0.62	102.29	3.54	102.29	3.54
47	105.58	-2.56	0.13	0.00	-0.33	-0.33	105.48	-4.72	105.48	-4.72

Table III.2.b. - Laser Velocimeter Results: Selected signal bursts – Statistics and First 100 selected.

48	101.61	2.14	0.82	0.93	-0.59	-0.59	101.54	3.79	101.54	3.79
49	101.24	5.01	0.05	0.31	-1.01	-1.01	100.85	8.85	100.85	8.85
50	105.53	0.47	-0.96	-0.94	0.38	0.38	105.52	0.87	105.52	0.87
51	101.78	2.43	-0.53	-0.40	-0.62	-0.62	101.69	4.32	101.69	4.32
52	99.07	3.58	-1.28	-1.09	0.54	0.54	98.87	6.18	98.87	6.18
53	100.62	3.43	-1.29	-1.11	1.13	1.13	100.44	6.03	100.44	6.03
54	98.68	-5.32	-1.44	-1.72	-0.82	-0.82	98.26	-9.15		
55	104.07	5.25	-1.39	-1.11	0.84	0.84	103.64	9.53	103.64	9.53
56	98.55	-0.39	0.89	0.87	-0.08	-0.08	98.55	-0.67	98.55	-0.67
57	100.93	-6.04	-1.08	-1.39	-0.17	-0.17	100.37	-10.61	100.37	-10.61
58	101.23	-1.68	1.47	1.39	-0.34	-0.34	101.18	-2.97	101.18	-2.97
59	94.35	-3.10	-0.02	-0.18	-0.52	-0.52	94.21	-5.11	94.21	-5.11
60	103.33	2.75	-0.15	0.00	-0.65	-0.65	103.21	4.96	103.21	4.96
61	98.44	-2.96	1.20	1.05	-1.00	-1.00	98.31	-5.09	98.31	-5.09
62	103.46	0.45	1.44	1.47	-0.16	-0.16	103.45	0.81	103.45	0.81
63	102.47	4.41	0.91	1.15	0.34	0.34	102.17	7.88	102.17	7.88
64	101.78	3.50	0.92	1.10	1.49	1.49	101.59	6.22	101.59	6.22
65	101.34	-4.53	1.43	1.20	0.88	0.88	101.03	-8.01	101.03	-8.01
66	101.18	-1.50	-0.94	-1.02	-1.21	-1.21	101.14	-2.65	101.14	-2.65
67	104.19	1.09	-1.06	-1.01	-1.05	-1.05	104.17	1.99	104.17	1.99
68	101.71	-0.37	-0.92	-0.94	-0.04	-0.04	101.71	-0.65	101.71	-0.65
69	104.24	1.67	-0.88	-0.79	-0.33	-0.33	104.20	3.03	104.20	3.03
70	104.97	-3.77	0.24	0.04	-0.91	-0.91	104.74	-6.91	104.74	-6.90
71	105.06	1.60	-0.85	-0.76	0.86	0.86	105.02	2.93	105.02	2.93
72	100.14	6.57	0.85	1.19	-0.55	-0.55	99.48	11.45	99.48	11.45
73	105.34	-1.02	-0.40	-0.46	-0.51	-0.51	105.32	-1.87	105.32	-1.87
74	95.88	1.37	0.07	0.15	-0.71	-0.71	95.86	2.29	95.86	2.29
75	99.00	-6.19	-1.21	-1.54	-1.50	-1.50	98.42	-10.67	98.42	-10.67
76	100.16	1.47	0.81	0.89	0.68	0.68	100.13	2.57	100.13	2.57
77	96.80	-0.84	-0.38	-0.43	-1.41	-1.41	96.79	-1.42	96.79	-1.42
78	98.61	-1.83	-0.74	-0.84	-0.78	-0.78	98.56	-3.15	98.56	-3.15
79	99.63	-0.72	0.17	0.13	0.09	0.09	99.62	-1.25	99.62	-1.25
80	106.14	-2.08	-0.81	-0.92	-0.82	-0.82	106.07	-3.85	106.07	-3.85
81	101.79	7.53	-1.45	-1.05	-0.24	-0.24	100.91	13.34	100.91	13.34
82	97.77	5.82	-1.39	-1.08	0.11	0.11	97.26	9.92	97.26	9.92
83	96.23	-1.46	-1.10	-1.18	-1.02	-1.02	96.20	-2.45	96.20	-2.45
84	99.68	-5.59	-1.12	-1.41	0.96	0.96	99.20	-9.71	99.20	-9.71
85	99.64	-0.74	0.82	0.78	0.38	0.38	99.63	-1.29	99.63	-1.29
86	100.77	-6.75	0.62	0.26	0.45	0.45	100.07	-11.84	100.07	-11.84
87	97.16	-5.12	-0.99	-1.26	-1.32	-1.32	96.77	-8.68	96.77	-8.68
88	97.54	-1.67	-0.67	-0.76	-1.44	-1.44	97.50	-2.85	97.50	-2.84
89	98.32	-6.37	-1.11	-1.44	0.44	0.44	97.72	-10.91	97.72	-10.91
90	95.68	10.60	-0.47	0.09	-0.23	-0.23	94.04	17.60	94.04	17.60
91	101.11	-2.58	-0.22	-0.36	0.34	0.34	101.01	-4.56	101.01	-4.56
92	96.25	-1.79	-1.29	-1.39	-0.11	-0.11	96.20	-3.01	96.20	-3.01
93	103.74	6.30	0.36	0.69	1.36	1.36	103.11	11.38	103.11	11.37
94	101.04	1.68	0.53	0.62	-0.95	-0.95	100.99	2.97	100.99	2.97
95	98.01	-2.92	-1.19	-1.34	-0.93	-0.93	97.89	-5.00	97.89	-5.00
96	100.19	2.19	-0.11	0.01	-0.52	-0.52	100.12	3.82	100.11	3.82
97	99.81	-6.59	-1.08	-1.42	0.83	0.83	99.15	-11.45	99.15	-11.45
98	101.49	3.80	-0.64	-0.44	-1.36	-1.36	101.27	6.73	101.27	6.73
99	100.88	3.78	-0.34	-0.14	-0.50	-0.50	100.66	6.66	100.66	6.66
100	100.60	4.50	-1.39	-1.15	0.29	0.29	100.29	7.89	100.29	7.89

Table III.2.b. (cont'd) - Laser Velocimeter Results: Selected signal bursts – Statistics and First 100 selected.

	Vel-mag	Alpha	Mag-meas	Alpha-meas	Error-Mag	Error-Alpha	U-select	V-select	U-meas	V-meas	Error U	Error V
Number	4264	4264	4264	4264	4264	4264	4264	4264	4264	4264	4264	4264
Maximum	106.03	3.59	105.03	3.05	1.92	0.93	105.95	6.13	104.68	4.94	1.93	1.55
Minimum	89.95	-5.83	90.48	-5.39	-1.78	-0.73	89.83	-9.97	90.47	-8.54	-1.75	-1.29
Mean	99.73	-0.69	99.83	-0.65	0.09	0.04	99.64	-1.19	99.73	-1.12	0.09	0.07
Standard Dev	2.76	2.42	2.83	2.41	0.70	0.38	2.77	4.21	2.83	4.19	0.70	0.66
Skew	-0.21	-0.19	-0.23	-0.20	0.05	0.03	-0.21	-0.19	-0.23	-0.19	0.05	0.03
Excess	-0.21	-1.02	-0.28	-1.06	-1.08	-1.14	-0.22	-1.03	-0.29	-1.07	-1.09	-1.15
? Mean	0.08	0.07	0.09	0.07	0.02	0.01	0.08	0.13	0.09	0.13	0.02	0.02
? Standard Dev	0.06	0.04	0.06	0.04	0.01	0.01	0.06	0.06	0.06	0.06	0.01	0.01

Particle	Vel-mag	Alpha	Mag-meas	Alpha-meas	Error-Mag	Error-Alpha	U-select	V-select	U-meas	V-meas	Error U	Error V
2	101.80	-4.64	102.67	-4.77	0.87	-0.13	101.47	-8.24	102.32	-8.54	0.85	-0.30
4	101.44	0.86	102.32	0.25	0.87	-0.61	101.43	1.52	102.32	0.45	0.88	-1.08
9	96.60	-4.50	97.95	-5.00	1.35	-0.50	96.30	-7.58	97.58	-8.54	1.28	-0.96
11	96.54	-3.54	95.42	-3.78	-1.13	-0.24	96.36	-5.96	95.21	-6.29	-1.15	-0.33
14	97.87	2.76	97.70	2.90	-0.17	0.14	97.76	4.71	97.58	4.94	-0.18	0.23
15	98.23	-1.36	97.60	-1.06	-0.63	0.31	98.20	-2.34	97.58	-1.80	-0.62	0.54
18	102.15	0.50	102.32	0.25	0.17	-0.25	102.15	0.89	102.32	0.45	0.17	-0.44
21	98.96	-1.04	99.96	-1.03	1.00	0.01	98.95	-1.79	99.95	-1.80	1.00	-0.01
22	97.90	-4.40	97.95	-5.00	0.06	-0.60	97.61	-7.52	97.58	-8.54	-0.03	-1.02
23	99.15	1.35	99.98	1.55	0.84	0.19	99.12	2.34	99.95	2.70	0.83	0.36
25	102.59	-0.69	102.33	-1.01	-0.26	-0.31	102.58	-1.24	102.32	-1.80	-0.26	-0.56
26	102.14	0.07	102.32	0.25	0.18	0.19	102.14	0.12	102.32	0.45	0.18	0.33
30	101.83	-0.50	102.33	-1.01	0.50	-0.50	101.83	-0.89	102.32	-1.80	0.49	-0.90
35	104.14	-5.26	105.03	-4.66	0.90	0.60	103.70	-9.54	104.68	-8.54	0.99	1.00
38	99.12	-1.10	99.96	-1.03	0.85	0.07	99.10	-1.91	99.95	-1.80	0.85	0.11
44	102.20	2.07	102.35	1.51	0.15	-0.56	102.13	3.69	102.32	2.70	0.18	-0.99
45	101.06	3.18	100.07	2.83	-0.99	-0.35	100.91	5.60	99.95	4.94	-0.96	-0.66
46	102.35	1.98	102.35	1.51	0.00	-0.47	102.29	3.54	102.32	2.70	0.03	-0.84
47	105.58	-2.56	104.76	-2.21	-0.82	0.35	105.48	-4.72	104.68	-4.04	-0.79	0.68
48	101.61	2.14	102.35	1.51	0.74	-0.63	101.54	3.79	102.32	2.70	0.77	-1.09
50	105.53	0.47	104.69	0.25	-0.84	-0.23	105.52	0.87	104.68	0.45	-0.84	-0.42
51	101.78	2.43	102.44	2.77	0.65	0.33	101.69	4.32	102.32	4.94	0.63	0.62
56	98.55	-0.39	97.58	0.26	-0.97	0.65	98.55	-0.67	97.58	0.45	-0.97	1.12
59	94.35	-3.10	95.30	-2.43	0.95	0.67	94.21	-5.11	95.21	-4.04	1.00	1.07
60	103.33	2.75	102.44	2.77	-0.90	0.01	103.21	4.96	102.32	4.94	-0.90	-0.02
68	101.71	-0.37	102.33	-1.01	0.62	-0.64	101.71	-0.65	102.32	-1.80	0.61	-1.15
69	104.24	1.67	104.72	1.48	0.48	-0.19	104.20	3.03	104.68	2.70	0.49	-0.33
70	104.97	-3.77	104.87	-3.44	-0.10	0.33	104.74	-6.91	104.68	-6.29	-0.06	0.62
71	105.06	1.60	104.72	1.48	-0.34	-0.12	105.02	2.93	104.68	2.70	-0.33	-0.23
73	105.34	-1.02	104.70	-0.98	-0.64	0.03	105.32	-1.87	104.68	-1.80	-0.63	0.07
74	95.89	1.37	95.25	1.62	-0.64	0.25	95.86	2.29	95.21	2.70	-0.65	0.41
76	100.16	1.47	99.98	1.55	-0.18	0.08	100.13	2.57	99.95	2.70	-0.18	0.13
77	96.80	-0.84	97.60	-1.06	0.80	-0.21	96.79	-1.42	97.58	-1.80	0.79	-0.38
78	98.61	-1.83	97.66	-2.37	-0.95	-0.54	98.56	-3.15	97.58	-4.04	-0.98	-0.89
79	99.63	-0.72	99.96	-1.03	0.34	-0.31	99.62	-1.25	99.95	-1.80	0.33	-0.55
85	99.64	-0.74	99.96	-1.03	0.32	-0.29	99.63	-1.29	99.95	-1.80	0.31	-0.51
91	101.11	-2.58	102.40	-2.26	1.28	0.32	101.01	-4.56	102.32	-4.04	1.31	0.51
94	101.04	1.68	99.98	1.55	-1.05	-0.14	100.99	2.97	99.95	2.70	-1.05	-0.27
96	100.19	2.19	100.07	2.83	-0.12	0.65	100.12	3.82	99.95	4.94	-0.17	1.12

Table III.2.c. - Laser Velocimeter Results: Peak Signal Processing – Statistics and First 100 selected.

	Vel-mag	Alpha	Mag-meas	Alpha-meas	Error-Mag	Error-Alpha	U-select	V-select	U-meas	V-meas	Error U	Error V
Number	5909	5909	5909	5909	5909	5909	5909	5909	5909	5909	5909	5909
Maximum	108.21	8.91	108.08	8.76	1.61	0.77	108.12	15.19	107.31	14.23	1.70	1.33
Minimum	89.23	-11.93	88.64	-11.77	-1.42	-0.62	88.86	-20.88	88.35	-20.06	-1.39	-1.08
Mean	99.90	-0.18	100.01	-0.13	0.11	0.04	99.68	-0.31	99.78	-0.23	0.11	0.08
Standard Dev	2.91	3.83	2.96	3.83	0.51	0.28	2.93	6.66	2.97	6.67	0.51	0.48
Skew	-0.07	-0.17	-0.07	-0.18	0.04	0.02	-0.07	-0.17	-0.07	-0.18	0.04	0.01
Excess	-0.07	-0.34	-0.09	-0.34	-0.97	-1.07	-0.08	-0.35	-0.08	-0.35	-0.97	-1.08
? Mean	0.08	0.10	0.08	0.10	0.01	0.01	0.08	0.17	0.08	0.17	0.01	0.01
? Standard Dev	0.05	0.06	0.05	0.06	0.01	0.00	0.05	0.11	0.05	0.11	0.01	0.01

Particle	Vel-mag	Alpha	Mag-meas	Alpha-meas	Error-Mag	Error-Alpha	U-select	V-select	U-meas	V-meas	Error U	Error V
2	101.80	-4.64	102.55	-4.65	0.74	-0.01	101.47	-8.24	102.21	-8.31	0.74	-0.07
4	101.44	0.86	102.05	0.41	0.61	-0.46	101.43	1.52	102.05	0.72	0.62	-0.80
6	98.63	4.11	98.15	4.19	-0.48	0.08	98.37	7.07	97.88	7.18	-0.49	0.10
7	102.65	3.79	102.62	3.96	-0.03	0.17	102.42	6.78	102.38	7.09	-0.05	0.31
9	96.60	-4.50	97.57	-4.82	0.97	-0.32	96.30	-7.58	97.22	-8.20	0.92	-0.62
10	99.53	3.46	100.05	3.96	0.53	0.50	99.34	6.00	99.82	6.90	0.47	0.90
11	96.54	-3.54	95.74	-3.71	-0.80	-0.17	96.36	-5.96	95.54	-6.20	-0.82	-0.24
14	97.87	2.76	97.67	2.88	-0.21	0.12	97.76	4.71	97.54	4.91	-0.22	0.20
15	98.23	-1.36	97.84	-1.10	-0.39	0.26	98.20	-2.34	97.82	-1.89	-0.38	0.45
18	102.15	0.50	102.36	0.31	0.21	-0.19	102.15	0.89	102.36	0.55	0.21	-0.34
19	99.59	-9.05	99.07	-8.96	-0.52	0.09	98.35	-15.66	97.86	-15.43	-0.49	0.23
20	100.34	-6.08	100.50	-6.12	0.15	-0.04	99.78	-10.63	99.92	-10.71	0.14	-0.08
21	98.96	-1.04	99.76	-0.97	0.80	0.07	98.95	-1.79	99.75	-1.69	0.80	0.10
22	97.90	-4.40	97.96	-4.82	0.07	-0.42	97.61	-7.52	97.62	-8.24	0.01	-0.72
23	99.15	1.35	99.82	1.51	0.67	0.16	99.12	2.34	99.78	2.63	0.66	0.29
24	105.90	-0.42	106.83	-0.84	0.94	-0.41	105.89	-0.78	106.82	-1.56	0.93	-0.78
25	102.59	-0.69	102.44	-0.92	-0.14	-0.23	102.58	-1.24	102.43	-1.64	-0.15	-0.40
26	102.14	0.07	102.27	0.22	0.13	0.15	102.14	0.12	102.27	0.39	0.13	0.27
29	97.03	6.65	97.95	6.78	0.92	0.13	96.38	11.24	97.26	11.57	0.88	0.33
30	101.83	-0.50	102.23	-0.88	0.40	-0.38	101.83	-0.89	102.22	-1.57	0.39	-0.67
34	99.96	4.87	100.33	5.27	0.37	0.40	99.60	8.48	99.90	9.21	0.31	0.73
35	104.14	-5.26	104.85	-4.77	0.72	0.49	103.70	-9.54	104.49	-8.71	0.79	0.83
38	99.12	-1.10	99.71	-1.03	0.59	0.07	99.10	-1.91	99.69	-1.79	0.59	0.12
42	104.88	5.32	105.15	5.20	0.27	-0.12	104.43	9.73	104.72	9.54	0.29	-0.19
43	96.88	8.06	96.44	8.25	-0.44	0.20	95.92	13.58	95.44	13.84	-0.48	0.27
44	102.20	2.07	102.30	1.66	0.10	-0.41	102.13	3.69	102.25	2.96	0.12	-0.73
45	101.06	3.18	100.41	2.95	-0.65	-0.22	100.91	5.60	100.28	5.17	-0.63	-0.43
46	102.35	1.98	102.44	1.67	0.09	-0.31	102.29	3.54	102.40	2.98	0.11	-0.56
47	105.58	-2.56	104.94	-2.28	-0.64	0.28	105.48	-4.72	104.86	-4.17	-0.61	0.55
48	101.61	2.14	102.18	1.69	0.57	-0.45	101.54	3.79	102.14	3.01	0.60	-0.78
49	101.24	5.01	100.73	5.29	-0.51	0.28	100.85	8.85	100.30	9.29	-0.55	0.44
50	105.53	0.47	104.97	0.33	-0.56	-0.14	105.52	0.87	104.97	0.60	-0.56	-0.27
51	101.78	2.43	102.26	2.69	0.47	0.25	101.69	4.32	102.14	4.79	0.45	0.47
56	98.55	-0.39	97.87	0.10	-0.68	0.49	98.55	-0.67	97.87	0.17	-0.68	0.84
59	94.35	-3.10	95.02	-2.62	0.68	0.48	94.21	-5.11	94.92	-4.35	0.72	0.76
60	103.33	2.75	102.74	2.77	-0.59	0.02	103.21	4.96	102.62	4.97	-0.59	0.01
63	102.47	4.41	102.56	4.16	0.09	-0.25	102.17	7.88	102.29	7.43	0.13	-0.45
68	101.71	-0.37	102.24	-0.88	0.53	-0.51	101.71	-0.65	102.23	-1.56	0.52	-0.91
69	104.24	1.67	104.61	1.55	0.36	-0.11	104.20	3.03	104.57	2.84	0.37	-0.19
70	104.97	-3.77	104.91	-3.51	-0.06	0.26	104.74	-6.91	104.72	-6.42	-0.03	0.48
71	105.06	1.60	104.82	1.54	-0.23	-0.06	105.02	2.93	104.79	2.81	-0.23	-0.12
72	100.14	6.57	100.47	6.69	0.33	0.12	99.48	11.45	99.79	11.70	0.31	0.24
73	105.34	-1.02	104.93	-0.99	-0.41	0.03	105.32	-1.87	104.91	-1.80	-0.41	0.07
74	95.89	1.37	95.45	1.56	-0.43	0.20	95.86	2.29	95.42	2.61	-0.44	0.32
76	100.16	1.47	100.11	1.53	-0.05	0.06	100.13	2.57	100.08	2.67	-0.05	0.10
77	96.80	-0.84	97.42	-0.92	0.62	-0.08	96.79	-1.42	97.41	-1.57	0.62	-0.14
78	98.61	-1.83	98.02	-2.23	-0.59	-0.40	98.56	-3.15	97.95	-3.82	-0.61	-0.66
79	99.63	-0.72	99.90	-0.92	0.28	-0.20	99.62	-1.25	99.89	-1.60	0.27	-0.36
80	106.14	-2.08	106.86	-2.19	0.72	-0.11	106.07	-3.85	106.78	-4.09	0.71	-0.24
81	101.79	7.53	103.07	7.73	1.28	0.21	100.91	13.34	102.13	13.87	1.22	0.54
85	99.64	-0.74	99.92	-0.93	0.28	-0.19	99.63	-1.29	99.91	-1.62	0.28	-0.33
86	100.77	-6.75	100.60	-6.29	-0.17	0.46	100.07	-11.84	99.99	-11.02	-0.08	0.82
91	101.11	-2.58	102.13	-2.33	1.01	0.26	101.01	-4.56	102.04	-4.14	1.03	0.41
94	101.04	1.68	100.30	1.61	-0.74	-0.07	100.99	2.97	100.26	2.82	-0.73	-0.15
96	100.19	2.19	100.12	2.66	-0.07	0.48	100.12	3.82	100.01	4.65	-0.11	0.83
99	100.88	3.79	100.41	4.06	-0.48	0.27	100.66	6.66	100.15	7.10	-0.51	0.44

Table III.2.d. - Laser Velocimeter Results: Gaussian Signal Processing – Statistics and First 100 selected.

	Vel-mag	Alpha	Mag-meas	Alpha-meas	Error-Mag	Error-Alpha	U-select	V-select	U-meas	V-meas	Error U	Error V
Number	7633	7633	7633	7633	7633	7633	7633	7633	7633	7633	7633	7633
Maximum	110.31	13.96	110.59	14.06	1.85	1.02	110.10	25.12	109.89	25.20	1.85	1.71
Minimum	89.23	-15.34	88.96	-15.20	-1.53	-1.14	88.86	-26.45	88.40	-26.36	-1.56	-1.97
Mean	99.95	-0.03	100.06	0.01	0.11	0.05	99.70	-0.06	99.81	0.02	0.11	0.08
Standard Dev	2.97	4.03	2.98	4.03	0.31	0.18	2.98	7.01	3.00	7.02	0.31	0.31
Skew	-0.01	-0.01	0.00	-0.01	0.10	-0.07	-0.01	-0.01	0.00	-0.01	0.07	-0.10
Excess	0.01	0.00	0.03	0.01	1.46	2.66	0.00	-0.01	0.02	0.00	1.47	2.54
? Mean	0.07	0.09	0.07	0.09	0.01	0.00	0.07	0.16	0.07	0.16	0.01	0.01
? Standard Dev	0.05	0.07	0.05	0.07	0.01	0.00	0.05	0.11	0.05	0.11	0.01	0.01

Particle	Vel-mag	Alpha	Mag-meas	Alpha-meas	Error-Mag	Error-Alpha	U-select	V-select	U-meas	V-meas	Error U	Error V
2	101.80	-4.64	102.34	-4.40	0.54	0.24	101.47	-8.24	102.04	-7.85	0.57	0.39
4	101.44	0.86	101.55	0.65	0.11	-0.21	101.43	1.52	101.54	1.15	0.11	-0.37
6	98.63	4.11	98.57	4.09	-0.06	-0.03	98.37	7.07	98.32	7.02	-0.06	-0.05
7	102.65	3.79	102.75	3.84	0.10	0.06	102.42	6.78	102.52	6.89	0.09	0.11
9	96.60	-4.50	97.12	-4.56	0.52	-0.06	96.30	-7.58	96.81	-7.72	0.51	-0.14
10	99.53	3.46	99.83	3.72	0.31	0.27	99.34	6.00	99.62	6.48	0.28	0.48
11	96.54	-3.54	96.24	-3.64	-0.30	-0.10	96.36	-5.96	96.05	-6.12	-0.31	-0.15
14	97.87	2.76	97.58	2.87	-0.29	0.11	97.76	4.71	97.46	4.89	-0.30	0.18
15	98.23	-1.36	98.13	-1.14	-0.10	0.23	98.20	-2.34	98.11	-1.95	-0.09	0.39
17	97.20	4.19	97.16	4.22	-0.04	0.03	96.94	7.10	96.90	7.15	-0.04	0.05
18	102.15	0.50	102.42	0.39	0.27	-0.11	102.15	0.89	102.41	0.70	0.27	-0.19
19	99.59	-9.05	99.52	-9.07	-0.07	-0.02	98.35	-15.66	98.27	-15.69	-0.08	-0.03
20	100.34	-6.08	100.46	-6.04	0.11	0.04	99.78	-10.63	99.90	-10.58	0.12	0.05
21	98.96	-1.04	99.51	-0.83	0.54	0.21	98.95	-1.79	99.49	-1.44	0.55	0.35
22	97.90	-4.40	97.97	-4.57	0.07	-0.16	97.61	-7.52	97.66	-7.80	0.05	-0.28
23	99.15	1.35	99.61	1.45	0.46	0.10	99.12	2.34	99.58	2.52	0.46	0.18
24	105.90	-0.42	106.40	-0.60	0.51	-0.18	105.89	-0.78	106.40	-1.11	0.51	-0.33
25	102.59	-0.69	102.59	-0.82	0.00	-0.12	102.58	-1.24	102.58	-1.46	0.00	-0.22
26	102.14	0.07	102.27	0.15	0.13	0.09	102.14	0.12	102.27	0.27	0.13	0.16
27	99.33	-2.96	99.66	-2.72	0.33	0.24	99.20	-5.13	99.54	-4.74	0.35	0.40
28	100.95	-4.65	100.76	-4.74	-0.20	-0.09	100.62	-8.18	100.41	-8.32	-0.21	-0.14
29	97.03	6.65	97.65	6.70	0.61	0.05	96.38	11.24	96.98	11.39	0.60	0.15
30	101.83	-0.50	102.03	-0.66	0.20	-0.16	101.83	-0.89	102.02	-1.17	0.20	-0.28
32	101.79	-6.21	102.23	-6.28	0.44	-0.07	101.19	-11.01	101.62	-11.17	0.42	-0.16
34	99.96	4.87	100.24	5.05	0.29	0.19	99.60	8.48	99.85	8.83	0.26	0.35
35	104.14	-5.26	104.53	-4.88	0.39	0.38	103.70	-9.54	104.15	-8.89	0.45	0.65
36	103.87	-1.06	103.50	-1.05	-0.37	0.01	103.85	-1.93	103.48	-1.90	-0.37	0.03
37	104.94	-2.36	104.95	-2.27	0.01	0.08	104.85	-4.31	104.87	-4.17	0.02	0.15
38	99.12	-1.10	99.24	-1.01	0.13	0.09	99.10	-1.91	99.23	-1.75	0.13	0.15
40	93.67	-2.37	93.73	-2.78	0.06	-0.41	93.59	-3.88	93.62	-4.55	0.03	-0.67
42	104.88	5.32	105.31	5.29	0.43	-0.03	104.43	9.73	104.86	9.71	0.43	-0.02
43	96.88	8.06	96.71	8.15	-0.16	0.09	95.92	13.58	95.74	13.71	-0.18	0.13
44	102.20	2.07	102.20	1.93	0.00	-0.14	102.13	3.69	102.14	3.45	0.01	-0.24
45	101.06	3.18	100.85	3.16	-0.21	-0.02	100.91	5.60	100.70	5.56	-0.21	-0.04
46	102.35	1.98	102.58	1.96	0.23	-0.02	102.29	3.54	102.52	3.51	0.23	-0.03
47	105.58	-2.56	105.29	-2.42	-0.30	0.15	105.48	-4.72	105.19	-4.44	-0.28	0.28
48	101.61	2.14	101.99	1.94	0.38	-0.20	101.54	3.79	101.94	3.44	0.39	-0.35
49	101.24	5.01	101.18	5.13	-0.06	0.12	100.85	8.85	100.77	9.05	-0.08	0.20
50	105.53	0.47	105.41	0.47	-0.12	0.00	105.52	0.87	105.41	0.86	-0.12	-0.01
51	101.78	2.43	102.05	2.56	0.27	0.12	101.69	4.32	101.95	4.55	0.26	0.23
52	99.07	3.58	99.59	3.66	0.52	0.09	98.87	6.18	99.38	6.36	0.51	0.18
56	98.55	-0.39	98.34	-0.14	-0.21	0.25	98.55	-0.67	98.34	-0.25	-0.21	0.42
57	100.93	-6.04	100.93	-5.91	0.00	0.13	100.37	-10.61	100.39	-10.39	0.02	0.23
59	94.35	-3.10	94.71	-2.88	0.36	0.22	94.21	-5.11	94.59	-4.76	0.38	0.35
60	103.33	2.75	103.19	2.78	-0.14	0.03	103.21	4.96	103.07	5.01	-0.15	0.05
63	102.47	4.41	102.56	4.38	0.09	-0.03	102.17	7.88	102.26	7.84	0.09	-0.04
68	101.71	-0.37	102.04	-0.64	0.32	-0.27	101.71	-0.65	102.03	-1.14	0.32	-0.49
69	104.24	1.67	104.48	1.70	0.24	0.03	104.20	3.03	104.43	3.10	0.24	0.07
70	104.97	-3.77	104.94	-3.63	-0.03	0.14	104.74	-6.91	104.73	-6.64	-0.02	0.27
71	105.06	1.60	104.95	1.63	-0.11	0.03	105.02	2.93	104.91	2.98	-0.11	0.06
72	100.14	6.57	100.38	6.75	0.24	0.19	99.48	11.45	99.68	11.81	0.20	0.35
73	105.34	-1.02	105.29	-0.98	-0.05	0.03	105.32	-1.87	105.27	-1.81	-0.05	0.06
74	95.89	1.37	95.75	1.48	-0.13	0.11	95.86	2.29	95.72	2.47	-0.14	0.18
76	100.16	1.47	100.28	1.50	0.12	0.03	100.13	2.57	100.25	2.63	0.12	0.06
77	96.80	-0.84	96.77	-0.65	-0.02	0.19	96.79	-1.42	96.77	-1.10	-0.02	0.32
78	98.61	-1.83	98.56	-2.02	-0.05	-0.19	98.56	-3.15	98.50	-3.48	-0.06	-0.32
79	99.63	-0.72	99.83	-0.74	0.21	-0.02	99.62	-1.25	99.82	-1.28	0.21	-0.04
80	106.14	-2.08	106.40	-2.29	0.26	-0.21	106.07	-3.85	106.31	-4.25	0.24	-0.41
81	101.79	7.53	102.87	7.66	1.08	0.14	100.91	13.34	101.95	13.72	1.04	0.38
82	97.77	5.82	98.01	5.55	0.24	-0.27	97.26	9.92	97.55	9.48	0.29	-0.44
85	99.64	-0.74	99.88	-0.73	0.24	0.01	99.63	-1.29	99.87	-1.28	0.24	0.01
86	100.77	-6.75	100.75	-6.49	-0.02	0.26	100.07	-11.84	100.10	-11.38	0.03	0.46
88	97.54	-1.67	97.51	-0.94	-0.04	0.73	97.50	-2.85	97.49	-1.60	-0.01	1.24
89	98.32	-6.37	98.14	-6.30	-0.18	0.07	97.72	-10.91	97.55	-10.77	-0.17	0.14
90	95.68	10.60	96.06	10.70	0.39	0.10	94.04	17.60	94.39	17.84	0.35	0.24
91	101.11	-2.58	101.64	-2.44	0.53	0.15	101.01	-4.56	101.55	-4.32	0.54	0.23
92	96.25	-1.79	95.50	-1.46	-0.75	0.33	96.20	-3.01	95.47	-2.44	-0.74	0.57
93	103.74	6.30	103.33	6.21	-0.41	-0.09	103.11	11.38	102.72	11.18	-0.39	-0.20
94	101.04	1.68	100.84	1.68	-0.19	-0.01	100.99	2.97	100.80	2.95	-0.19	-0.02
96	100.19	2.19	100.16	2.40	-0.02	0.21	100.12	3.82	100.08	4.19	-0.04	0.37
97	99.81	-6.59	99.71	-5.93	-0.10	0.66	99.15	-11.45	99.18	-10.30	0.02	1.15
98	101.49	3.80	101.60	3.97	0.10	0.17	101.27	6.73	101.35	7.04	0.08	0.31
99	100.88	3.79	100.70	3.96	-0.18	0.18	100.66	6.66	100.46	6.96	-0.20	0.30
100	100.60	4.50	100.60	4.37	0.00	-0.13	100.29	7.89	100.31	7.66	0.02	-0.23

Table III.2.e. - Laser Velocimeter Results: Histogram (3) Signal Processing – Statistics and First 100 selected.

	Vel-mag	Alpha	Mag-meas	Alpha-meas	Error-Mag	Error-Alpha	U-select	V-select	U-meas	V-meas	Error U	Error V
Number	7633	7633	7633	7633	7633	7633	7633	7633	7633	7633	7633	7633
Maximum	110.31	13.96	110.75	14.02	2.84	1.41	110.10	25.12	110.49	25.23	2.85	2.36
Minimum	89.23	-15.34	88.44	-15.24	-2.33	-1.33	88.86	-26.45	87.85	-26.35	-2.61	-2.31
Mean	99.95	-0.03	100.07	0.01	0.12	0.05	99.70	-0.06	99.82	0.02	0.12	0.08
Standard Dev	2.97	4.03	2.99	4.03	0.40	0.23	2.98	7.01	3.01	7.03	0.41	0.40
Skew	-0.01	-0.01	0.00	-0.01	-0.05	-0.18	-0.01	-0.01	-0.01	-0.01	-0.09	-0.19
Excess	0.01	0.00	0.04	0.00	2.85	4.83	0.00	-0.01	0.03	-0.01	2.93	4.74
? Mean	0.07	0.09	0.07	0.09	0.01	0.01	0.07	0.16	0.07	0.16	0.01	0.01
? Standard Dev	0.05	0.07	0.05	0.07	0.01	0.01	0.05	0.11	0.05	0.11	0.01	0.01

Particle	Vel-mag	Alpha	Mag-meas	Alpha-meas	Error-Mag	Error-Alpha	U-select	V-select	U-meas	V-meas	Error U	Error V
2	101.80	-4.64	102.65	-4.01	0.85	0.63	101.47	-8.24	102.40	-7.18	0.93	1.06
4	101.44	0.86	100.83	0.85	-0.62	-0.01	101.43	1.52	100.82	1.49	-0.62	-0.03
6	98.63	4.11	98.81	3.92	0.19	-0.19	98.37	7.07	98.58	6.76	0.21	-0.31
7	102.65	3.79	103.02	3.78	0.38	-0.01	102.42	6.78	102.80	6.79	0.38	0.01
9	96.60	-4.50	97.04	-4.38	0.44	0.12	96.30	-7.58	96.76	-7.41	0.46	0.17
10	99.53	3.46	99.75	3.49	0.22	0.03	99.34	6.00	99.56	6.07	0.22	0.07
11	96.54	-3.54	96.55	-3.63	0.01	-0.09	96.36	-5.96	96.36	-6.12	0.00	-0.15
14	97.87	2.76	97.80	2.85	-0.07	0.09	97.76	4.71	97.68	4.87	-0.08	0.15
15	98.23	-1.36	98.18	-1.13	-0.05	0.24	98.20	-2.34	98.16	-1.93	-0.04	0.40
17	97.20	4.19	96.75	4.24	-0.45	0.05	96.94	7.10	96.48	7.15	-0.45	0.05
18	102.15	0.50	102.44	0.43	0.29	-0.07	102.15	0.89	102.44	0.78	0.29	-0.12
19	99.59	-9.05	99.13	-9.31	-0.46	-0.26	98.35	-15.66	97.82	-16.03	-0.53	-0.37
20	100.34	-6.08	100.43	-5.92	0.09	0.16	99.78	-10.63	99.89	-10.36	0.11	0.27
21	98.96	-1.04	99.47	-0.50	0.50	0.54	98.95	-1.79	99.46	-0.87	0.52	0.92
22	97.90	-4.40	97.95	-4.39	0.05	0.02	97.61	-7.52	97.66	-7.49	0.05	0.02
23	99.15	1.35	99.59	1.32	0.45	-0.03	99.12	2.34	99.57	2.30	0.45	-0.04
24	105.90	-0.42	106.00	-0.35	0.10	0.07	105.89	-0.78	105.99	-0.65	0.10	0.13
25	102.59	-0.69	102.34	-0.80	-0.25	-0.11	102.58	-1.24	102.33	-1.44	-0.25	-0.19
26	102.14	0.07	102.27	0.02	0.13	-0.05	102.14	0.12	102.27	0.03	0.13	-0.09
27	99.33	-2.96	99.96	-2.80	0.64	0.16	99.20	-5.13	99.85	-4.88	0.65	0.25
28	100.95	-4.65	100.90	-4.69	-0.05	-0.04	100.62	-8.18	100.56	-8.25	-0.06	-0.07
29	97.03	6.65	97.62	6.65	0.59	0.00	96.38	11.24	96.96	11.31	0.59	0.07
30	101.83	-0.50	101.67	-0.49	-0.16	0.01	101.83	-0.89	101.67	-0.87	-0.16	0.03
32	101.79	-6.21	101.89	-6.51	0.10	-0.31	101.19	-11.01	101.23	-11.56	0.04	-0.55
34	99.96	4.87	100.61	4.85	0.65	-0.02	99.60	8.48	100.25	8.50	0.65	0.02
35	104.14	-5.26	104.07	-4.97	-0.07	0.29	103.70	-9.54	103.68	-9.01	-0.02	0.53
36	103.87	-1.06	102.92	-1.18	-0.95	-0.11	103.85	-1.93	102.90	-2.11	-0.96	-0.19
37	104.94	-2.36	104.95	-2.27	0.01	0.09	104.85	-4.31	104.87	-4.15	0.02	0.16
38	99.12	-1.10	98.99	-0.96	-0.13	0.14	99.10	-1.91	98.97	-1.67	-0.13	0.24
40	93.67	-2.37	93.36	-3.31	-0.31	-0.94	93.59	-3.88	93.21	-5.39	-0.38	-1.51
42	104.88	5.32	105.33	5.43	0.45	0.11	104.43	9.73	104.86	9.97	0.43	0.24
43	96.88	8.06	96.96	8.09	0.08	0.03	95.92	13.58	95.99	13.65	0.07	0.07
44	102.20	2.07	101.94	2.16	-0.26	0.09	102.13	3.69	101.87	3.84	-0.26	0.15
45	101.06	3.18	101.14	3.35	0.08	0.18	100.91	5.60	100.96	5.91	0.06	0.32
46	102.35	1.98	102.80	2.15	0.45	0.17	102.29	3.54	102.73	3.86	0.44	0.32
47	105.58	-2.56	105.73	-2.59	0.15	-0.03	105.48	-4.72	105.62	-4.77	0.14	-0.05
48	101.61	2.14	102.03	2.12	0.42	-0.02	101.54	3.79	101.96	3.77	0.42	-0.02
49	101.24	5.01	101.45	5.06	0.21	0.05	100.85	8.85	101.06	8.95	0.21	0.10
50	105.53	0.47	105.22	0.54	-0.31	0.06	105.52	0.87	105.22	0.98	-0.31	0.11
51	101.78	2.43	102.04	2.50	0.26	0.07	101.69	4.32	101.94	4.45	0.25	0.13
52	99.07	3.58	100.03	3.33	0.96	-0.25	98.87	6.18	99.86	5.81	0.99	-0.37
56	98.55	-0.39	98.68	-0.21	0.13	0.19	98.55	-0.67	98.68	-0.35	0.13	0.32
57	100.93	-6.04	101.37	-5.70	0.44	0.34	100.37	-10.61	100.87	-10.07	0.50	0.54
59	94.35	-3.10	94.72	-3.02	0.38	0.09	94.21	-5.11	94.59	-4.99	0.38	0.12
60	103.33	2.75	103.54	2.78	0.21	0.03	103.21	4.96	103.42	5.02	0.20	0.06
63	102.47	4.41	102.25	4.61	-0.22	0.20	102.17	7.88	101.92	8.22	-0.24	0.34
68	101.71	-0.37	101.89	-0.42	0.18	-0.05	101.71	-0.65	101.89	-0.74	0.18	-0.09
69	104.24	1.67	104.58	1.76	0.33	0.09	104.20	3.03	104.53	3.21	0.33	0.18
70	104.97	-3.77	104.94	-3.67	-0.03	0.10	104.74	-6.91	104.73	-6.72	-0.01	0.18
71	105.06	1.60	104.95	1.67	-0.11	0.07	105.02	2.93	104.91	3.06	-0.11	0.13
72	100.14	6.57	100.17	6.94	0.03	0.37	99.48	11.45	99.43	12.10	-0.05	0.65
73	105.34	-1.02	105.43	-0.98	0.10	0.03	105.32	-1.87	105.42	-1.81	0.10	0.06
74	95.89	1.37	96.00	1.34	0.11	-0.03	95.86	2.29	95.97	2.24	0.11	-0.05
76	100.16	1.47	100.54	1.51	0.38	0.04	100.13	2.57	100.51	2.64	0.38	0.07
77	96.80	-0.84	96.42	-0.27	-0.38	0.57	96.79	-1.42	96.42	-0.46	-0.37	0.97
78	98.61	-1.83	98.79	-1.66	0.18	0.17	98.56	-3.15	98.75	-2.87	0.19	0.29
79	99.63	-0.72	99.85	-0.62	0.23	0.10	99.62	-1.25	99.85	-1.08	0.23	0.16
80	106.14	-2.08	105.86	-2.60	-0.28	-0.52	106.07	-3.85	105.75	-4.80	-0.32	-0.95
81	101.79	7.53	102.49	7.47	0.70	-0.06	100.91	13.34	101.62	13.33	0.71	-0.01
82	97.77	5.82	98.42	5.53	0.65	-0.29	97.26	9.92	97.96	9.48	0.70	-0.44
85	99.64	-0.74	99.89	-0.53	0.25	0.21	99.63	-1.29	99.89	-0.92	0.25	0.37
86	100.77	-6.75	100.81	-6.55	0.04	0.20	100.07	-11.84	100.15	-11.50	0.08	0.34
88	97.54	-1.67	98.65	-0.78	1.11	0.89	97.50	-2.85	98.64	-1.35	1.14	1.49
89	98.32	-6.37	98.14	-6.55	-0.19	-0.18	97.72	-10.91	97.50	-11.20	-0.22	-0.29
90	95.68	10.60	95.70	10.61	0.02	0.01	94.04	17.60	94.06	17.62	0.02	0.02
91	101.11	-2.58	101.01	-2.49	-0.10	0.09	101.01	-4.56	100.92	-4.40	-0.09	0.16
92	96.25	-1.79	95.59	-1.85	-0.67	-0.06	96.20	-3.01	95.54	-3.08	-0.67	-0.08
93	103.74	6.30	103.71	6.05	-0.03	-0.25	103.11	11.38	103.13	10.92	0.02	-0.45
94	101.04	1.68	101.19	1.69	0.15	0.00	100.99	2.97	101.15	2.98	0.15	0.01
96	100.19	2.19	100.14	2.21	-0.05	0.03	100.12	3.82	100.07	3.87	-0.05	0.04
97	99.81	-6.59	100.06	-6.01	0.25	0.57	99.15	-11.45	99.51	-10.48	0.36	0.97
98	101.49	3.80	102.33	3.98	0.83	0.17	101.27	6.73	102.08	7.09	0.81	0.36
99	100.88	3.79	100.78	3.93	-0.10	0.15	100.66	6.66	100.54	6.91	-0.12	0.25
100	100.60	4.50	100.89	4.54	0.29	0.05	100.29	7.89	100.58	7.99	0.29	0.11

Table III.2.f. - Laser Velocimeter Results: Histogram (5) Signal Processing – Statistics and First 100 selected.

	Vel-mag	Alpha	Mag-meas	Alpha-meas	Error-Mag	Error-Alpha	U-select	V-select	U-meas	V-meas	Error U	Error V
Number	6040	6040	6040	6040	6040	6040	6040	6040	6040	6040	6040	6040
Maximum	110.31	13.96	110.68	13.99	1.64	0.64	110.10	25.12	110.42	25.18	1.66	1.08
Minimum	89.23	-15.34	89.40	-15.29	-1.30	-0.71	88.86	-26.45	89.07	-26.41	-1.40	-1.12
Mean	99.94	-0.02	100.07	0.02	0.12	0.05	99.69	-0.04	99.82	0.04	0.12	0.08
Standard Dev	2.96	4.05	2.96	4.06	0.33	0.16	2.97	7.06	2.98	7.07	0.33	0.28
Skew	0.00	-0.01	0.01	-0.01	-0.03	-0.03	0.00	-0.01	0.01	-0.01	-0.03	-0.03
Excess	0.05	0.01	0.09	0.01	-0.04	-0.12	0.04	0.00	0.07	0.01	-0.01	-0.14
? Mean	0.08	0.10	0.08	0.10	0.01	0.00	0.08	0.18	0.08	0.18	0.01	0.01
? Standard Dev	0.05	0.07	0.06	0.07	0.01	0.00	0.05	0.13	0.06	0.13	0.01	0.00

Particle	Vel-mag	Alpha	Mag-meas	Alpha-meas	Error-Mag	Error-Alpha	U-select	V-select	U-meas	V-meas	Error U	Error V
2	101.80	-4.64	102.41	-4.22	0.61	0.42	101.47	-8.24	102.13	-7.54	0.66	0.70
4	101.44	0.86	101.22	0.88	-0.23	0.02	101.43	1.52	101.21	1.55	-0.23	0.03
6	98.63	4.11	98.94	4.14	0.31	0.02	98.37	7.07	98.68	7.13	0.31	0.06
7	102.65	3.79	102.66	3.92	0.02	0.13	102.42	6.78	102.42	7.01	0.00	0.23
9	96.60	-4.50	96.70	-4.40	0.10	0.10	96.30	-7.58	96.41	-7.43	0.11	0.16
10	99.53	3.46	99.19	3.52	-0.34	0.07	99.34	6.00	99.00	6.10	-0.34	0.09
11	96.54	-3.54	96.54	-3.66	0.00	-0.12	96.36	-5.96	96.35	-6.16	-0.02	-0.20
14	97.87	2.76	97.63	2.88	-0.24	0.12	97.76	4.71	97.51	4.90	-0.25	0.19
15	98.23	-1.36	98.62	-1.12	0.39	0.25	98.20	-2.34	98.60	-1.92	0.40	0.42
18	102.15	0.50	102.38	0.34	0.23	-0.16	102.15	0.89	102.38	0.61	0.23	-0.28
19	99.59	-9.05	100.06	-9.33	0.47	-0.28	98.35	-15.66	98.74	-16.22	0.38	-0.56
20	100.34	-6.08	100.48	-6.09	0.14	-0.01	99.78	-10.63	99.91	-10.66	0.13	-0.03
21	98.96	-1.04	98.95	-0.93	-0.01	0.11	98.95	-1.79	98.94	-1.60	-0.01	0.19
22	97.90	-4.40	97.92	-4.36	0.02	0.05	97.61	-7.52	97.64	-7.44	0.03	0.08
23	99.15	1.35	99.73	1.49	0.58	0.13	99.12	2.34	99.69	2.59	0.57	0.25
24	105.90	-0.42	106.66	-0.36	0.76	0.06	105.89	-0.78	106.66	-0.68	0.76	0.11
25	102.59	-0.69	102.51	-0.87	-0.08	-0.18	102.58	-1.24	102.50	-1.56	-0.08	-0.32
26	102.14	0.07	102.27	0.19	0.13	0.13	102.14	0.12	102.27	0.34	0.13	0.23
29	97.03	6.65	97.14	6.80	0.11	0.15	96.38	11.24	96.46	11.50	0.08	0.26
30	101.83	-0.50	102.15	-0.41	0.32	0.09	101.83	-0.89	102.14	-0.74	0.32	0.16
34	99.96	4.87	100.23	4.80	0.27	-0.07	99.60	8.48	99.87	8.39	0.28	-0.10
35	104.14	-5.26	104.01	-4.85	-0.13	0.41	103.70	-9.54	103.63	-8.79	-0.06	0.75
38	99.12	-1.10	98.90	-1.04	-0.22	0.07	99.10	-1.91	98.88	-1.79	-0.22	0.12
42	104.88	5.32	105.21	5.24	0.33	-0.08	104.43	9.73	104.77	9.60	0.34	-0.12
43	96.88	8.06	97.23	8.15	0.35	0.10	95.92	13.58	96.25	13.79	0.33	0.21
44	102.20	2.07	102.28	2.14	0.08	0.07	102.13	3.69	102.21	3.81	0.08	0.12
45	101.06	3.18	101.28	3.40	0.22	0.22	100.91	5.60	101.10	6.01	0.20	0.41
46	102.35	1.98	102.52	2.12	0.17	0.14	102.29	3.54	102.45	3.79	0.16	0.25
47	105.58	-2.56	105.08	-2.33	-0.51	0.23	105.48	-4.72	104.99	-4.27	-0.49	0.45
48	101.61	2.14	101.40	2.15	-0.21	0.01	101.54	3.79	101.33	3.80	-0.21	0.01
49	101.24	5.01	101.53	5.19	0.29	0.18	100.85	8.85	101.11	9.19	0.26	0.34
50	105.53	0.47	105.82	0.38	0.29	-0.09	105.52	0.87	105.82	0.71	0.30	-0.17
51	101.78	2.43	101.43	2.65	-0.35	0.22	101.69	4.32	101.33	4.70	-0.37	0.37
56	98.55	-0.39	98.75	-0.39	0.20	0.01	98.55	-0.67	98.75	-0.67	0.20	0.01
59	94.35	-3.10	94.29	-3.10	-0.06	0.00	94.21	-5.11	94.15	-5.10	-0.06	0.01
60	103.33	2.75	103.59	2.76	0.25	0.01	103.21	4.96	103.47	4.99	0.25	0.02
63	102.47	4.41	102.62	4.62	0.15	0.21	102.17	7.88	102.28	8.26	0.12	0.38
68	101.71	-0.37	102.17	-0.78	0.46	-0.42	101.71	-0.65	102.16	-1.40	0.45	-0.75
69	104.24	1.67	104.54	1.61	0.30	-0.06	104.20	3.03	104.50	2.94	0.30	-0.09
70	104.97	-3.77	104.93	-3.56	-0.04	0.21	104.74	-6.91	104.72	-6.51	-0.02	0.39
71	105.06	1.60	104.88	1.57	-0.18	-0.02	105.02	2.93	104.84	2.88	-0.18	-0.05
72	100.14	6.57	99.71	6.75	-0.43	0.19	99.48	11.45	99.02	11.72	-0.46	0.27
73	105.34	-1.02	105.79	-0.98	0.45	0.04	105.32	-1.87	105.77	-1.81	0.45	0.06
74	95.89	1.37	96.25	1.52	0.37	0.15	95.86	2.29	96.22	2.55	0.36	0.26
76	100.16	1.47	100.92	1.51	0.76	0.04	100.13	2.57	100.88	2.65	0.75	0.08
77	96.80	-0.84	96.72	-0.47	-0.08	0.37	96.79	-1.42	96.71	-0.80	-0.07	0.63
78	98.61	-1.83	98.79	-1.74	0.18	0.09	98.56	-3.15	98.74	-3.01	0.19	0.15
79	99.63	-0.72	99.86	-0.47	0.24	0.25	99.62	-1.25	99.86	-0.82	0.24	0.42
80	106.14	-2.08	106.01	-2.24	-0.13	-0.16	106.07	-3.85	105.93	-4.13	-0.14	-0.29
81	101.79	7.53	102.98	7.71	1.19	0.18	100.91	13.34	102.04	13.82	1.13	0.48
85	99.64	-0.74	99.90	-0.85	0.26	-0.11	99.63	-1.29	99.89	-1.49	0.26	-0.20
86	100.77	-6.75	100.73	-6.76	-0.04	-0.01	100.07	-11.84	100.03	-11.86	-0.04	-0.02
90	95.68	10.60	95.65	10.50	-0.03	-0.10	94.04	17.60	94.05	17.43	0.01	-0.18
91	101.11	-2.58	101.22	-2.39	0.11	0.20	101.01	-4.56	101.13	-4.22	0.12	0.34
94	101.04	1.68	101.12	1.63	0.08	-0.05	100.99	2.97	101.08	2.88	0.09	-0.09
96	100.19	2.19	100.11	2.20	-0.07	0.01	100.12	3.82	100.04	3.84	-0.08	0.02
99	100.88	3.79	101.25	3.99	0.37	0.20	100.66	6.66	101.01	7.04	0.35	0.38

Table III.2.g. - Laser Velocimeter Results: Half Power Signal Processing – Statistics and First 100 selected.

	Vel-mag	Alpha	Mag-meas	Alpha-meas	Error-Mag	Error-Alpha	U-select	V-select	U-meas	V-meas	Error U	Error V
Number	6040	6040	6040	6040	6040	6040	6040	6040	6040	6040	6040	6040
Maximum	110.31	13.96	110.62	13.99	1.53	0.56	110.10	25.12	110.39	25.19	1.55	1.02
Minimum	89.23	-15.34	89.39	-15.27	-1.21	-0.64	88.86	-26.45	88.97	-26.39	-1.28	-1.01
Mean	99.94	-0.02	100.07	0.02	0.12	0.05	99.69	-0.04	99.82	0.04	0.12	0.08
Standard Dev	2.96	4.05	2.96	4.05	0.28	0.14	2.97	7.06	2.97	7.07	0.28	0.24
Skew	0.00	-0.01	0.01	-0.01	-0.02	-0.06	0.00	-0.01	0.01	-0.01	-0.02	-0.05
Excess	0.05	0.01	0.09	0.01	0.22	0.15	0.04	0.00	0.06	0.01	0.26	0.15
? Mean	0.08	0.10	0.08	0.10	0.01	0.00	0.08	0.18	0.08	0.18	0.01	0.01
? Standard Dev	0.05	0.07	0.06	0.07	0.01	0.00	0.05	0.13	0.05	0.13	0.01	0.00

Particle	Vel-mag	Alpha	Mag-meas	Alpha-meas	Error-Mag	Error-Alpha	U-select	V-select	U-meas	V-meas	Error U	Error V
2	101.80	-4.64	102.35	-4.24	0.55	0.41	101.47	-8.24	102.07	-7.56	0.60	0.68
4	101.44	0.86	101.22	0.87	-0.22	0.01	101.43	1.52	101.21	1.54	-0.22	0.01
6	98.63	4.11	98.91	4.12	0.28	0.01	98.37	7.07	98.65	7.11	0.28	0.03
7	102.65	3.79	102.69	3.88	0.05	0.10	102.42	6.78	102.46	6.96	0.04	0.18
9	96.60	-4.50	96.71	-4.41	0.11	0.10	96.30	-7.58	96.42	-7.43	0.12	0.16
10	99.53	3.46	99.29	3.53	-0.23	0.07	99.34	6.00	99.11	6.11	-0.24	0.10
11	96.54	-3.54	96.53	-3.64	-0.02	-0.10	96.36	-5.96	96.33	-6.13	-0.03	-0.17
14	97.87	2.76	97.61	2.87	-0.26	0.11	97.76	4.71	97.49	4.89	-0.27	0.18
15	98.23	-1.36	98.56	-1.13	0.34	0.23	98.20	-2.34	98.54	-1.95	0.34	0.39
18	102.15	0.50	102.40	0.37	0.25	-0.13	102.15	0.89	102.40	0.66	0.25	-0.24
19	99.59	-9.05	100.02	-9.29	0.42	-0.25	98.35	-15.66	98.70	-16.15	0.35	-0.49
20	100.34	-6.08	100.47	-6.07	0.12	0.01	99.78	-10.63	99.90	-10.63	0.12	0.00
21	98.96	-1.04	99.02	-0.89	0.06	0.15	98.95	-1.79	99.01	-1.54	0.06	0.25
22	97.90	-4.40	97.93	-4.36	0.04	0.04	97.61	-7.52	97.65	-7.45	0.04	0.07
23	99.15	1.35	99.66	1.47	0.51	0.12	99.12	2.34	99.63	2.56	0.51	0.22
24	105.90	-0.42	106.53	-0.36	0.64	0.06	105.89	-0.78	106.53	-0.68	0.64	0.11
25	102.59	-0.69	102.55	-0.84	-0.03	-0.15	102.58	-1.24	102.54	-1.50	-0.04	-0.26
26	102.14	0.07	102.26	0.18	0.12	0.11	102.14	0.12	102.26	0.31	0.12	0.20
29	97.03	6.65	97.19	6.76	0.16	0.11	96.38	11.24	96.51	11.45	0.13	0.21
30	101.83	-0.50	102.09	-0.43	0.26	0.07	101.83	-0.89	102.09	-0.77	0.26	0.12
34	99.96	4.87	100.21	4.82	0.25	-0.05	99.60	8.48	99.86	8.42	0.26	-0.06
35	104.14	-5.26	104.06	-4.88	-0.08	0.37	103.70	-9.54	103.68	-8.86	-0.02	0.68
38	99.12	-1.10	98.93	-1.03	-0.19	0.07	99.10	-1.91	98.92	-1.78	-0.18	0.13
42	104.88	5.32	105.24	5.26	0.36	-0.06	104.43	9.73	104.80	9.65	0.37	-0.08
43	96.88	8.06	97.16	8.14	0.28	0.08	95.92	13.58	96.18	13.75	0.26	0.17
44	102.20	2.07	102.25	2.14	0.05	0.07	102.13	3.69	102.18	3.81	0.05	0.12
45	101.06	3.18	101.26	3.38	0.19	0.21	100.91	5.60	101.08	5.97	0.17	0.38
46	102.35	1.98	102.55	2.12	0.20	0.14	102.29	3.54	102.48	3.80	0.19	0.26
47	105.58	-2.56	105.18	-2.37	-0.40	0.20	105.48	-4.72	105.09	-4.34	-0.38	0.38
48	101.61	2.14	101.49	2.14	-0.12	0.01	101.54	3.79	101.42	3.80	-0.12	0.01
49	101.24	5.01	101.51	5.16	0.27	0.14	100.85	8.85	101.10	9.12	0.25	0.27
50	105.53	0.47	105.80	0.42	0.28	-0.05	105.52	0.87	105.80	0.78	0.28	-0.09
51	101.78	2.43	101.52	2.61	-0.26	0.18	101.69	4.32	101.42	4.63	-0.27	0.31
56	98.55	-0.39	98.74	-0.38	0.19	0.01	98.55	-0.67	98.73	-0.65	0.19	0.02
59	94.35	-3.10	94.34	-3.08	-0.01	0.02	94.21	-5.11	94.20	-5.08	-0.01	0.03
60	103.33	2.75	103.57	2.77	0.24	0.01	103.21	4.96	103.45	5.00	0.24	0.03
63	102.47	4.41	102.60	4.61	0.14	0.20	102.17	7.88	102.27	8.25	0.11	0.37
68	101.71	-0.37	102.11	-0.72	0.40	-0.35	101.71	-0.65	102.11	-1.28	0.40	-0.63
69	104.24	1.67	104.50	1.65	0.26	-0.01	104.20	3.03	104.46	3.01	0.26	-0.02
70	104.97	-3.77	104.94	-3.59	-0.03	0.18	104.74	-6.91	104.73	-6.57	-0.01	0.33
71	105.06	1.60	104.92	1.60	-0.14	0.00	105.02	2.93	104.88	2.93	-0.14	0.00
72	100.14	6.57	99.83	6.76	-0.31	0.20	99.48	11.45	99.14	11.76	-0.35	0.30
73	105.34	-1.02	105.74	-0.98	0.41	0.04	105.32	-1.87	105.73	-1.81	0.41	0.06
74	95.89	1.37	96.18	1.50	0.30	0.13	95.86	2.29	96.15	2.51	0.29	0.22
76	100.16	1.47	100.80	1.50	0.64	0.03	100.13	2.57	100.77	2.64	0.64	0.07
77	96.80	-0.84	96.80	-0.48	0.00	0.36	96.79	-1.42	96.79	-0.82	0.01	0.61
78	98.61	-1.83	98.79	-1.77	0.18	0.07	98.56	-3.15	98.74	-3.05	0.19	0.11
79	99.63	-0.72	99.84	-0.51	0.22	0.21	99.62	-1.25	99.84	-0.89	0.22	0.36
80	106.14	-2.08	106.01	-2.26	-0.13	-0.18	106.07	-3.85	105.93	-4.18	-0.14	-0.33
81	101.79	7.53	102.90	7.69	1.11	0.16	100.91	13.34	101.98	13.77	1.07	0.44
85	99.64	-0.74	99.89	-0.80	0.25	-0.06	99.63	-1.29	99.88	-1.40	0.24	-0.10
86	100.77	-6.75	100.75	-6.74	-0.01	0.01	100.07	-11.84	100.06	-11.83	-0.01	0.02
90	95.68	10.60	95.66	10.53	-0.01	-0.07	94.04	17.60	94.05	17.48	0.01	-0.12
91	101.11	-2.58	101.22	-2.41	0.11	0.17	101.01	-4.56	101.13	-4.26	0.12	0.30
94	101.04	1.68	101.12	1.66	0.08	-0.03	100.99	2.97	101.08	2.92	0.08	-0.05
96	100.19	2.19	100.14	2.20	-0.05	0.02	100.12	3.82	100.06	3.85	-0.05	0.03
99	100.88	3.79	101.19	3.97	0.30	0.18	100.66	6.66	100.94	7.00	0.28	0.34

Table III.2.h. - Laser Velocimeter Results: True Half Power Signal Processing – Statistics and First 100 selected.

Peak Processing						
Measurements	**Mag-meas**	**Alpha-meas**	**U-select**	**U-meas**	**V-select**	**V-meas**
Number	6040	6040	9382	6040	9382	6040
Mean	100.05	0.02	99.72	99.80	-0.01	0.04
Standard Deviation	3.05	4.07	2.98	3.03	6.97	7.09
Errors:						
Mean	0.11	0.04		0.10		0.08
Standard Deviation	0.70	0.38		0.70		0.65
Outliers Removed						
Number	4264	4264	4264	4264	4264	4264
Mean	99.83	-0.65	99.64	99.73	-1.19	-1.12
Standard Deviation	2.83	2.41	2.77	2.83	4.21	4.19
Errors:						
Mean	0.09	0.04		0.09		0.07
Standard Deviation	0.70	0.38		0.70		0.66

Gaussian Processing						
	Mag-meas	**Alpha-meas**	**U-select**	**U-meas**	**V-select**	**V-meas**
Number	6040	6040	9382	6040	9382	6040
Mean	100.05	0.02	99.72	99.80	-0.01	0.04
Standard Deviation	3.00	4.06	2.98	3.02	6.97	7.07
Errors:						
Mean	0.11	0.04		0.11		0.08
Standard Deviation	0.51	0.28		0.51		0.48
Outliers Removed						
Number	5909	5909	5909	5909	5909	5909
Mean	100.01	-0.13	99.68	99.78	-0.31	-0.23
Standard Deviation	2.96	3.83	2.93	2.97	6.66	6.67
Errors:						
Mean	0.11	0.04		0.11		0.08
Standard Deviation	0.51	0.28		0.51		0.48

Histogram 3 Processing						
	Mag-meas	**Alpha-meas**	**U-select**	**U-meas**	**V-select**	**V-meas**
Number	7633	7633	9382	7633	9382	7633
Mean	100.06	0.01	99.72	99.81	-0.01	0.02
Standard Deviation	2.99	4.03	2.98	2.99	6.97	7.02
Errors:						
Mean	0.11	0.05		0.11		0.08
Standard Deviation	0.31	0.18		0.31		0.31
Outliers Removed						
Number	7633	7633	7633	7633	7633	7633
Mean	100.06	0.01	99.70	99.81	-0.06	0.02
Standard Deviation	2.98	4.03	2.98	3.00	7.01	7.02
Errors:						
Mean	0.11	0.05		0.11		0.08
Standard Deviation	0.31	0.18		0.31		0.31

Table III.2.i. - Laser Velocimeter Results: Statistics and Errors – Peak, Gaussian and Histogram (3) Signal Processing.

	Histogram 5 Processing					
	Mag-meas	Alpha-meas	U-select	U-meas	V-select	V-meas
Number	7633	7633	9382	7633	9382	7633
Mean	100.07	0.01	99.72	99.82	-0.01	0.02
Standard Deviation	3.00	4.03	2.98	3.01	6.97	7.03
Errors:						
Mean	0.12	0.05		0.12		0.08
Standard Deviation	0.40	0.23		0.41		0.40
Outliers Removed						
Number	7633	7633	7633	7633	7633	7633
Mean	100.07	0.01	99.70	99.82	-0.06	0.02
Standard Deviation	2.99	4.03	2.98	3.01	7.01	7.03
Errors:						
Mean	0.12	0.05		0.12		0.08
Standard Deviation	0.40	0.23		0.41		0.40

	Half Power Processing					
	Mag-meas	Alpha-meas	U-select	U-meas	V-select	V-meas
Number	6040	6040	9382	6040	9382	6040
Mean	100.07	0.02	99.72	99.82	-0.01	0.04
Standard Deviation	2.97	4.06	2.98	2.98	6.97	7.07
Errors:						
Mean	0.12	0.05		0.12		0.08
Standard Deviation	0.33	0.16		0.33		0.28
Outliers Removed						
Number	6040	6040	6040	6040	6040	6040
Mean	100.07	0.02	99.69	99.82	-0.04	0.04
Standard Deviation	2.96	4.06	2.97	2.98	7.06	7.07
Errors:						
Mean	0.12	0.05		0.12		0.08
Standard Deviation	0.33	0.16		0.33		0.28

	True Half Power Processing					
	Mag-meas	Alpha-meas	U-select	U-meas	V-select	V-meas
Number	6040	6040	9382	6040	6040	9382
Mean	100.07	0.02	99.72	99.82	-0.01	0.04
Standard Deviation	2.96	4.05	2.98	2.97	6.97	7.07
Errors:						
Mean	0.12	0.05		0.12		0.08
Standard Deviation	0.28	0.14		0.28		0.24
Outliers Removed						
Number	6040	6040	6040	6040	6040	6040
Mean	100.07	0.02	99.69	99.82	-0.04	0.04
Standard Deviation	2.96	4.05	2.97	2.97	7.06	7.07
Errors:						
Mean	0.12	0.05		0.12		0.08
Standard Deviation	0.28	0.14		0.28		0.24

Table III.2.i. (cont'd) - Laser Velocimeter Results: Statistics and Errors – Histogram (5), Half Power, and True Half Power Signal Processing.

Theoretical Distribution

Velocity Magnitude		Vertical Flow Angle (alpha)	
Mean	Sigma	Mean	Sigma
(m/s)	(m/s)	(degree)	(degree)
100.00	3.00	0.00	4.00

Distribution of particles randomly selected from the Theoretical Distributions

Number of	Velocity Magnitude:		Vertical Flow Angle (alpha)		U-component		V-component	
Particles	Mean	Sigma	Mean	Sigma	Mean	Sigma	Mean	Sigma
	(m/s)	(m/s)	(degree)	(degree)	(m/s)	(m/s)	(m/s)	(m/s)
10000	99.98	2.97	0.01	4.02	99.74	2.98	0.02	7.00

Distribution of particles whose signals trigger the oscilloscope based on high-trigger levels with pretriggering

Number of	Velocity Magnitude:		Vertical Flow Angle (alpha)		U-component		V-component	
Particles	Mean	Sigma	Mean	Sigma	Mean	Sigma	Mean	Sigma
	(m/s)	(m/s)	(degree)	(degree)	(m/s)	(m/s)	(m/s)	(m/s)
9382	99.94	2.97	-0.02	4.05	99.72	2.98	-0.01	6.97

Measurement statistics of the processed signals

	Number of	Velocity Magnitude				Vertical Flow Angle (alpha)			
	Particles	Mean	Error in Mean	Sigma	Error in Sigma	Mean	Error in Mean	Sigma	Error in Sigma
		(m/s)	(m/s)	(m/s)	(degree)	(degree)	(degree)	(degree)	(degree)
Peak	6040	100.05	0.11	3.05	0.70	0.02	0.04	4.07	0.38
Gaussian	6040	100.05	0.11	3.00	0.51	0.02	0.04	4.06	0.28
Histogram (3)	7633	100.06	0.11	2.99	0.31	0.01	0.05	4.03	0.18
Histogram (5)	7633	100.07	0.12	3.00	0.40	0.01	0.05	4.03	0.23
Half Power	6040	100.07	0.12	2.97	0.33	0.02	0.05	4.06	0.16
Half Power True	6040	100.07	0.12	2.96	0.28	0.02	0.05	4.05	0.14

	Number of	U-component				V-component			
	Particles	Mean	Error in Mean	Sigma	Error in Sigma	Mean	Error in Mean	Sigma	Error in Sigma
		(m/s)	(m/s)	(m/s)	(m/s)	(m/s)	(m/s)	(m/s)	(m/s)
Peak	6040	99.80	0.10	3.03	0.70	0.04	0.08	7.09	0.65
Gaussian	6040	99.80	0.11	3.02	0.51	0.04	0.08	7.07	0.48
Histogram (3)	7633	99.81	0.11	2.99	0.31	0.02	0.08	7.02	0.31
Histogram (5)	7633	99.82	0.12	3.01	0.41	0.02	0.08	7.03	0.40
Half Power	6040	99.82	0.12	2.98	0.33	0.04	0.08	7.07	0.28
Half Power True	6040	99.82	0.12	2.97	0.28	0.04	0.08	7.07	0.24

Measurement statistics of the processed signals – outliers removed

	Number of	Velocity Magnitude				Vertical Flow Angle (alpha)			
	Particles	Mean	Error in Mean	Sigma	Error in Sigma	Mean	Error in Mean	Sigma	Error in Sigma
		(m/s)	(m/s)	(m/s)	(m/s)	(degree)	(degree)	(degree)	(degree)
Peak	4264	99.83	0.09	2.82	0.70	-0.65	0.04	2.41	0.38
Gaussian	5909	100.01	0.11	2.96	0.51	-0.13	0.04	3.83	0.28
Histogram (3)	7633	100.06	0.11	2.99	0.31	0.01	0.05	4.03	0.18
Histogram (5)	7633	100.07	0.12	3.00	0.40	0.01	0.05	4.03	0.23
Half Power	6040	100.07	0.12	2.97	0.33	0.02	0.05	4.06	0.16
Half Power True	6040	100.07	0.12	2.96	0.28	0.02	0.05	4.05	0.14

	Number of	U-component				V-component			
	Particles	Mean	Error in Mean	Sigma	Error in Sigma	Mean	Error in Mean	Sigma	Error in Sigma
		(m/s)	(m/s)	(m/s)	(m/s)	(m/s)	(m/s)	(m/s)	(m/s)
Peak	4264	99.73	0.09	2.80	0.70	-1.12	0.07	4.19	0.66
Gaussian	5909	99.78	0.11	2.97	0.51	-0.23	0.08	6.67	0.48
Histogram (3)	7633	99.81	0.11	2.99	0.31	0.02	0.08	7.02	0.31
Histogram (5)	7633	99.82	0.12	3.01	0.41	0.02	0.08	7.03	0.40
Half Power	6040	99.82	0.12	2.98	0.33	0.04	0.08	7.07	0.28
Half Power True	6040	99.82	0.12	2.97	0.28	0.04	0.08	7.07	0.24

Table III.3. - Laser Velocimeter Results: Comparison of signal processing results, with and without outliers.

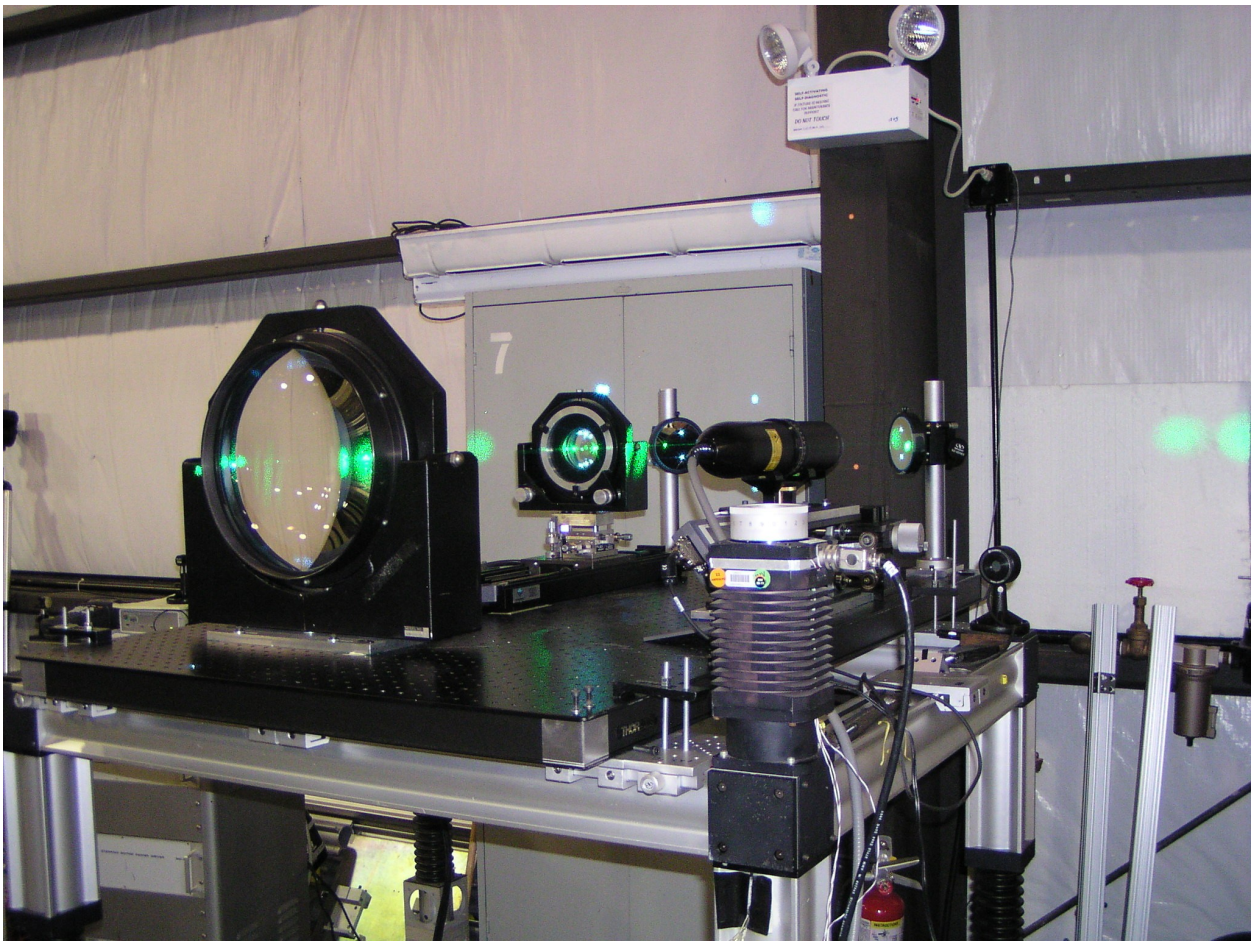

Figure III.1.- Upgraded laser velocimeter optical system installed in BART.

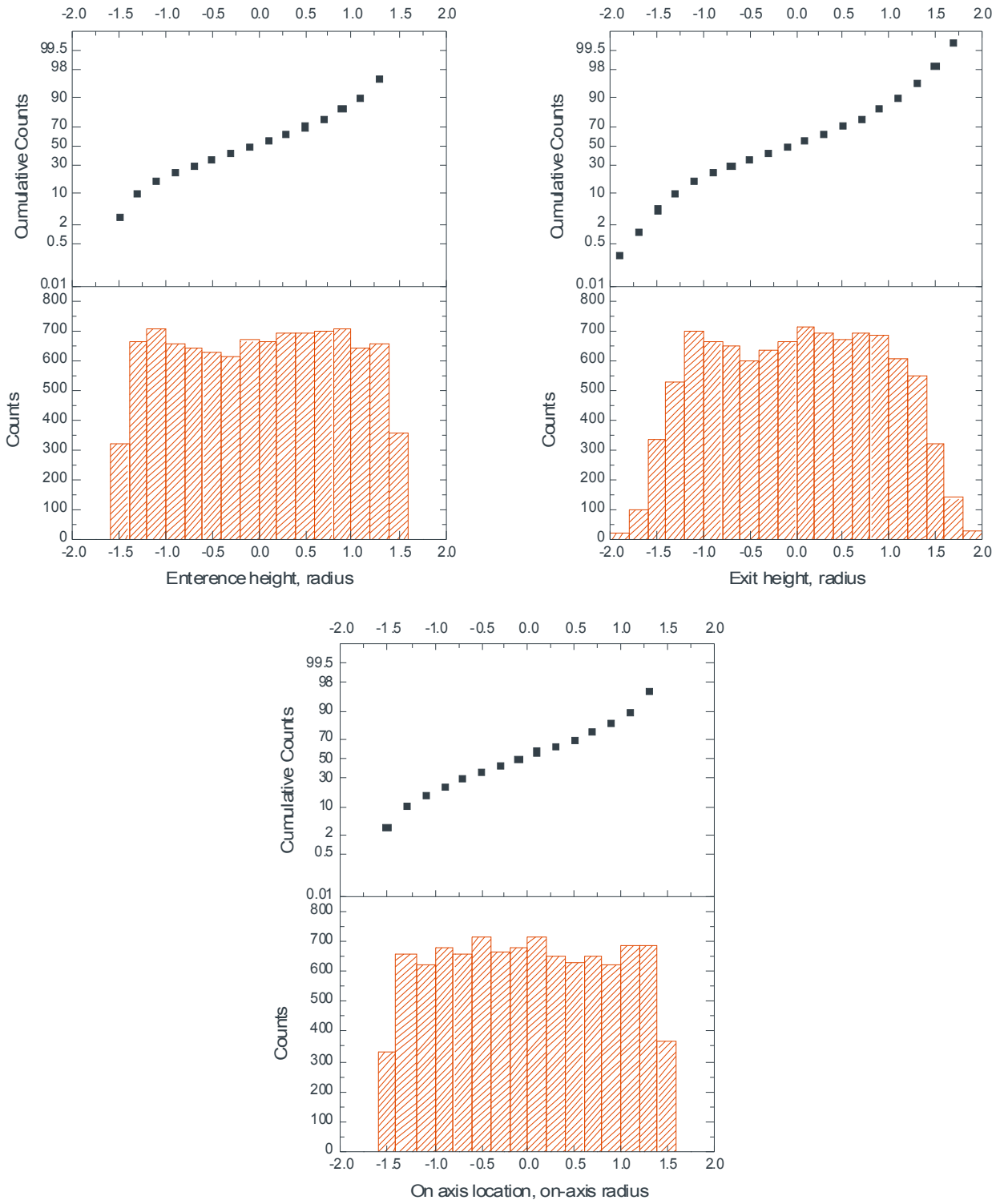

Figure III.2.- Particle injection distribution in the vertical and on-axis plane based on uniform statistics over a window defined by ±150-percent of the beam waist radius (radius defined by the $1/e^2$ power locus).

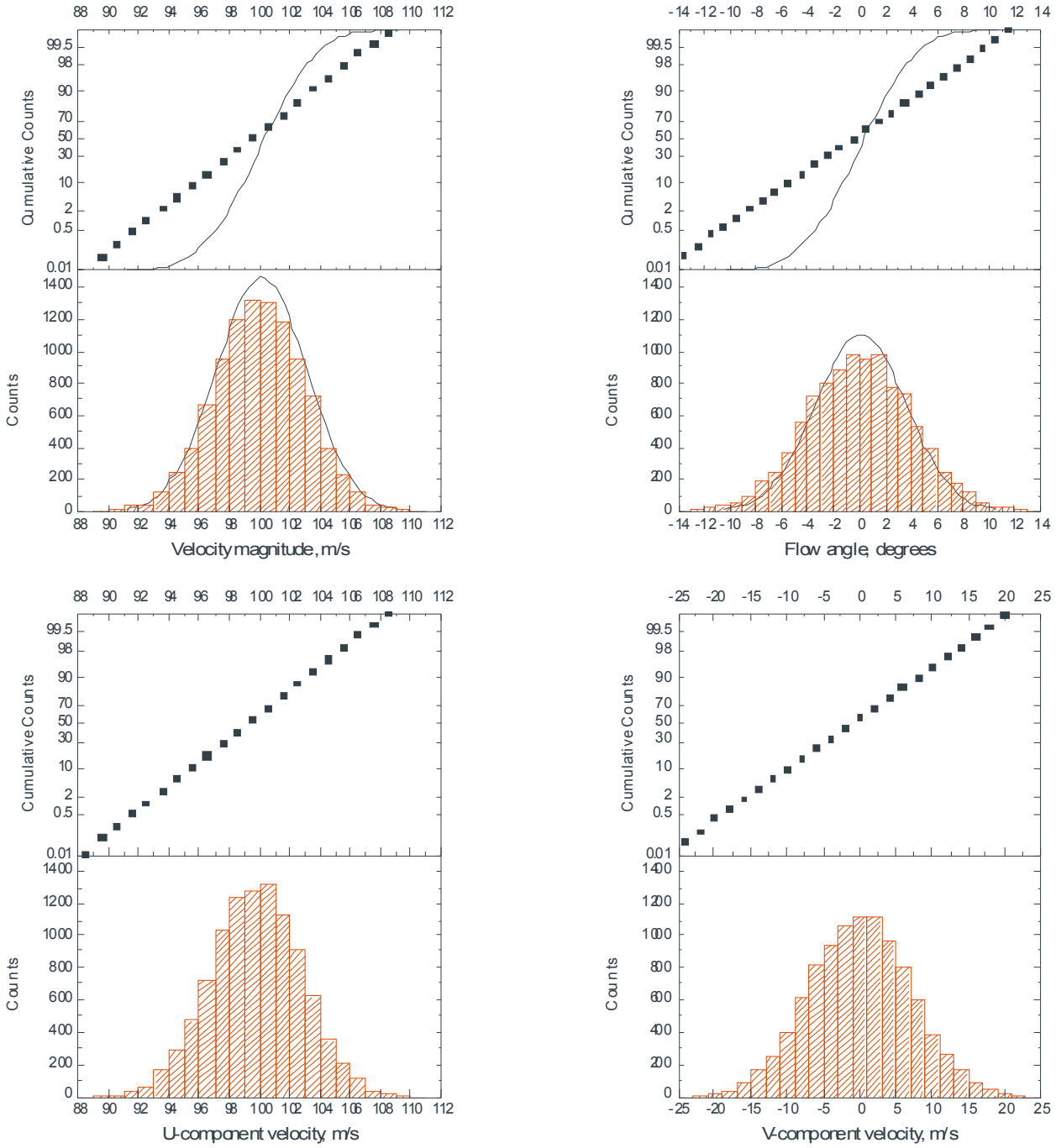

Figure III.3.- Velocity and flow angle distributions obtained by Gaussian random number selection based on the overlaid Gaussian distributions: Velocity magnitude = 100.0 m/s with a standard deviation of 3.0 m/s, and a vertical flow angle = 0.0 degrees with a standard deviation of 4.0 degrees, total number of particles = 10,000.

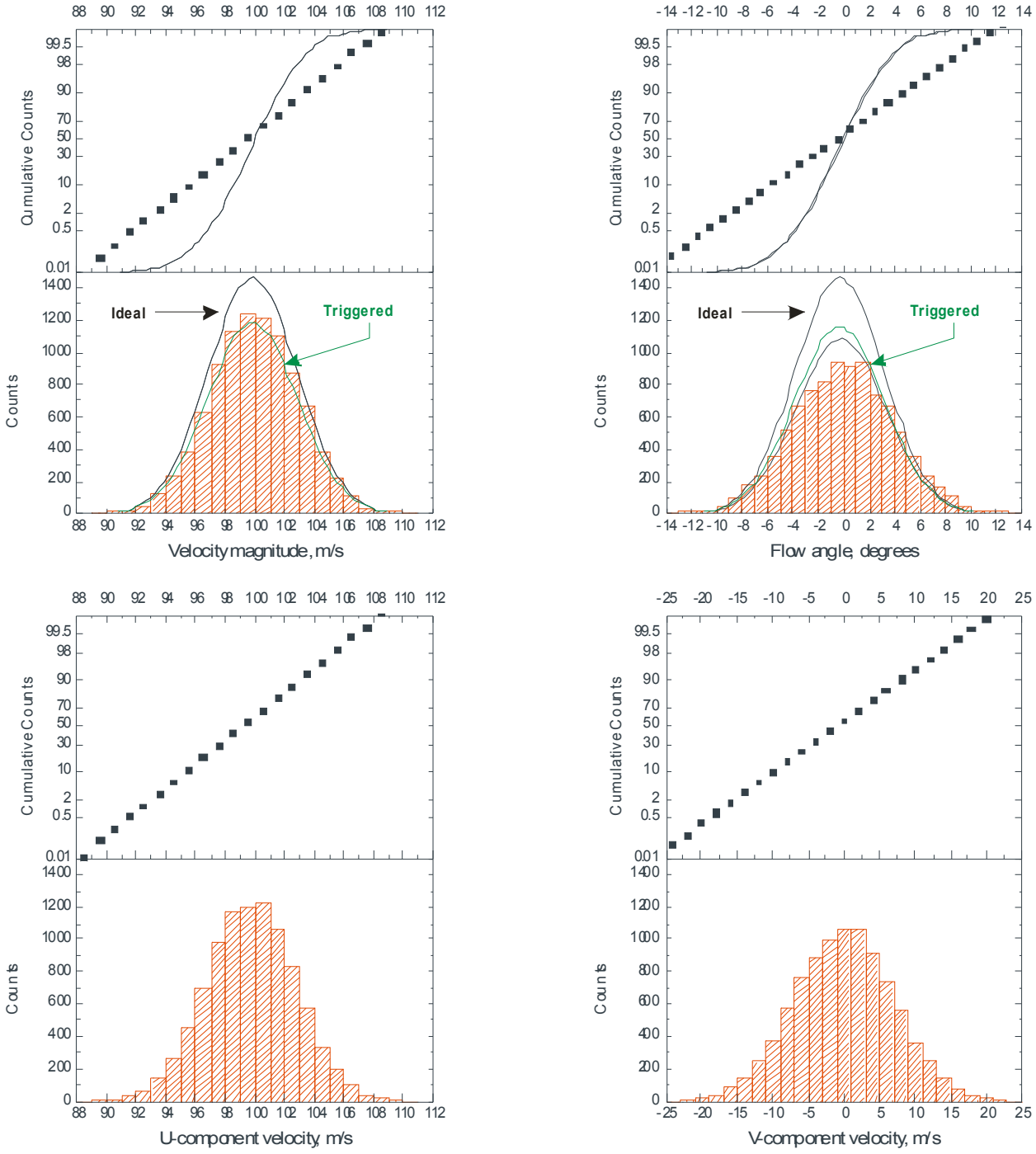

Figure III.4.- Velocity and flow angle distributions from particles with sufficient signal strength to trigger the oscilloscope, total number of particles = 9382.

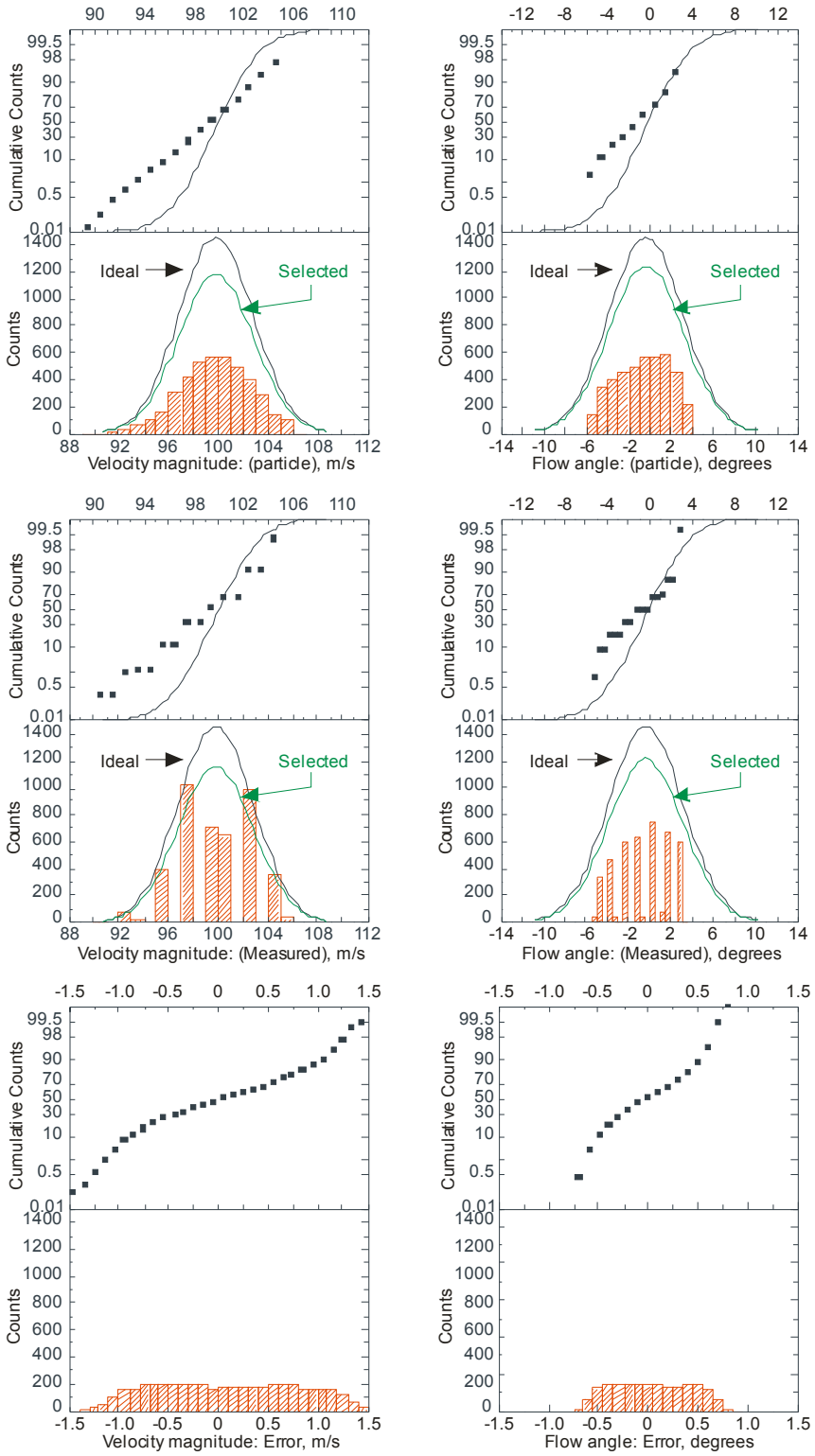

Figure III.5.- Velocity and flow angle distributions from particles that yielded velocity measurements based on the particle velocity determined by the peak signal frequency, total number of particles = 4264.

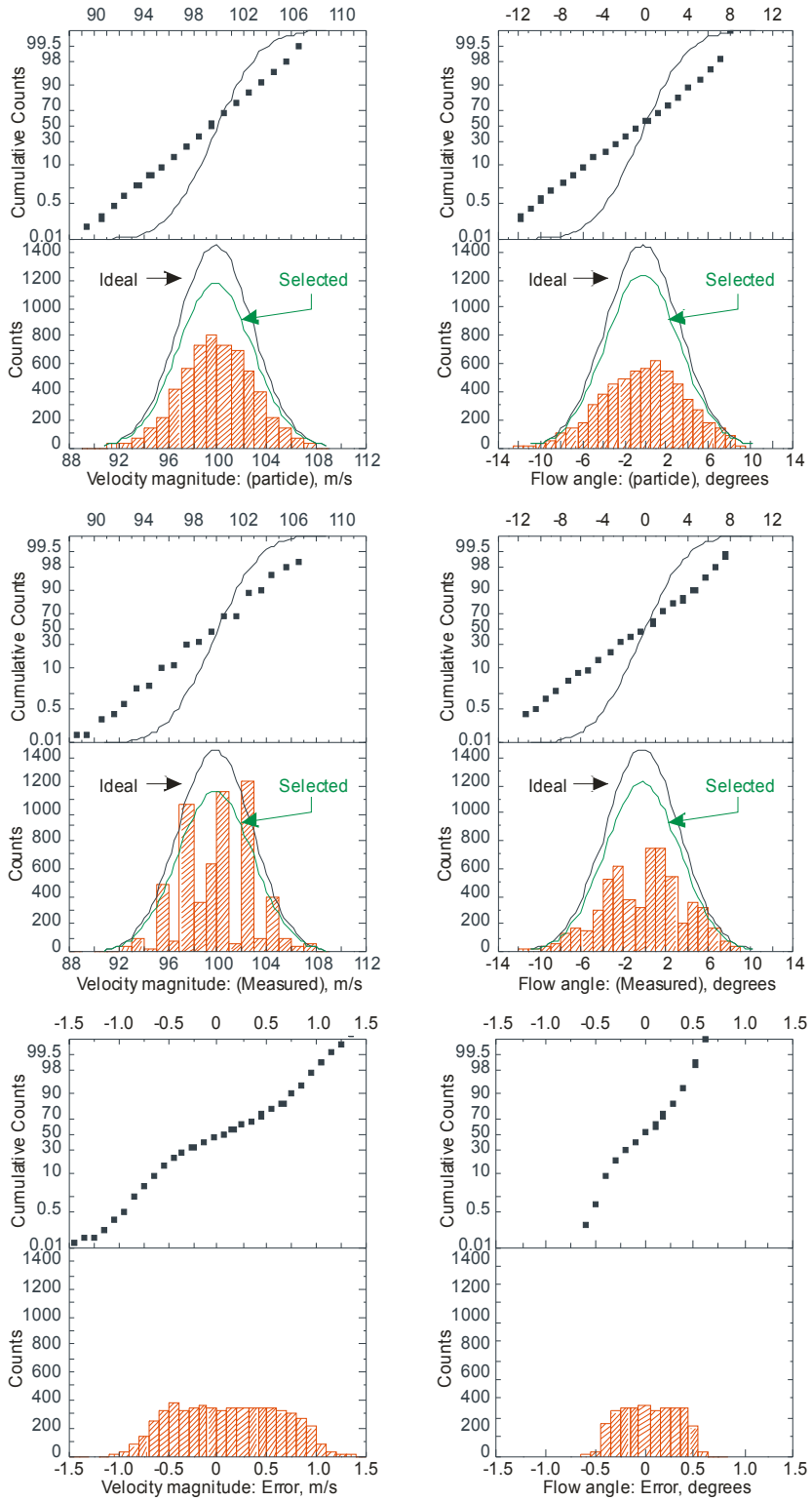

Figure III.6.- Velocity and flow angle distributions from particles that yielded velocity measurements based on the particle velocity determined by a Gaussian fit of the peak signal frequency, total number of particles = 5909.

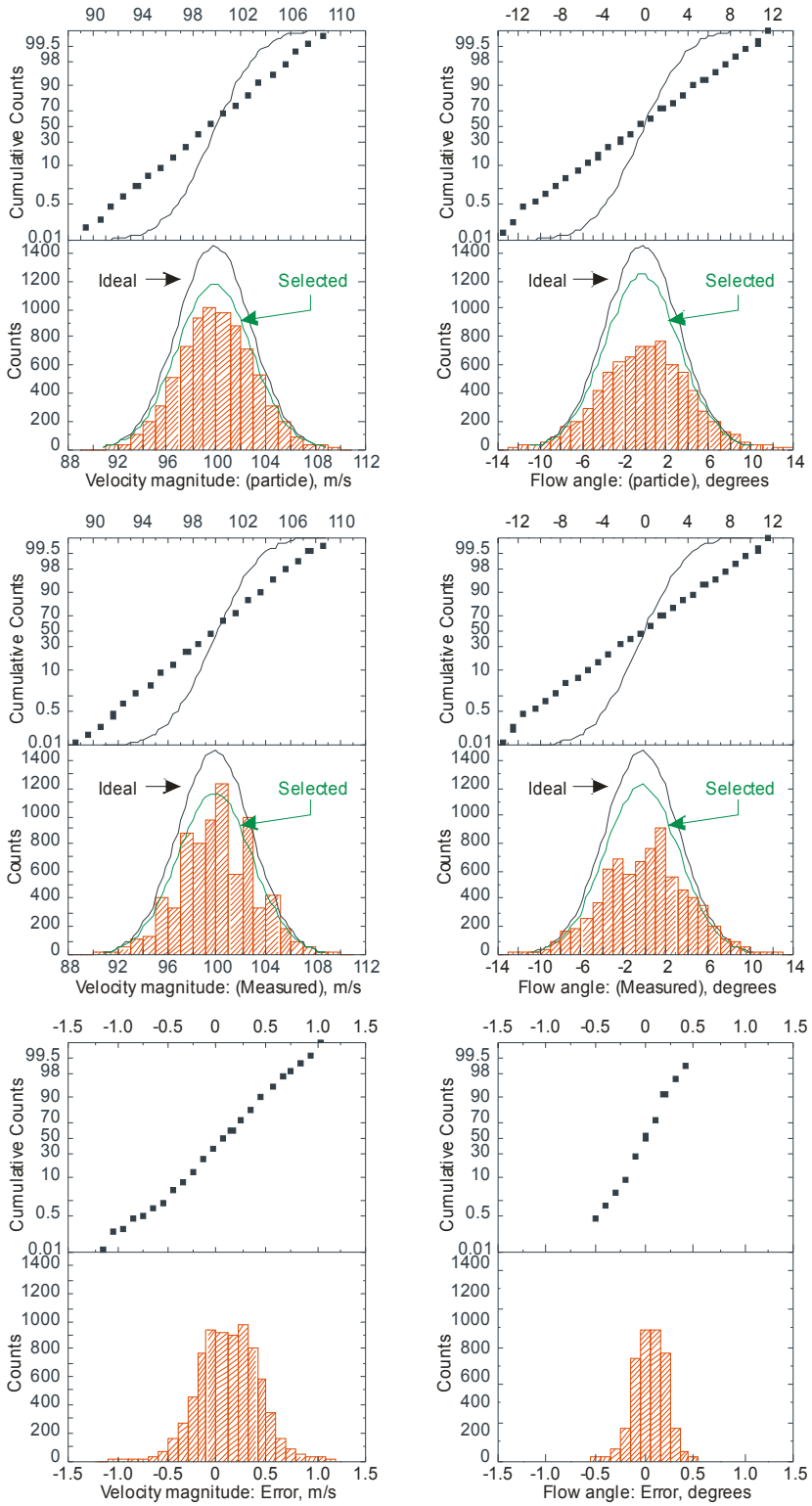

Figure III.7.- Velocity and flow angle distributions from particles that yielded velocity measurements based on the particle velocity determined by 3-bin histogram average of the peak signal frequency, total number of particles = 7633.

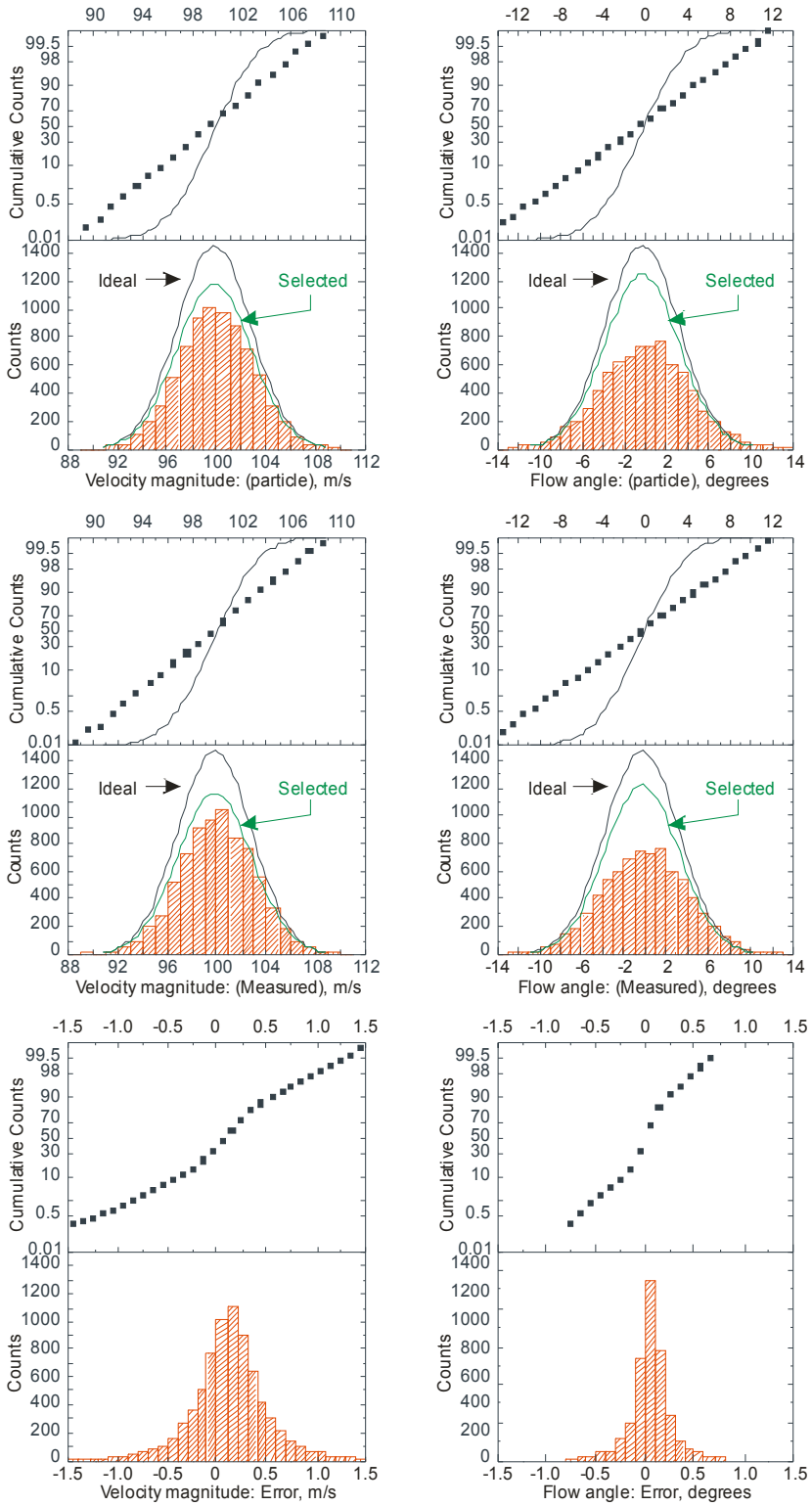

Figure III.8.-Velocity and flow angle distributions from particles that yielded velocity measurements based on the particle velocity determined by 5-bin histogram average of the peak signal frequency, total number of particles = 7633.

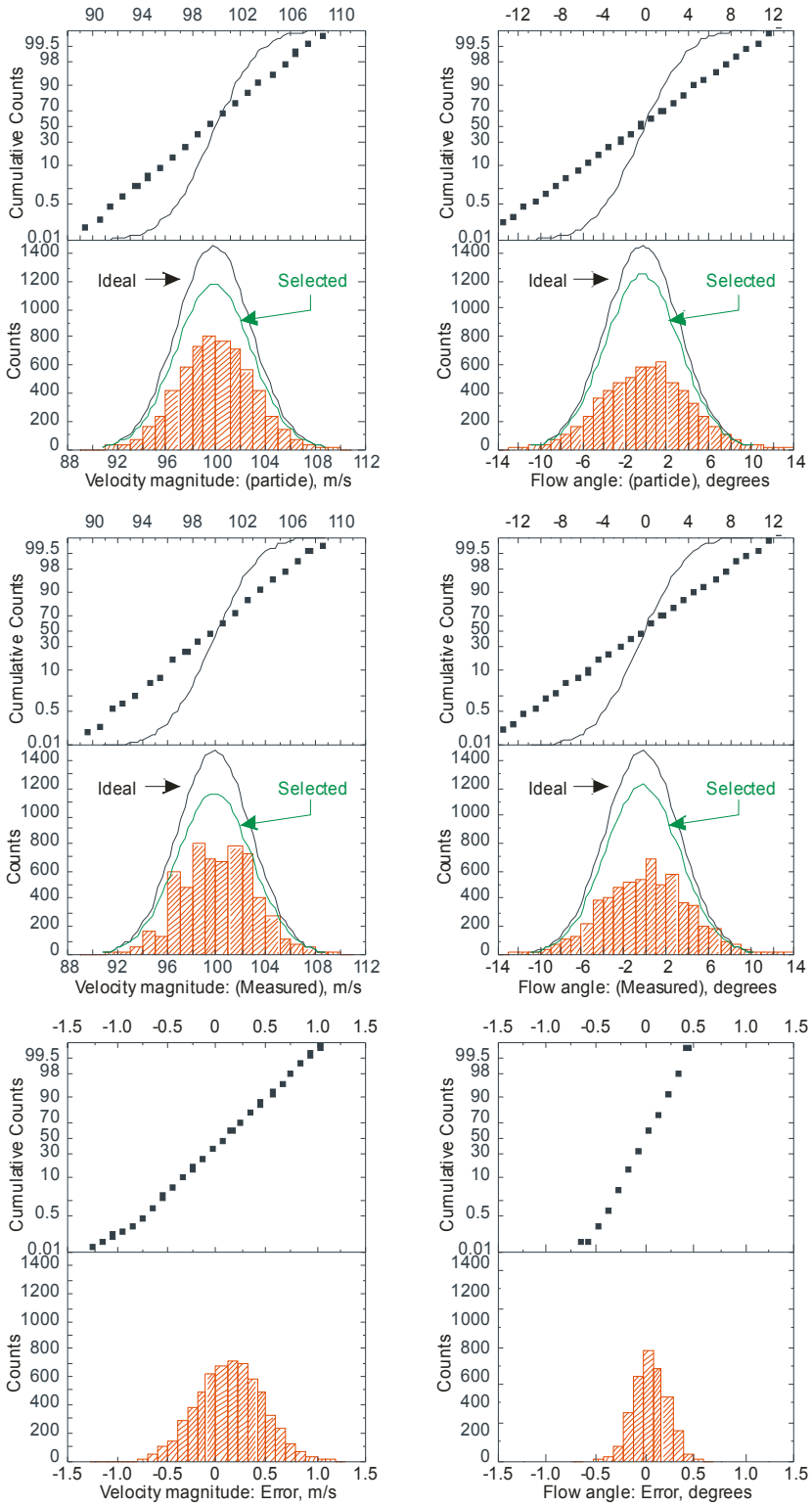

Figure III.9.- Velocity and flow angle distributions from particles that yielded velocity measurements based on the particle velocity determined by half power average of the peak signal frequency, total number of particles = 6040.

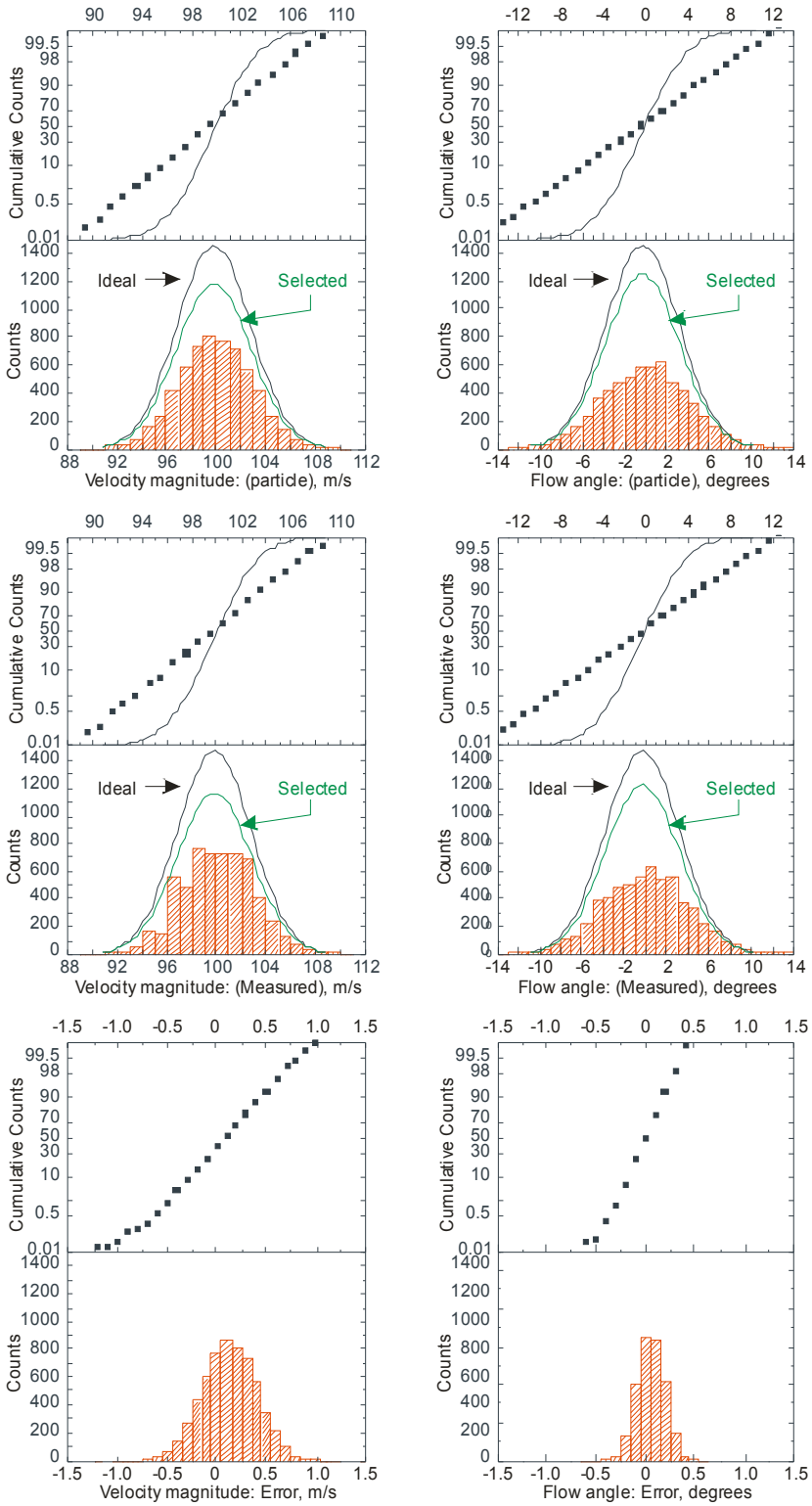

Figure III.10.- Velocity and flow angle distributions from particles that yielded velocity measurements based on the particle velocity determined by interpolated half power average of the peak signal frequency, total number of particles = 6040.

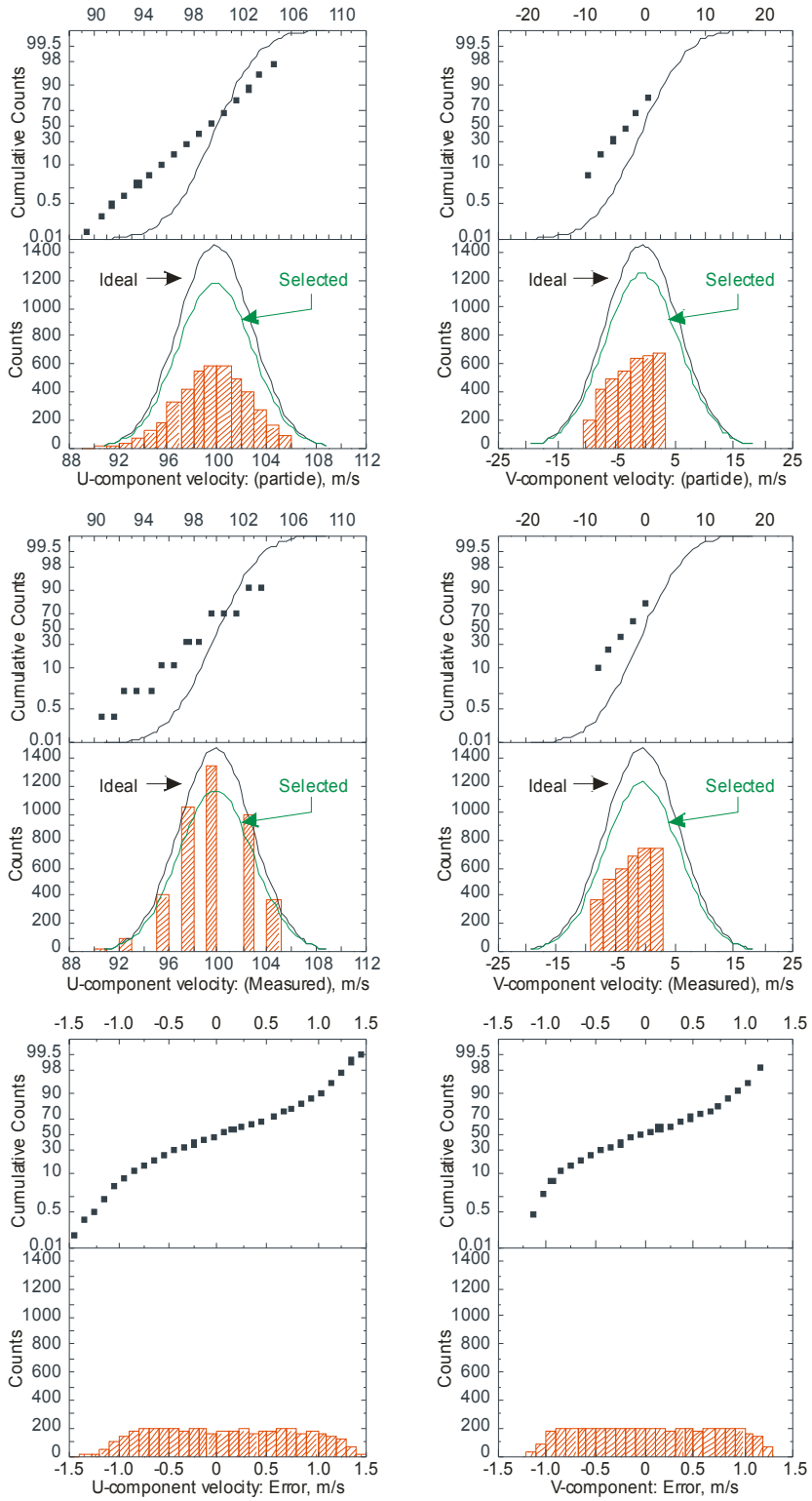

Figure III.11.- U- and V-component distributions from particles that yielded velocity measurements based on the particle velocity determined by the peak signal frequency, total number of particles = 4264.

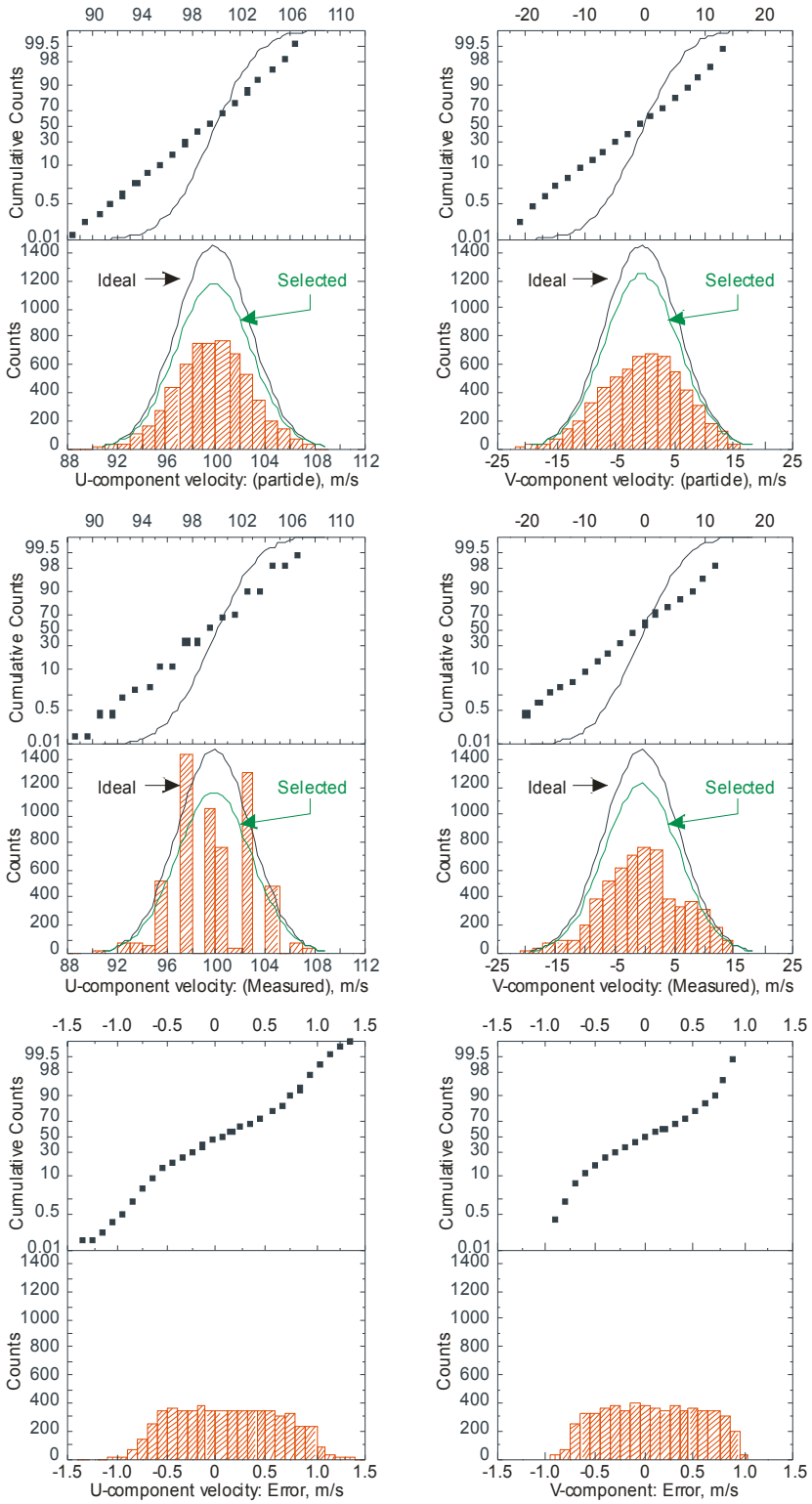

Figure III.12.- U- and V-component distributions from particles that yielded velocity measurements based on the particle velocity determined by a Gaussian fit of the peak signal frequency, total number of particles = 6040.

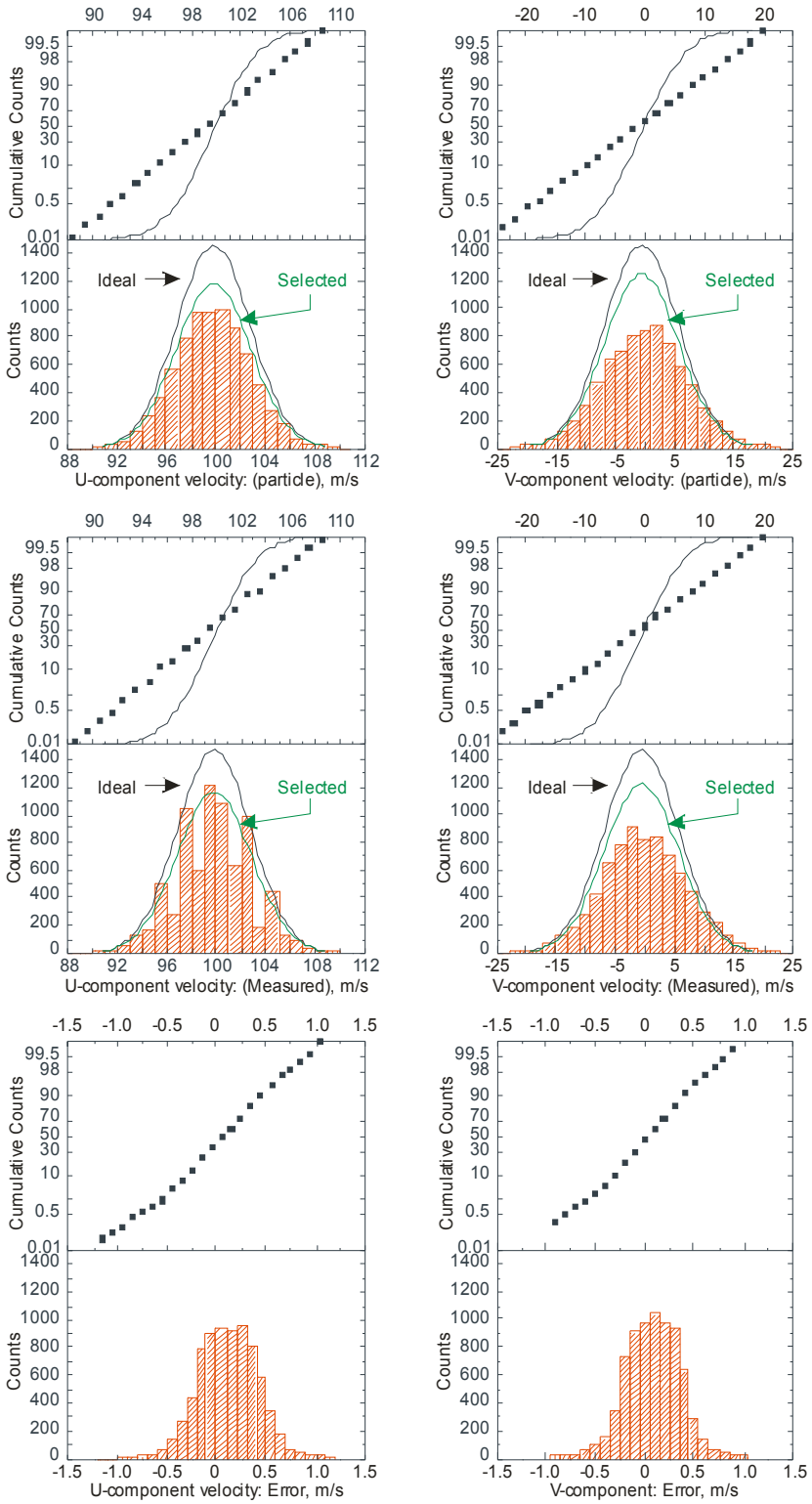

Figure III.13.- U- and V-component distributions from particles that yielded velocity measurements based on the particle velocity determined by 3-bin histogram average of the peak signal frequency, total number of particles = 7633.

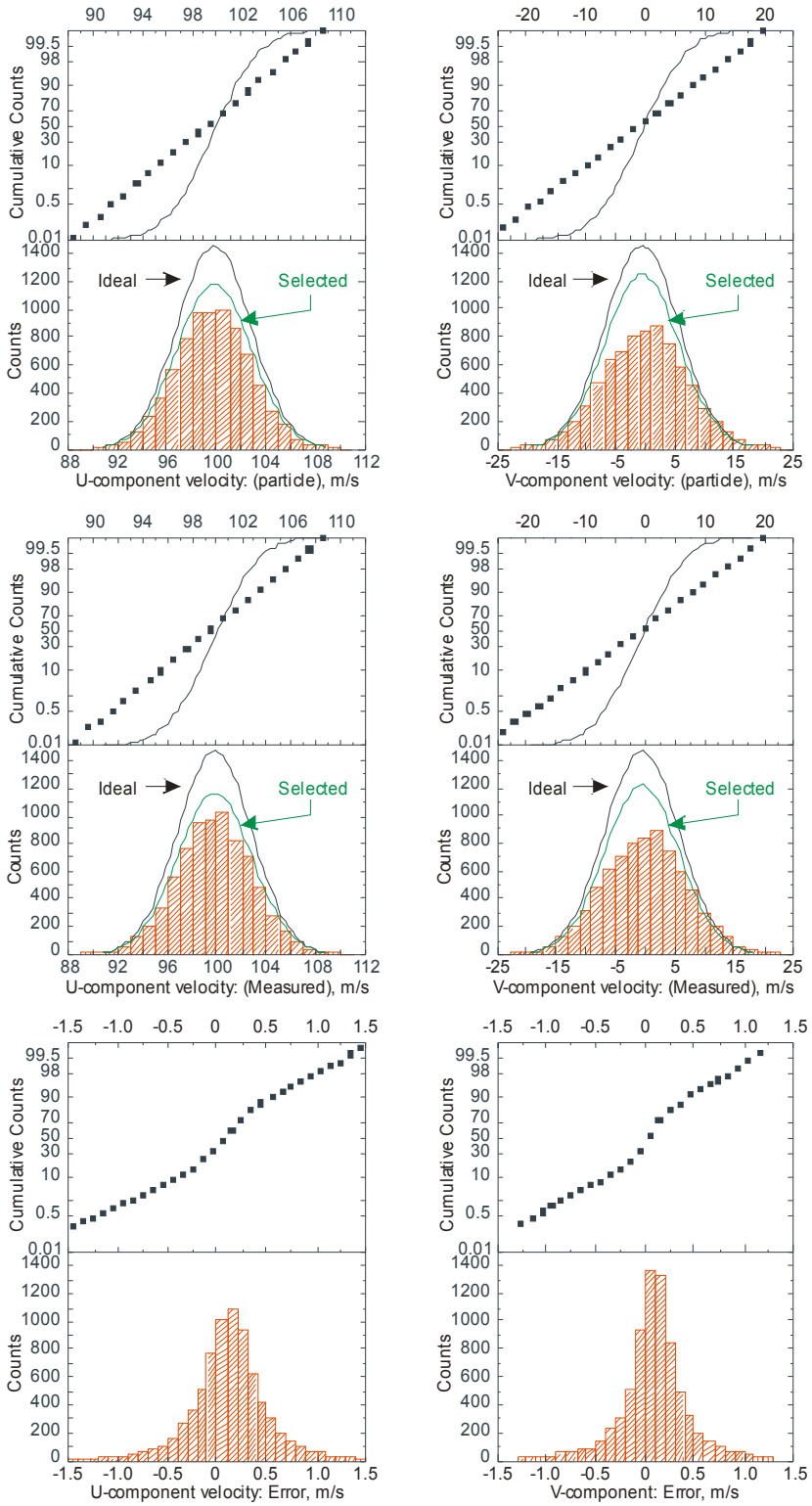

Figure III.14.- U- and V-component distributions from particles that yielded velocity measurements based on the particle velocity determined by 5-bin histogram average of the peak signal frequency, total number of particles = 7633.

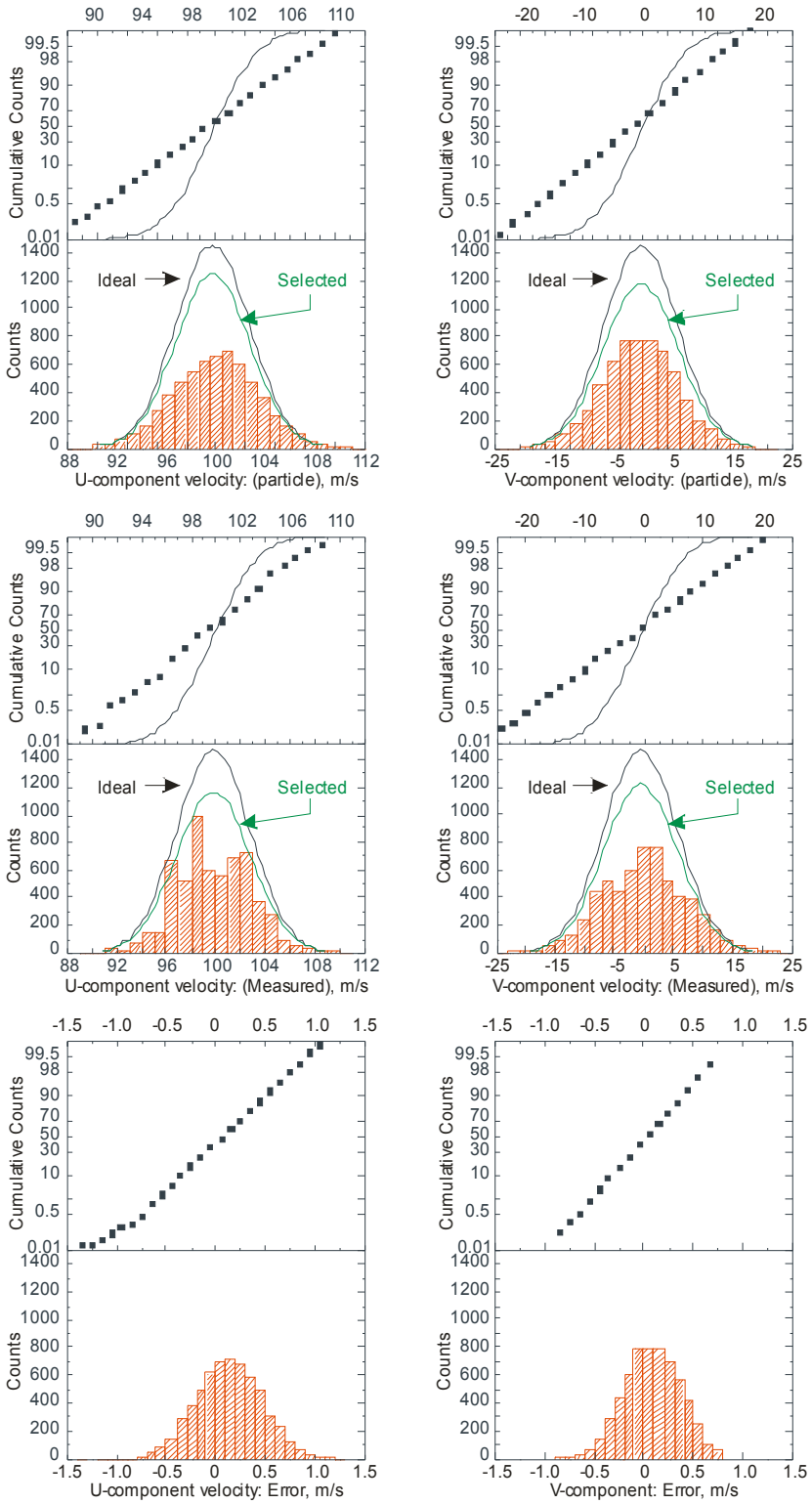

Figure III.15.- U- and V-component distributions from particles that yielded velocity measurements based on the particle velocity determined by half power average of the peak signal frequency, total number of particles = 6040.

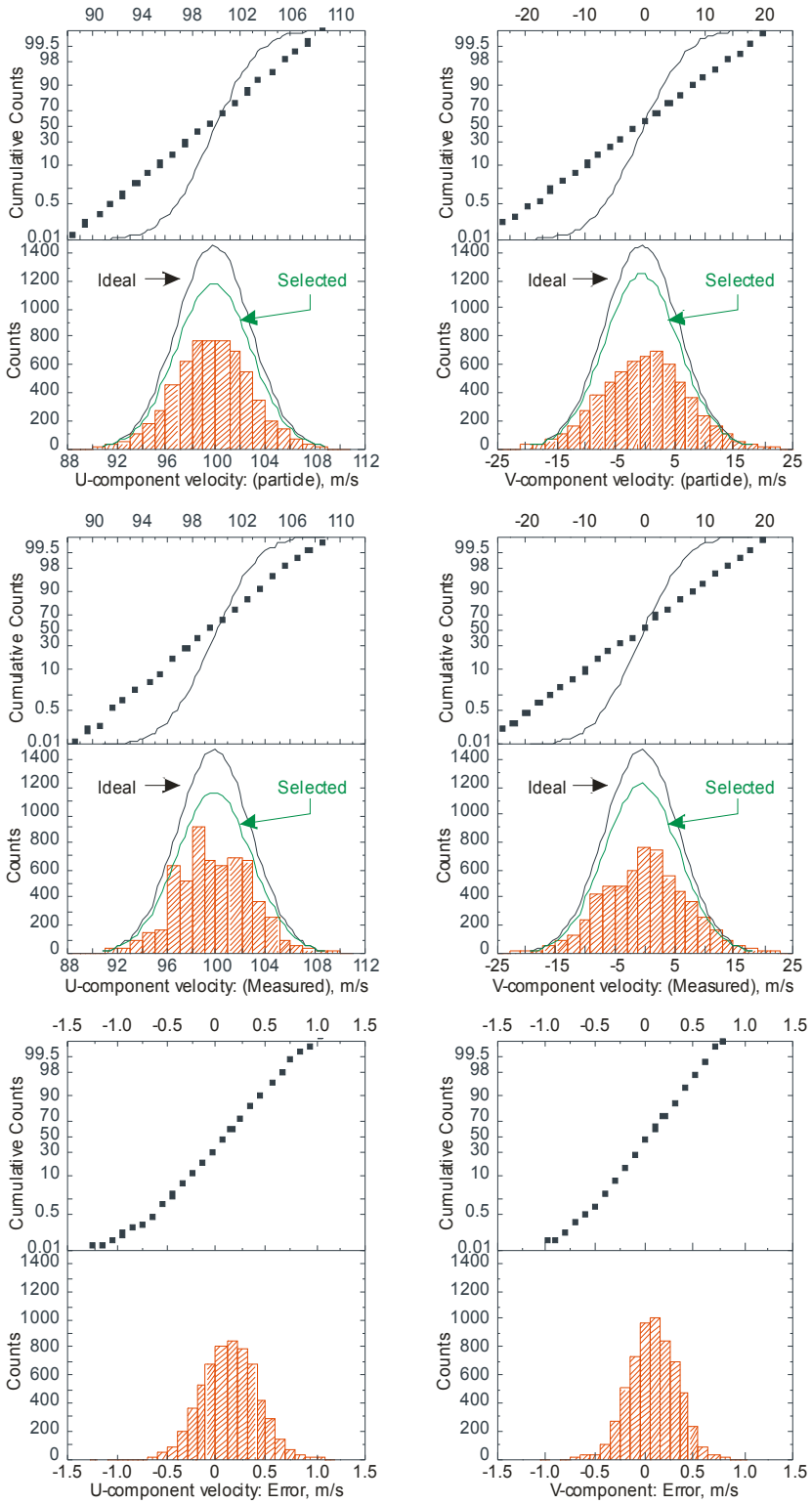

Figure III.16.- U- and V-component distributions from particles that yielded velocity measurements based on the particle velocity determined by interpolated half power average of the peak signal frequency, total number of particles = 6040.

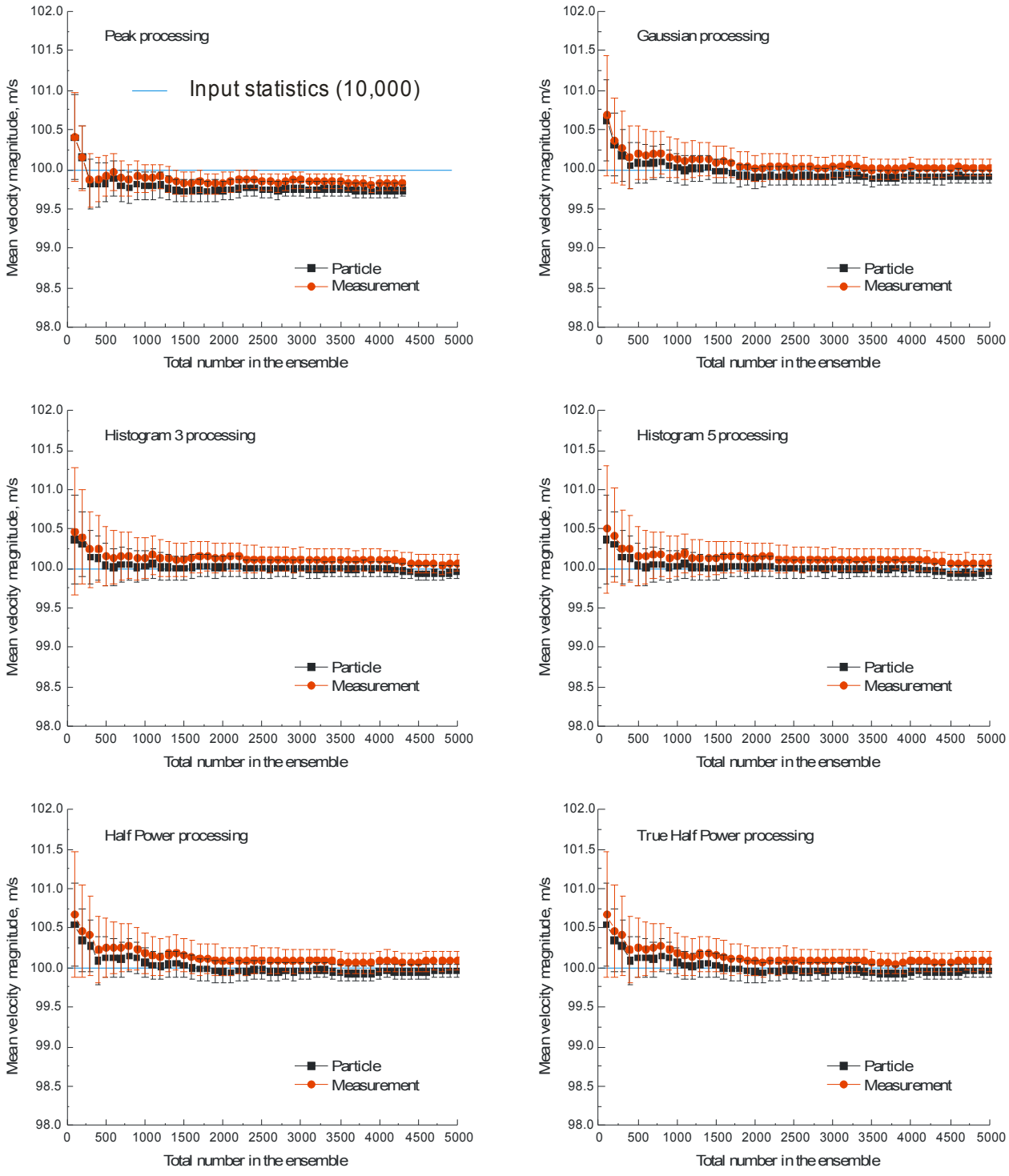

Figure III.17.- Statistical convergence of the mean velocity magnitude based on the six signal processing schemes.

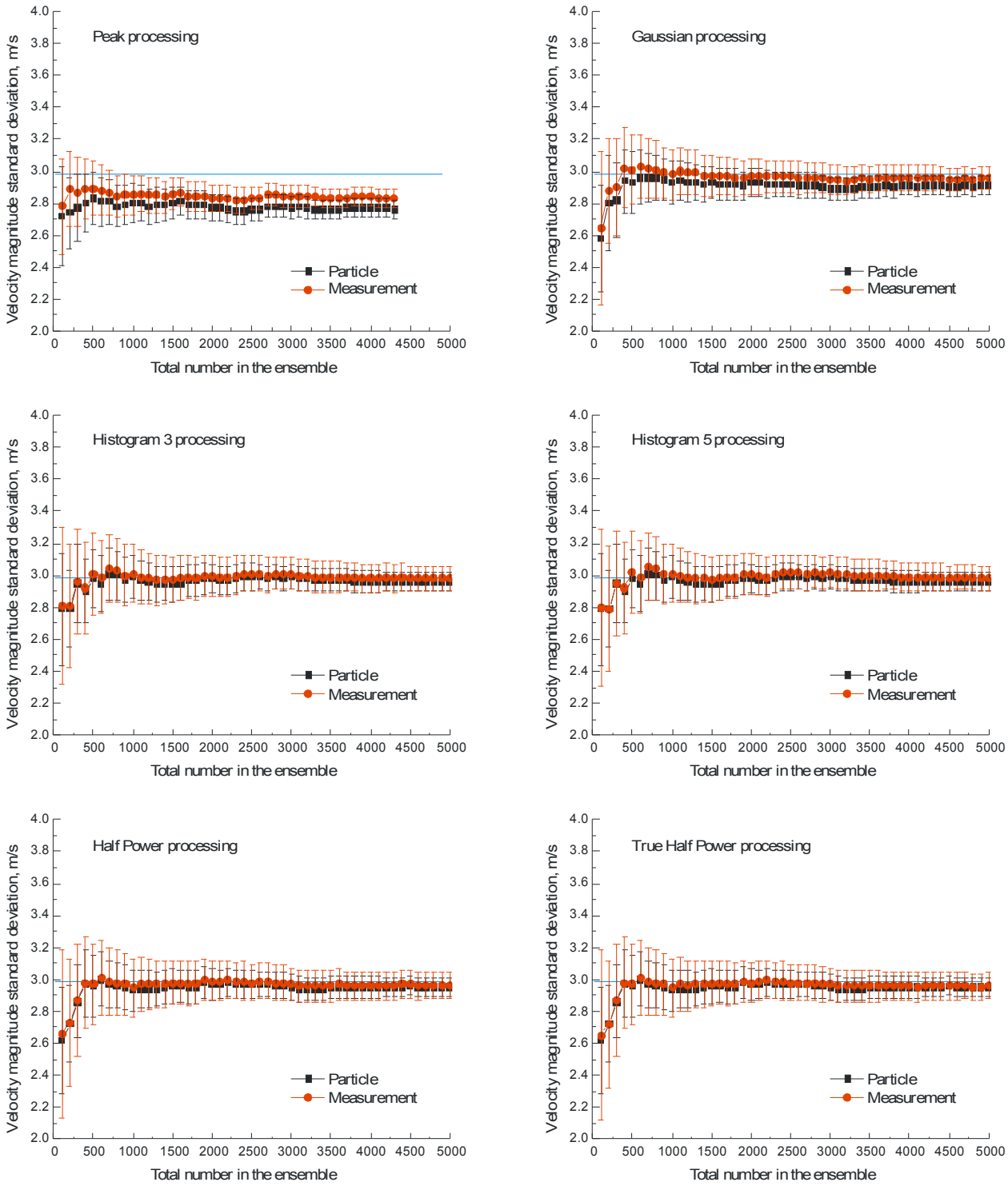

Figure III.18.- Statistical convergence of the velocity magnitude standard deviation based on the six signal processing schemes.

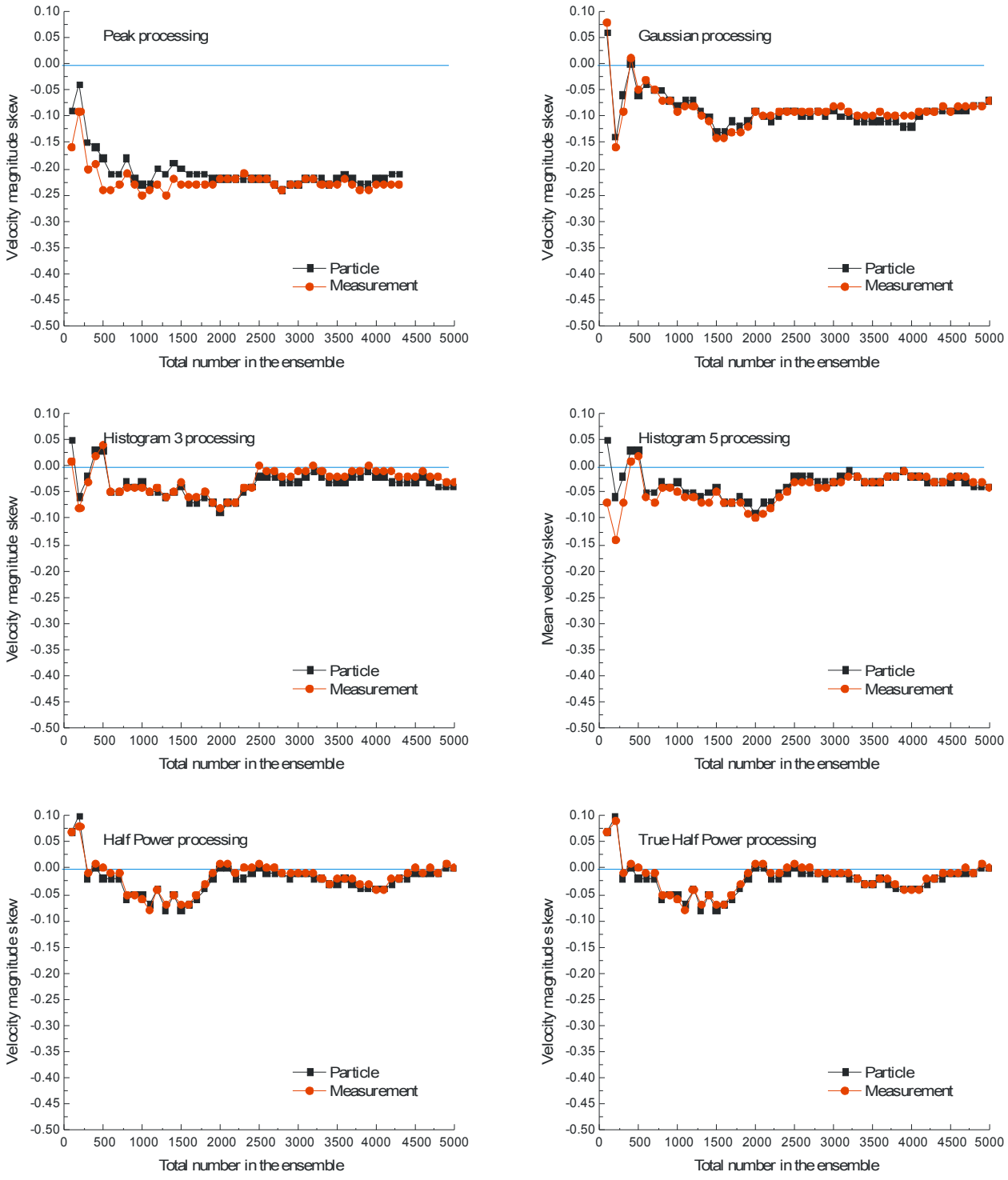

Figure III.19.- Statistical convergence of the velocity magnitude skew based on the six signal processing schemes.

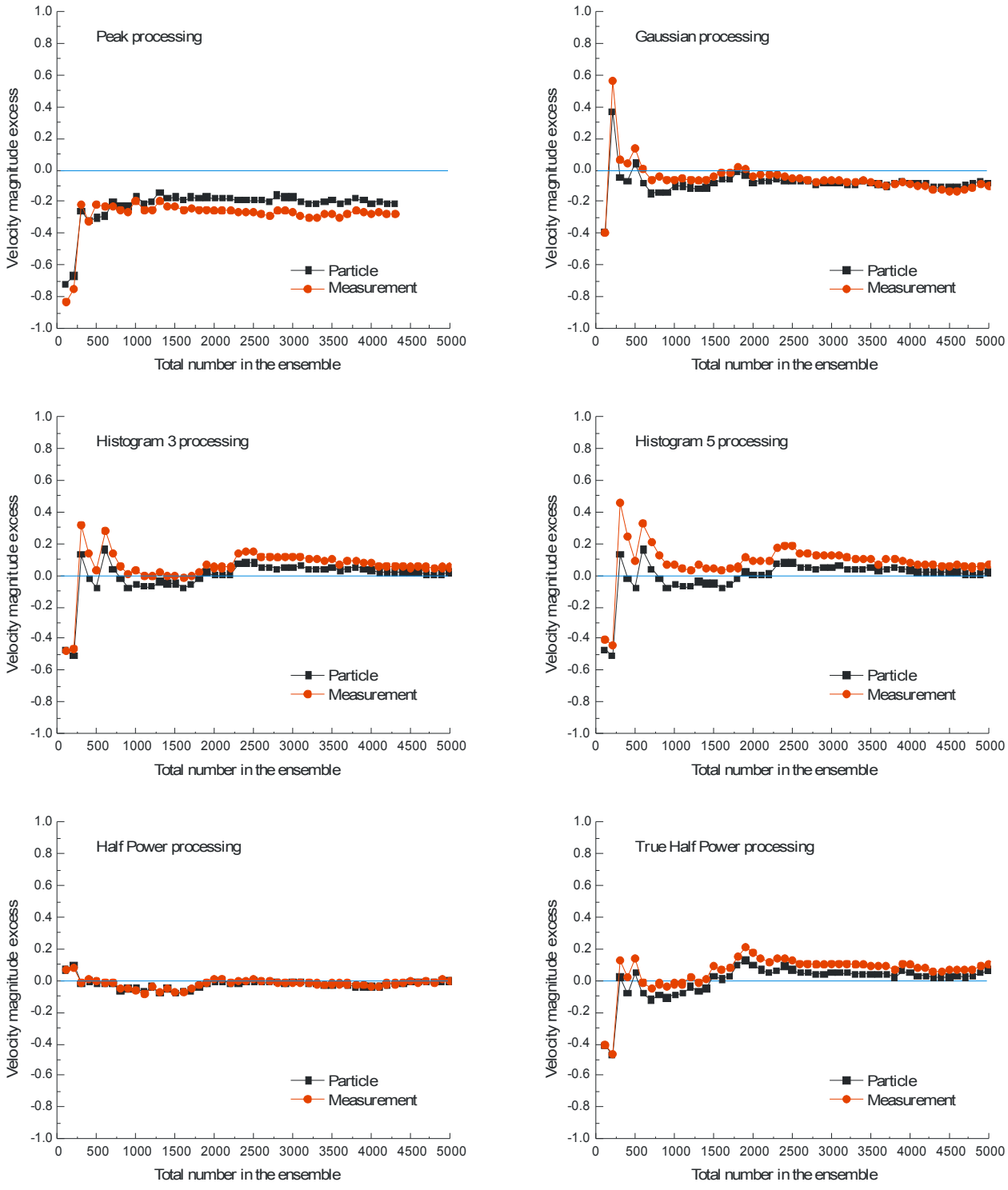

Figure III.20.- Statistical convergence of the velocity magnitude excess based on the six signal processing schemes.

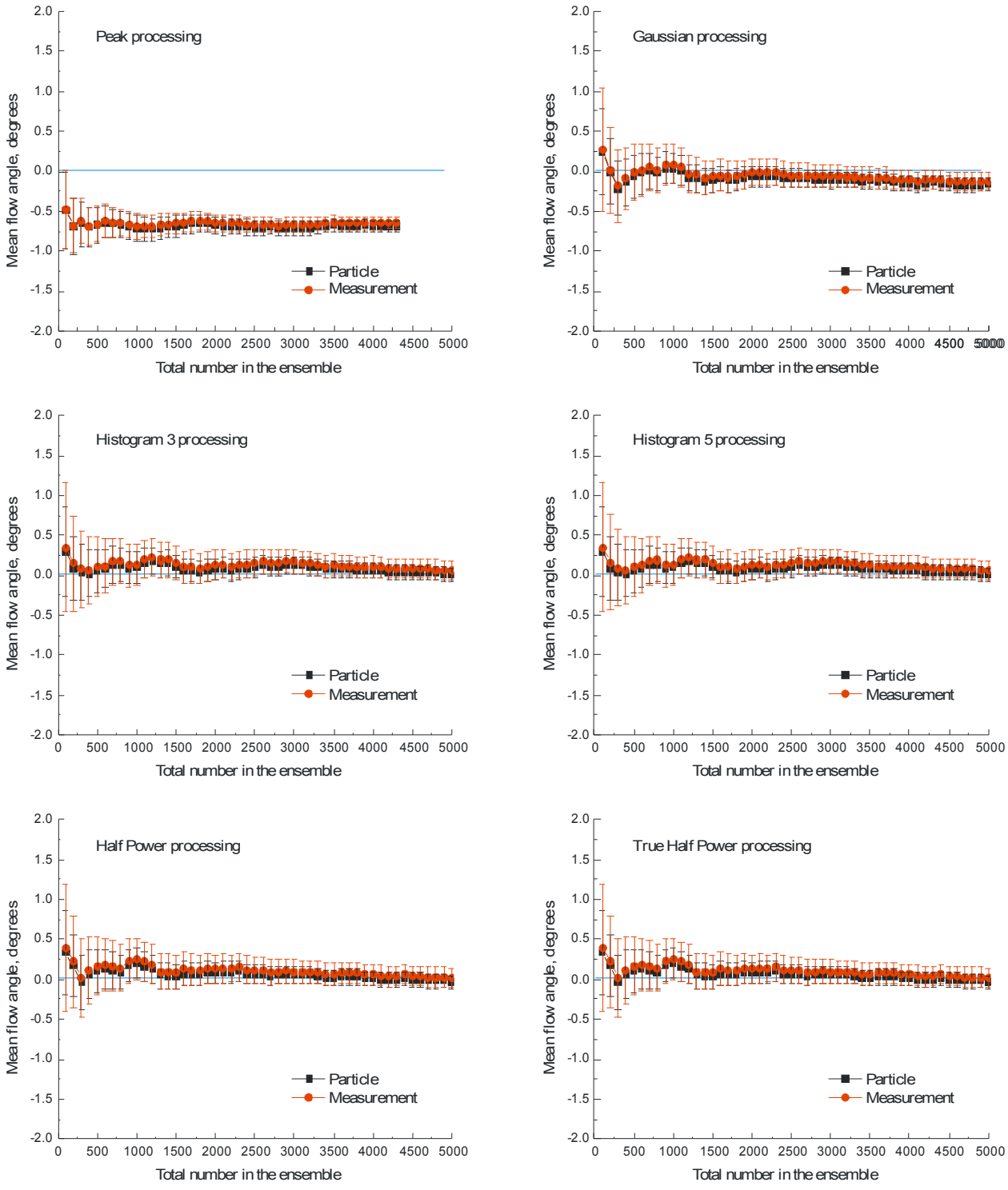

Figure III.21.- Statistical convergence of the mean flow angle based on the six signal processing schemes.

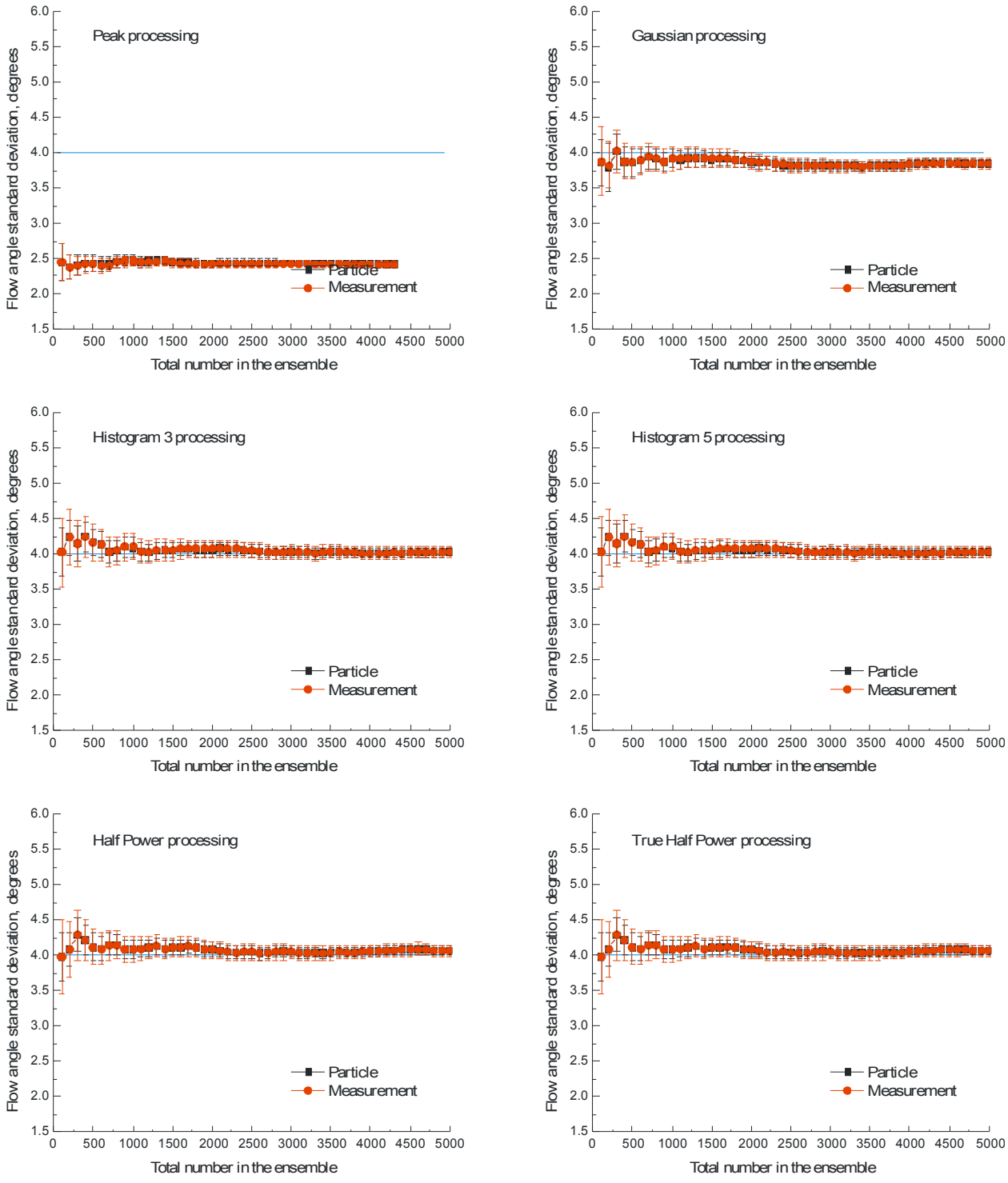

Figure III.22.- Statistical convergence of the flow angle standard deviation based on the six signal processing schemes.

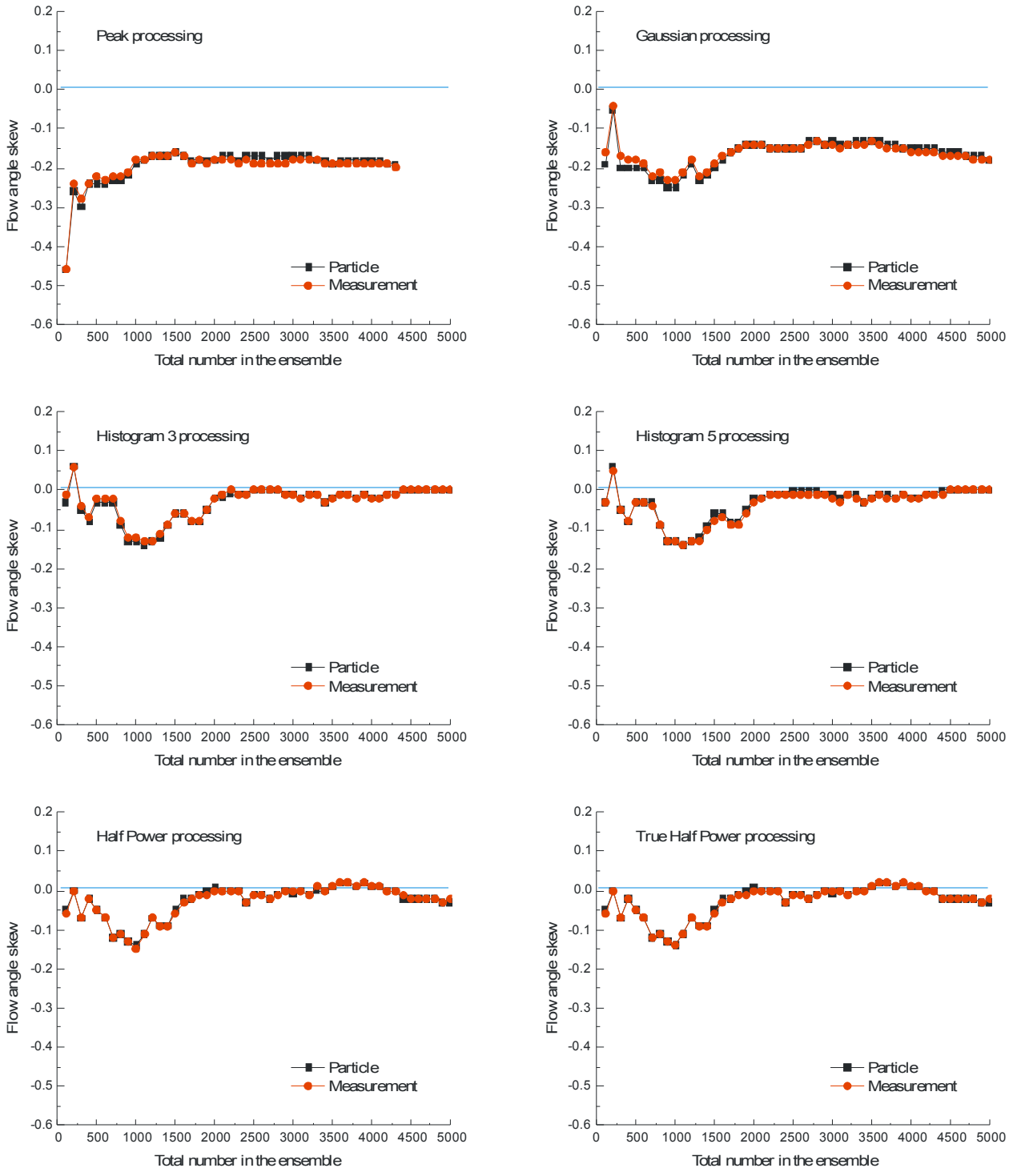

Figure III.23.- Statistical convergence of the flow angle skew based on the six signal processing schemes.

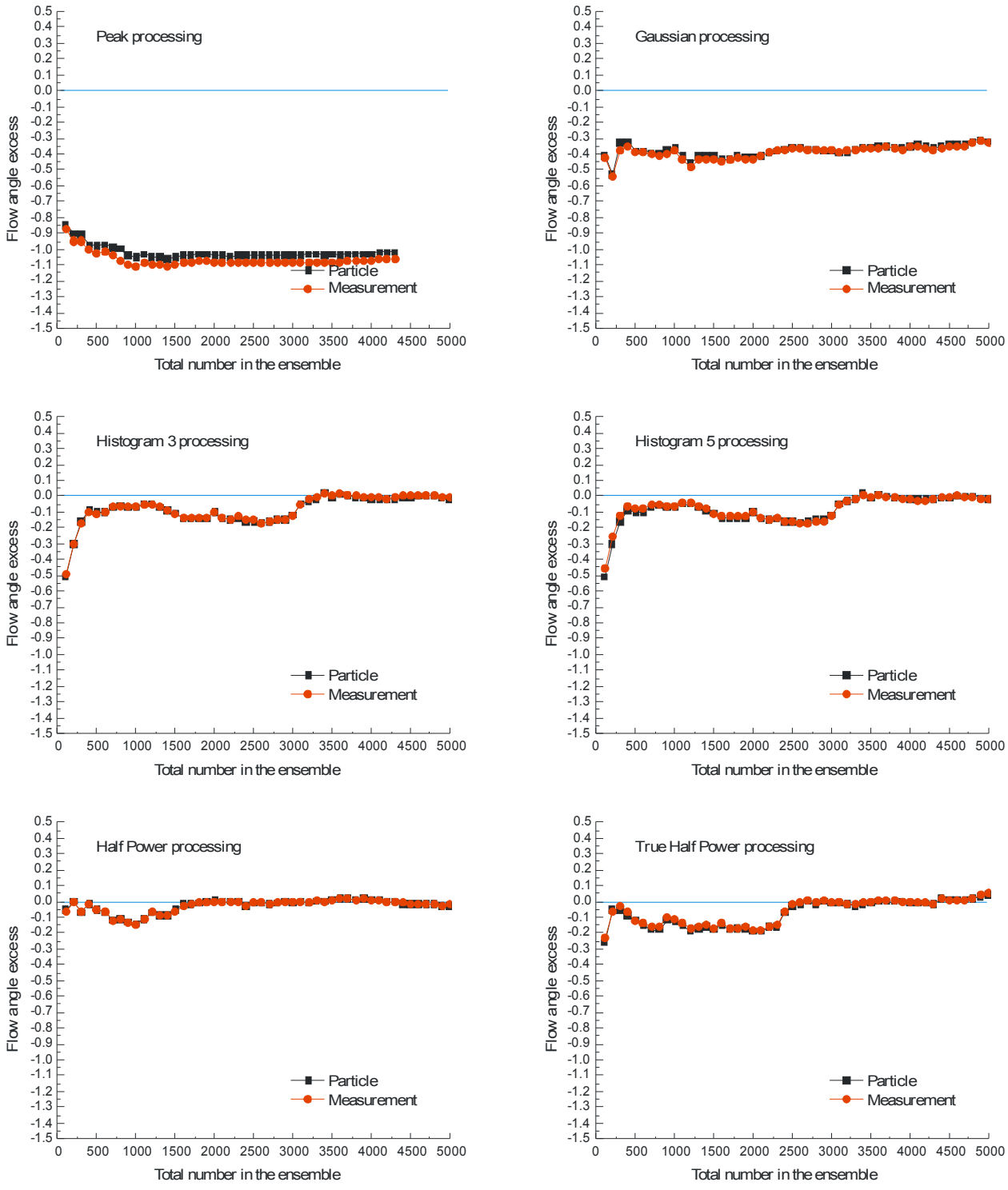

Figure III.24.- Statistical convergence of the flow angle excess based on the six signal processing schemes.

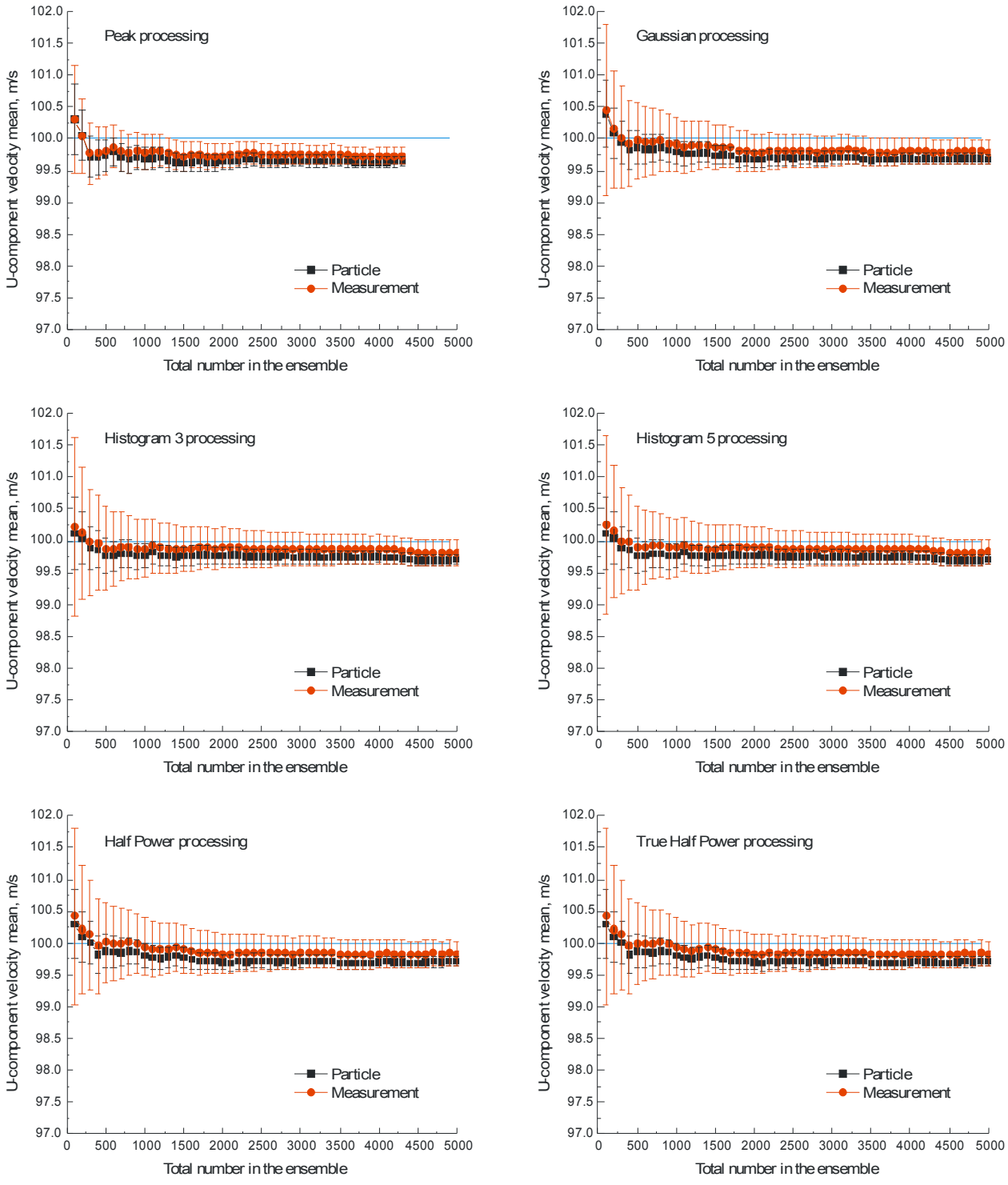

Figure III.25.- Statistical convergence of the mean U-component velocity based on the six signal processing schemes.

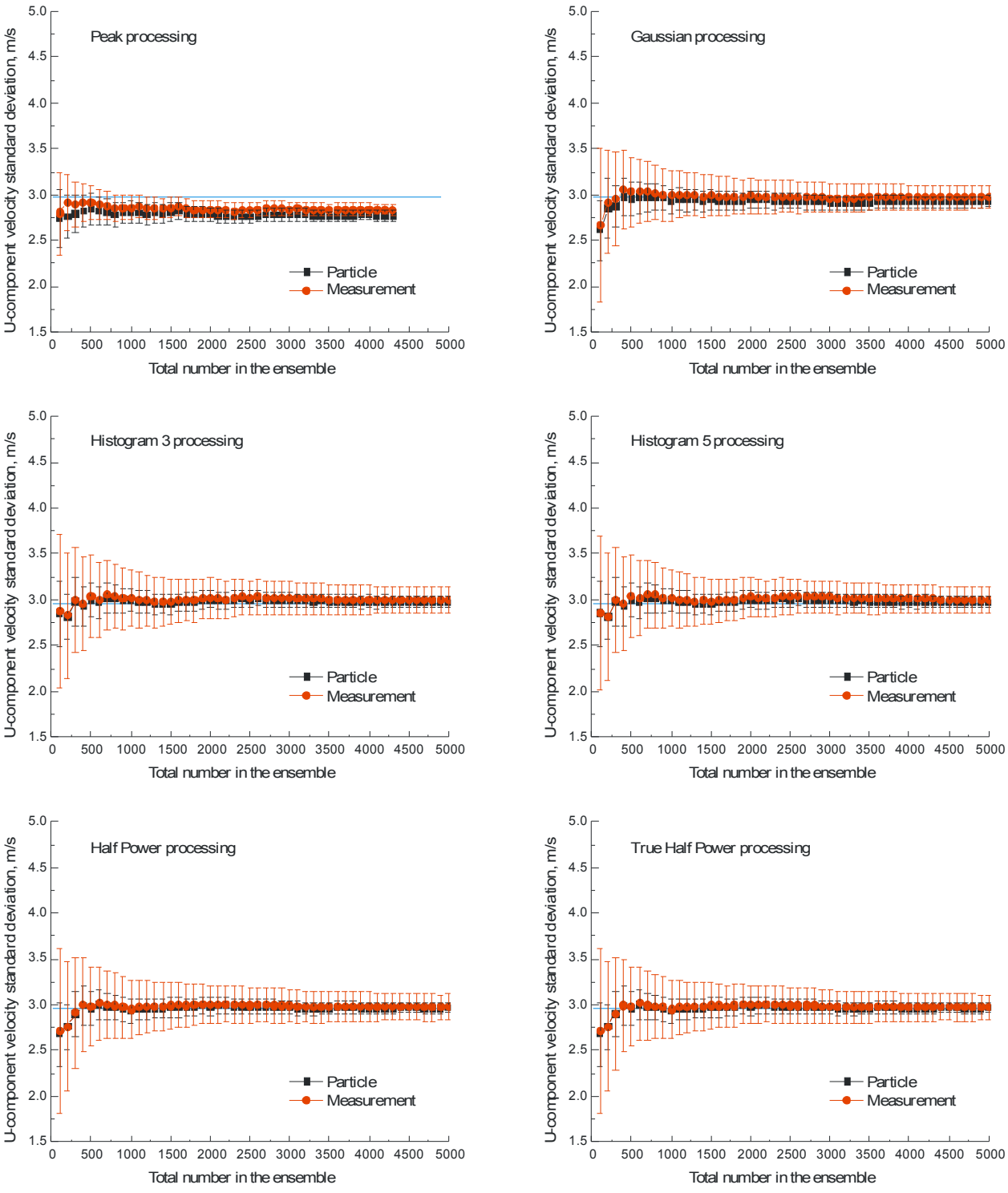

Figure III.26.- Statistical convergence of the U-component standard deviation based on the six signal processing schemes.

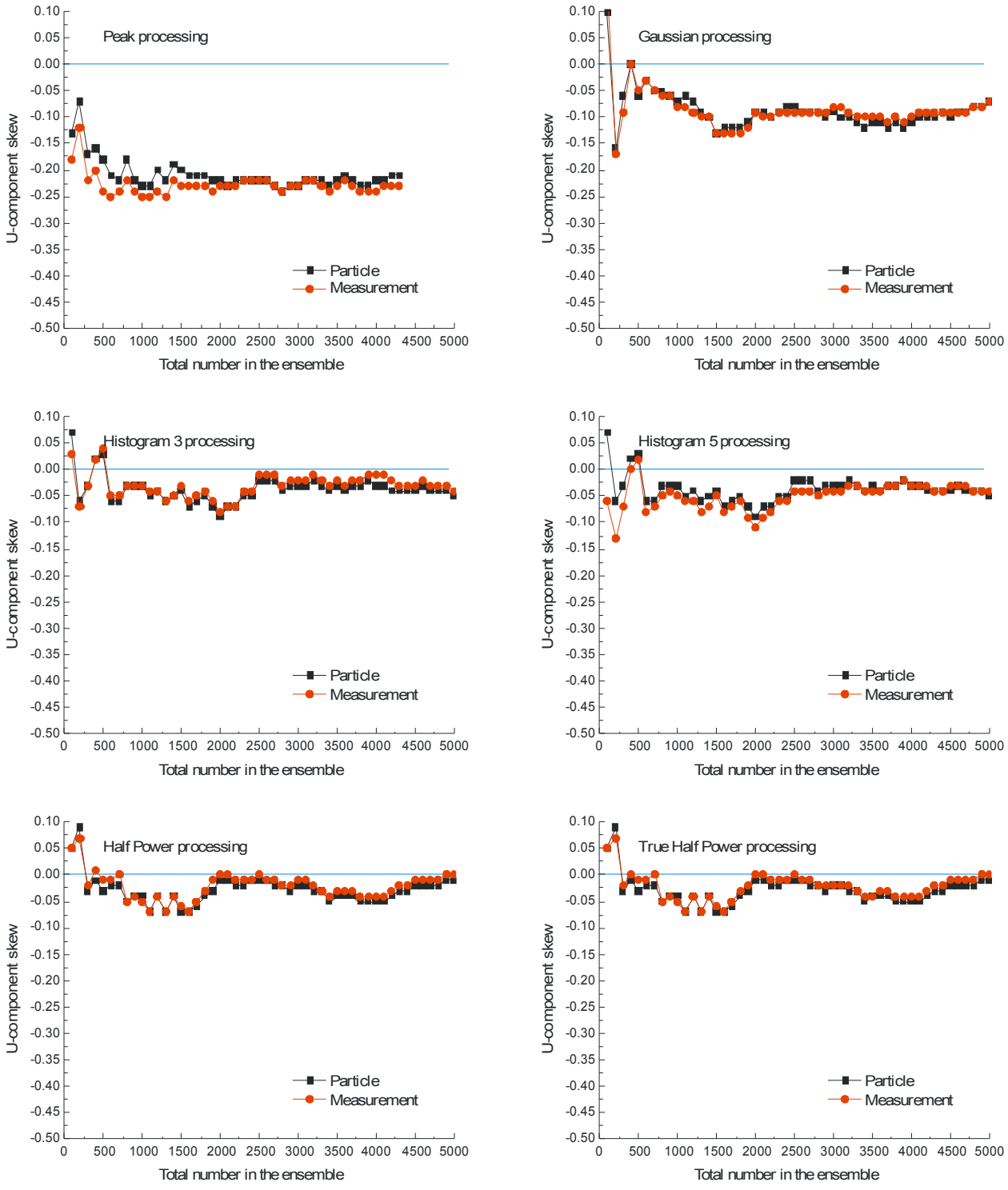

Figure III.27.- Statistical convergence of the U-component skew based on the six signal processing schemes.

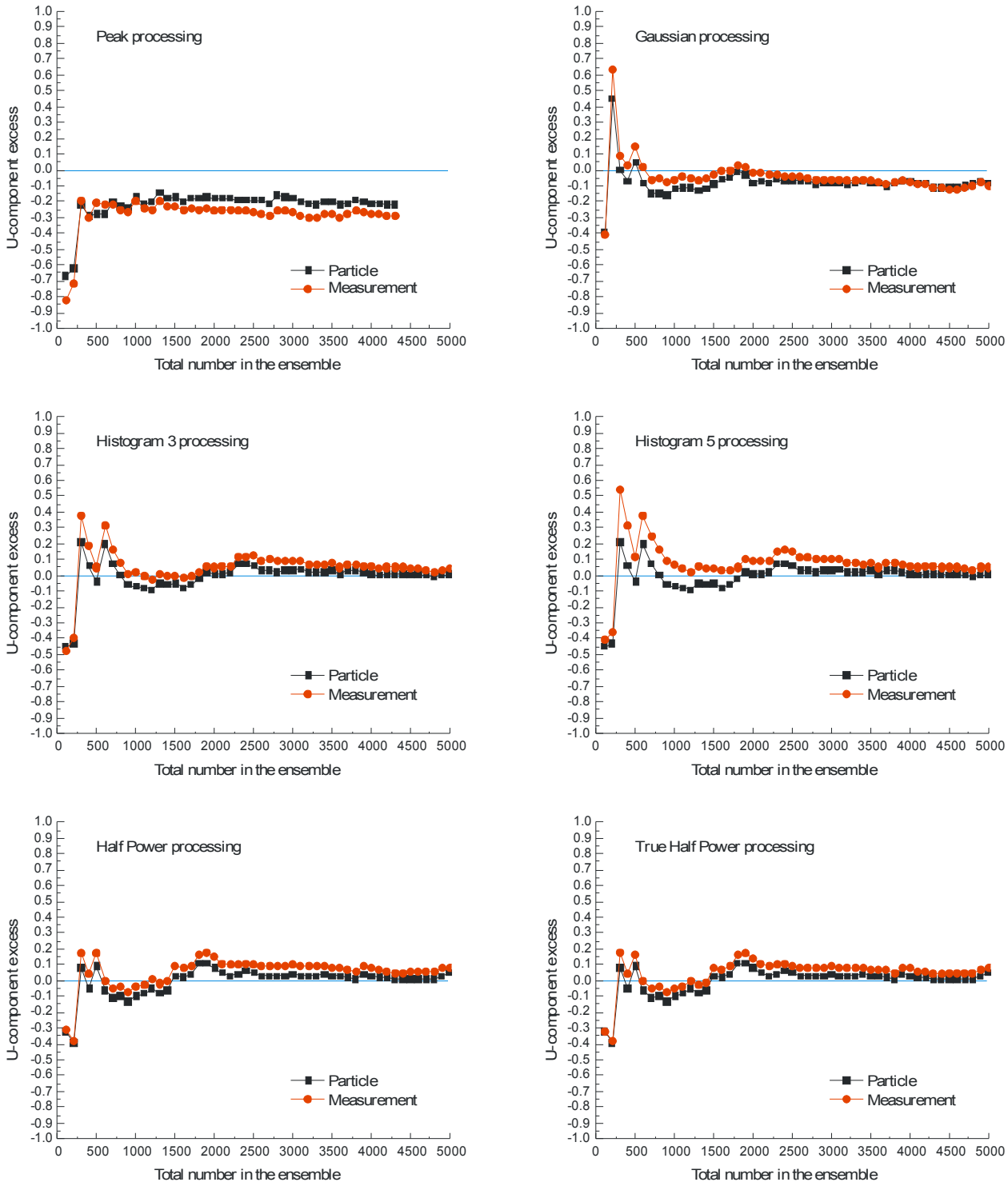

Figure III.28.- Statistical convergence of the U-component excess based on the six signal processing schemes.

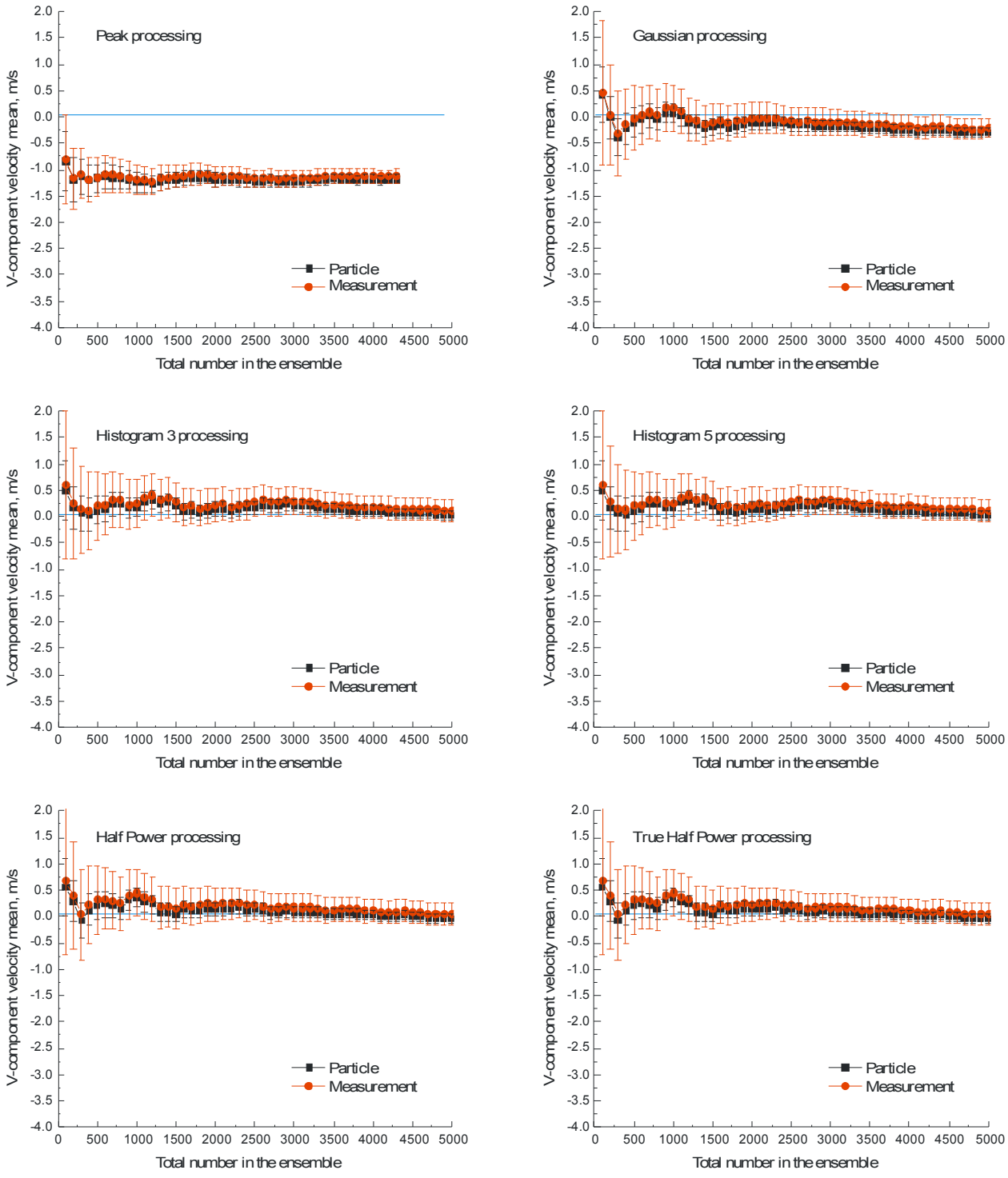

Figure III.29.- Statistical convergence of the mean V-component velocity based on the six signal processing schemes.

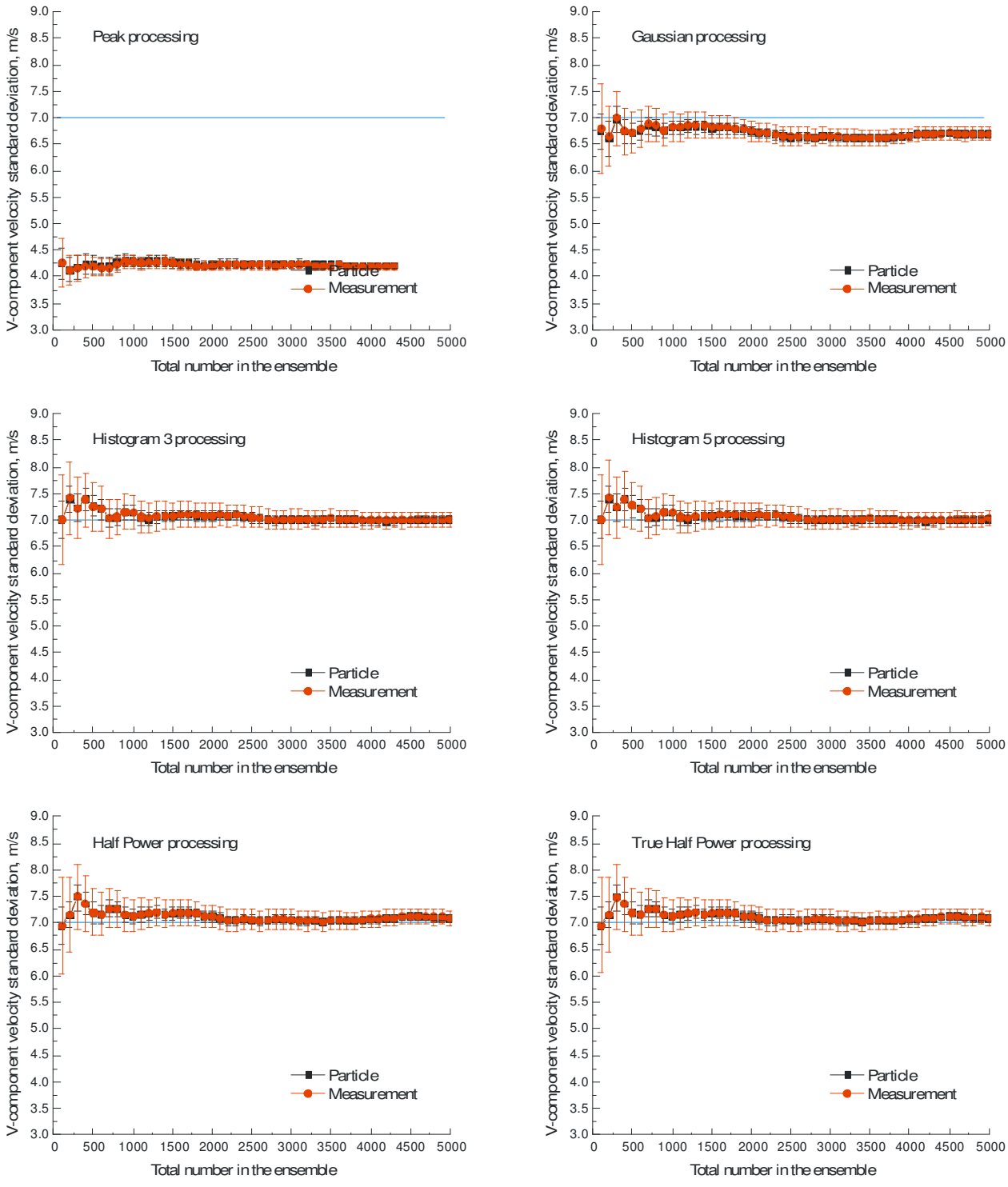

Figure III.30.- Statistical convergence of the V-component standard deviation based on the six signal processing schemes.

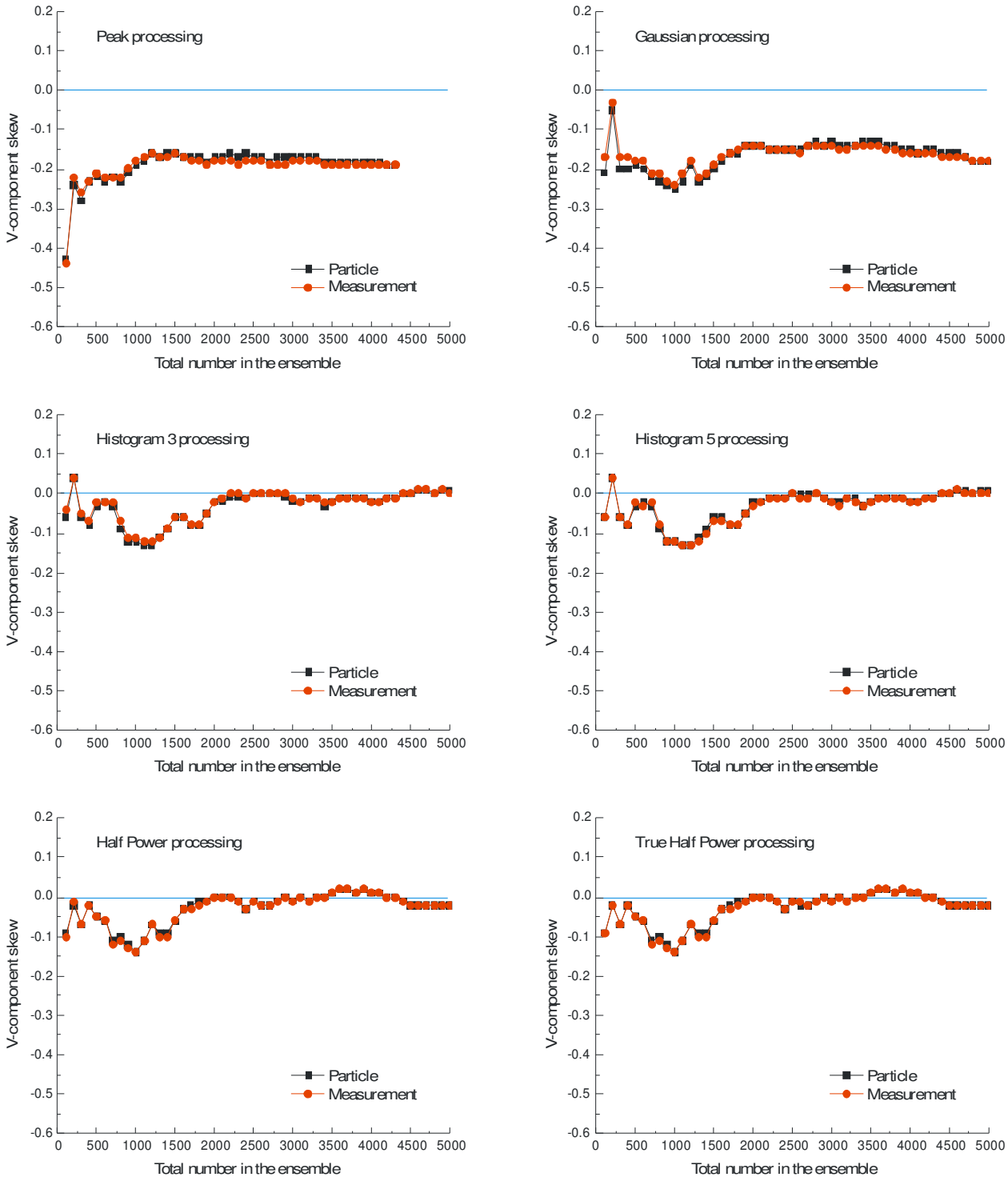

Figure III.31.- Statistical convergence of the V-component skew based on the six signal processing schemes.

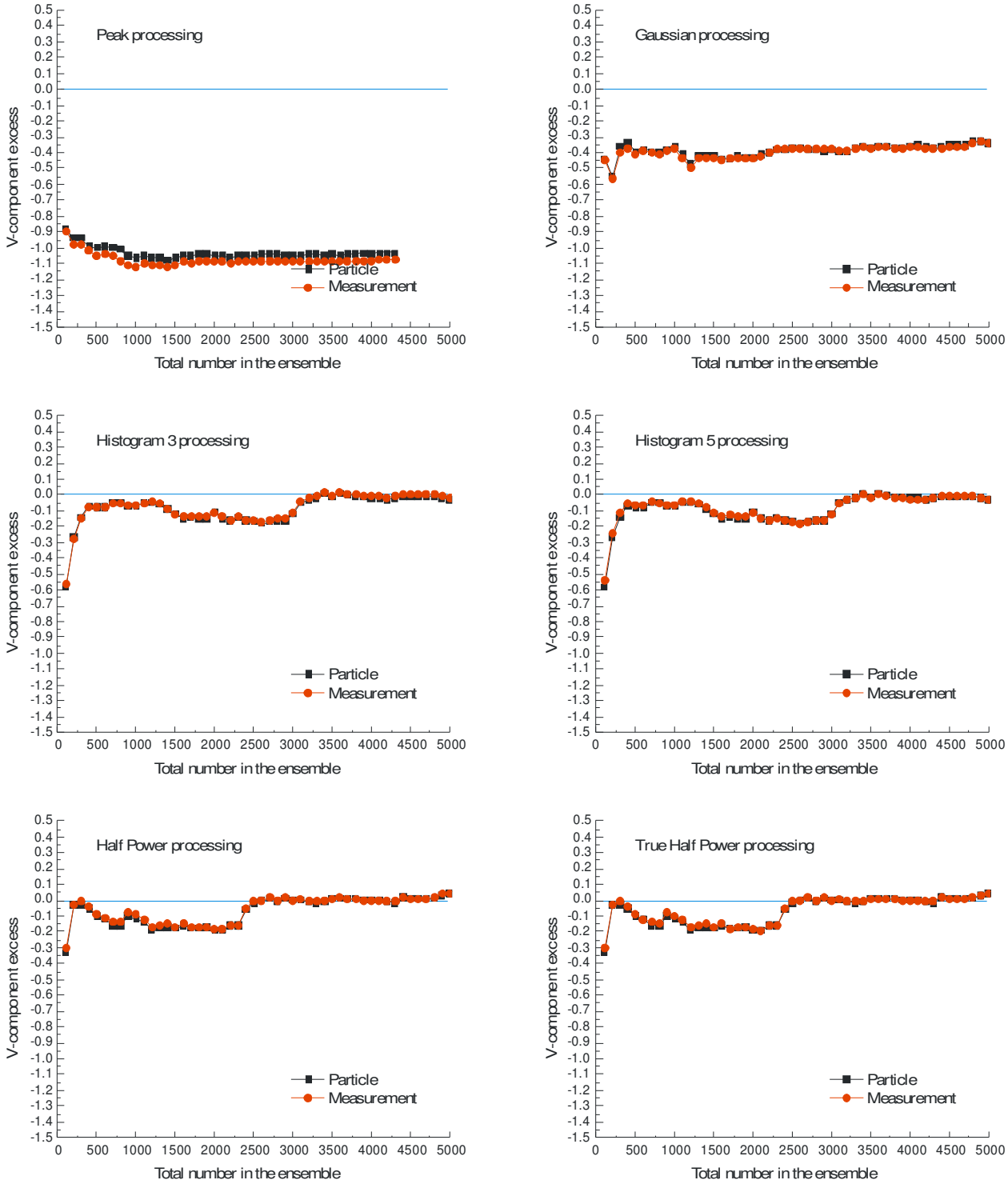

Figure III.32.- Statistical convergence of the V-component excess based on the six signal processing schemes.

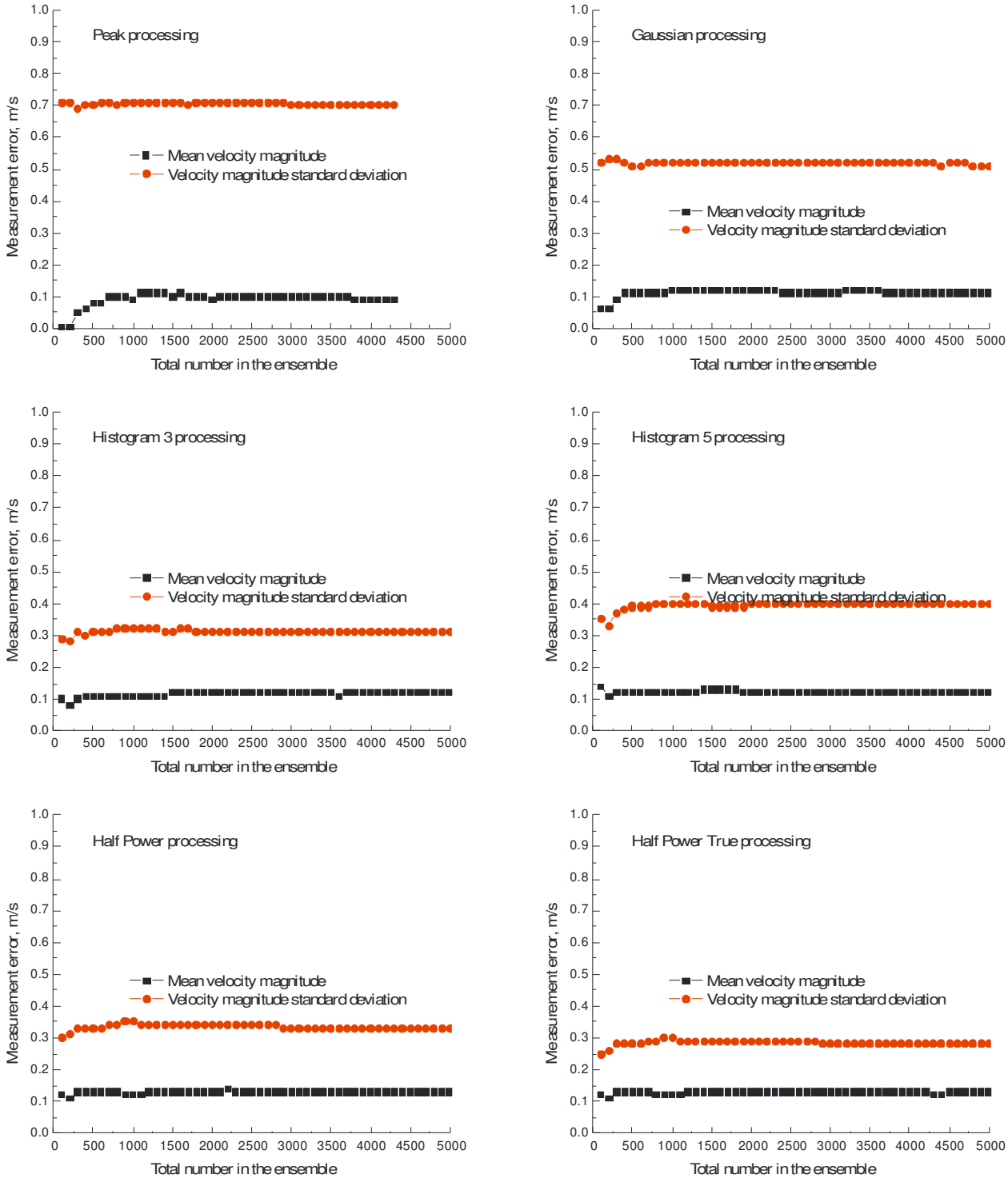

Figure III.33.- Statistical convergence of the velocity magnitude measurement errors based on the six signal processing schemes.

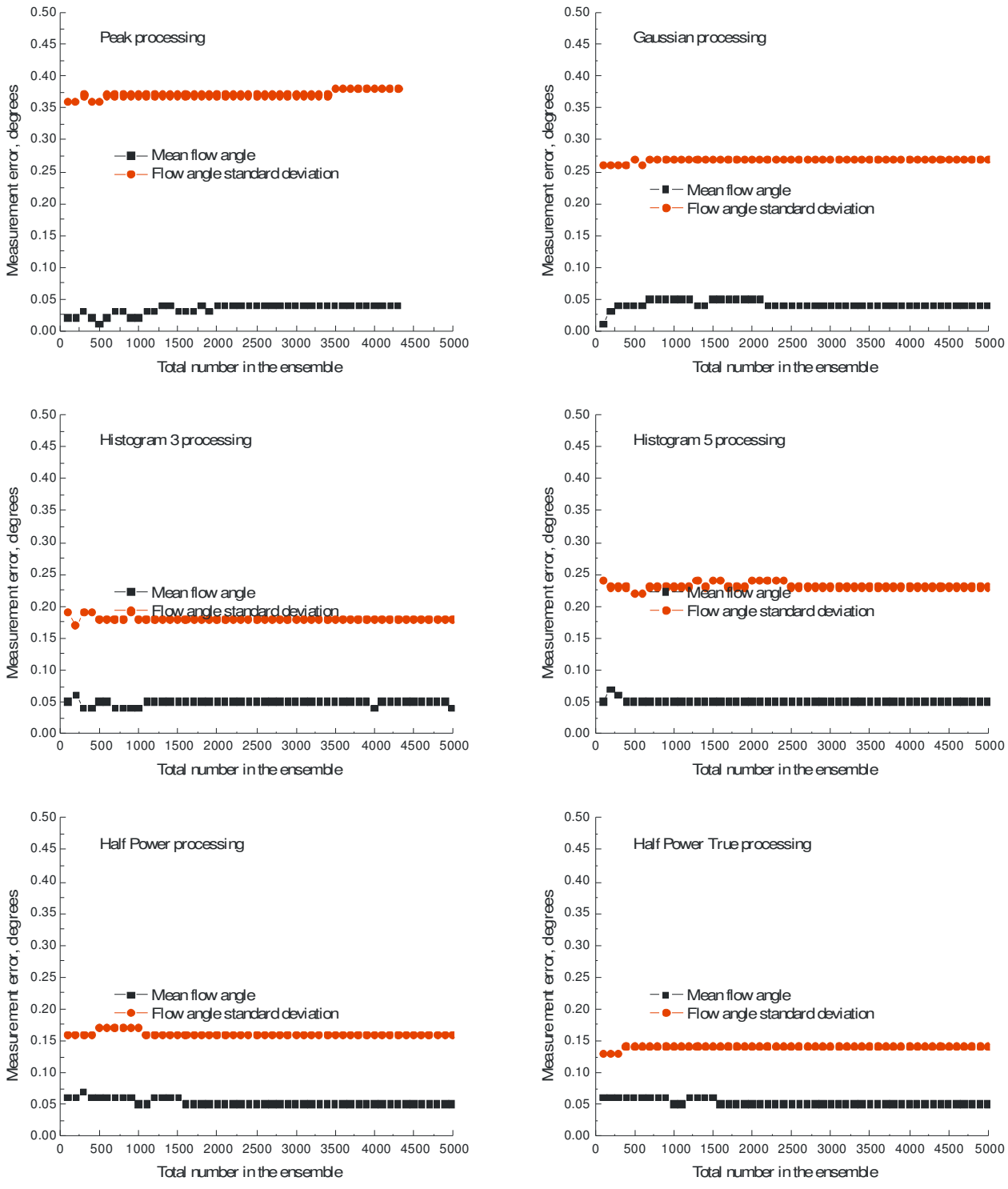

Figure III.34.- Statistical convergence of the flow angle measurement errors based on the six signal processing schemes.

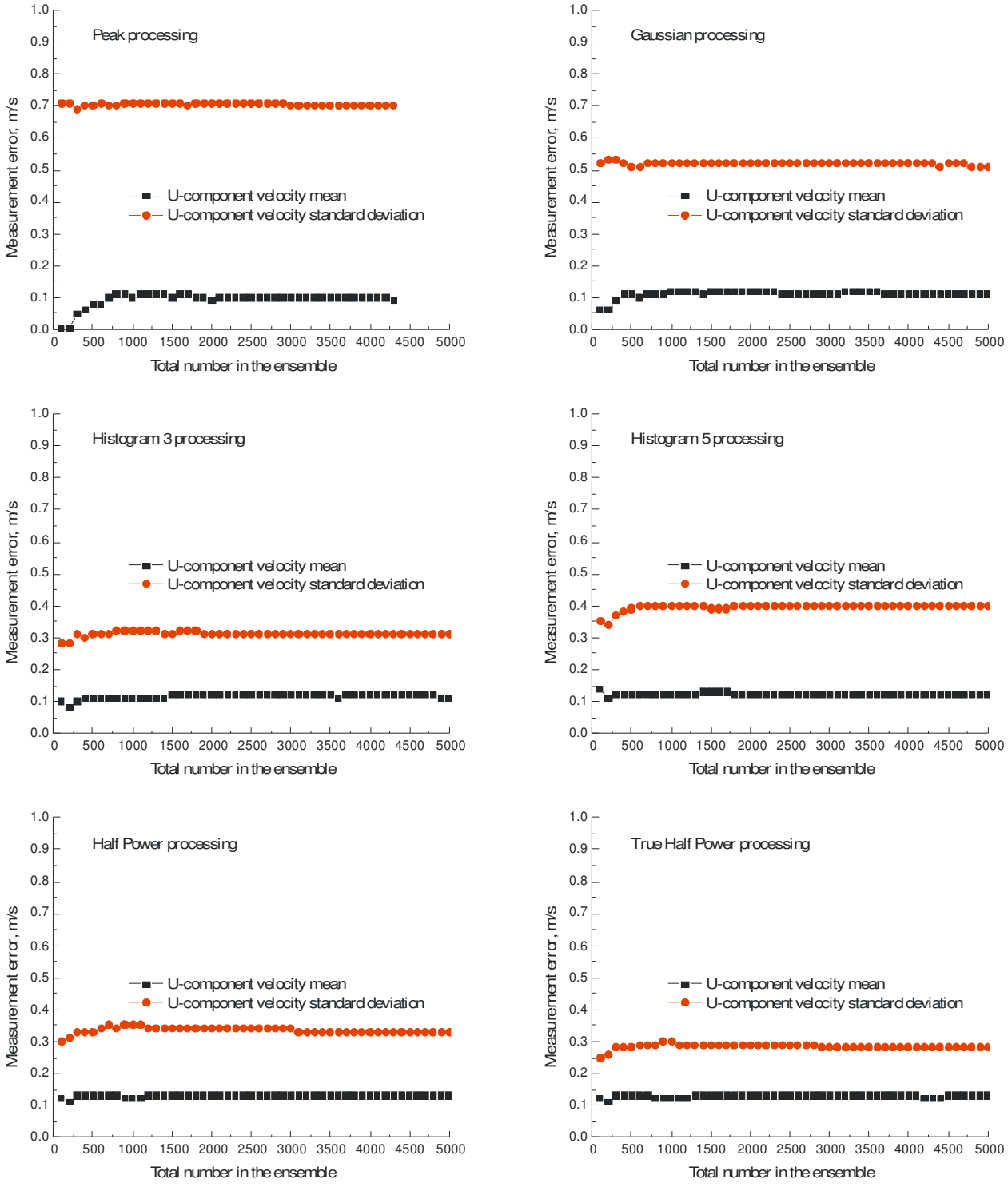

Figure III.35.- Statistical convergence of the U-component measurement errors based on the six signal processing schemes.

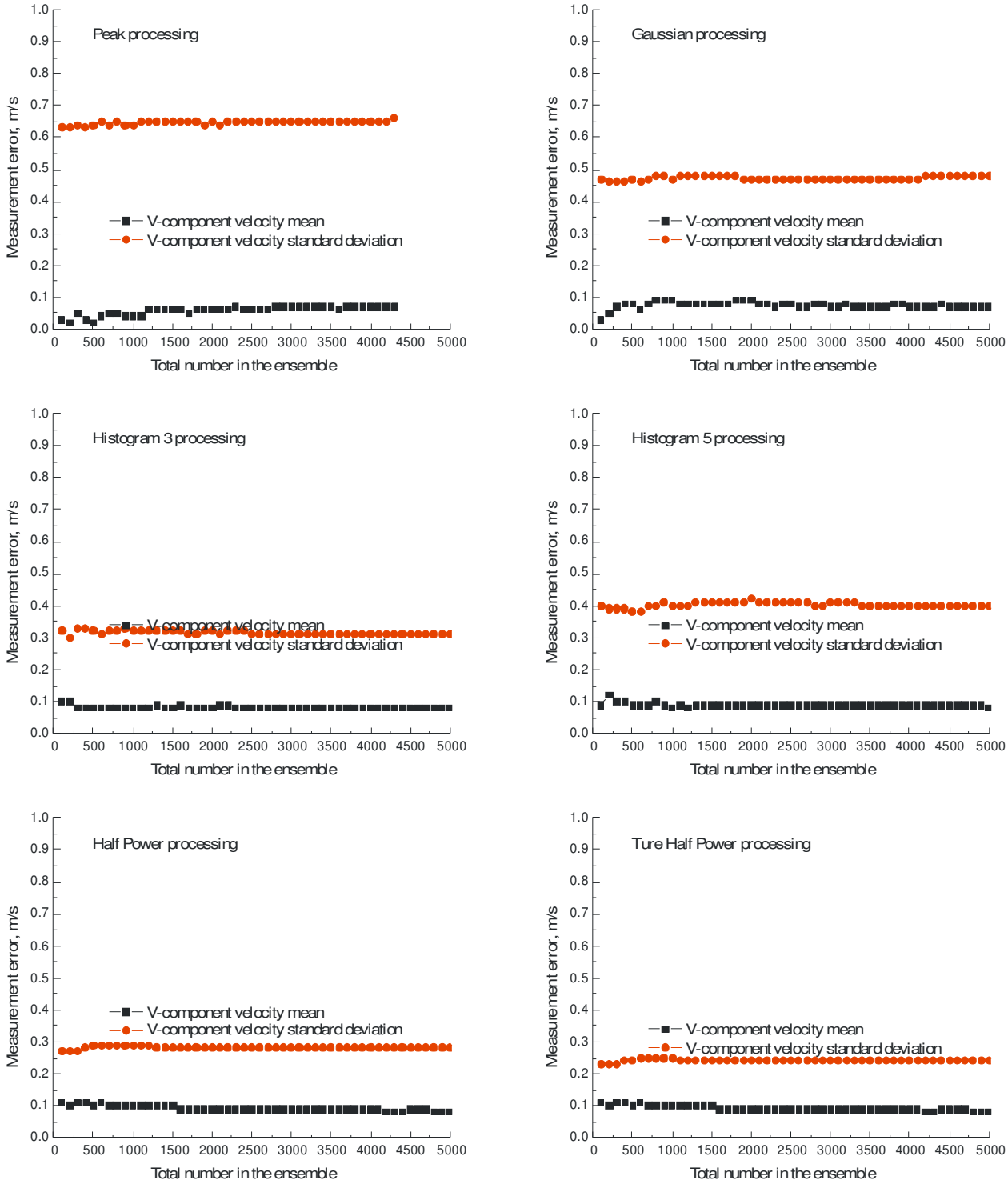

Figure III.36.- Statistical convergence of the V-component measurement errors based on the six signal processing schemes.

Laser Velocimeter Data Acquisition System Implementation

Now that the Monte Carlo simulation has demonstrated that the proposed system would have the ability to satisfy the required measurement accuracy, and that signal processing could be performed within the time constraints needed for real time processing, the data acquisition system was constructed. It consisted of two parts: hardware to capture the signal bursts, acquire auxiliary data, temporarily store the data, and then transfer it to the computers; and the software necessary to control the data acquisition process and conduct the signal/data processing of the captured signal bursts. To minimize the risk in a production environment, the data acquisition and signal/data processing functions were separated by using two computers connected by a 1.0 Gb/s data link. The system would be configured such that the data acquisition computer would have total control of the process including control of the signal/data processing computer. The signal/data processing would be autonomous with the data acquisition program responsible for transferring the data and the corresponding control file to the signal/data processing computer. Once the transfers are completed, the signal/data processing program will recognize the update of the control file and begin processing the new data.

Hardware

The upgraded laser velocimeter data acquisition system employs a dual channel, high-speed digitizer, along with a general purpose data acquisition system and a general purpose counter/timer mounted in a PXI chassis (Compact PCI standard) as the data acquisition hardware. Two networked PC-server class computers are used in support of this hardware. One computer provides the control, setup and arming of the digitizers, and data transfer from the digitizers to permanent storage. The second computer provides the signal/data processing capabilities in an automated manner to provide real-time statistics and distributions of the U- and V-component velocity measurement ensembles, along with the velocity magnitude and flow angle results computed signal burst-by-signal burst from the component measurements. These results are displayed in real time as feedback to the user to provide insight into data quality and help guide the development of the test matrix. The detailed specifications of the acquisition hardware follow.

PXI Data Acquisition System Specifications

The PXI-hosted data acquisition system was constructed using components manufactured by National Instruments, Inc. (NI). The system consists of the following subsystems:

NI PXI-1042 PXI Chassis

This 8-slot, 3U size form factor, rack-mountable chassis provides a high-output power supply with cooling, and a signal interconnection backplane to house and interface the various data acquisition modules together as a complete system. The chassis houses

modular 3U-sized, Eurocard standard compliant, printed circuit boards adhering to the compact PCI specifications. The backplane provides standardized interfacing and synchronization signals to allow communication and control between the various modules inserted in the chassis. The unit operates as an extension of the host computer's PCI bus.

NI PXI-PCI8331 Interface

This module provides the control and data transfer interface to the host computer. The module is composed of two components – a plug-in board that resides in the PXI chassis, and a PCI plug-in board residing in the host computer. The two boards are interconnected via a system bus cable. This interface provides MXI-4 link information transfer rates of up to 132 Mbytes/s (peak) and 78 Mbytes/s (sustained)

NI PXI-5152 High-Speed Digitizers

This 8-bit digitizer is the key component in the data acquisition process as it simultaneously digitizes the signal bursts from both the U- and V-components of the laser velocimeter. It was selected because its bandwidth and sample rate were sufficient to obtain five samples per cycle from the highest signal frequency obtainable from the photomultipliers. These capabilities also allow direct measurement of the Bragg shifted signal frequency, thus eliminating the noise imposed by a double-balanced mixer commonly used in laser velocimetry to bring the signal frequencies within range of the current signal processors. The significant specifications of the two-channel, high-speed digitizer are:

- Sample Rates: 2 GS/s single channel, 1 GS/s simultaneous two channel;
- 8-bit resolution;
- 100 mV_{pp} to 10 V_{pp} analog signal input range;
- 300 MHz analog signal bandwidth;
- 256 Mbyte/channel on-board memory (512 Mbyte total);
- Programmable sample rate, record length, and amplitude range;
- Edge, window, and external triggering capabilities;
- Programmable pretrigger and post-trigger capabilities; and,
- Time Stamp capabilities for each digitized trace (interarrival times).

NI PXI-6120 Multifunction Data Acquisition Module

This module provides the capability to sample analog or digital signals produced by peripheral measurement devices that must be captured each time a laser velocimeter signal burst is acquired (conditional sampling). Additionally this module contains analog and digital output channels that are available for controlling external devices, and counter/timers that can be used to time external events. The significant specifications of the multifunction data acquisition module are:

- 4 Analog input channels – simultaneously sampled
  ±200 mV_{pp} to ±12 V_{pp} Analog signal input range
  16-bit Digitizer resolution
  800 kS/s Sample rate;
- 2 Analog output channels
  ±10 V Output voltage range
  8-bit Digital output;
- 2 Counter/timers
  24-bit;
- Analog or digital triggering capability.

NI PXI-6602 Counter/Timer Module

This module provides the capability to asynchronously record rotor azimuth position by counting the pulses from the shaft encoder and storing the current value when the trigger signifying the capture of a signal burst occurs. The counter continues counting the encoder pulses until reset by the one-per-rev pulse from the encoder. It is recommended that all shaft encoders provide at least 1024 counts per shaft revolution for maximum azimuth measurement accuracy. The module can also be configured to simulate the functionality of the azimuth encoder for system verification. The significant specifications for the counter/timer are:

- 8-channel, 32-bit up/down counter/timer;
- 32 digital I/O lines (5 V TTL/CMOS);
- 80 MHz maximum source frequency.

Computer Specifications

Two identical PC-server class computers are networked together with 1.0 Gb/s communication capability to provide data acquisition hardware control and data transfer (data acquisition computer), and signal/data processing/display functions (signal processing computer). The computers use the Microsoft Windows 7, 64-bit Professional operating system. The data acquisition computer is equipped with LabVIEW version 11 and the LabVIEW compiler. The signal/data processing computer is equipped with the Intel Fortran 90, version 11 compiler with both 32-bit and 64-bit versions. The GrWin graphics libraries, in both 32-bit and 64-bit versions are available. Both computers have software to preform diagnostics, data manipulation, code development along with plotting and display software used for *in situ* tasks in code development, report writing, and data interrogation and plotting. The computers consist of the following components:

- Rack mount system case;
- SuperMicro X7DAL-E Server Motherboard with 2 Socket-J Processor Sockets, 24-Gbyte max memory support;

- Intel Xeon Quad Core Processor with 2.33 GHz clock speed, 1.33 GHz front side bus, 12 Mbyte L2 cache;
- 8 Gbyte RAM;
- 6 open 5.25-inch bays that include:
  - 1 RAID 0 drive using two 1.0 Tbyte SATA drives, 7200 rpm;
  - 1 1.0 Tbyte SATA drive, 7200 rpm – hot swappable for data backup/transfer;
  - 1 500 Mbyte ATA drive, 7200 rpm – hot swappable for data backup/transfer;
  - 1 DVD player/recorder;
- 2 in-chassis 3.5-inch bays that include:
  - 1 750 Mbyte SATA drive, 7200 rpm – operating system, programs, etc.
- Sapphire Radeon HD 3870 Graphics Card with on-board 512 Mbyte memory and 775 MHz graphics processor;
- 2 1.0 Gb network ports;
- 620 W Power Supply;
- 24-inch LCD display with 1920x1200 pixel resolution.

Peripheral Components

The two peripheral components that are used during laser velocimetry investigations and system testing are the high-speed digital oscilloscope and the arbitrary waveform generator. The generator is used to convert the signal bursts created by the Monte Carlo laser velocimeter simulation program into known frequency electronic signal bursts for system testing.

Tektronix TDS 5054B Digital Phosphor Oscilloscope

Along with being a general purpose oscilloscope used during system set-up, it is also a critical element in the data acquisition system where it performs three functions. The first is to evaluate the quality of the signals obtained from the two laser velocimeter components before initiating a data acquisition. This evaluation can identify seeding number density problems, e.g., generators running out of particles, and low or mismatched signal levels which could be caused by laser or optics misalignment. The second task is to provide the user with a visual display of the signal bursts so that the trigger level can be set for optimum measurement accuracy. And, finally the oscilloscope provides the trigger to initiate the digitization of the signal burst as a particle passes through the measurement volume. This trigger also initiates the sampling of the auxiliary channels and counter/timer to conditionally sample voltages from other instrumentation and read the rotor azimuth encoder. The specifications of the digital oscilloscope are:

- 500 MHz bandwidth;
- 4 channels;
- 8-bit resolution;
- Max 5 GS/s sample rate;
- Max 16 M record length;

- Max 100,000 /s waveform capture rate;
- 50-/1000k-ohm input impedance;
- Multiple acquisition modes;
- Multiple triggering modes;
- External trigger output capability.

Agilent 81150A Pulse Function Arbitrary Waveform Generator

Measurement accuracy and instrument precision can be predicted by the Monte Carlo laser velocimeter simulation program. This is possible, even with the randomness involved in the flow model, photon statistics, etc., since the velocity trajectory of every particle is known. Further the particle velocity can be tracked through every phase of signal processing to the final statistics. Any differences between the *real* particle velocity and the *measured* velocity is attributed to instrument precision. Measurement accuracy can be determined by comparing the statistical measurements of the generated particle velocities with the statistics of the measured velocities, assuming sufficient signal bursts are measured to reach statistical stationarity of the flow – real or simulated. Carrying this even further, instead of comparing the generated particle velocity statistics, the statistical characteristics of the particles actually passing through the measurement volume should be compared with the measured velocity statistics to determine the *true* measurement accuracy.

Unfortunately, these theoretical predictions do not provide the actual instrument precision or measurement accuracy. Comparisons of the laser velocimeter measurements with other techniques or even other laser velocimeter measurements will not provide a measure of accuracy since the true velocities are unknown. Only the relative statistical differences between the two data sets can be determined.

The solution to this dilemma was to use the signal records developed by the Monte Carlo simulation to drive an arbitrary waveform generator and send them to the data acquisition system as if they originated from the photomultiplier. A normal data acquisition cycle was initiated and the measurements determined from the results of the signal/data processing software. Since the *particle* velocities are now known for particles that yield acceptable signal bursts, the real instrument precision can be determined (discounting errors attributed to inaccuracies in the optical cross-beam angle which would impose a bias error in the mean velocity). As with the simulation, the real measurement accuracy can also be determined by comparing the measurement statistics with the input statistical characteristics and/or the randomly selected particle velocities. The only point of concern was whether the arbitrary waveform generator accurately reproduced the signal burst waveforms. A comparison of several signal bursts produced by the simulator with the corresponding electronic signals captured by the high-speed digitizer in the PXI system, as produced by the arbitrary waveform generator, were identical. Additionally the determination of instrument precision and measurement accuracies, this time performed

on the actual hardware, produced results that compared exactly with the predictions from the Monte Carlo simulation.

The specifications for the arbitrary waveform generator include:

- 1μ – 120 MHz pulse generation with variable rise/fall time;
- 1μ – 240 MHz sine waveform output;
- 14-bit, 2 GS/s arbitrary waveforms;
- 512k samples, arbitrary waveform memory per channel;
- Noise with a selectable crest factor and signal repetition time of 26 days;
- FM, AM, PW, PWM, FSK modulation capabilities up to 10 MHz;
- 1 or 2 channel, coupled and uncoupled;
- Differential outputs;
- Internal or external triggering capability;
- 50-/1000k-ohm output impedance;
- Fully programmable.

Software

The data acquisition and signal/data processing computers utilized Microsoft Windows 7, 64-bit Professional as the operating system.

The instrument control and data acquisition software was developed using the National Instruments LabVIEW development environment. The program provides the user with an easy to navigate interface (GUI) that controls the configuration and operation of the PXI data acquisition hardware, transfer of data from the acquisition hardware to permanent storage on the hard drives of the data acquisition and signal/data processing computers, and constructing the initiation (trigger) file that executes the signal/data processing software. The primary capabilities of this software are as follows:

- Hardware initialization and control;
- Data acquisition management;
- Interarrival time recording;
- Conditional sampling of auxiliary signals;
- Data retrieval and archival;
- Scan rig management via GPIB-488 interface.

The details of the installation and operation of the data acquisition and control software are given in Appendix C with the specific variable glossary given in Appendix D. The details of operating the signal/data processing software along with the glossary of variables are given in Appendix E. Additionally several programs were written in support of the development of the upgraded laser velocimeter, outlined in Appendix C, and programs to assist in post processing the data, outlined in Appendix E.

Laboratory Testing of the Upgraded 14- by 22-Foot Subsonic Tunnel Laser Velocimeter

The first shakedown test of the upgraded laser velocimeter for the 14- by 22-Foot Subsonic Tunnel was conducted in the laboratory. The laser velocimeter was configured to operate at a focal distance of 4.5-meters, equivalent to reaching tunnel centerline. A small jet flow was used to provide an example flow with relatively low turbulence and a centerline velocity of approximately 70 m/s. The optical axis was angled approximately 55-degrees with the flow centerline because of physical constraints in the laboratory. The objective was to determine if the system would yield signals from 1.9-micron PSL particles with levels sufficient to yield acceptable velocity measurements. It is noted that 1.9-micron particles were used to provide a small safety factor in signal amplitude over the normally used 1.7-micron particles. The investigation would also serve as an operational test of the data acquisition electronics and software, data transmission to both acquisition and processing computers, and automatic data processing and display of the measurement results. The test would be conducted in a production mode manner to determine the time required for each step in the data acquisition/processing sequence.

The jet flow apparatus was driven by a squirrel cage fan exiting into a 100-mm diameter, 1.575-m long pipe before entering a series of screens and straws. The pipe necked down to a 50-mm diameter, 0.56-m long pipe following the flow straighteners where the flow exits to form the low turbulence jet, Figures V.1 and V.2. The optical axis of the laser velocimeter passed through the axis of the jet with an inclination angle of approximately 55-degrees, and located just downstream of the pipe exit, Figure V.1. The seeding particles, embedded in a 50:50 solution of water and ethanol, were injected into the inlet of the squirrel cage fan using a spray atomizer with 6 Laskin nozzles. Typically only one nozzle was used. The 100-mm diameter pipe allowed sufficient transit time for the water/ethanol solution to evaporate. The jet flow along with the entrained particles were exhausted to the outside of the laboratory by a blower-driven collector.

The center of the laser velocimeter measurement volume was positioned on the flow axis and five sets of 10,000 data point ensembles were acquired. The oscilloscope trigger level was set to 0.05 V (same level as used in the Monte Carlo simulation: ADC captured signals in Figures A.1. - A.7.). Examples of the captured signals by the high-speed digitizer, as triggered by the oscilloscope, are shown in Figure V.3. It is noted that all U-component signals, which generate the trigger, were virtually identical whereas the V-component signals vary by a factor of up to six. All of these signals produced acceptable measurements illustrating the robust nature of the signal processing algorithm. Other captures, Figure V.4, consisted of a fairly high level noise pulse that was a spontaneous emission from the photomultiplier which triggered the oscilloscope. Although these pulses were rejected by the signal processing software, their presence reduced the number of potential acquisitions of acceptable signal bursts. The seeding rate was sufficient in the jet that the noise represented a relatively small percentage of the data. However, when the measurement volume was traversed to the shear region at the edge of the jet, the particle

data rate was overwhelmed by the noise pulses leaving too few acceptable measurements for any statistical meaning, and thus this data was excluded from the following comparisons. Histograms of peak signal level for the U- and V-component acquisitions for the five ensembles along with an ensemble obtained with the measurement volume located at half radius in the jet are shown in Figure V.5. As expected with PSL particles, the histograms were virtually identical. The difference between the U-component signal levels and the V-component signals was attributed to the lower laser energy in the 0.488-micron wavelength used in the V-component.

Each 10,000 element ensemble was acquired in approximately 110 seconds then stored locally to the disk drives installed in the data acquisition computer and to disk drives residing on the networked data processing computer thus supporting in-situ data backup. This redundant transfer of data was fairly slow, but increasing its transfer rate was not considered a priority at this time. Once the data was stored on both computers, the acquisition computer triggered the signal processing software which then began determining the signal frequency of each burst in the ensemble. Processing of the data ensembles was completed in approximately 20 seconds and the resolved distributions of velocity magnitude, flow angle, and the U- and V- component velocities along with their statistical results were presented on the processing computer's monitor. Images of the histograms, statistical results, and the full measurement log including interarrival times and azimuth angles for each particle were stored in a LOG file for that data ensemble on the processing computer. Once complete, the signal processing software automatically entered a sleep state where it was idled until the next trigger occurred from the data acquisition software. The system was designed to allow another acquisition cycle to be initiated after a new trigger pulse was generated by the acquisition program. In practice however, acquisition was delayed until the distributions and statistics were displayed. This allowed researchers to evaluate whether the data ensemble was acceptable before continuing the data acquisition activity.

The next phase of the laboratory investigation was to determine the convergence of the measurement statistics, as was performed with the Monte Carlo simulation results. For the data convergence study only the Histogram (5) and True Half Power processing approaches were used. The simulation results indicated that the Histogram (5) yielded the most accurate velocity distribution results, but with slightly greater uncertainties in the statistical results. The True Half Power method yielded the most accurate statistical results but suffered from “binning” (results that have specific values, not continuous, e.g, integer numbers versus floating point – 1.4 would be 1 in integer, but 1.4 in floating point) in the distribution results and thus did not produce a true representation of the velocity distribution. The convergence results of velocity magnitude, shown in Figure V.6 indicate that the mean and standard deviation trends with increased ensemble size were identical in form as predicted by the simulation. Additionally the trends show increased sensitivity in the standard deviation trends, again as predicted by the simulation. The True Half Power converged slightly faster, but both methods reached statistical stationarity with ensemble sizes of 2,500. Acceptable convergence occurs at approximately 1,000 signal bursts, indicated by a jitter of less than 0.1-m/s out of a “turbulence” of 0.5-m/s found in

the 59.2 m/s jet flow (Note: freestream velocity of 72 m/s times cos(35 degrees)). The mean velocity magnitude varies approximately 0.2-m/s among the five data ensembles, most likely a measure of the long term instability of the fan and potential back pressure changes in the collector caused by wind external to the laboratory. This variation appears in both processing methods, and thus it was most likely real. These trends remain consistent for the flow angle, and the U- and V-component velocity measurements shown in Figures V.7-V.9, respectively. However, the flow angle and V-component measurements indicate small, but not insignificant differences in their results computed by each method. Since the true flow characteristics are unknown, it is impossible to ascertain which measurement was correct, and the simulation provided no insight into any differences in the statistically stationary results. The question is whether 0.25-degree differences in flow angle and its associated standard deviation differences of 0.25-degrees between the two processing methods are significant.

As predicted by the simulation, the True Half Power method converged faster, but the question "Do the associated velocity and flow angle distributions have the predicted characteristics?" remained to be answered. The distribution obtained from each processing method for a given data ensemble was then analyzed to determine consistency and if any deviations from the expected smooth distributions were found. For example, the velocity magnitude of the first ensemble (T144647 → 14 hours, 46 minutes, 47 seconds → time of data acquisition start) is shown in Figure V.10. As predicted by the simulation, the Histogram (5) yielded a smooth distribution whereas the True Half Power method showed significant binning. For this example all statistical results converge at low ensemble sizes and track well between the two methods. These trends continue for the next three data ensembles, Figures V.11 to V.13. However, data set T152338, Figure V.14, shows significant differences in the skew and excess results between the two processing methods at smaller ensemble sizes, but they converged to virtually the same level at larger ensemble sizes.

The flow angle results varied from virtually identical statistical trends to completely different with a great variation in convergence results, Figures V.15-V.19. It is also noted that the Histogram (5) approach would suddenly change value in skew and excess and begin a new convergence trace. The Histogram (5) distributions remained smooth in all cases and the True Half Power distributions always contained significant binning. Again the significance of these results must be left to the reader. As expected for low turbulent centerline flows, the characteristics of the U-component results, Figures V.20-V.24, track the characteristics found in the velocity magnitude. Likewise the characteristics of the V-component results, Figures V.25-V.29, track the characteristics found in the flow angle.

By moving the measurement volume away from the centerline to the half radius position, it was expected that there should be a drop in velocity magnitude and a potential increase in flow angle, Figures V.30 and V.31 respectively. While this was the case, the trends found at the centerline continued with the statistics, tracking well between the two methods. However, the skew and excess results for both methods suddenly jumped to new convergences for the velocity magnitude, Figure V.30. Again the U- and V-component

results, Figures V.32 and V.33, track the velocity magnitude and flow angle trends, respectively.

The laboratory investigation yielded the following conclusions:

1) The trends predicted by the Monte Carlo simulation were found in the laser velocimetry measurements:
   a) Histogram (5) distributions were smooth, True Half Power distributions were binned;
   b) There was a distinct convergence of the statistical results as the ensemble size was increased;
   c) The True Half Power statistics converged faster and had lower excursions at small ensemble sizes than the Histogram (5) method; and,
   d) In general the two methods yielded virtually identical converged results.
2) There were sudden excursions in the convergence trends by both methods (more often in the Histogram (5) method) in skew and excess which caused new convergence trends to begin. This might be attributed to an errant data point that was not rejected by the data processing software because it remained within the threshold limits imposed by the software on the distribution, but significantly affected the skew and excess.
3) Measurement standard deviation convergence was more sensitive than the convergence of the mean and did not suffer from bias problems as did the mean nor did it exhibit sudden excursions as did the skew and excess convergences – thus standard deviation will be chosen to be the defining variable for statistical convergence.
4) The signal processing techniques proved to be robust based on the number of successful coincident measurements even with the variation in the V-component signal level. Although this variation may have contributed to the differences found in the flow angle and V-component statistics.
5) High-level noise pulses were generated by the photomultipliers; as these signals satisfied triggering requirements, they were accepted thus reducing the number of valid signal bursts within a given ensemble.
6) U- and V- coincidence measurements were obtained at acceptable rates for production testing (90 measurements per second).
7) Data transfer to the acquisition and processing computer hard drives was slow.
8) Automatic signal/data processing was successful and completed within an acceptable time with the display of the results being used to assess the data ensemble before the next data ensemble was acquired.
9) The more realistic distribution produced by the Histogram (5) method, even though the statistical measurements had slightly larger uncertainties, validated its selection as the method of choice for final implementation of the signal processing software. It is noted that since the original captured signals were saved, off-line processing using the same program can be conducted with any of the six processing methods described or any new method developed in the future. Manual triggering of the data processing program can be achieved by editing the trigger files generated by the data

acquisition program during data collection activities that reflect the configuration of the targeted data ensemble(s). If more than a few ensembles are to be processed, the batch processing program: batchlvprocessing.exe, should be used. This program automatically copies the respective trigger file for each data ensemble to the target location, making processing totally automated. New processing techniques can also be easily incorporated into the existing data processing program by developing a subroutine to replace the Histogram (5) subroutine currently installed. It is noted that the new subroutine must conform to the calling variable sequence in order to compile without error.

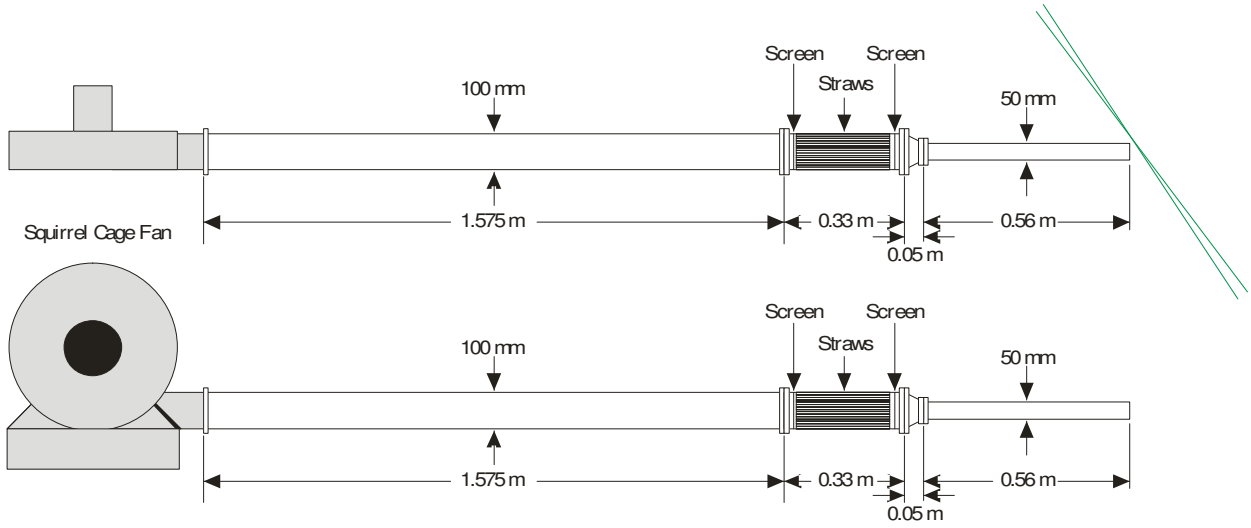

Figure V.1.- Schematic of the 50-mm diameter jet used during laboratory testing of the upgraded laser velocimeter, along with the location and orientation of the crossing laser beams.

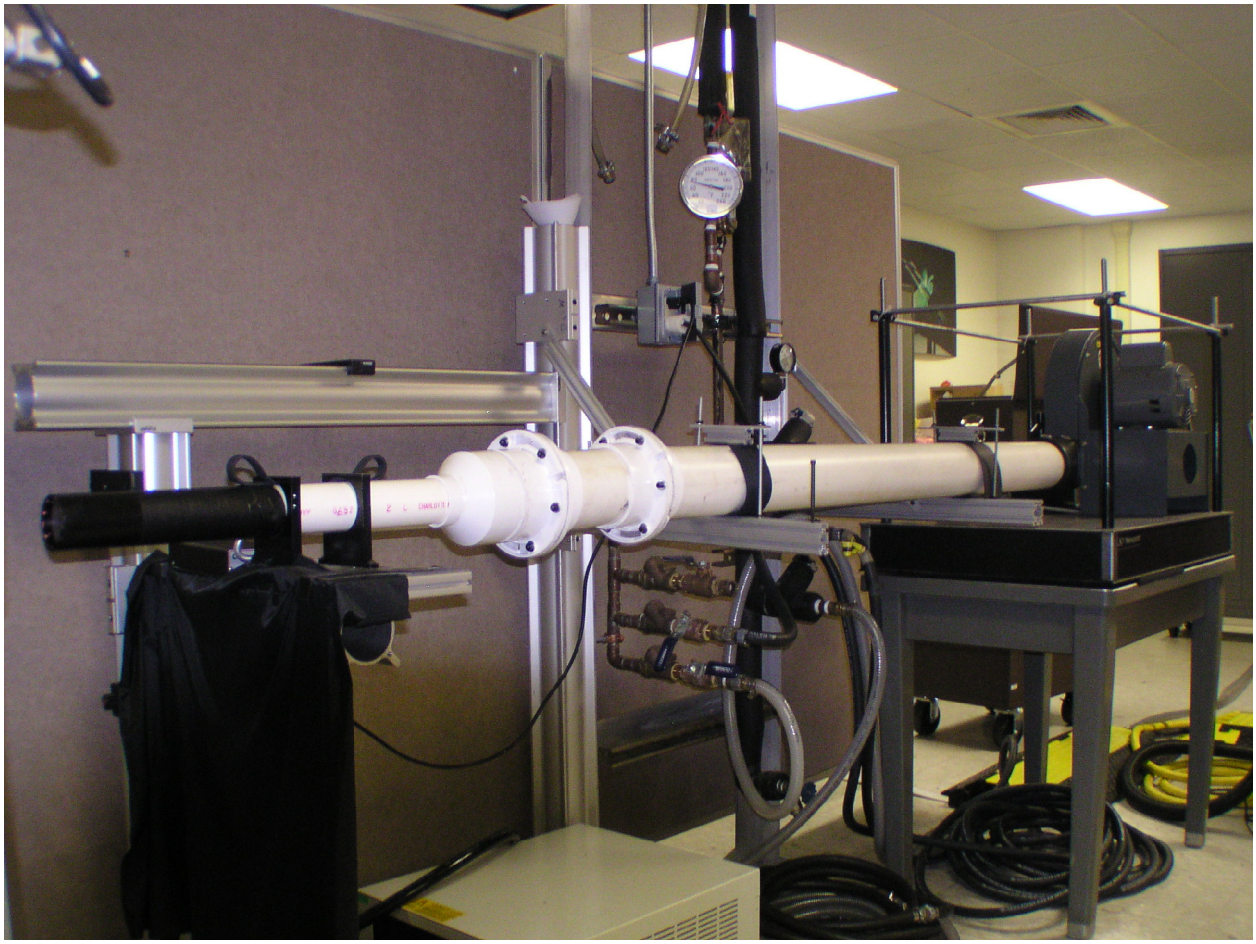

Figure V.2.- Photograph of the 50-mm diameter jet used during laboratory testing of the upgraded laser velocimeter.

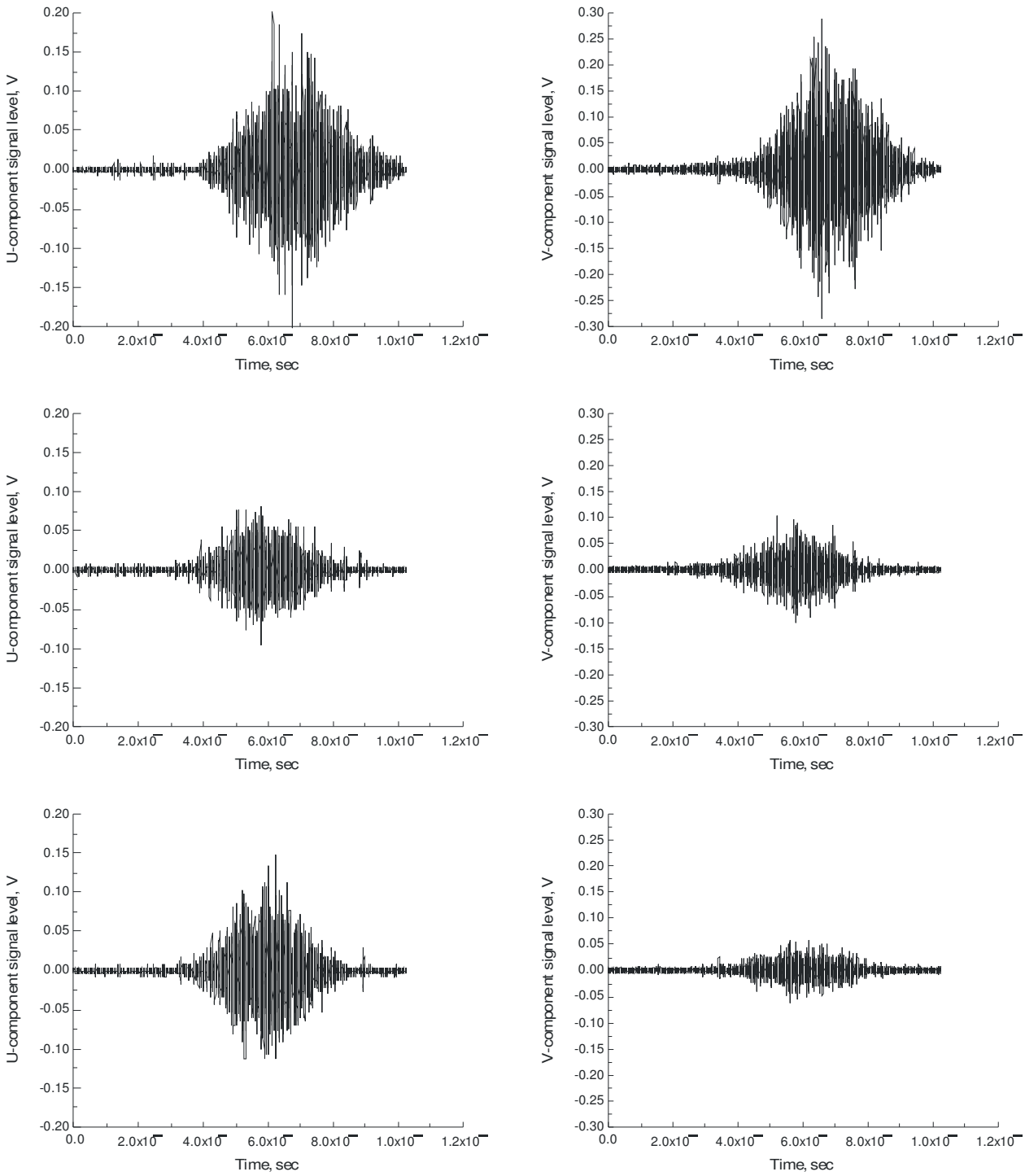

Figure V.3.- Example signal bursts obtained from 1.9-micron particles embedded in the 2-inch diameter jet flow, U-component trigger level 0.05 V. Signals produced by the upgraded LV receiver.

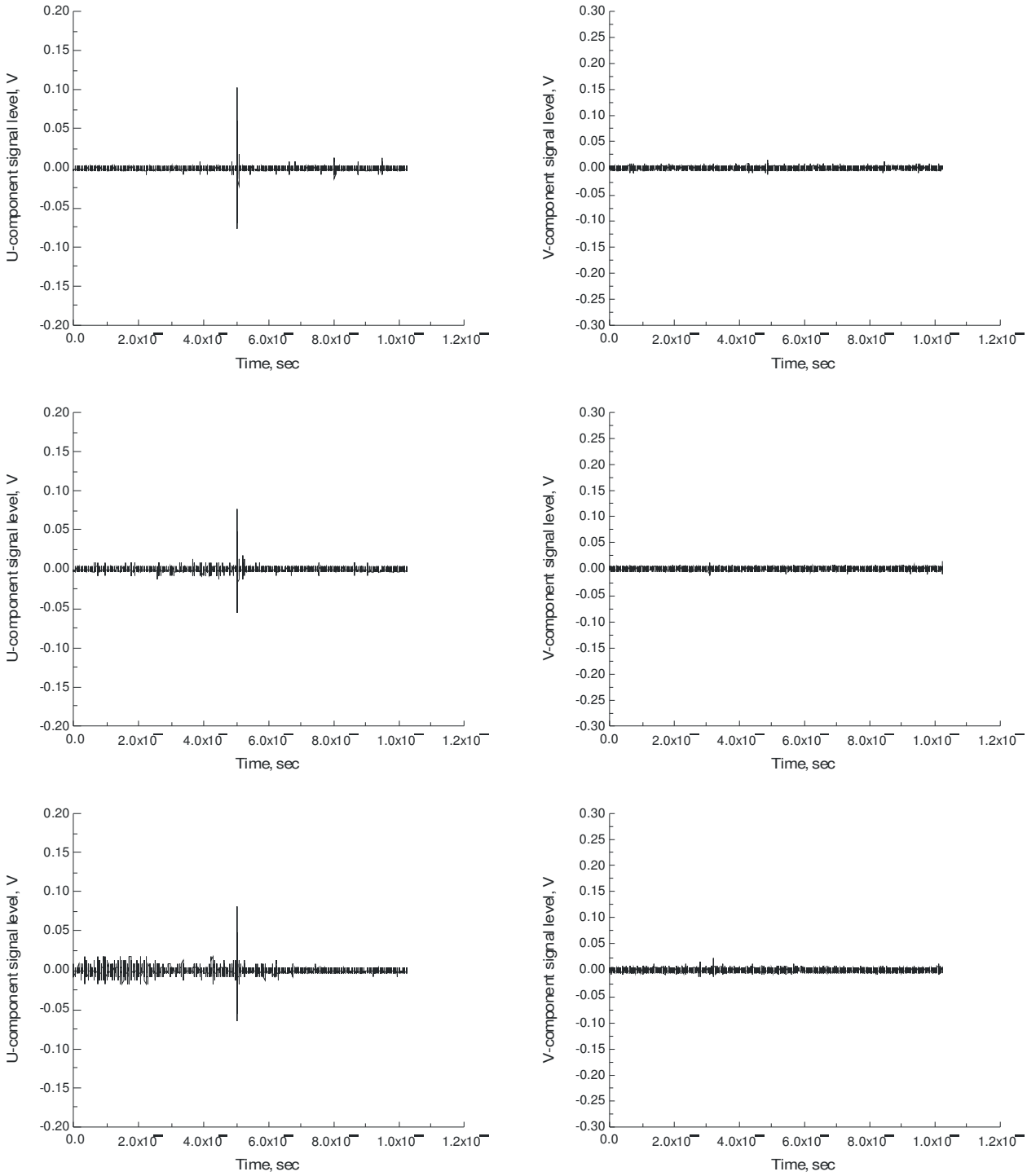

Figure V.4.- Example noise pulses produced by the upgraded LV receiver, U-component trigger level 0.05 V.

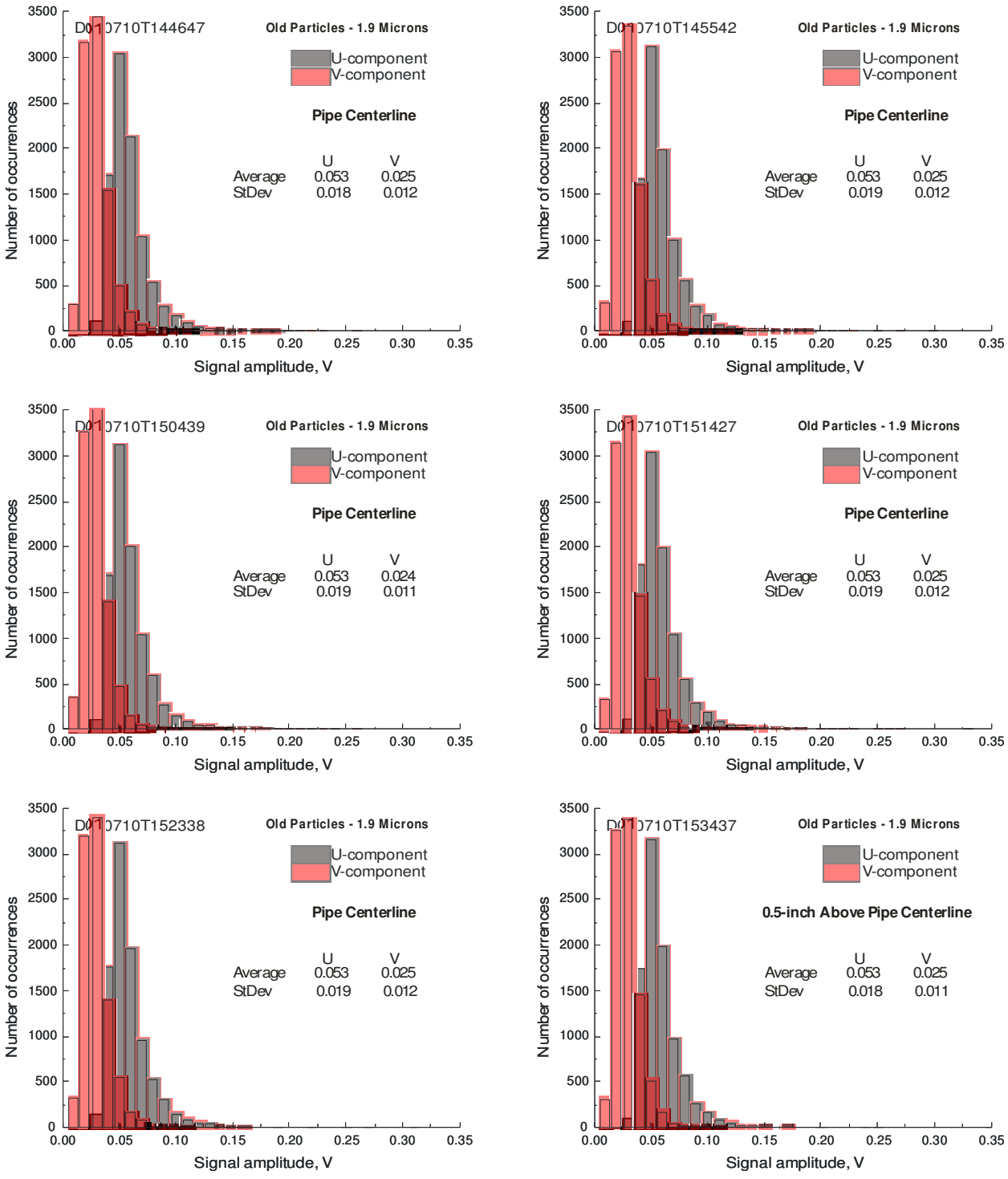

Figure V.5.- Distributions of peak signal level obtained from 1.9-micron particles embedded in the 2-inch diameter jet flow, U-component trigger level 0.05 V.

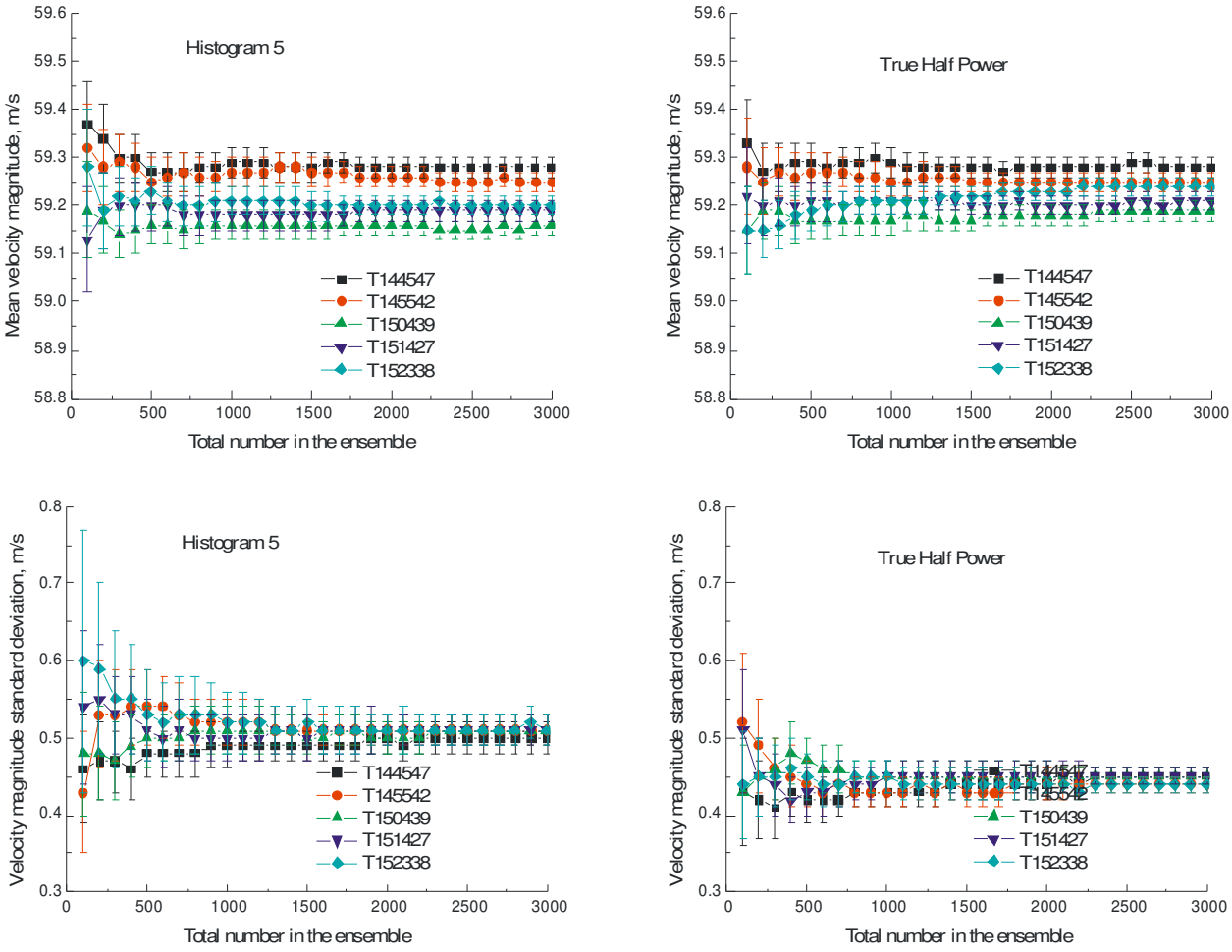

Figure V.6.- Convergence of the velocity magnitude mean and standard deviation for five repeated ensembles at the centerline of a 2-inch diameter jet in the laboratory using Histogram (5) and True Half Power processing.

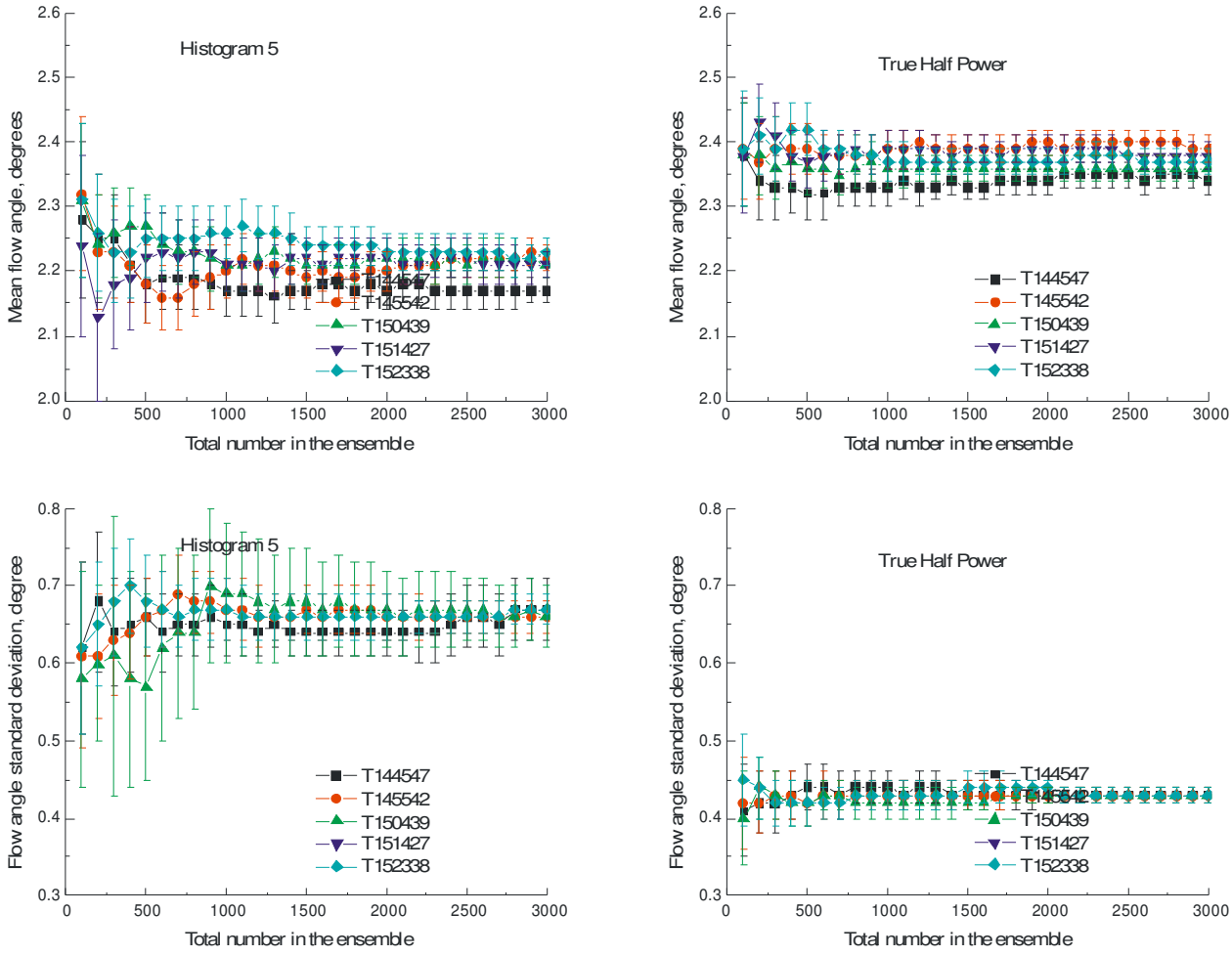

Figure V.7.- Convergence of the flow angle mean and standard deviation for five repeated ensembles at the centerline of a 2-inch diameter jet in the laboratory using Histogram (5) and True Half Power processing.

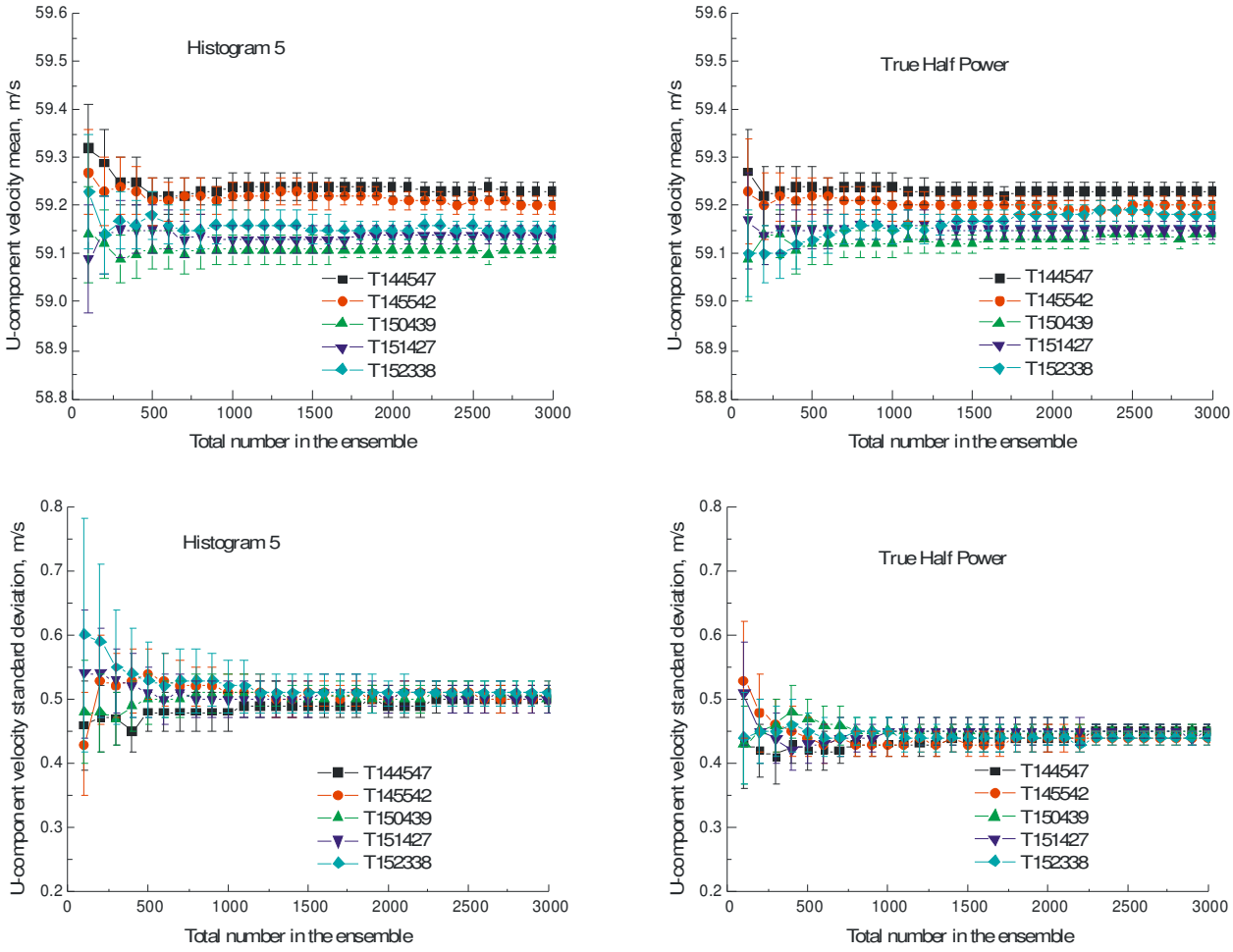

Figure V.8.- Convergence of the U-component velocity mean and standard deviation for five repeated ensembles at the centerline of a 2-inch diameter jet in the laboratory using Histogram (5) and True Half Power processing.

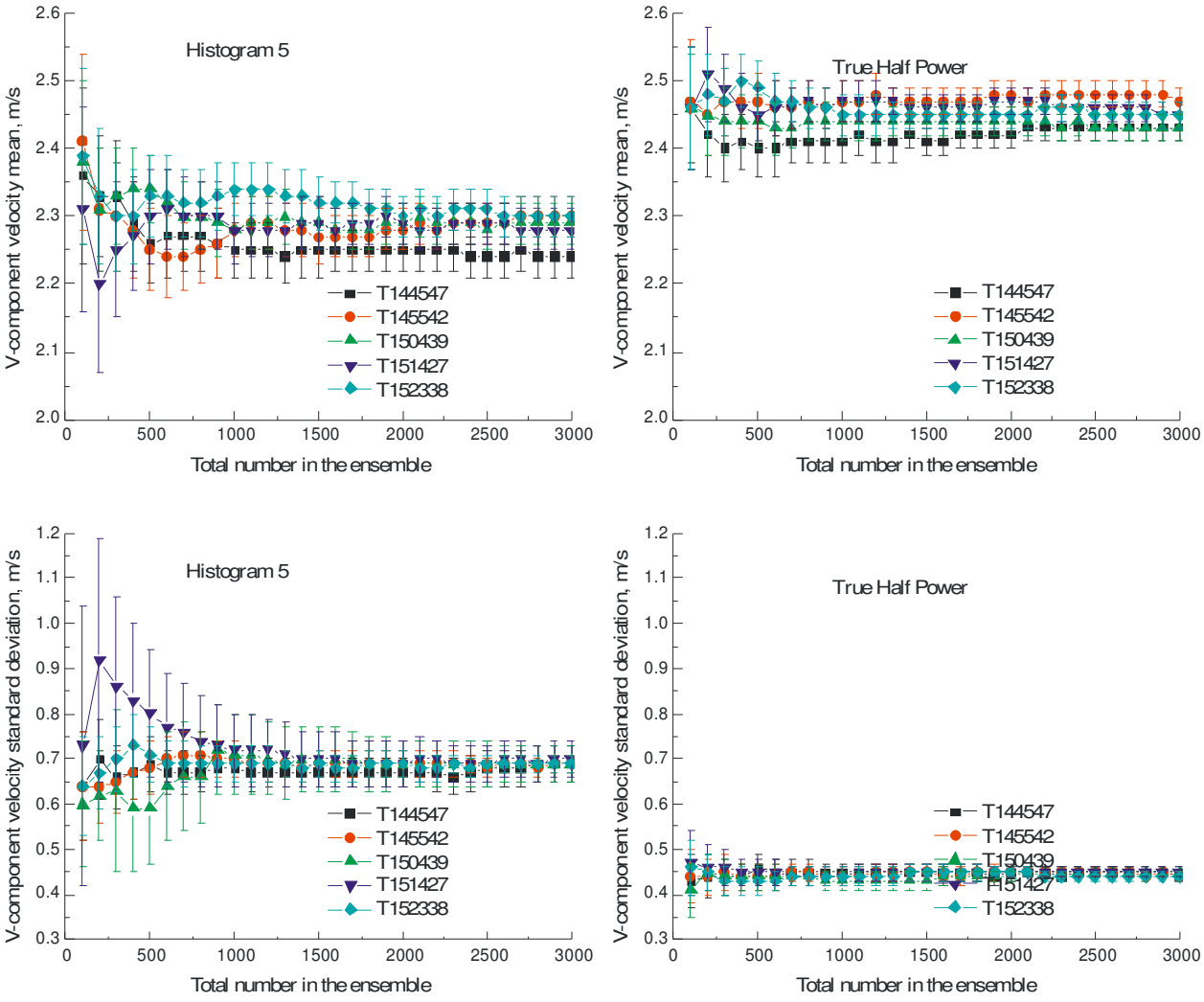

Figure V.9.- Convergence of the V-component velocity mean and standard deviation for five repeated ensembles at the centerline of a 2-inch diameter jet in the laboratory using Histogram (5) and True Half Power processing.

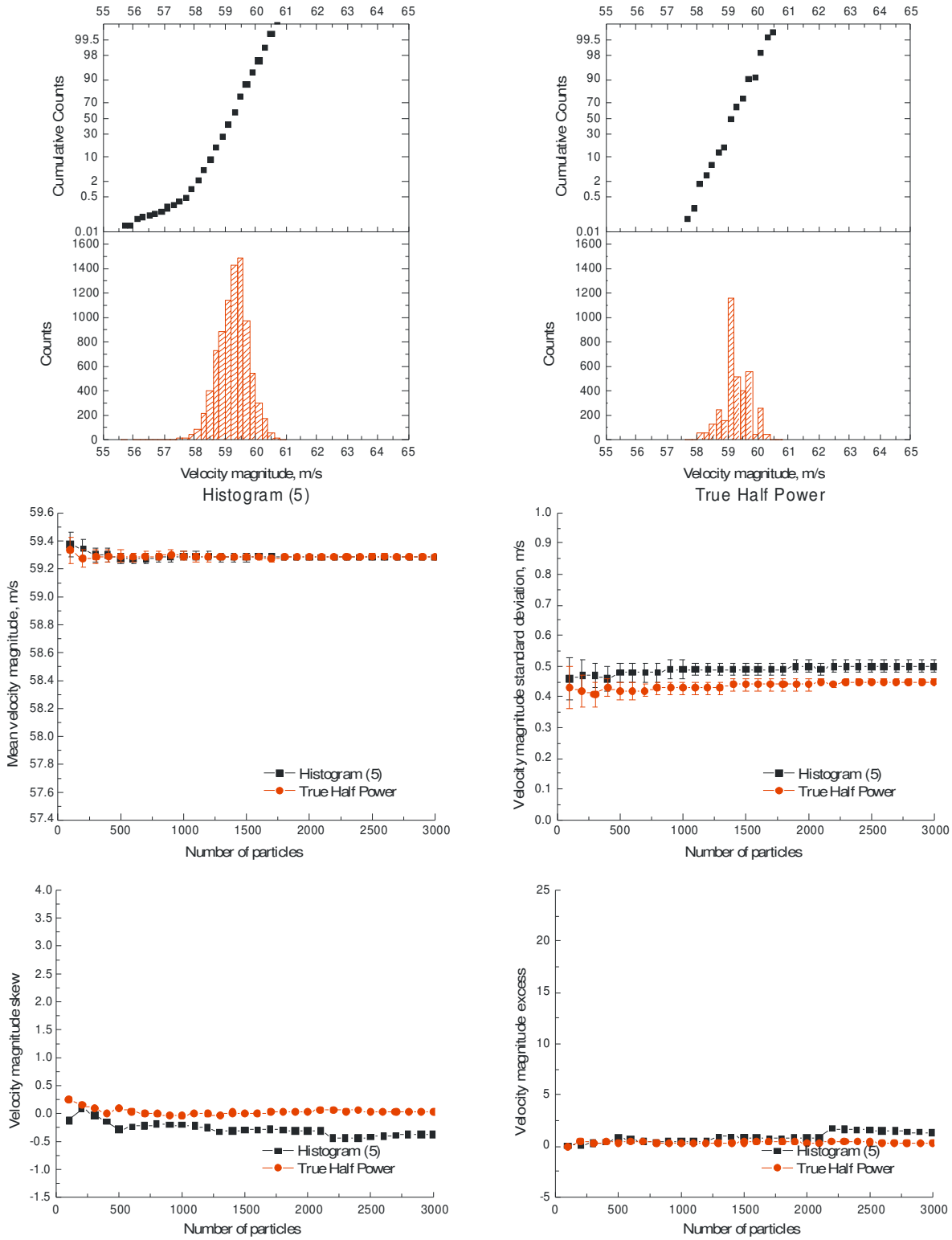

Figure V.10.- Convergence of the velocity magnitude statistics and full ensemble histograms at the centerline of a 2-inch diameter jet in the laboratory using Histogram (5) and True Half Power processing – ensemble T144647.

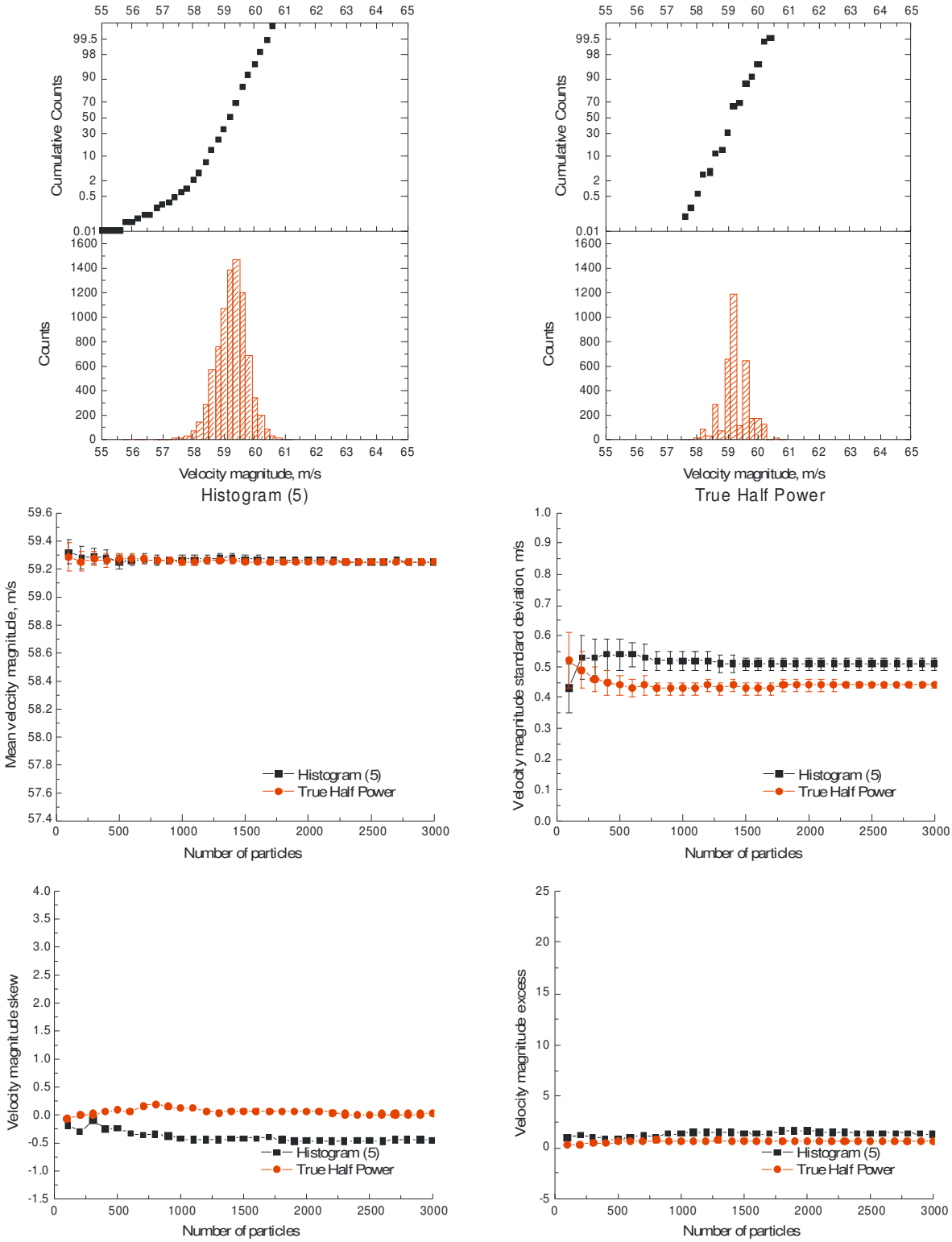

Figure V.11.- Convergence of the velocity magnitude statistics and full ensemble histograms at the centerline of a 2-inch diameter jet in the laboratory using Histogram (5) and True Half Power processing – ensemble T145542.

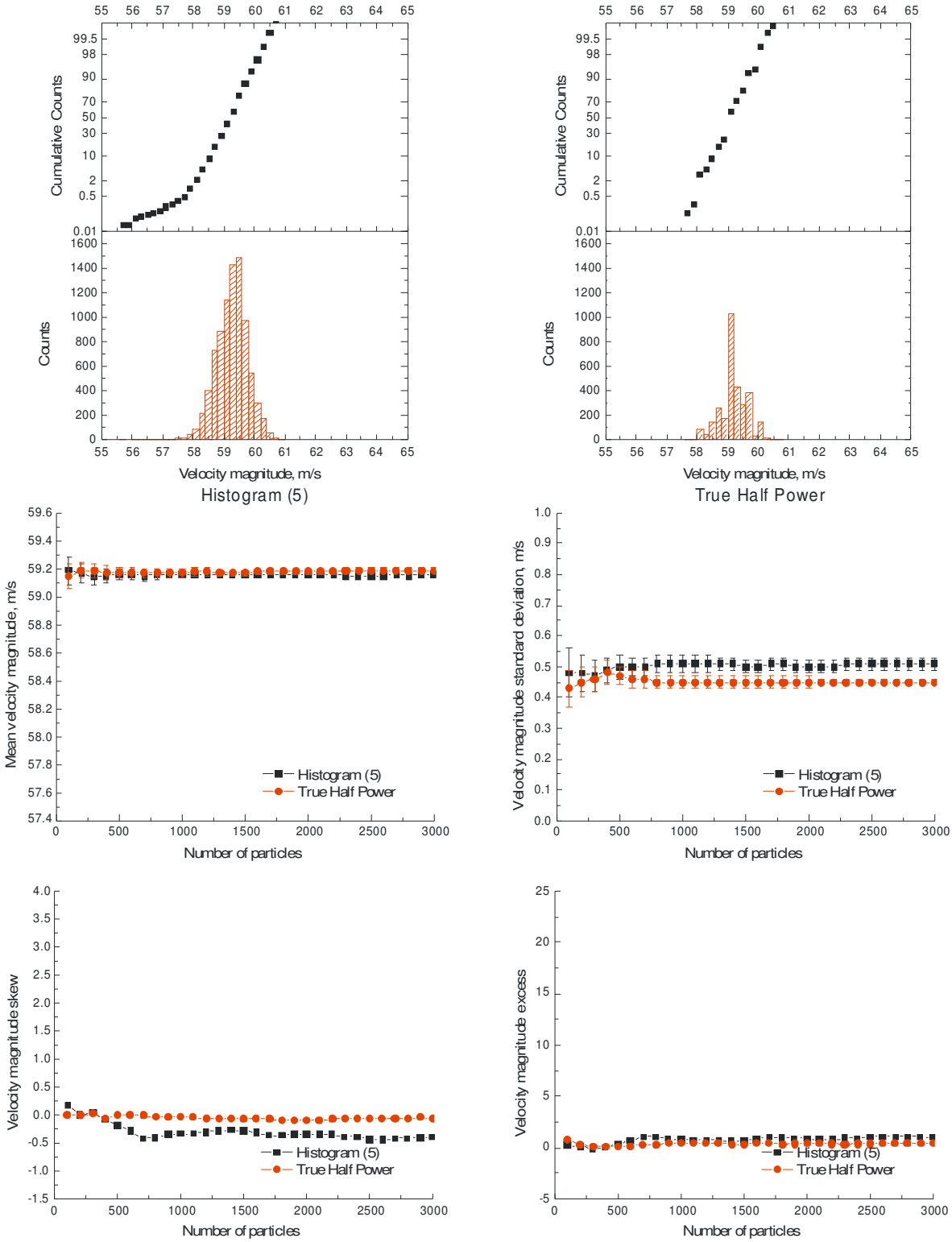

Figure V.12.- Convergence of the velocity magnitude statistics and full ensemble histograms at the centerline of a 2-inch diameter jet in the laboratory using Histogram (5) and True Half Power processing – ensemble T150439.

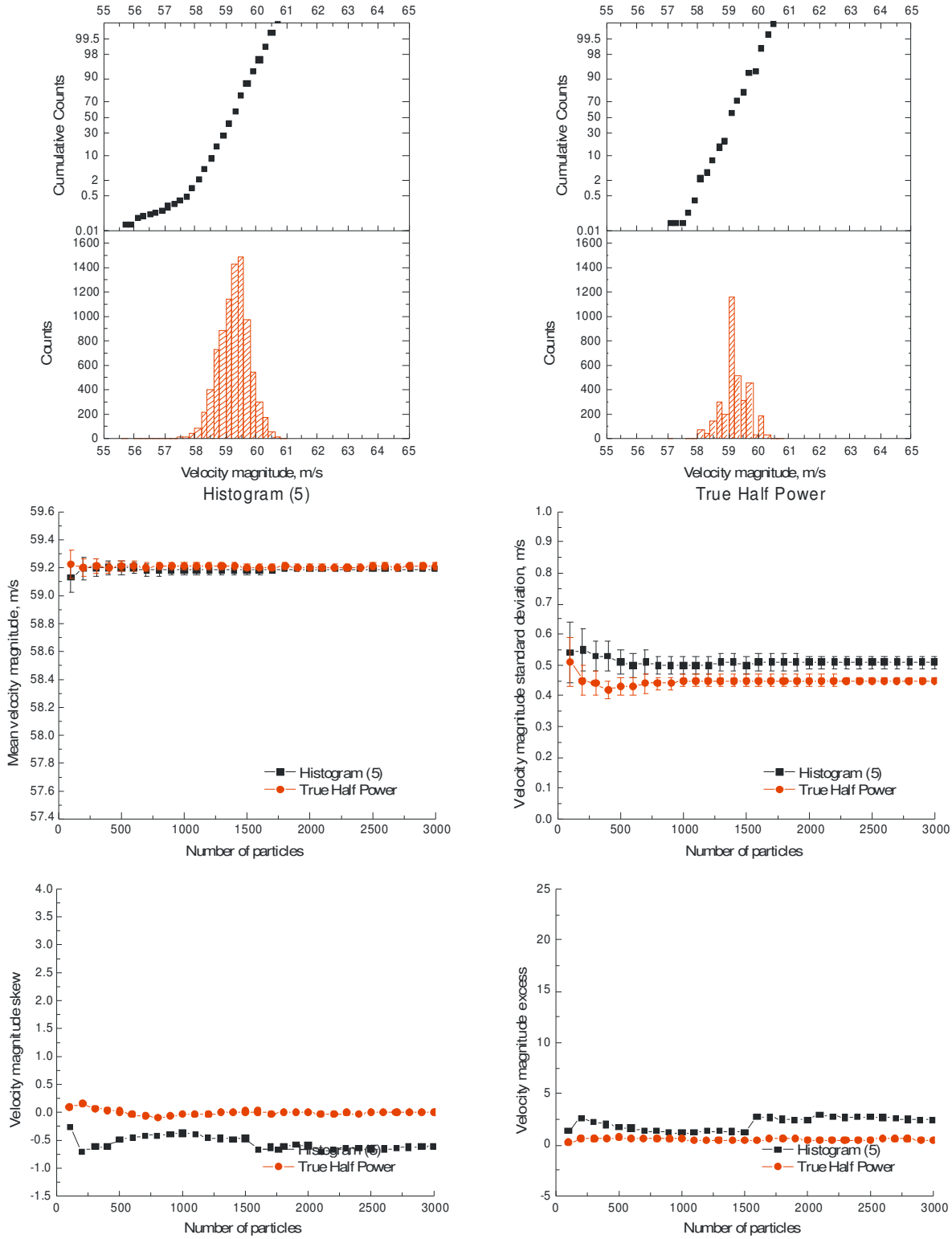

Figure V.13.- Convergence of the velocity magnitude statistics and full ensemble histograms at the centerline of a 2-inch diameter jet in the laboratory using Histogram (5) and True Half Power processing – ensemble T151427.

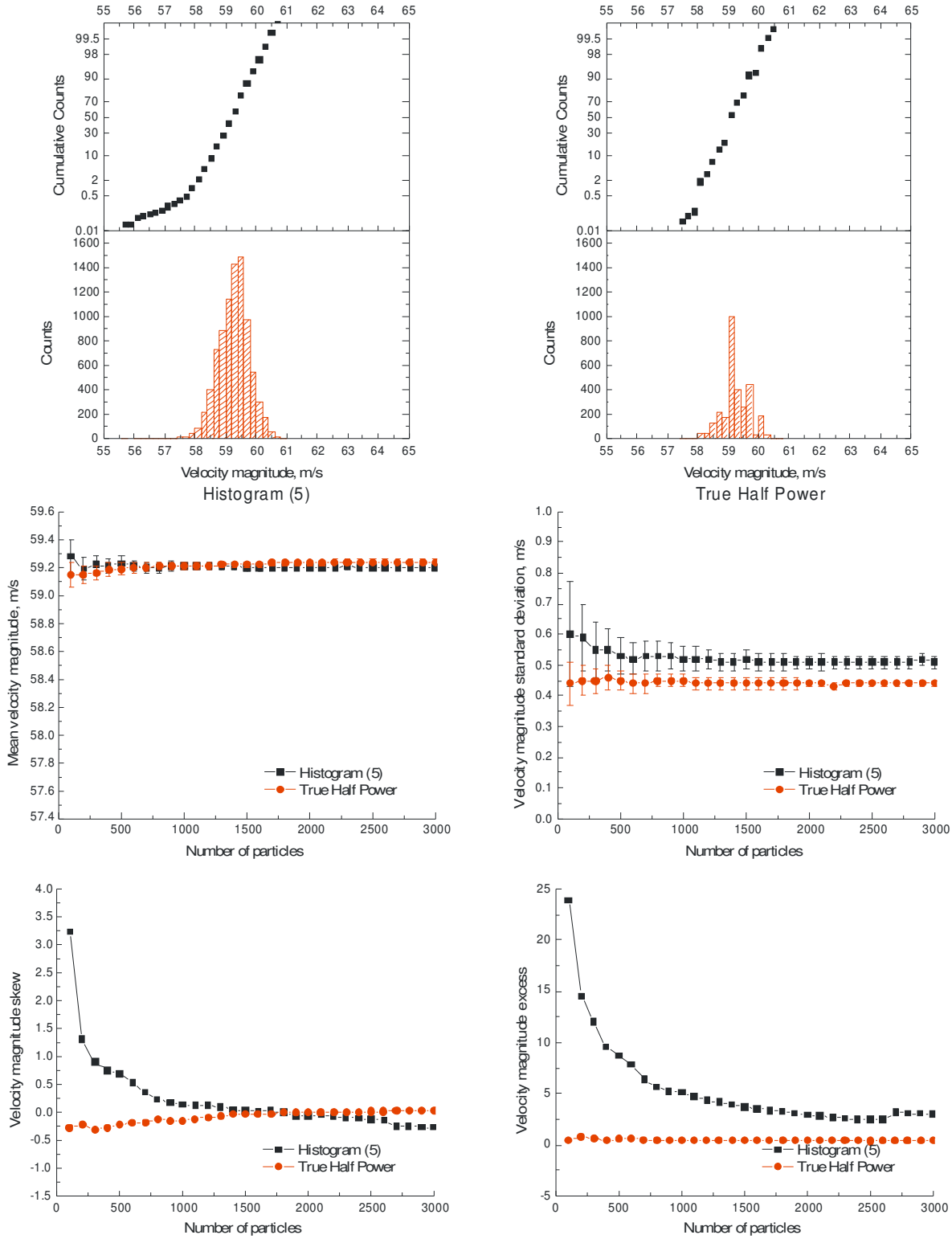

Figure V.14.- Convergence of the velocity magnitude statistics and full ensemble histograms at the centerline of a 2-inch diameter jet in the laboratory using Histogram (5) and True Half Power processing – ensemble T152338.

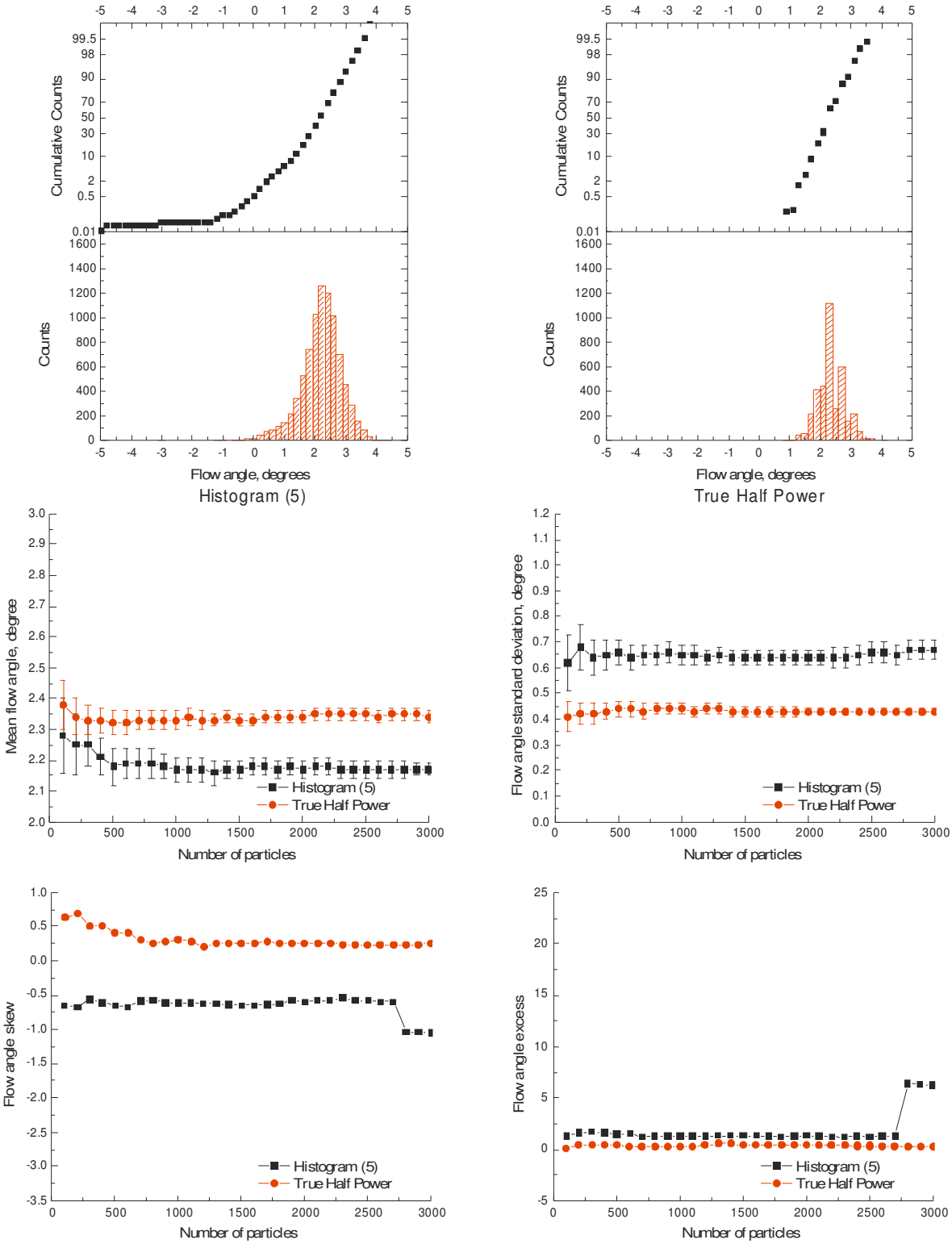

Figure V.15.- Convergence of the flow angle statistics and full ensemble histograms at the centerline of a 2-inch diameter jet in the laboratory using Histogram (5) and True Half Power processing – ensemble T144647.

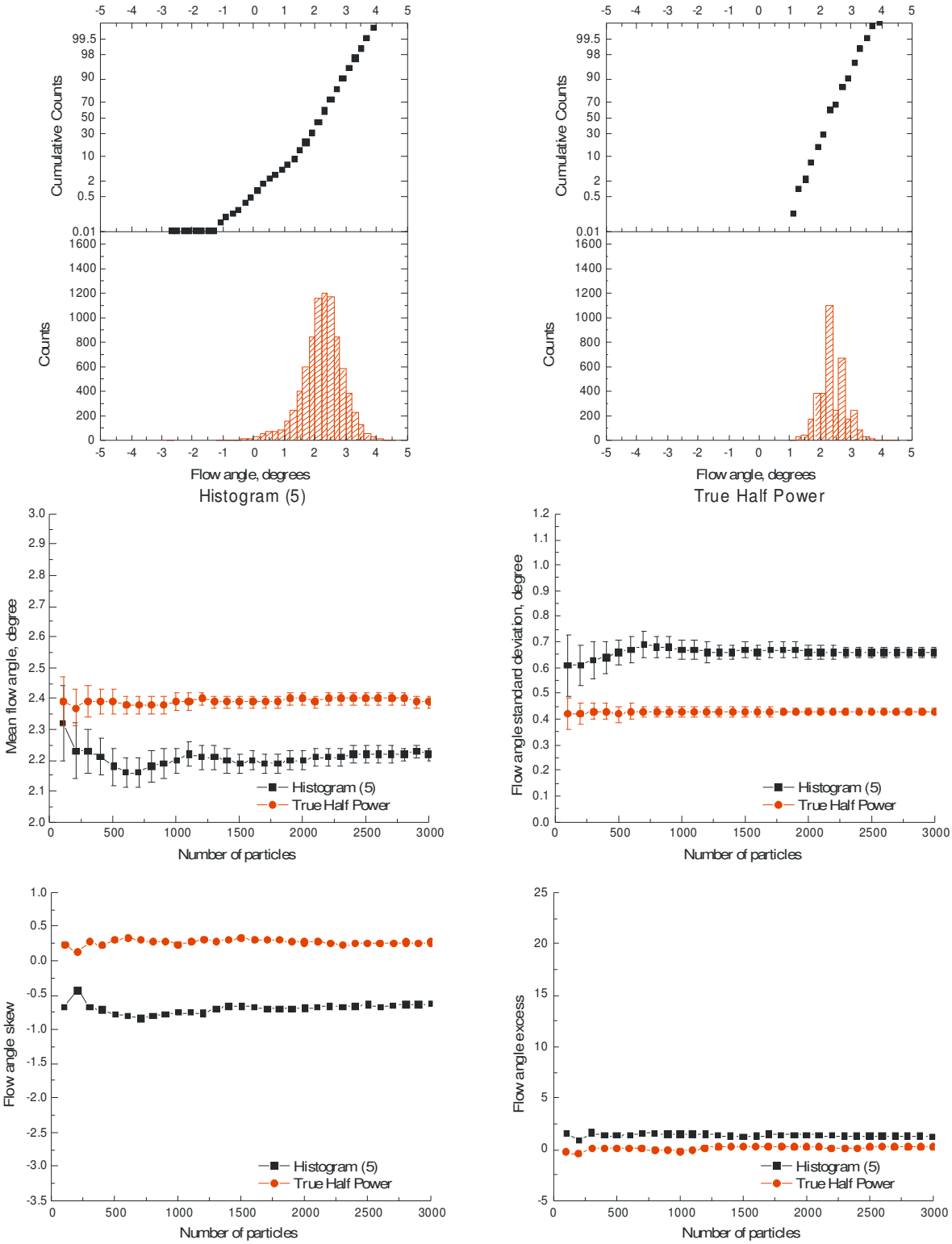

Figure V.16.- Convergence of the flow angle statistics and full ensemble histograms at the centerline of a 2-inch diameter jet in the laboratory using Histogram (5) and True Half Power processing – ensemble T145542.

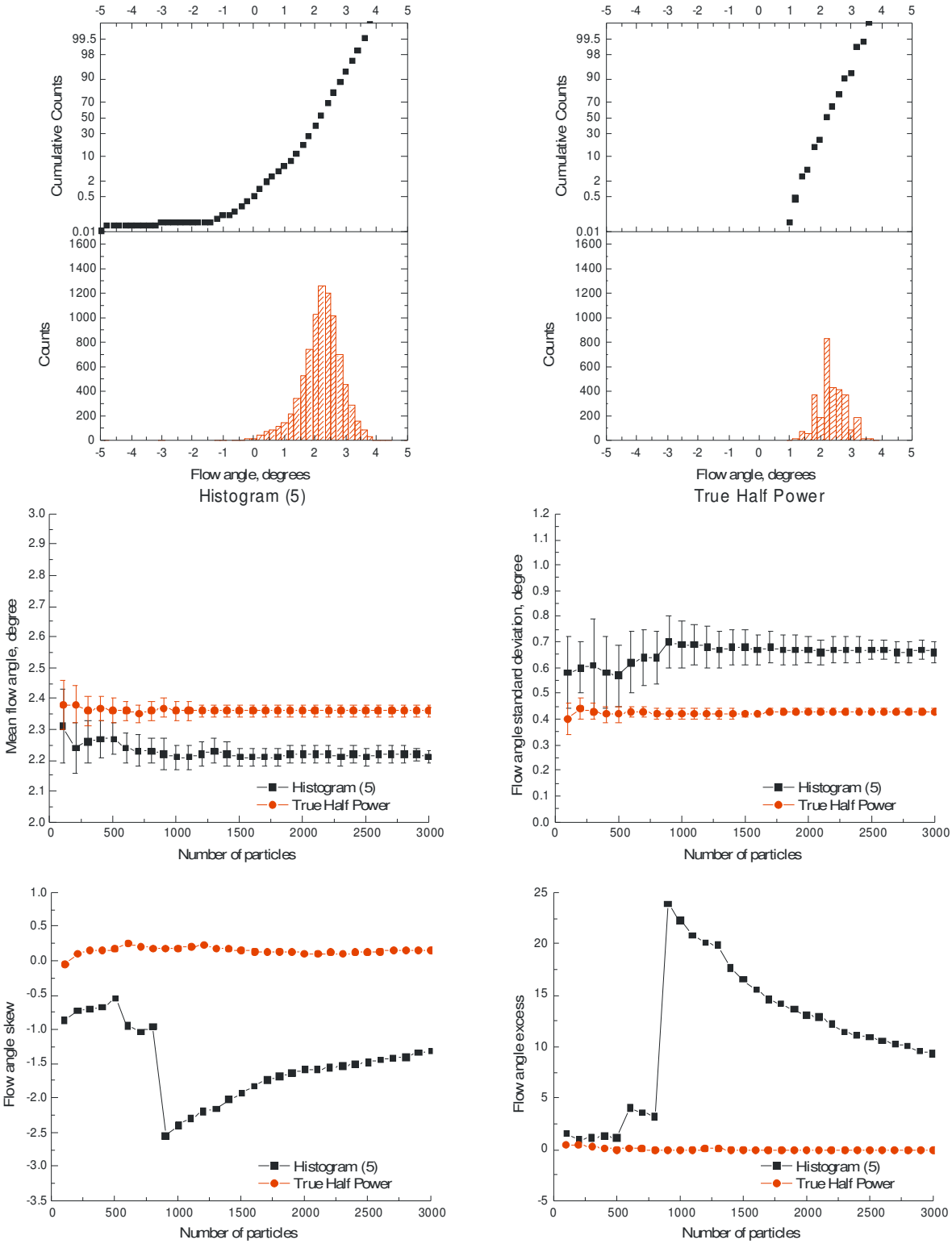

Figure V.17.- Convergence of the flow angle statistics and full ensemble histograms at the centerline of a 2-inch diameter jet in the laboratory using Histogram (5) and True Half Power processing – ensemble T150439.

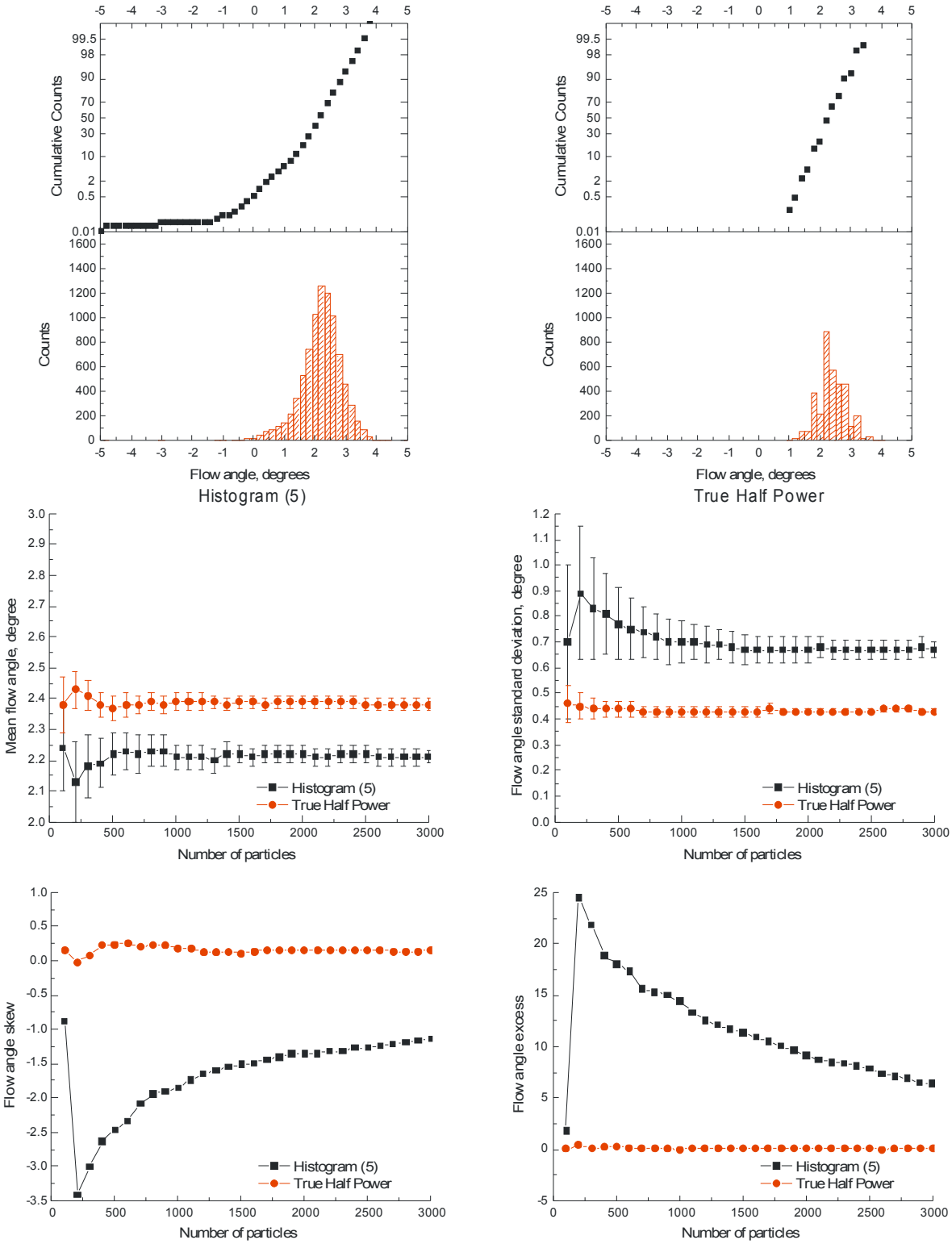

Figure V.18.- Convergence of the flow angle statistics and full ensemble histograms at the centerline of a 2-inch diameter jet in the laboratory using Histogram (5) and True Half Power processing – ensemble T151427.

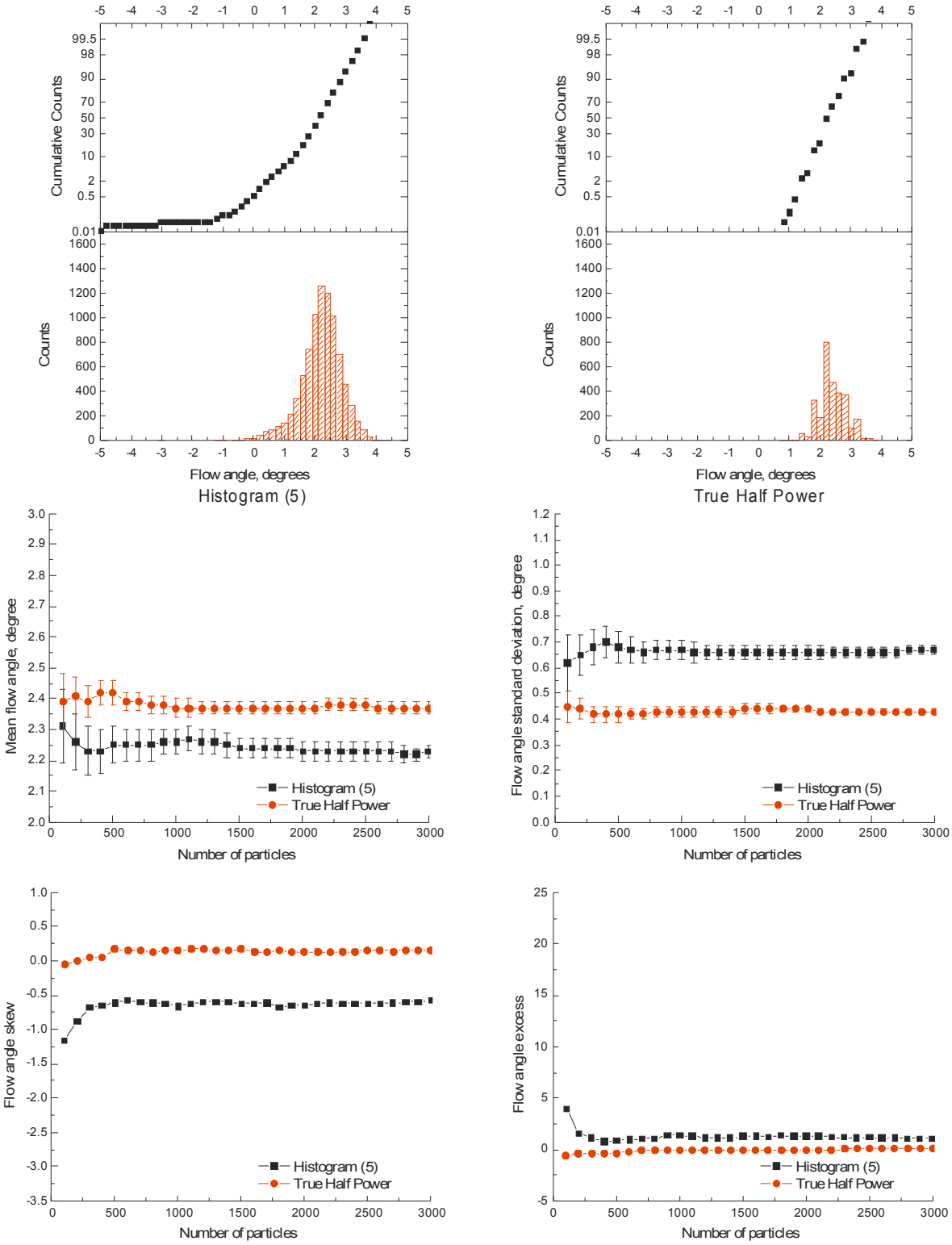

Figure V.19.- Convergence of the flow angle statistics and full ensemble histograms at the centerline of a 2-inch diameter jet in the laboratory using Histogram (5) and True Half Power processing – ensemble T152338.

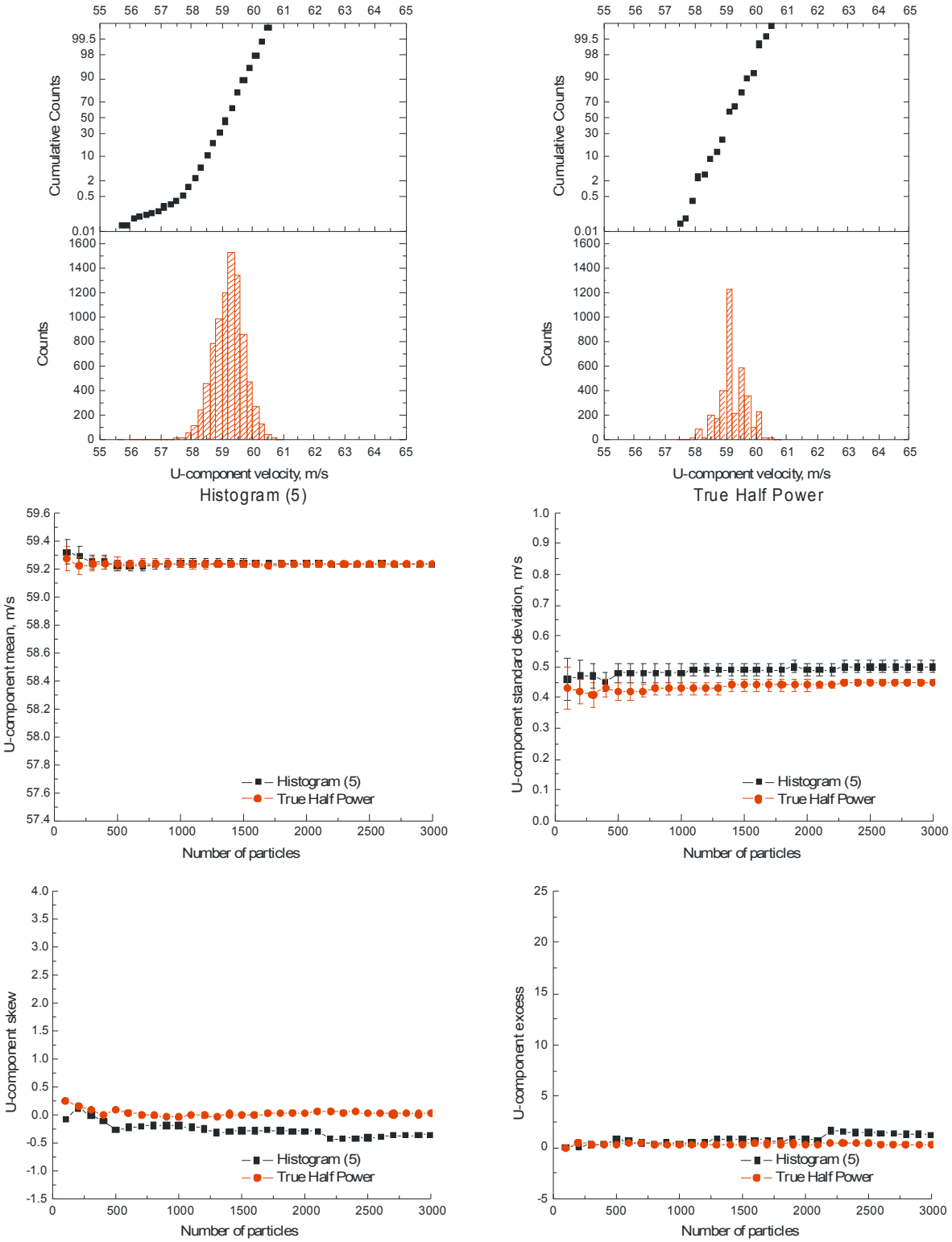

Figure V.20.- Convergence of the U-component statistics and full ensemble histograms at the centerline of a 2-inch diameter jet in the laboratory using Histogram (5) and True Half Power processing – ensemble T144647.

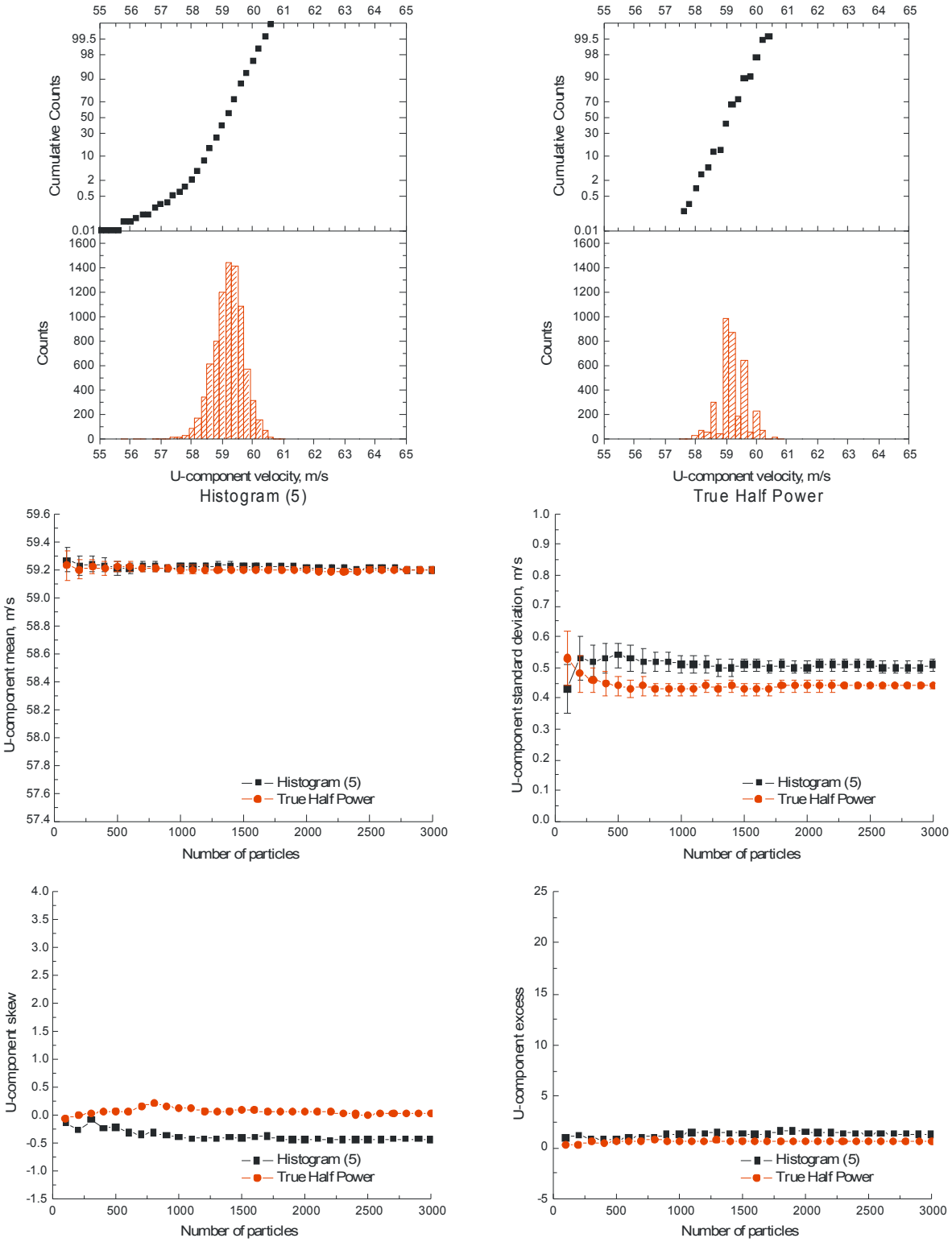

Figure V.21.- Convergence of the U-component statistics and full ensemble histograms at the centerline of a 2-inch diameter jet in the laboratory using Histogram (5) and True Half Power processing – ensemble T145542.

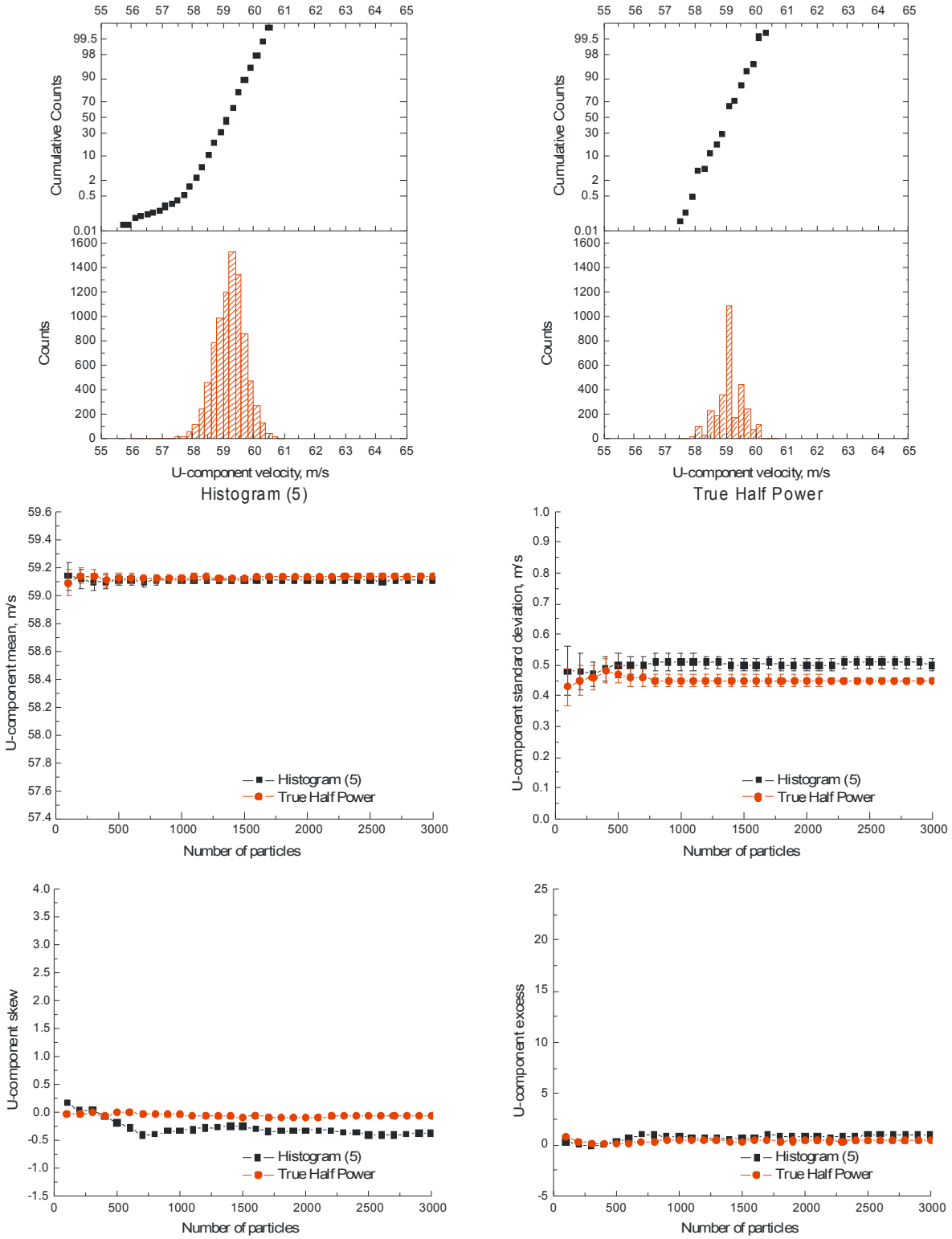

Figure V.22.- Convergence of the U-component statistics and full ensemble histograms at the centerline of a 2-inch diameter jet in the laboratory using Histogram (5) and True Half Power processing – ensemble T150439.

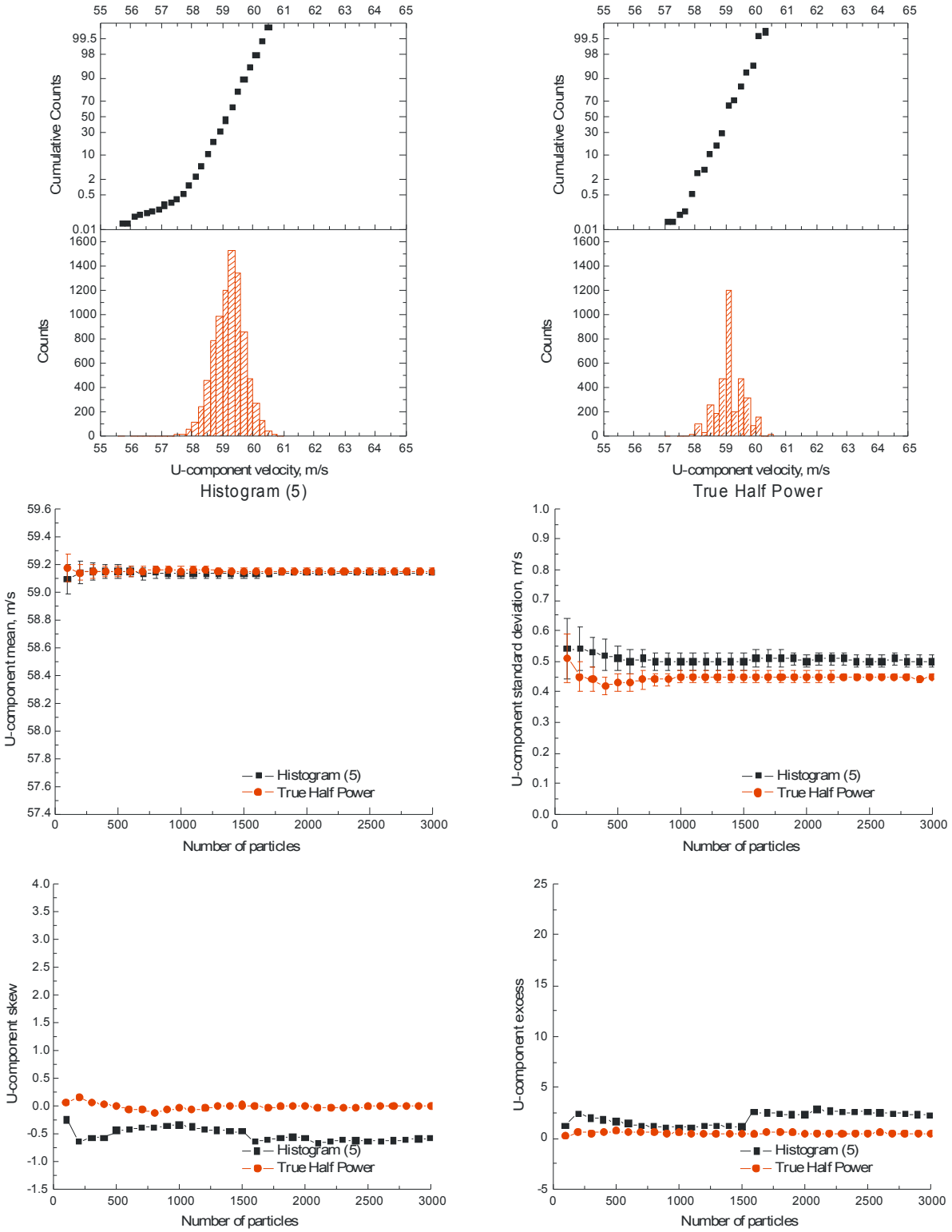

Figure V.23.- Convergence of the U-component statistics and full ensemble histograms at the centerline of a 2-inch diameter jet in the laboratory using Histogram (5) and True Half Power processing – ensemble T151427.

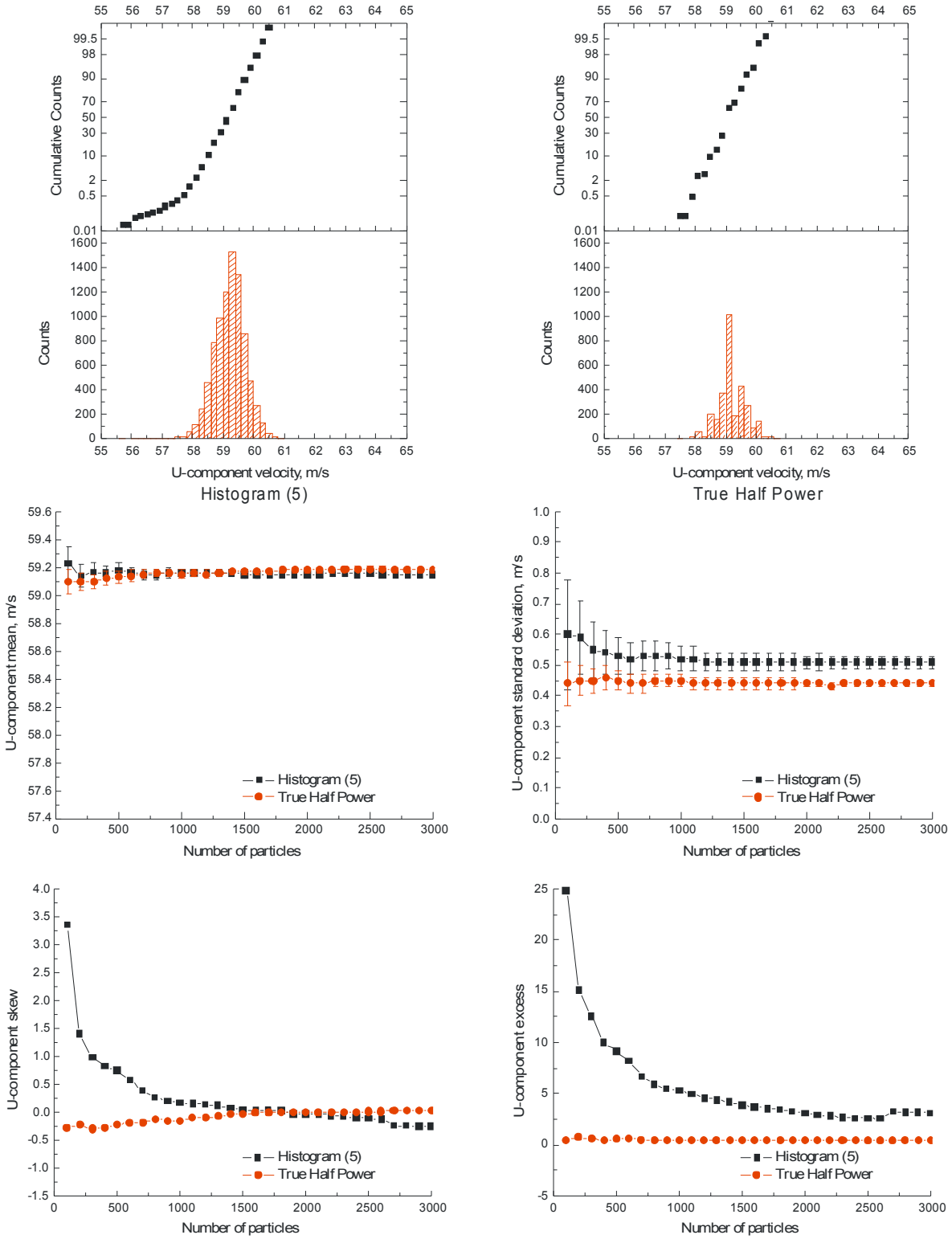

Figure V.24.- Convergence of the U-component statistics and full ensemble histograms at the centerline of a 2-inch diameter jet in the laboratory using Histogram (5) and True Half Power processing – ensemble T152338.

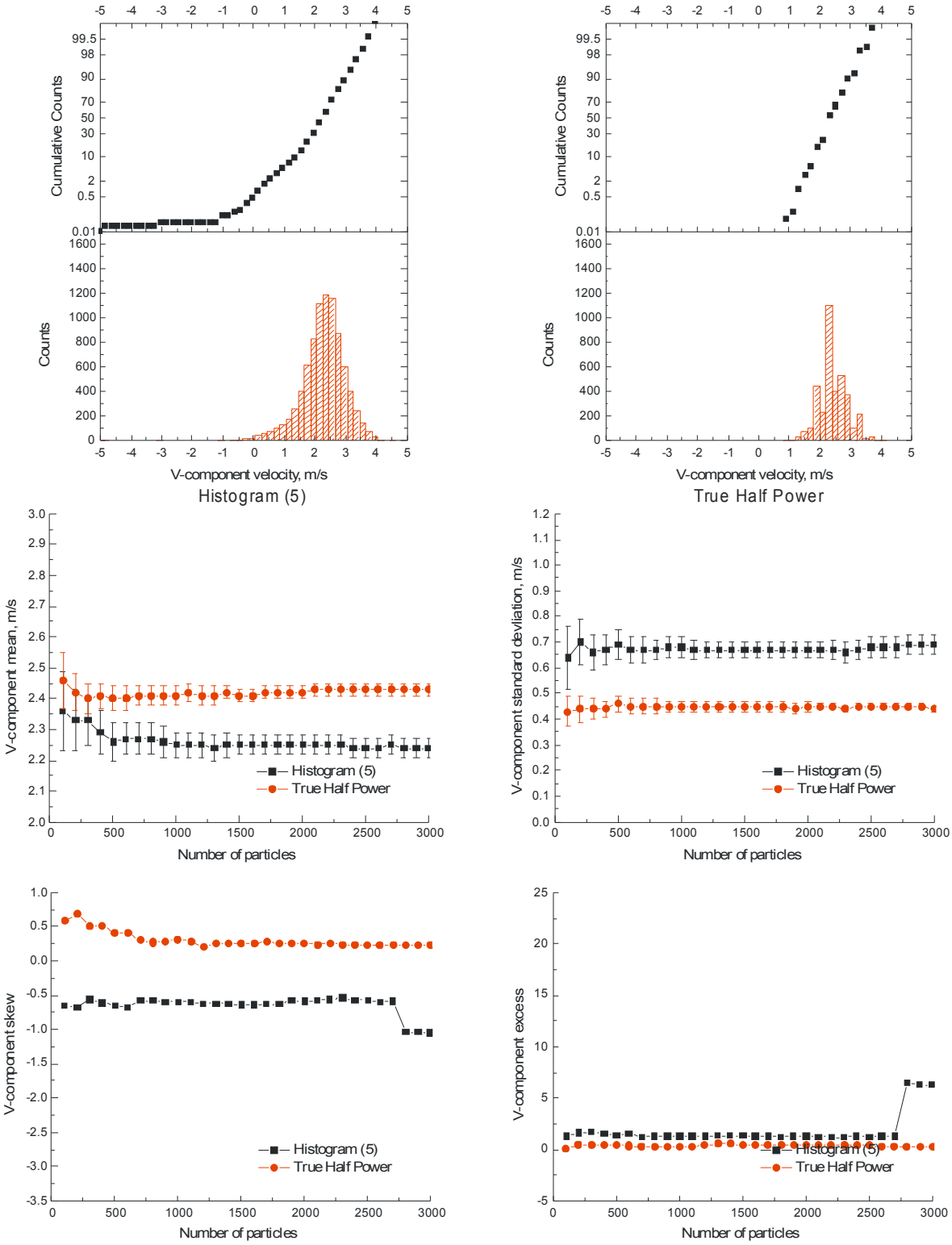

Figure V.25.- Convergence of the V-component statistics and full ensemble histograms at the centerline of a 2-inch diameter jet in the laboratory using Histogram (5) and True Half Power processing – ensemble T144647.

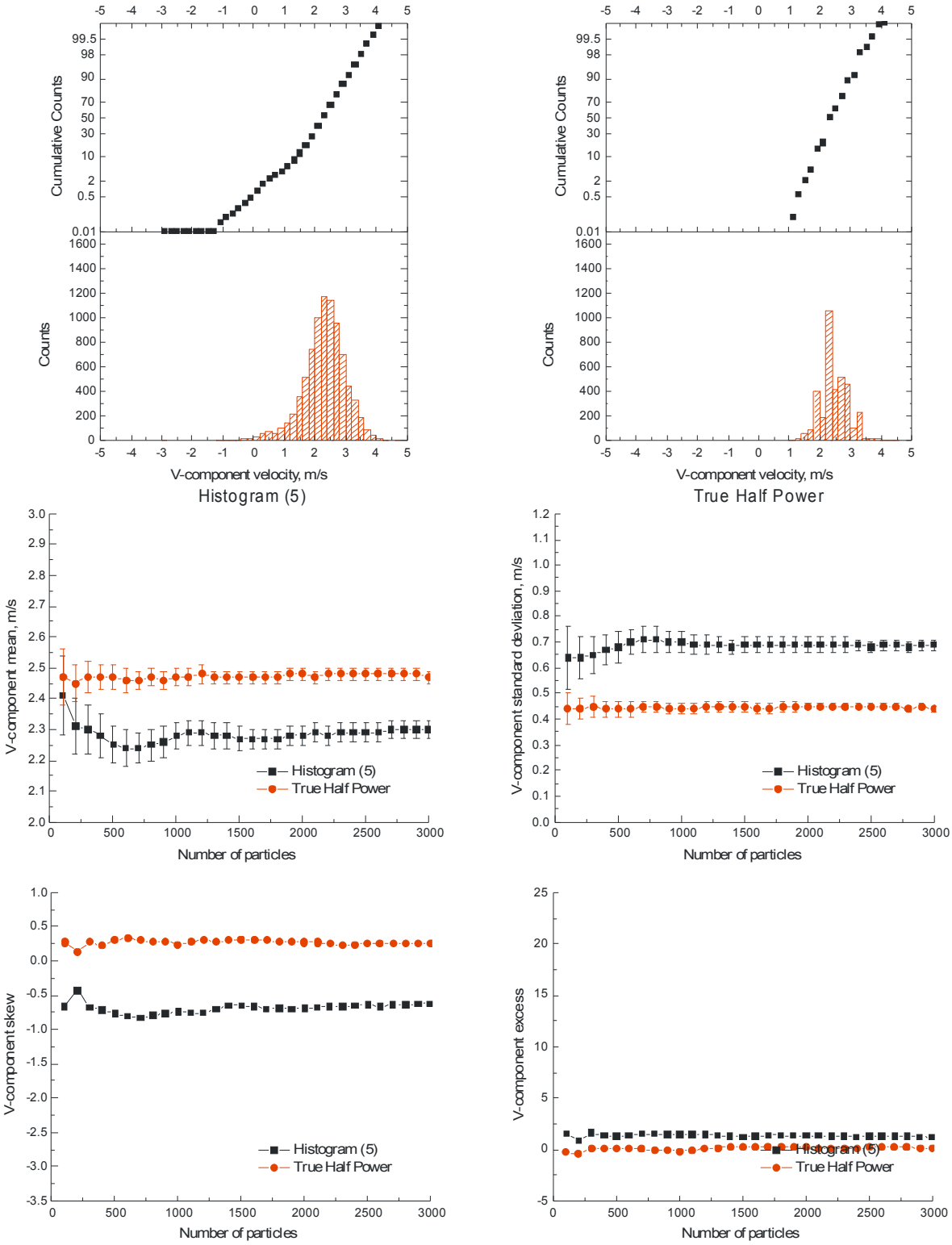

Figure V.26.- Convergence of the V-component statistics and full ensemble histograms at the centerline of a 2-inch diameter jet in the laboratory using Histogram (5) and True Half Power processing – ensemble T145542.

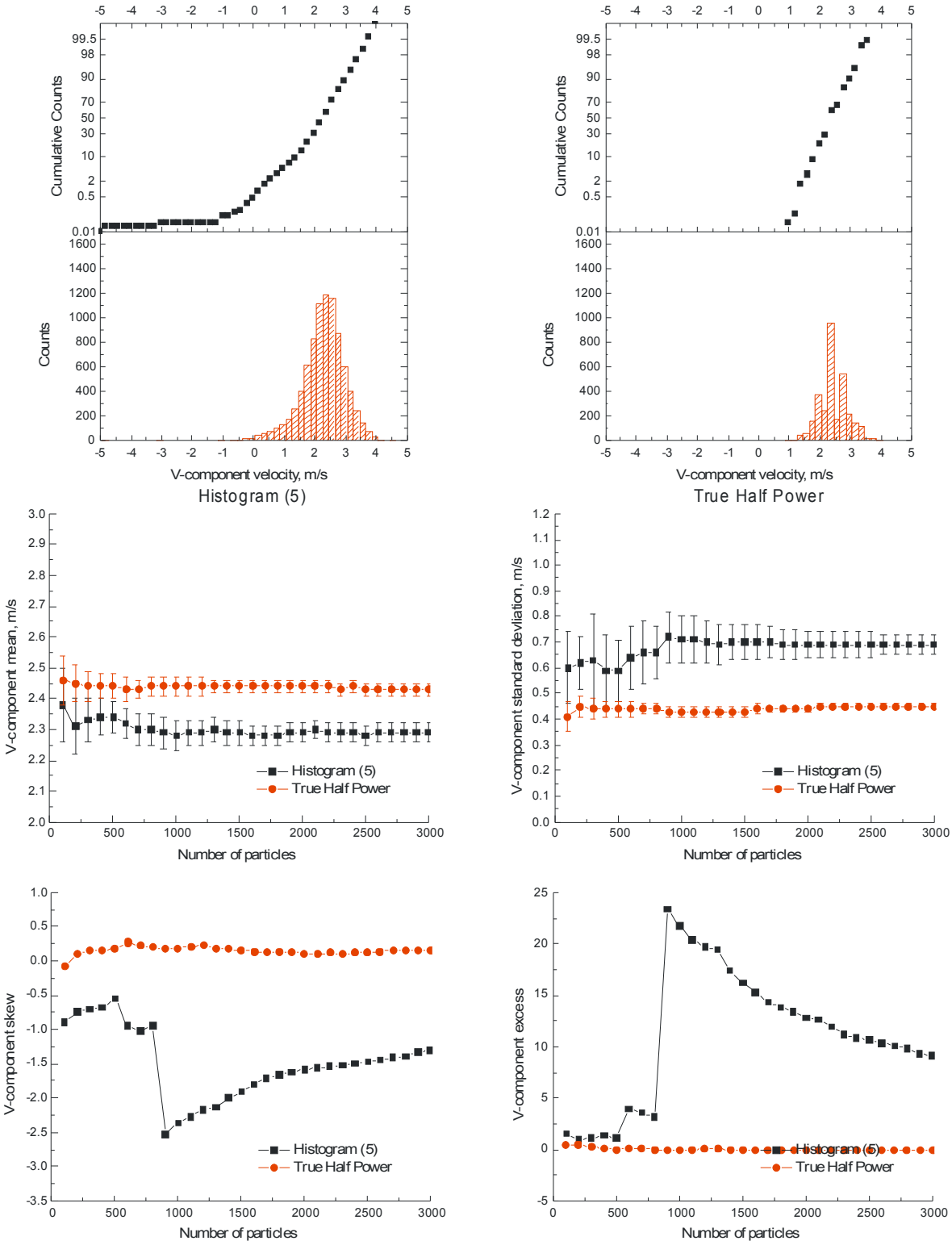

Figure V.27.- Convergence of the V-component statistics and full ensemble histograms at the centerline of a 2-inch diameter jet in the laboratory using Histogram (5) and True Half Power processing – ensemble T150439.

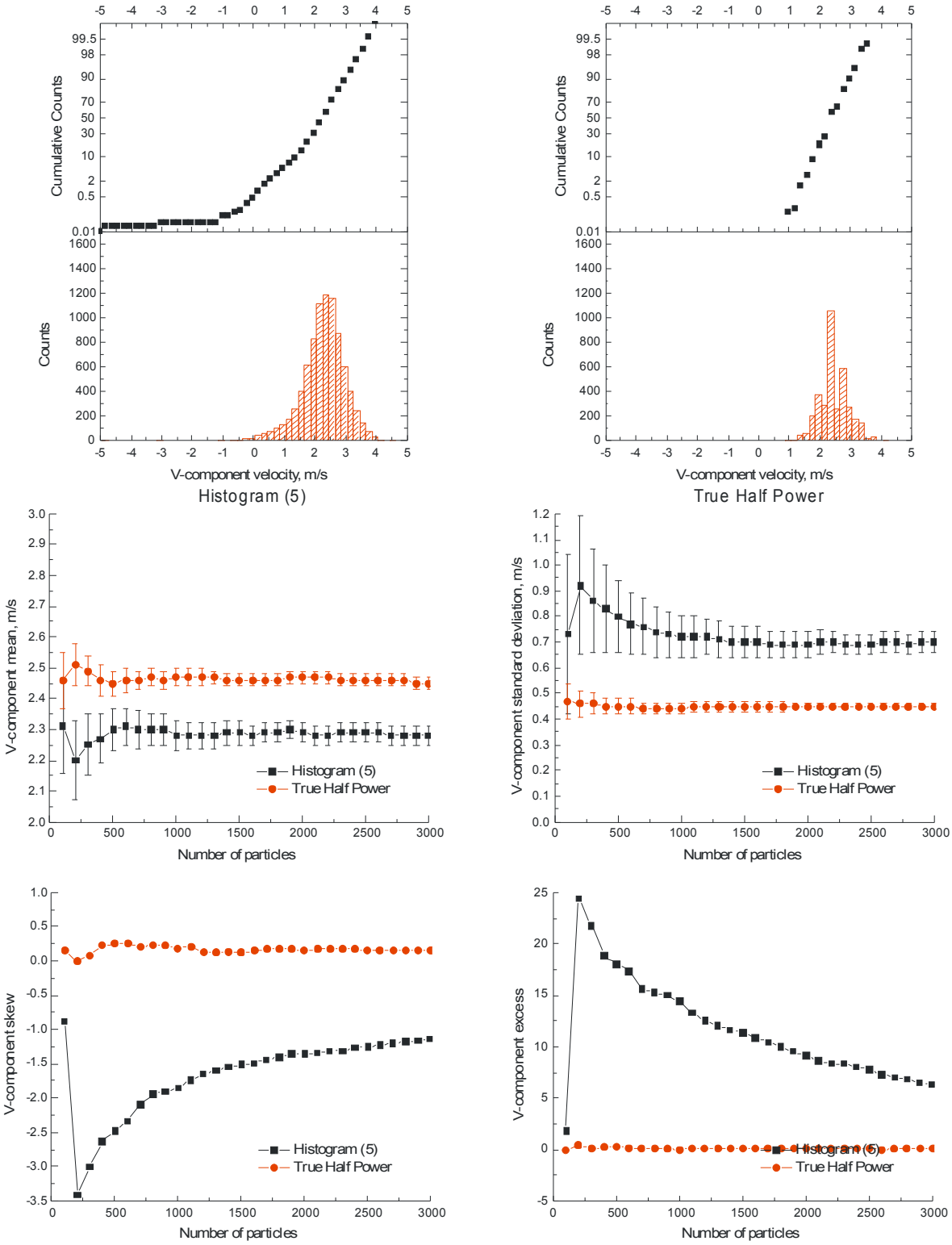

Figure V.28.- Convergence of the V-component statistics and full ensemble histograms at the centerline of a 2-inch diameter jet in the laboratory using Histogram (5) and True Half Power processing – ensemble T151427.

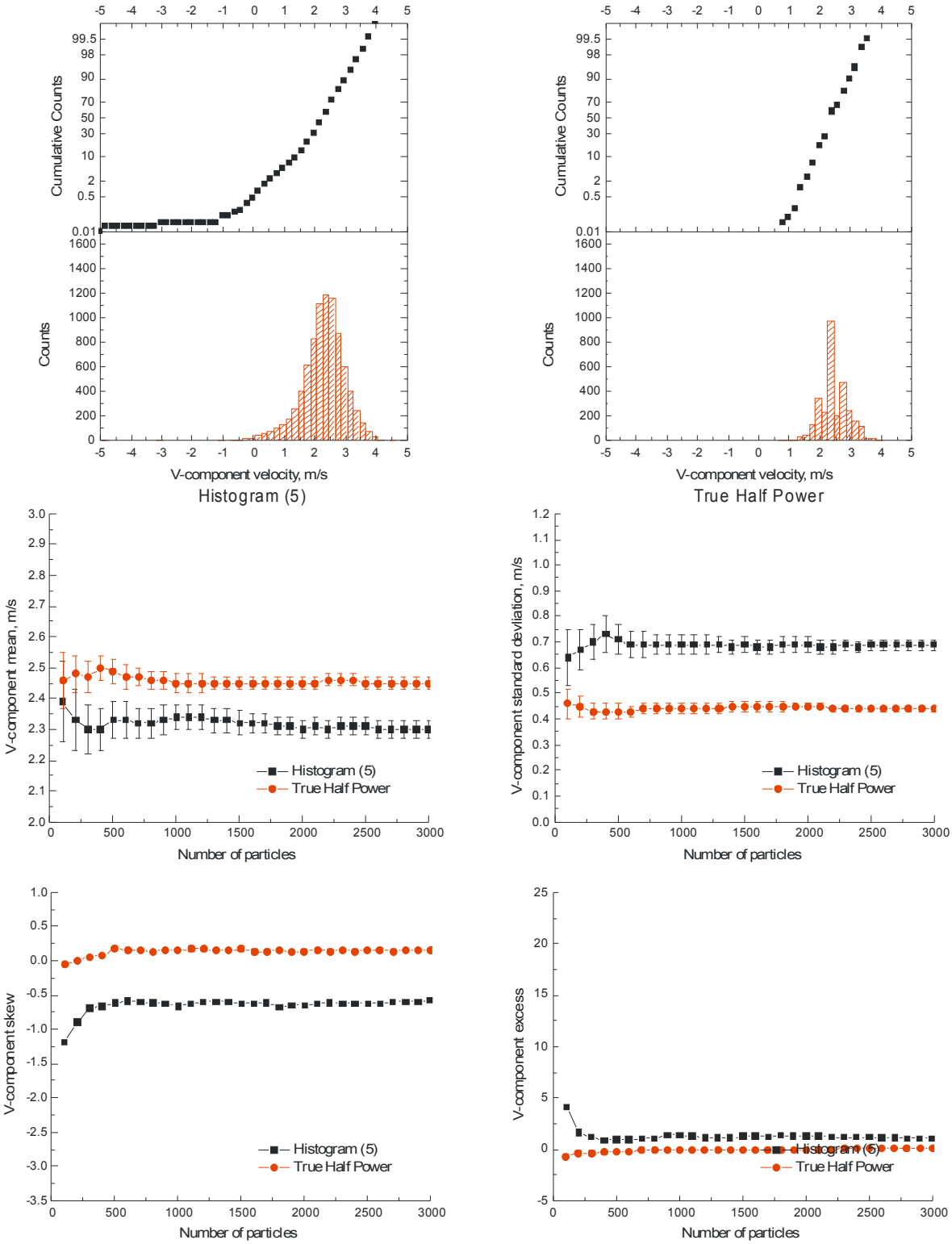

Figure V.29.- Convergence of the V-component statistics and full ensemble histograms at the centerline of a 2-inch diameter jet in the laboratory using Histogram (5) and True Half Power processing – ensemble T152338.

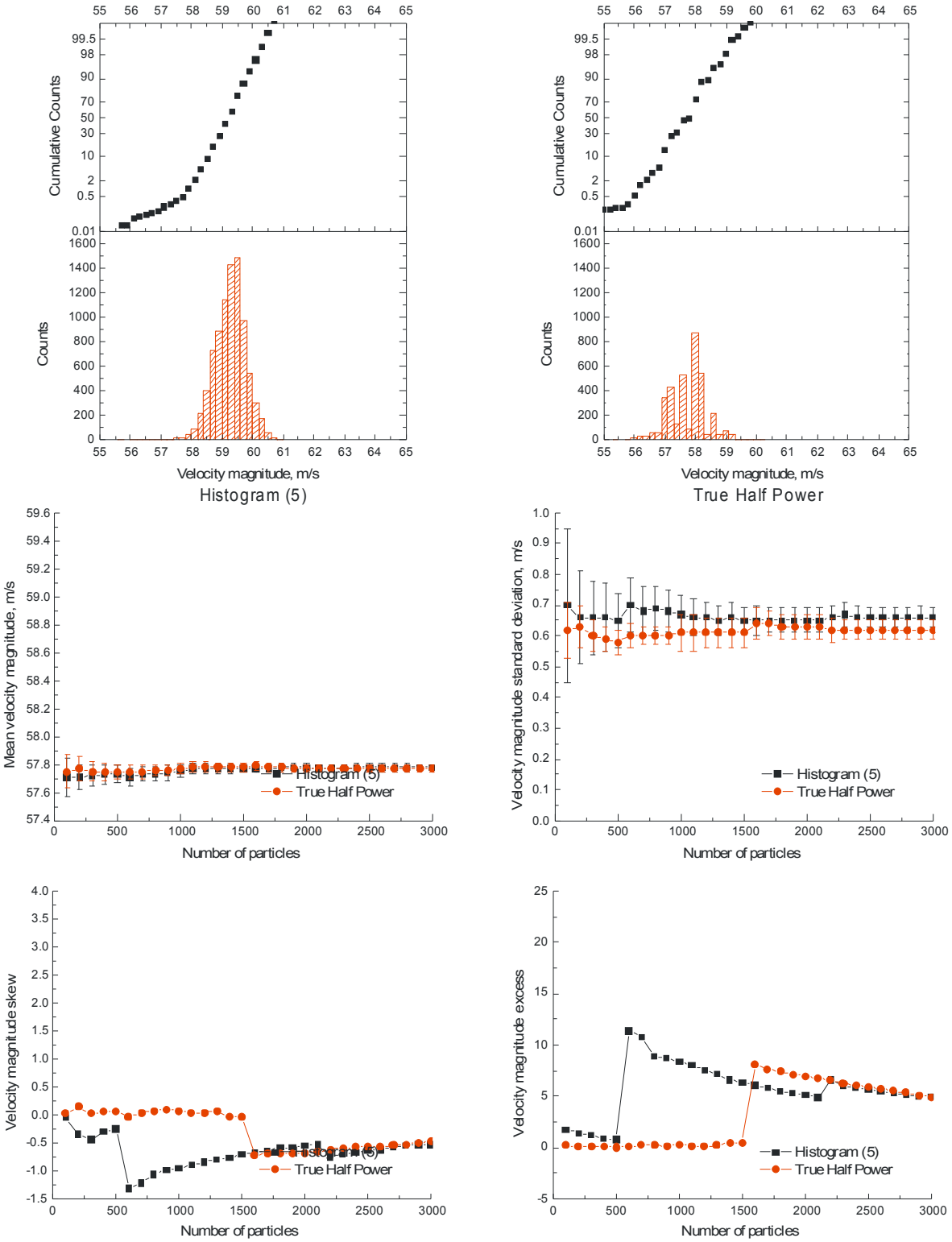

Figure V.30.- Convergence of the velocity magnitude statistics and histograms at 0.5-inch above center-line of a 2-inch diameter jet in the laboratory using Histogram (5) and True Half Power processing – ensemble T153437.

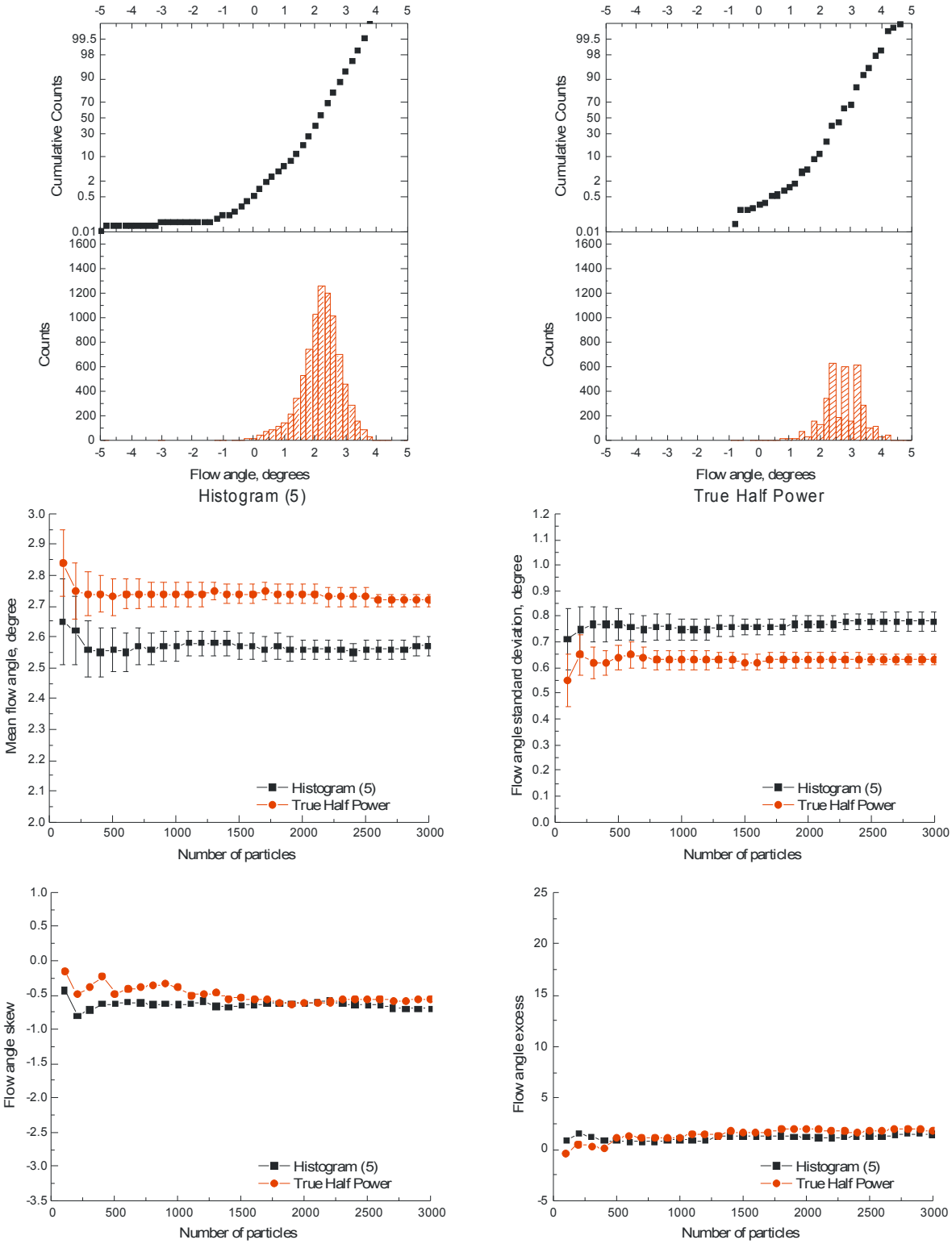

Figure V.31.- Convergence of the flow angle statistics and histograms at 0.5-inch above center-line of a 2-inch diameter jet in the laboratory using Histogram (5) and True Half Power processing – ensemble T153437.

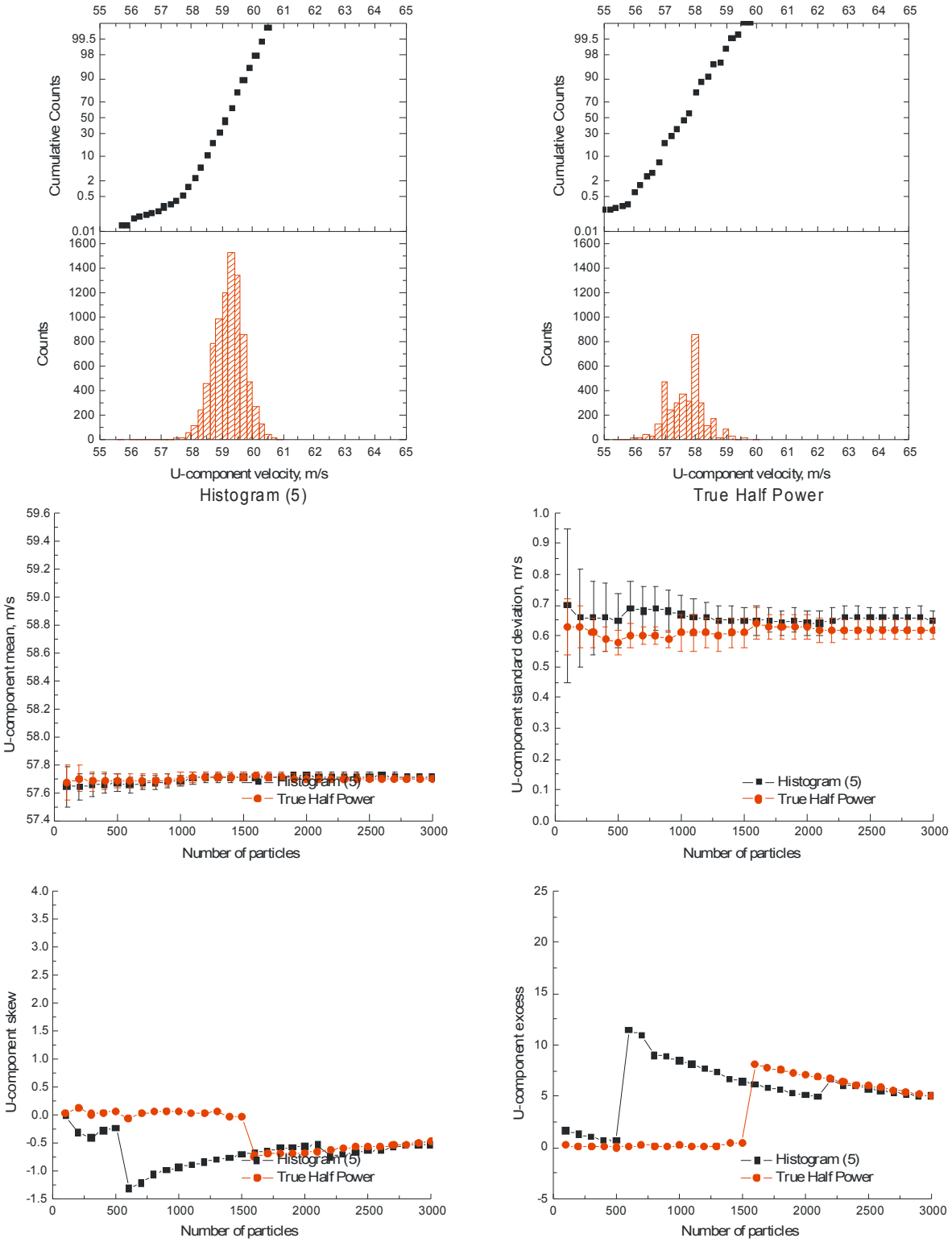

Figure V.32.- Convergence of the U-component statistics and histograms at 0.5-inch above center-line of a 2-inch diameter jet in the laboratory using Histogram (5) and True Half Power processing – ensemble T153437.

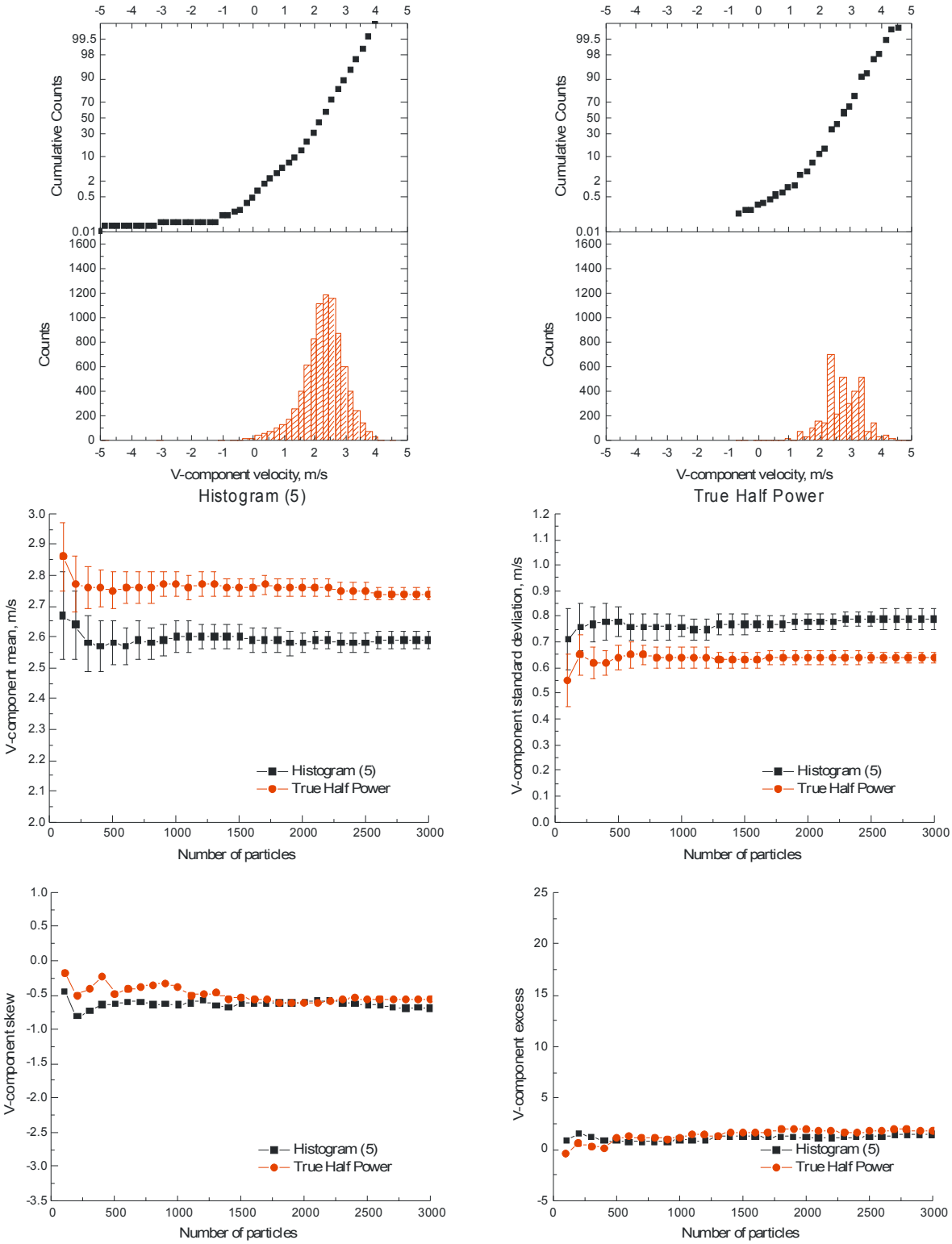

Figure V.33.- Convergence of the V-component statistics and histograms at 0.5-inch above center-line of a 2-inch diameter jet in the laboratory using Histogram (5) and True Half Power processing – ensemble T153437.

Evaluation Testing of the Upgraded 14- by 22-Foot Subsonic Tunnel Laser Velocimeter in the Basic Aerodynamics Research Tunnel

The next phase of the validation of the upgraded laser velocimeter for the 14- by 22-Foot Subsonic Tunnel was to measure the flow field about a backward facing step in the Basic Aerodynamics Research Tunnel (BART), schematic below. This model was chosen because the velocity flow field ranges from low turbulence freestream to a recirculating flow along with the associated shear flow region. In addition, this flow field has been previously measured by two different fringe-type laser velocimeter systems (Meyers *et al* (1990) and Hart *et al* (2001)).

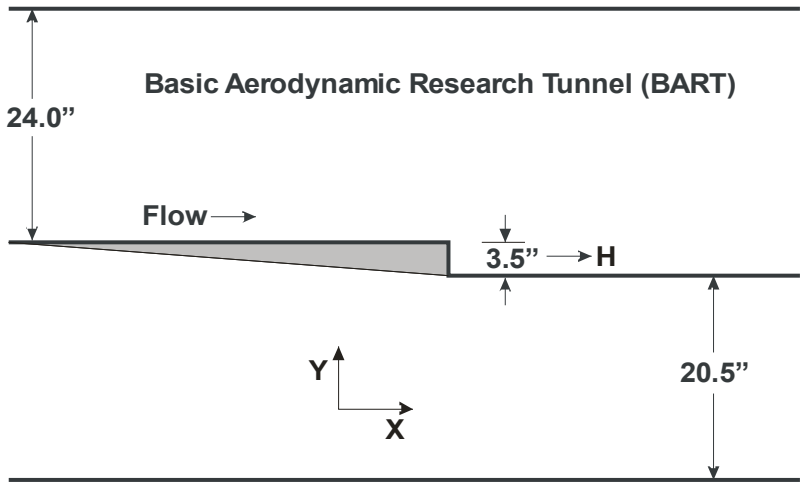

The upgraded laser velocimeter was installed in the BART with the final configuration that will be used in the 14- by 22-Foot Subsonic Tunnel. The system, shown in Figure VI.1, consists of two subsystems. The subsystem containing the final zoom lens and the laser transceiver, Figures VI.2-VI.3, would be placed in the tunnel plenum chamber. The laser, beam splitting and fiber coupling optics along with the photomultipliers, Figure VI.1, would be located in the laser velocimetry laboratory adjacent to the wind tunnel test section to protect these components from the harsh environment in the plenum chamber, and to allow minor optical adjustments to be made while the tunnel is in operation. The two subsystems are connected with a 15-meter-long fiber optic bundle – containing four polarization preserving fibers to transmit the laser beams to the transceiver probe and a single multi-mode fiber to return the collected scattered light to the photomultipliers, Figure VI.4. As shown in Figure VI.4, both subsystems were located in the return leg of the BART for the system evaluation test. A photograph of the system in operation with the laser beams passing through the freestream flow at the backward facing step location is shown in Figure VI.5. The four photo-diode array used to measure the leakage power of the four laser beams through the final turning mirror just prior to the zoom lens is shown in Figure VI.6. This array provides the feedback needed to adjust the fiber optic coupling efficiency of the laser beam should the laser resonator alignment drift during testing.

Evaluation of the Laser Velocimeter in Various Flow Fields

The first part of the evaluation was to obtain large data ensembles at several locations about the step to determine the statistical convergence characteristics in freestream, shear region, and reverse flows. The primary question was whether the statistics converged in the manner found in the simulation and laboratory tests, and to see if convergence varies with flow conditions. Since the laboratory tests indicated that the Histogram (5) approach provided a better representation of the flow velocity distributions, it was the only processing method used during this investigation. The 1.7-micron PSL particles, suspended in a 50:50 mixture of water and ethanol, were injected at the tunnel inlet using two paint sprayers. The measurement volume was set above the 3.5-inch step and slightly downstream (y/H = 0.34, x/H = 0.32) to evaluate the system in freestream conditions. The freestream velocity was set to 16.6 m/s. Four data ensembles were acquired, each with 5,000 measurements, with the distribution for all measurements plotted along with the convergence statistics for the first 3,000 measurements of each ensemble. The results for the velocity magnitude are shown in Figure VI.7. The distribution was nearly Gaussian as would be expected in the freestream and the convergences occur almost immediately in the standard deviation with very small differences (~20 mm/s) in the stationary values. It is also noted that the convergence plots do not extend to 3,000 data points because the lower data rate, as compared to the laboratory tests, allowed the noise pulses described in Chapter V and shown in Figure V.4, to become a significant fraction of the data ensemble. These trends continued with the flow angle, U- and V-component velocity results, Figures VI.8-VI.10 respectively. It is also noted that, as with the laboratory data, the flow angle and V-component velocity means had larger differences among the four stationary values, in this case by 1.4-degrees and 0.4 m/s respectively. The distributions for each of the four ensembles are shown in Figures VI.11-VI.14. Although there are slight differences among the distributions, the overall characteristics remain very similar for the four ensembles.

This process was repeated with the measurement volume located in the shear region just downstream of the step (y/H = -0.17, x/H = 0.32). In this case the velocity magnitude distribution, Figure VI.15, has decreased indicating that the measurement volume is below freestream, yet the skew toward higher velocities may indicate some influence of freestream. The convergence of the standard deviation was very rapid for this data ensemble – approximately 700 measurements. However only 1,250 signal bursts were processed, an indication that the data rate was lower than freestream as expected, with a corresponding increase in the number of spurious noise pulses within the ensemble. Moving to the flow angle results, Figure VI.16, the peak of the distribution was located at 130-degrees. The U- and V-component velocity distributions, Figures VI-17-VI.18, were nearly Gaussian which may indicate that a coupling of the component velocities caused the skew in the velocity magnitude distribution and not freestream. Based on these distributions, the flow at this location was directed upstream with an upward angle of 50-degrees indicating that this location was near the top of the upstream portion of the primary separation vortex. However the large spread in the flow angle distribution also appears to indicate that the flow is very turbulent with angles extending from the

freestream direction to fully reversed flow. At this position, the flow was varying about 1.4-m/s in the x-axis and 0.9-m/s in the vertical axis. The separation in mean flow angle and V-component velocity found in the freestream data was not as noticeable at this location, but then again convergence did not occur in the flow angle or the V-component standard deviations. The individual distributions are shown in Figures VI.19-VI.22.

The measurement volume was then moved further downstream directly behind the top of the step (y/H = 0.0, x/H = 0.69). This should have located the measurement volume in the primary shear region between the freestream flow and the recirculation zone. In this case the distribution of the velocity magnitude, Figure VI.23, had a marked skew toward lower velocities indicating the presence of the recirculation zone part of the time, with the peak of the distribution approximately 20-percent below the freestream velocity. Based on previous studies, Meyers *et al* (1990), Meyers (1991), this location should have generated measurements that had a fairly high velocity:data rate correlation indicating the presence of particle sampling bias. Also, as shown by Meyers (1991), the level and sign of the correlation coefficient was also dependent on the measurement instrumentation. In this case the data rate was sufficiently low so that there was no correlation indicating that each measurement was truly an independent measure of the flow. However, it does not confirm that sampling bias was not present because the physics of two interacting flows with different seeding densities would still produce a bias. This will be addressed again when the current measurements are compared with the results from previous investigations. The number of signal bursts acquired increased at this location because of the high seeding density in the freestream. However the high "turbulence" in this region, greater than 10-percent of freestream, delayed convergence of the velocity magnitude standard deviation until 2,500 signal bursts were included in the ensemble. Excess statistics never converged for this data ensemble. As seen in Figure VI.24, the flow angle was directed approximately 5-degrees downward indicating that the freestream flow was expanding to fill the void behind the separation zone which also explains the lower mean velocity magnitude. The U- and V-component results are shown in Figures VI.25-VI.26 and the individual distributions shown in Figures VI.27-VI.30.

The measurement volume was then positioned deep within the separation zone at this downstream location (y/H = -0.40, x/H = 0.69). This location should provide a strong reverse flow with relatively low influence from freestream. The results presented in Figures VI.31-VI.34 indicate nearly Gaussian distributions in the U- and V-components and rapid convergence of the standard deviations occurring at approximately 1,500 signal bursts. However, the number of measurements was unexpectedly high with the noise pulses making a much smaller contribution. The distribution characteristics were similar to the results obtained at y/H = -0.17, x/H = 0.32, except the peak of the flow angle distribution was approximately 150-degrees. The Gaussian distributions in the U- and V-components indicated that there was no influence from freestream at this location as expected, and that the measurement volume was positioned at the upstream part of the primary separation vortex, but lower since the flow angle was approaching horizontal. The individual distributions are given in Figures VI.35-VI.38.

The final measurement location was slightly below the top of the step and further downstream (y/H = -0.17, x/H =1.37). The flow in this region should be an expansion of the freestream with a fair amount of turbulence as the shear layer mixing would be more significant. The results, Figures VI.39-VI.42, indicate that the turbulence was approximately 20-percent of the local mean velocity indicating that for a period of time the flow was in the upstream direction, Figure VI.41. Here again the data rate was fairly high and the flow was primarily in the downstream direction, but occasionally a portion of the separated flow passes through the measurement volume as indicated by the low level, noise-like segments in the flow angle distribution, Figure VI.40. Here again the standard deviation convergence was quite rapid occurring at approximately 1,500 signal bursts. The individual distributions are shown in Figures VI.43-VI.46.

In summary for this portion of the laser velocimeter evaluation, the performance was very similar to that observed during laboratory testing. The use of standard deviation convergence proved to be a good indicator of the realization of statistical stationarity. The spurious voltage pulses spontaneously generated by the photomultiplier were still present and had a significant influence on the number of signal bursts acquired, especially with the low data rates found in the separated region. The distributions appeared nearly Gaussian except in the shear region where the expected skew was found. The velocity:data rate correlations were nominally zero indicating that the measurements were independent; however there were also indications that particle sampling bias was still present. When comparing these findings with previous investigations there appears to be two parts to the origin of the sampling bias: 1) the influence of the instrumentation in accepting measurements, as shown by Meyers (1991) when the correlation coefficient changed signs after the instrument dead time was changed, and 2) the physical characteristics involved when two adjacent flows with different seed densities mix.

Comparison With Other Measurements

Although the Monte Carlo simulation results indicated that the precision of the upgraded laser velocimeter was better than 0.3-m/s at a velocity of 100 m/s (even with direct measure of the 40-MHz Bragg shifted signal), a comparison with previous measurements of the same/similar flow is the true indicator as to system performance. The comparison data were obtained from two sources:

1) One component laser velocimeter measurements using the dedicated short focal length system in the BART to measure about a 1.5-inch backward facing step with a freestream velocity of 45 m/s (Hart *et al* (2001); and,

2) Three component laser velocimeter measurements using a 1-meter focal length system in a 6-inch channel with a 3-inch backward facing step and a freestream velocity of 50 m/s (Meyers *et al* (1990)).

Since the first source used a 1.5-inch step, the 3.5-inch step was removed from the test section and the 1.5-inch step inserted and further velocity measurements obtained.

Measurement volume location was normalized by step height so that data from both steps could be included in the comparisons. The freestream velocity was maintained at 16.6 m/s during all testing with only a single scan obtained with a freestream velocity of 45 m/s at the furthest downstream location (x/H = 1.6) using the 1.5-inch step. Here again, to allow direct comparison among the various freestream velocities, all measured velocities were normalized by freestream.

The first task in this comparative investigation was to determine if there was any indication of particle sampling bias. Using the velocity:data rate correlation coefficient in the manner described by Meyers *et al* (1990), the coefficient traces were plotted for both steps, Figure VI.47. The results from the 3.5-inch step investigation indicate a zero correlation in freestream at all stations, then a slow trend in the negative direction until approximately y/H = 0.3 where the correlation remains at -0.1. Likewise the results from the 1.5-inch step investigation indicate a zero correlation in freestream, but the trend in the negative direction did not begin until y/H = 0.4 with no indication of flattening even when the correlation reaches -0.15 at the lowest point measured. The estimated correlation time (Meyers *et al* (1990)), shown in Figure VI.47, was short in freestream increasing through the shear layer and fairly long, approximately 0.15 seconds, within the separated flow region for both steps. The long excursions shown in the figures were caused by very low data rates. These trends are in agreement which those found by Meyers *et al* (1990), but not to the level previously found. This was most likely the influence of the longer instrument dead time (time when the data acquisition system cannot accept a new measurement because it is processing/storing the current signal burst) of the current system.

During a Laser Induced Thermal Acoustics (LITA) proof of concept test (Hart *et al* (2001)), the dedicated laser velocimeter in the BART was used to establish the velocity characteristics of the flow. The laser velocimetry measurements were made at x/H = 0.53 downstream of the 1.5-inch step with a freestream velocity of 45.0 m/s. The mean and standard deviation profiles measured at that location for three separate traverses are shown in Figure VI.48. The overlaid profiles for the current investigation are also shown in the Figure along with an overlay of both data sets near x/H = 0.53. Although the trends are very similar, there are differences in the slope of the mean velocity and the location of the maximum standard deviations. These differences are most likely due to the differences in the freestream velocity: 45.0 m/s for the previous investigation and 15.24 m/s for the current investigation. A further comparison is presented in Figure VI.49., where the vertical traverse obtained in the original investigation at x/H = 6.64 is included, and the current investigation about the 3.5-inch step is added. A visual comparison between the current data obtained from the two step heights clearly shows that they are not scalable. This visual difference in the data traces is accentuated by the overlays in the scaled velocity and flow region comparison. Here again the mean velocity near freestream and deep within the recirculation region match, but there are differences between the two investigations through the shear region. Although scalability was one problem, measurement volume size may also influence spatial averaging within this region. The problem with scalability based on step height is clearly seen with the overlay of the

standard deviations. There is no match between the data obtained with the 3.5-inch step and the other data except when the sampling bias noise floor is reached below the shear layer. However, the current data obtained from the 1.5-inch step is a reasonable match with the previous data except at and just below the peak of the turbulence – again this may be traced to the differences in measurement volume size and the associated averaging of the particle velocities.

The final comparison was obtained in a channel flow where the step height was 3-inches, half the height of the downstream channel, Figure VI.50 (Meyers *et al* (1990)). Although a three-component laser velocimeter was used, only the U-component velocity profiles would be compared and those only to the extent where the measurement locations were approximately the same. A photograph of the installation is shown in Figure VI.51 and the measured mean velocity and standard deviation maps are shown in Figure VI.52. Again the comparable scans for the previous investigation along with a repeat of the current investigation are shown in Figure VI.53. Here the basic trends of the data are similar, but not directly comparable. The peak standard deviations did not occur at the same location but had approximately the same amplitude. The residual standard deviations below the shear regions nearly match along with the mean velocity in the same region. Based on the inability to scale measurement location with step height as determined above, along with the potential influence of the channel ceiling on the flow field, one should expect differences between the results of the two investigations. However, the trends indicate that sampling bias is an issue of concern since the previous investigation found significant velocity:data rate correlations that varied with location while the current investigation had far less of an indication. The instrument-based biases were corrected in the previous investigation resulting in the data used for this comparison. Thus both data sets were derived from independent measures of the flow field, but both were still influenced by sampling bias. If the velocity:data rate correlation can not be used as an indicator of particle sampling bias, then another indicator must be found to provide the researcher with information as to when the measurements would be accurate.

In order to insure that particle dynamics were not an issue regarding the fidelity of the flow measurements with the current system, signal level distributions were determined for a scan downstream of the 1.5-inch step (x/H = 1.6). Several sizes of PSL particles were used with the 50:50 mixture of water and ethanol and injected into the flow with the same paint sprayers. The theoretical distribution of signal levels for 1.7-micron particles passing randomly through the measurement volume is shown in Figure VI.54. Also the distribution of signal levels obtained in the laboratory using the Royco particle generator is also shown in Figure VI.54. A comparison of the two distributions show consistency, as do the distributions obtained from the 2-inch jet flow, Figure V.5. The distributions of signal level from 0.68-micron and 1.7-micron particles are shown in Figure VI.55 as a function of vertical distance. While the distributions obtained from the 0.68-micron particles are similar to the theoretical and laboratory distributions, the 1.7-micron distribution is totally different producing considerably higher signal levels. These distributions remain the same until the shear layer was entered where the 1.7-micron signal levels begin to reduce until the bottom of the scan is reached (y/H = -0.47). Here the distributions become similar to

the theoretical and laboratory distributions. This change in distribution is characteristic of an evaporating liquid particle. There would be little evaporation in freestream because of the lower transit time between particle generation and measurement location versus the longer transit time experienced by a particle entrained in the recirculation zone. Since the distributions for the 0.68-micron particles did not vary, it must be concluded that the amount of liquid attached to these particles was far less which evaporated before the test section was reached. Thus it appears that the use of the paint sprayer may have affected the results of the current investigation. A direct comparison with signal levels from the previous investigations is not possible as the instrumentation used did not preserve the signals.

In summary, the comparative investigation indicates that the upgraded laser velocimeter yields data comparable with previous investigations, however allowances must be made for differences in freestream velocity and step heights. The following conclusions can be made based on this comparative investigation:

1) Given the differences in the investigations, the current system yielded measurements that traced the main structures within the flow found in the previous investigations.
2) All measurement distributions were smooth and most nearly Gaussian, with the only exceptions being in the region of the shear layer where skewed distributions would be expected – thus the Histogram (5) method performs as predicted and as was found in the laboratory experiments.
3) The statistical convergence method also performed as predicted and as found in the laboratory to determine at which ensemble size statistical stationarity was reached.
4) The distribution of signal levels indicate that the water:ethanol used to transport the 1.7-micron PSL particles from the paint sprayer in the current investigation did not fully evaporate, which may have affected the measurement accuracy.
5) The Monte Carlo simulation investigation indicated that the measurement precision of the upgraded system was better than 0.3 m/s and that measurement accuracy was highly dependent on the number of measurements obtained before the statistics were calculated. Based on the simulation results, laboratory findings, and the comparative results presented above, it can be concluded that the upgraded laser velocimeter satisfies the required ± 1.5 m/s accuracy – provided sufficient signal bursts are processed to reach statistical stationarity.

Recommendations

During the simulation, laboratory and especially the comparative investigations in the BART, several areas needing attention were found which generated the following recommendations:

1) Develop a method to eliminate the spurious electronic pulses spontaneously generated by the photomultiplier which lead to false triggers in the data acquisition system – A circuit has been designed, built and tested that eliminates these spurious pulses from the signal before it reaches the data acquisition system: problem eliminated.
2) Develop a method to increase data transfer speeds to reasonable levels for production testing – Software has been developed to increase the transfer speed by almost an order of magnitude to bring the transfer times to acceptable levels.
3) Improve measurement accuracy by better defining the extent of the measurement distributions – Data processing software was improved to yield better accuracies than obtained previously. It is noted that all data, simulation and measurements, were reprocessed using the new software and the results presented in this document were obtained using the new software.
4) Develop a method to use the convergence of the measured standard deviations as a function of ensemble size to determine when statistical stationarity is reached and provide feedback to the data acquisition system when sufficient data has been acquired – To be implemented in the future.
5) Develop a method to separate bi-modal velocity distributions so that each of the two flows can be studied together and separately – To be implemented in the future.
6) Use Monte Carlo simulation techniques to determine the measurement precision of other velocimeters, e.g., PIV, LITA, pDv, DGV, Rayleigh, etc.

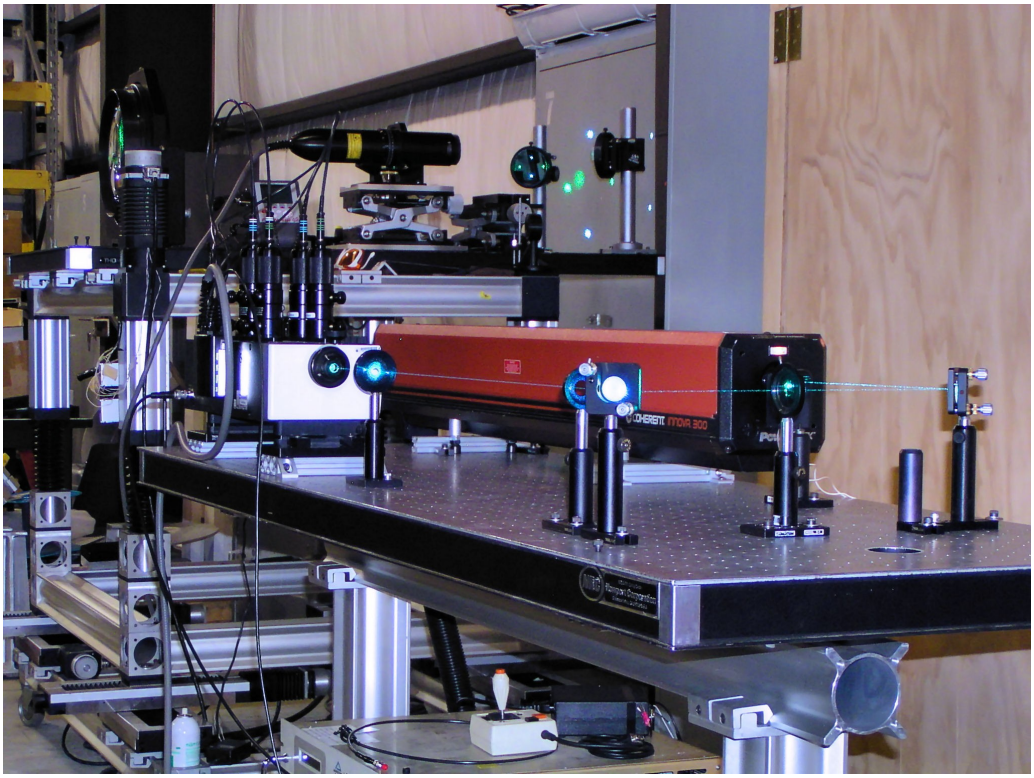

Figure VI.1.- Upgraded 14- by 22-Foot Subsonic Tunnel laser velocimeter optics system.

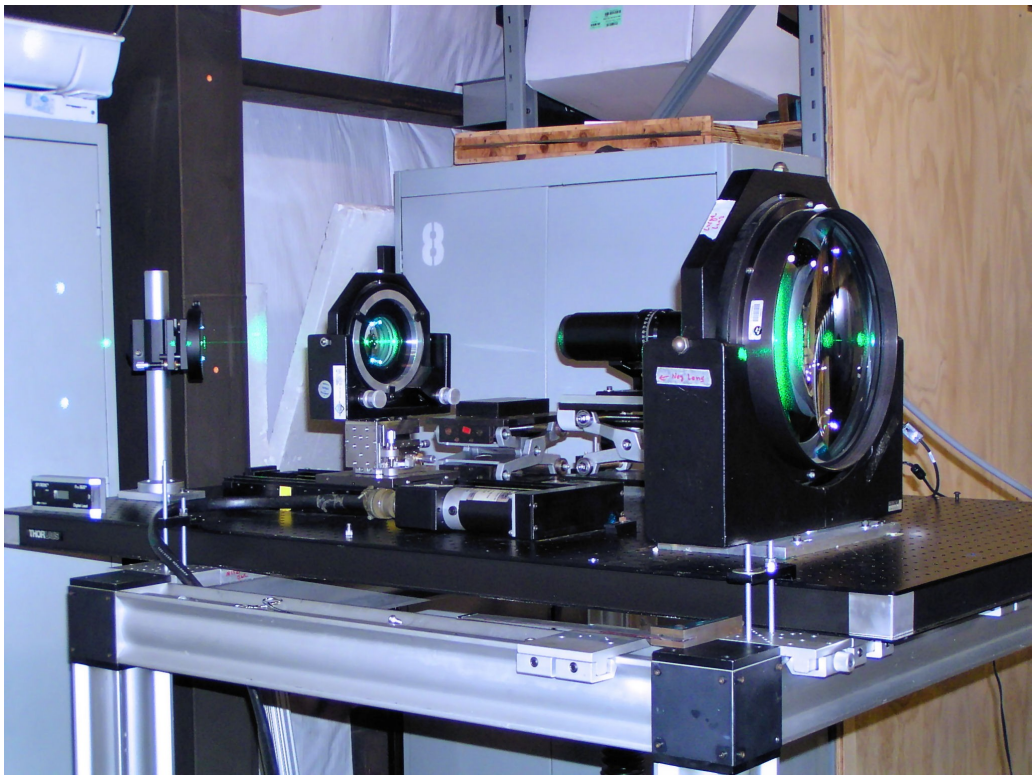

Figure VI.2.- Subsystem of the upgraded laser velocimeter that will be placed in the tunnel plenum chamber.

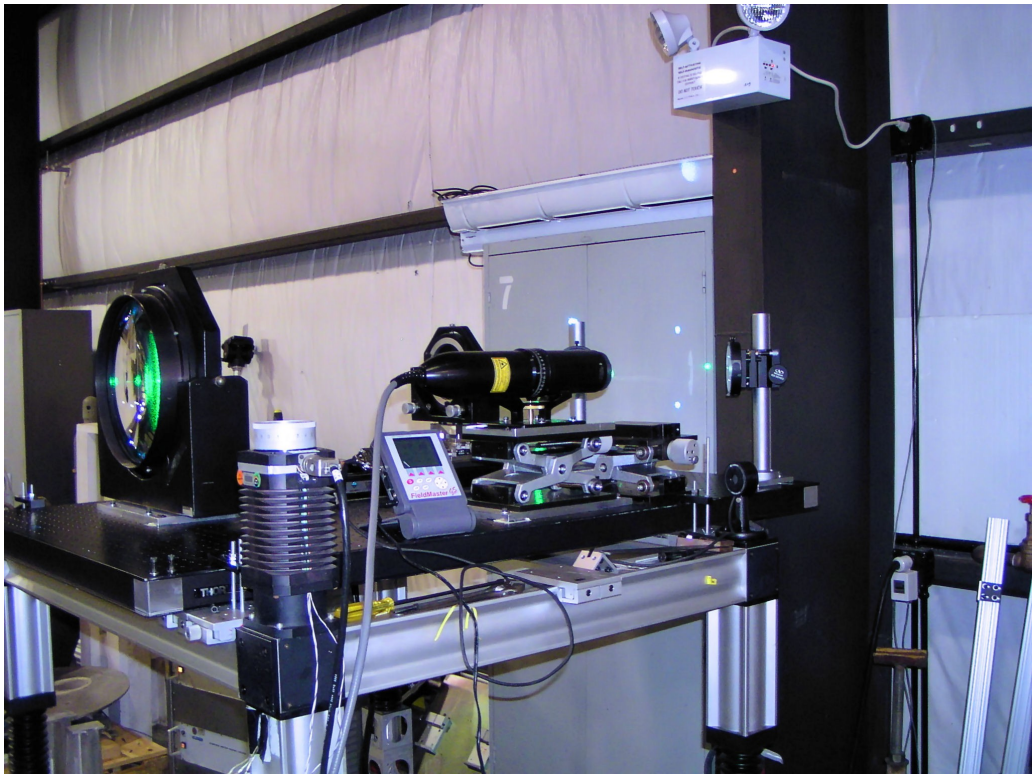

Figure VI.3.- Subsystem of the upgraded laser velocimeter that will be placed in the tunnel plenum chamber.

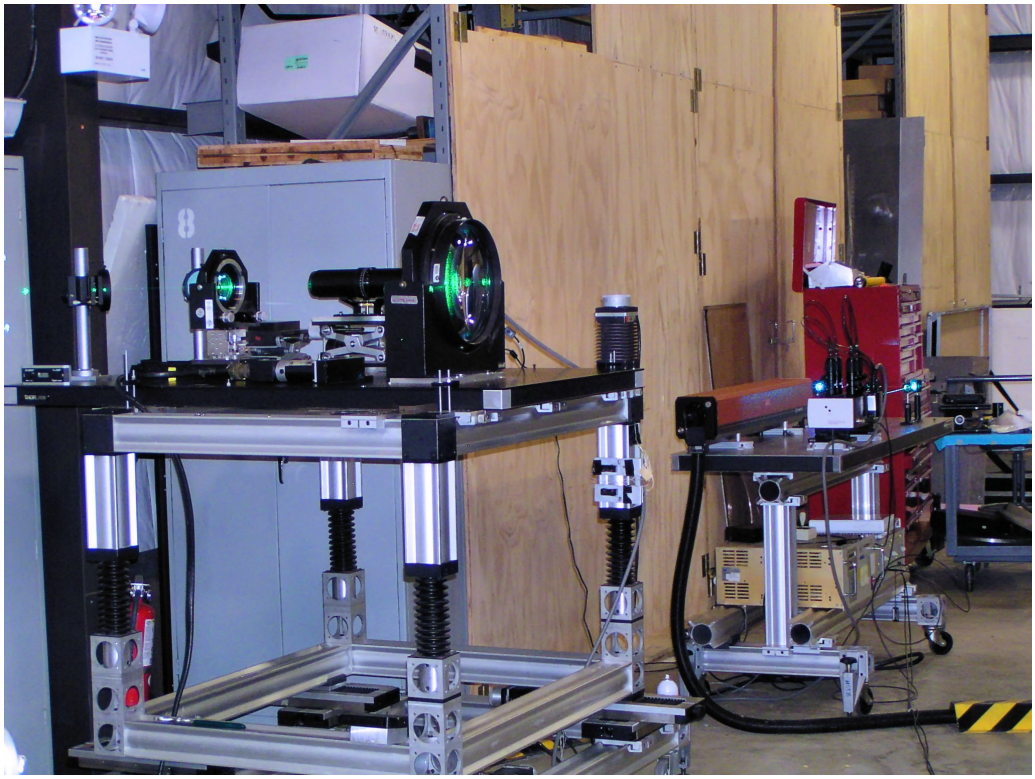

Figure VI.4.- Subsystem of the upgraded laser velocimeter that will be placed in the tunnel plenum chamber connected with the subsystem and laser that will be placed outside the tunnel via fiber optics.

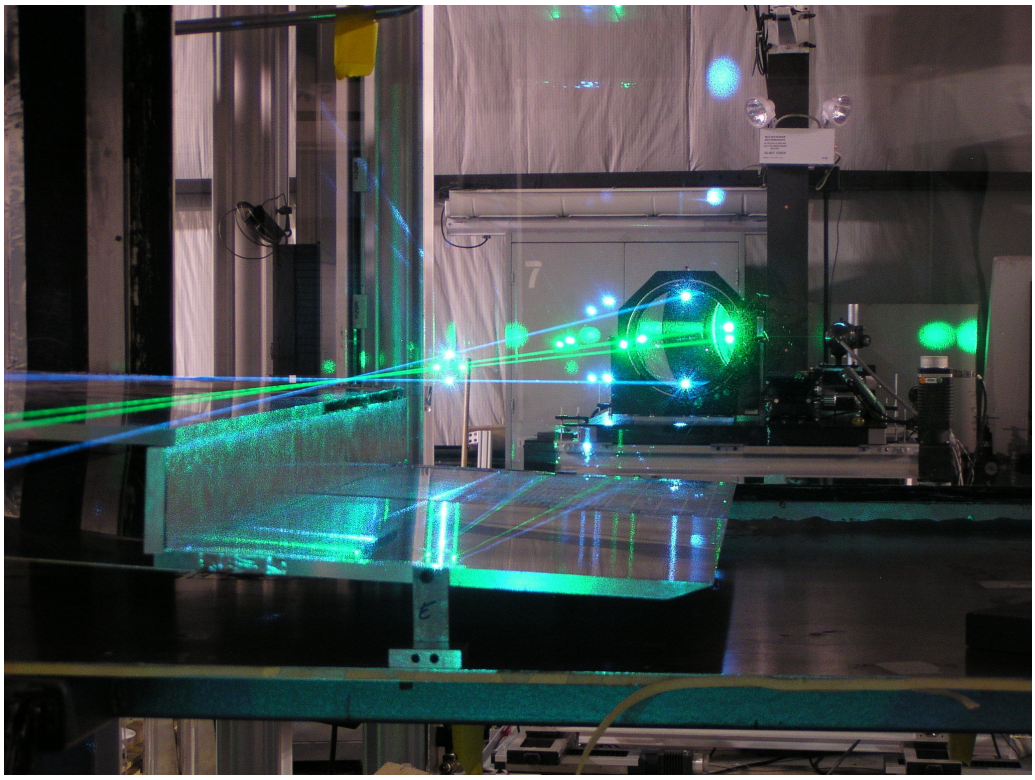

Figure VI.5.- Upgraded laser velocimeter under test in the BART – Measure the velocity flow field about a backward facing step.

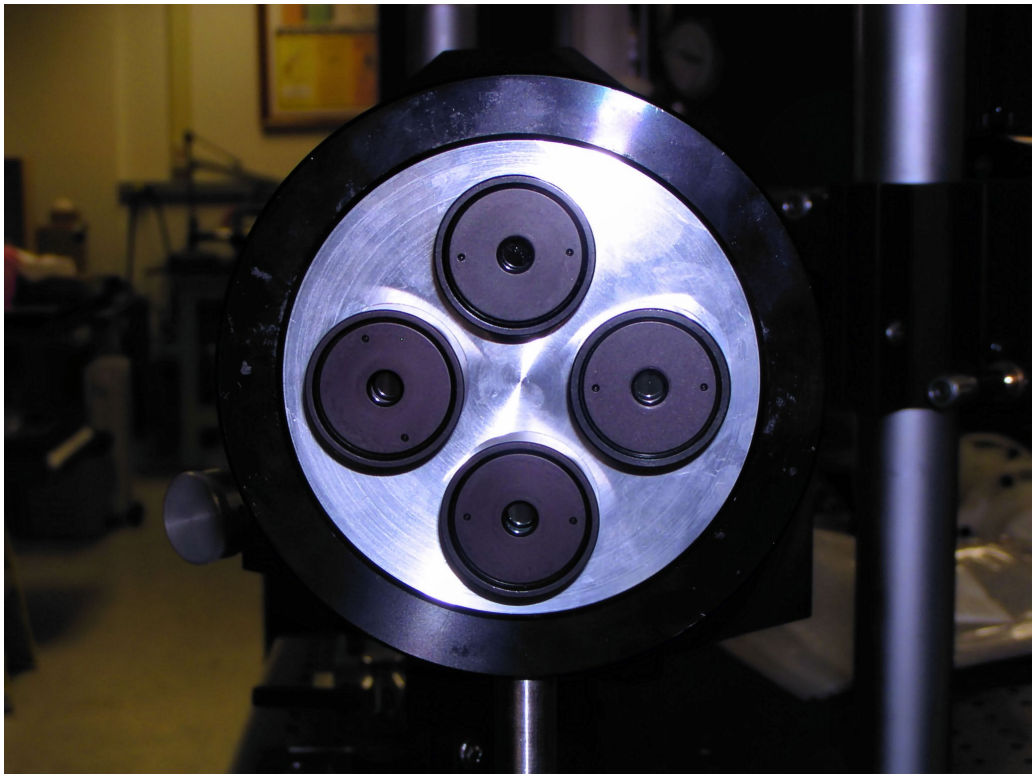

Figure VI.6.- Prototype optical alignment sensor that will provide the signals needed to remotely realign the LV transmission optical system should there be alignment drifts caused by the wind tunnel environment.

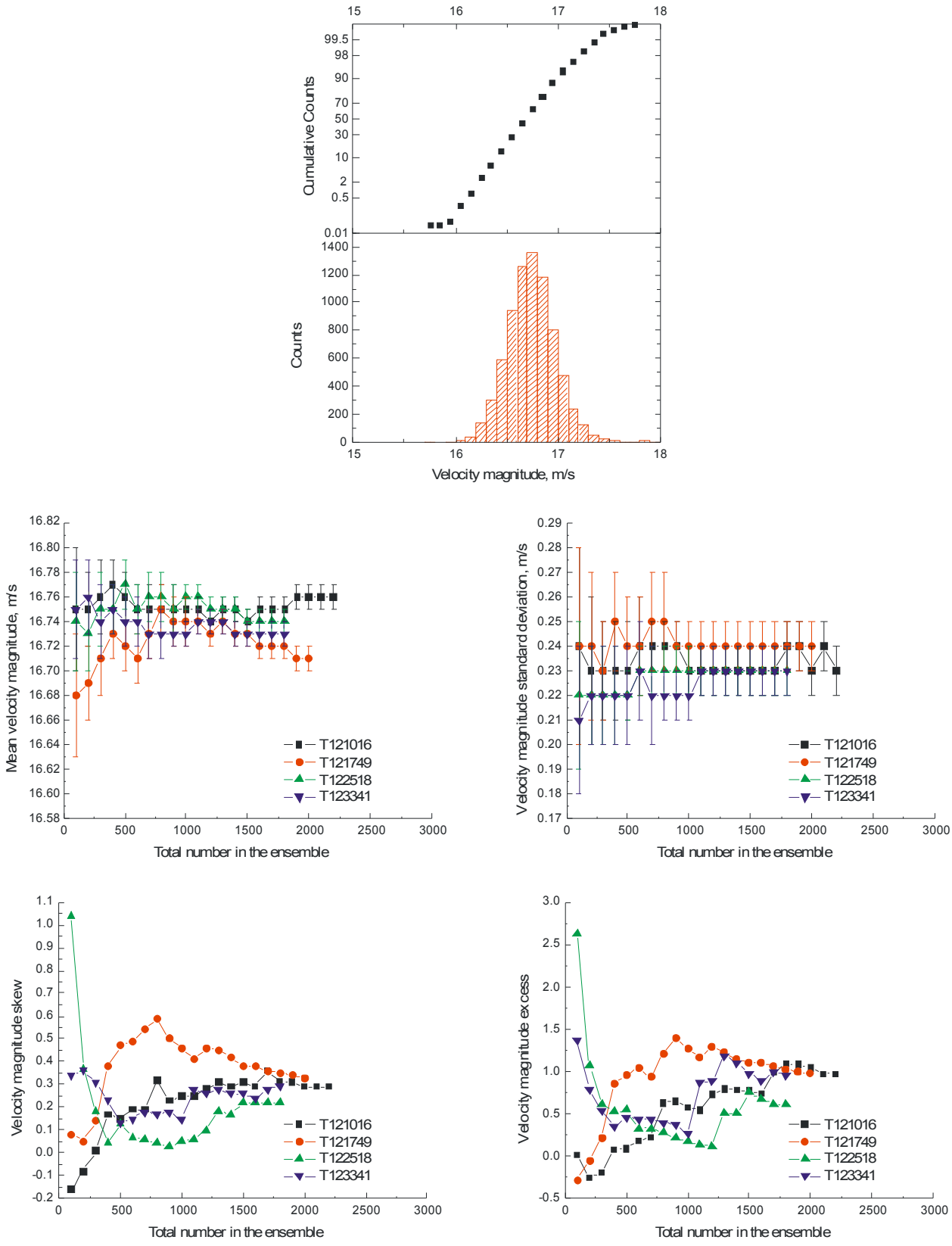

Figure VI.7.- Convergence of the velocity magnitude statistics and full ensemble histogram in the freestream area above of the backward facing step (y/H = 0.34, x/H = 0.32).

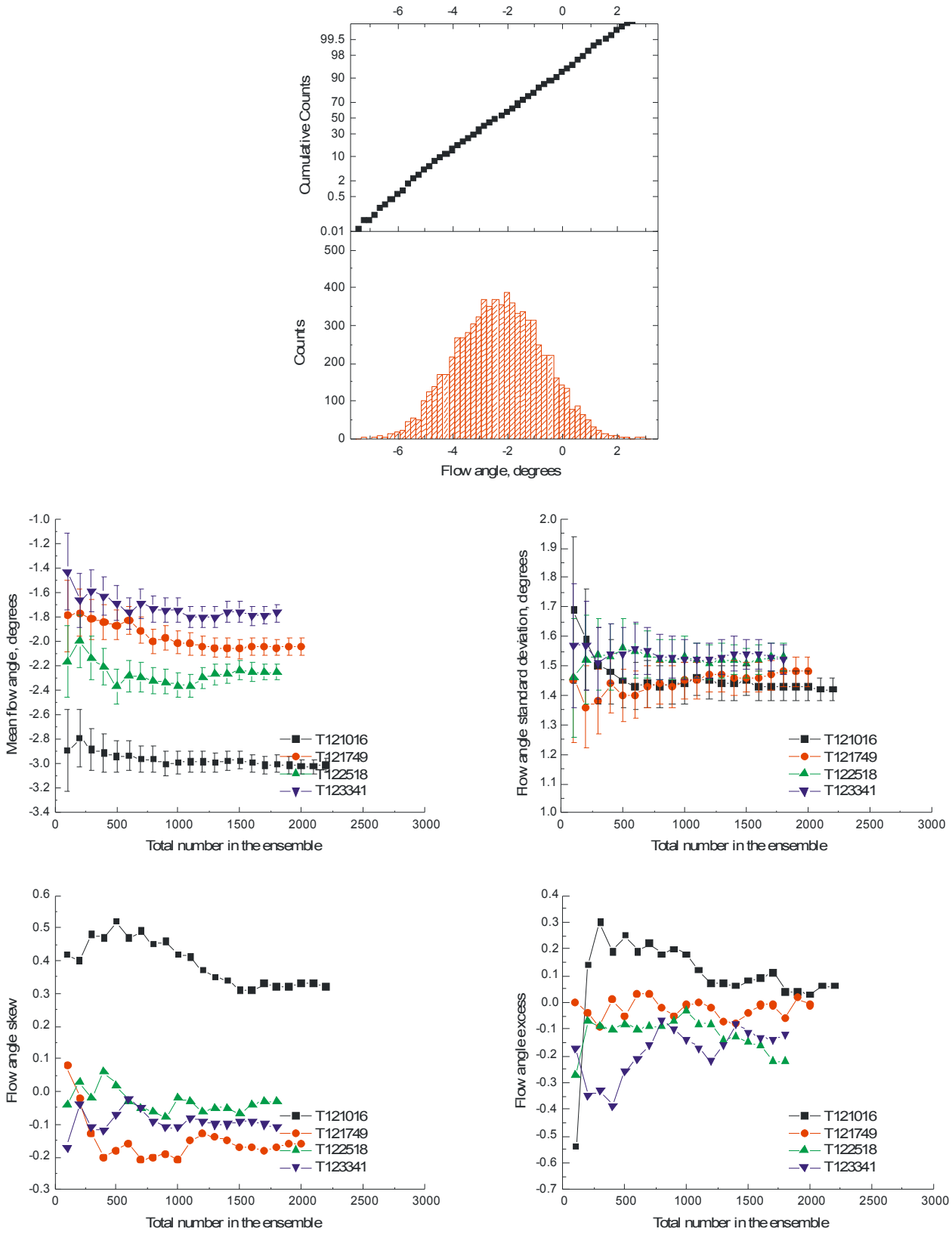

Figure VI.8.- Convergence of the flow angle statistics and full ensemble histogram in the freestream area above of the backward facing step (y/H = 0.34, x/H = 0.32).

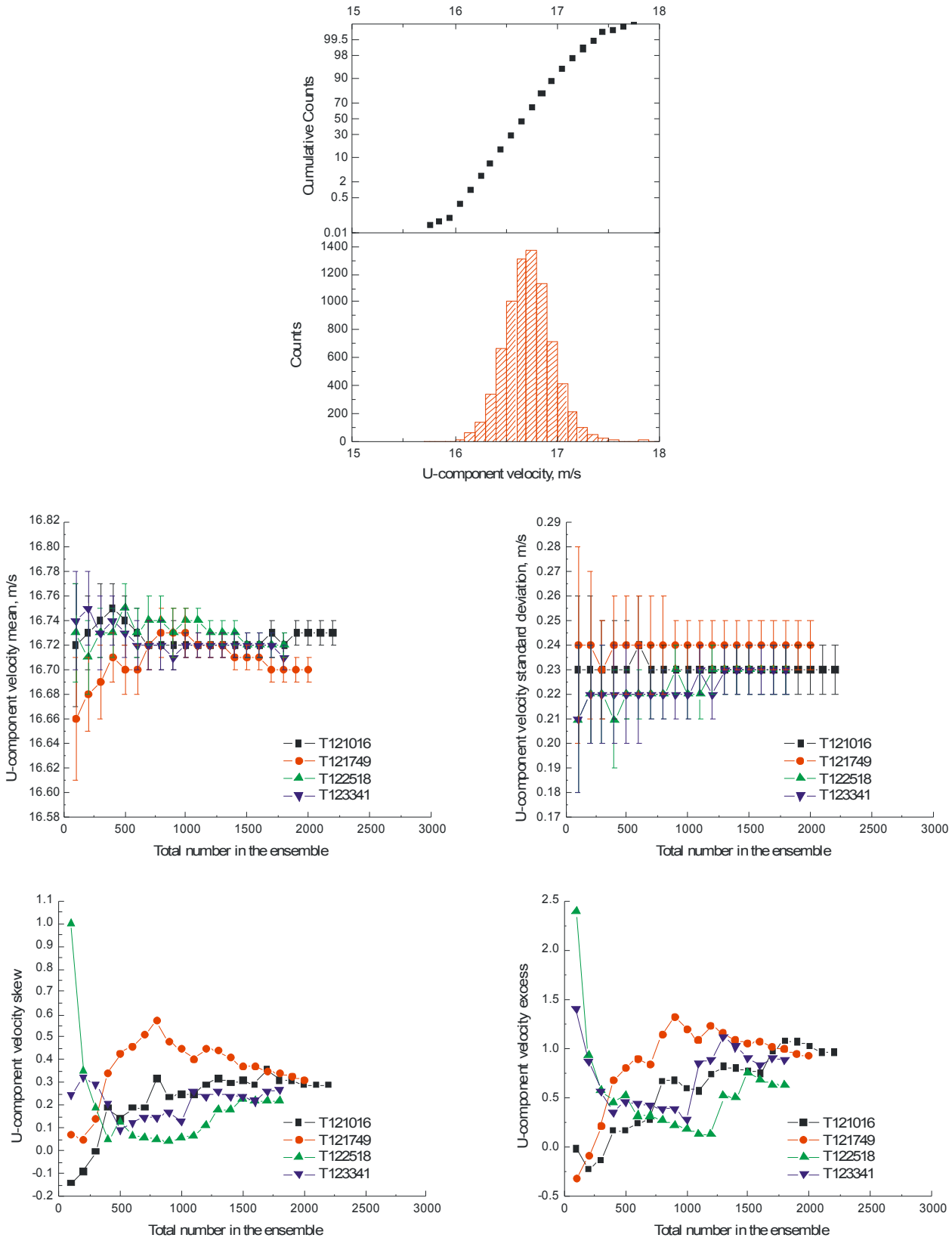

Figure VI.9.- Convergence of the U-component velocity statistics and full ensemble histogram in the freestream area above of the backward facing step (y/H = 0.34, x/H = 0.32).

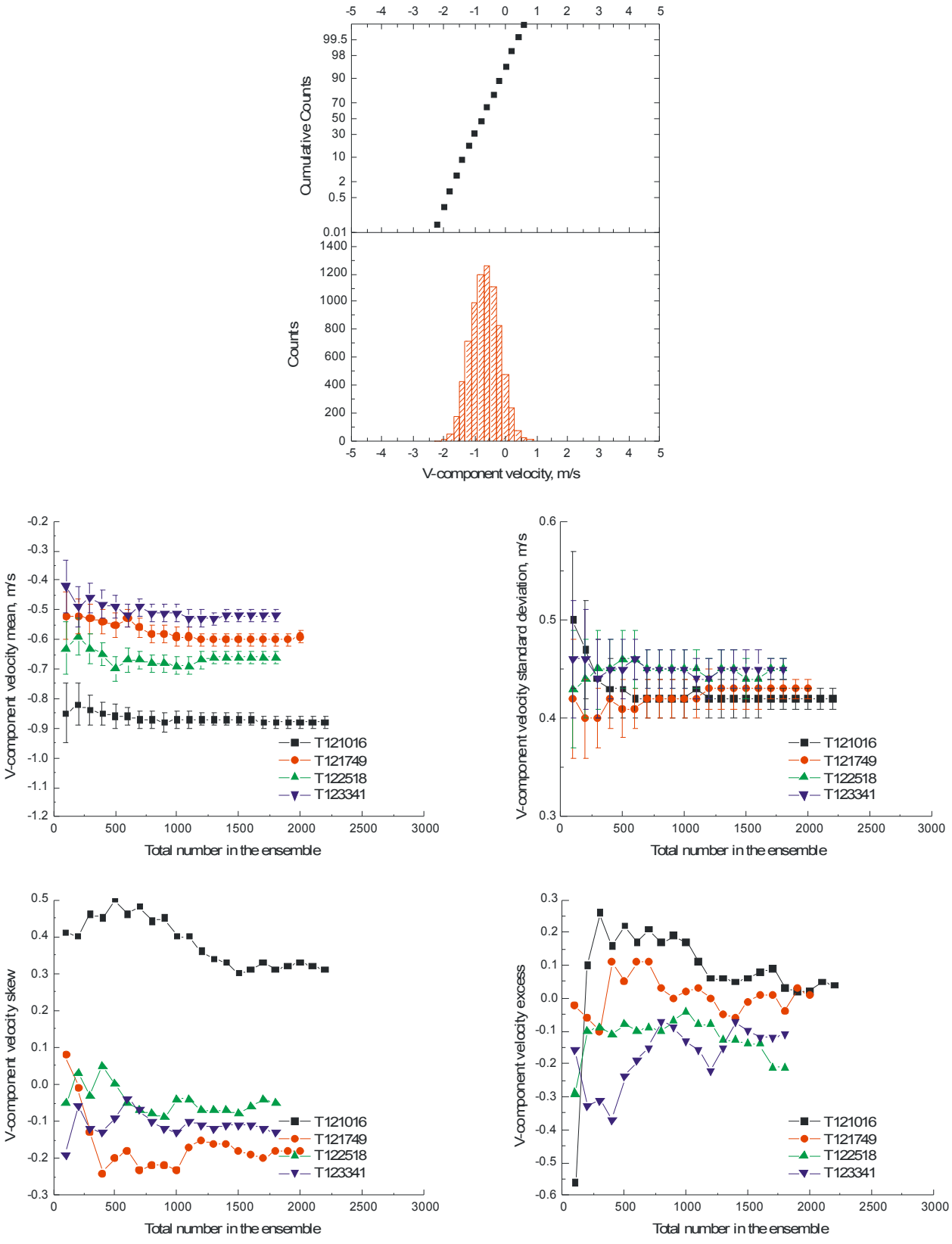

Figure VI.10.- Convergence of the V-component velocity statistics and full ensemble histogram in the freestream area above of the backward facing step (y/H = 0.34, x/H = 0.32).

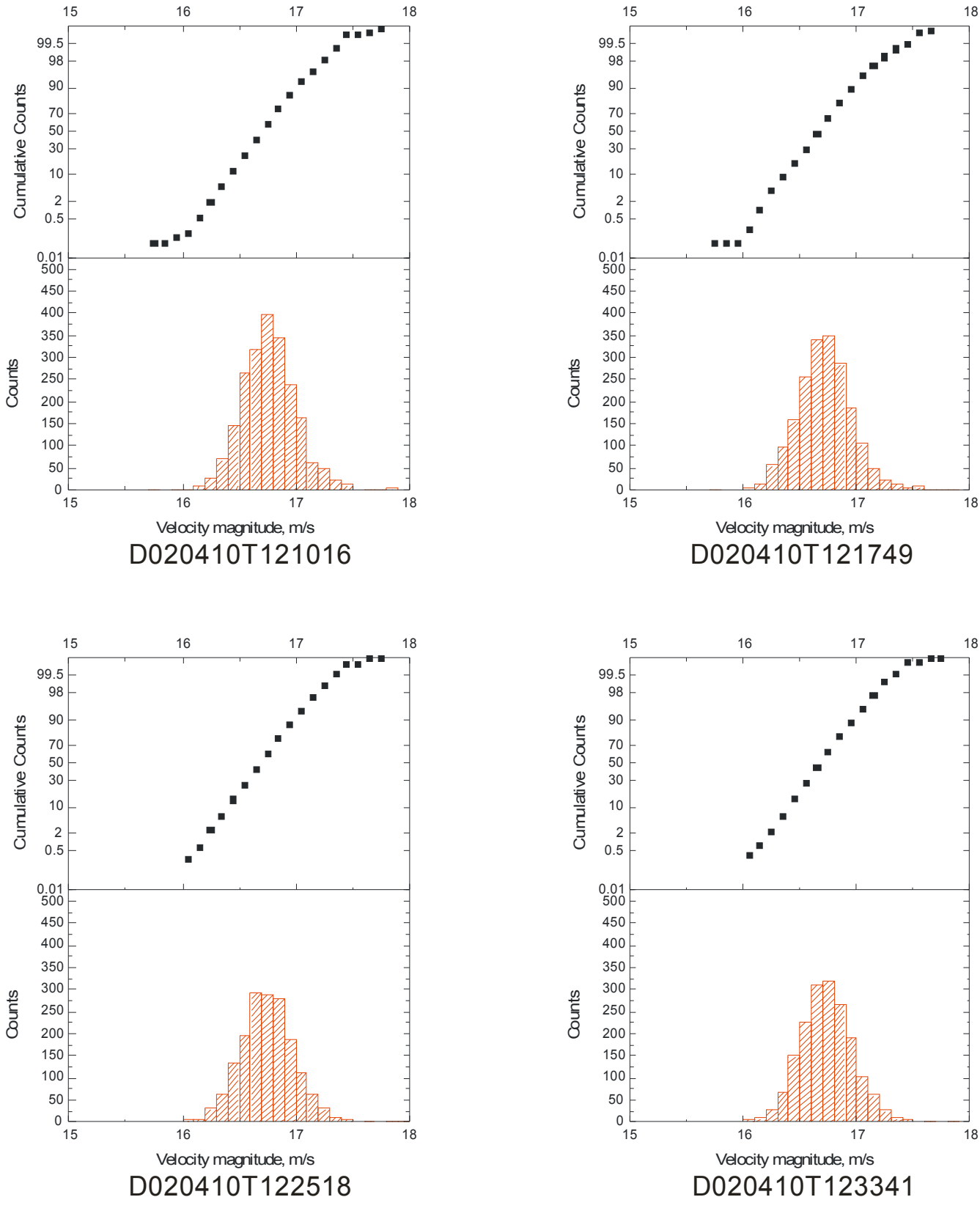

Figure VI.11.- Distribution of velocity magnitude for the individual data ensembles in the freestream area above of the backward facing step (y/H = 0.34, x/H = 0.32).

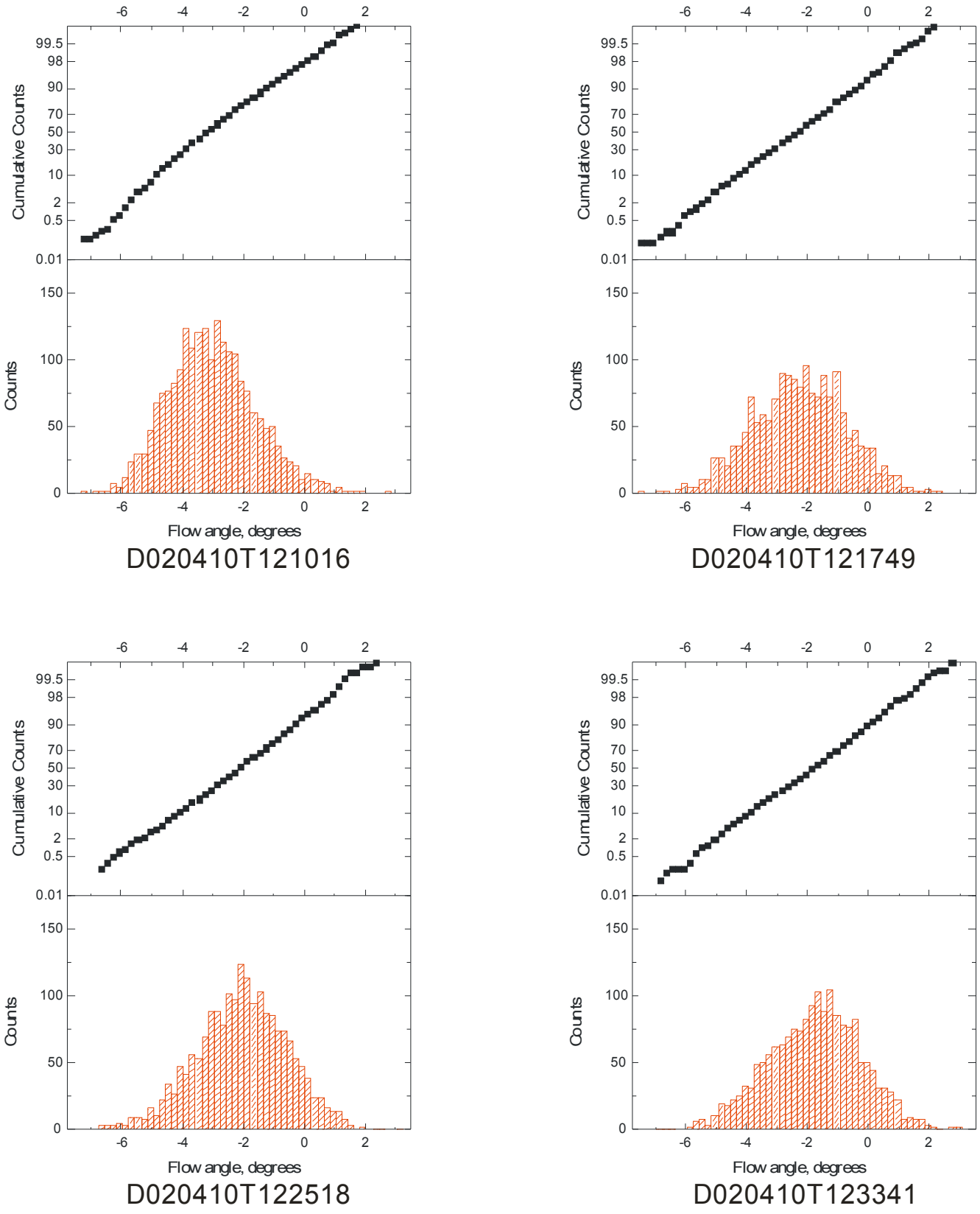

Figure VI.12.- Distribution of flow angle for the individual data ensembles in the freestream area above of the backward facing step (y/H = 0.34, x/H = 0.32).

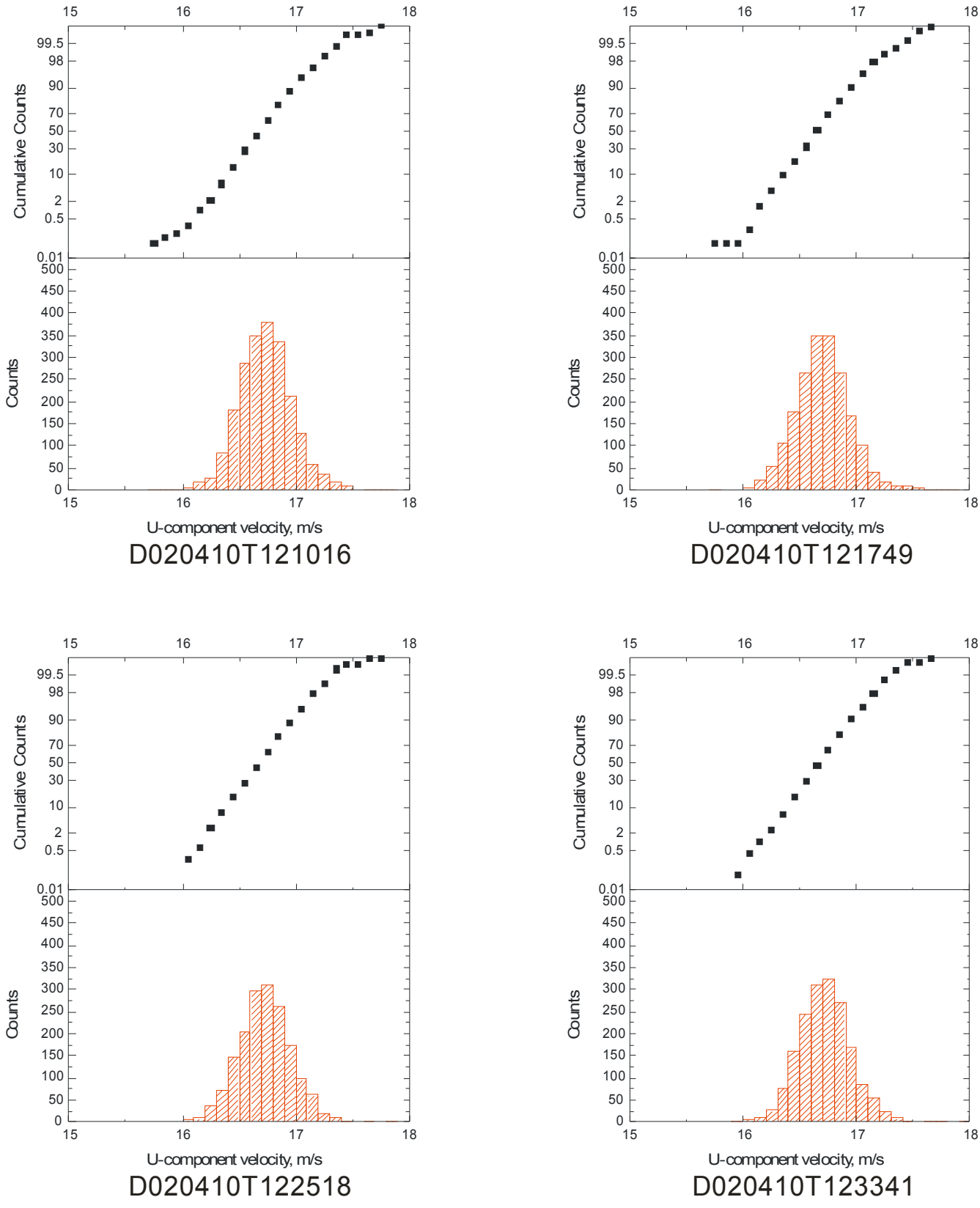

Figure VI.13.- Distribution of U-component velocity for the individual data ensembles in the freestream area above of the backward facing step (y/H = 0.34, x/H = 0.32).

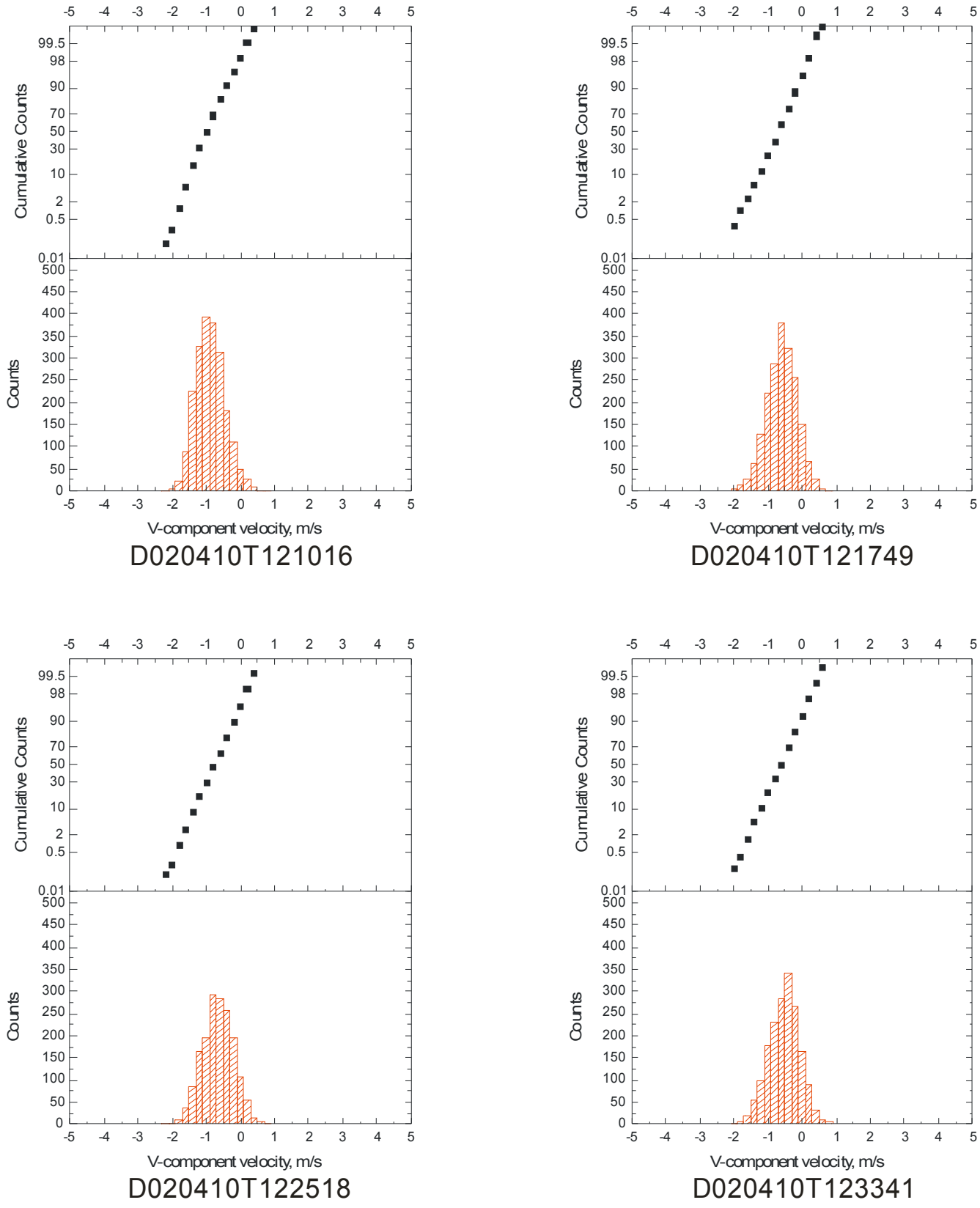

Figure VI.14.- Distribution of V-component velocity for the individual data ensembles in the freestream area above of the backward facing step (y/H = 0.34, x/H = 0.32).

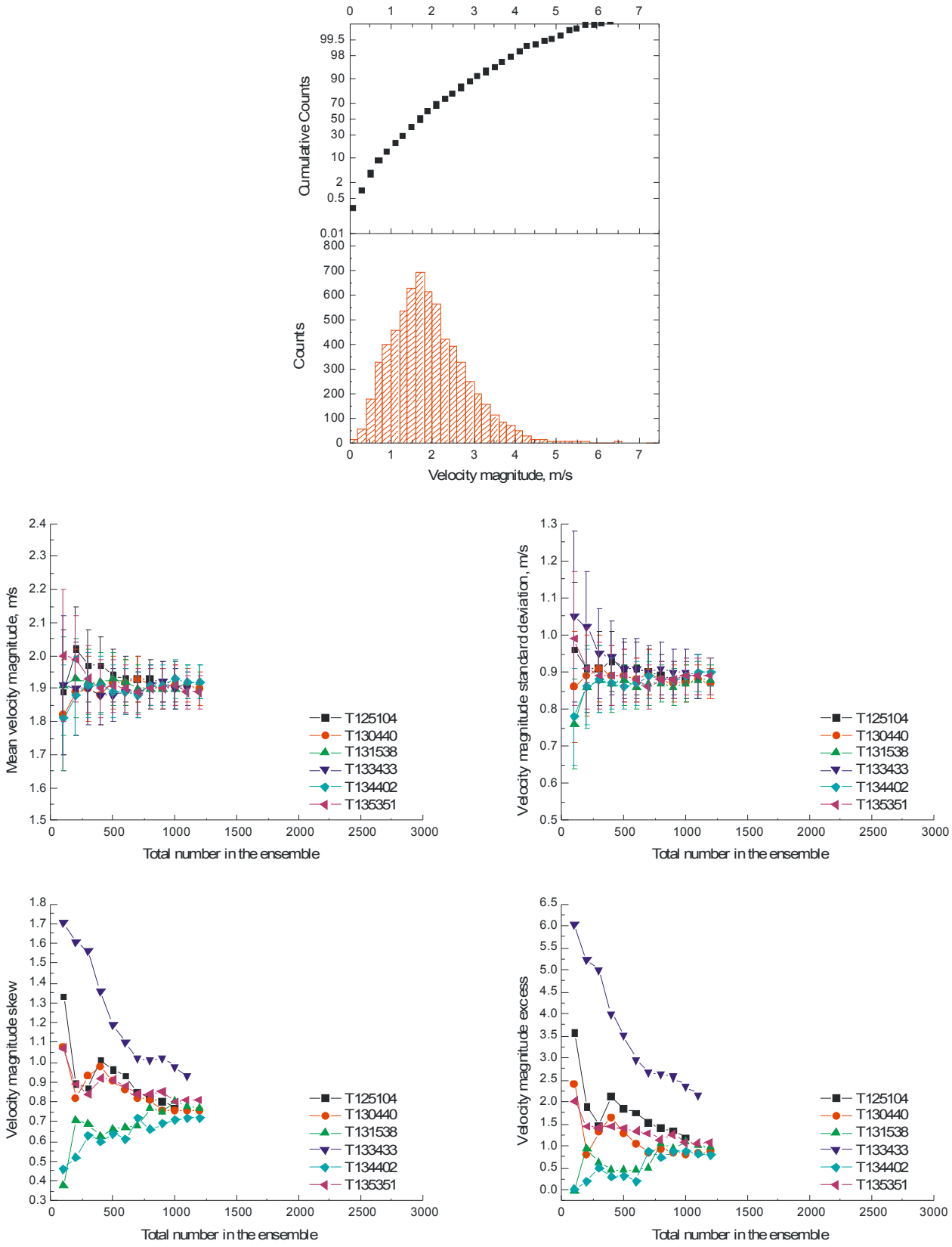

Figure VI.15.- Convergence of the velocity magnitude statistics and full ensemble histogram in the shear flow region just behind the backward facing step (y/H = -0.17, x/H = 0.32).

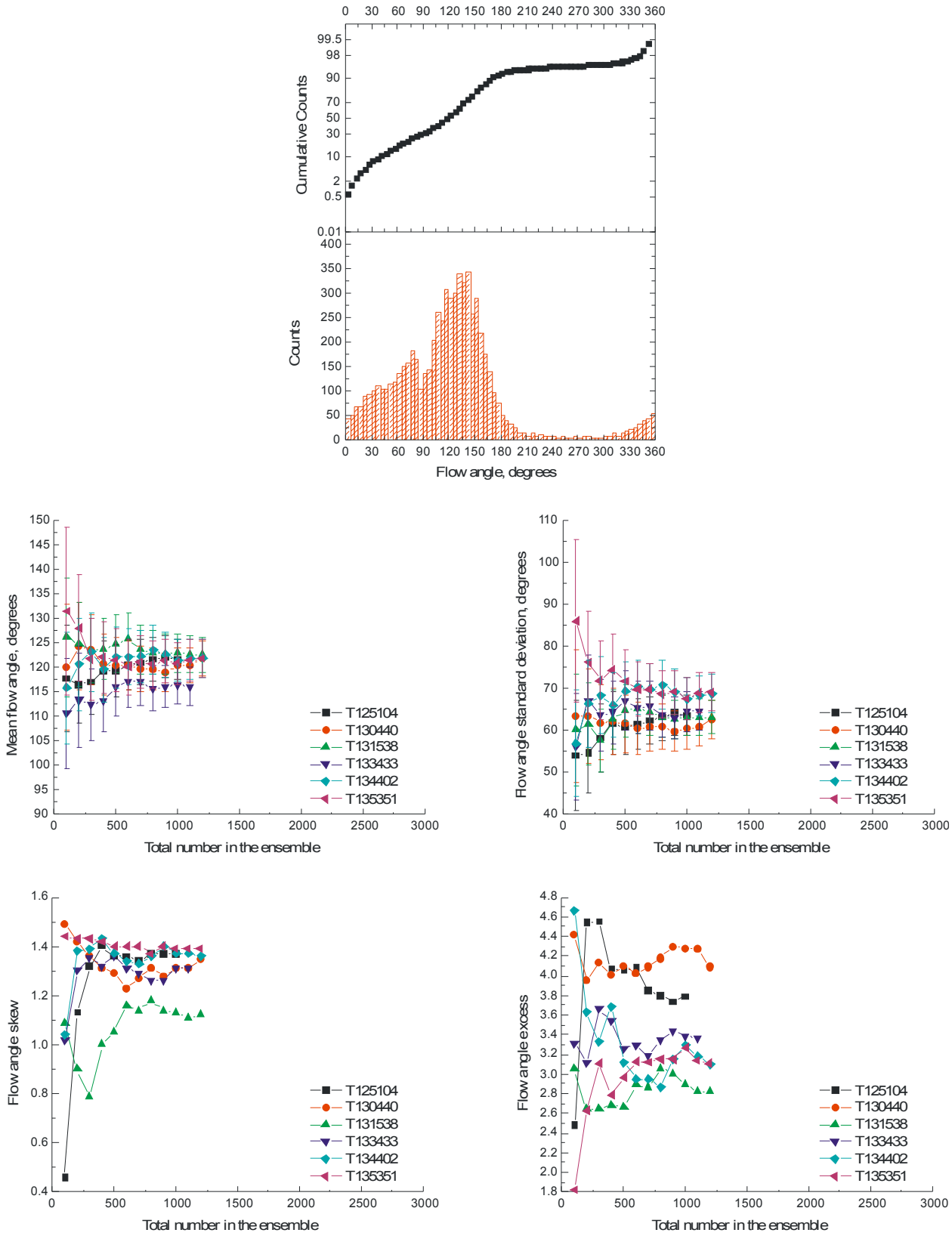

Figure VI.16.- Convergence of the flow angle statistics and full ensemble histogram in the shear flow region just behind the backward facing step (y/H = -0.17, x/H = 0.32).

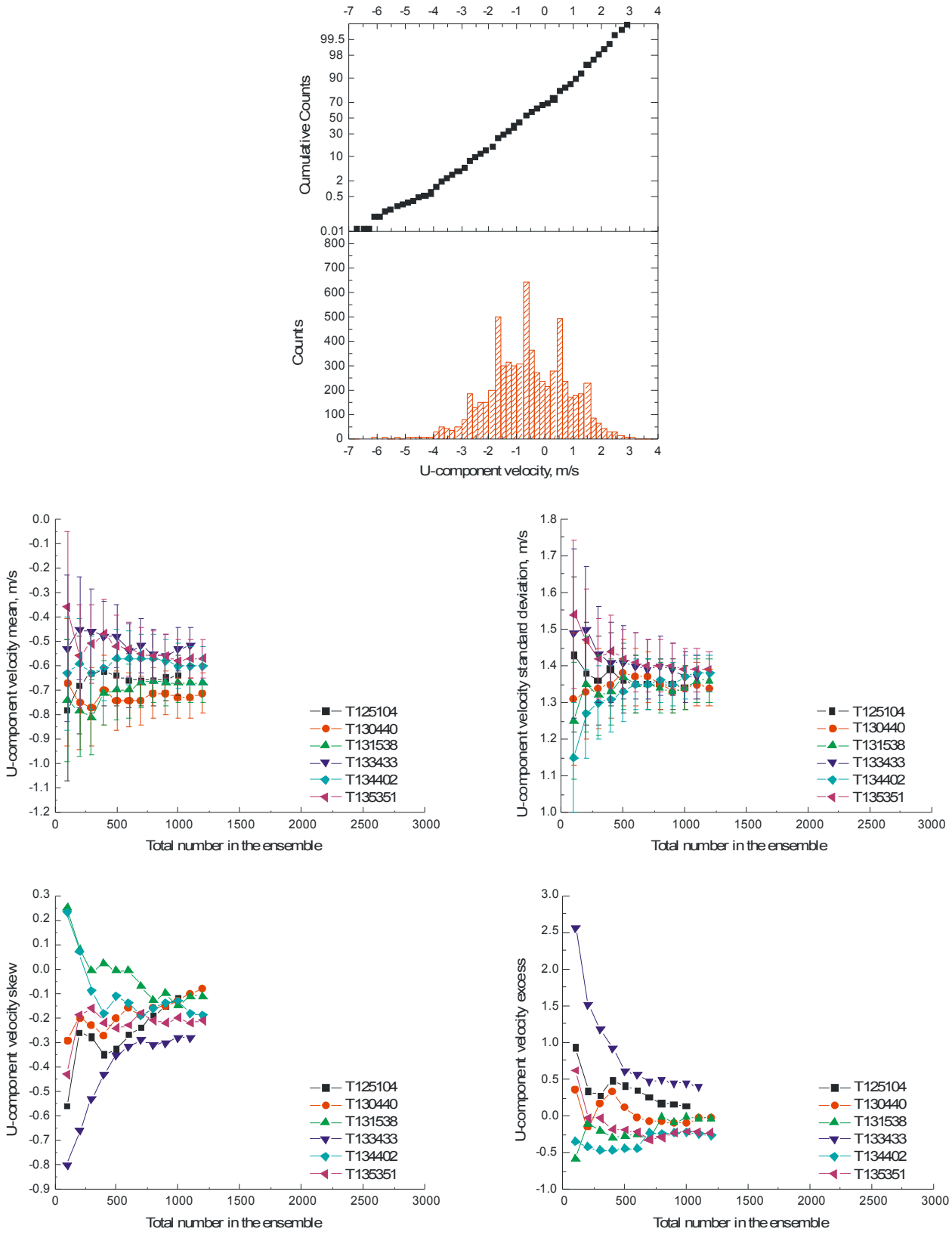

Figure VI.17.- Convergence of the U-component velocity statistics and full ensemble histogram in the shear flow region just behind the backward facing step (y/H = -0.17, x/H = 0.32).

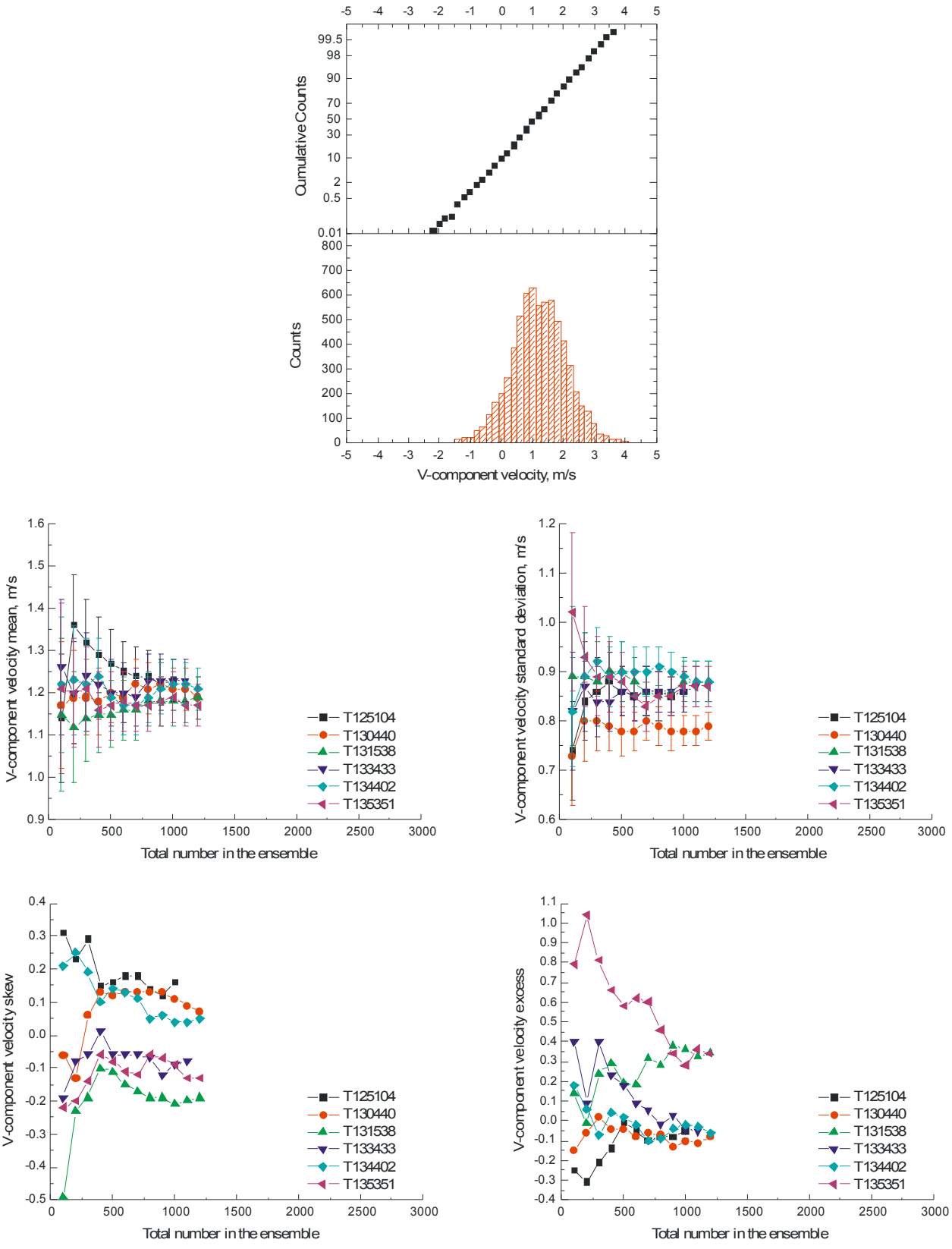

Figure VI.18.- Convergence of the V-component velocity statistics and full ensemble histogram in the shear flow region just behind the backward facing step (y/H = -0.17, x/H = 0.32).

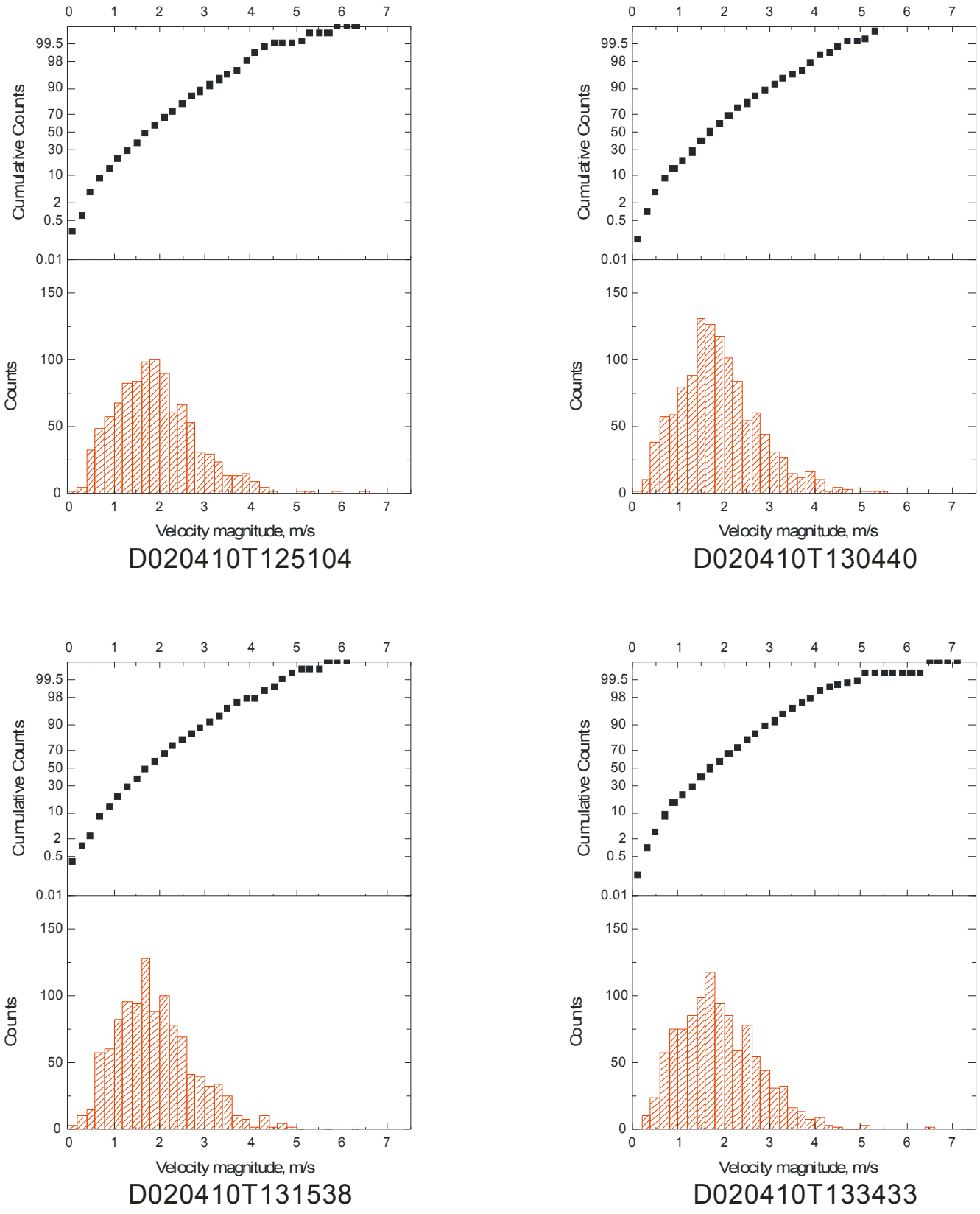

Figure VI.19.- Distribution of velocity magnitude for the individual data ensembles in the shear flow region just behind the backward facing step (y/H = -0.17, x/H = 0.32).

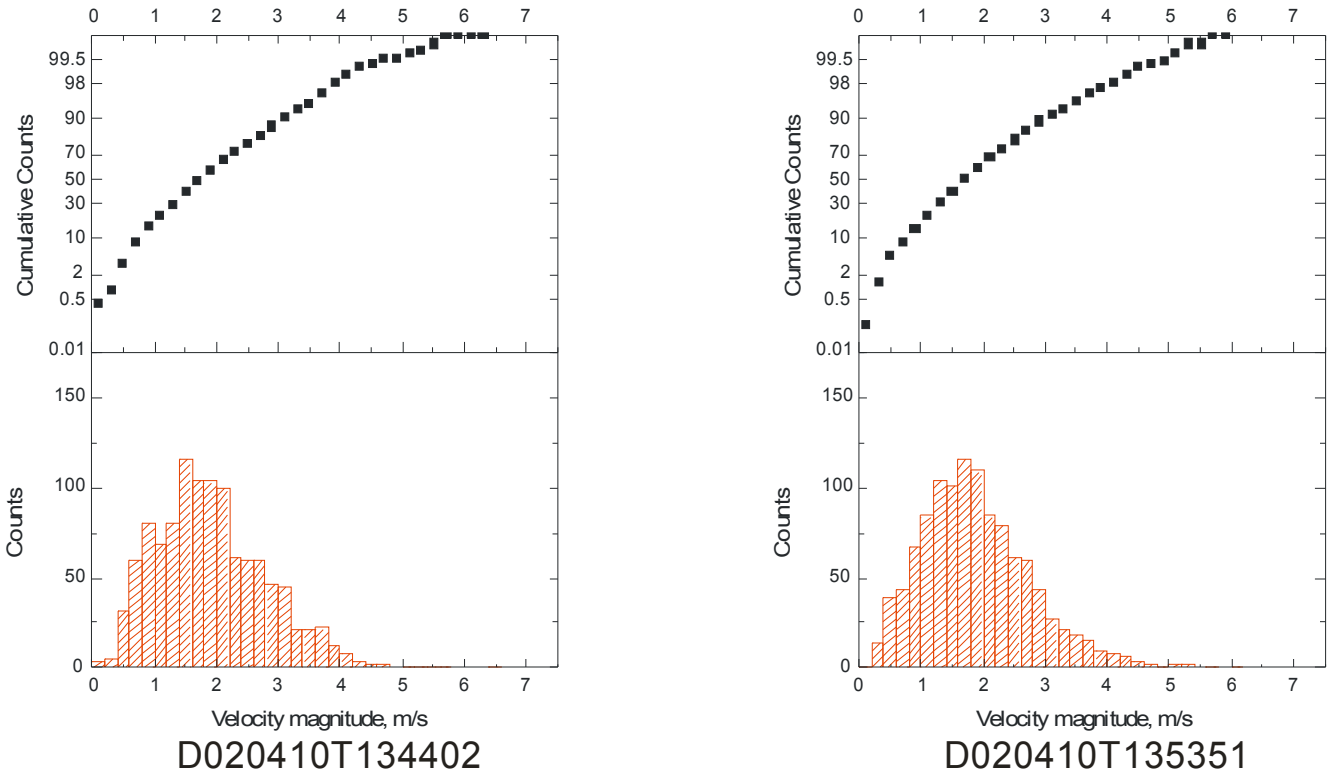

Figure VI.19 (cont'd).- Distribution of velocity magnitude for the individual data ensembles in the shear flow region just behind the backward facing step (y/H = -0.17, x/H = 0.32).

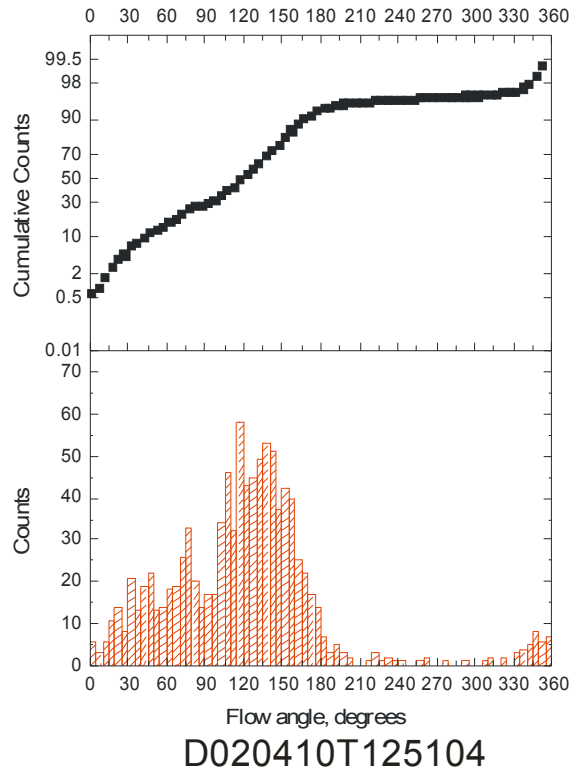

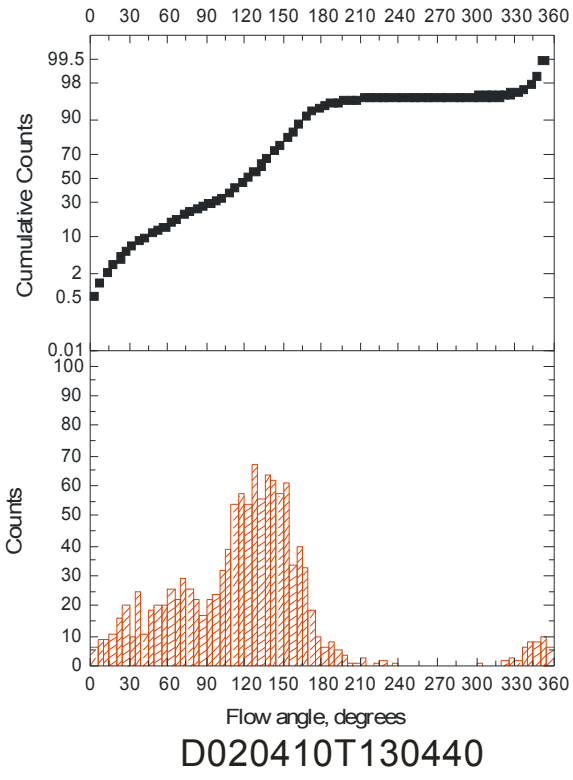

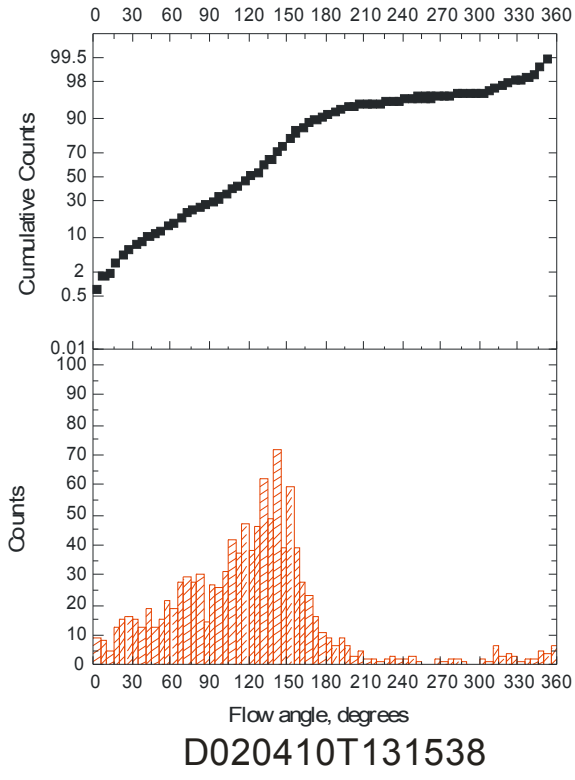

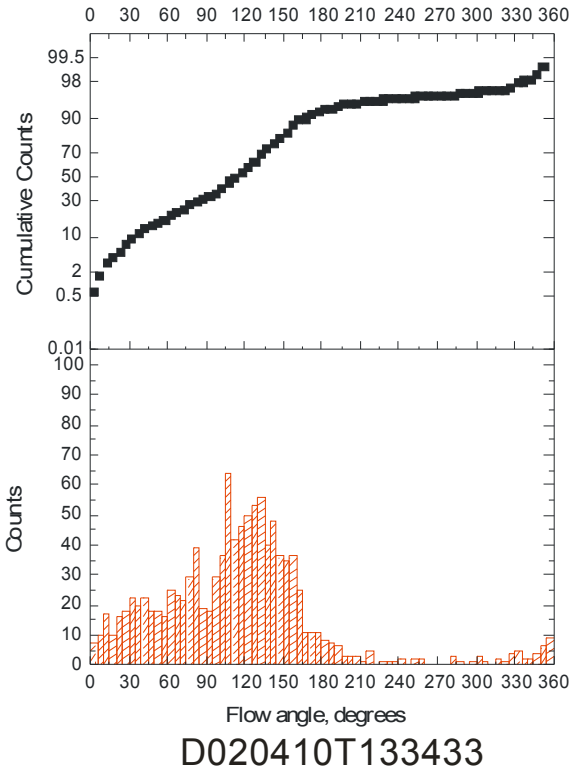

Figure VI.20.- Distribution of flow angle for the individual data ensembles in the shear flow region just behind the backward facing step (y/H = -0.17, x/H = 0.32).

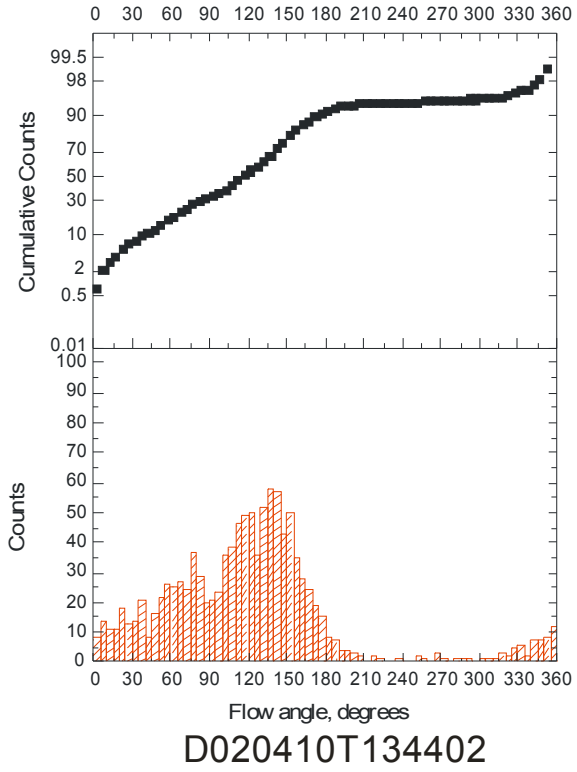

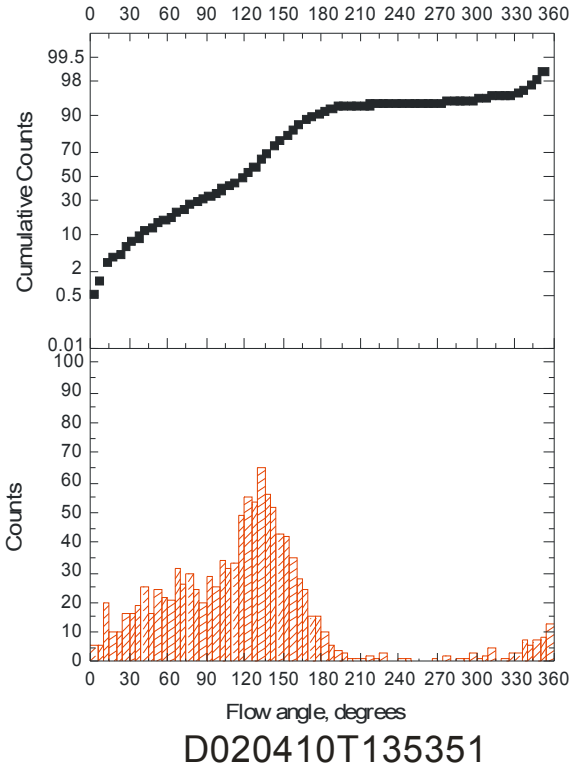

Figure VI.20 (cont'd).- Distribution of flow angle for the individual data ensembles in the shear flow region just behind the backward facing step (y/H = -0.17, x/H = 0.32).

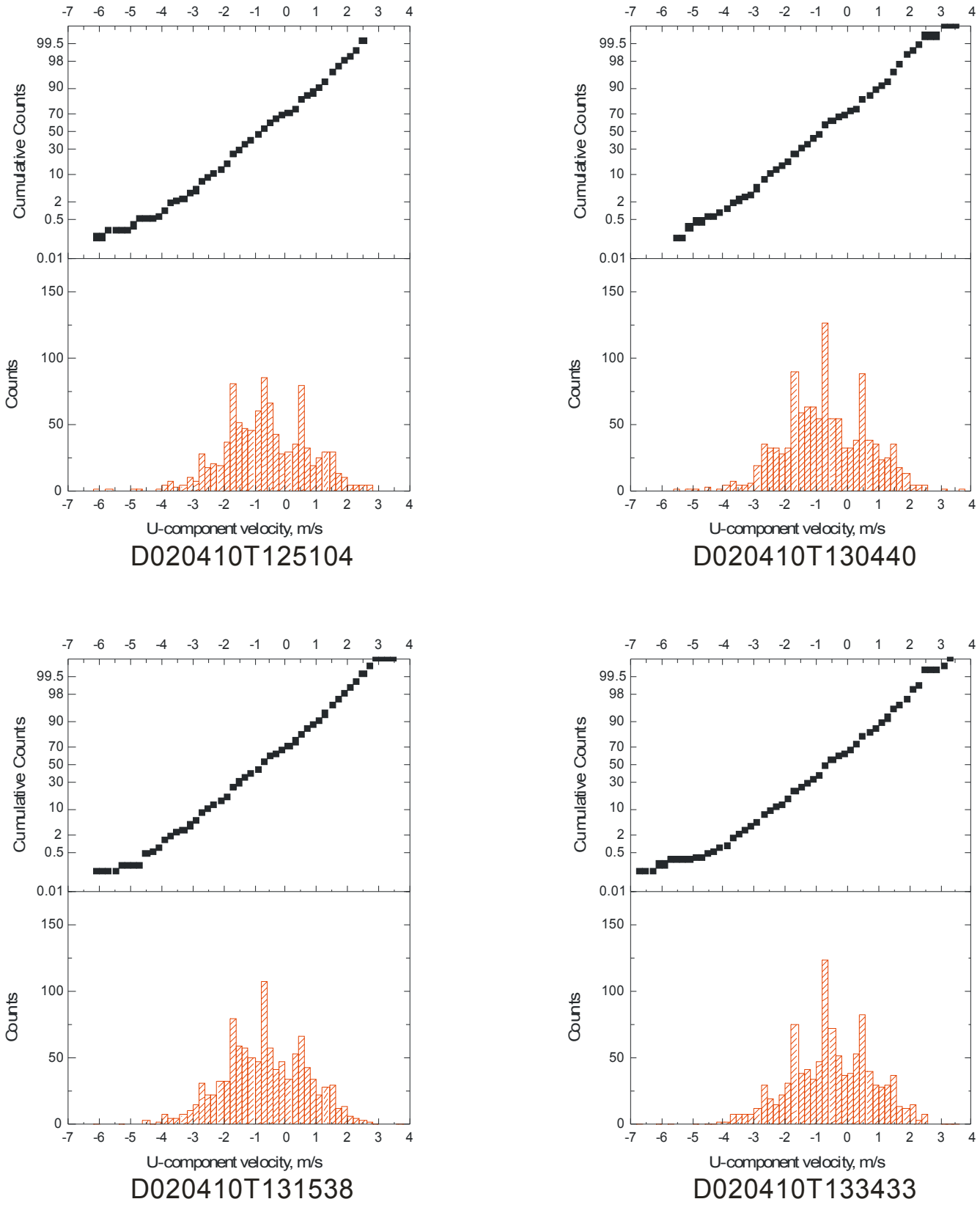

Figure VI.21.- Distribution of U-component velocity for the individual data ensembles in the shear flow region just behind the backward facing step (y/H = -0.17, x/H = 0.32).

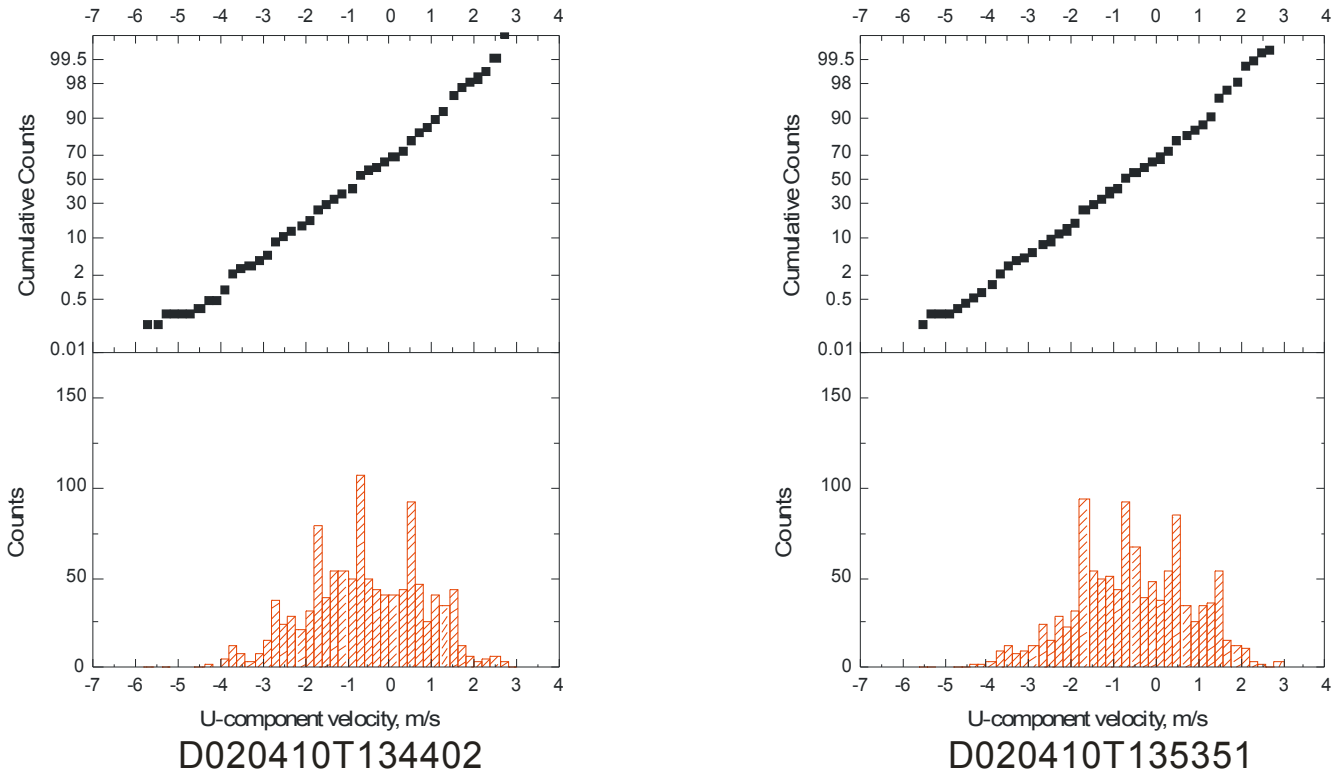

Figure VI.21 (cont'd).- Distribution of U-component velocity for the individual data ensembles in the shear flow region just behind the backward facing step (y/H = -0.17, x/H = 0.32).

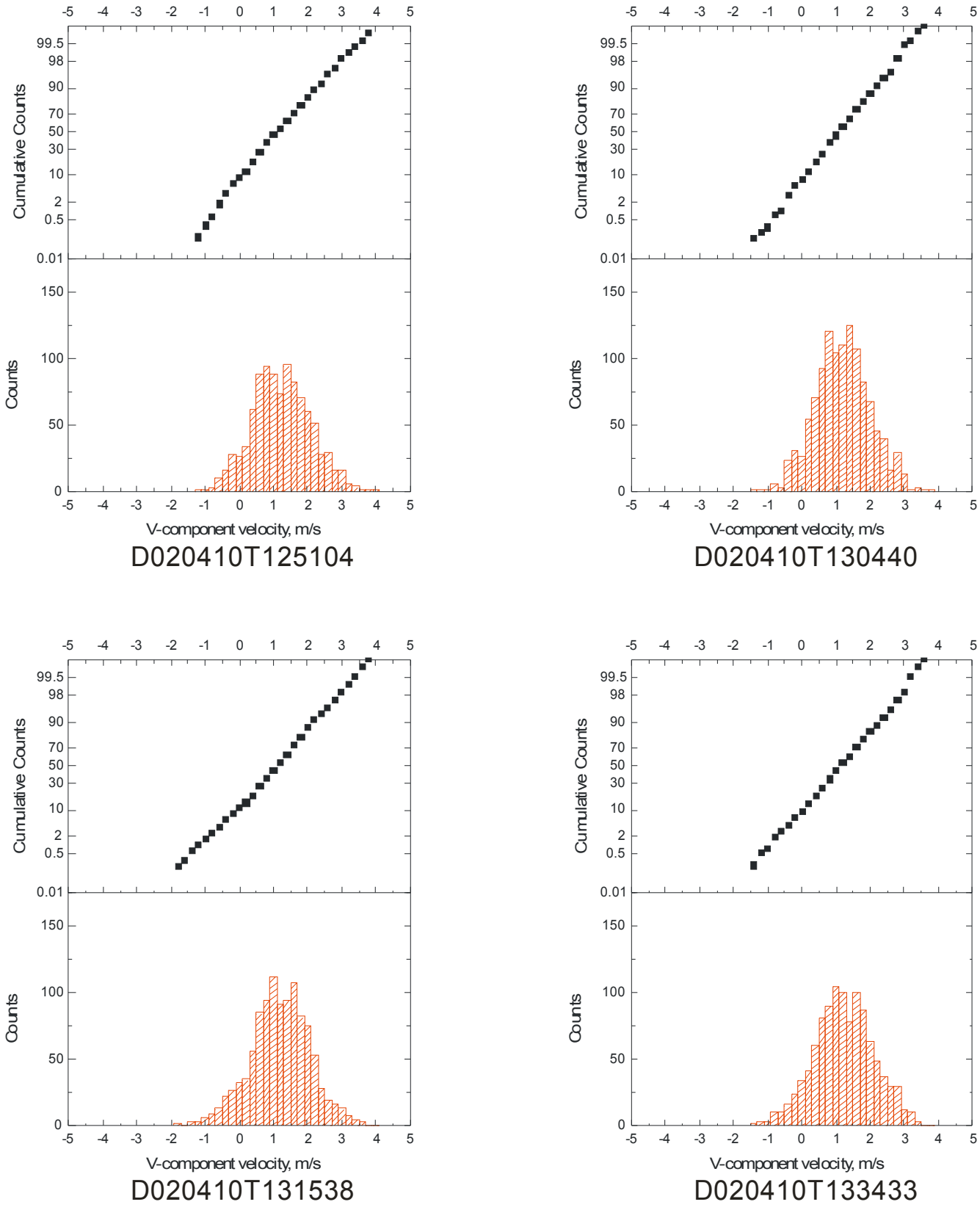

Figure VI.22.- Distribution of V-component velocity for the individual data ensembles in the shear flow region just behind the backward facing step (y/H = -0.17, x/H = 0.32).

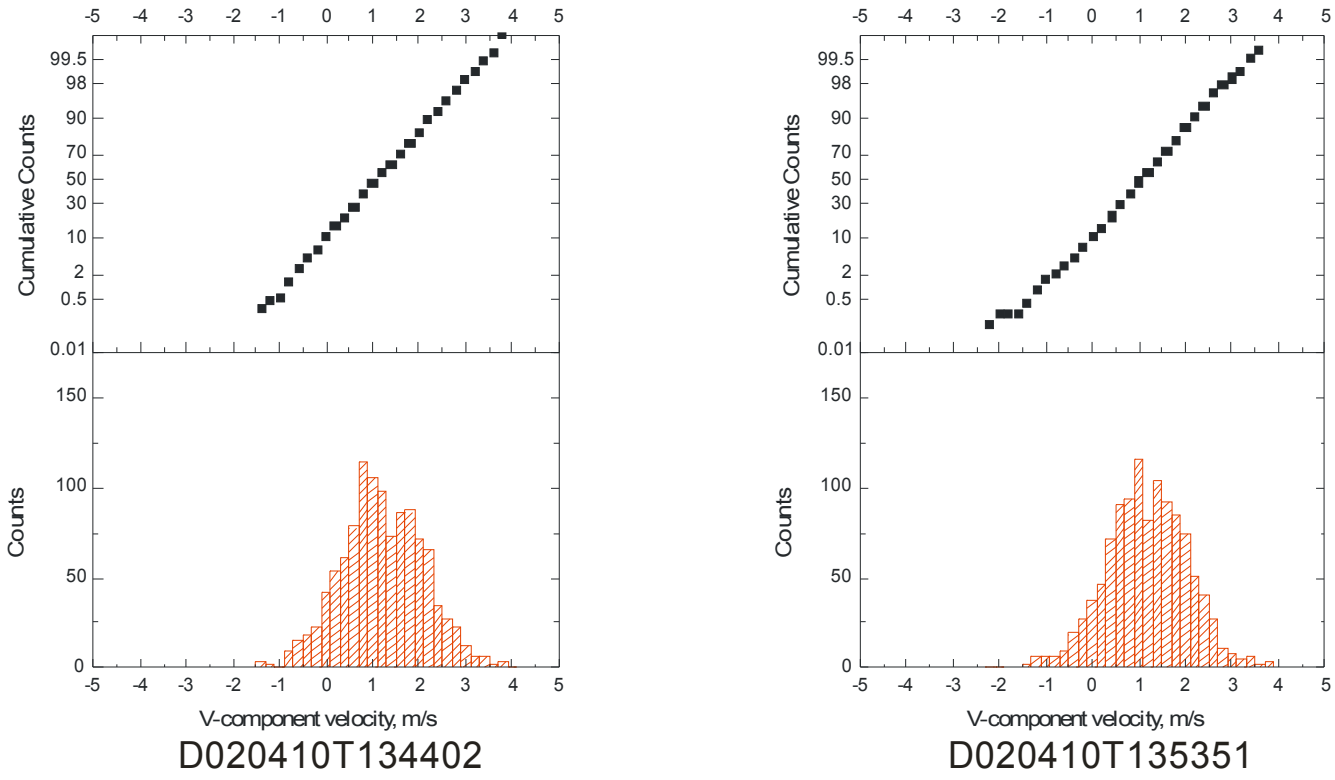

Figure VI.22 (cont'd).- Distribution of V-component velocity for the individual data ensembles in the shear flow region just behind the backward facing step (y/H = -0.17, x/H = 0.32).

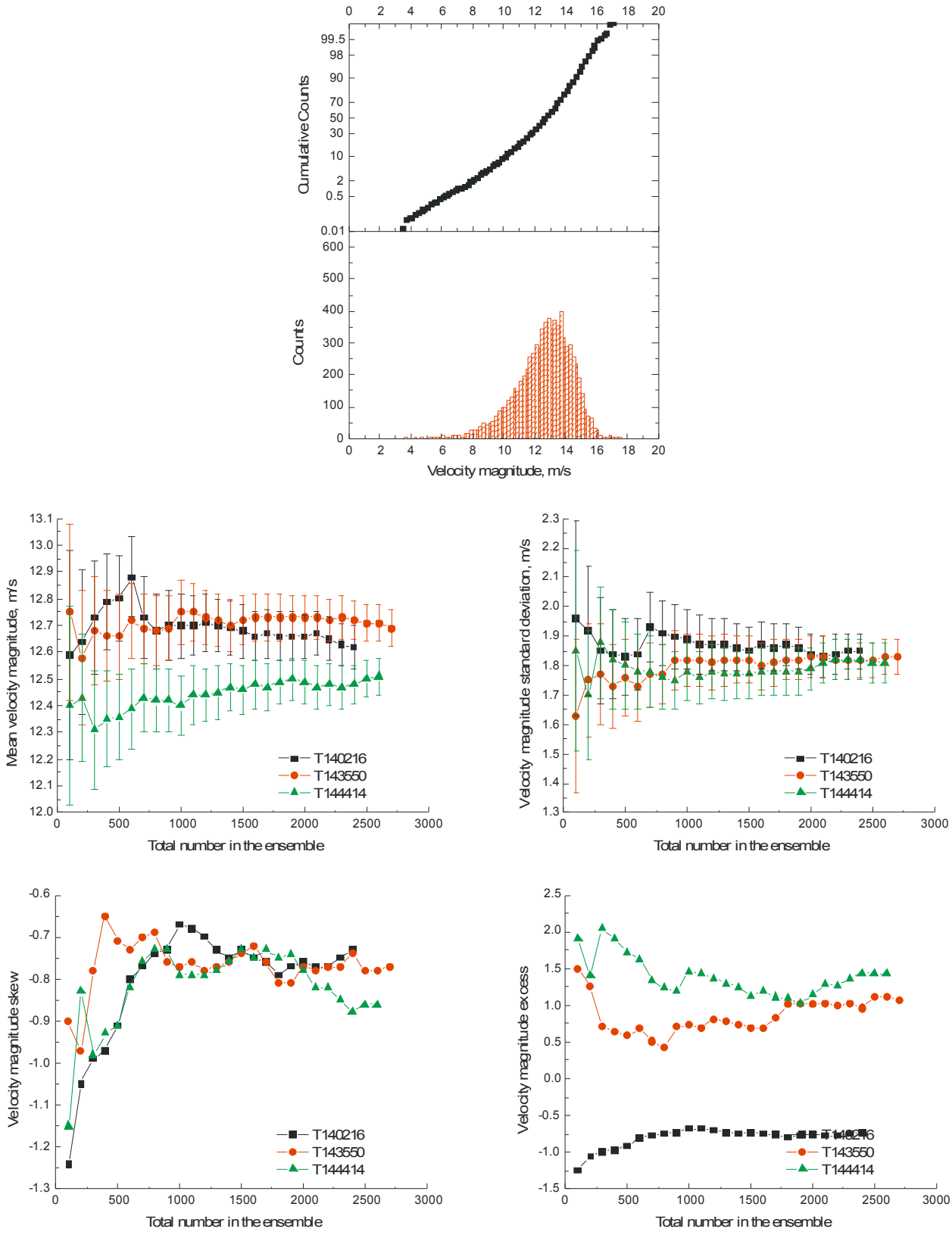

Figure VI.23.- Convergence of the velocity magnitude statistics and full ensemble histogram in the region directly behind the backward facing step (y/H = 0.0, x/H = 0.69).

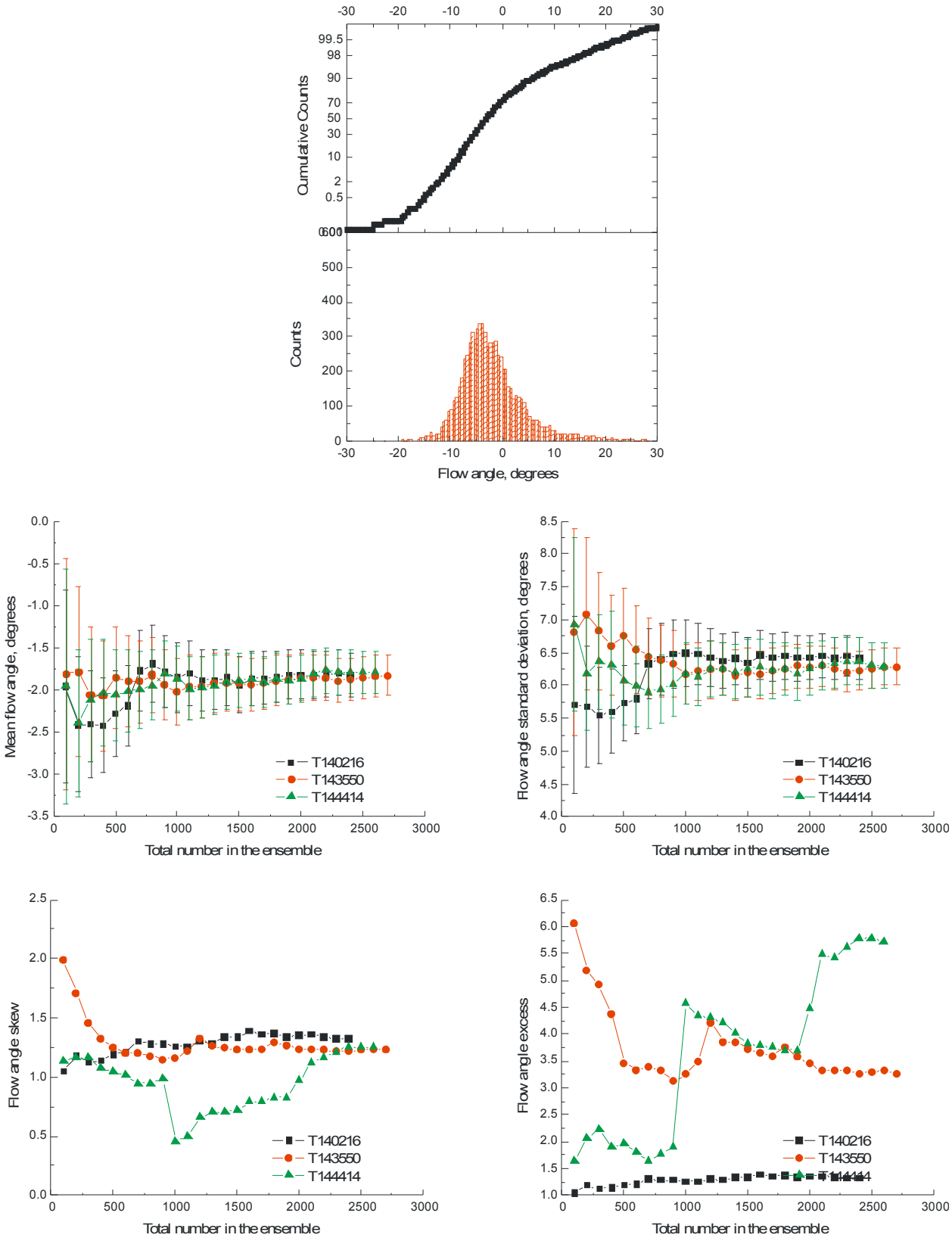

Figure VI.24.- Convergence of the flow angle statistics and full ensemble histogram in the region directly behind the backward facing step (y/H = 0.0, x/H = 0.69).

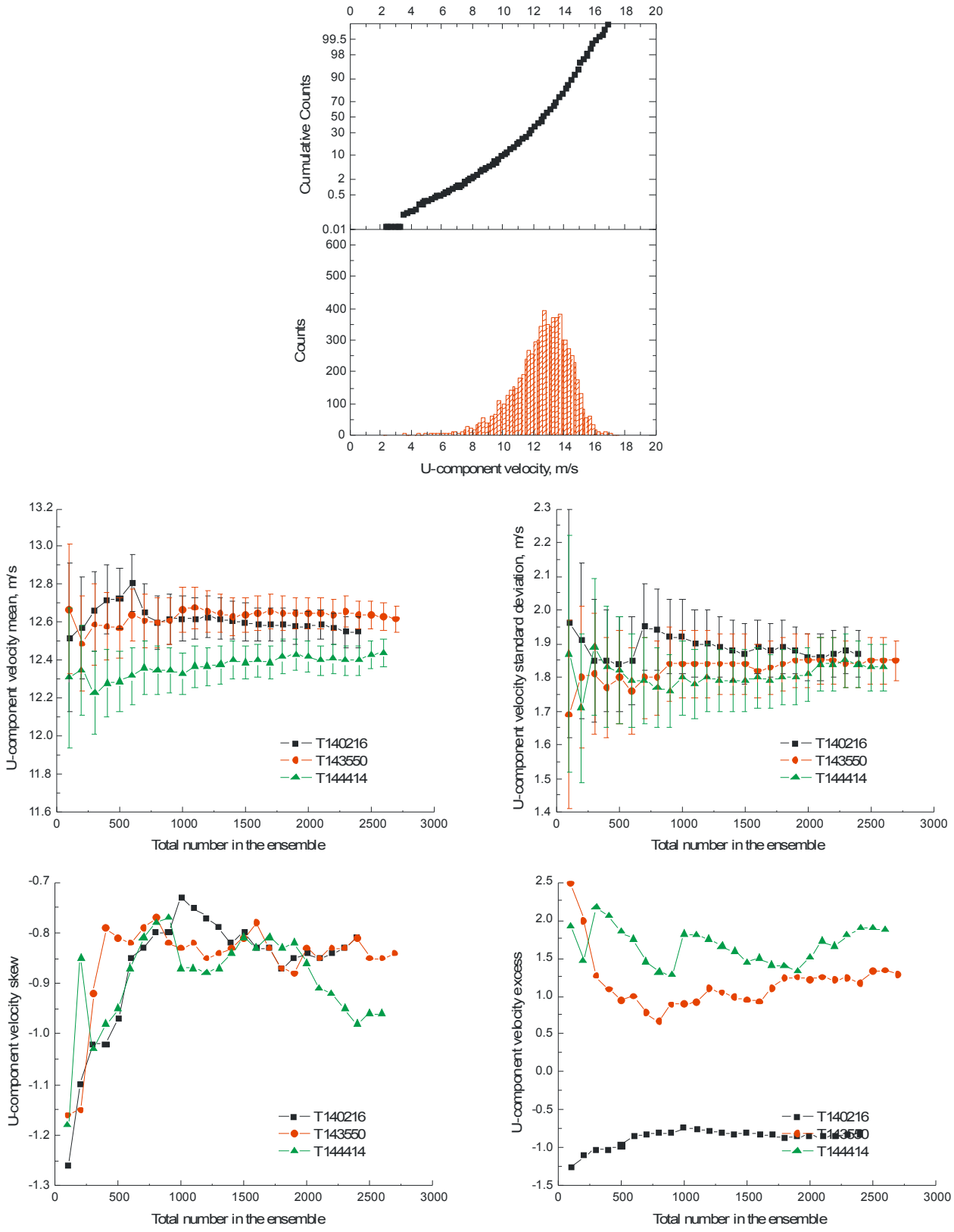

Figure VI.25.- Convergence of the U-component velocity statistics and full ensemble histogram in the region directly behind the backward facing step (y/H = 0.0, x/H = 0.69).

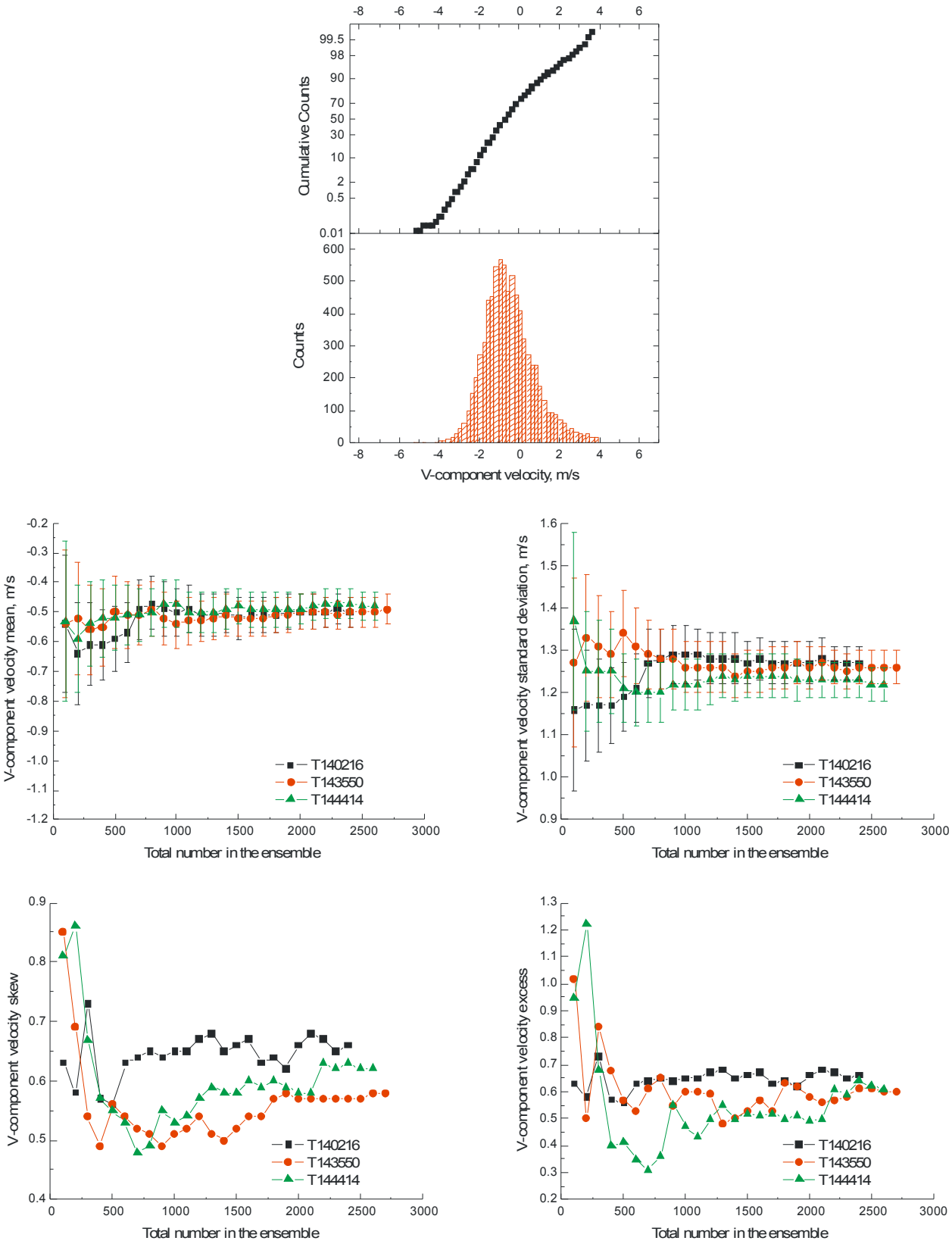

Figure VI.26.- Convergence of the V-component velocity statistics and full ensemble histogram in the region directly behind the backward facing step (y/H = 0.0, x/H = 0.69).

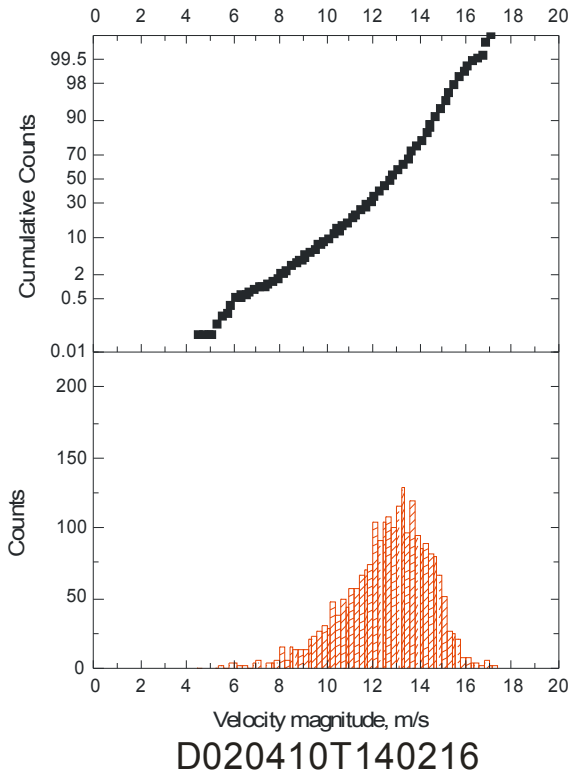

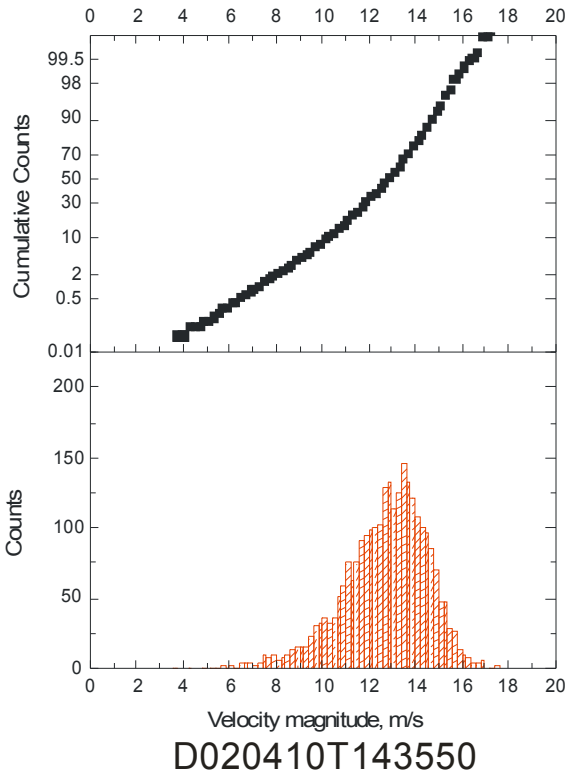

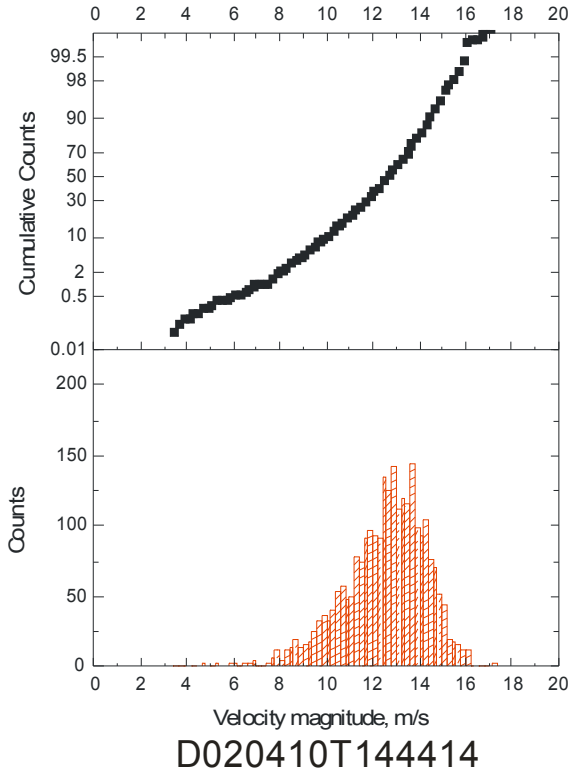

Figure VI.27.- Distribution of velocity magnitude for the individual data ensembles in the region directly behind the backward facing step (y/H = 0.0, x/H = 0.69).

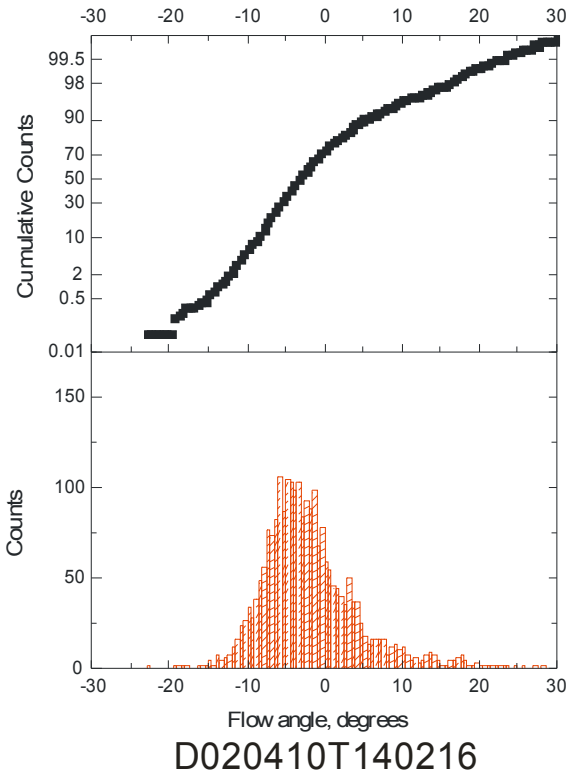

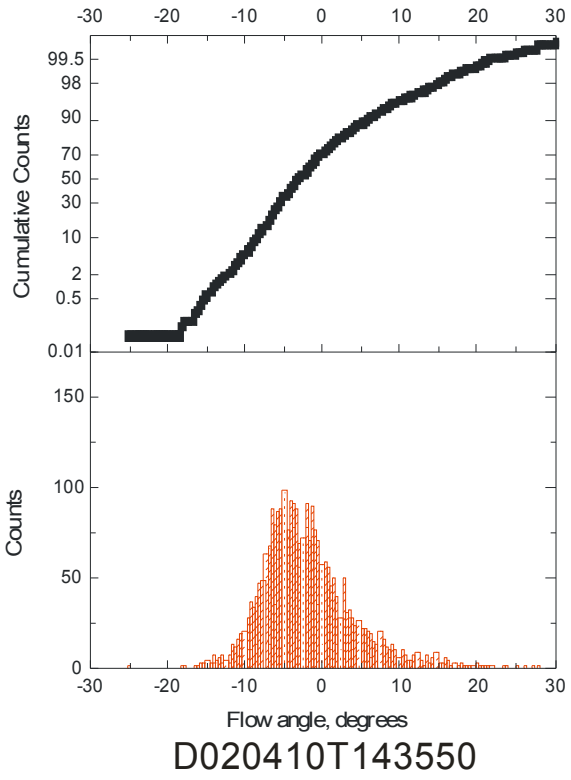

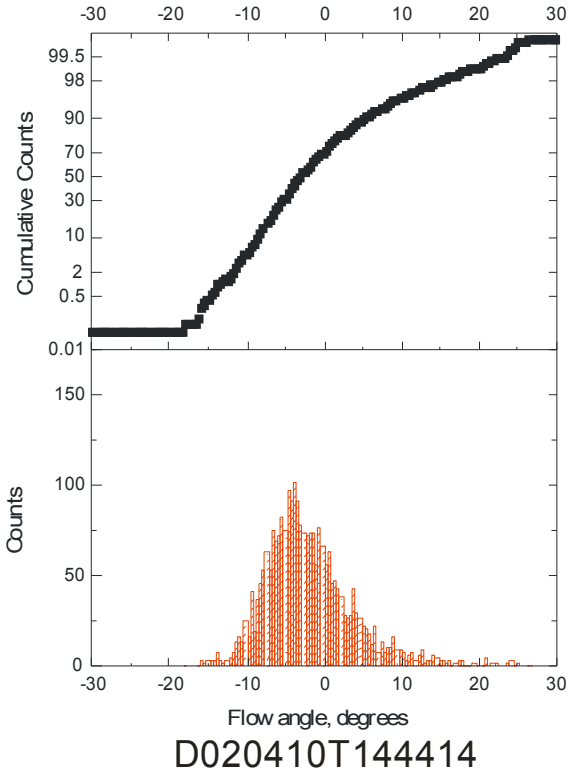

Figure VI.28.- Distribution of flow angle for the individual data ensembles in the region directly behind the backward facing step (y/H = 0.0, x/H = 0.69).

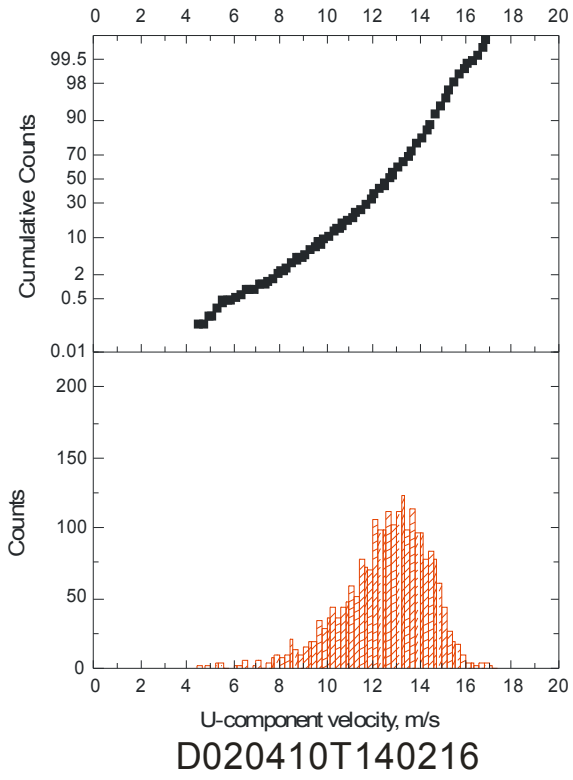

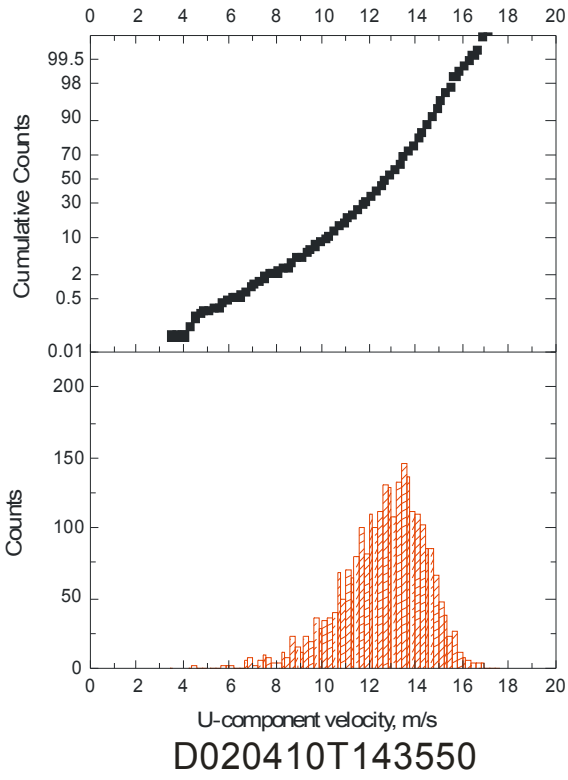

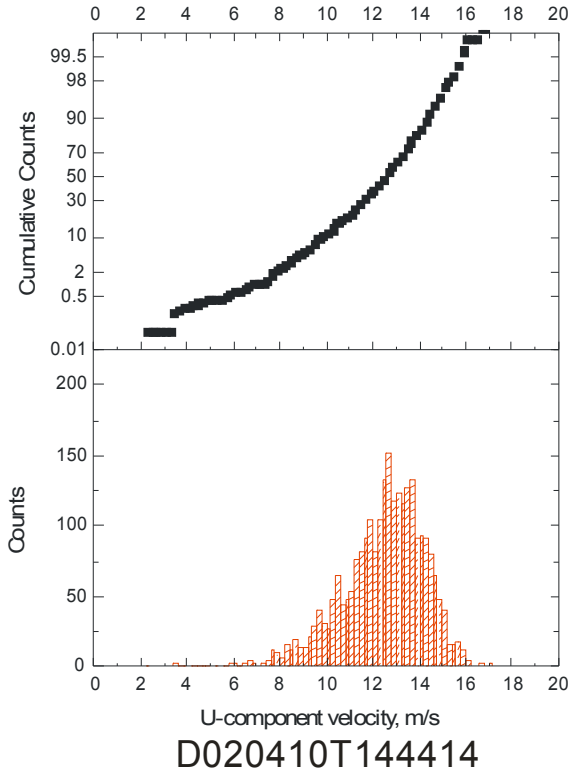

Figure VI.29.- Distribution of U-component velocity for the individual data ensembles in the region directly behind the backward facing step (y/H = 0.0, x/H = 0.69).

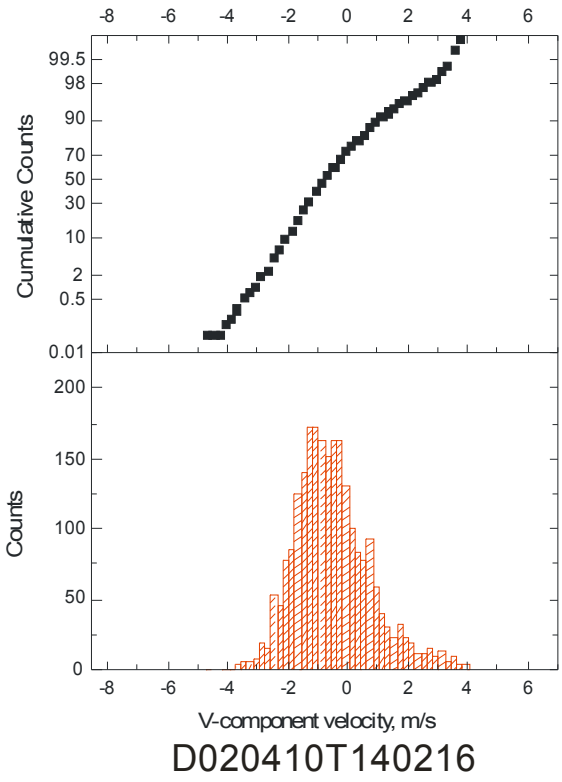

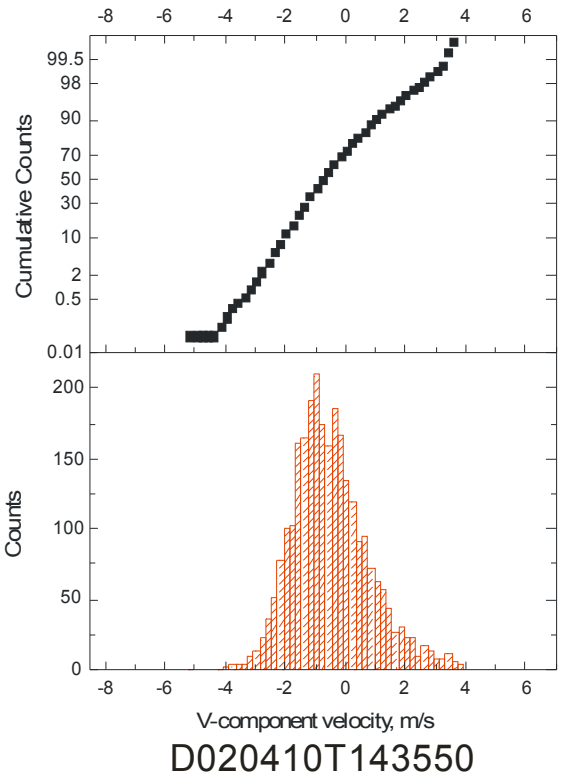

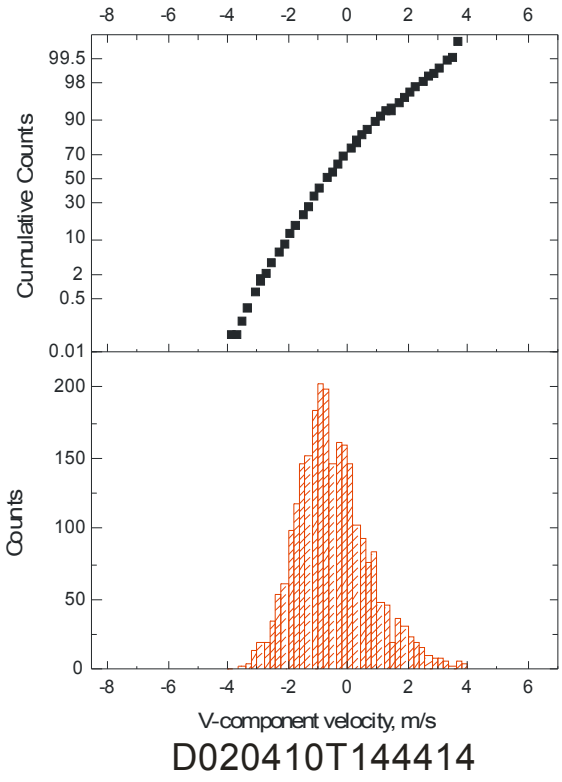

Figure VI.30.- Distribution of V-component velocity for the individual data ensembles in the region directly behind the backward facing step (y/H = 0.0, x/H = 0.69).

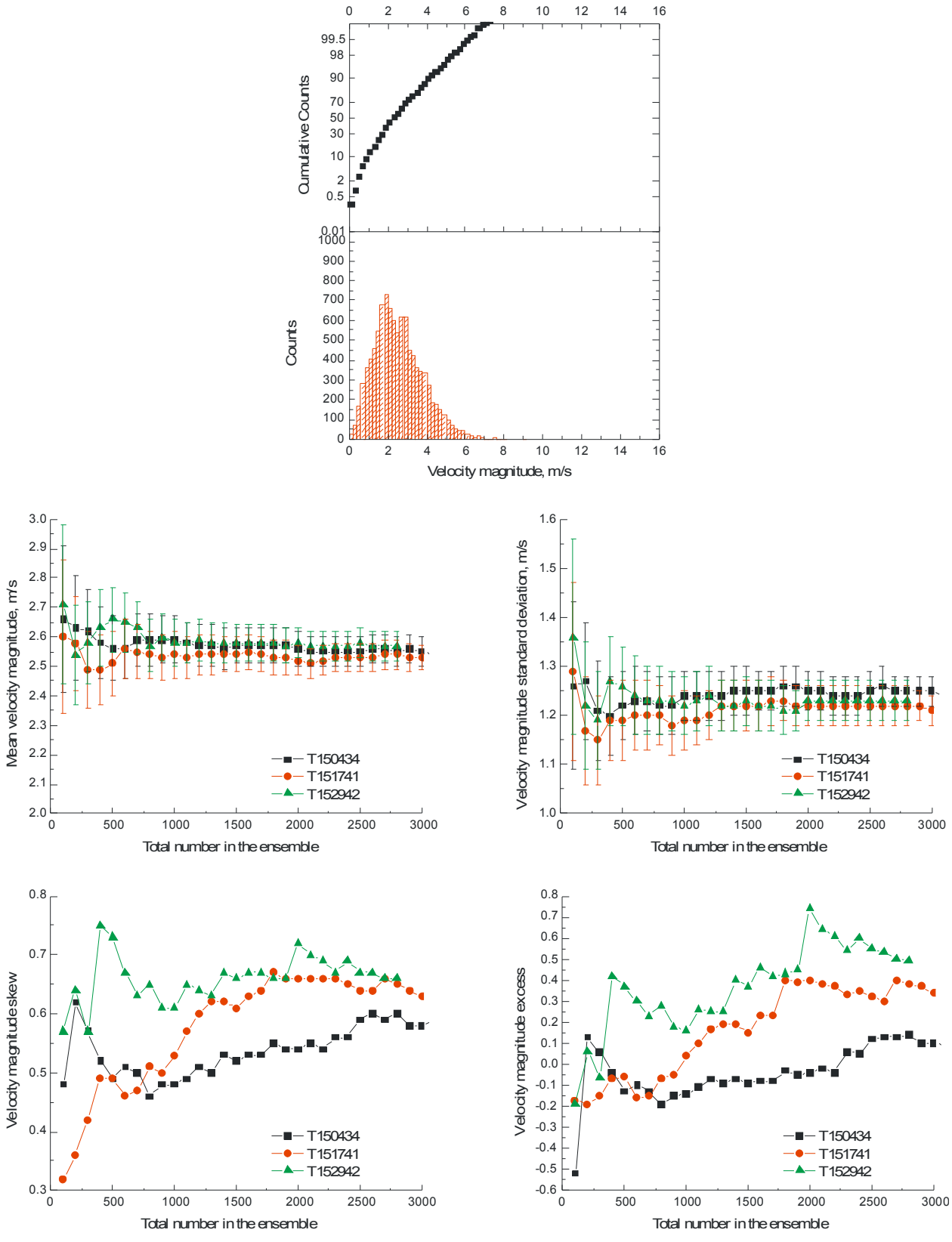

Figure VI.31.- Convergence of the velocity magnitude statistics and full ensemble histogram in the reverse flow region behind the backward facing step (y/H = -0.40, x/H = 0.69).

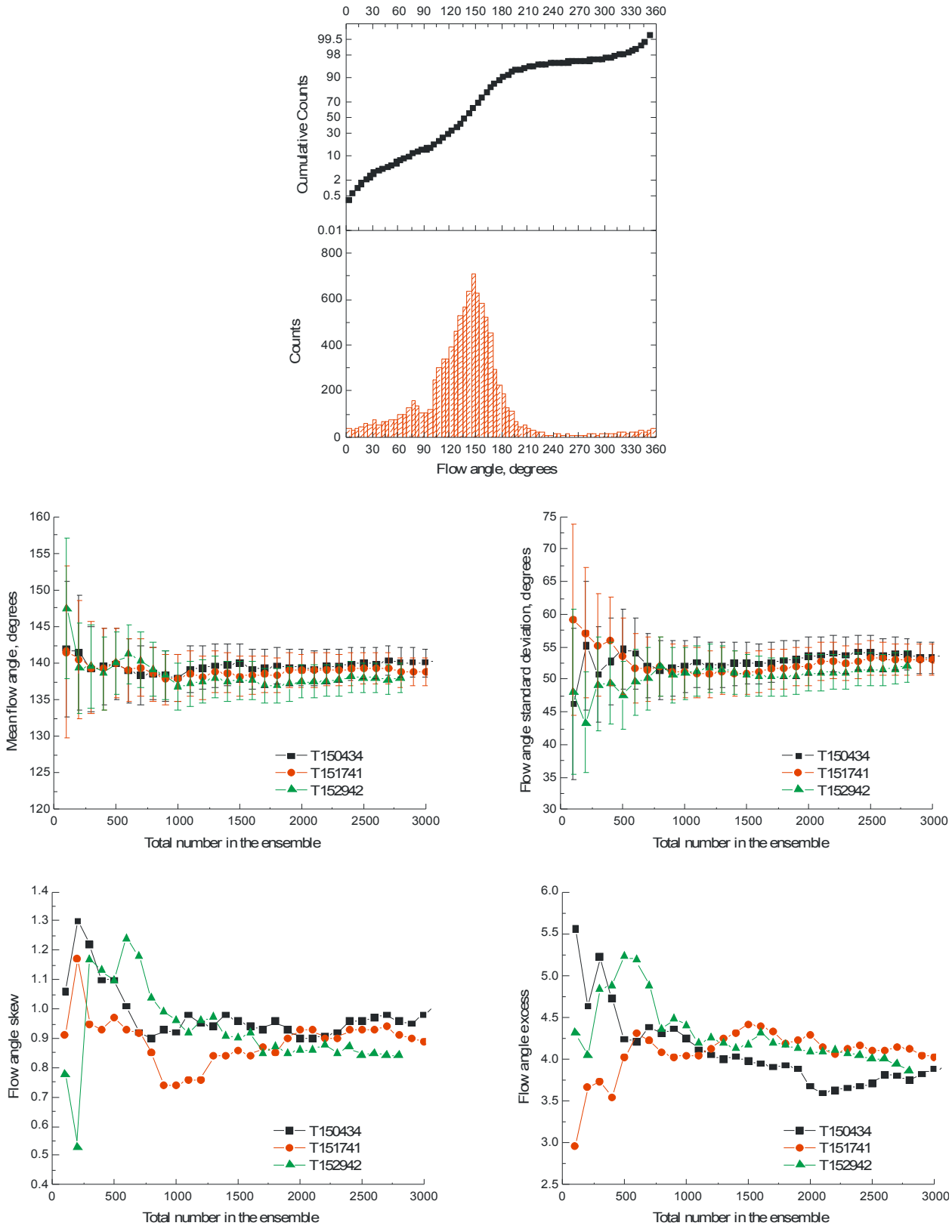

Figure VI.32.- Convergence of the flow angle statistics and full ensemble histogram in the reverse flow region behind the backward facing step (y/H = -0.40, x/H = 0.69).

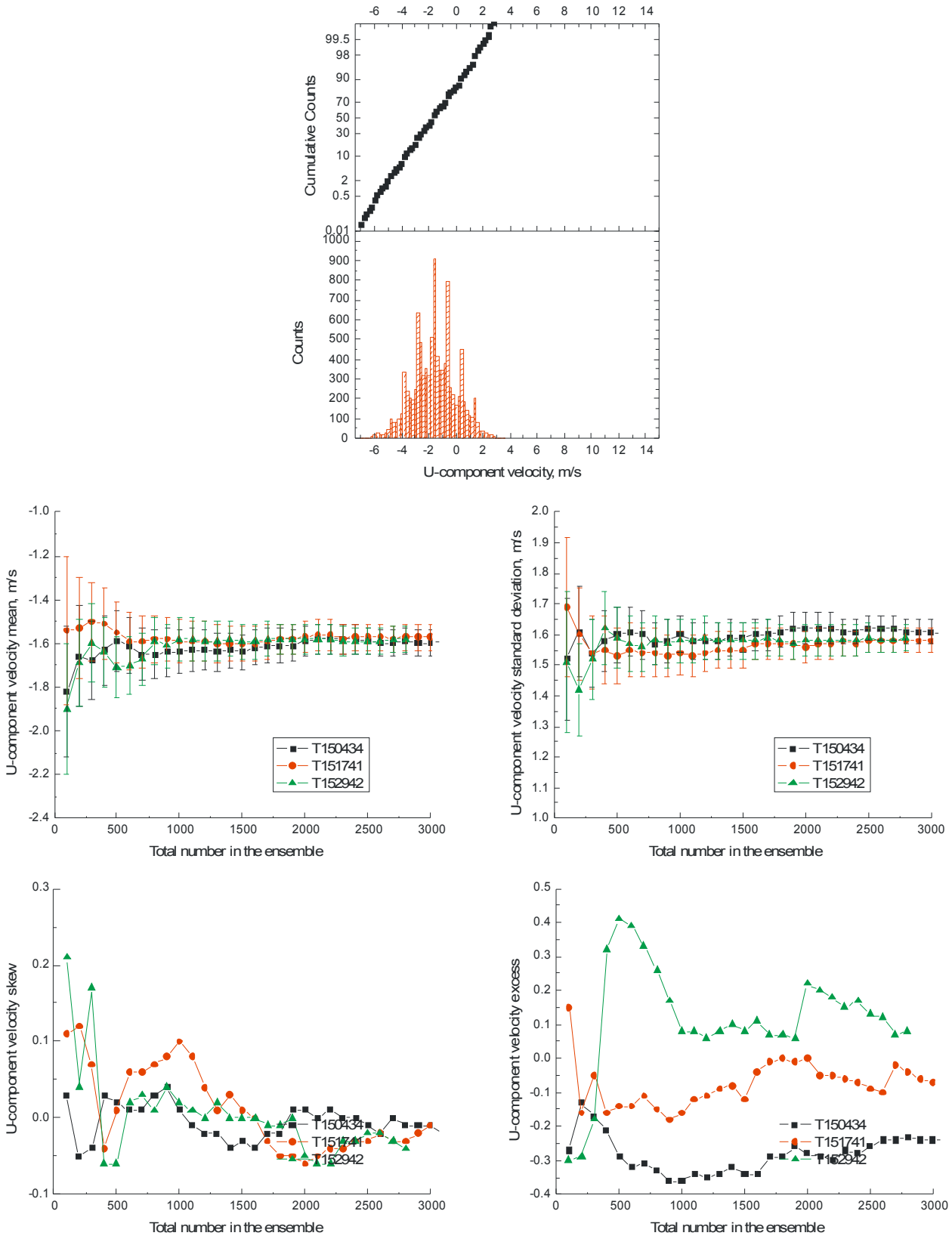

Figure VI.33.- Convergence of the U-component velocity statistics and full ensemble histogram in the reverse flow region behind the backward facing step (y/H = -0.40, x/H = 0.69).

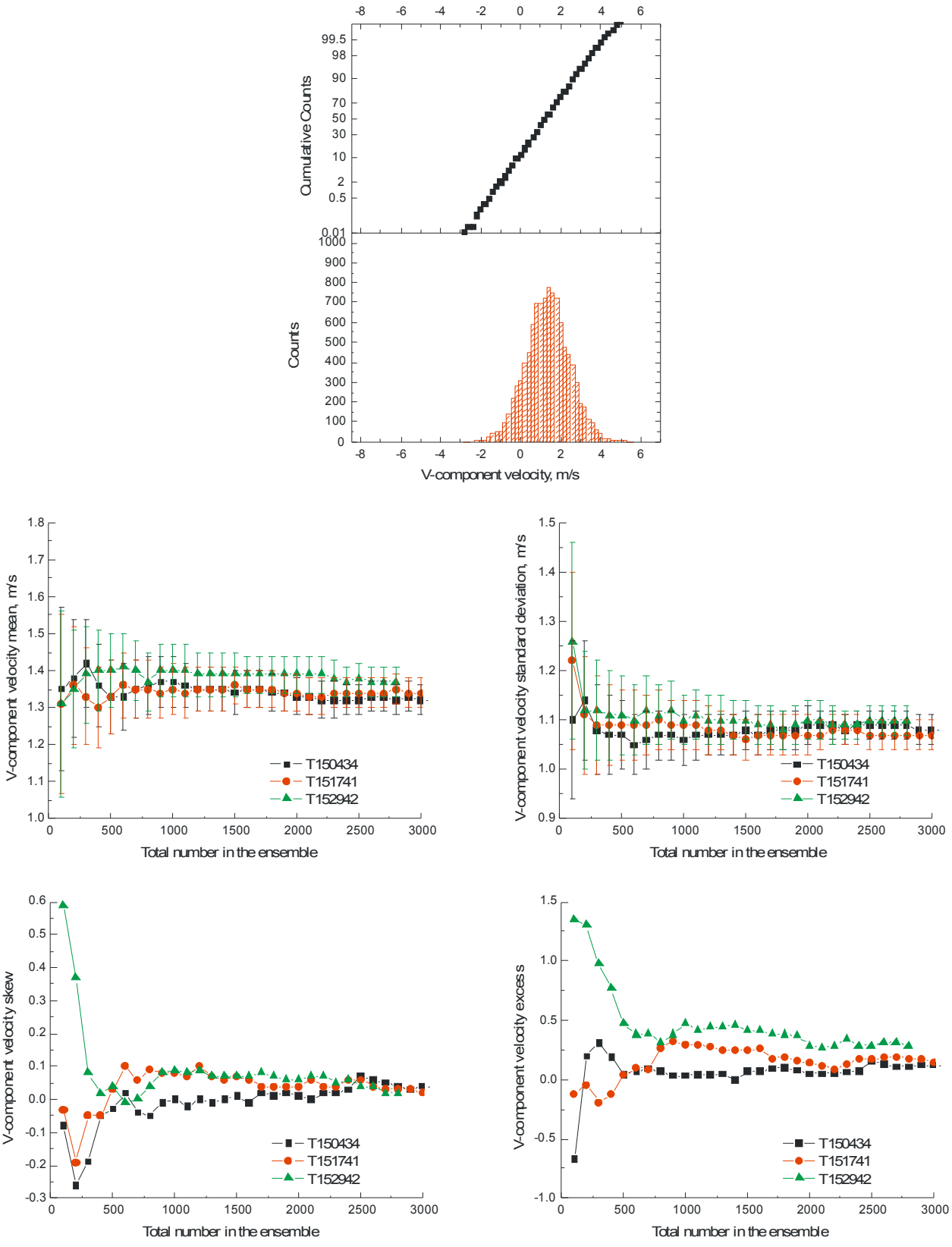

Figure VI.34.- Convergence of the V-component velocity statistics and full ensemble histogram in the reverse flow region behind the backward facing step (y/H = -0.40, x/H = 0.69).

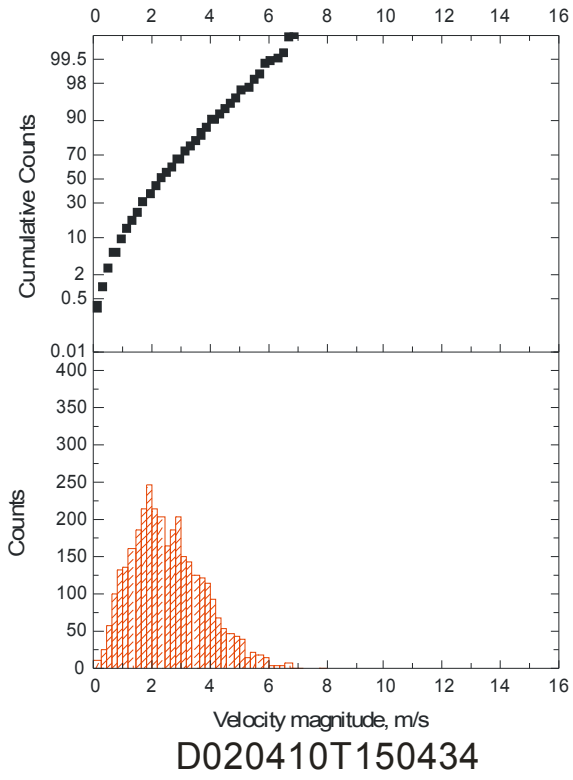

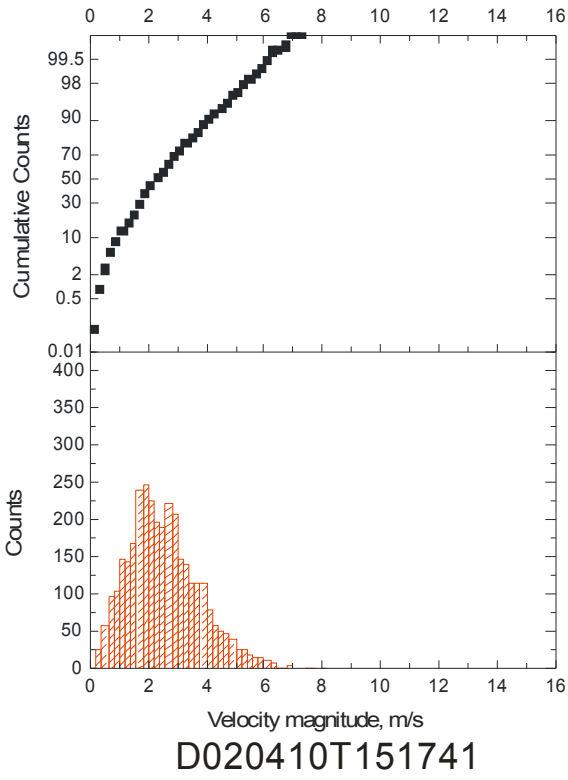

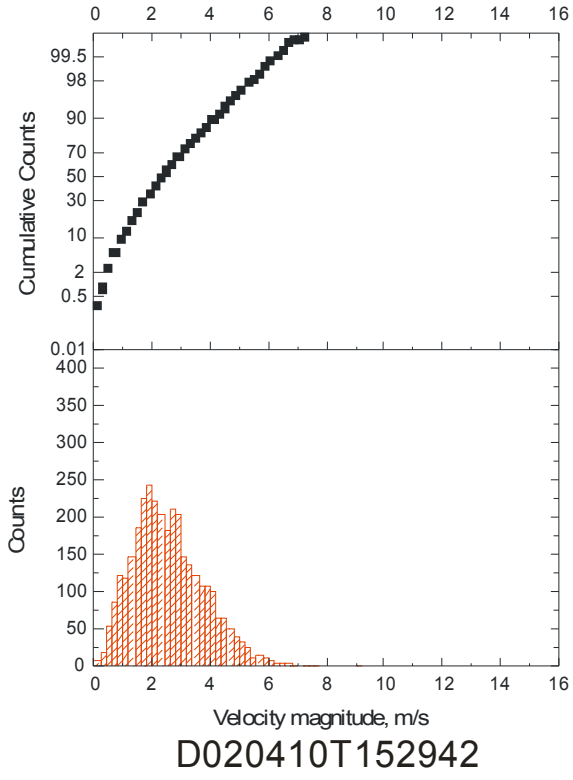

Figure VI.35.- Distribution of velocity magnitude for the individual data ensembles in the reverse flow region behind the backward facing step (y/H = -0.40, x/H = 0.69).

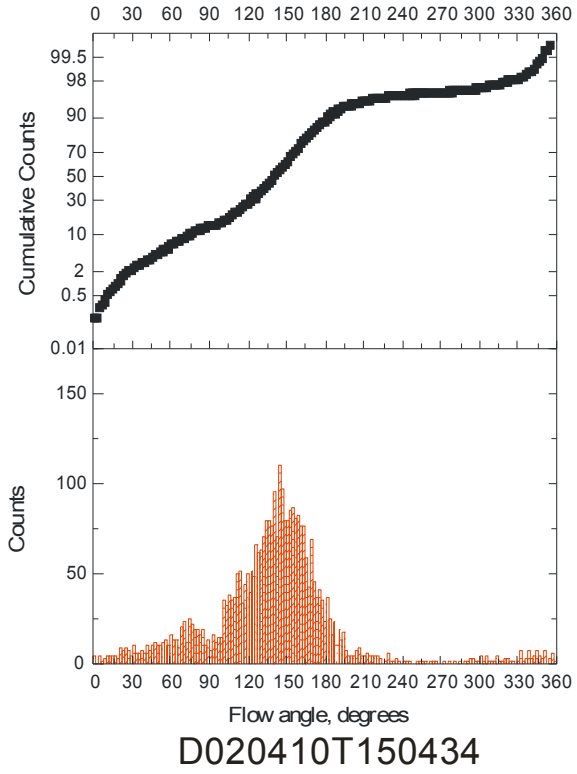

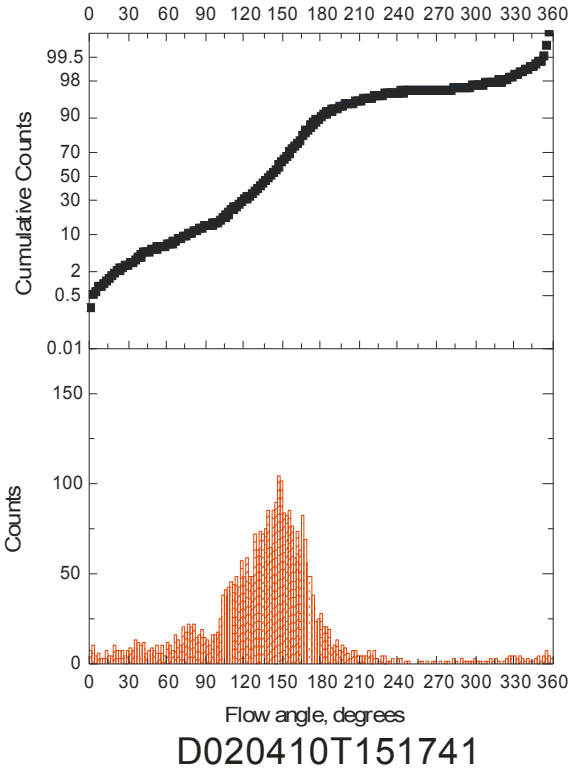

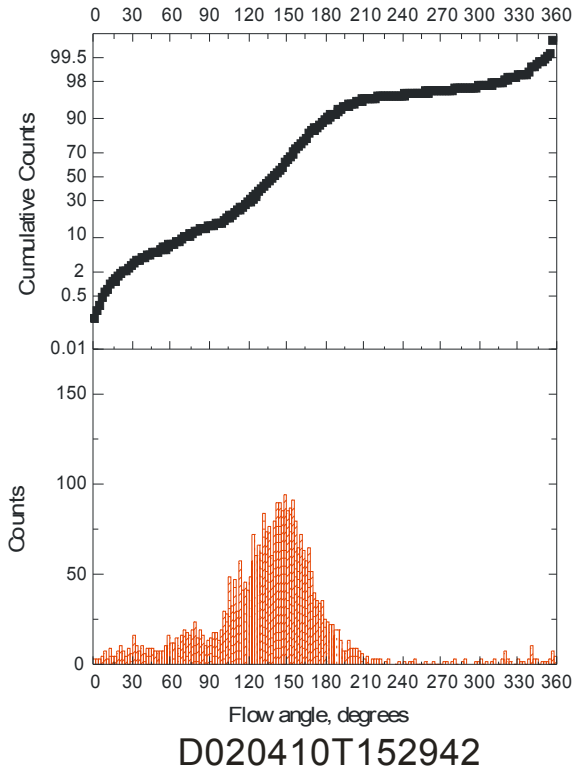

Figure VI.36.- Distribution of flow angle for the individual data ensembles in the reverse flow region behind the backward facing step (y/H = -0.40, x/H = 0.69).

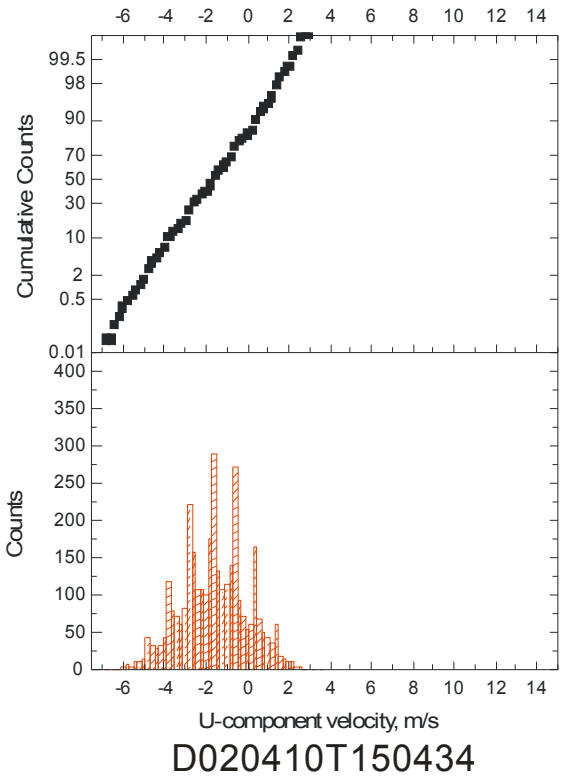

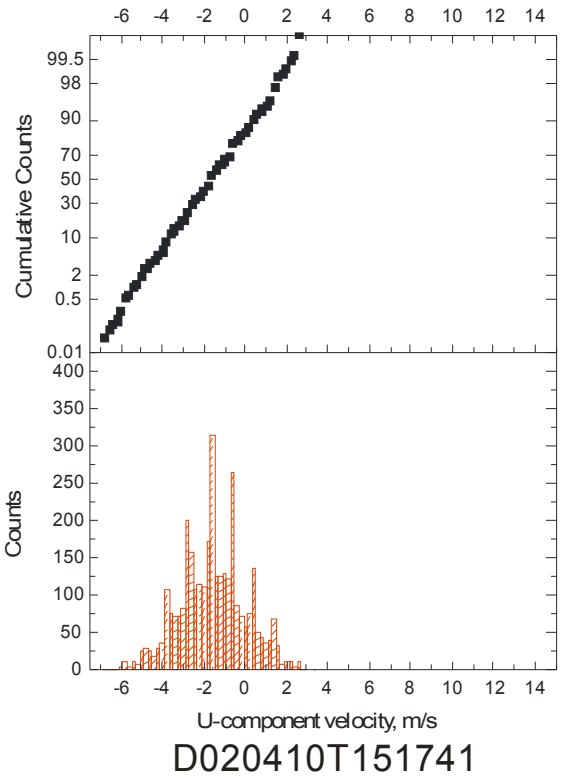

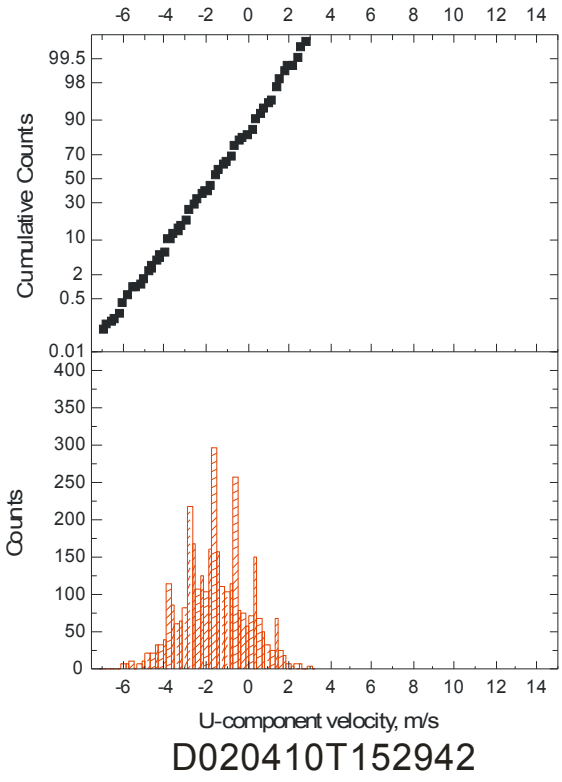

Figure VI.37.- Distribution of U-component velocity for the individual data ensembles in the reverse flow region behind the backward facing step (y/H = -0.40, x/H = 0.69).

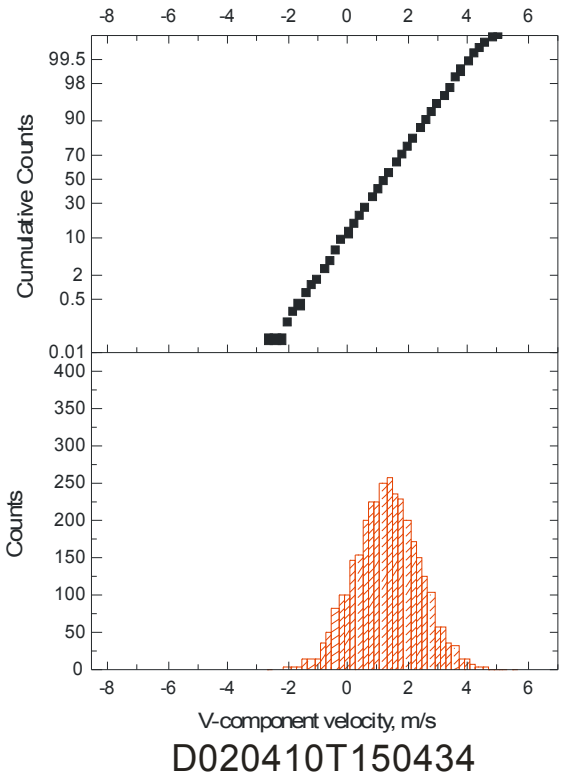

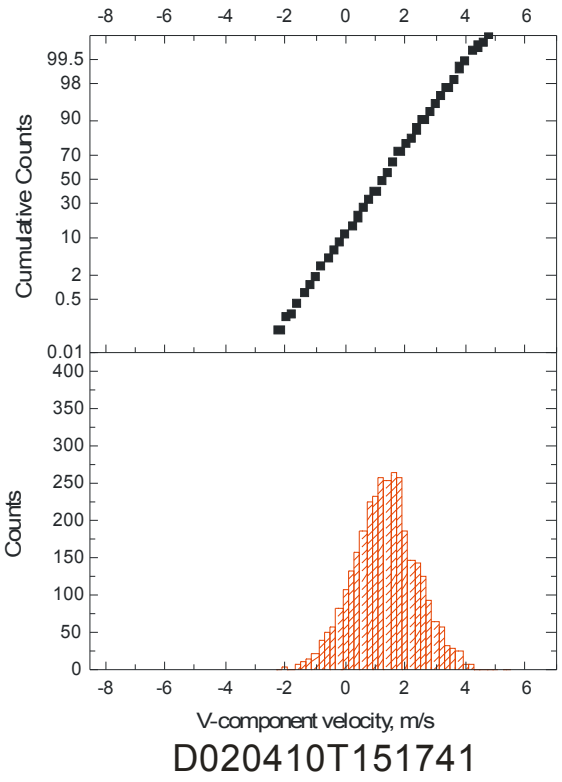

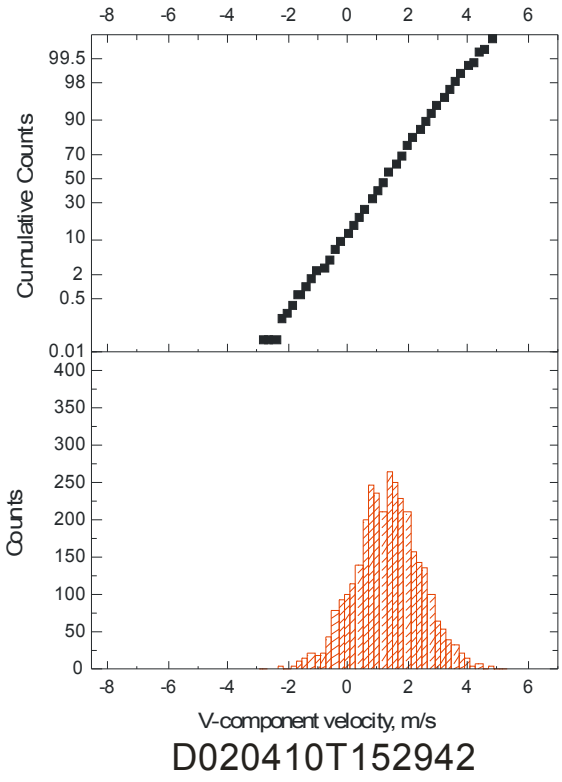

Figure VI.38.- Distribution of V-component velocity for the individual data ensembles in the reverse flow region behind the backward facing step (y/H = -0.40, x/H = 0.69).

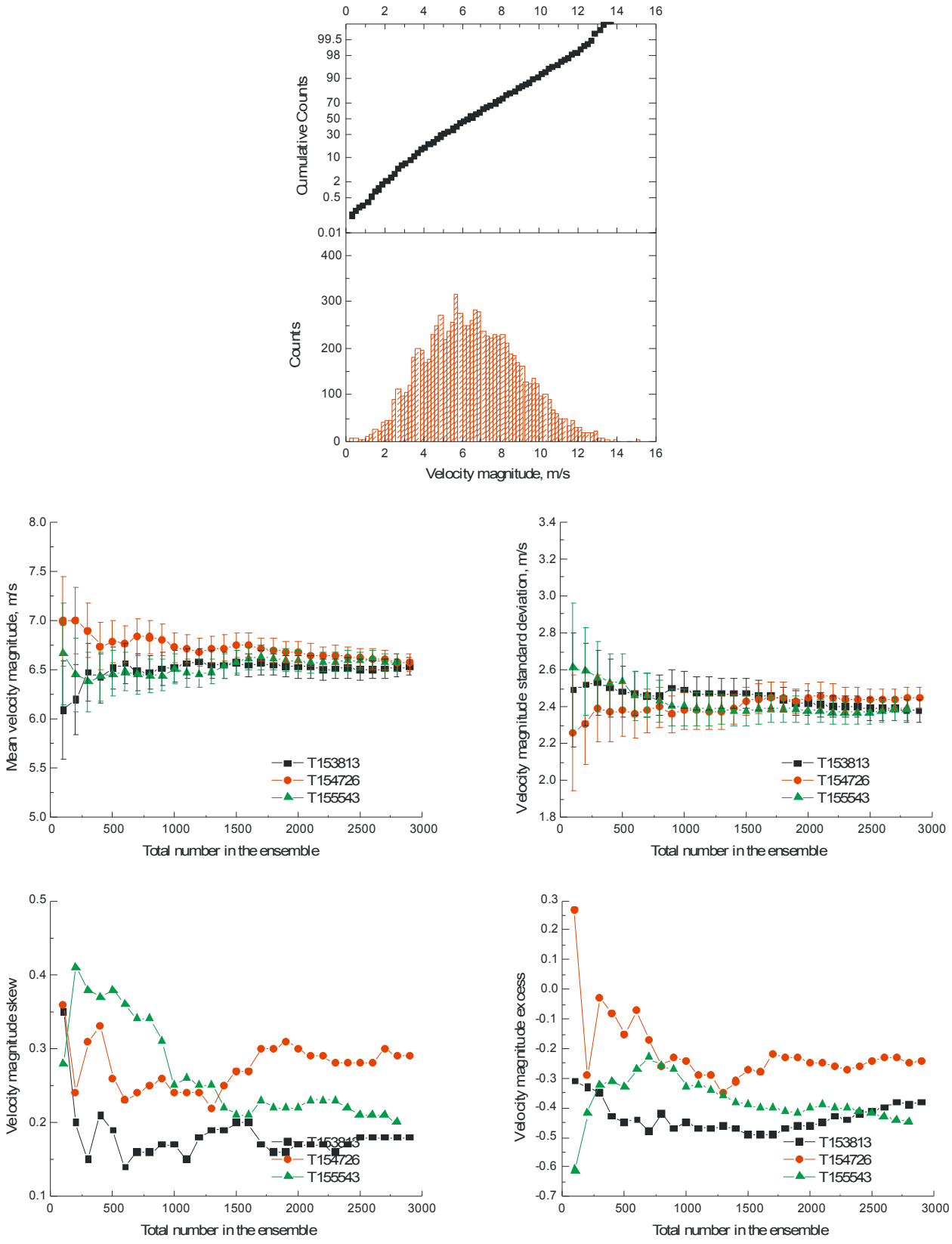

Figure VI.39.- Convergence of the velocity magnitude statistics and full ensemble histogram in the shear flow region downstream from the backward facing step (y/H = -0.17, x/H = 1.37).

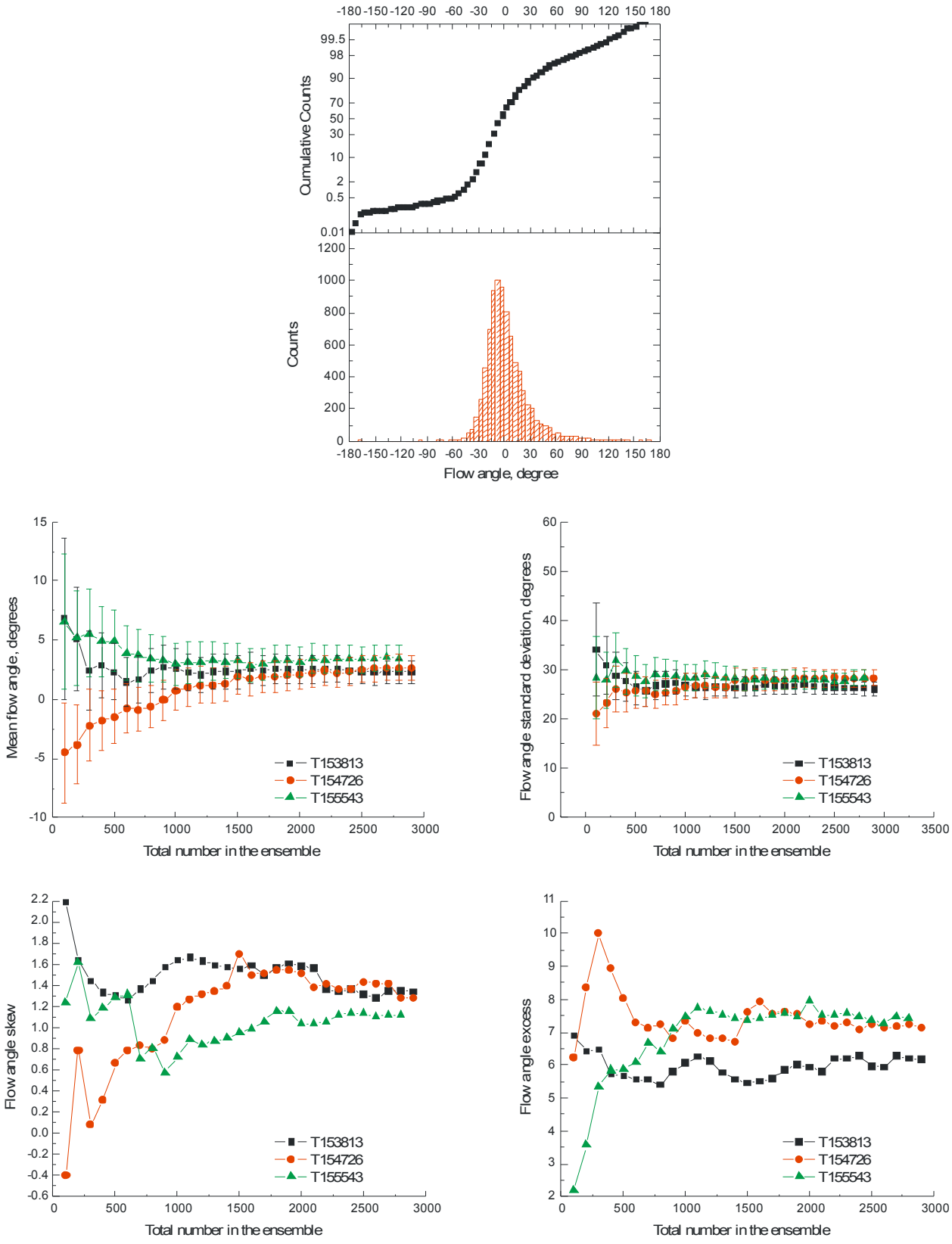

Figure VI.40.- Convergence of the flow angle statistics and full ensemble histogram in the shear flow region downstream from the backward facing step (y/H = -0.17, x/H = 1.37).

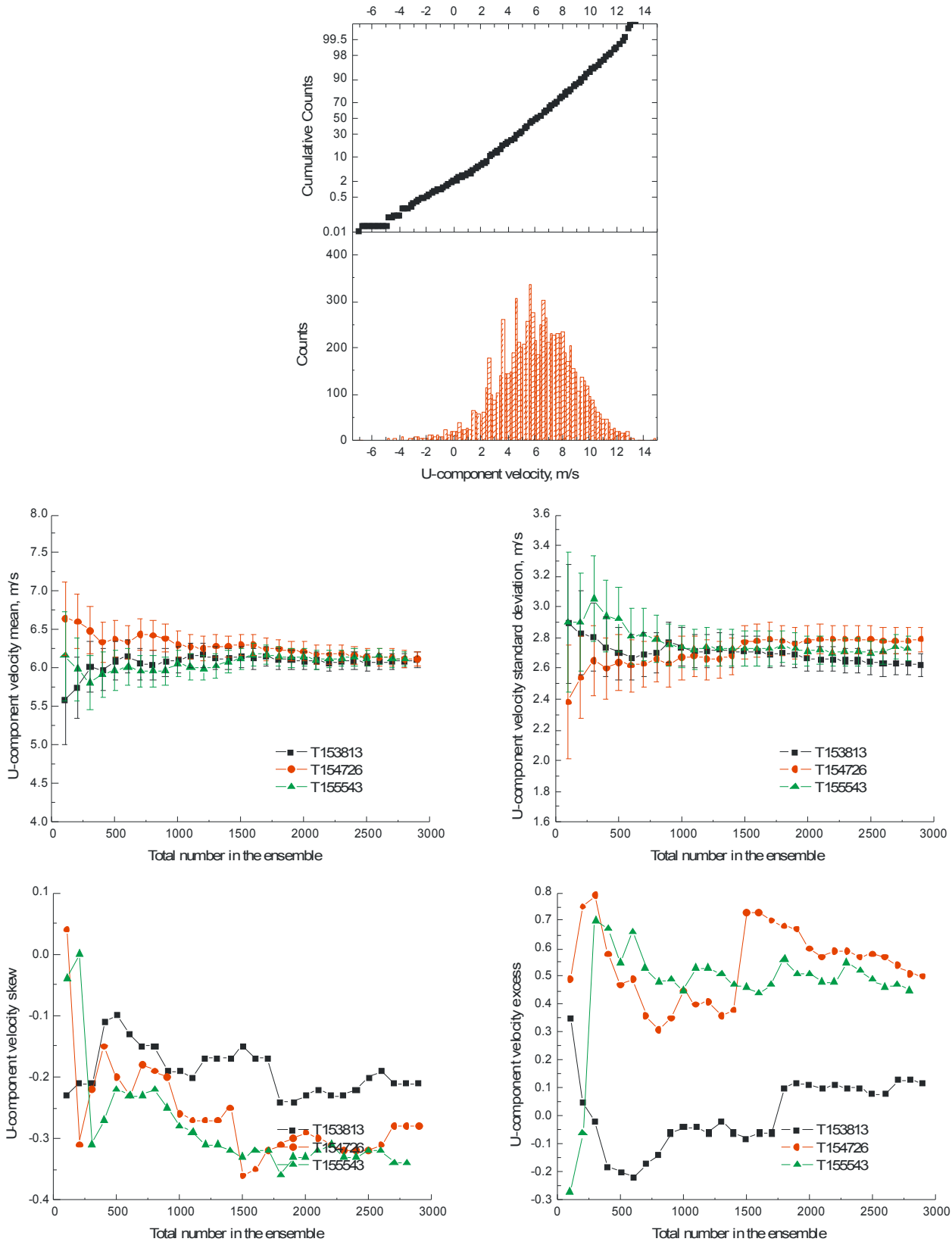

Figure VI.41.- Convergence of the U-component velocity statistics and full ensemble histogram in the shear flow region downstream from the backward facing step (y/H = -0.17, x/H = 1.37).

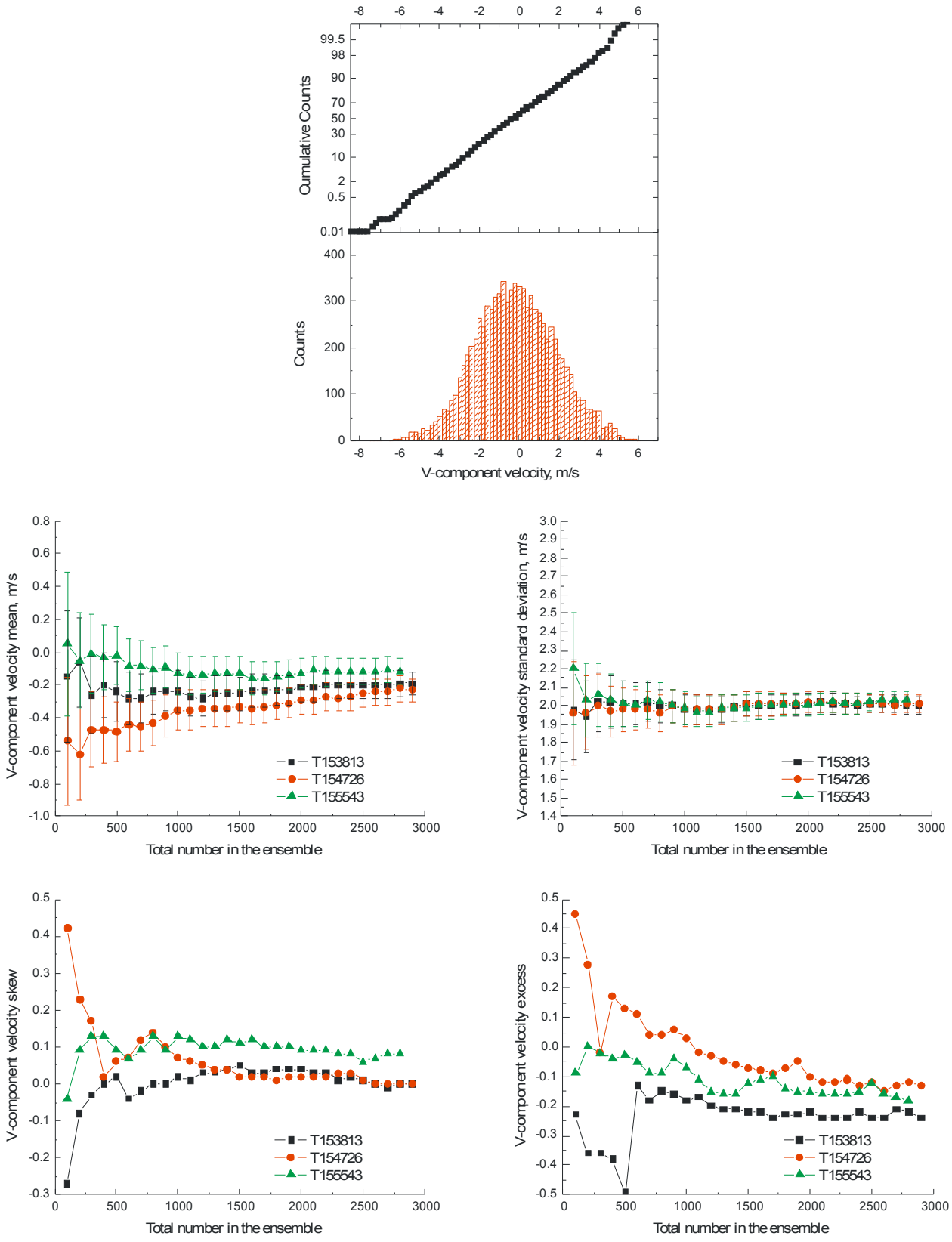

Figure VI.42.- Convergence of the V-component velocity statistics and full ensemble histogram in the shear flow region downstream from the backward facing step (y/H = -0.17, x/H = 1.37).

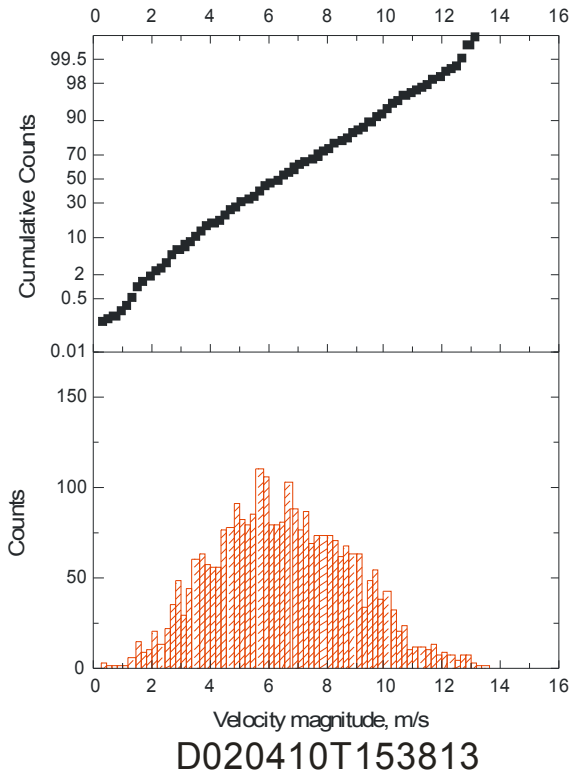

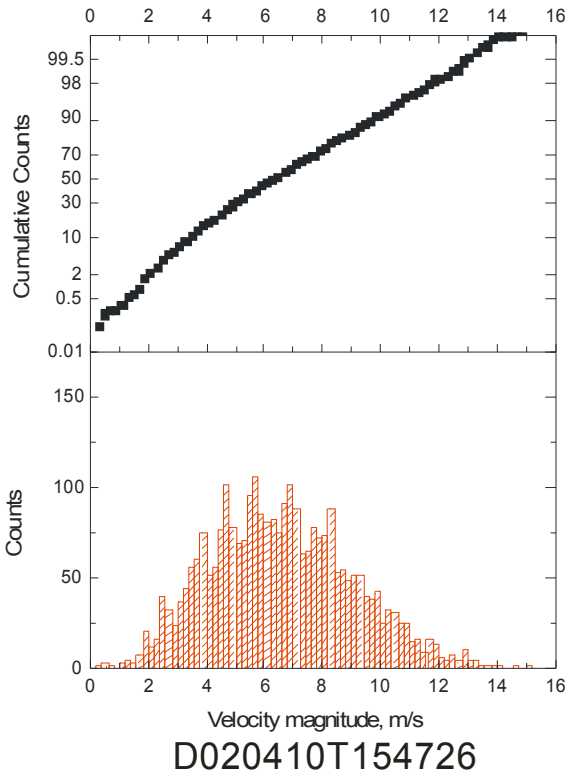

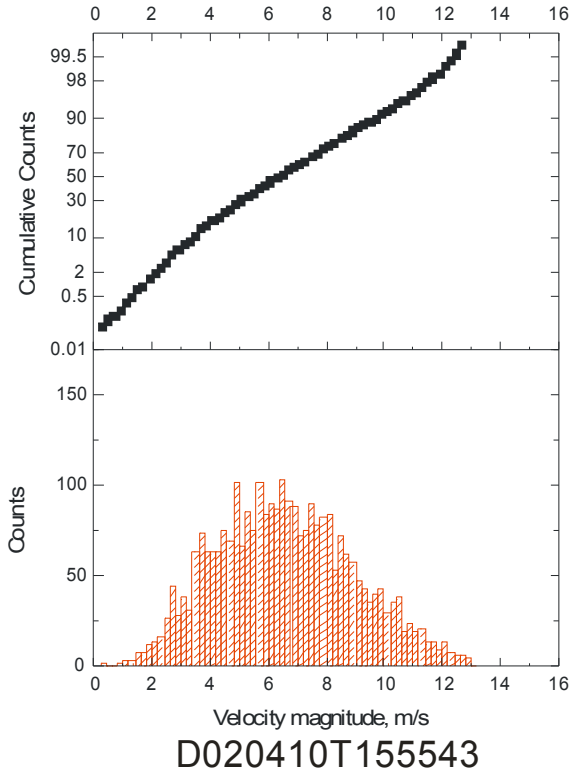

Figure VI.43.- Distribution of velocity magnitude for the individual data ensembles in the shear flow region downstream from the backward facing step (y/H = -0.17, x/H = 1.37).

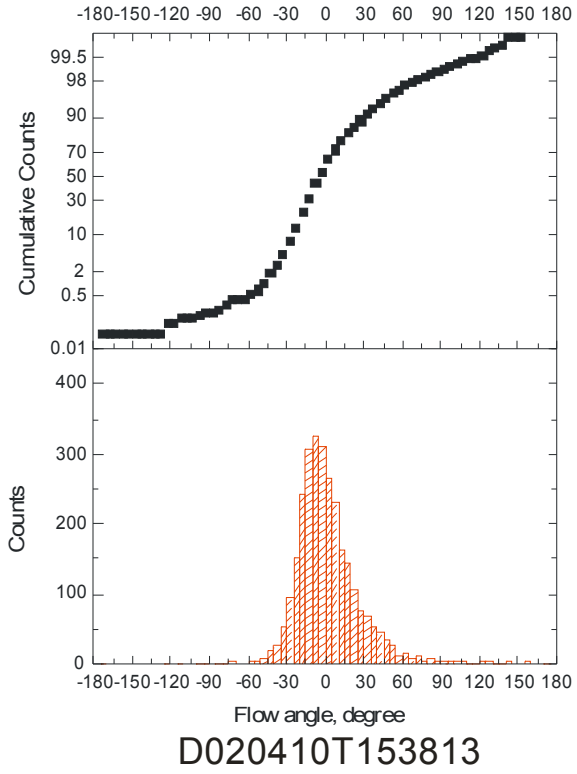

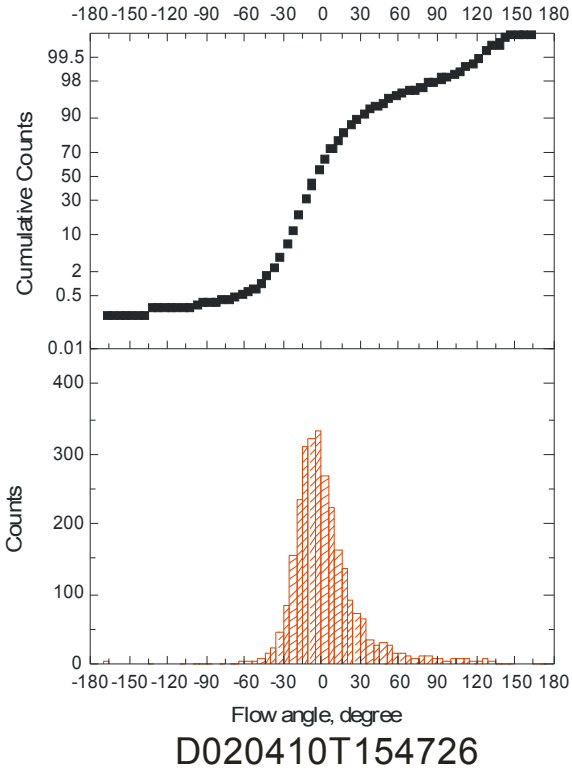

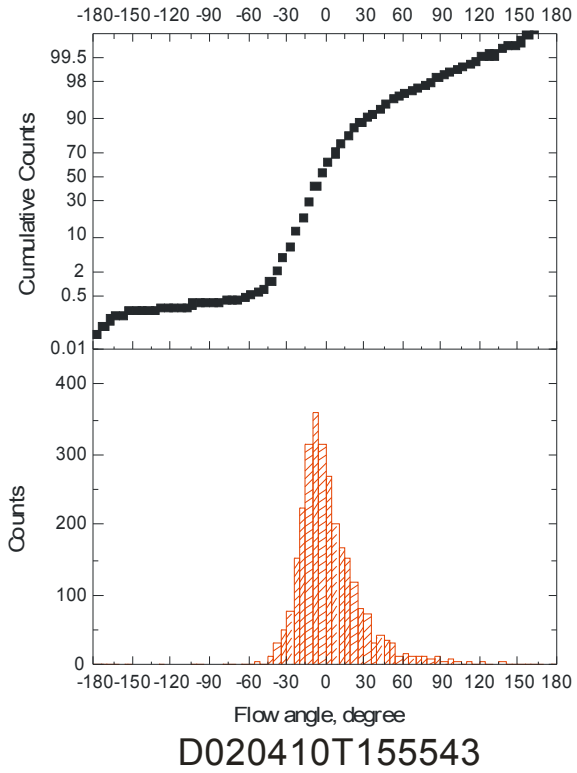

Figure VI.44.- Distribution of flow angle for the individual data ensembles in the shear flow region downstream from the backward facing step (y/H = -0.17, x/H = 1.37).

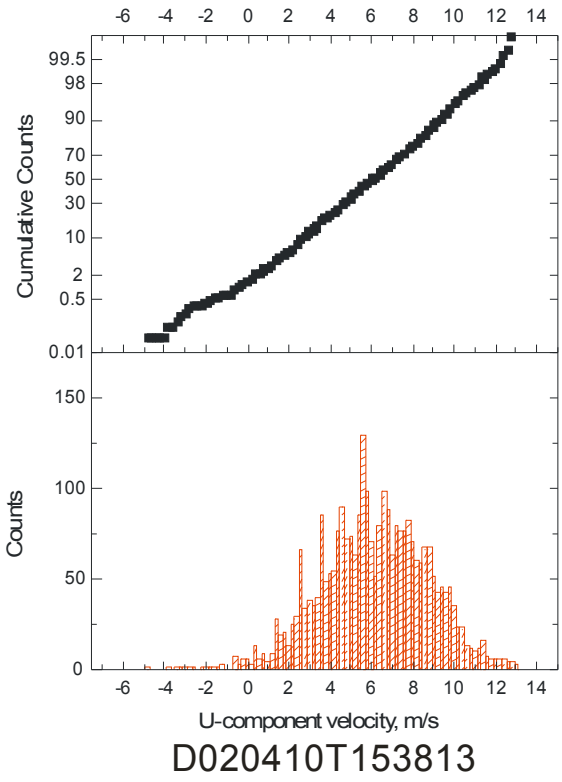

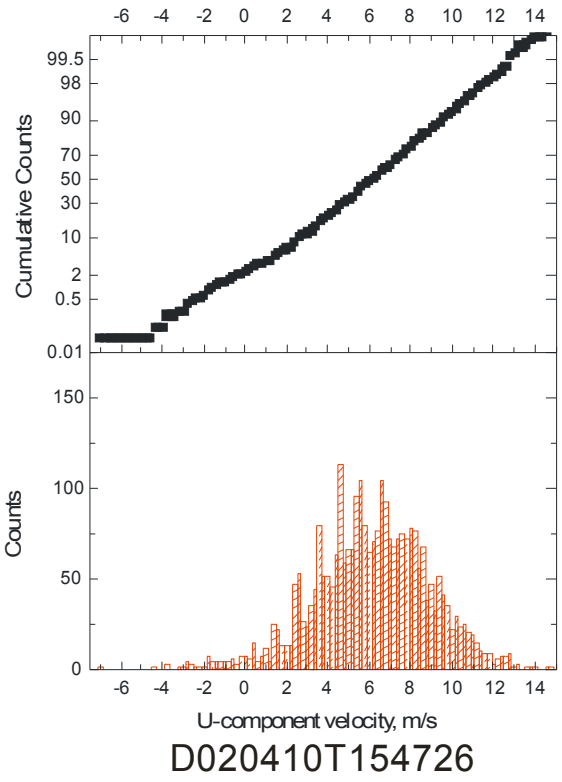

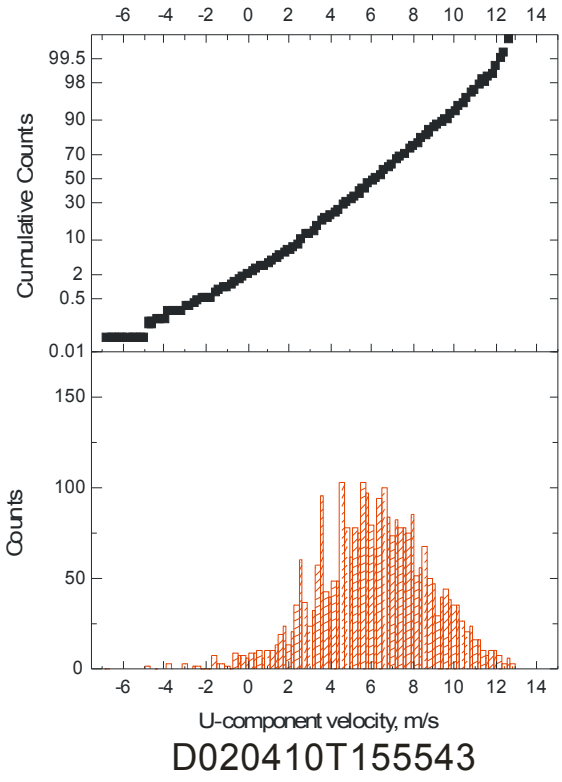

Figure VI.45.- Distribution of U-component velocity for the individual data ensembles in the shear flow region downstream from the backward facing step (y/H = -0.17, x/H = 1.37).

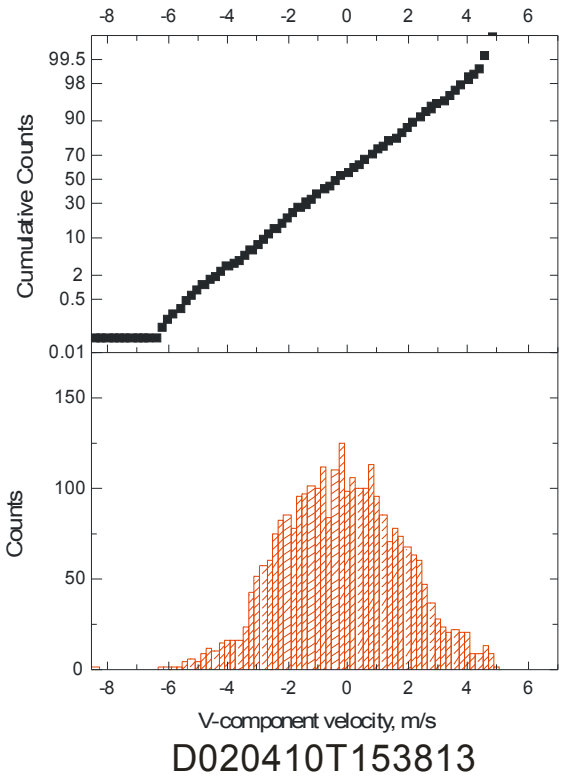

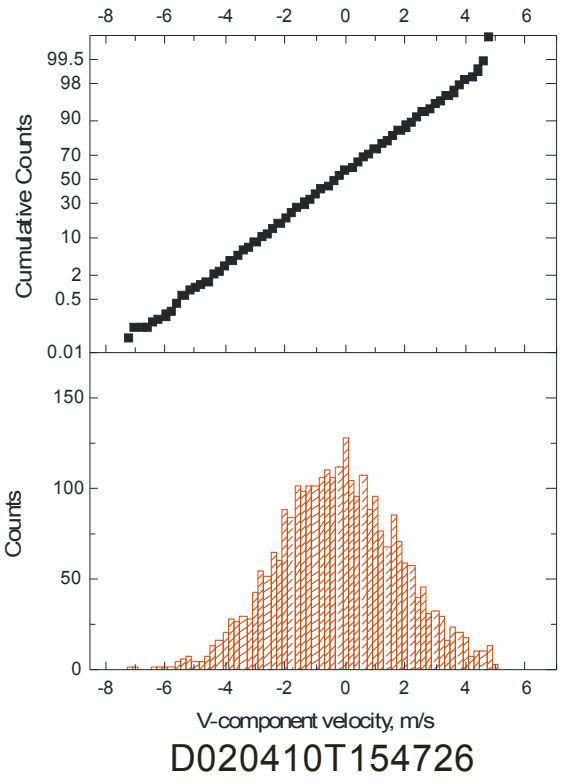

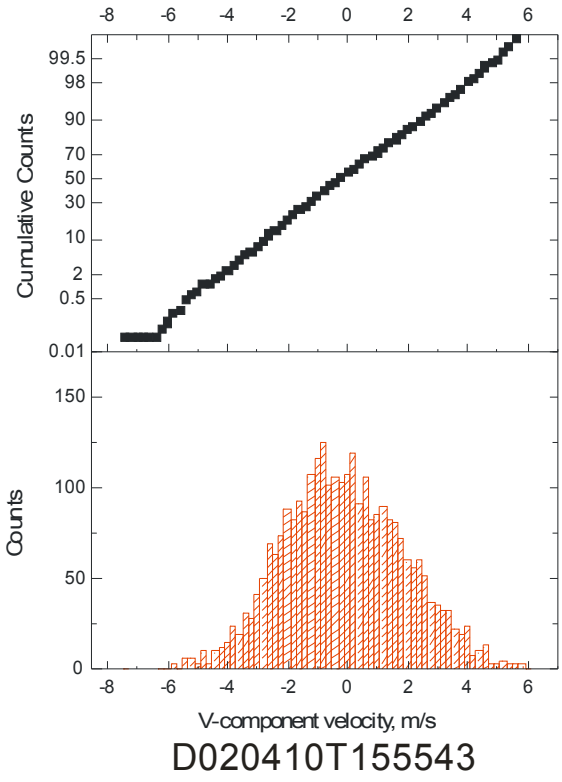

Figure VI.46.- Distribution of V-component velocity for the individual data ensembles in the shear flow region downstream from the backward facing step (y/H = -0.17, x/H = 1.37).

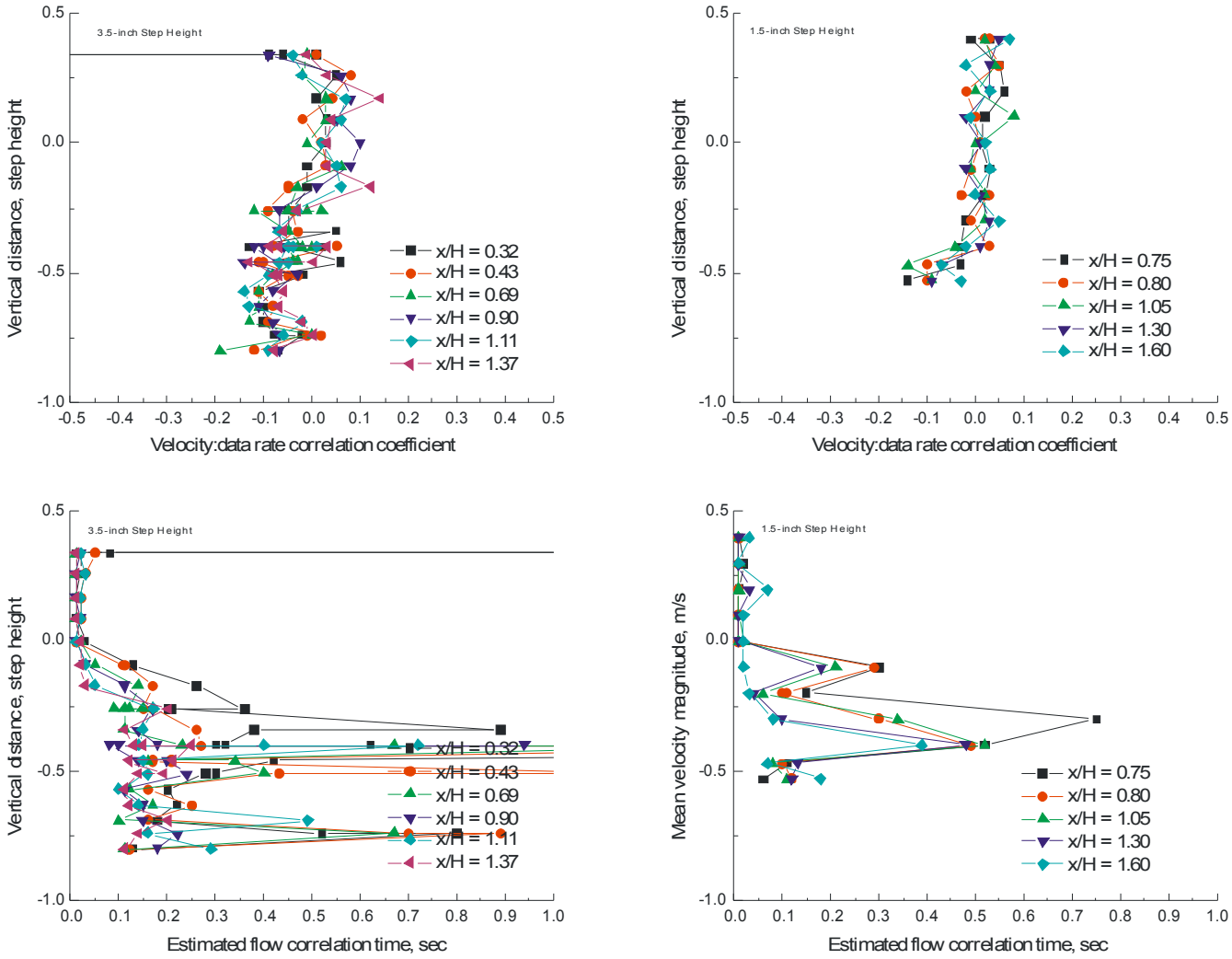

Figure VI.47.- Velocity:data rate correlation coefficient and estimated flow correlation time as a function of position about the 3.5-inch and 1.5-inch backward facing steps in the BART.

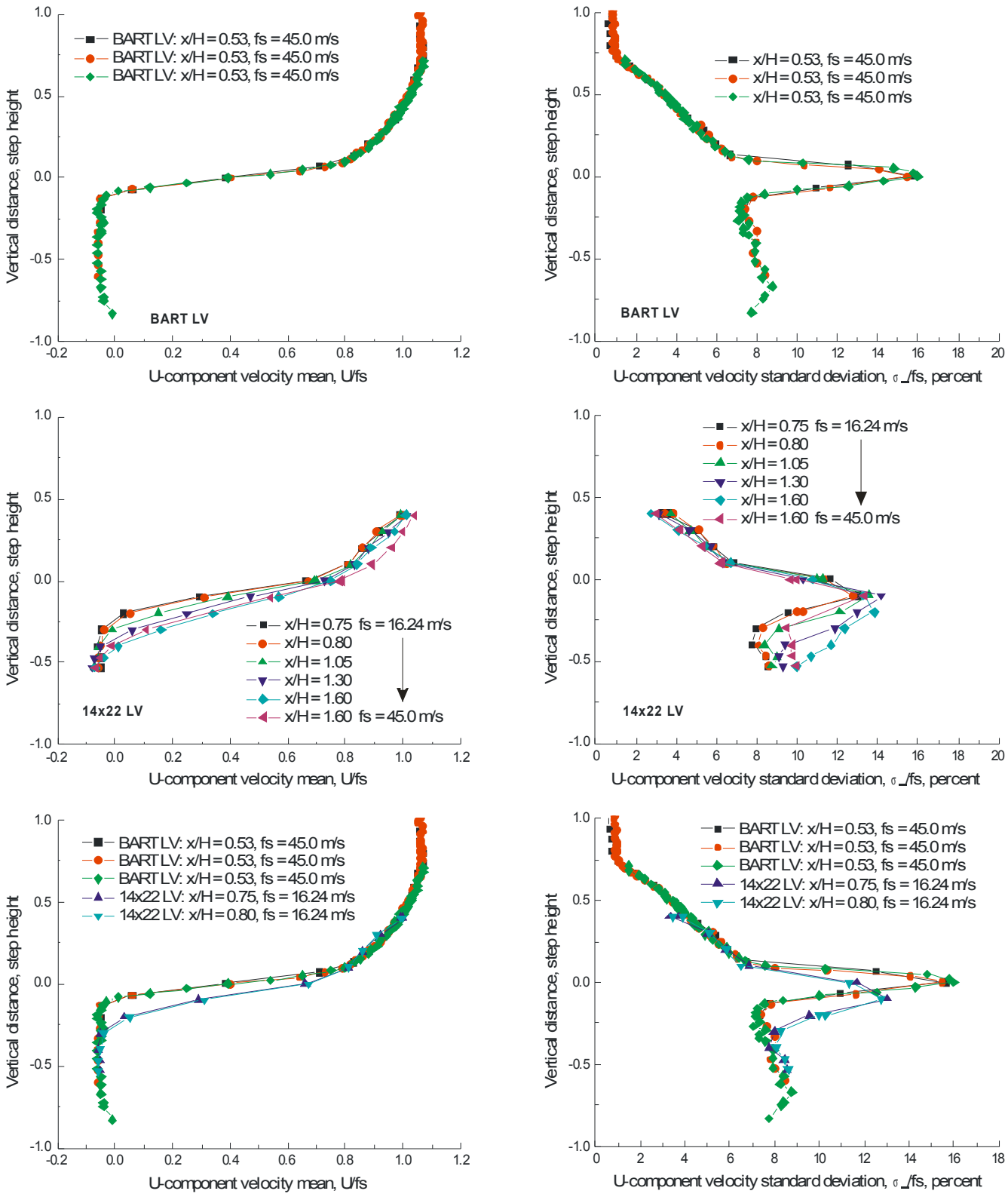

Figure VI.48.- Comparison of U-component velocity measurements obtained with the upgraded laser velocimeter and the measurements obtained with the short focal length BART laser velocimeter at various stations downstream of the 1.5-inch backward facing step.

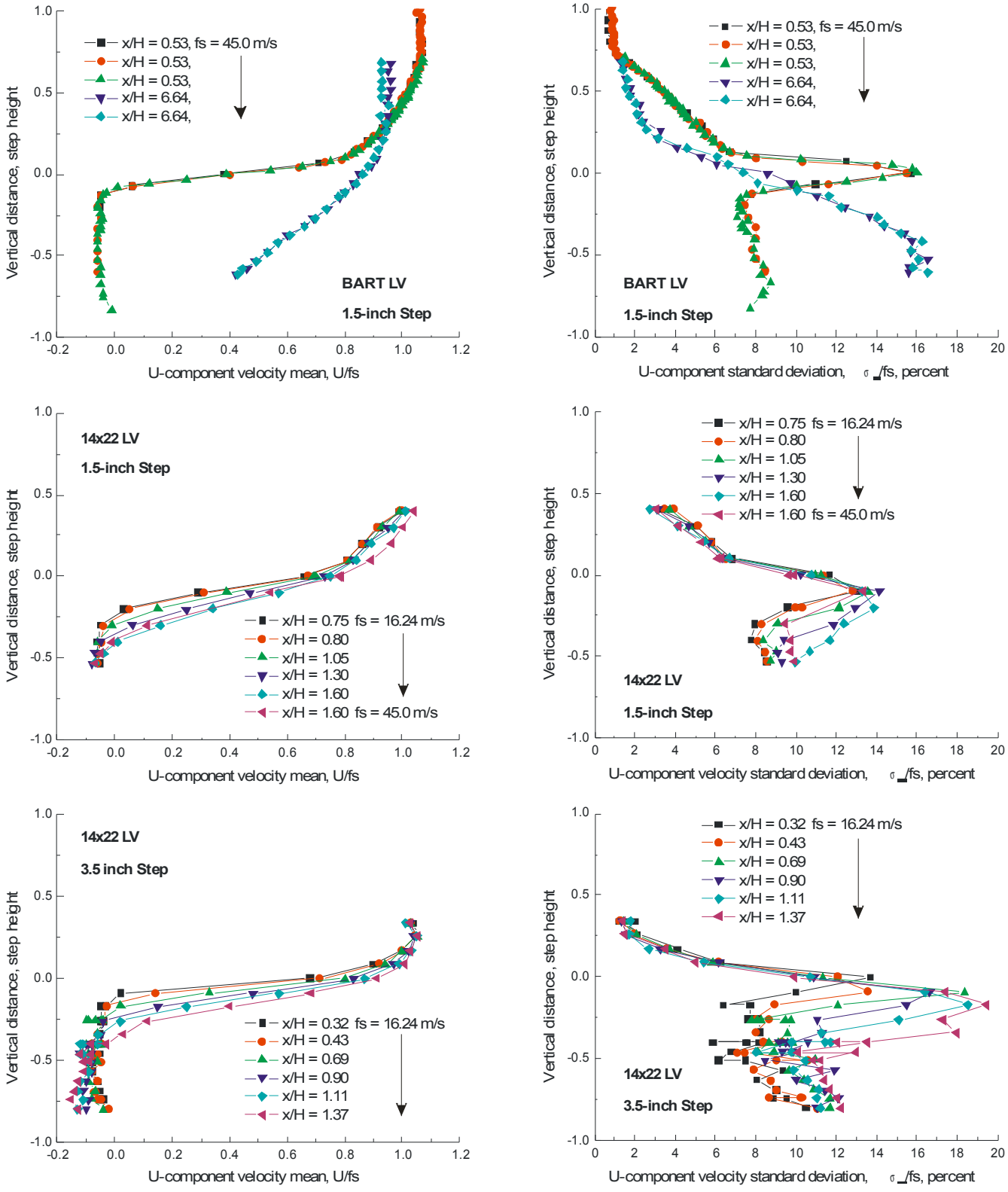

Figure VI.49.- Comparison of U-component velocity measurements obtained with the upgraded laser velocimeter and the measurements obtained using a short focal length laser velocimeter in the BART at various stations downstream of the backward facing step.

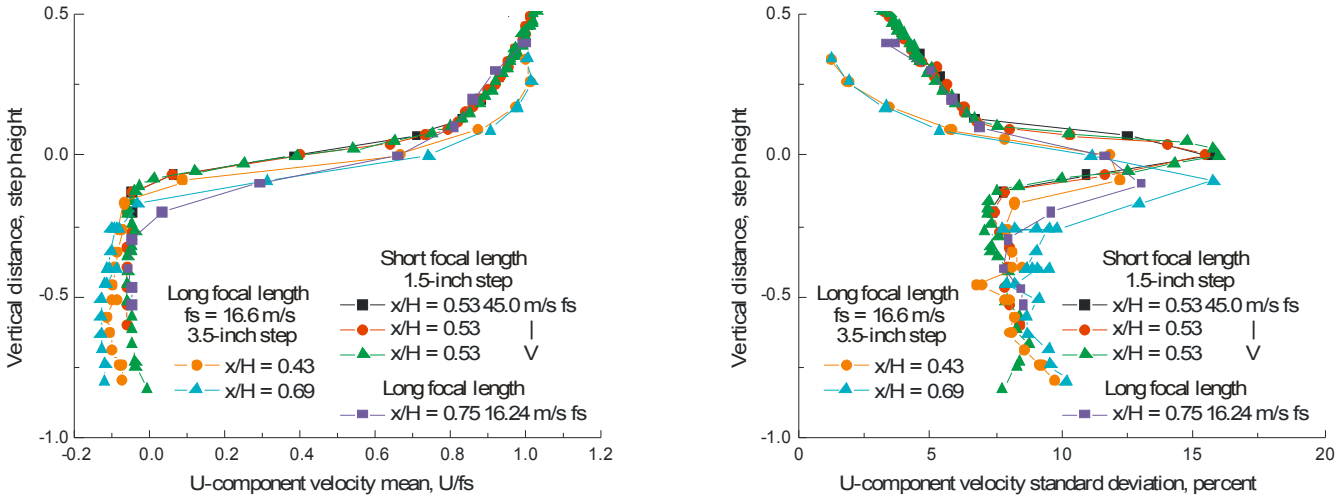

Figure VI.49 (cont'd).- Comparison of U-component velocity measurements obtained with the upgraded laser velocimeter and the measurements obtained using a short focal length laser velocimeter in the BART at various stations downstream of the backward facing step.

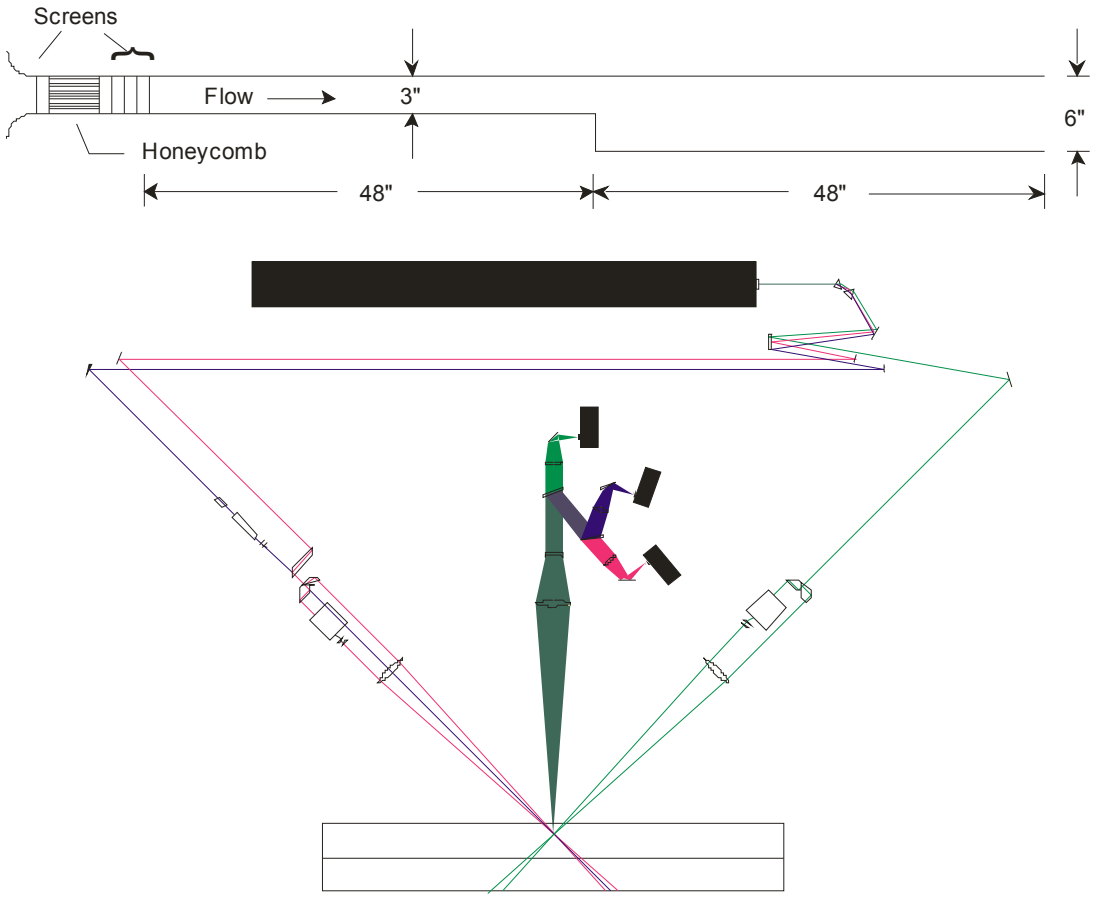

Figure VI.50.- Schematic of the channel flow generator with an internal backward facing step, and the schematic of the three-component, three-color laser velocimeter.

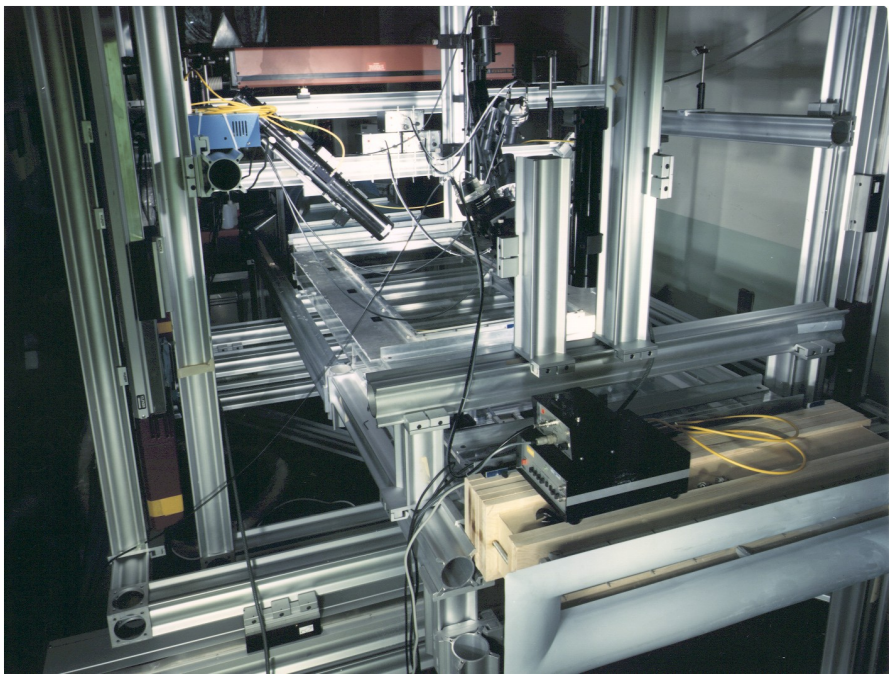

Figure VI.51.- Photograph of the channel flow generator with the internal backward facing step along with the three-component laser velocimeter installed about the channel.

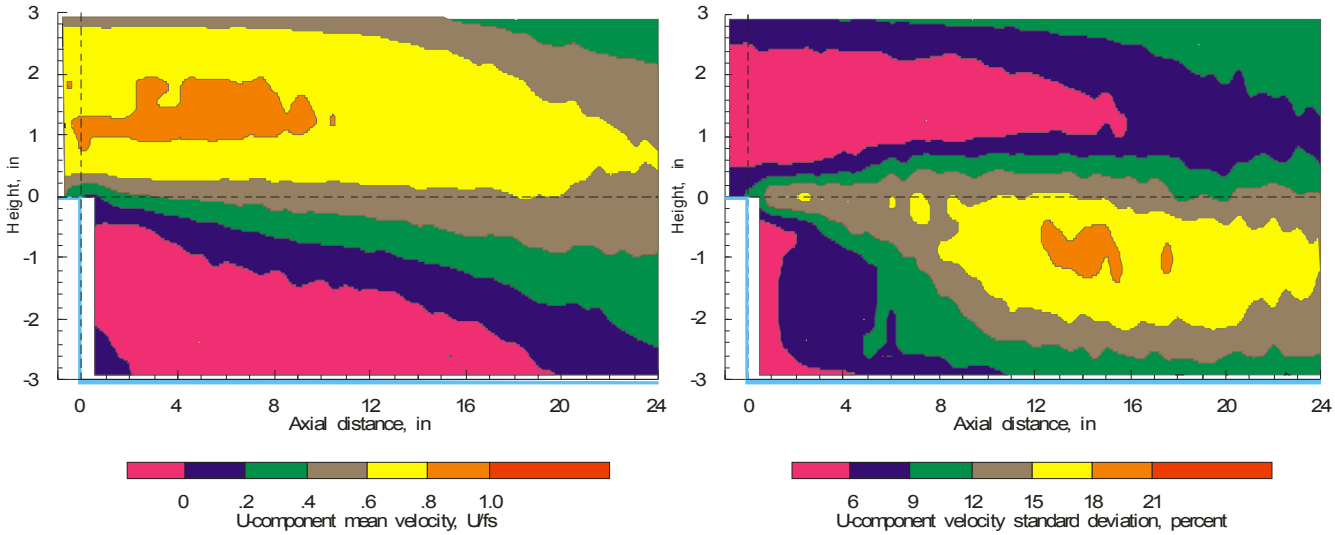

Figure VI.52.- U-component velocity maps of the flow about the backward facing step embedded within the channel flow generator.

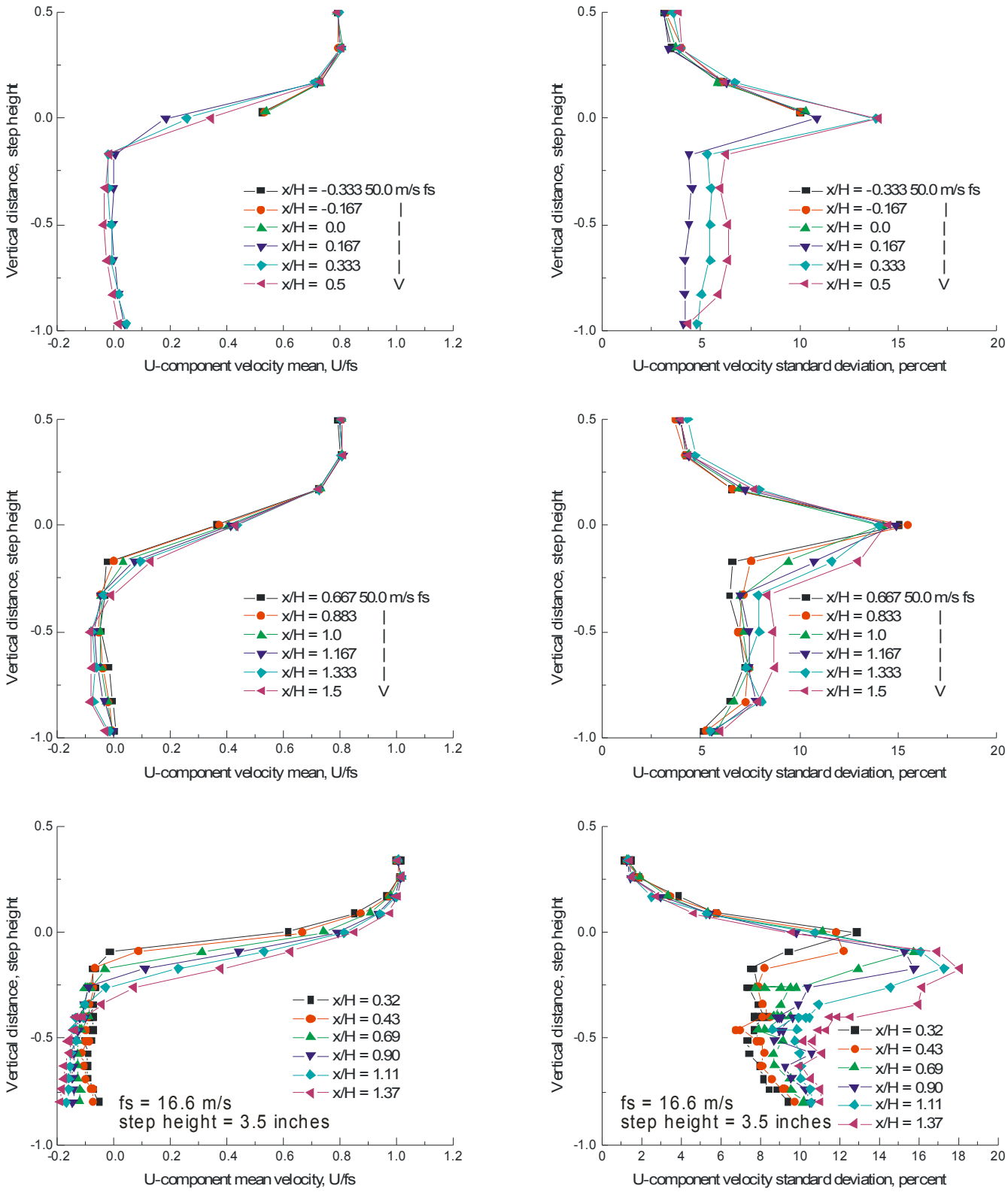

Figure VI.53.- Comparison of U-component velocity measurements obtained with the upgraded laser velocimeter and the measurements obtained using a short focal length laser velocimeter in a channel at various stations downstream of the backward facing step.

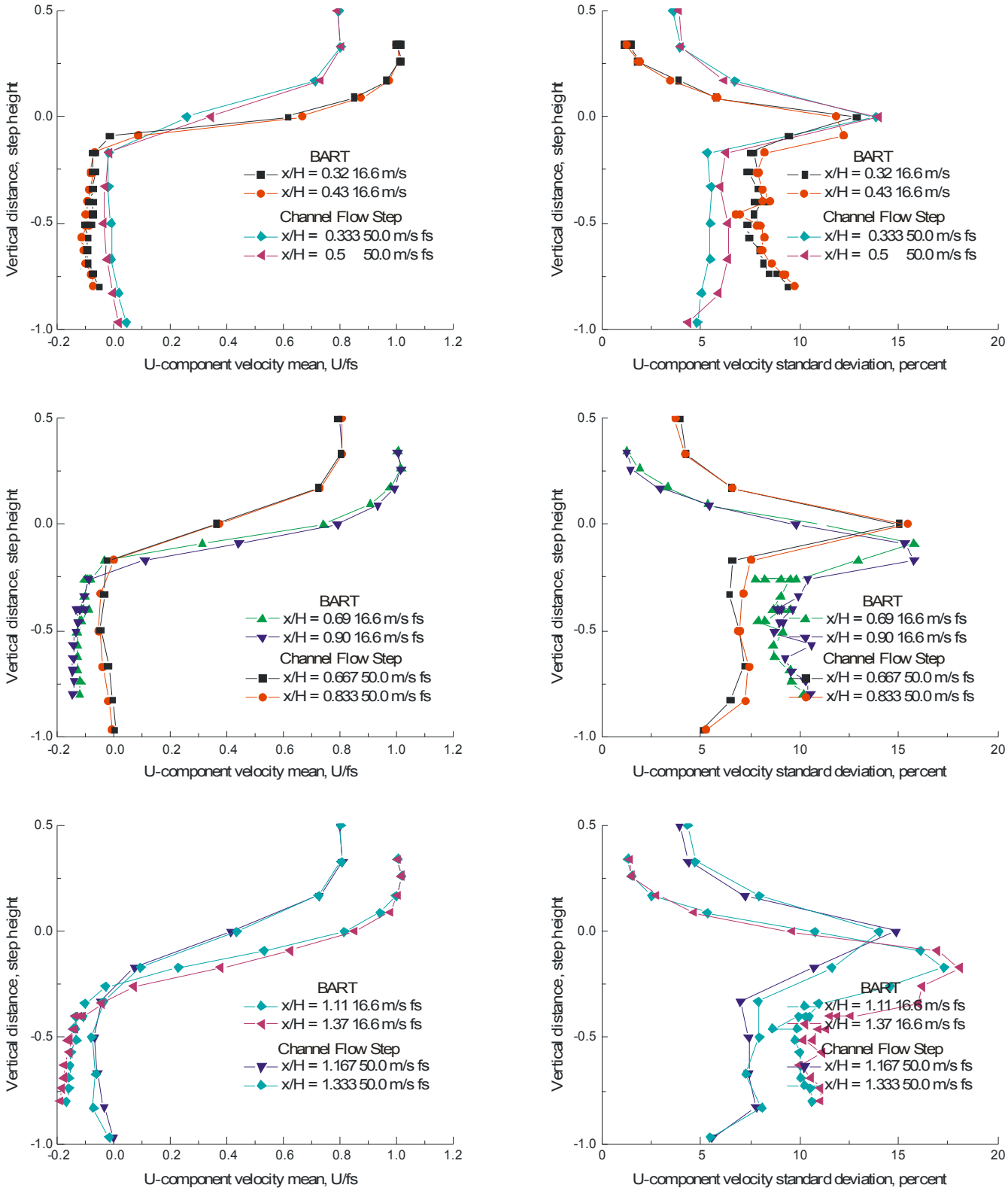

Figure VI.53 (cont'd).- Comparison of U-component velocity measurements obtained with the upgraded laser velocimeter and the measurements obtained using a short focal length laser velocimeter in a channel at various stations downstream of the backward facing step.

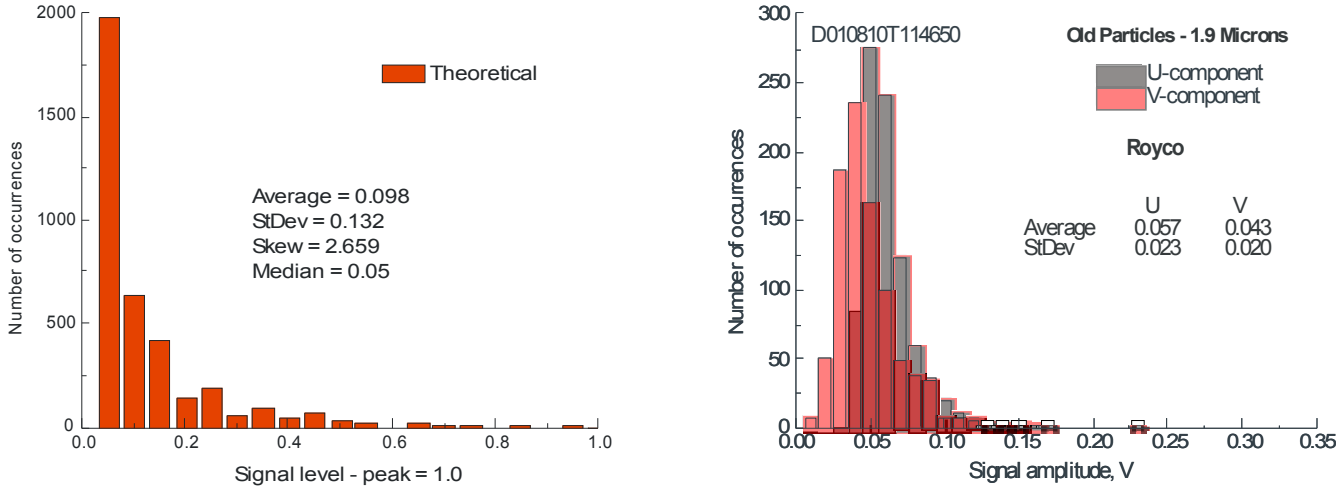

Figure VI.54.- Theoretical signal level distributions from 1.7-micron PSL particles along with the measurement distribution obtained from latex particles exiting the Royco particle generator.

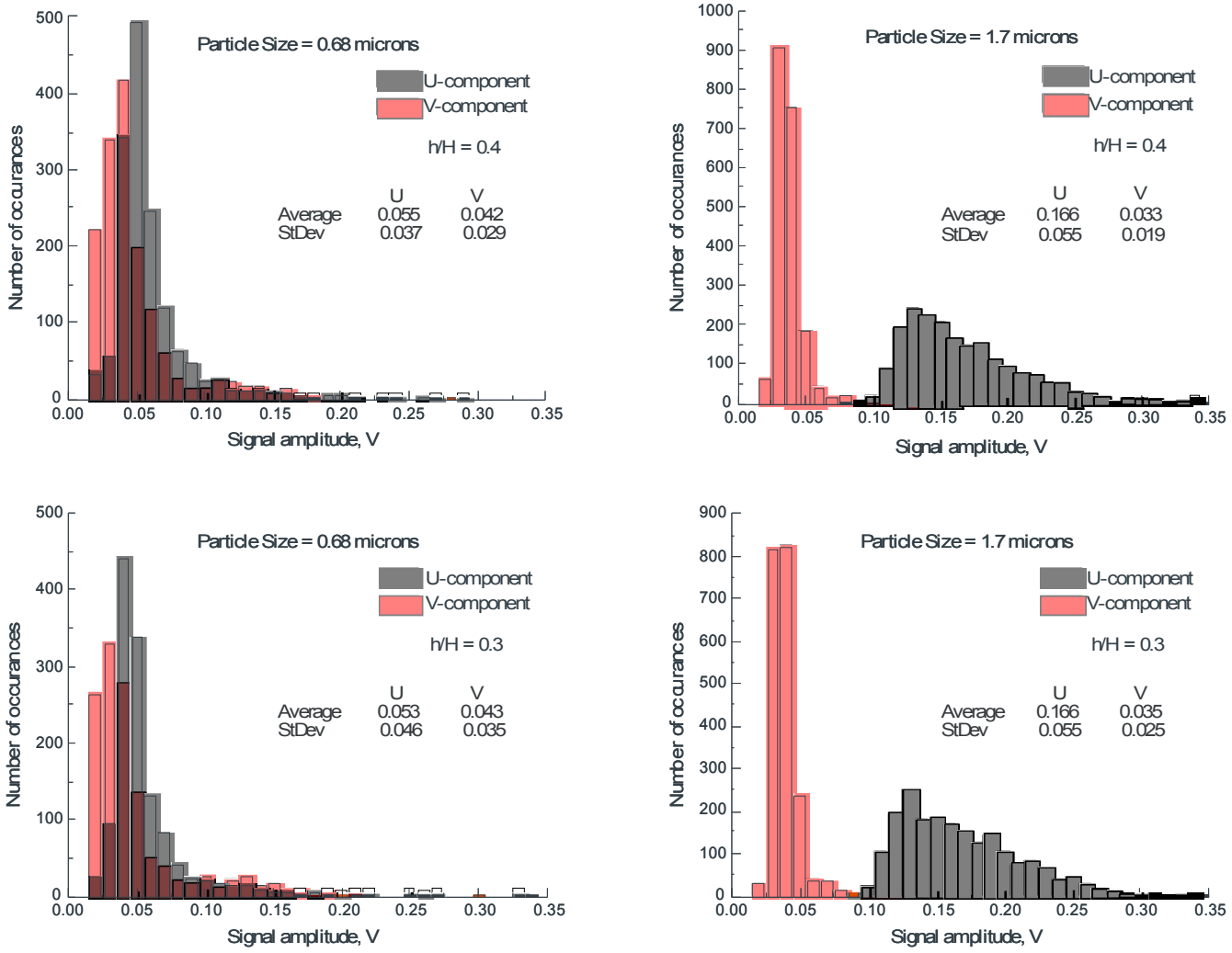

Figure VI.55.- Distributions of signal level obtained from the upgraded laser velocimeter using two sizes of PSL particles injected in the BART with a paint sprayer.

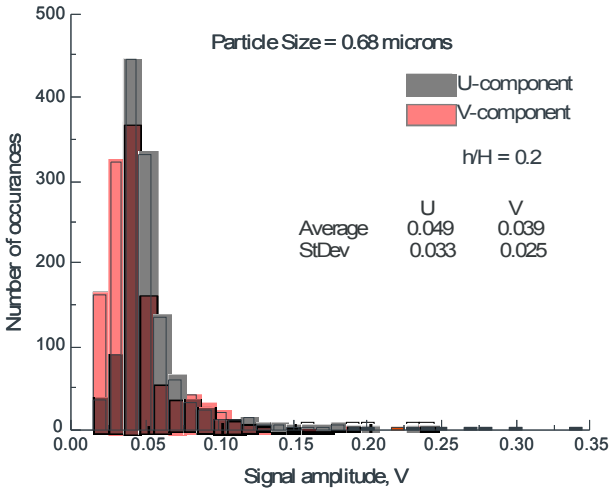

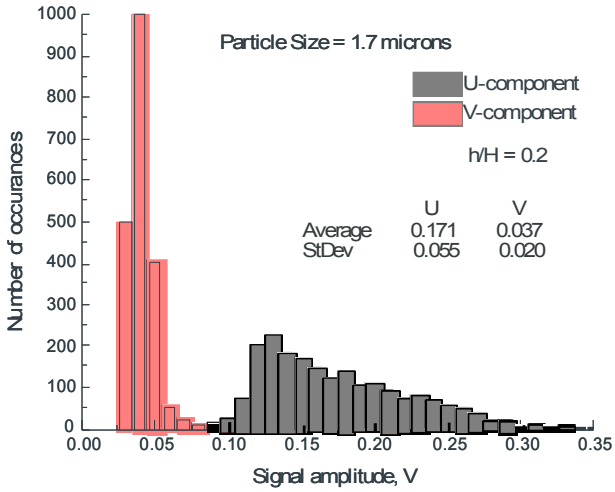

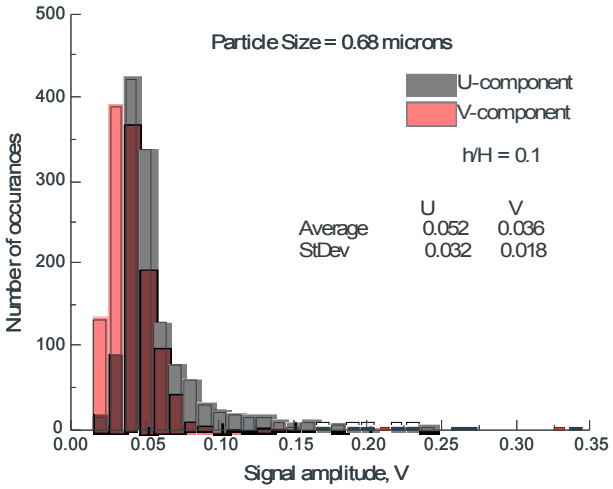

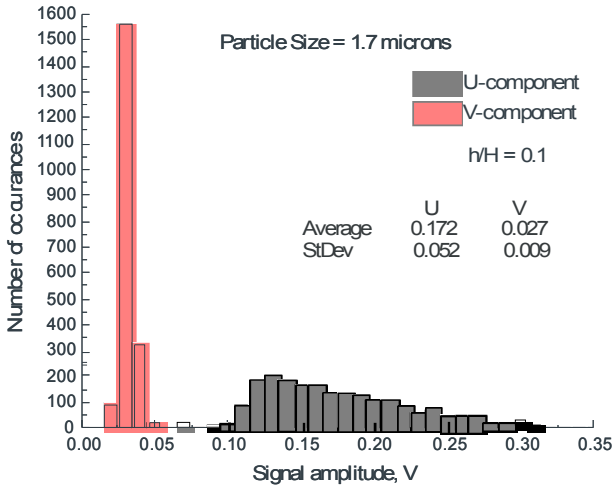

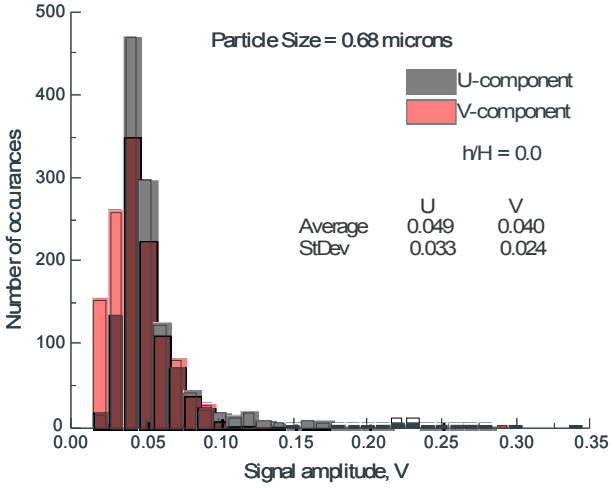

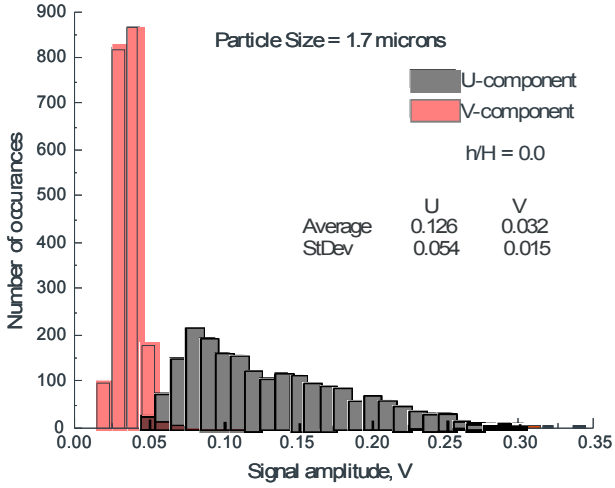

Figure VI.55 (cont'd).- Distributions of signal level obtained from the upgraded laser velocimeter using two sizes of PSL particles injected in the BART with a paint sprayer.

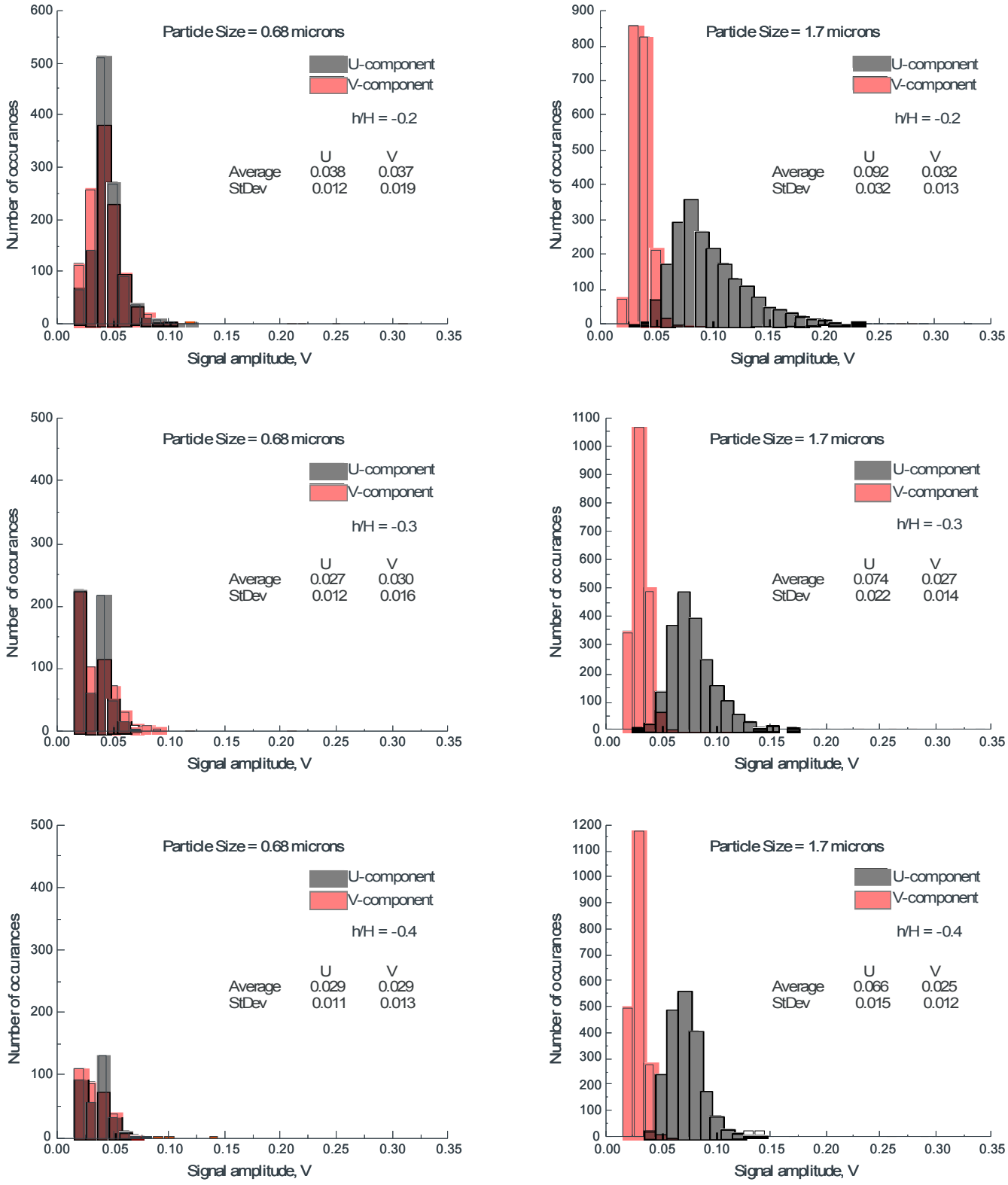

Figure VI.55 (cont'd).- Distributions of signal level obtained from the upgraded laser velocimeter using two sizes of PSL particles injected in the BART with a paint sprayer.

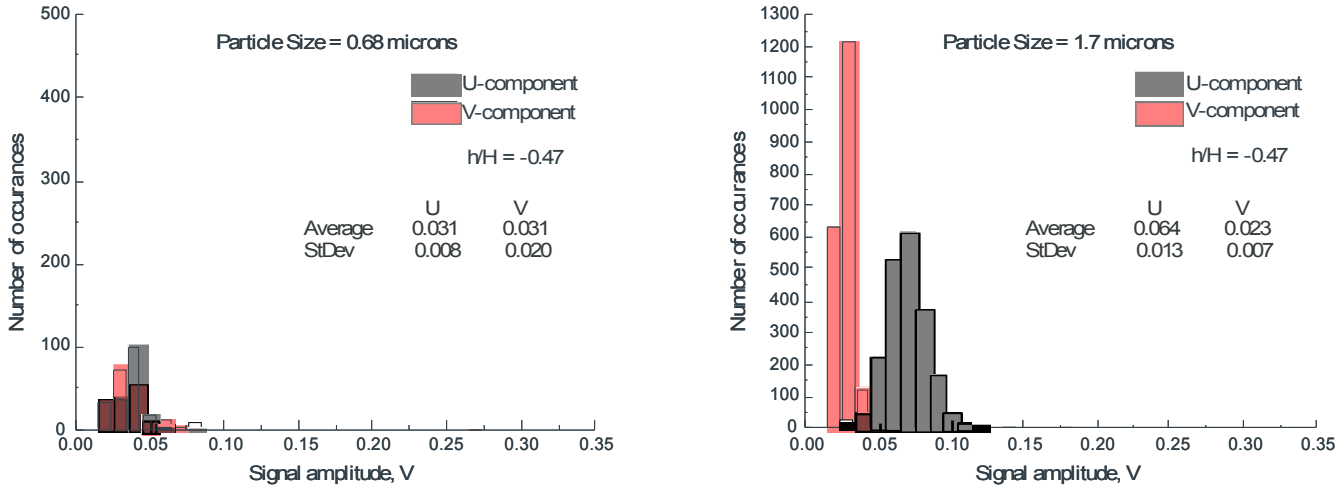

Figure VI.55 (cont'd).- Distributions of signal level obtained from the upgraded laser velocimeter using two sizes of PSL particles injected in the BART with a paint sprayer.

Testing the Upgraded
14- by 22-Foot Subsonic Tunnel Laser Velocimeter
Phase II

The two issues found during the risk reduction test in BART were the length of time needed to transfer the data from the data acquisition computer memory to the hard drives on the two computers, and the false data triggers traced to spurious noise spikes produced by the photomultiplier. The time required to transfer the measurement data was reduced by writing a multi-thread C-program to transfer the data in binary format to the disk drives. Previously it took approximately 77-seconds to store 1,000 measurements whereas the C-program reduced the time to 8.8-seconds. A measurement consisted of 10,000 floating point samples of the U- and V-component amplitudes along with the clock time trace. Additionally a header was attached that included, for example, the measurement location, inter-arrival time, azimuth angle, and conditionally sampled signal readings.

The false triggers were eliminated through the development of a signal identification circuit. The false triggers were found to have a high amplitude spike followed by a few low amplitude oscillations, most likely caused by ringing in the filtering circuits in the TSI electronics, whereas a signal burst generated by a particle passage through the LV measurement volume contained numerous oscillations. Using these characteristics a circuit was developed that, once triggered by the oscilloscope external trigger, would count positive zero crossings. Only if the number of zero crossings was greater than eight, a trigger pulse would be generated to command the high-speed analog-to-digital converter (ADC) to capture the signal burst. The pretrigger capabilities of the ADC insured that the entire signal burst would be captured, thus negating any time delay imposed by the signal identification circuit.

An auxiliary display program was developed to provide a running display of the results as the measurement volume was scanned through the flow field. The program provides profiles of the U- and V-component results along with velocity magnitude and flow angle. Each profile contains the means and standard deviations along with error bars based on statistical uncertainty for each of the four measurements. The plots update automatically as each new ensemble is processed.

The investigations also afforded the opportunity to determine whether particles smaller than the 1.7-micron PSL particles used previously could provide signals with sufficient amplitudes and signal-to-noise ratios to yield accurate velocity measurements.

Laboratory Investigation

A laboratory investigation was conducted to determine if the improvements to the laser velocimeter corrected the issues found in the BART test. The investigation was conducted under production conditions by measuring vertical velocity profiles at the flow centerline of the jet exiting the 50-mm diameter jet flow apparatus. A profile consisted of a series of

measurements made every 2.5-mm across the diameter of the jet cross section to yield profiles containing up to 38 measurement locations. Signal traces from 1000 signal bursts were processed at each measurement location. If statistical stationarity was not found, based on the real time plots of velocity/standard as a function of number of measurements, additional measurement ensembles were acquired at that location until stationarity was reached. The signal/data processing program was modified to automatically combine the repeated ensembles with the original ensemble to process the entire data set at that location. Status data based on the average of the standard deviations of the last five means for each of the four measurements (U- and V-components, velocity magnitude and flow angle) were returned to the data acquisition program for comparison with the user selected threshold that would indicate flow statistical stationarity. If the average standard deviation was larger than the threshold value, an alert was presented to the user by the data acquisition program suggesting that another data ensemble should be acquired.

The laser velocimeter was configured to a focal distance of 5.0 meters to approximate the focal distance to the centerline of the 14- by 22-Foot Subsonic Tunnel. A folding mirror was used to direct the optical axis orthogonal to the centerline of the jet flow to measure the streamwise and vertical velocity components. The vertical measurement profile was obtained by moving the optical system with a mechanical traversing mechanism. The laser power was set to 1.0-W, all-lines. A single Laskin nozzle was used to inject 1.0-micron PSL particles into the inlet of the squirrel-cage fan used to drive the flow apparatus. The average high-pass filtered signal output was ± 0.6 V with a data rate of 207 acceptable signal bursts per second at 0.125-inch downstream of the jet exit. The rate dropped to 44 and 131 acceptable signal bursts per second at the ± 1.0 radii locations respectively. At two jet diameters downstream, the centerline data rate dropped to 10 acceptable signal bursts per second. The peak signal values had a standard deviation of 0.2 V in all cases. This indicated that all of the water:ethanol carrier had evaporated, and that the Gaussian characteristics of the laser power throughout the measurement volume cross section were maintained.

Vertical scans were obtained at six downstream stations, Figure VII.1. These data sets were acquired and processed during a five hour test session. A repeatability test was conducted at the 10.25-inch downstream location, Figure VII.2. As shown in Figure VII.2, the two data sets are virtually identical not only in mean and standard deviation, but in skew and excess. During the acquisition phase, a uniform random number generator was used to obtain a synthetic “azimuth” angle for each signal burst that was processed. Since a uniform random number was used, the resulting statistics plotted as a function of “azimuth” should have the same value within the bounds of statistical uncertainty. This was found to be the case for all of the statistical calculations, Figure VII.3.

The laboratory investigation showed that the system upgrades provided acquisition rates that would satisfy production requirements, and that there were no acquisitions from noise spikes originating from the photomultiplier. Further the signal levels obtained from 1.0-micron PSL particles were sufficient to yield results that were comparable to those

from the larger particles. However, the velocity measurements should be more accurate based on the ability of the smaller particles to track the flow field with better fidelity.

Basic Aerodynamic Research Tunnel
Backward-facing Step

The laser velocimeter system was installed in the BART with the same configuration used in the first backward-facing step investigation, Chapter VI. For this entry, the 1.5-inch step model was installed first with the flow conditions set to match the conditions used to obtain the validation laser velocimetry measurements (Hart *et al* (2001)), Figure VI.48. Several additional vertical profiles were obtained beside the matching profile at x/H = 53 downstream of the step to determine if the data from the current investigation yielded a reasonable description of the flow field. The second investigation was the flow about the 3.5-inch backward-facing step. Instead of repeating the previous LV measurement locations from Chapter VI, the locations were extrapolated based on step height from the smaller step, and the test conditions fixed to the same settings as used with the smaller step. This would provide a direct comparison of measurements to determine if the two flow fields had similar characteristics.

1.5-inch backward facing step

A series of vertical profiles was obtained at downstream stations beginning at x/H = 0.262 with increments of 0.262 x/H to nominally x/H = 4.0 to obtain a grid mapping of the flow downstream of the backward-facing step. The series of velocity profiles for the U- and V-components is shown in Figure VII.4. The plots include mean and standard deviation of the two velocity components along with the number of validated measurements within the ensemble and the levels of convergence for those ensembles. The U-component mean and standard deviation profiles obtained from the BART laser velocimeter, Figure VI.48., is overlaid for comparison. The comparison of the profiles at the same downstream location, Figure VII.4.b., shows almost identical results. Thus the measurements obtained by the upgraded laser velocimeter have been shown to be of sufficient accuracy for wind tunnel applications. By plotting the data as a function of downstream location, Figure VII.5, the boundary of the separated flow can be found. For example, near the step at z/H = 0.050, (Figure VII.5.d.) the effects of the step can be seen with the drop in velocity even though the location is above the step. At z/H = -0.090, Figure VII.5.e., the velocity has dropped to nearly 0.0 U/fs, and at z/H = -0.220, Figure VII.5.f., the U-component velocity has become negative. Finally at z/H = -0.755, Figure VII.5.k., the entire profile is negative.

The flow characteristics can be viewed in another way by computing the velocity magnitude and flow angle statistics, Figures VII.6 (vertical scans) and VII.7 (horizontal scans). This is possible since the data processing software can extract the coincident U- and V-component measurements from the data ensembles. While the velocity magnitude basically tracks the characteristics of the U-component velocity until the flow reverses, the flow angle provides a bit more insight into the flow characteristics. The flow reversal point has a very strong demarcation with an associated strong spike in standard deviation. The

vertical scan at the 0.525 x/H station, Figure VII.6.b, indicates that the measurement volume went below the rotational flow since the mean flow angle was no longer reversed, and may even indicate the entrance into the secondary vortex. However at stations close to the step, the standard deviations in flow angle reached up to 100-degrees. Moving further downstream a spike in the standard deviation developed at the reversal point. The high standard deviations began to fall near the floor at the 1.050 x/H station, Figure VII.6.d, and continued to fall further downstream, reaching 30-degrees at the 2.362 x/H station, Figure VII.6.i. The standard deviation near the floor rose again further downstream as the spike moved closer to the floor. These characteristics form a clear trend in the horizontal plots, Figure VII.7, showing the reversal point moving downstream as the floor is approached, with the maximum standard deviation tracking the reversal.

Although the current measurements are nearly identical to the reference measurements obtain by the dedicated laser velocimeter in BART, there is still a concern about sampling bias affecting the accuracy of the measurements. Edwards and Meyers (1984) showed that sampling bias could be corrected if the data rate was higher than the integral time scale of the flow at the measurement location. However, the current data acquisition system has reset times greater than typical flow integral time scales. Thus each measurement is independent of the previous measurements and correction is not necessary or possible. However, the probability that the freestream will contribute more particles, and thus more measurements, than the recirculation flow will still produce sampling bias as the two flow states randomly switch at a given measurement location within the shear region. Therefore it is concluded that uncorrectable sampling bias exists in the measurements obtained within the shear region.

The improvements in the LV data acquisition and signal/data processing software had no apparent effect on the characteristics of the velocity standard deviation trends found in the first investigation in BART, Figures VII.4-VII.5 and VI.48-VI.49. Applying the same test used to determine if statistical stationarity had been reached described above during laboratory testing, the number of measurements required remained fairly constant until the recirculation zone was entered, Figures VII.4 and VII.5. In general the average standard deviations, used as the test for statistical stationarity as described above, were less than 0.02 m/s outside recirculation. Within the region the average standard deviation reached 0.07 m/s, primarily because of the lack of acceptable signals within the vortex. These trends, however, provided no insight into the large standard deviations found below the shear region since the statistical uncertainties of the standard deviation measurements were relatively small.

Skewness of the velocity distributions should not only be an indicator of the amount of time the freestream flow is present versus the recirculation flow at a given location, but also an indicator of sampling bias. If the measurement location is in freestream, there should be no contribution from the recirculation flow resulting in a skew near zero. As the measurement location is lowered into the shear region, a small contribution from the recirculation region should be present affecting the skew results. Particle seeding should follow the same pattern, with the majority of the particles found in the freestream

segments, not only because of the greater presence of the freestream flow, but its increased seeding density as compared to the recirculation region. This should produce a skew of the velocity distribution toward the higher velocities. With the measurement location in the center of the shear region, the percentage of time the flow originates from freestream is equal to the percentage from the recirculation. However, the particle number density distribution will cause the freestream flow to be over sampled as compared to the recirculation. Again this would result in a smaller, but still positive skew instead of the actual near zero skew that would be expected. Finally, at the lower extent of the shear region, the primary contributor would be the recirculation flow which should produce a negative skew, although sampling bias could lessen the amount of skew even to zero. Once within the core of the recirculation region, the levels of skew should be near zero as the velocity gradient is linear through the measurement volume diameter. The effects of sampling bias, if any, would be unknown within the recirculation region.

From the trends shown in Figure VII.8, the U-component had a fairly strong negative skew in freestream while the V-component had a fairly positive skew. Inspecting the traces further downstream of the step, the U-component developed a strong negative peak in skew just above the step height, while the V-component developed a strong negative peak in skew below the step height. At approximately three step heights downstream, the peak in the V-component disappeared while the U-component peak continued although falling below the step height. These trends continued further downstream. The streamwise profiles of component skew, Figure VII.9, were fairly random with no indication of the sharp shifts in skew found in the vertical traces. However, there was a sharp shift in flow angle skew that translated downstream. The shift is first found at a height of 0.090 z/H, Figure VII.9.e, below the step just downstream of the step. The shift continued downstream until a height of -0.606 z/H, Figure VII.9.j, is reached when the artifact moves downstream of the interrogation region.

The Reynolds stress traces in the streamwise direction, Figure VII.9, have a significant change from a measurement height of 0.050 z/H to -0.090 z/H, Figures VII.9.d and VII.9.e, respectively. This artifact moves downstream becoming narrower and stronger as the height above the floor is reduced. The vertical scans of Reynolds stress, Figure VII.8, show a sharp negative stress artifact at the step height for a downstream location of 0.262 x/H, Figure VII.8.a. This artifact grows stronger while dropping in height as the measurement location is moved downstream. These results appear to show that the artifact in the Reynolds stress measurements is an indicator of the center of the shear region. The artifact appeared to have the same location profile as found with the flow angle standard deviation peak locations, Figure VII.6.

3.5-inch backward facing step

After the model change to a 3.5-inch backward facing step, a repeat investigation was conducted with the measurement locations selected to scale with step height, matching the equivalent locations measured downstream of the 1.5-inch step. The size of the step,

however, limited the number of locations that could be measured because of beam blocking by the model and the equivalent reduction in traversing range.

The results, shown in Figures VII.10-VII.13, U-and V-component velocities (vertical and streamwise scans) and Magnitude and Flow Angle (vertical and streamwise scans) respectively, have similar characteristics found in the results from the 1.5-inch step. The component standard deviations also remained elevated below the shear region. The characteristics found in the skew results and the Reynolds stress found in the 1.5-inch step investigation were also found in the 3.5-inch step study, Figures VII.14 and VII.15.

Comparison as normalized by step height

In order to obtain a better visual comparison, the results from both LV investigations were scaled by step height and plotted in Figures VII.16 - VII.18 (vertical scans), and VII.19 - VII.21 (streamwise scans). From the comparison of the U-component measurements in Figure VII.16, it was found that the velocity above the 3.5-inch step was slightly higher than above the 1.5-inch step. Also the flow had a greater negative velocity in the separation region below the 3.5-inch step. However the characteristics of the U-component standard deviations were almost identical except the peak in the standard deviation grew in strength and width at further downstream locations from the 3.5-inch step. These characteristics were also found in the V-component measurements except that the mean measurements were consistently higher about the 3.5-inch step.

The characteristics of the velocity magnitude found in Figure VII.17 were similar to those found in the U-component measurements. However, the flow angle measurements had some differences, especially in standard deviation. It appears that the shear region is slightly higher downstream of the 3.5-inch step. Further the standard deviation of flow angle is consistently higher below the shear region for the 1.5-inch step. Measurements of skew shown in Figure VII.18 are loosely similar, but there is a great deal of randomness in the results. However, the Reynolds stress measurements are virtually identical except for the greater stress values obtained in the shear region further downstream of the 3.5-inch step.

Plotting the data as a function of downstream location at fixed heights above the floor appear to remove much of the randomness in the data. Here in Figures VII.19 – VII.21, the similarities and differences between the measurements are clearly seen. Overall the data show consistent patterns indicating that the they represent reasonable indicators of the true flow field. The differences between the two steps may be attributed to Reynolds number effects – we leave this conclusion to the Aerodynamicists.

Flow measurements downstream of a NACA 0012 airfoil

Since one of the prime flow structures to be investigated is the rotor tip vortex, it seemed appropriate to determine if the measurement volume length would compromise the measurements of a vortical flow. Thus the backward-facing step was removed from the

test section and a NACA 0012 airfoil was installed on the floor of the test section which placed the wing tip near the test section centerline. The model could be manually rotated to select the angle-of-attack. Three tests were conducted: 1) stable vortex flow with the wing set to an 8.0-degree angle-of-attack; 2) burst vortex with the wing angle-of-attack set to 20.0-degrees; and, 3) an investigation of the wake region with the wing returned to an 8.0-degree angle-of-attack. In each case the measurement volume was scanned across the test section, orthogonal to the wing span.

Measurements of the vortex generated by the airfoil set to 8.0-degrees angle-of-attack were conducted on three successive days, Figure VII.22.a. The three U-component velocity profiles were virtually identical. They showed a slight change in velocity along the scan plus the characteristic deficit found within the vortex. The standard deviation measurements remained low and repeatable throughout the profile. The V-component velocity profiles were also virtually identical with the characteristic shape expected from the radial spin found in a stable vortex. The significant peak in the standard deviation at the vortex core shows the effect of the finite size of the measurement volume. Unlike other techniques that average the flow over the measurement volume, classic laser velocimetry measures each particle velocity within the volume, but can not determine its location within the volume. For example, if the volume extends through a velocity gradient, as in the case of the vortex core, high-speed particles may be measured at one end of the volume and low-speed particles at the other. The calculation of the mean velocity will basically negate the differences, but the standard deviation will be very high caused by the velocity gradient, not turbulence. If the measurement volume was infinitely small, the standard deviation would not measure the gradient effects, but just the turbulence in the flow. While the V-component results indicate that the size of the measurement volume is affecting the measurement accuracy, a better indicator is the profile of the flow angle, Figure VII.23.a. Ideally the flow angle profile should swing ±90-degrees (assuming that the scan is through the exact center of the vortex), but the measurements indicate only a swing of ±20-degrees. This means that either the scan was not through the center of the vortex, or that the length of the measurement volume has spatially low-pass filtered the flow gradient, or both. Here again the peak in the standard deviation of upwards of 8-degrees indicate the averaging effects typical of laser velocimetry. However, considering the focal distance, the measurement volume effects appear to be less than expected for a vortex core approximately 0.4-inches in diameter.

The airfoil angle-of-attack was then increased to 20.0-degrees to establish a burst vortex. The results from the U- and V-component measurements, along with a repeat of one of the profiles obtained at 8.0-degrees for reference, are shown in Figure VII.22.b. The results show that the vortex has moved from approximately 0.5-inches below the wing, to 2.0-inches above the wing. The U-component profiles show a significant deficit in velocity with an associated increase in standard deviation (15-percent of the local mean velocity). The V-component profiles show a less sharp vortical profile with an increase in standard deviation far greater than can be attributed to gradient effects. The velocity magnitude and flow angle profiles, Figure VII.23.b, are very similar to the U- and V-component profiles, respectively. Here the flow angle standard deviation peaks at 12-degrees. Based

on these measurements, one would conclude that the flow in a burst vortex was very turbulent. However, measurements made using Doppler global velocimetry of a burst vortex generated by a delta wing at high angle-of-attack (Meyers *et al* (1994)) showed the cross-flow mapping of a solid body of revolution with only small scale turbulence, not the massive turbulence indicated by, for example, laser light sheet visualization. Each captured frame (1/60 of a second) showed the mapping of a solid body of revolution, except that the average velocity varied considerably from frame to frame. Thus a burst vortex is structured in space with a large variation in velocity with time which gives rise to the large standard deviations measured by the laser velocimeter.

The investigation of the wake region with the wing set at 8-degrees angle-of-attack, found the small deficit (5-percent) in the streamwise velocity in the wake centered about an inch above the wing, Figure VII.22.c. There was an accompanying small rise in standard deviation. The V-component showed only a slight rise in velocity from negative in-board to positive out-board. The extent of the rise was approximately the same as the width of the deficit found in the U-component. Again there was only a small increase in standard deviation at the wake. These same characteristics were found in the velocity magnitude and flow angle, Figure VII.23.c, respectively.

The measurements of velocity skew and flow angle skew, Figure VII.24, appear to have some structure, but there is considerable noise in the profiles not found in the backward-facing step investigations. The reason for these large excursions in skew is unknown, but they do not originate from statistical uncertainty attributed to small data ensembles as the number of accepted signal bursts, Figure VII.22, was over 98-percent of bursts generating triggers. On the other hand, the Reynolds stress profiles distinct structures occurring at the vortices. A profile similar to that shown by the U-component mean in Figure VII.22.a was found at the vortex location with the wing set to 8.0-degrees angle-of-attack, Figure VII.24.a. When the angle-of-attack was increased to 20.0-degrees, the Reynolds stress profile, Figure VII.24.b, had the shape of the V-component mean in Figure VII.22.a. Finally, there was absolutely no stress measured in the cross-flow profile through the wake region, Figure VII.24.c. The significance of these results are left for the Aerodynamicists to determine.

BART test summary

To summarize the results from the investigations conducted in BART, the laser velocimeter performed in a manner acceptable for production testing in the 14- by 22-Foot Subsonic Tunnel. Acceptable signal acquisitions from 1.0-micron PSL particles yielded high quality measurements with comparable flow field profiles that match the previous investigation with 1.7-micron PSL particles. The limitations of data transfer rate and acceptance of spurious noise spikes found in the first investigation were totally eliminated as issues. Plots to monitor statistical stationarity of the flow and scan profiles of the measurement results provide the user with additional information to better guide the flow investigation in real time.

Tying Up the Loose Ends

The laser velocimeter was moved back to the laboratory to experimentally determine several system characteristics. All measurement volume characteristics were previously determined using diffraction limited theory. Since the optical system is not diffraction limited, measurements of the actual diameter and length of the measurement volume were needed as a function of focal distance. Additionally an investigation of surface scatter was undertaken to find the surface preparation that would allow the closest approach of the measurement volume to the surface while yielding acceptable measurement signal-to-noise ratios. Finally, the signal/data processing software was linked back to the data acquisition software to transfer the results of the statistical stationarity test to the acquisition program. The acquisition program then compared the test result with the user supplied threshold, and if greater than the threshold, alert the user that stationarity had not been reached and that additional data should be acquired at that location and test condition. The signal/data processing program was also modified to combine the original and any repeat data ensembles to yield statistics for all data acquired at a given location and test condition.

Zoom lens calibrations

The investigation of the optical characteristics included the calibration of focal distance and cross-beam angle as a function of negative lens traverse position, and the determination of signal strength and signal-to-noise ratio from 1.0-micron PSL particles throughout the focal distance range. The manufacturer's specifications for the zoom lens are:

Transmission Mode	
Laser Beam Input	
Diameter, each beam	2.0 mm
Separation	50 mm
Beam Output	
Diameter, each beam	0.44 to 0.50 inch
Separation	10.0 to 11.4 inches
Scan Distance	118 to 217 inches
Scan Element Movement	5.2 inches
Receiver Mode	
Input Aperture Diameter	12 inches
Collimated Output Diameter	2.05 inches
General Parameters	
Antireflection Coatings	Magnesium Fluoride
Wavelengths	514.5 and 488.0 nm

In this investigation the limits set by the manufacturer would be extended to determine the practical limits of focal distance based on signal strength and signal-to-noise ratio. To begin the negative lens was moved away from the focusing lens until the center of the beams reached the clear aperture of 12-inches. At this setting the focal distance was 108 inches, but the available laser power was halved. Even with the reduced laser energy, the short focal distance allowed sufficient scattered light to be collected to obtain usable velocity measurements. The traversing mechanism was zeroed at this negative lens location. The lens was then moved to obtain calibration points at 108-, 126-, 180-, and 300-inch focal distances, Figure VII.25. Although the zoom lens calibration of the original system was lost to history, the focal distance calibration was exponential and the cross-beam angle calibration was linear. The four-point calibration, Figures VII.25.a-d, have these same characteristics.

At each of the four calibration locations, 1.0-micron PSL particles were sent through the measurement volume by a small particle generator to determine the signal amplitude and whether the signal-to-noise ratio was sufficient to obtain usable measurements. The captured signals that were accepted as viable measurements were interrogated to determine the peak of the high-pass filtered signal burst. The resulting histograms for the U-component (wavelength = 0.488 microns) are presented in Figure VII.25.e, and the histograms for the V-component (wavelength = 0.5145 microns) are presented in Figure VII.25.f. The lower amplitudes of the U-component signals were related to the lower efficiency of the fiber optics to transmit the blue light versus the green light in the V-component. In order to increase the probability of obtaining coincident measurements of the two components, the U-component was selected as the triggering source. The logic was if the lower amplitude signal was acceptable, the higher amplitude signal should also be acceptable. Additionally, any signal that failed to pass the signal-to-noise test in the signal/data processing software, that signal was most likely a U-component signal. The histograms show that the most efficient focal distance was 126 inches, and that signals obtained at 300 inches were within a factor of two of those obtained at 108 inches.

Although the four point calibration resulted in excellent curve fit results, a more detailed calibration was conducted on April 21, 2011 with a repeat conducted on April 28. The results are presented in Figures VII.26.a-d and found to be repeatable and within the uncertainty of the curve fits of the four point calibration. The calibrations were inverted, Figures VII.26.e and VII.26.f, to provide the user with negative lens position as a function of focal length so that the data acquisition program could automatically zoom the lens based on the desired focal distance.

Measurement volume characteristics

With the calibrations completed to allow the user to select a focal distance and command the zoom lens to place the measurement volume at that position, the next parameters to be determined were the diameter and length of the measurement volume as a function of focal distance. The diameter of the measurement volume was determined by first measuring the velocity of particles passing through the volume using the laser velocimeter. Then the

peak amplitude of each unfiltered signal was determined along with the temporal positions where the signal amplitude is 13.5-percent of the peak. The time difference between these two points equate to the time it took the particle to pass through the measurement volume based on the $1/e^2$ intensity points which are classically used to define the diameter. The diameter is then found by multiplying the measured velocity of a given particle and its passage time through the measurement volume. The results of this test are shown in Figure VII.27.a. The fact that the measurements do not track the theoretical predictions may be due to the use of fixed triggering of the PSL generated signal bursts which electronically reduce the measurement volume.

The length of the measurement volume was obtained by attaching a 127 micron (0.005-inch) diameter wire to a spinning wheel and aligning it so that the unattached end of the wire passed through the measurement volume. With the laser power greatly reduced, the wheel was translated along the optical axis until the peak signal was found. After noting the location, the wheel was first translated toward the zoom lens until the signal level was 80-percent of the peak, and the location noted. The wheel was then translated away from the zoom lens, passing through the peak signal to 80-percent of the peak at the far side. The difference between the two 80-percent locations represents the measurement volume length when the triggering oscilloscope is set to 80-percent of the peak of the signal bursts generated by the passage of PSL through the volume. The results of this test are compared to the diffraction limit theoretical predictions in Figure VII.27.b. As expected, the measurement volume length is greater than the predicted values, but not significantly, especially since the major increase in length is beyond lens specifications: 324-inch focal distance versus the specification limit of 217-inches. This investigation was repeated with amplitudes from the 50-percent locations. These results are presented in Figure VII.27.c. The ability to electronically control the length of the measurement volume has the potential to increase spatial resolution in areas of high velocity gradients, yet increase data rate in quiescent flows by lowering the triggering threshold to increase the length of the measurement volume.

Flare from surfaces

A classic limitation of laser velocimetry is the inability to obtain measurements near surfaces because of flare from the impact and/or reflection of the laser light on/from the surface. This is especially true with coaxial backscatter configurations where the surface is orthogonal to the optical centerline because the flare occurs within the depth-of-field of the lens. For this configuration the only possible solution is finding a surface preparation that minimizes the flare generated by the impact of the laser beams. It is noted that the longer the focal distance, the greater the problem as the cross-beam angle decreases with focal distance bringing the impacts closer to the optical centerline, thus increasing the effective depth-of-field.

A laboratory investigation was conducted to determine the closest approach of a surface to the measurement volume for the following surface preparations:

1) Flat black paint – classic standard used in previous laser velocimetry applications;
2) Untreated aluminum plate – Worse case sample;
3) Aeroglaze – a smooth surface, flat black type of surface preparation;
4) ChemGlaze – a glossy surface without the structure found in gloss paint;
5) Semi-gloss black paint with Rhodamine B added – Worked well for Doppler global velocimetry applications – NOTE: All camera views in DGV were at least 30degrees from the light sheet optical axis; and,
6) Nanotube – a three-dimensional surface preparation composed of carbon nanotubes.

The test sequence began by setting the lens focal distance (120-, 180-, 228-, or 276-inches) and placing the target sample orthogonal to the optical axis 36-inches beyond the center of the measurement volume. Two standard, 4096 sample data acquisitions were obtained from 1.0-micron PSL particles emitted from the Royco particle generator placed at the center of the measurement volume and approximately 0.5-inches orthogonal to the optical axis so as to eliminate flare from the generator, yet close enough to obtain a usable flow velocity. The sample was then moved to a point 12-inches from the measurement volume and two data acquisitions were obtained. The sample was moved to a distance of 9-inches, then 6-inches with respective data ensembles acquired. Following the data acquisition at the 6-inch separation, the scan rig was used to move the measurement volume and particle generator toward the target sample until the sample was centered in the particle flow and measurement volume. The scan rig origin was reset to zero at this point. The rig was then scanned 3-inches away from the surface to obtain the scattering characteristics at that spatial distance. This method was used in order to obtain greater spatial accuracy at the smaller spatial distances than could be found using the tape measure employed at the greater spatial distances. The scan rig was used to move the measurement volume and Royco closer to the fixed surface location in a sequence of spatial distances until the signal bursts from the particle passage were buried in noise to the point where oscilloscope triggering was not possible. At longer focal distances, some surfaces produced sufficient noise that even the 6-inch station could not be reached.

The signal-to-noise ratio for this investigation was determined by dividing the peak spectral power by the average level throughout the power spectral density. The signal-to-noise ratio was computed for each captured signal burst, whether or not it was an accepted measurement. The mean and standard deviation of the signal-to-noise ratios were then determined and the results plotted for all surfaces at the four focal distances, Figure VII.28. The signal-to-noise ratio used to determine acceptable signal bursts was 5.0 (7 dB). As shown in the figures, at the closer approaches a significant number of signal bursts were below the accepted threshold, and thus would be rejected from the velocity measurement statistics. Also it can be seen in the figures that the V-component had a far greater signal-to-noise ratio than the U-component, primarily due to its greater laser power. Thus, for coincident measurements, the U-component was the controller regarding size of the data ensemble and measurement quality.

In general the signal-to-noise ratios obtained at the 36-inch spatial distance remained constant until the spatial distance decreased to the point where surface flare began to be collected by the optical system, thus increasing the noise level. Once this break point was reached, the decrease in signal-to-noise ratio followed a linear slope as plotted in semi-log. It is noted that the differences in signal-to-noise ratios at the 36-inch spatial distance were not sample surface dependent, but set primarily by the laser power for that particular test case. Although set nominally at 0.5 W (1.0 W at 276-inch focal distance) all-line output for each test, differences were found. As expected the closest approaches were obtained at the 120-inch focal distance with the minimal approach distance increasing with increased focal distance. Also, as expected, the average signal-to-noise ratios also decreased with increased focal distance because the collecting solid angle decreased while the laser beam impacts occurred closer to the optical axis, thus resulting in decreasing signal strength while increasing the flare contribution to the noise level. Although the nanotube sample provided the closest approach at the 120- and 276-inch focal distances, the surface with the best overall characteristics was the Aeroglaze. It is also noted that the Rhodamine B doped semi-gloss black paint showed little overall improvement over plane semi-gloss black paint, Figure VII.28.a, even though it provided an improvement in DGV applications. This is most likely caused by the saturation of the absorption characteristics in the Rhodamine B because of the high power density at the laser beam impact locations versus the lower power densities found in laser light sheets.

Comparisons of signal-to-noise characteristics as a function of focal distance for each sample surface are presented in Figure VII.29. Again, the signal-to-noise levels at the 36-inch separation distance are dependent on laser power and focal distance, and at the longer focal distances, contributions from surface flare. While each sample exhibits the onset of the flare effect at the 120-inch station, all of the samples, except the Aeroglaze, have no break point at the longer focal distances indicating that flare influences the measurements even at the 36-inch separation distance. During the course of testing a portion of the nanotube sample was damaged which may have affected its efficiency. Thus a comparison of the characteristics from the damaged section with the original was performed at the 276-inch focal distance, Figure VII.29.h. Surprisingly the damaged surface performed better than the original in having a clear break point and a closer approach distance.

In order to determine the optimal signal-to-noise threshold, the data was reprocessed with thresholds of 2.5 (5 dB) and 10.0 (10 dB) and the results presented in Figures VII.30-39. As an example, consider the characteristics found from the flat black painted sample, Figure VII.30.a. At the 120-inch focal distance, the number of acceptable signal bursts obtained using the 2.5 and 5.0 signal-to-noise levels are similar while there is a significant reduction in acceptable signal bursts at the 10.0 level as expected based on the number of signal bursts with signal-to-noise ratios below the threshold. However, the plots of mean velocity and standard deviation do not indicate any significant differences among the three thresholds. The mean velocity and standard deviation results were curve fit using iterative procedures to minimize error to fit a first order exponential decay function. As shown, there were significant changes in velocity and standard deviation that correlates with the

loss of signal-to-noise ratio, Figure VII.29.a. As the signal-to-noise ratio decreases with the inclusion of noise from surface flare, the probability density function widens, Figure VII.30.a.(2). The mean velocity is also affected by the loss of the lower signal-to-noise ratio bursts that are obtained from particles passing through the edge of the measurement volume which, in this case, are lower velocity since the measurement volume encompasses the entire diameter of the jet flow especially at the longer focal distances. As the focal distance increases the differences in the number of acceptable signal bursts becomes significant, while measurement accuracies decrease. The decrease in measurement accuracy is found first in the signal-to-noise ratio threshold of 2.5 as shown in the plots of mean velocity and standard deviation along with the histograms. Data processed using the threshold of 5.0 remain consistent until the focal distance reaches 276-inches. At that focal distance the threshold of 10.0 remains consistent except that the number of acceptable signal bursts becomes so low that statistical uncertainty becomes an issue. Thus it is recommended that a threshold of 5.0 be used during real time data processing because of its relative insensitivity to noise while providing higher numbers of acceptable signal bursts to minimize statistical uncertainties. The threshold of 5.0 was used during the processing of all data acquired in both BART entries, the results of which are presented in this document.

The above characteristics were found with all of the surface samples:

Figure VII.31 – Unpainted aluminum sample;
Figure VII.32 – Semi-gloss black paint (no Rhodamine);
Figure VII.33 – Aeroglaze;
Figure VII.34 – Chem Glaze;
Figure VII.35 – Semi-gloss black paint with Rhodamine B added;
Figures VII.36-38 – illustrate the effect of aging of the Rhodamine B; and,
Figure VII.39 – Nanotube.

Since testing in facilities would normally scan the measurement volume in a plane normal to the optical axis at a fixed focal distance, any flare from the model surface could not be predicted because of the lack of a clear break point, as found in this investigation, leading to the potential of unknown measurement uncertainties. While monitoring the oscilloscope traces of the signal bursts would provide an indication of the increase in noise caused by surface flare, this is not a practical solution in the hectic world of wind tunnel testing. Thus it is recommended that post processing be conducted using the 2.5 and 10.0 signal-to-noise thresholds along with the real time processing using the 5.0 threshold to ascertain the onset of measurement uncertainty due to surface flare. It is noted that the loss of signal-to-noise ratio related to focal distance or lower laser power has a far lower effect on measurement accuracy than the increase in noise caused by surface flare. It is further recommended that Aeroglaze be used as a surface coating on the areas of the model that would be impacted by the laser beams during testing. Also, if found to be practical, off-axis collection of the scattered light will greatly reduce the amount of collected flare light, thus allowing a closer approach to the surface without compromising measurement accuracy, (Meyers and Hepner (1984)).

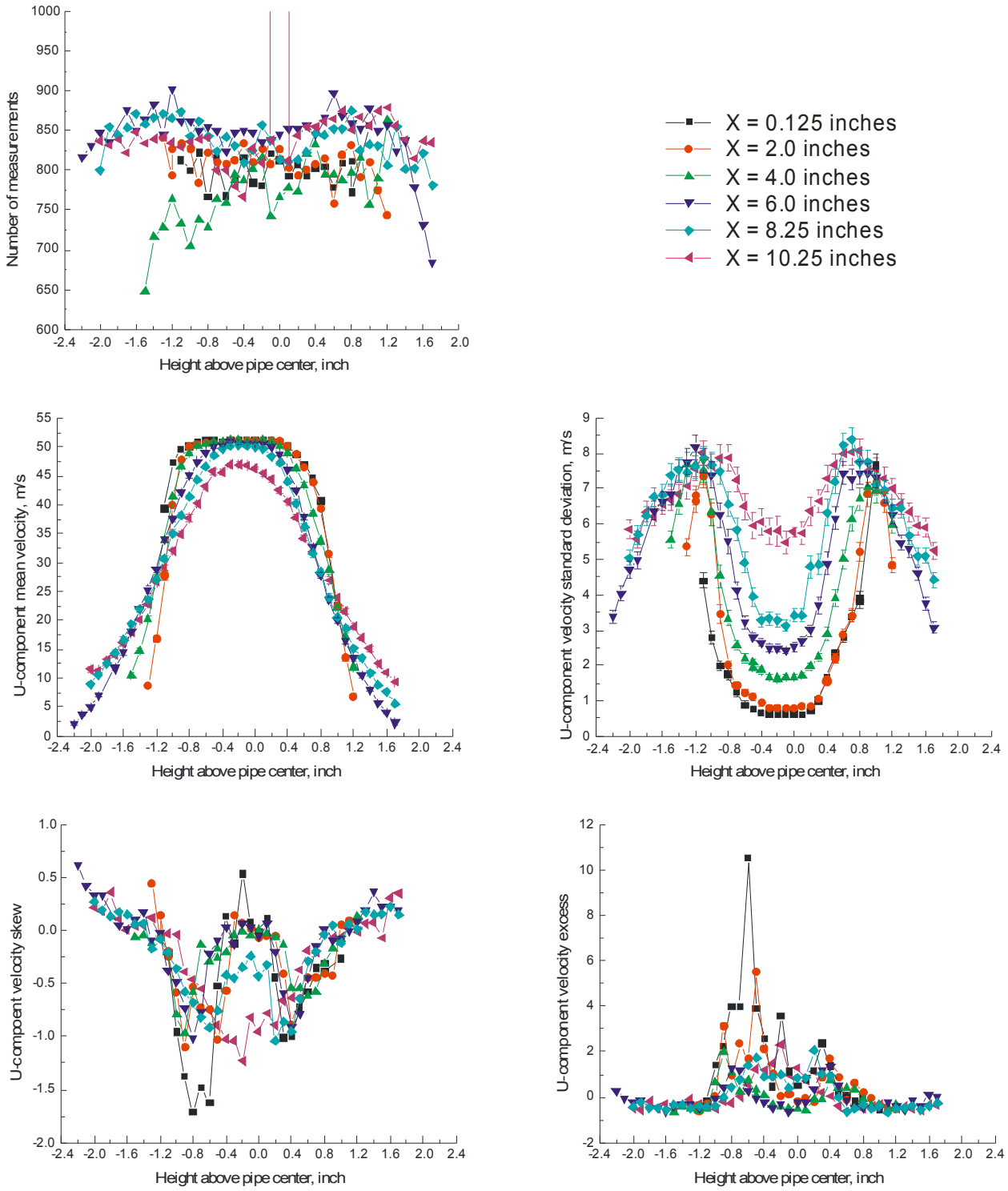

Figure VII.1.a.- Vertical scans at several downstream locations in the jet exiting the 2-inch jet: Streamwise velocity.

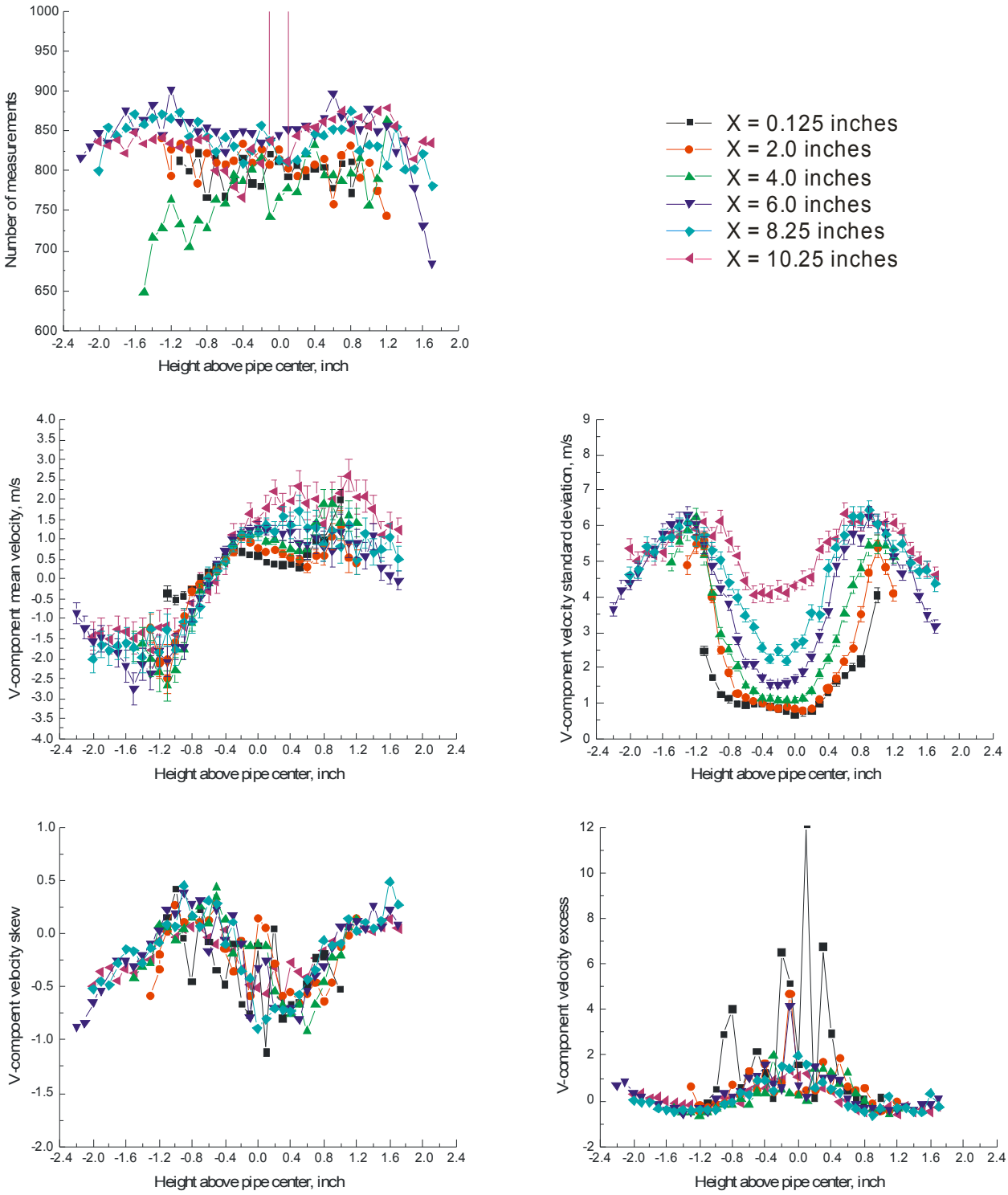

Figure VII.1.b.- Vertical scans at several downstream locations in the jet exiting the 2-inch jet: Vertical velocity.

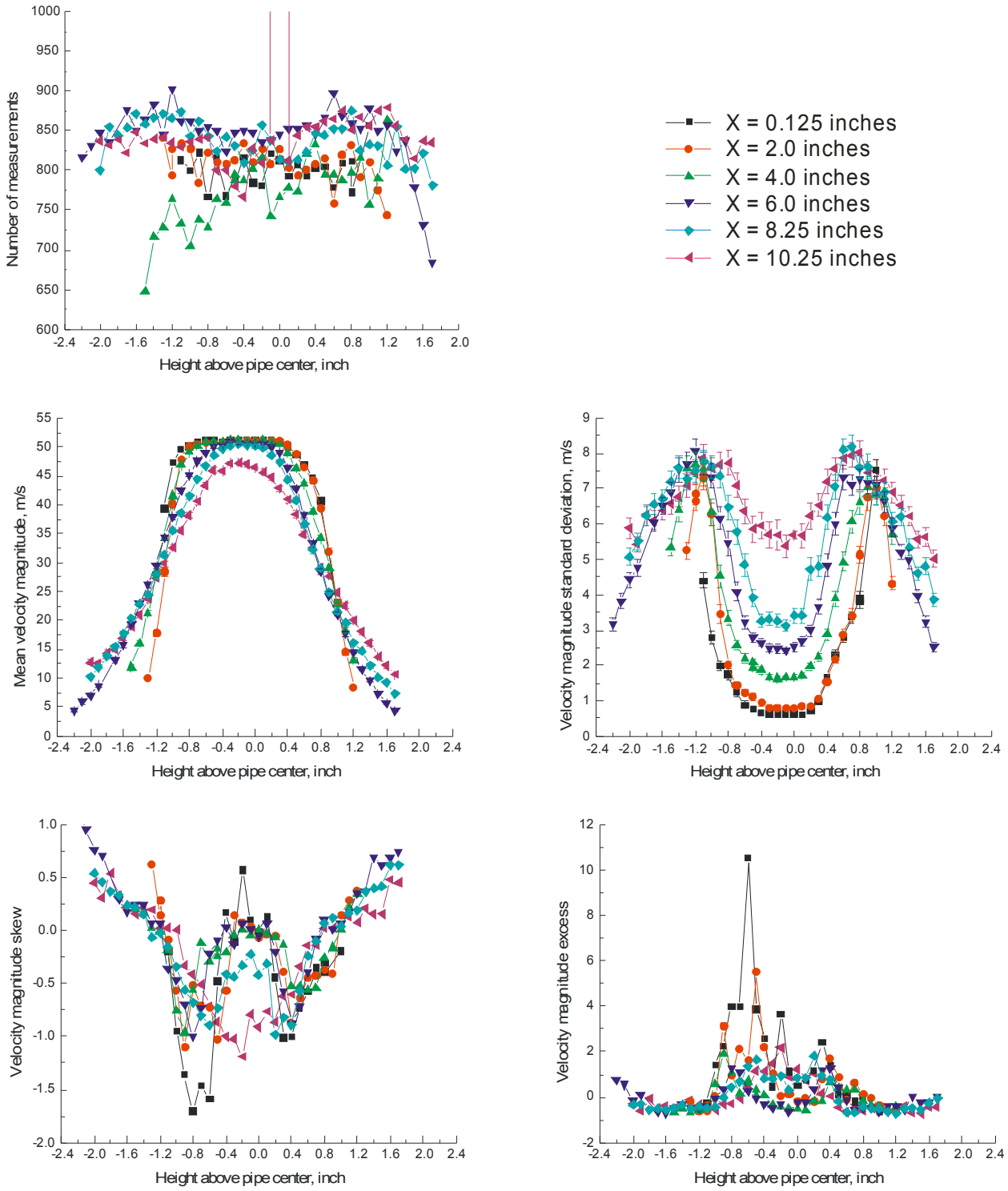

Figure VII.1.c.- Vertical scans at several downstream locations in the jet exiting the 2-inch jet: Velocity magnitude.

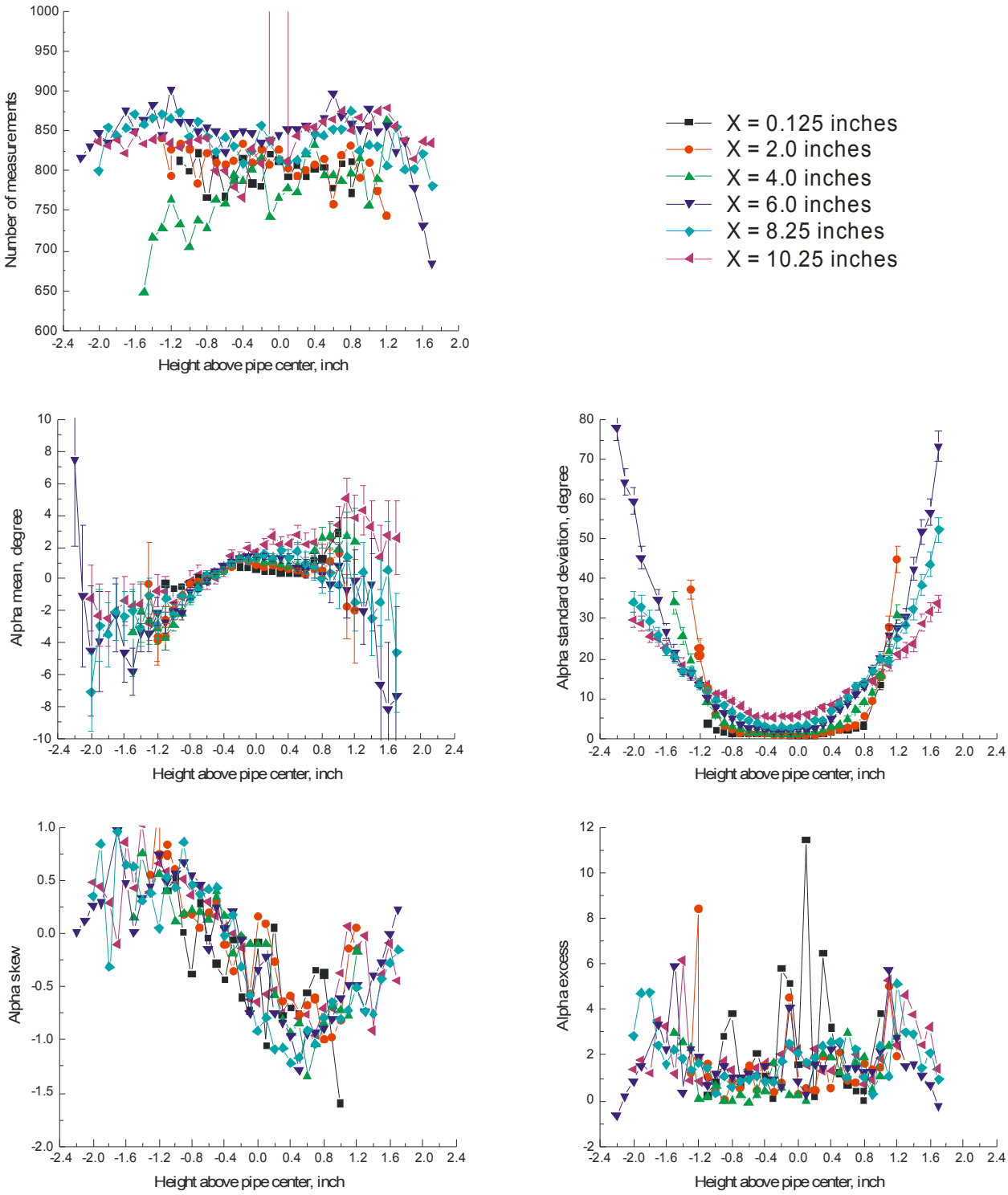

Figure VII.1.d.- Vertical scans at several downstream locations in the jet exiting the 2-inch jet: Flow angle.

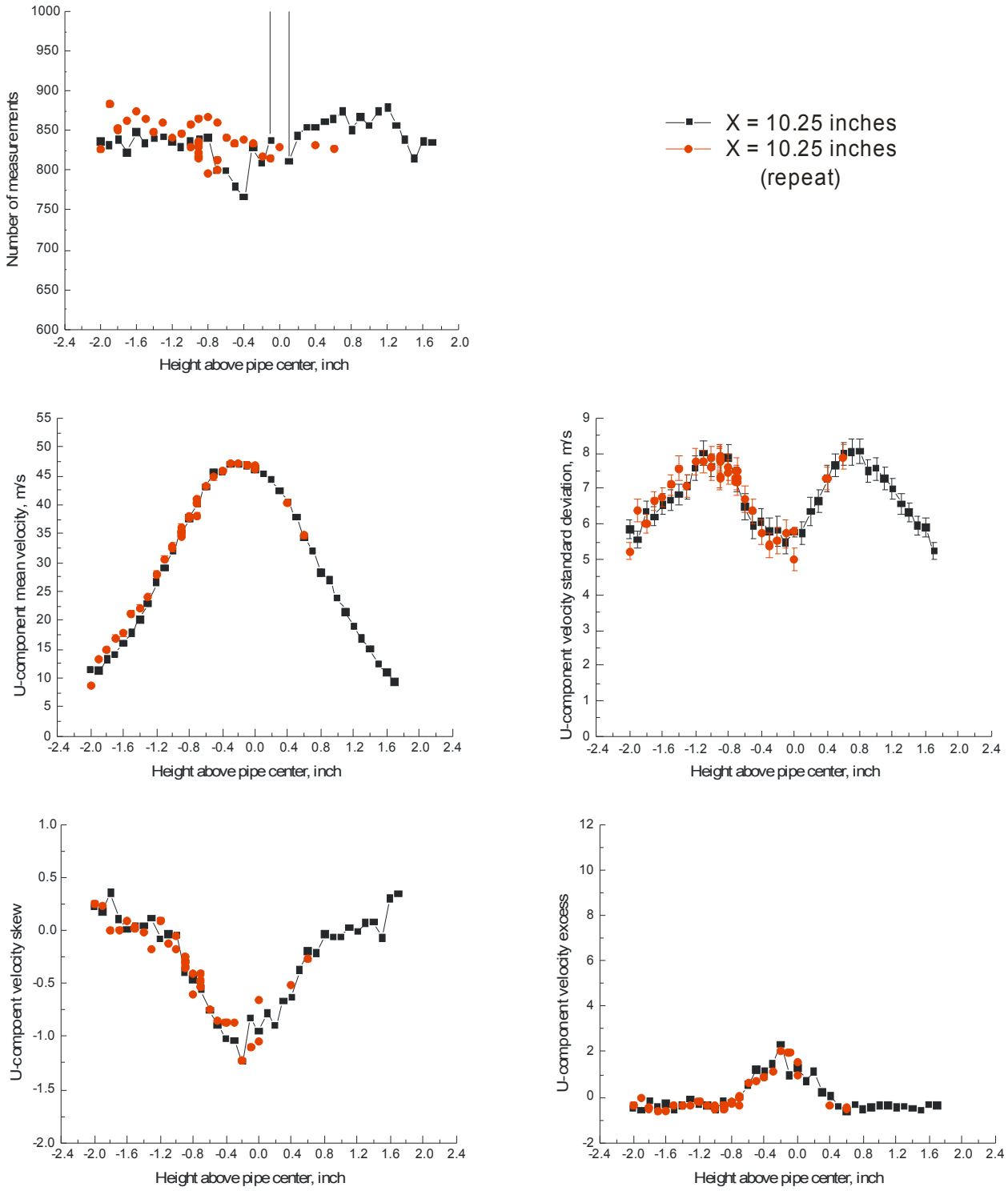

Figure VII.2.a.- Vertical scan repeat test at 10.25-inches downstream: Streamwise velocity.

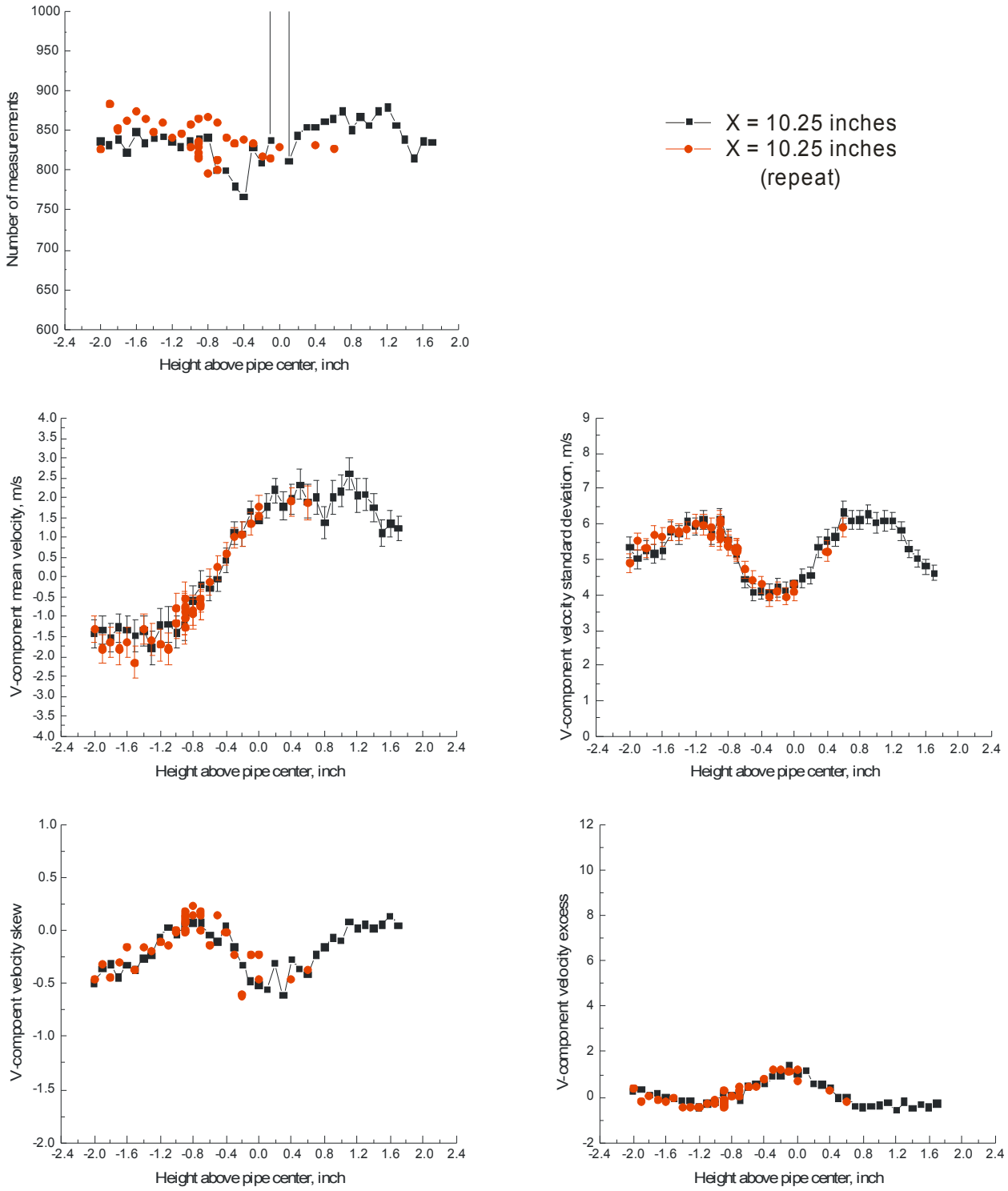

Figure VII.2.b.- Vertical scan repeat test at 10.25-inches downstream: Vertical velocity.

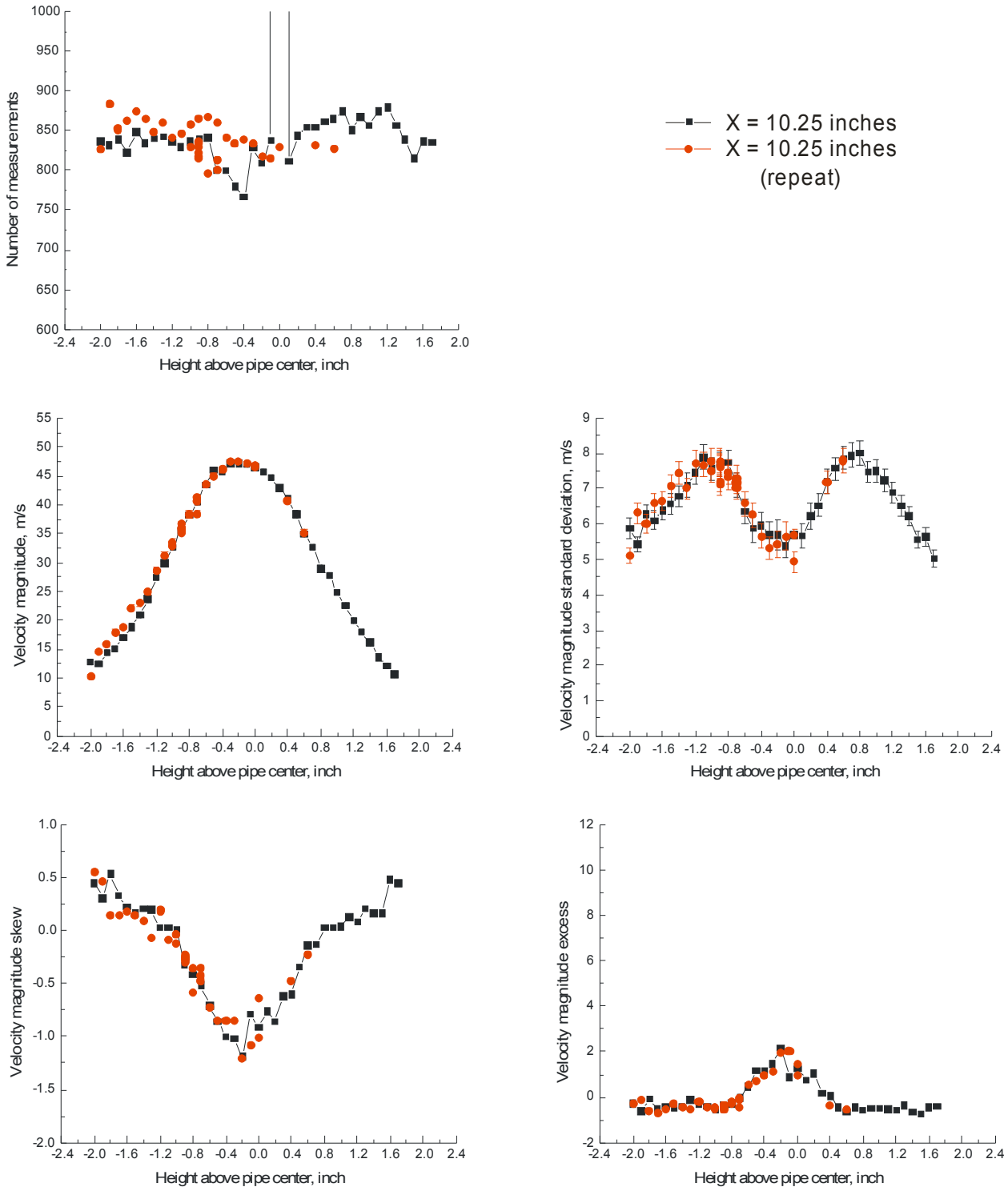

Figure VII.2.c.- Vertical scan repeat test at 10.25-inches downstream: Velocity magnitude.

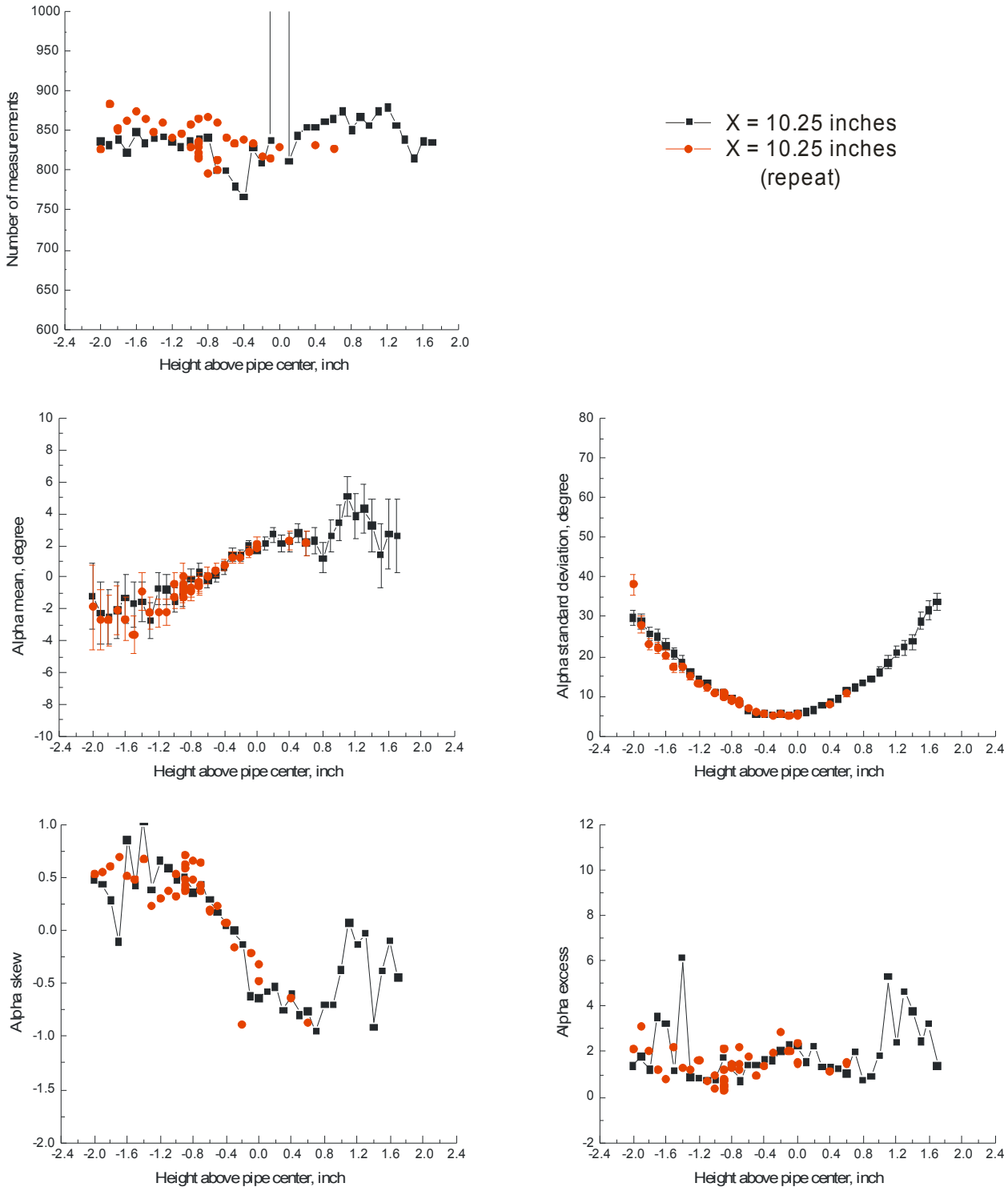

Figure VII.2.d.- Vertical scan repeat test at 10.25-inches downstream: Flow angle.

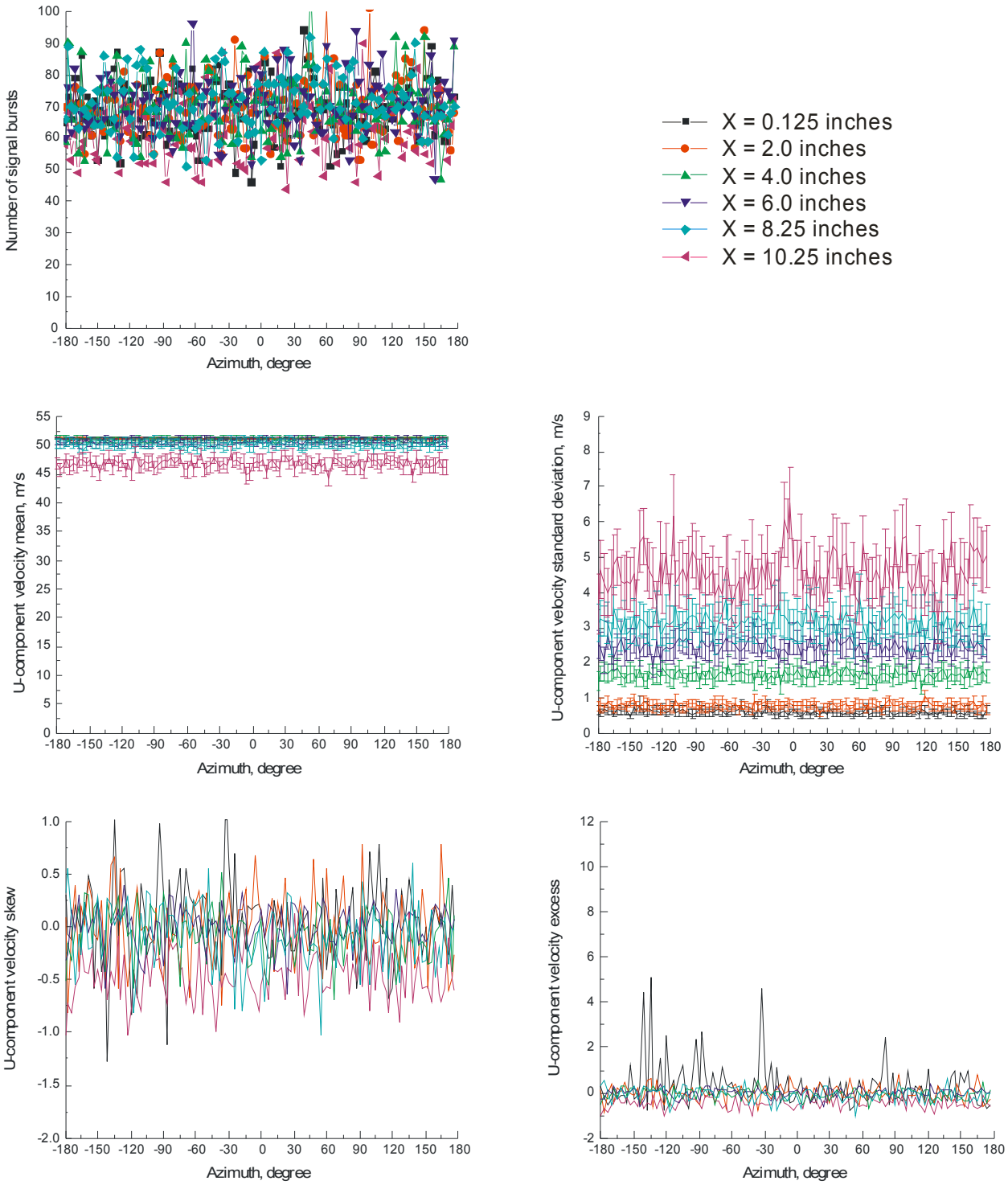

Figure VII.3.a.- Vertical scan azimuth test (uniform random number based) at several downstream locations: Streamwise velocity.

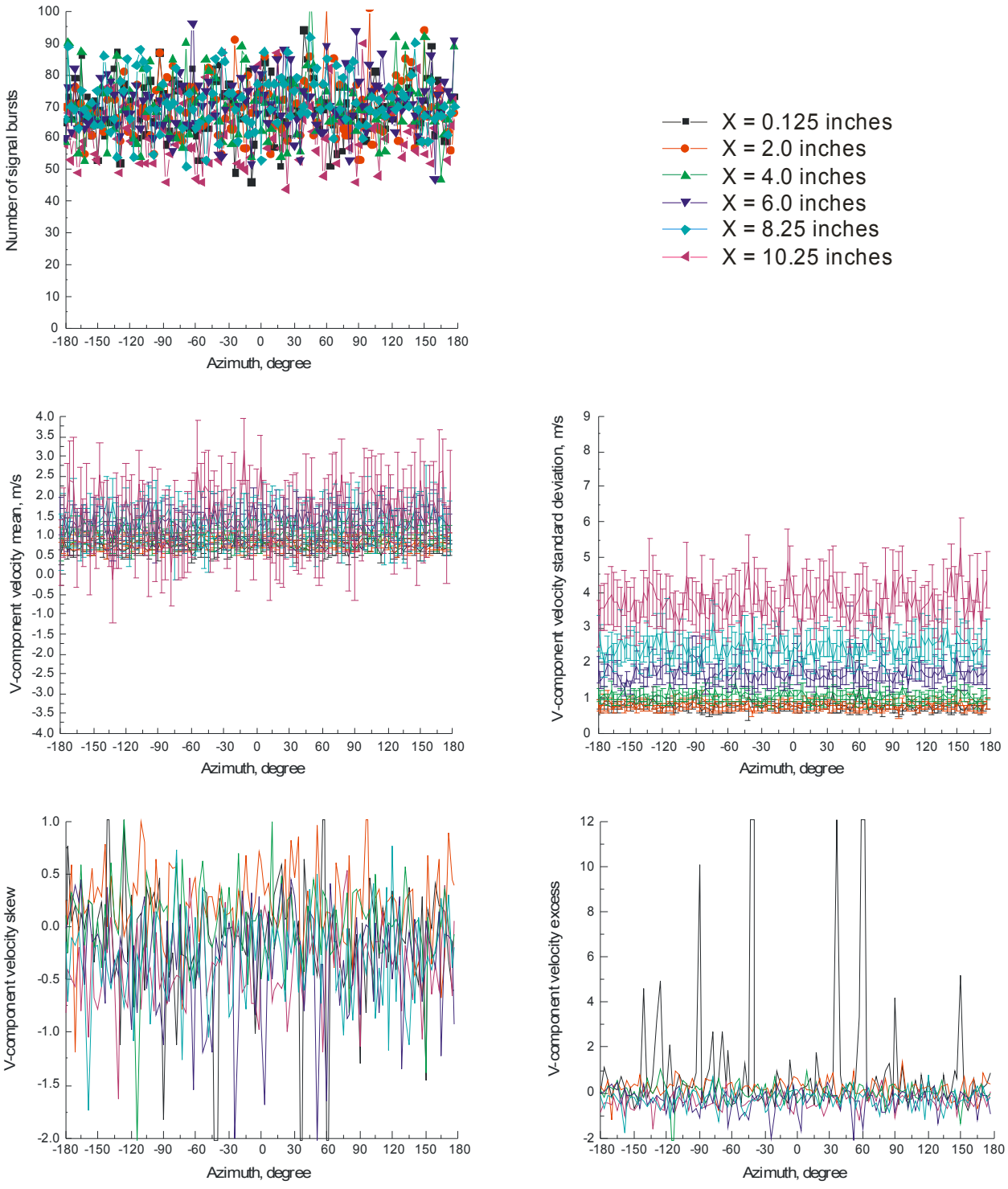

Figure VII.3.b.- Vertical scan azimuth test (uniform random number based) at several downstream locations: Vertical velocity.

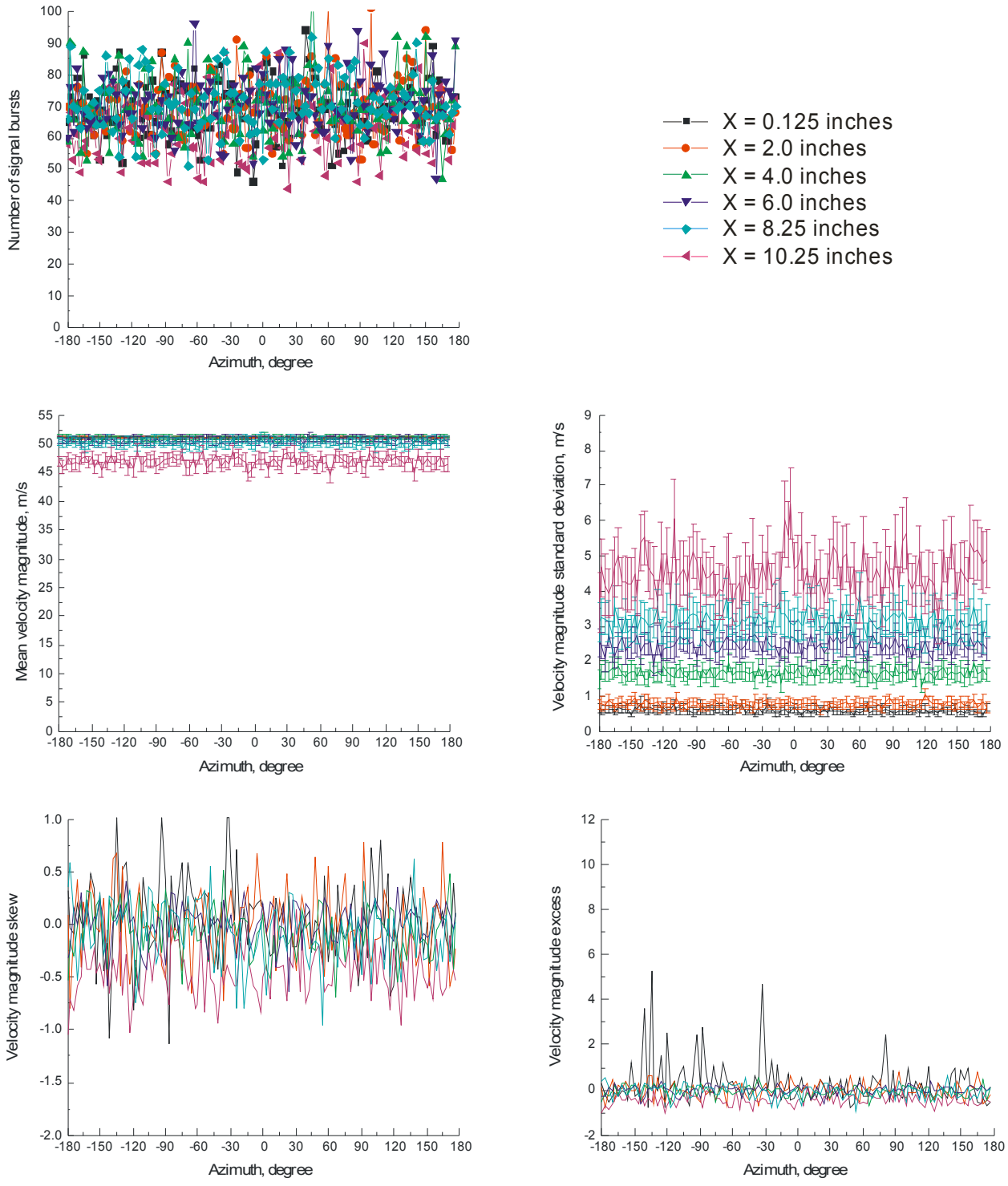

Figure VII.3.c.- Vertical scan azimuth test (uniform random number based) at several downstream locations: Velocity magnitude.

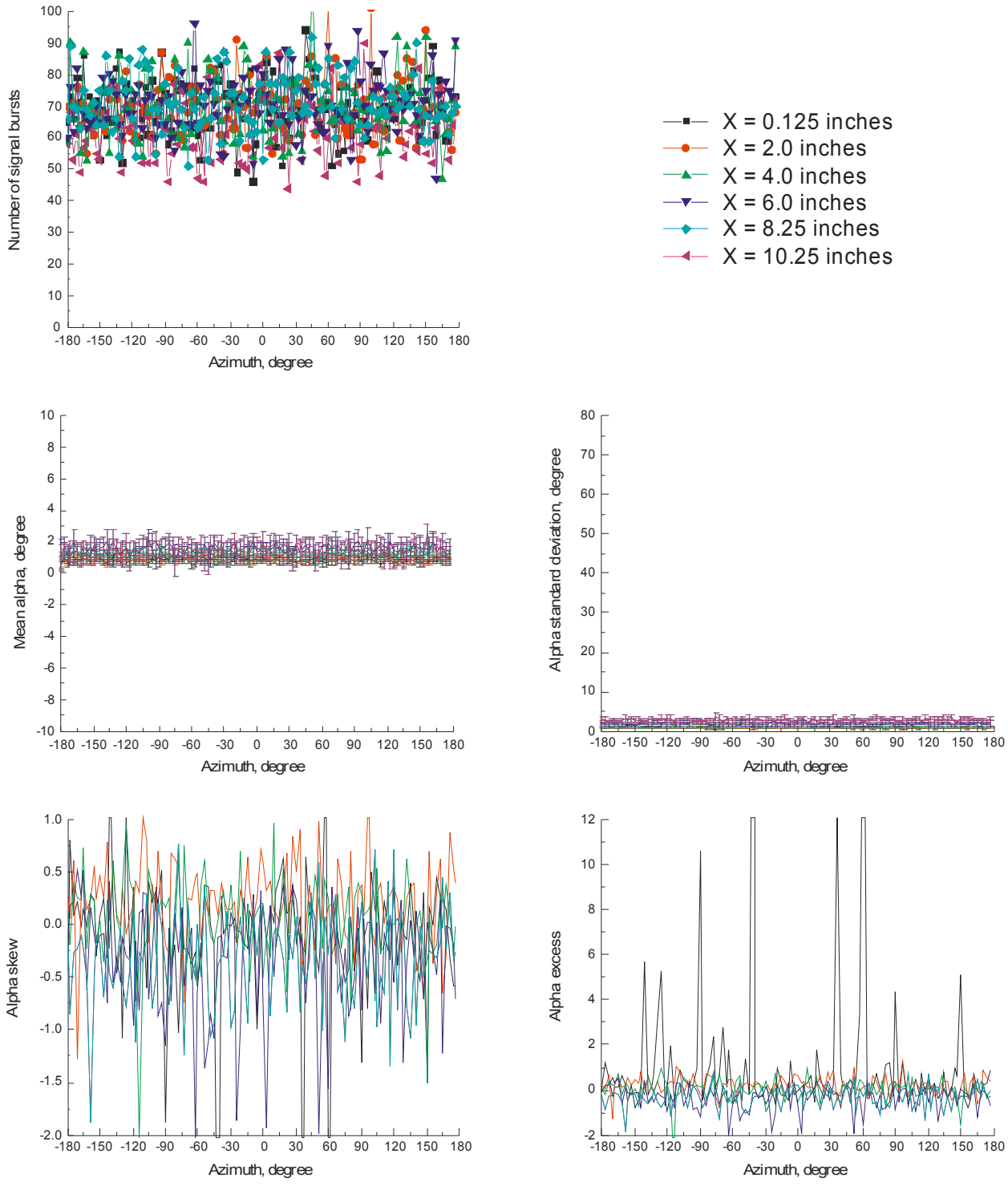

Figure VII.3.d.- Vertical scan azimuth test (uniform random number based) at several downstream locations: Flow angle.

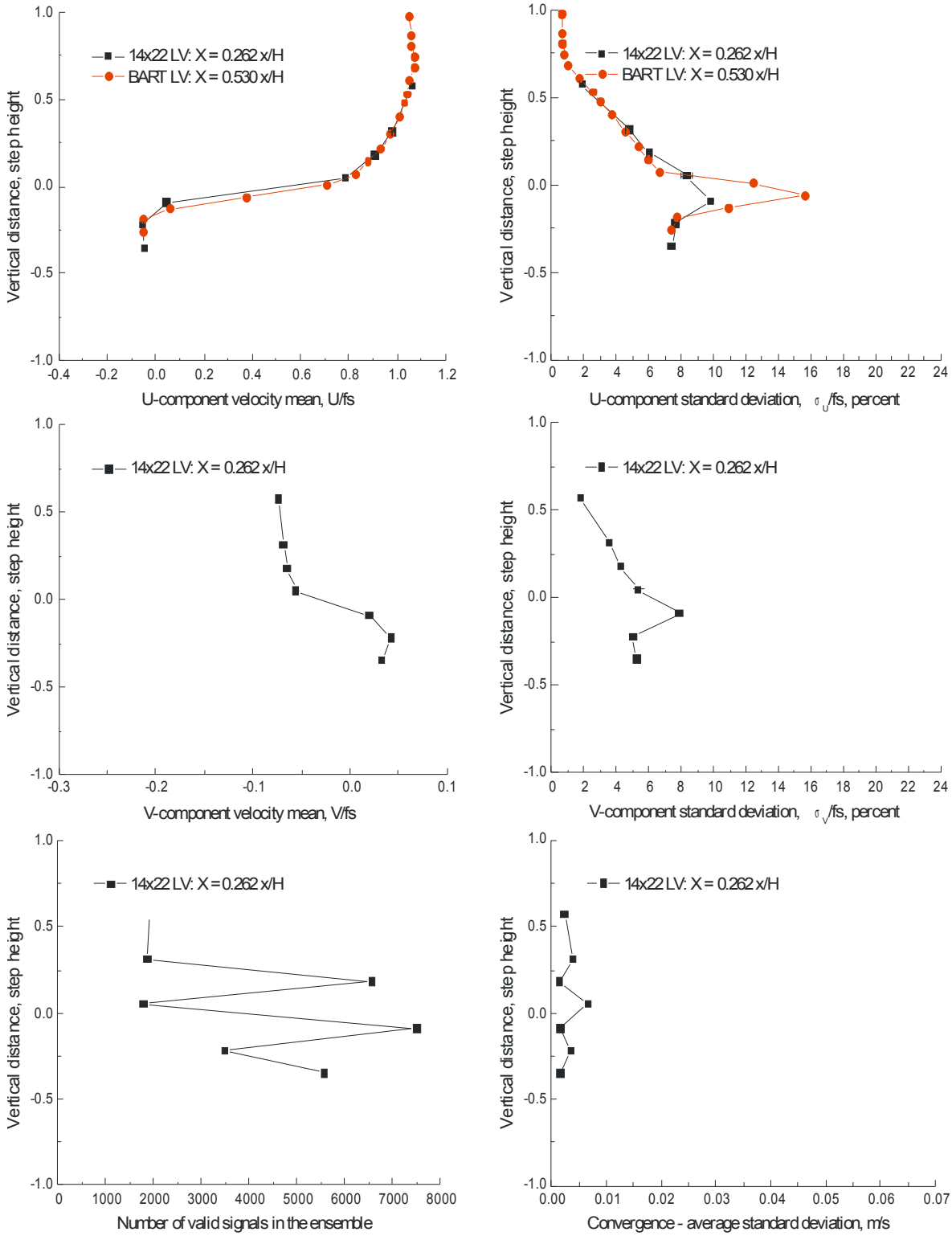

Figure VII.4.a.- Vertical scan 0.262 x/H downstream of a 1.5-inch backward-facing step: streamwise and vertical velocity components, number of accepted signal bursts, and statistical stationarity convergence standard deviation, fs = 45.0 m/s.

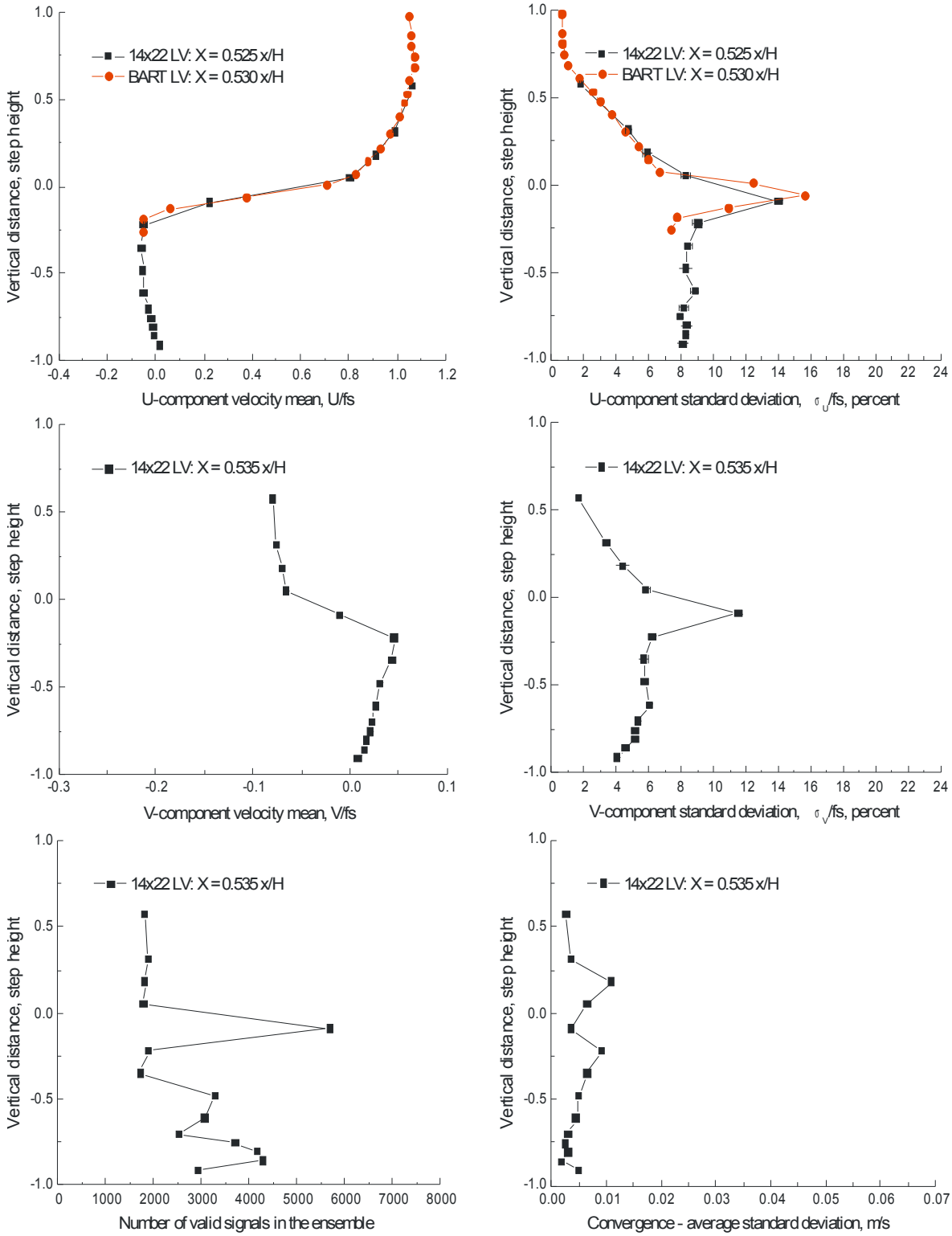

Figure VII.4.b.- Vertical scan 0.535 x/H downstream of a 1.5-inch backward-facing step: streamwise and vertical velocity components, number of accepted signal bursts, and statistical stationarity convergence standard deviation, fs = 45.0 m/s.

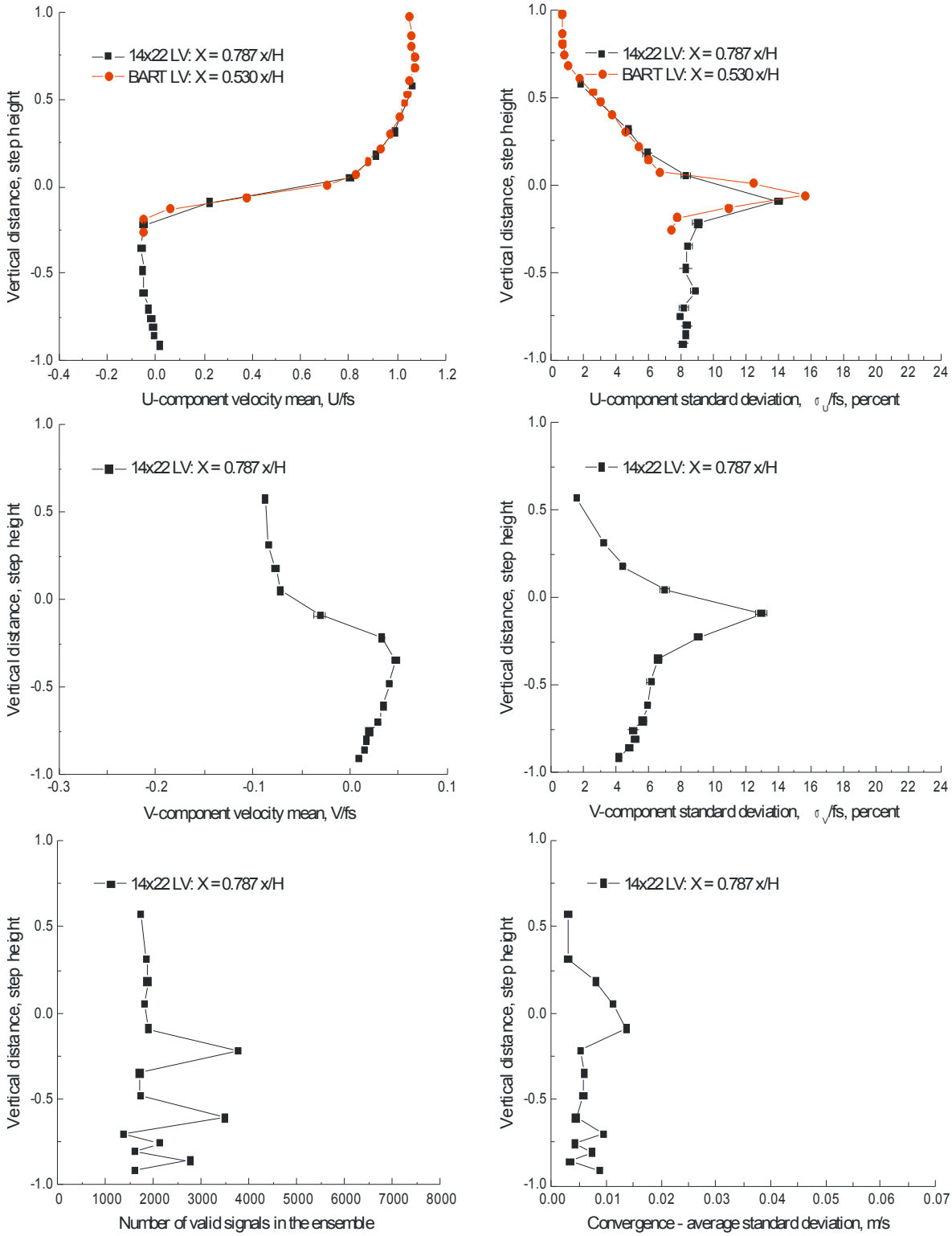

Figure VII.4.c.- Vertical scan 0.787 x/H downstream of a 1.5-inch backward-facing step: streamwise and vertical velocity components, number of accepted signal bursts, and statistical stationarity convergence standard deviation, fs = 45.0 m/s.

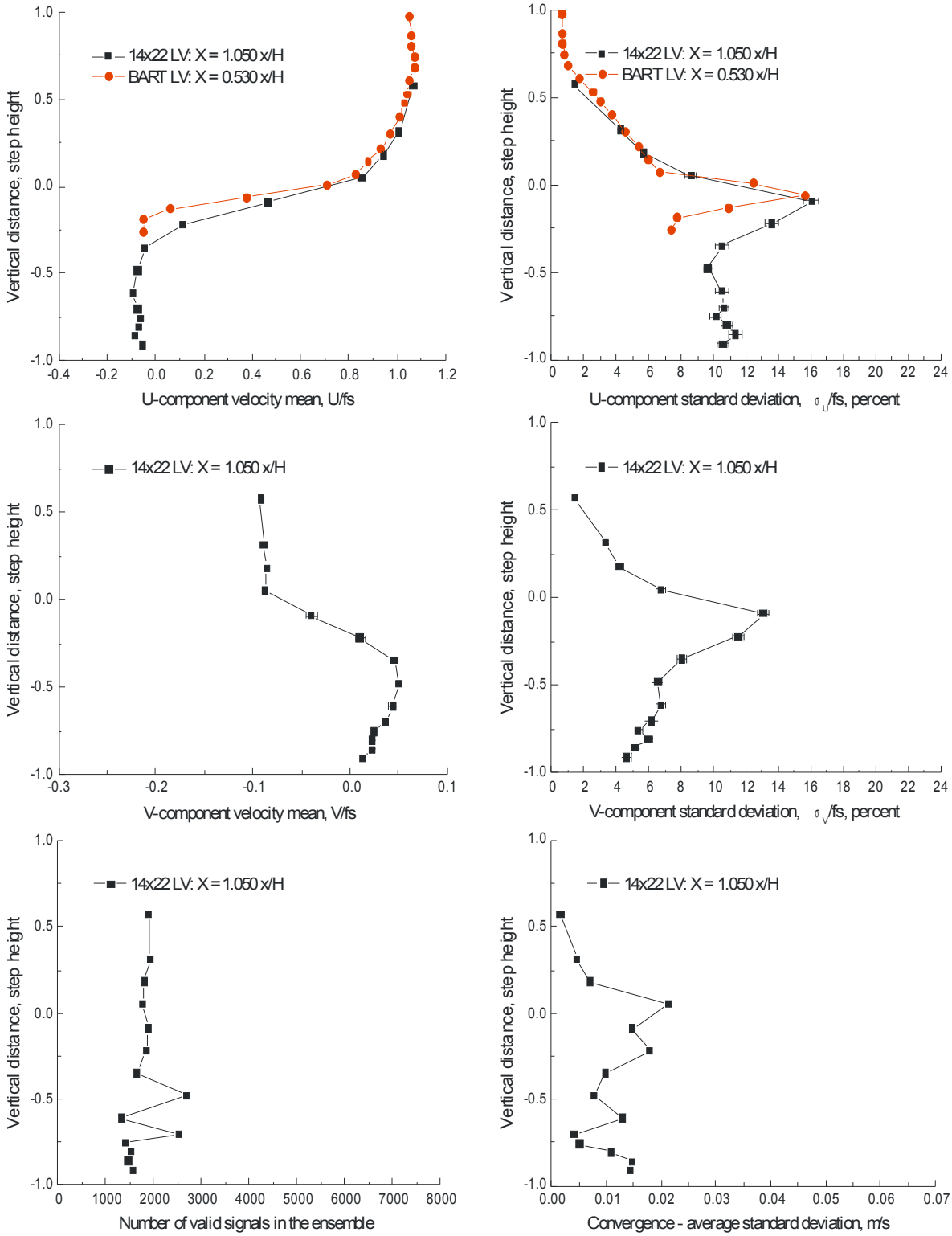

Figure VII.4.d.- Vertical scan 1.050 x/H downstream of a 1.5-inch backward-facing step: streamwise and vertical velocity components, number of accepted signal bursts, and statistical stationarity convergence standard deviation, fs = 45.0 m/s.

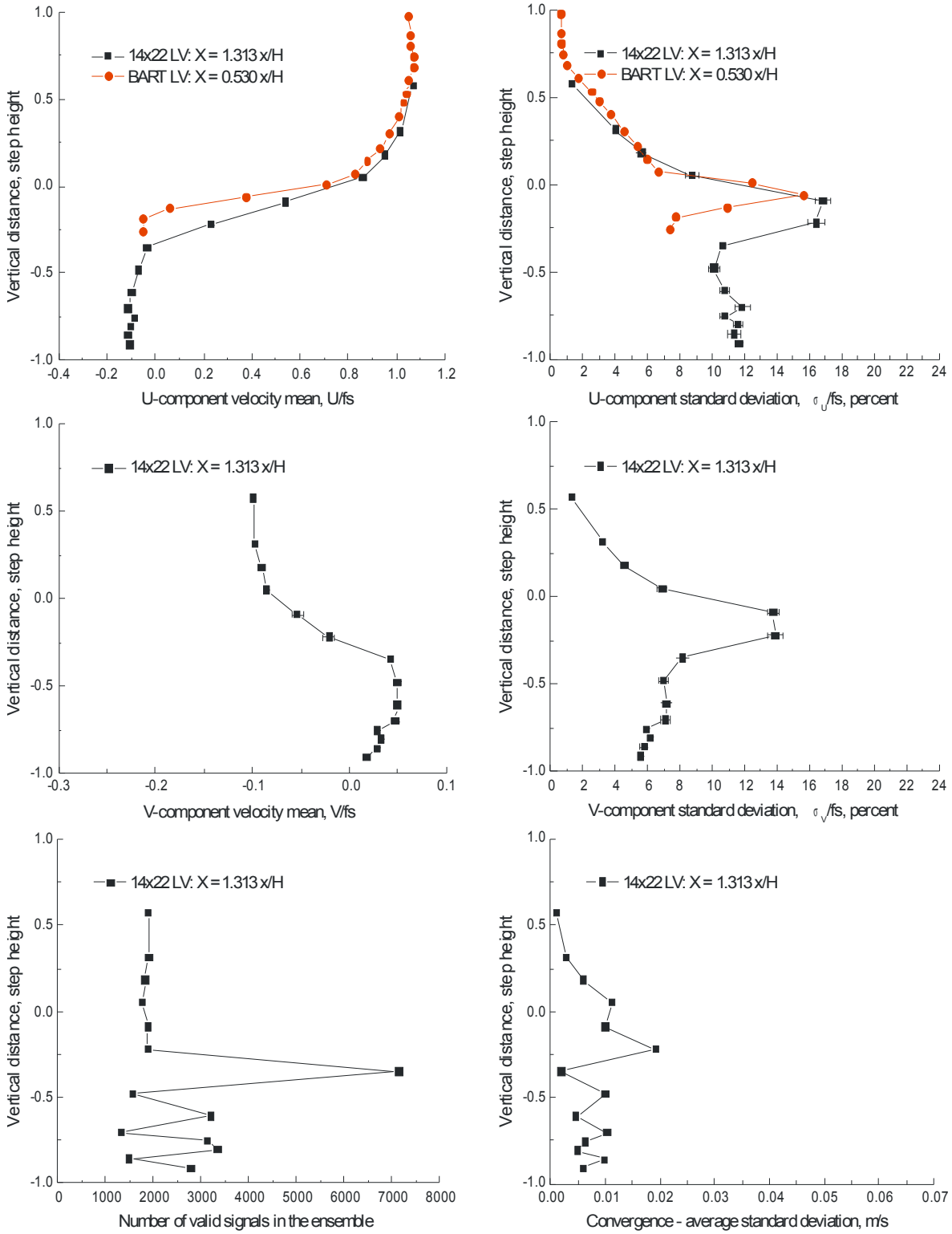

Figure VII.4.e.- Vertical scan 1.313 x/H downstream of a 1.5-inch backward-facing step: streamwise and vertical velocity components, number of accepted signal bursts, and statistical stationarity convergence standard deviation, fs = 45.0 m/s.

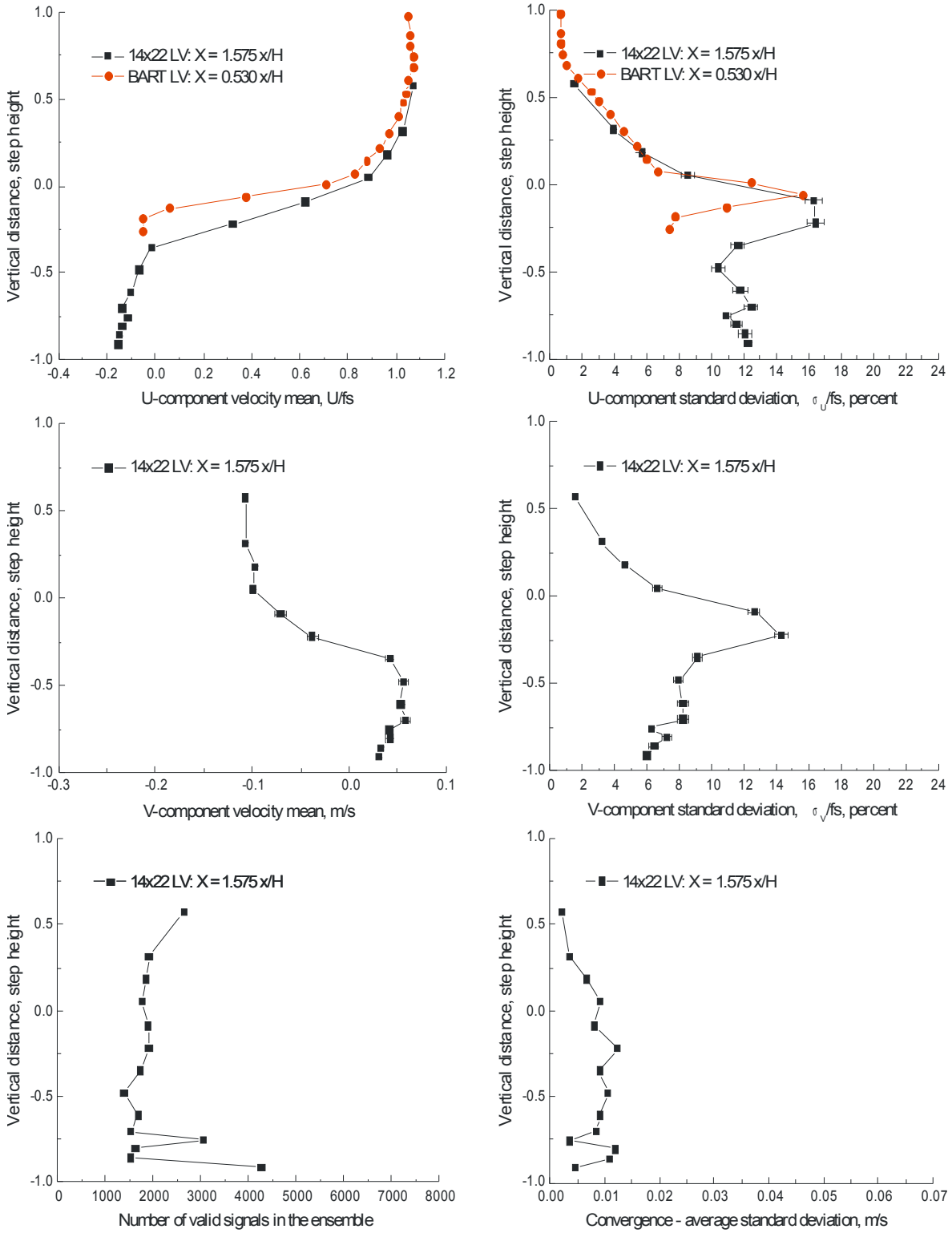

Figure VII.4.f.- Vertical scan 1.575 x/H downstream of a 1.5-inch backward-facing step: streamwise and vertical velocity components, number of accepted signal bursts, and statistical stationarity convergence standard deviation, fs = 45.0 m/s.

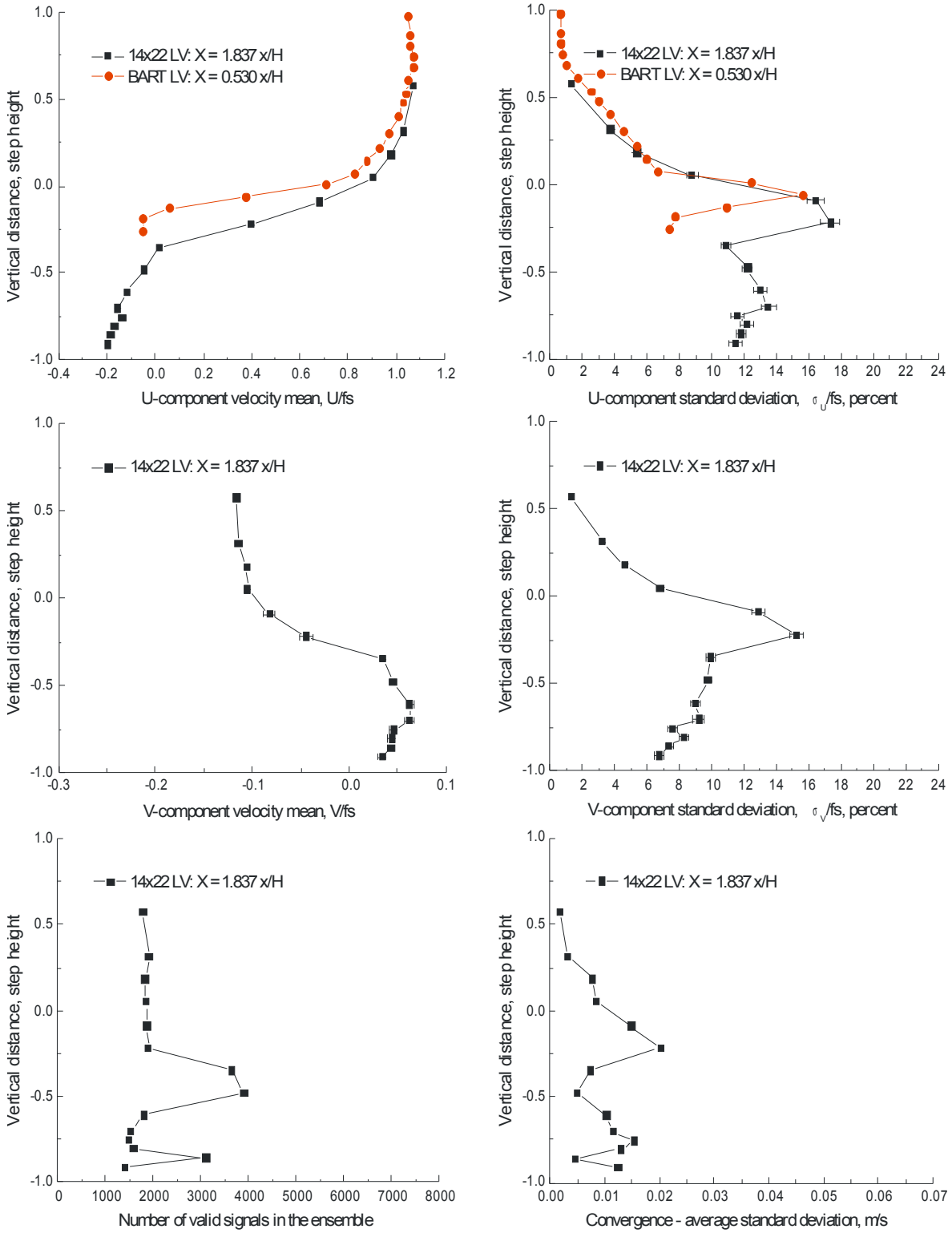

Figure VII.4.g.- Vertical scan 1.837 x/H downstream of a 1.5-inch backward-facing step: streamwise and vertical velocity components, number of accepted signal bursts, and statistical stationarity convergence standard deviation, fs = 45.0 m/s.

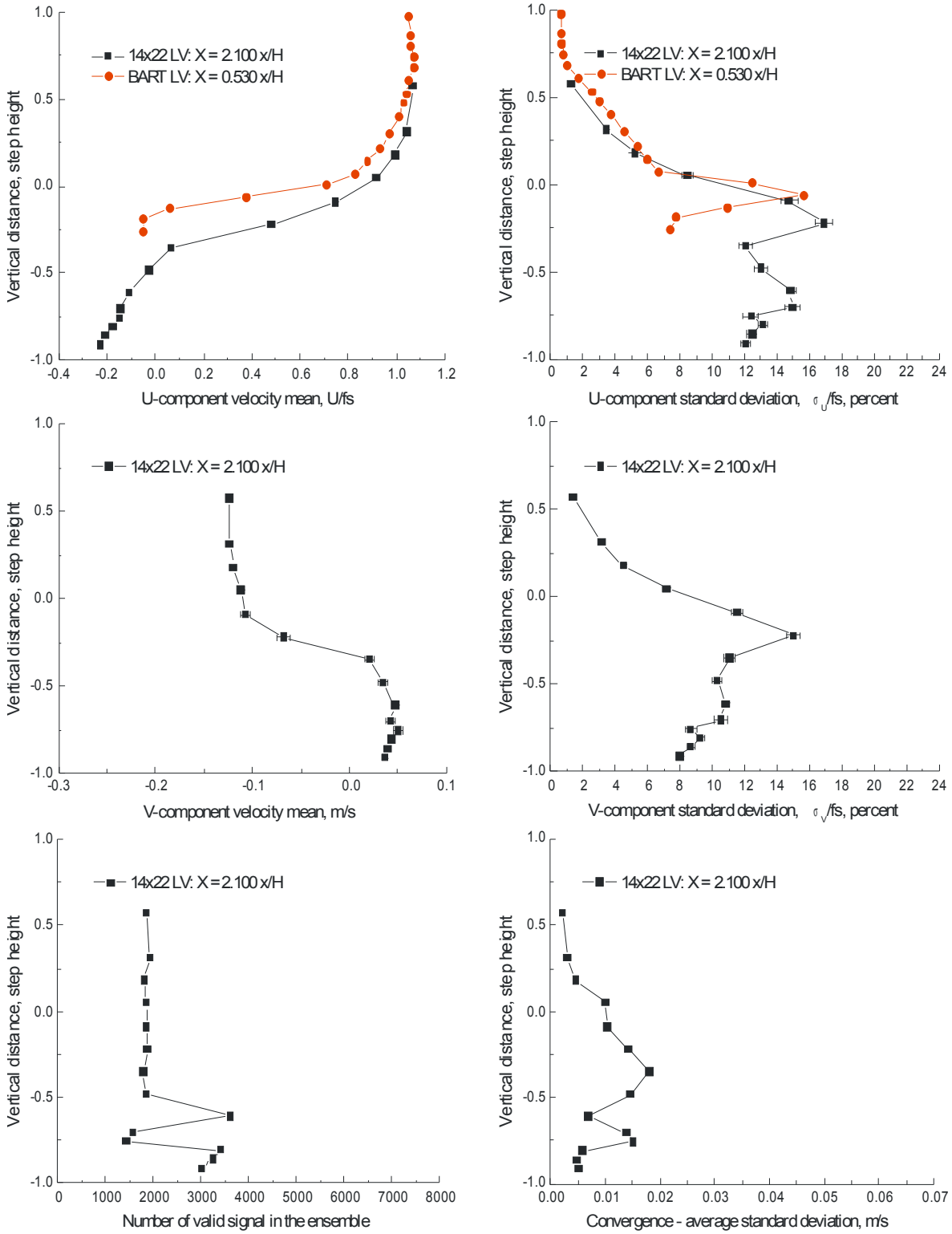

Figure VII.4.h.- Vertical scan 2.1 x/H downstream of a 1.5-inch backward-facing step: streamwise and vertical velocity components, number of accepted signal bursts, and statistical stationarity convergence standard deviation, fs = 45.0 m/s.

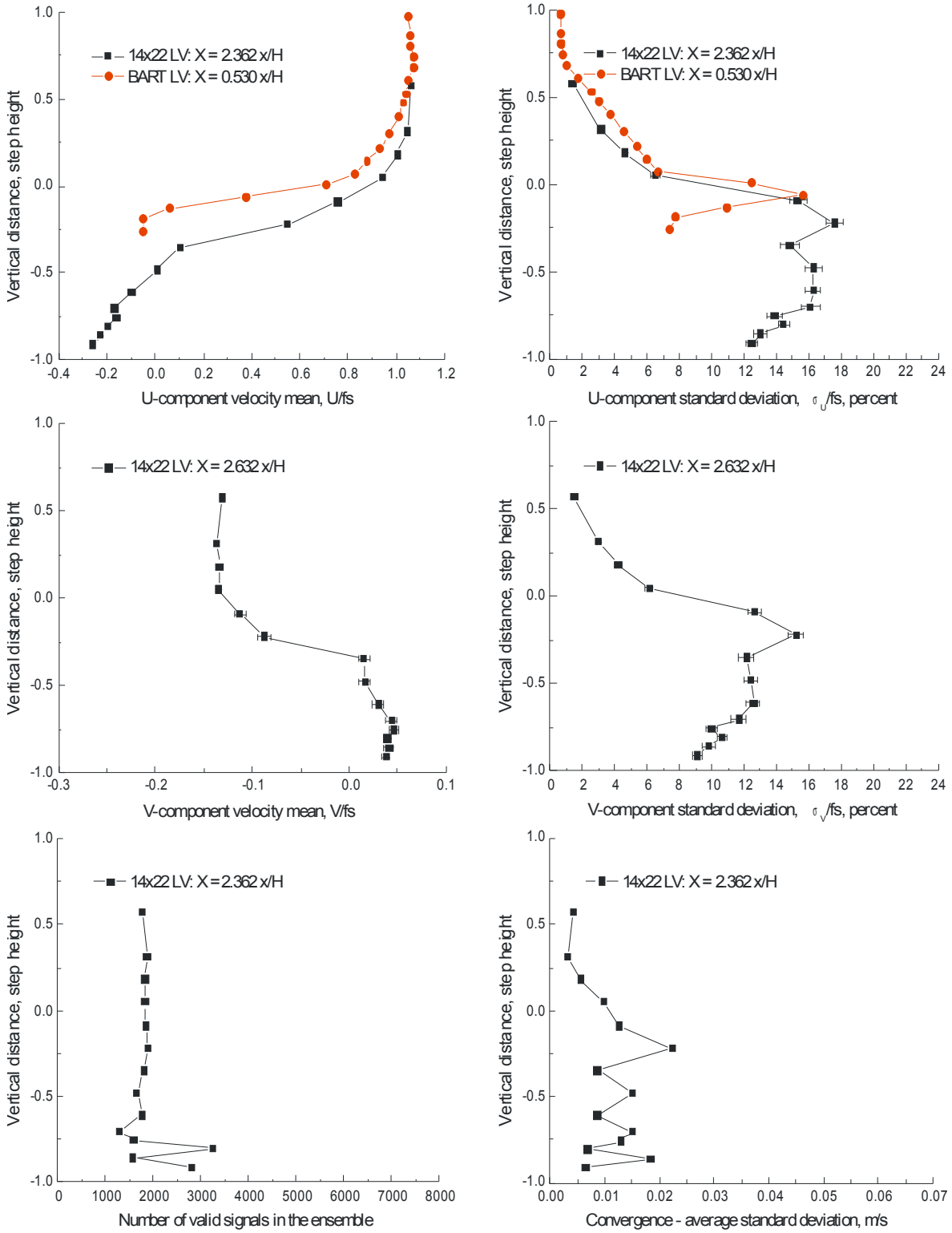

Figure VII.4.i.- Vertical scan 2.362 x/H downstream of a 1.5-inch backward-facing step: streamwise and vertical velocity components, number of accepted signal bursts, and statistical stationarity convergence standard deviation, fs = 45.0 m/s.

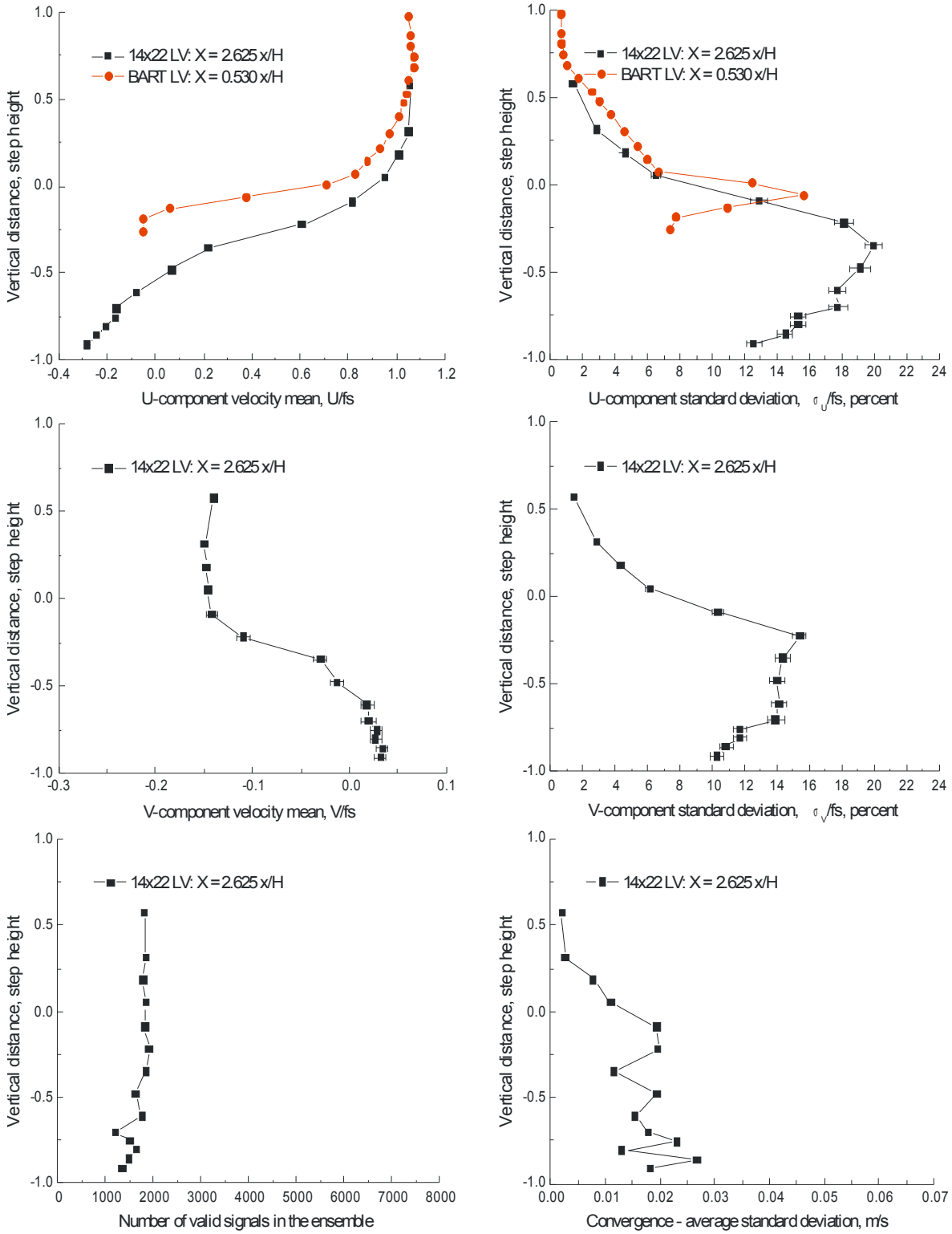

Figure VII.4.j.- Vertical scan 2.625 x/H downstream of a 1.5-inch backward-facing step: streamwise and vertical velocity components, number of accepted signal bursts, and statistical stationarity convergence standard deviation, fs = 45.0 m/s.

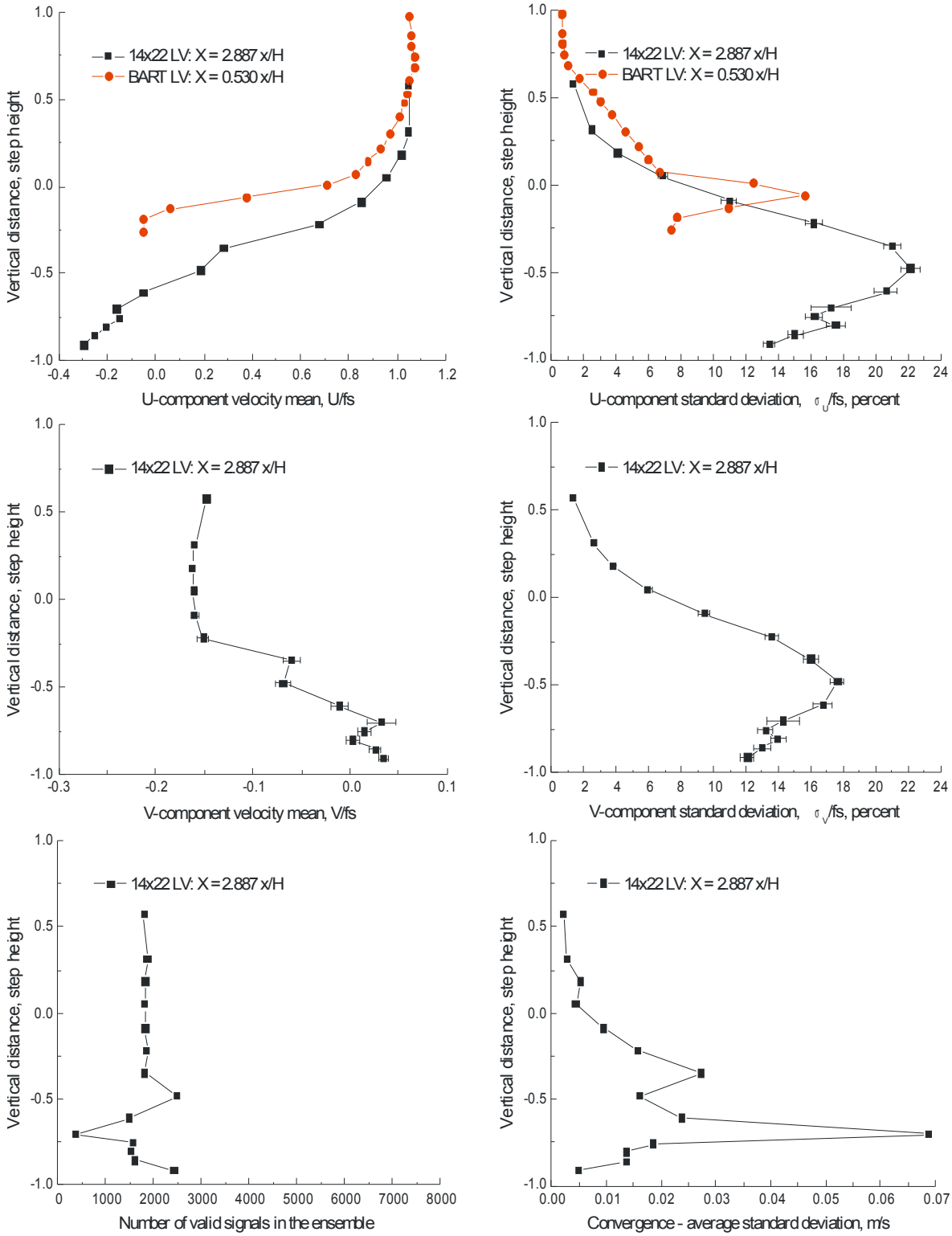

Figure VII.4.k.- Vertical scan 2.887 x/H downstream of a 1.5-inch backward-facing step: streamwise and vertical velocity components, number of accepted signal bursts, and statistical stationarity convergence standard deviation, fs = 45.0 m/s.

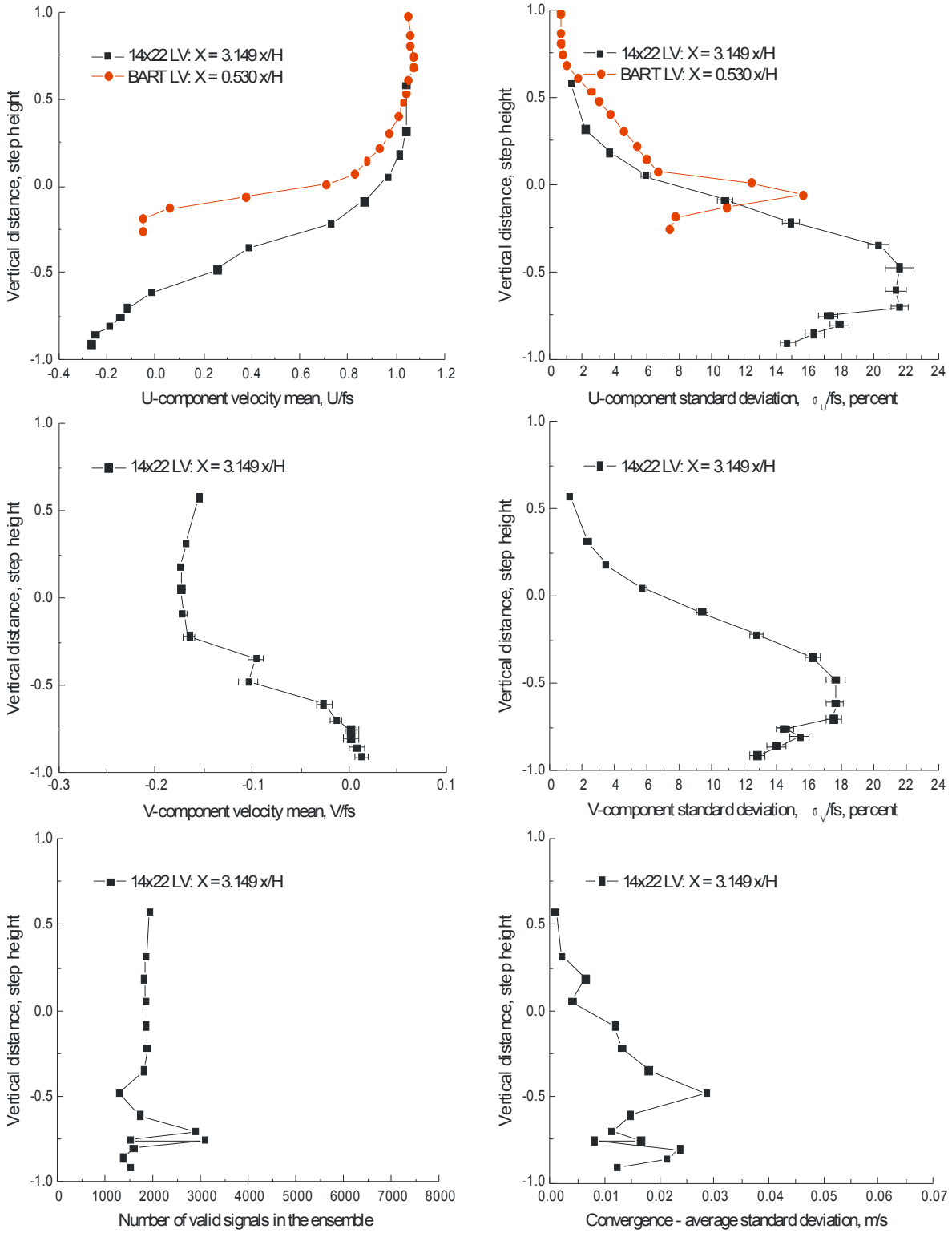

Figure VII.4.I.- Vertical scan 3.149 x/H downstream of a 1.5-inch backward-facing step: streamwise and vertical velocity components, number of accepted signal bursts, and statistical stationarity convergence standard deviation, fs = 45.0 m/s.

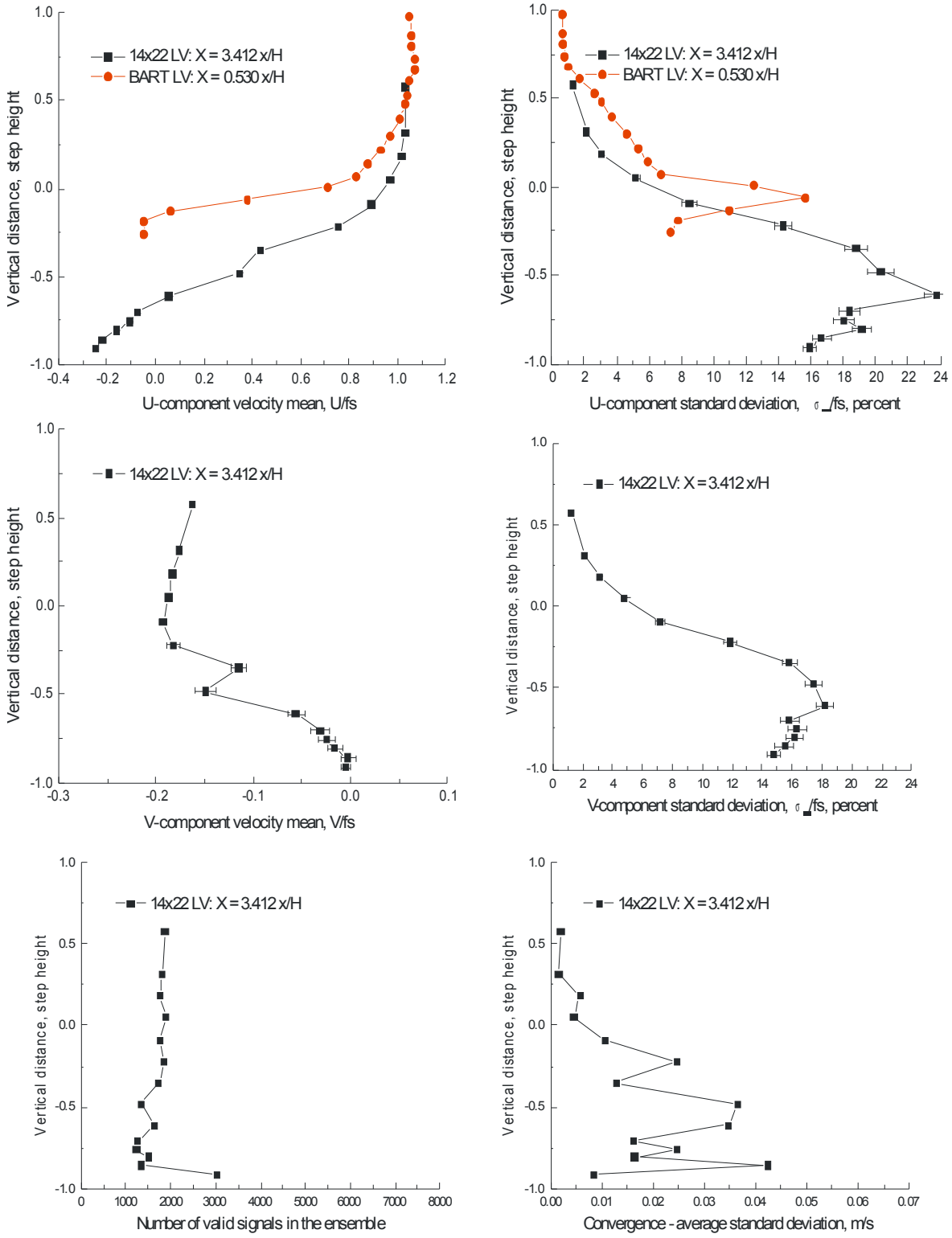

Figure VII.4.m.- Vertical scan 3.412 x/H downstream of a 1.5-inch backward-facing step: streamwise and vertical velocity components, number of accepted signal bursts, and statistical stationarity convergence standard deviation, fs = 45.0 m/s.

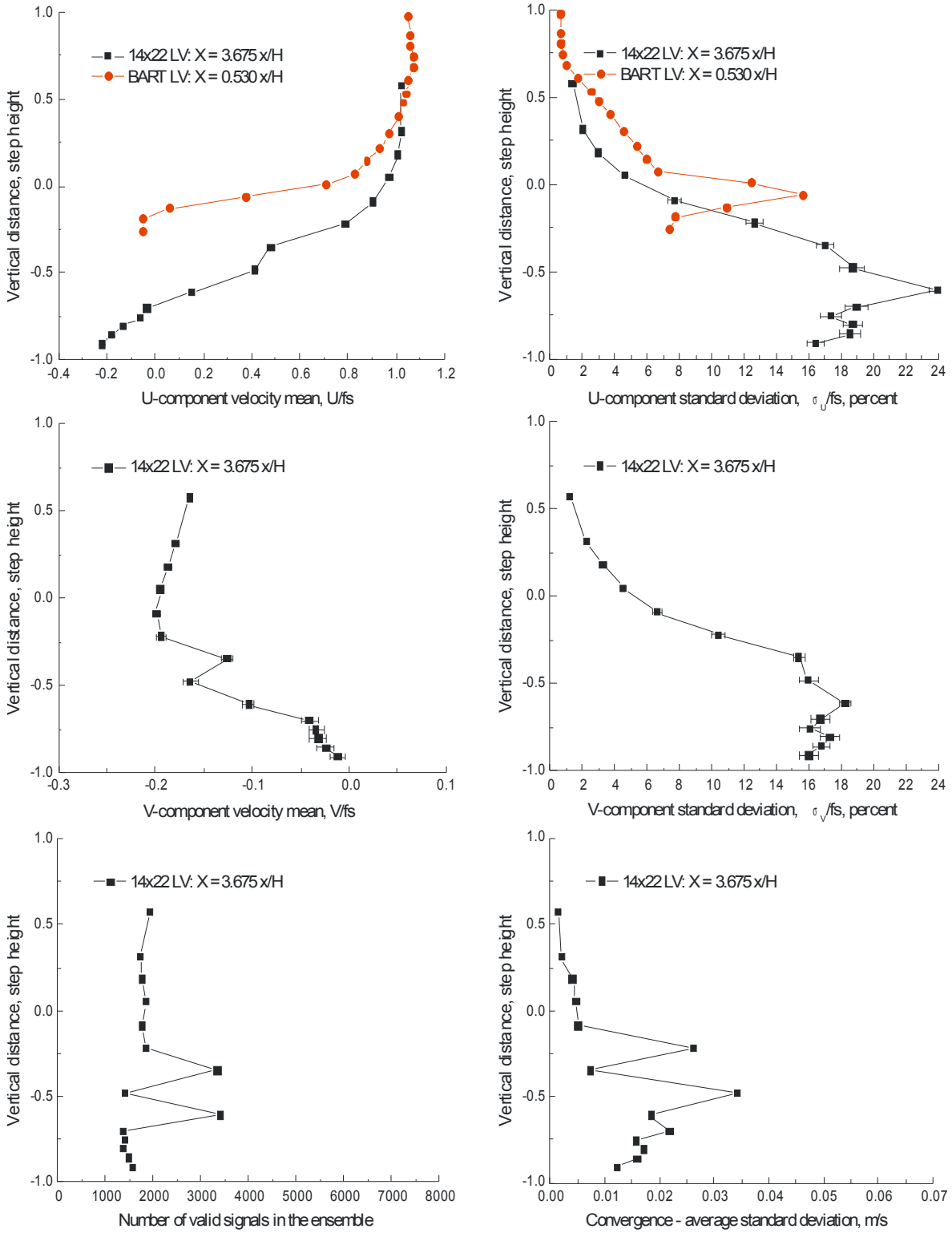

Figure VII.4.n.- Vertical scan 3.675 x/H downstream of a 1.5-inch backward-facing step: streamwise and vertical velocity components, number of accepted signal bursts, and statistical stationarity convergence standard deviation, fs = 45.0 m/s.

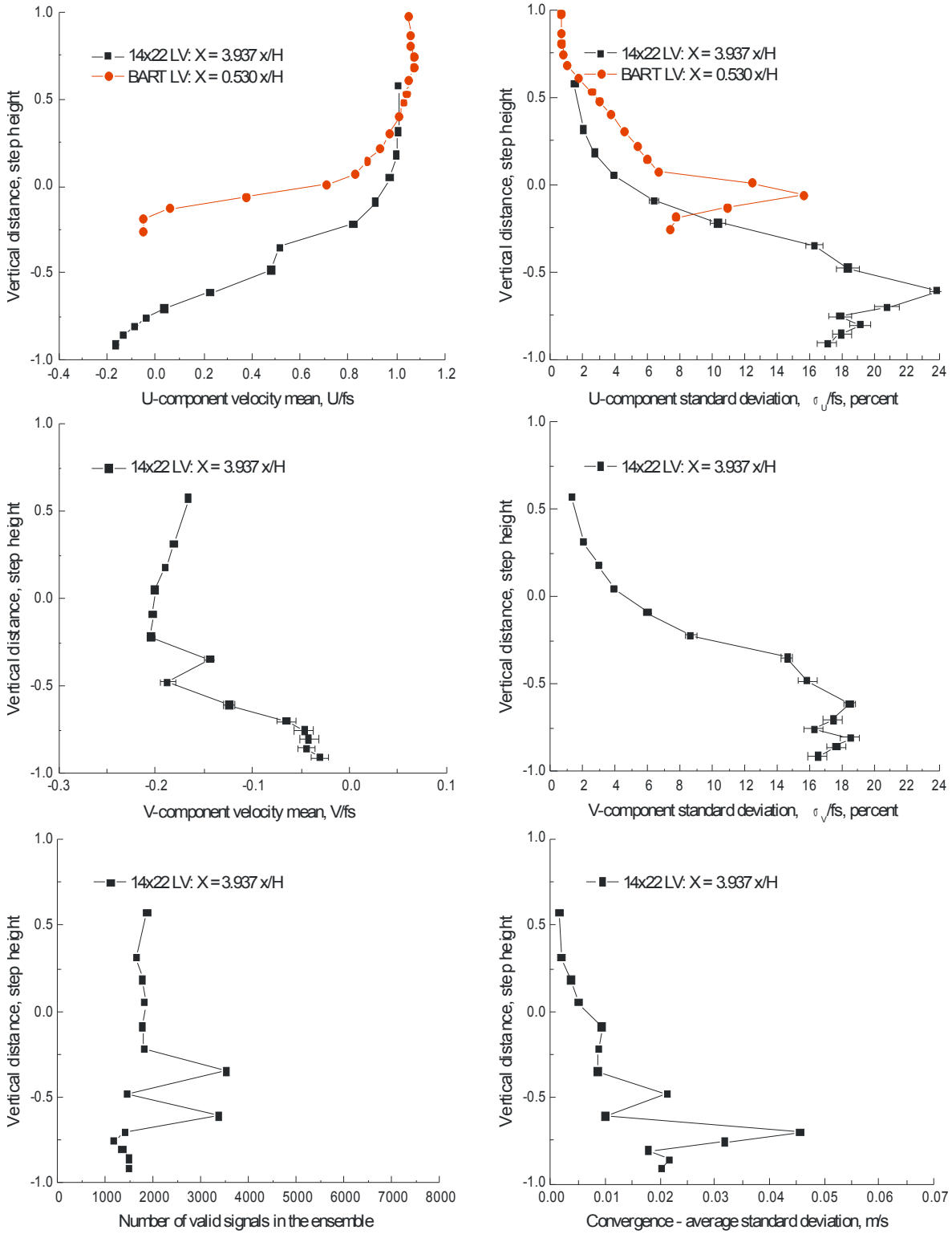

Figure VII.4.o.- Vertical scan 3.937 x/H downstream of a 1.5-inch backward-facing step: streamwise and vertical velocity components, number of accepted signal bursts, and statistical stationarity convergence standard deviation, fs = 45.0 m/s.

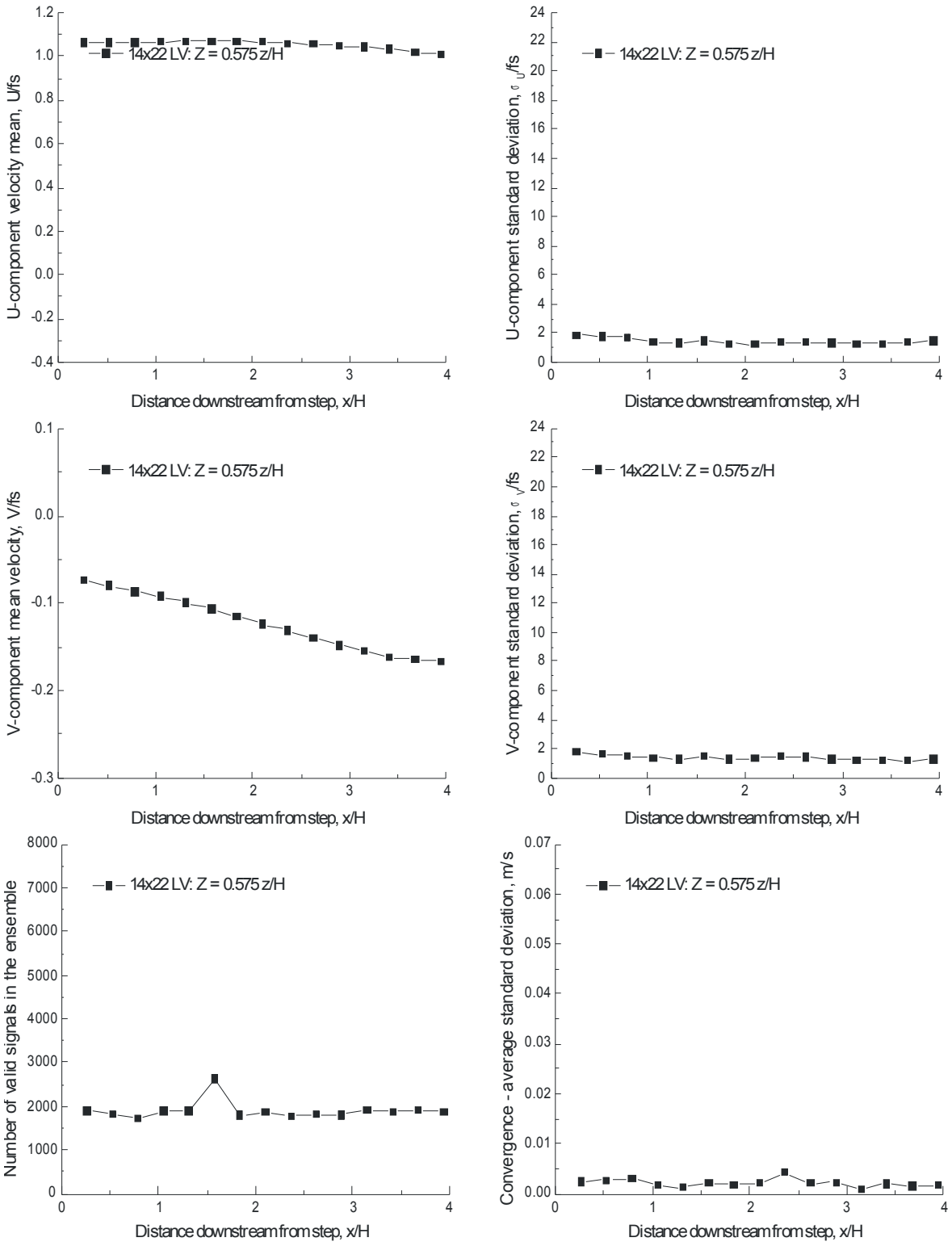

Figure VII.5.a.- Horizontal scan 0.575 z/H above a 1.5-inch backward-facing step: streamwise and vertical velocity components, number of accepted signal bursts, and statistical stationarity convergence standard deviation, fs = 45.0 m/s.

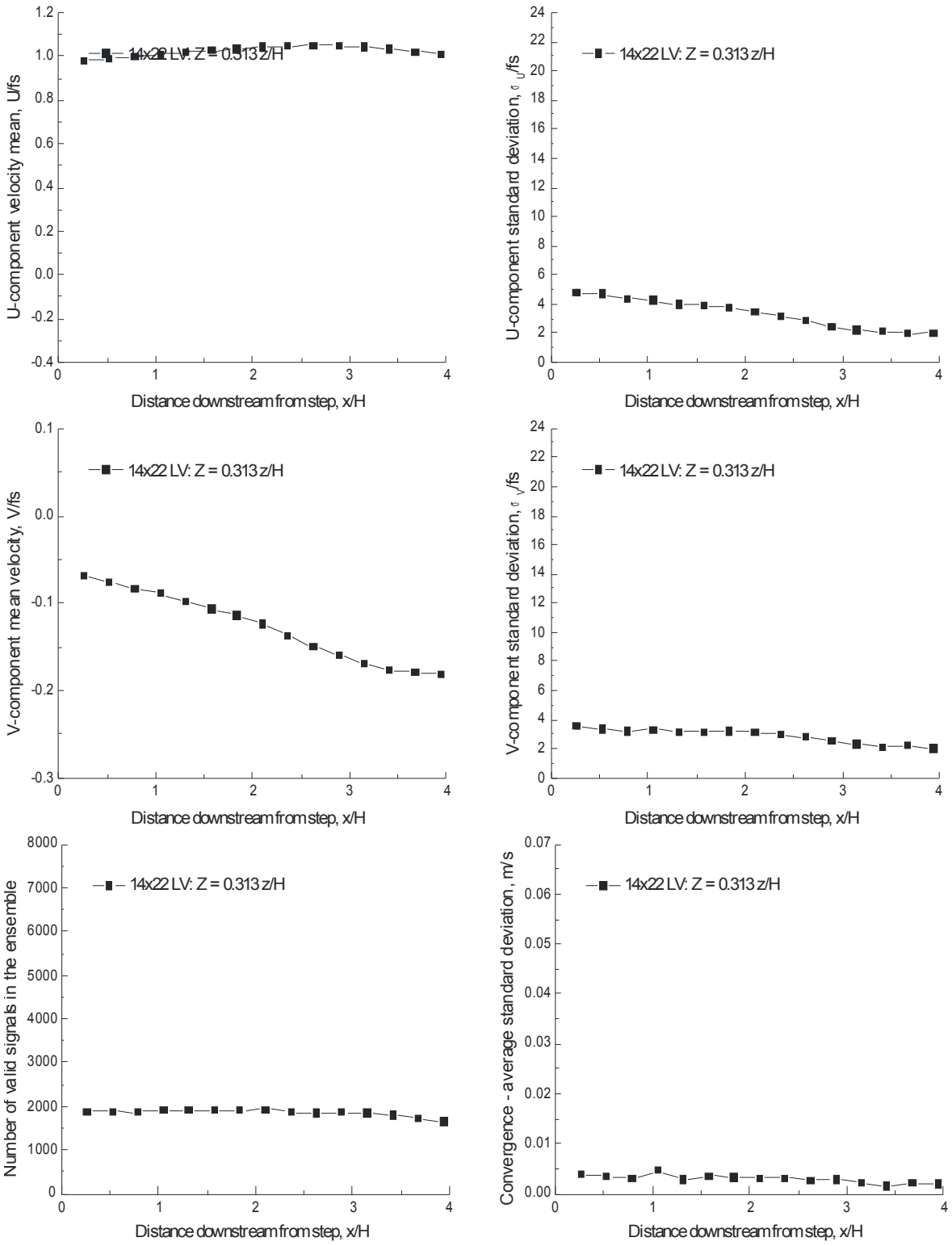

Figure VII.5.b.- Horizontal scan 0.313 z/H above a 1.5-inch backward-facing step: streamwise and vertical velocity components, number of accepted signal bursts, and statistical stationarity convergence standard deviation, fs = 45.0 m/s.

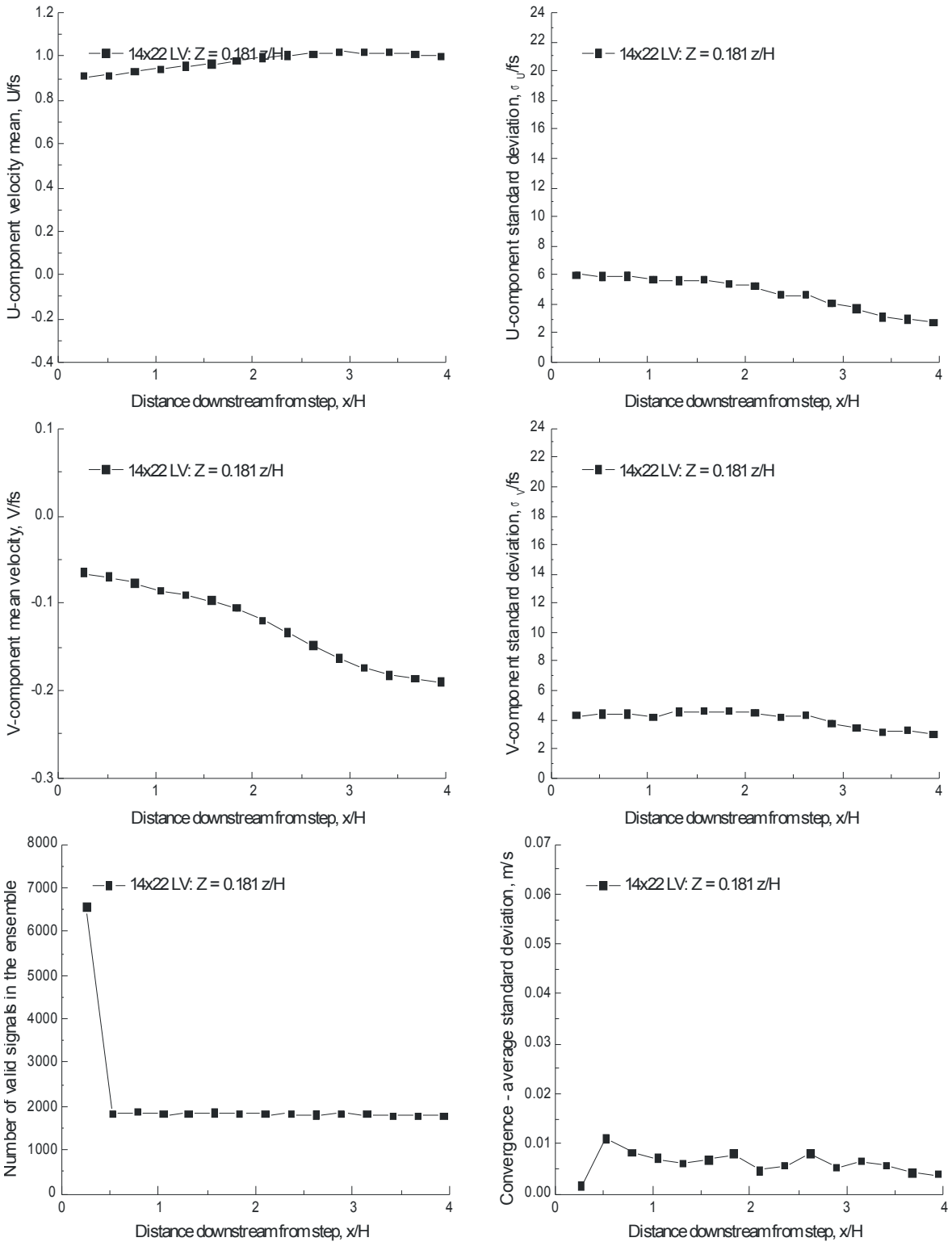

Figure VII.5.c.- Horizontal scan 0.181 z/H above a 1.5-inch backward-facing step: streamwise and vertical velocity components, number of accepted signal bursts, and statistical stationarity convergence standard deviation, fs = 45.0 m/s.

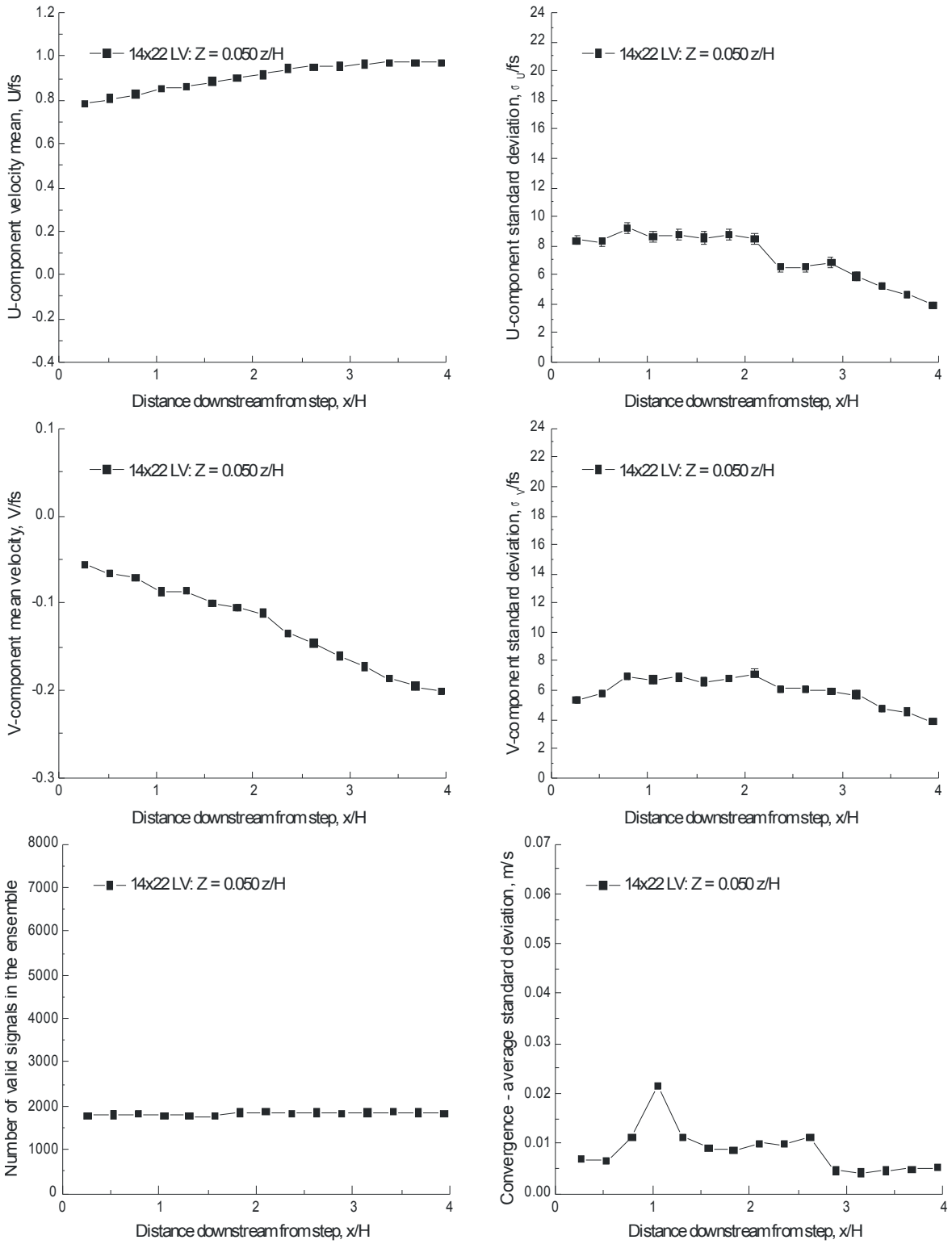

Figure VII.5.d.- Horizontal scan 0.050 z/H above a 1.5-inch backward-facing step: streamwise and vertical velocity components, number of accepted signal bursts, and statistical stationarity convergence standard deviation, fs = 45.0 m/s.

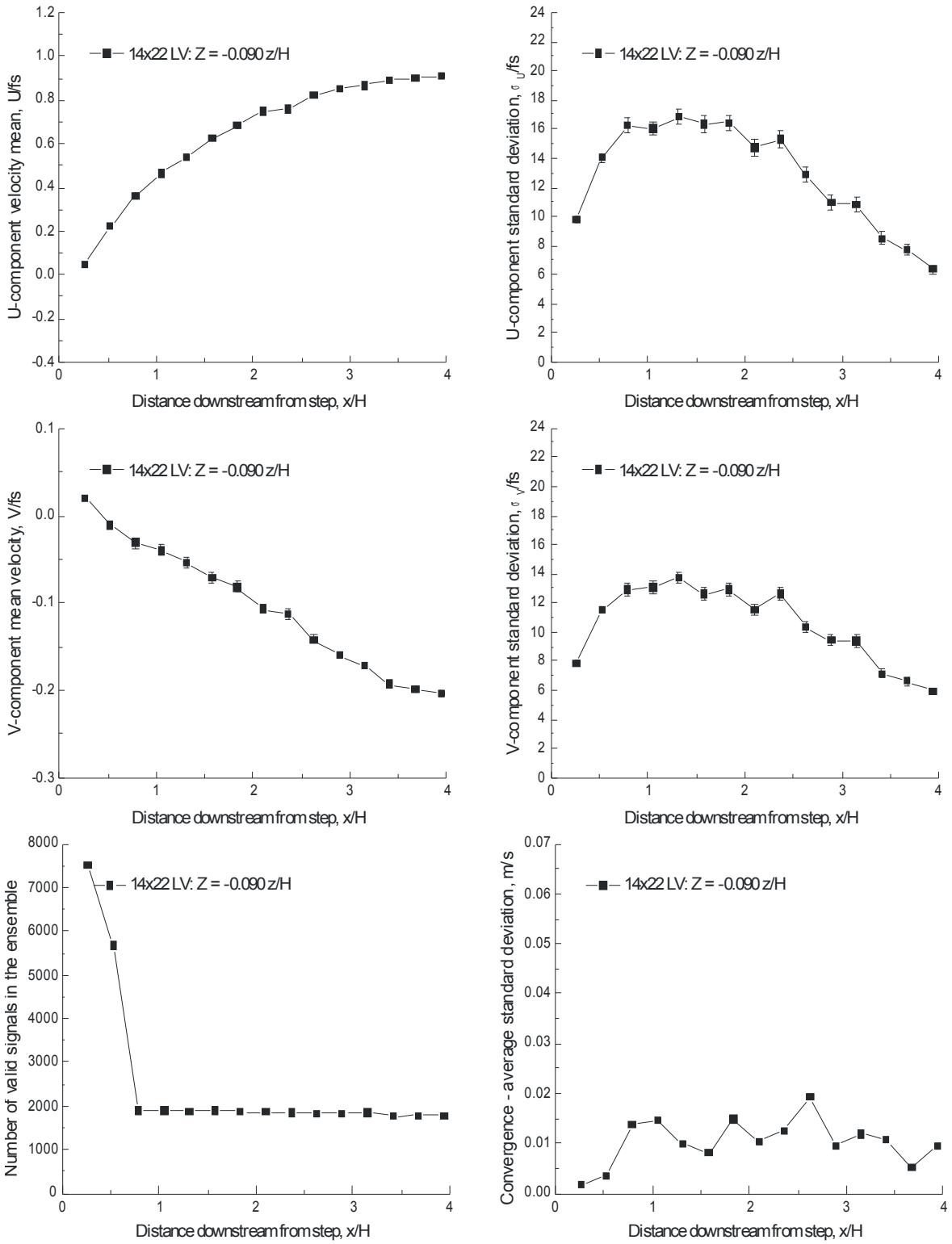

Figure VII.5.e.- Horizontal scan 0.090 z/H below a 1.5-inch backward-facing step: streamwise and vertical velocity components, number of accepted signal bursts, and statistical stationarity convergence standard deviation, fs = 45.0 m/s.

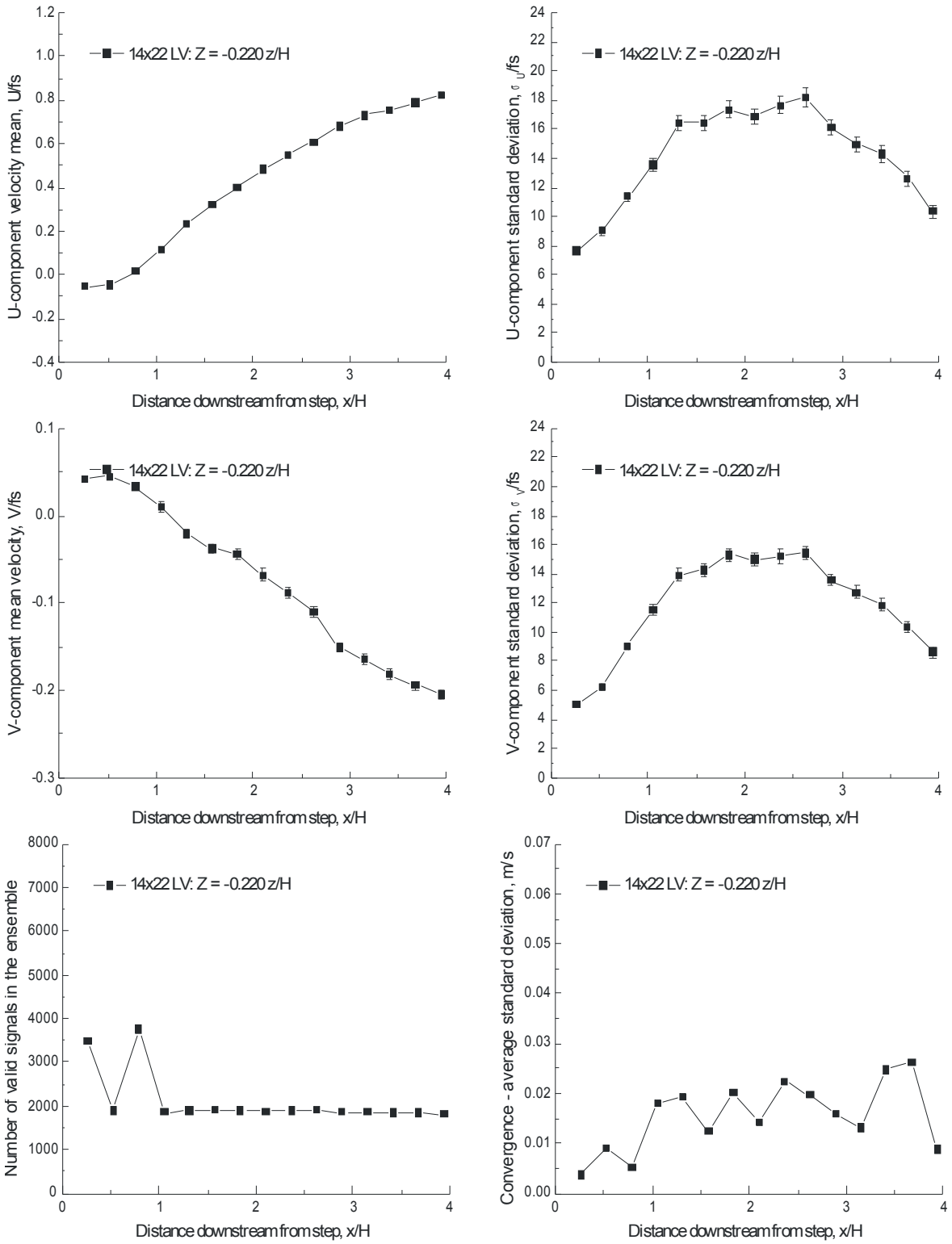

Figure VII.5.f.- Horizontal scan 0.220 z/H below a 1.5-inch backward-facing step: streamwise and vertical velocity components, number of accepted signal bursts, and statistical stationarity convergence standard deviation, fs = 45.0 m/s.

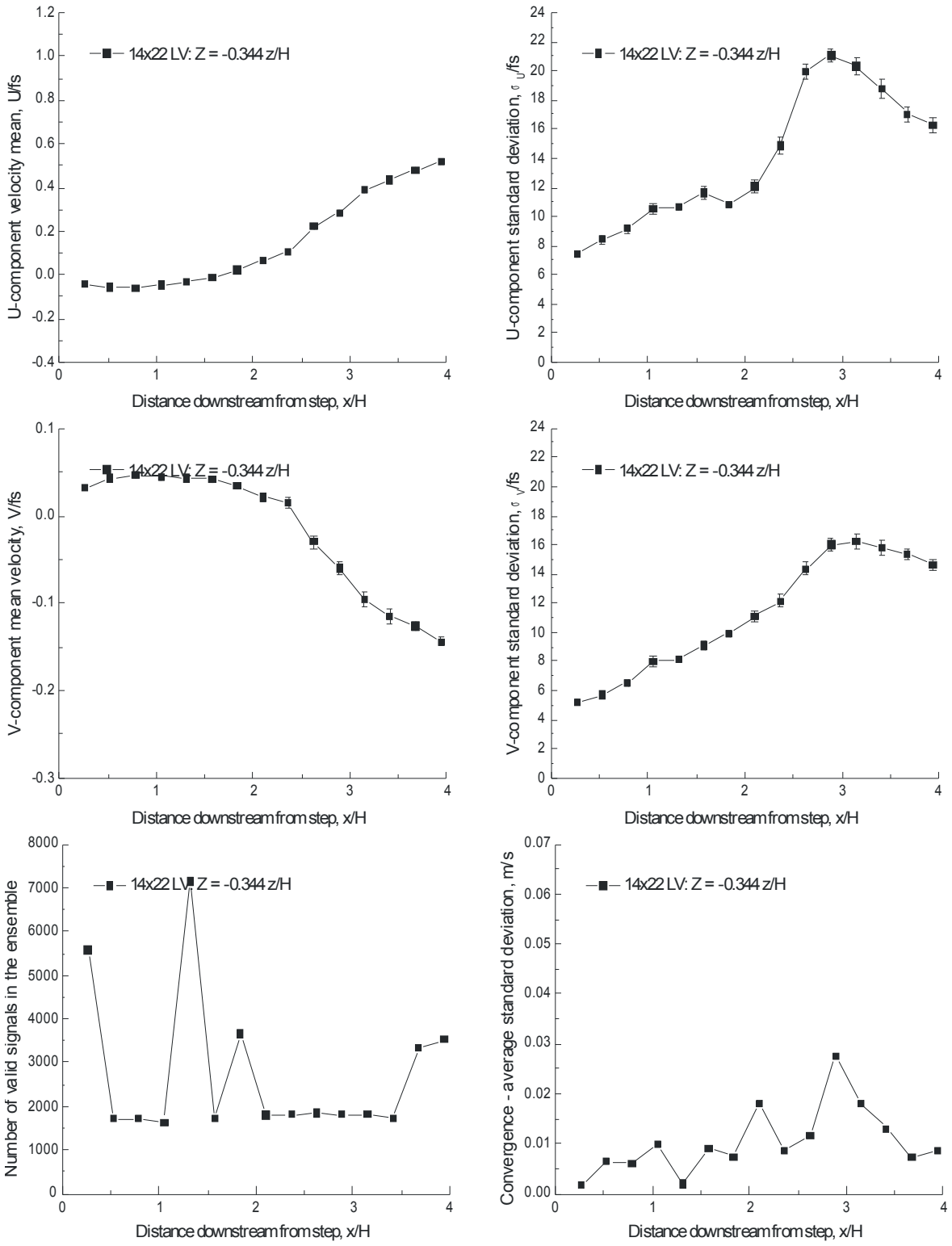

Figure VII.5.g.- Horizontal scan 0.344 z/H below a 1.5-inch backward-facing step: streamwise and vertical velocity components, number of accepted signal bursts, and statistical stationarity convergence standard deviation, fs = 45.0 m/s.

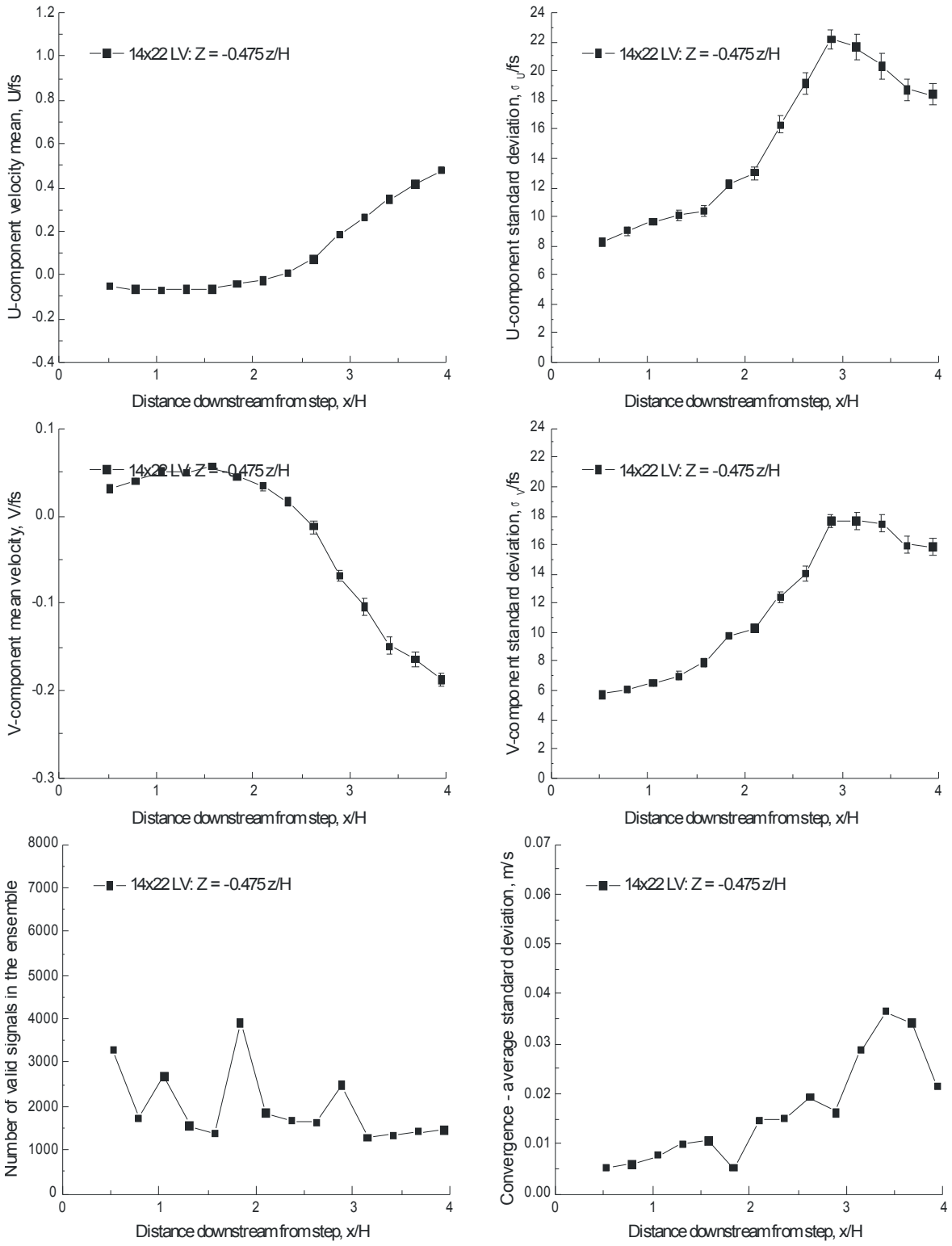

Figure VII.5.h.- Horizontal scan 0.475 z/H below a 1.5-inch backward-facing step: streamwise and vertical velocity components, number of accepted signal bursts, and statistical stationarity convergence standard deviation, fs = 45.0 m/s.

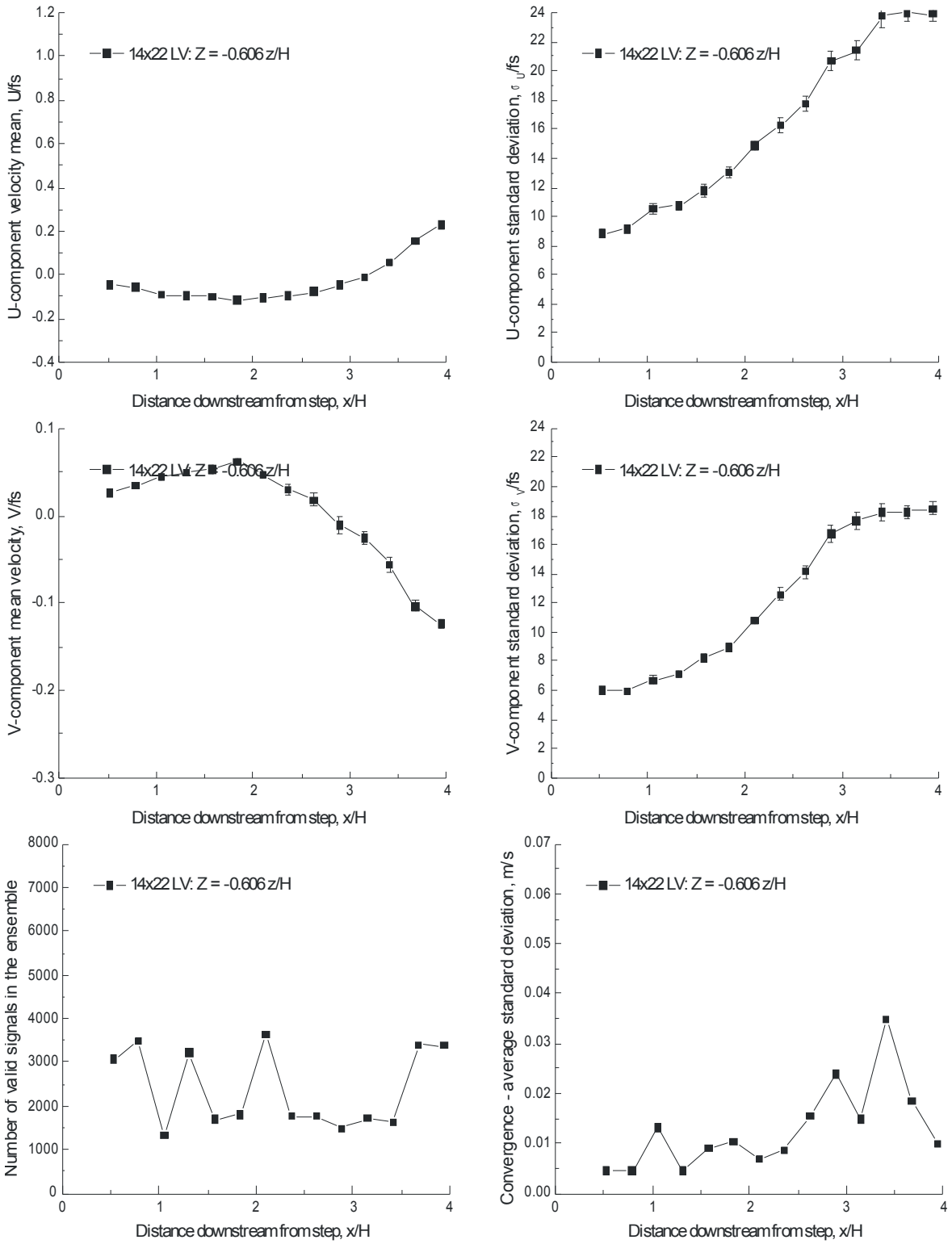

Figure VII.5.i.- Horizontal scan 0.606 z/H below a 1.5-inch backward-facing step: streamwise and vertical velocity components, number of accepted signal bursts, and statistical stationarity convergence standard deviation, fs = 45.0 m/s.

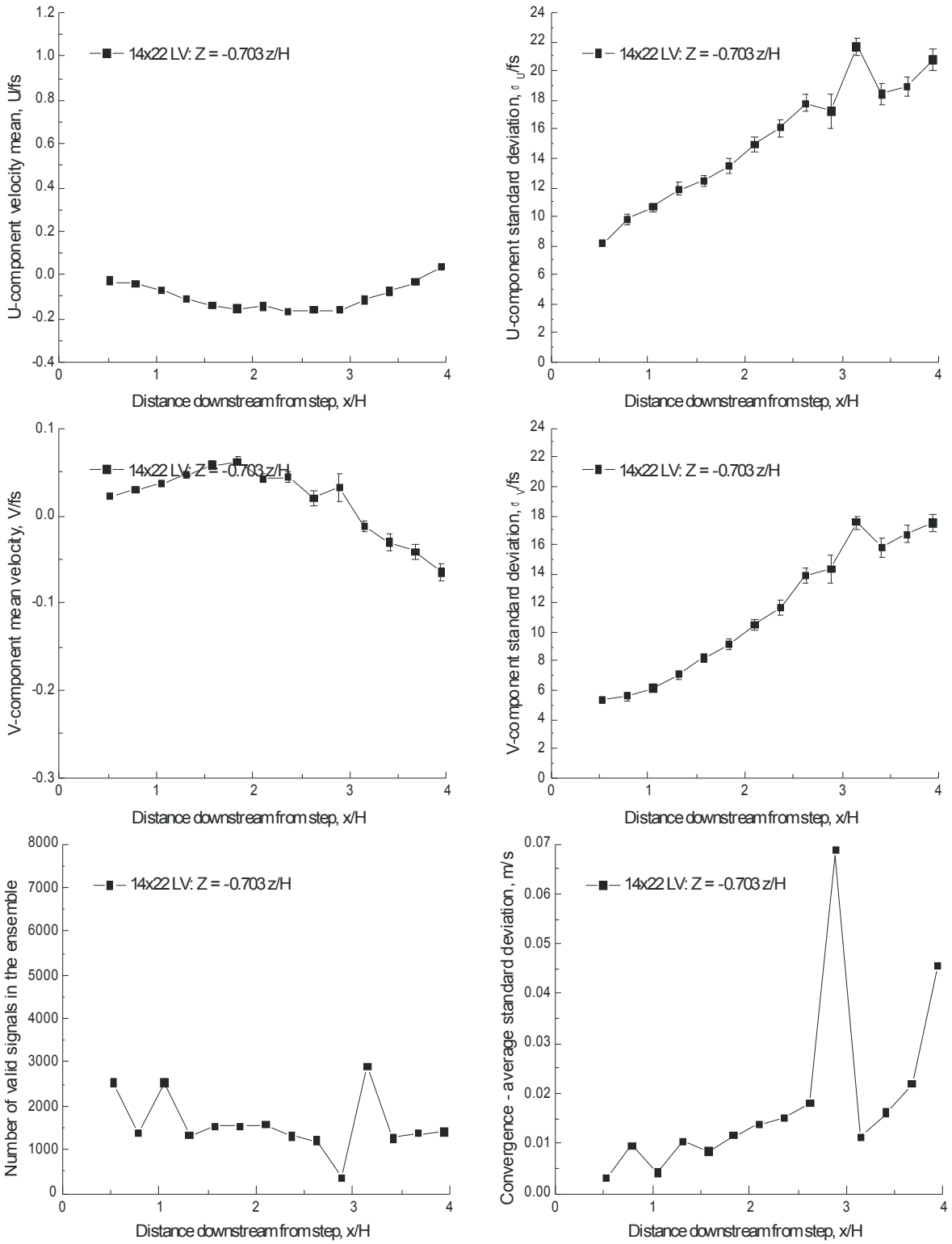

Figure VII.5.j.- Horizontal scan 0.703 z/H below a 1.5-inch backward-facing step: streamwise and vertical velocity components, number of accepted signal bursts, and statistical stationarity convergence standard deviation, fs = 45.0 m/s.

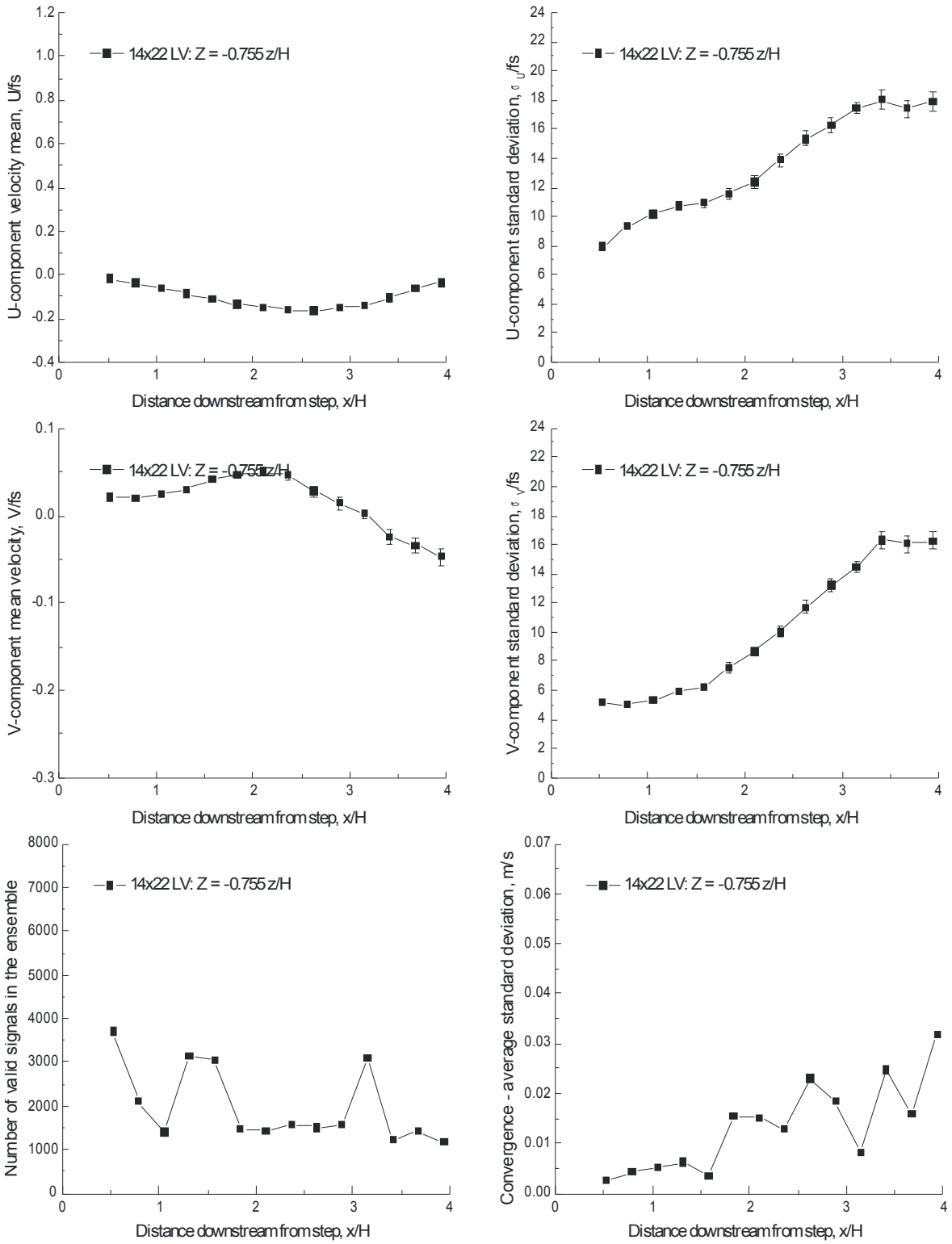

Figure VII.5.k.- Horizontal scan 0.755 z/H below a 1.5-inch backward-facing step: streamwise and vertical velocity components, number of accepted signal bursts, and statistical stationarity convergence standard deviation, fs = 45.0 m/s.

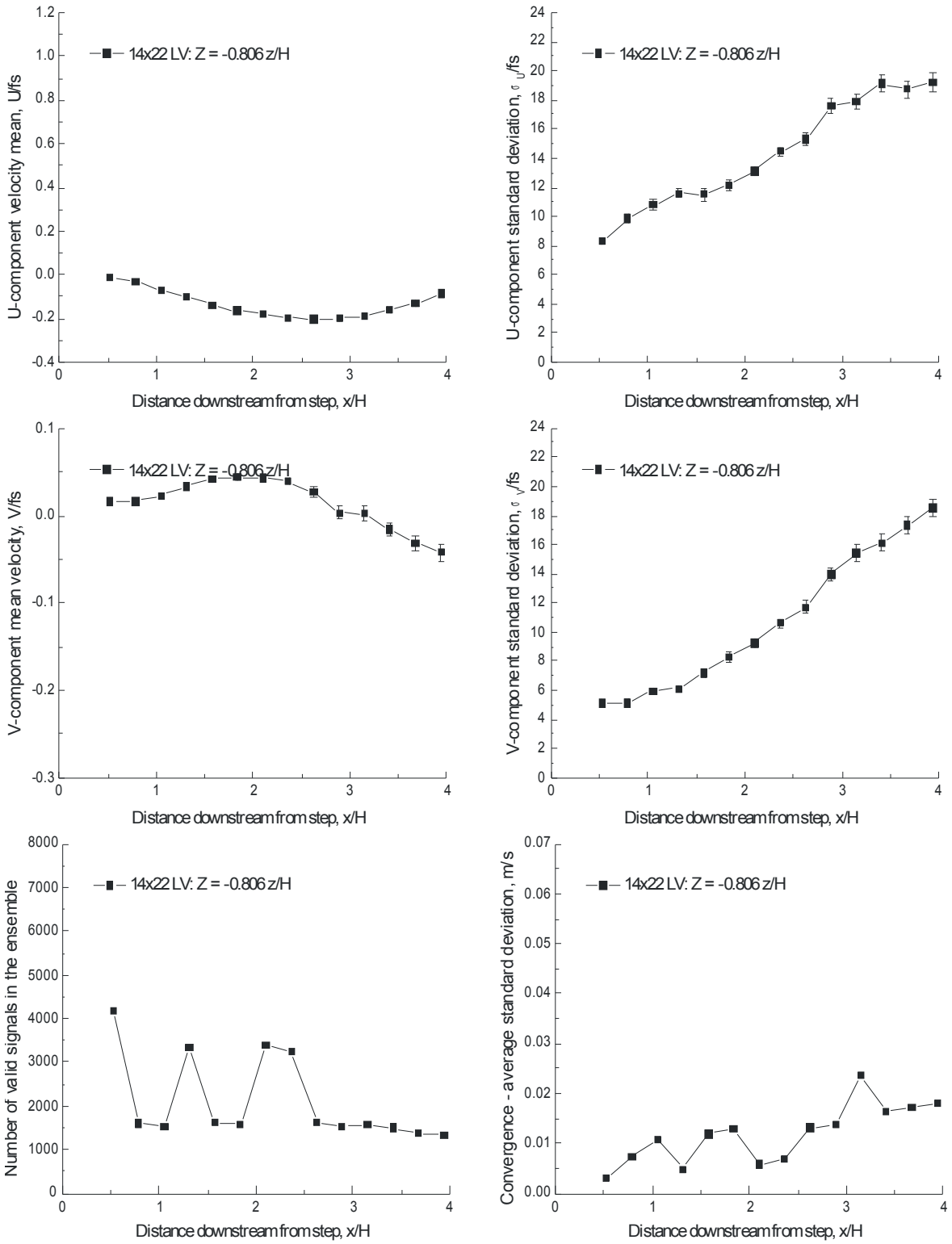

Figure VII.5.l.- Horizontal scan 0.806 z/H below a 1.5-inch backward-facing step: streamwise and vertical velocity components, number of accepted signal bursts, and statistical stationarity convergence standard deviation, fs = 45.0 m/s.

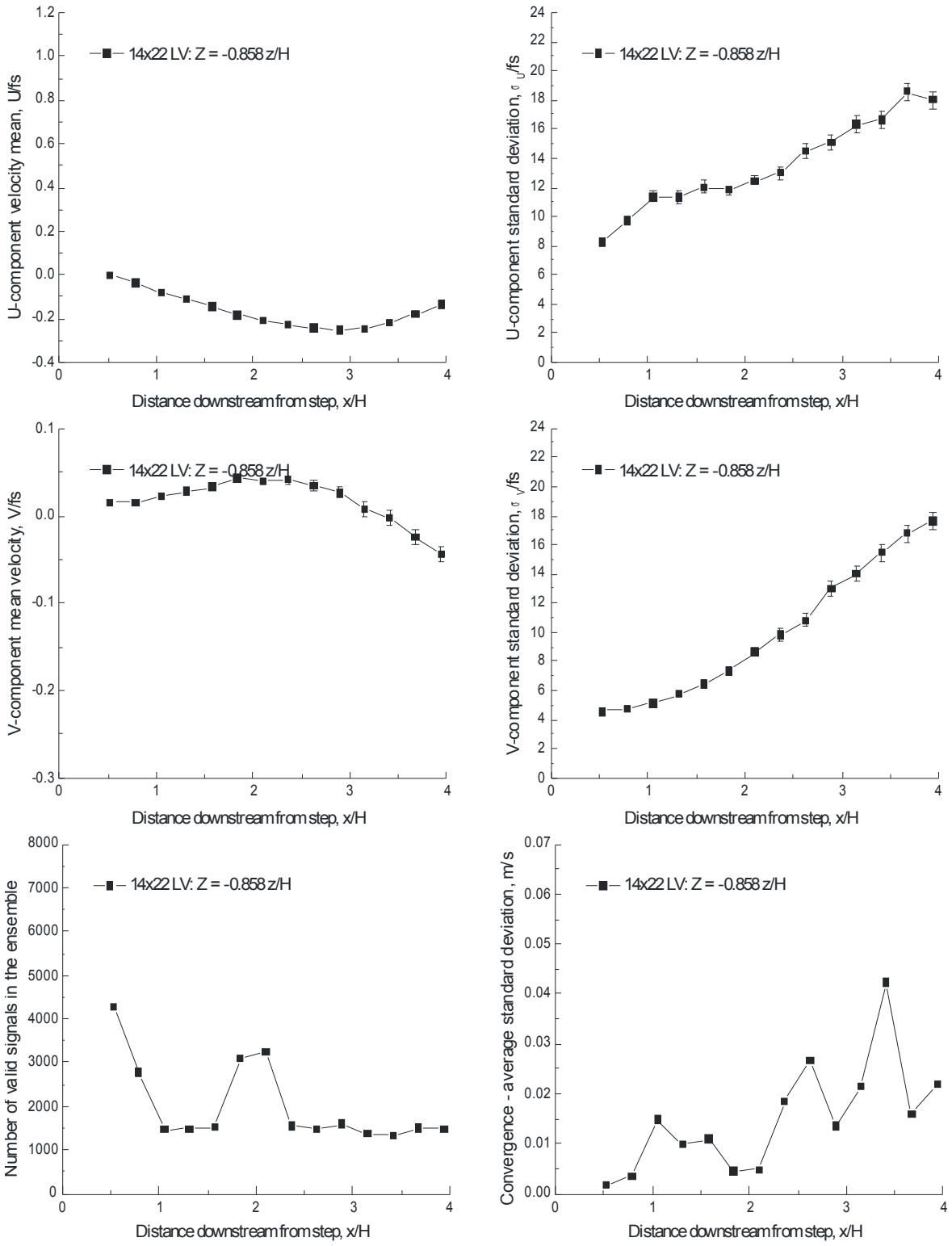

Figure VII.5.m.- Horizontal scan 0.858 z/H below a 1.5-inch backward-facing step: streamwise and vertical velocity components, number of accepted signal bursts, and statistical stationarity convergence standard deviation, fs = 45.0 m/s.

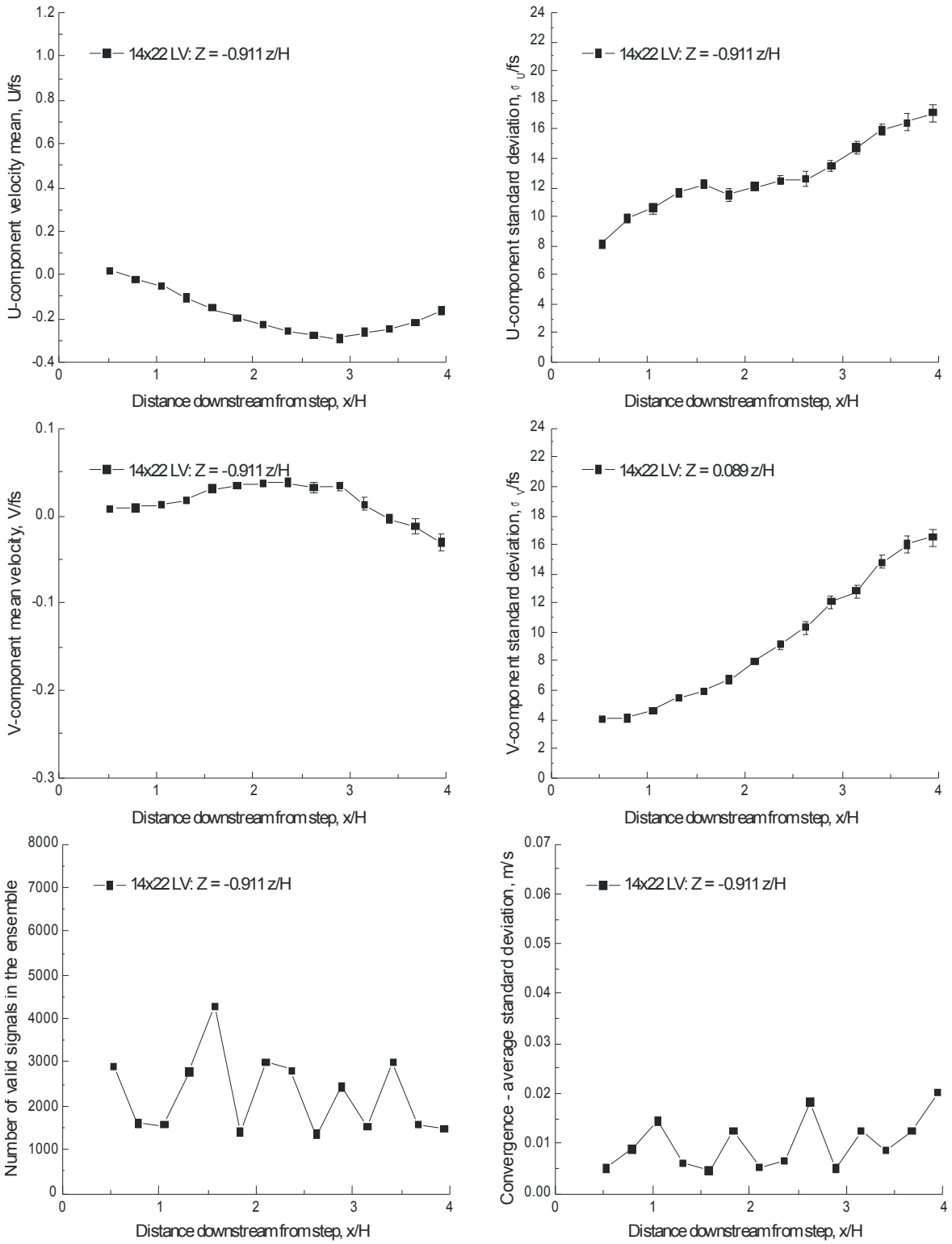

Figure VII.5.n.- Horizontal scan 0.911 z/H below a 1.5-inch backward-facing step: streamwise and vertical velocity components, number of accepted signal bursts, and statistical stationarity convergence standard deviation, fs = 45.0 m/s.

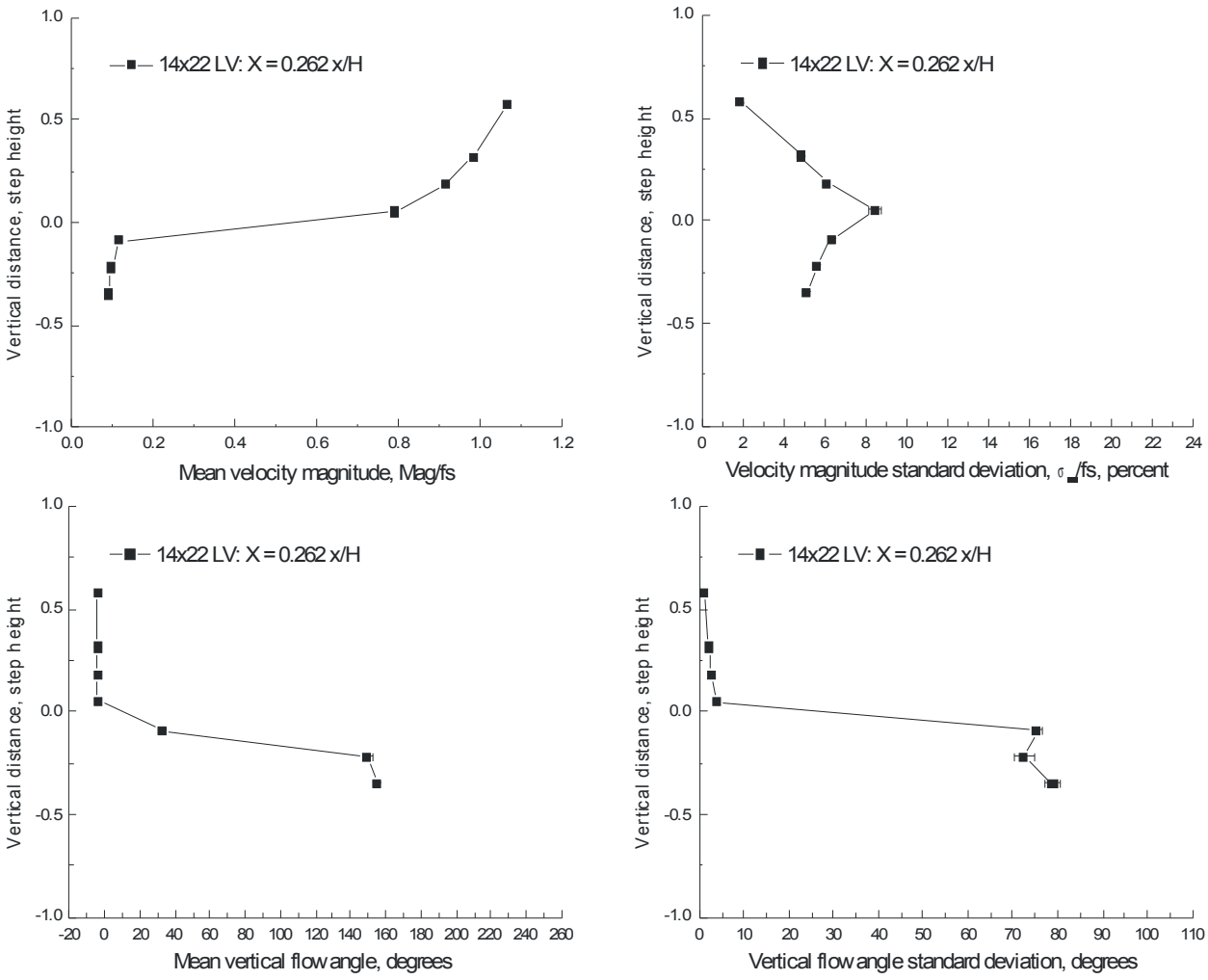

Figure VII.6.a.- Vertical scan 0.262 x/H downstream of a 1.5-inch backward-facing step: velocity magnitude and flow angle, fs = 45.0 m/s.

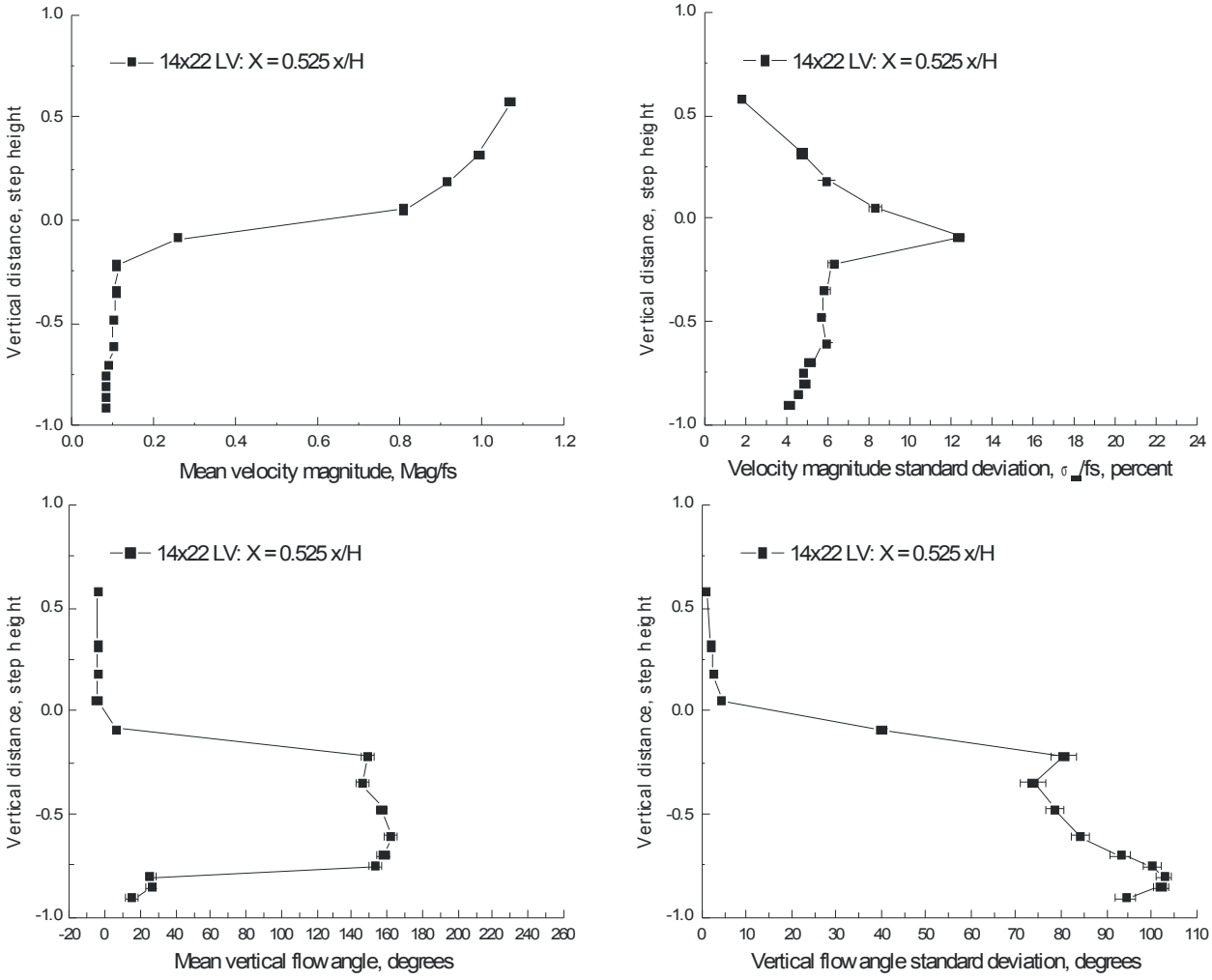

Figure VII.6.b.- Vertical scan 0.525 x/H downstream of a 1.5-inch backward-facing step: velocity magnitude and flow angle, fs = 45.0 m/s.

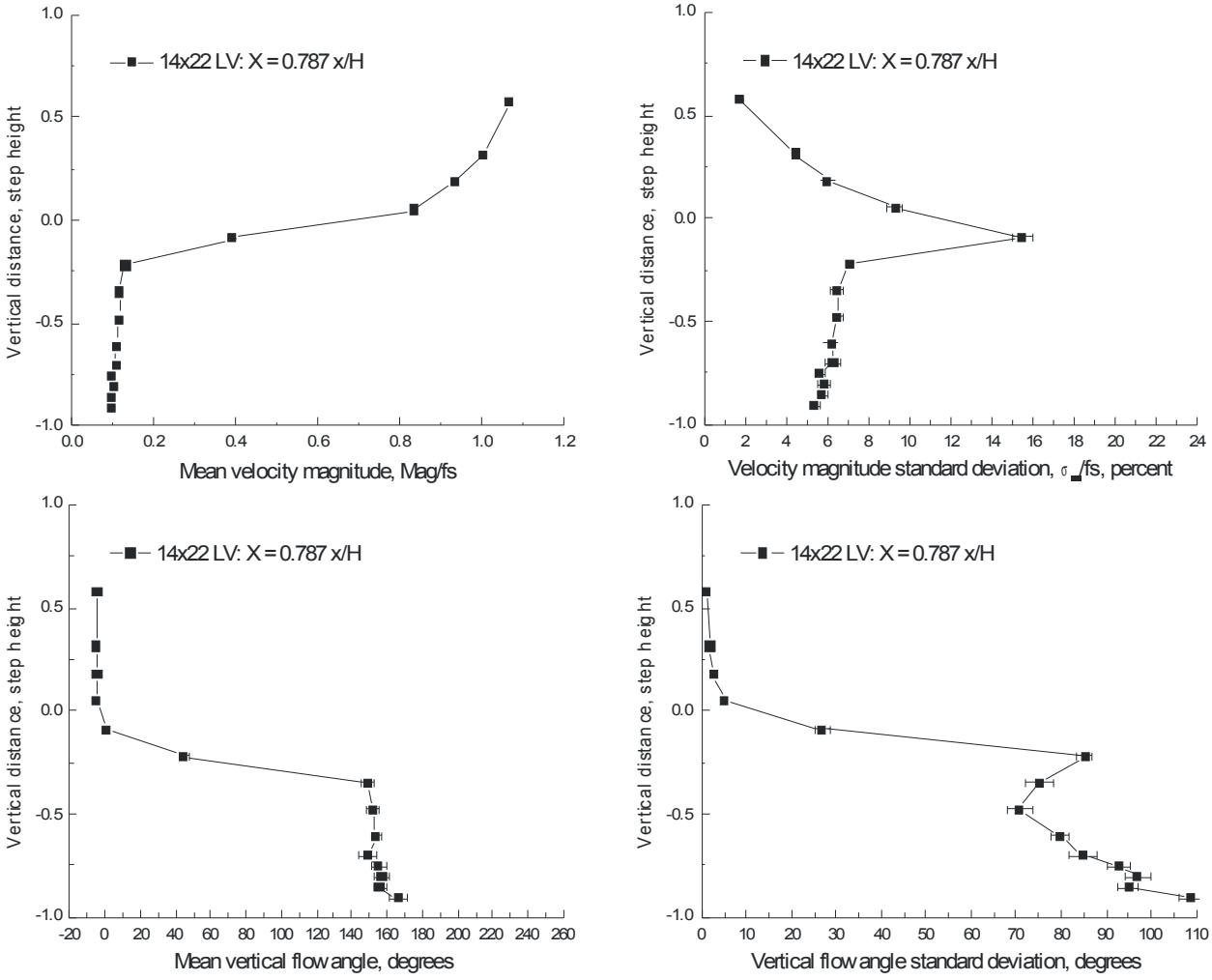

Figure VII.6.c.- Vertical scan 0.787 x/H downstream of a 1.5-inch backward-facing step: velocity magnitude and flow angle, fs = 45.0 m/s.

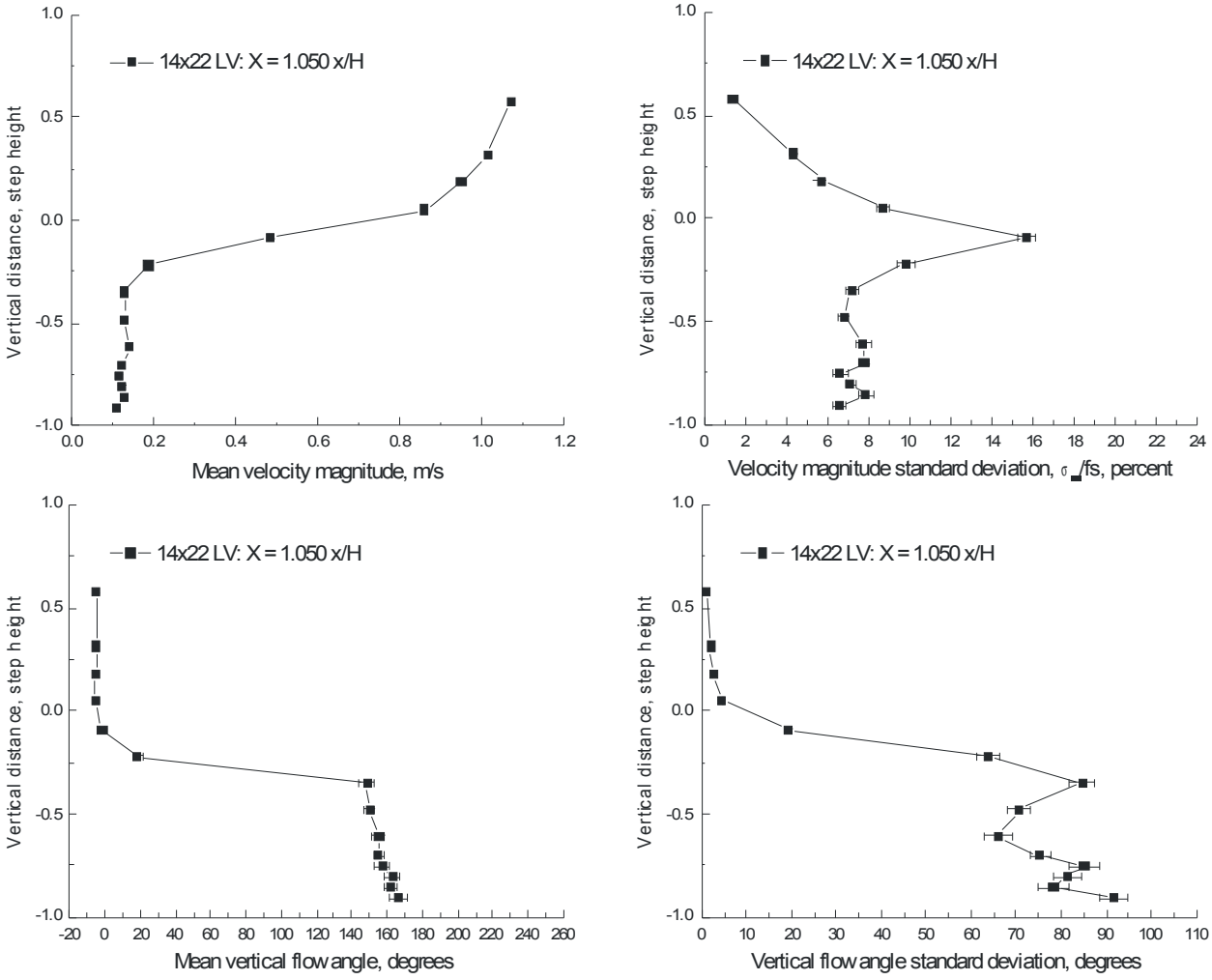

Figure VII.6.d.- Vertical scan 1.050 x/H downstream of a 1.5-inch backward-facing step: velocity magnitude and flow angle, fs = 45.0 m/s.

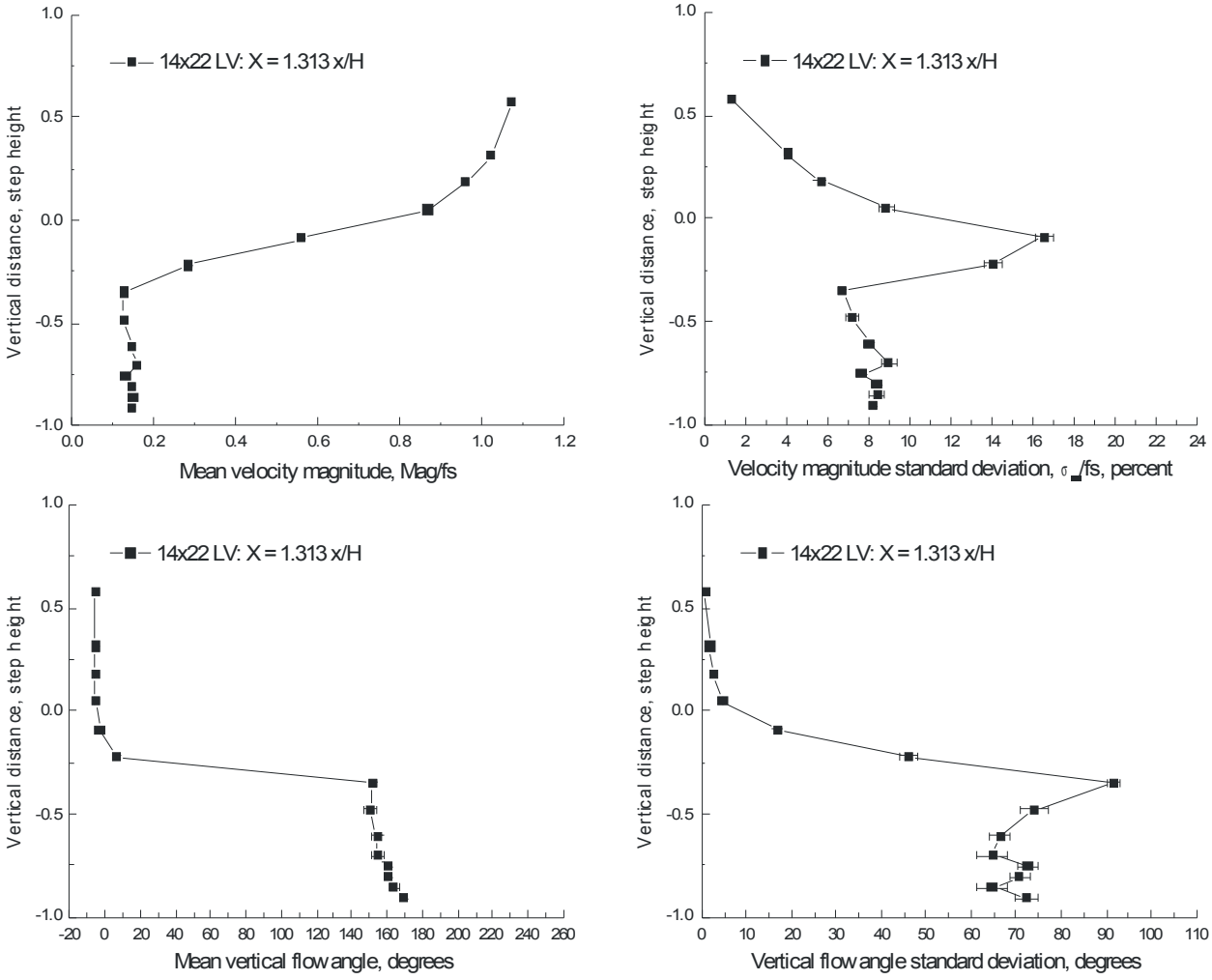

Figure VII.6.e.- Vertical scan 1.313 x/H downstream of a 1.5-inch backward-facing step: velocity magnitude and flow angle, fs = 45.0 m/s.

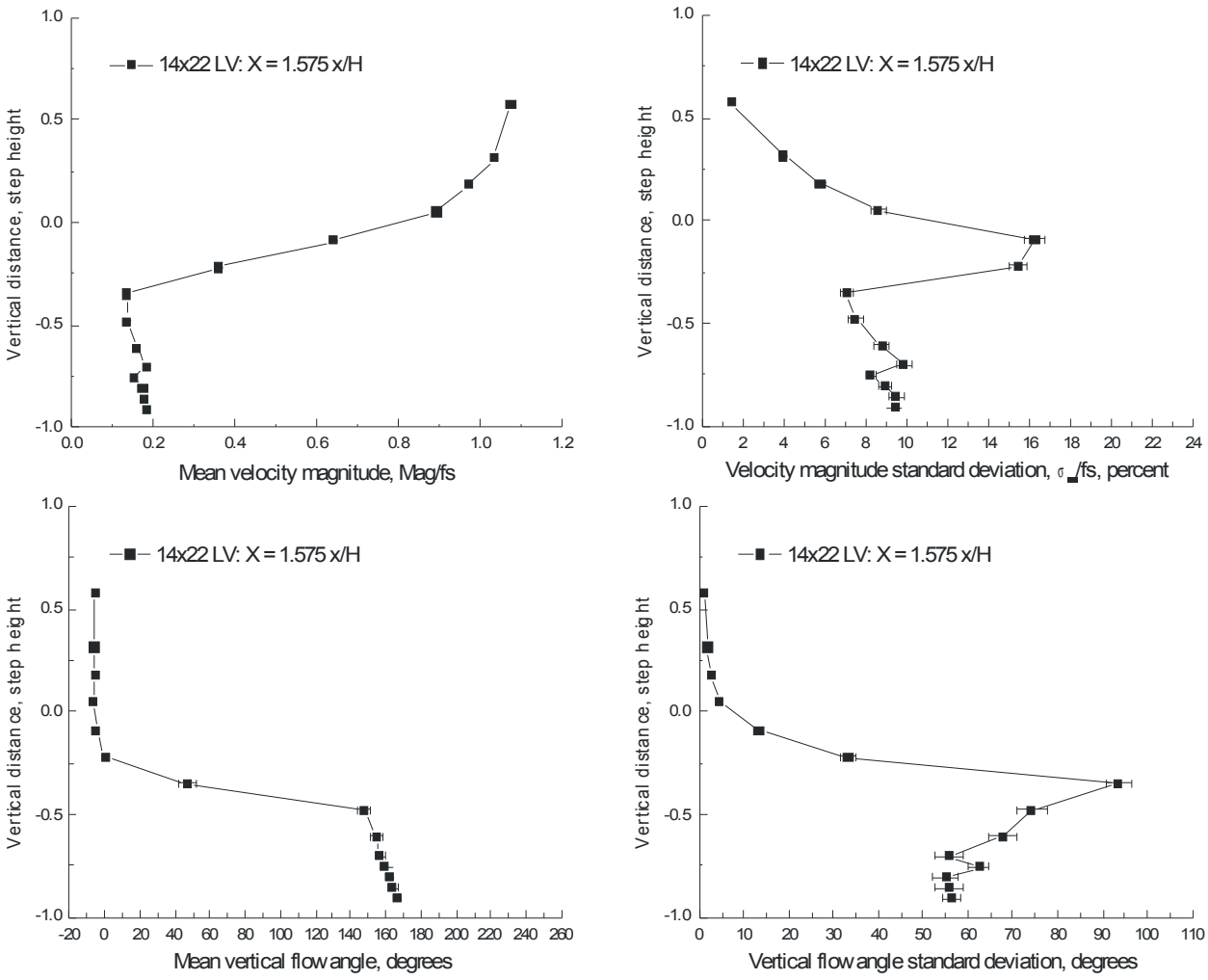

Figure VII.6.f.- Vertical scan 1.575 x/H downstream of a 1.5-inch backward-facing step: velocity magnitude and flow angle, fs = 45.0 m/s.

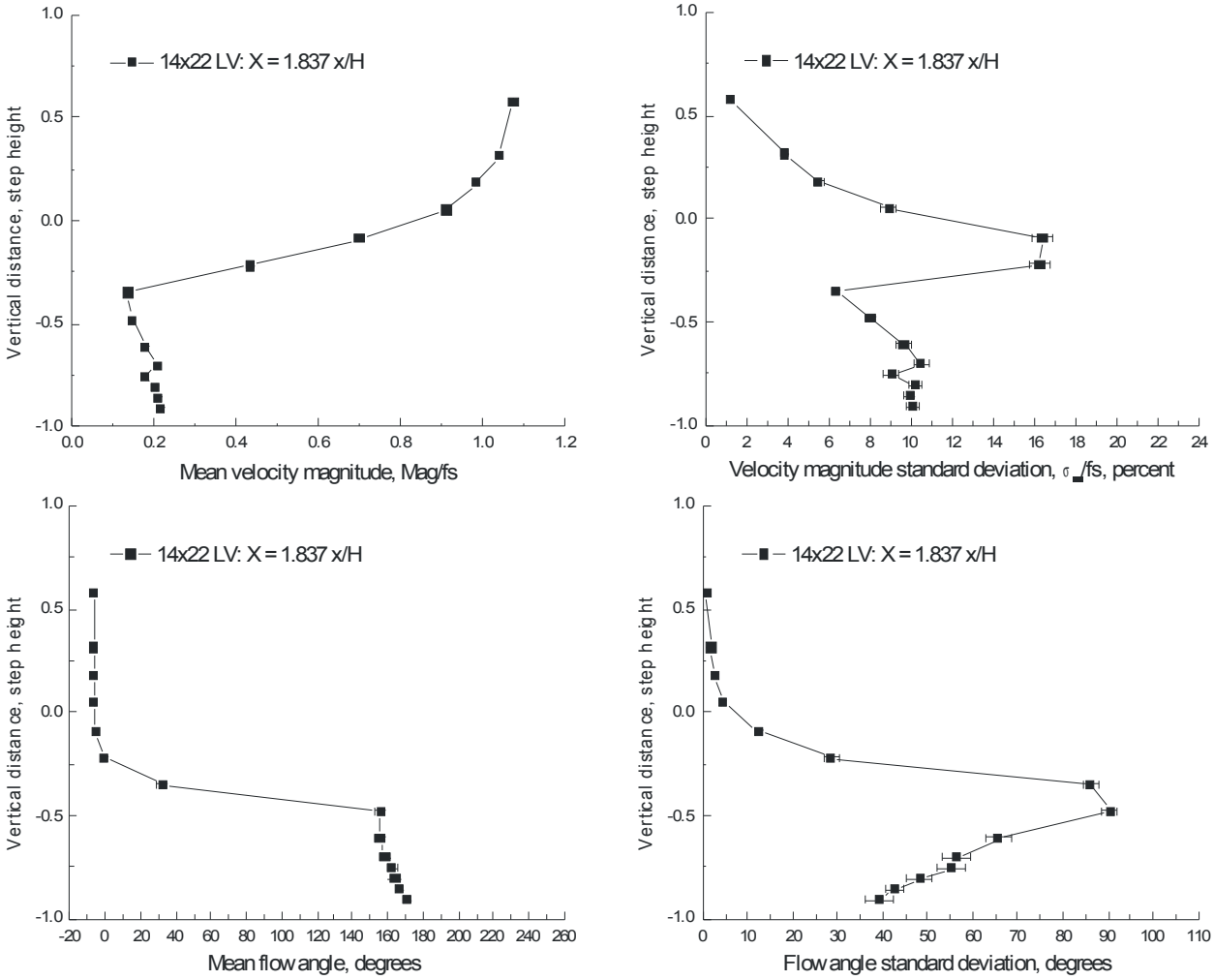

Figure VII.6.g.- Vertical scan 1.837 x/H downstream of a 1.5-inch backward-facing step: velocity magnitude and flow angle, fs = 45.0 m/s.

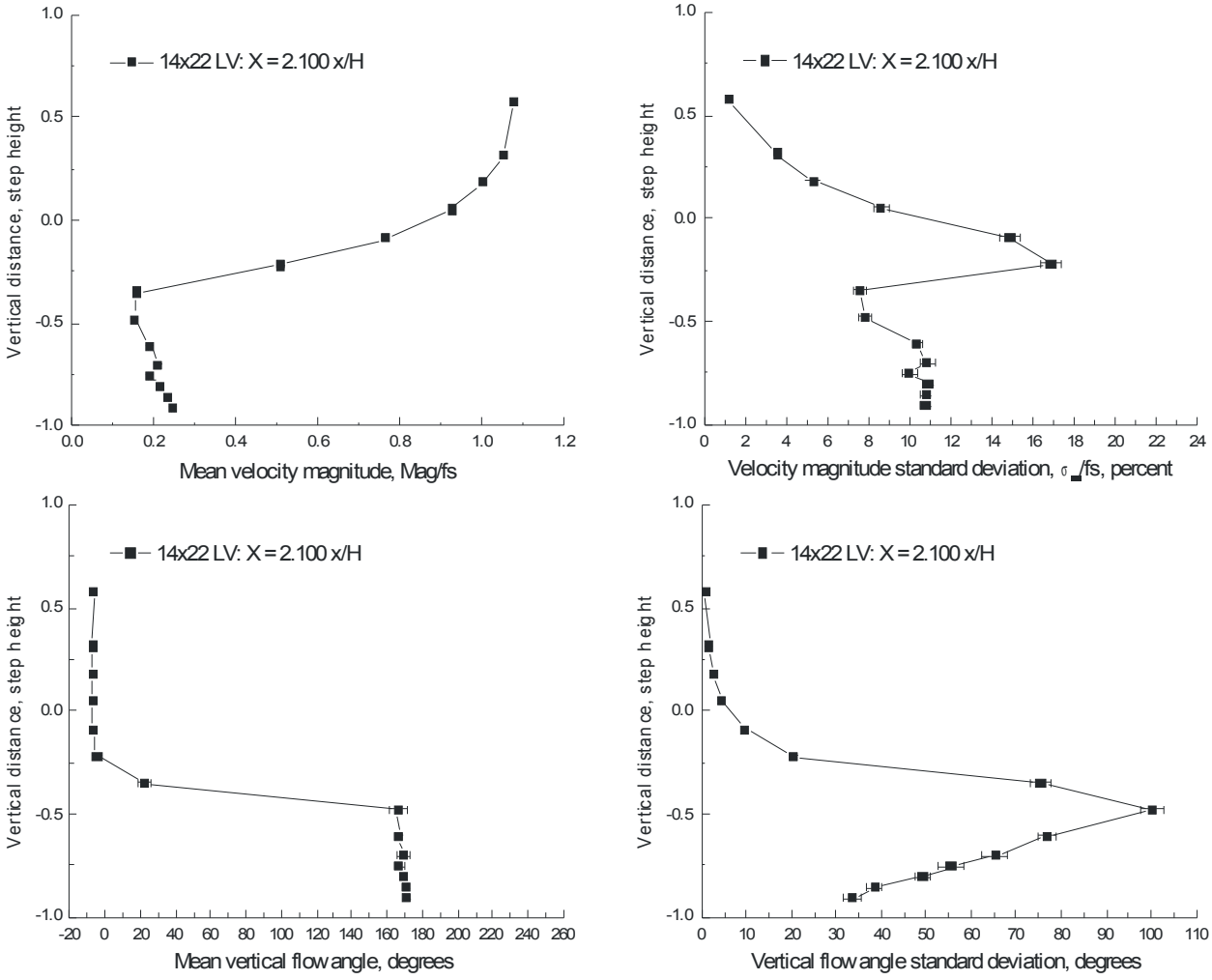

Figure VII.6.h.- Vertical scan 2.1 x/H downstream of a 1.5-inch backward-facing step: velocity magnitude and flow angle, fs = 45.0 m/s.

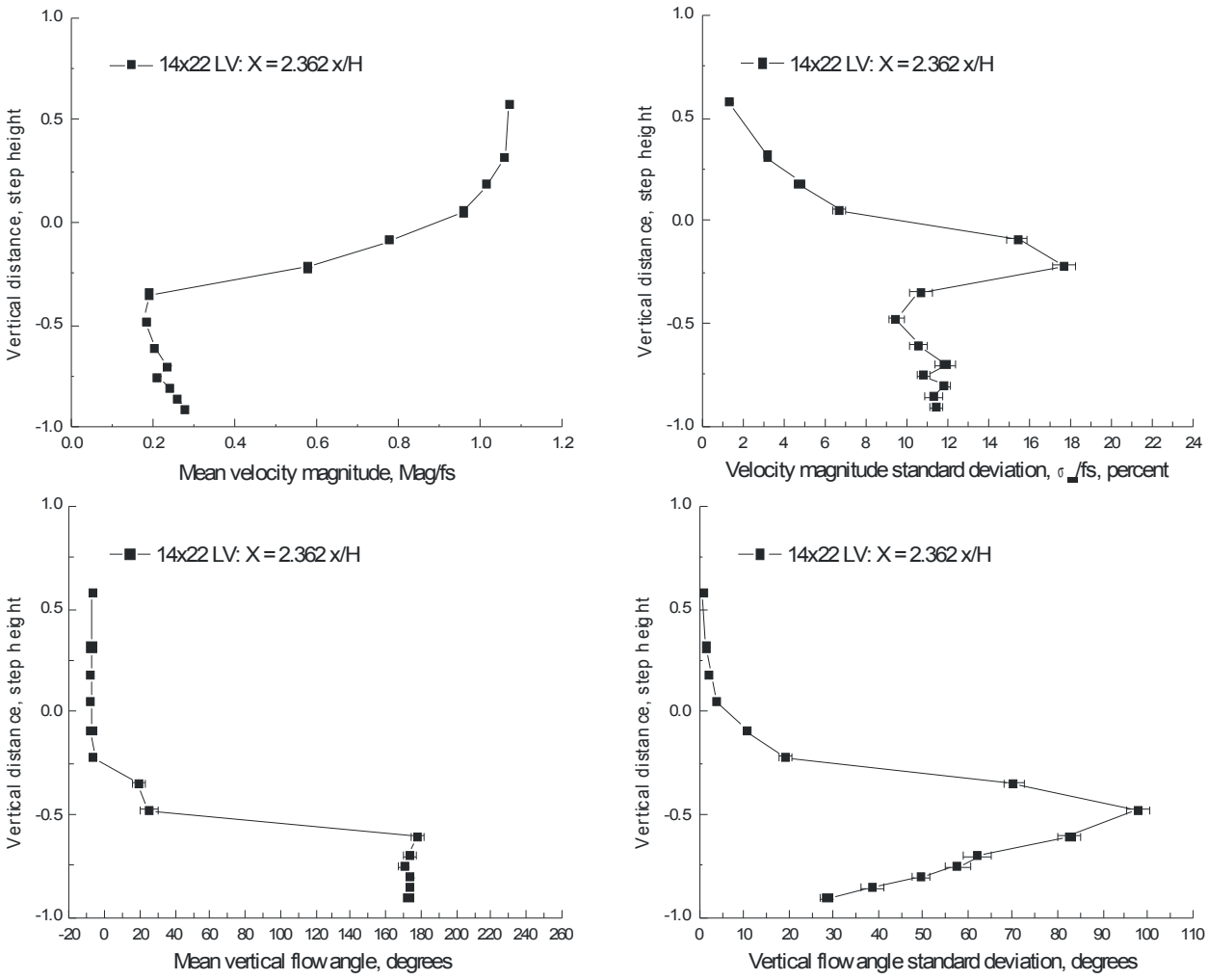

Figure VII.6.i.- Vertical scan 2.362 x/H downstream of a 1.5-inch backward-facing step: velocity magnitude and flow angle, fs = 45.0 m/s.

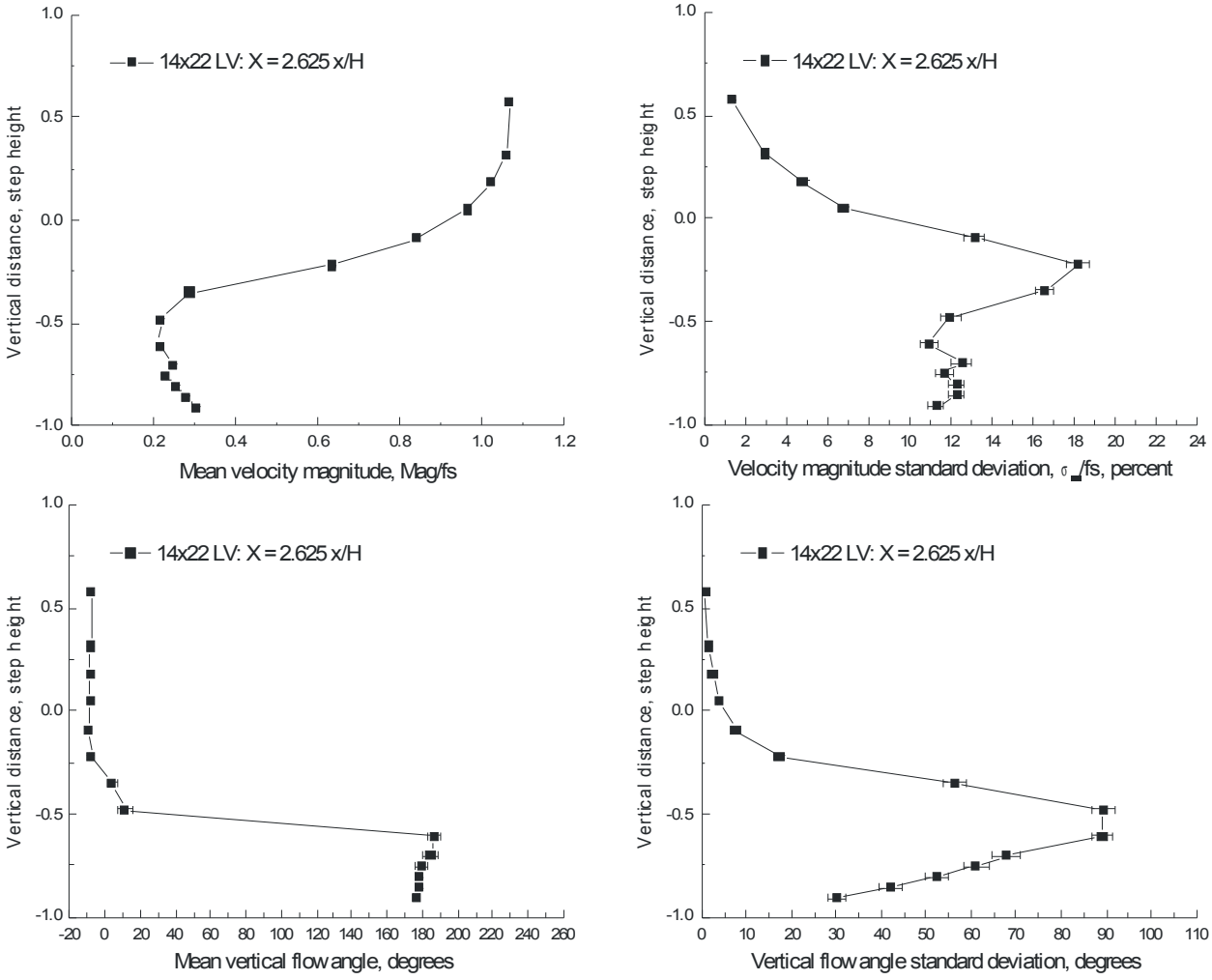

Figure VII.6.j.- Vertical scan 2.625 x/H downstream of a 1.5-inch backward-facing step: velocity magnitude and flow angle, fs = 45.0 m/s.

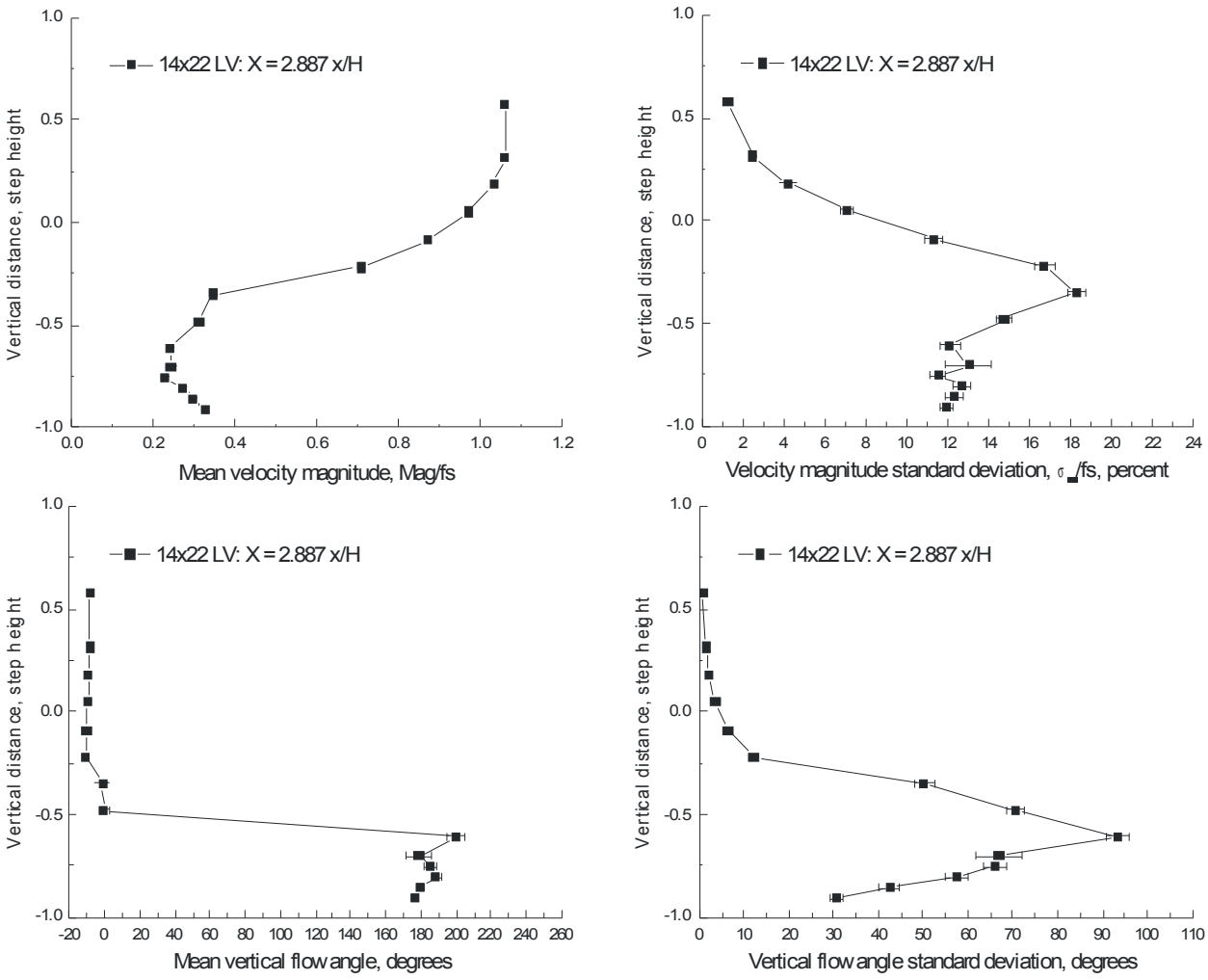

Figure VII.6.k.- Vertical scan 2.887 x/H downstream of a 1.5-inch backward-facing step: velocity magnitude and flow angle, fs = 45.0 m/s.

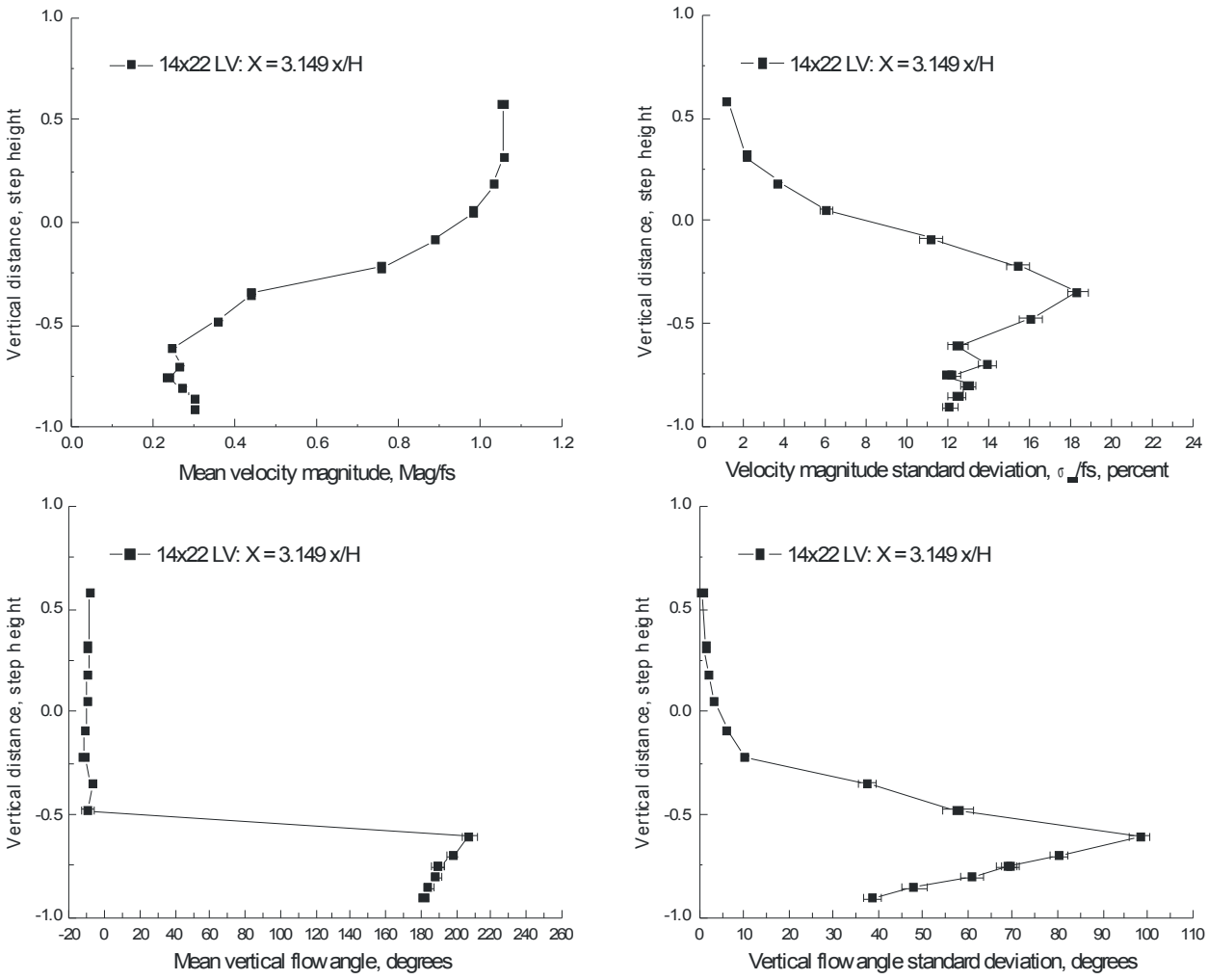

Figure VII.6.l.- Vertical scan 3.149 x/H downstream of a 1.5-inch backward-facing step: velocity magnitude and flow angle, fs = 45.0 m/s.

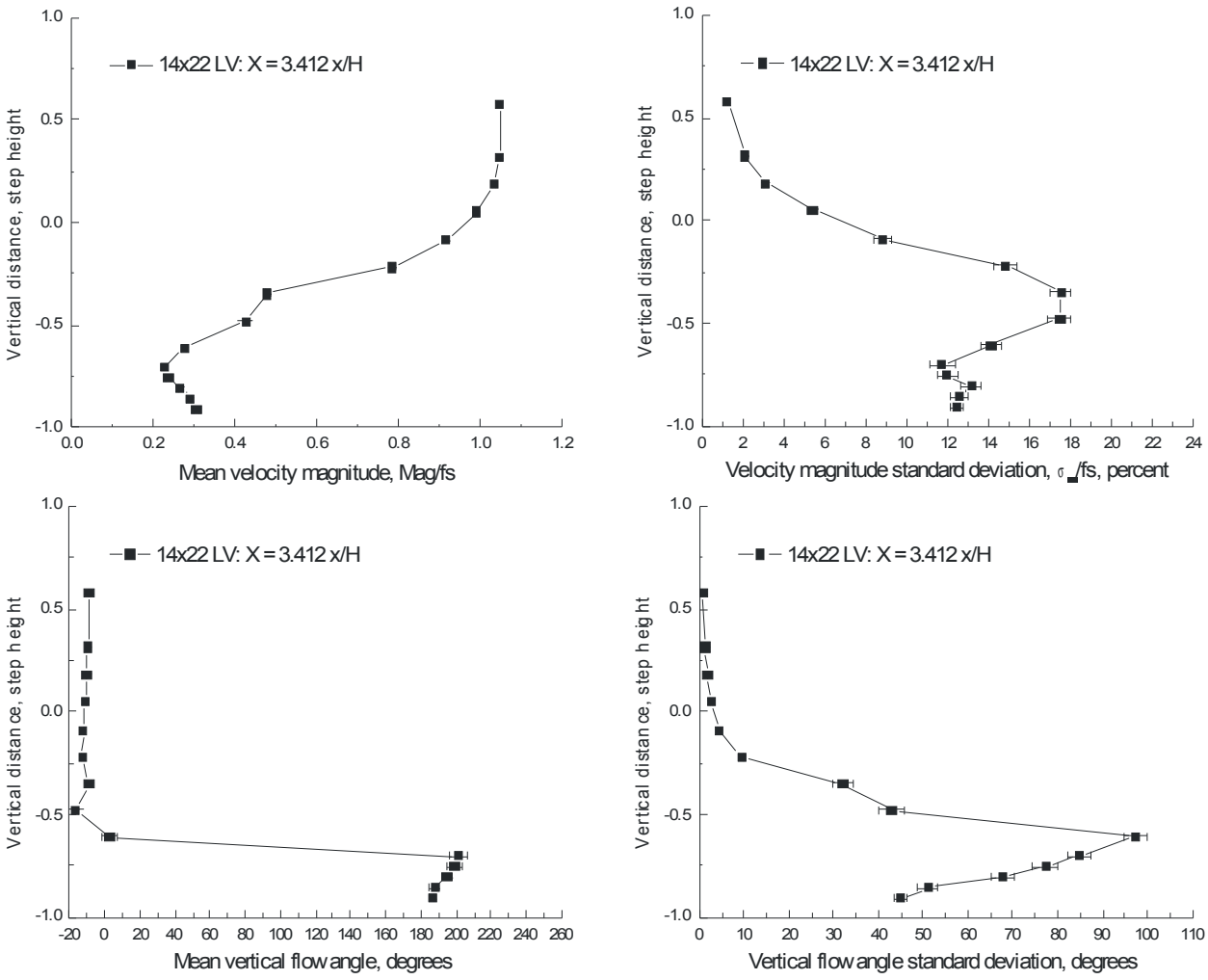

Figure VII.6.m.- Vertical scan 3.412 x/H downstream of a 1.5-inch backward-facing step: velocity magnitude and flow angle, fs = 45.0 m/s.

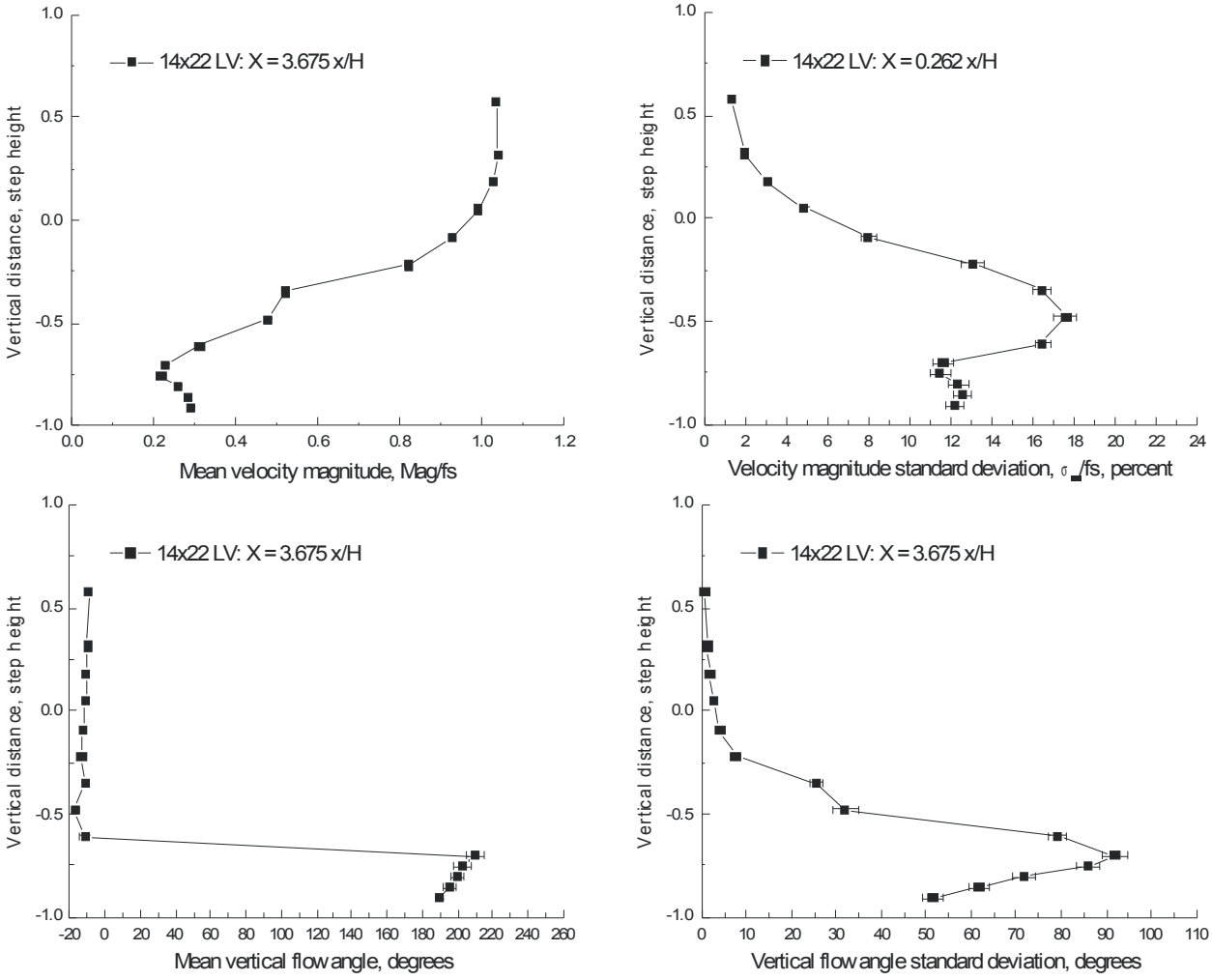

Figure VII.6.n.- Vertical scan 3.675 x/H downstream of a 1.5-inch backward-facing step: velocity magnitude and flow angle, fs = 45.0 m/s.

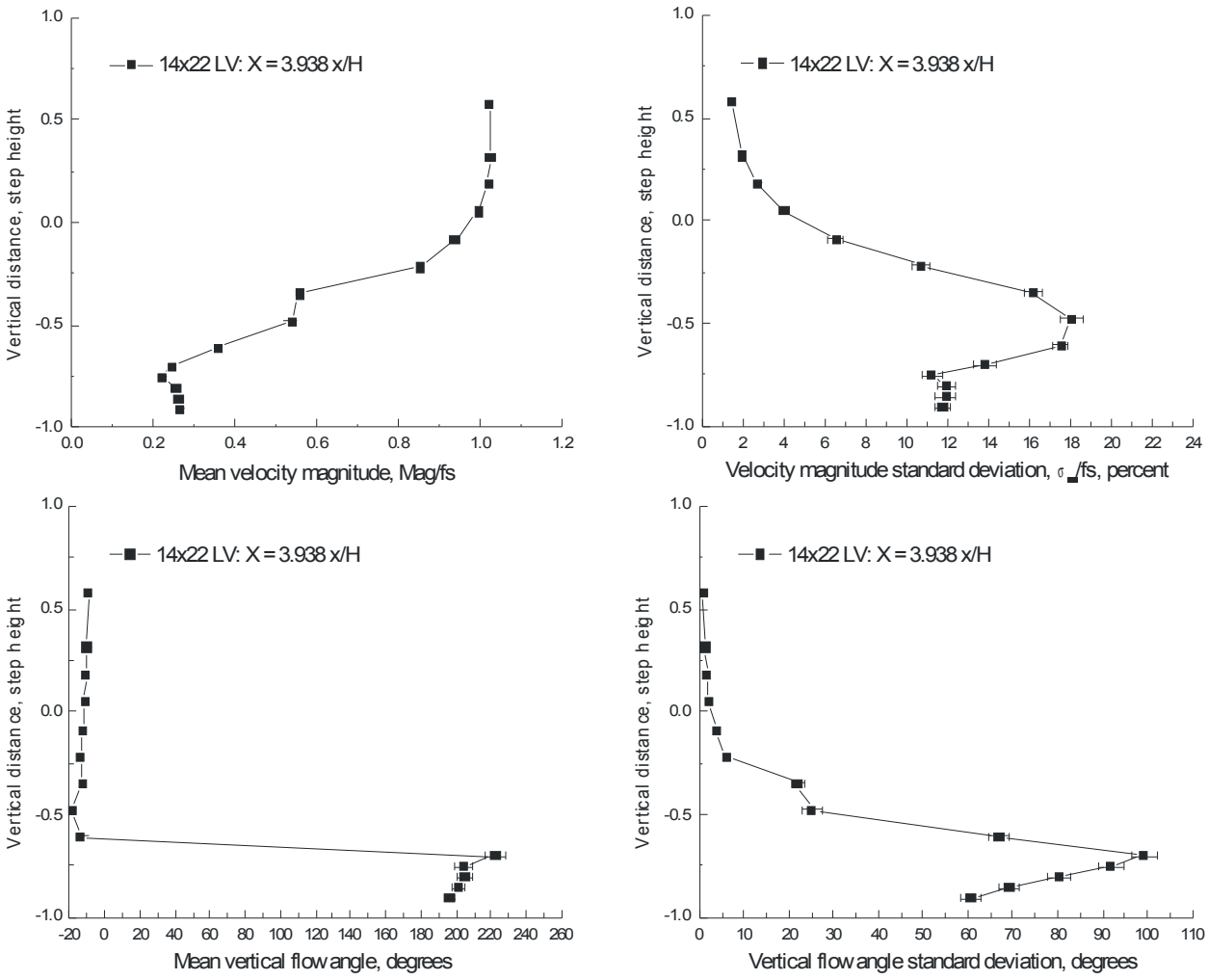

Figure VII.6.o.- Vertical scan 3.938 x/H downstream of a 1.5-inch backward-facing step: velocity magnitude and flow angle, fs = 45.0 m/s.

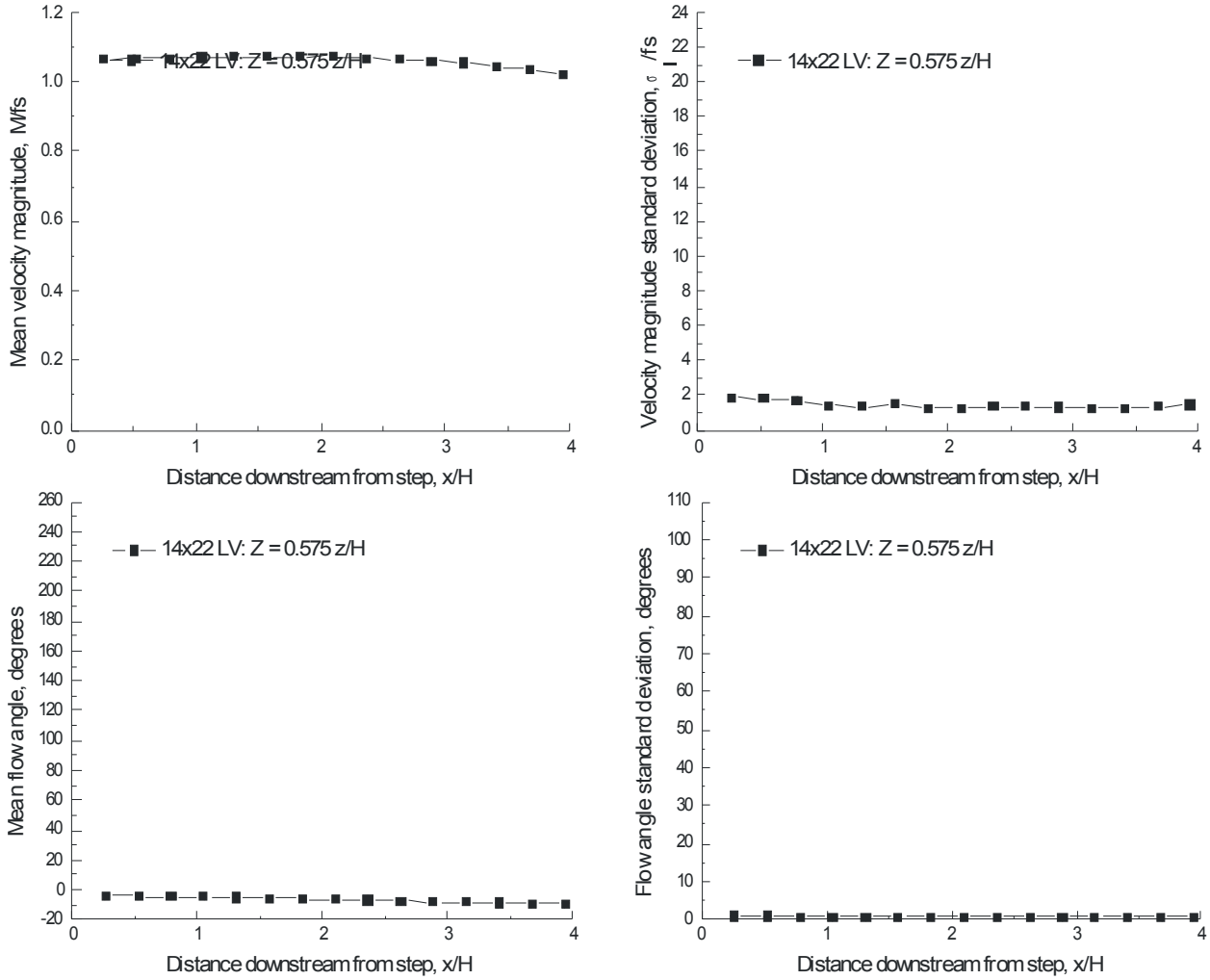

Figure VII.7.a.- Horizontal scan 0.575 z/H above a 1.5-inch backward-facing step: velocity magnitude and flow angle, fs = 45.0 m/s.

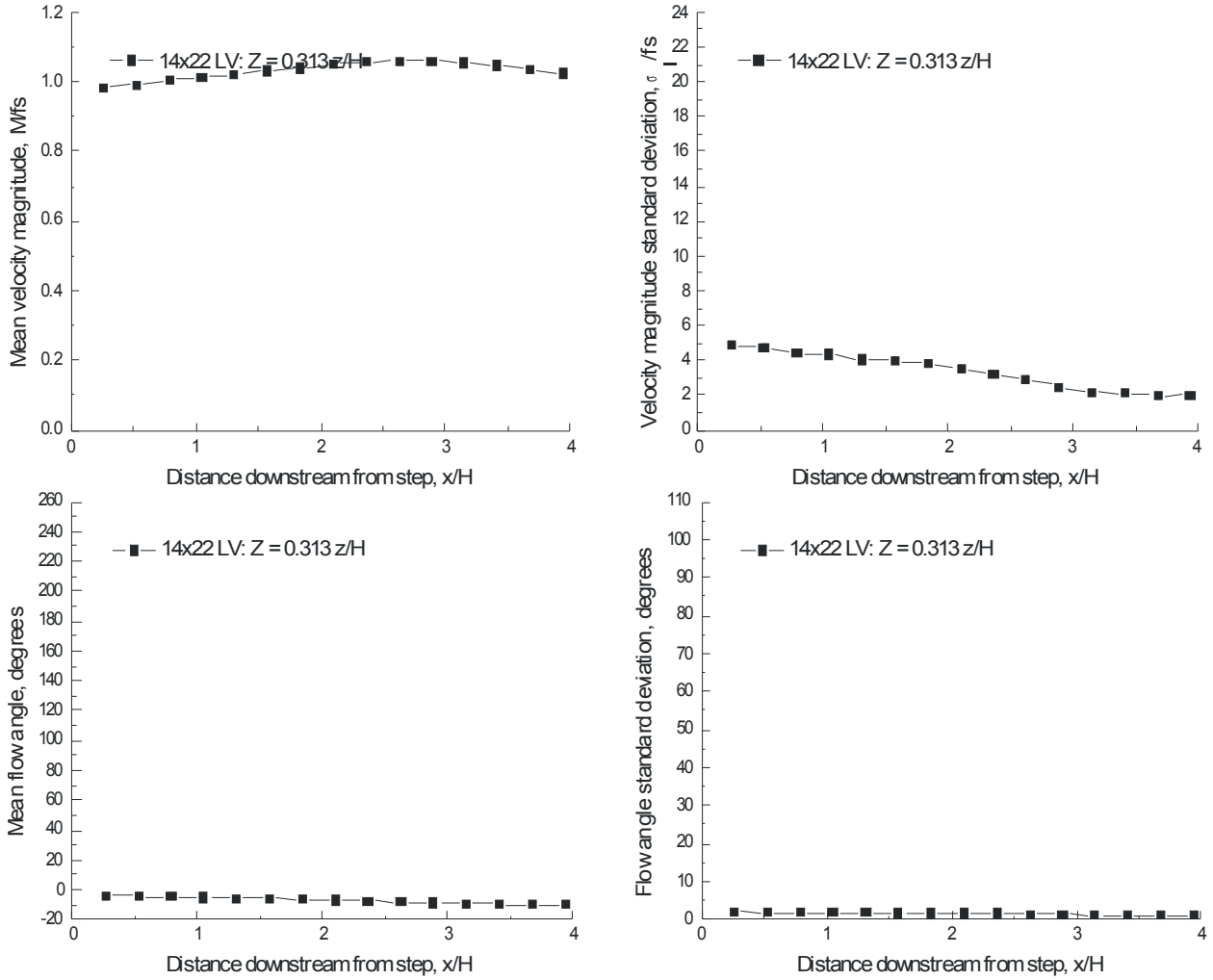

Figure VII.7.b.- Horizontal scan 0.313 z/H above a 1.5-inch backward-facing step: velocity magnitude and flow angle, fs = 45.0 m/s.

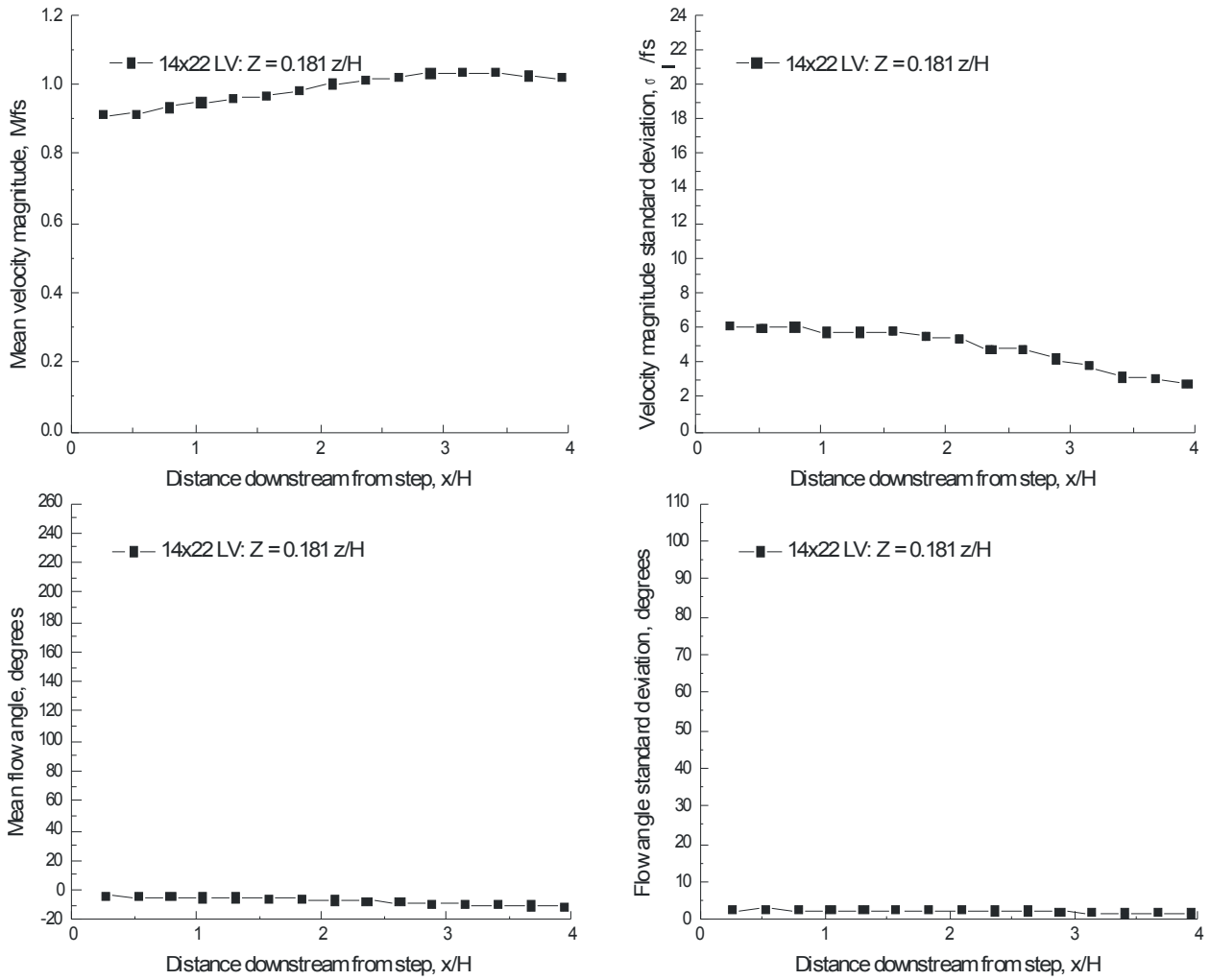

Figure VII.7.c.- Horizontal scan 0.181 z/H above a 1.5-inch backward-facing step: velocity magnitude and flow angle, fs = 45.0 m/s.

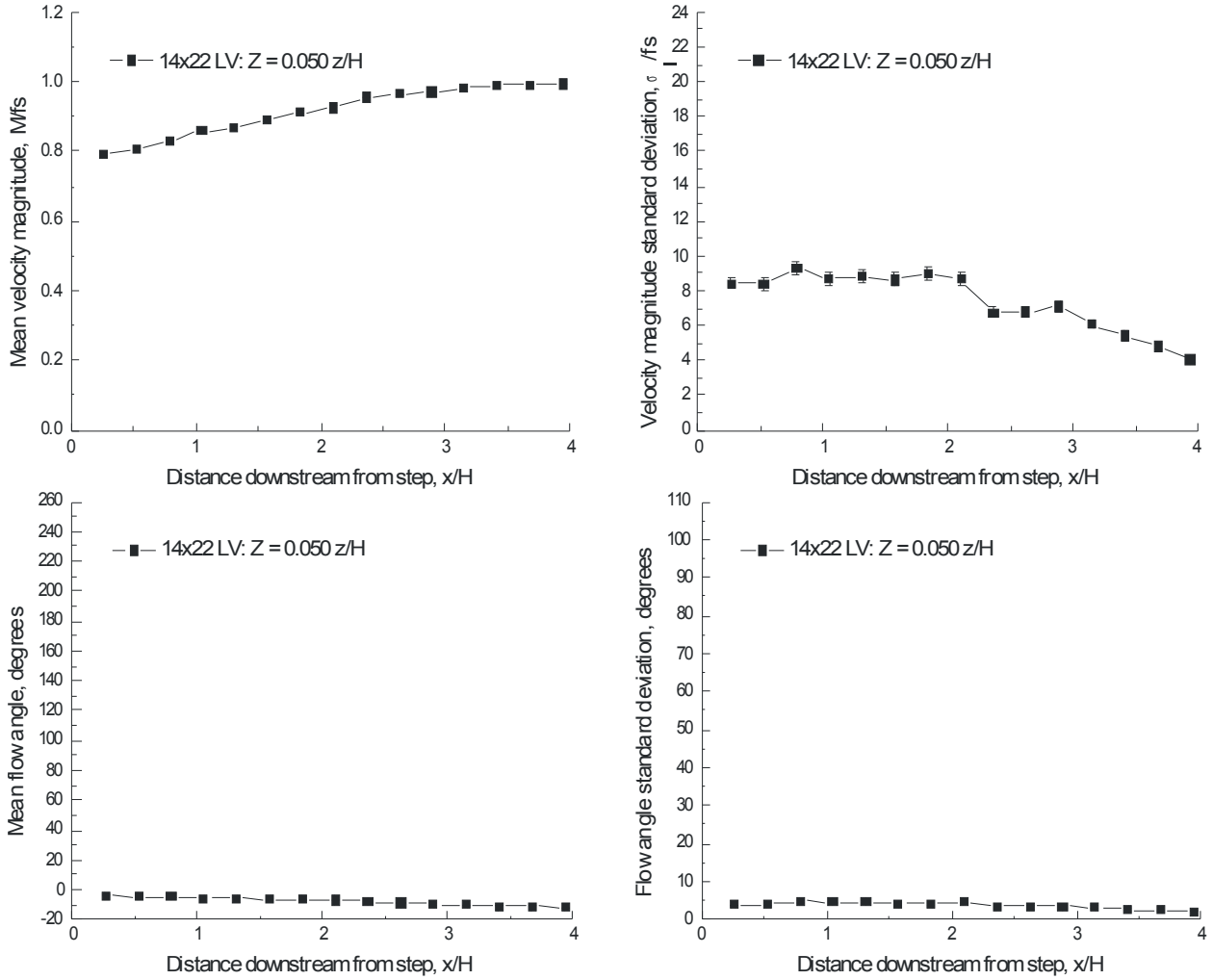

Figure VII.7.d.- Horizontal scan 0.050 z/H above a 1.5-inch backward-facing step: velocity magnitude and flow angle, fs = 45.0 m/s.

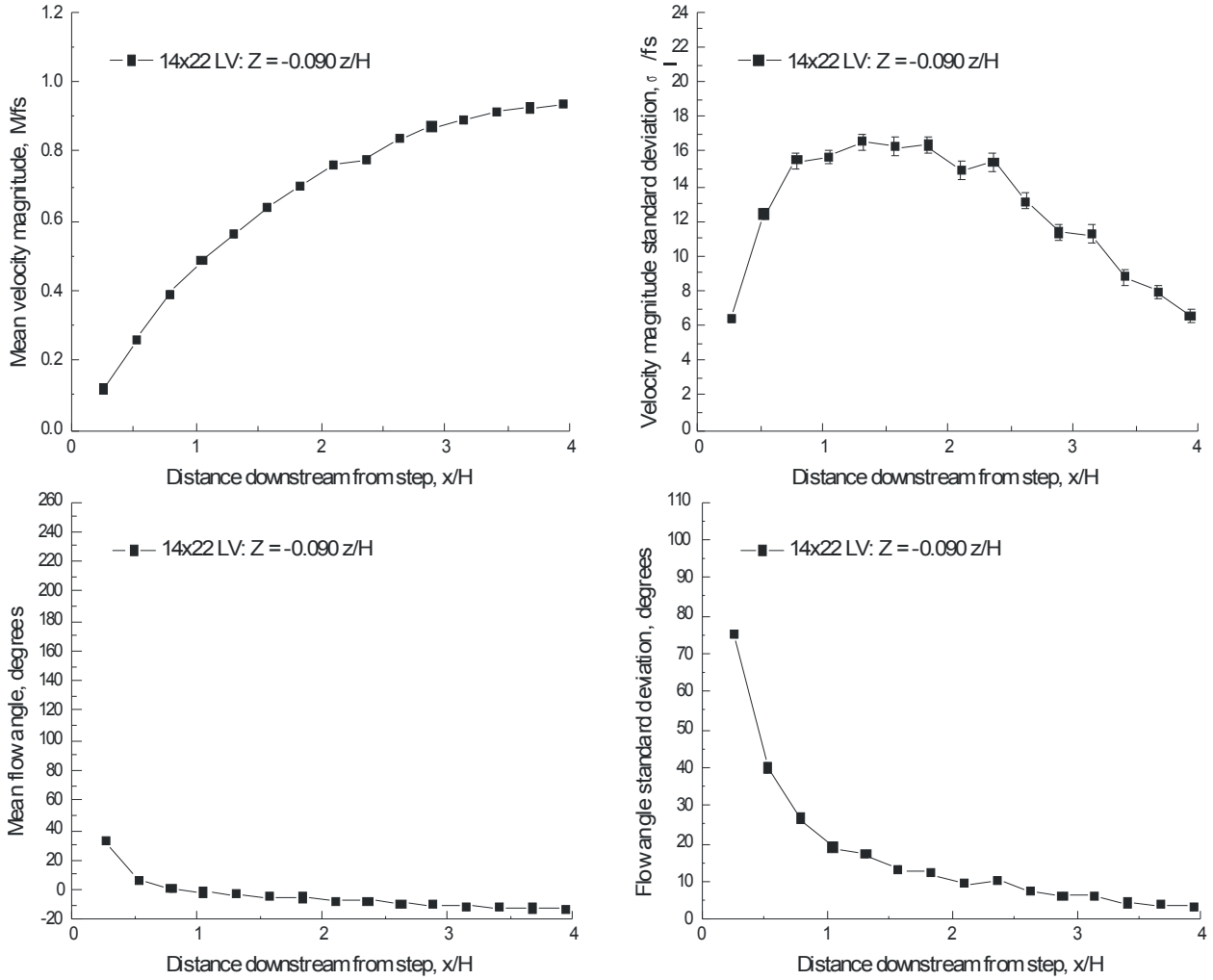

Figure VII.7.e.- Horizontal scan 0.090 z/H below a 1.5-inch backward-facing step: velocity magnitude and flow angle, fs = 45.0 m/s.

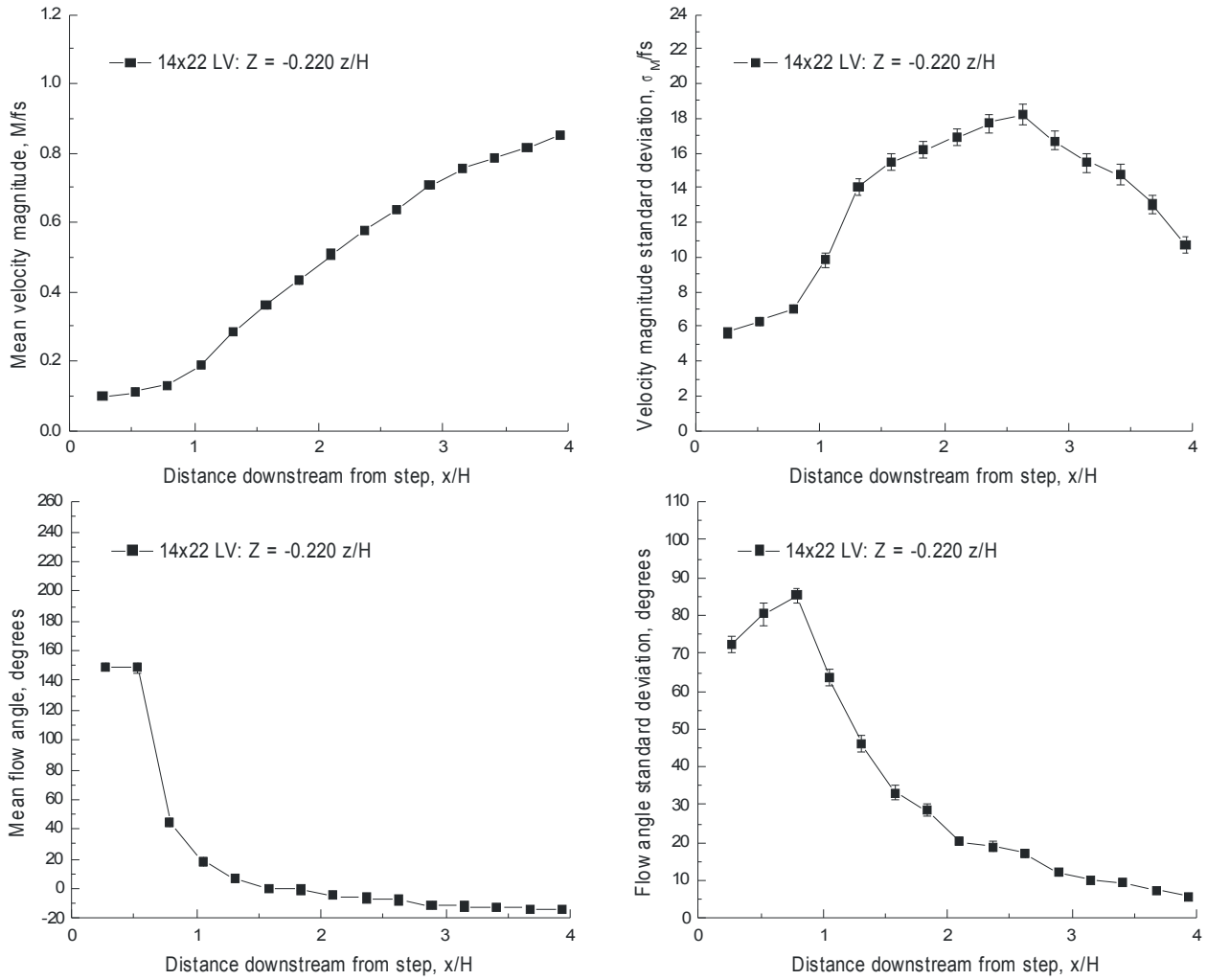

Figure VII.7.f.- Horizontal scan 0.220 z/H below a 1.5-inch backward-facing step: velocity magnitude and flow angle, fs = 45.0 m/s.

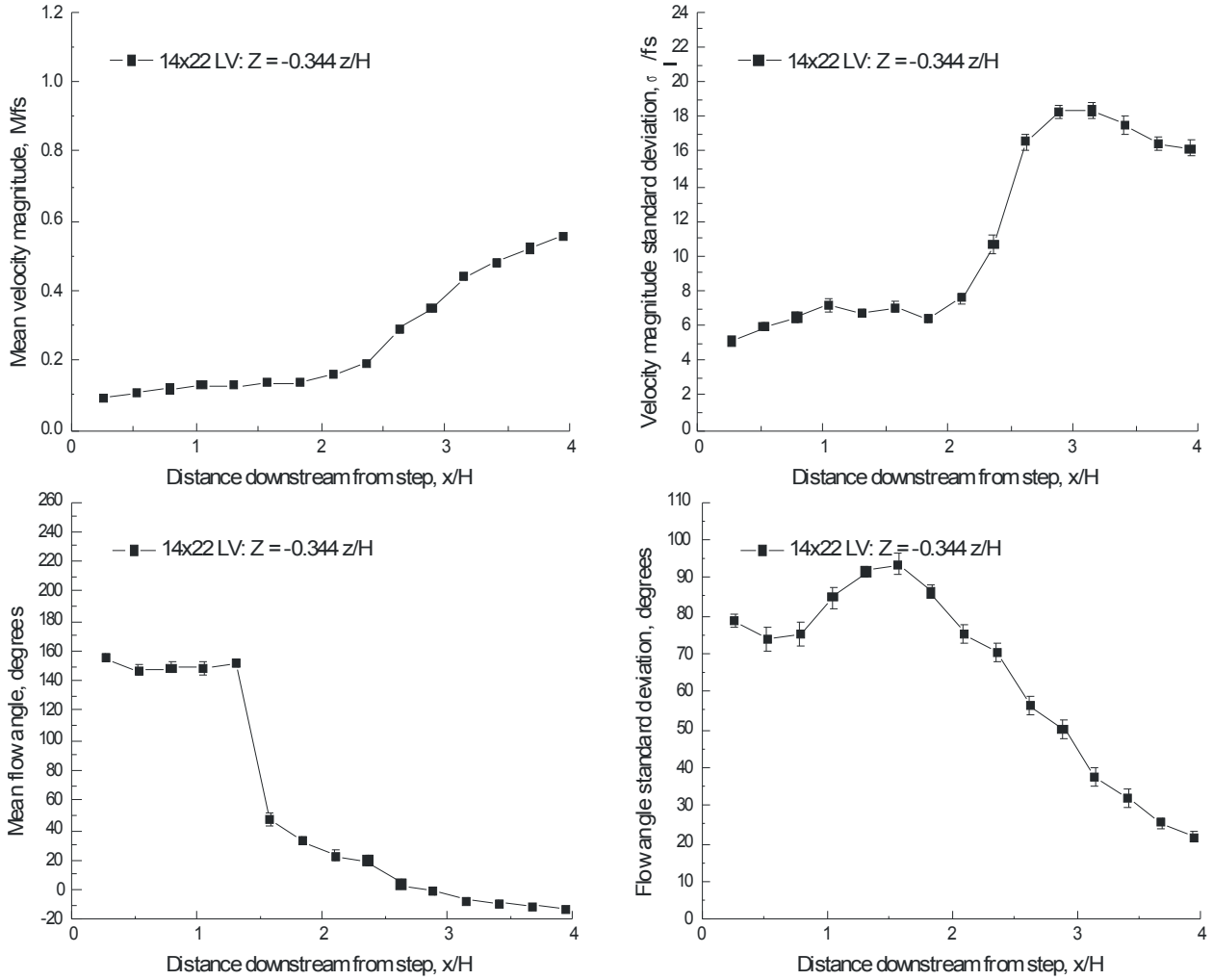

Figure VII.7.g.- Horizontal scan 0.344 z/H below a 1.5-inch backward-facing step: velocity magnitude and flow angle, fs = 45.0 m/s.

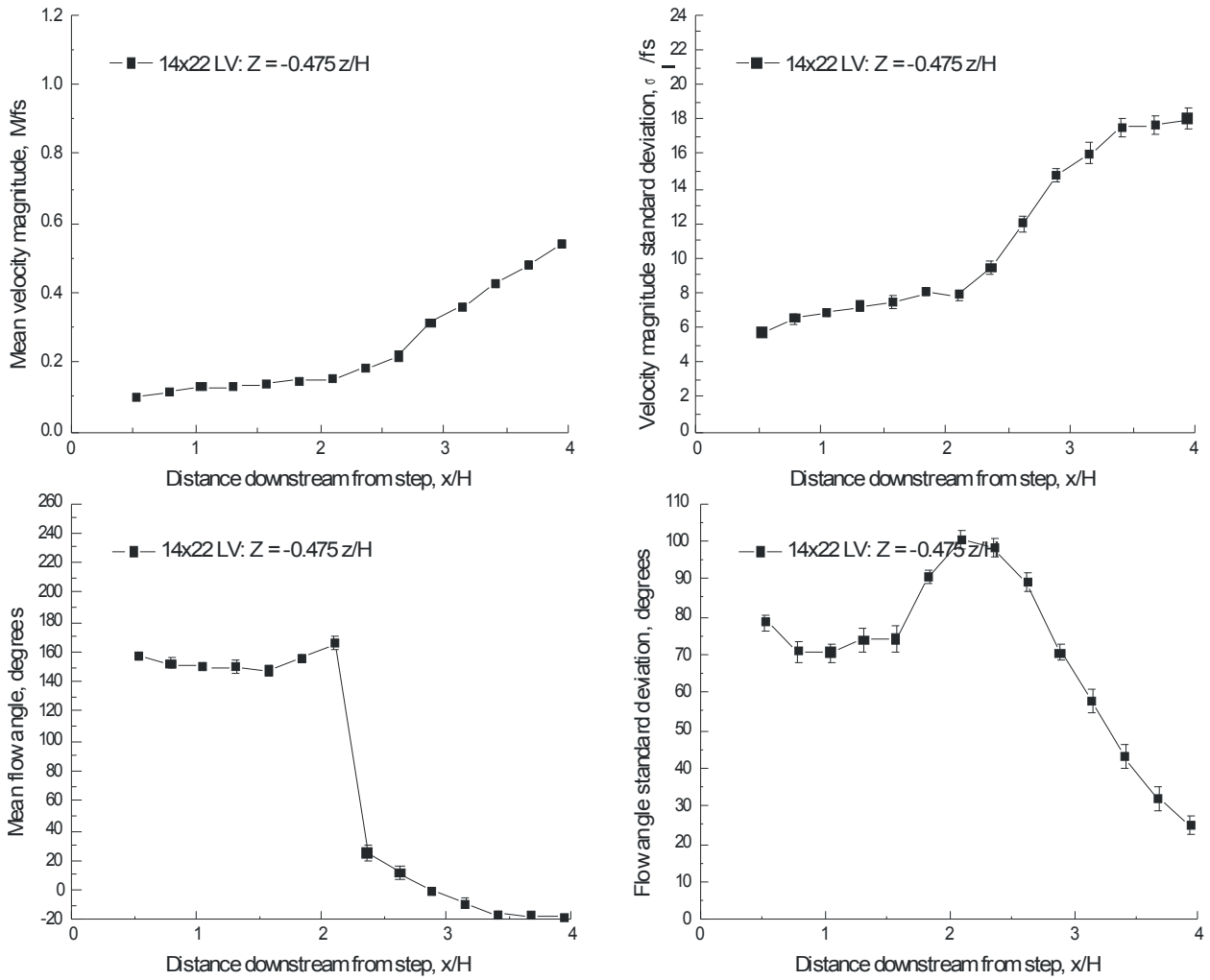

Figure VII.7.h.- Horizontal scan 0.475 z/H below a 1.5-inch backward-facing step: velocity magnitude and flow angle, fs = 45.0 m/s.

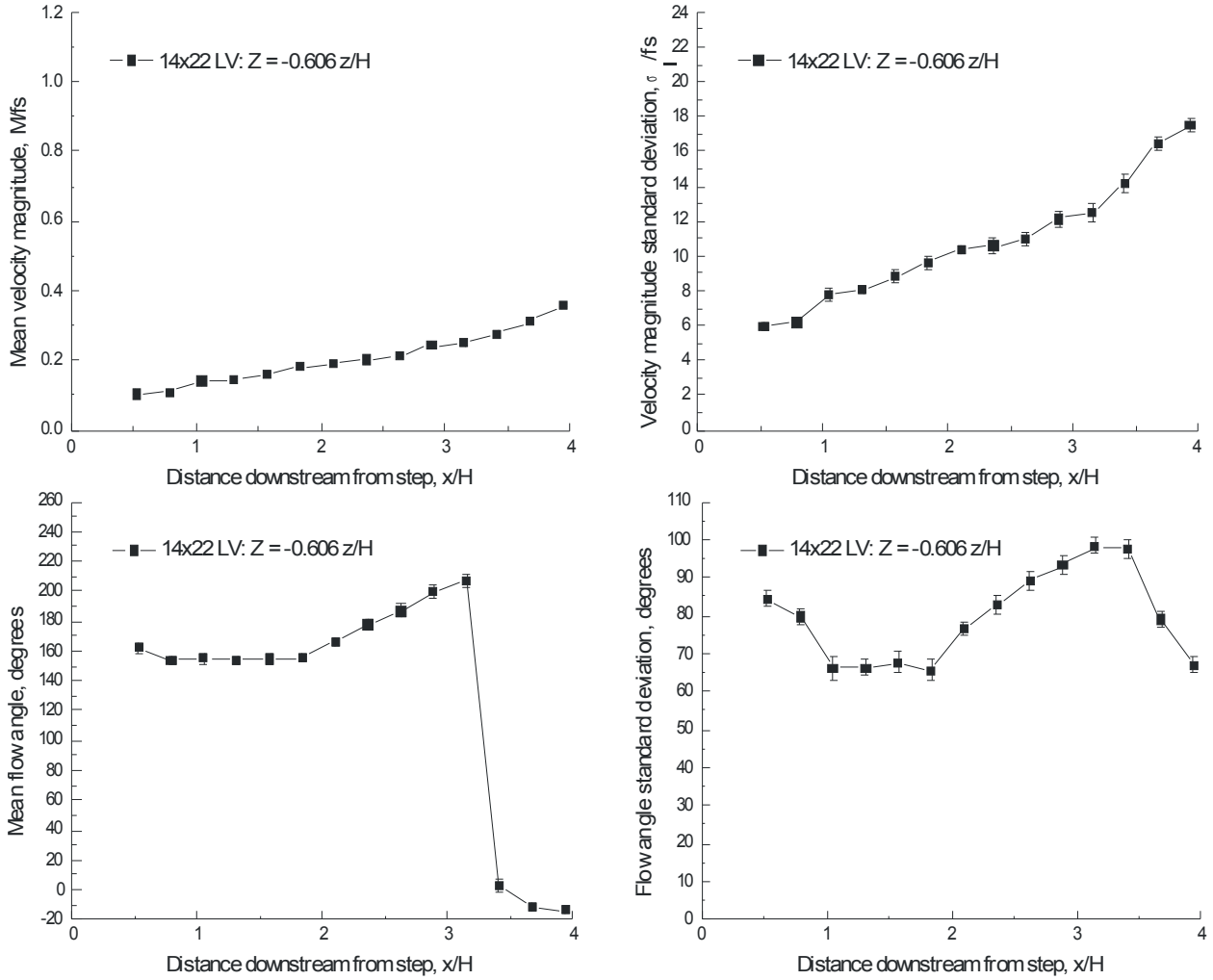

Figure VII.7.i.- Horizontal scan 0.606 z/H below a 1.5-inch backward-facing step: velocity magnitude and flow angle, fs = 45.0 m/s.

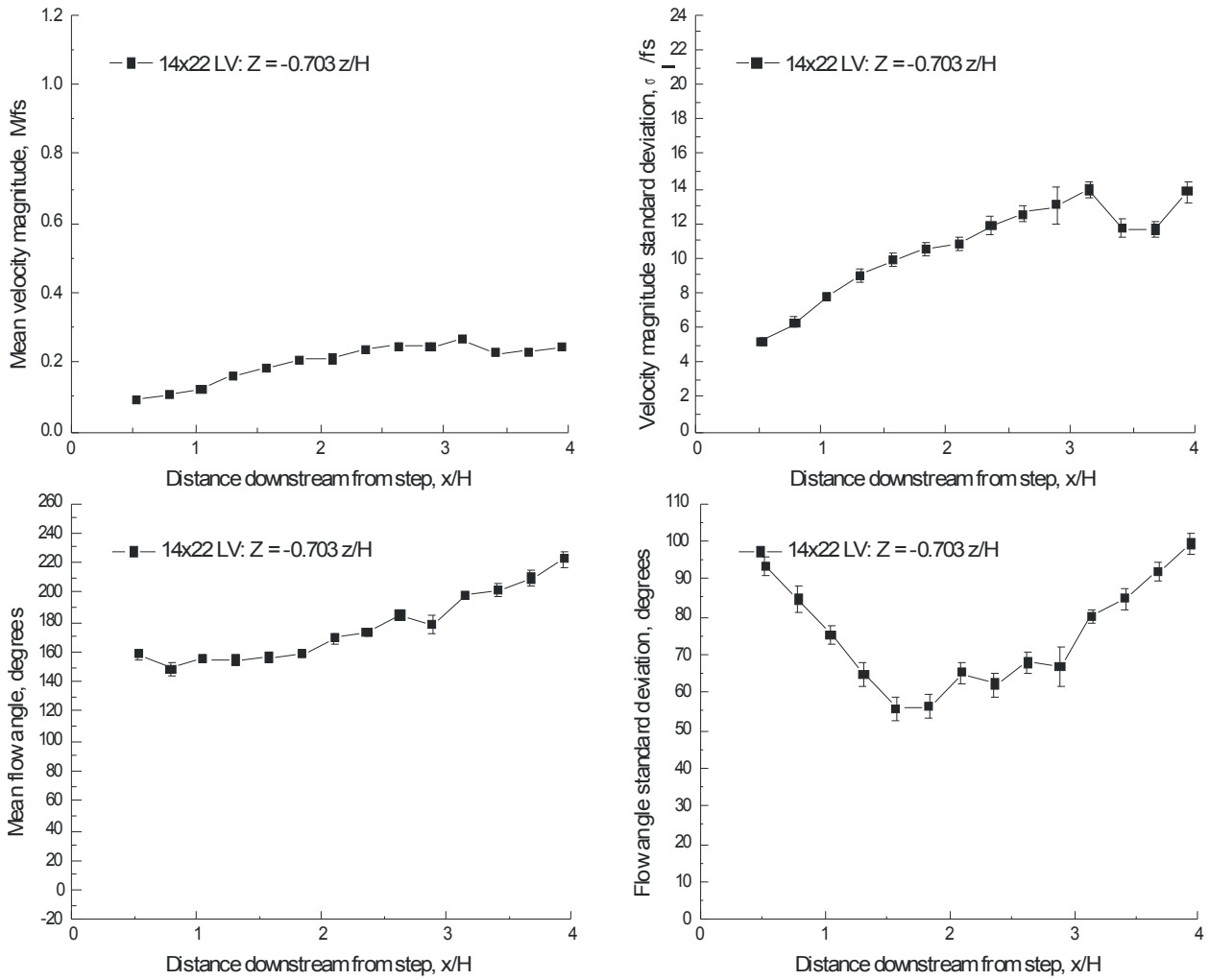

Figure VII.7.j.- Horizontal scan 0.703 z/H below a 1.5-inch backward-facing step: velocity magnitude and flow angle, fs = 45.0 m/s.

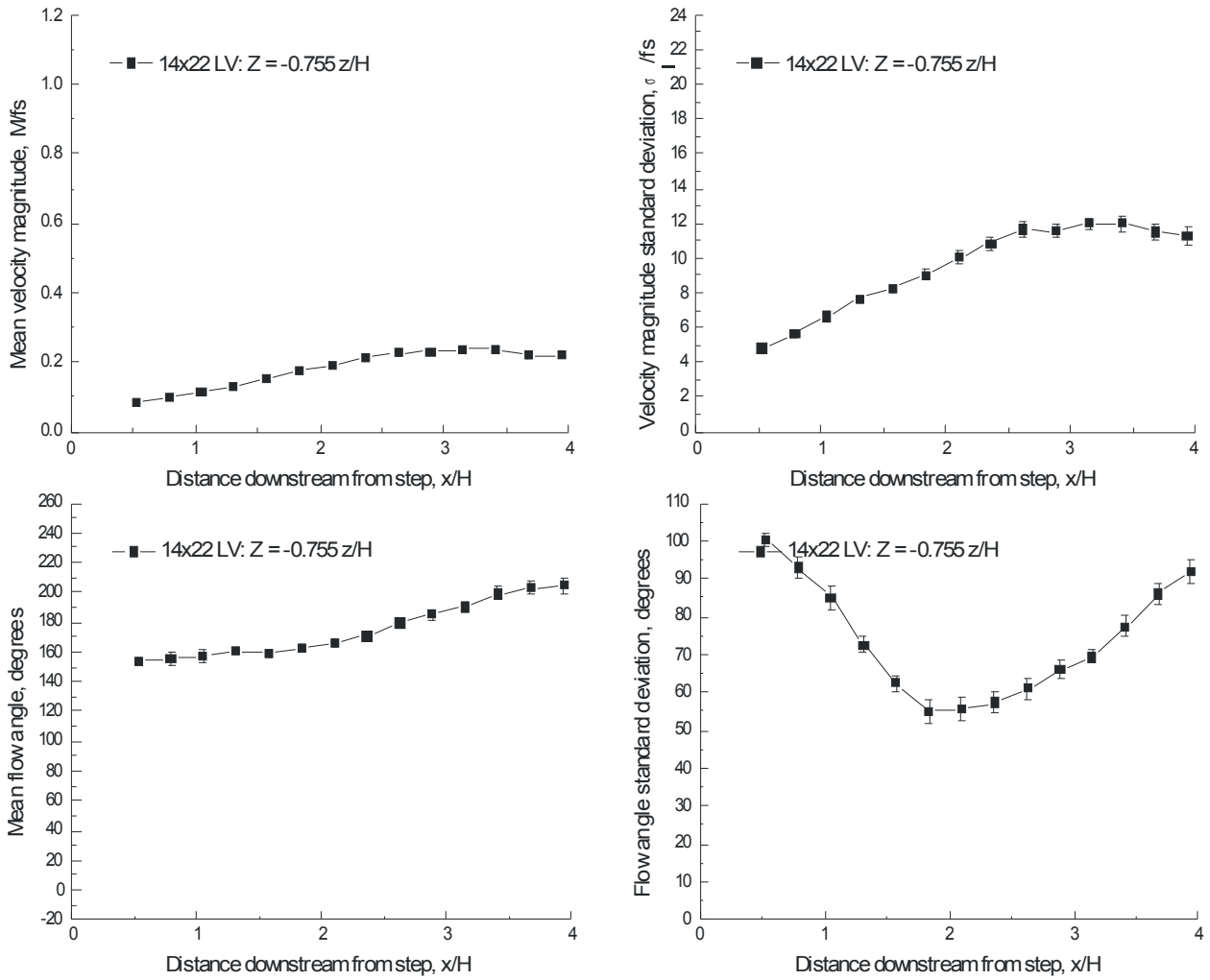

Figure VII.7.k.- Horizontal scan 0.755 z/H below a 1.5-inch backward-facing step: velocity magnitude and flow angle, fs = 45.0 m/s.

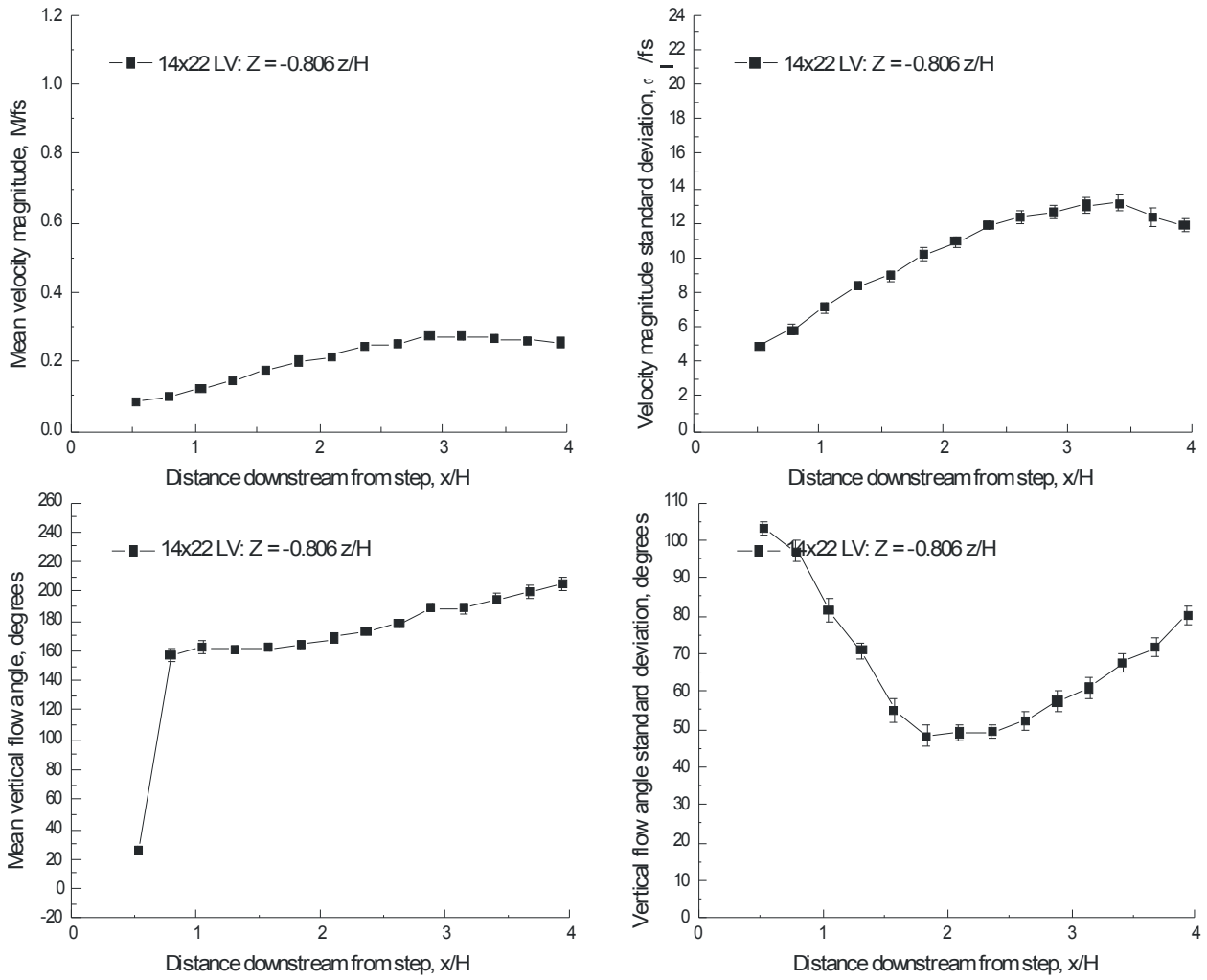

Figure VII.7.l.- Horizontal scan 0.806 z/H below a 1.5-inch backward-facing step: velocity magnitude and flow angle, fs = 45.0 m/s.

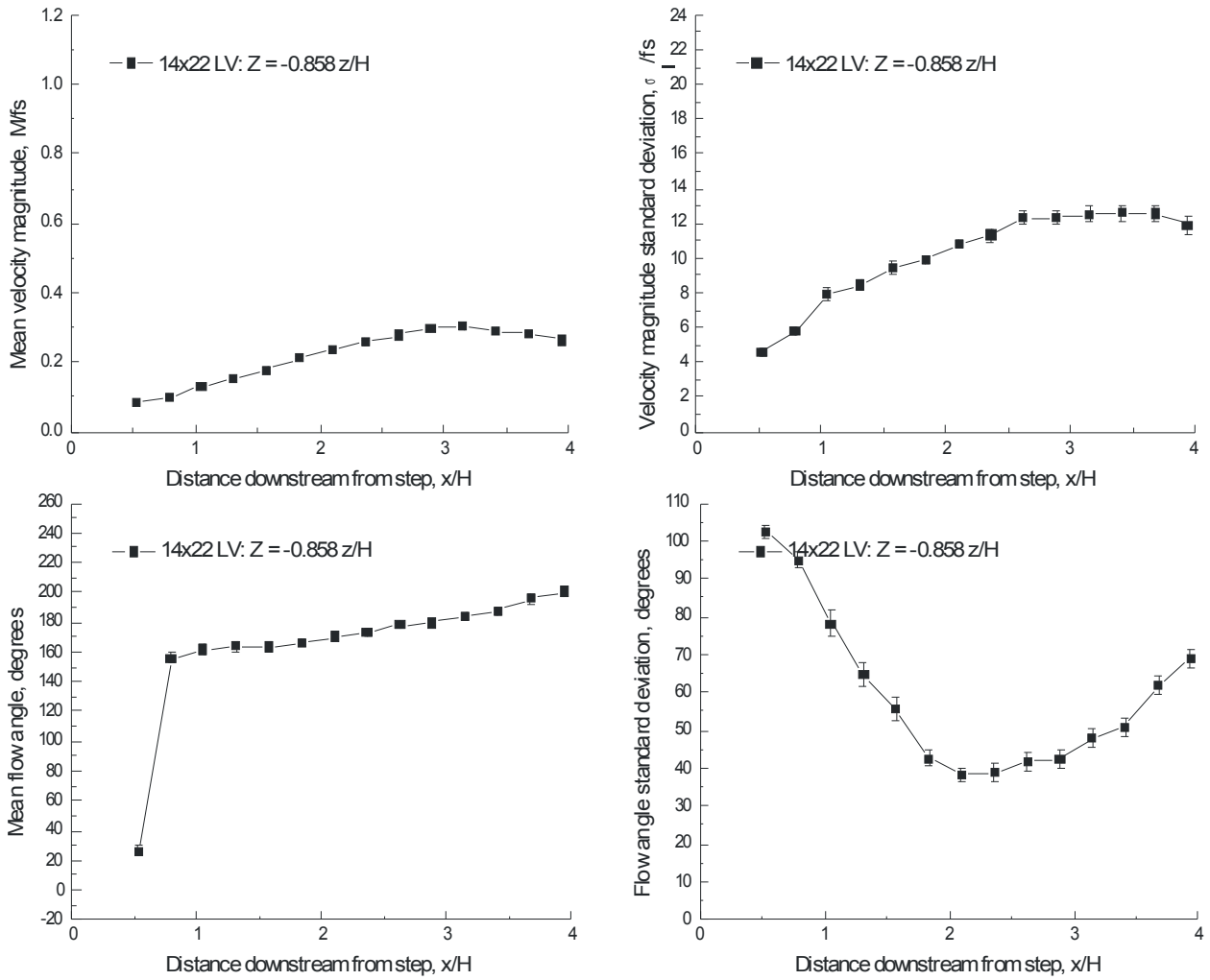

Figure VII.7.m.- Horizontal scan 0.858 z/H below a 1.5-inch backward-facing step: velocity magnitude and flow angle, fs = 45.0 m/s.

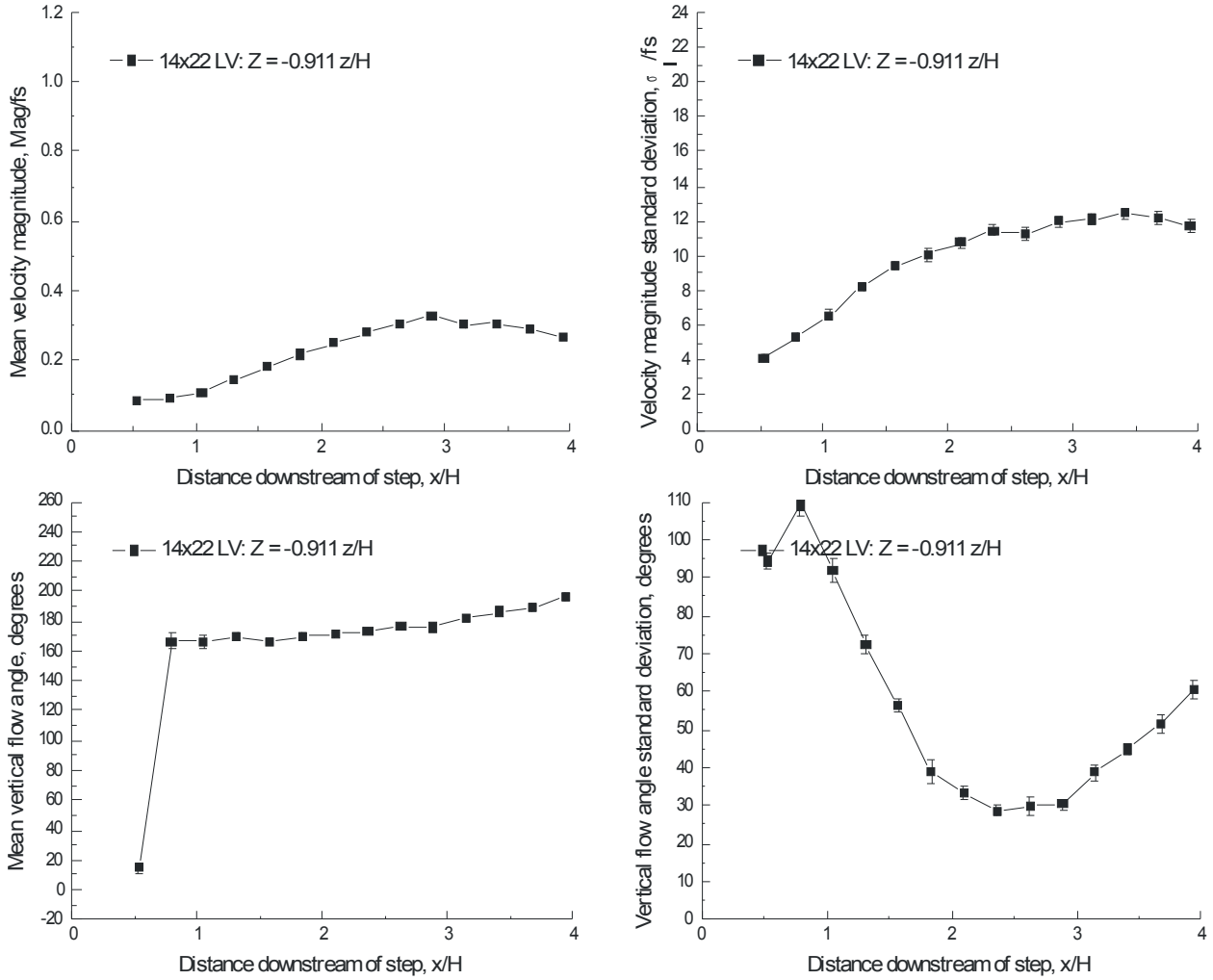

Figure VII.7.n.- Horizontal scan 0.911 z/H below a 1.5-inch backward-facing step: velocity magnitude and flow angle, fs = 45.0 m/s.

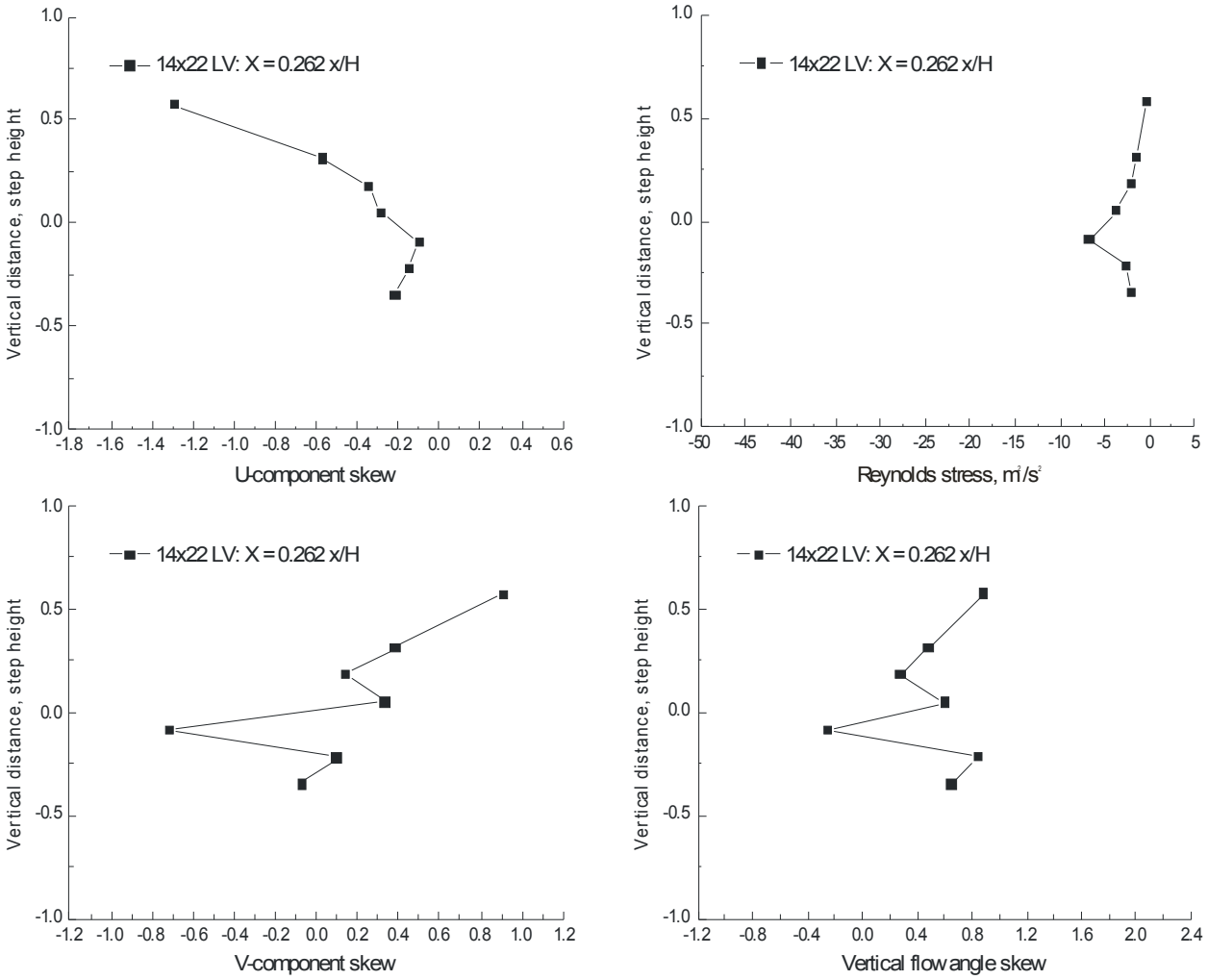

Figure VII.8.a.- Vertical scan 0.262 x/H downstream of a 1.5-inch backward-facing step: streamwise and vertical velocity skew, flow angle skew and Reynolds stress, fs = 45.0 m/s.

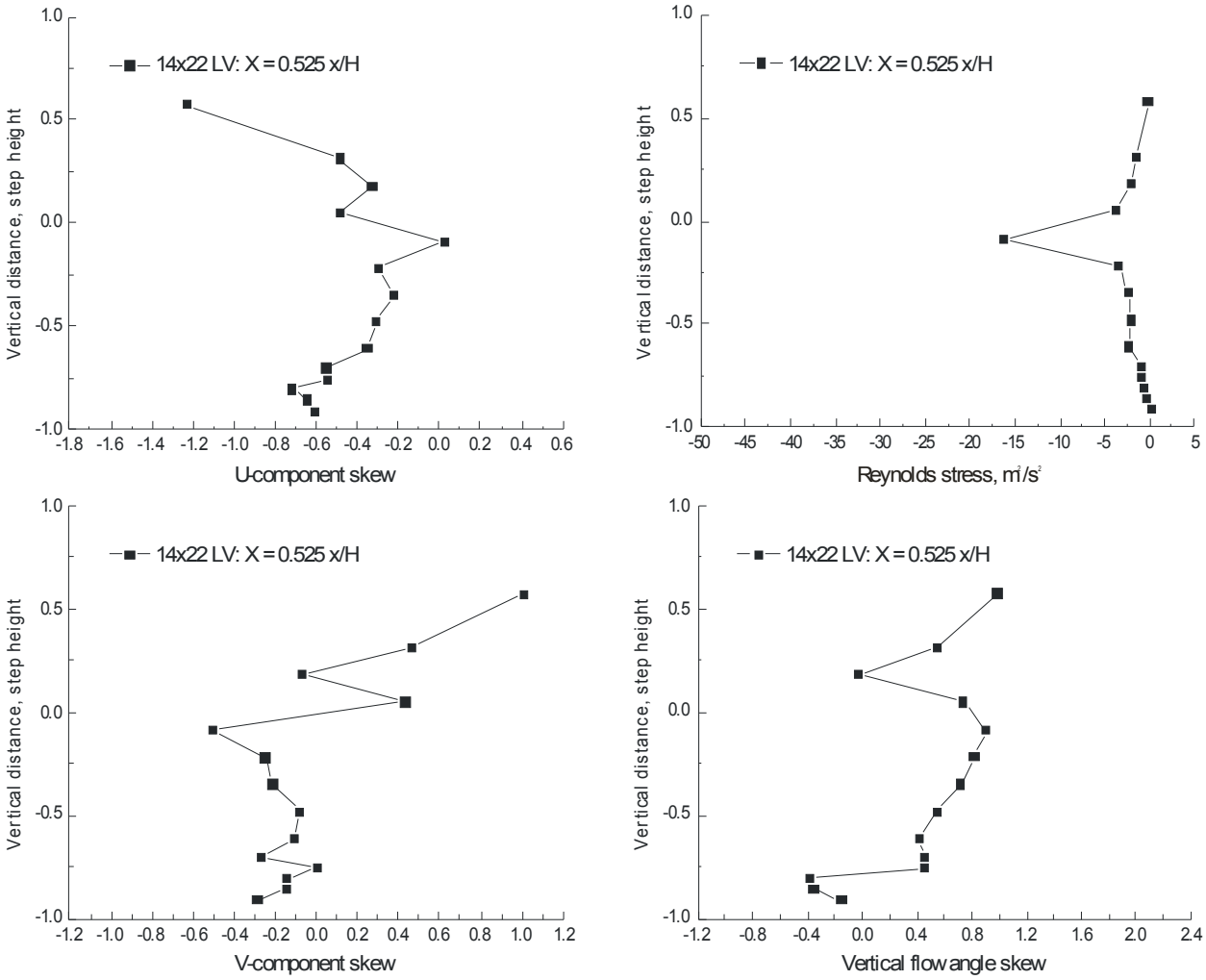

Figure VII.8.b.- Vertical scan 0.525 x/H downstream of a 1.5-inch backward-facing step: streamwise and vertical velocity skew, flow angle skew and Reynolds stress, fs = 45.0 m/s.

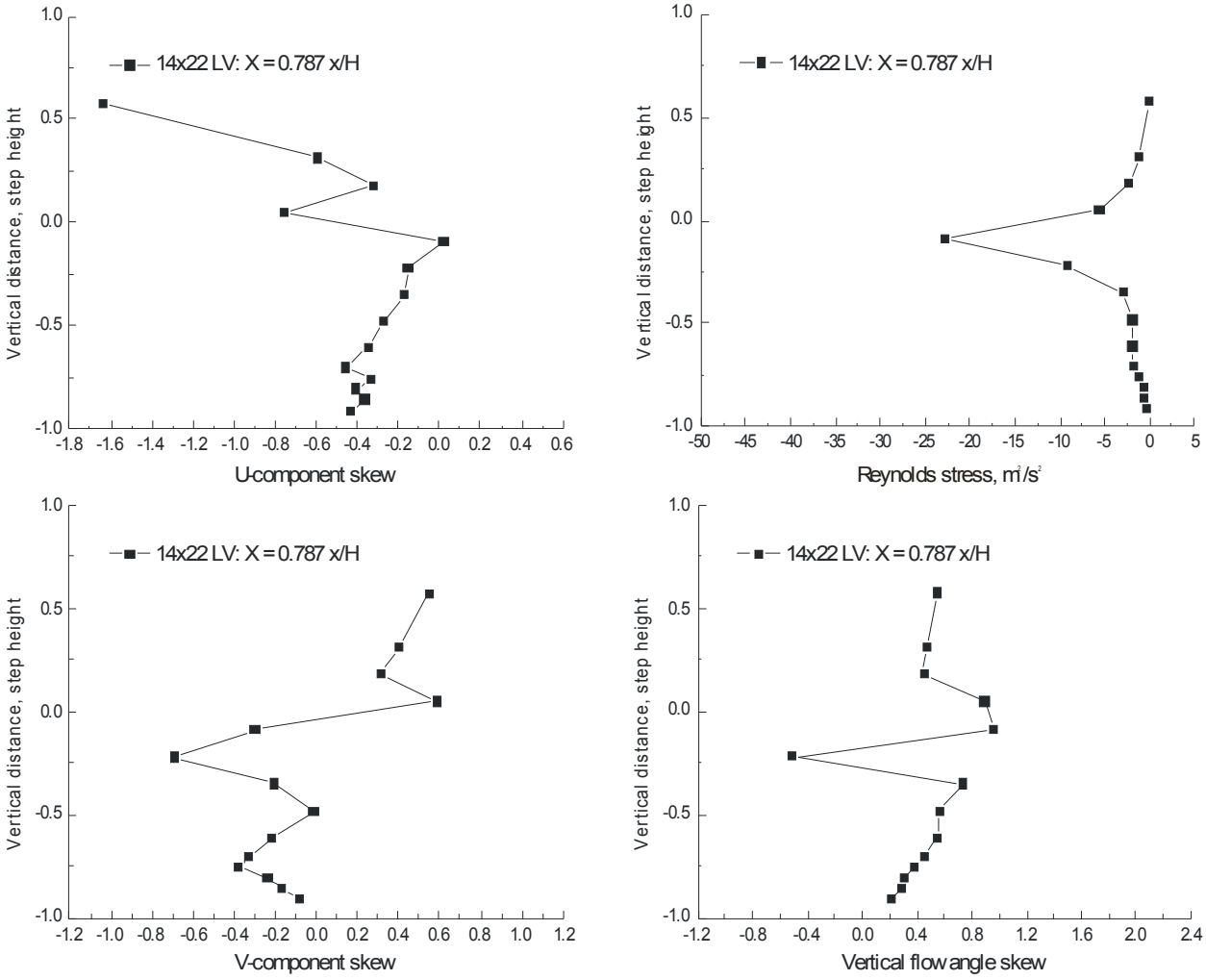

Figure VII.8.c.- Vertical scan 0.787 x/H downstream of a 1.5-inch backward-facing step: streamwise and vertical velocity skew, flow angle skew and Reynolds stress, fs = 45.0 m/s.

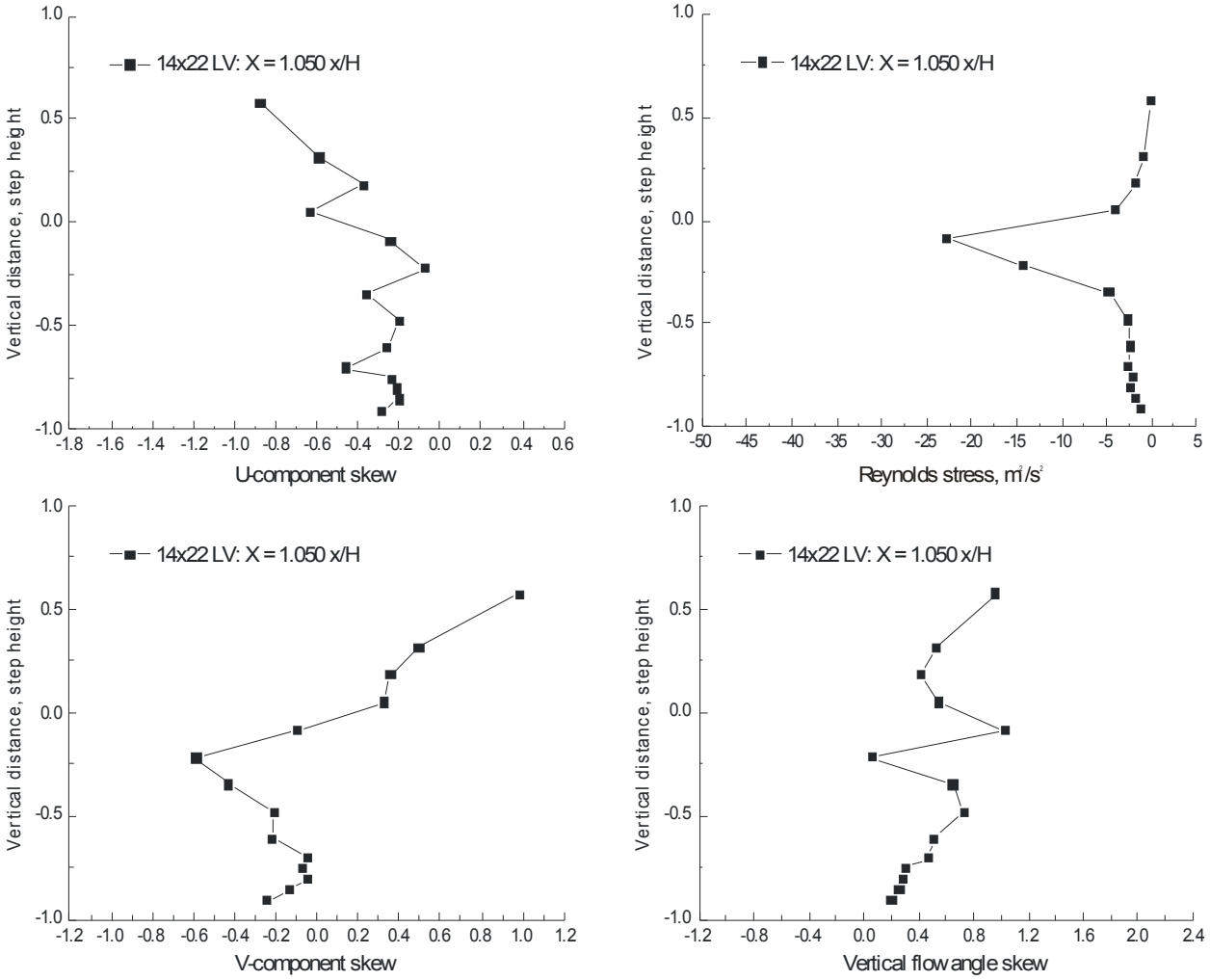

Figure VII.8.d.- Vertical scan 1.050 x/H downstream of a 1.5-inch backward-facing step: streamwise and vertical velocity skew, flow angle skew and Reynolds stress, fs = 45.0 m/s.

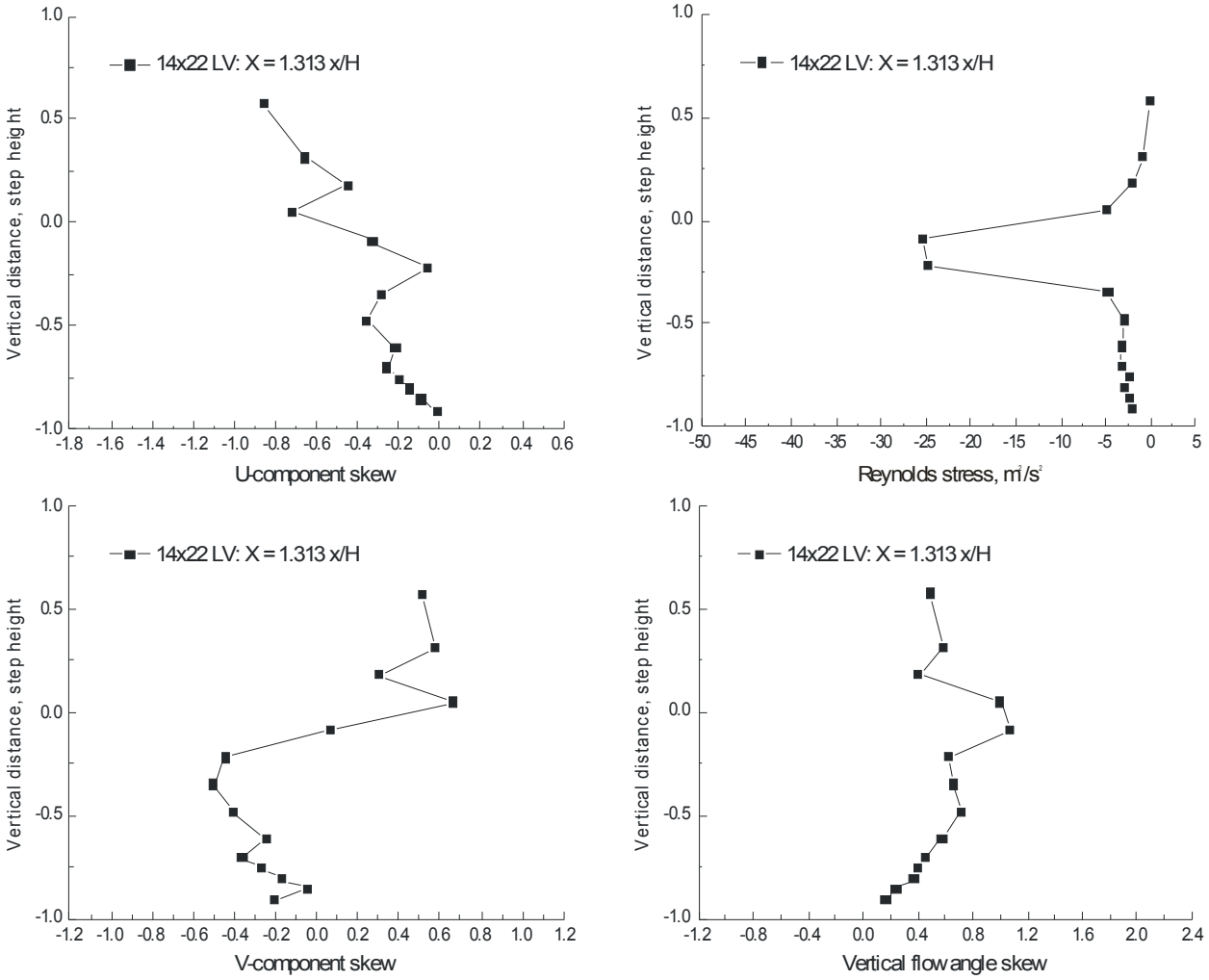

Figure VII.8.e.- Vertical scan 1.313 x/H downstream of a 1.5-inch backward-facing step: streamwise and vertical velocity skew, flow angle skew and Reynolds stress, fs = 45.0 m/s.

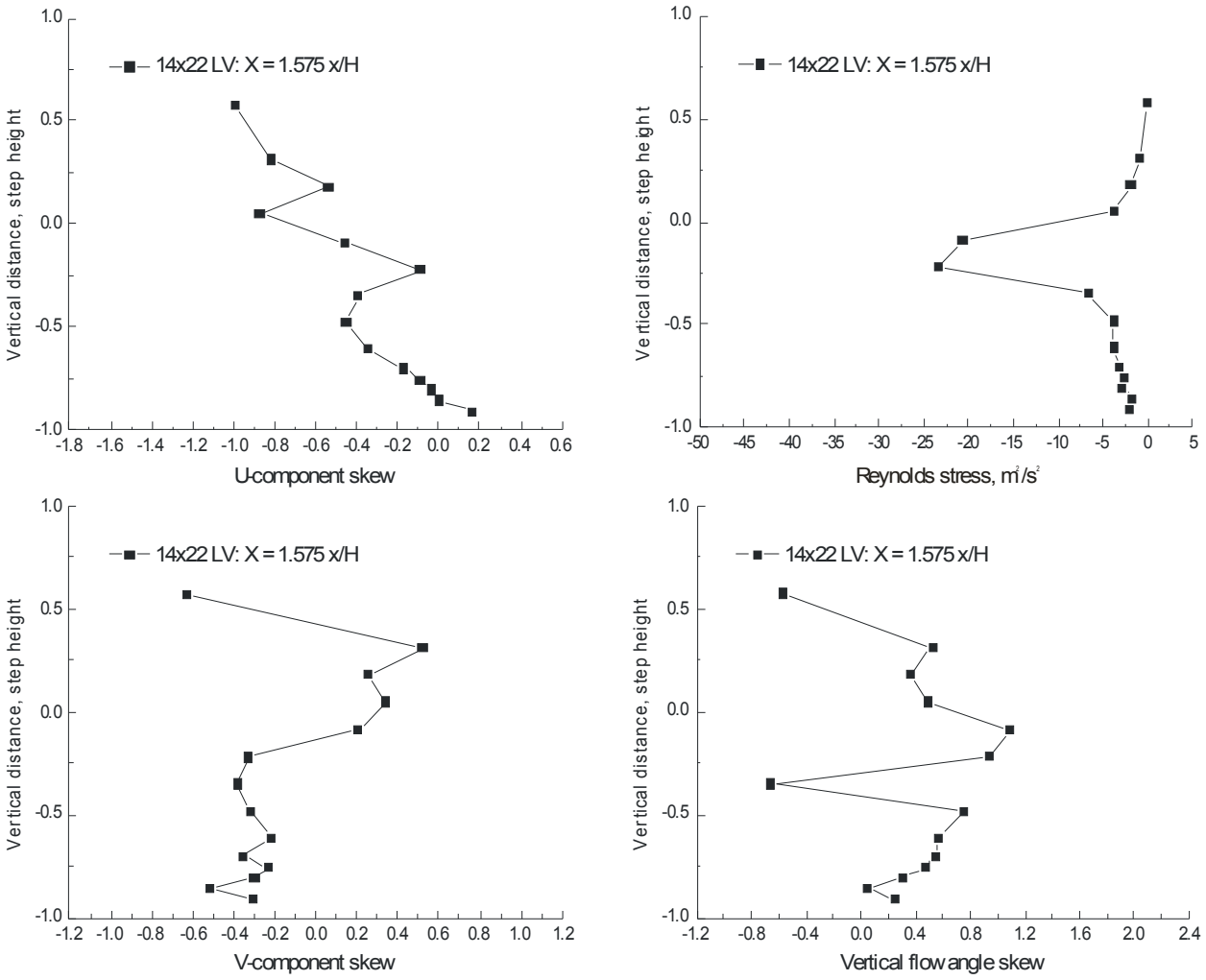

Figure VII.8.f.- Vertical scan 1.575 x/H downstream of a 1.5-inch backward-facing step: streamwise and vertical velocity skew, flow angle skew and Reynolds stress, fs = 45.0 m/s.

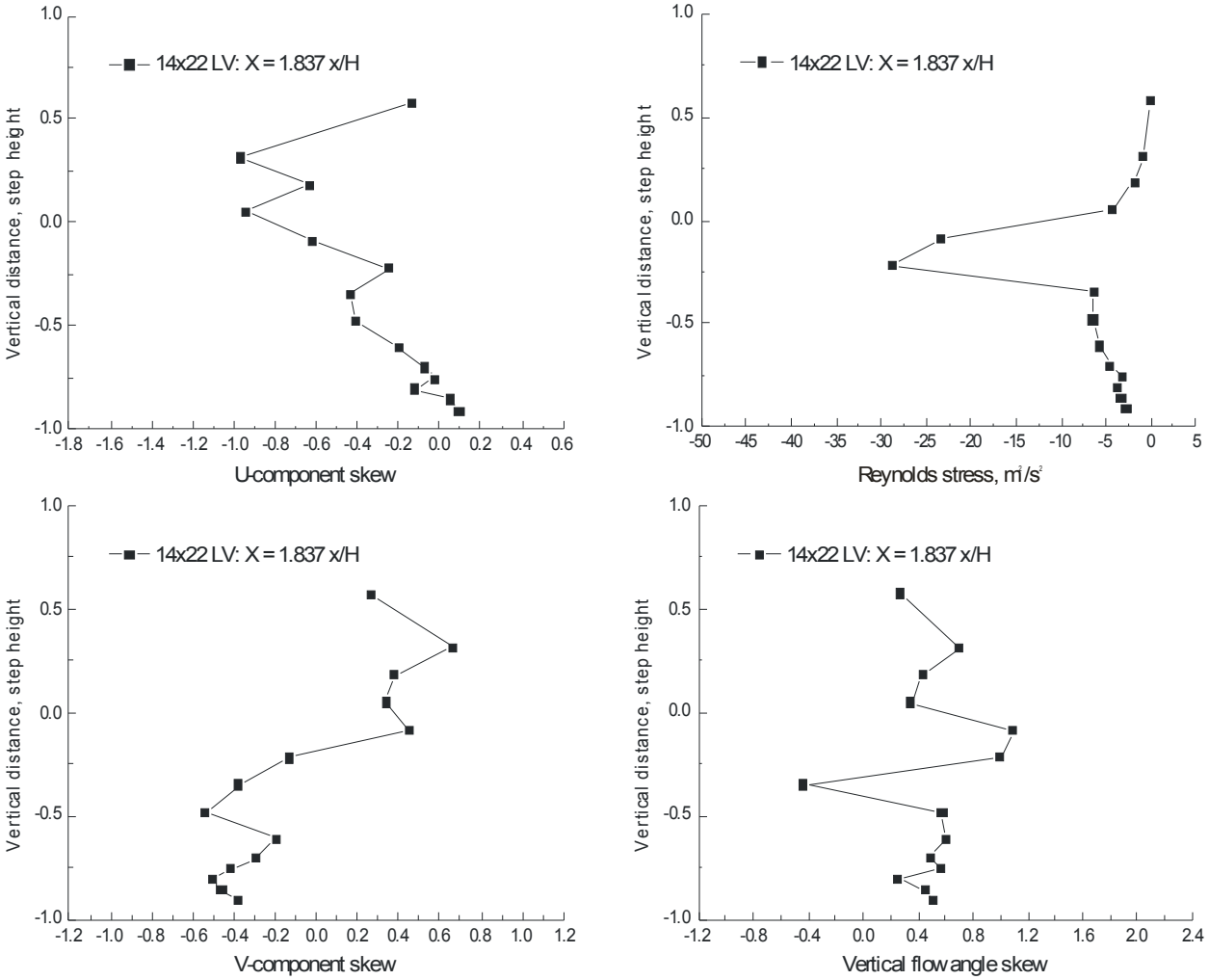

Figure VII.8.g.- Vertical scan 1.837 x/H downstream of a 1.5-inch backward-facing step: streamwise and vertical velocity skew, flow angle skew and Reynolds stress, fs = 45.0 m/s.

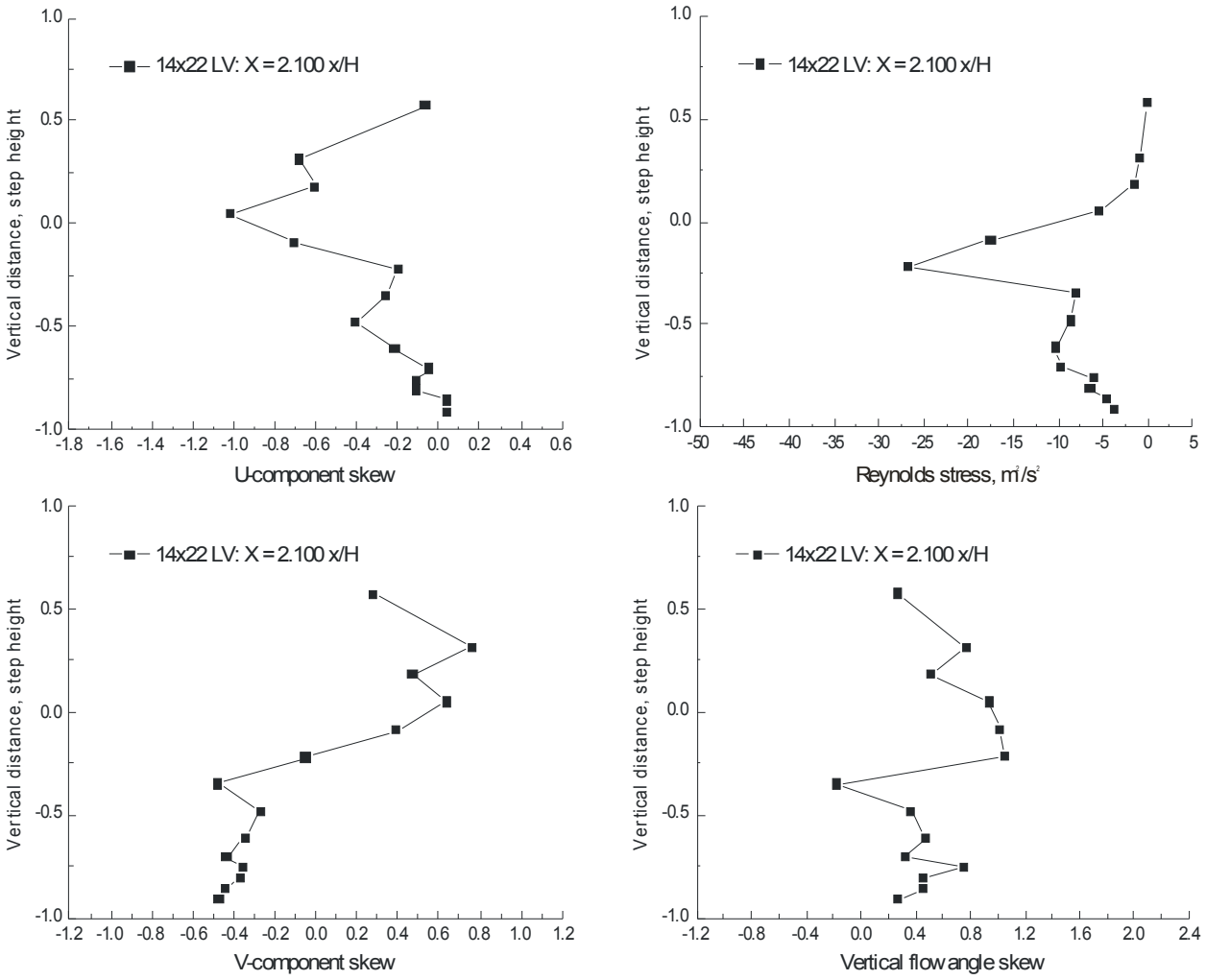

Figure VII.8.h.- Vertical scan 2.1 x/H downstream of a 1.5-inch backward-facing step: streamwise and vertical velocity skew, flow angle skew and Reynolds stress, fs = 45.0 m/s.

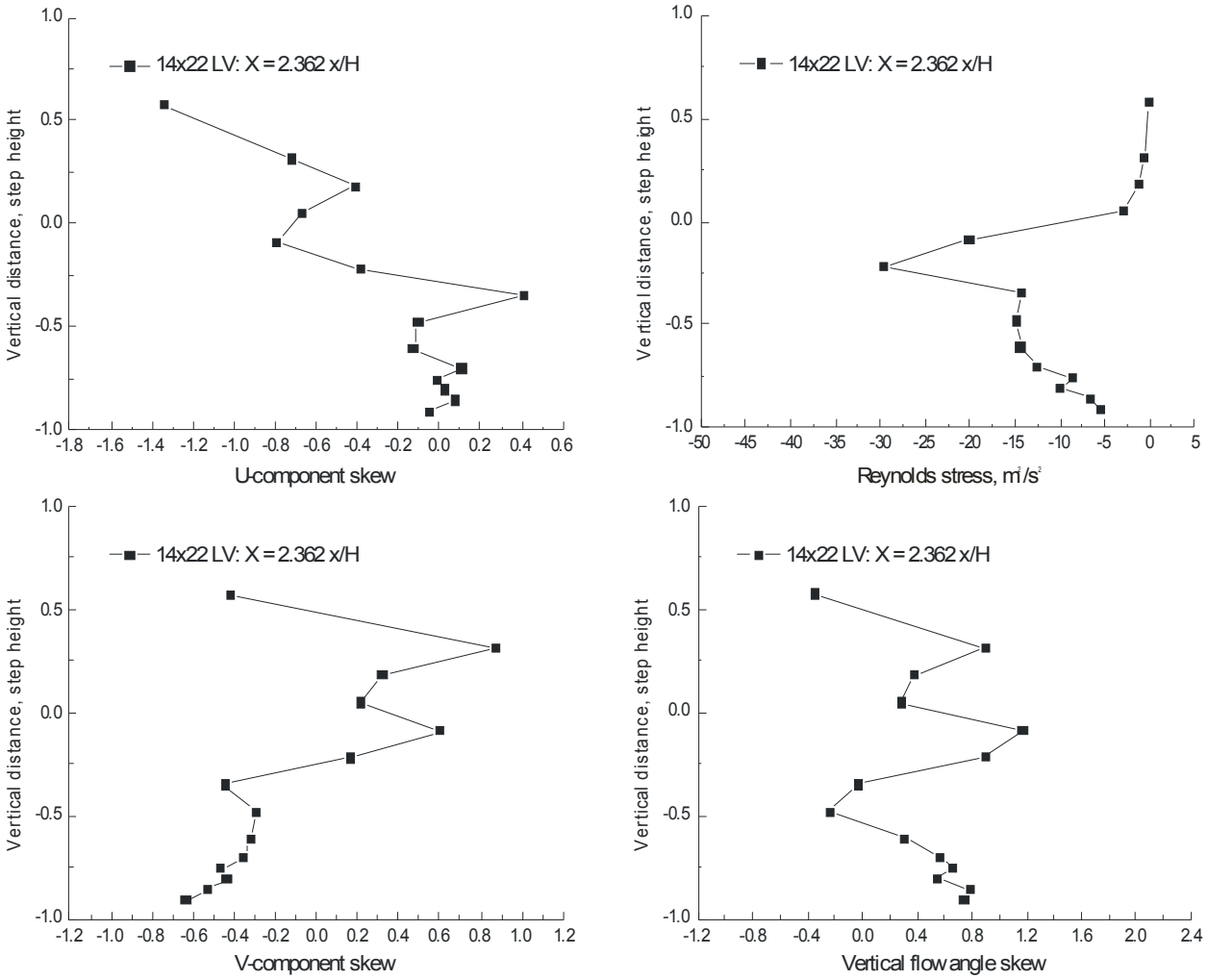

Figure VII.8.i.- Vertical scan 2.362 x/H downstream of a 1.5-inch backward-facing step: streamwise and vertical velocity skew, flow angle skew and Reynolds stress, fs = 45.0 m/s.

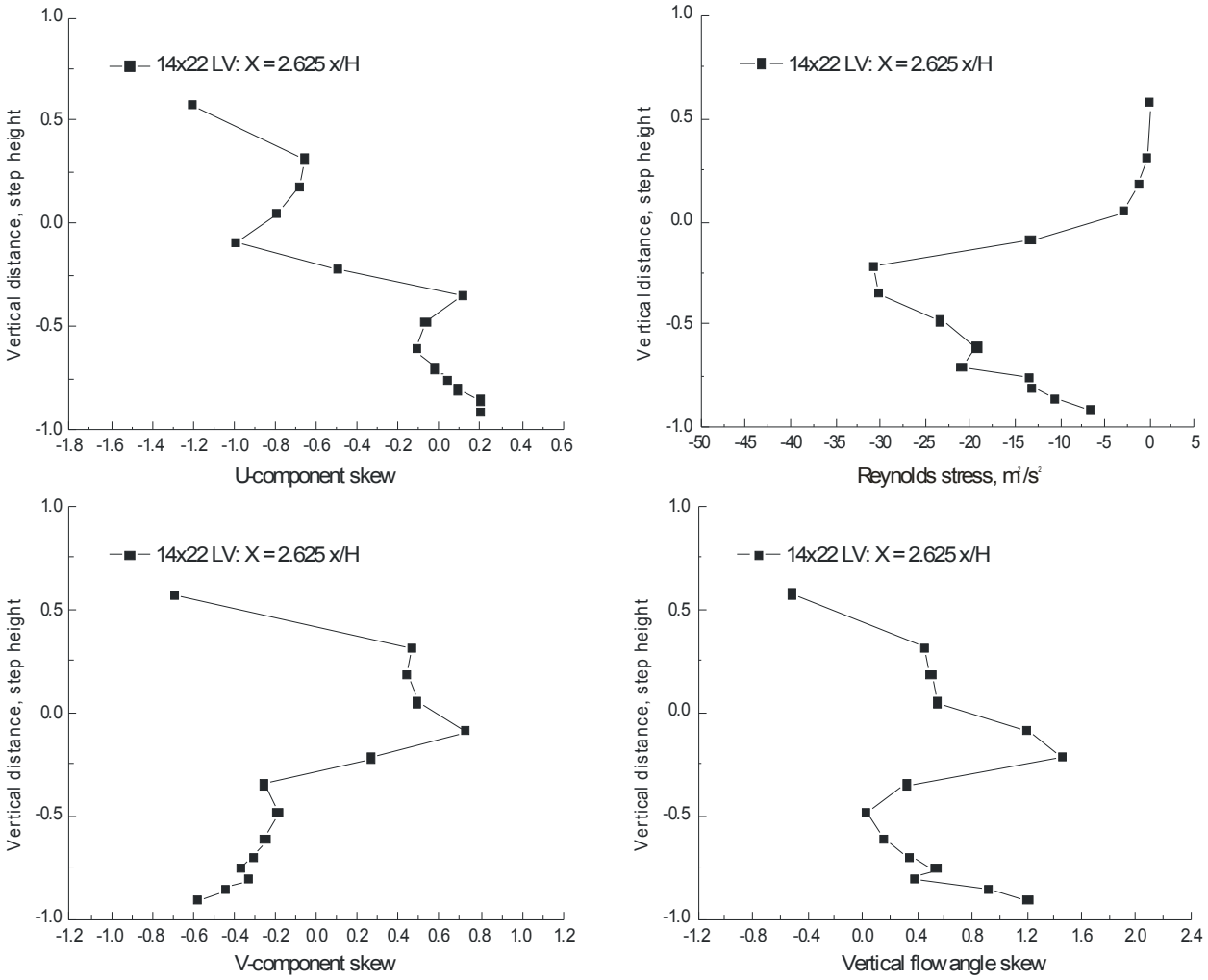

Figure VII.8.j.- Vertical scan 2.625 x/H downstream of a 1.5-inch backward-facing step: streamwise and vertical velocity skew, flow angle skew and Reynolds stress, fs = 45.0 m/s.

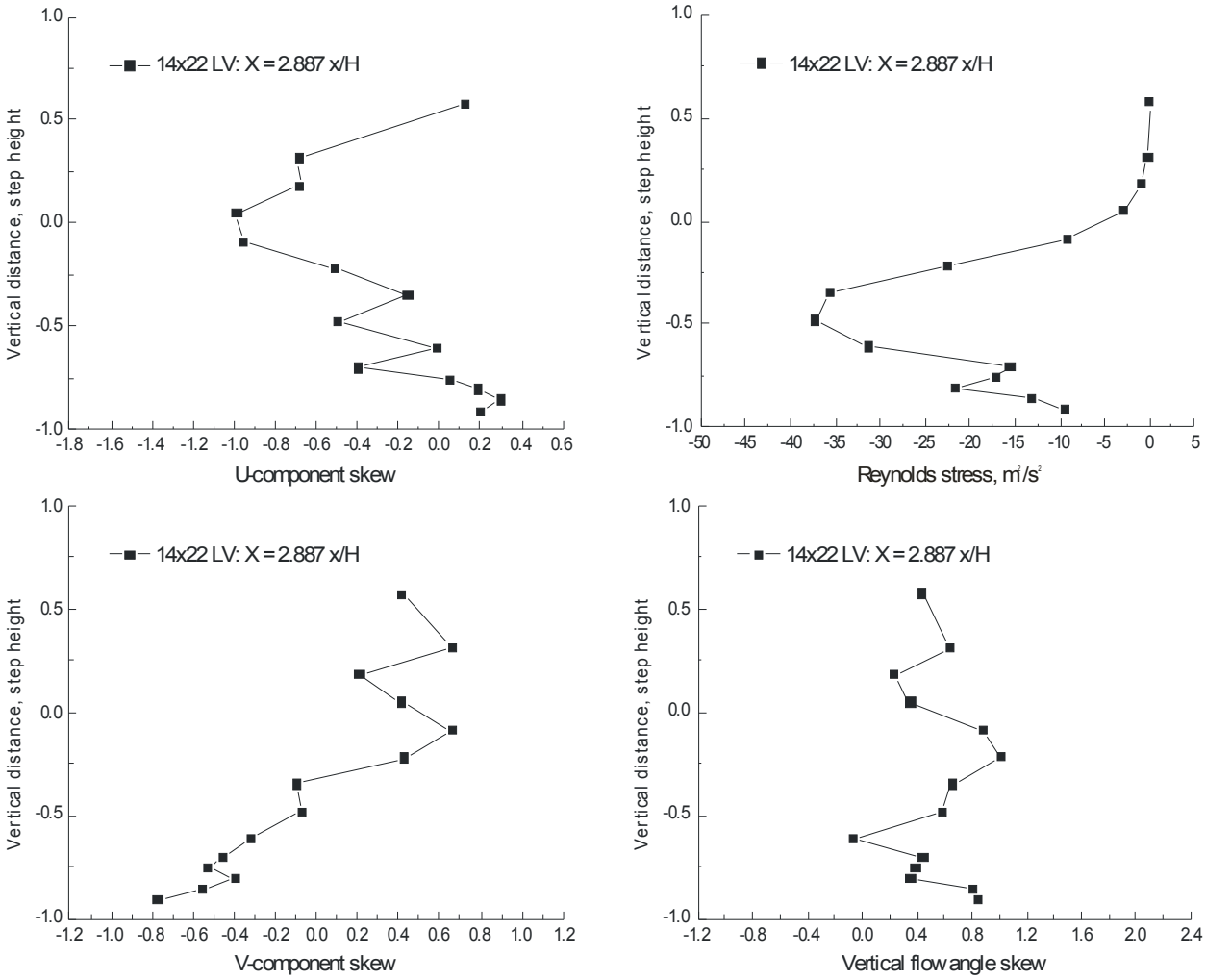

Figure VII.8.k.- Vertical scan 2.887 x/H downstream of a 1.5-inch backward-facing step: streamwise and vertical velocity skew, flow angle skew and Reynolds stress, fs = 45.0 m/s.

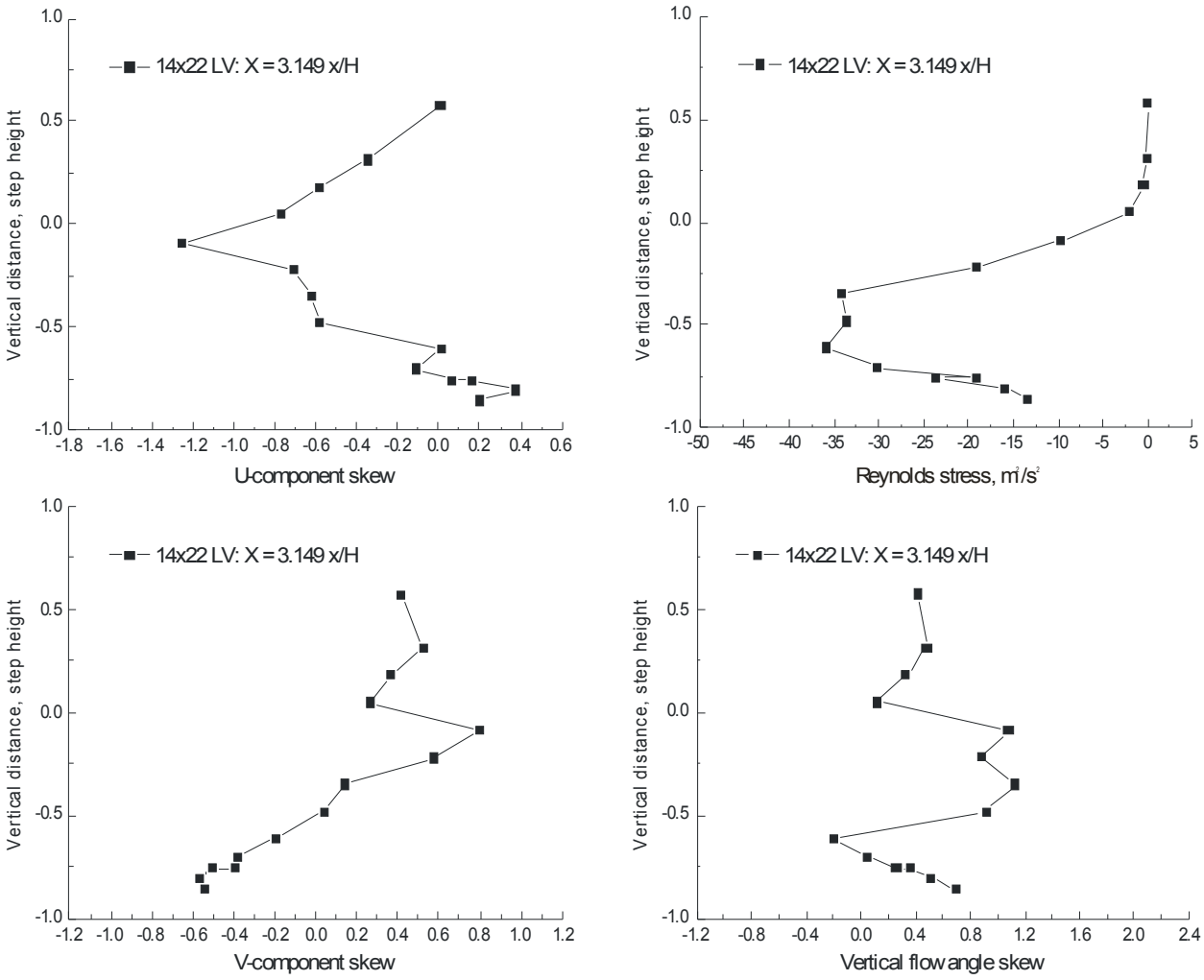

Figure VII.8.l.- Vertical scan 3.149 x/H downstream of a 1.5-inch backward-facing step: streamwise and vertical velocity skew, flow angle skew and Reynolds stress, fs = 45.0 m/s.

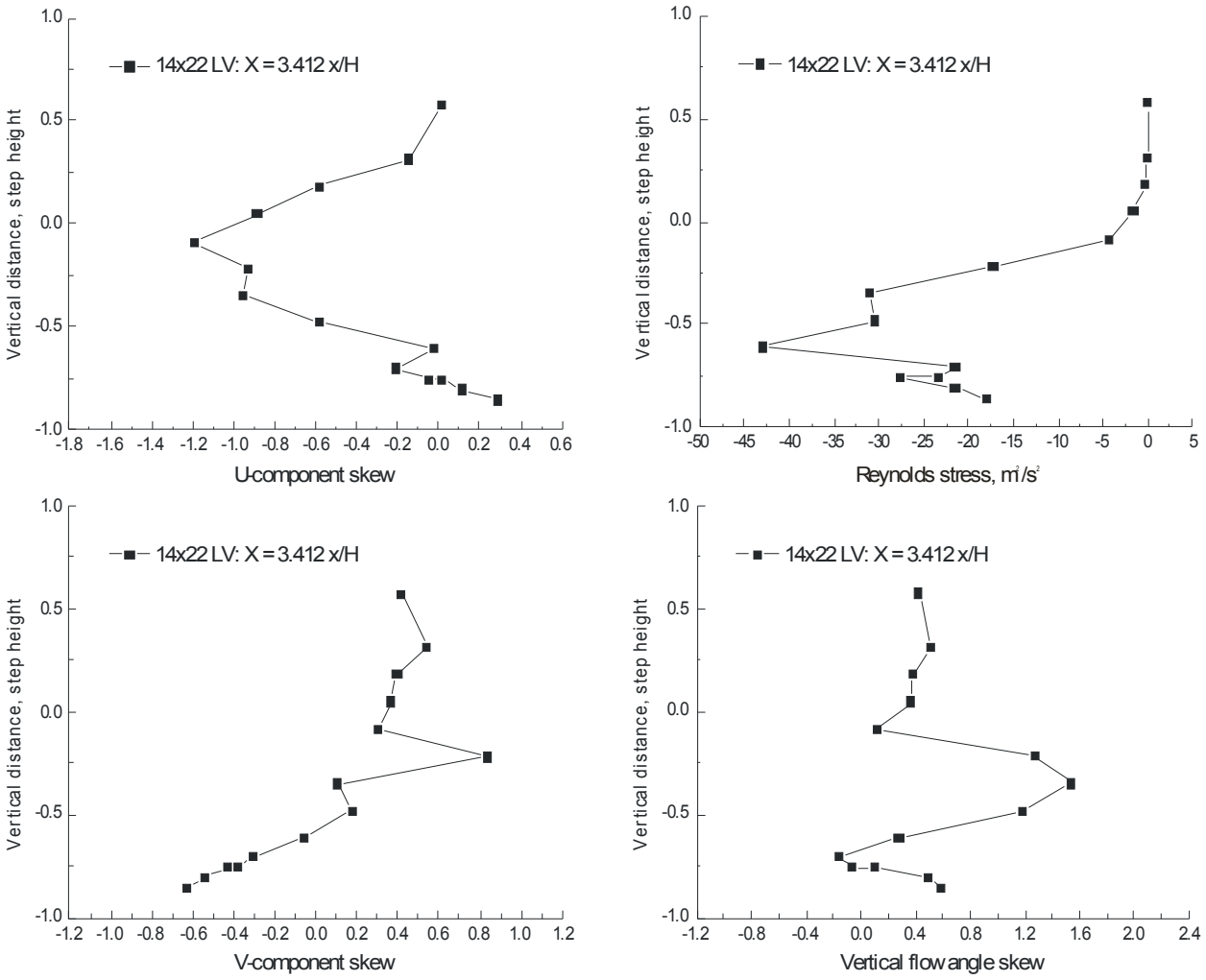

Figure VII.8.m.- Vertical scan 3.412 x/H downstream of a 1.5-inch backward-facing step: streamwise and vertical velocity skew, flow angle skew and Reynolds stress, fs = 45.0 m/s.

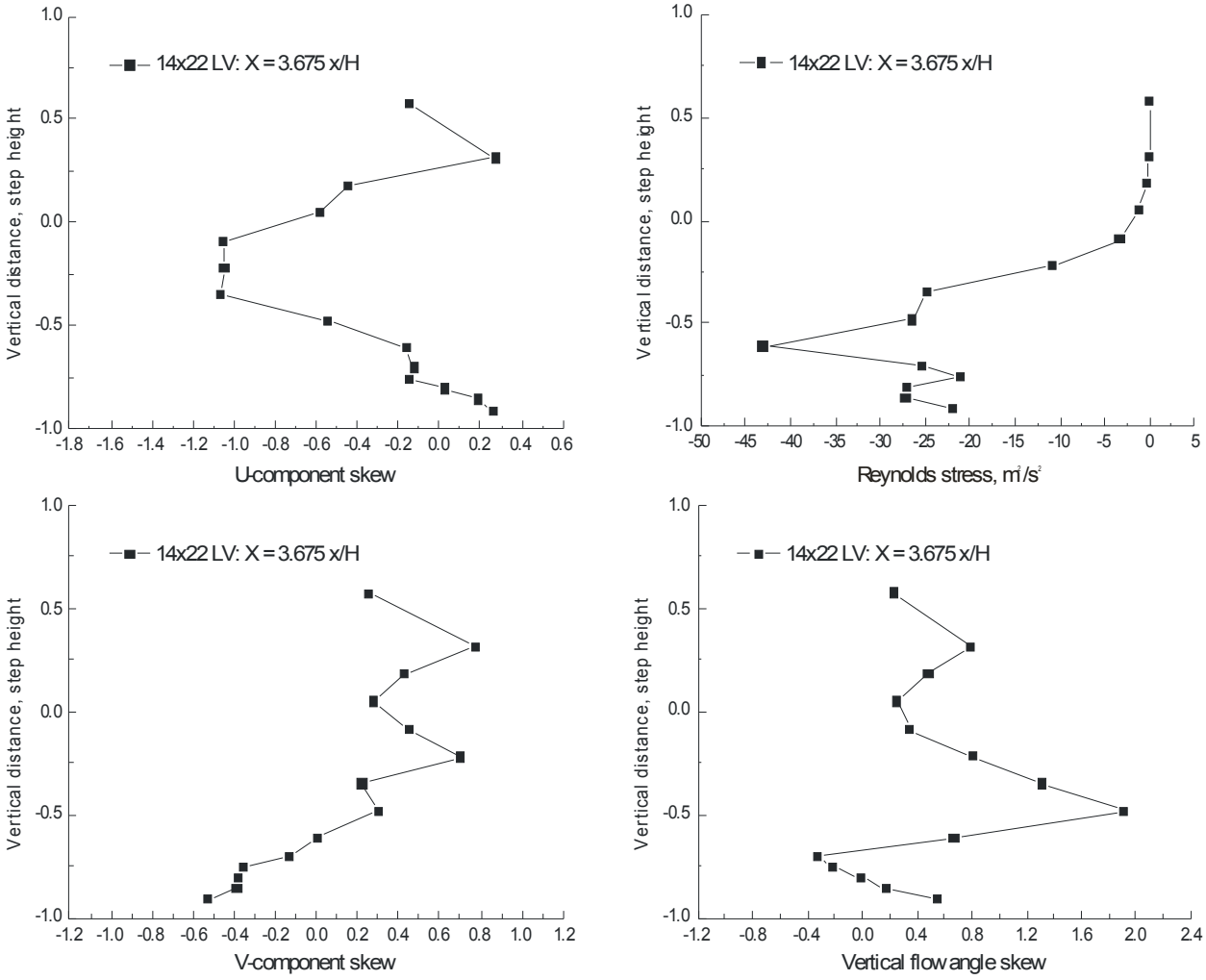

Figure VII.8.n.- Vertical scan 3.675 x/H downstream of a 1.5-inch backward-facing step: streamwise and vertical velocity skew, flow angle skew and Reynolds stress, fs = 45.0 m/s.

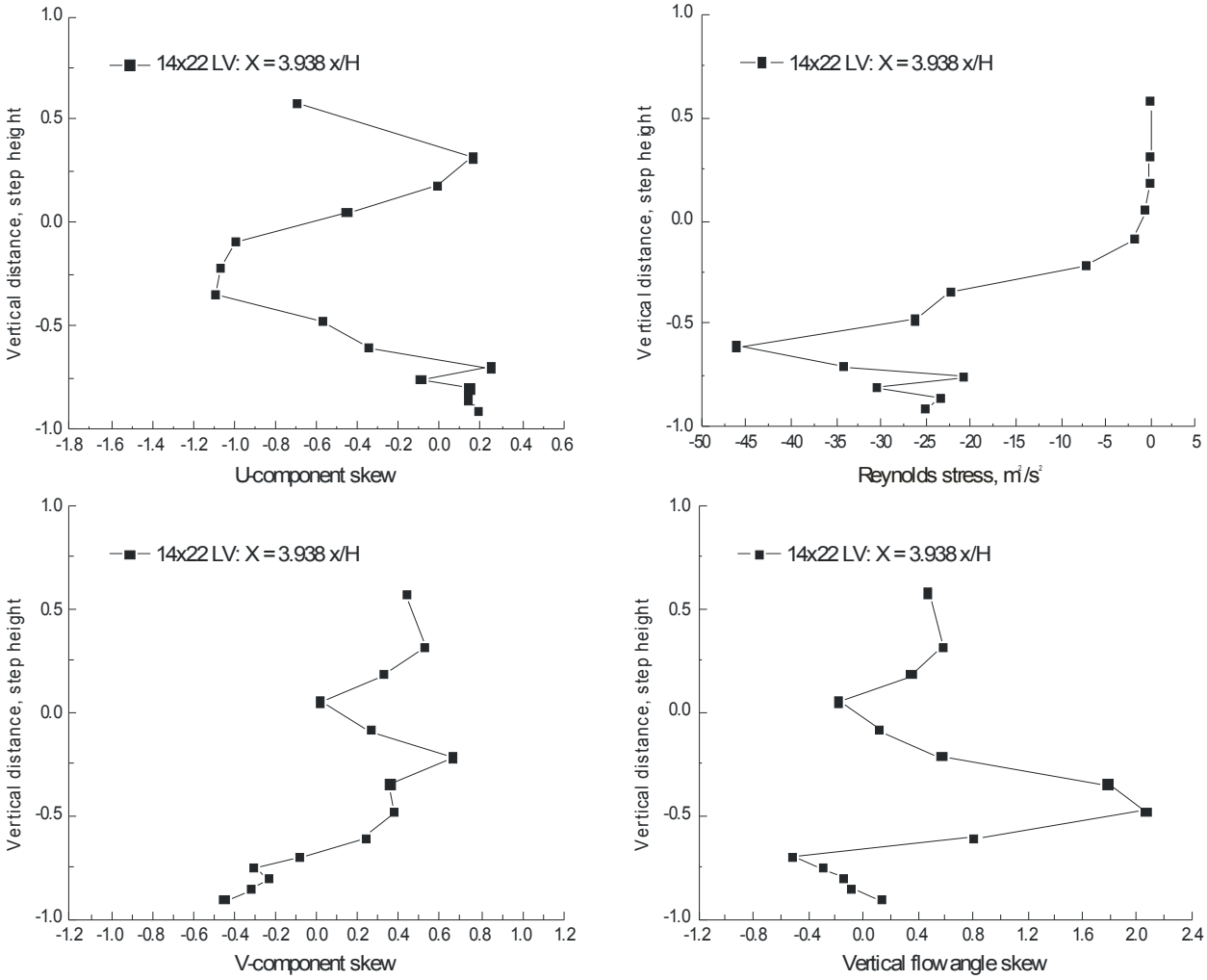

Figure VII.8.o.- Vertical scan 3.938 x/H downstream of a 1.5-inch backward-facing step: streamwise and vertical velocity skew, flow angle skew and Reynolds stress, fs = 45.0 m/s.

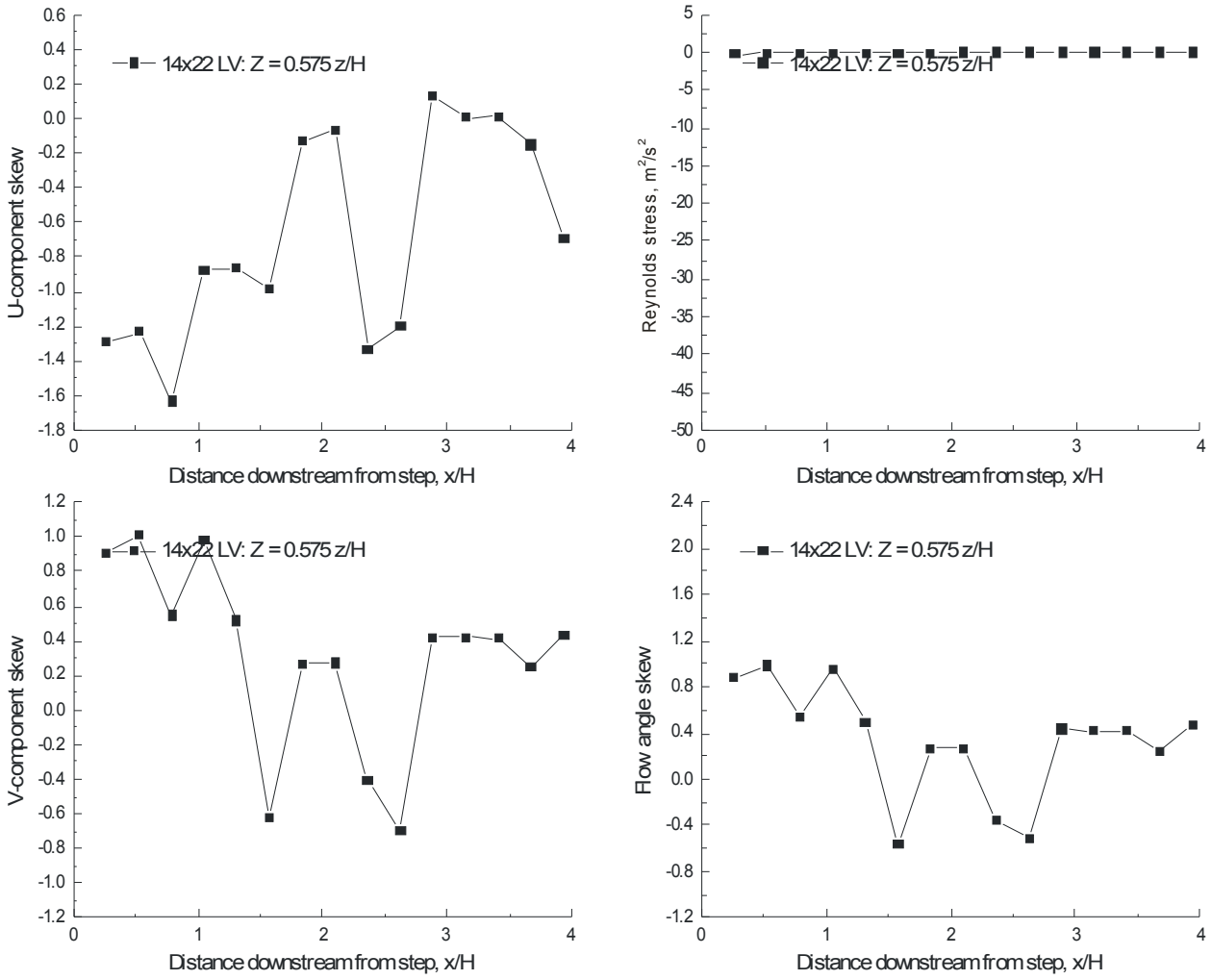

Figure VII.9.a.- Horizontal scan 0.575 z/H above a 1.5-inch backward-facing step: streamwise and vertical velocity skew, flow angle skew and Reynolds stress, fs = 45.0 m/s.

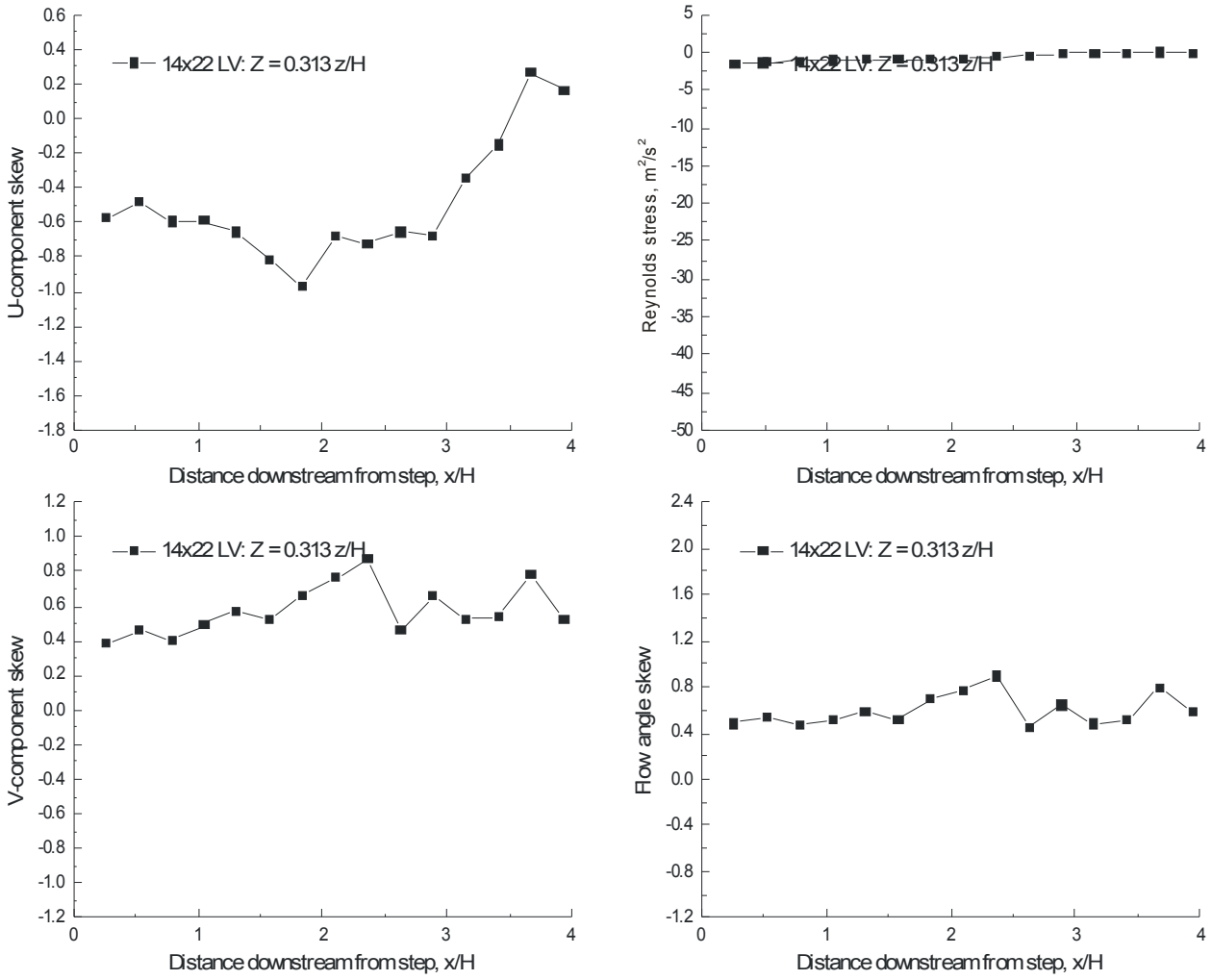

Figure VII.9.b.- Horizontal scan 0.313 z/H above a 1.5-inch backward-facing step: streamwise and vertical velocity skew, flow angle skew and Reynolds stress, fs = 45.0 m/s.

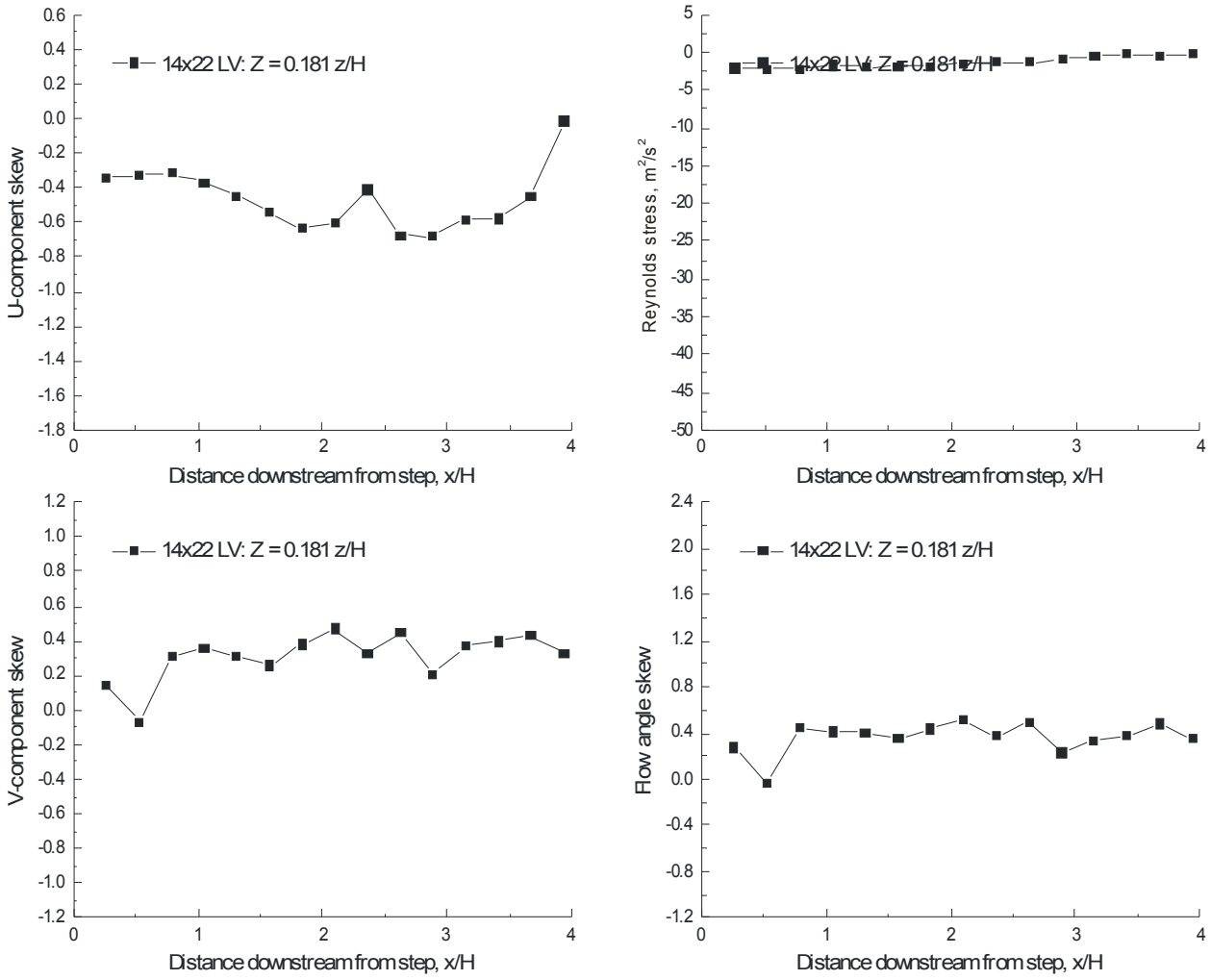

Figure VII.9.c.- Horizontal scan 0.181 z/H above a 1.5-inch backward-facing step: streamwise and vertical velocity skew, flow angle skew and Reynolds stress, fs = 45.0 m/s.

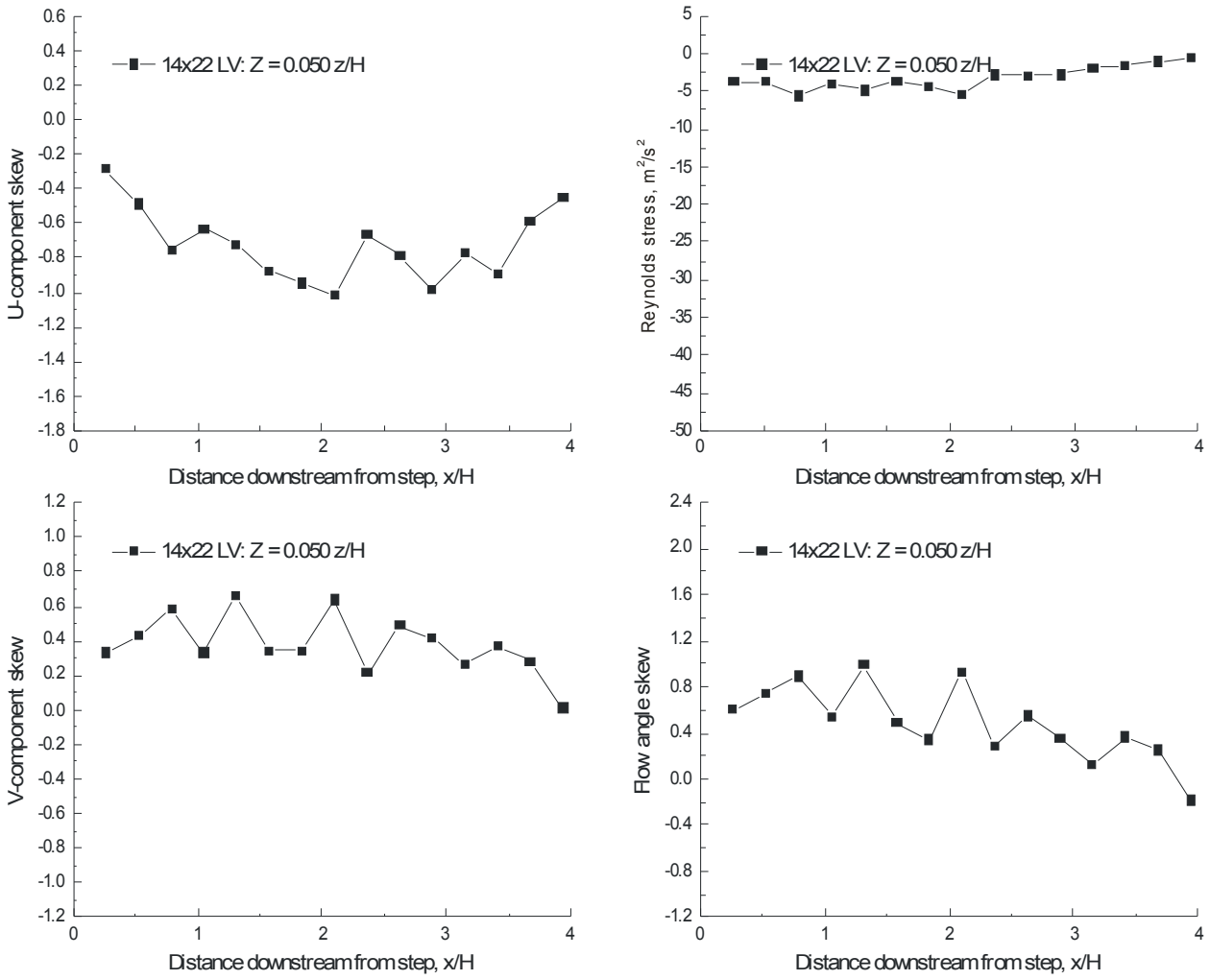

Figure VII.9.d.- Horizontal scan 0.050 z/H above a 1.5-inch backward-facing step: streamwise and vertical velocity skew, flow angle skew and Reynolds stress, fs = 45.0 m/s.

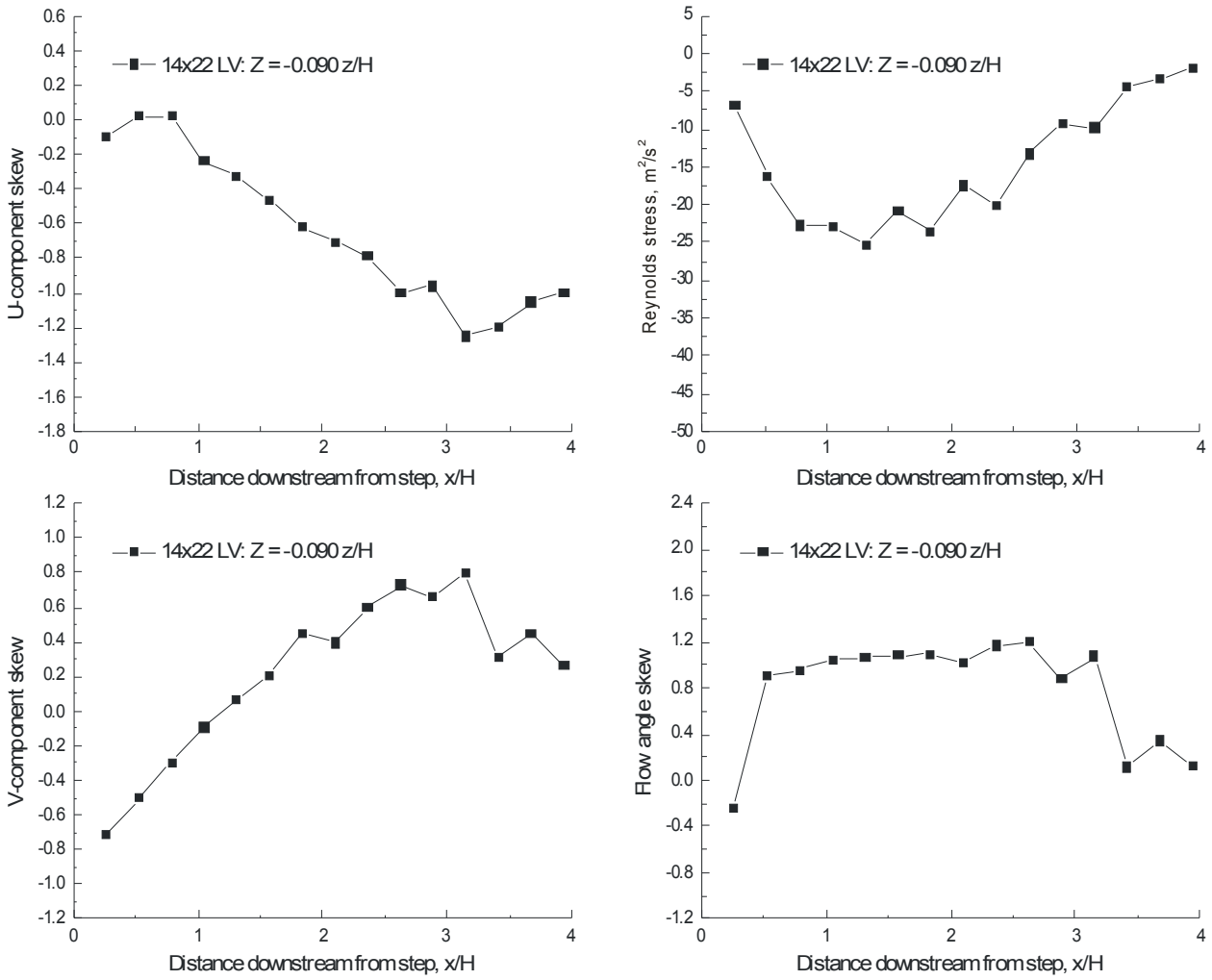

Figure VII.9.e.- Horizontal scan 0.090 z/H below a 1.5-inch backward-facing step: streamwise and vertical velocity skew, flow angle skew and Reynolds stress, fs = 45.0 m/s.

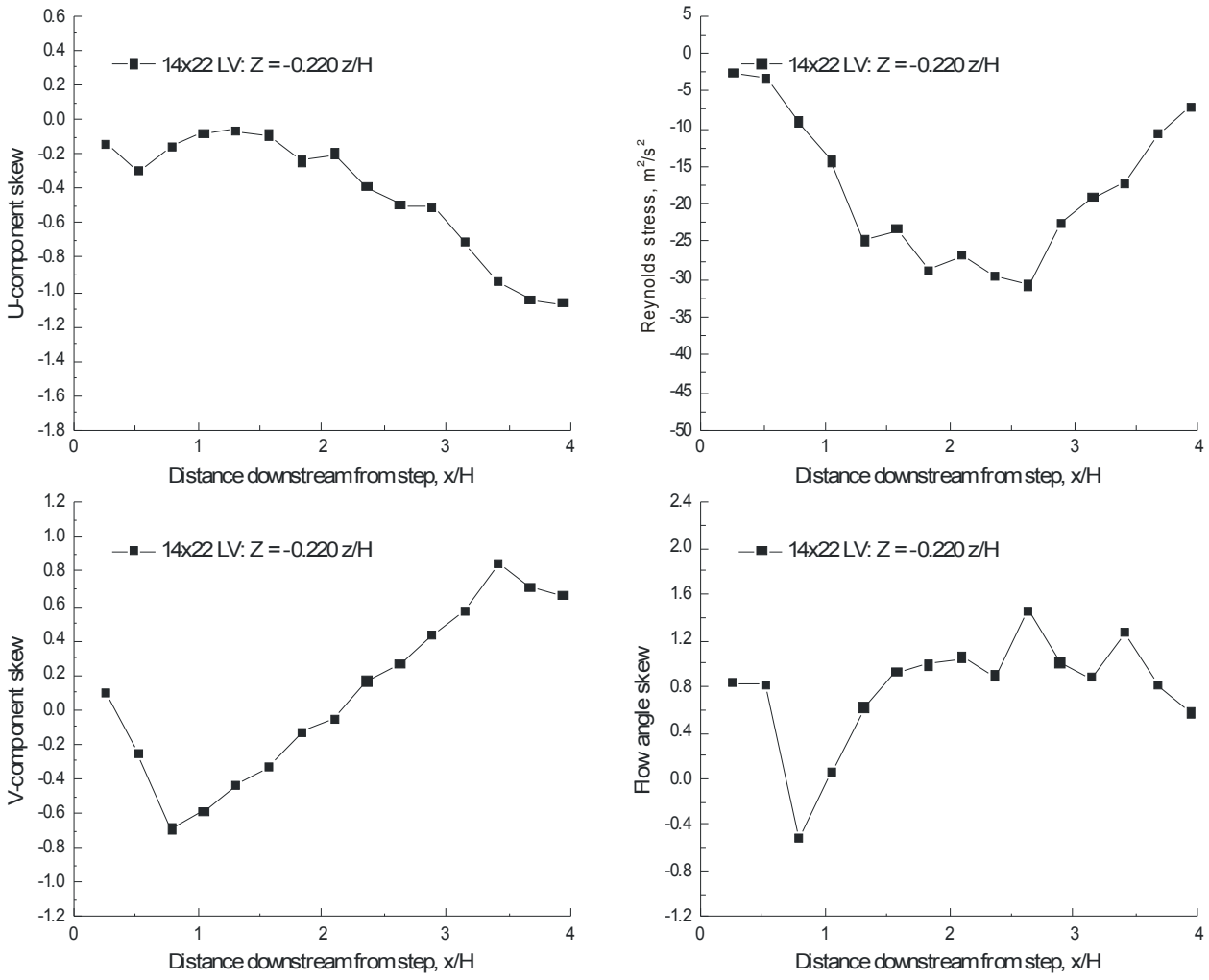

Figure VII.9.f.- Horizontal scan 0.220 z/H below a 1.5-inch backward-facing step: streamwise and vertical velocity skew, flow angle skew and Reynolds stress, fs = 45.0 m/s.

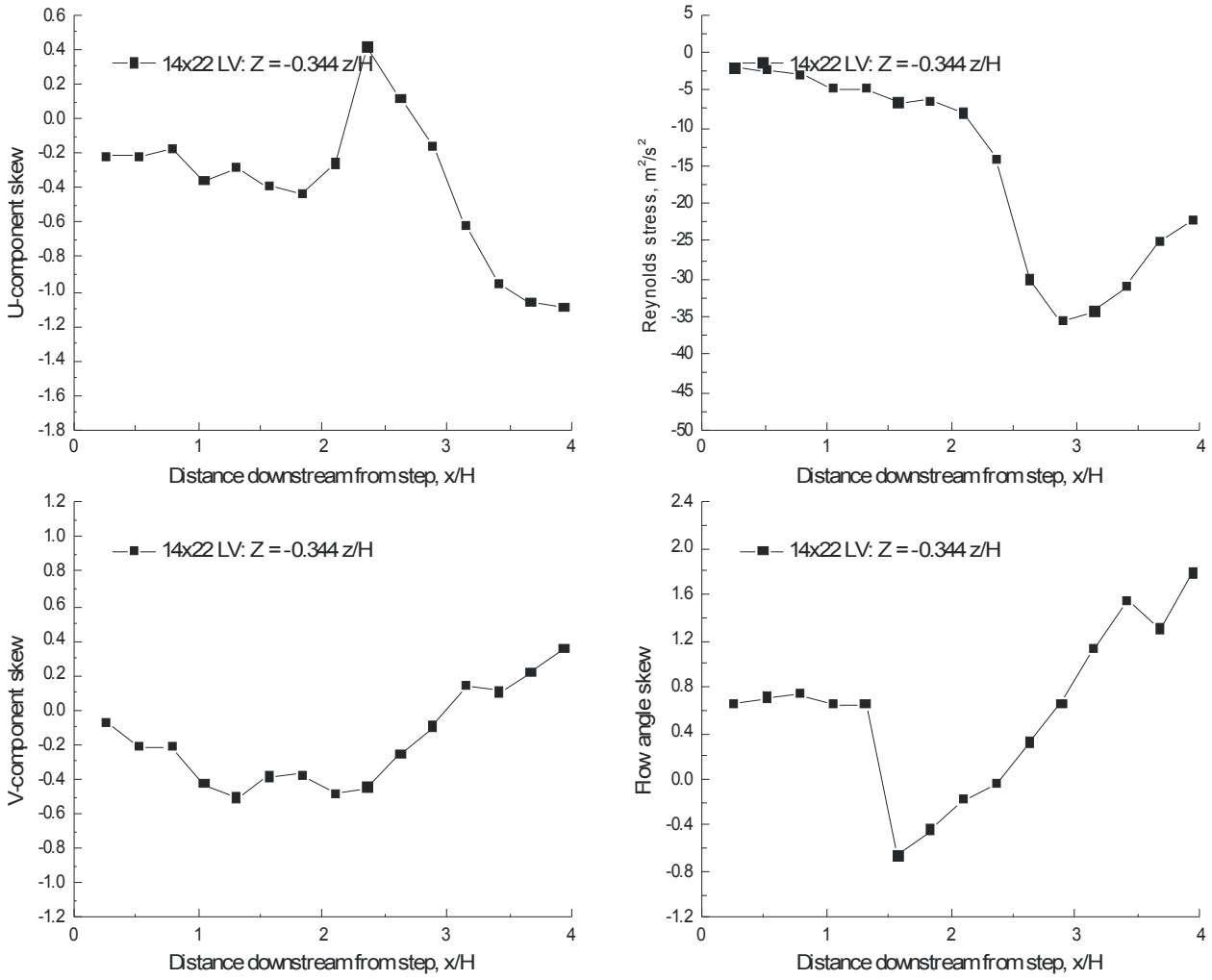

Figure VII.9.g.- Horizontal scan 0.344 z/H below a 1.5-inch backward-facing step: streamwise and vertical velocity skew, flow angle skew and Reynolds stress, fs = 45.0 m/s.

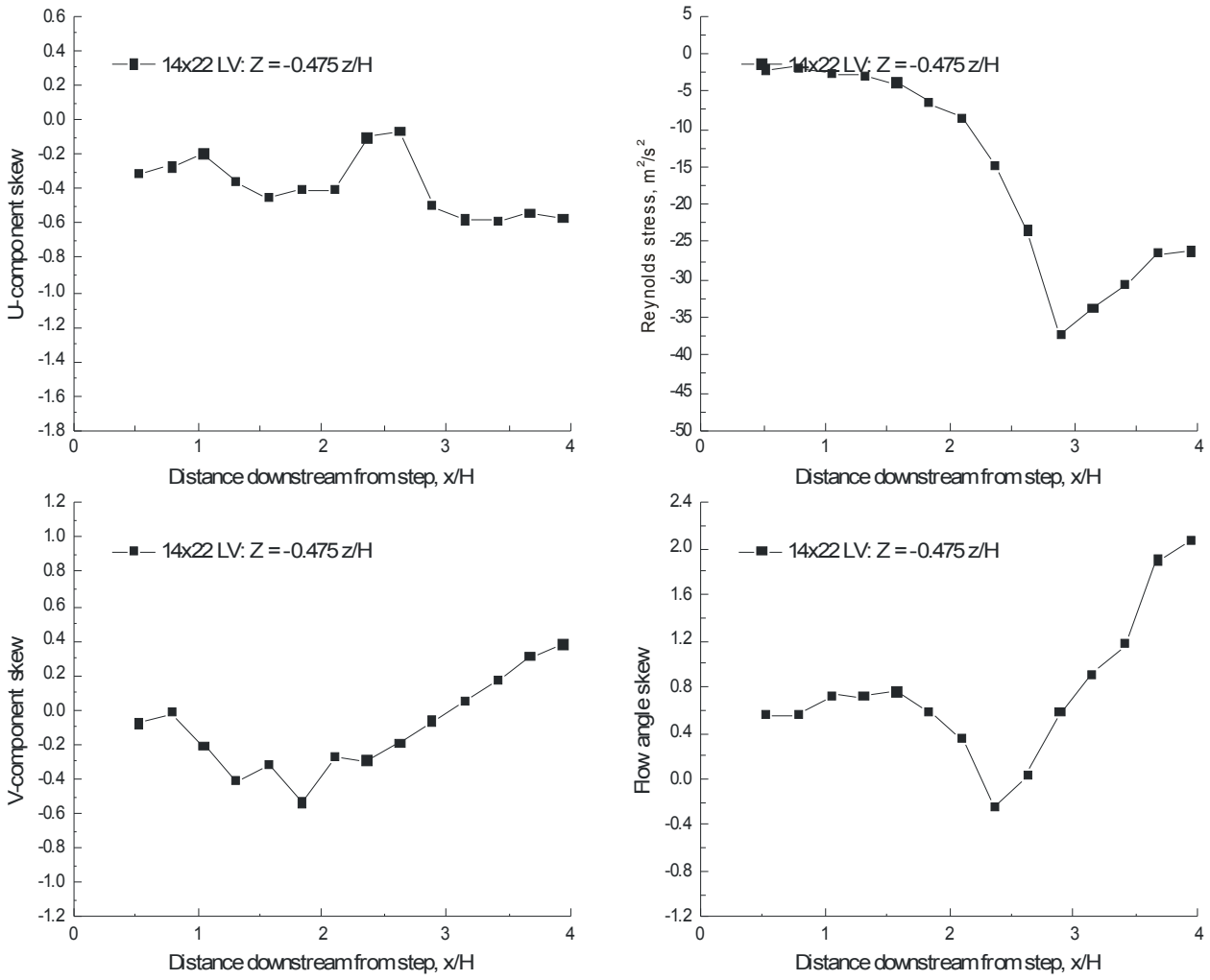

Figure VII.9.h.- Horizontal scan 0.475 z/H below a 1.5-inch backward-facing step: streamwise and vertical velocity skew, flow angle skew and Reynolds stress, fs = 45.0 m/s.

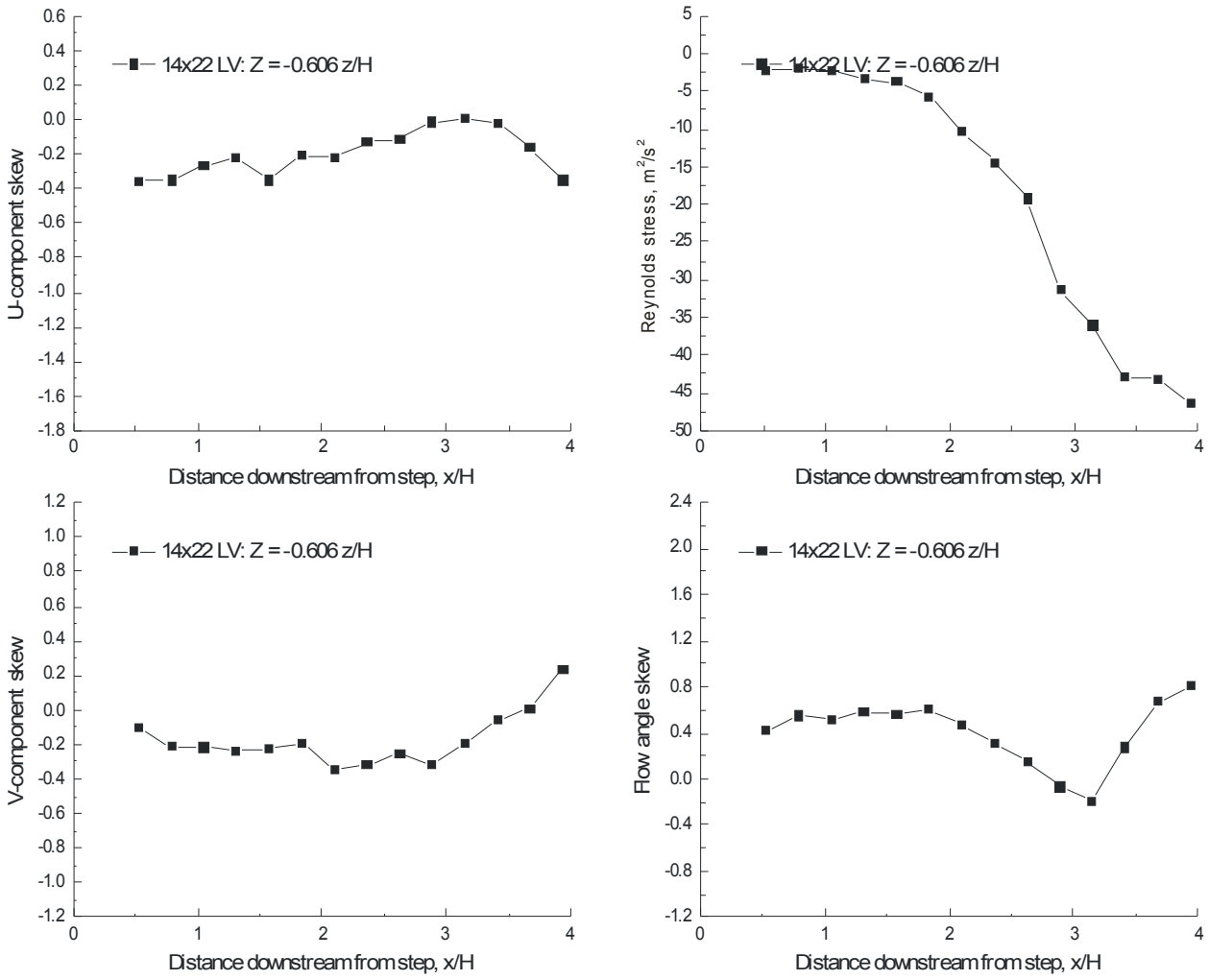

Figure VII.9.i.- Horizontal scan 0.606 z/H below a 1.5-inch backward-facing step: streamwise and vertical velocity skew, flow angle skew and Reynolds stress, fs = 45.0 m/s.

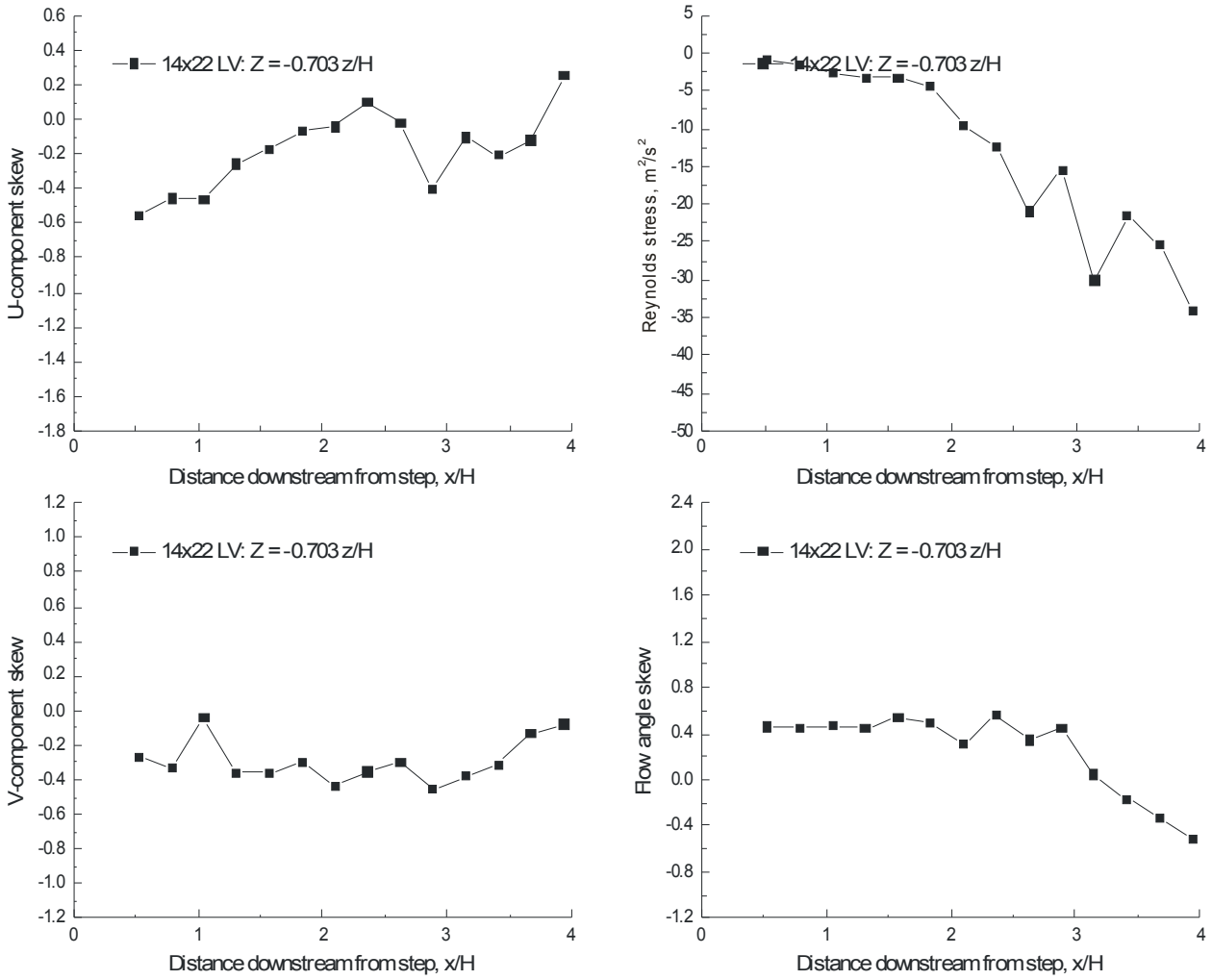

Figure VII.9.j.- Horizontal scan 0.703 z/H below a 1.5-inch backward-facing step: streamwise and vertical velocity skew, flow angle skew and Reynolds stress, fs = 45.0 m/s.

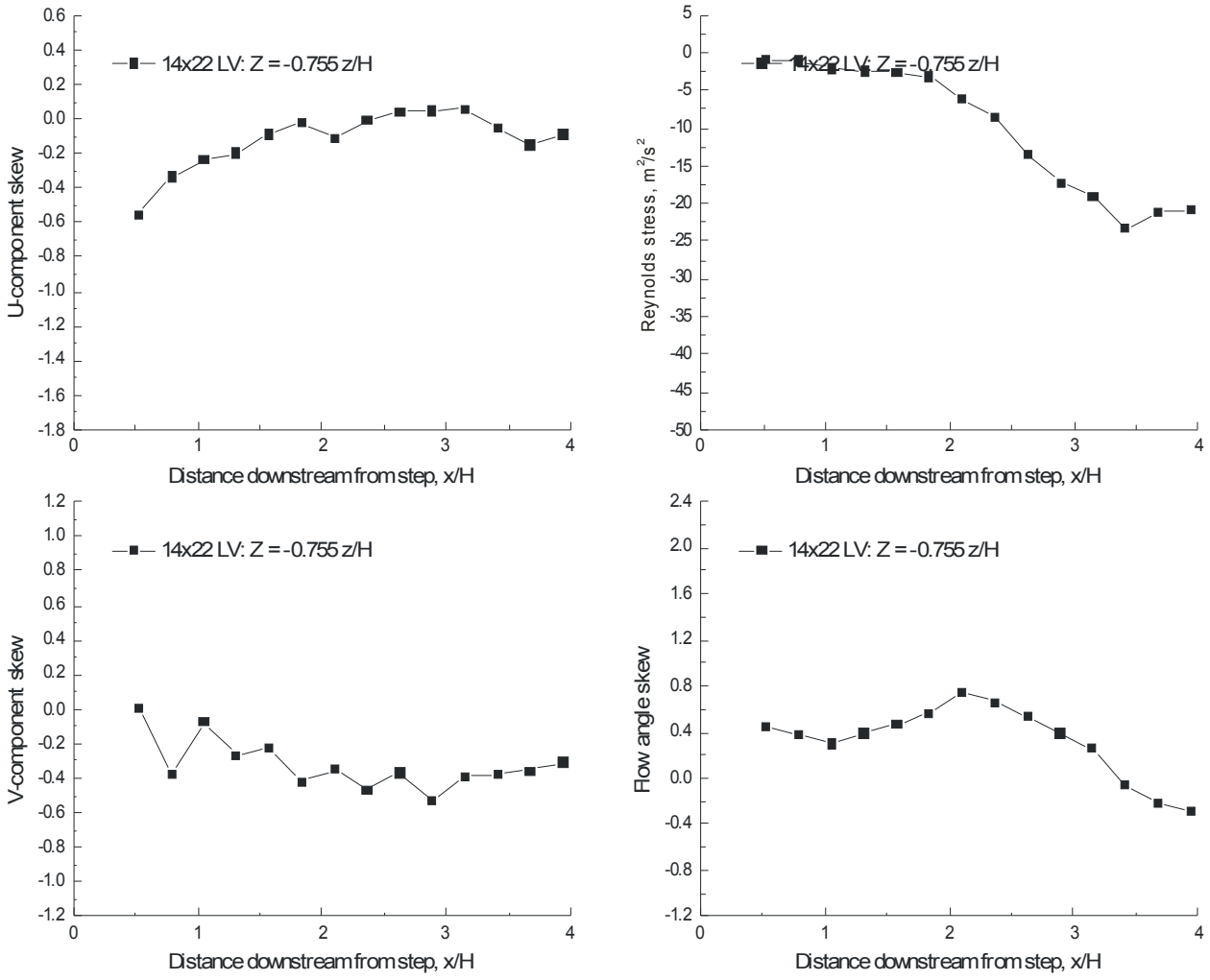

Figure VII.9.k.- Horizontal scan 0.755 z/H below a 1.5-inch backward-facing step: streamwise and vertical velocity skew, flow angle skew and Reynolds stress, fs = 45.0 m/s.

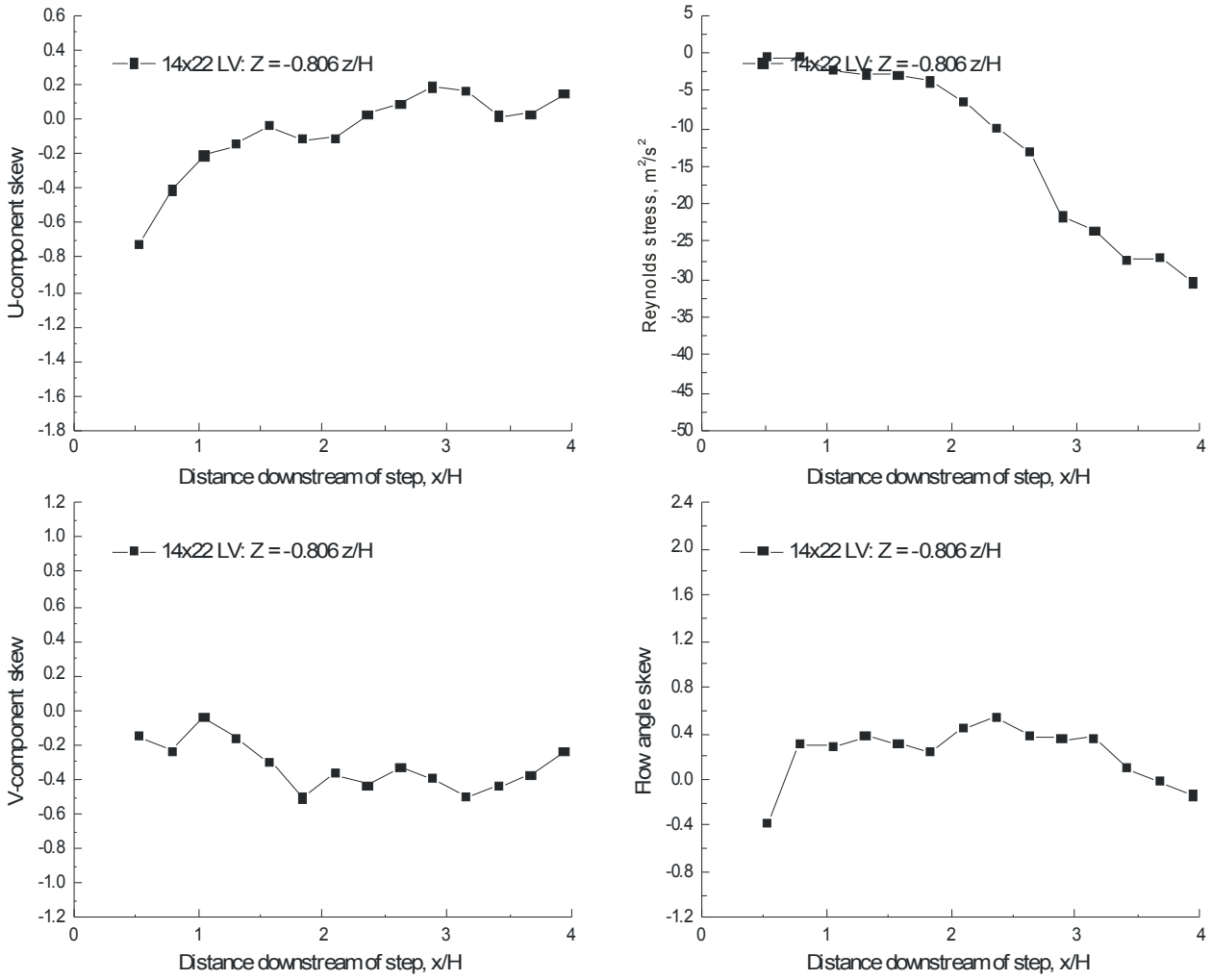

Figure VII.9.I.- Horizontal scan 0.806 z/H below a 1.5-inch backward-facing step: streamwise and vertical velocity skew, flow angle skew and Reynolds stress, fs = 45.0 m/s.

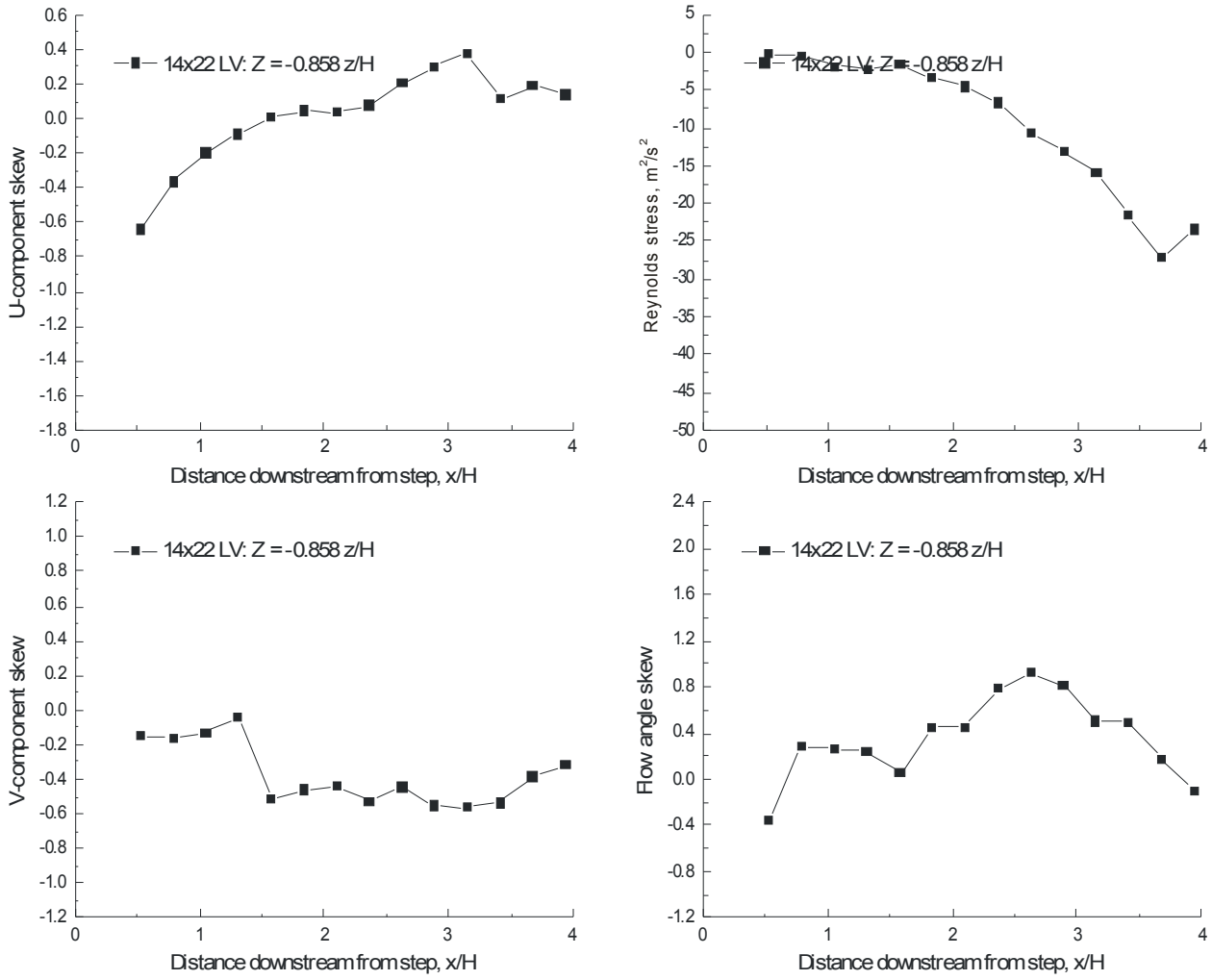

Figure VII.9.m.- Horizontal scan 0.858 z/H below a 1.5-inch backward-facing step: streamwise and vertical velocity skew, flow angle skew and Reynolds stress, fs = 45.0 m/s.

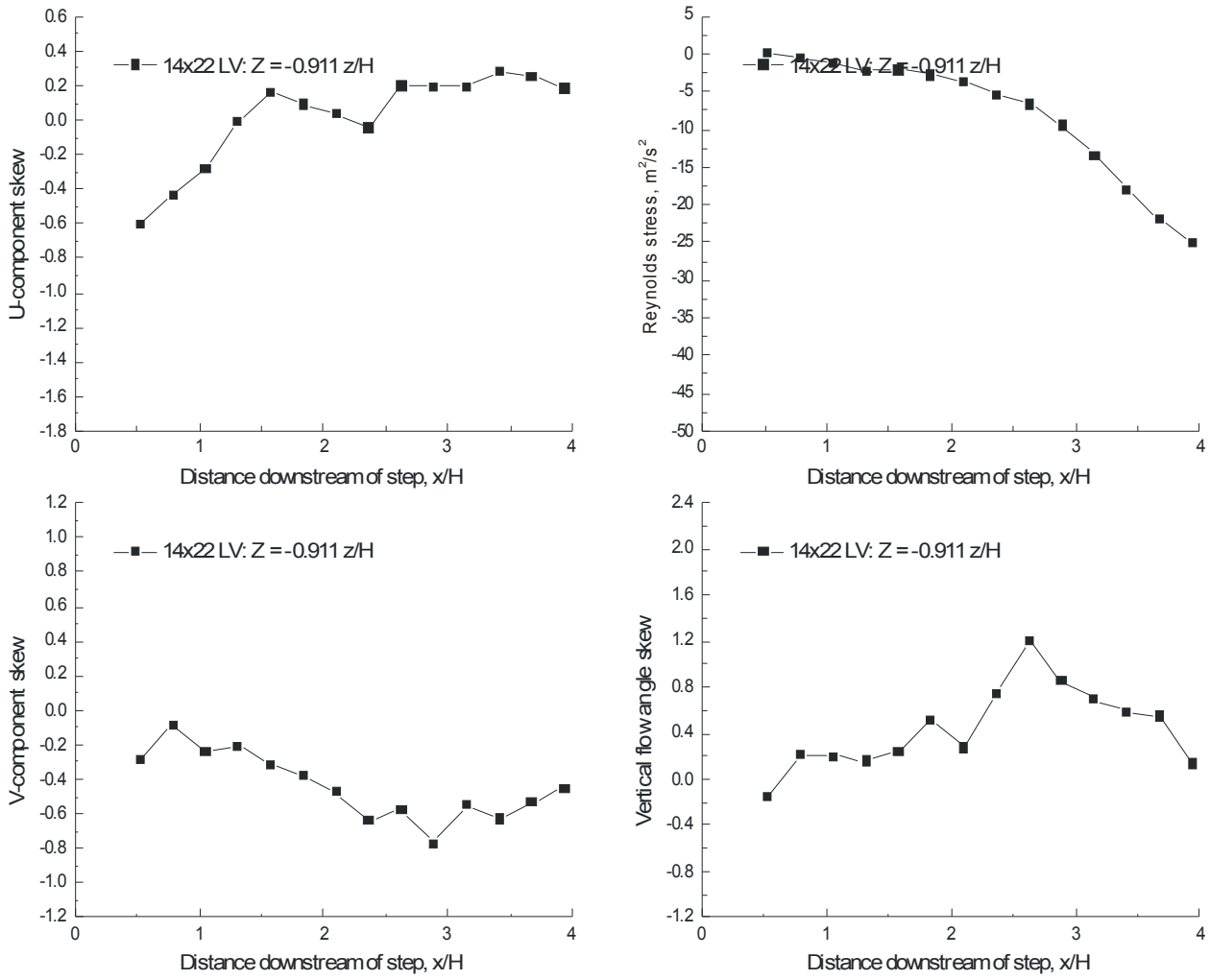

Figure VII.9.n.- Horizontal scan 0.911 z/H below a 1.5-inch backward-facing step: streamwise and vertical velocity skew, flow angle skew and Reynolds stress, fs = 45.0 m/s.

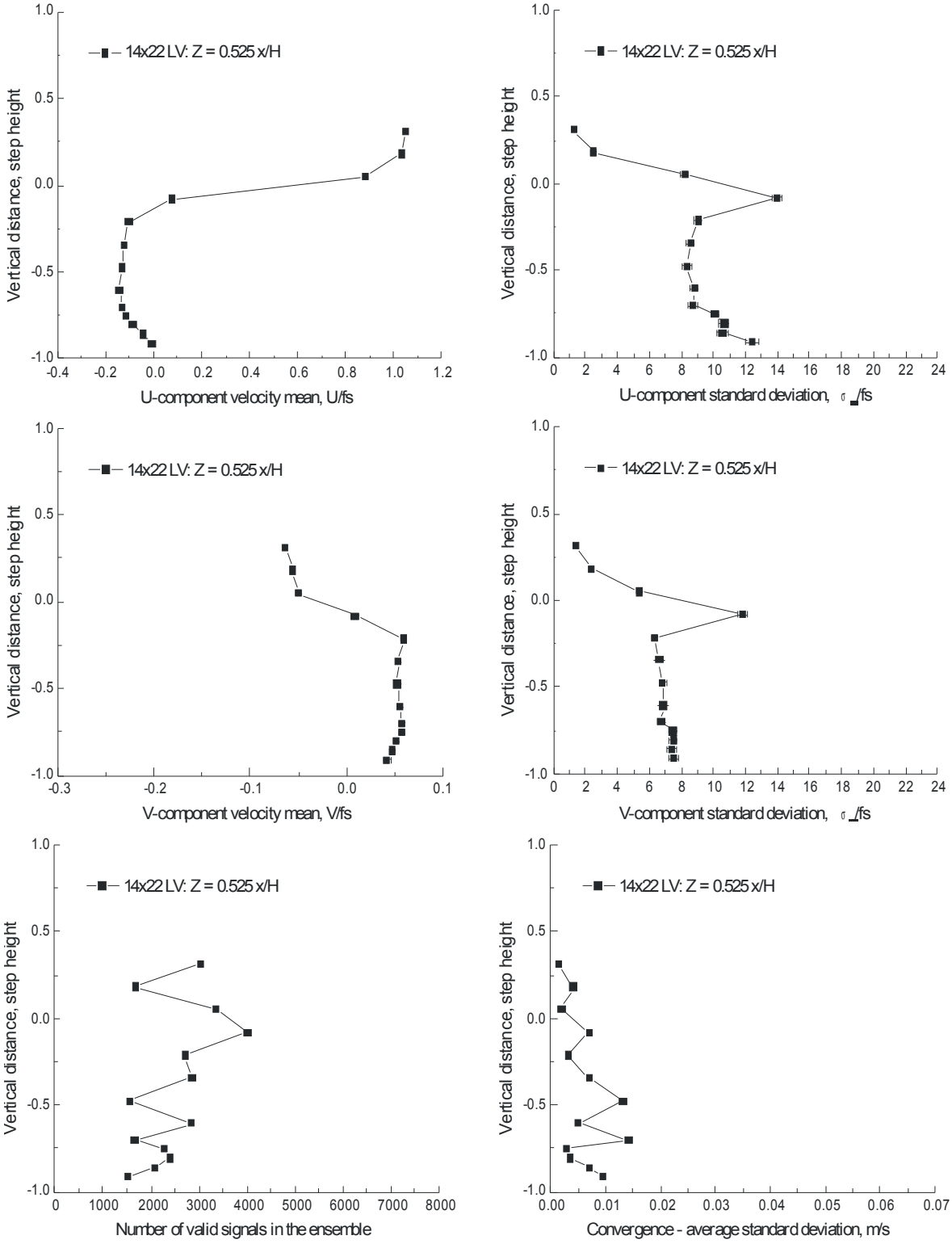

Figure VII.10.a.- Vertical scan 0.525 x/H downstream of a 3.5-inch backward-facing step (compares to Figure VII.4.b): streamwise and vertical velocity components, number of accepted signal bursts, and statistical stationarity convergence standard deviation, fs = 45.0 m/s.

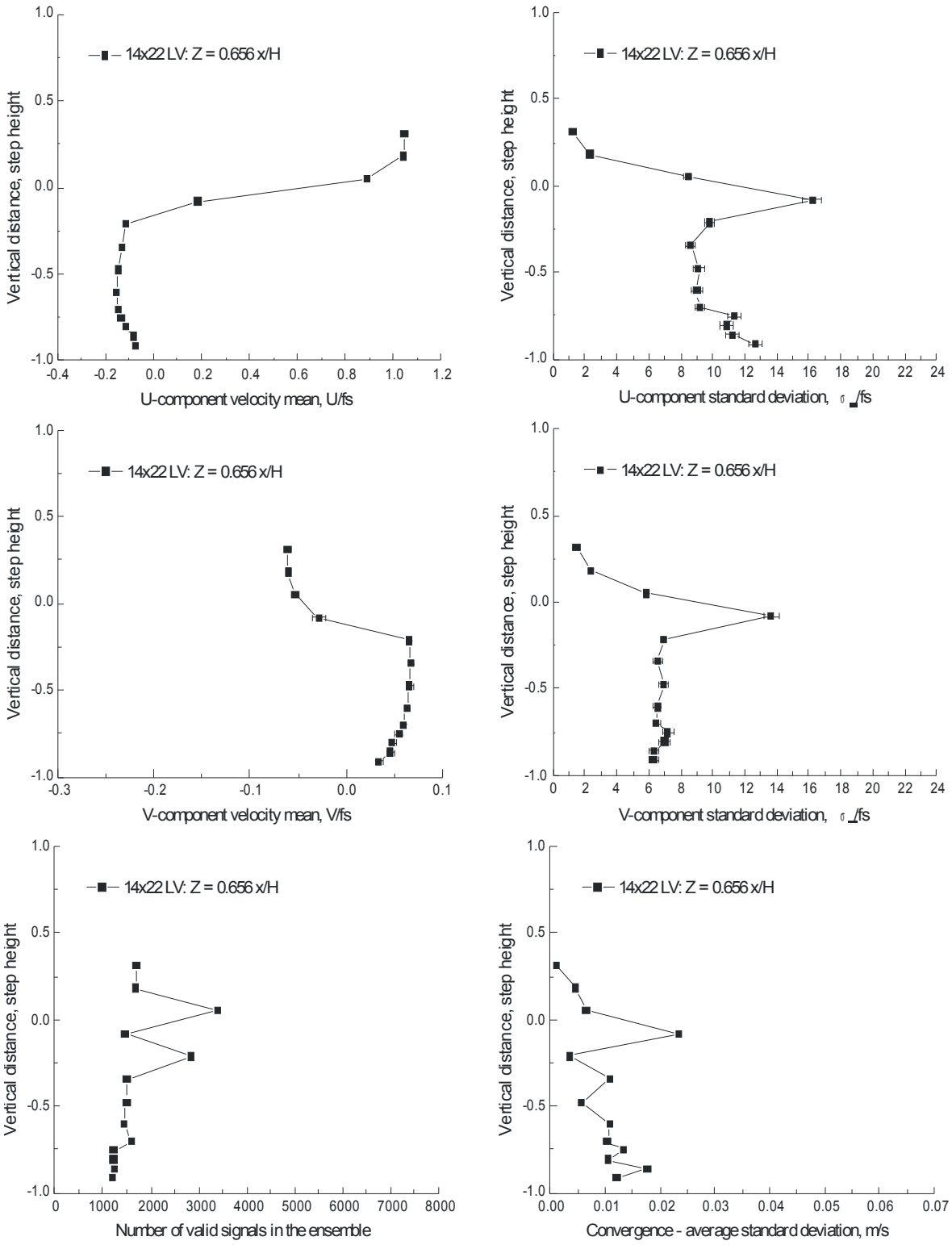

Figure VII.10.b.- Vertical scan 0.656 x/H downstream of a 3.5-inch backward-facing step: streamwise and vertical velocity components, number of accepted signal bursts, and statistical stationarity convergence standard deviation, fs = 45.0 m/s.

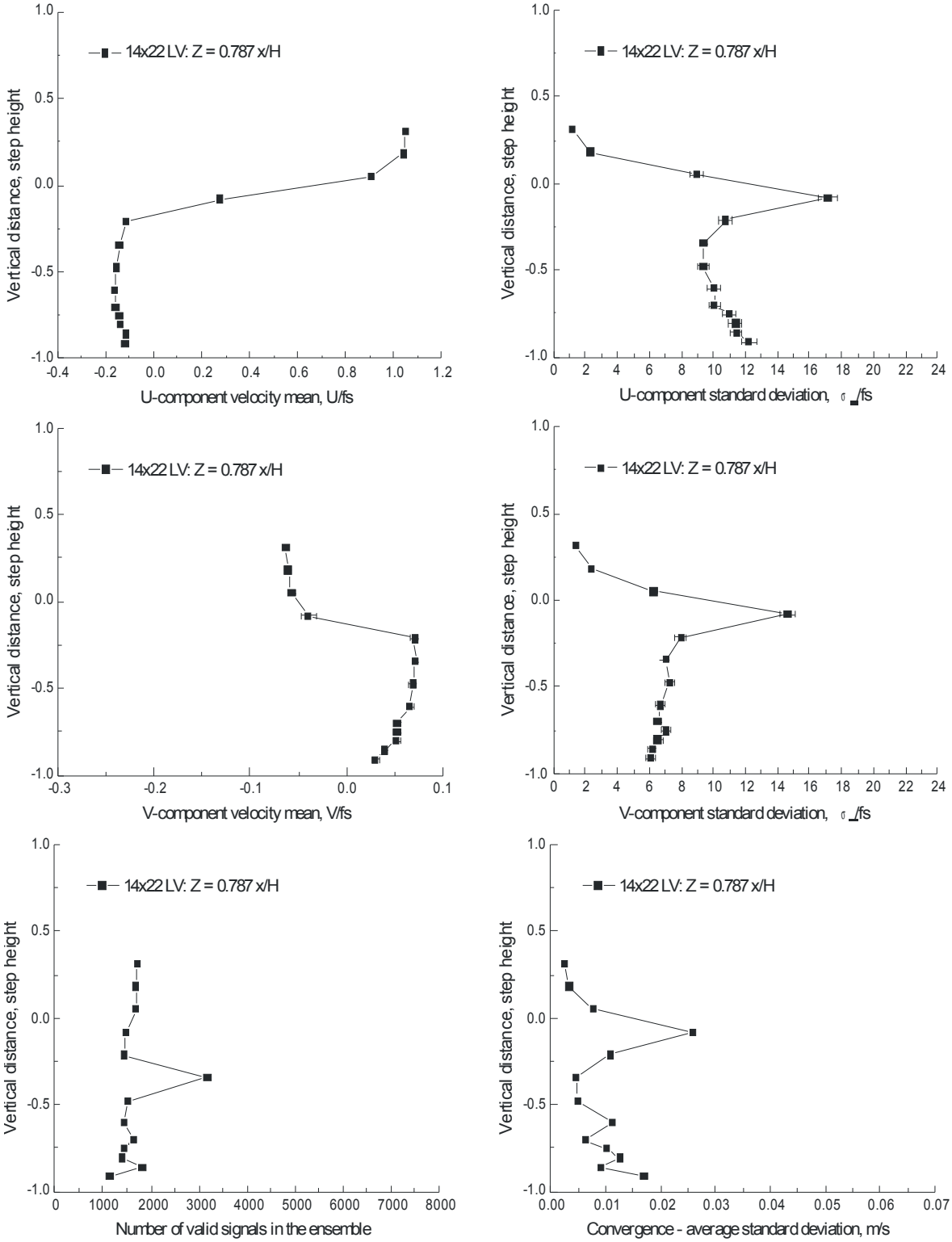

Figure VII.10.c.- Vertical scan 0.787 x/H downstream of a 3.5-inch backward-facing step (compares to Figure VII.4.c): streamwise and vertical velocity components, number of accepted signal bursts, and statistical stationarity convergence standard deviation, fs = 45.0 m/s.

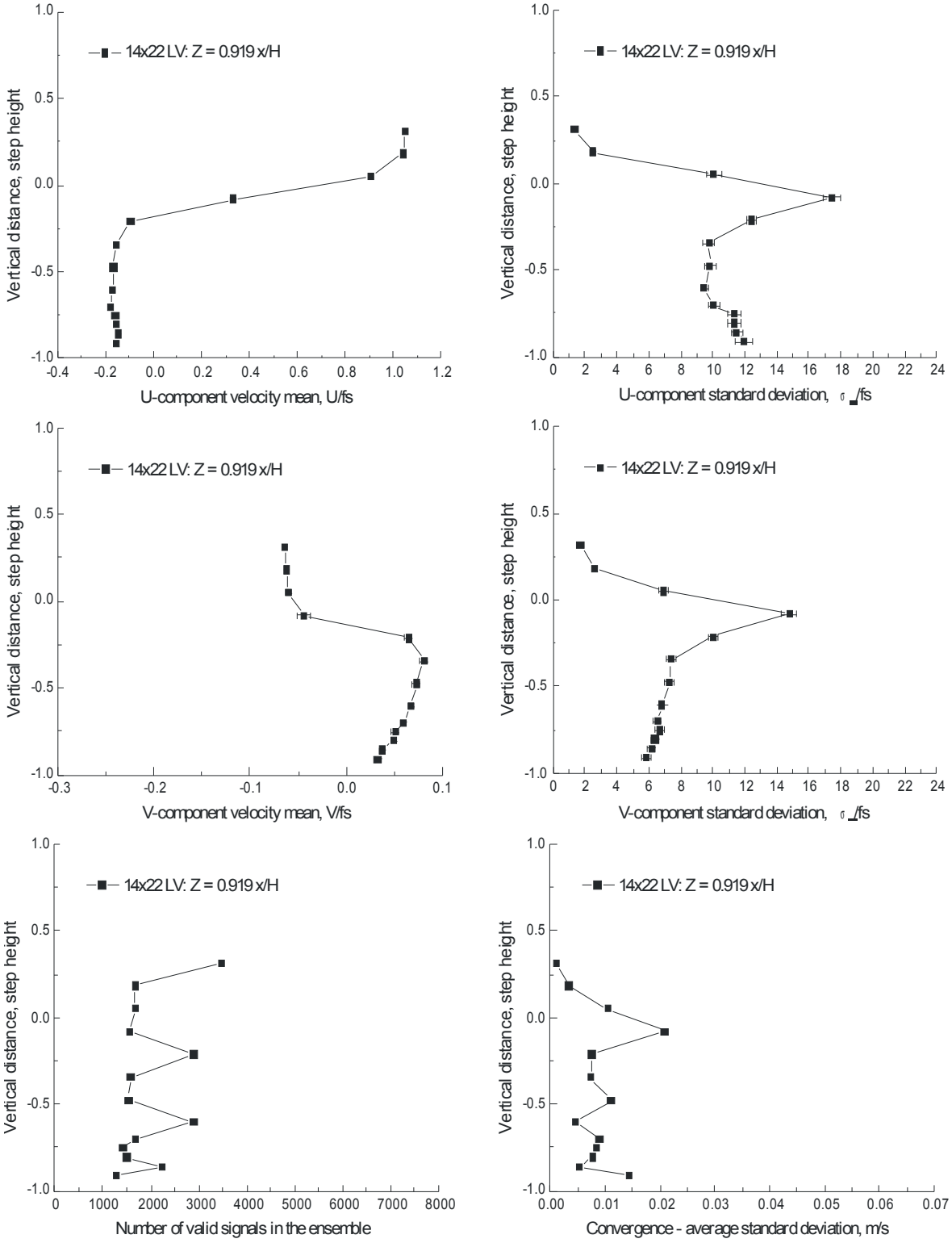

Figure VII.10.d.- Vertical scan 0.919 x/H downstream of a 3.5-inch backward-facing step: streamwise and vertical velocity components, number of accepted signal bursts, and statistical stationarity convergence standard deviation, fs = 45.0 m/s.

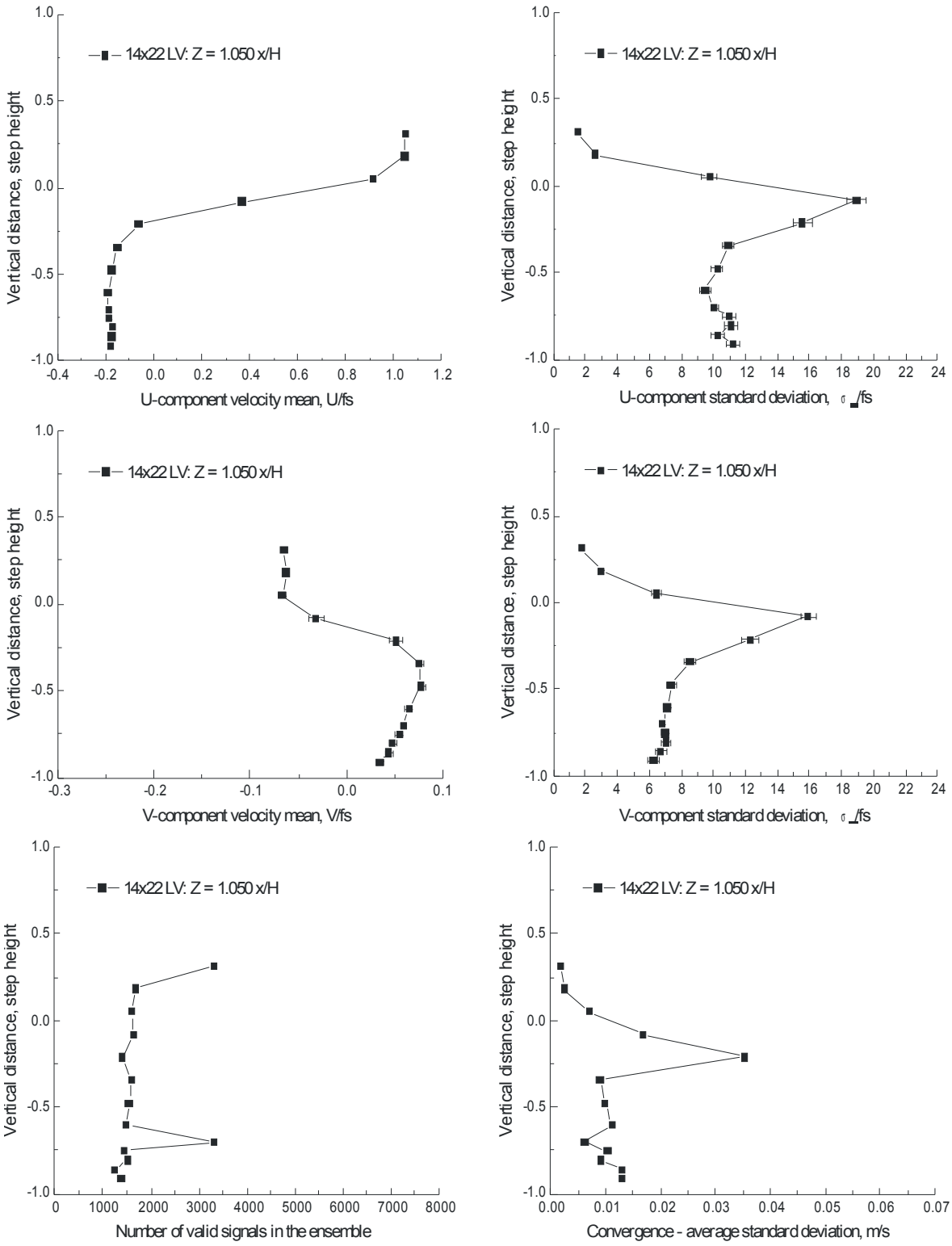

Figure VII.10.e.- Vertical scan 1.050 x/H downstream of a 3.5-inch backward-facing step (compares to Figure VII.4.d): streamwise and vertical velocity components, number of accepted signal bursts, and statistical stationarity convergence standard deviation, fs = 45.0 m/s.

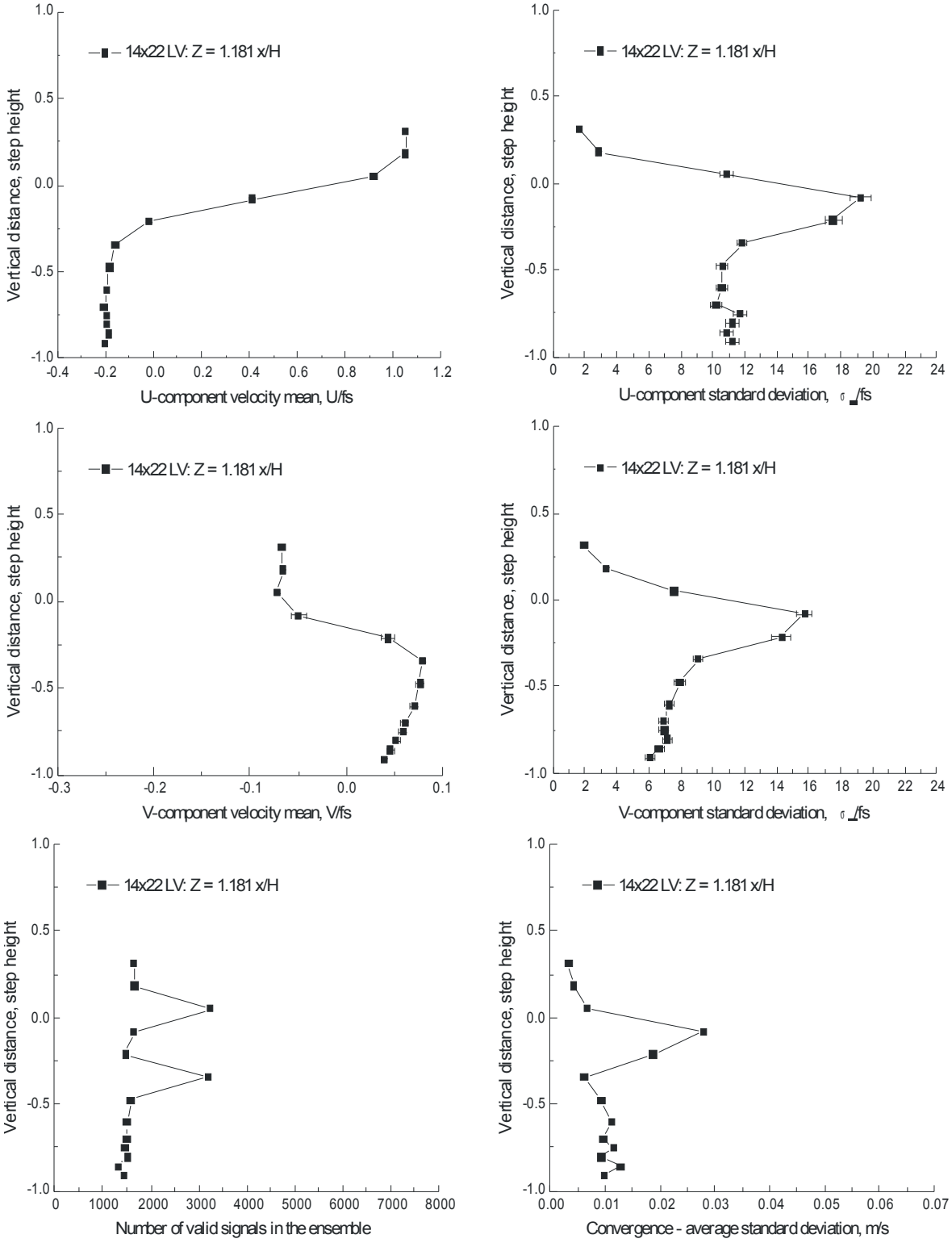

Figure VII.10.f.- Vertical scan 1.181 x/H downstream of a 3.5-inch backward-facing step: streamwise and vertical velocity components, number of accepted signal bursts, and statistical stationarity convergence standard deviation, fs = 45.0 m/s.

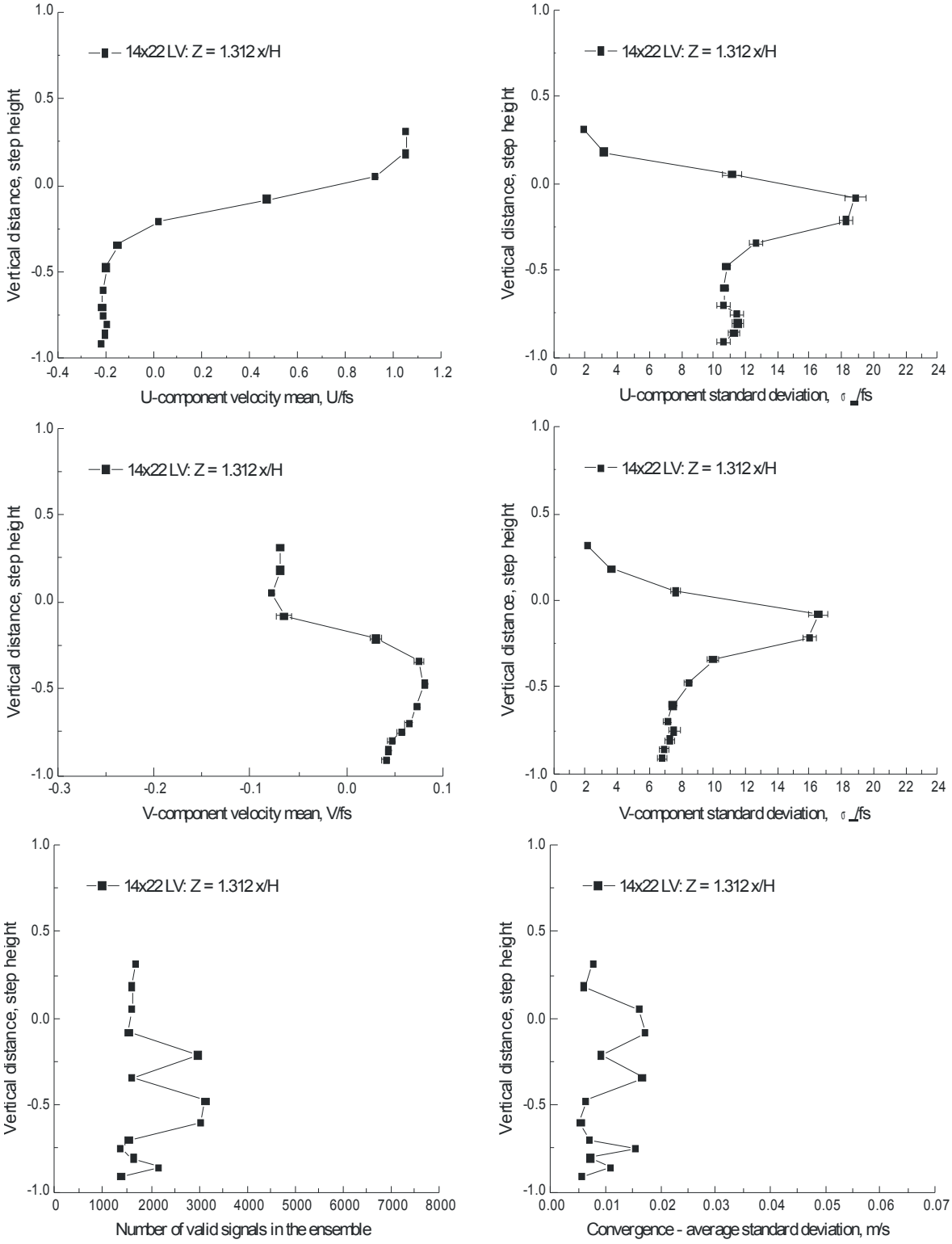

Figure VII.10.g.- Vertical scan 1.312 x/H downstream of a 3.5-inch backward-facing step (compares to Figure VII.4.e): streamwise and vertical velocity components, number of accepted signal bursts, and statistical stationarity convergence standard deviation, fs = 45.0 m/s.

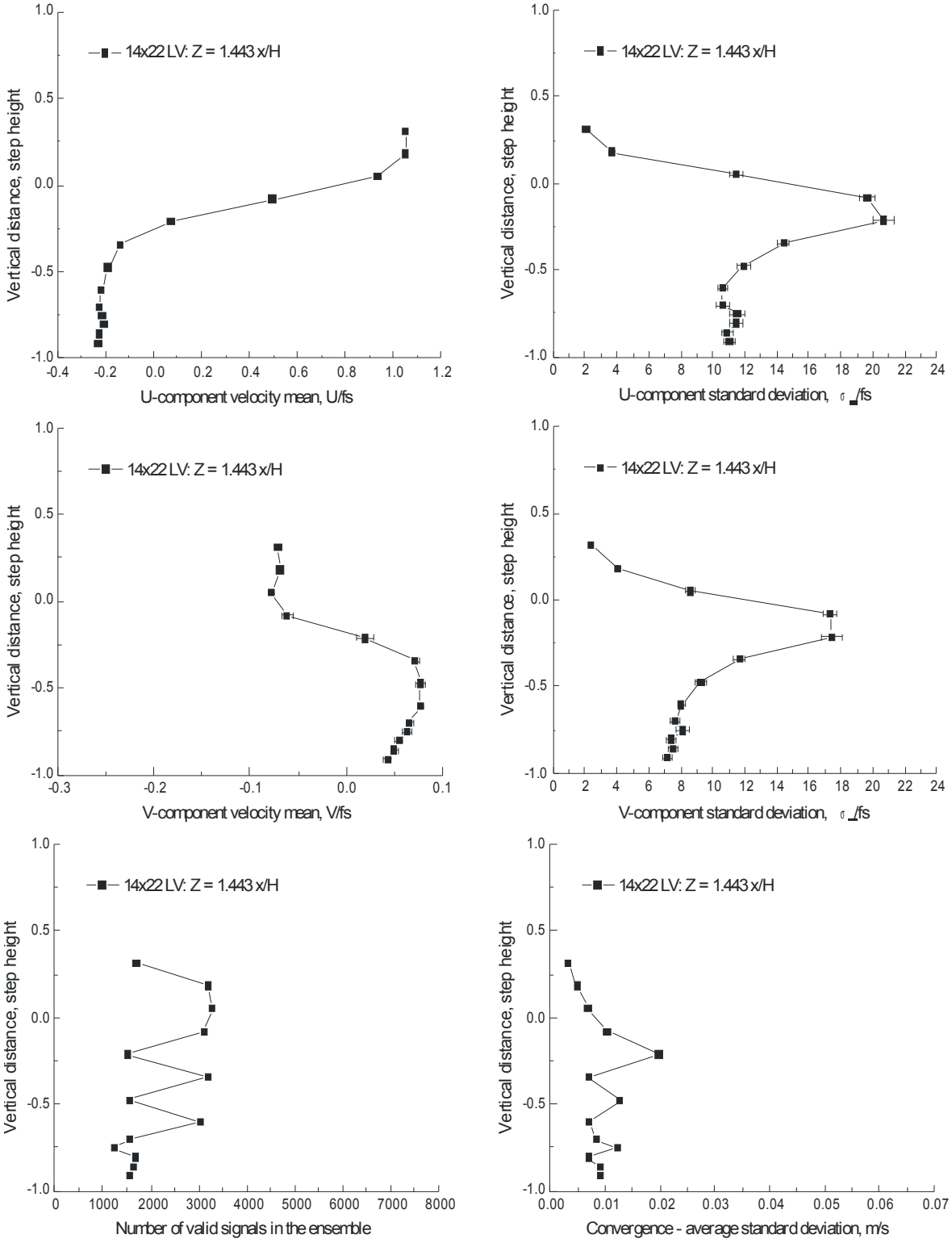

Figure VII.10.h.- Vertical scan 1.443 x/H downstream of a 3.5-inch backward-facing step: streamwise and vertical velocity components, number of accepted signal bursts, and statistical stationarity convergence standard deviation, fs = 45.0 m/s.

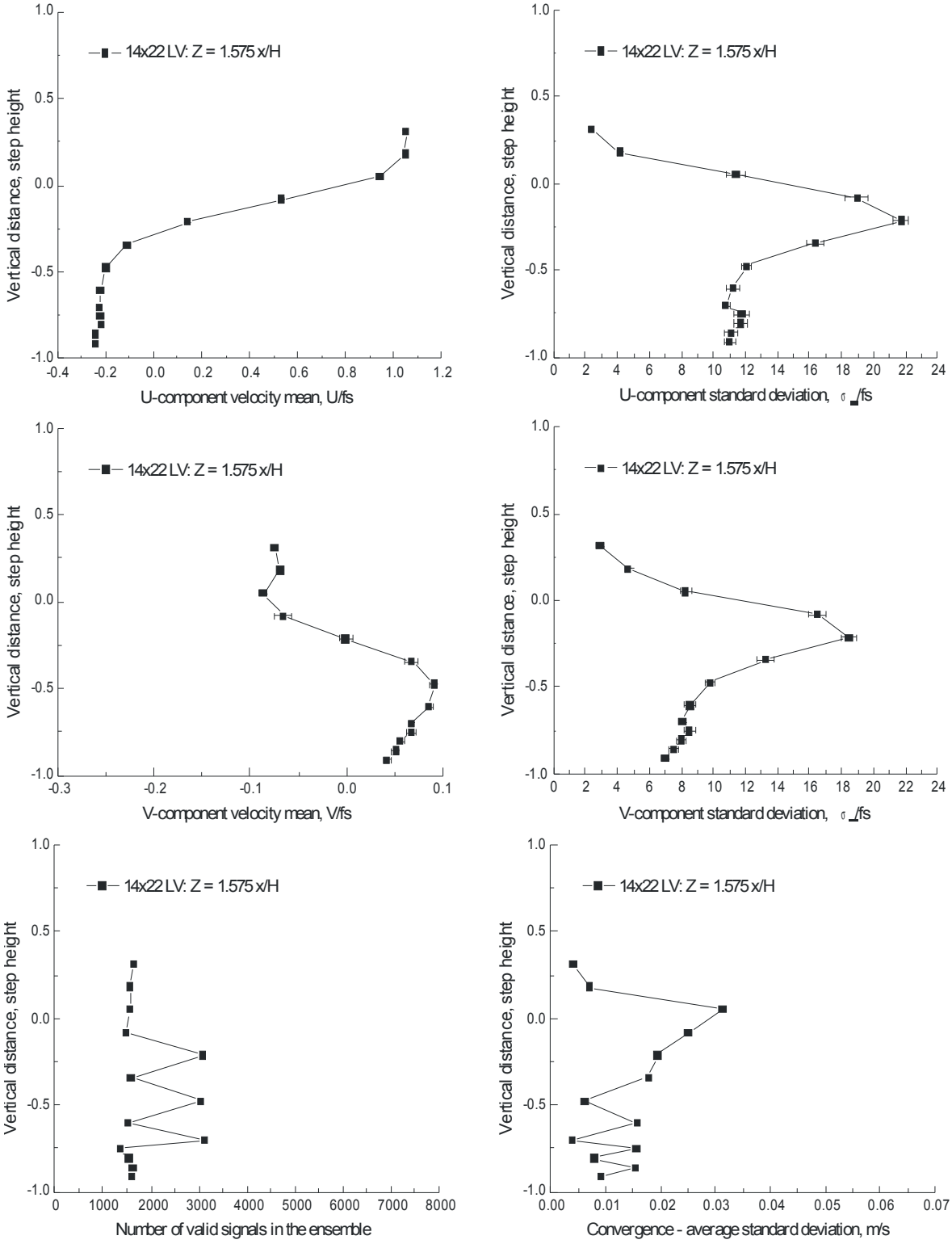

Figure VII.10.i.- Vertical scan 1.575 x/H downstream of a 3.5-inch backward-facing step (compares to Figure VII.4.f): streamwise and vertical velocity components, number of accepted signal bursts, and statistical stationarity convergence standard deviation, fs = 45.0 m/s.

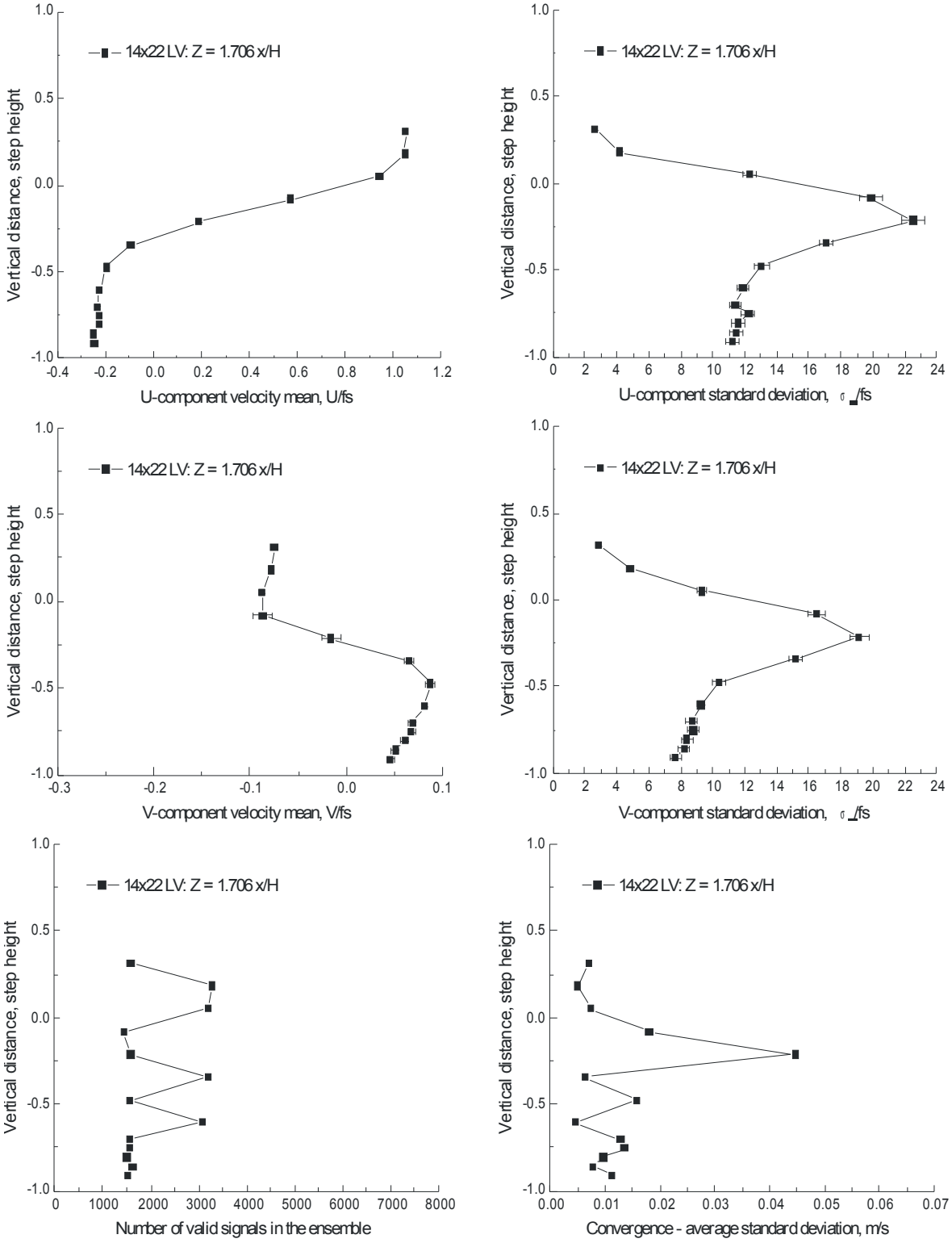

Figure VII.10.j.- Vertical scan 1.706 x/H downstream of a 3.5-inch backward-facing step: streamwise and vertical velocity components, number of accepted signal bursts, and statistical stationarity convergence standard deviation, fs = 45.0 m/s.

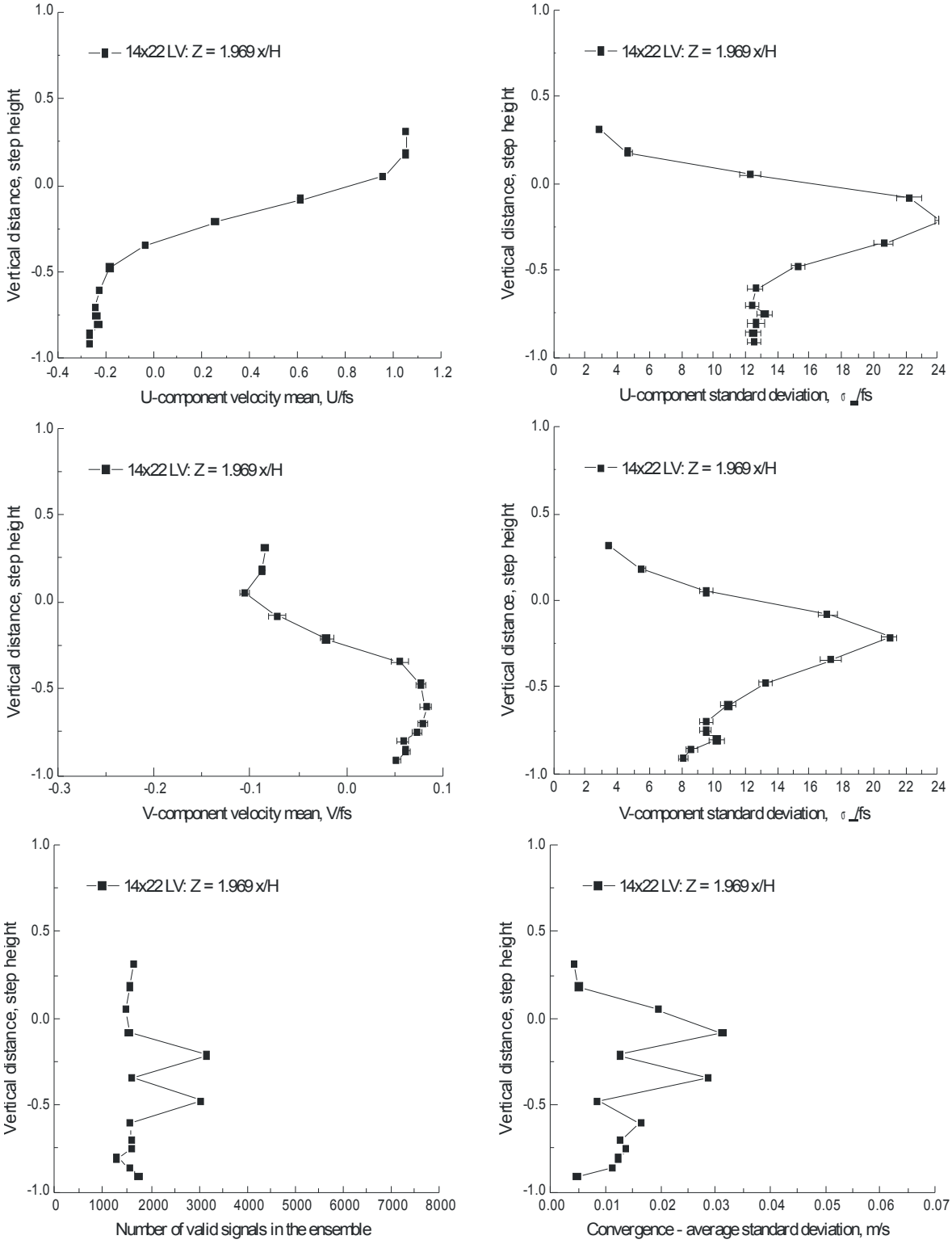

Figure VII.10.k.- Vertical scan 1.969 x/H downstream of a 3.5-inch backward-facing step (compares to Figure VII.4.g): streamwise and vertical velocity components, number of accepted signal bursts, and statistical stationarity convergence standard deviation, fs = 45.0 m/s.

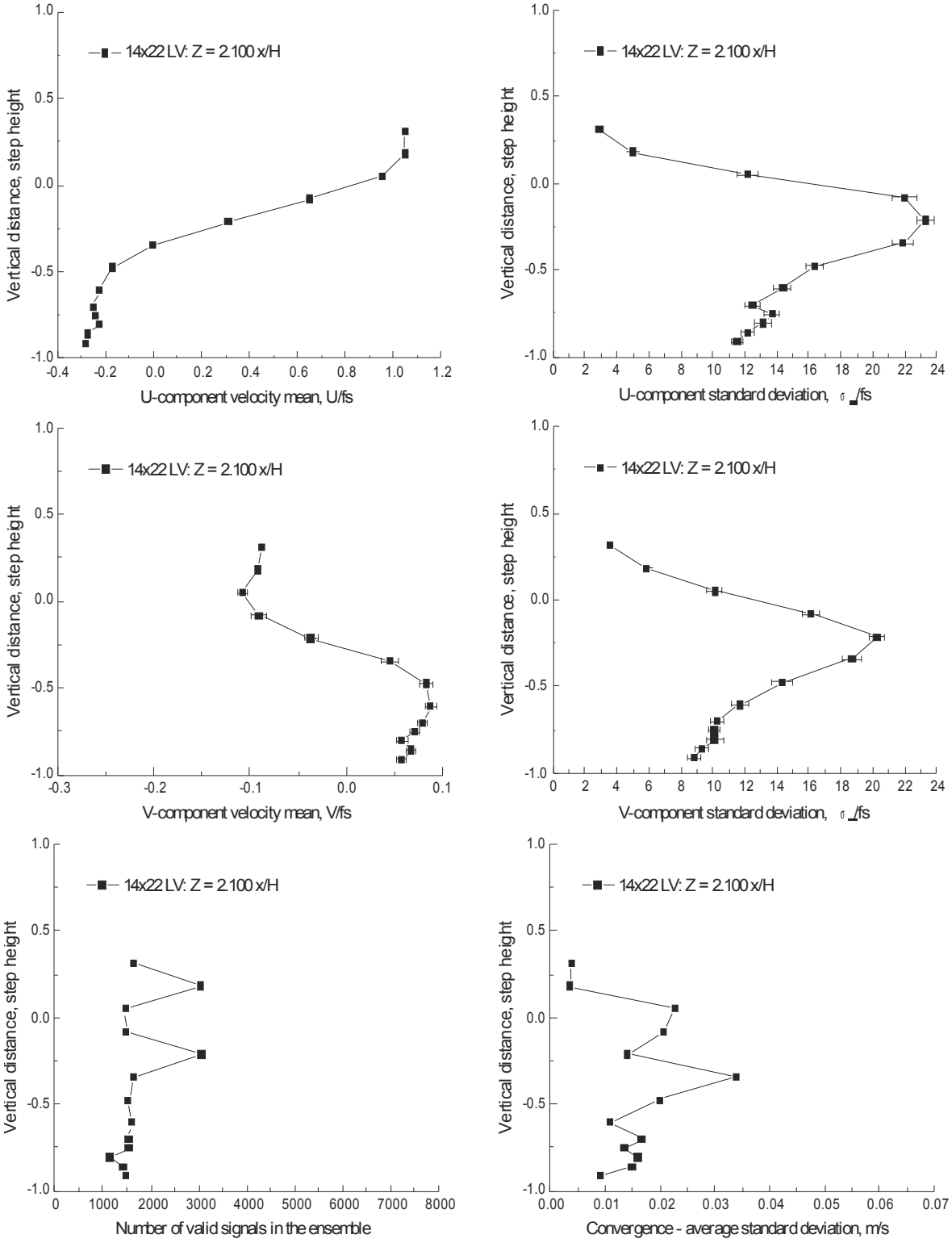

Figure VII.10.l.- Vertical scan 2.1 x/H downstream of a 3.5-inch backward-facing step: streamwise and vertical velocity components, number of accepted signal bursts, and statistical stationarity convergence standard deviation, fs = 45.0 m/s.

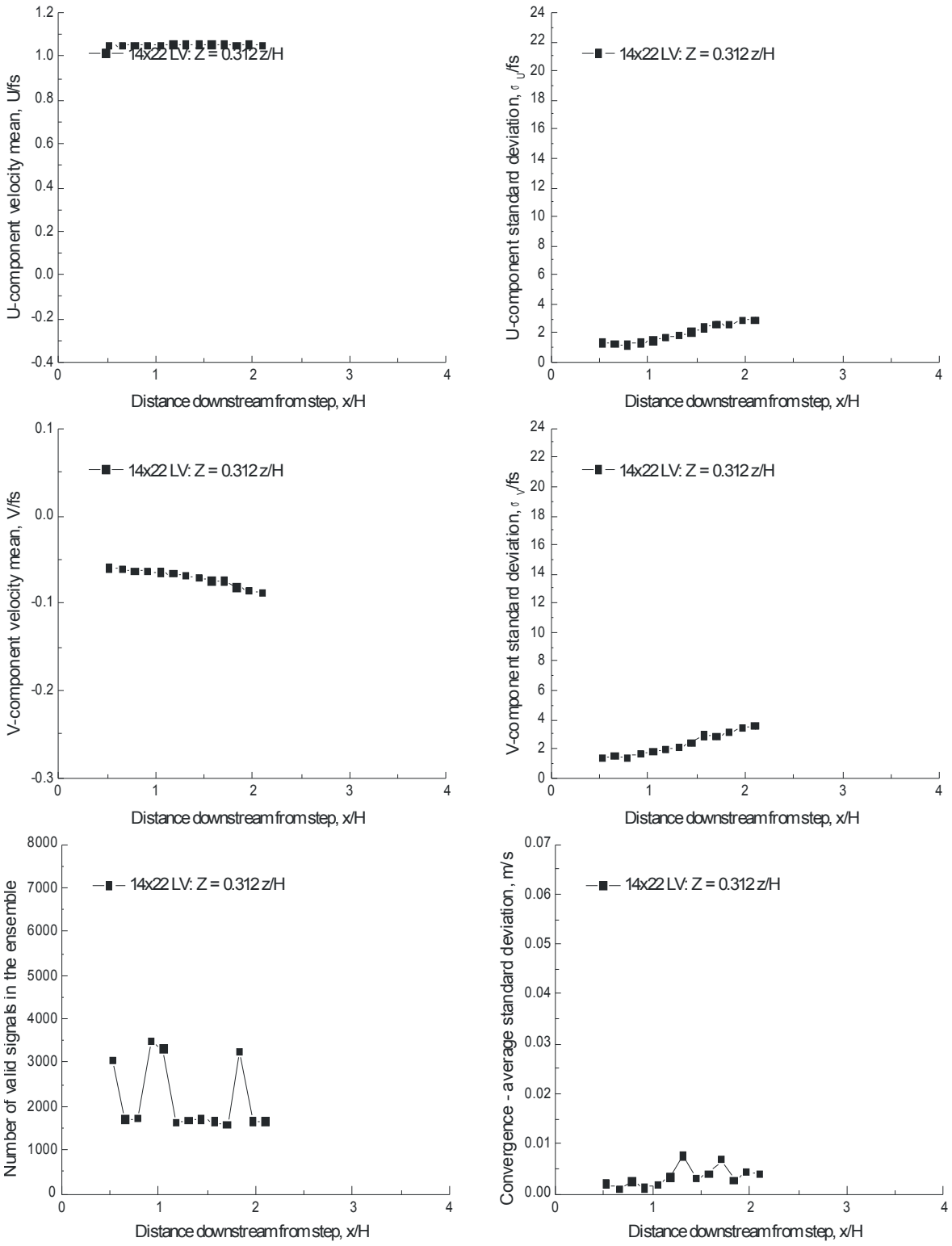

Figure VII.11.a. - Horizontal scan 0.312 z/H above a 3.5-inch backward-facing step (compares to Figure VII.5.b): streamwise and vertical velocity components, number of accepted signal bursts, and statistical stationarity convergence standard deviation, fs = 45.0 m/s.

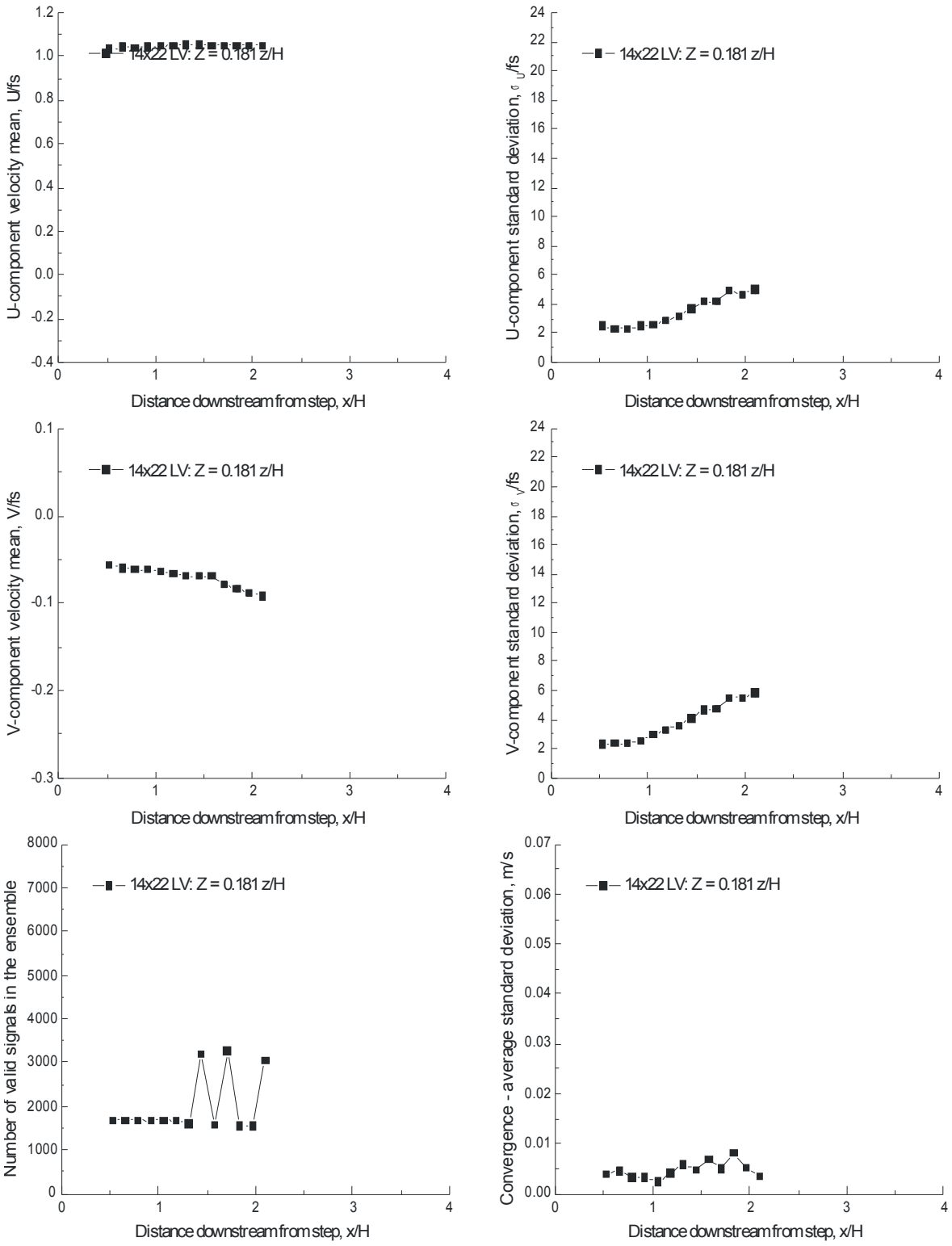

Figure VII.11.b. - Horizontal scan 0.181 z/H above a 3.5-inch backward-facing step (compares to Figure VII.5.c): streamwise and vertical velocity components, number of accepted signal bursts, and statistical stationarity convergence standard deviation, fs = 45.0 m/s.

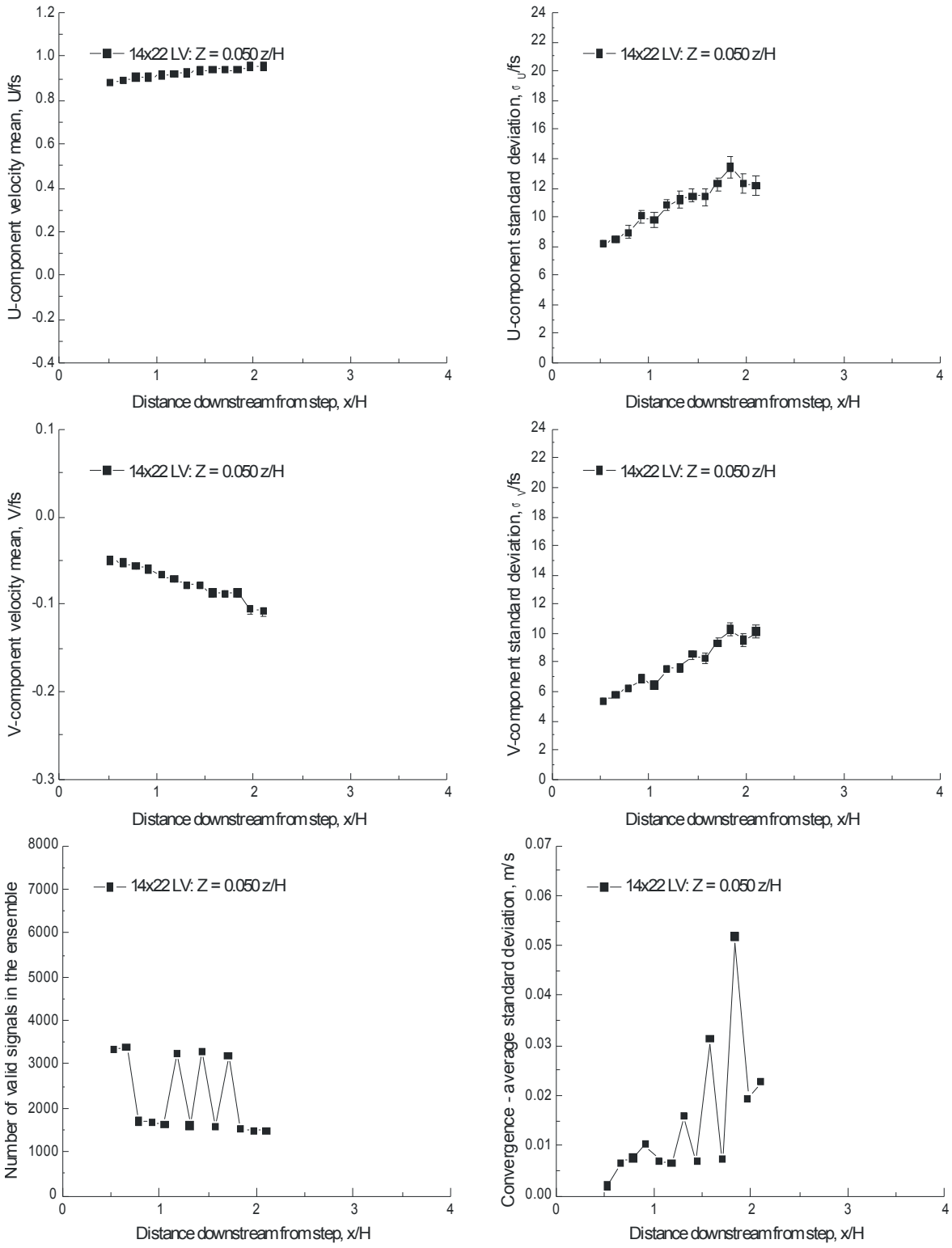

Figure VII.11.c. - Horizontal scan 0.050 z/H above a 3.5-inch backward-facing step (compares to Figure VII.5.d): streamwise and vertical velocity components, number of accepted signal bursts, and statistical stationarity convergence standard deviation, fs = 45.0 m/s.

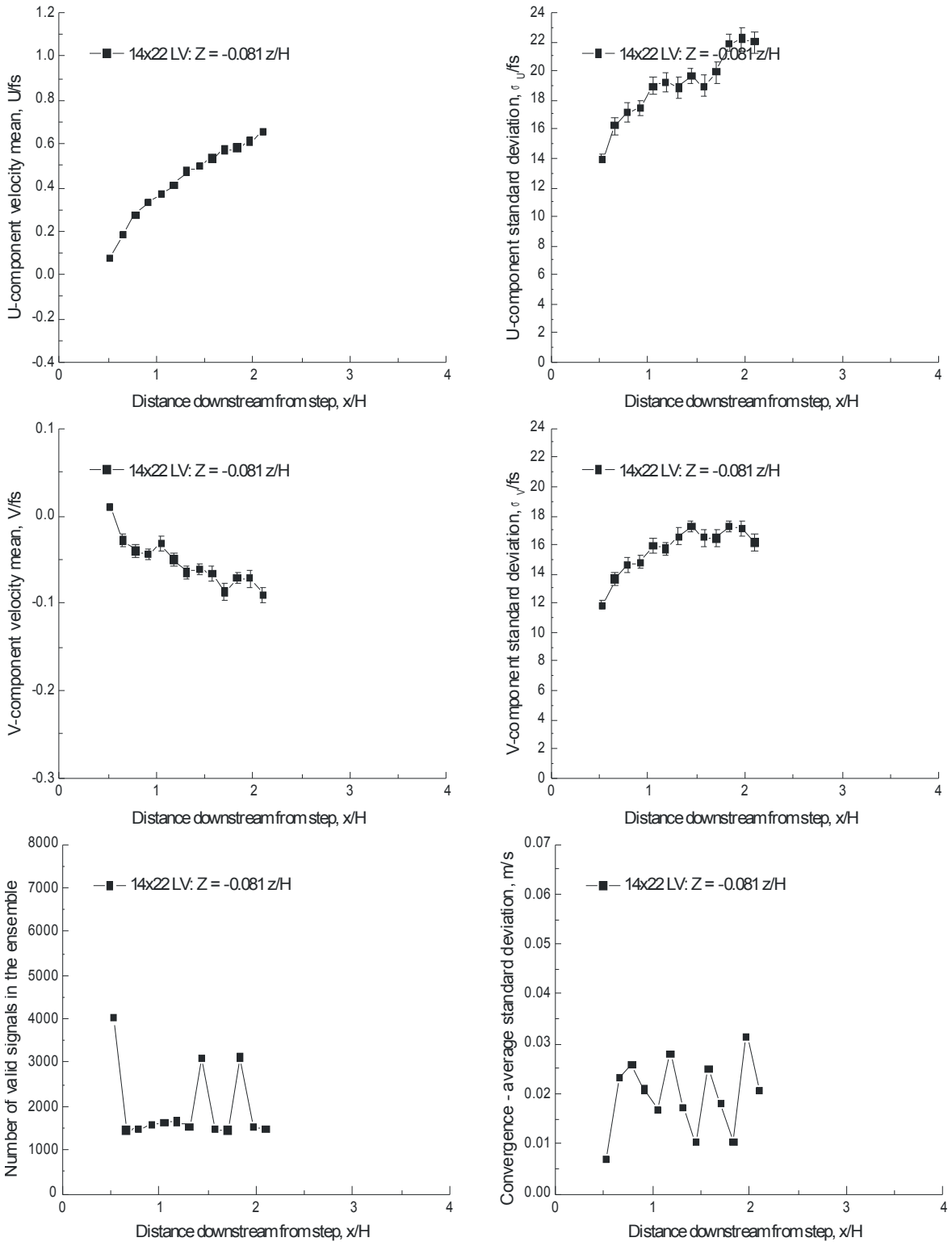

Figure VII.11.d. - Horizontal scan 0.081 z/H below a 3.5-inch backward-facing step (compares to Figure VII.5.e): streamwise and vertical velocity components, number of accepted signal bursts, and statistical stationarity convergence standard deviation, fs = 45.0 m/s.

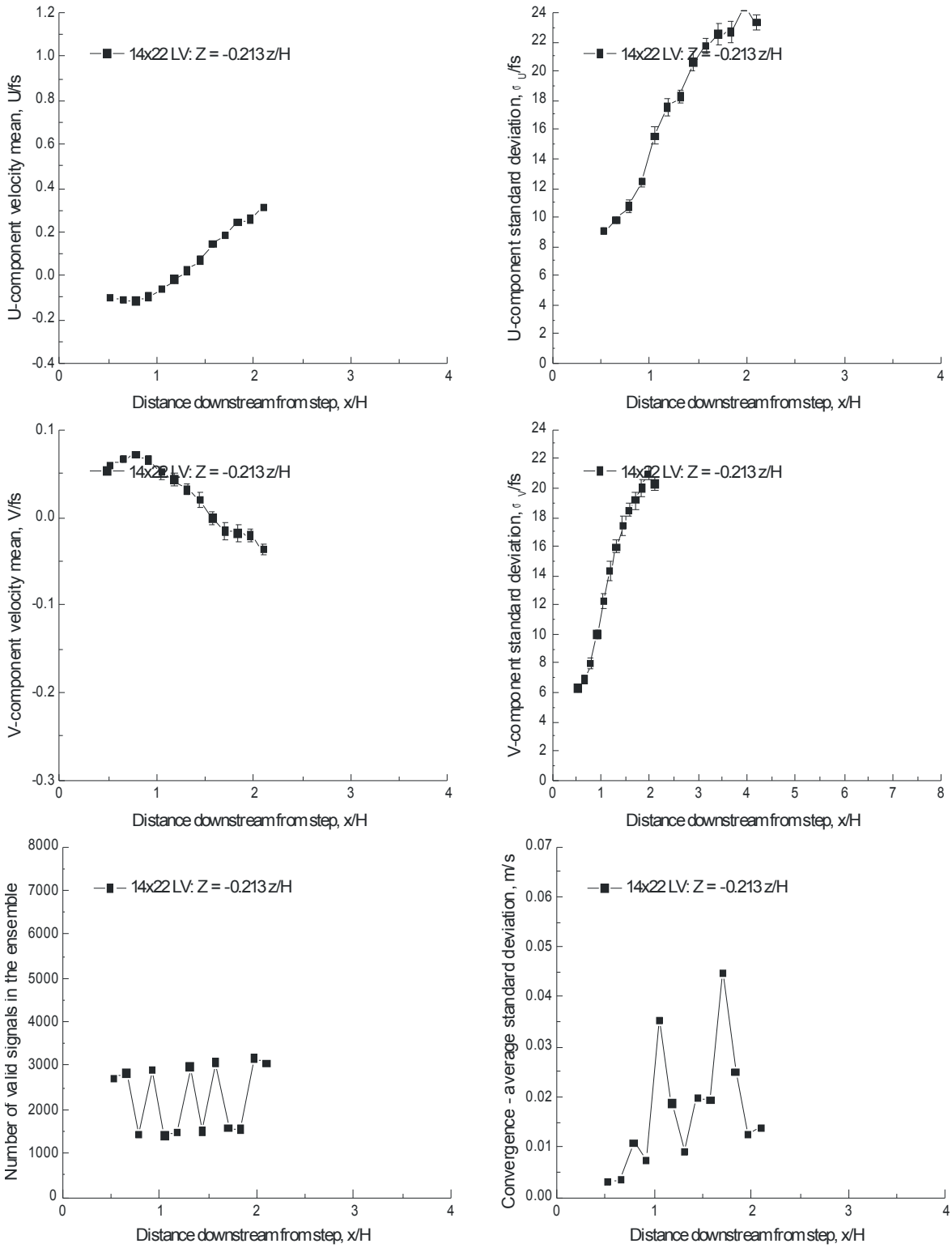

Figure VII.11.e. - Horizontal scan 0.213 z/H below a 3.5-inch backward-facing step (compares to Figure VII.5.f): streamwise and vertical velocity components, number of accepted signal bursts, and statistical stationarity convergence standard deviation, fs = 45.0 m/s.

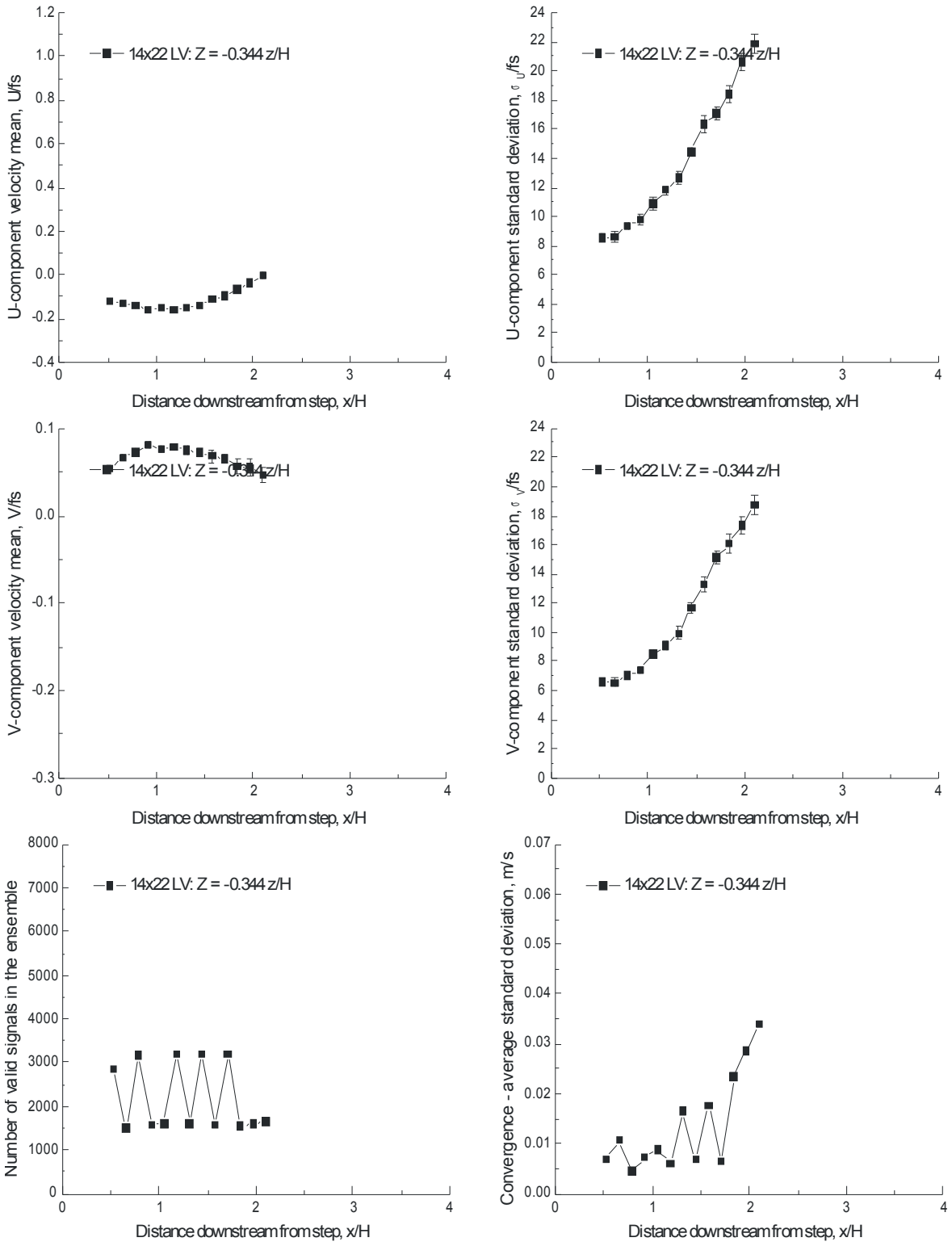

Figure VII.11.f. - Horizontal scan 0.344 z/H below a 3.5-inch backward-facing step (compares to Figure VII.5.g): streamwise and vertical velocity components, number of accepted signal bursts, and statistical stationarity convergence standard deviation, fs = 45.0 m/s.

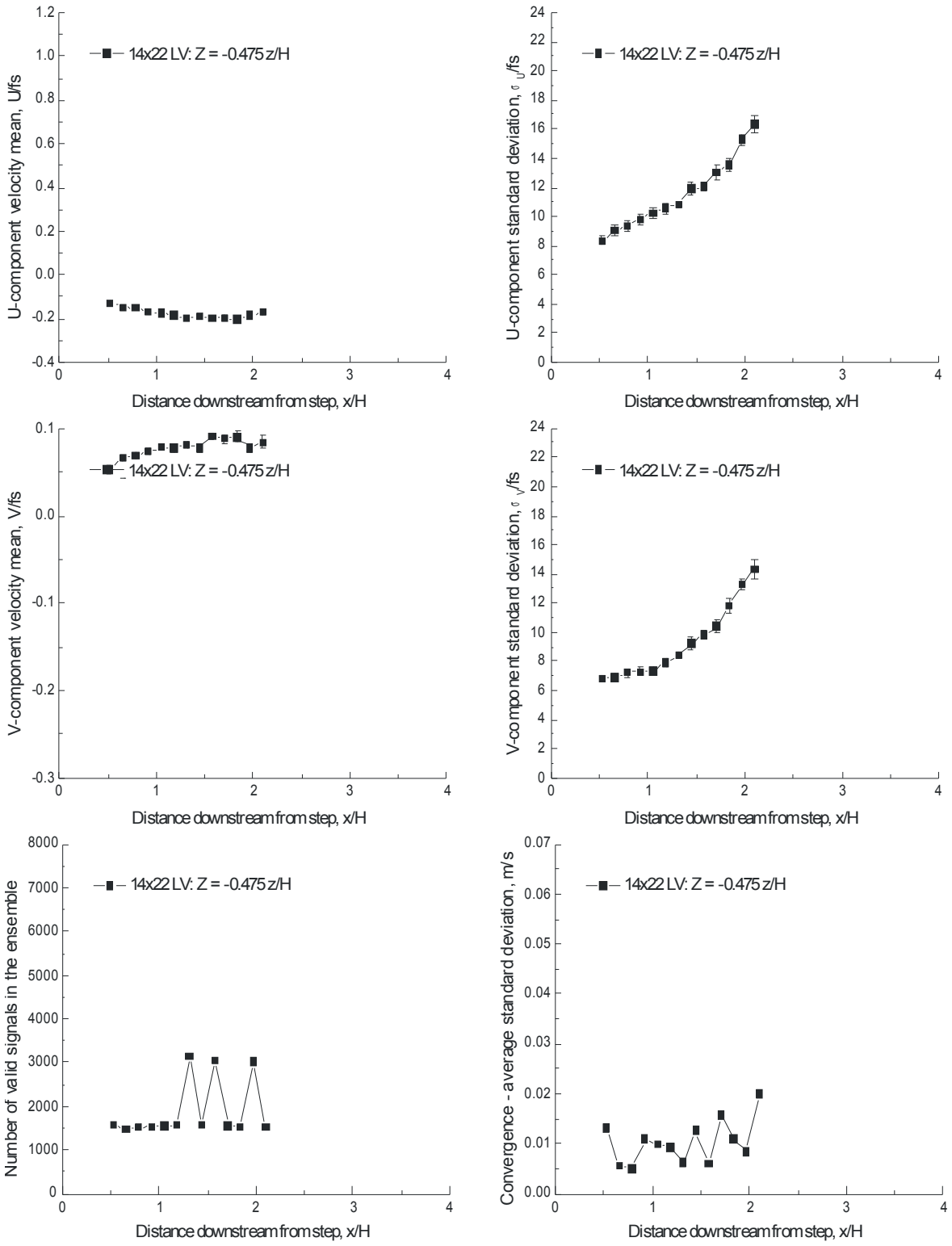

Figure VII.11.g. - Horizontal scan 0.475 z/H below a 3.5-inch backward-facing step (compares to Figure VII.5.h): streamwise and vertical velocity components, number of accepted signal bursts, and statistical stationarity convergence standard deviation, fs = 45.0 m/s.

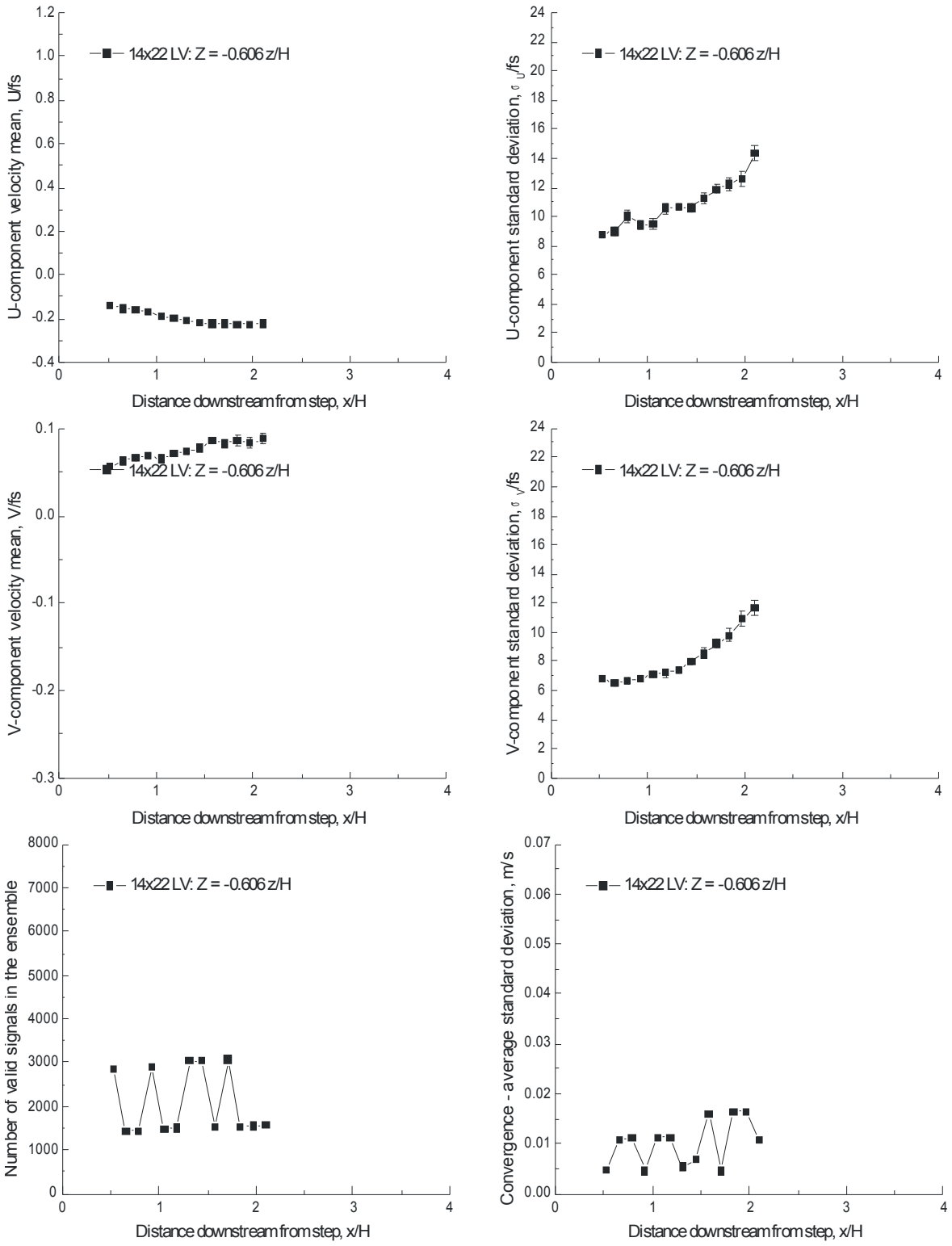

Figure VII.11.h. - Horizontal scan 0.606 z/H below a 3.5-inch backward-facing step (compares to Figure VII.5.i): streamwise and vertical velocity components, number of accepted signal bursts, and statistical stationarity convergence standard deviation, fs = 45.0 m/s.

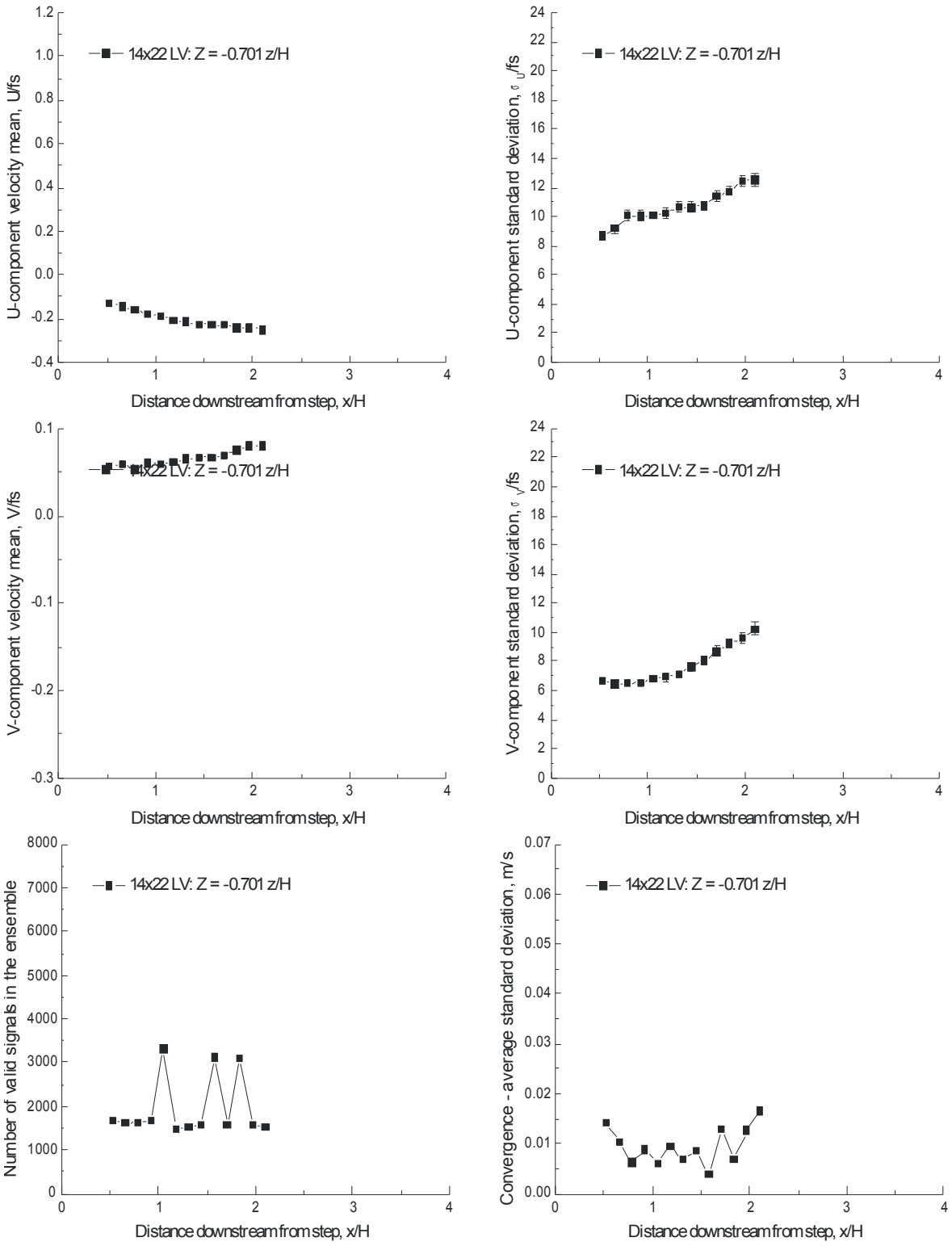

Figure VII.11.i. - Horizontal scan 0.701 z/H below a 3.5-inch backward-facing step (compares to Figure VII.5.j): streamwise and vertical velocity components, number of accepted signal bursts, and statistical stationarity convergence standard deviation, fs = 45.0 m/s.

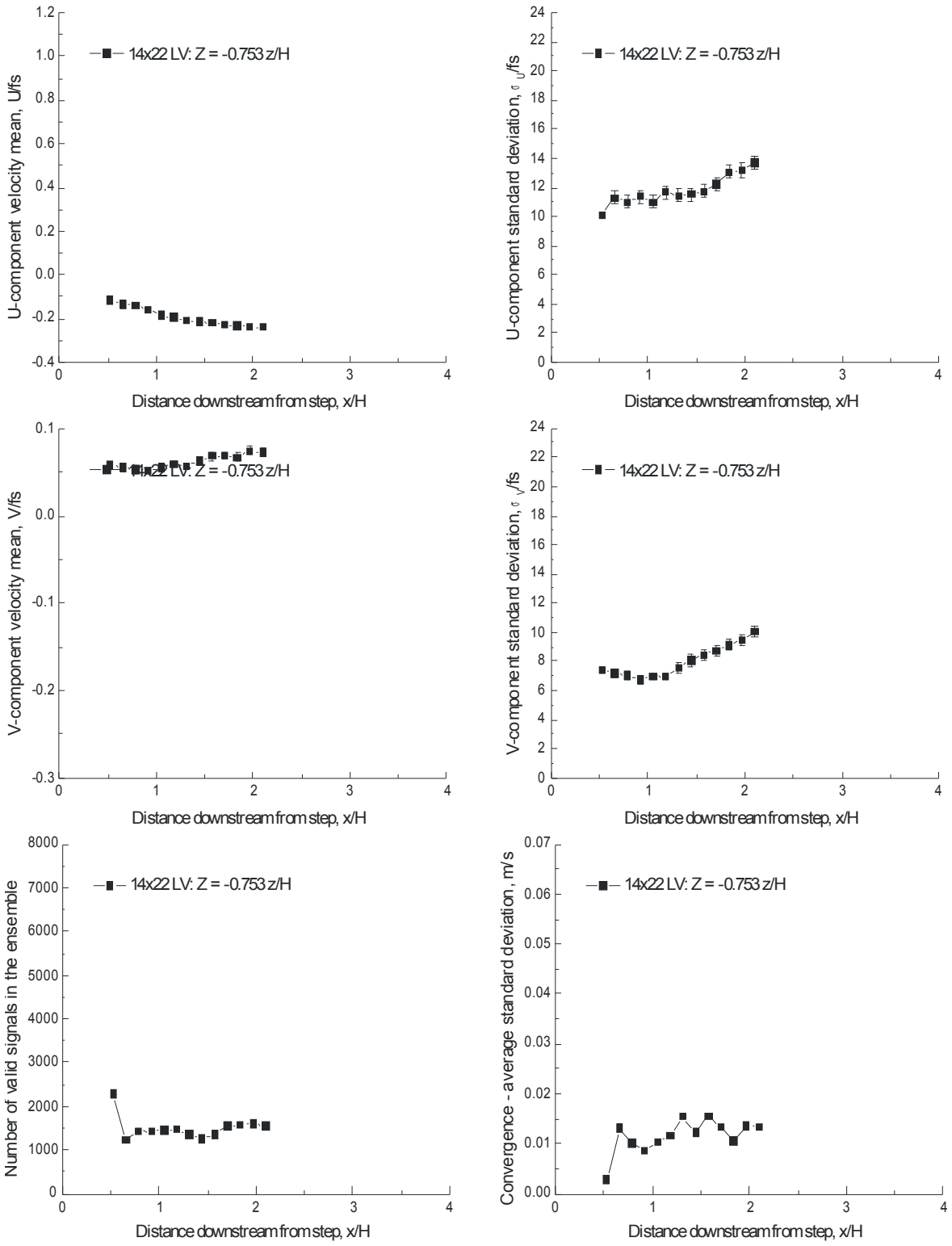

Figure VII.11.j. - Horizontal scan 0.753 z/H below a 3.5-inch backward-facing step (compares to Figure VII.5.k): streamwise and vertical velocity components, number of accepted signal bursts, and statistical stationarity convergence standard deviation, fs = 45.0 m/s.

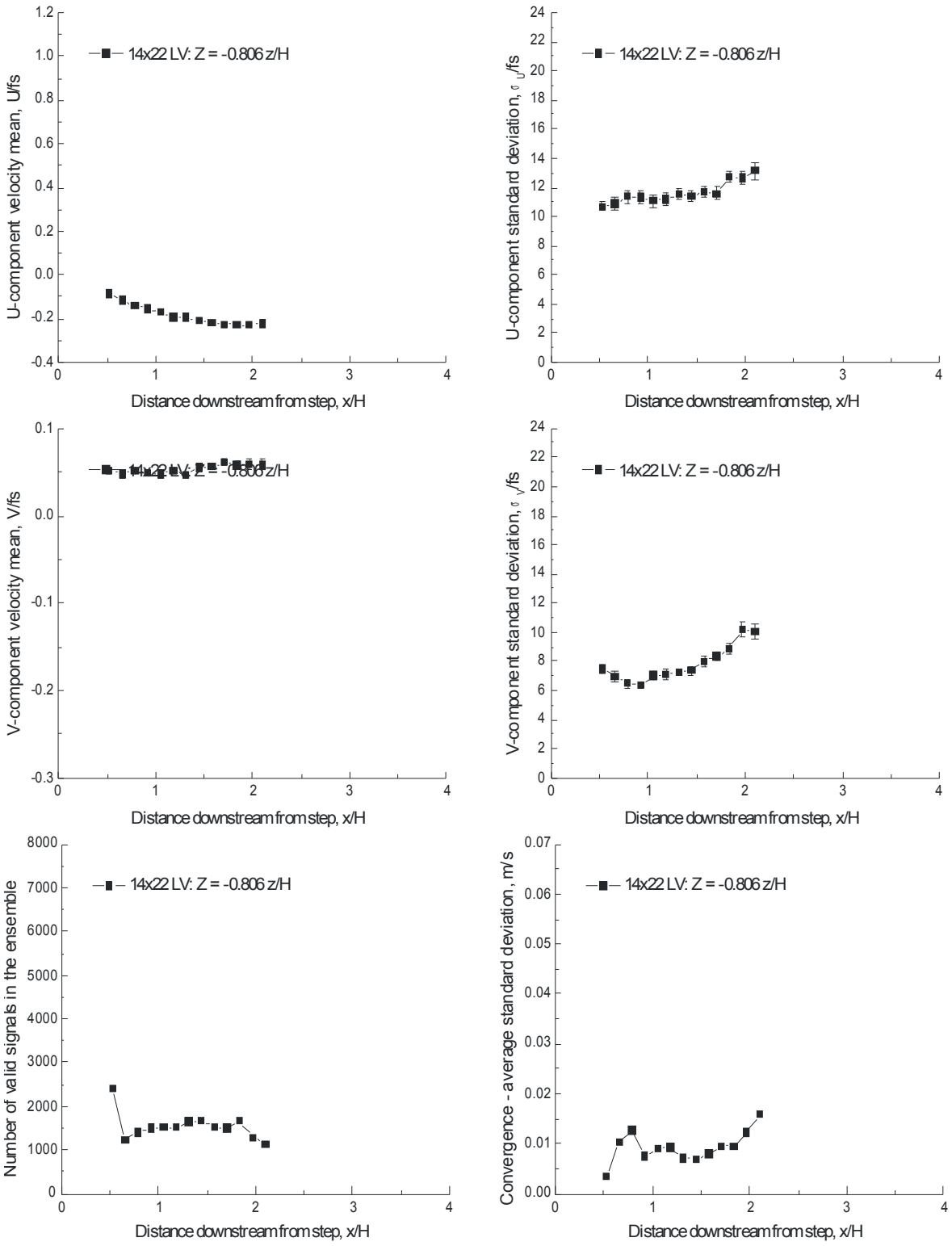

Figure VII.11.k. - Horizontal scan 0.806 z/H below a 3.5-inch backward-facing step (compares to Figure VII.5.l): streamwise and vertical velocity components, number of accepted signal bursts, and statistical stationarity convergence standard deviation, fs = 45.0 m/s.

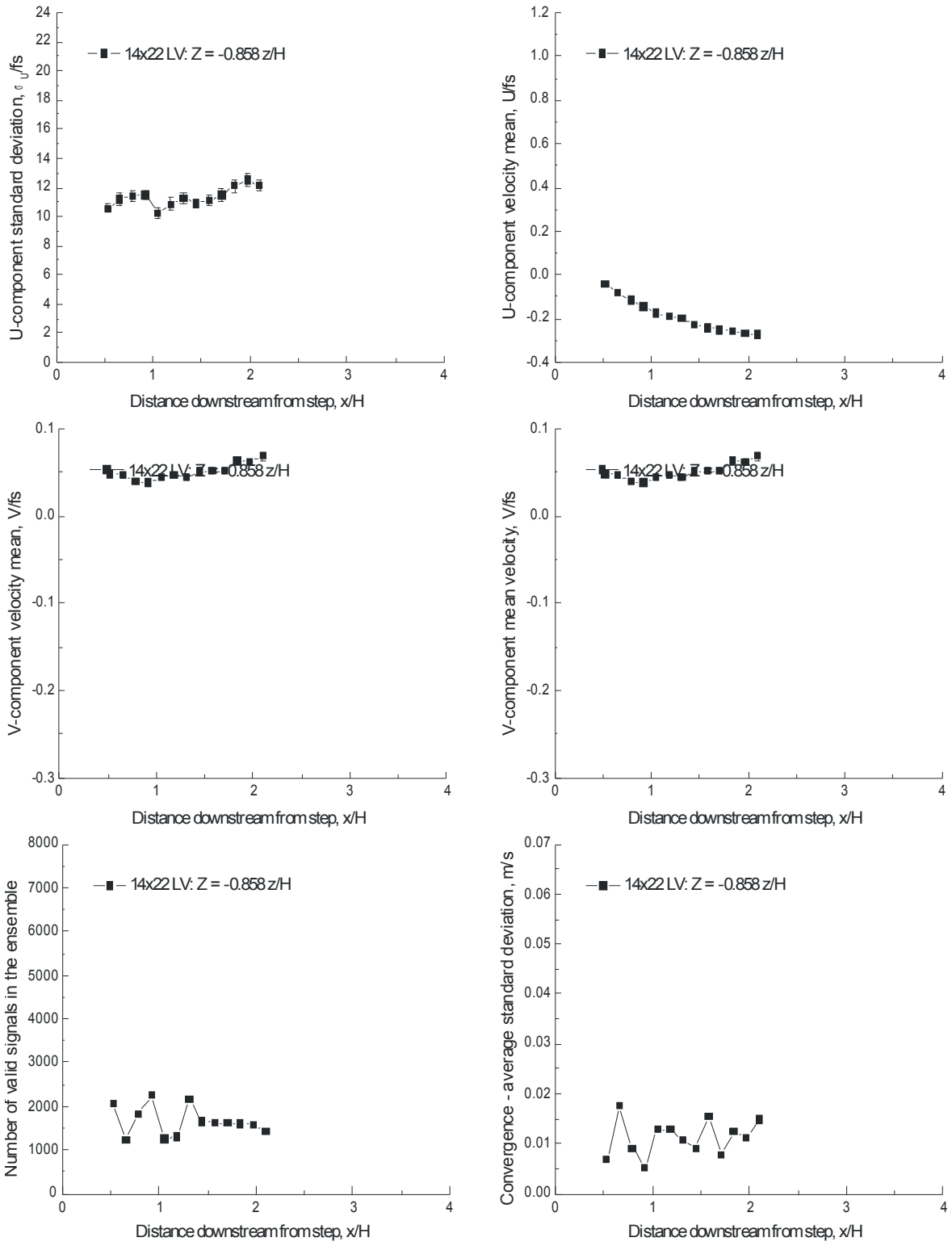

Figure VII.11.l. - Horizontal scan 0.858 z/H below a 3.5-inch backward-facing step (compares to Figure VII.5.m): streamwise and vertical velocity components, number of accepted signal bursts, and statistical stationarity convergence standard deviation, fs = 45.0 m/s.

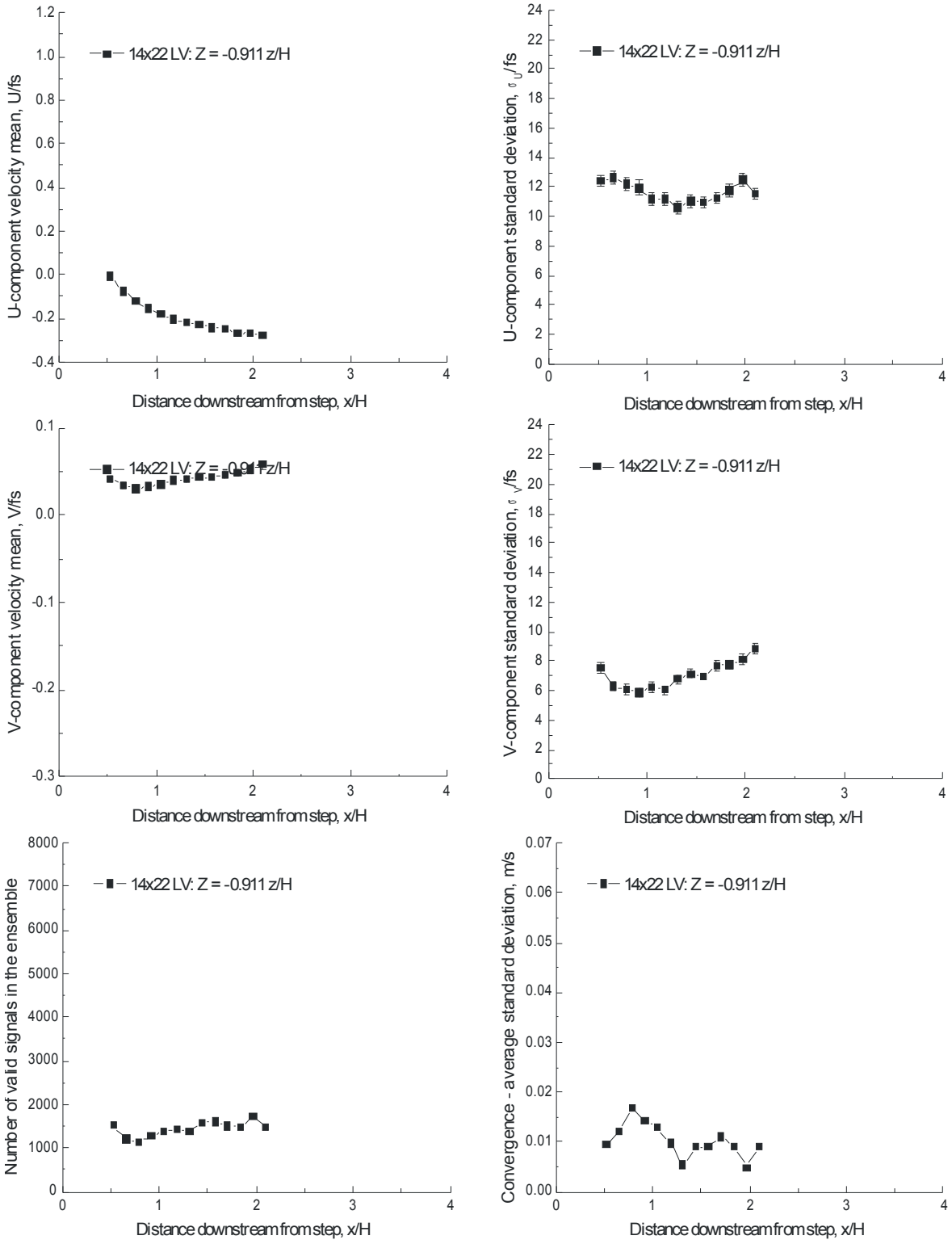

Figure VII.11.m. - Horizontal scan 0.911 z/H below a 3.5-inch backward-facing step (compares to Figure VII.5.n): streamwise and vertical velocity components, number of accepted signal bursts, and statistical stationarity convergence standard deviation, fs = 45.0 m/s.

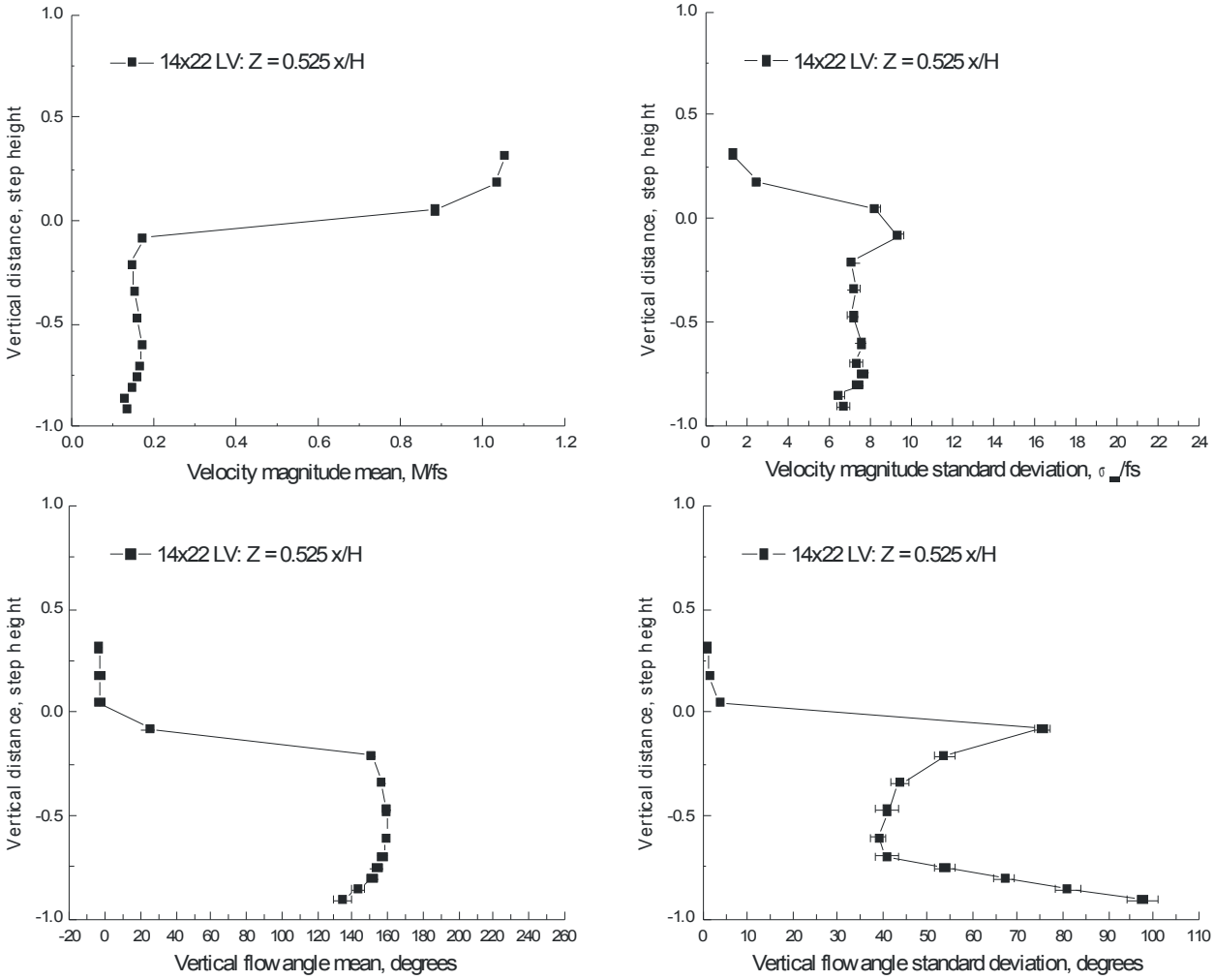

Figure VII.12.a.- Vertical scan 0.525 x/H downstream of a 3.5-inch backward-facing step (compares to Figure VII.6.b): velocity magnitude and flow angle, fs = 45.0 m/s.

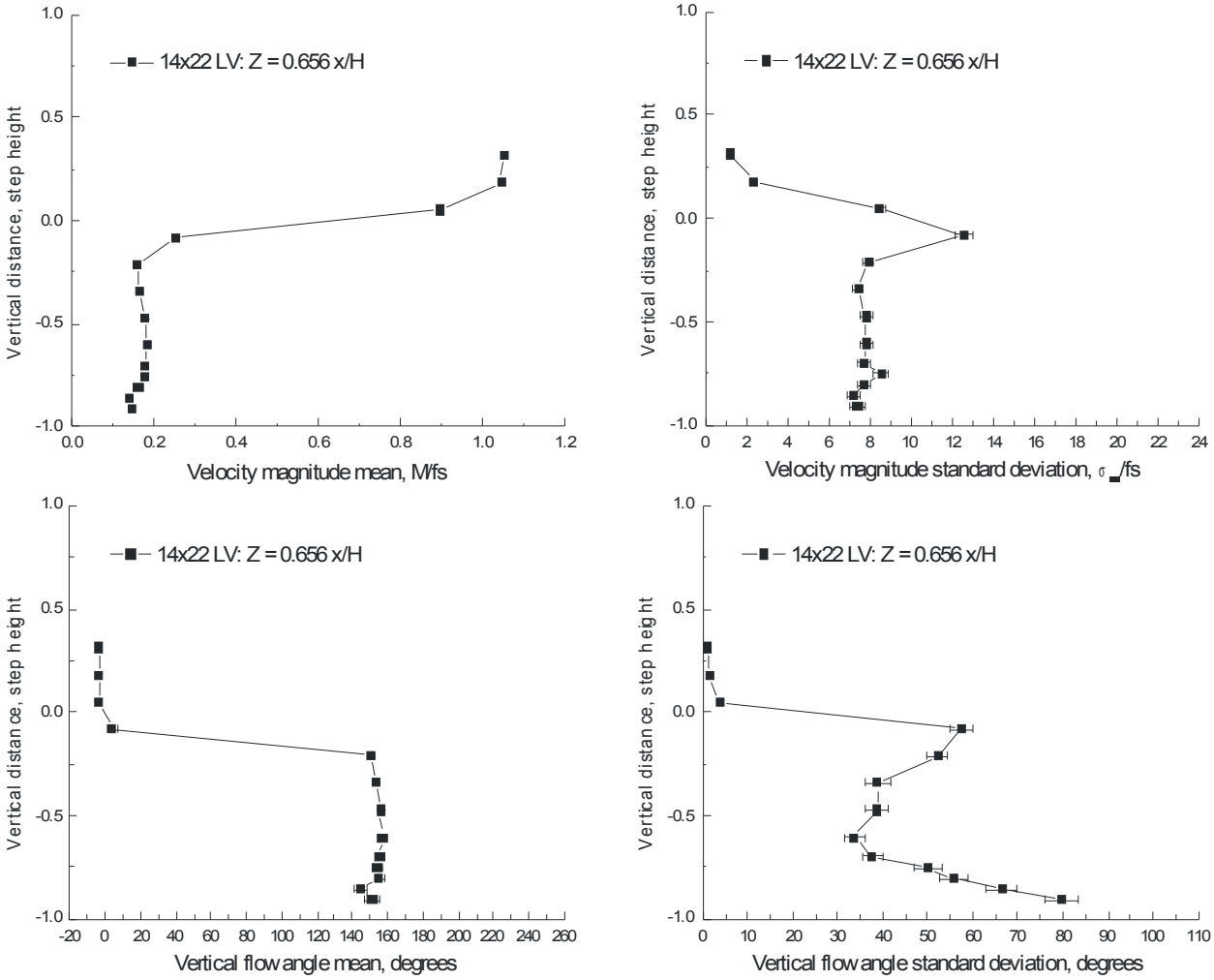

Figure VII.12.b.- Vertical scan 0.656 x/H downstream of a 3.5-inch backward-facing step: velocity magnitude and flow angle, fs = 45.0 m/s.

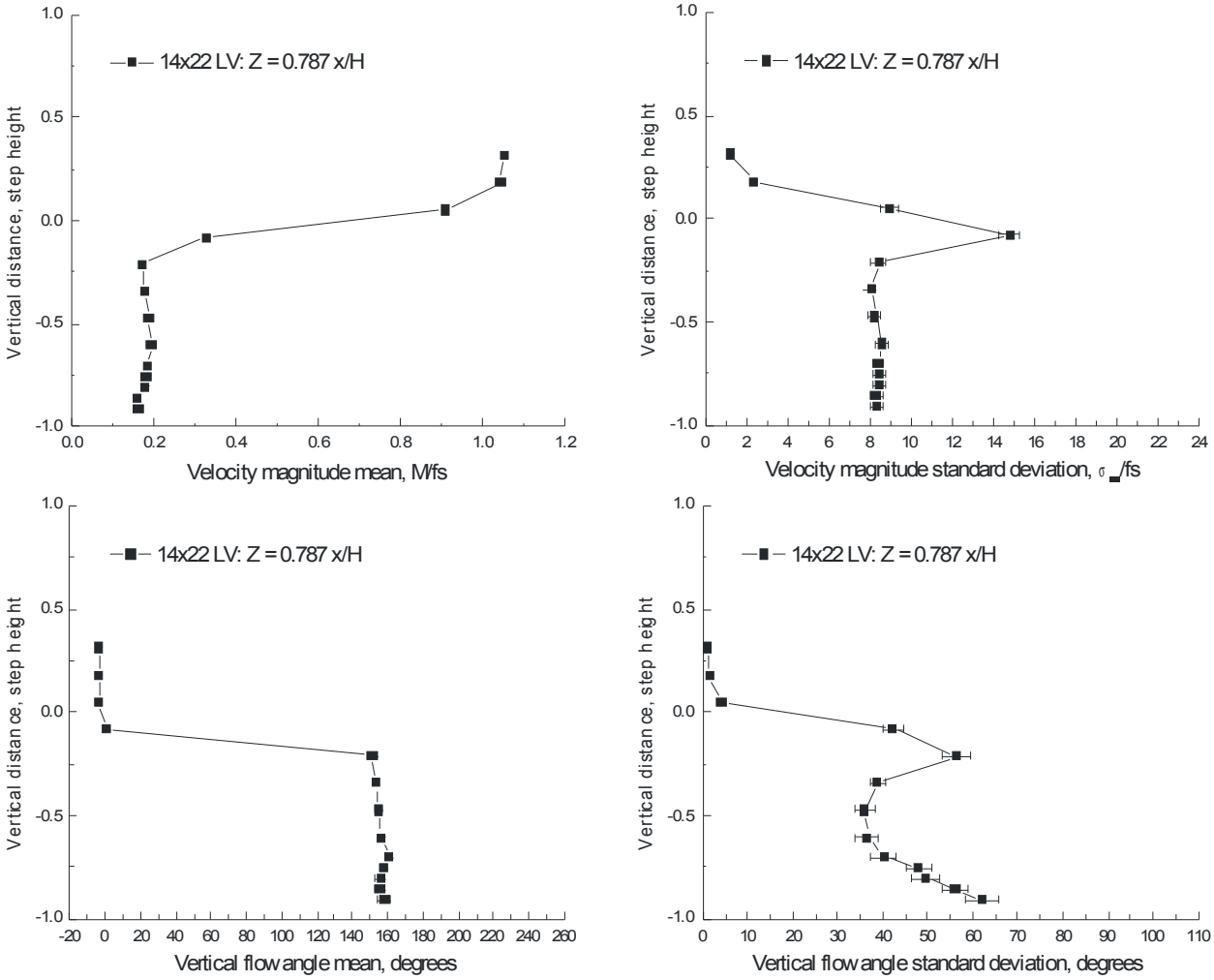

Figure VII.12.c.- Vertical scan 0.787 x/H downstream of a 3.5-inch backward-facing step (compares to Figure VII.6.c): velocity magnitude and flow angle, fs = 45.0 m/s.

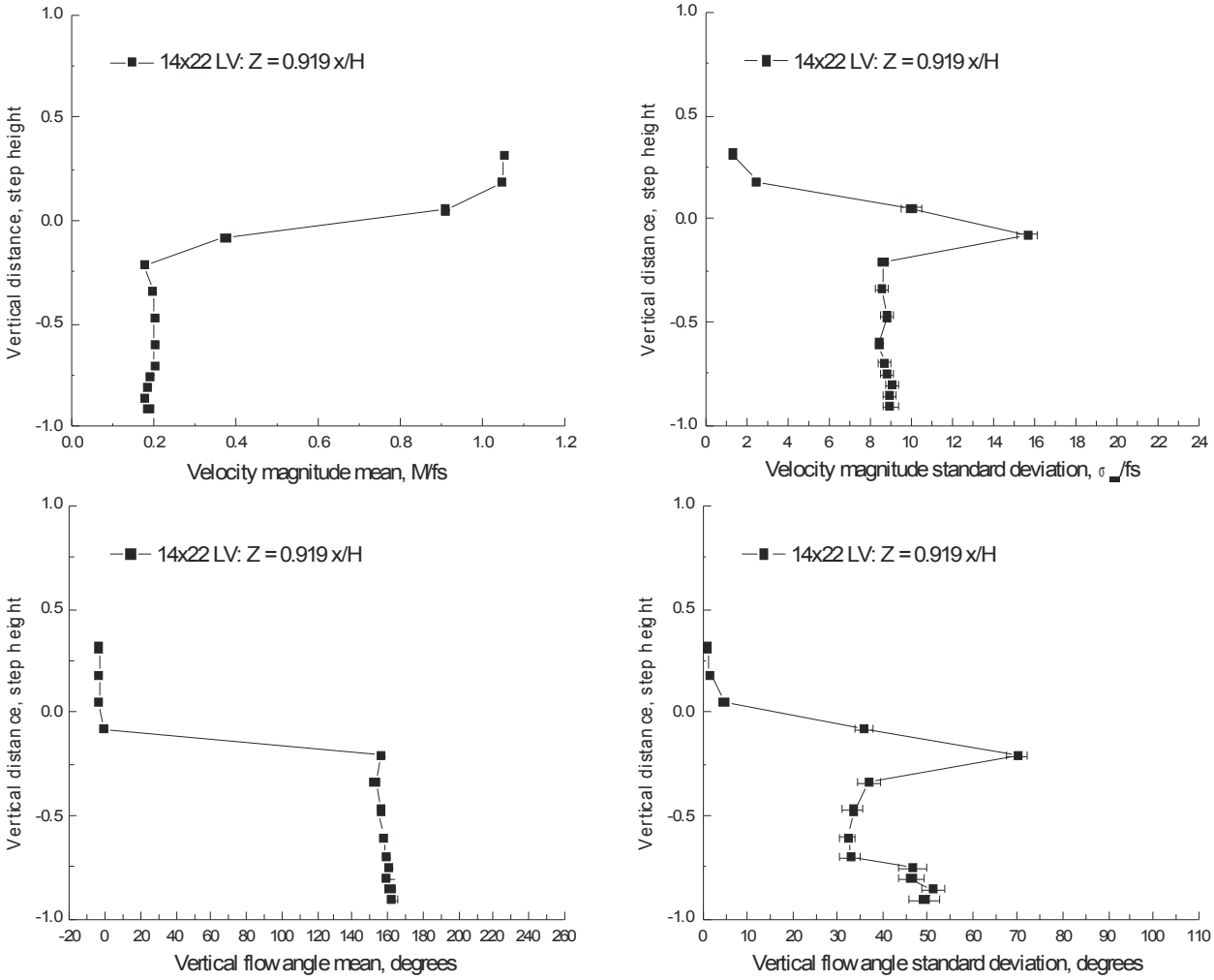

Figure VII.12.d.- Vertical scan 0.919 x/H downstream of a 3.5-inch backward-facing step: velocity magnitude and flow angle, fs = 45.0 m/s.

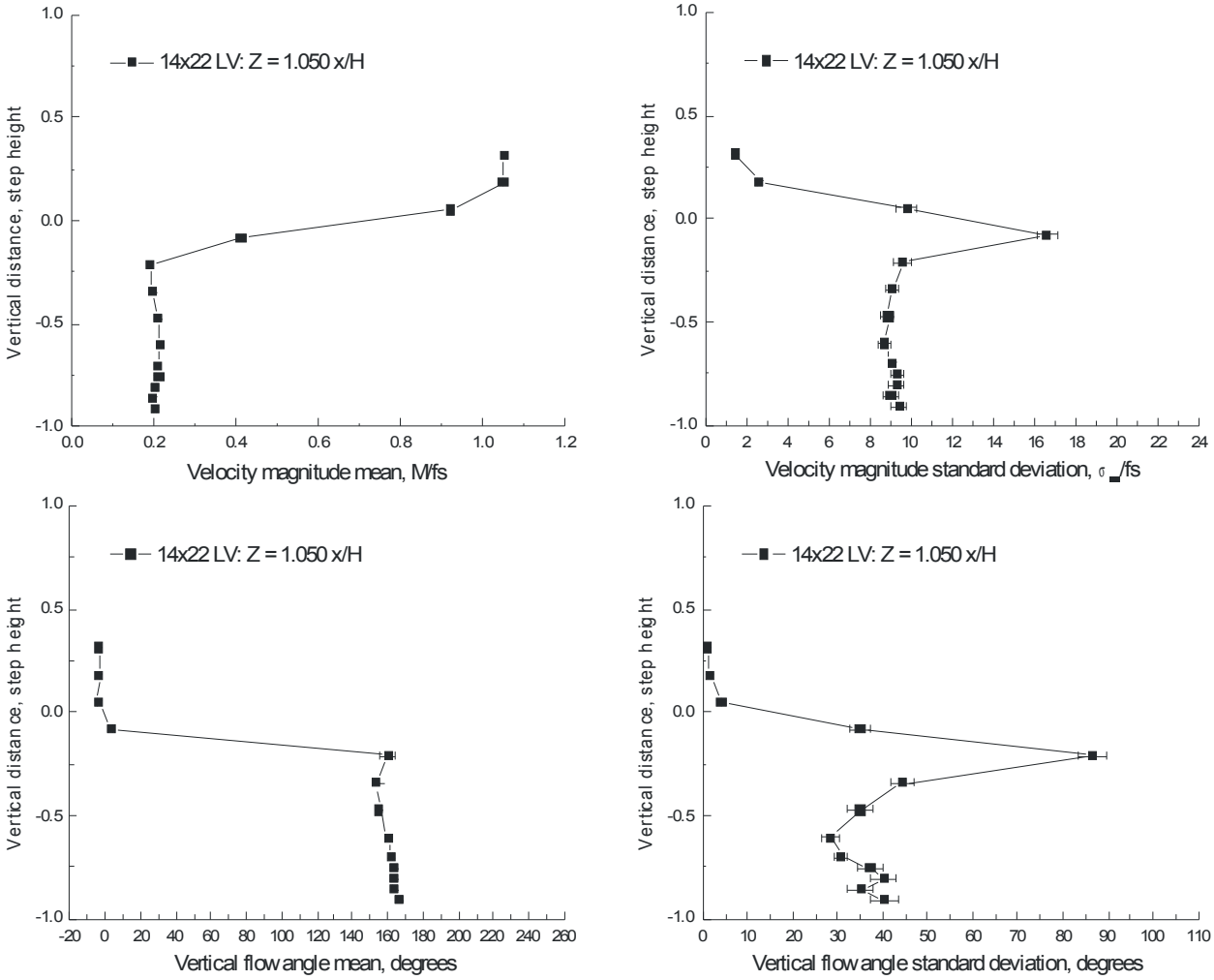

Figure VII.12.e.- Vertical scan 1.050 x/H downstream of a 3.5-inch backward-facing step (compares to Figure VII.6.d): velocity magnitude and flow angle, fs = 45.0 m/s.

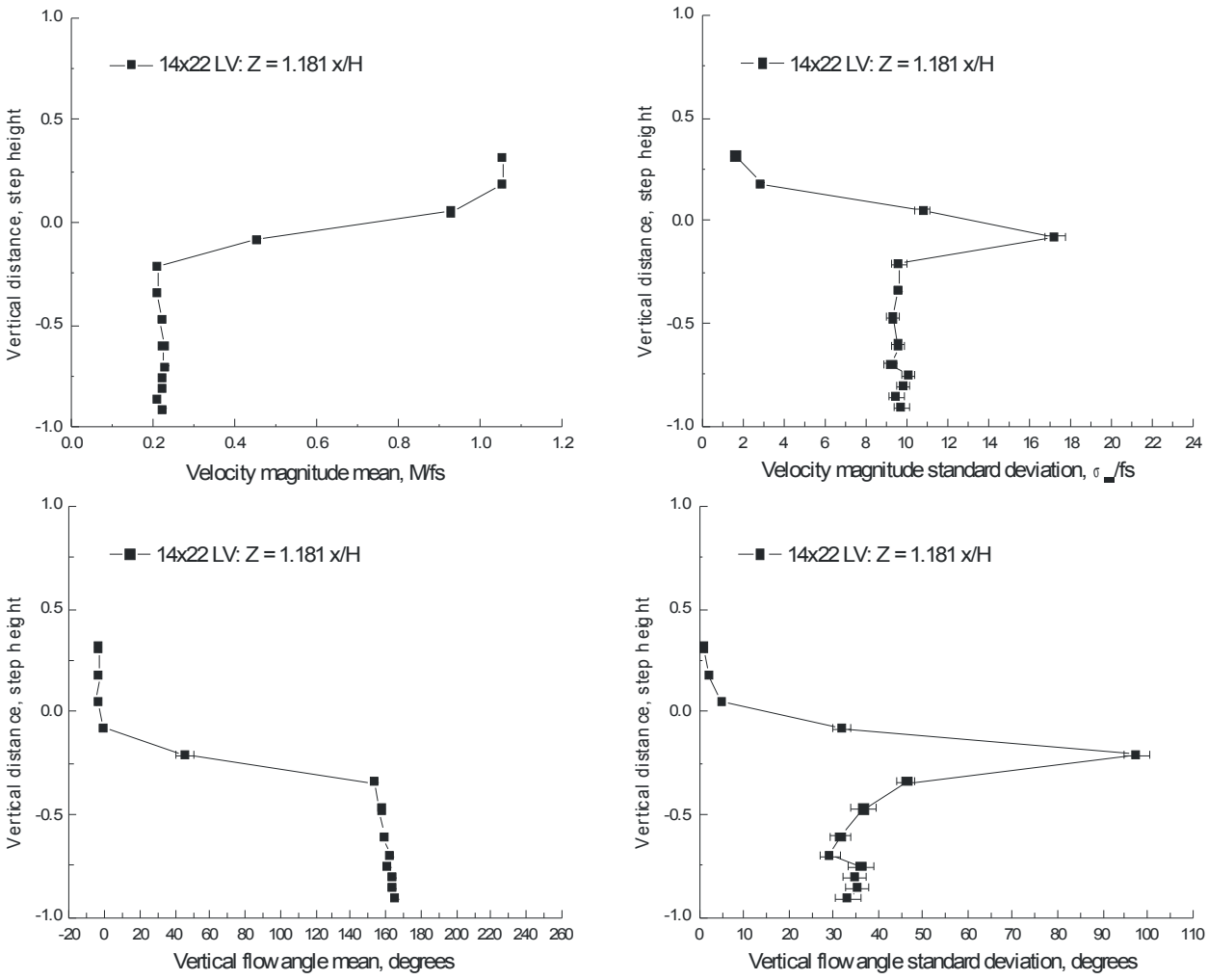

Figure VII.12.f.- Vertical scan 1.181 x/H downstream of a 3.5-inch backward-facing step: velocity magnitude and flow angle, fs = 45.0 m/s.

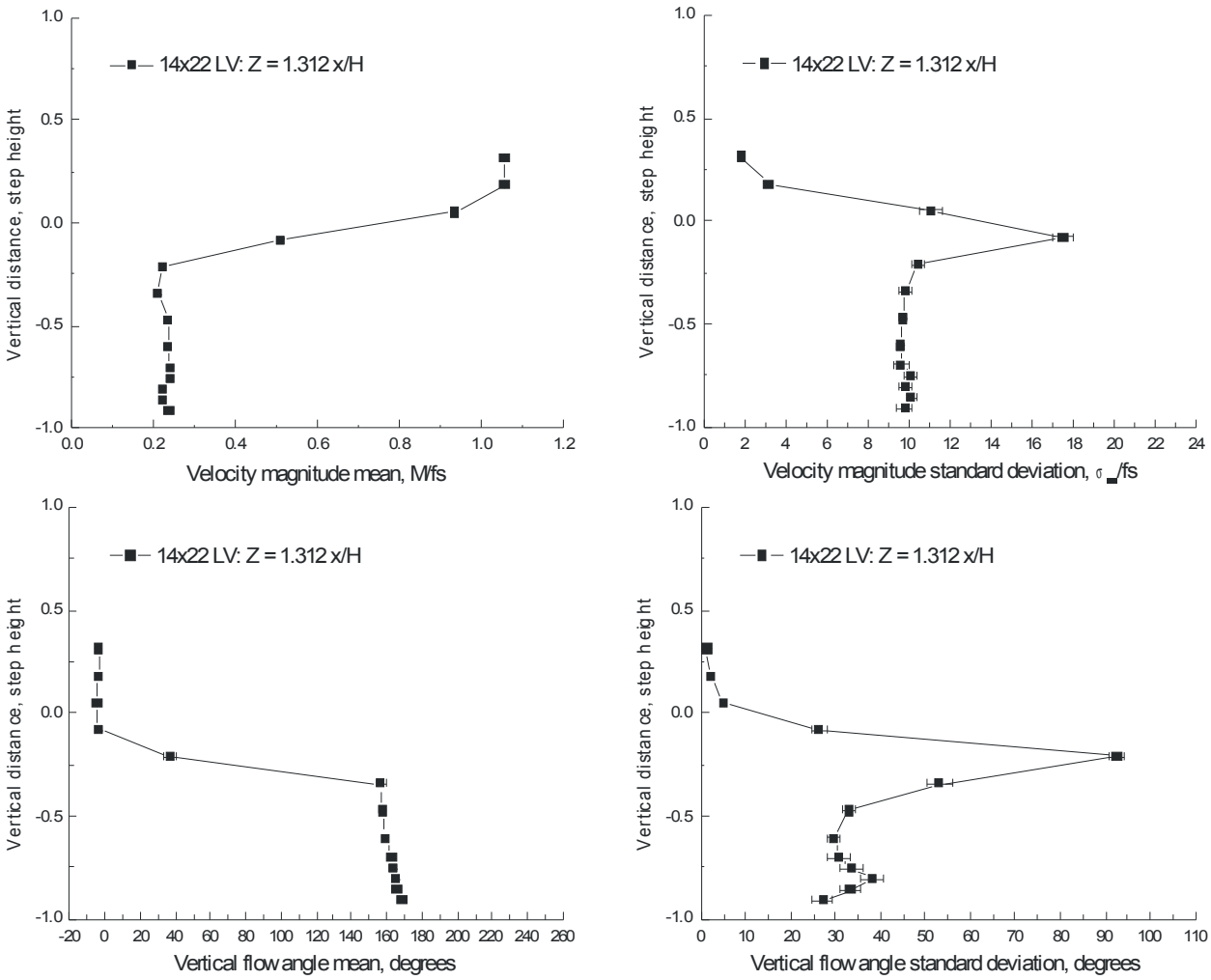

Figure VII.12.g.- Vertical scan 1.312 x/H downstream of a 3.5-inch backward-facing step (compares to Figure VII.6.e): velocity magnitude and flow angle, fs = 45.0 m/s.

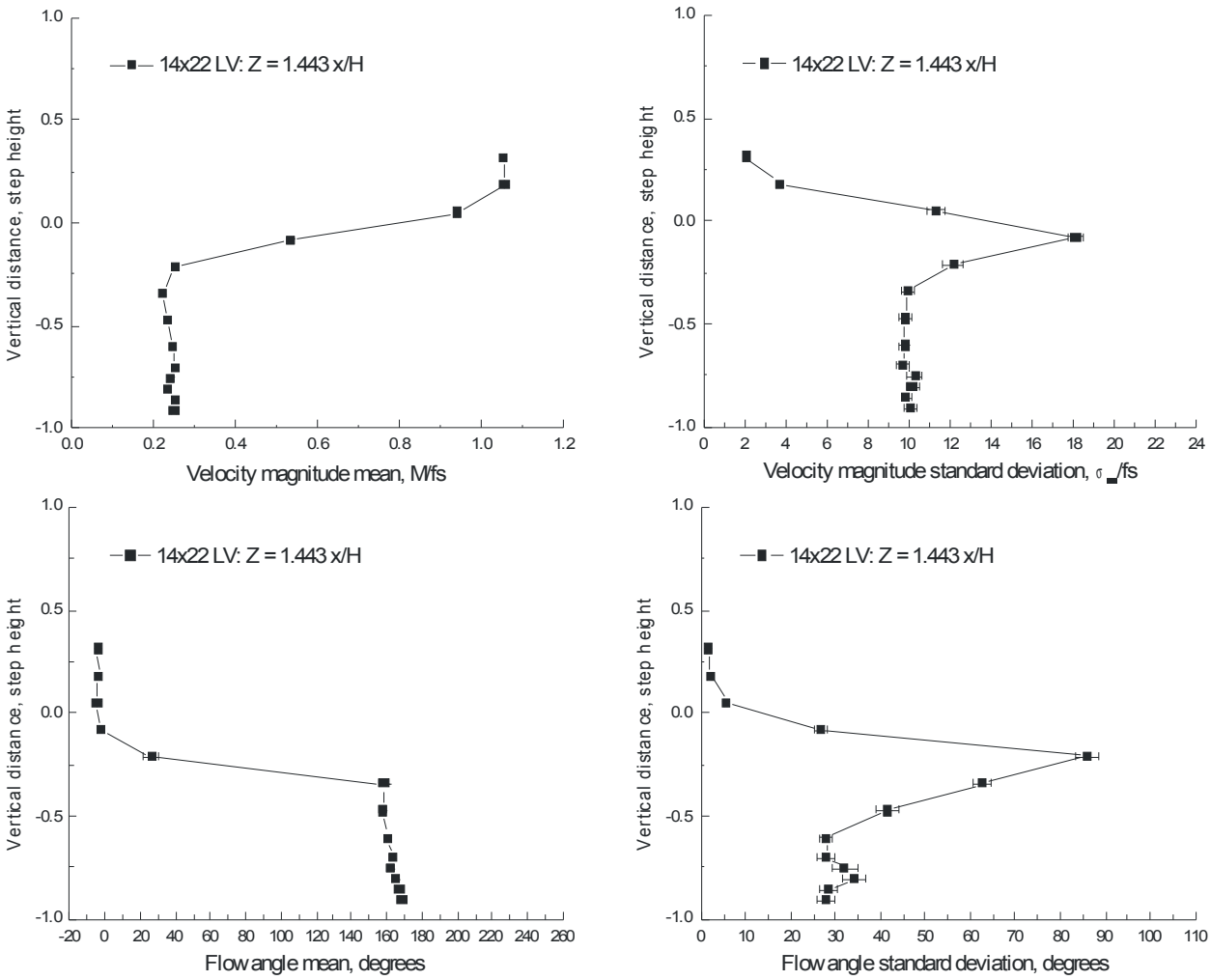

Figure VII.12.h.- Vertical scan 1.443 x/H downstream of a 3.5-inch backward-facing step: velocity magnitude and flow angle, fs = 45.0 m/s.

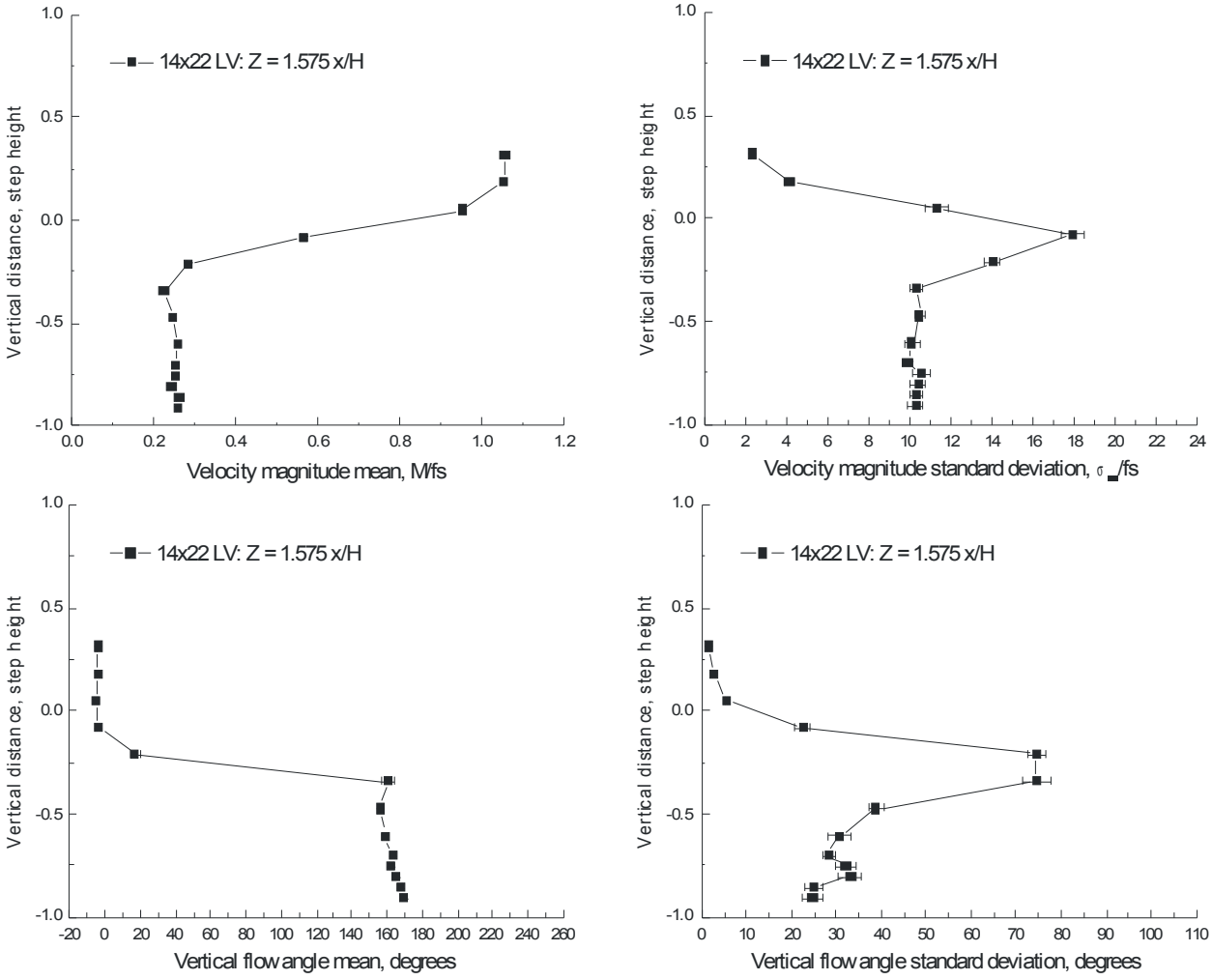

Figure VII.12.i.- Vertical scan 1.575 x/H downstream of a 3.5-inch backward-facing step (compares to Figure VII.6.f): velocity magnitude and flow angle, fs = 45.0 m/s.

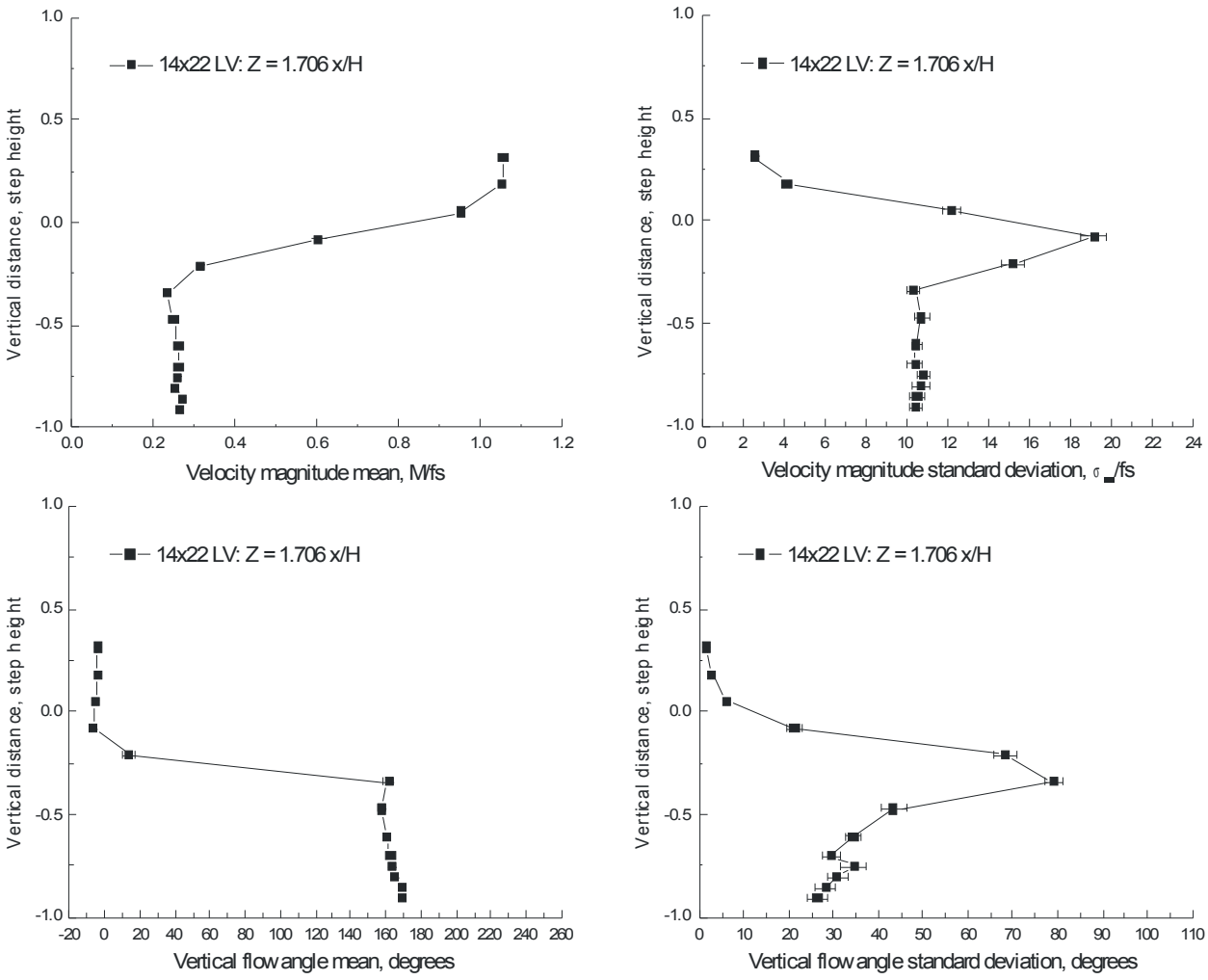

Figure VII.12.j.- Vertical scan 1.706 x/H downstream of a 3.5-inch backward-facing step: velocity magnitude and flow angle, fs = 45.0 m/s.

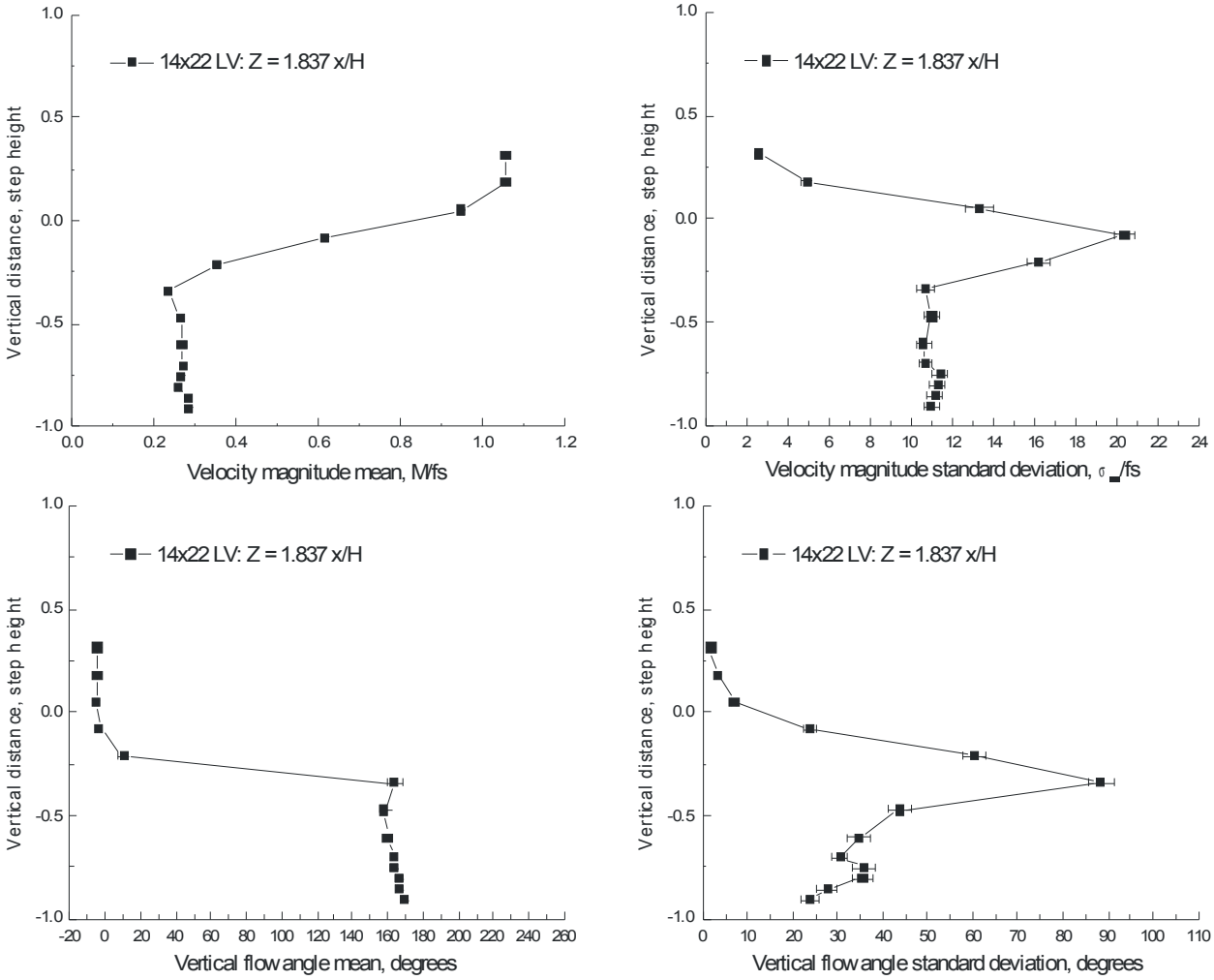

Figure VII.12.k.- Vertical scan 1.837 x/H downstream of a 3.5-inch backward-facing step (compares to Figure VII.6.g): velocity magnitude and flow angle, fs = 45.0 m/s.

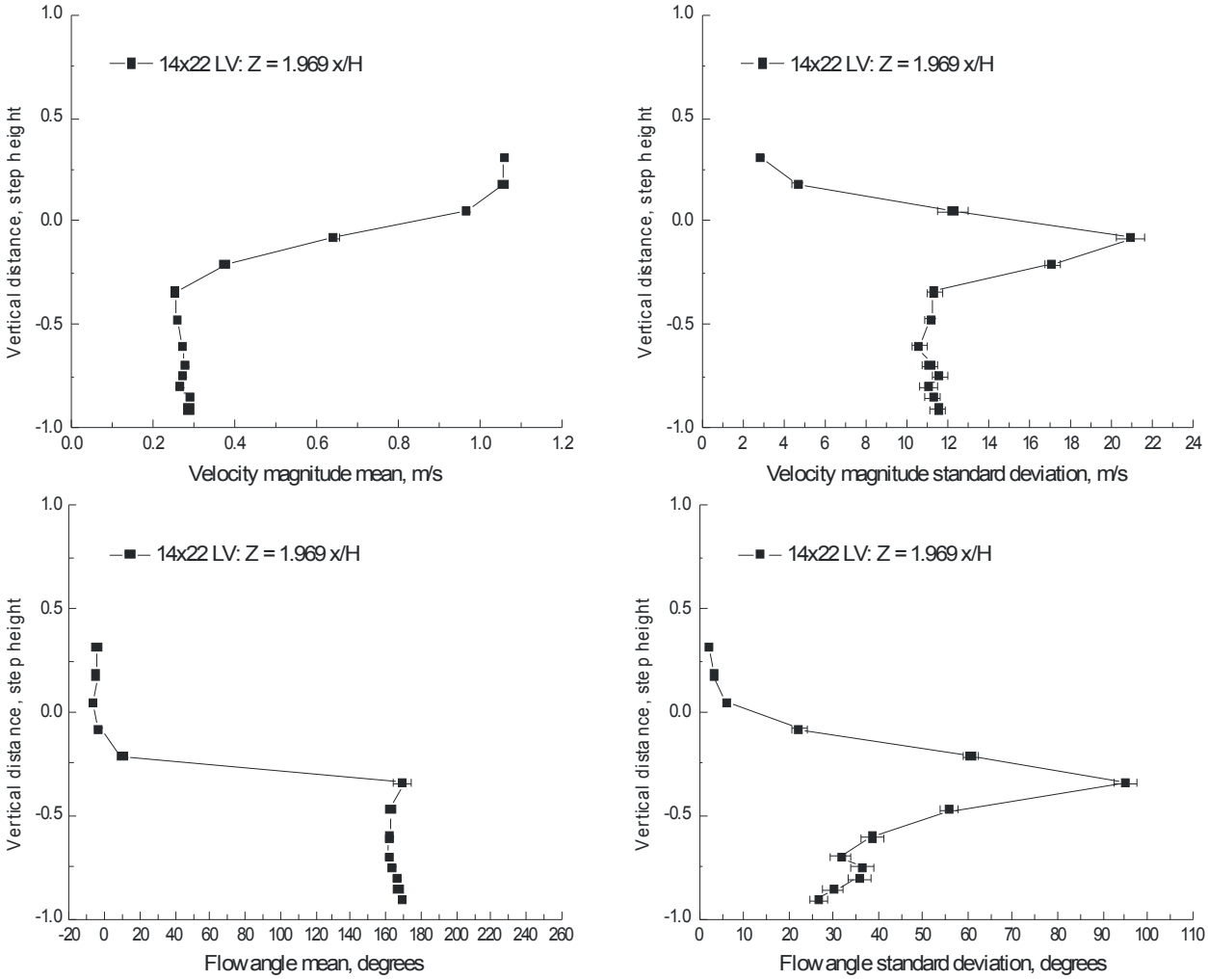

Figure VII.12.l.- Vertical scan 1.969 x/H downstream of a 3.5-inch backward-facing step: velocity magnitude and flow angle, fs = 45.0 m/s.

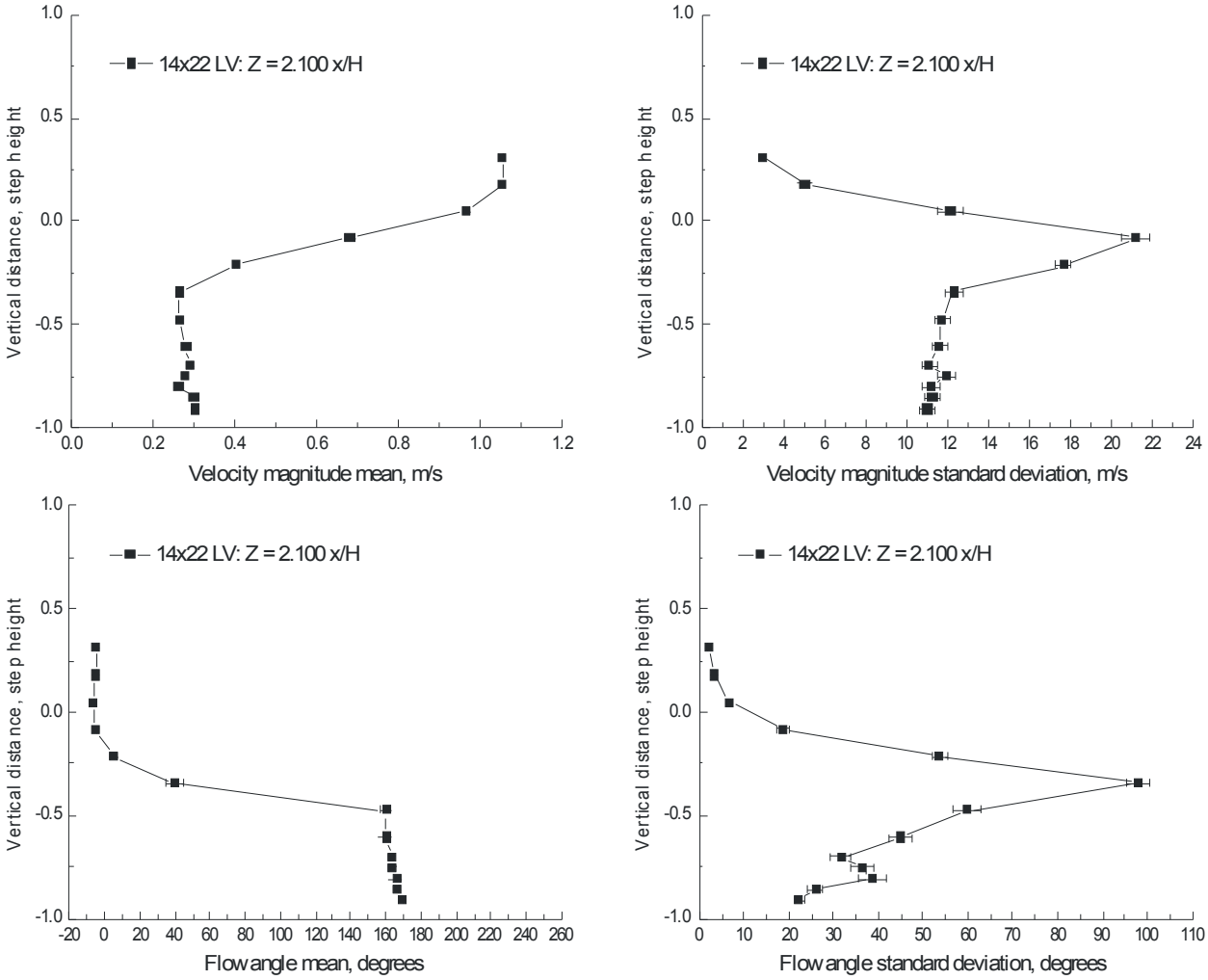

Figure VII.12.m.- Vertical scan 2.1 x/H downstream of a 3.5-inch backward-facing step (compares to Figure VII.6.h): velocity magnitude and flow angle, fs = 45.0 m/s.

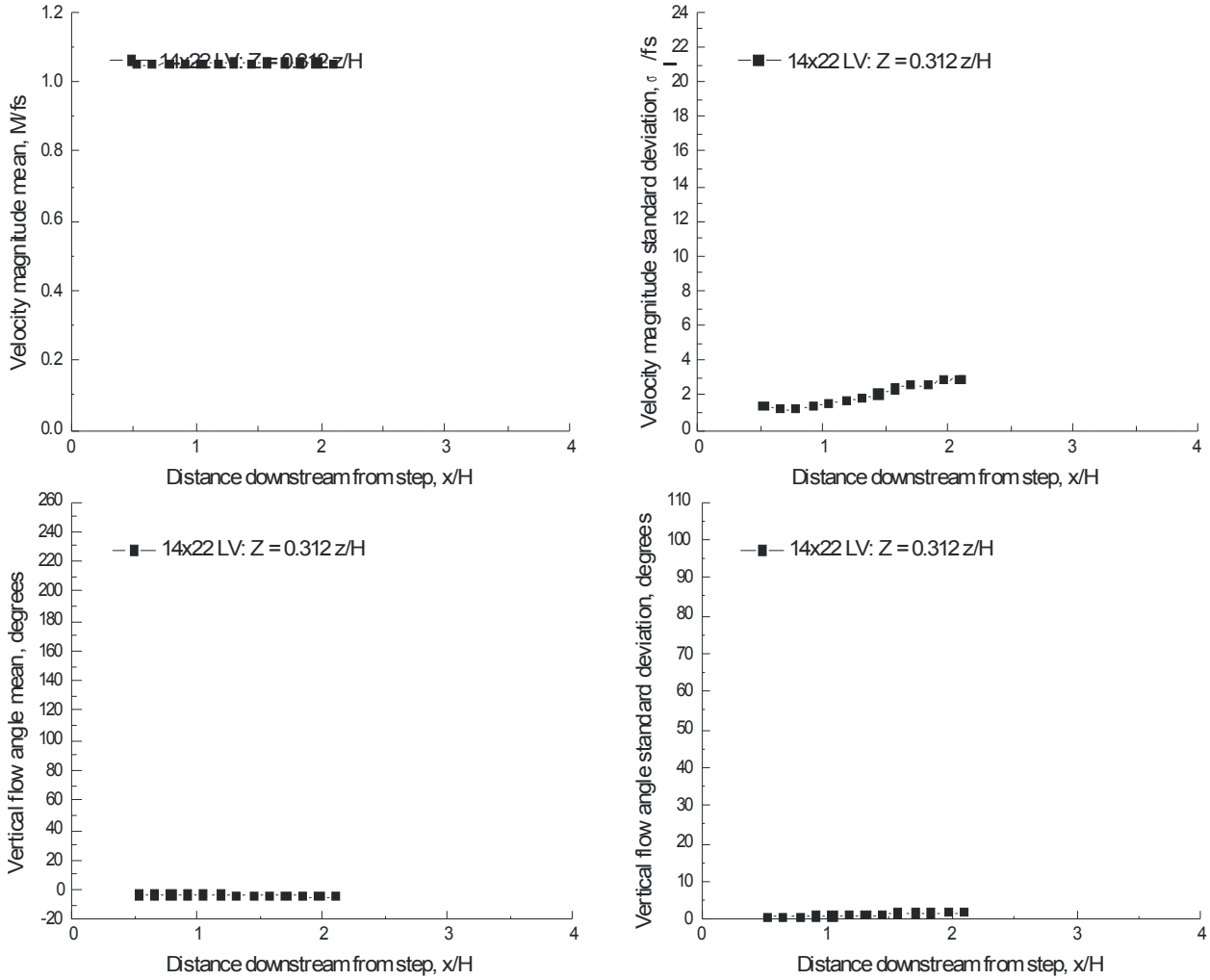

Figure VII.13.a.- Horizontal scan 0.312 z/H above a 3.5-inch backward-facing step (compares to Figure VII.7.b): velocity magnitude and flow angle, fs = 45.0 m/s.

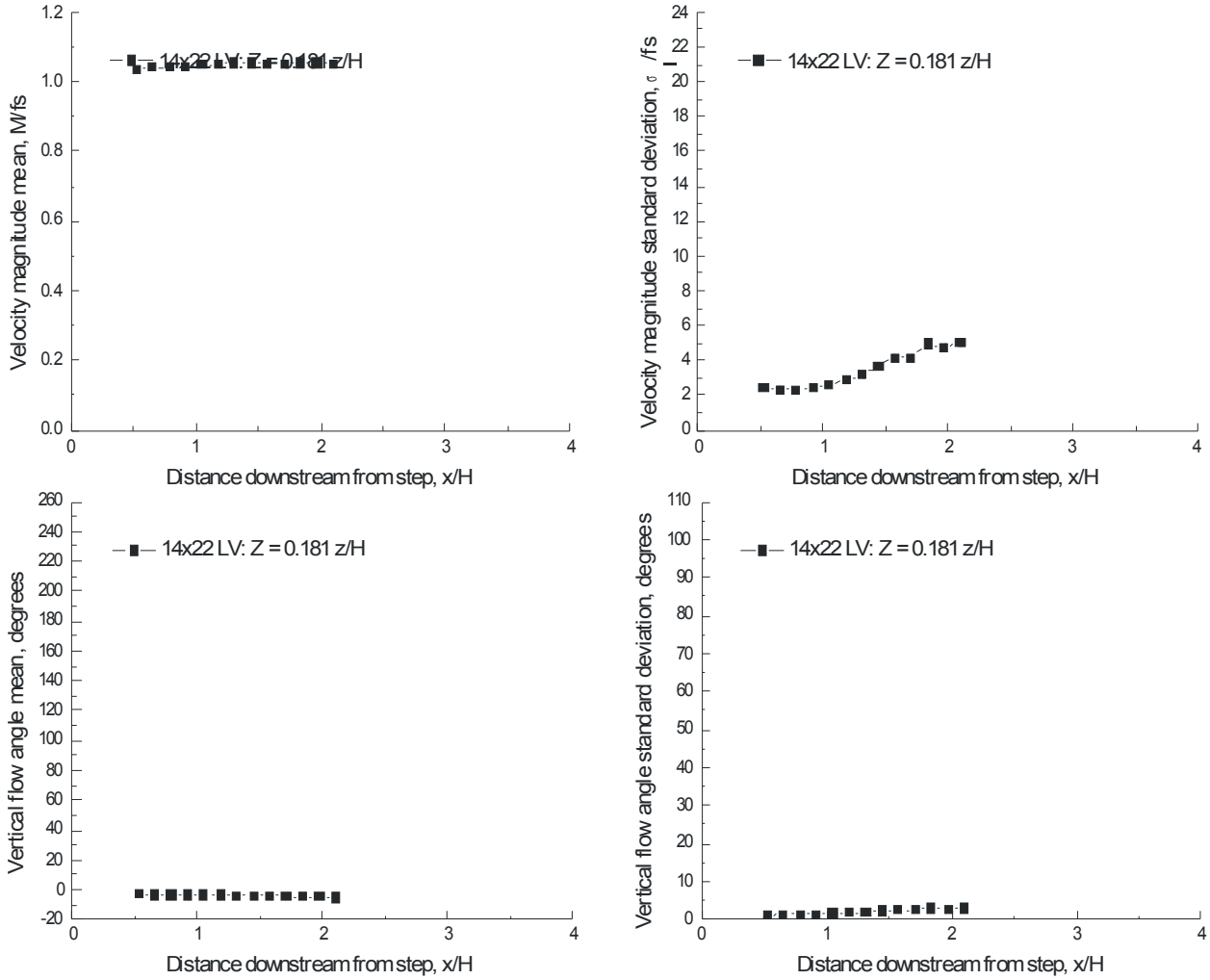

Figure VII.13.b.- Horizontal scan 0.181 z/H above a 3.5-inch backward-facing step (compares to Figure VII.7.c): velocity magnitude and flow angle, fs = 45.0 m/s.

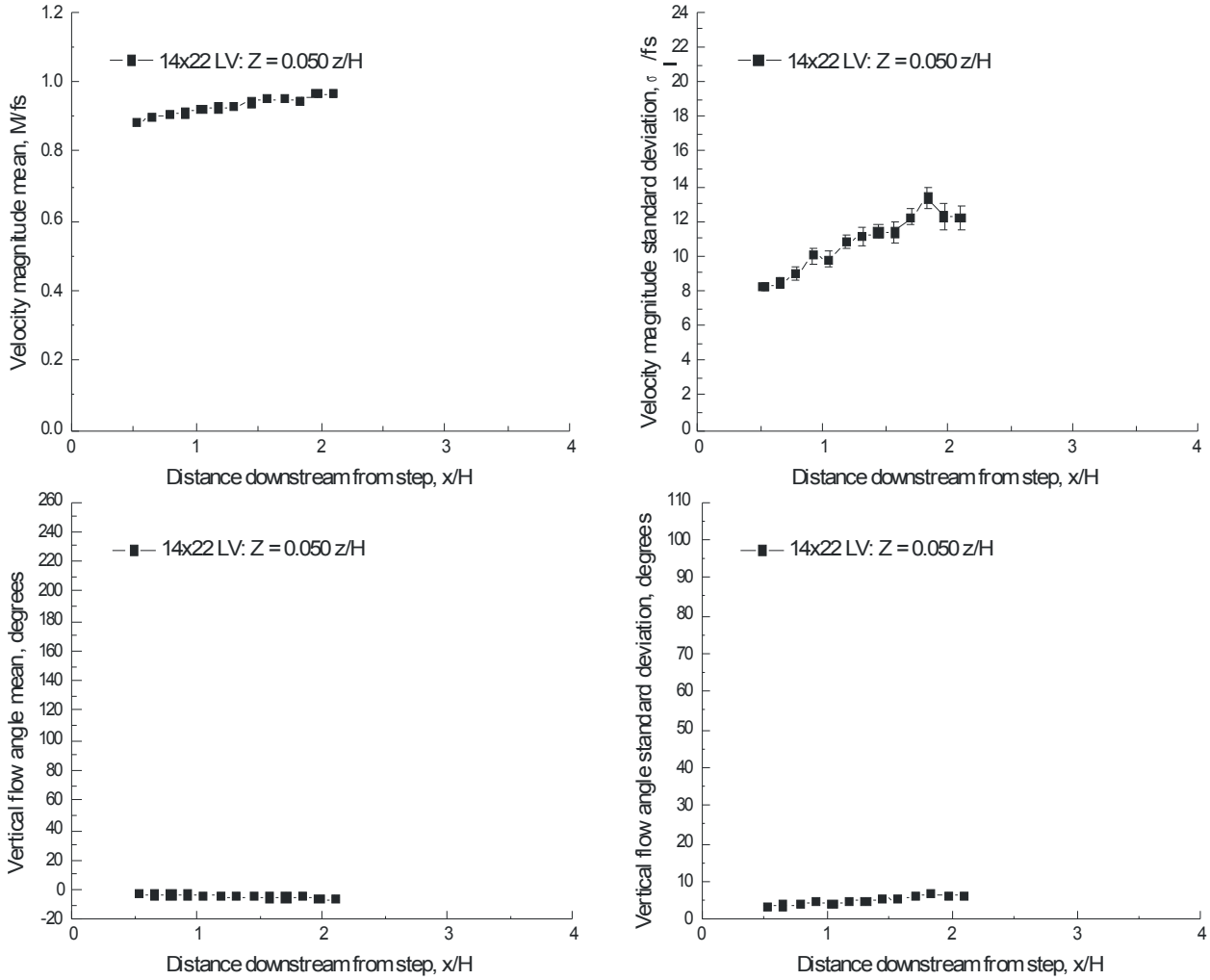

Figure VII.13.c.- Horizontal scan 0.050 z/H above a 3.5-inch backward-facing step (compares to Figure VII.7.d): velocity magnitude and flow angle, fs = 45.0 m/s.

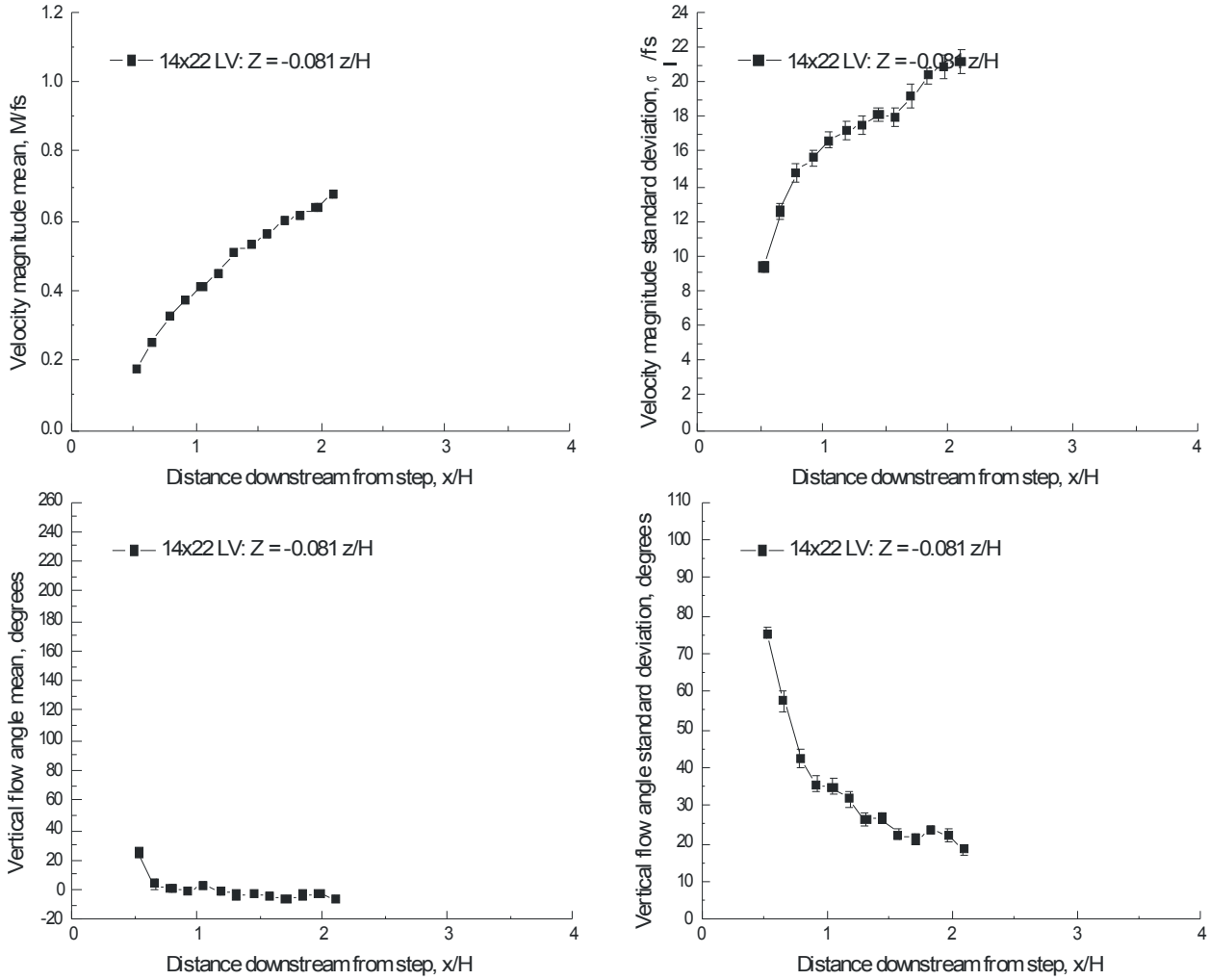

Figure VII.13.d.- Horizontal scan 0.081 z/H below a 3.5-inch backward-facing step (compares to Figure VII.7.e): velocity magnitude and flow angle, fs = 45.0 m/s.

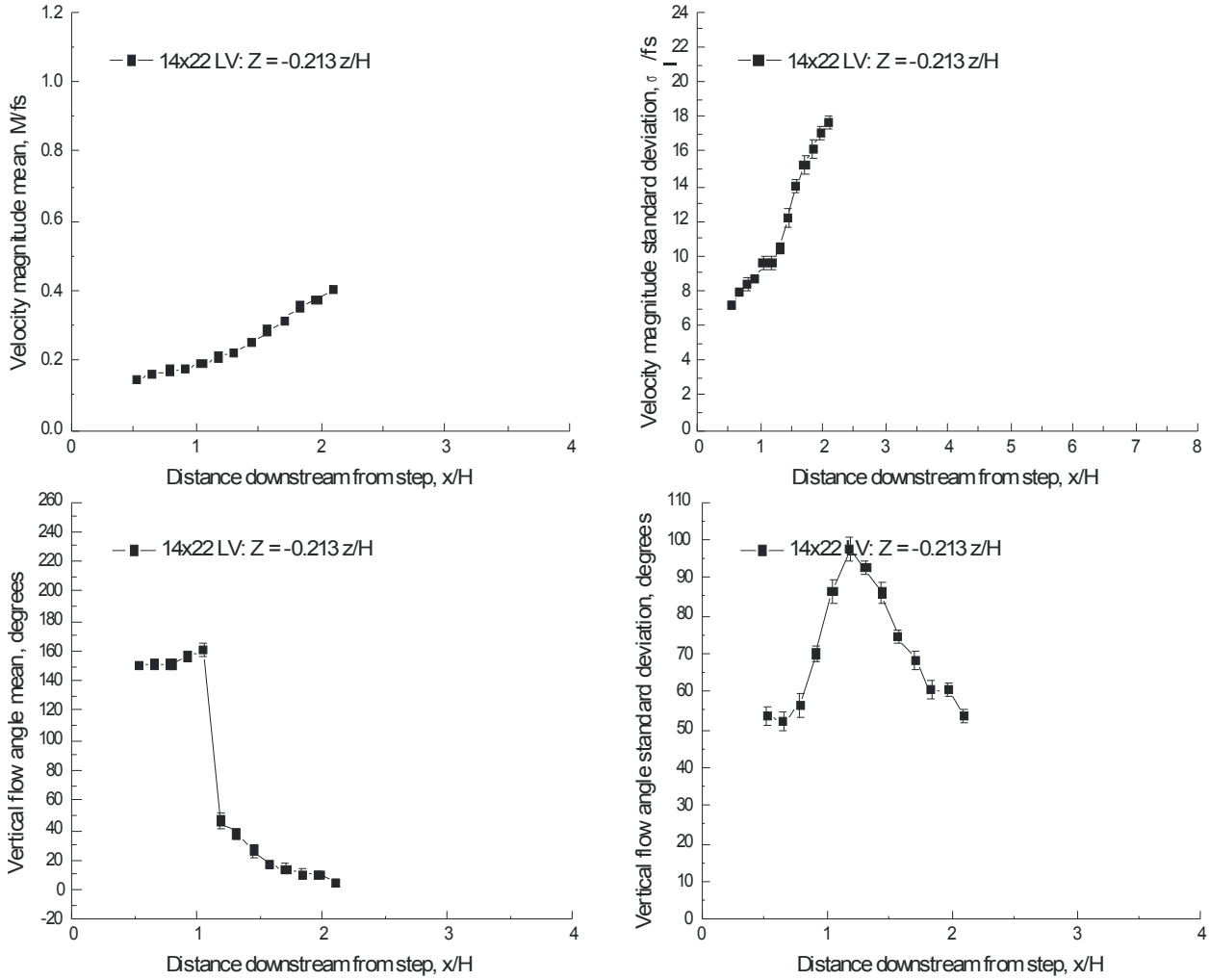

Figure VII.13.e.- Horizontal scan 2.13 z/H below a 3.5-inch backward-facing step (compares to Figure VII.7.f): velocity magnitude and flow angle, fs = 45.0 m/s.

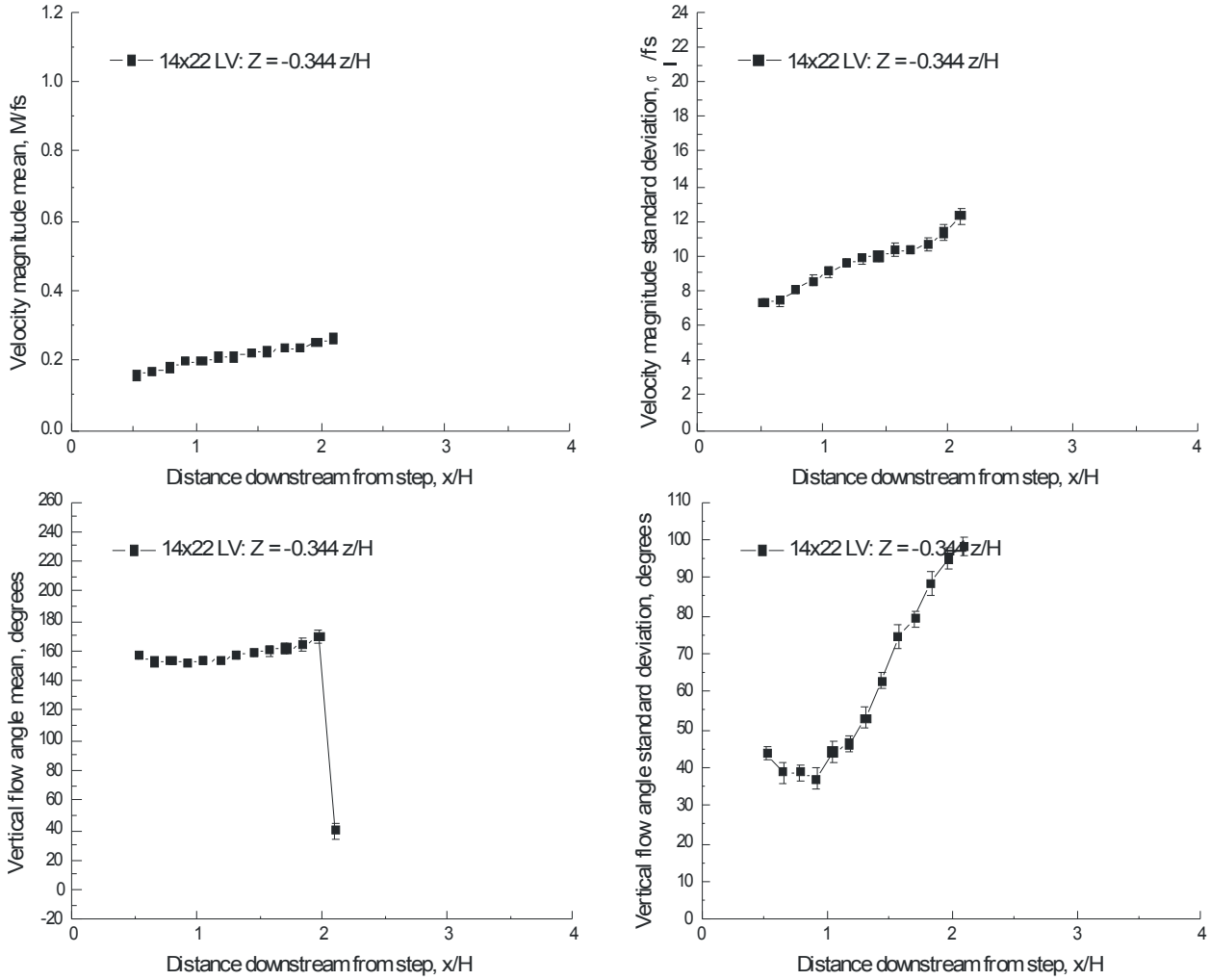

Figure VII.13.f.- Horizontal scan 0.344 z/H below a 3.5-inch backward-facing step (compares to Figure VII.7.g): velocity magnitude and flow angle, fs = 45.0 m/s.

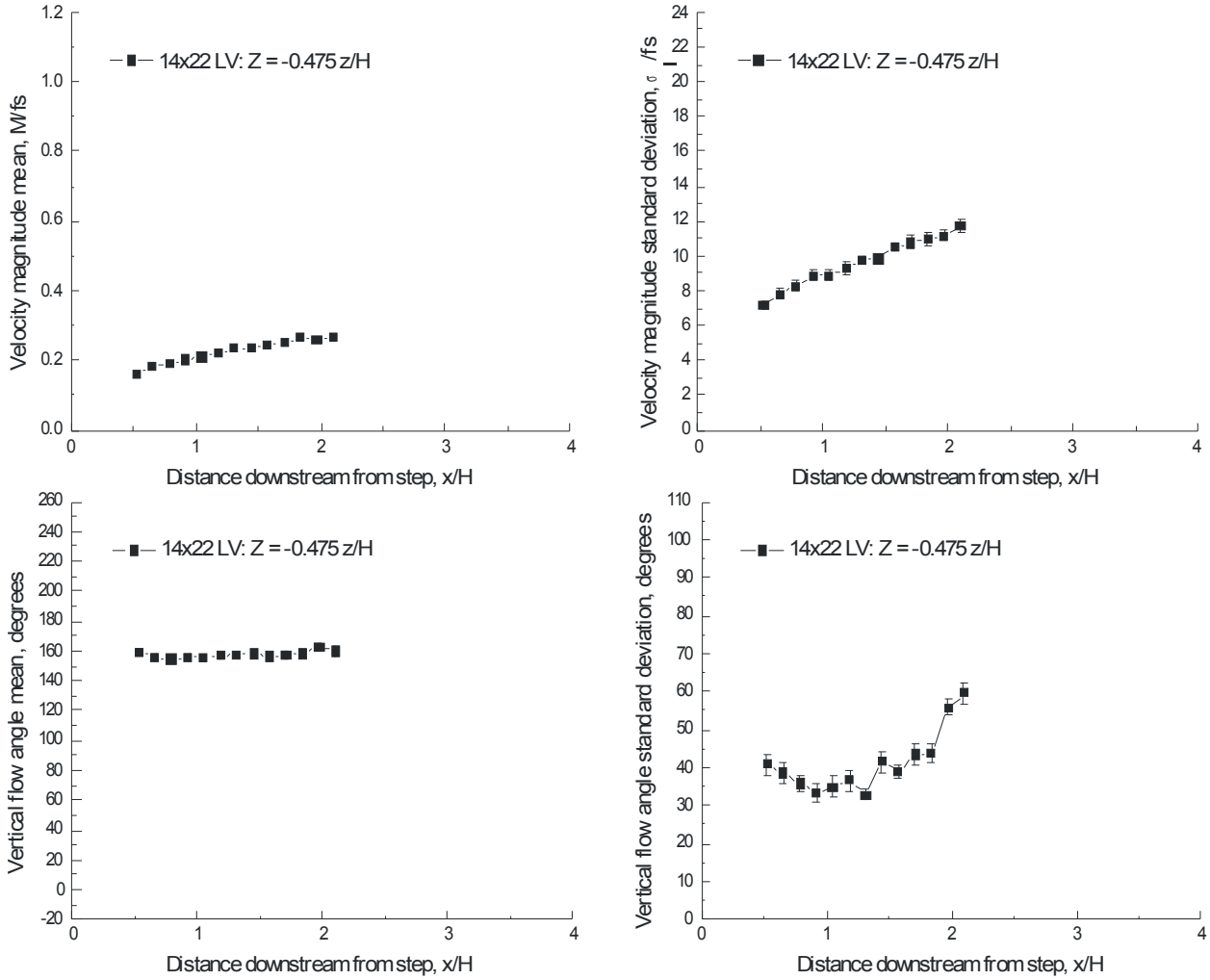

Figure VII.13.g.- Horizontal scan 0.475 z/H below a 3.5-inch backward-facing step (compares to Figure VII.7.h): velocity magnitude and flow angle, fs = 45.0 m/s.

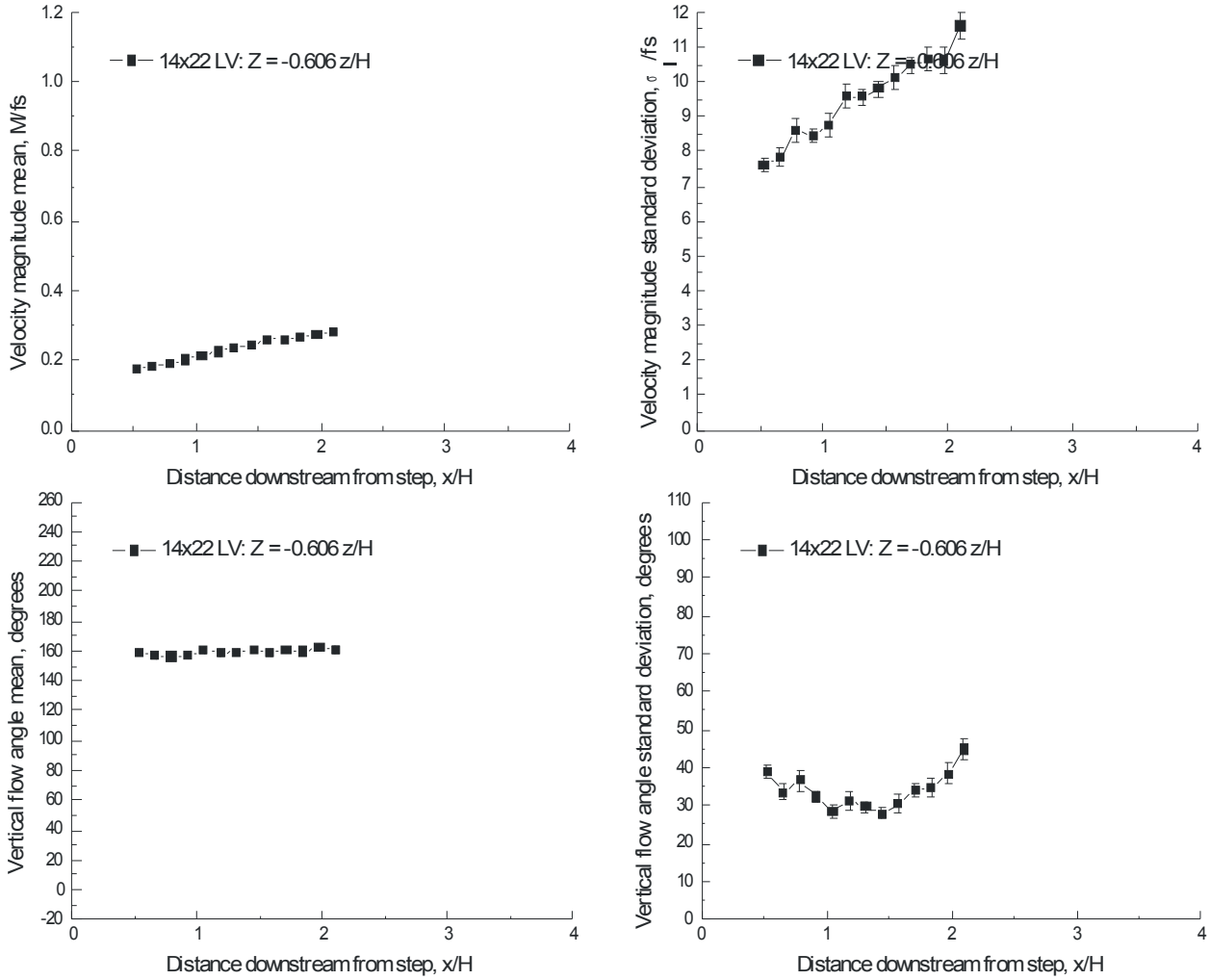

Figure VII.13.h.- Horizontal scan 0.606 z/H below a 3.5-inch backward-facing step (compares to Figure VII.7.i): velocity magnitude and flow angle, fs = 45.0 m/s.

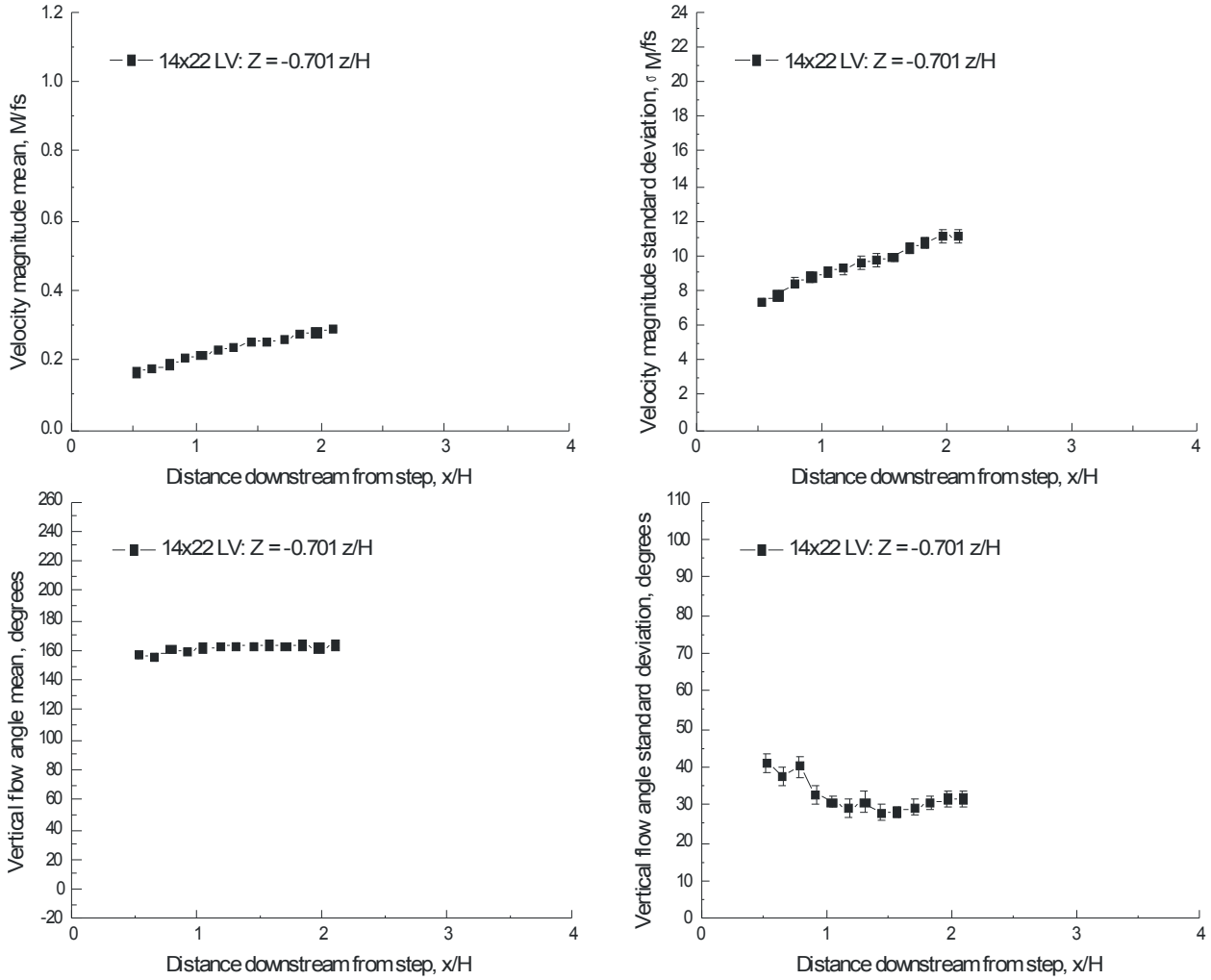

Figure VII.13.i.- Horizontal scan 0.701 z/H below a 3.5-inch backward-facing step (compares to Figure VII.7.j): velocity magnitude and flow angle, fs = 45.0 m/s.

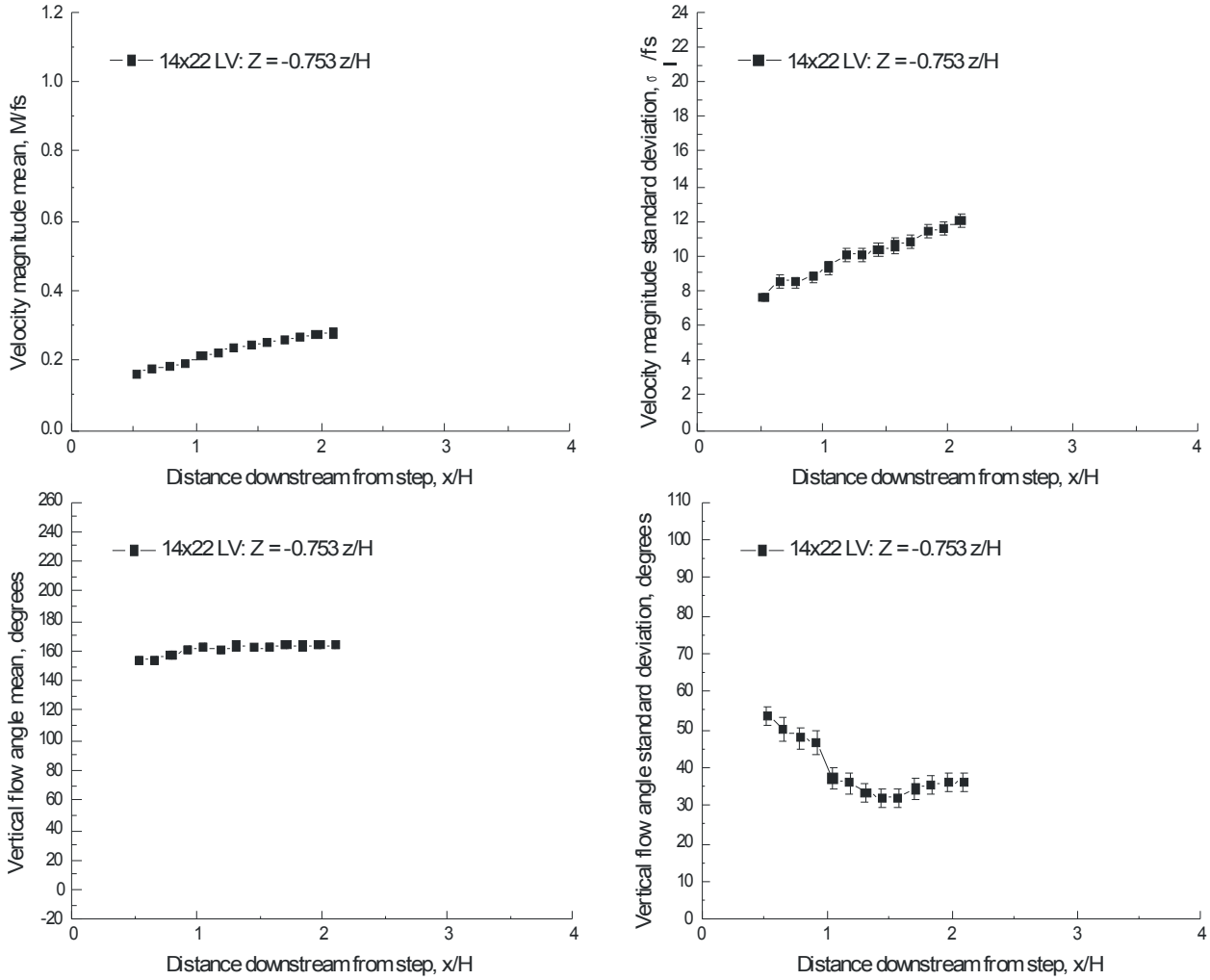

Figure VII.13.j.- Horizontal scan 0.753 z/H below a 3.5-inch backward-facing step (compares to Figure VII.7.k): velocity magnitude and flow angle, fs = 45.0 m/s.

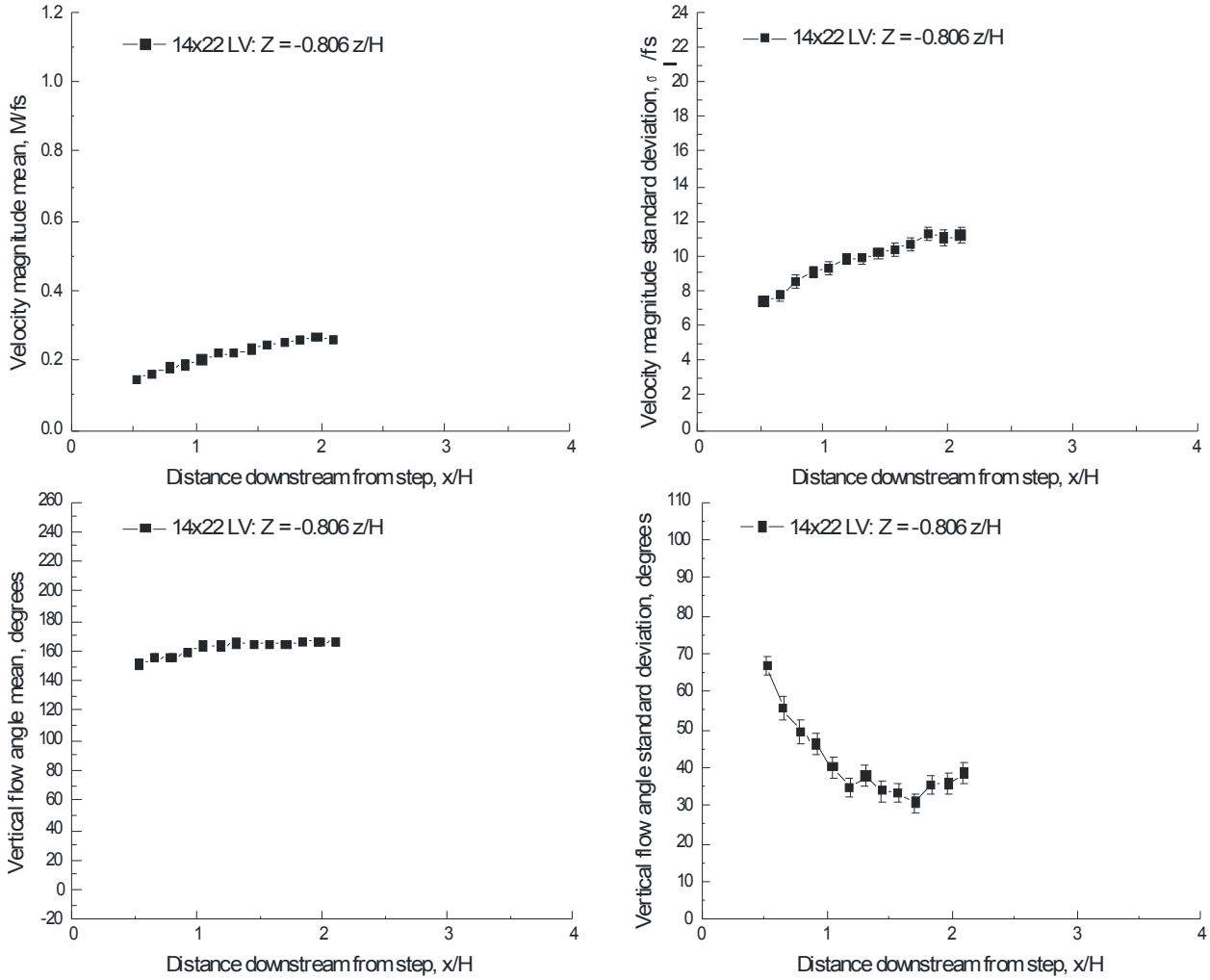

Figure VII.13.k.- Horizontal scan 0.806 z/H below a 3.5-inch backward-facing step (compares to Figure VII.7.l): velocity magnitude and flow angle, fs = 45.0 m/s.

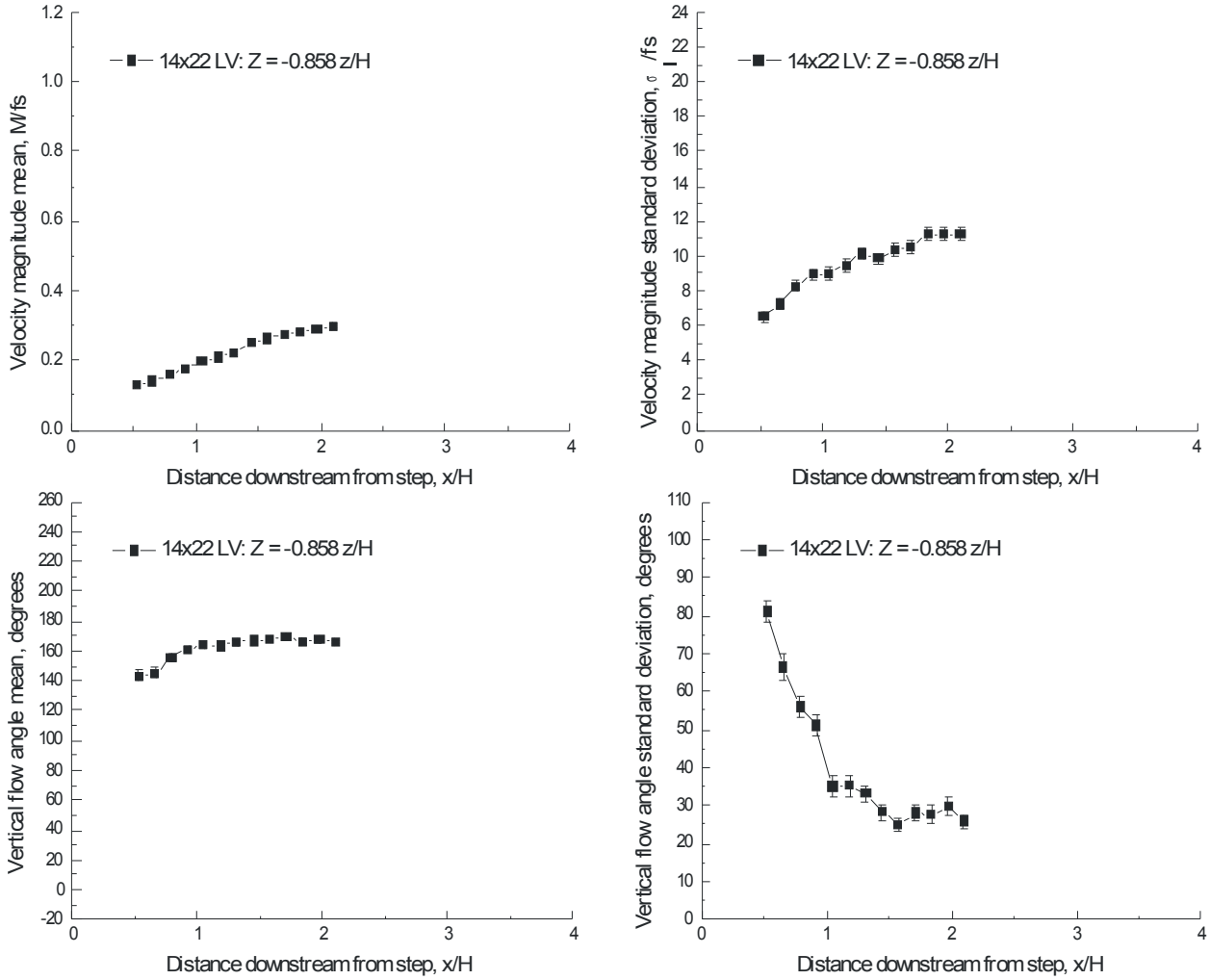

Figure VII.13.l.- Horizontal scan 0.858 z/H below a 3.5-inch backward-facing step (compares to Figure VII.7.m): velocity magnitude and flow angle, fs = 45.0 m/s.

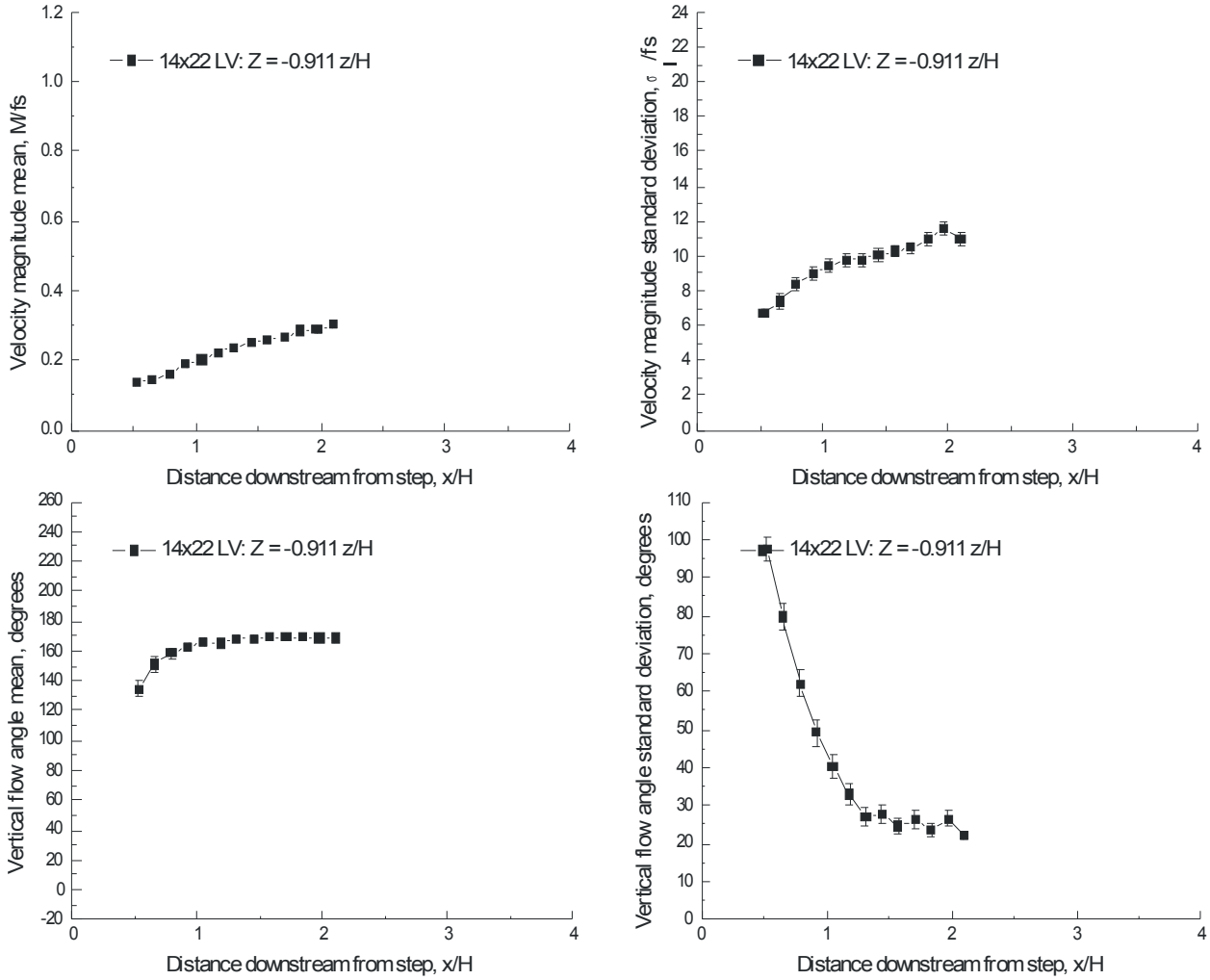

Figure VII.13.m.- Horizontal scan 0.911 z/H below a 3.5-inch backward-facing step (compares to Figure VII.7.n): velocity magnitude and flow angle, fs = 45.0 m/s.

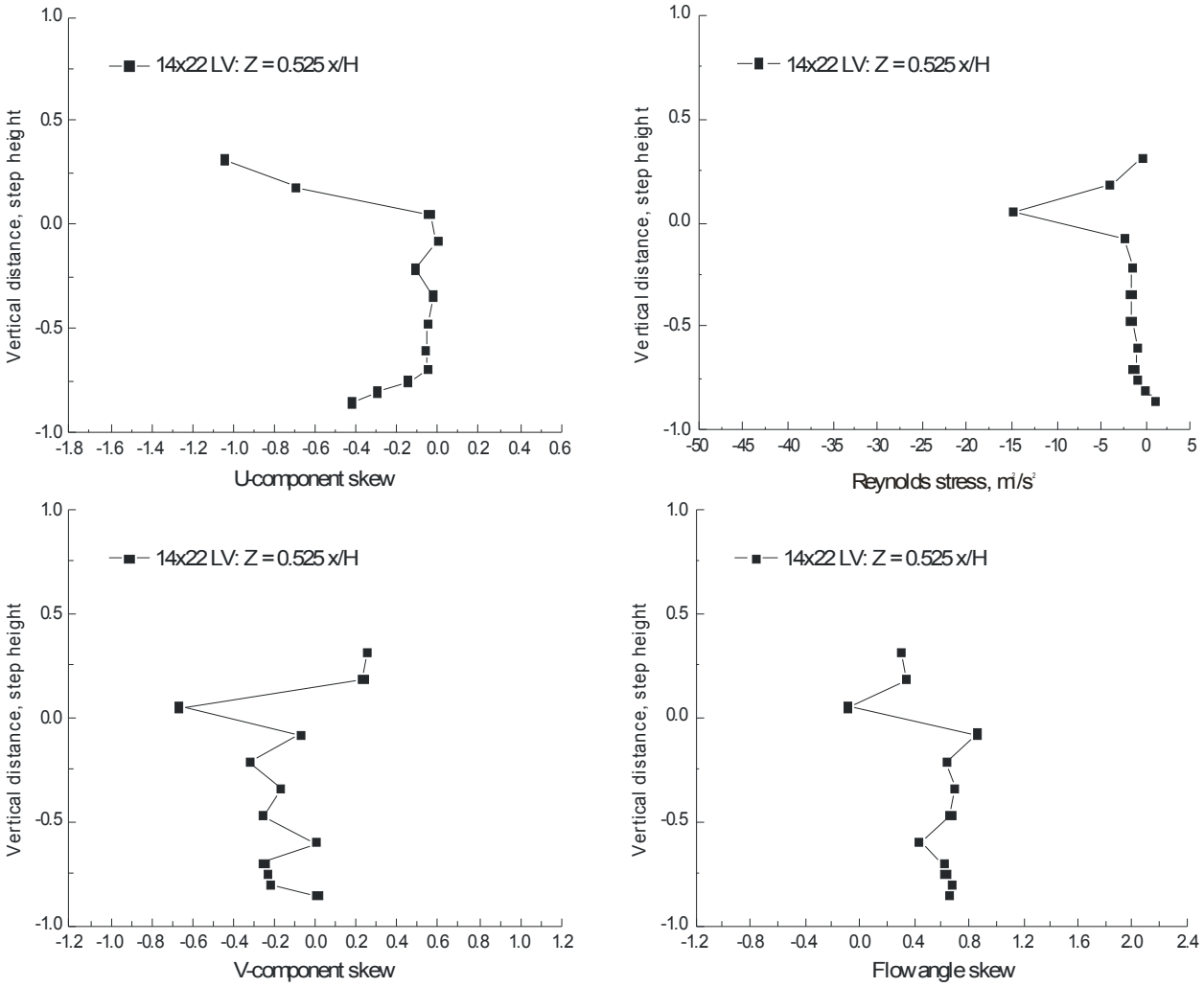

Figure VII.14.a.- Vertical scan 0.525 x/H downstream of a 3.5-inch backward-facing step (compares to Figure VII.8.b): streamwise and vertical velocity skew, flow angle skew and Reynolds stress, fs = 45.0 m/s.

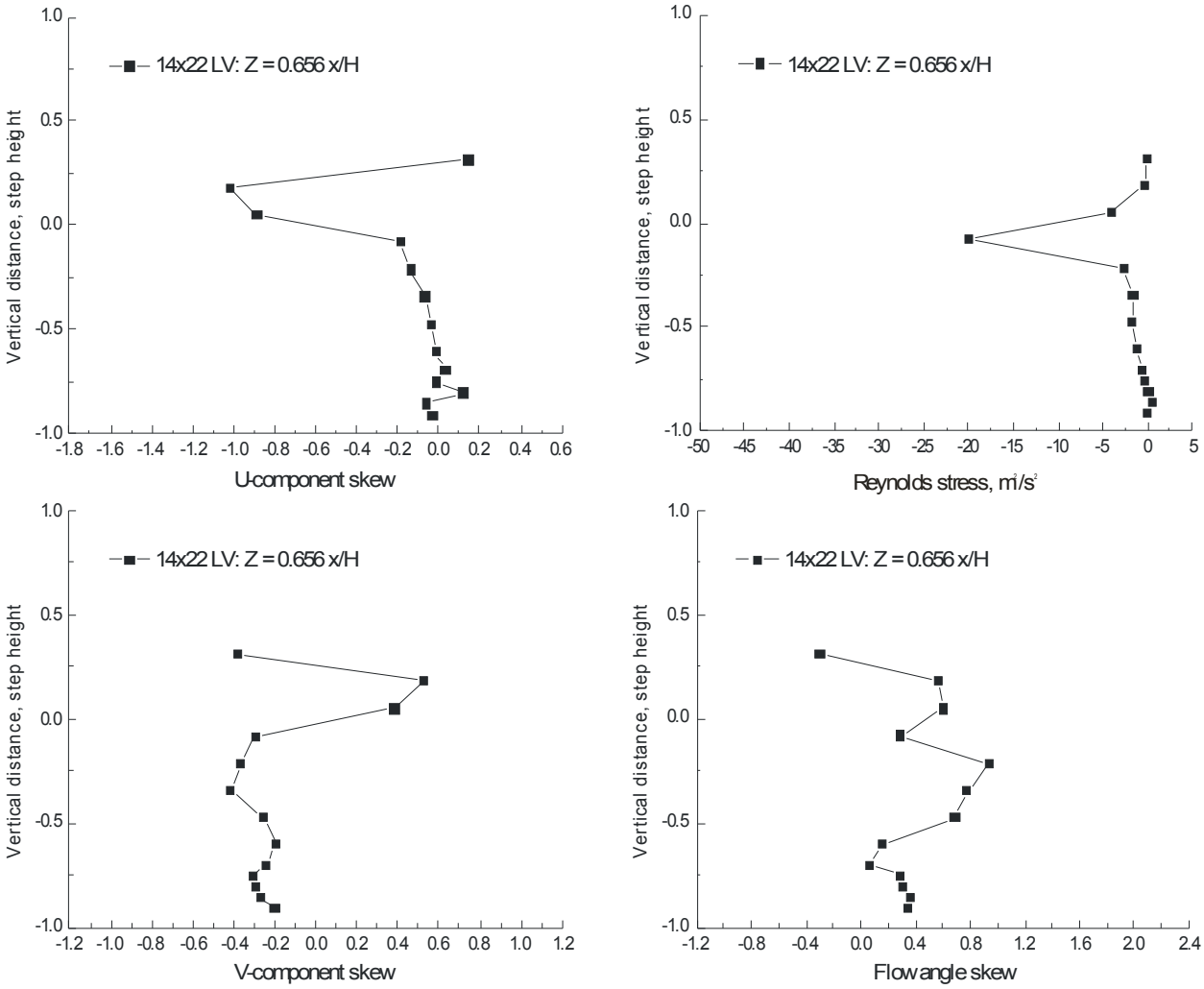

Figure VII.14.b.- Vertical scan 0.656 x/H downstream of a 3.5-inch backward-facing step: streamwise and vertical velocity skew, flow angle skew and Reynolds stress, fs = 45.0 m/s.

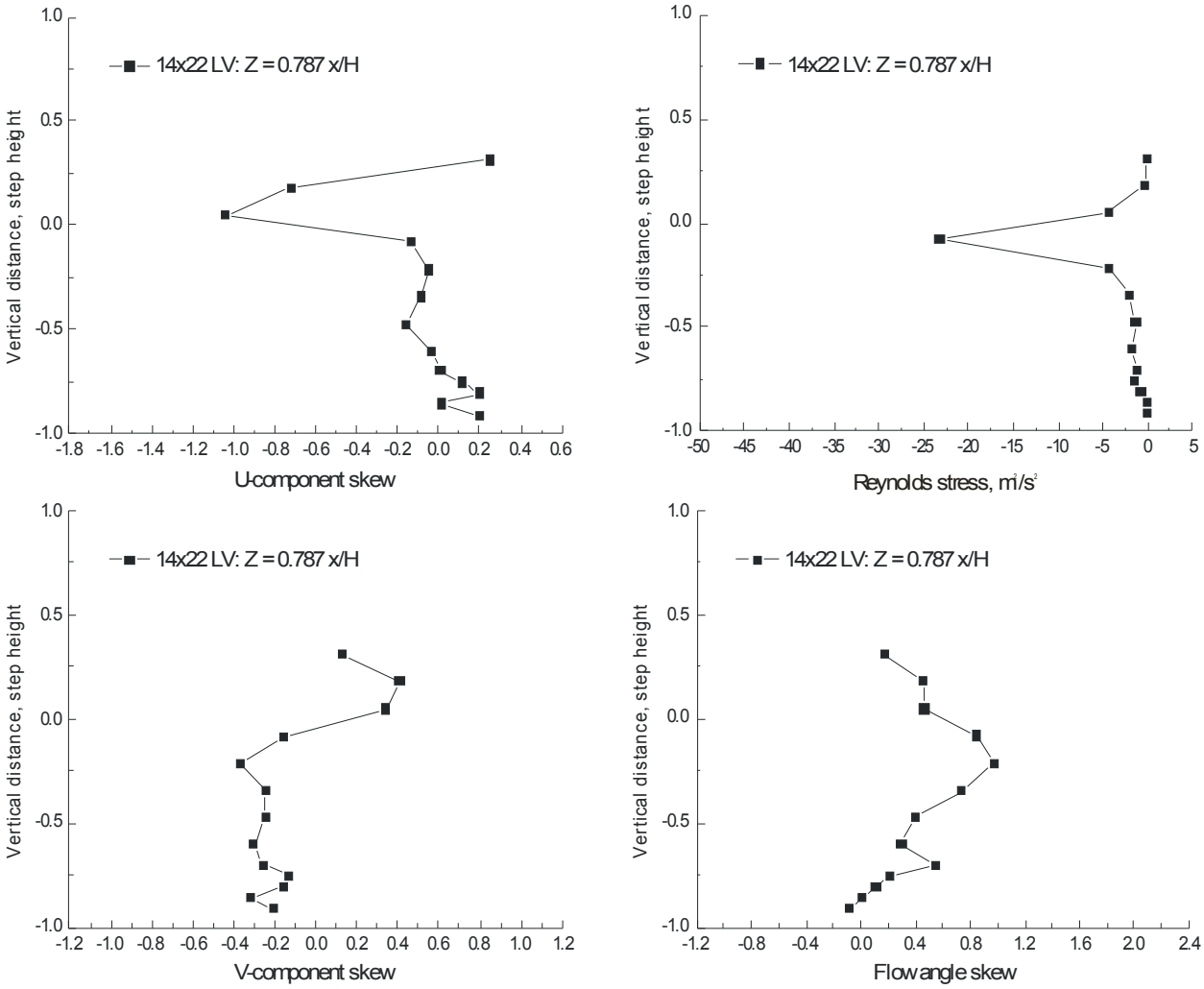

Figure VII.14.c.- Vertical scan 0.787 x/H downstream of a 3.5-inch backward-facing step (compares to Figure VII.8.c): streamwise and vertical velocity skew, flow angle skew and Reynolds stress, fs = 45.0 m/s.

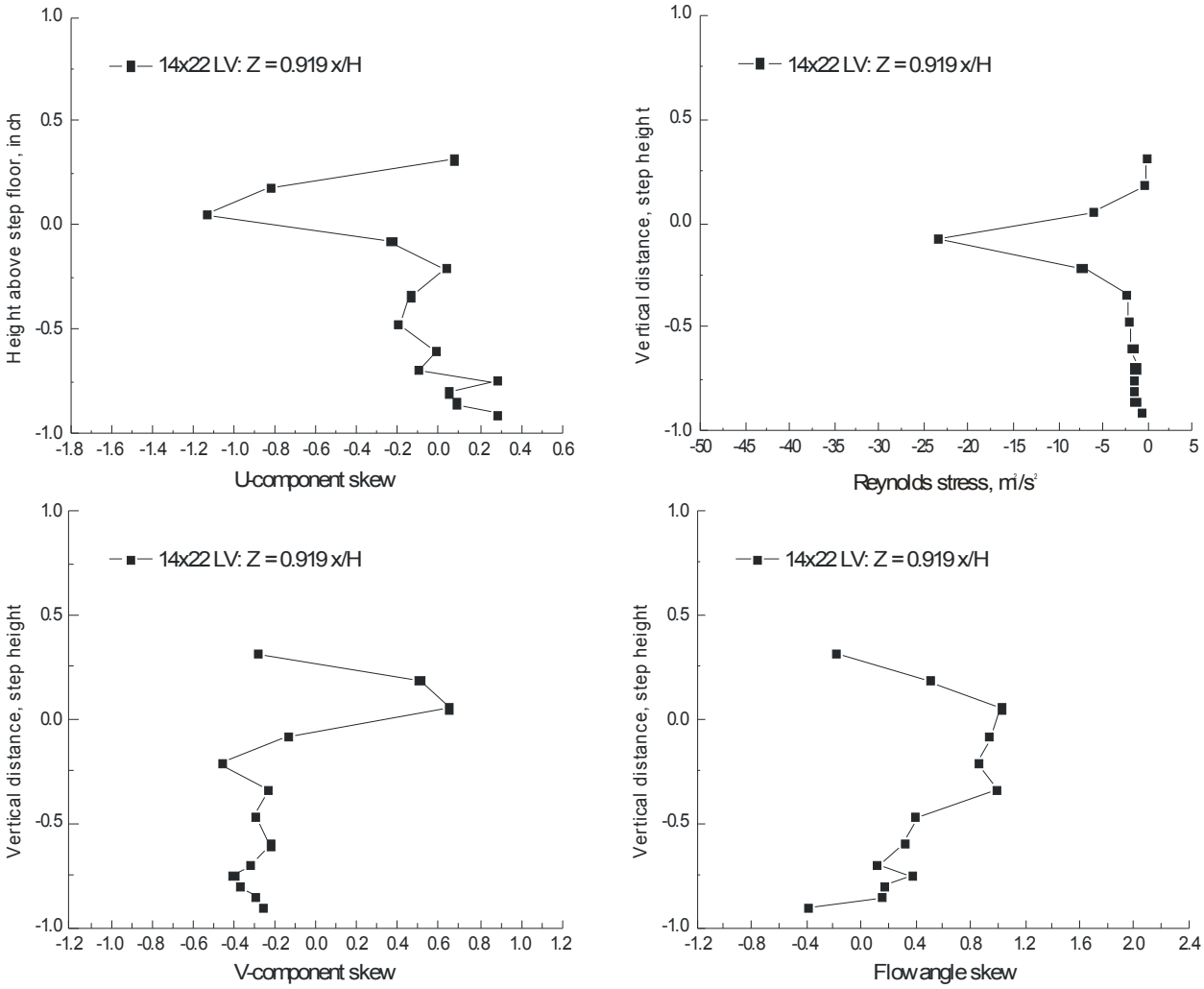

Figure VII.14.d.- Vertical scan 0.919 x/H downstream of a 3.5-inch backward-facing step: streamwise and vertical velocity skew, flow angle skew and Reynolds stress, fs = 45.0 m/s.

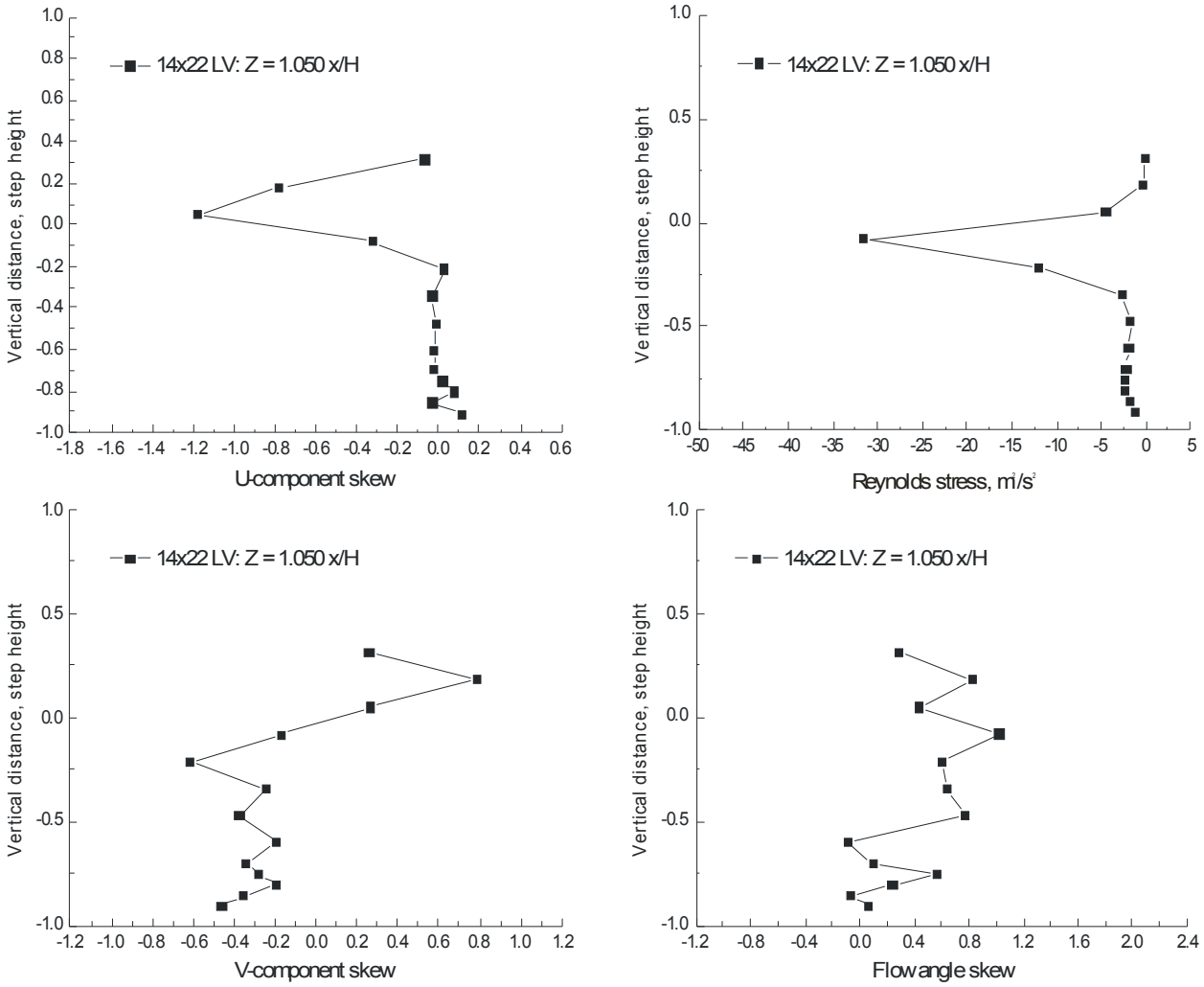

Figure VII.14.e.- Vertical scan 1.050 x/H downstream of a 3.5-inch backward-facing step (compares to Figure VII.8.d): streamwise and vertical velocity skew, flow angle skew and Reynolds stress, fs = 45.0 m/s.

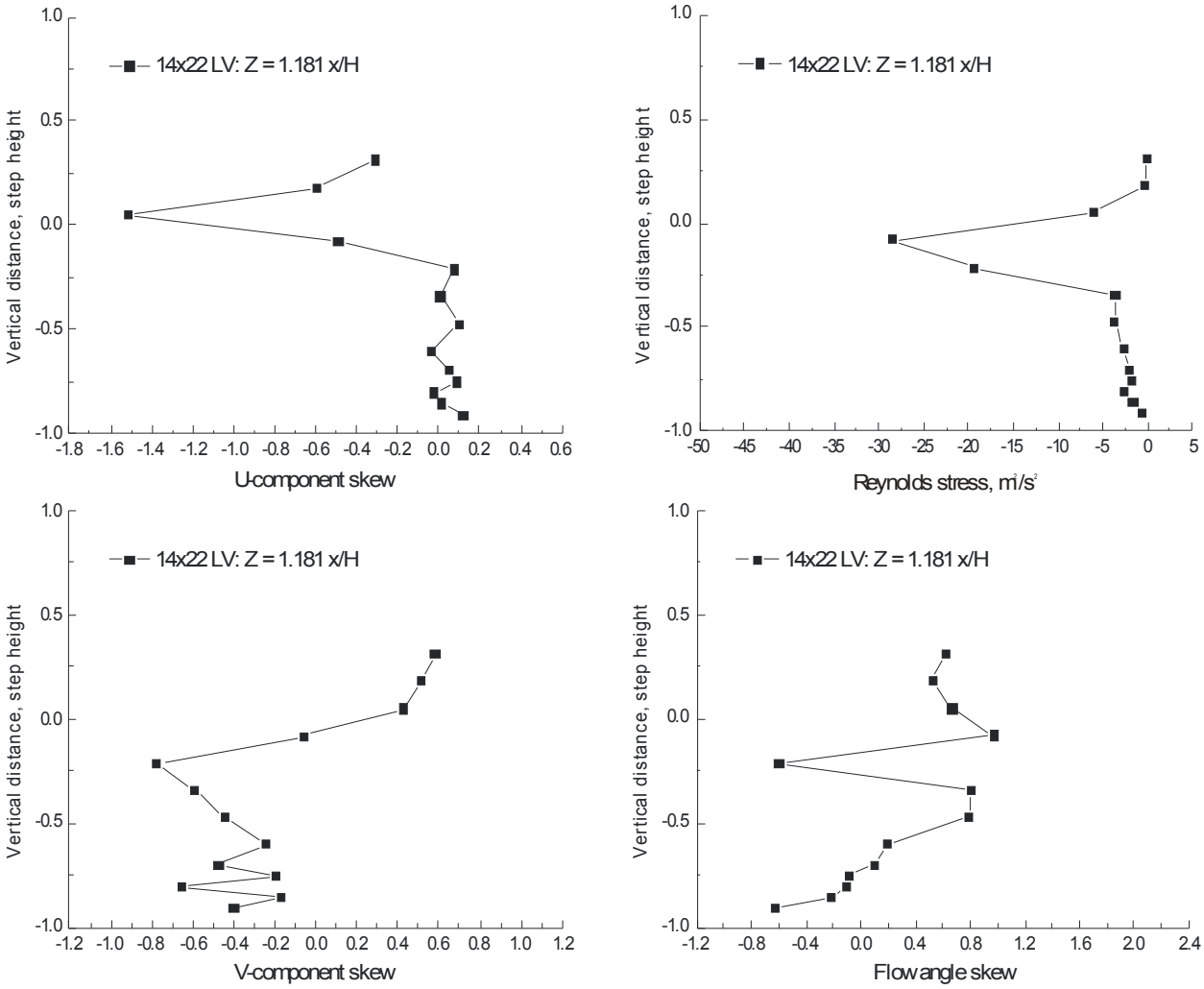

Figure VII.14.f.- Vertical scan 1.181 x/H downstream of a 3.5-inch backward-facing step: streamwise and vertical velocity skew, flow angle skew and Reynolds stress, fs = 45.0 m/s.

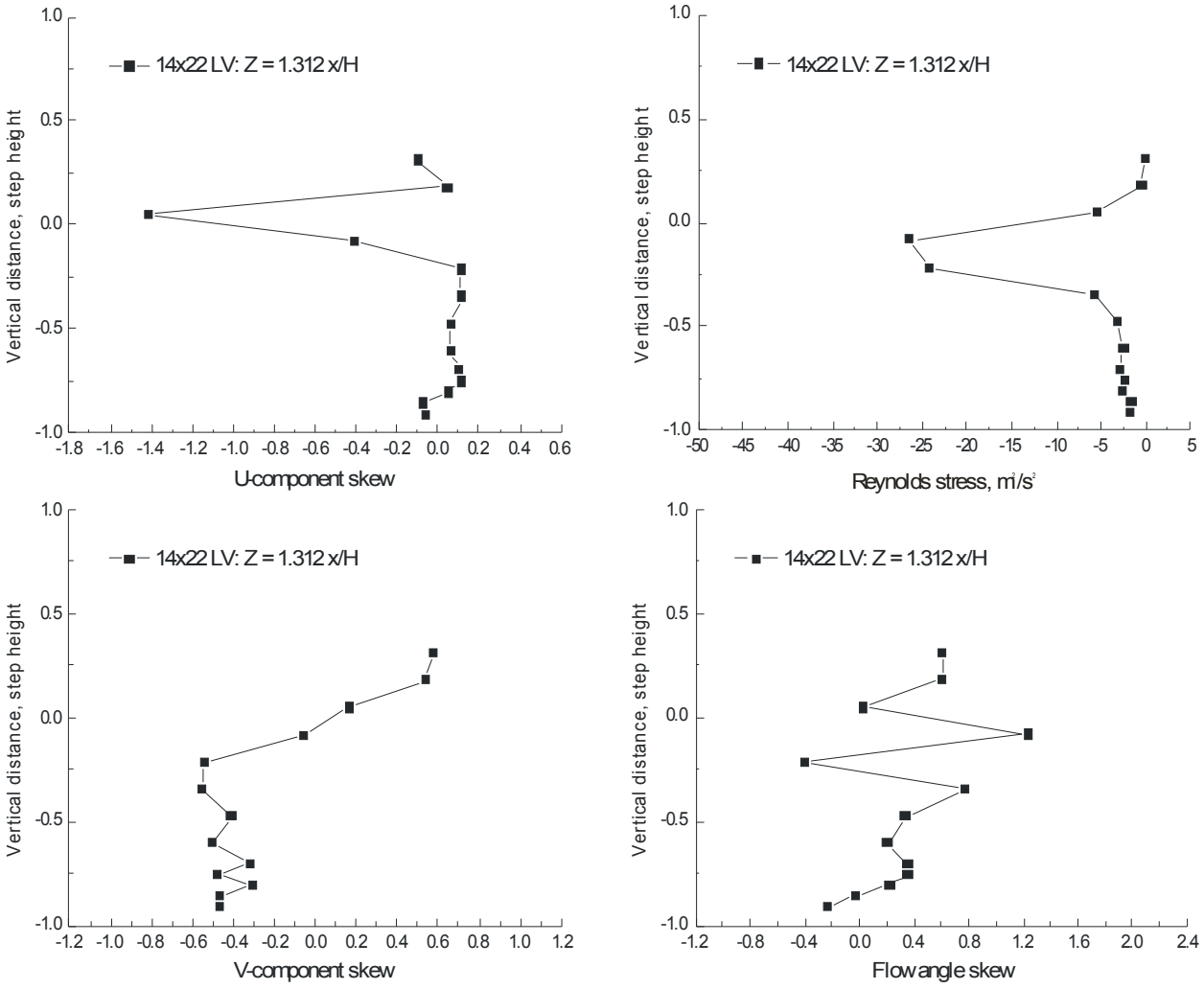

Figure VII.14.g.- Vertical scan 1.312 x/H downstream of a 3.5-inch backward-facing step (compares to Figure VII.8.e): streamwise and vertical velocity skew, flow angle skew and Reynolds stress, fs = 45.0 m/s.

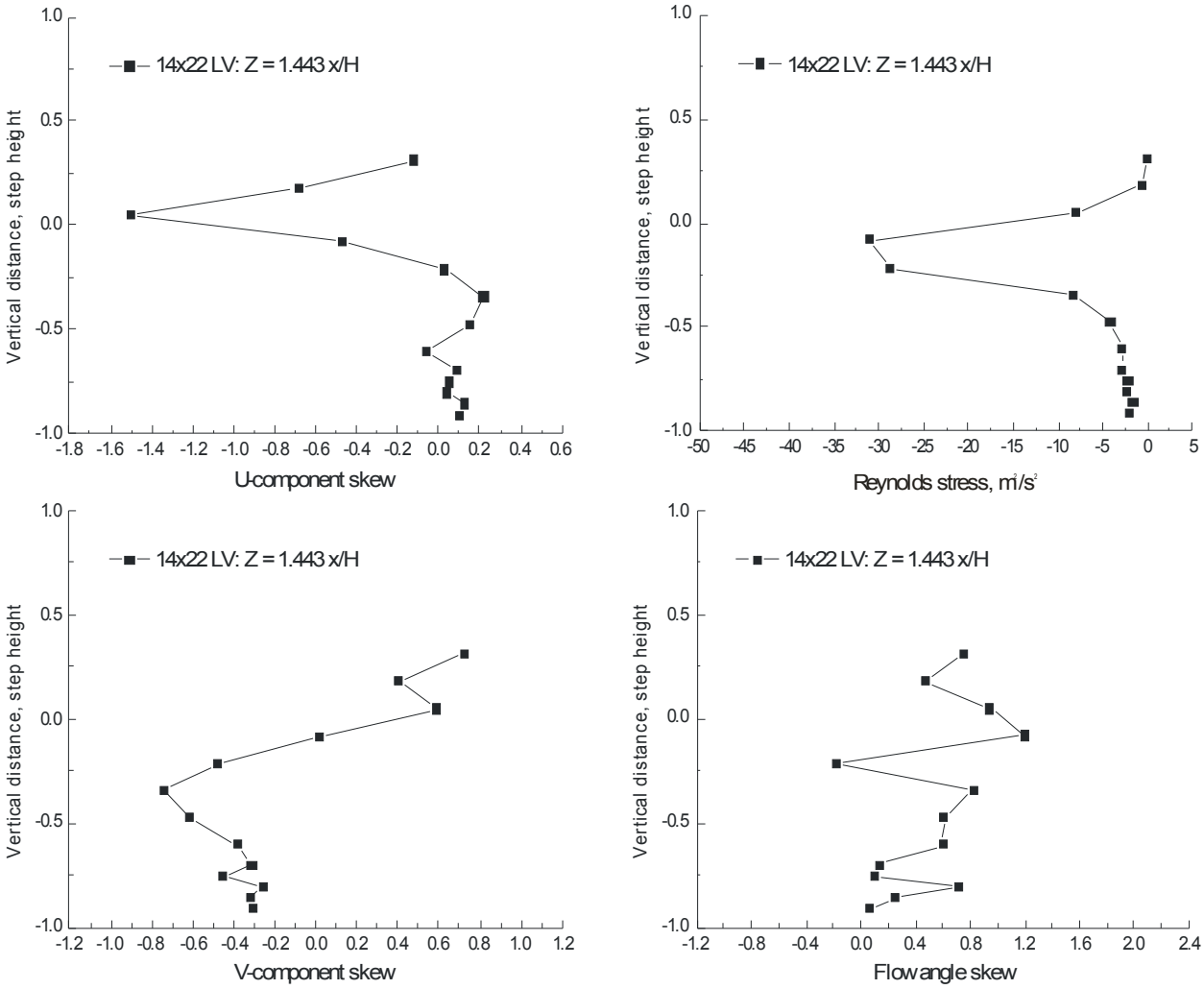

Figure VII.14.h.- Vertical scan 1.443 x/H downstream of a 3.5-inch backward-facing step: streamwise and vertical velocity skew, flow angle skew and Reynolds stress, fs = 45.0 m/s.

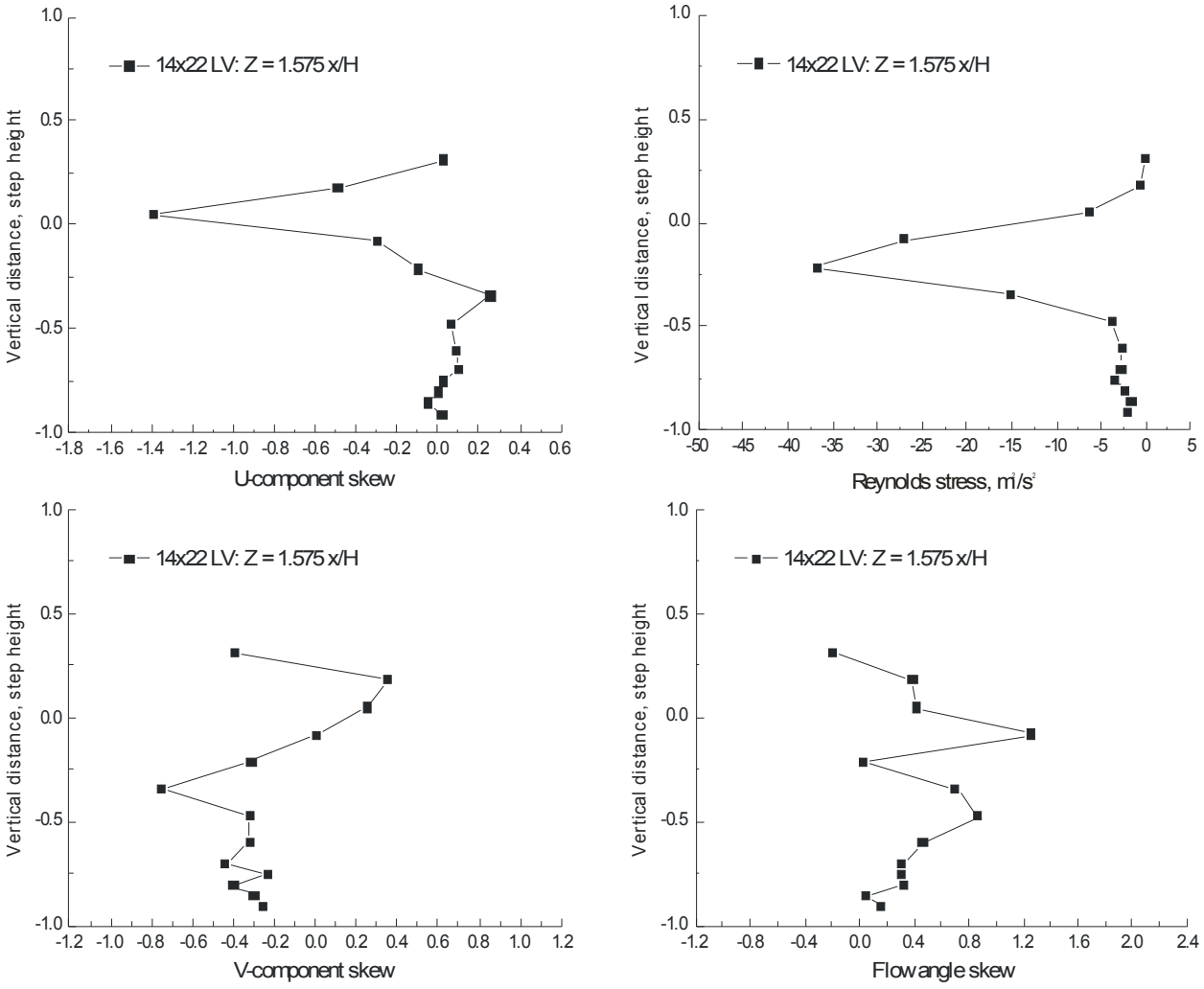

Figure VII.14.i.- Vertical scan 1.575 x/H downstream of a 3.5-inch backward-facing step (compares to Figure VII.8.f): streamwise and vertical velocity skew, flow angle skew and Reynolds stress, fs = 45.0 m/s.

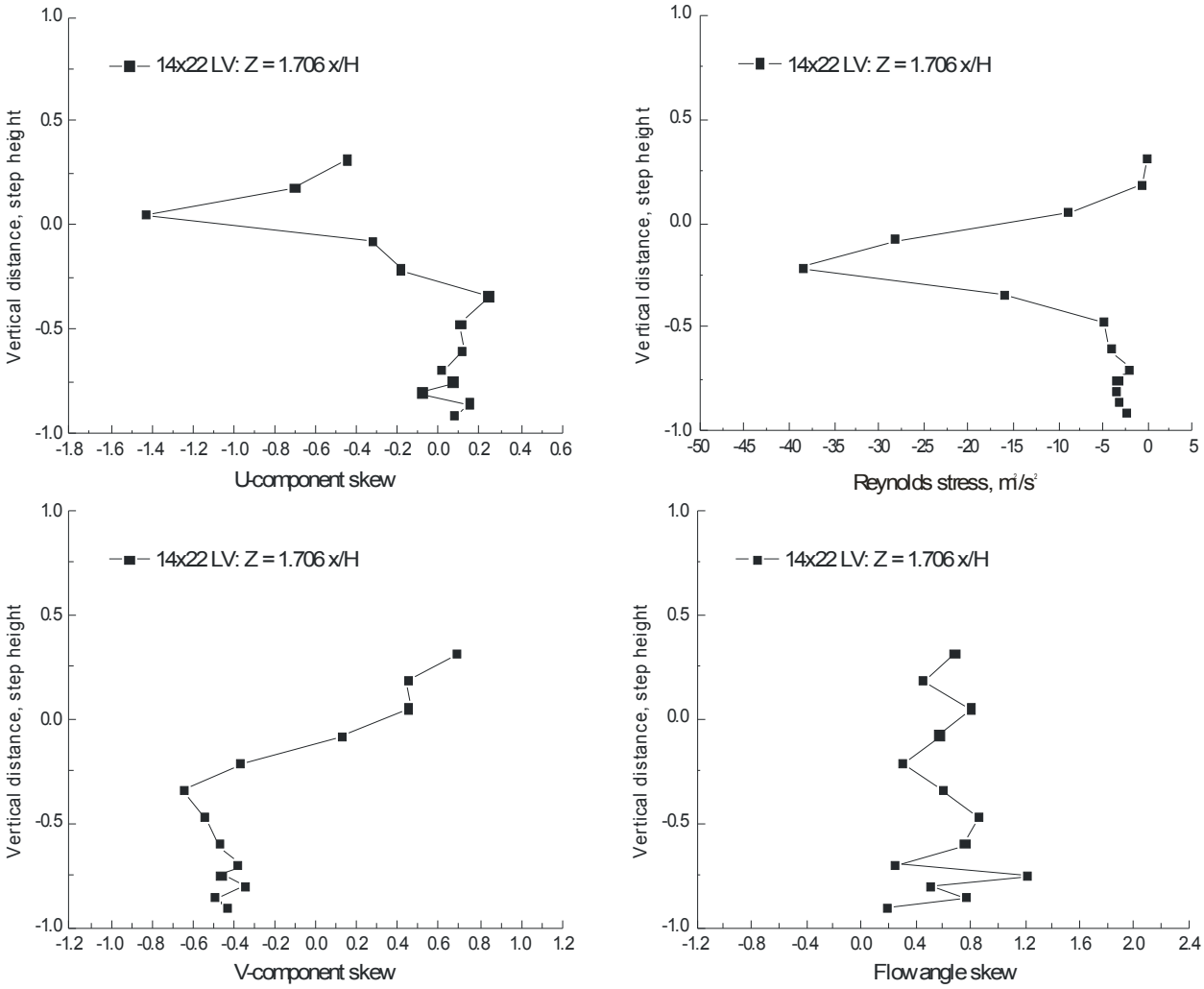

Figure VII.14.j.- Vertical scan 1.706 x/H downstream of a 3.5-inch backward-facing step: streamwise and vertical velocity skew, flow angle skew and Reynolds stress, fs = 45.0 m/s.

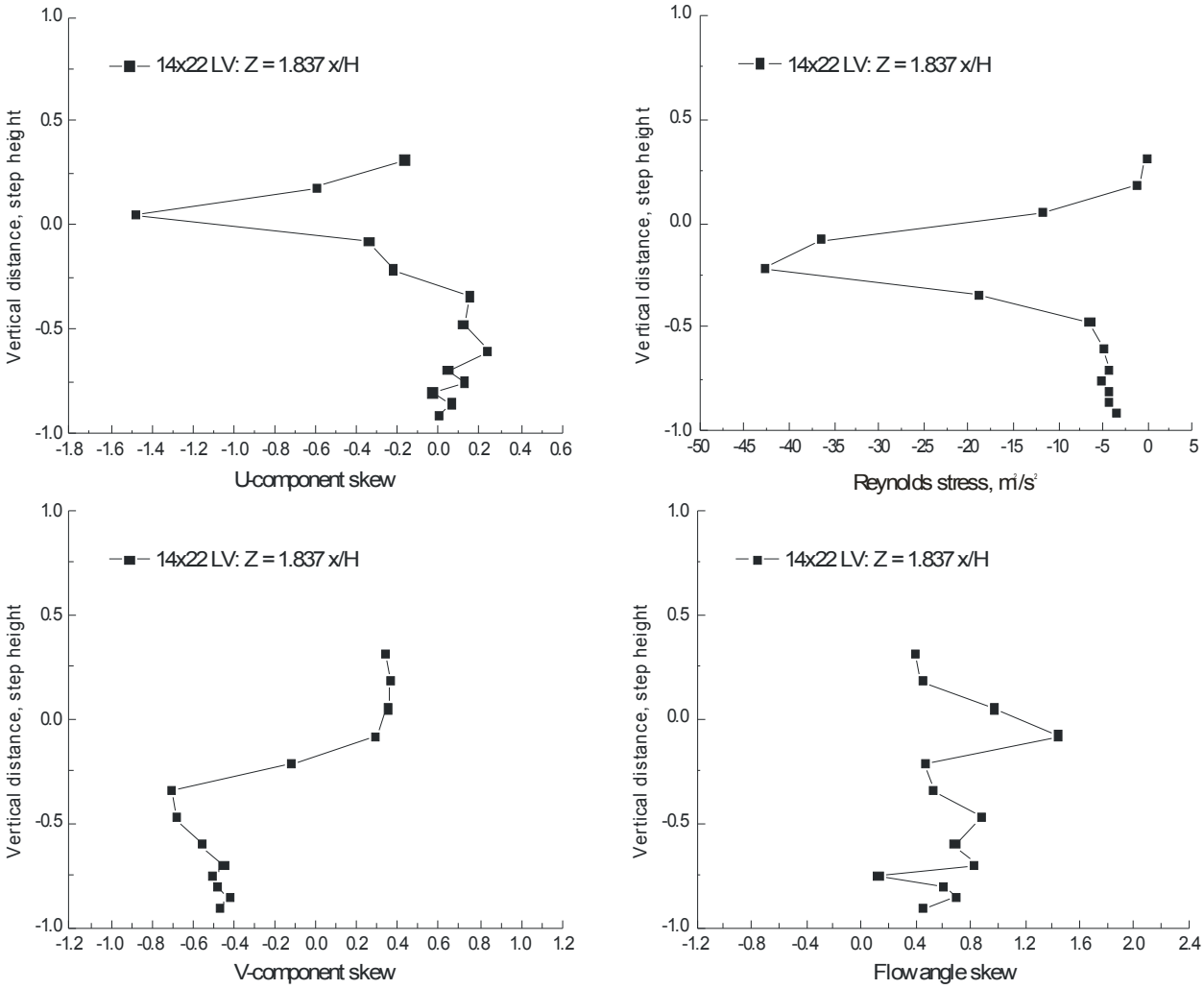

Figure VII.14.k.- Vertical scan 1.837 x/H downstream of a 3.5-inch backward-facing step (compares to Figure VII.8.g): streamwise and vertical velocity skew, flow angle skew and Reynolds stress, fs = 45.0 m/s.

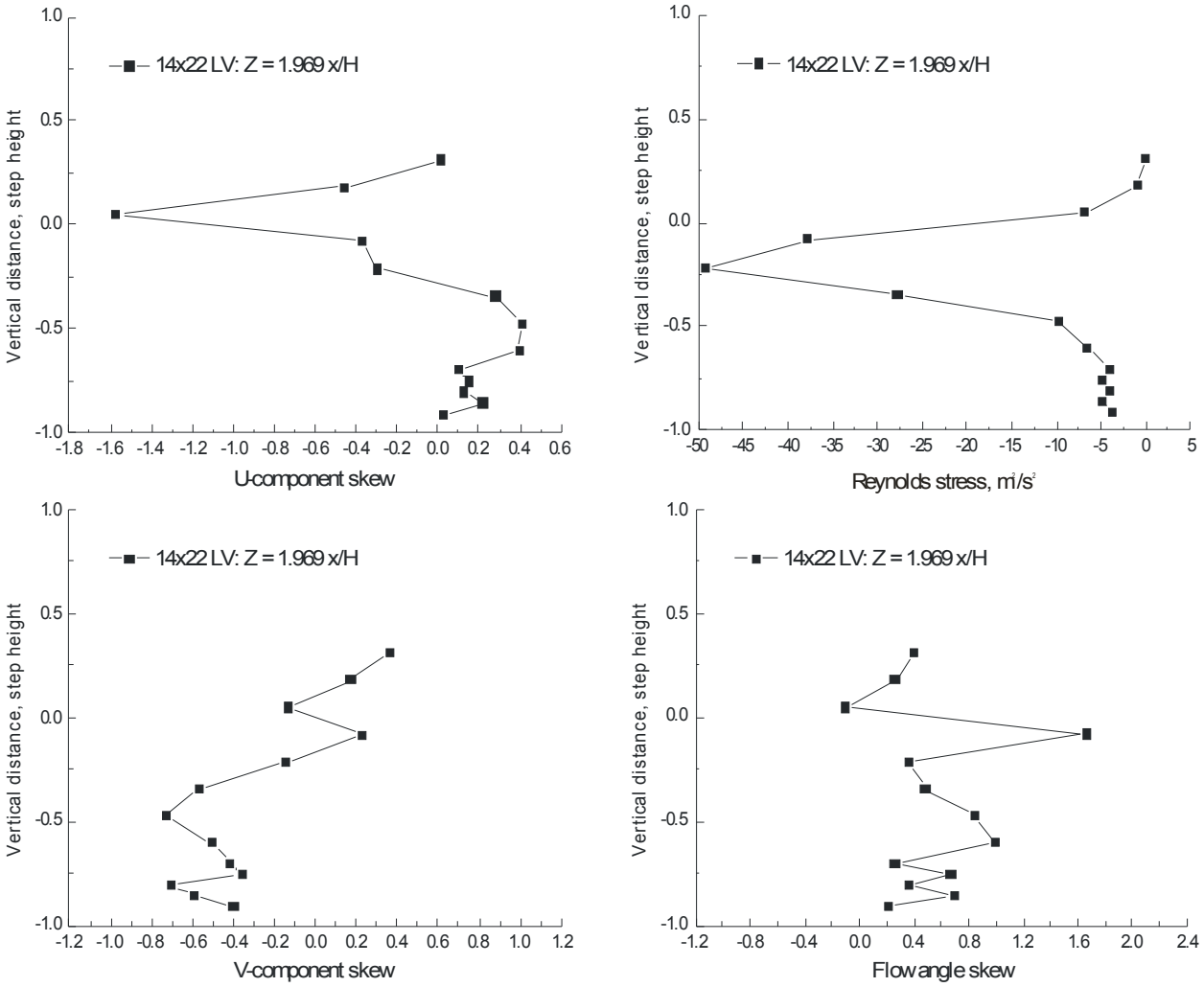

Figure VII.14.l.- Vertical scan 1.969 x/H downstream of a 3.5-inch backward-facing step: streamwise and vertical velocity skew, flow angle skew and Reynolds stress, fs = 45.0 m/s.

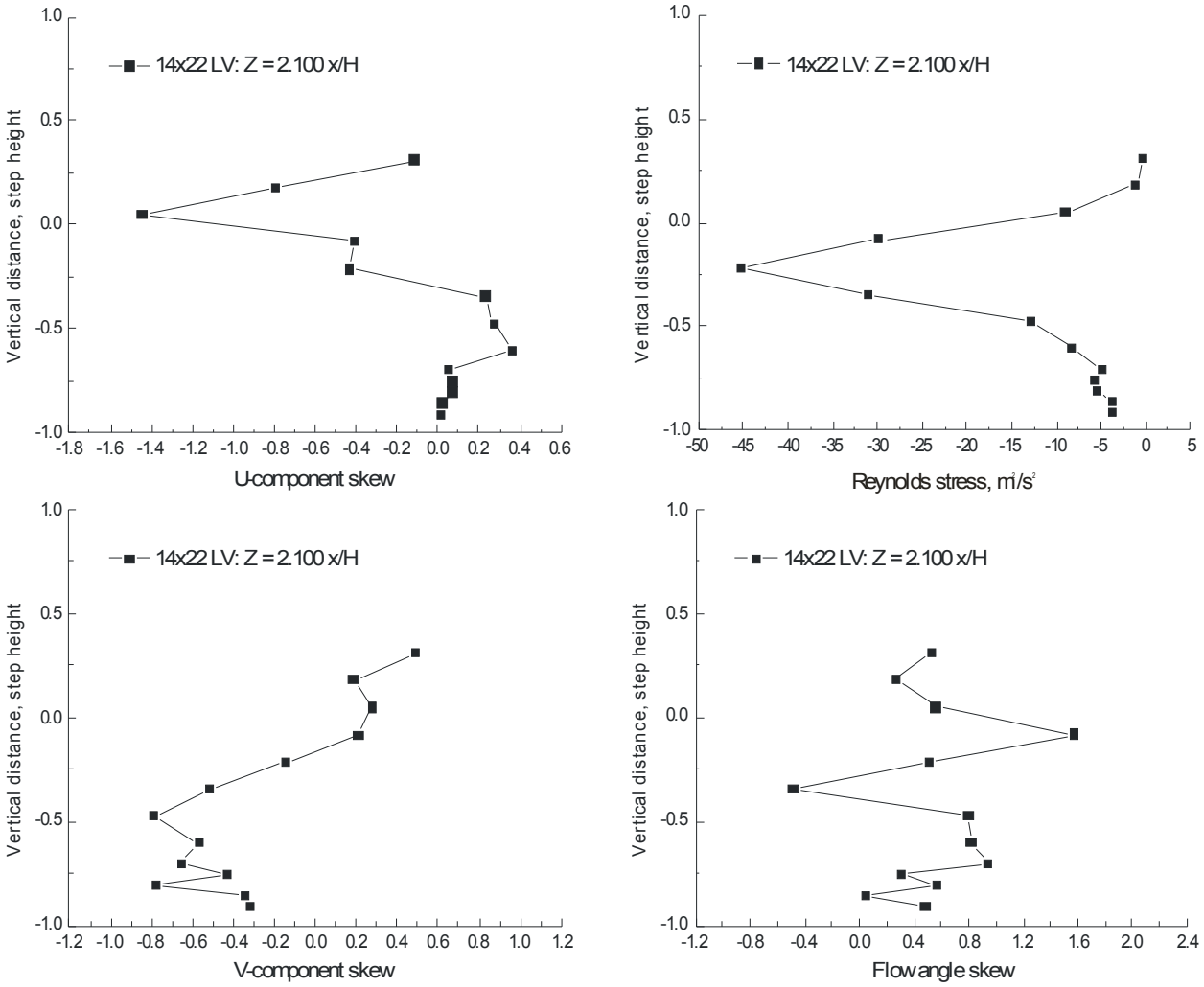

Figure VII.14.m.- Vertical scan 2.1 x/H downstream of a 3.5-inch backward-facing step (compares to Figure VII.8.h): streamwise and vertical velocity skew, flow angle skew and Reynolds stress, fs = 45.0 m/s.

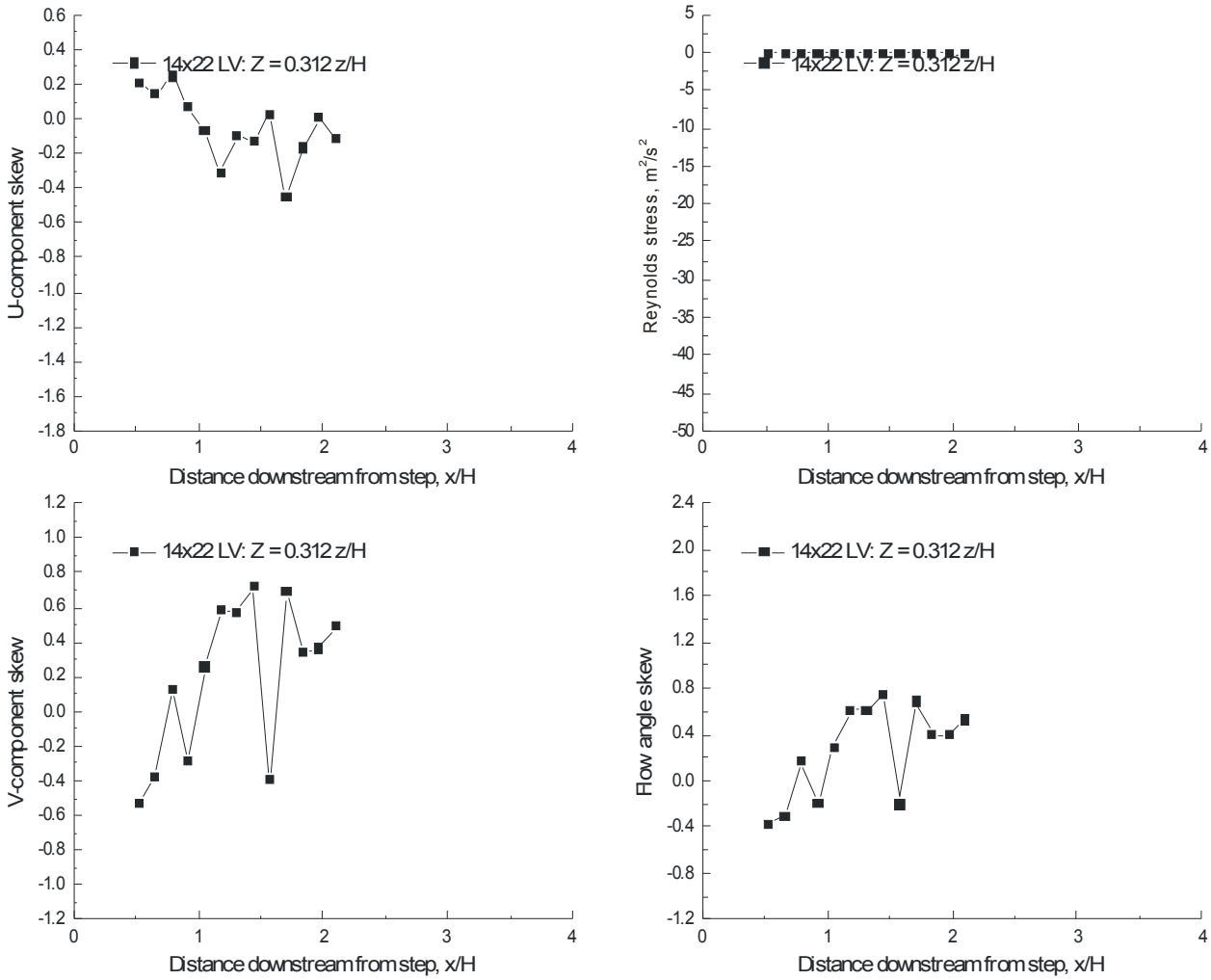

Figure VII.15.a.- Horizontal scan 0.312 z/H above a 3.5-inch backward-facing step (compares to Figure VII.9.b): streamwise and vertical velocity skew, flow angle skew and Reynolds stress, fs = 45.0 m/s.

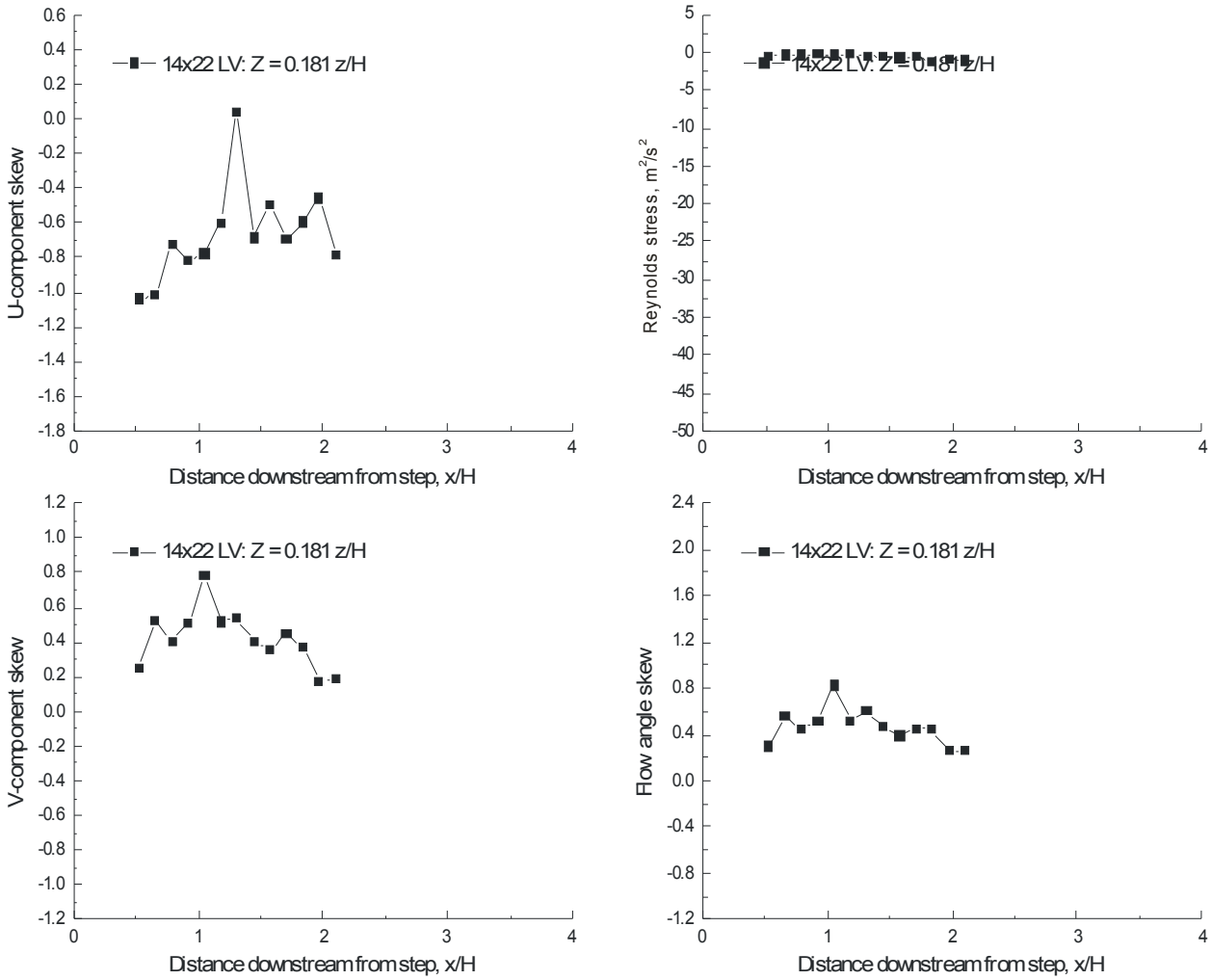

Figure VII.15.b.- Horizontal scan 0.181 z/H above a 3.5-inch backward-facing step (compares to Figure VII.9.c): streamwise and vertical velocity skew, flow angle skew and Reynolds stress, fs = 45.0 m/s.

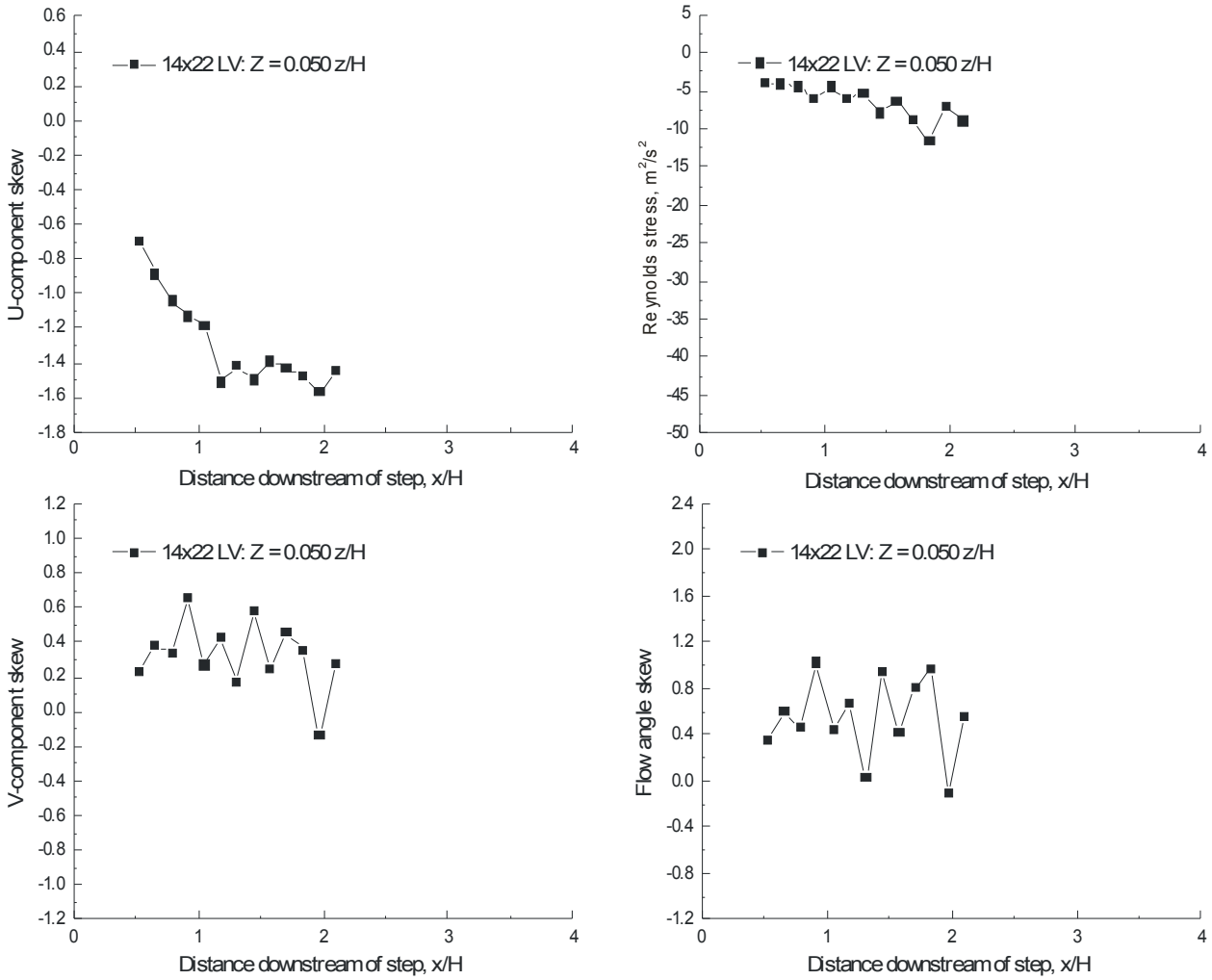

Figure VII.15.c.- Horizontal scan 0.050 z/H above a 3.5-inch backward-facing step (compares to Figure VII.9.d): streamwise and vertical velocity skew, flow angle skew and Reynolds stress, fs = 45.0 m/s.

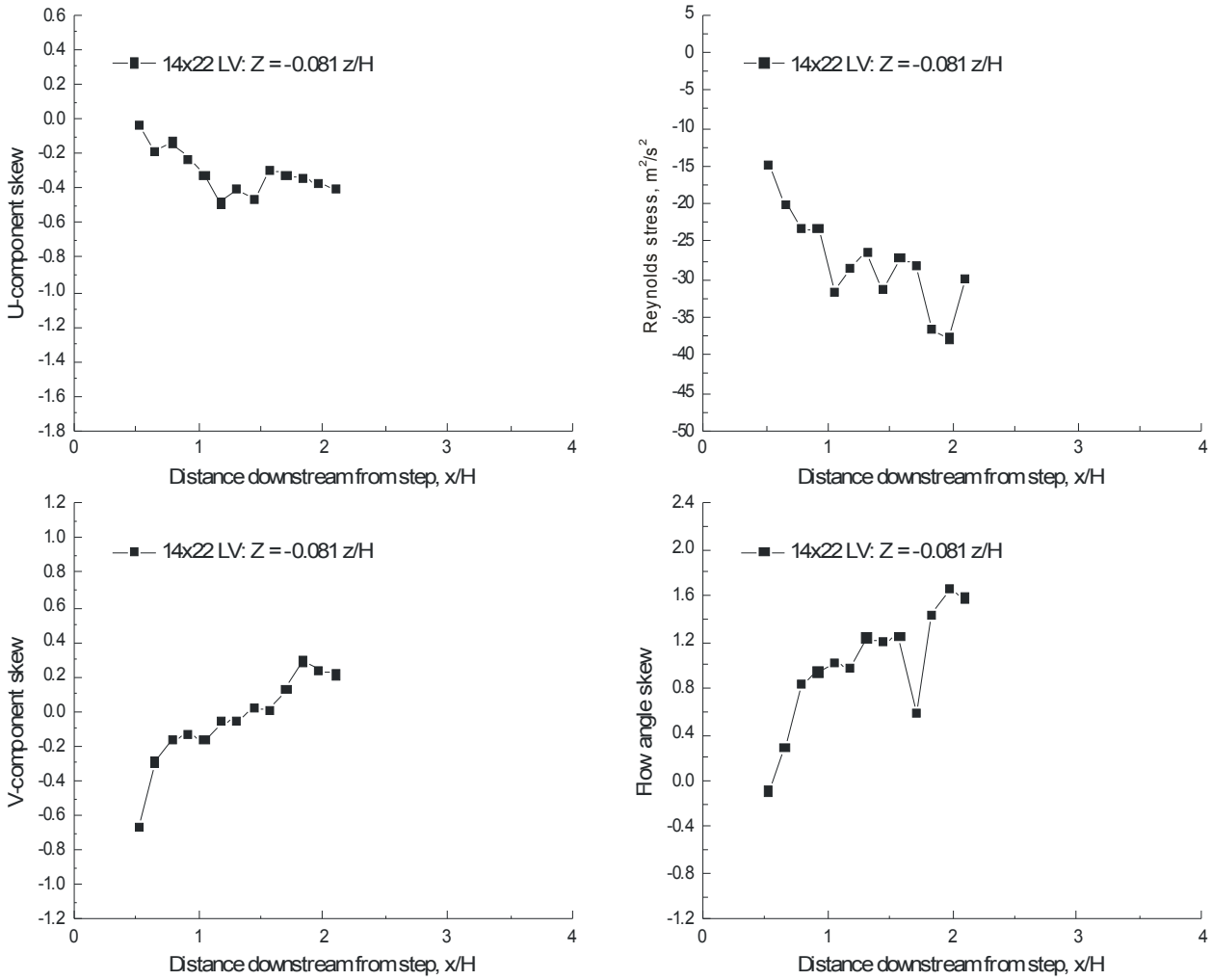

Figure VII.15.d.- Horizontal scan 0.081 z/H below a 3.5-inch backward-facing step (compares to Figure VII.9.e): streamwise and vertical velocity skew, flow angle skew and Reynolds stress, fs = 45.0 m/s.

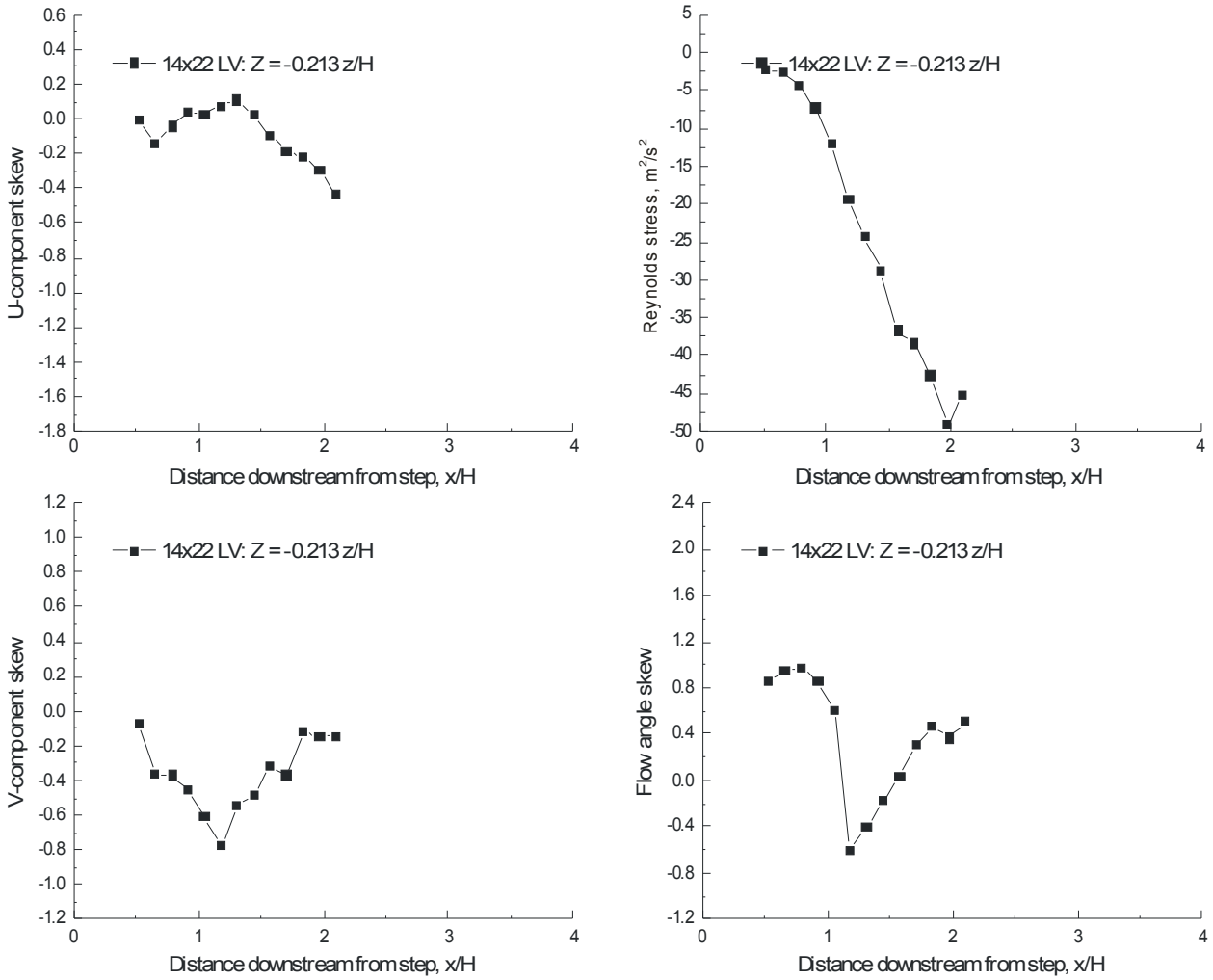

Figure VII.15.e.- Horizontal scan 0.213 z/H below a 3.5-inch backward-facing step (compares to Figure VII.9.f): streamwise and vertical velocity skew, flow angle skew and Reynolds stress, fs = 45.0 m/s.

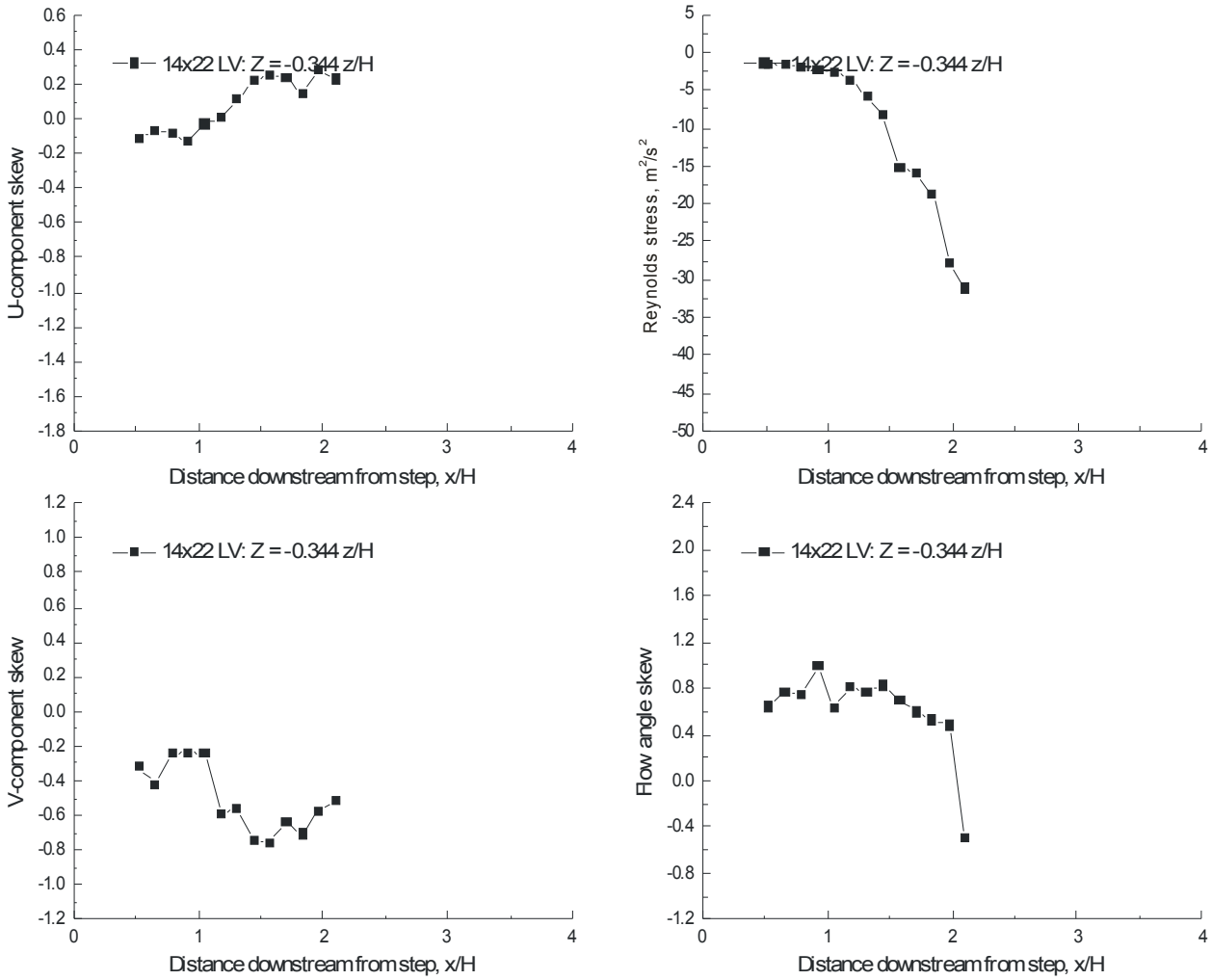

Figure VII.15.f.- Horizontal scan 0.344 z/H below a 3.5-inch backward-facing step (compares to Figure VII.9.g): streamwise and vertical velocity skew, flow angle skew and Reynolds stress, fs = 45.0 m/s.

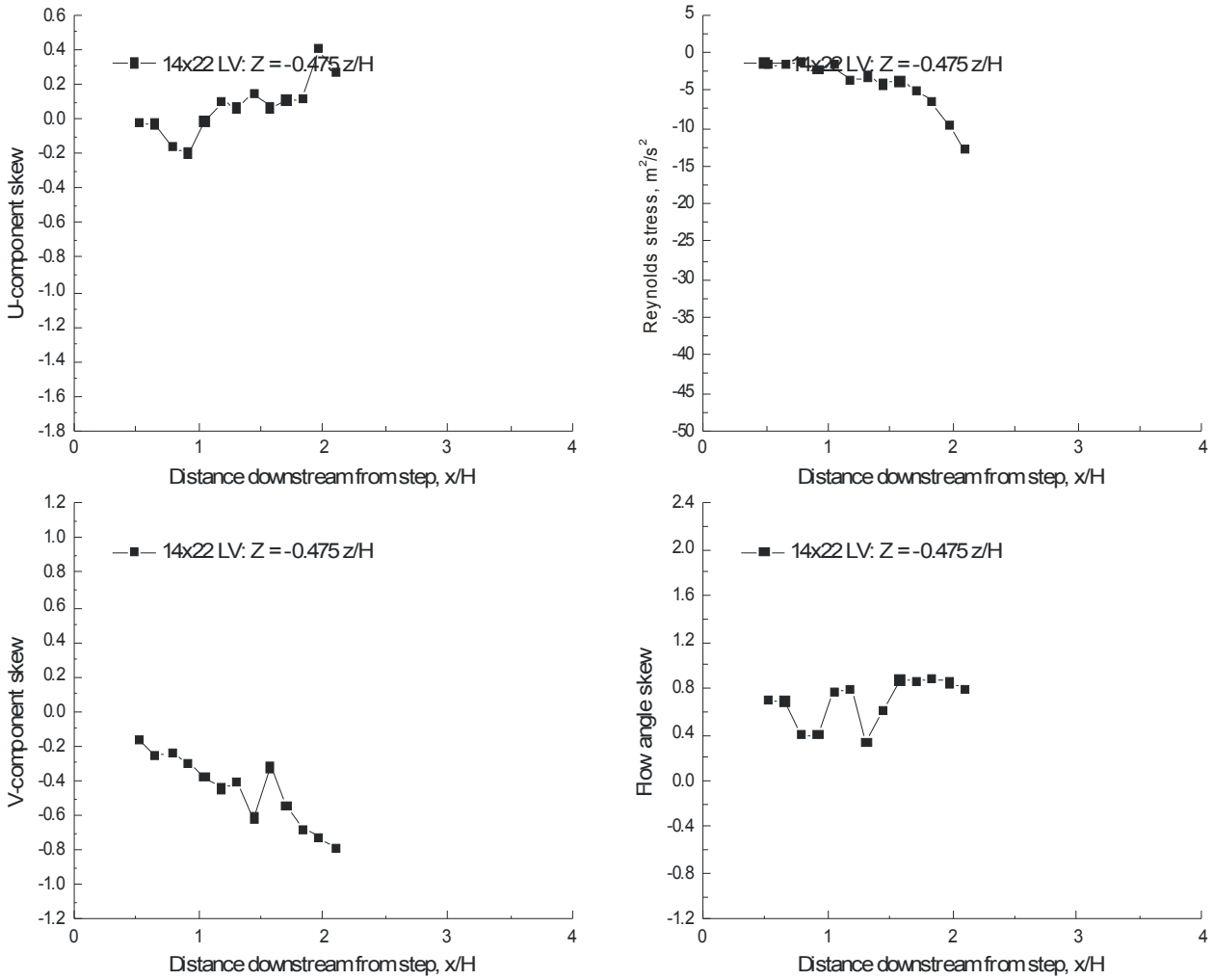

Figure VII.15.g.- Horizontal scan 0.475 z/H below a 3.5-inch backward-facing step (compares to Figure VII.9.h): streamwise and vertical velocity skew, flow angle skew and Reynolds stress, fs = 45.0 m/s.

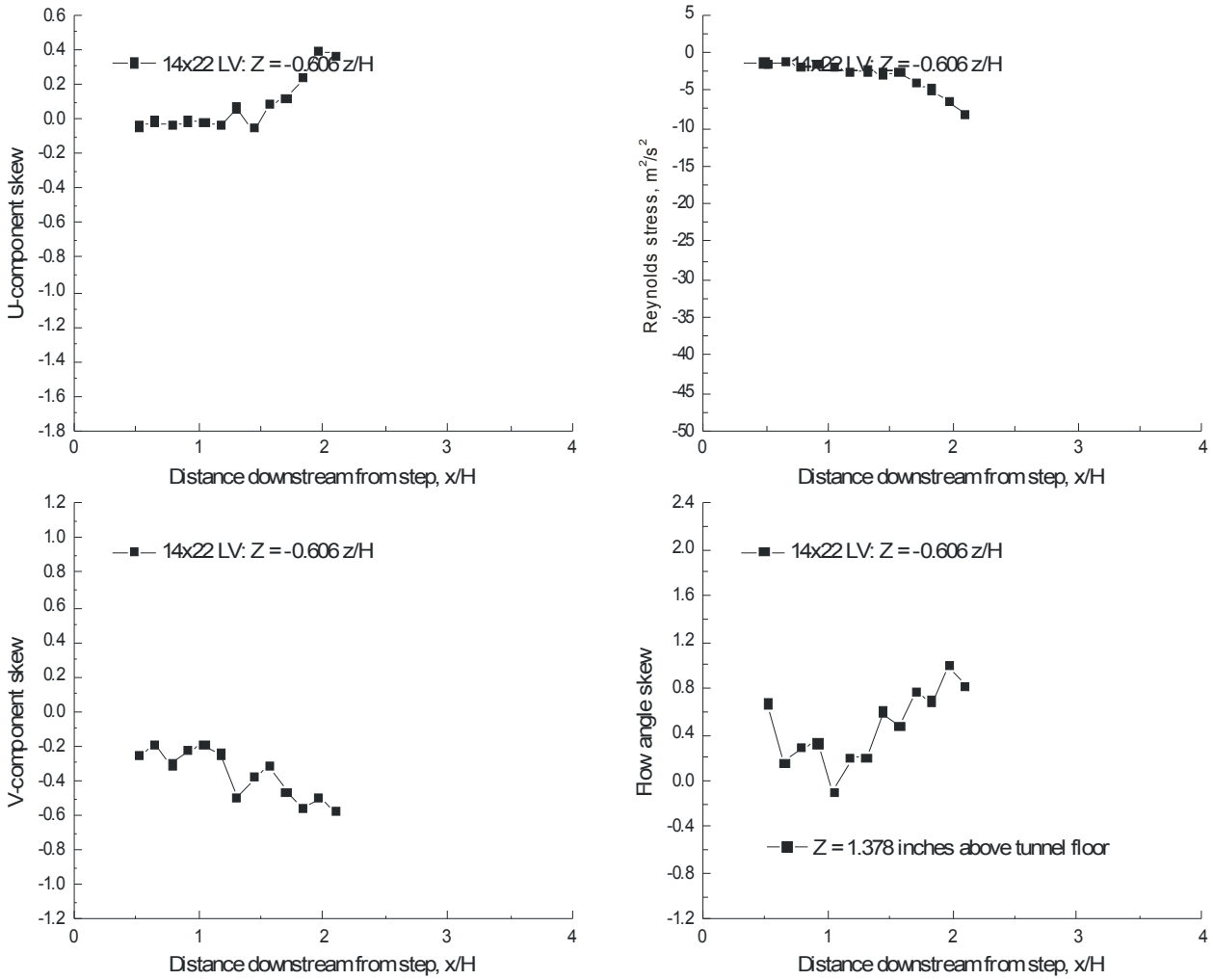

Figure VII.15.h.- Horizontal scan 0.606 z/H below a 3.5-inch backward-facing step (compares to Figure VII.9.i): streamwise and vertical velocity skew, flow angle skew and Reynolds stress, fs = 45.0 m/s.

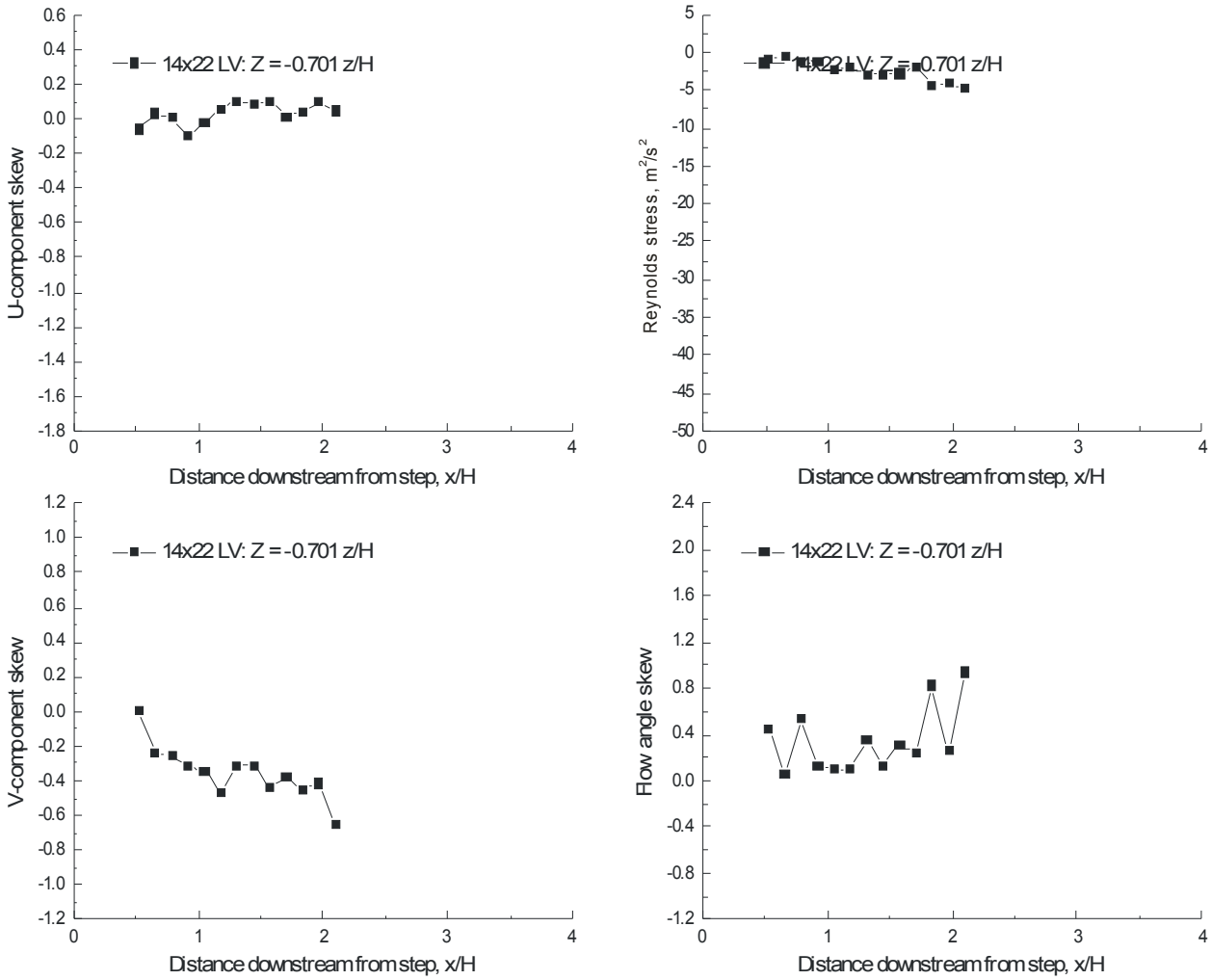

Figure VII.15.i.- Horizontal scan 0.701 z/H below a 3.5-inch backward-facing step (compares to Figure VII.9.j): streamwise and vertical velocity skew, flow angle skew and Reynolds stress, fs = 45.0 m/s.

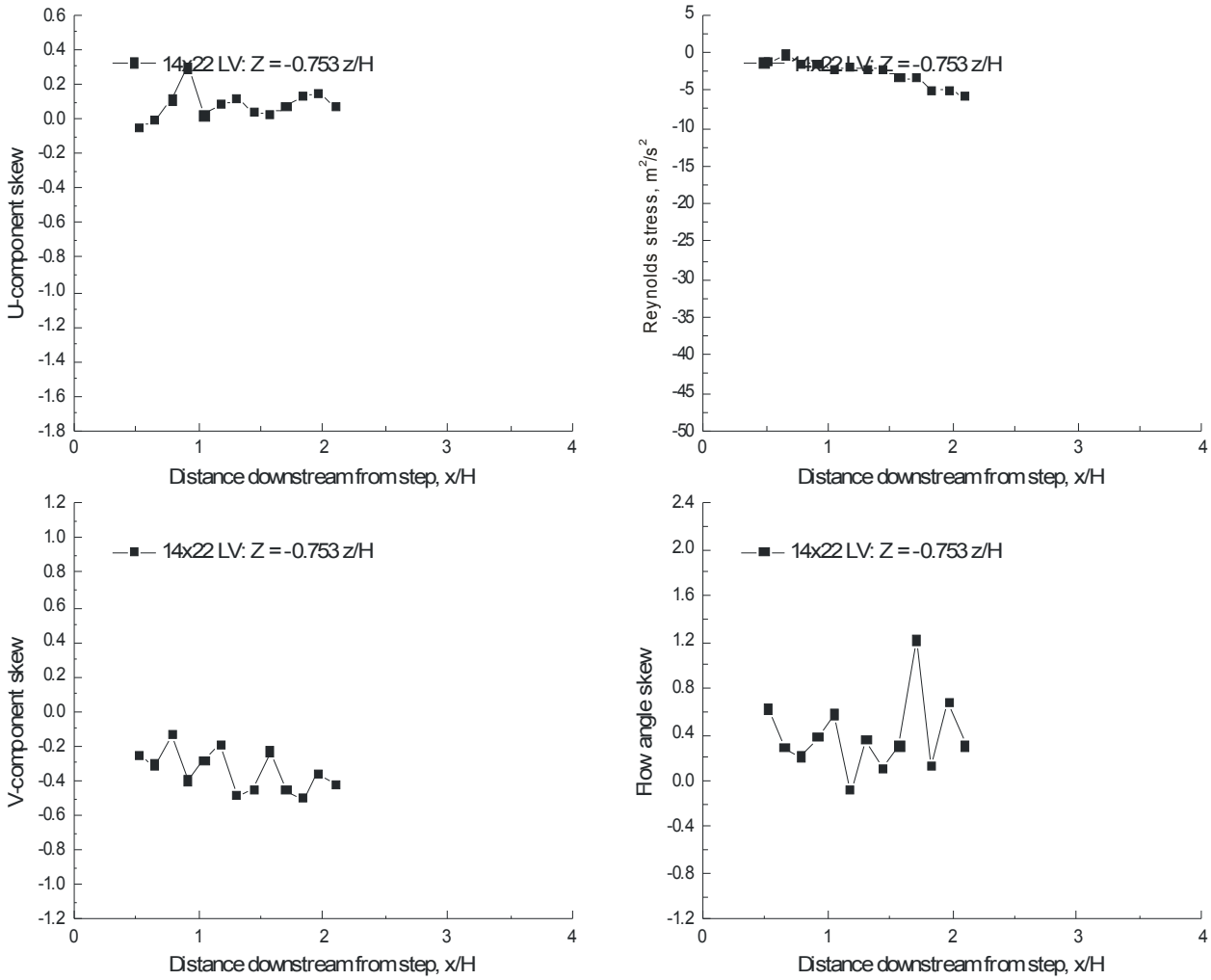

Figure VII.15.j.- Horizontal scan 0.753 z/H below a 3.5-inch backward-facing step (compares to Figure VII.9.k): streamwise and vertical velocity skew, flow angle skew and Reynolds stress, fs = 45.0 m/s.

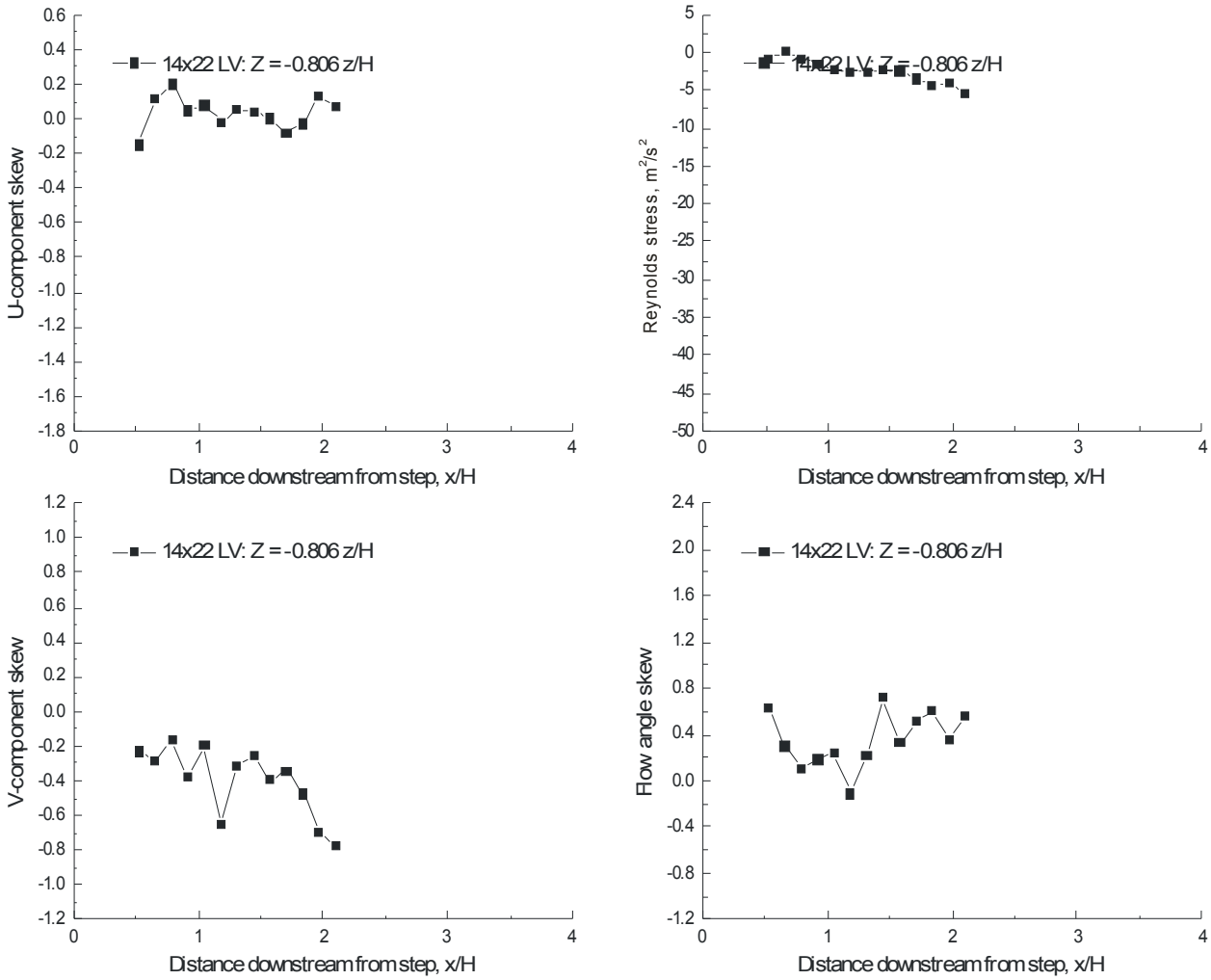

Figure VII.15.k.- Horizontal scan 0.806 z/H below a 3.5-inch backward-facing step (compares to Figure VII.9.l): streamwise and vertical velocity skew, flow angle skew and Reynolds stress, fs = 45.0 m/s.

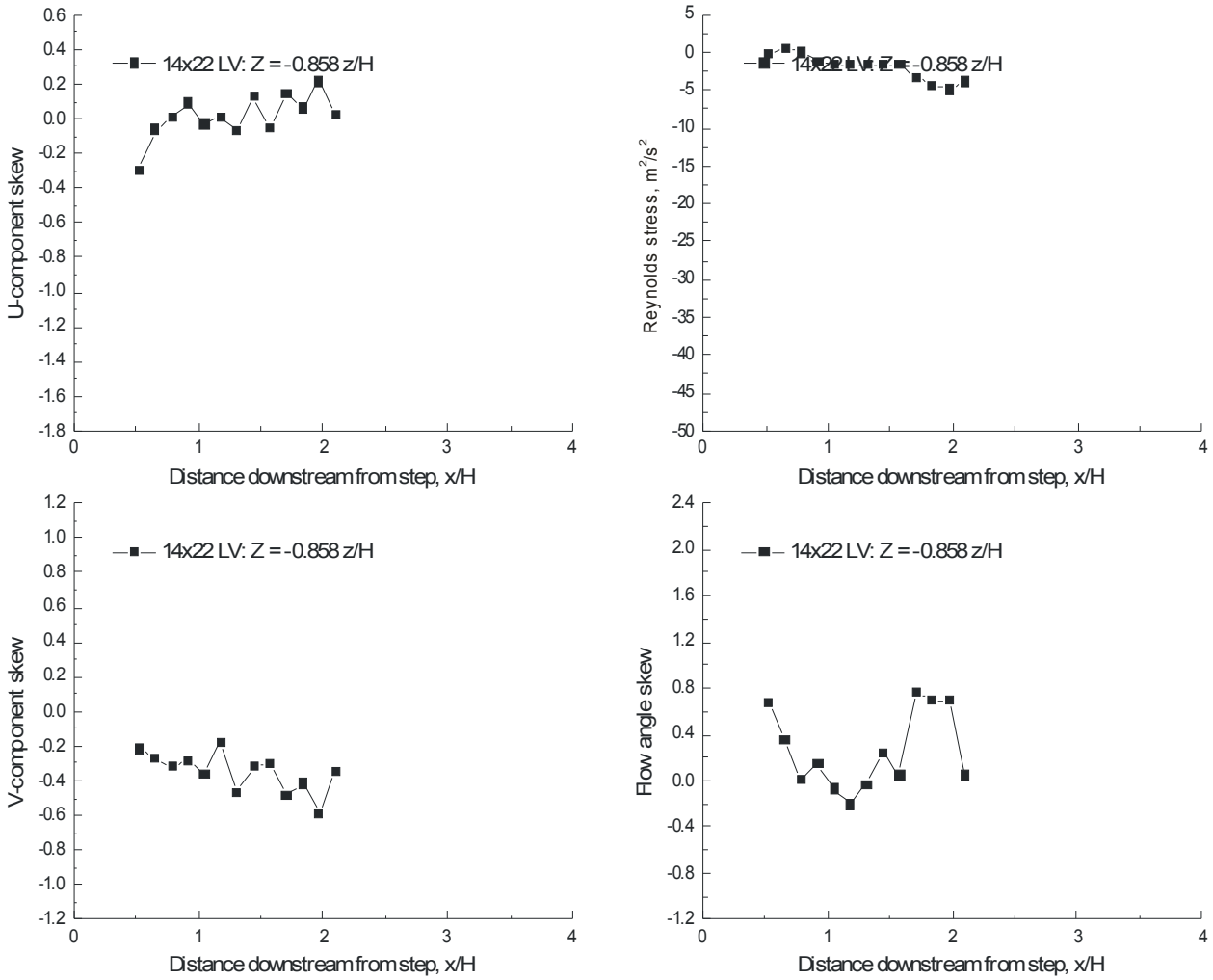

Figure VII.15.l.- Horizontal scan 0.858 z/H below a 3.5-inch backward-facing step (compares to Figure VII.9.m): streamwise and vertical velocity skew, flow angle skew and Reynolds stress, fs = 45.0 m/s.

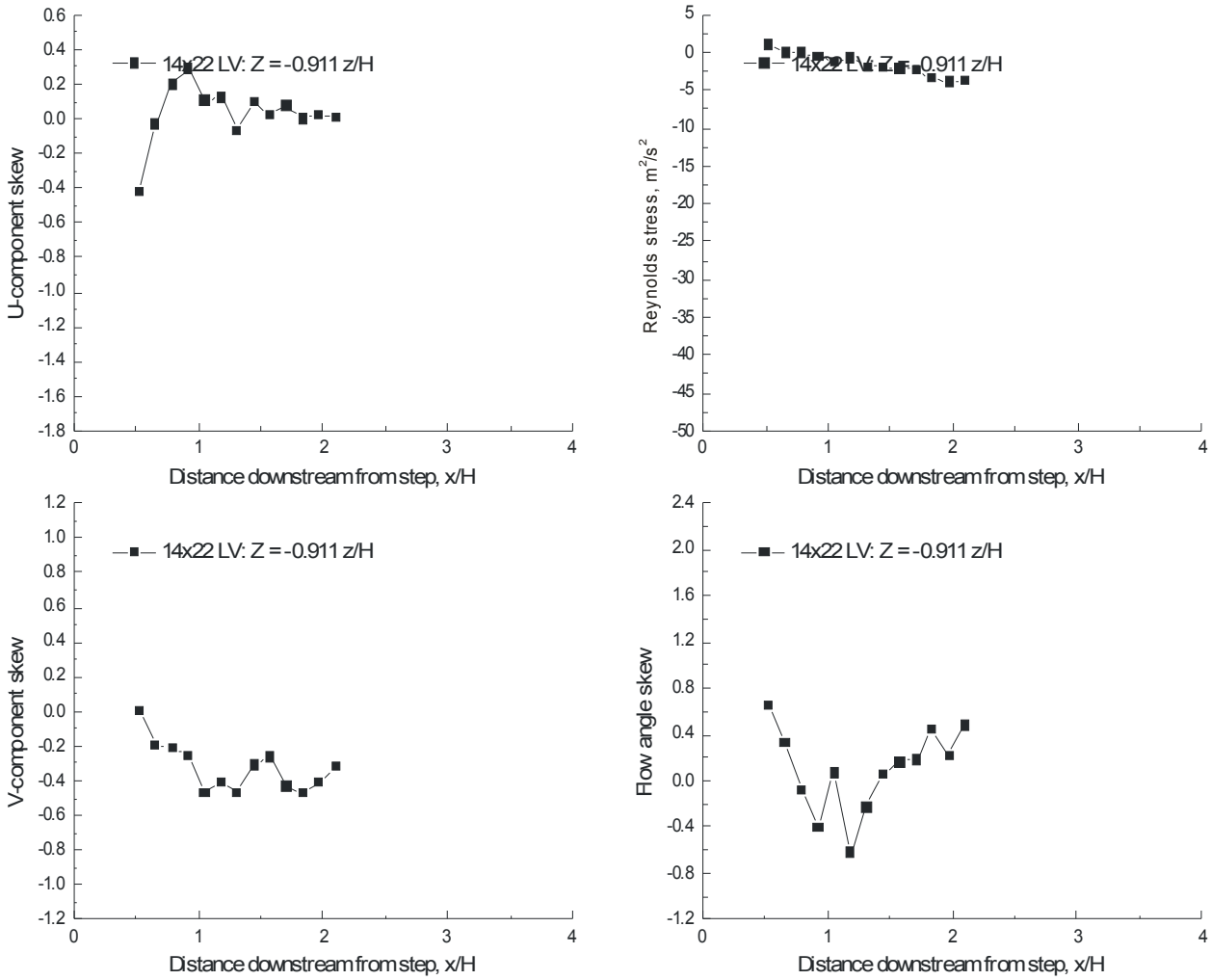

Figure VII.15.m.- Horizontal scan 0.911 z/H below a 3.5-inch backward-facing step (compares to Figure VII.9.n): streamwise and vertical velocity skew, flow angle skew and Reynolds stress, fs = 45.0 m/s.

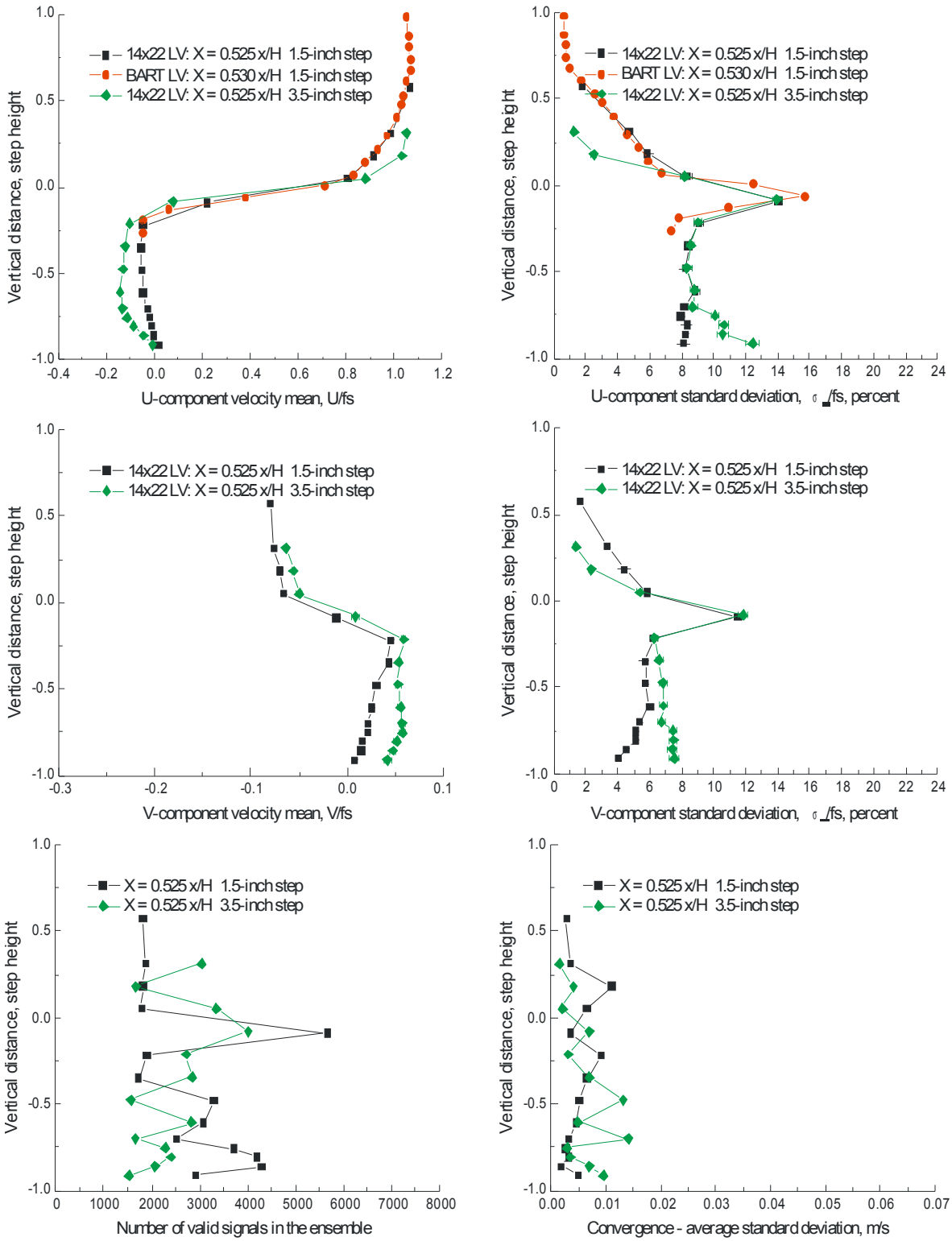

Figure VII.16.a.- Vertical scan 0.525-step heights downstream of the 1.5- and 3.5-inch backward-facing steps: streamwise and vertical velocity components, number of accepted signal bursts, and statistical stationarity convergence standard deviation.

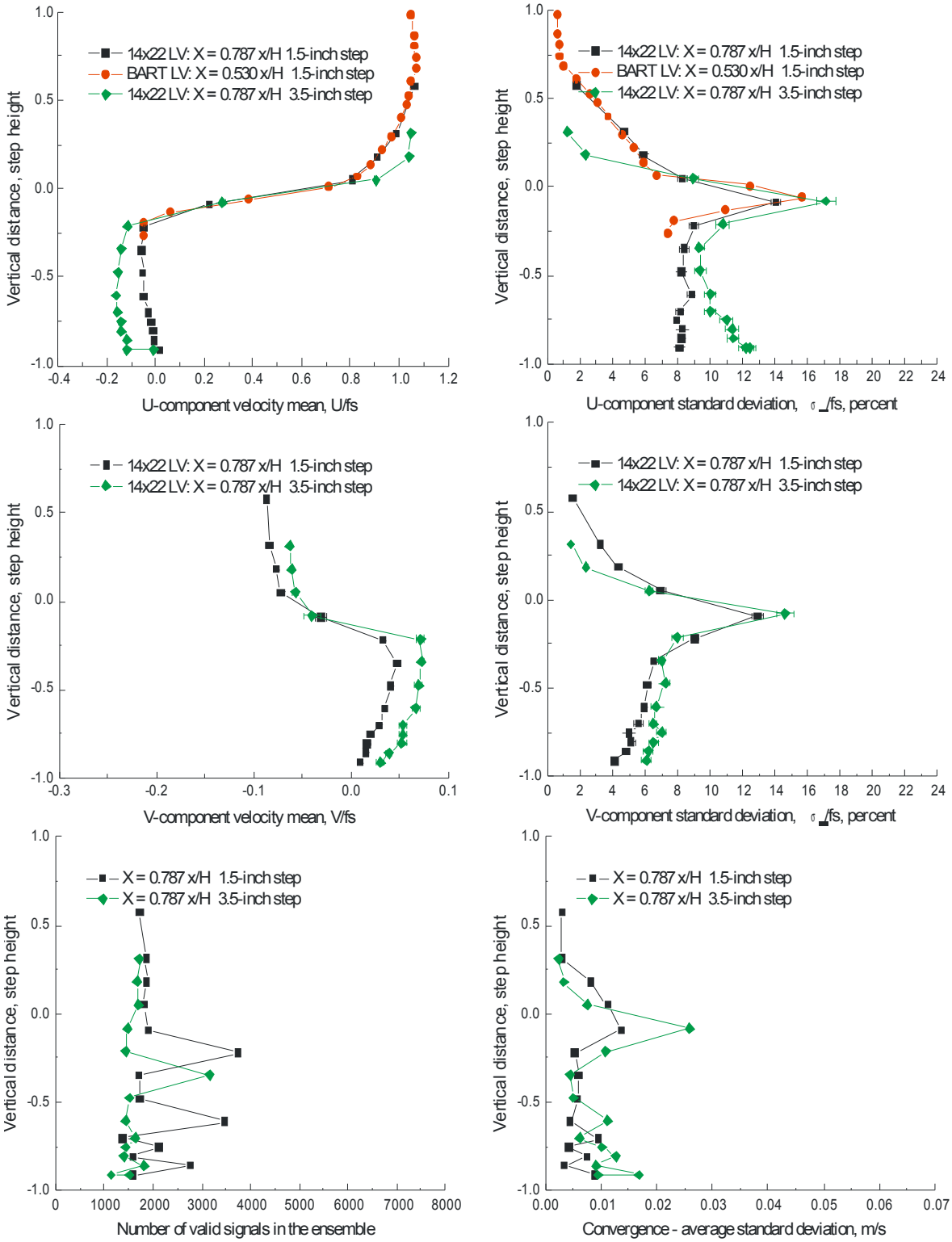

Figure VII.16.b.- Vertical scan 0.787-step heights downstream of the 1.5- and 3.5-inch backward-facing steps: streamwise and vertical velocity components, number of accepted signal bursts, and statistical stationarity convergence standard deviation.

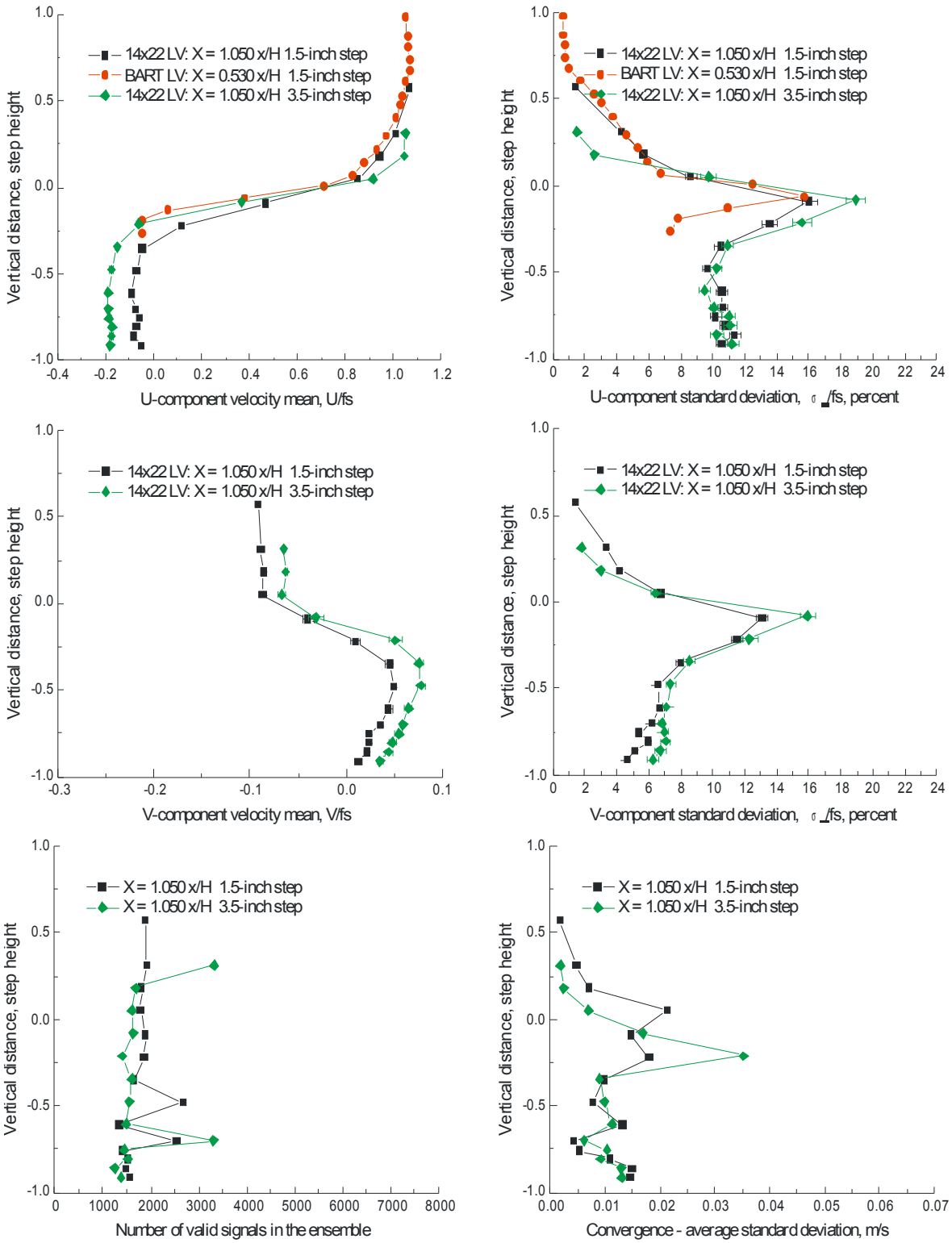

Figure VII.16.c.- Vertical scan 1.050-step heights downstream of the 1.5- and 3.5-inch backward-facing steps: streamwise and vertical velocity components, number of accepted signal bursts, and statistical stationarity convergence standard deviation.

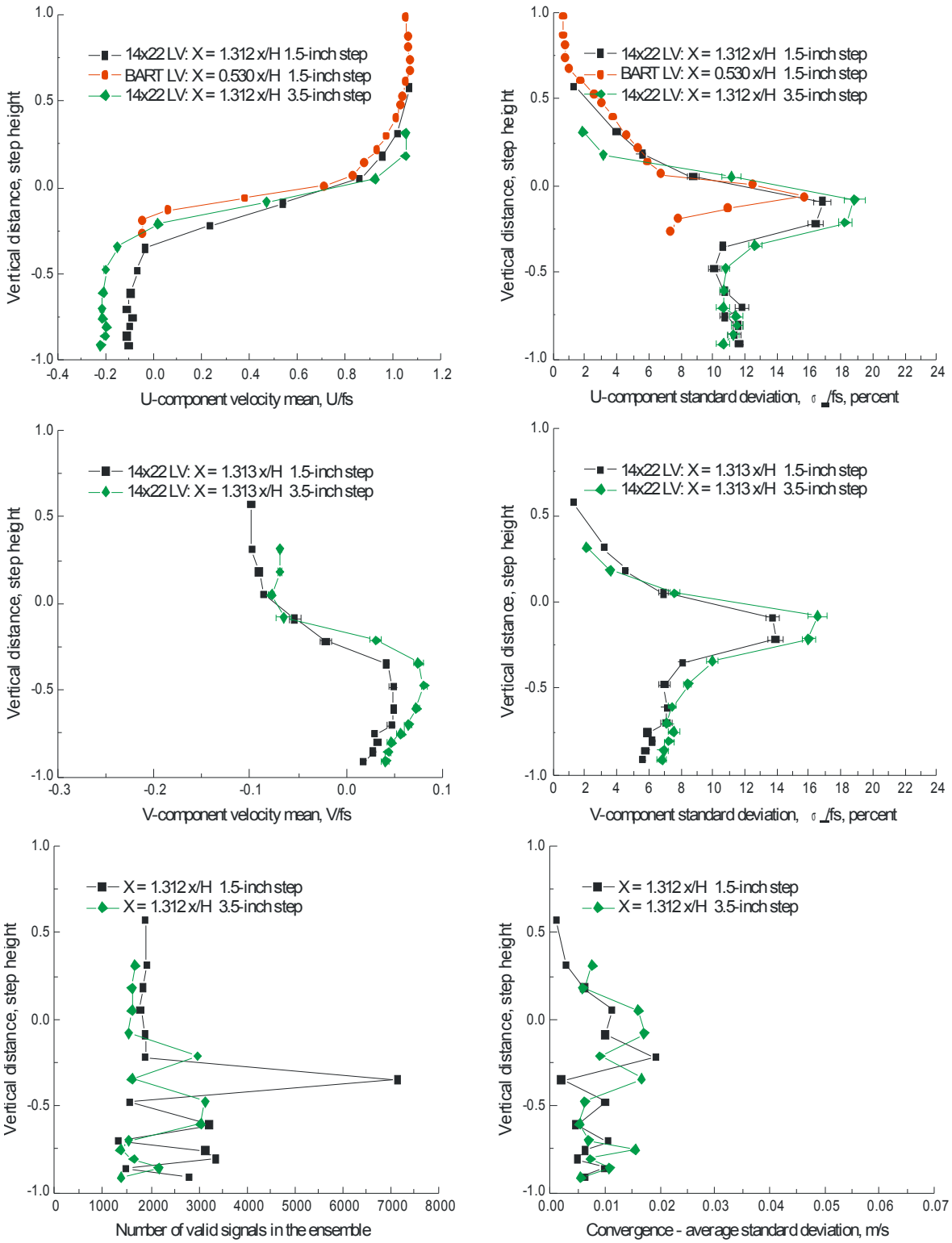

Figure VII.16.d.- Vertical scan 1.312-step heights downstream of the 1.5- and 3.5-inch backward-facing steps: streamwise and vertical velocity components, number of accepted signal bursts, and statistical stationarity convergence standard deviation.

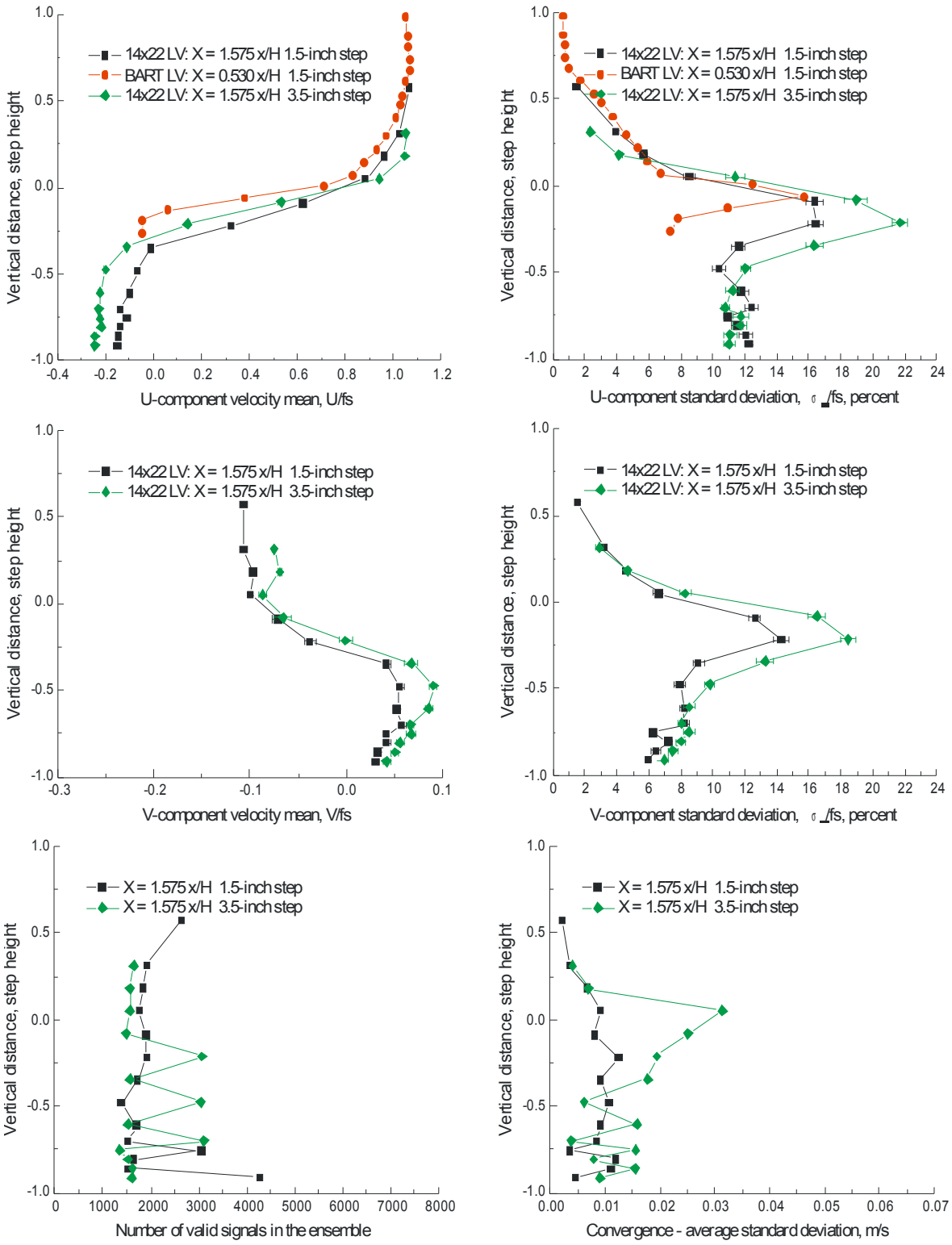

Figure VII.16.e.- Vertical scan 1.575-step heights downstream of the 1.5- and 3.5-inch backward-facing steps: streamwise and vertical velocity components, number of accepted signal bursts, and statistical stationarity convergence standard deviation.

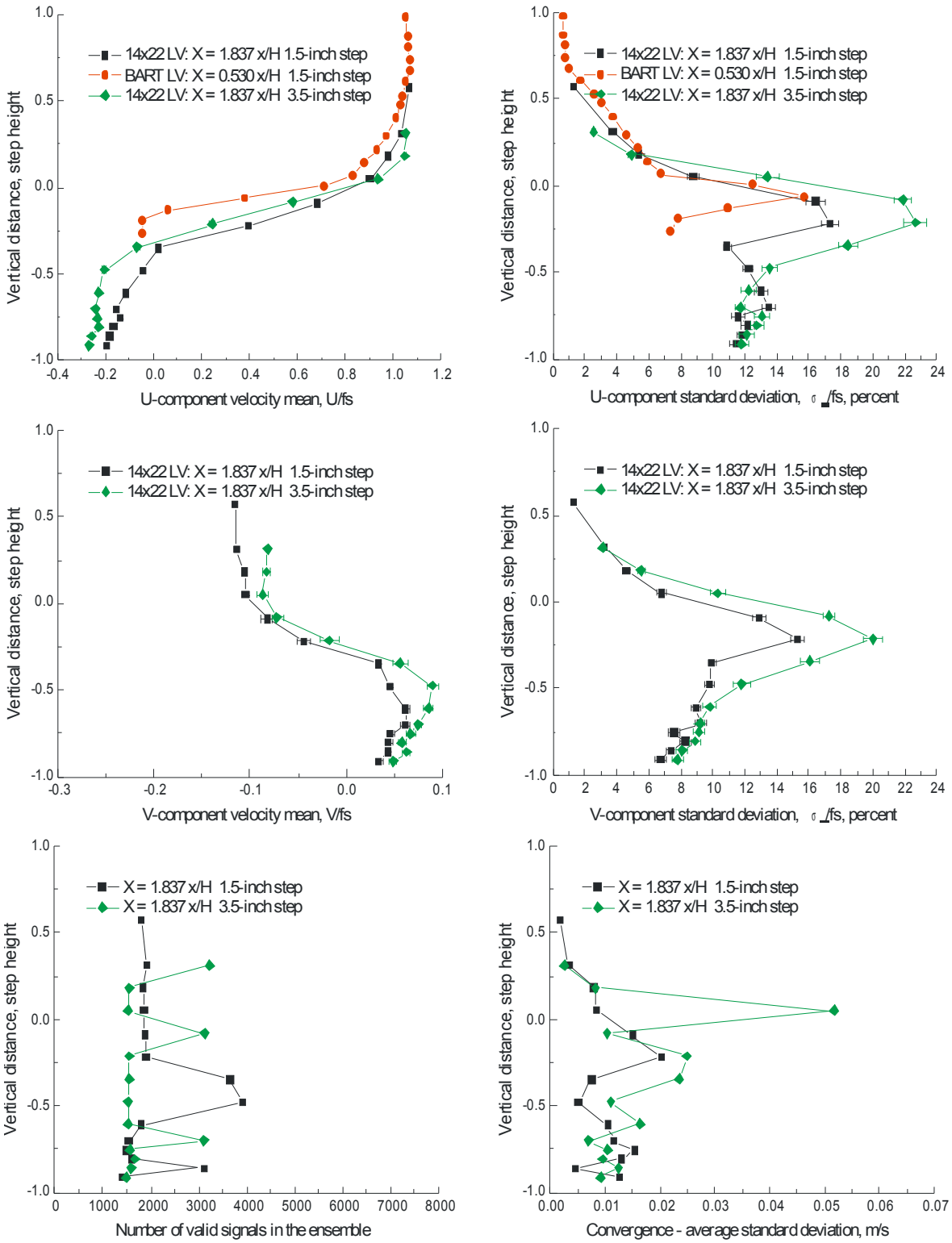

Figure VII.16.f.- Vertical scan 1.837-step heights downstream of the 1.5- and 3.5-inch backward-facing steps: streamwise and vertical velocity components, number of accepted signal bursts, and statistical stationarity convergence standard deviation.

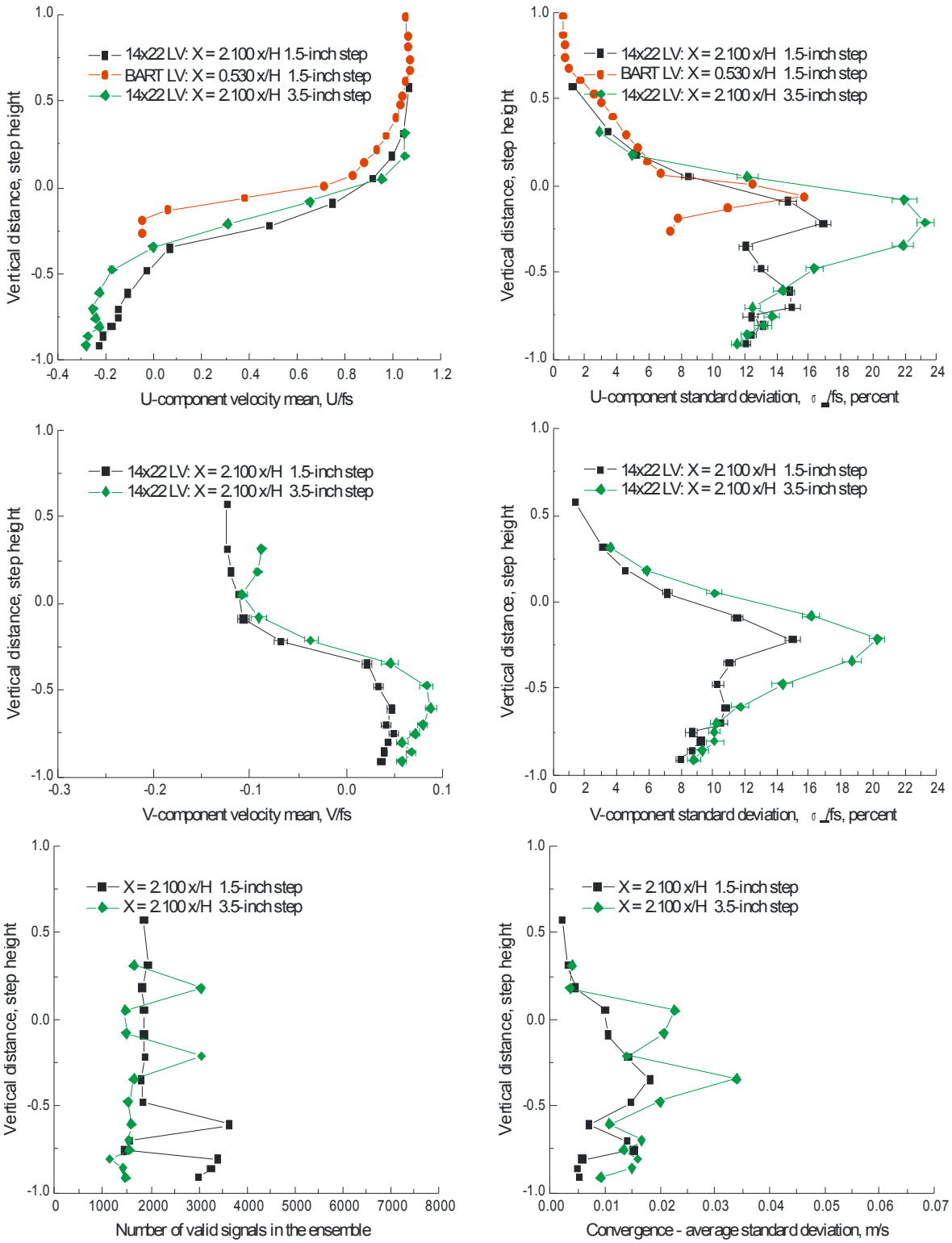

Figure VII.16.g.- Vertical scan 2.1-step heights downstream of the 1.5- and 3.5-inch backward-facing steps: streamwise and vertical velocity components, number of accepted signal bursts, and statistical stationarity convergence standard deviation.

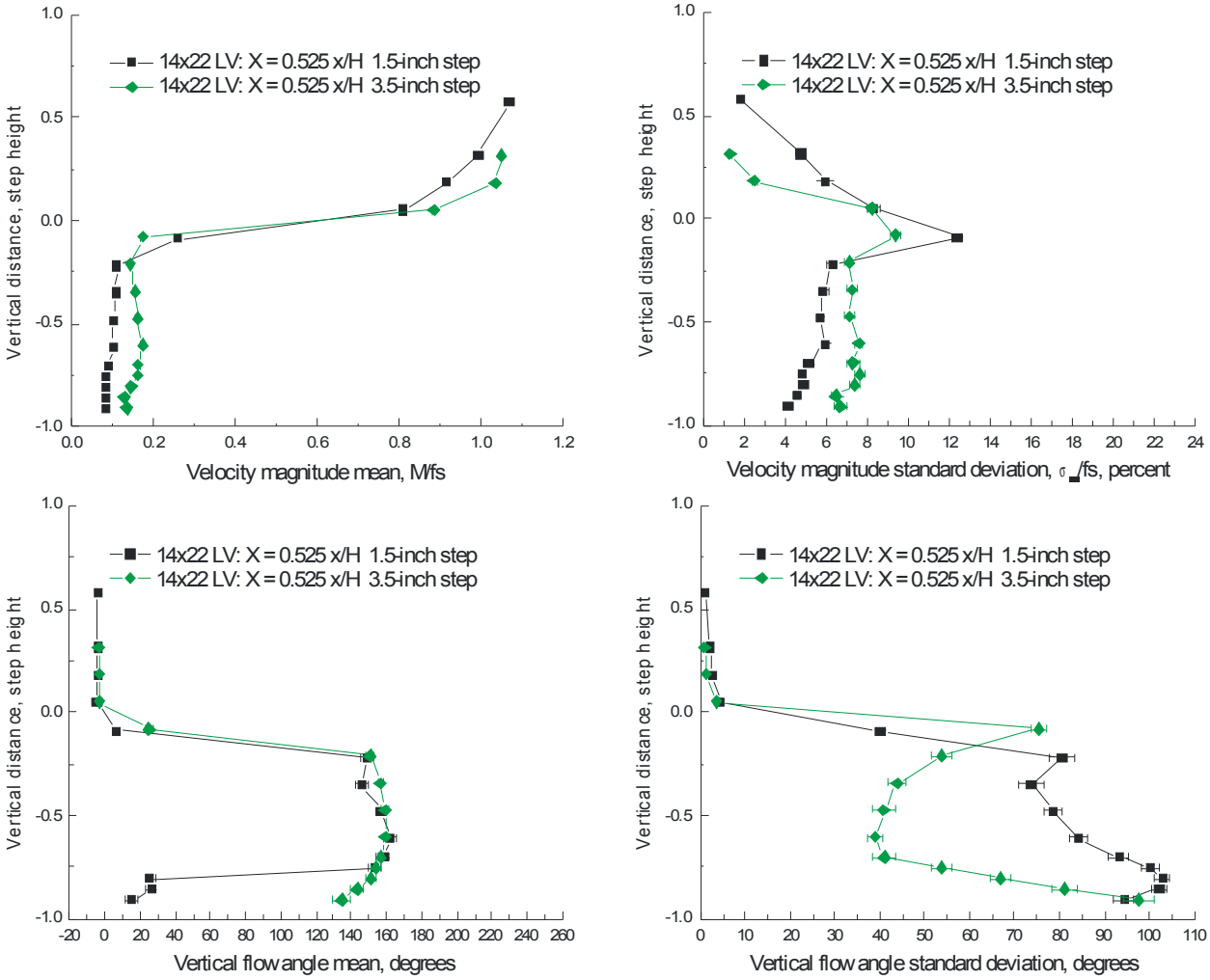

Figure VII.17.a.- Vertical scan 0.525-step heights downstream of the 1.5- and 3.5-inch backward-facing steps: velocity magnitude and flow angle.

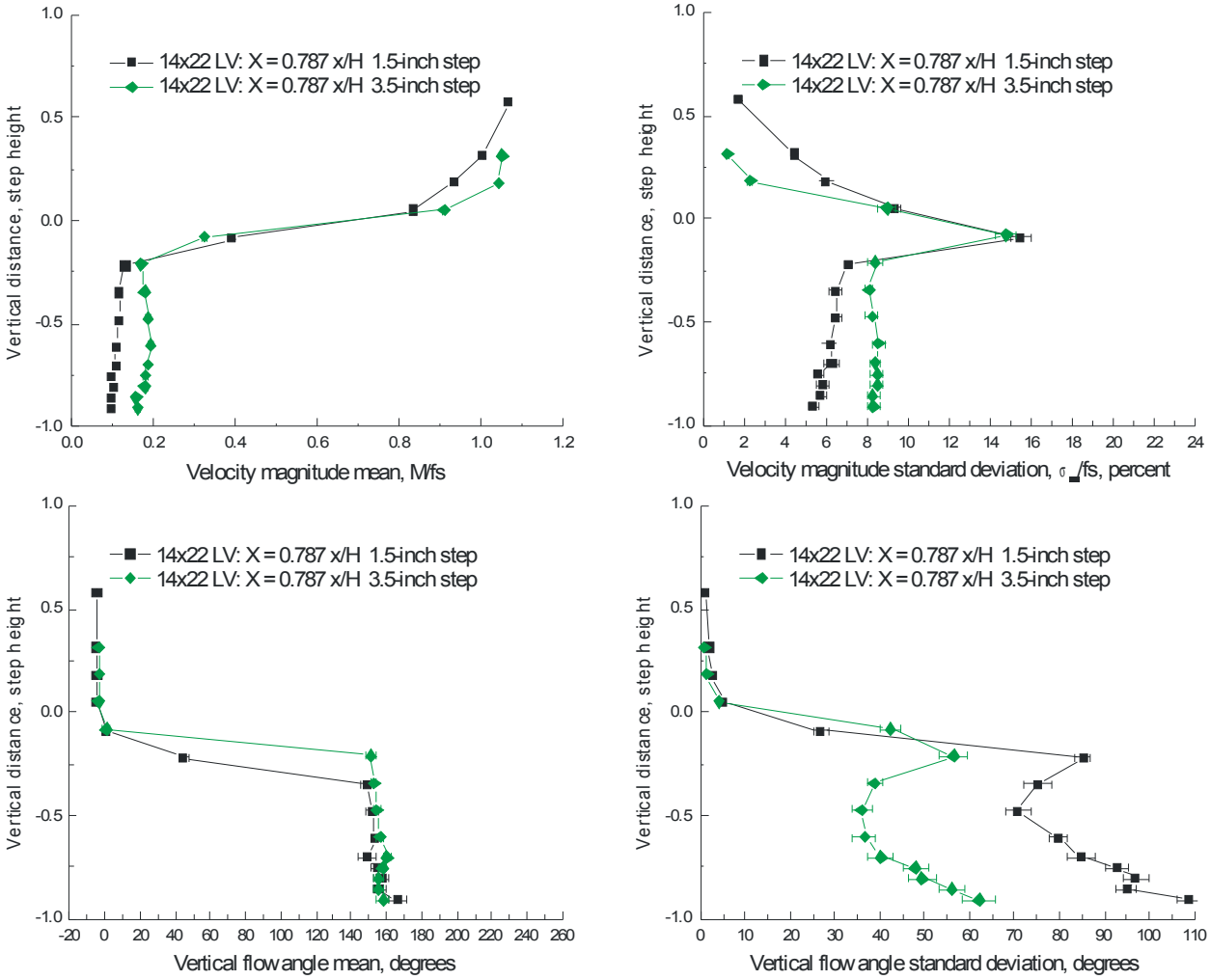

Figure VII.17.b.- Vertical scan 0.787-step heights downstream of the 1.5- and 3.5-inch backward-facing steps: velocity magnitude and flow angle.

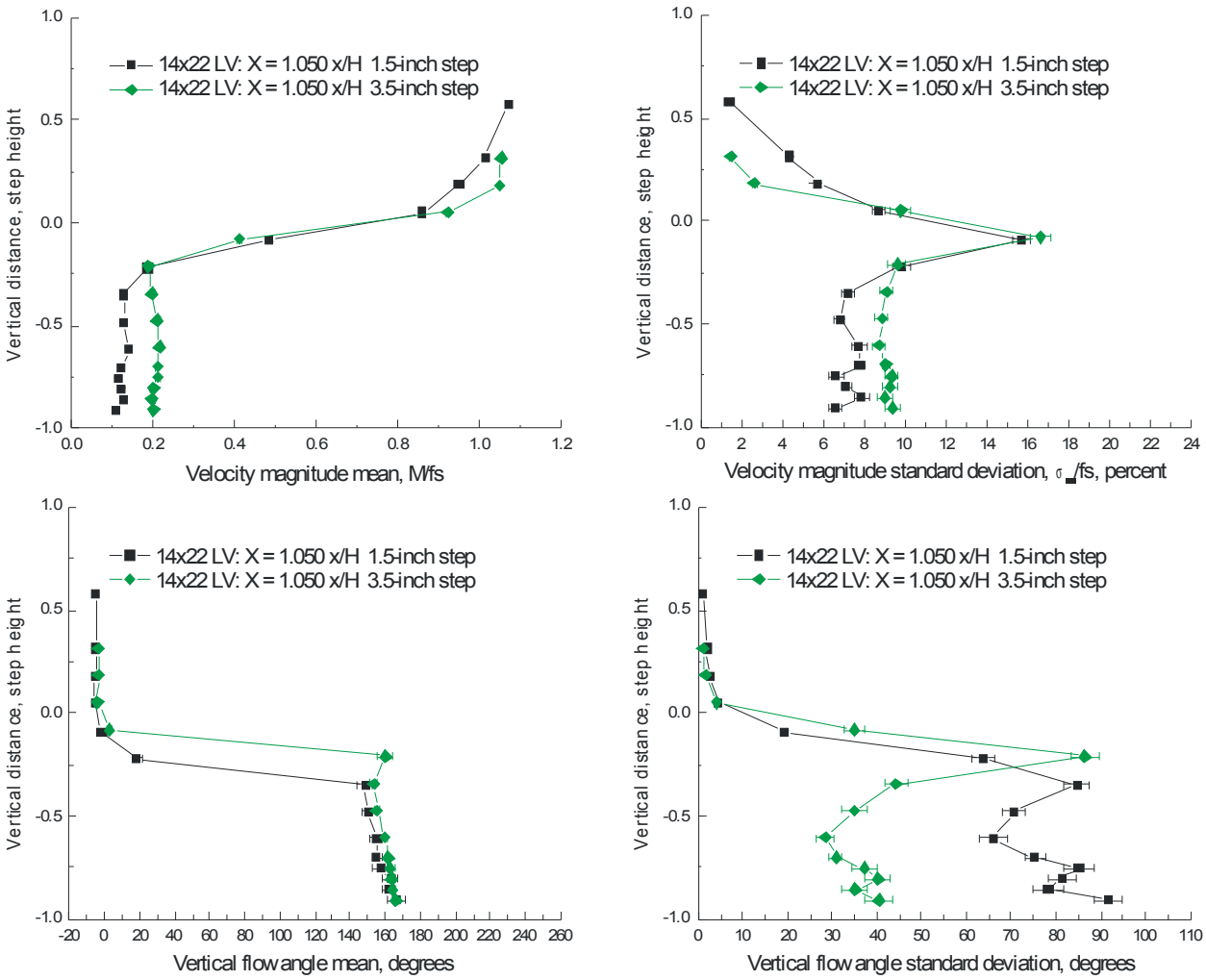

Figure VII.17.c.- Vertical scan 1.050-step heights downstream of the 1.5- and 3.5-inch backward-facing steps: velocity magnitude and flow angle.

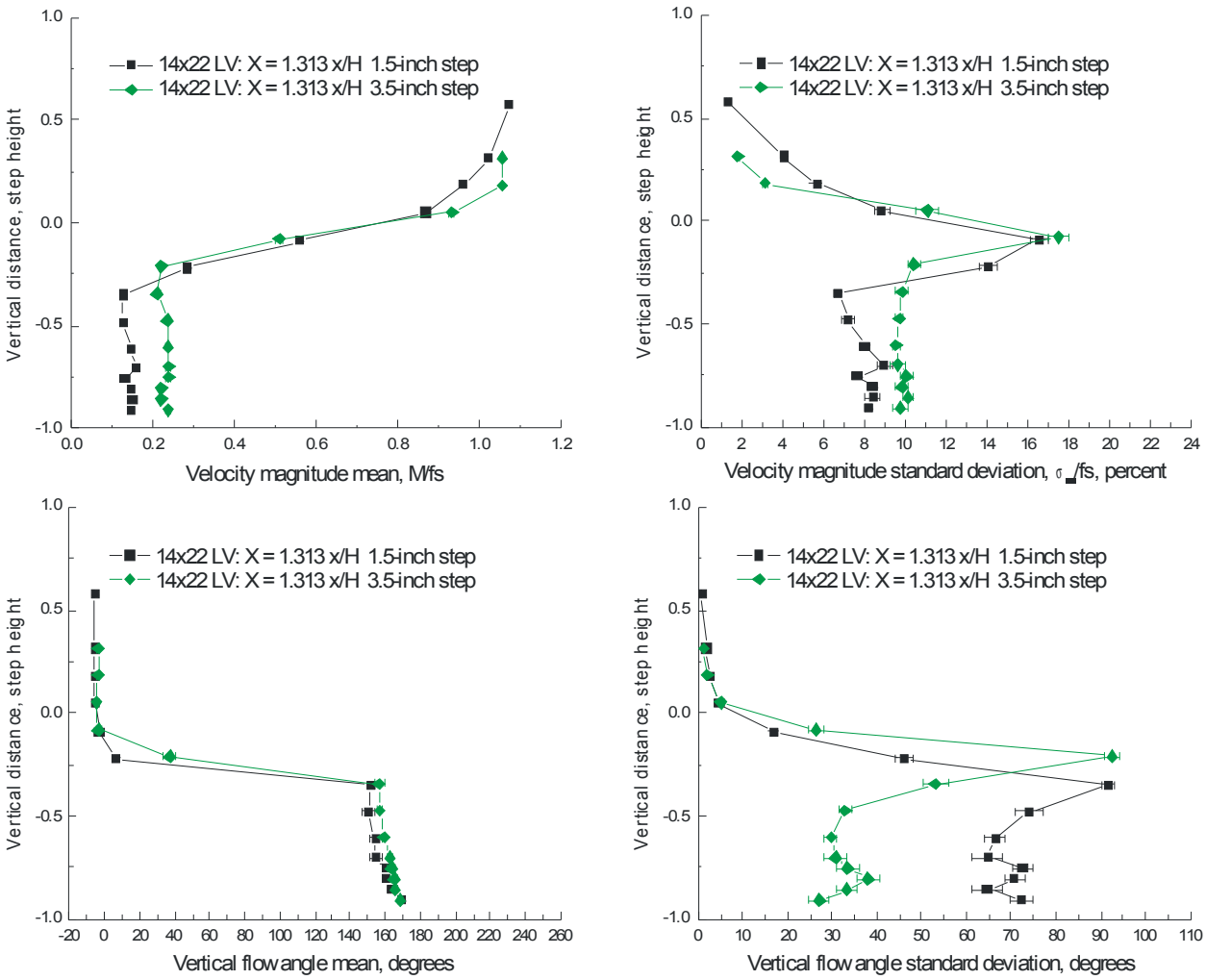

Figure VII.17.d.- Vertical scan 1.313-step heights downstream of the 1.5- and 3.5-inch backward-facing steps: velocity magnitude and flow angle.

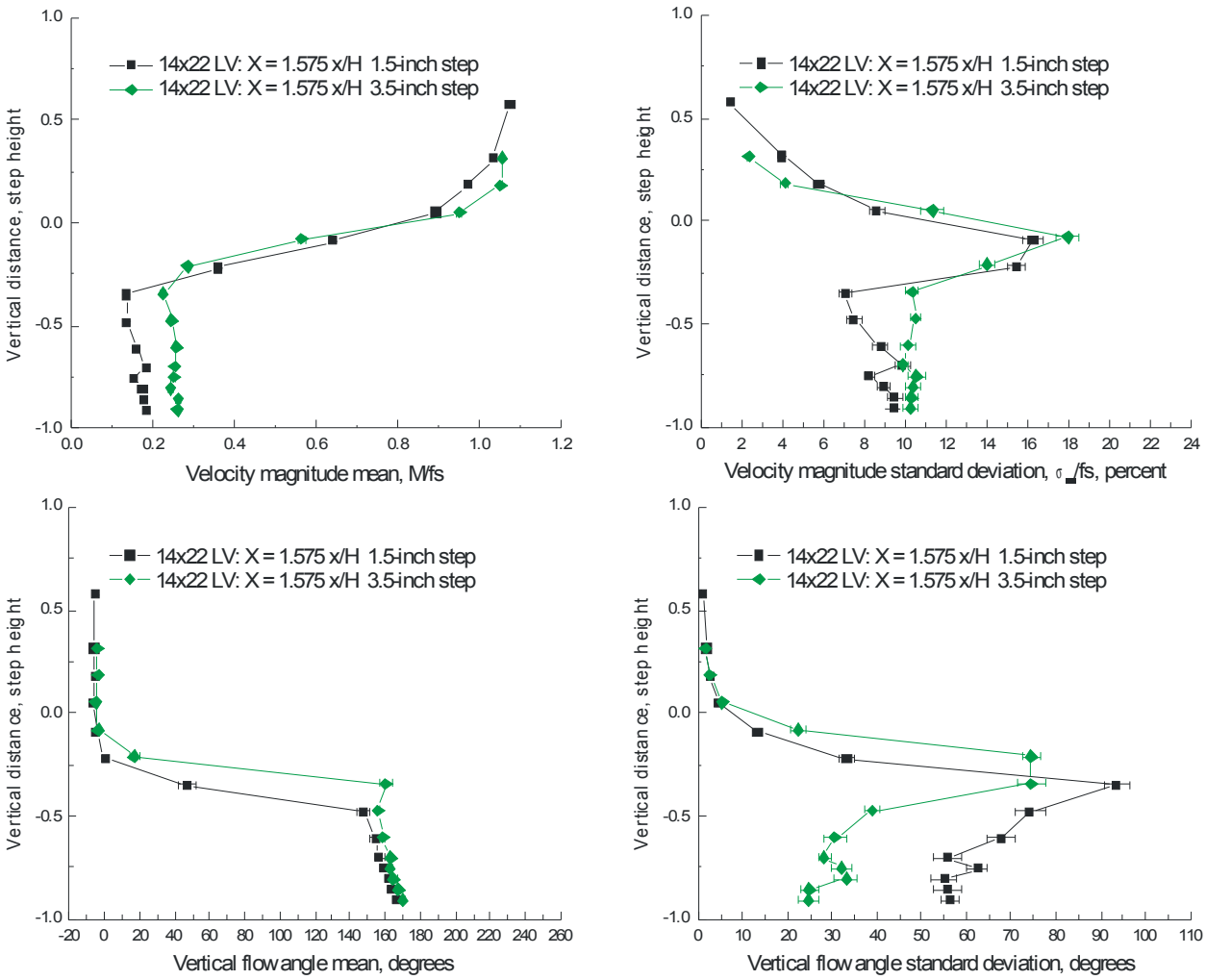

Figure VII.17.e.- Vertical scan 1.575-step heights downstream of the 1.5- and 3.5-inch backward-facing steps: velocity magnitude and flow angle.

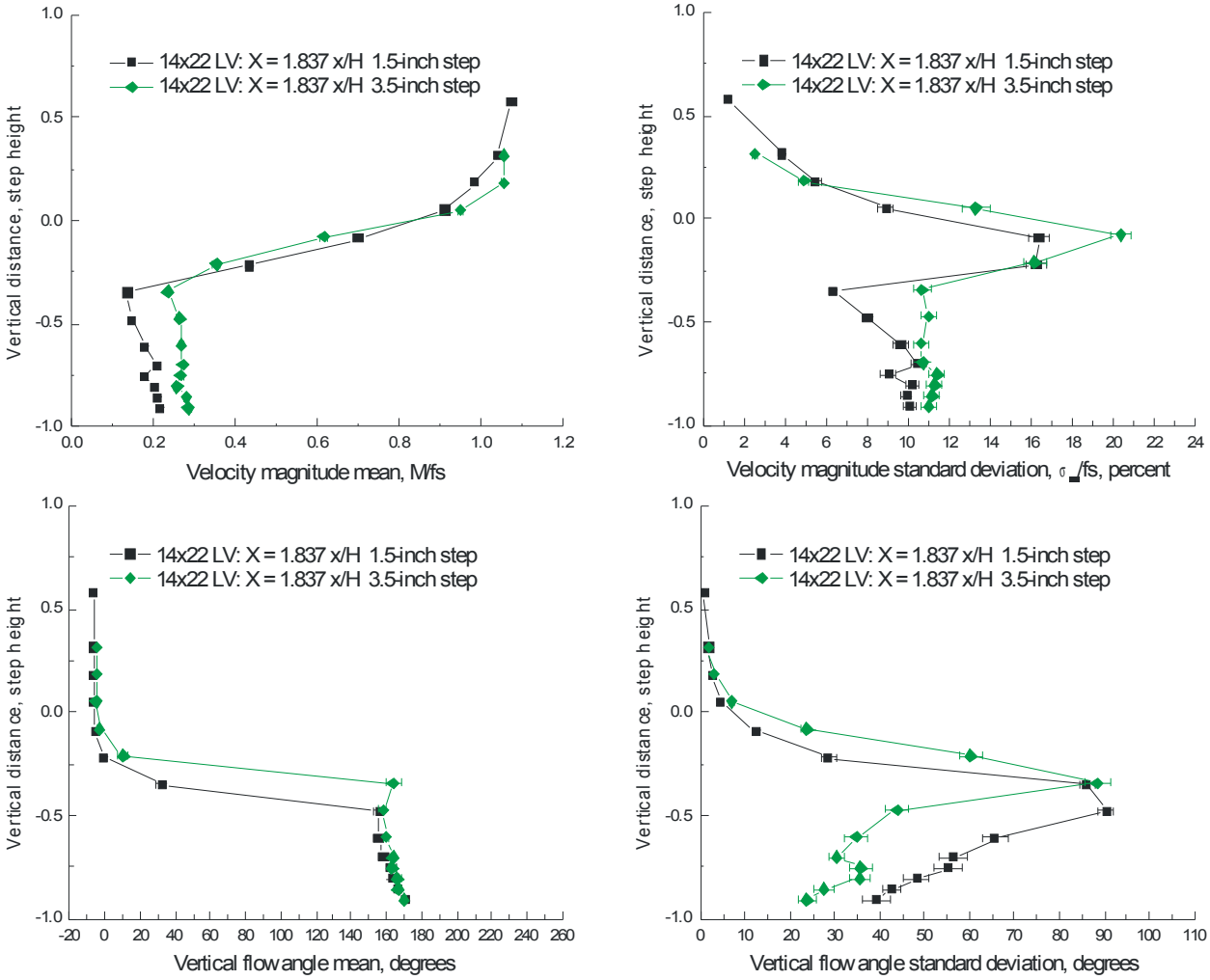

Figure VII.17.f.- Vertical scan 1.837-step heights downstream of the 1.5- and 3.5-inch backward-facing steps: velocity magnitude and flow angle.

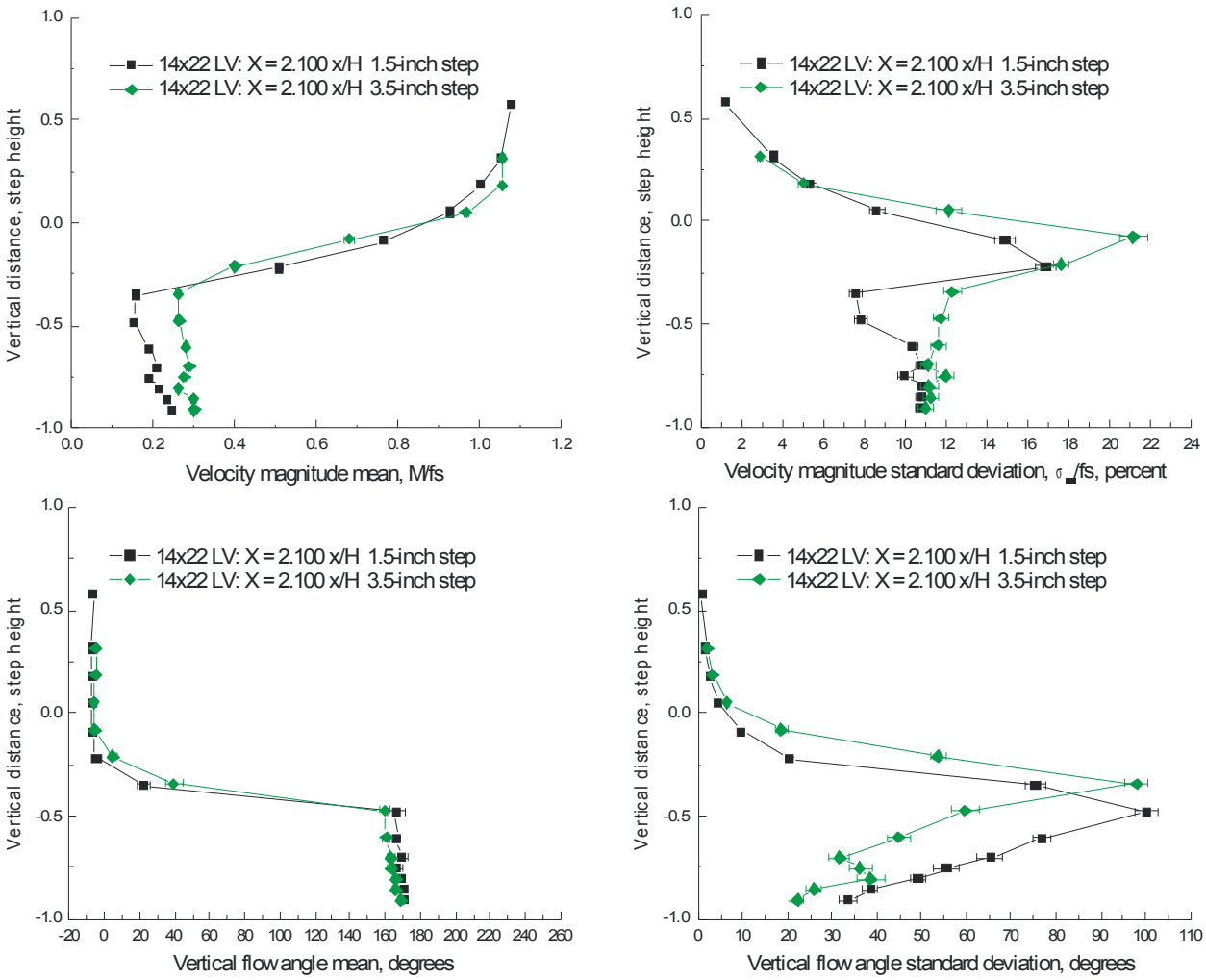

Figure VII.17.g.- Vertical scan 2.1-step heights downstream of the 1.5- and 3.5-inch backward-facing steps: velocity magnitude and flow angle.

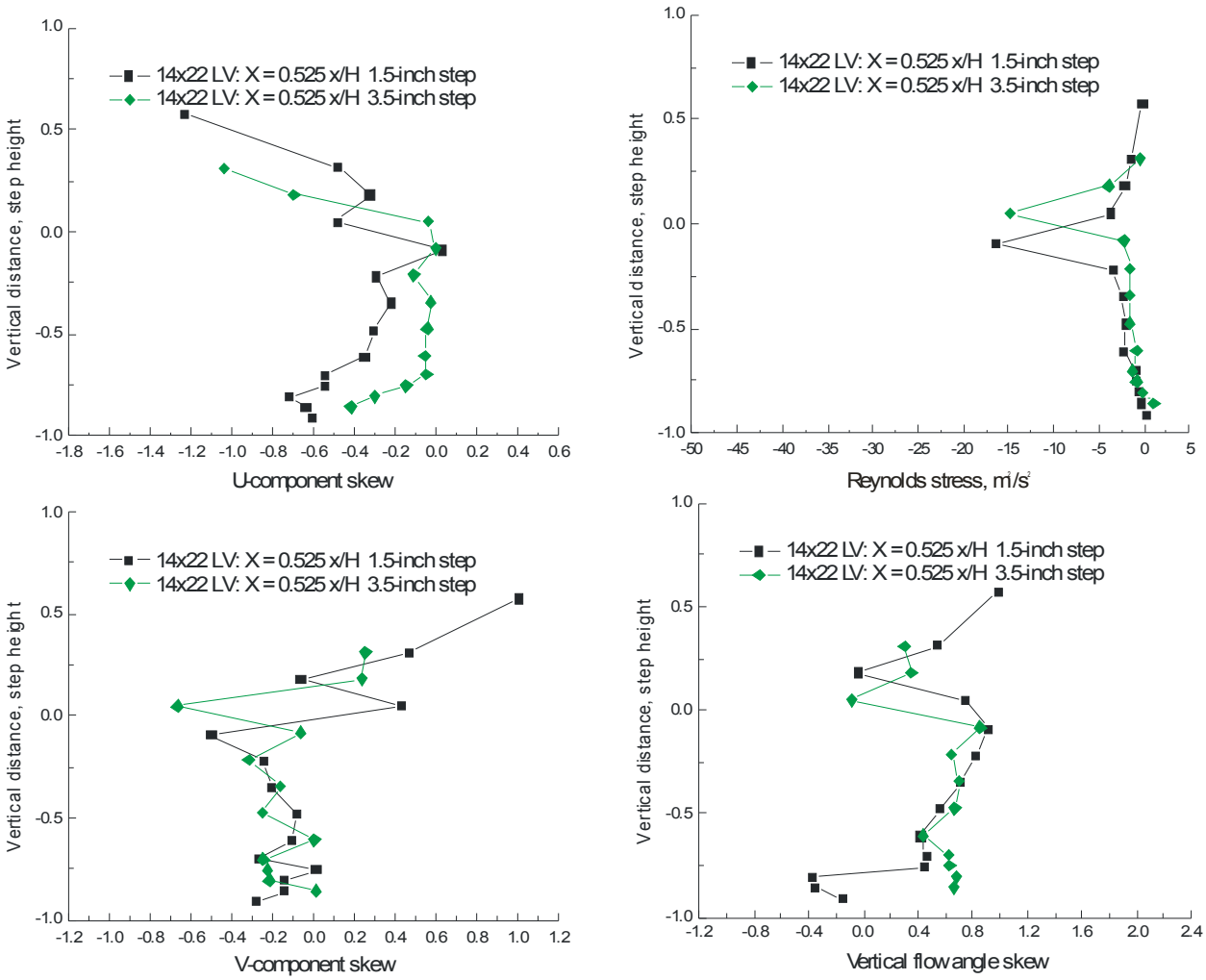

Figure VII.18.a.- Vertical scan 0.525-step heights downstream of the 1.5- and 3.5-inch backward-facing steps: streamwise and vertical velocity skew, flow angle skew and Reynolds stress.

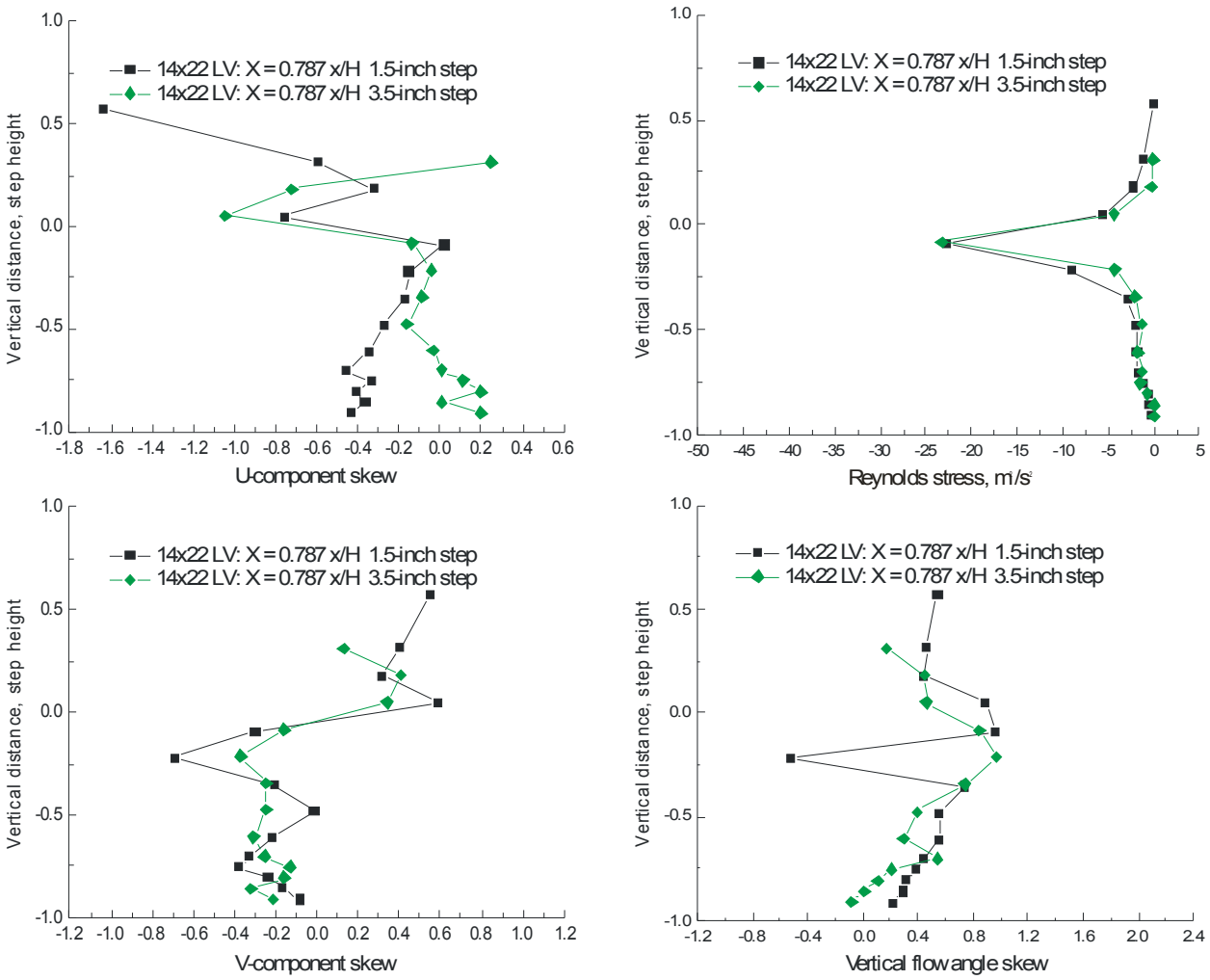

Figure VII.18.b.- Vertical scan 0.787-step heights downstream of the 1.5- and 3.5-inch backward-facing steps: streamwise and vertical velocity skew, flow angle skew and Reynolds stress.

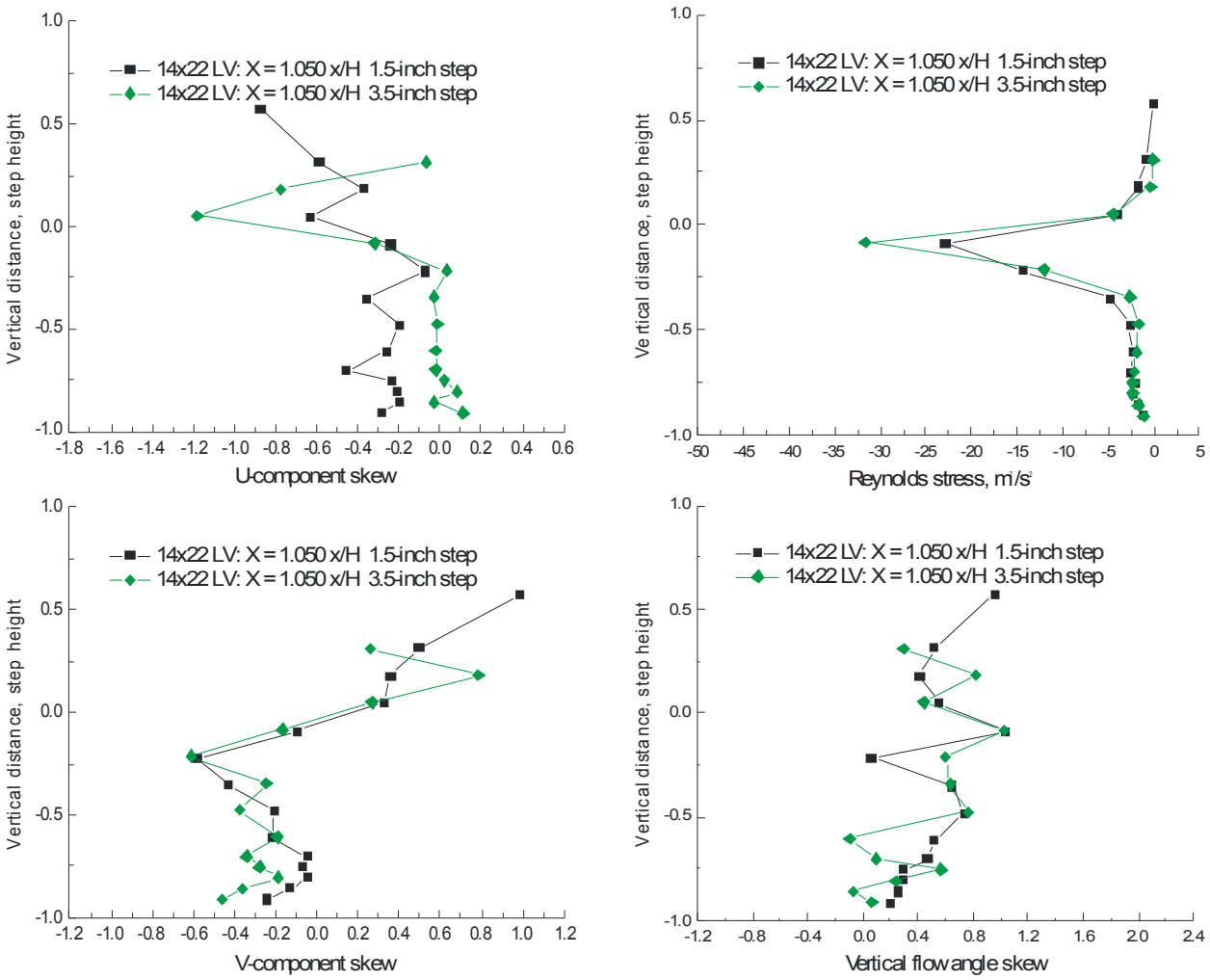

Figure VII.18.c.- Vertical scan 1.050-step heights downstream of the 1.5- and 3.5-inch backward-facing steps: streamwise and vertical velocity skew, flow angle skew and Reynolds stress.

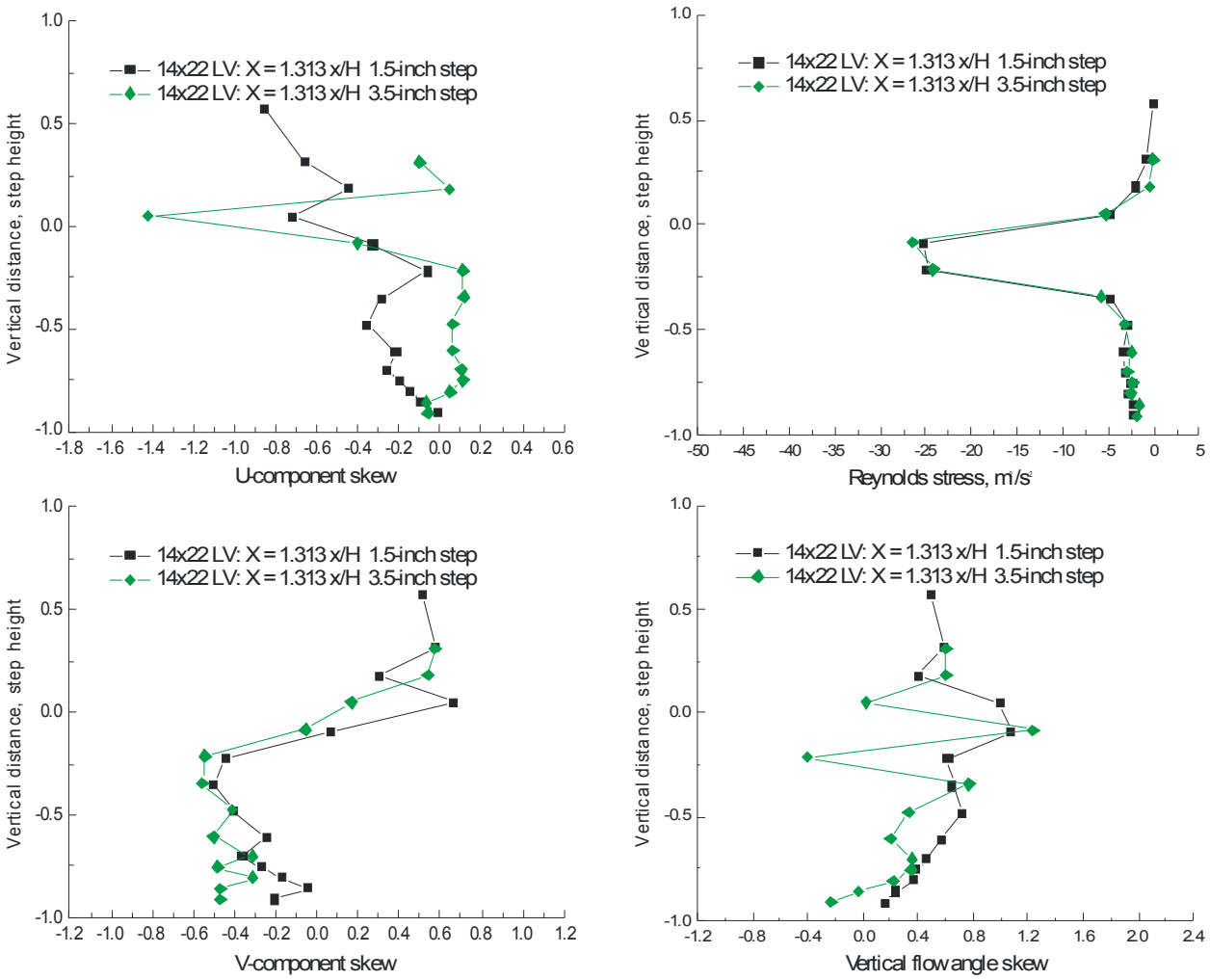

Figure VII.18.d.- Vertical scan 1.312-step heights downstream of the 1.5- and 3.5-inch backward-facing steps: streamwise and vertical velocity skew, flow angle skew and Reynolds stress.

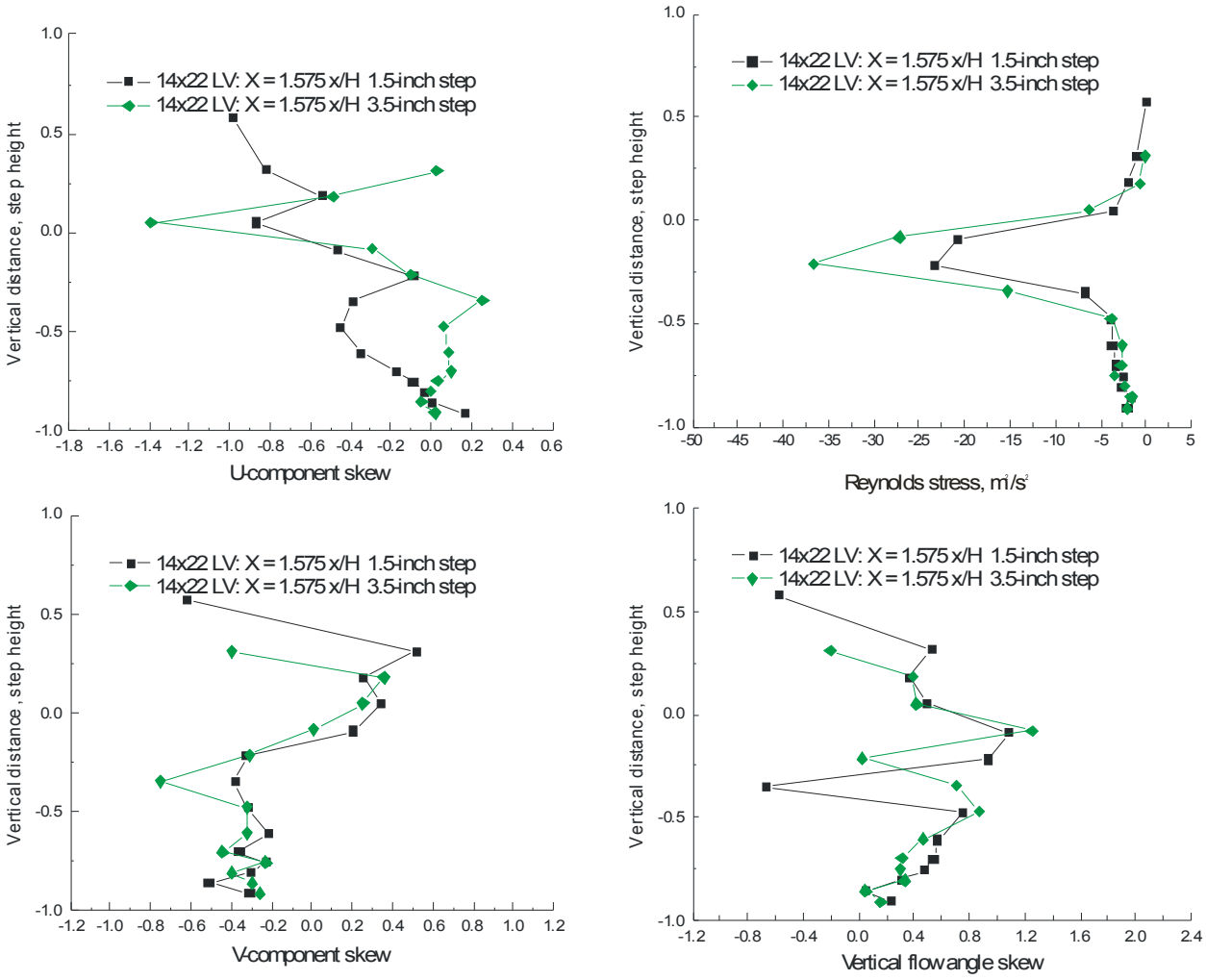

Figure VII.18.e.- Vertical scan 1.575-step heights downstream of the 1.5- and 3.5-inch backward-facing steps: streamwise and vertical velocity skew, flow angle skew and Reynolds stress.

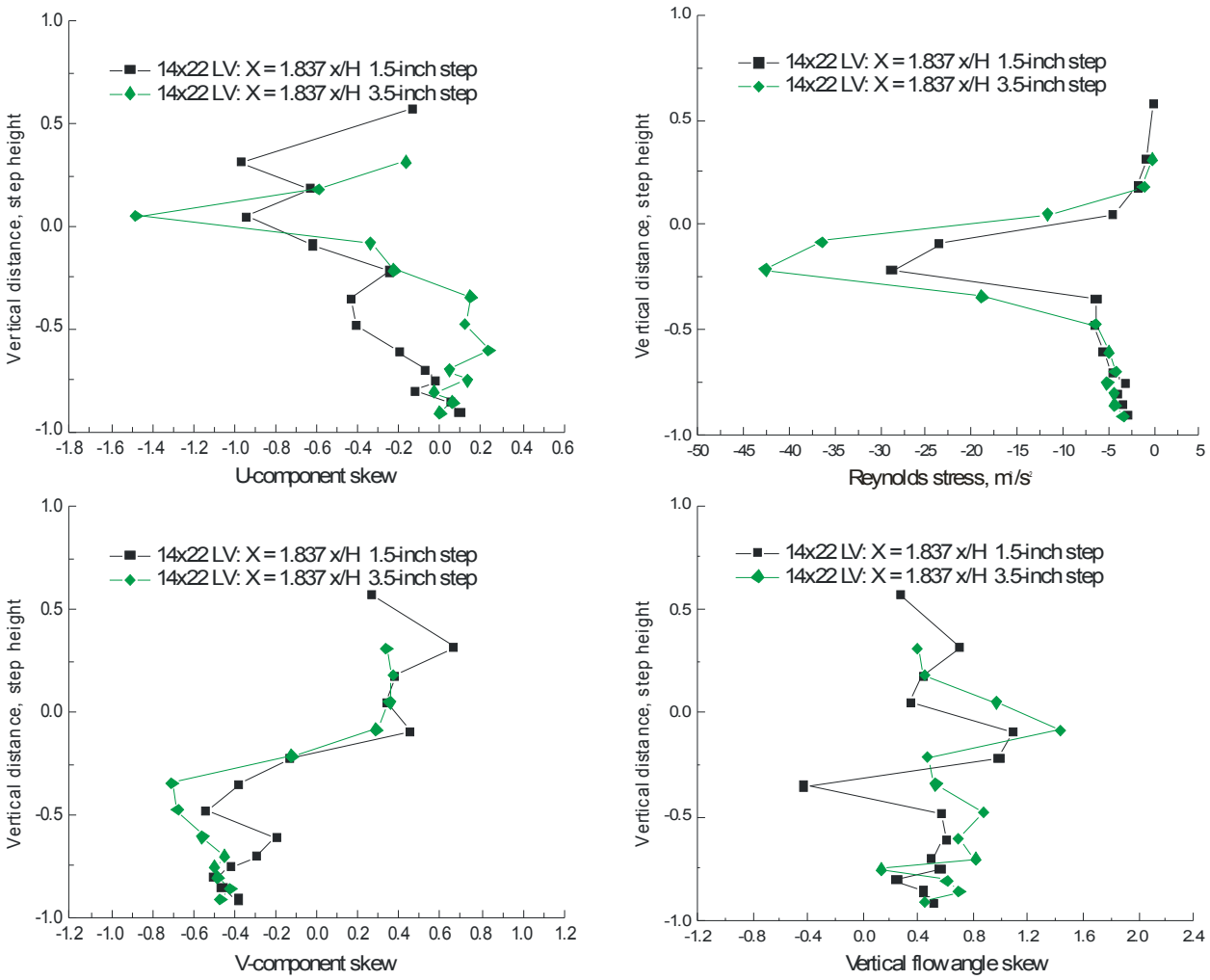

Figure VII.18.f.- Vertical scan 1.837-step heights downstream of the 1.5- and 3.5-inch backward-facing steps: streamwise and vertical velocity skew, flow angle skew and Reynolds stress.

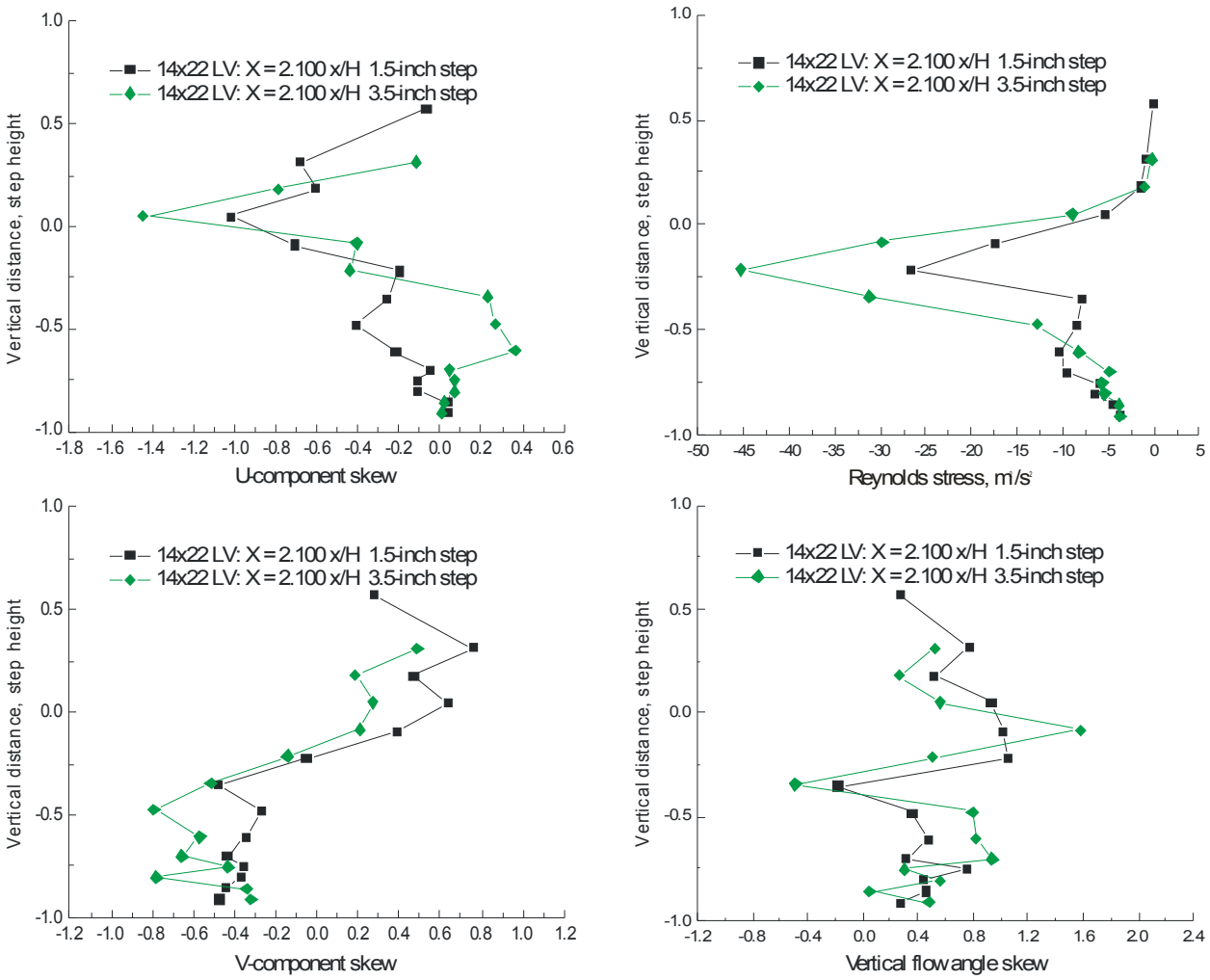

Figure VII.18.g.- Vertical scan 2.1-step heights downstream of the 1.5- and 3.5-inch backward-facing steps: streamwise and vertical velocity skew, flow angle skew and Reynolds stress.

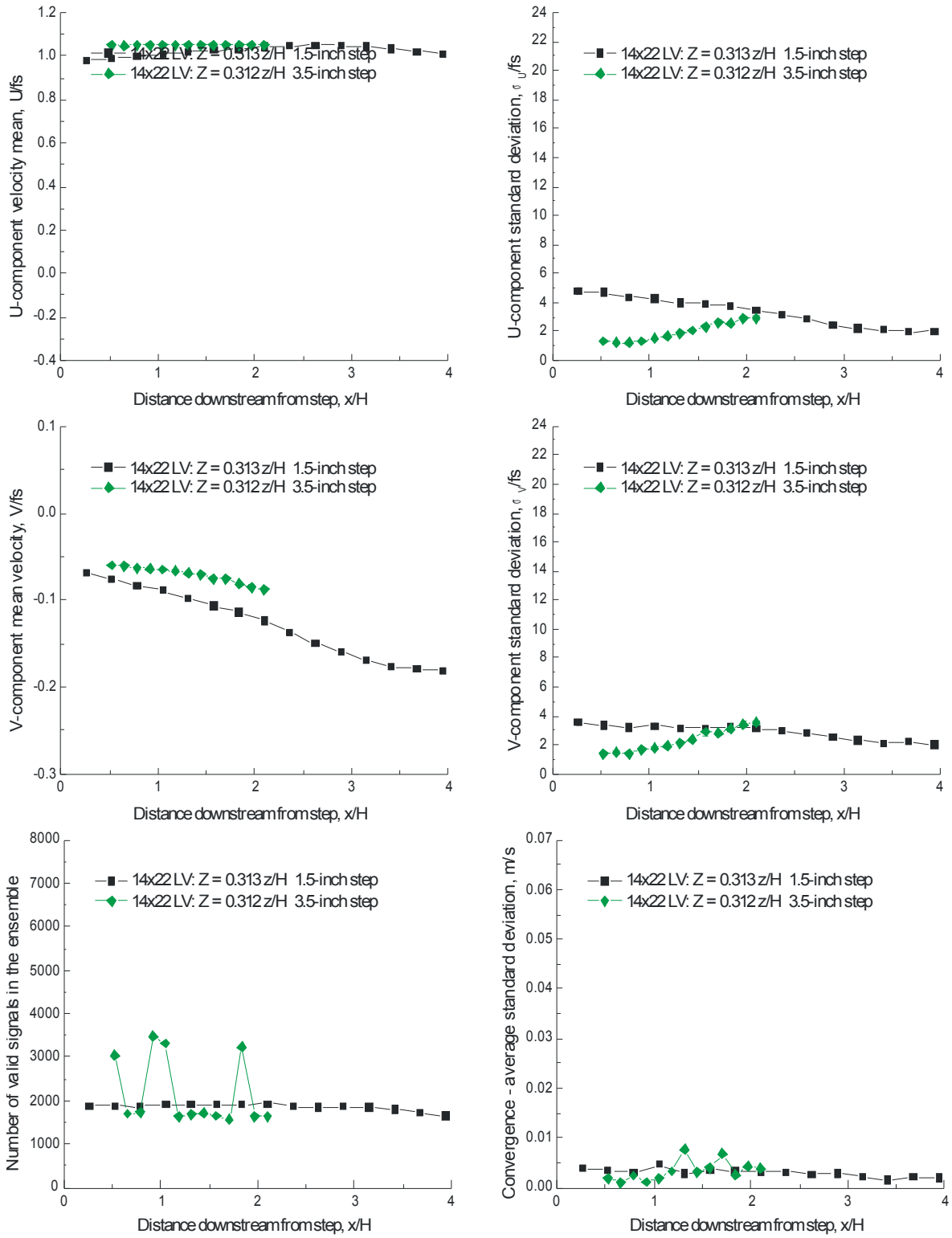

Figure VII.19.a.- Horizontal scan 0.313 z/H above the 1.5- and 3.5-inch backward-facing steps: streamwise and vertical velocity components, number of accepted signal bursts, and statistical stationarity convergence standard deviation.

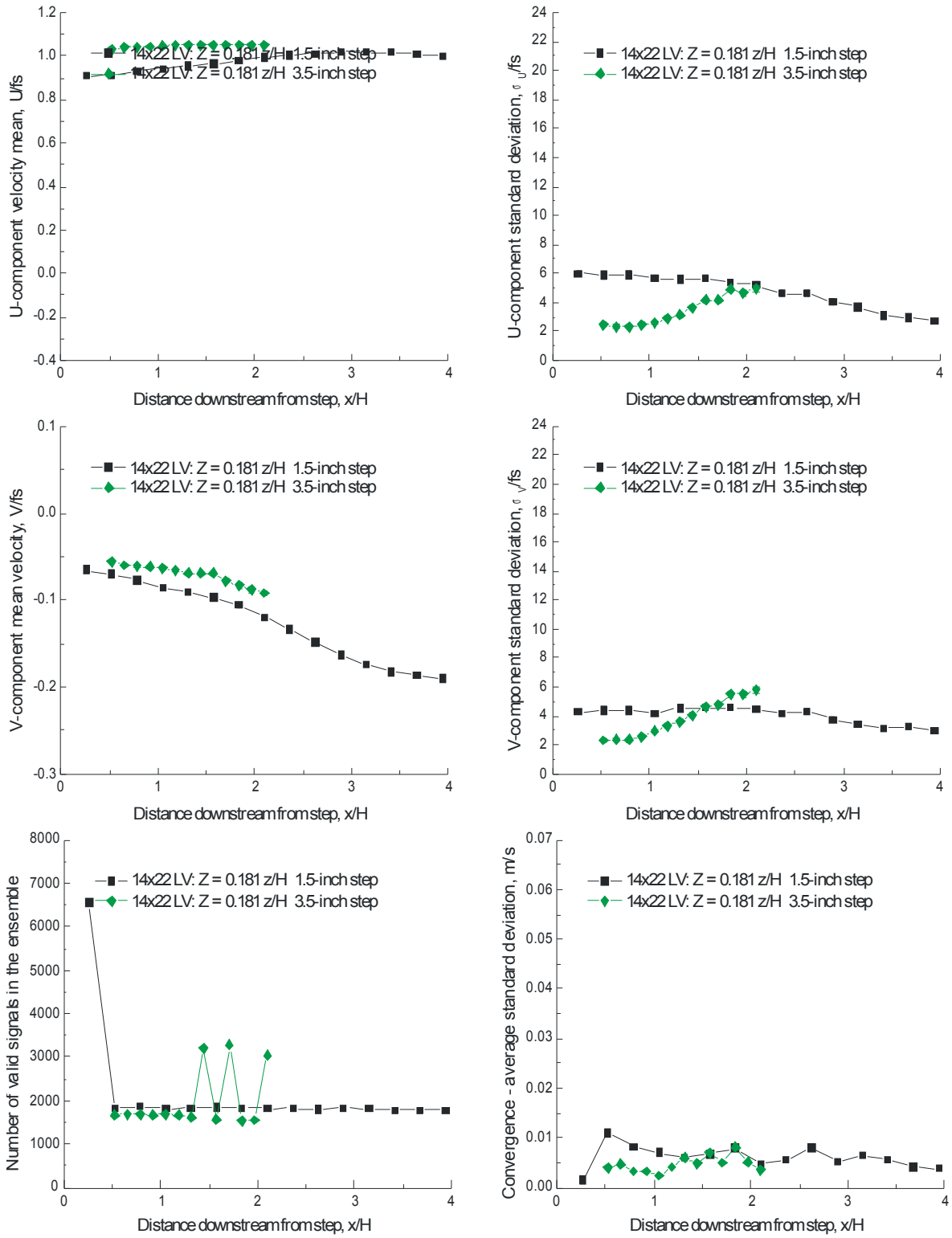

Figure VII.19.b.- Horizontal scan 0.181 z/H above the 1.5- and 3.5-inch backward-facing steps: streamwise and vertical velocity components, number of accepted signal bursts, and statistical stationarity convergence standard deviation.

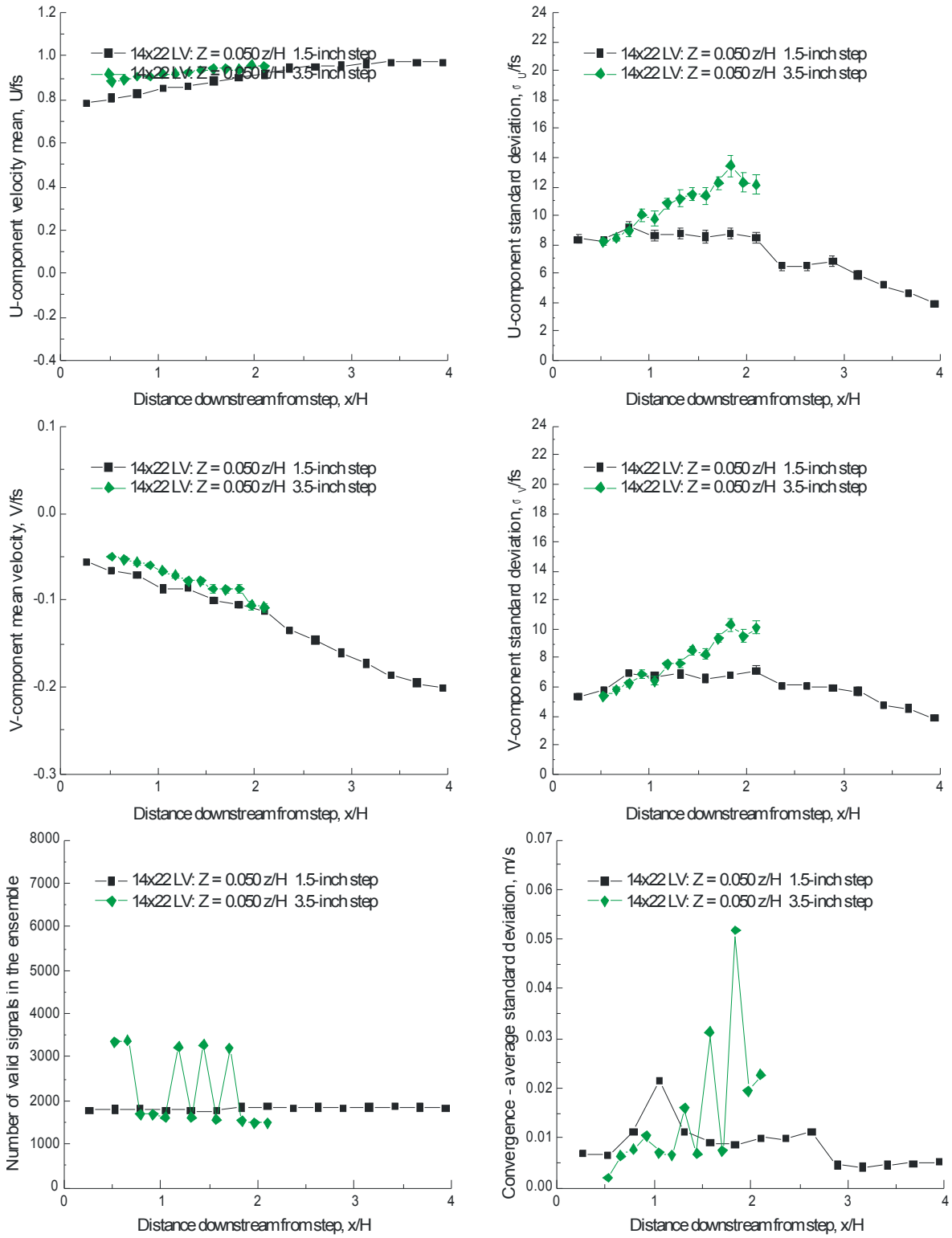

Figure VII.19.c.- Horizontal scan 0.050 z/H above the 1.5- and 3.5-inch backward-facing steps: streamwise and vertical velocity components, number of accepted signal bursts, and statistical stationarity convergence standard deviation.

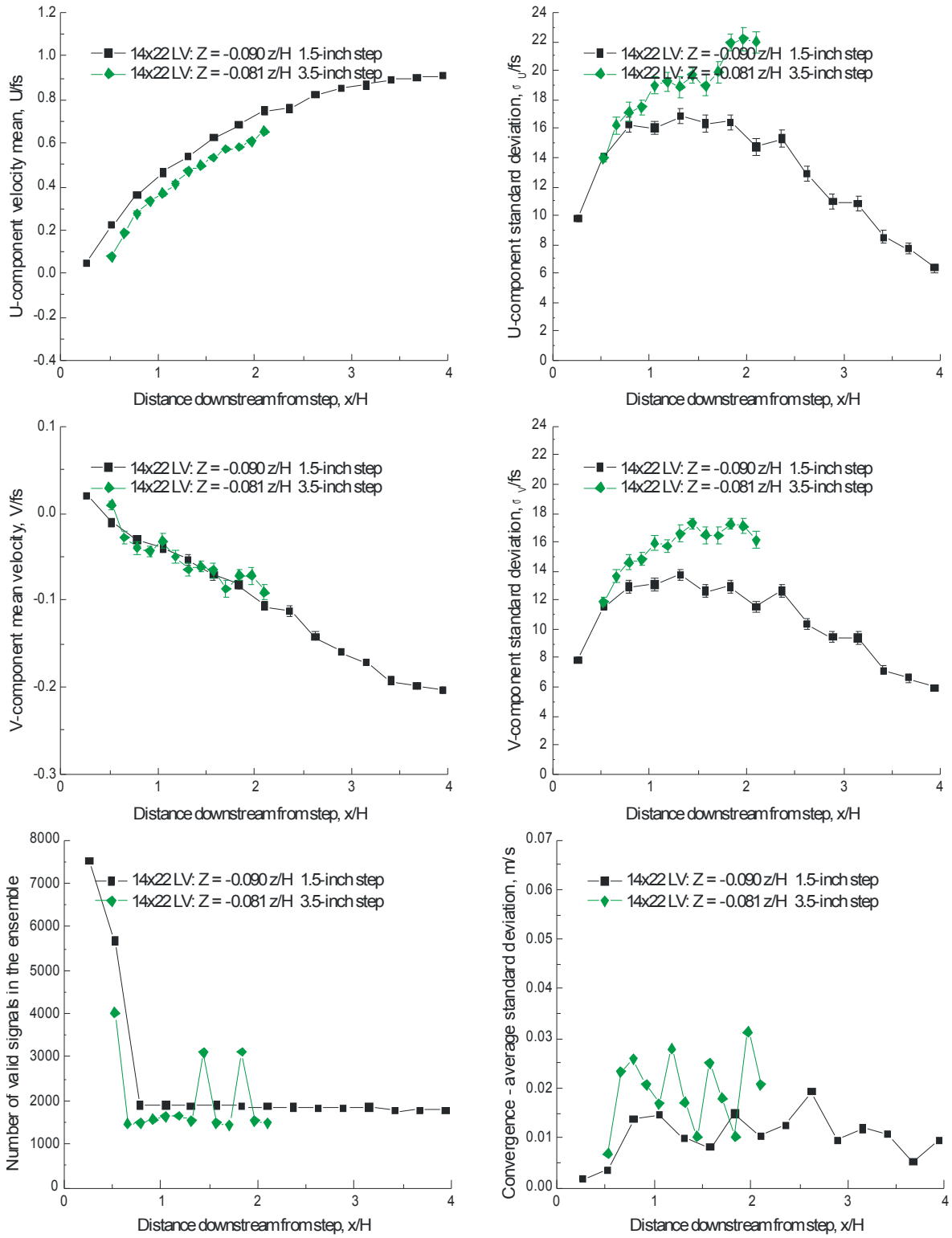

Figure VII.19.d.- Horizontal scan 0.090 z/H below the 1.5- and 3.5-inch backward-facing steps: streamwise and vertical velocity components, number of accepted signal bursts, and statistical stationarity convergence standard deviation.

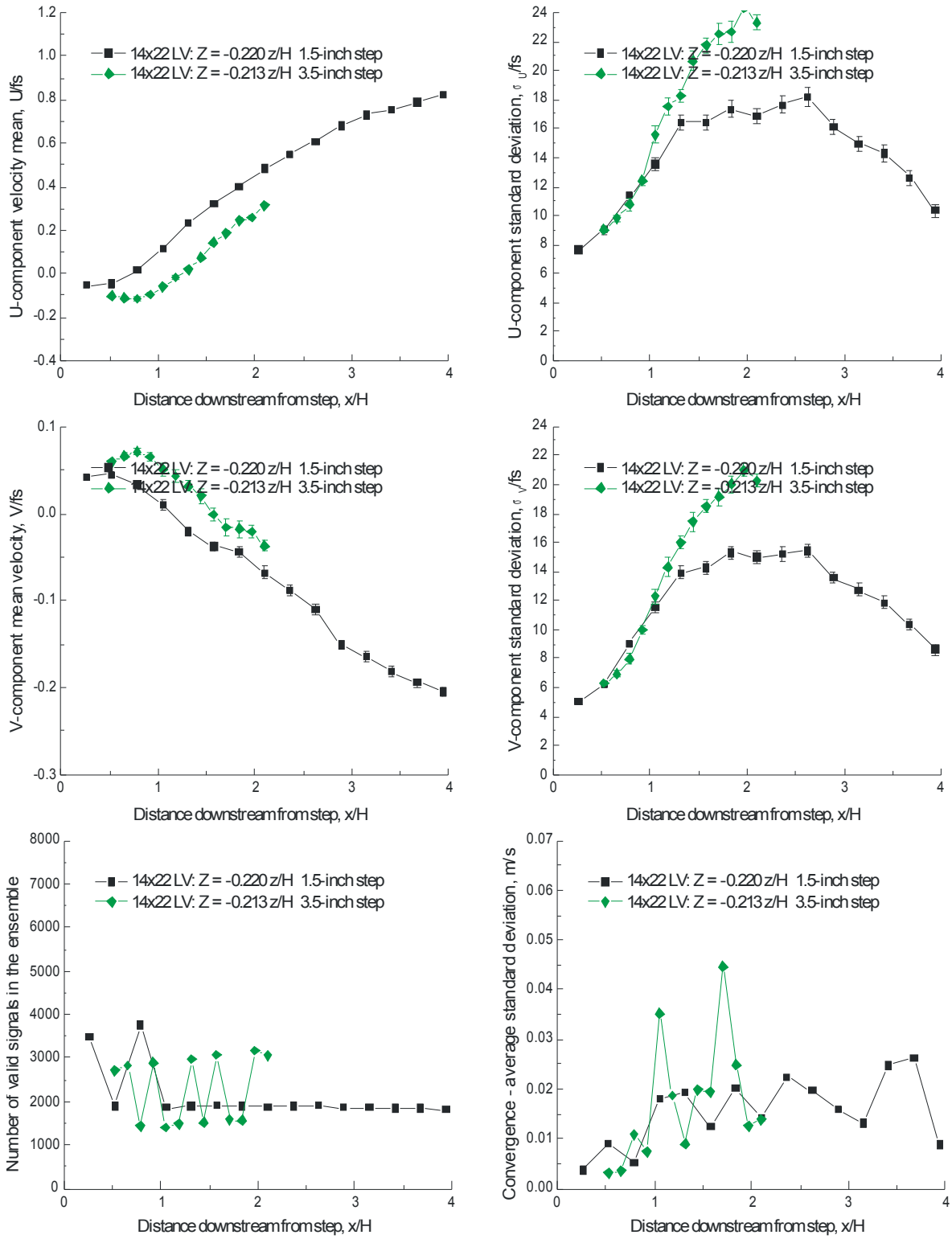

Figure VII.19.e.- Horizontal scan 0.220 z/H below the 1.5- and 3.5-inch backward-facing steps: streamwise and vertical velocity components, number of accepted signal bursts, and statistical stationarity convergence standard deviation.

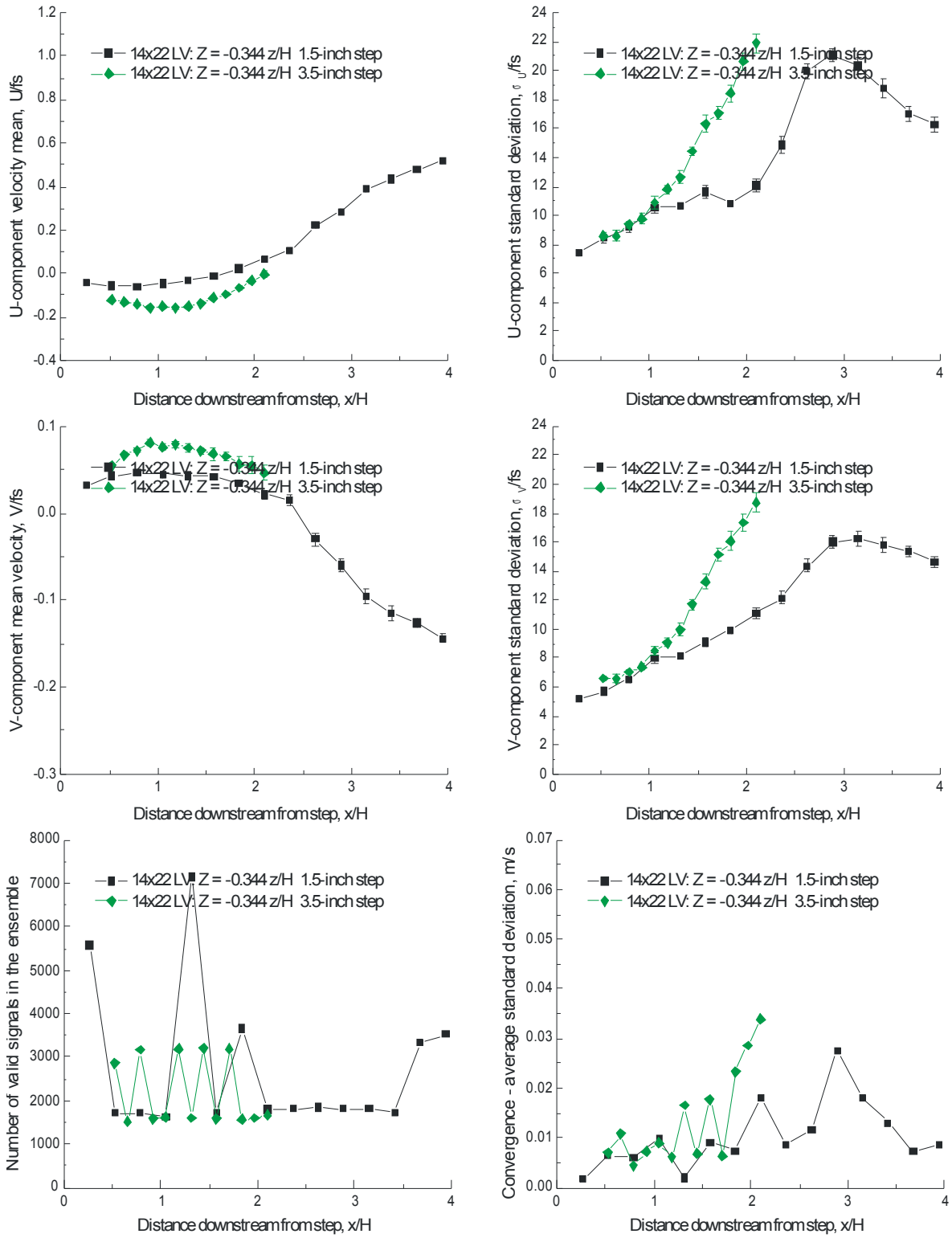

Figure VII.19.f.- Horizontal scan 0.344 z/H below the 1.5- and 3.5-inch backward-facing steps: streamwise and vertical velocity components, number of accepted signal bursts, and statistical stationarity convergence standard deviation.

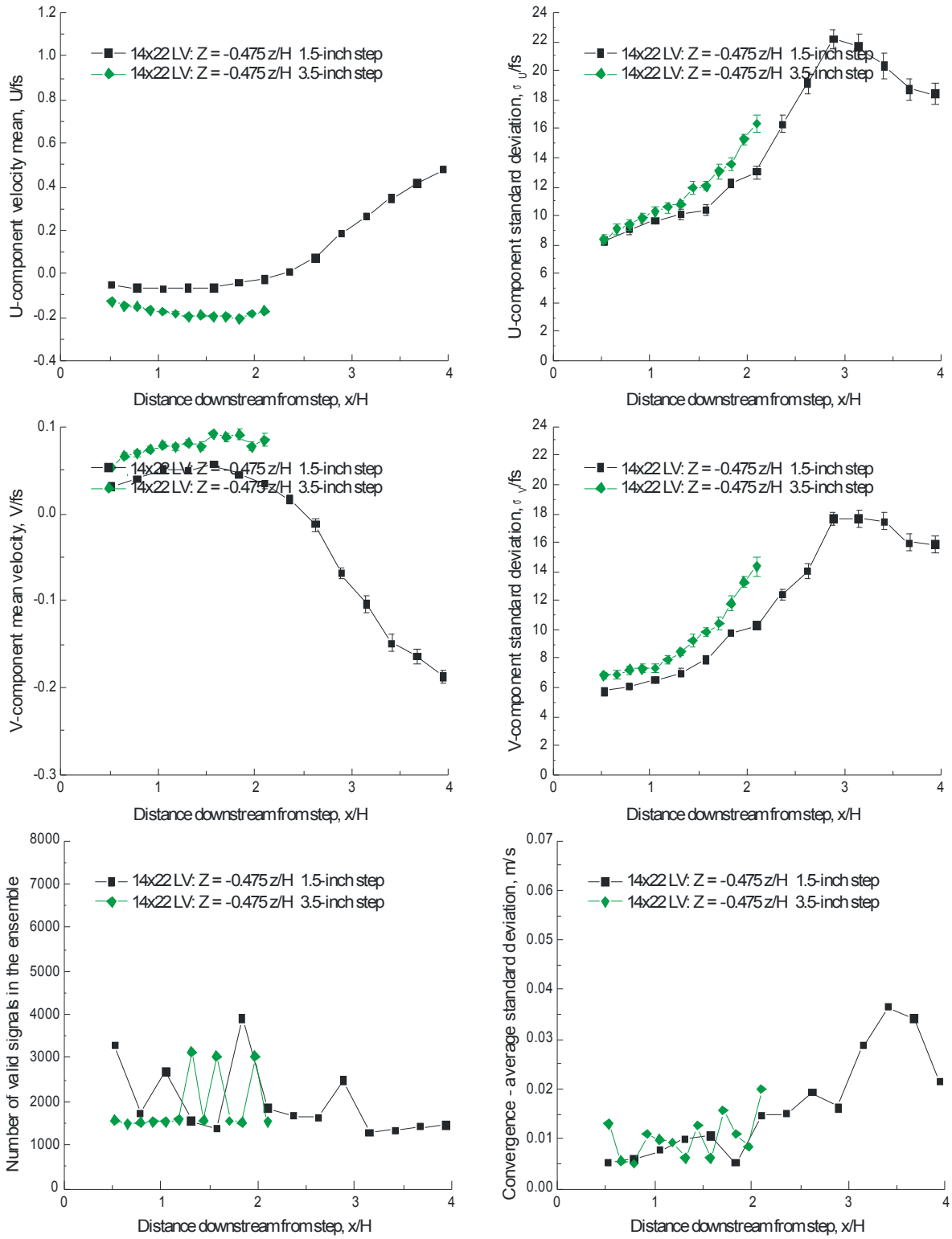

Figure VII.19.g.- Horizontal scan 0.475 z/H below the 1.5- and 3.5-inch backward-facing steps: streamwise and vertical velocity components, number of accepted signal bursts, and statistical stationarity convergence standard deviation.

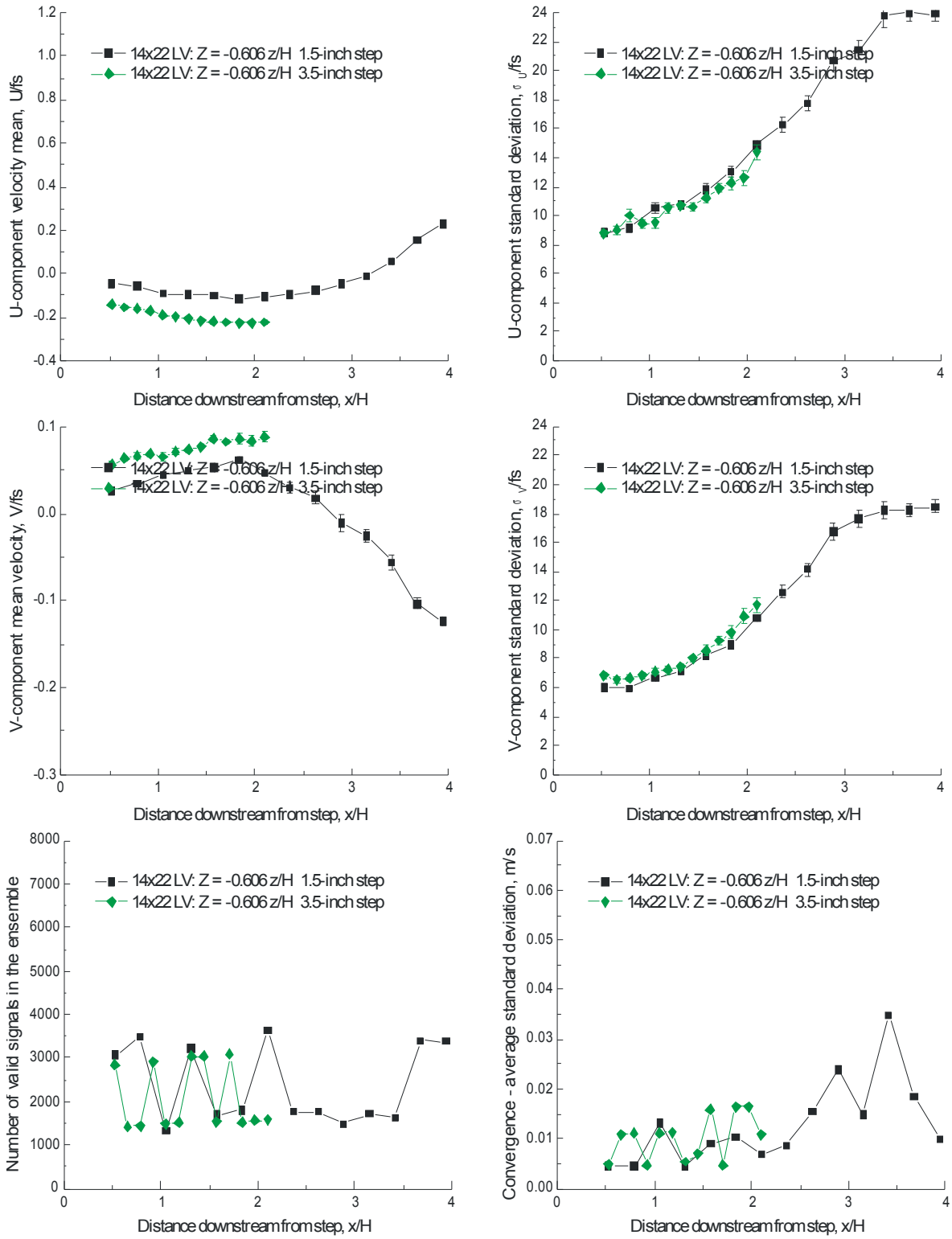

Figure VII.19.h.- Horizontal scan 0.606 z/H below the 1.5- and 3.5-inch backward-facing steps: streamwise and vertical velocity components, number of accepted signal bursts, and statistical stationarity convergence standard deviation.

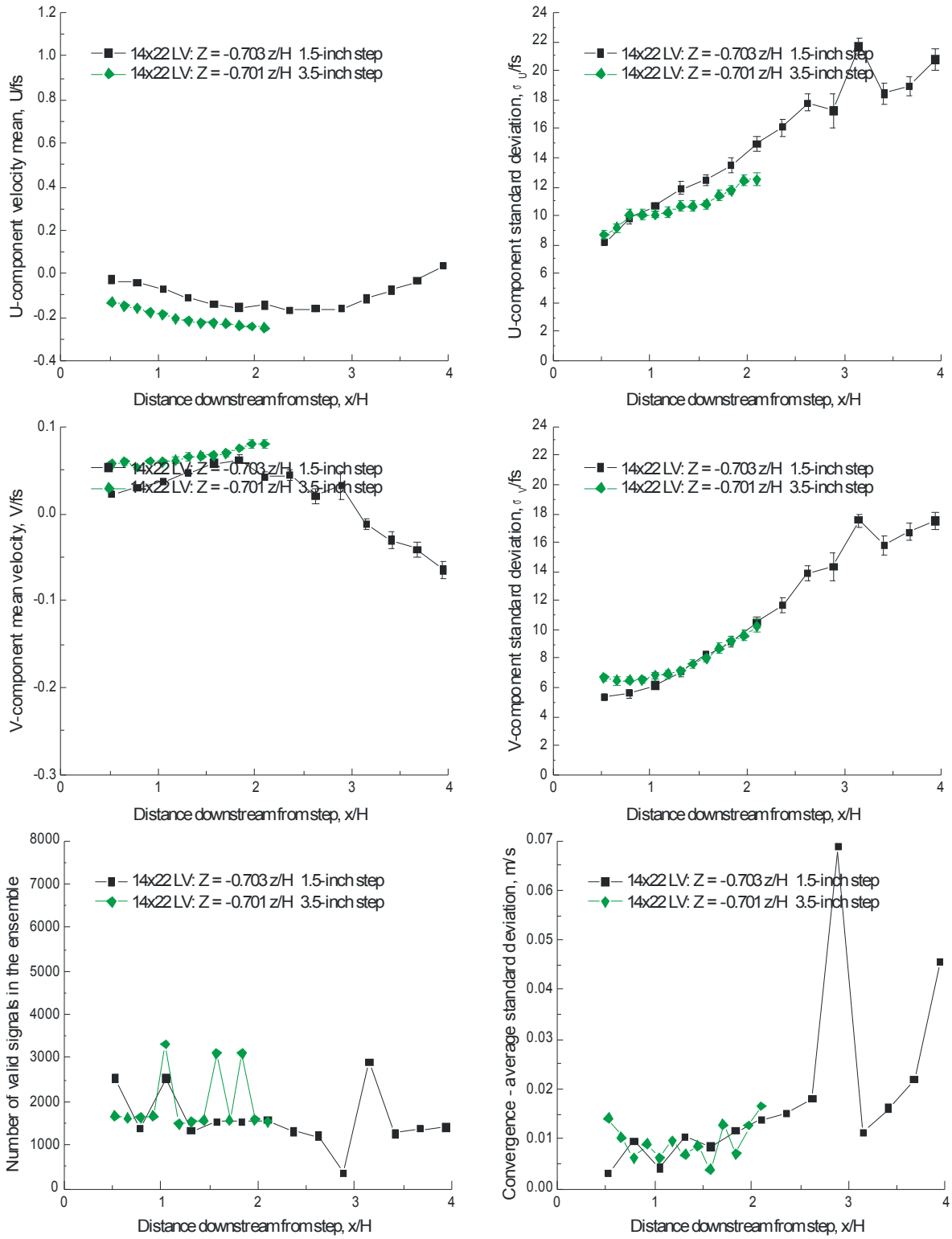

Figure VII.19.i.- Horizontal scan 0.703 z/H below the 1.5- and 3.5-inch backward-facing steps: streamwise and vertical velocity components, number of accepted signal bursts, and statistical stationarity convergence standard deviation.

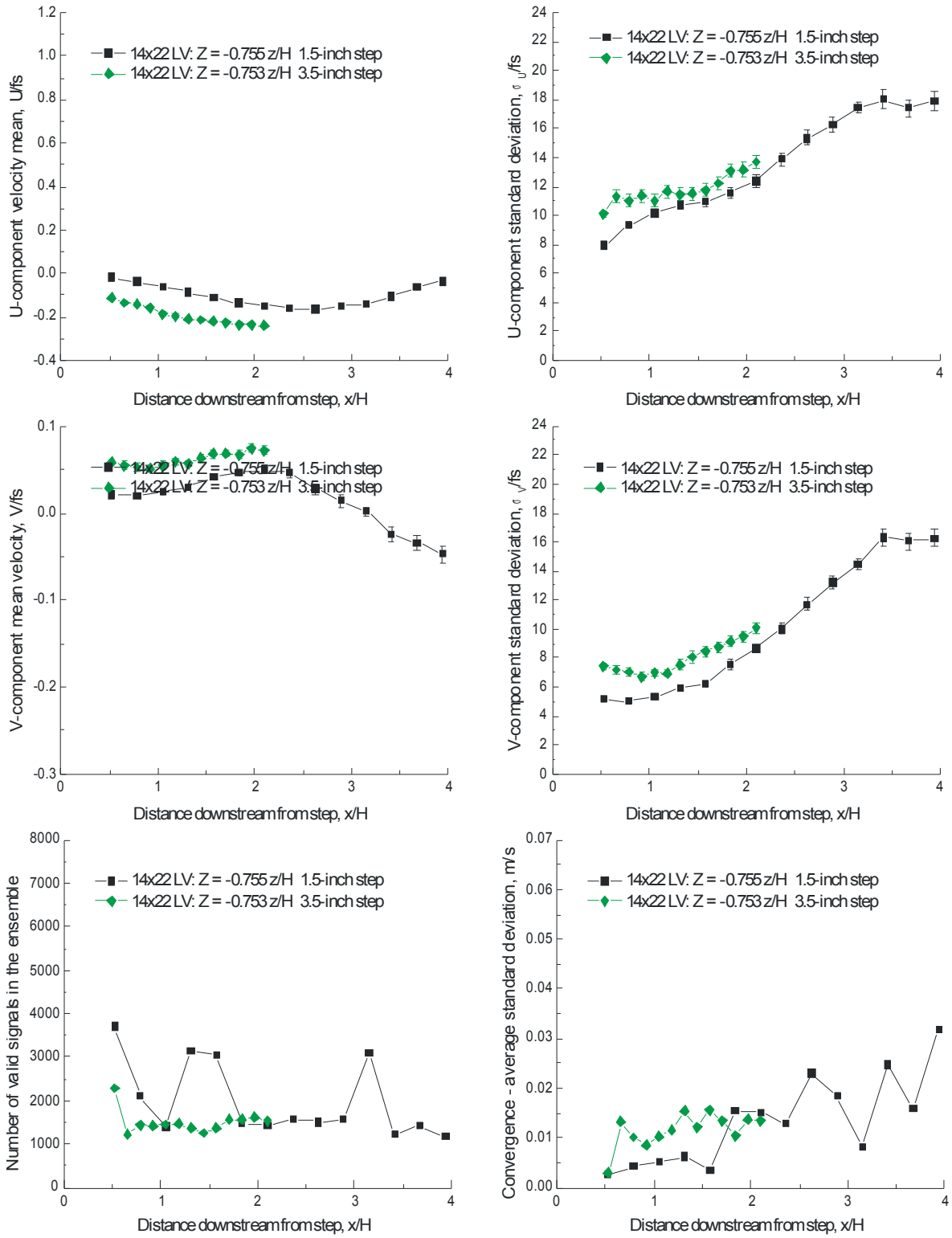

Figure VII.19.j.- Horizontal scan 0.755 z/H below the 1.5- and 3.5-inch backward-facing steps: streamwise and vertical velocity components, number of accepted signal bursts, and statistical stationarity convergence standard deviation.

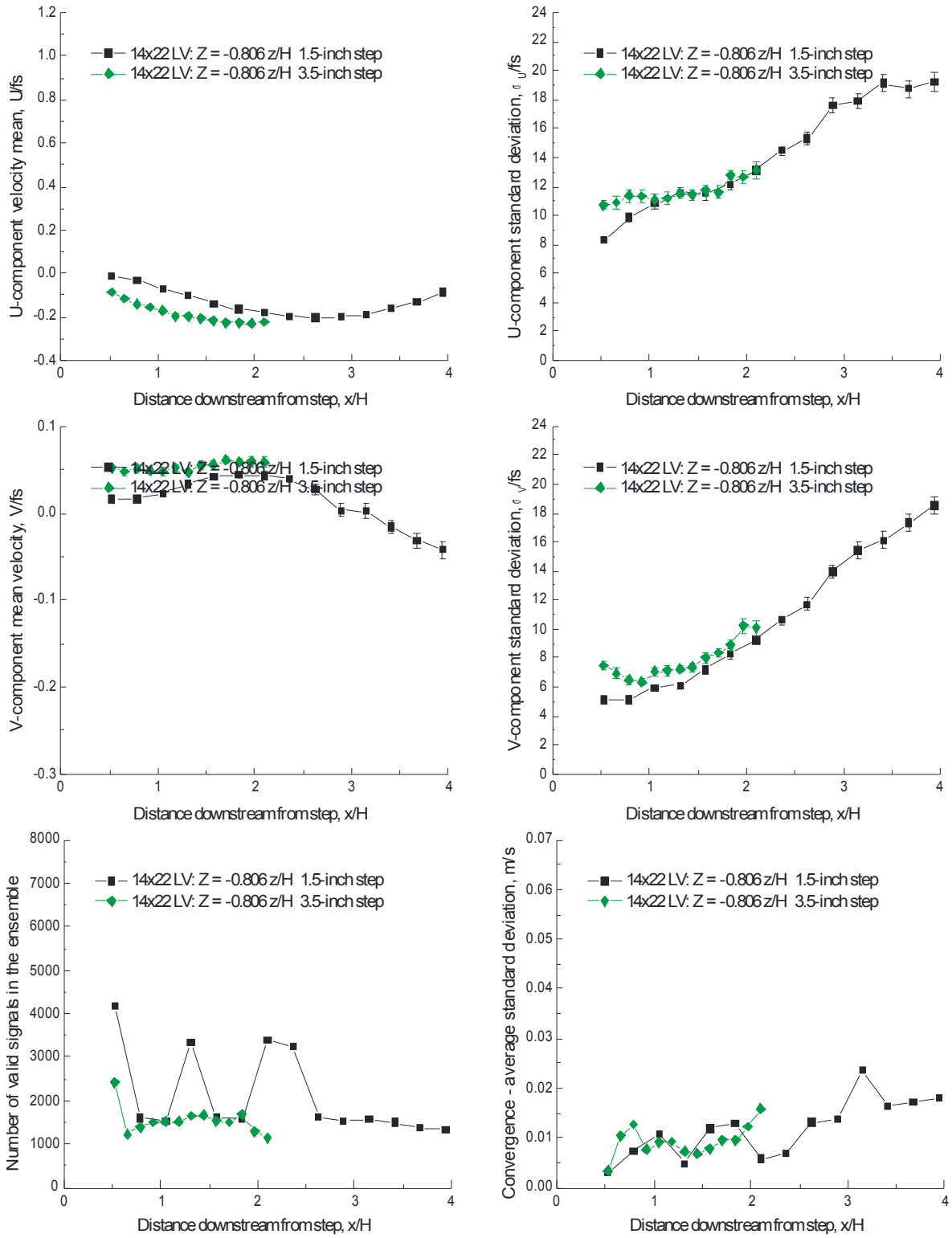

Figure VII.19.k.- Horizontal scan 0.806 z/H below the 1.5- and 3.5-inch backward-facing steps: streamwise and vertical velocity components, number of accepted signal bursts, and statistical stationarity convergence standard deviation.

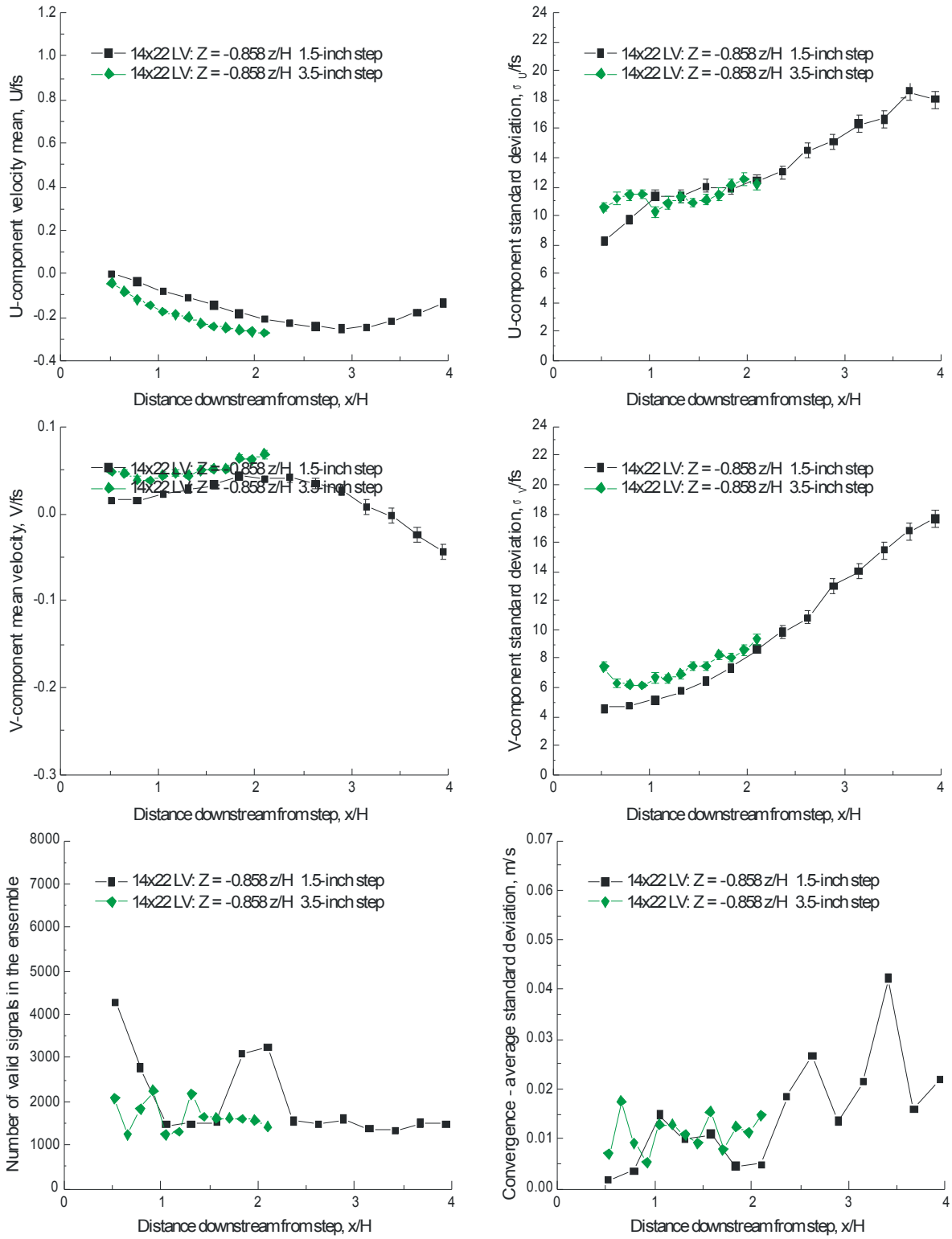

Figure VII.19.l.- Horizontal scan 0.858 z/H below the 1.5- and 3.5-inch backward-facing steps: streamwise and vertical velocity components, number of accepted signal bursts, and statistical stationarity convergence standard deviation.

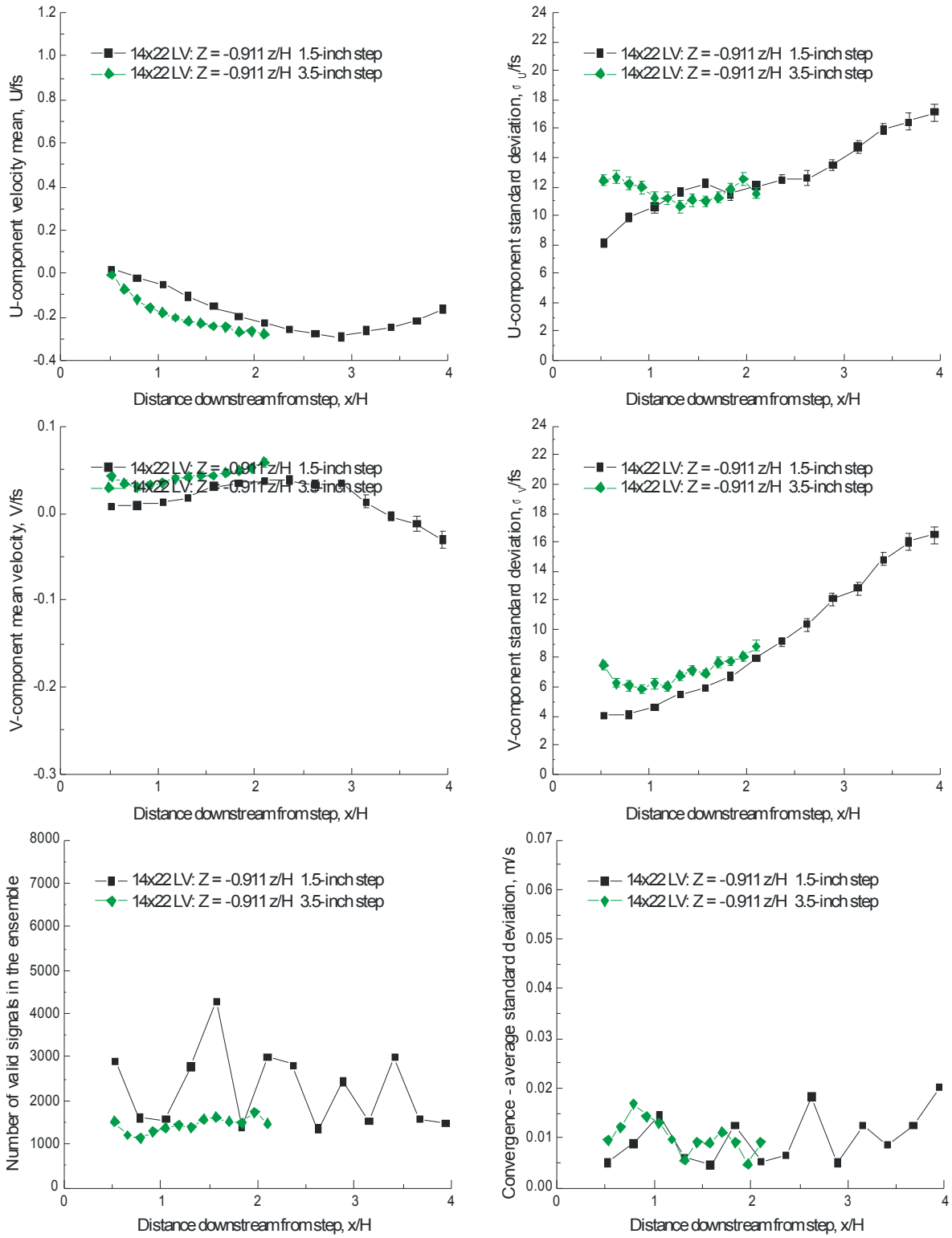

Figure VII.19.m.- Horizontal scan 0.911 z/H below the 1.5- and 3.5-inch backward-facing steps: streamwise and vertical velocity components, number of accepted signal bursts, and statistical stationarity convergence standard deviation.

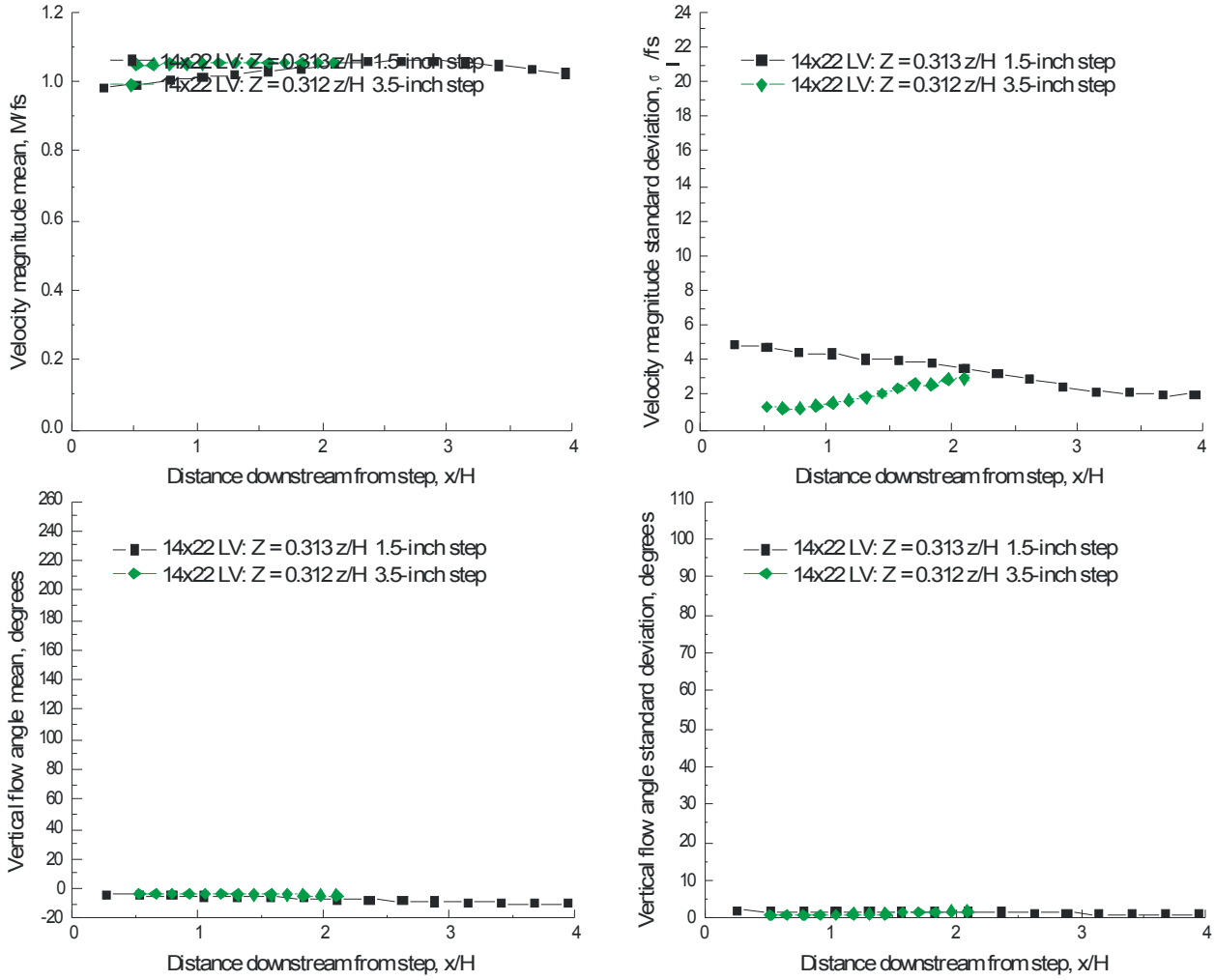

Figure VII.20.a.- Horizontal scan 0.313 z/H above the 1.5- and 3.5-inch backward-facing steps: velocity magnitude and flow angle.

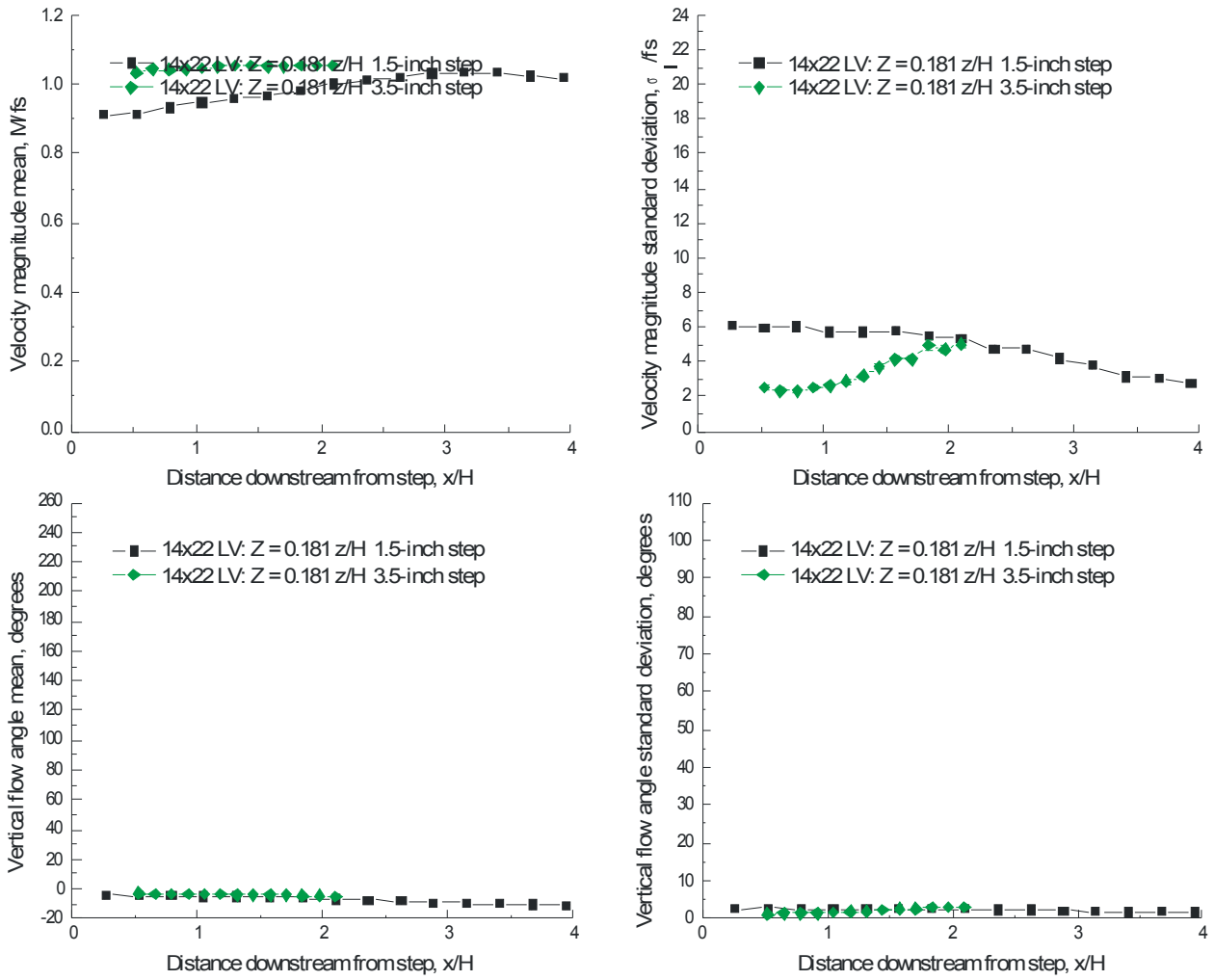

Figure VII.20.b.- Horizontal scan 0.181 z/H above the 1.5- and 3.5-inch backward-facing steps: velocity magnitude and flow angle.

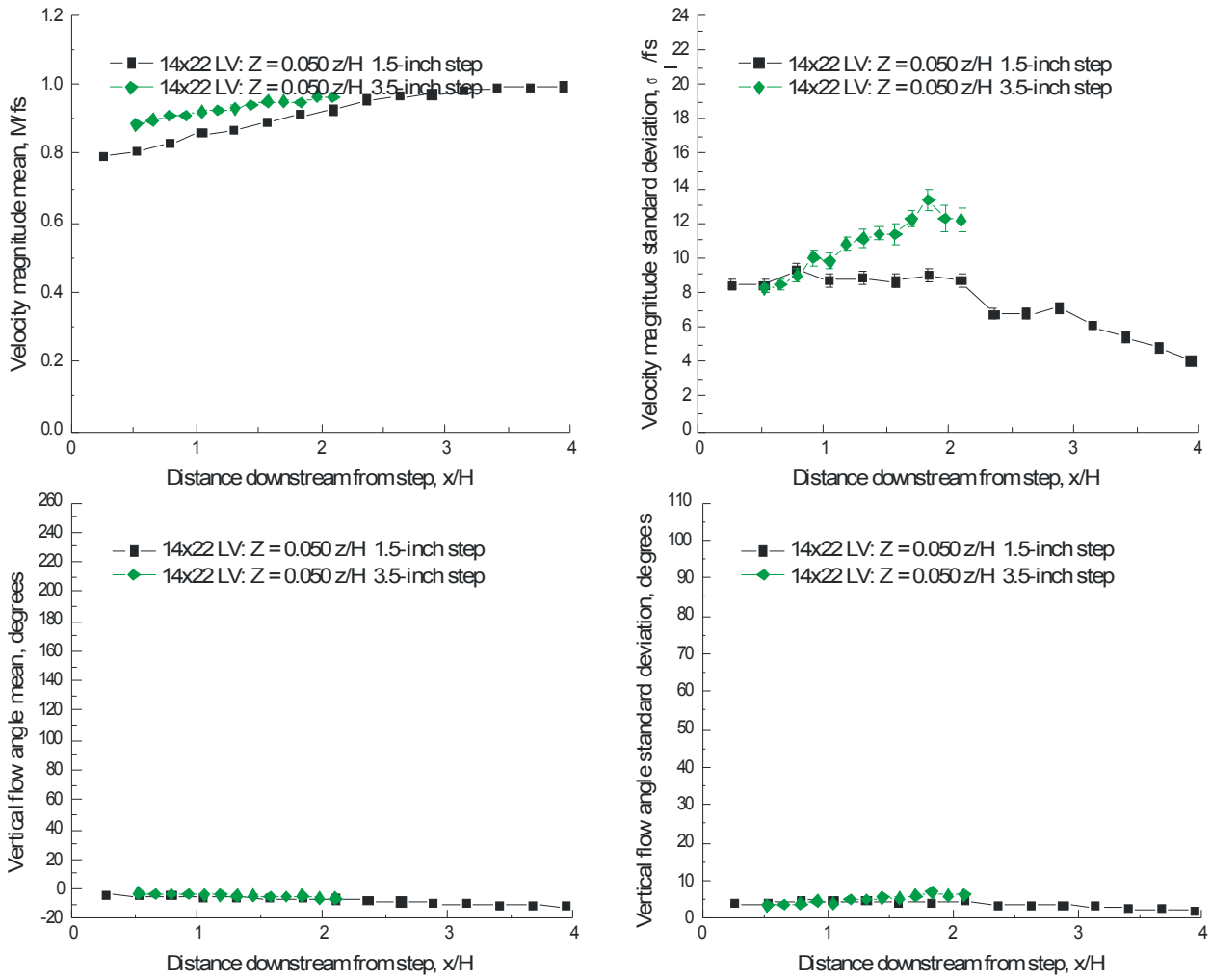

Figure VII.20.c.- Horizontal scan 0.050 z/H above the 1.5- and 3.5-inch backward-facing steps: velocity magnitude and flow angle.

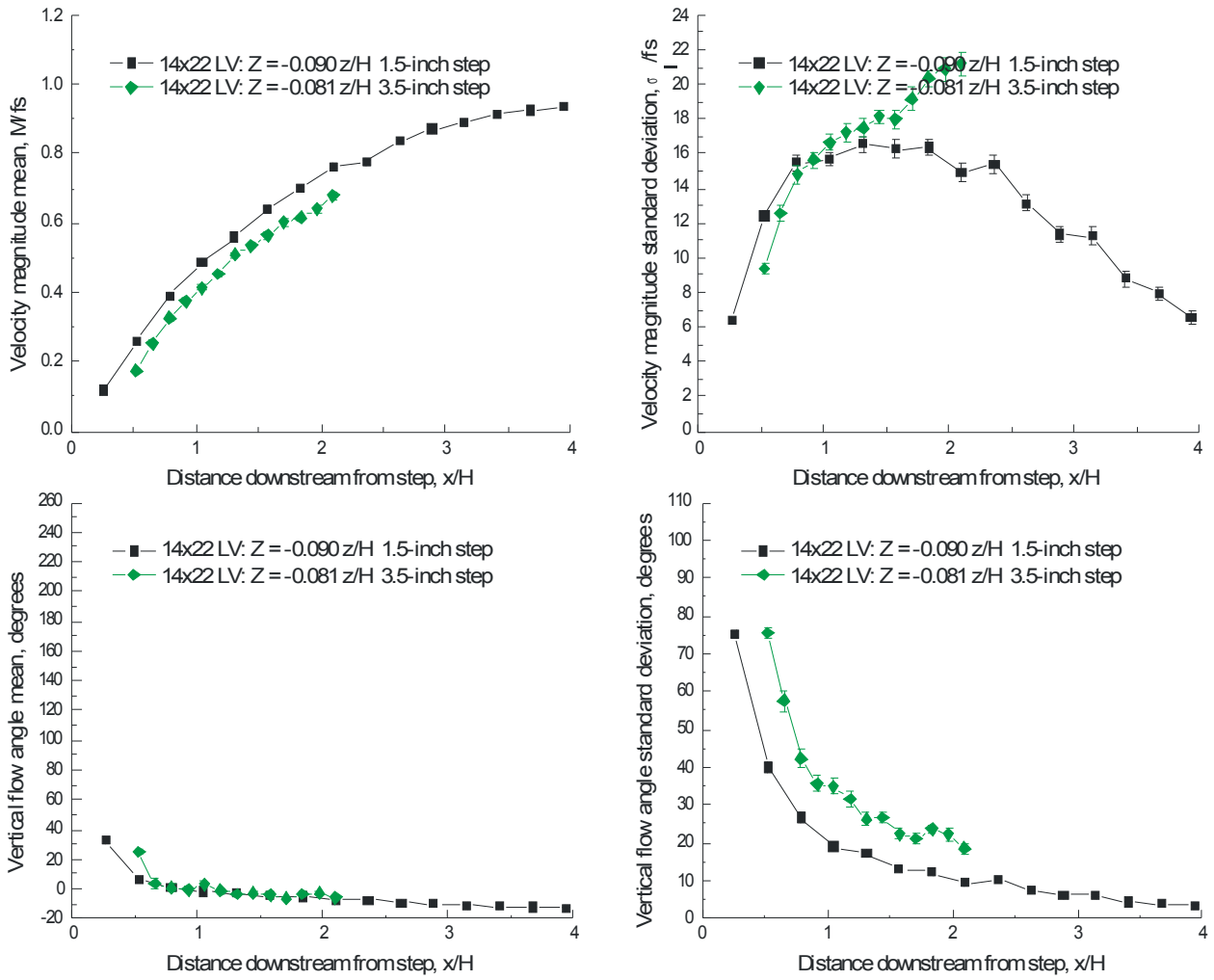

Figure VII.20.d.- Horizontal scan 0.090 z/H below the 1.5- and 3.5-inch backward-facing steps: velocity magnitude and flow angle.

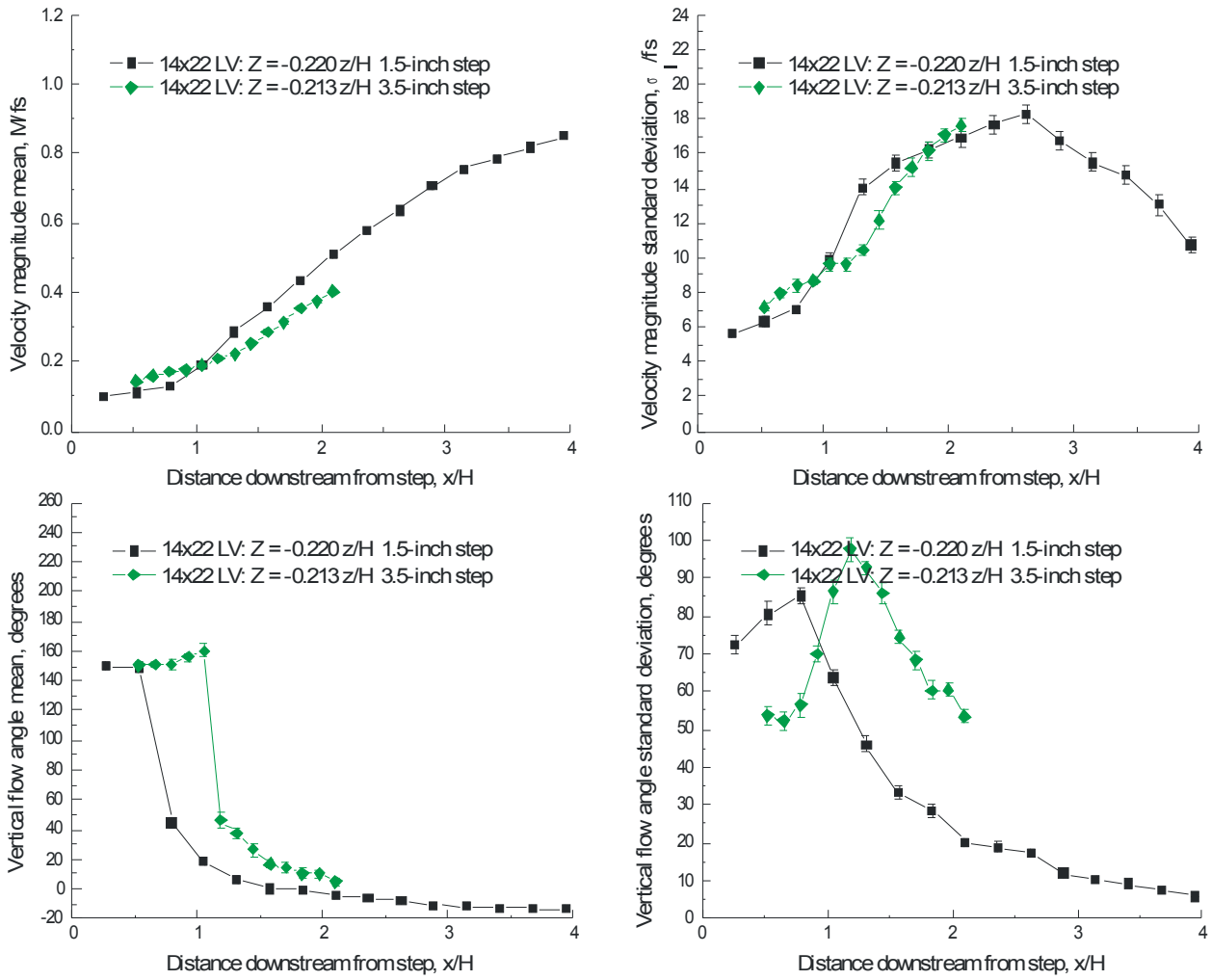

Figure VII.20.e.- Horizontal scan 0.220 z/H below the 1.5- and 3.5-inch backward-facing steps: velocity magnitude and flow angle.

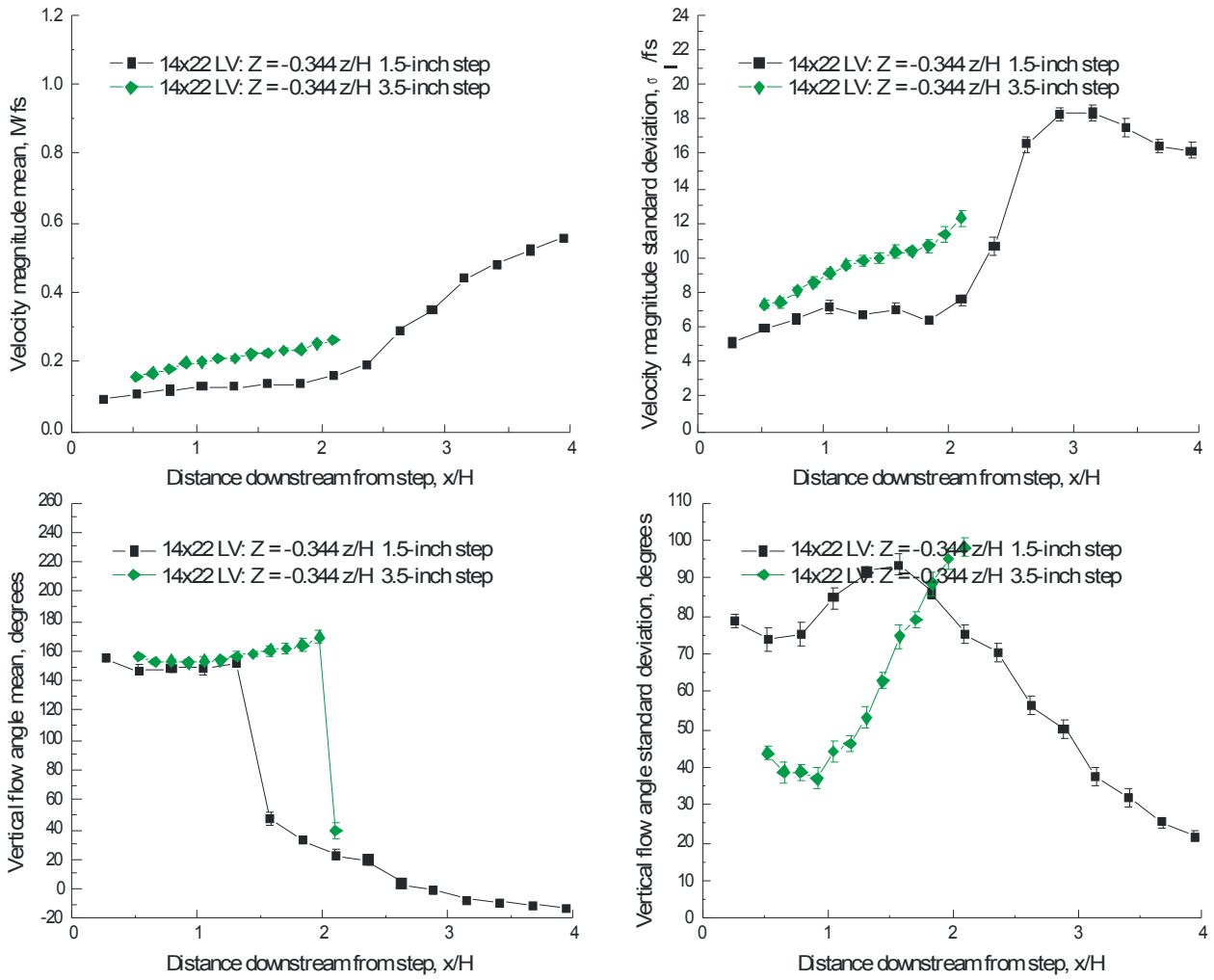

Figure VII.20.f.- Horizontal scan 0.344 z/H below the 1.5- and 3.5-inch backward-facing steps: velocity magnitude and flow angle.

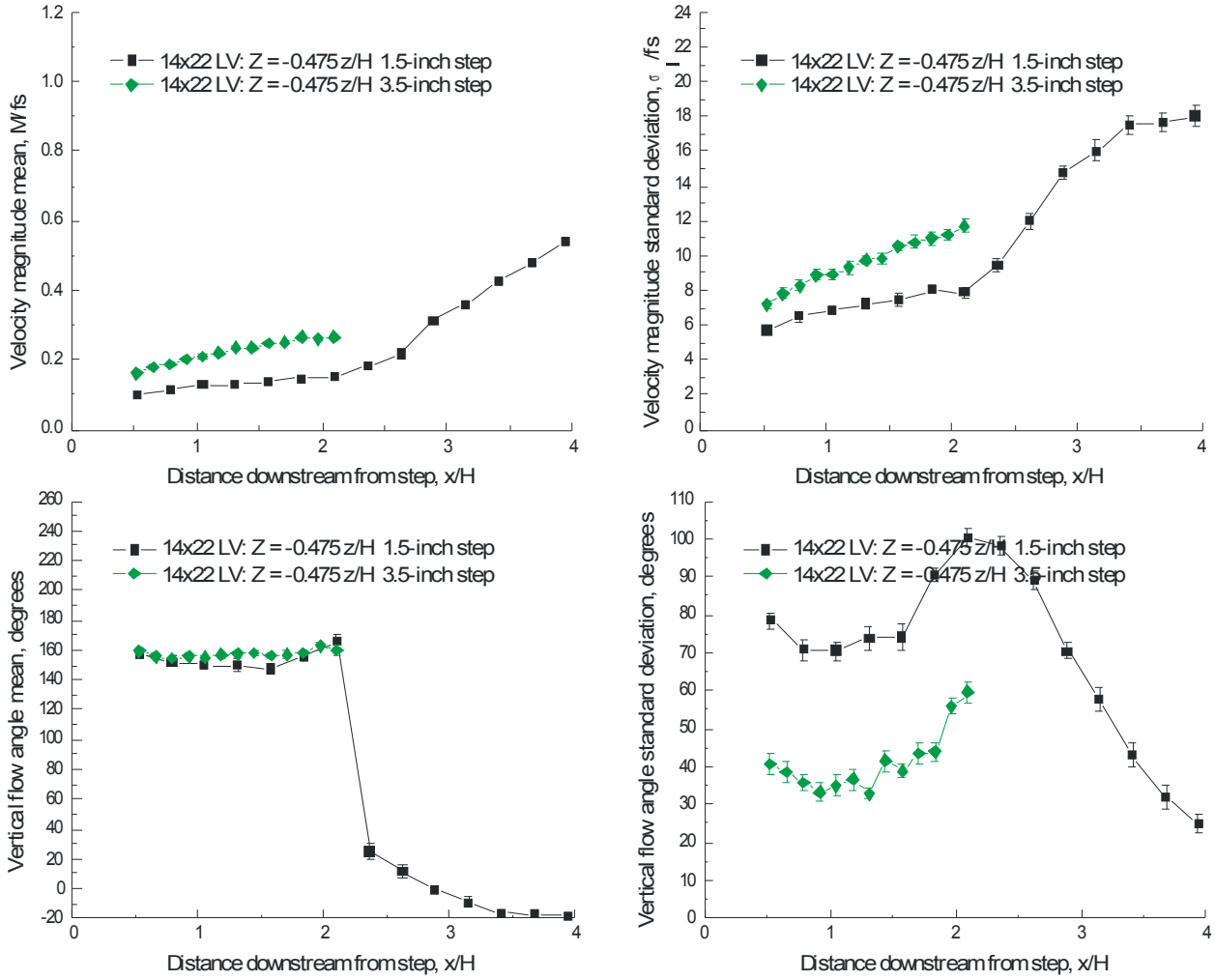

Figure VII.20.g.- Horizontal scan 0.475 z/H below the 1.5- and 3.5-inch backward-facing steps: velocity magnitude and flow angle.

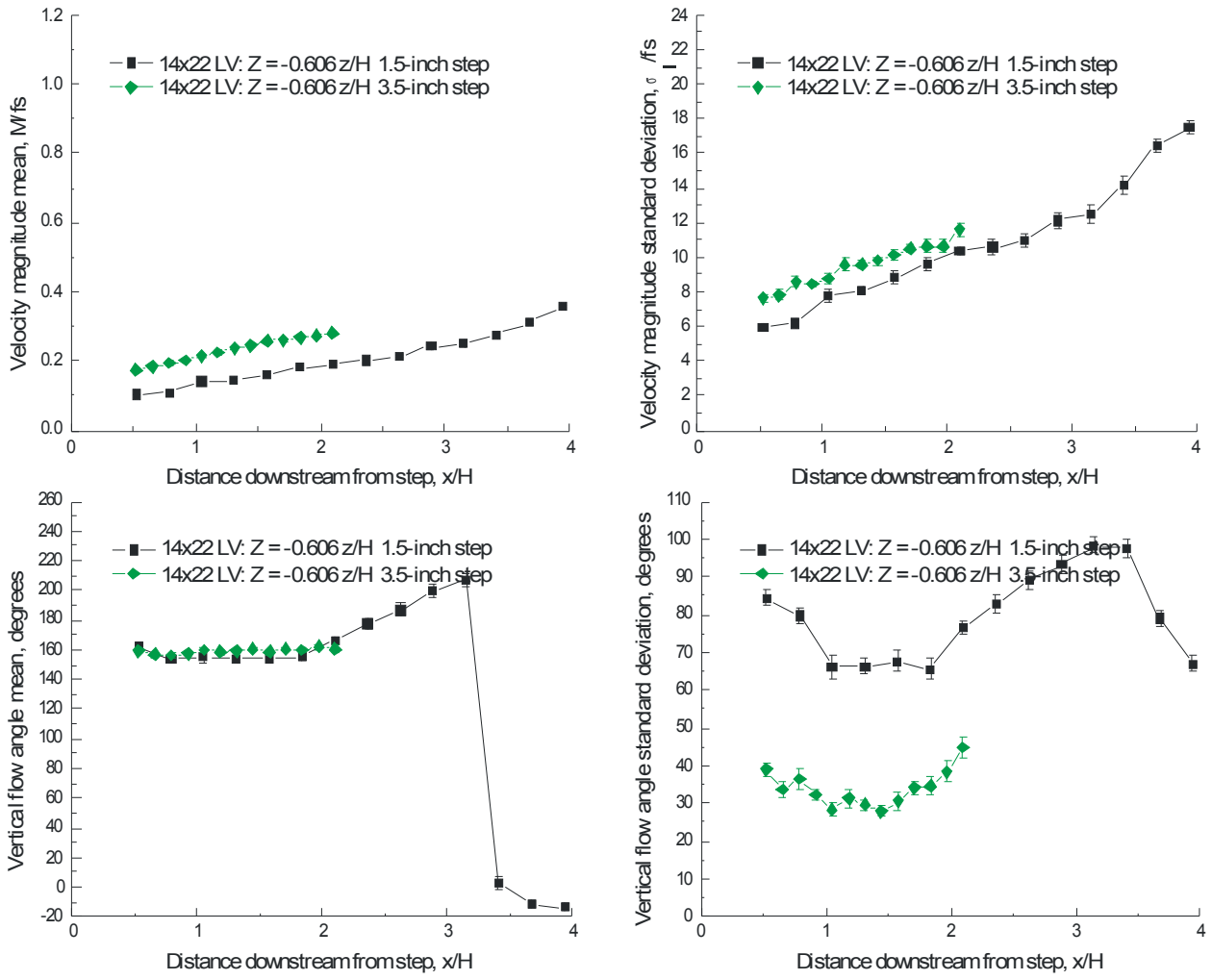

Figure VII.20.h.- Horizontal scan 0.606 z/H below the 1.5- and 3.5-inch backward-facing steps: velocity magnitude and flow angle.

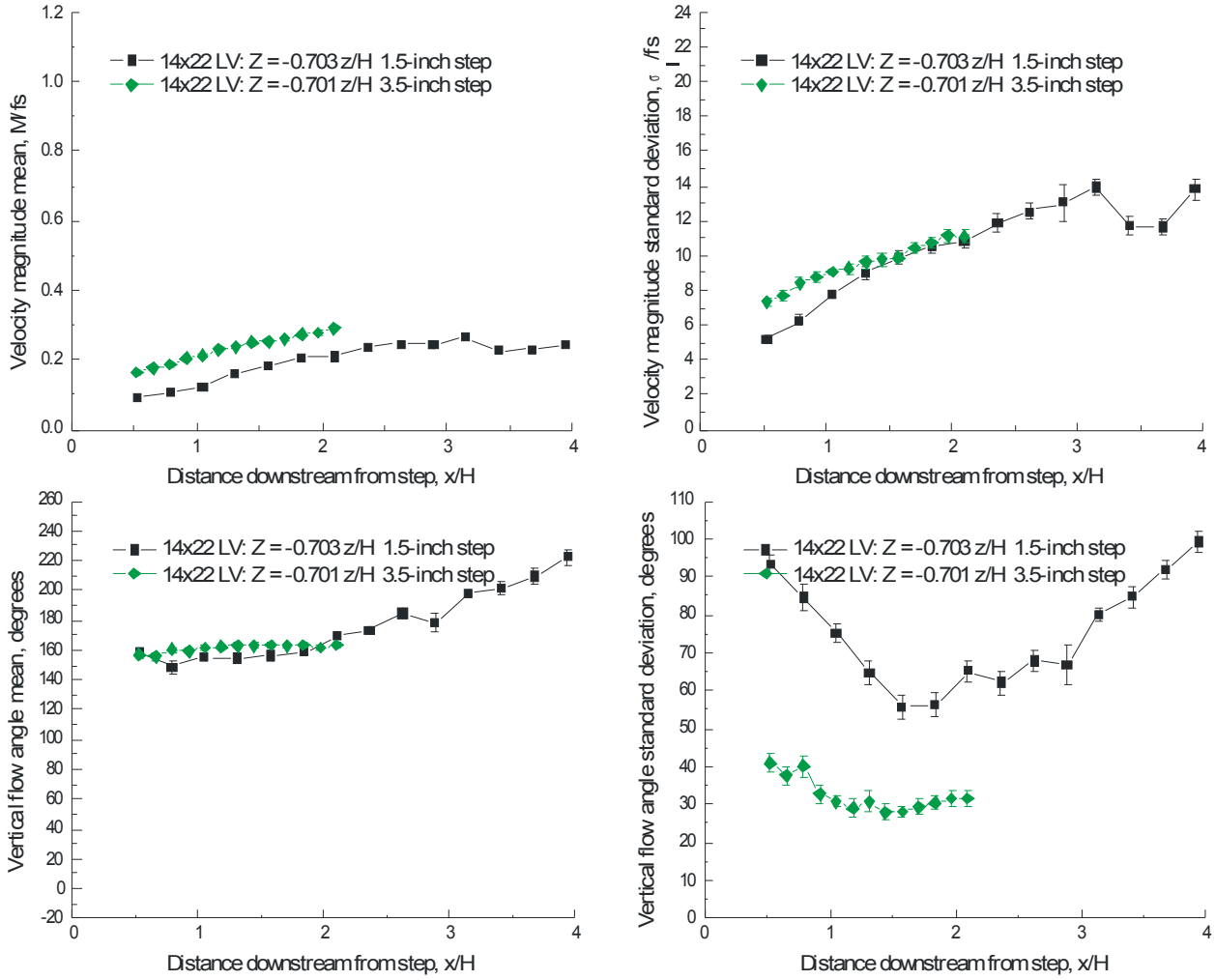

Figure VII.20.i.- Horizontal scan 0.703 z/H below the 1.5- and 3.5-inch backward-facing steps: velocity magnitude and flow angle.

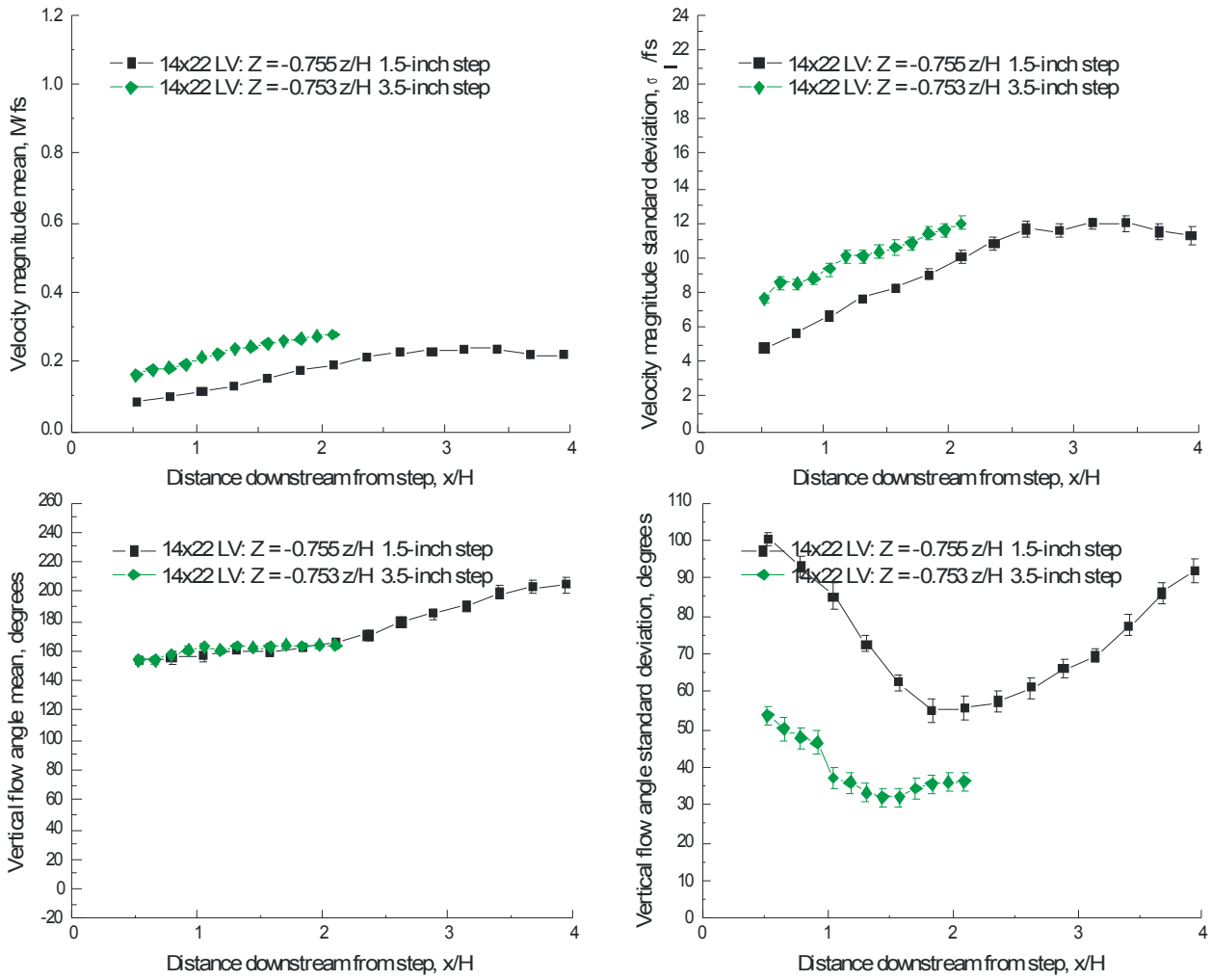

Figure VII.20.j.- Horizontal scan 0.755 z/H below the 1.5- and 3.5-inch backward-facing steps: velocity magnitude and flow angle.

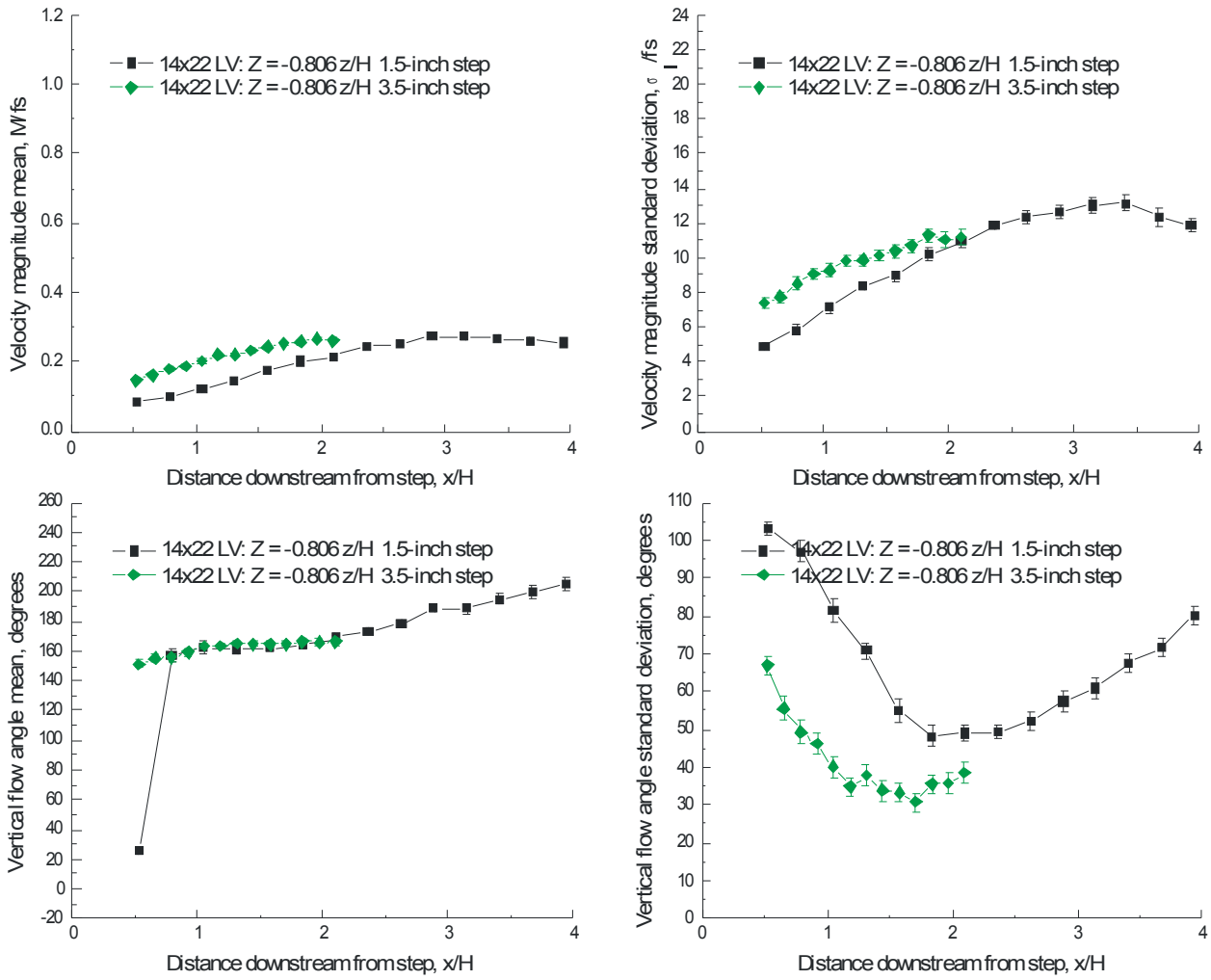

Figure VII.20.k.- Horizontal scan 0.806 z/H below the 1.5- and 3.5-inch backward-facing steps: velocity magnitude and flow angle.

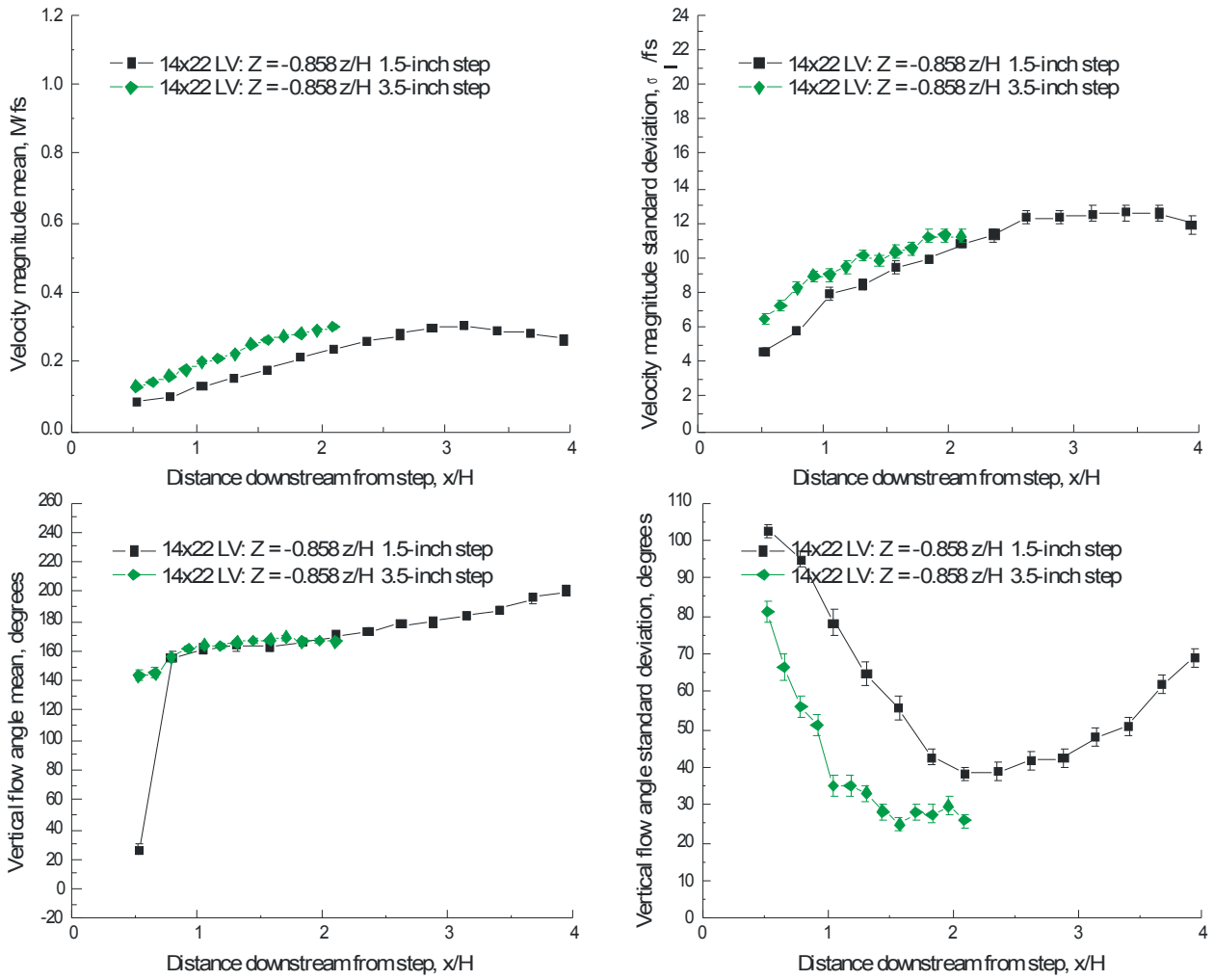

Figure VII.20.l.- Horizontal scan 0.858 z/H below the 1.5- and 3.5-inch backward-facing steps: velocity magnitude and flow angle.

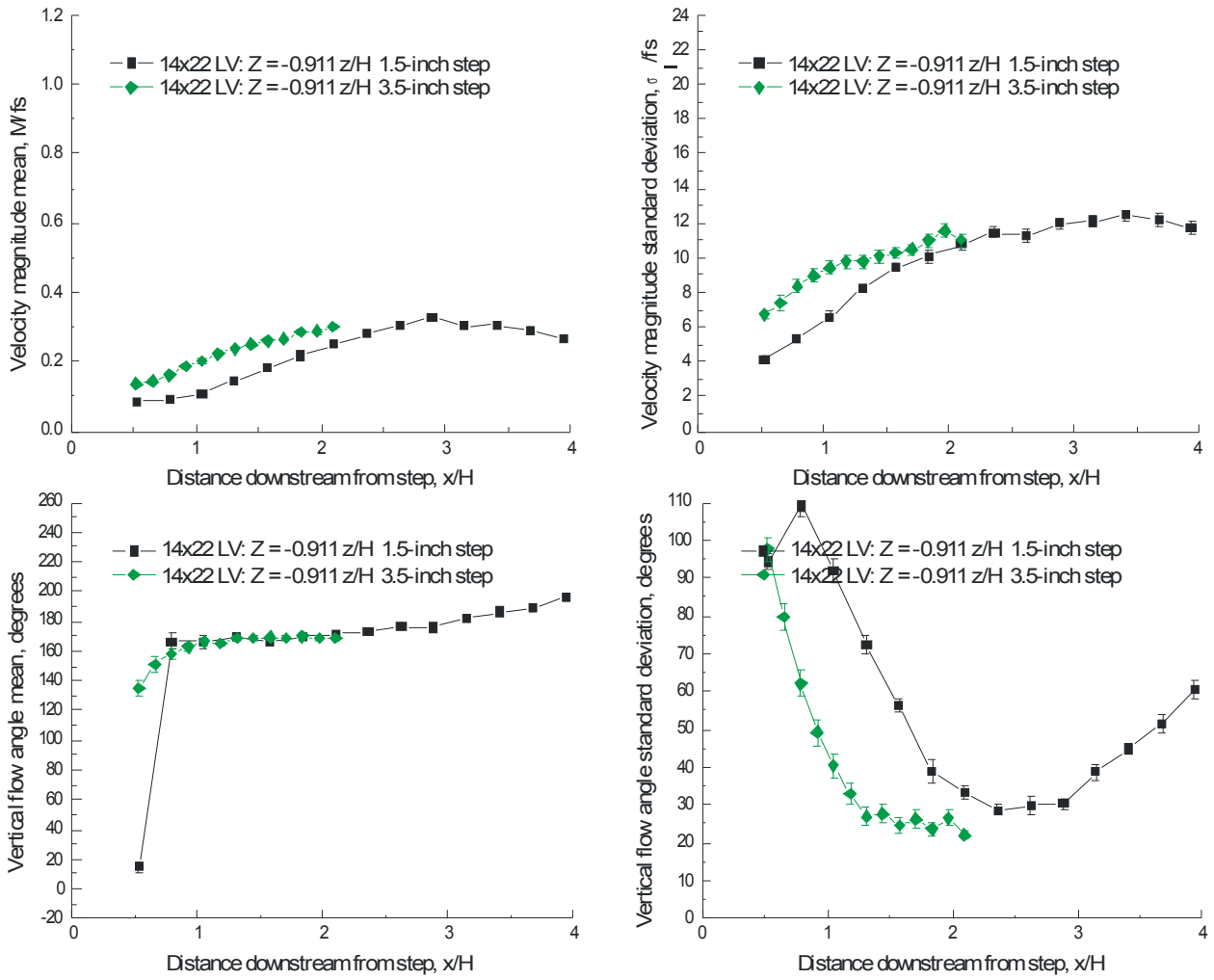

Figure VII.20.m.- Horizontal scan 0.911 z/H below the 1.5- and 3.5-inch backward-facing steps: velocity magnitude and flow angle.

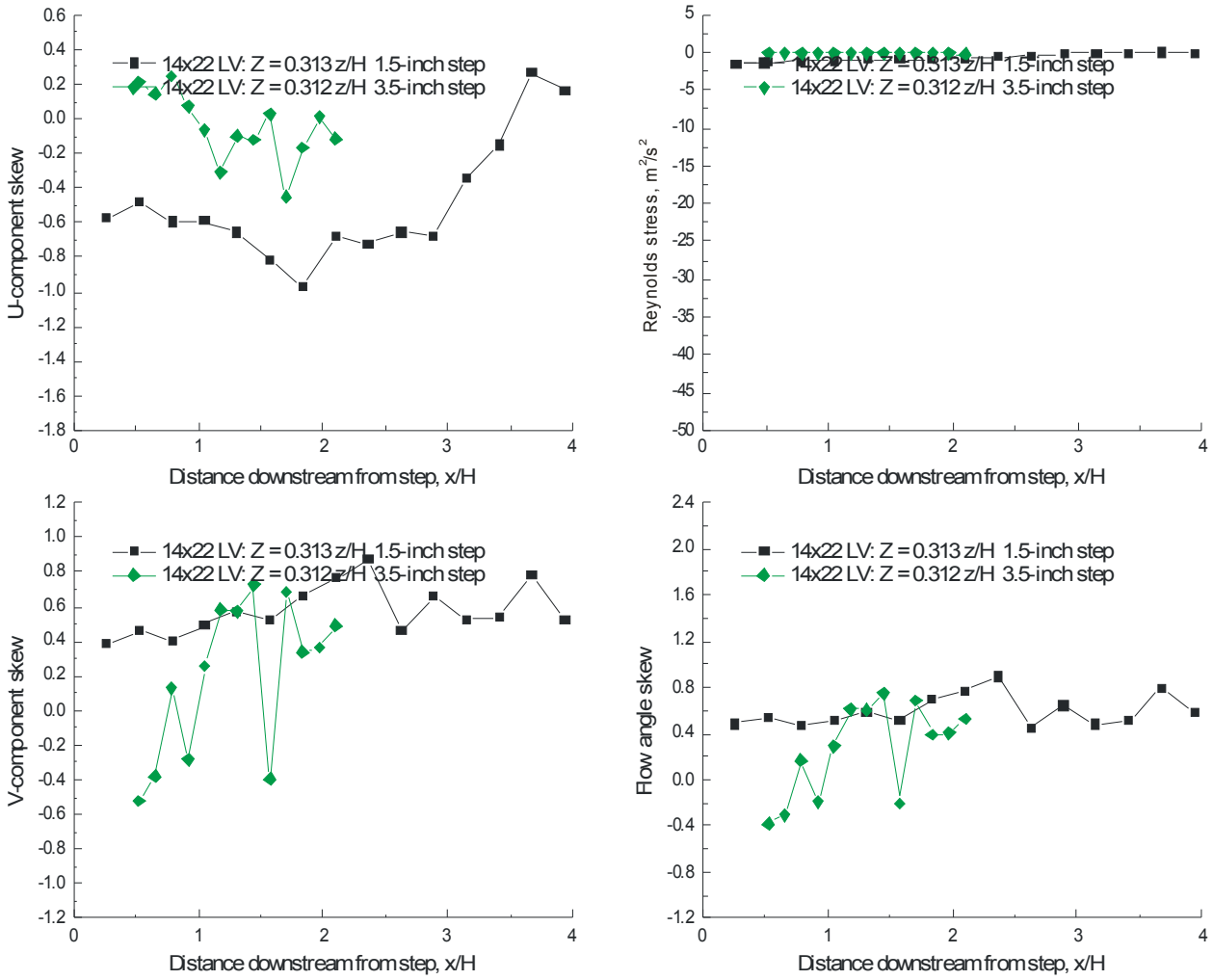

Figure VII.21.a.- Horizontal scan 0.313 z/H below the 1.5- and 3.5-inch backward-facing steps: streamwise and vertical velocity skew, flow angle skew and Reynolds stress.

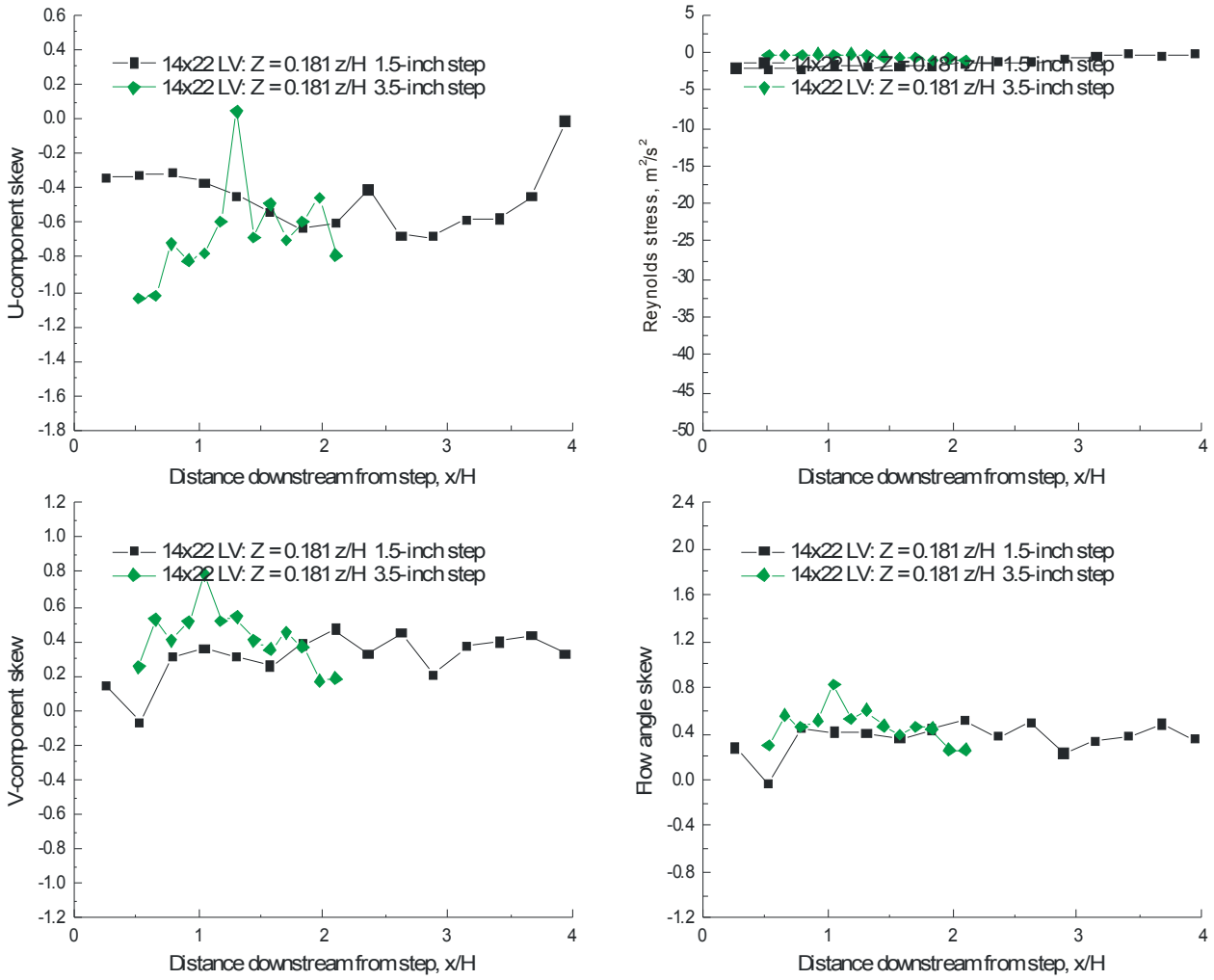

Figure VII.21.b.- Horizontal scan 0.181 z/H above the 1.5- and 3.5-inch backward-facing steps: streamwise and vertical velocity skew, flow angle skew and Reynolds stress.

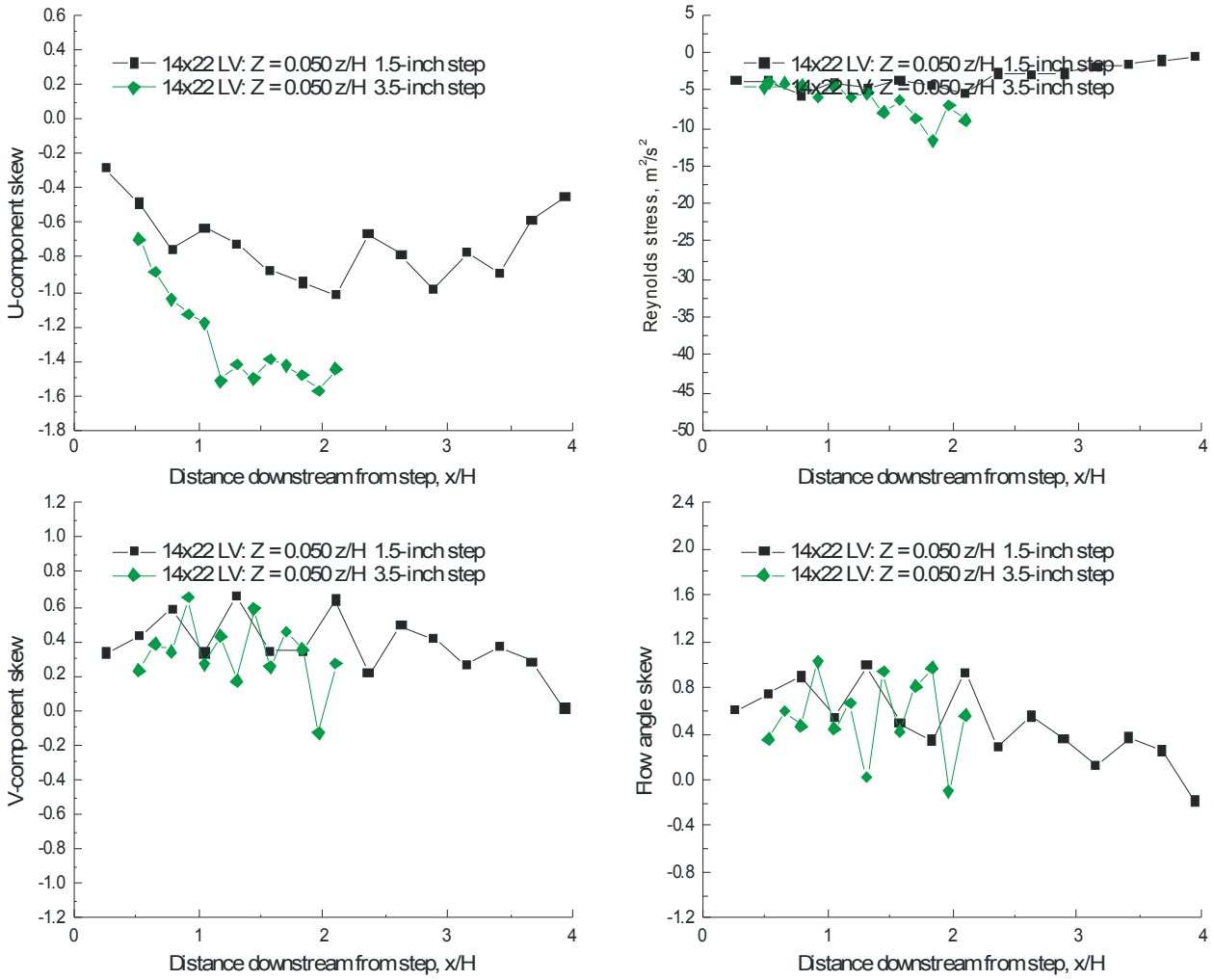

Figure VII.21.c.- Horizontal scan 0.050 z/H above the 1.5- and 3.5-inch backward-facing steps: streamwise and vertical velocity skew, flow angle skew and Reynolds stress.

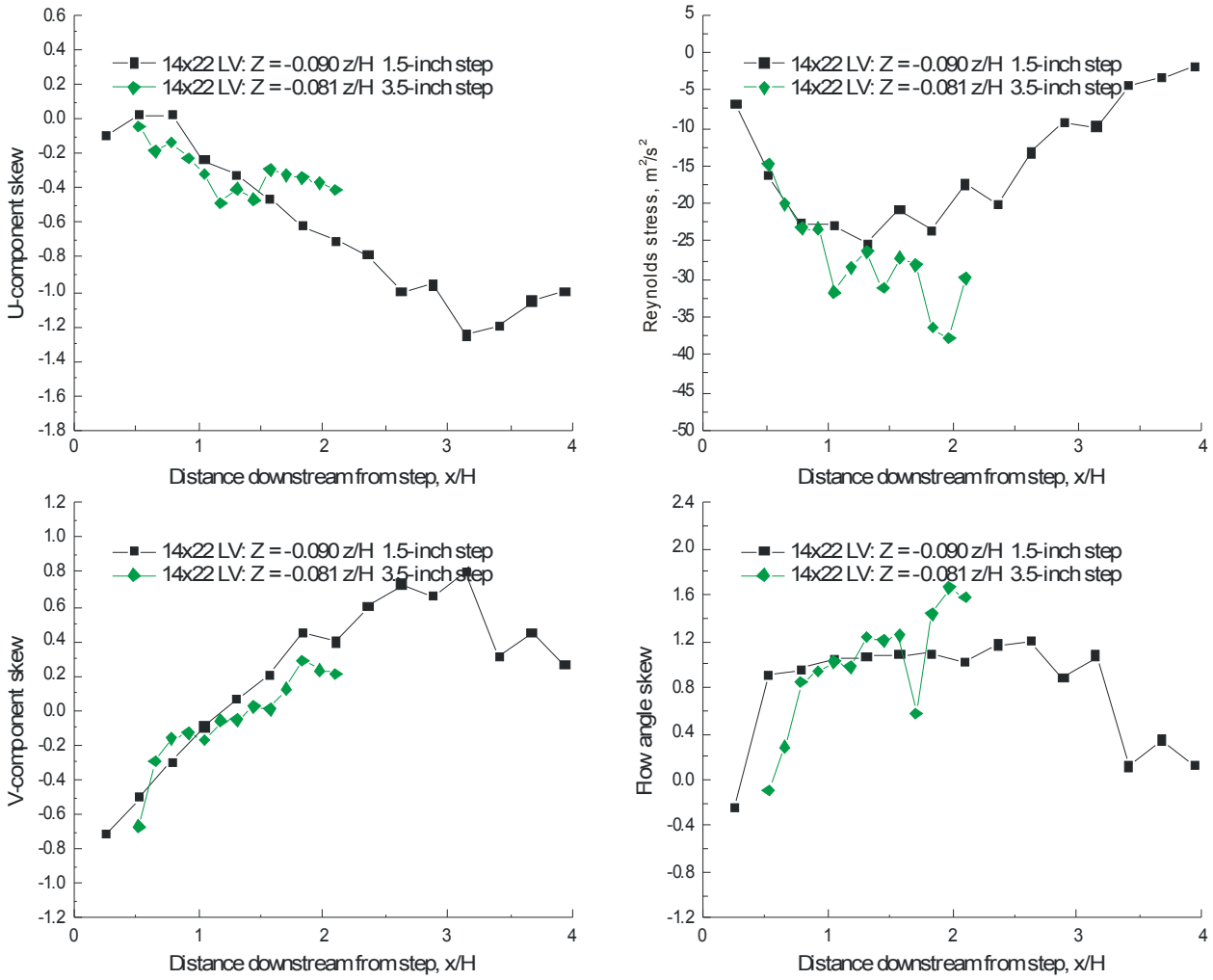

Figure VII.21.d.- Horizontal scan 0.090 z/H below the 1.5- and 3.5-inch backward-facing steps: streamwise and vertical velocity skew, flow angle skew and Reynolds stress.

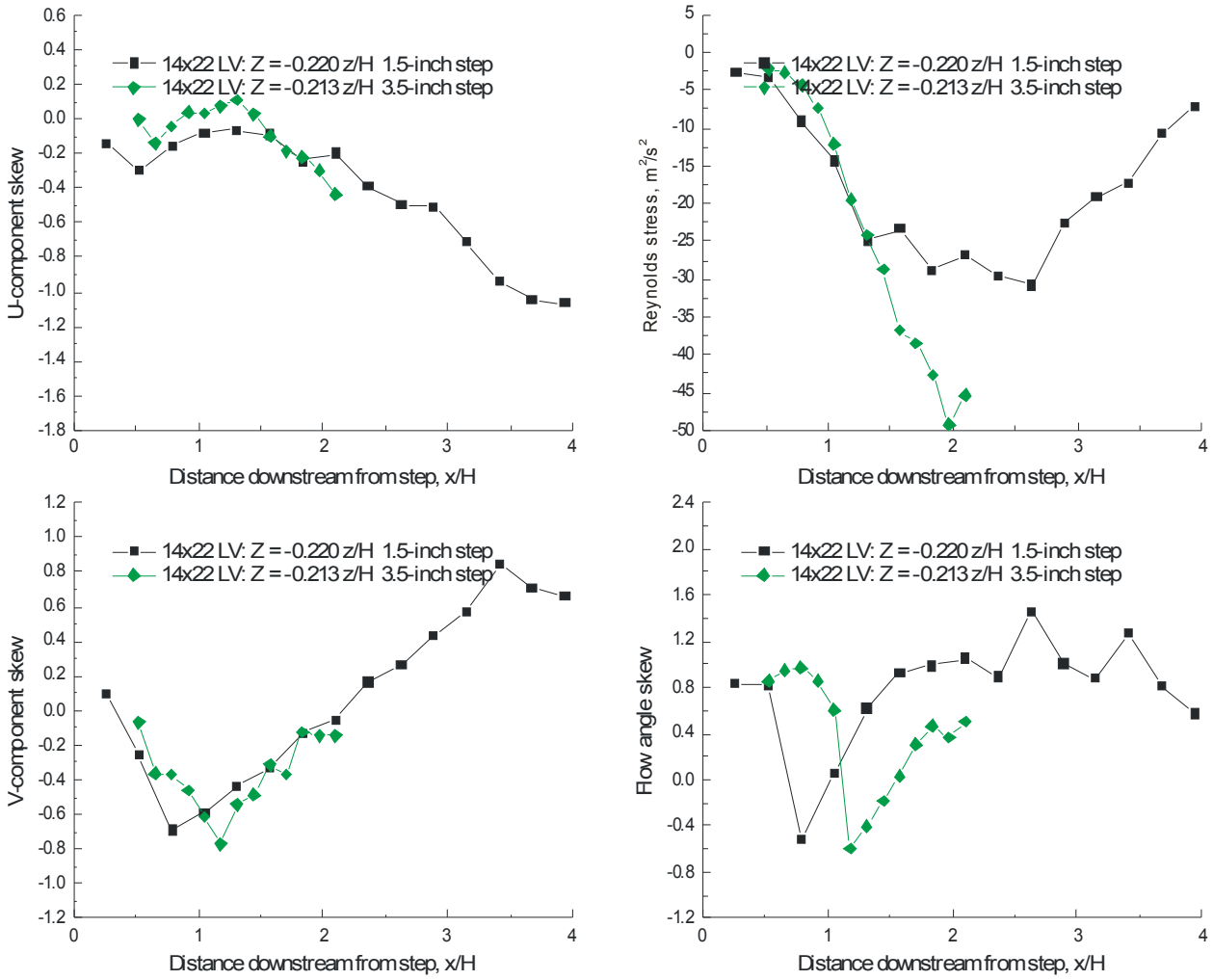

Figure VII.21.e.- Horizontal scan 0.220 z/H below the 1.5- and 3.5-inch backward-facing steps: streamwise and vertical velocity skew, flow angle skew and Reynolds stress.

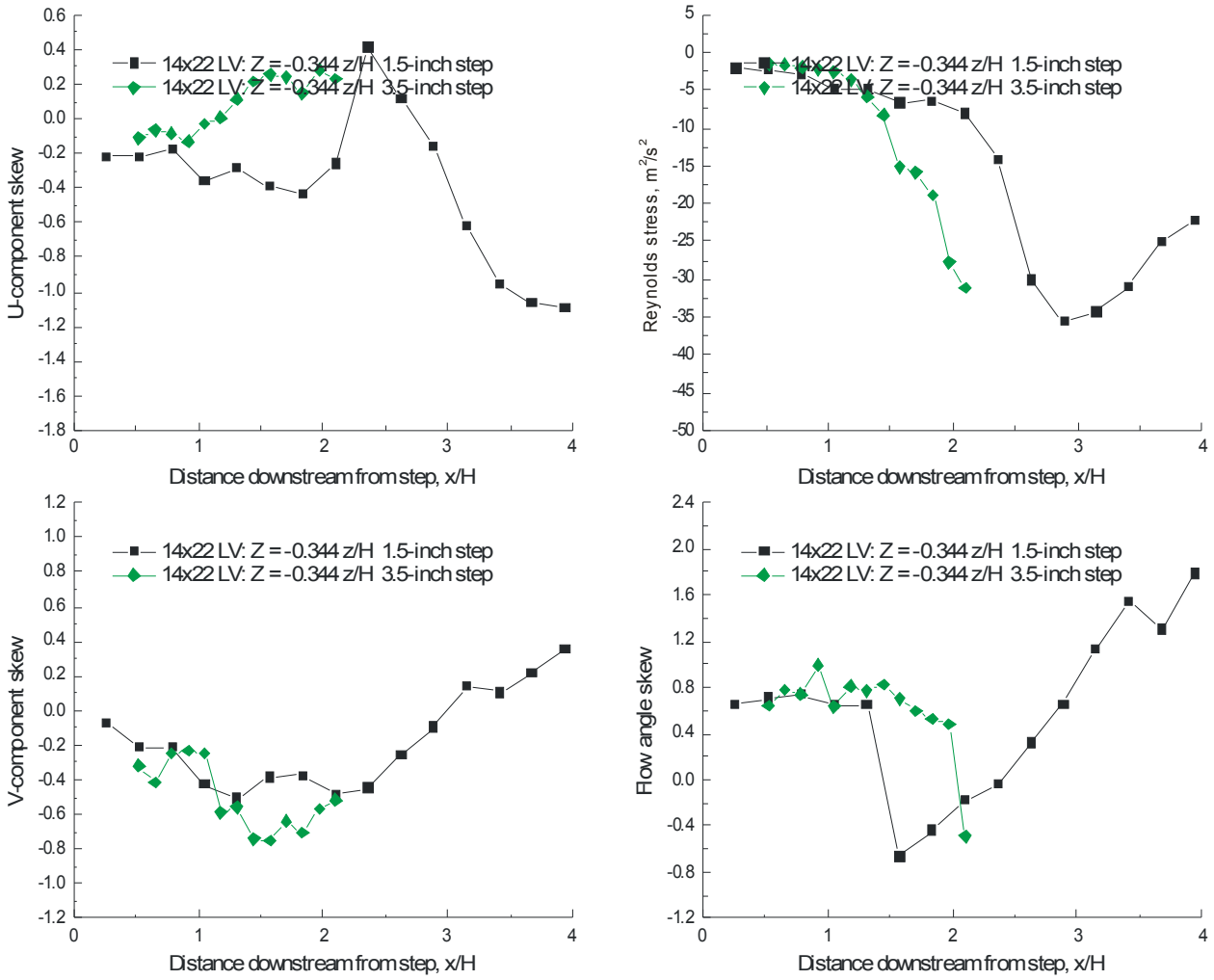

Figure VII.21.f.- Horizontal scan 0.344 z/H below the 1.5- and 3.5-inch backward-facing steps: streamwise and vertical velocity skew, flow angle skew and Reynolds stress.

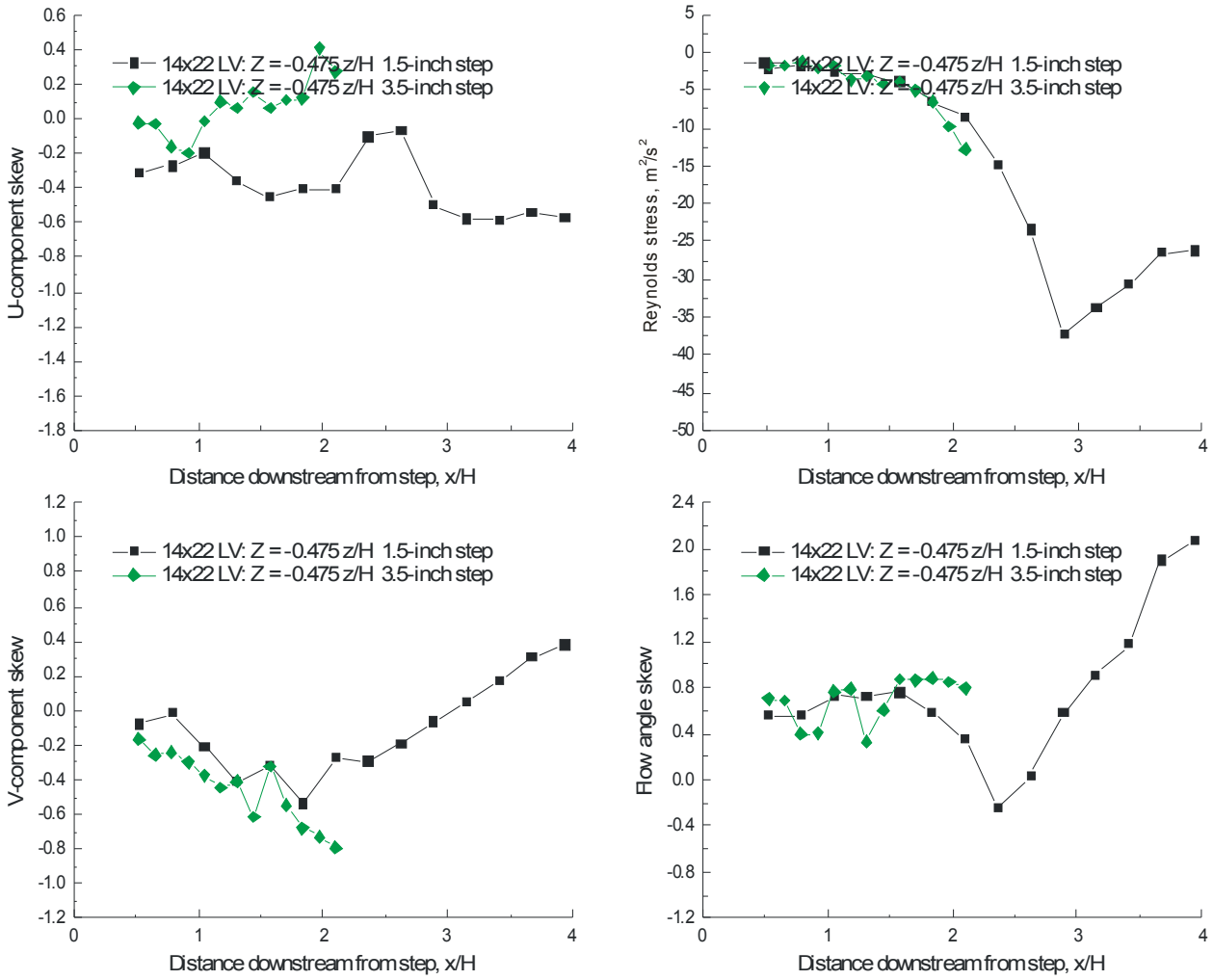

Figure VII.21.g.- Horizontal scan 0.475 z/H below the 1.5- and 3.5-inch backward-facing steps: streamwise and vertical velocity skew, flow angle skew and Reynolds stress.

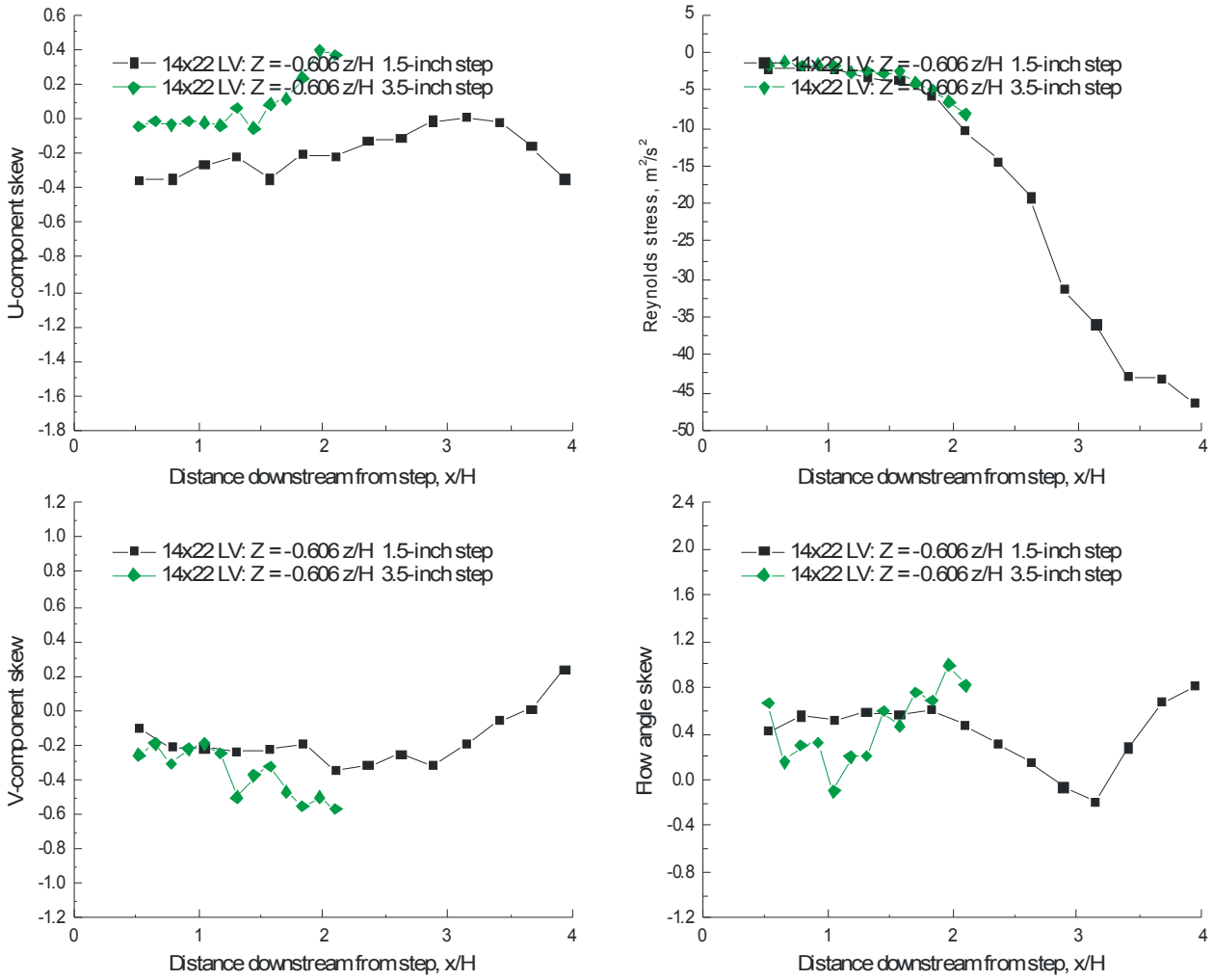

Figure VII.21.h.- Horizontal scan 0.606 z/H below the 1.5- and 3.5-inch backward-facing steps: streamwise and vertical velocity skew, flow angle skew and Reynolds stress.

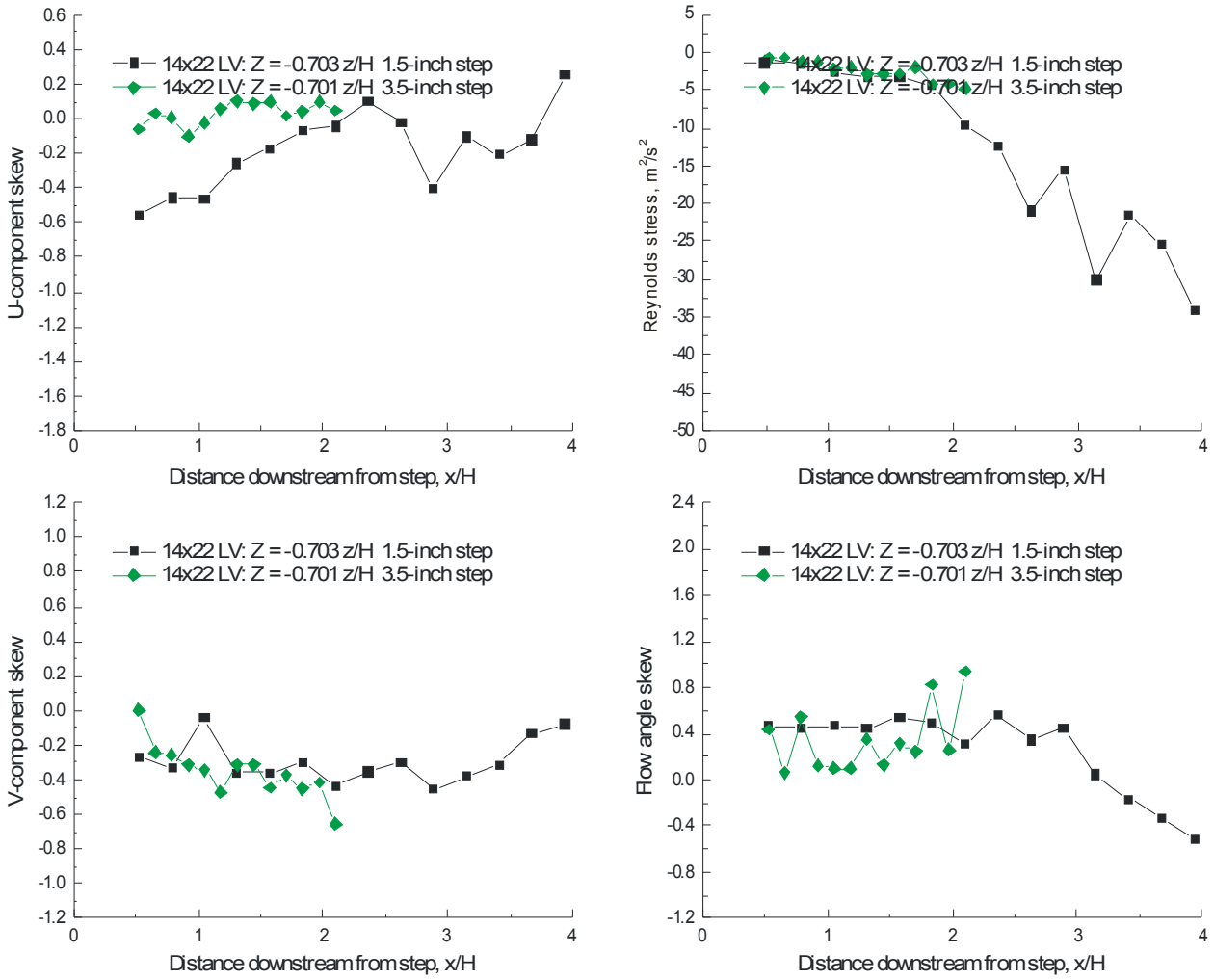

Figure VII.21.i.- Horizontal scan 0.703 z/H below the 1.5- and 3.5-inch backward-facing steps: streamwise and vertical velocity skew, flow angle skew and Reynolds stress.

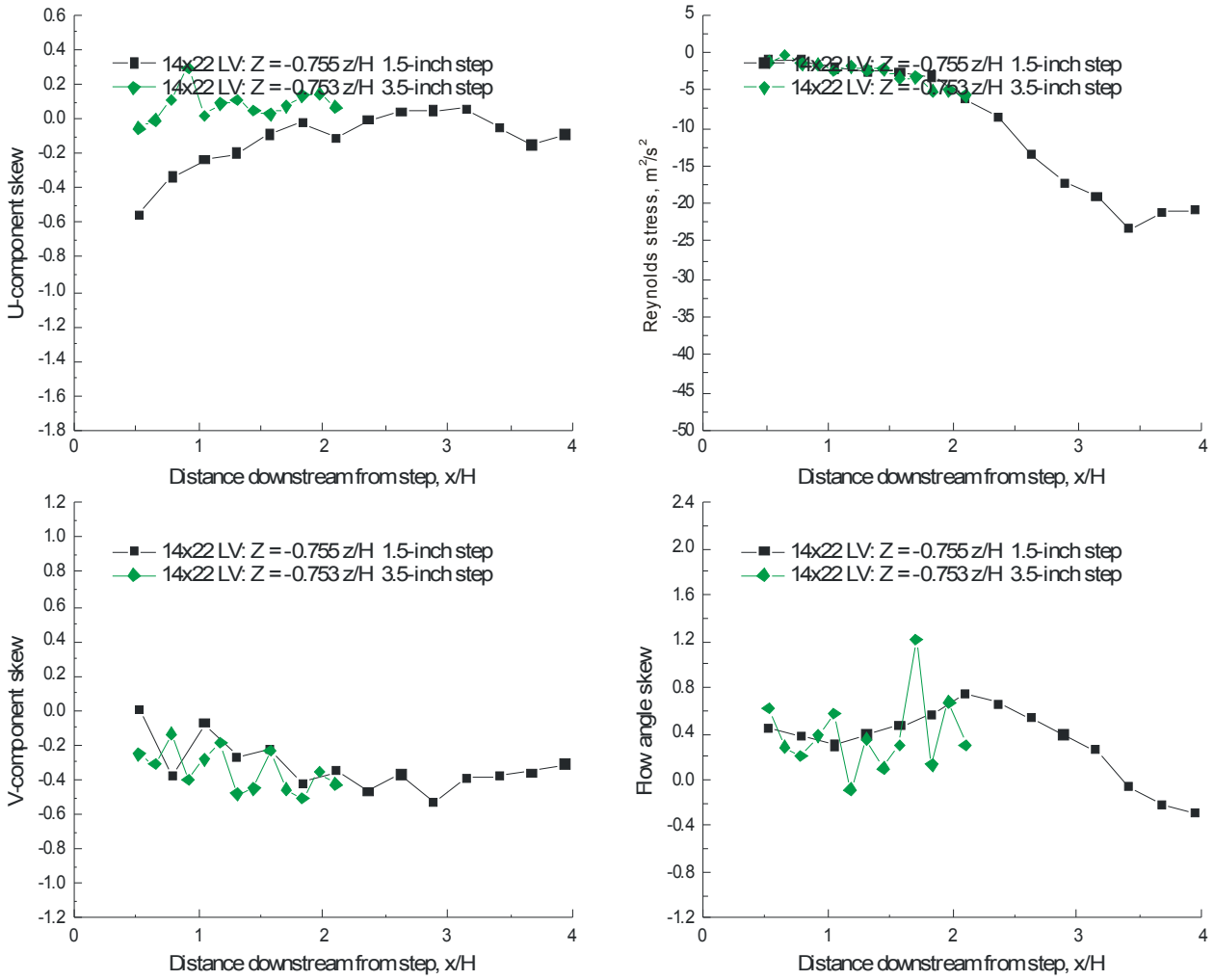

Figure VII.21.j.- Horizontal scan 0.755 z/H below the 1.5- and 3.5-inch backward-facing steps: streamwise and vertical velocity skew, flow angle skew and Reynolds stress.

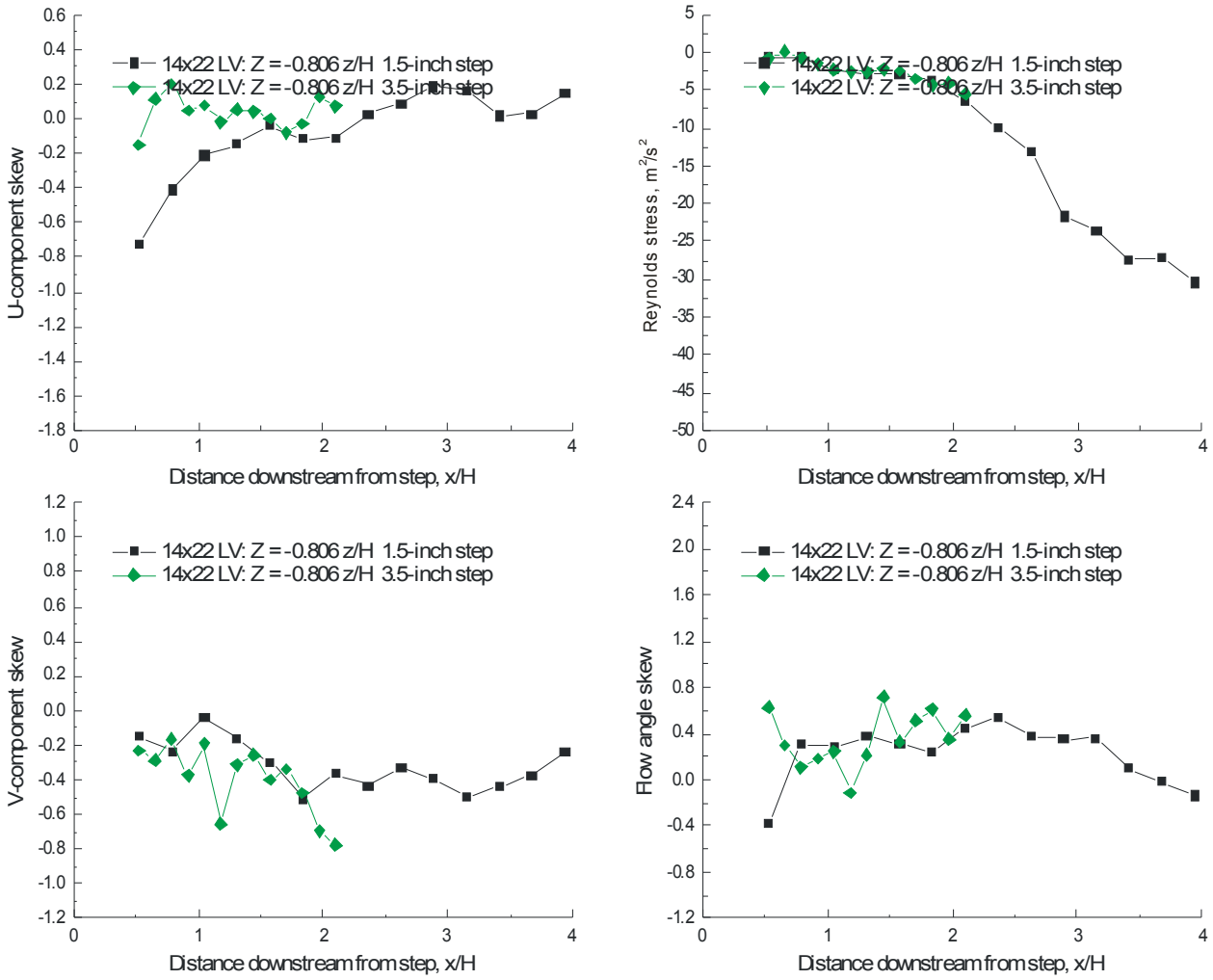

Figure VII.21.k.- Horizontal scan 0.806 z/H below the 1.5- and 3.5-inch backward-facing steps: streamwise and vertical velocity skew, flow angle skew and Reynolds stress.

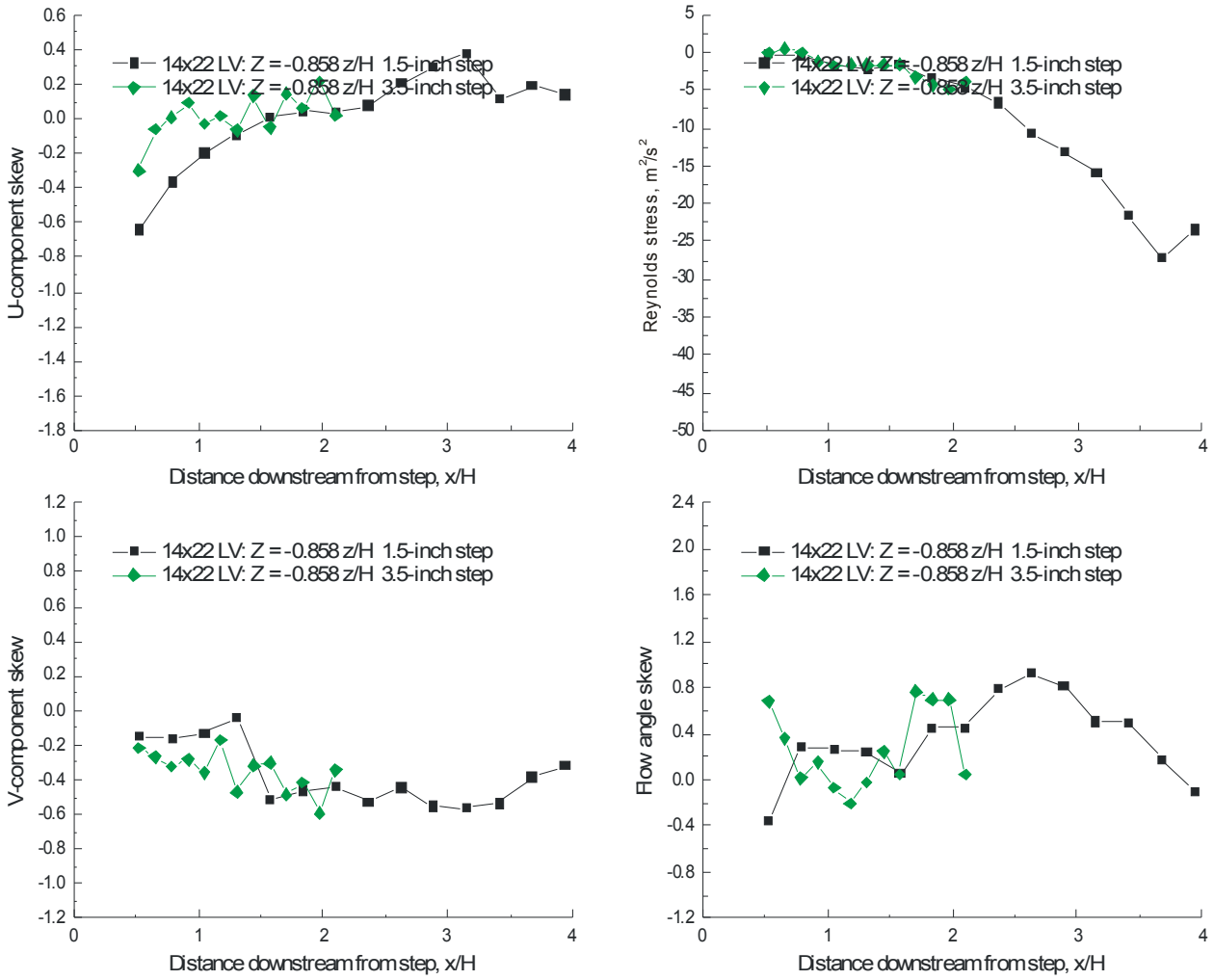

Figure VII.21.l.- Horizontal scan 0.858 z/H below the 1.5- and 3.5-inch backward-facing steps: streamwise and vertical velocity skew, flow angle skew and Reynolds stress.

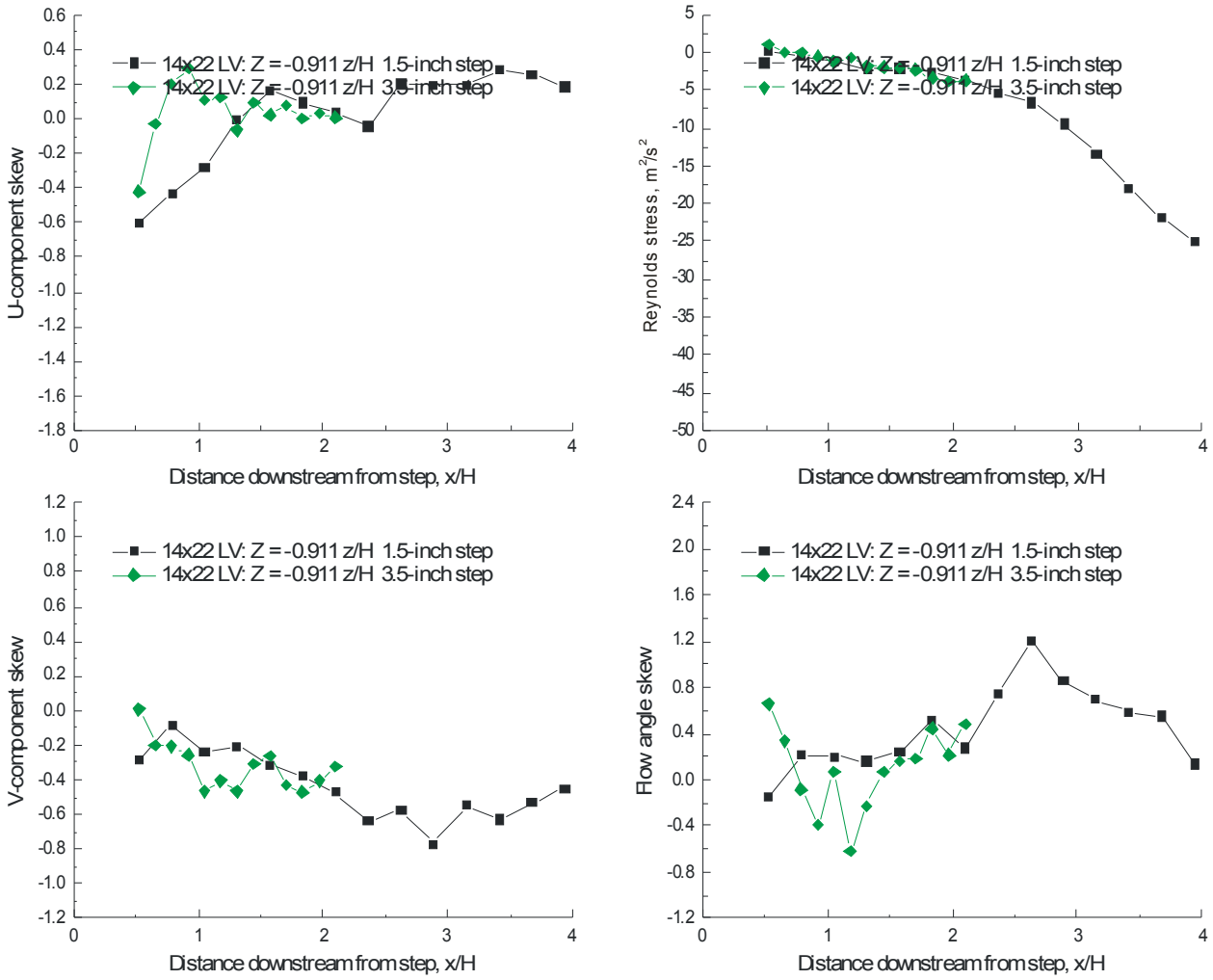

Figure VII.21.m.- Horizontal scan 0.911 z/H below the 1.5- and 3.5-inch backward-facing steps: streamwise and vertical velocity skew, flow angle skew and Reynolds stress.

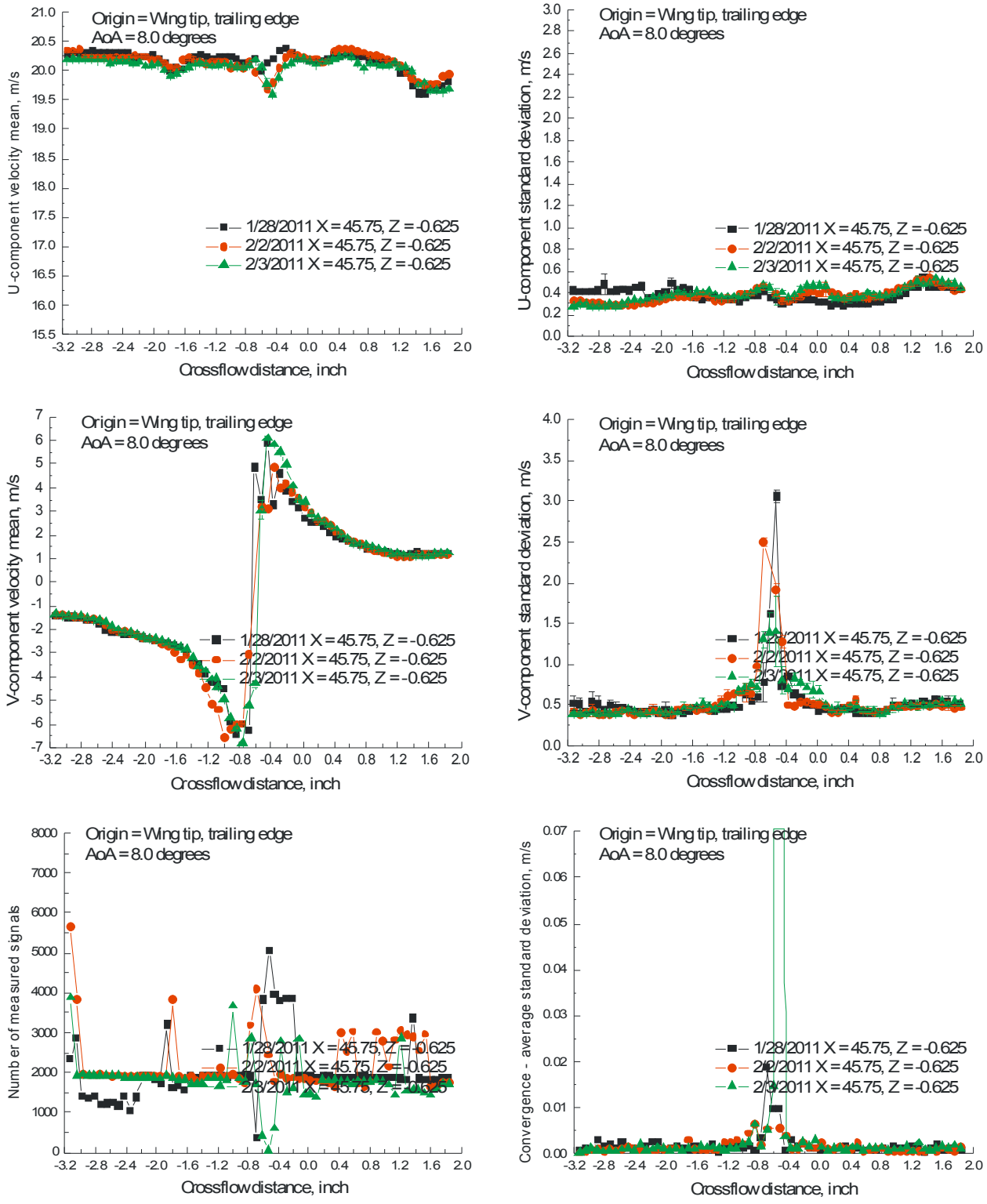

Figure VII.22.a.- Crossflow scans through a wing-tip vortex flow, wing angle of attack = 8.0 degrees: streamwise and vertical velocity components, number of accepted signal bursts, and statistical stationarity convergence standard deviation.

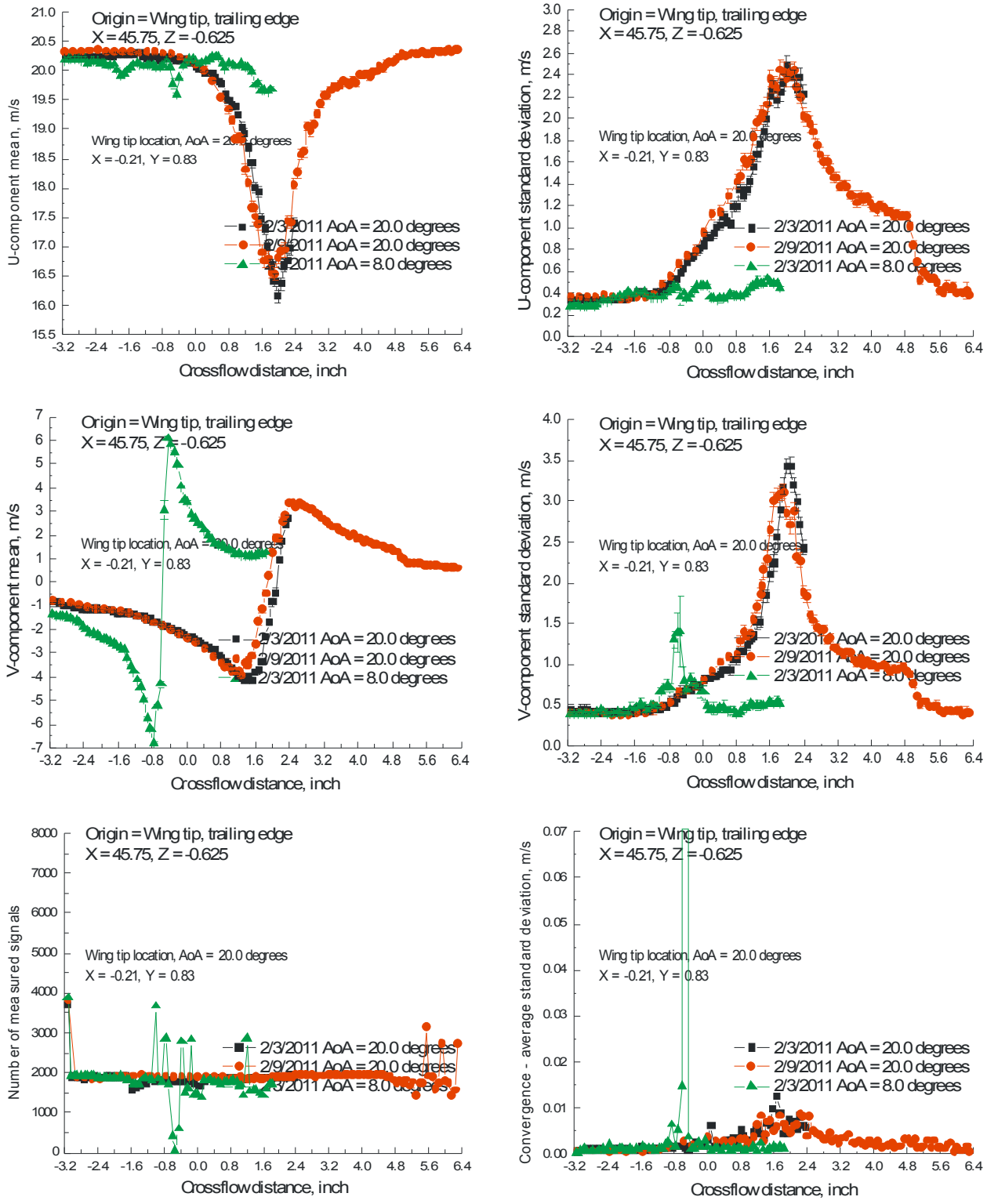

Figure VII.22.b.- Crossflow scans through a wing-tip vortex flow, wing angle of attack = 20.0 degrees as compared to 8.0 degrees: streamwise and vertical velocity components, number of accepted signal bursts, and statistical stationarity convergence standard deviation.

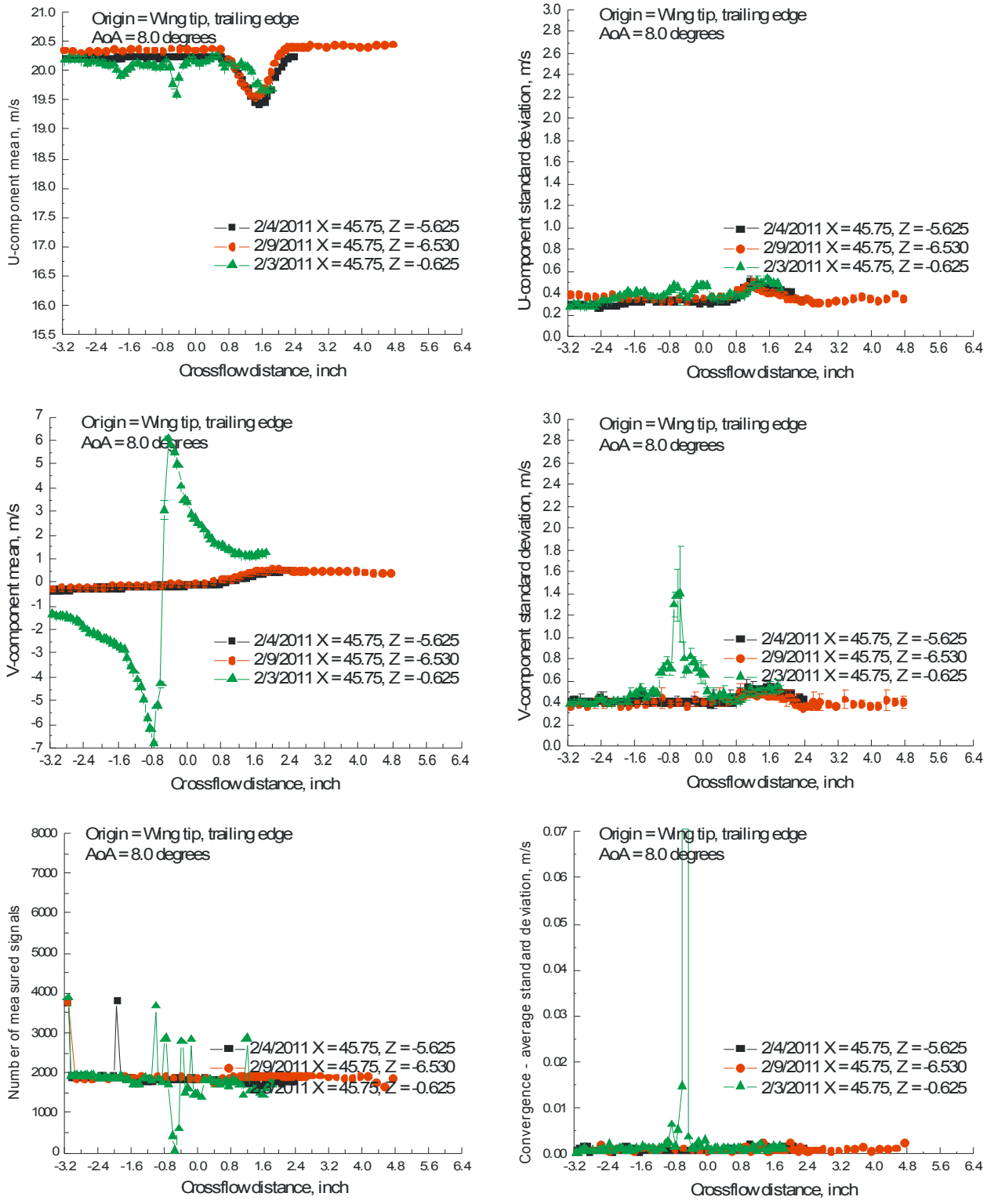

Figure VII.22.c.- Crossflow scans through the wake region, wing angle of attack = 8.0 degrees as compared to the scan through the vortex: streamwise and vertical velocity components, number of accepted signal bursts, and statistical stationarity convergence standard deviation.

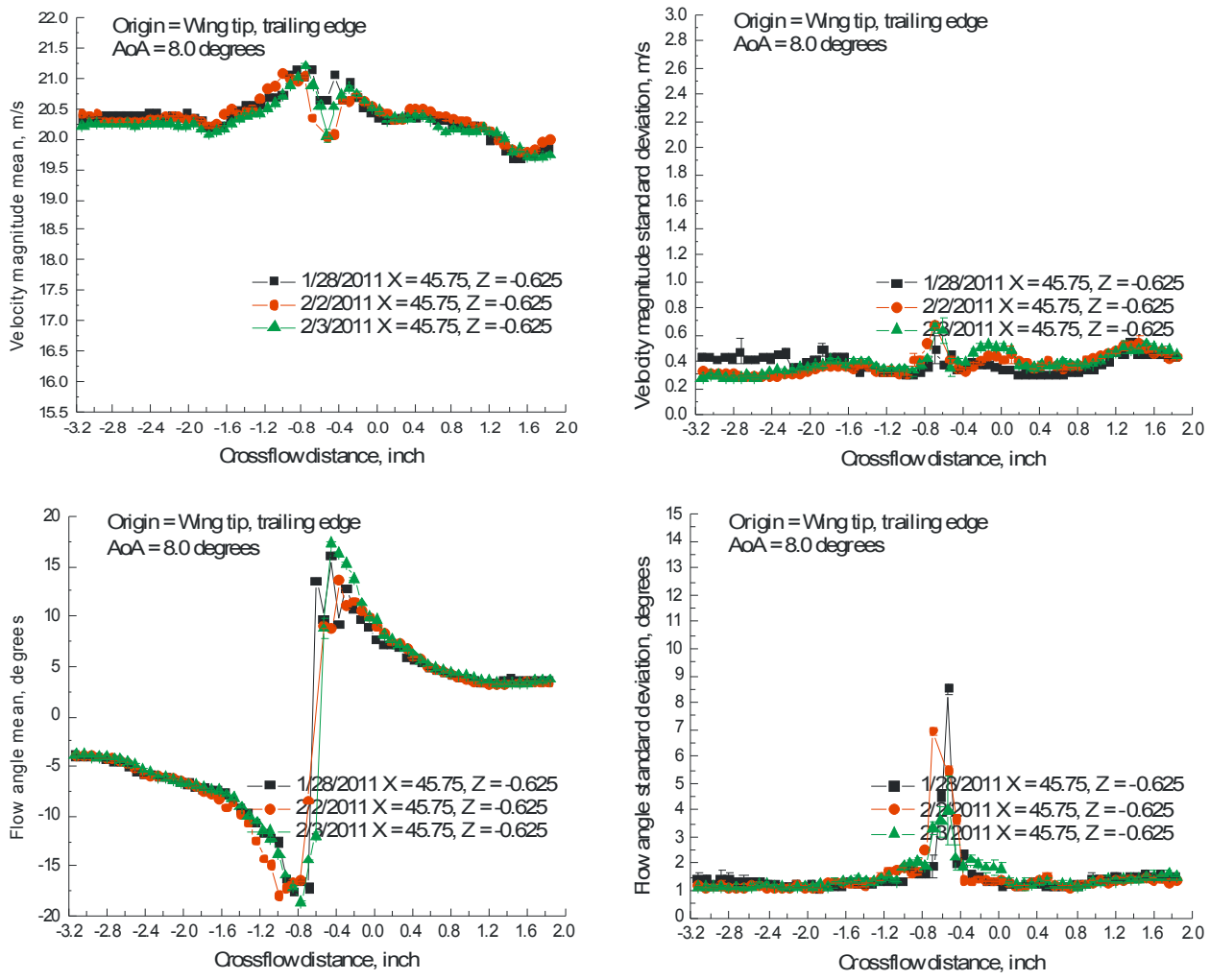

Figure VII.23.a.- Crossflow scans through a wing-tip vortex flow, wing angle of attack = 8.0 degrees: velocity magnitude and flow angle.

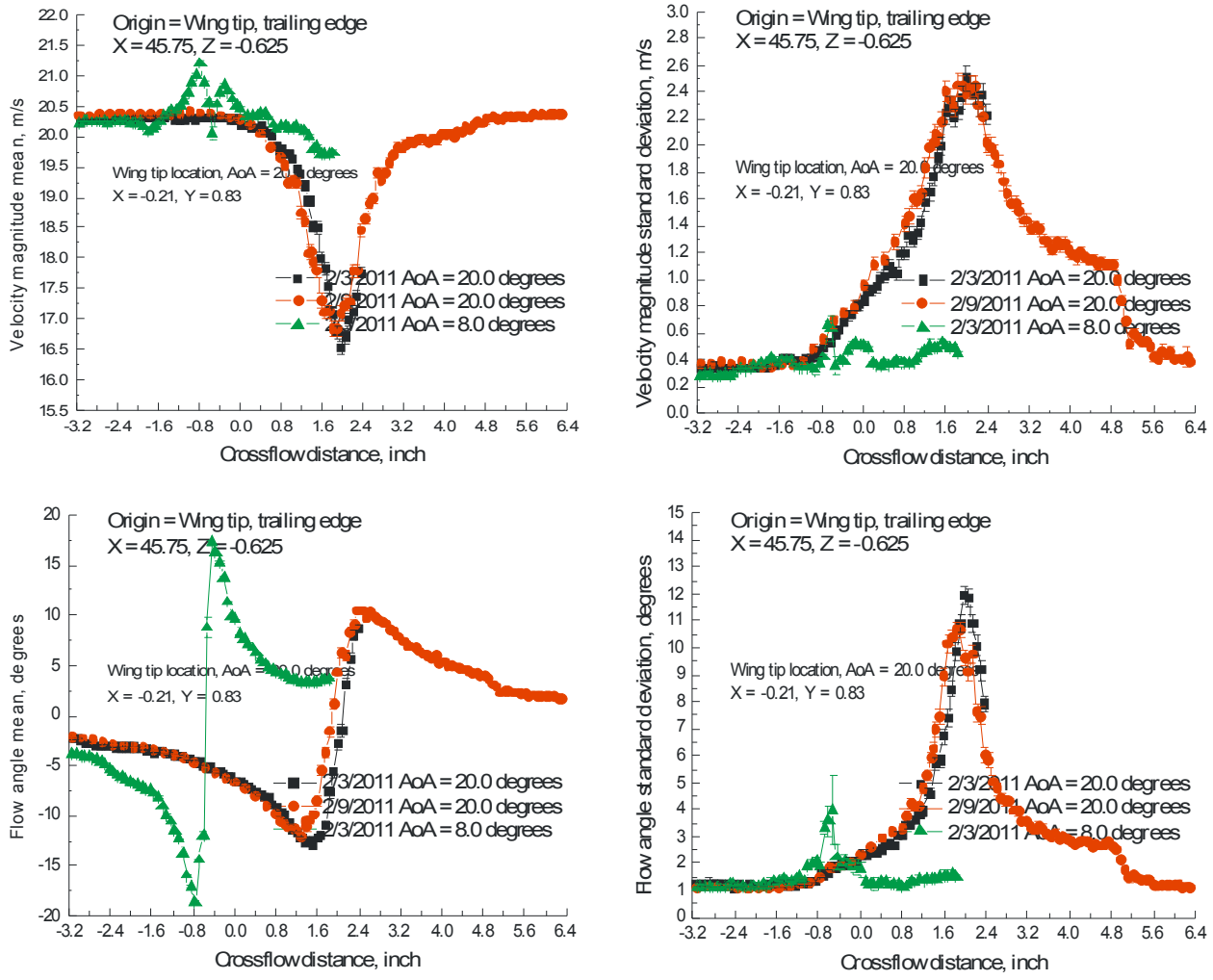

Figure VII.23.b.- Crossflow scans through a wing-tip vortex flow, wing angle of attack = 20.0 degrees as compared to 8.0 degrees: velocity magnitude and flow angle.

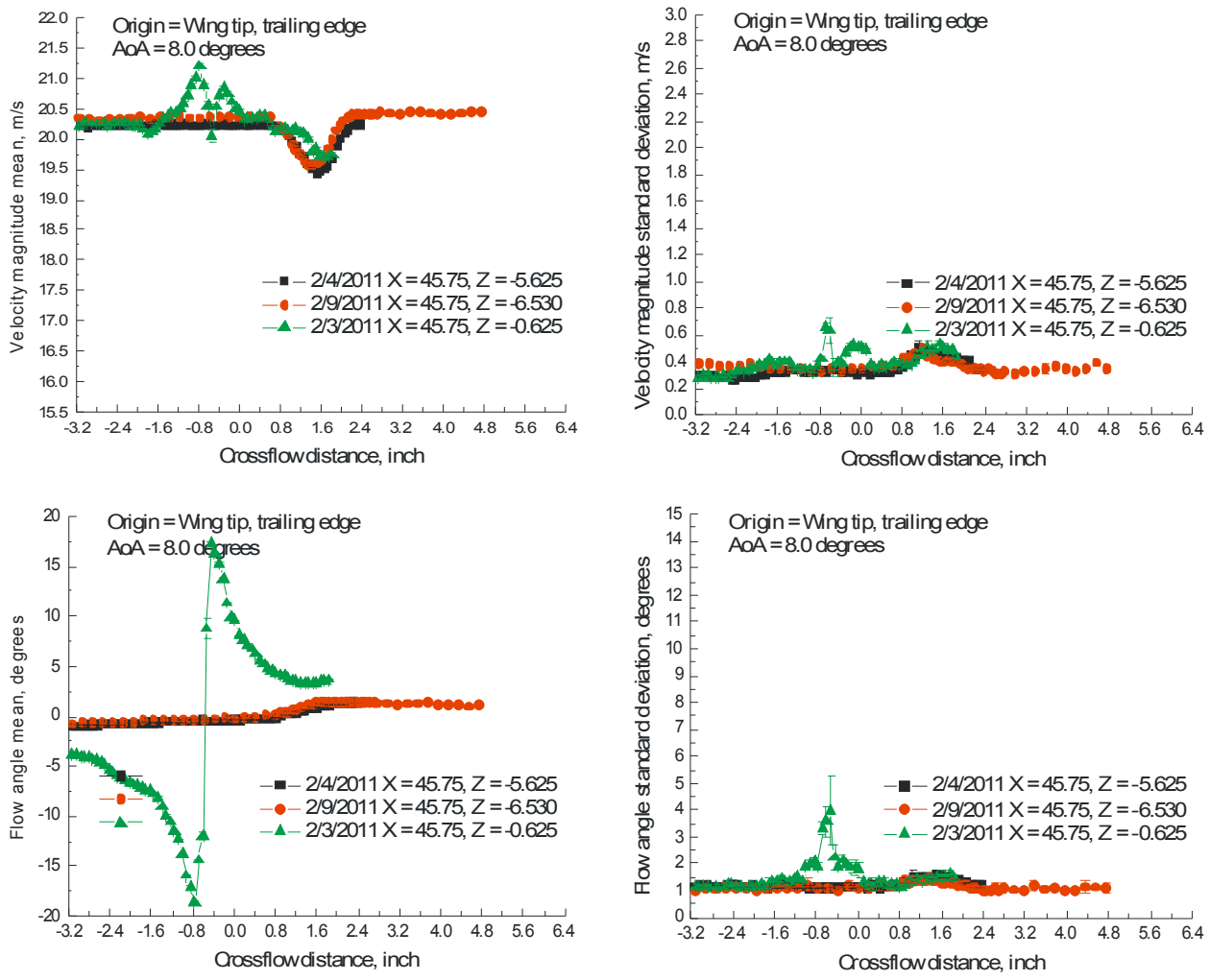

Figure VII.23.c.- Crossflow scans through the wake region, wing angle of attack = 8.0 degrees as compared to the scan through the vortex: velocity magnitude and flow angle.

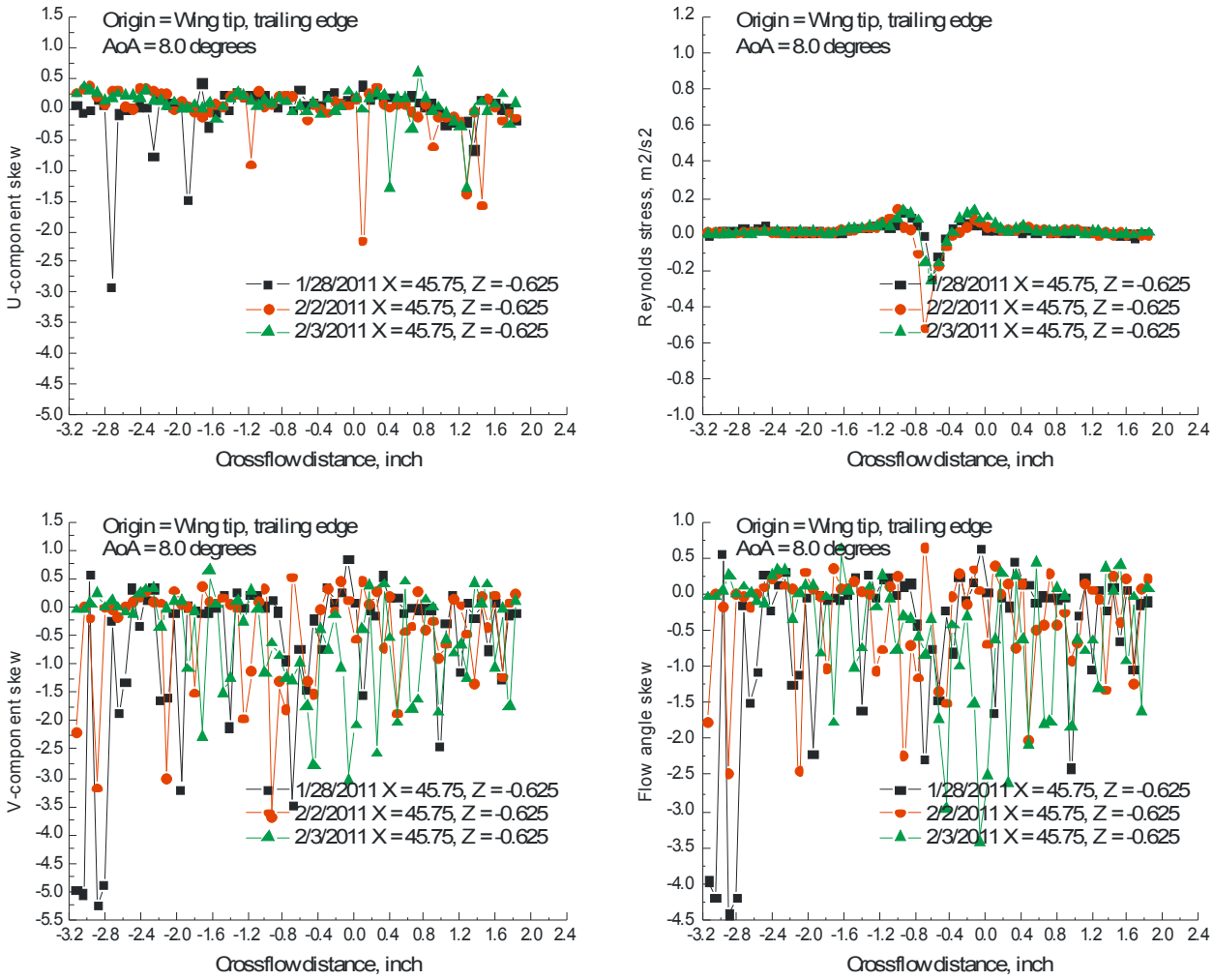

Figure VII.24.a.- Crossflow scans through a wing-tip vortex flow, wing angle of attack = 8.0 degrees: streamwise and vertical velocity skew, flow angle skew and Reynolds stress.

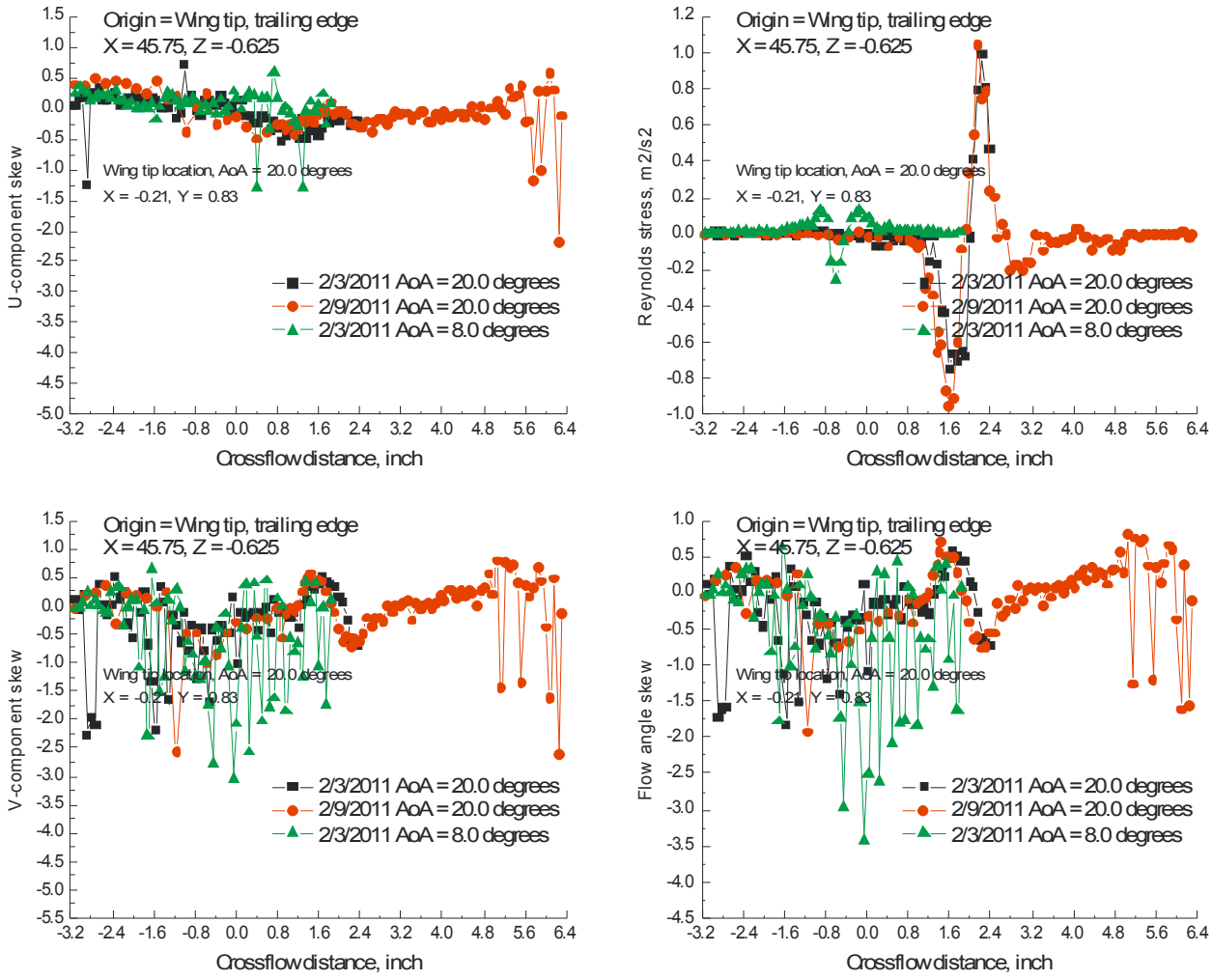

Figure VII.24.b.- Crossflow scans through a wing-tip vortex flow, wing angle of attack = 20.0 degrees as compared to 8.0 degrees: streamwise and vertical velocity skew, flow angle skew and Reynolds stress.

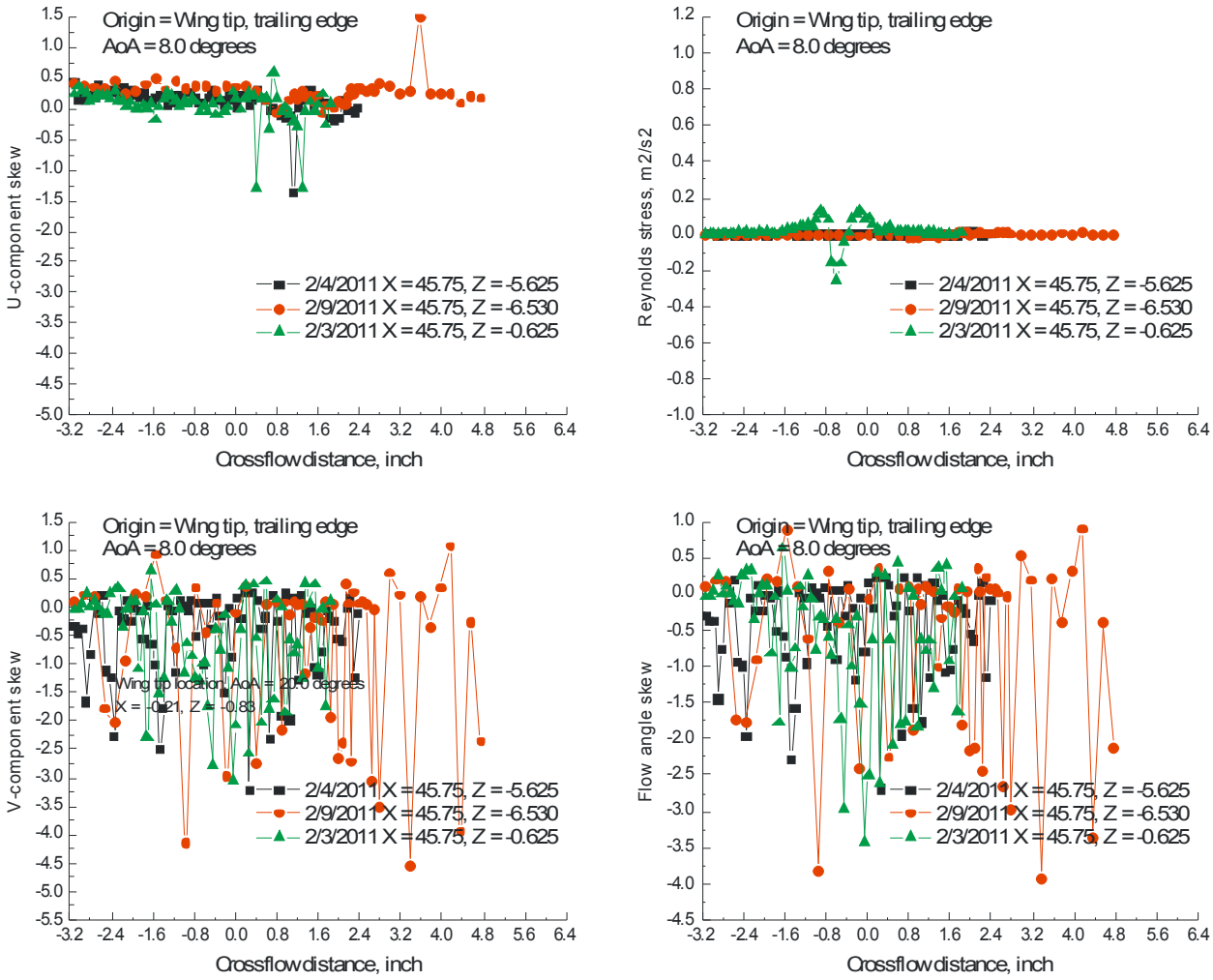

Figure VII.24.c.- Crossflow scans through the wake region, wing angle of attack = 8.0 degrees as compared to the scan through the vortex: streamwise and vertical velocity skew, flow angle skew and Reynolds stress.

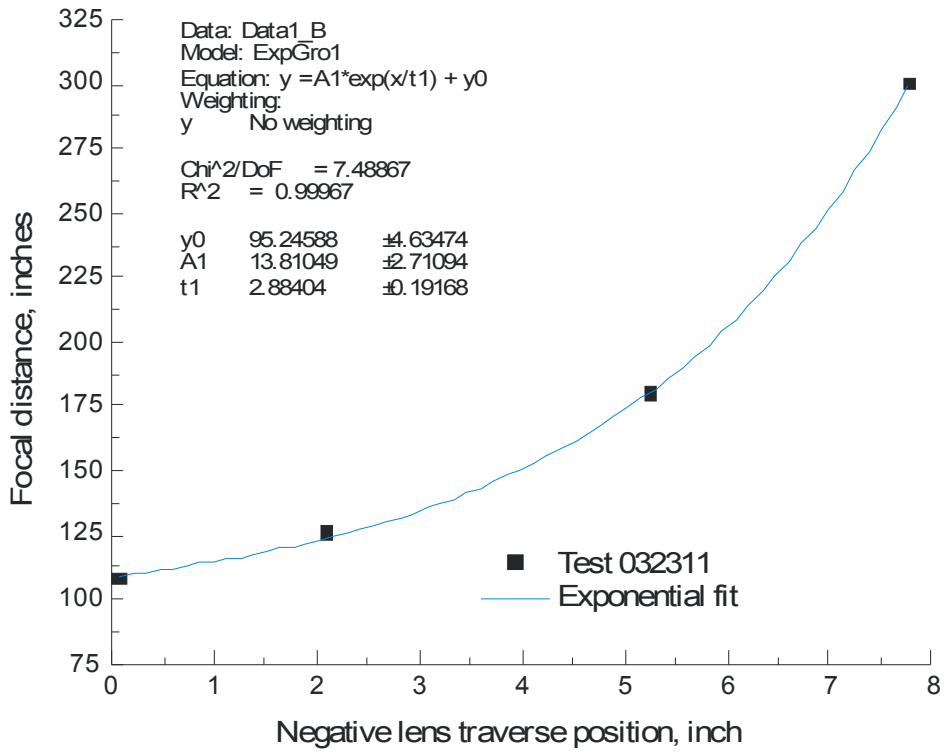

Figure VII.25.a.- Zoom lens focal distance as a function of negative lens traverse position.

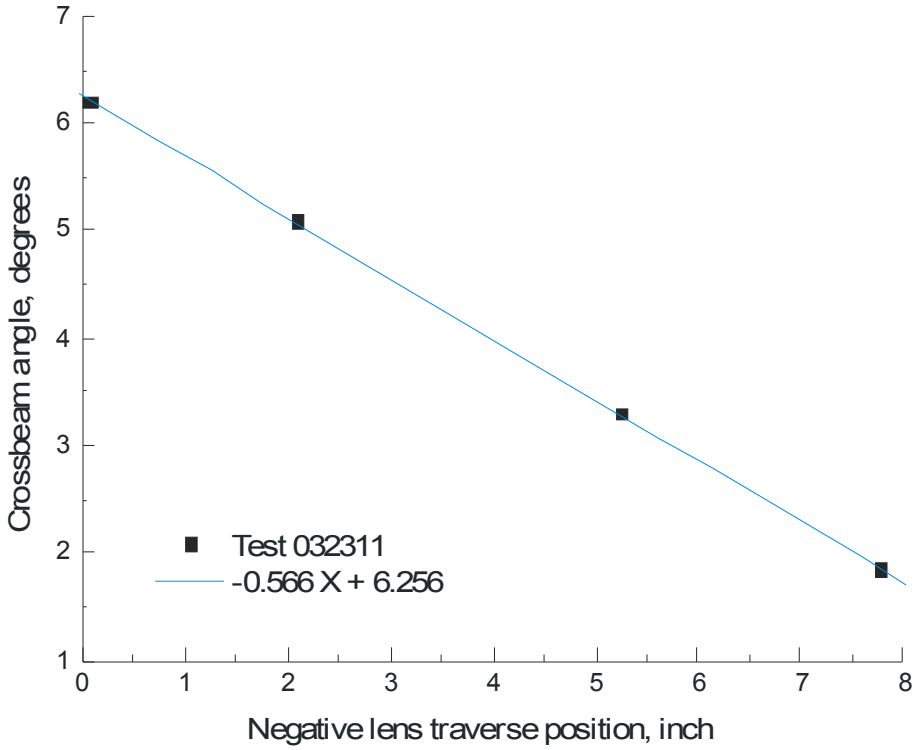

Figure VII.25.b.- Cross-beam angle as a function of negative lens traverse position.

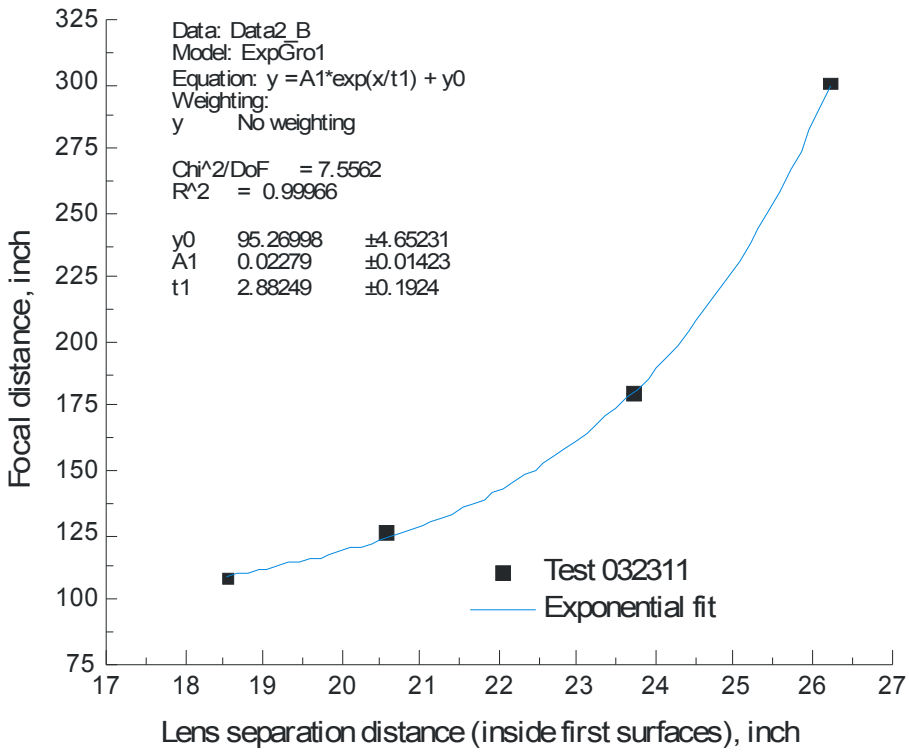

Figure VII.25.c.- Zoom lens focal distance as a function of lens separation.

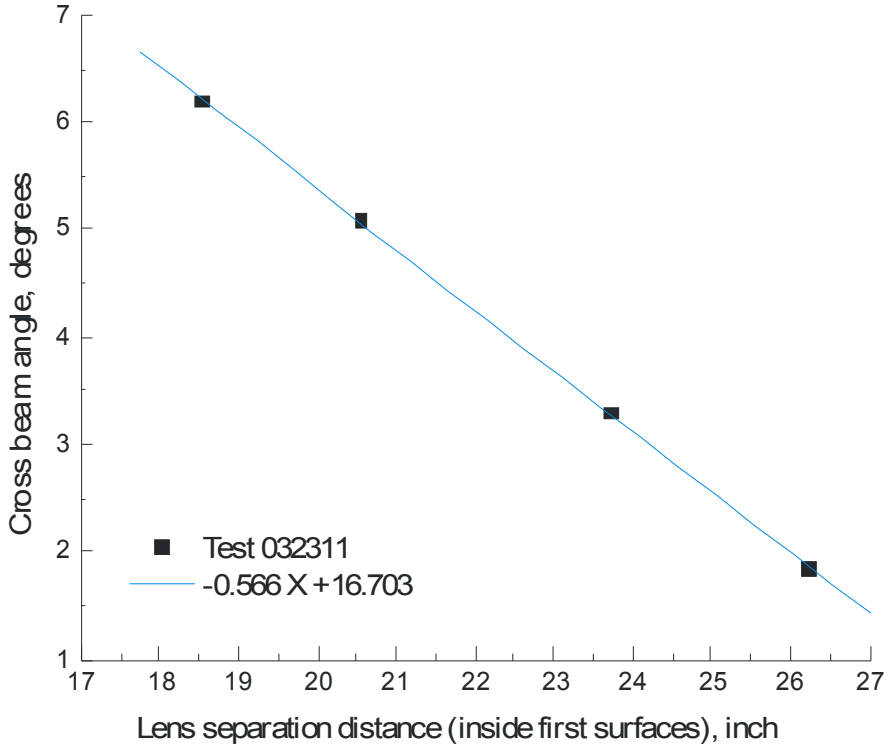

Figure VII.25.d.- Cross-beam angle as a function of lens separation.

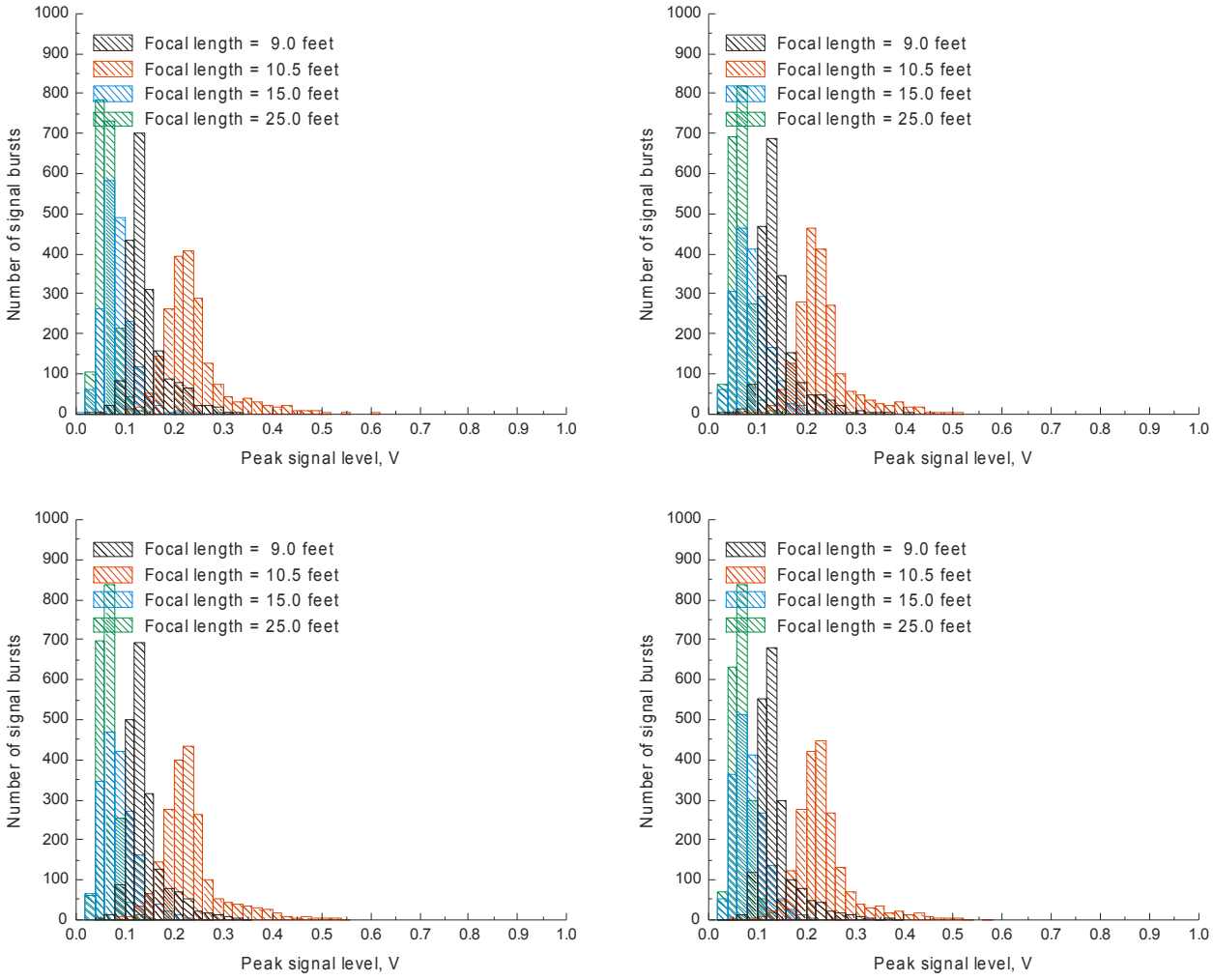

Figure VII.25.e.- Peak signal level distribution as a function of focal length - U-component.

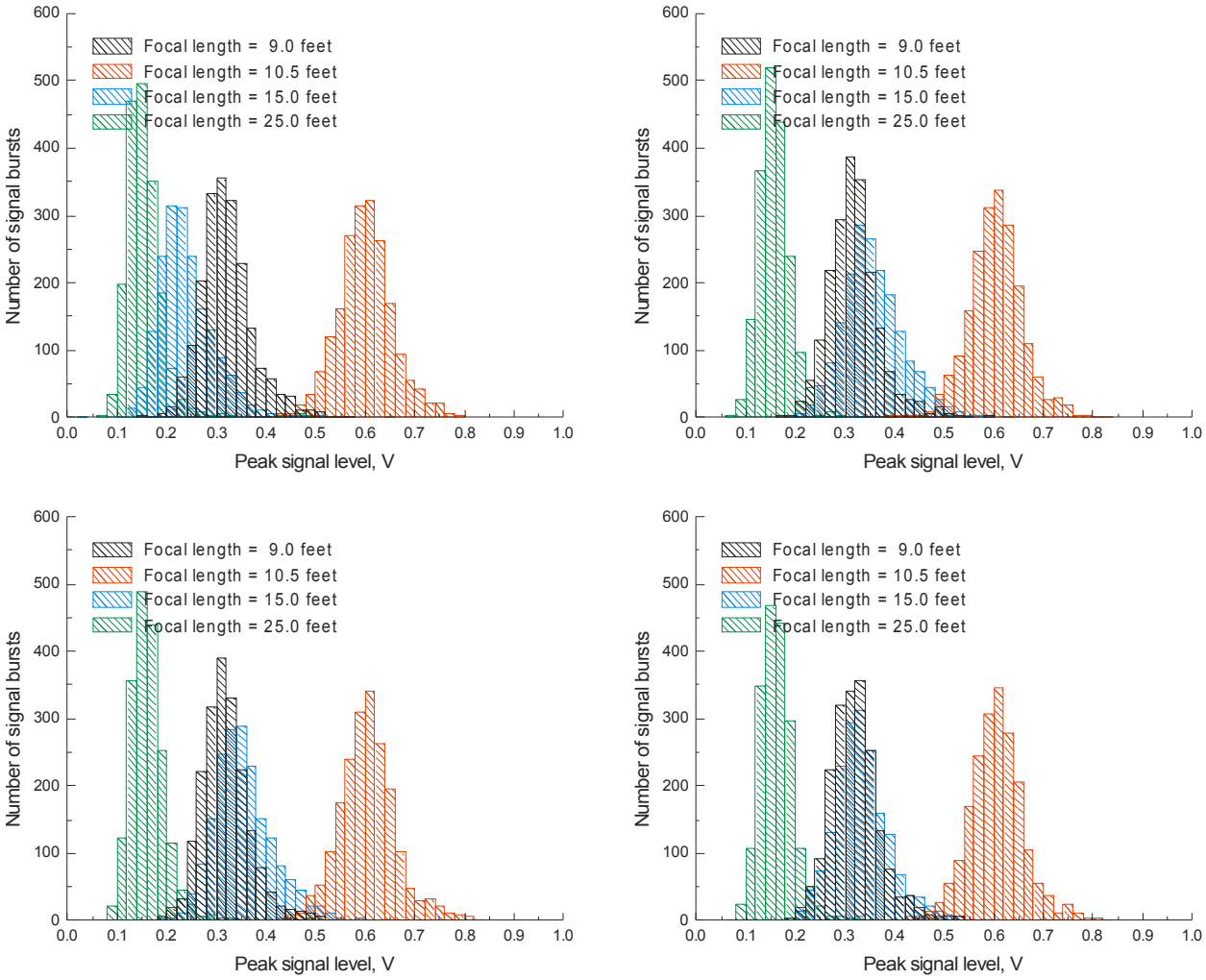

Figure VII.25.f.- Peak signal level distribution as a function of focal length - V-component.

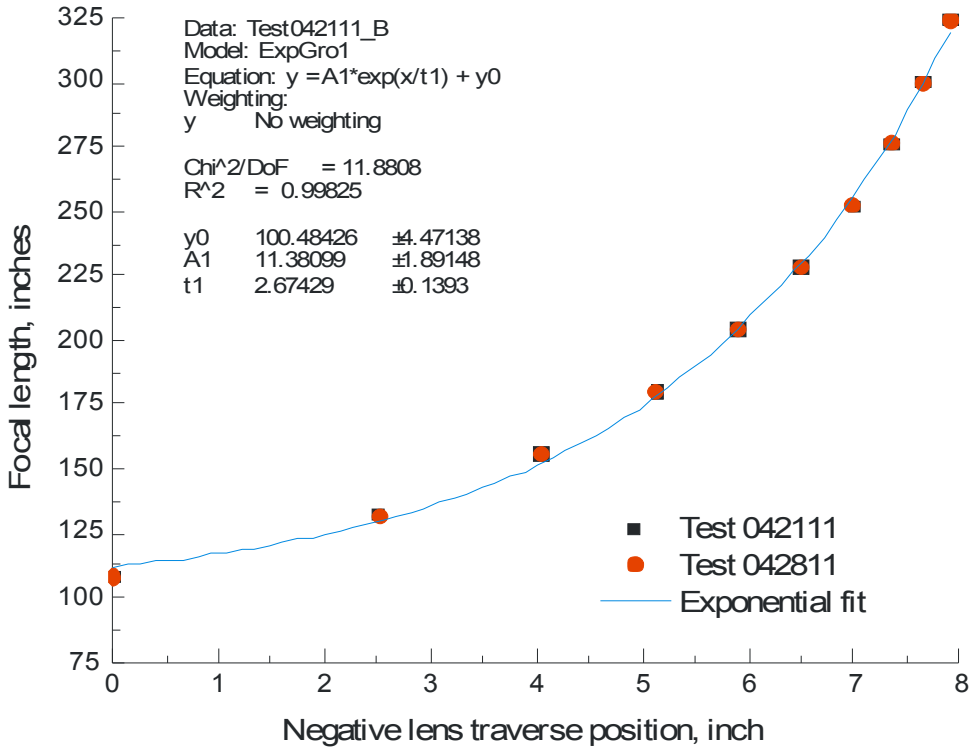

Figure VII.26.a.- Zoom lens focal distance as a function of negative lens traverse position - repeat.

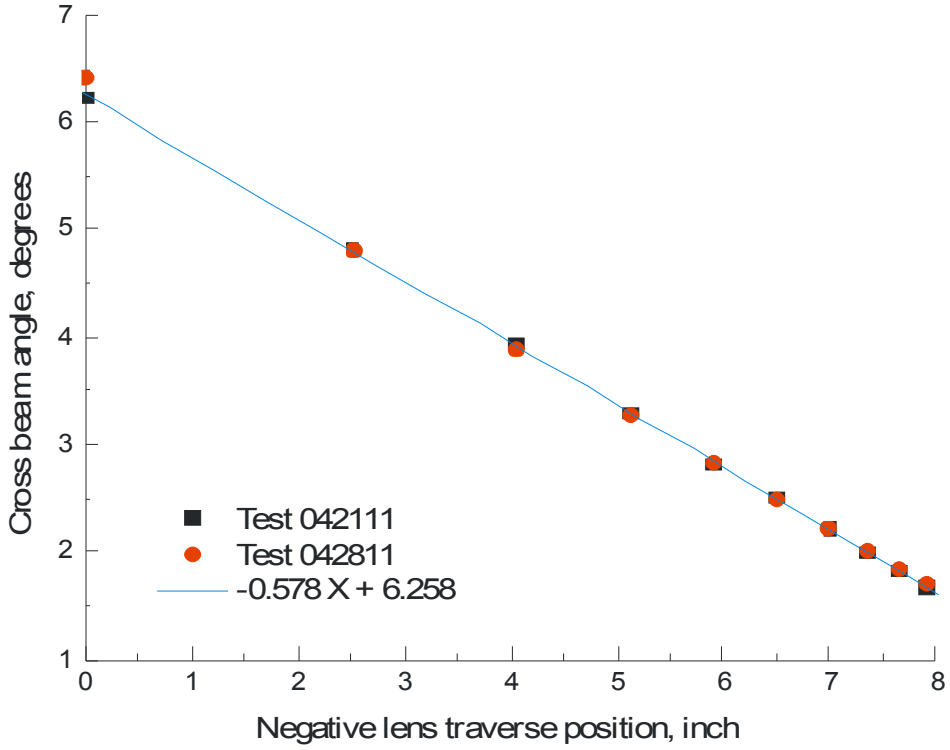

Figure VII.26.b.- Cross-beam angle as a function of negative lens traverse position - repeat.

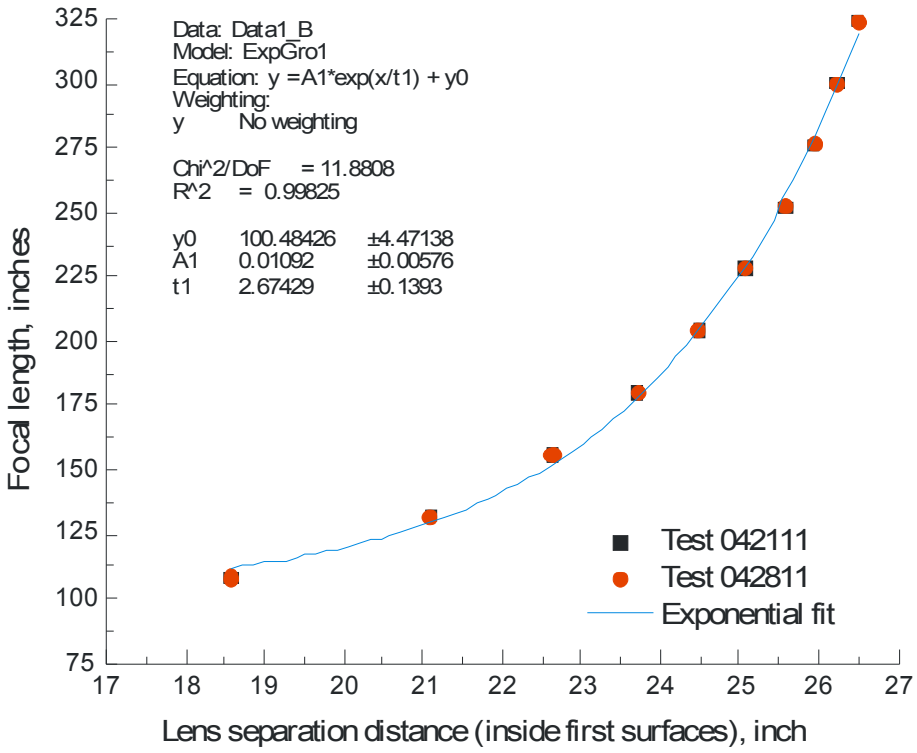

Figure VII.26.c.- Zoom lens focal distance as a function of lens separation - repeat.

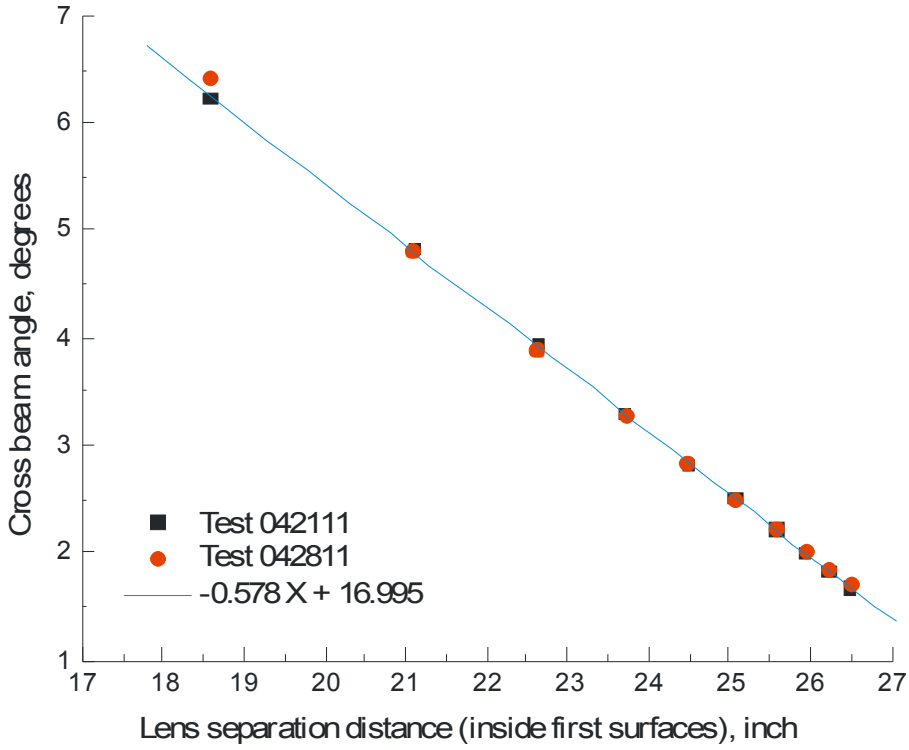

Figure VII.26.d.- Cross-beam angle as a function of lens separation - repeat.

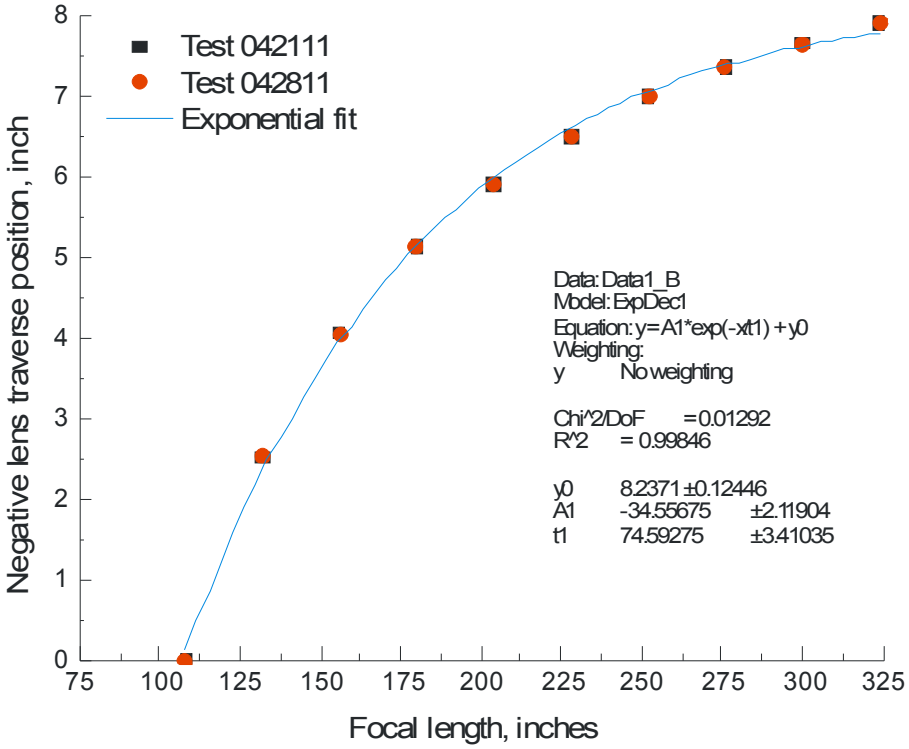

Figure VII.26.e.- Negative lens traverse position as a function of zoom lens focal distance.

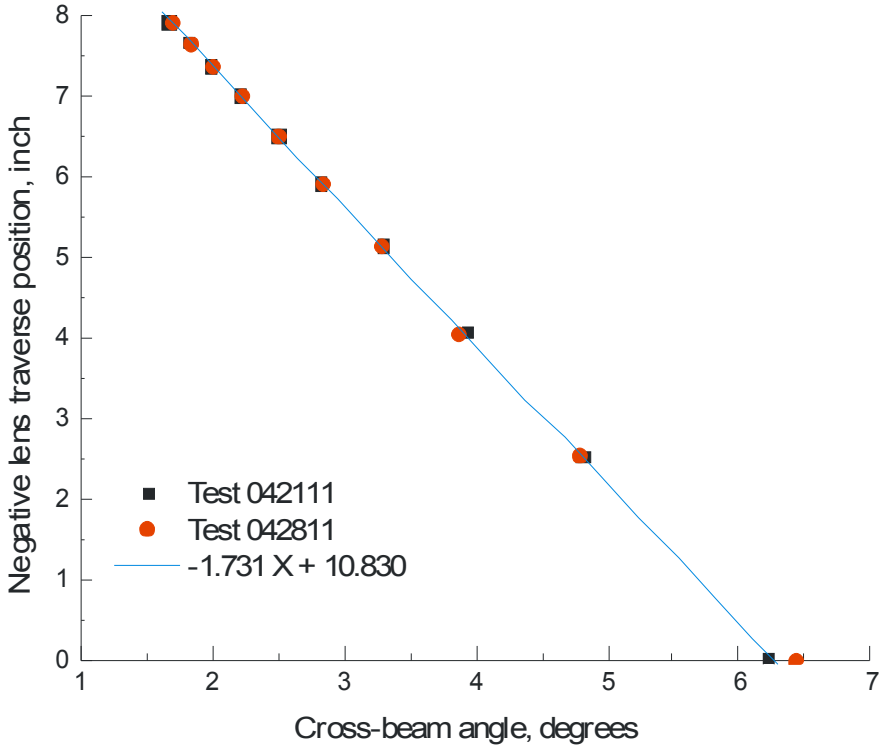

Figure VII.26.f.- Negative lens traverse position as a function of cross-beam angle.

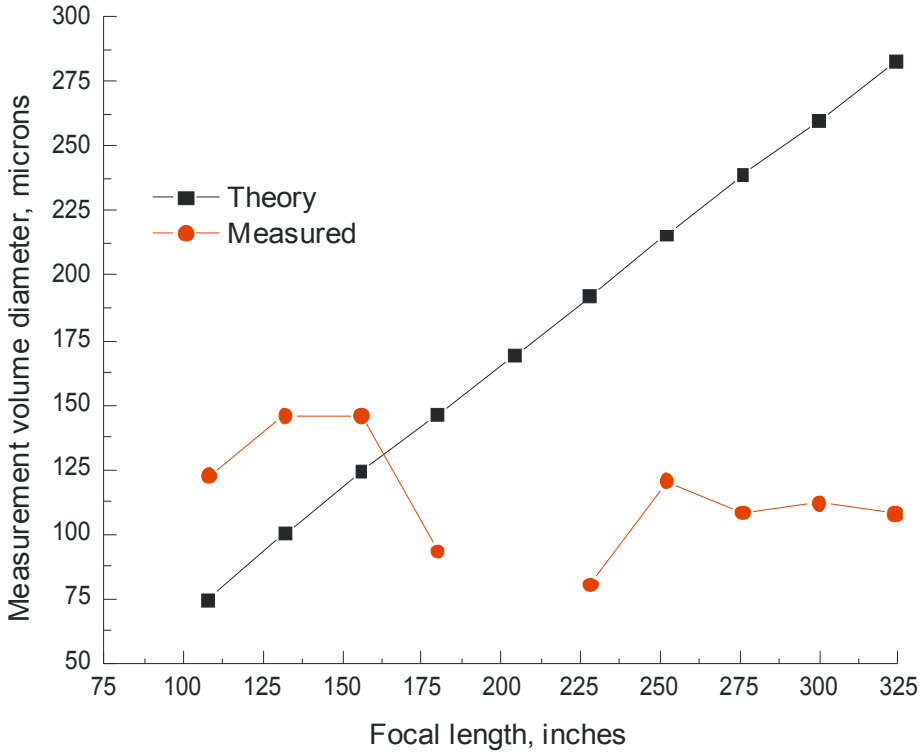

Figure VII.27.a.- Measurement volume diameter based on measured velocity magnitude and transit time from the $\pm 1/e^2$ amplitudes on the captured signal.

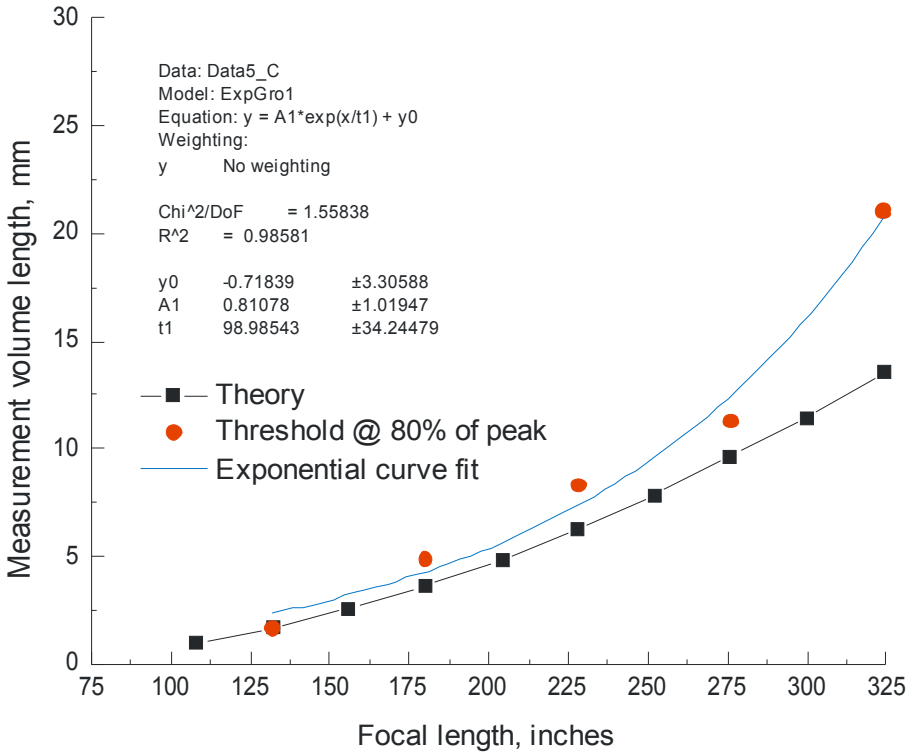

Figure VII.27.b.- Measurement volume length as a function of focal length: measured length based on signals reduced to 80% of peak, theoretical length based on $\pm 1/e^2$ locations.

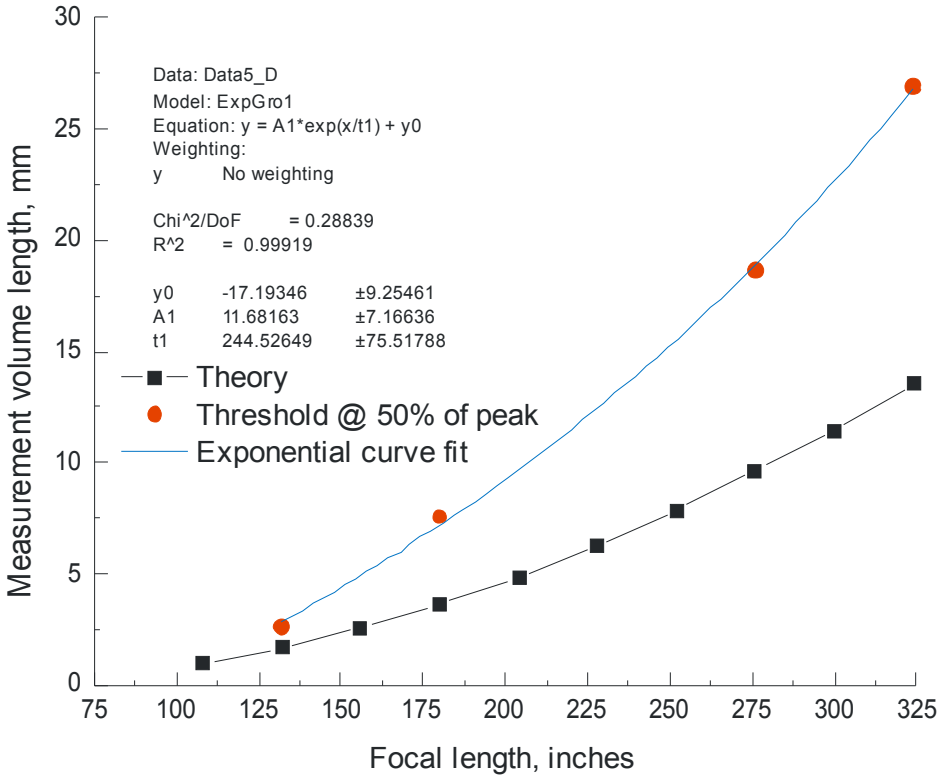

Figure VII.27.c.- Measurement volume length as a function of focal length: measured length based on signals reduced to 50% of peak, theoretical length based on $\pm 1/e^2$ locations.

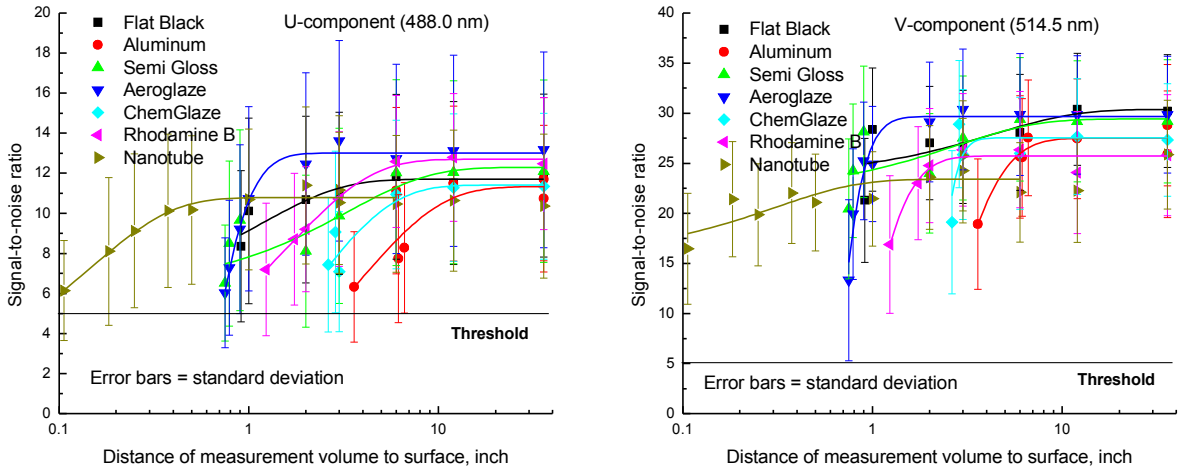

Figure VII.28.a.- Average signal-to-noise ratios of the signal bursts contained within each measurement ensemble as each surface is moved toward the measurement volume – Focal distance: 120 inches, particle size: 1.0 micron PSL, laser power: 0.5 W all-lines.

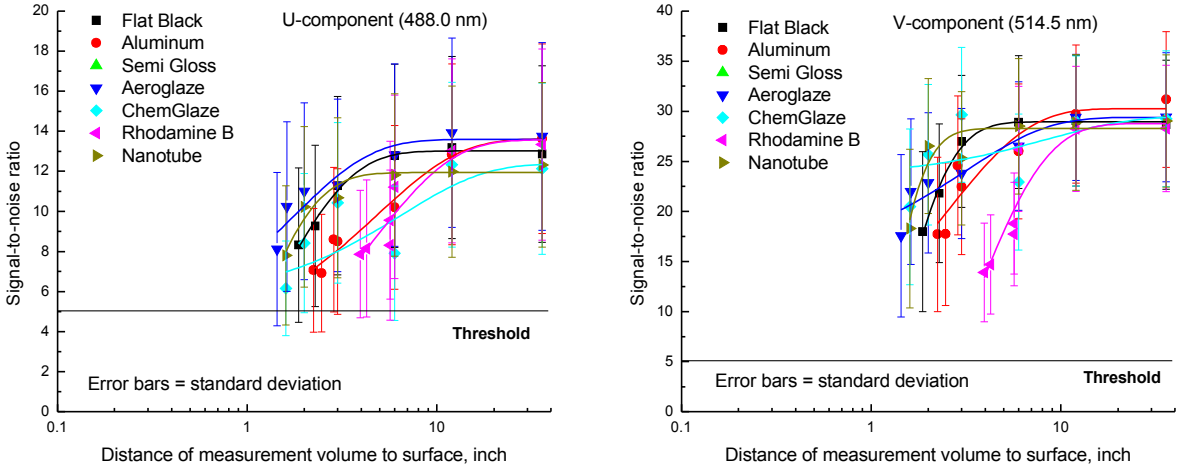

Figure VII.28.b.- Average signal-to-noise ratios of the signal bursts contained within each measurement ensemble as each surface is moved toward the measurement volume – Focal distance: 180 inches, particle size: 1.0 micron PSL, laser power: 0.5 W all-lines.

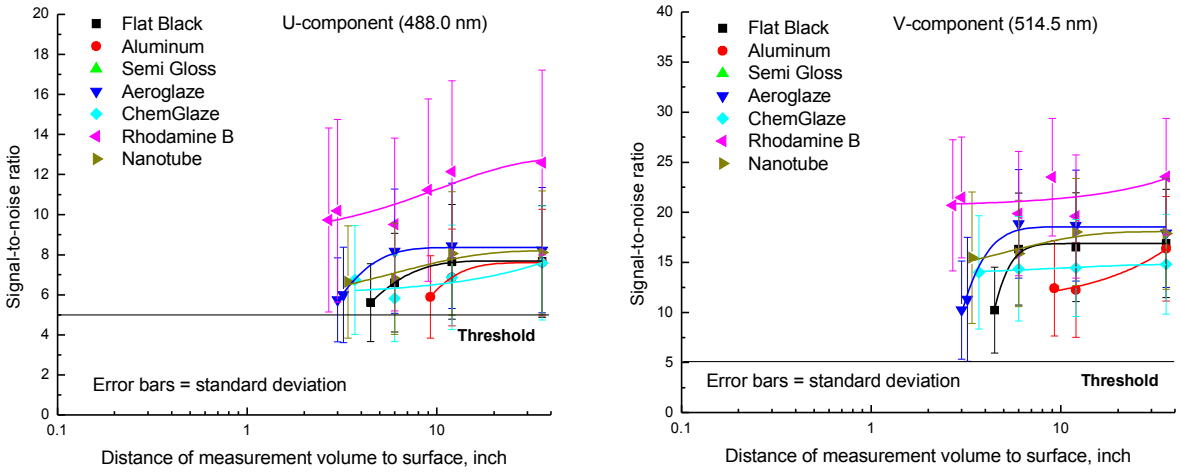

Figure VII.28.c.- Average signal-to-noise ratios of the signal bursts contained within each measurement ensemble as each surface is moved toward the measurement volume – Focal distance: 228 inches, particle size: 1.0 micron PSL, laser power: 0.5 W all-lines.

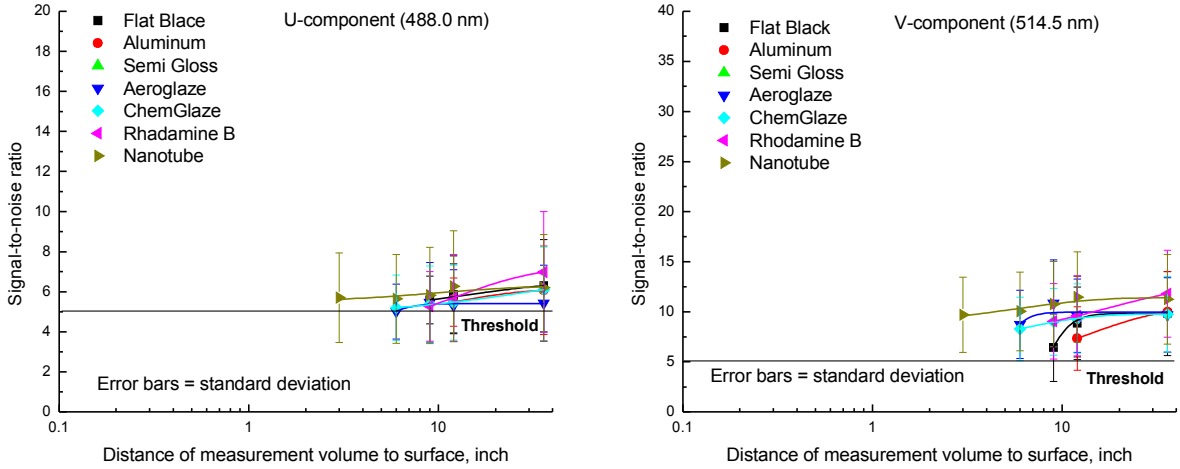

Figure VII.28.d.- Average signal-to-noise ratios of the signal bursts contained within each measurement ensemble as each surface is moved toward the measurement volume – Focal distance: 276 inches, particle size: 1.0 micron PSL, laser power: 1.0 W all-lines.

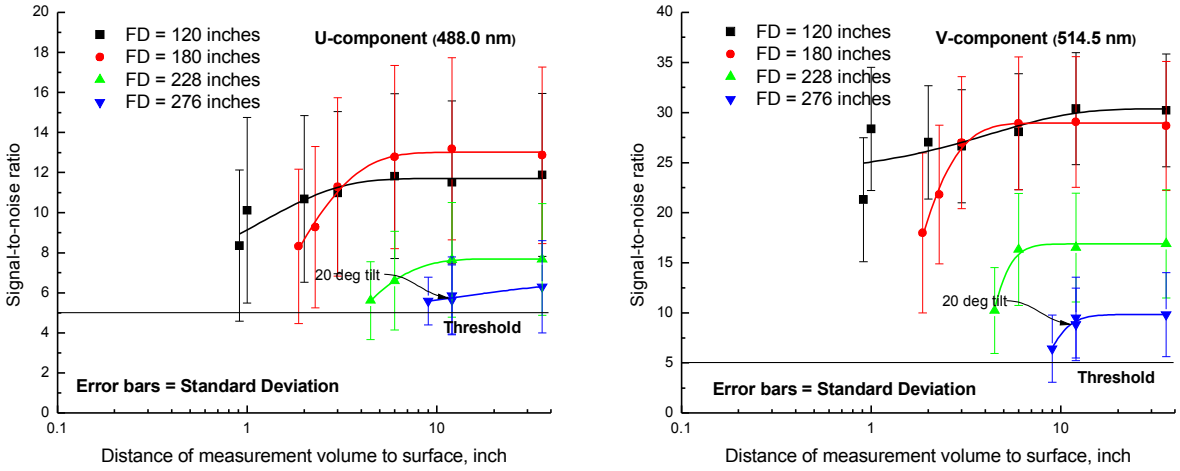

Figure VII.29.a.- Average signal-to-noise ratios of the signal bursts contained within each measurement ensemble as each surface is moved toward the measurement volume – Flat black, particle size: 1.0 micron PSL.

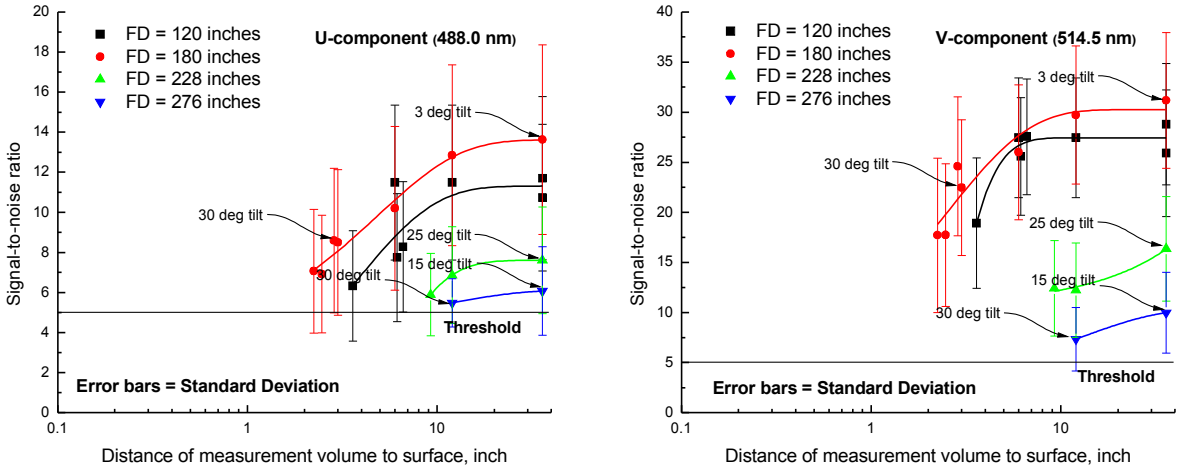

Figure VII.29.b.- Average signal-to-noise ratios of the signal bursts contained within each measurement ensemble as each surface is moved toward the measurement volume – Unpainted aluminum plate, particle size: 1.0 micron PSL.

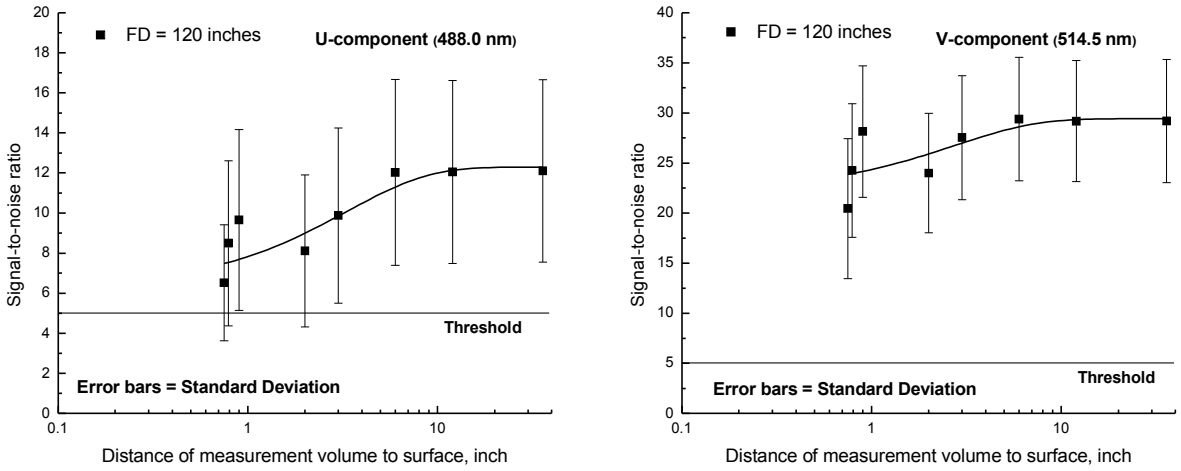

Figure VII.29.c.- Average signal-to-noise ratios of the signal bursts contained within each measurement ensemble as each surface is moved toward the measurement volume – Semi-gloss black paint, particle size: 1.0 micron PSL.

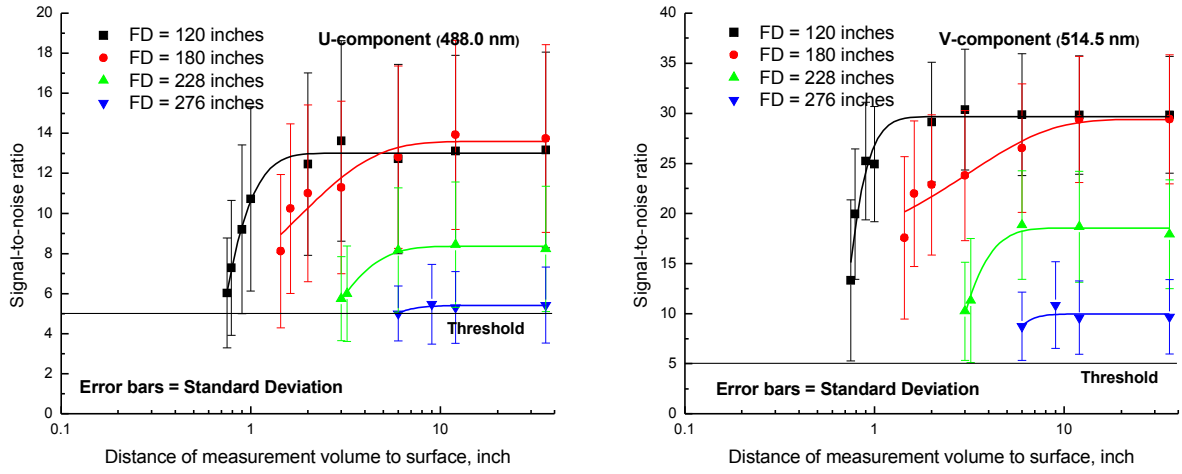

Figure VII.29.d.- Average signal-to-noise ratios of the signal bursts contained within each measurement ensemble as each surface is moved toward the measurement volume – Aeroglaze, particle size: 1.0 micron PSL.

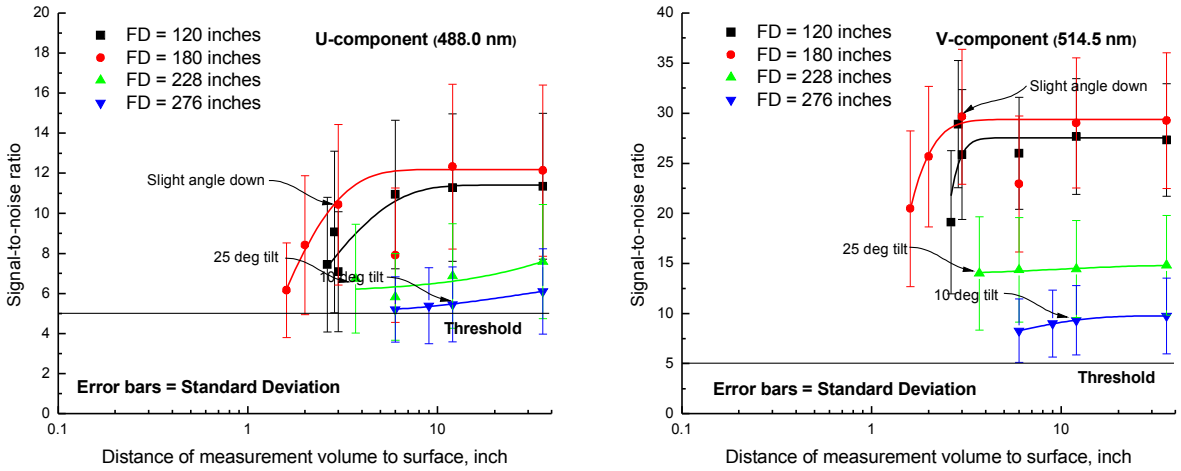

Figure VII.29.e.- Average signal-to-noise ratios of the signal bursts contained within each measurement ensemble as each surface is moved toward the measurement volume – Chem Glaze sample, particle size: 1.0 micron PSL.

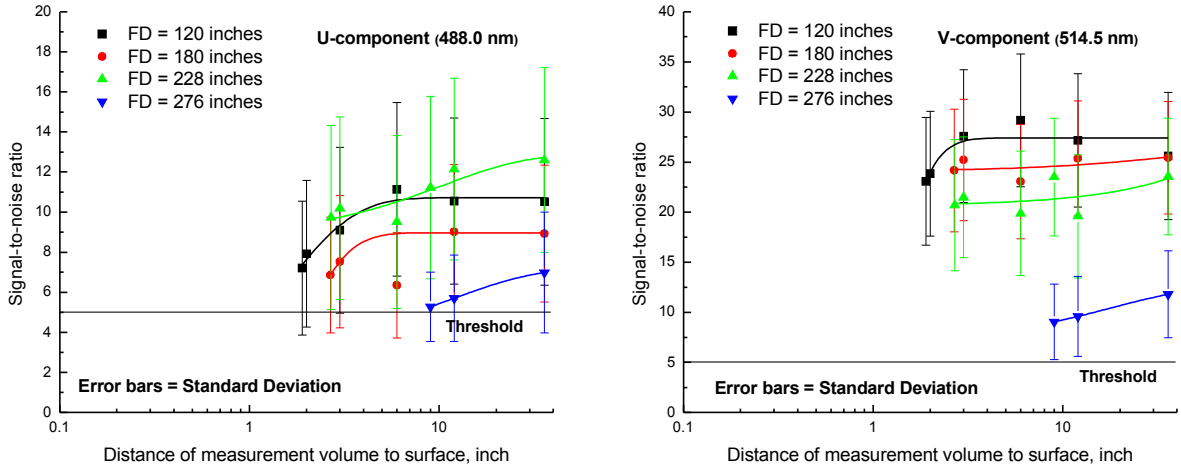

Figure VII.29.f.- Average signal-to-noise ratios of the signal bursts contained within each measurement ensemble as each surface is moved toward the measurement volume – Semi gloss black paint with Rhodamine B added, particle size: 1.0 micron PSL.

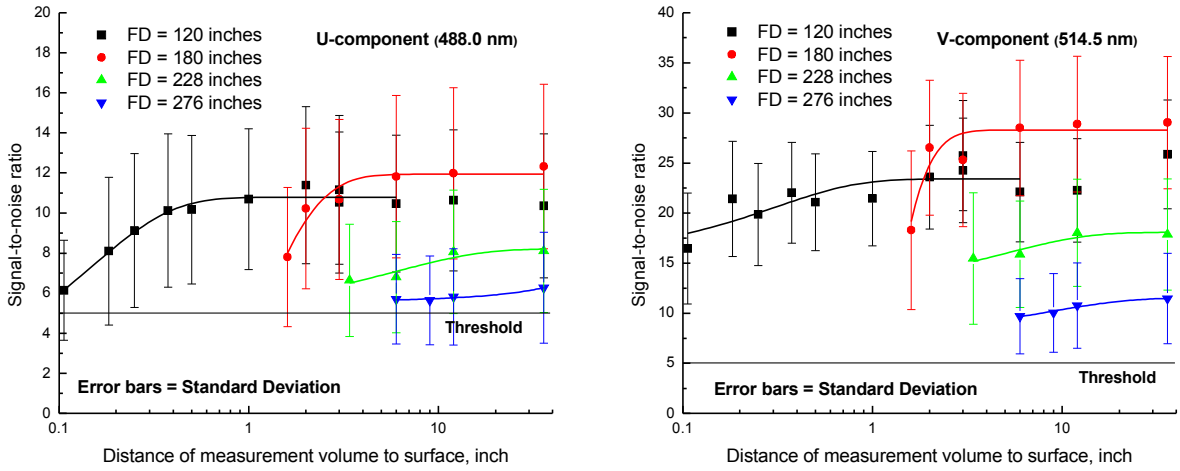

Figure VII.29.g.- Average signal-to-noise ratios of the signal bursts contained within each measurement ensemble as each surface is moved toward the measurement volume – Nanotube matrix sample, particle size: 1.0 micron PSL.

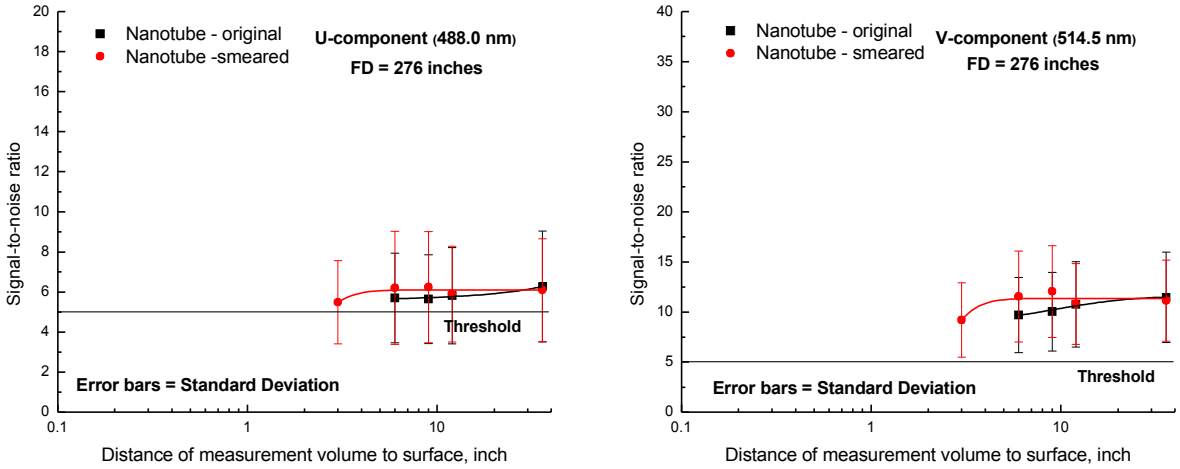

Figure VII.29.h.- Average signal-to-noise ratios of the signal bursts contained within each measurement ensemble as each surface is moved toward the measurement volume – Nanotube matrix sample: normal surface versus damaged surface, particle size: 1.0 micron PSL.

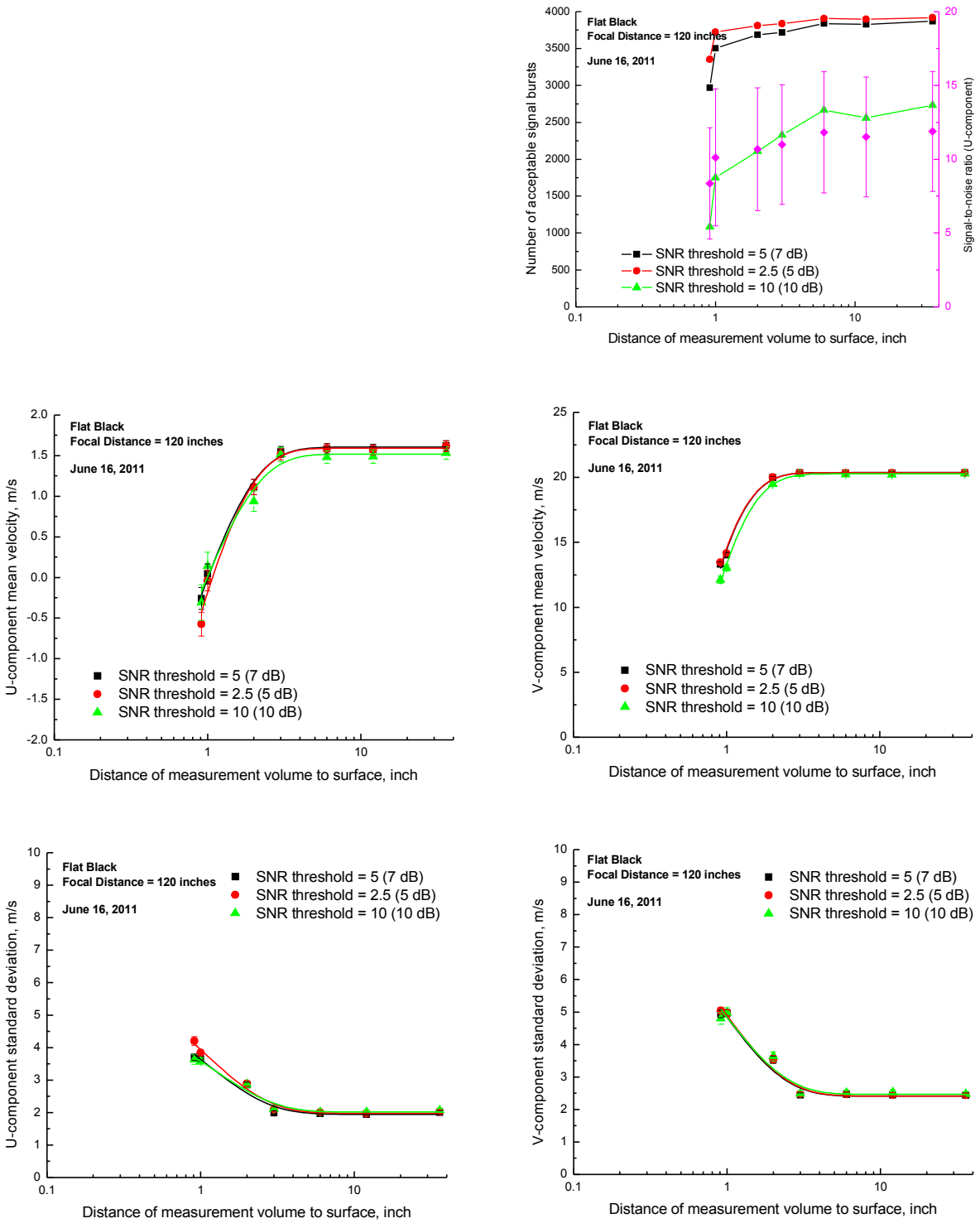

Figure VII.30.a.(1) - Velocity statistics as each surface is moved toward the measurement volume – Flat black sample, Focal distance = 120 inches.

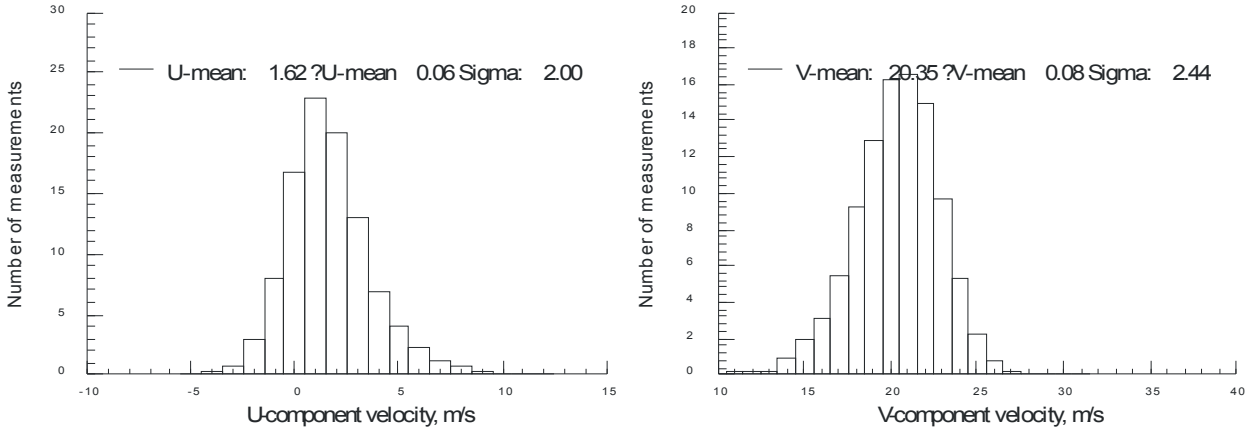

(i) Signal-to-noise ratio threshold = 5 (7 dB)

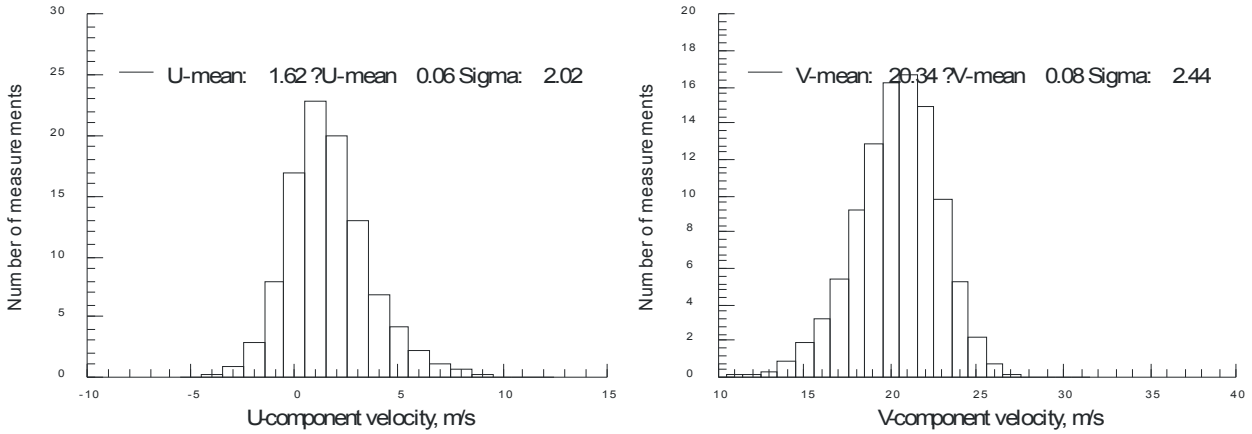

(ii) Signal-to-noise ratio threshold = 2.5 (5 dB)

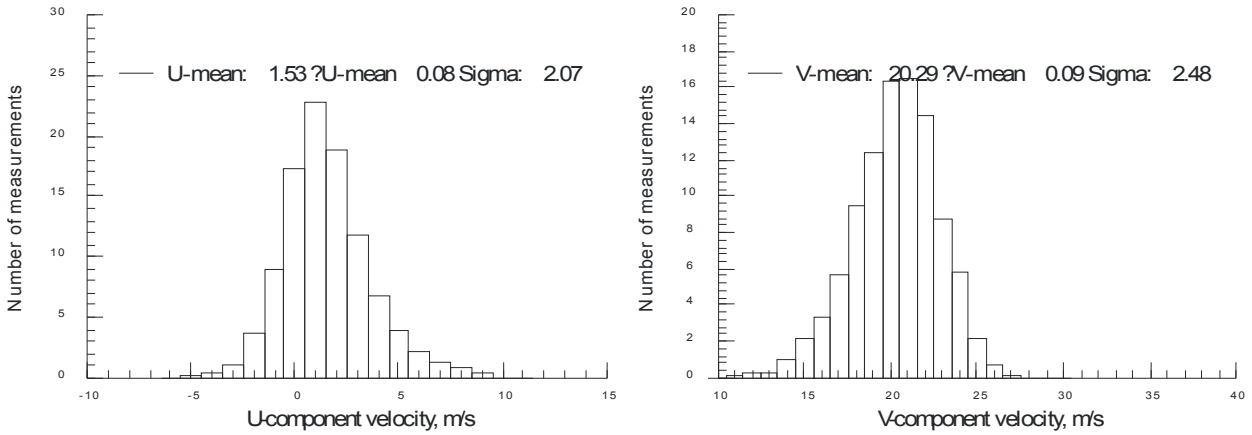

(iii) Signal-to-noise ratio threshold = 10 (10 dB)

Figure VII.30.a.(2)(a) - Velocity histograms obtained at 36-inch separation – Flat black sample, Focal distance = 120 inches.

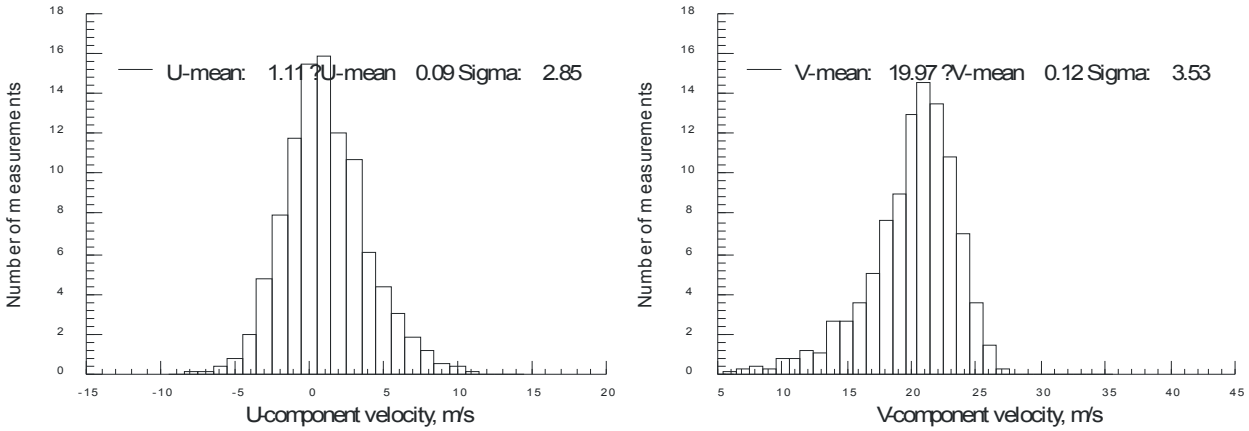

(i) Signal-to-noise ratio threshold = 5 (7 dB)

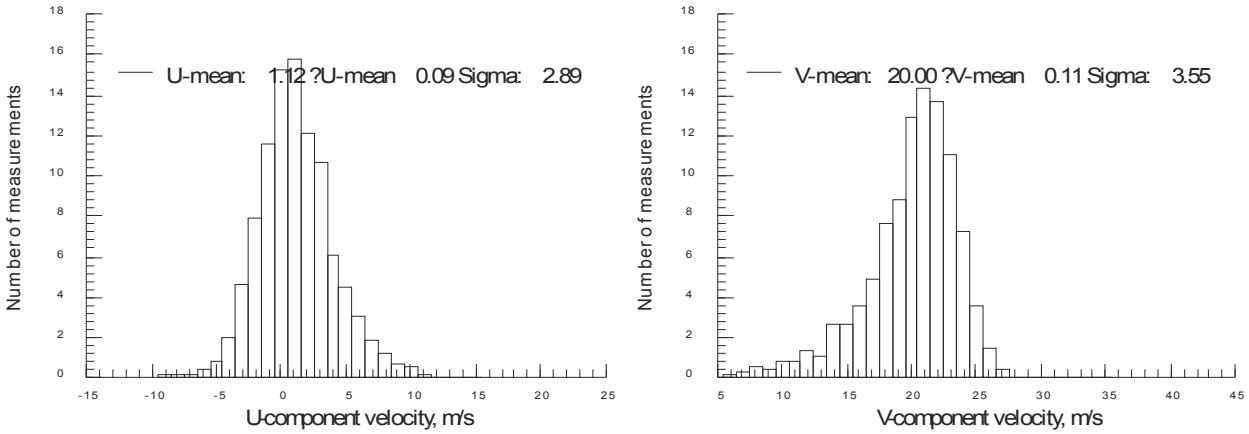

(ii) Signal-to-noise ratio threshold = 2.5 (5 dB)

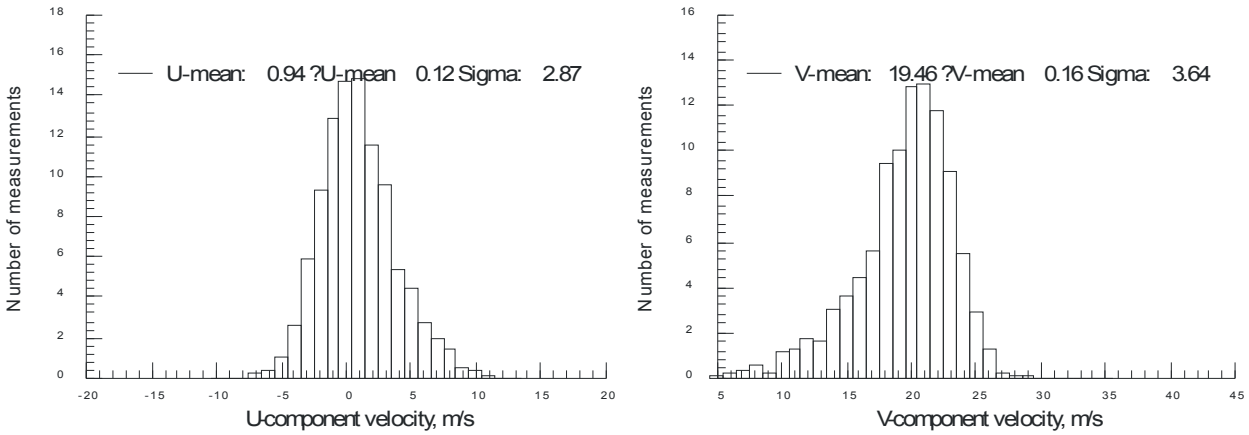

(iii) Signal-to-noise ratio threshold = 10 (10 dB)

Figure VII.30.a.(2)(b) - Velocity histograms obtained at first velocity/sigma deviation – Flat black sample, Focal distance = 120 inches.

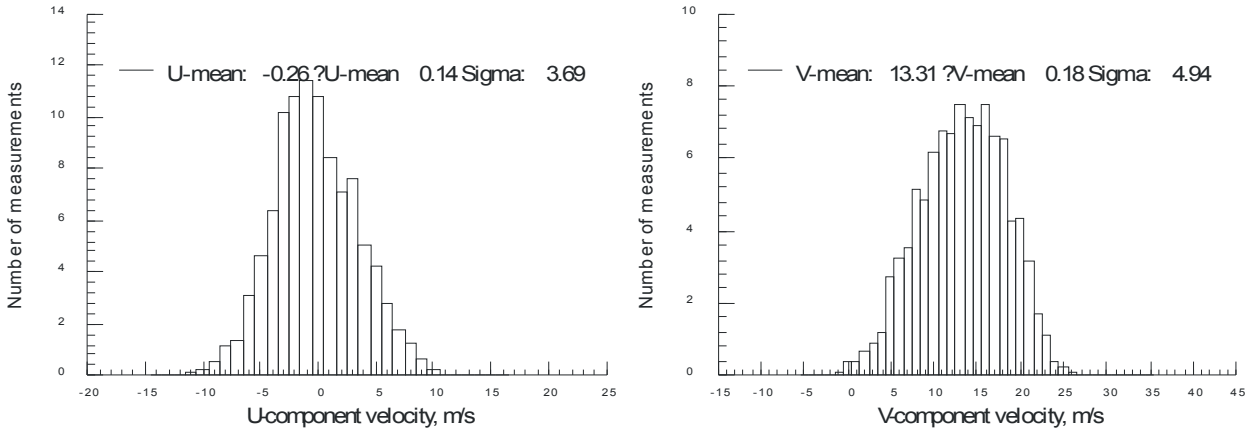

(i) Signal-to-noise ratio threshold = 5 (7 dB)

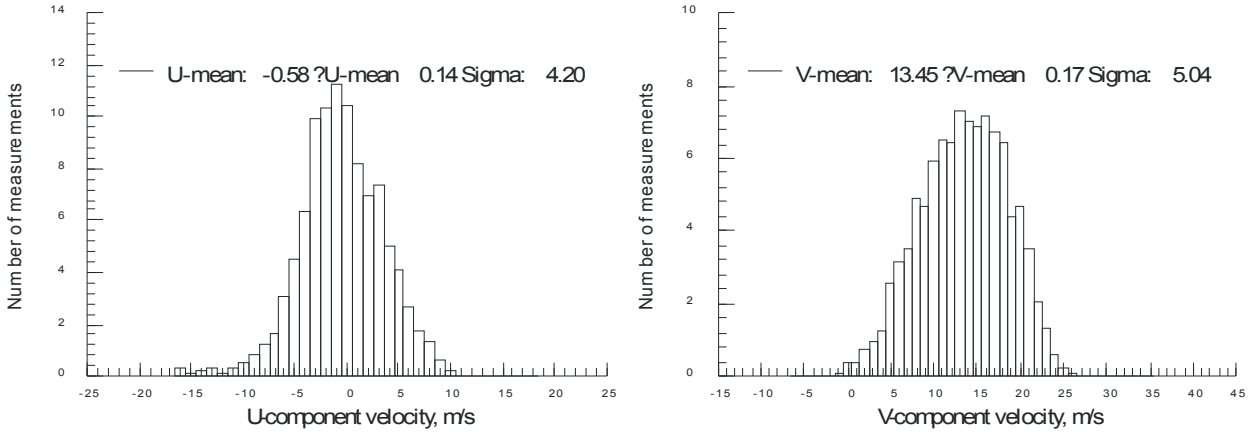

(ii) Signal-to-noise ratio threshold = 2.5 (5 dB)

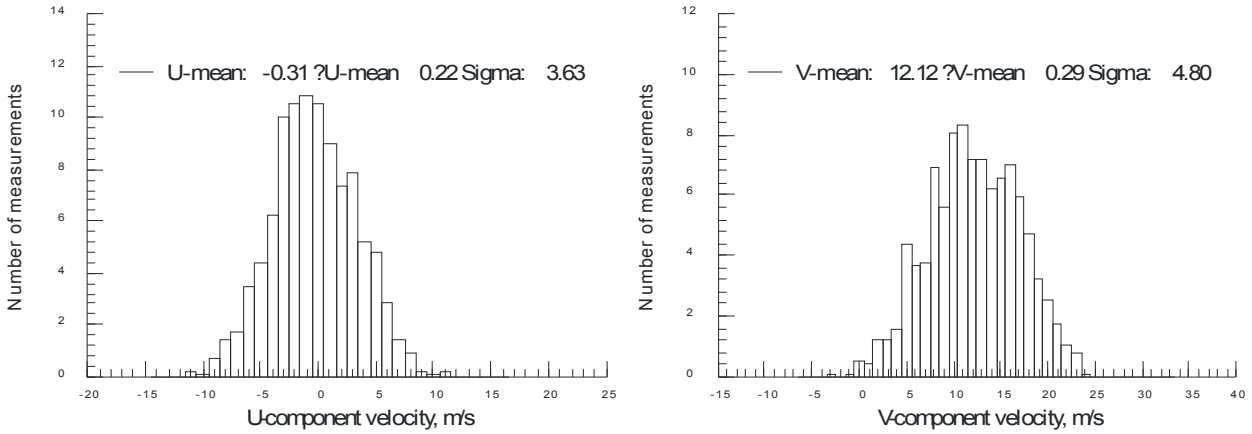

(iii) Signal-to-noise ratio threshold = 10 (10 dB)

Figure VII.30.a.(2)(c) - Velocity histograms obtained at closest approach – Flat black sample, Focal distance = 120 inches.

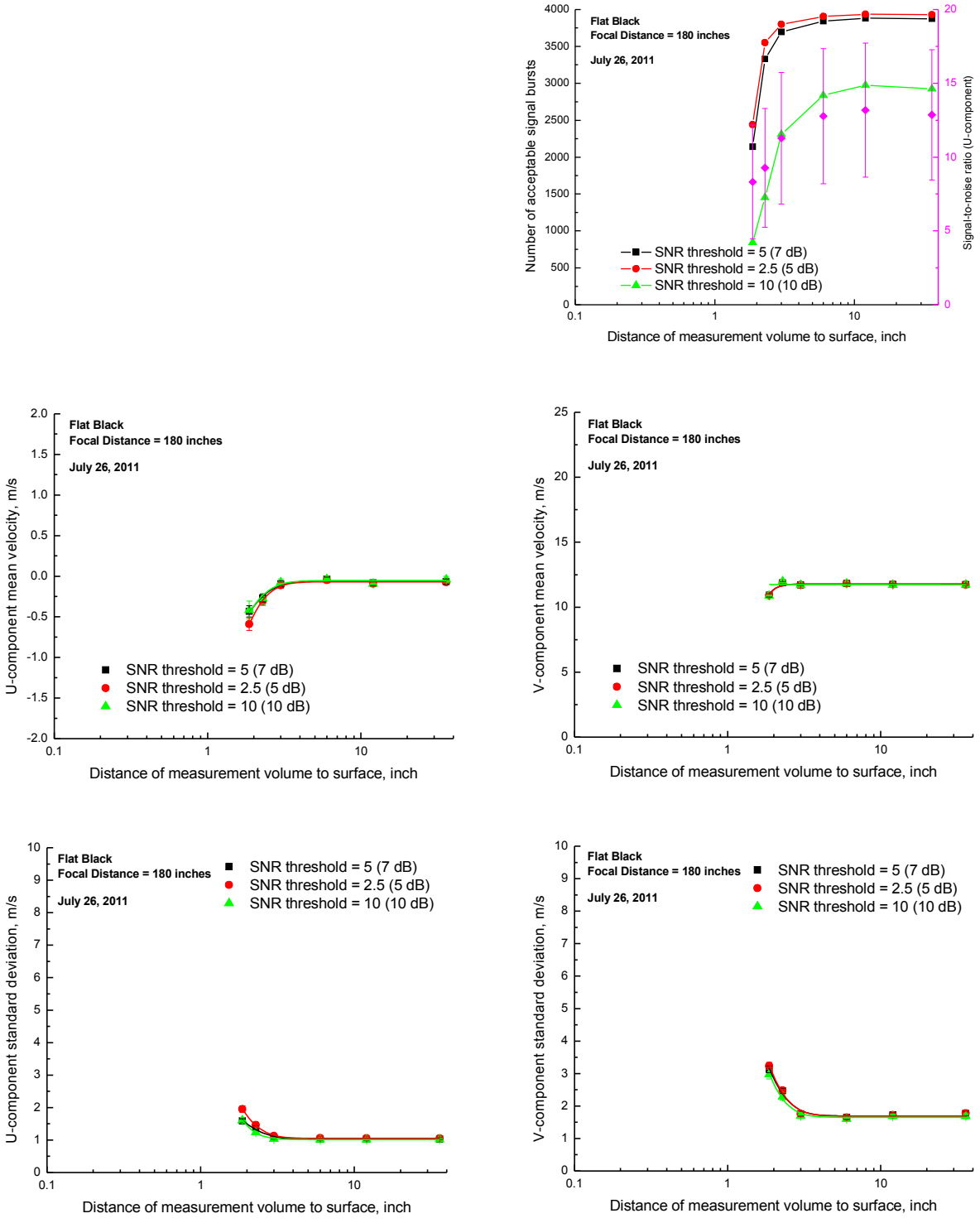

Figure VII.30.b.(1) - Velocity statistics as each surface is moved toward the measurement volume – Flat black sample, Focal distance = 180 inches.

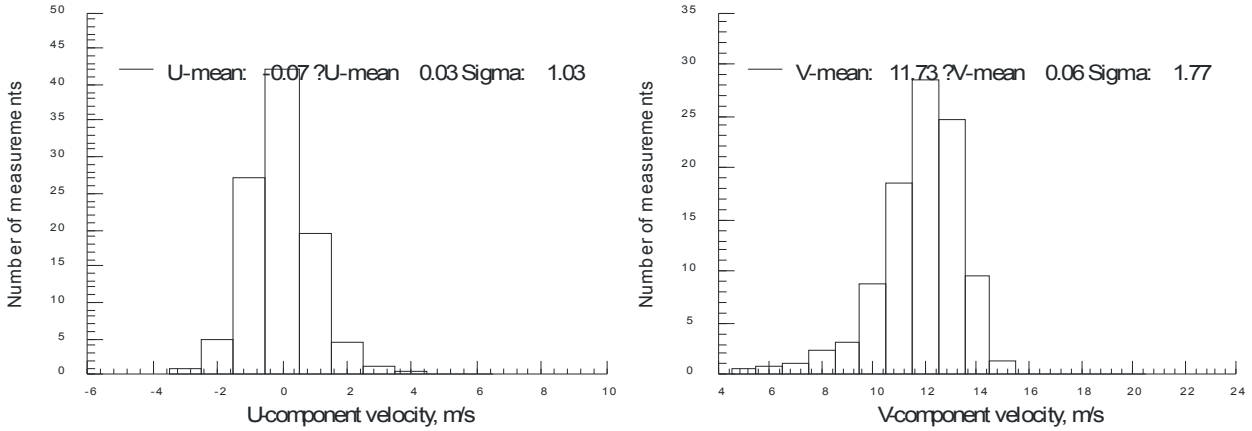

(i) Signal-to-noise ratio threshold = 5 (7 dB)

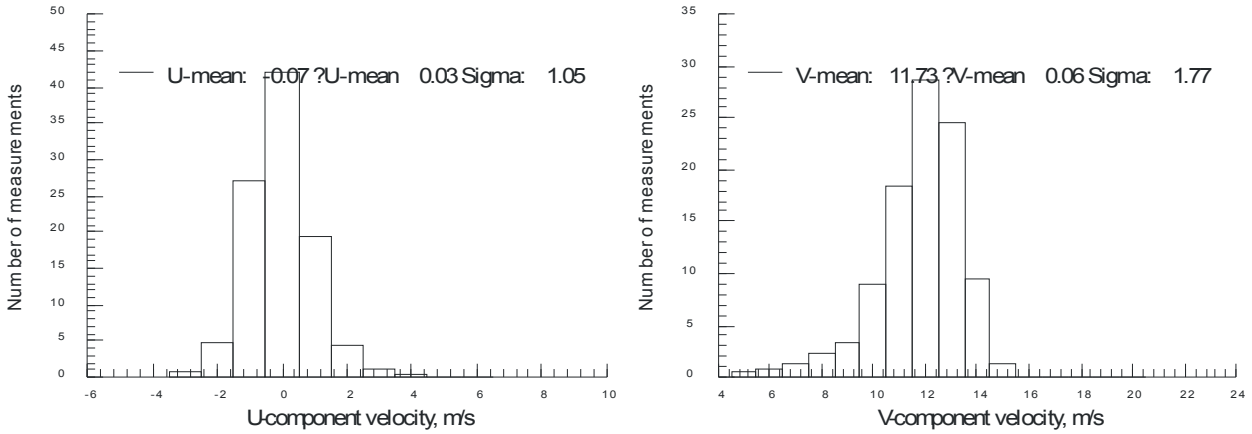

(ii) Signal-to-noise ratio threshold = 2.5 (5 dB)

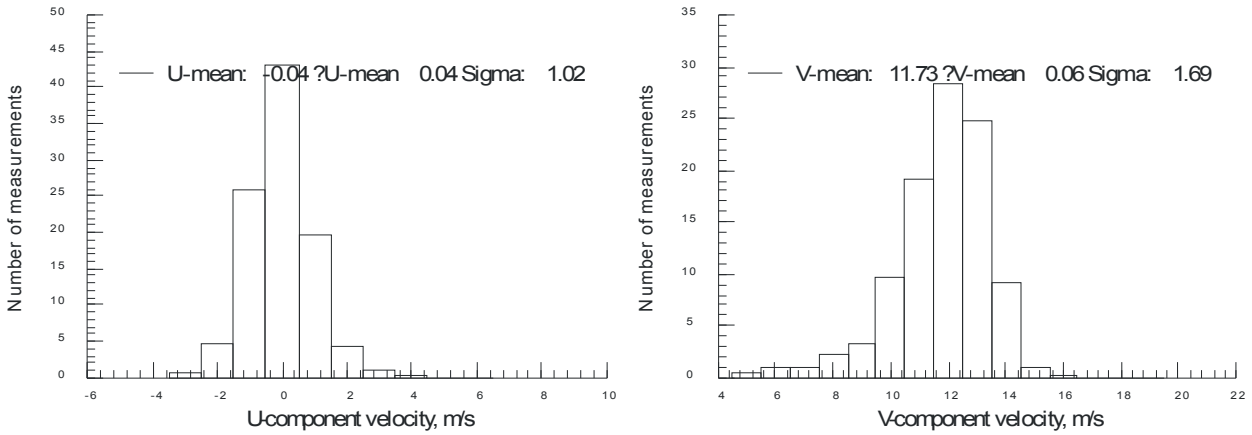

(iii) Signal-to-noise ratio threshold = 10 (10 dB)

Figure VII.30.b.(2)(a) - Velocity histograms obtained at 36-inch separation – Flat black sample, Focal distance = 180 inches.

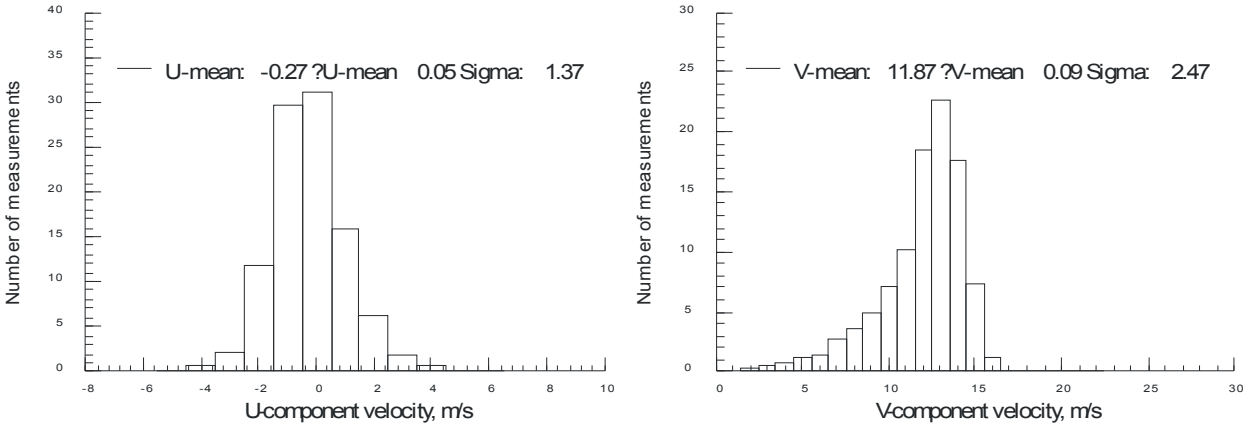

(i) Signal-to-noise ratio threshold = 5 (7 dB)

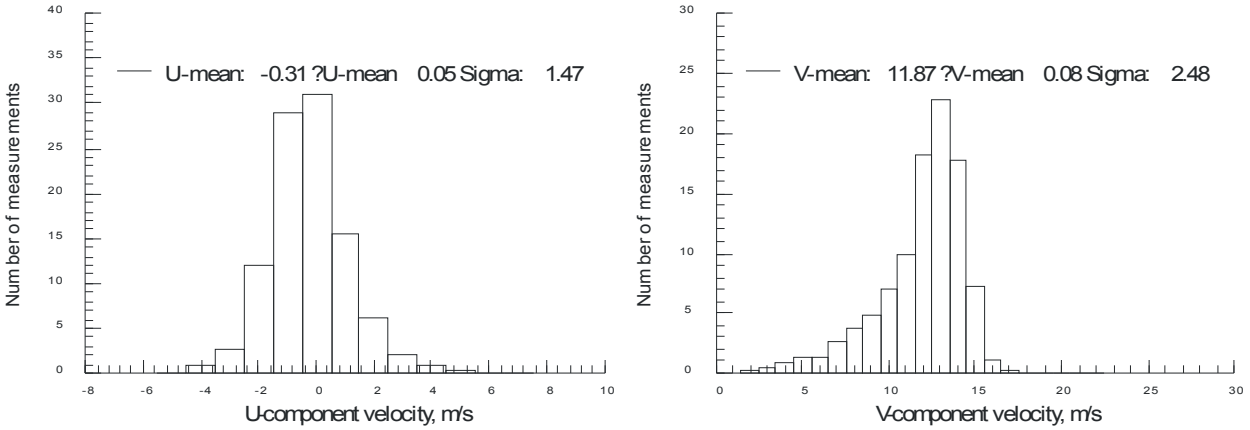

(ii) Signal-to-noise ratio threshold = 2.5 (5 dB)

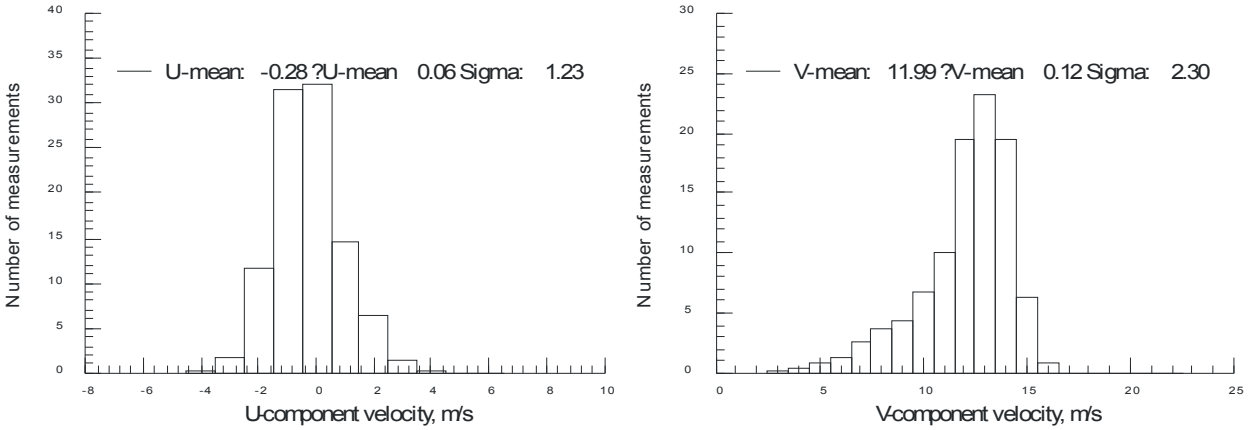

(iii) Signal-to-noise ratio threshold = 10 (10 dB)

Figure VII.30.b.(2)(b) - Velocity histograms obtained at first velocity/sigma deviation – Flat black sample, Focal distance = 180 inches.

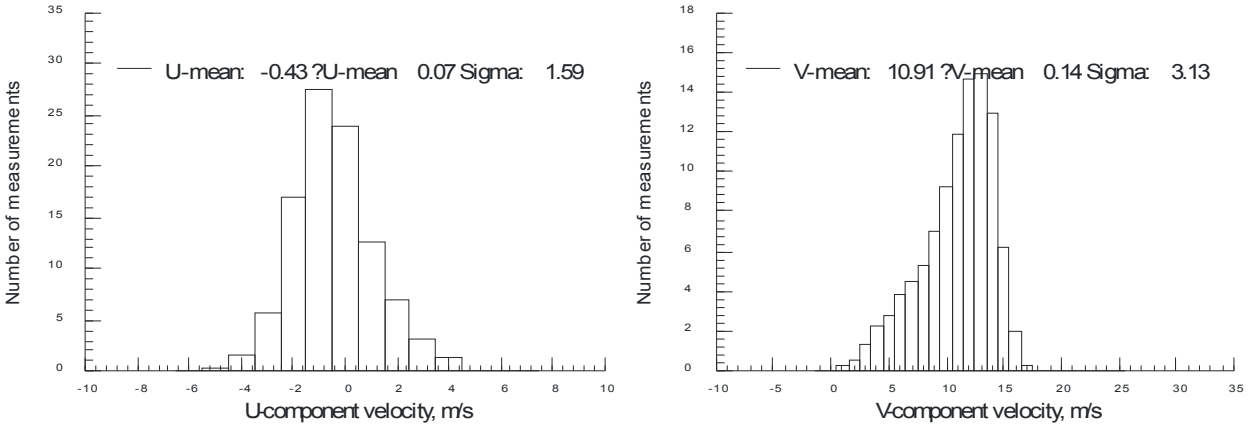

(i) Signal-to-noise ratio threshold = 5 (7 dB)

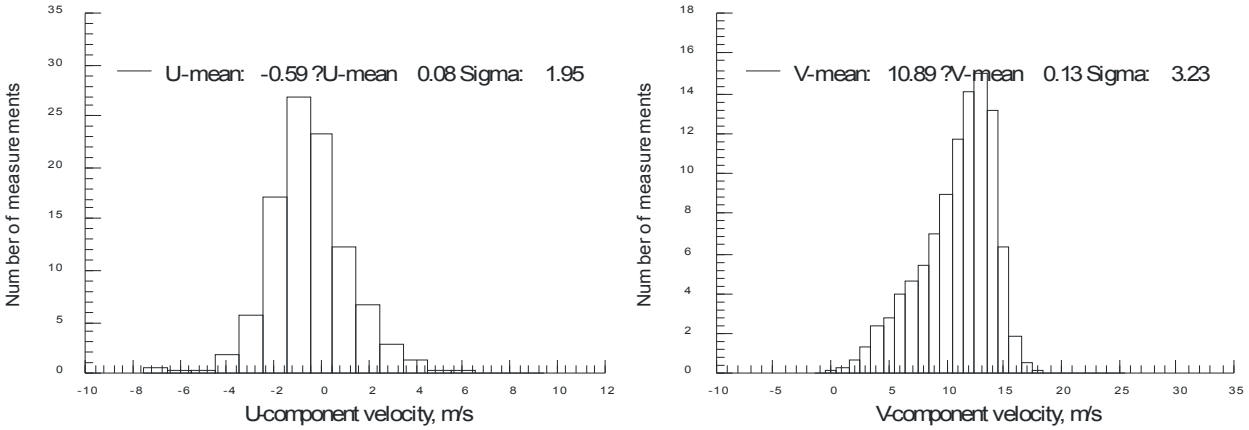

(ii) Signal-to-noise ratio threshold = 2.5 (5 dB)

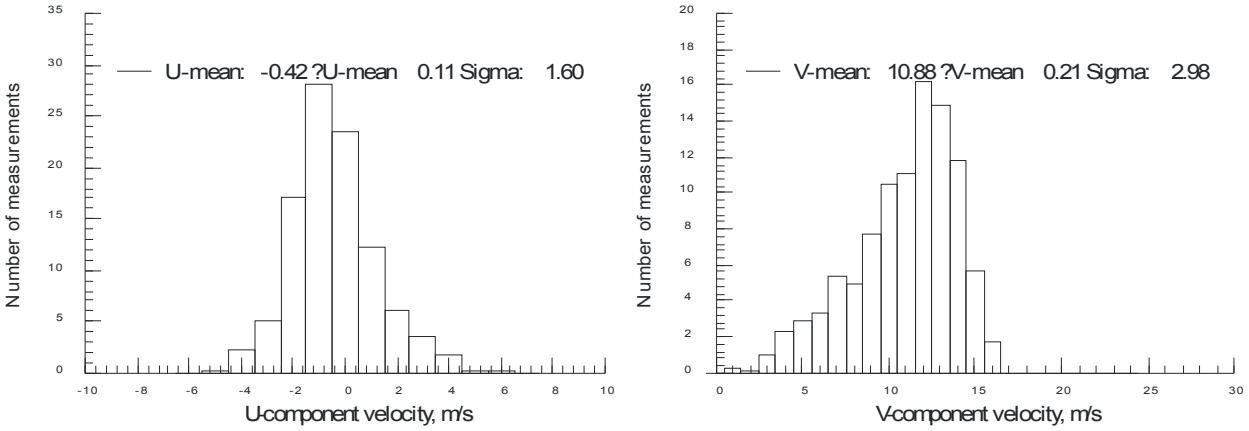

(iii) Signal-to-noise ratio threshold = 10 (10 dB)

Figure VII.30.b.(2)(c) - Velocity histograms obtained at closest approach – Flat black sample, Focal distance = 180 inches.

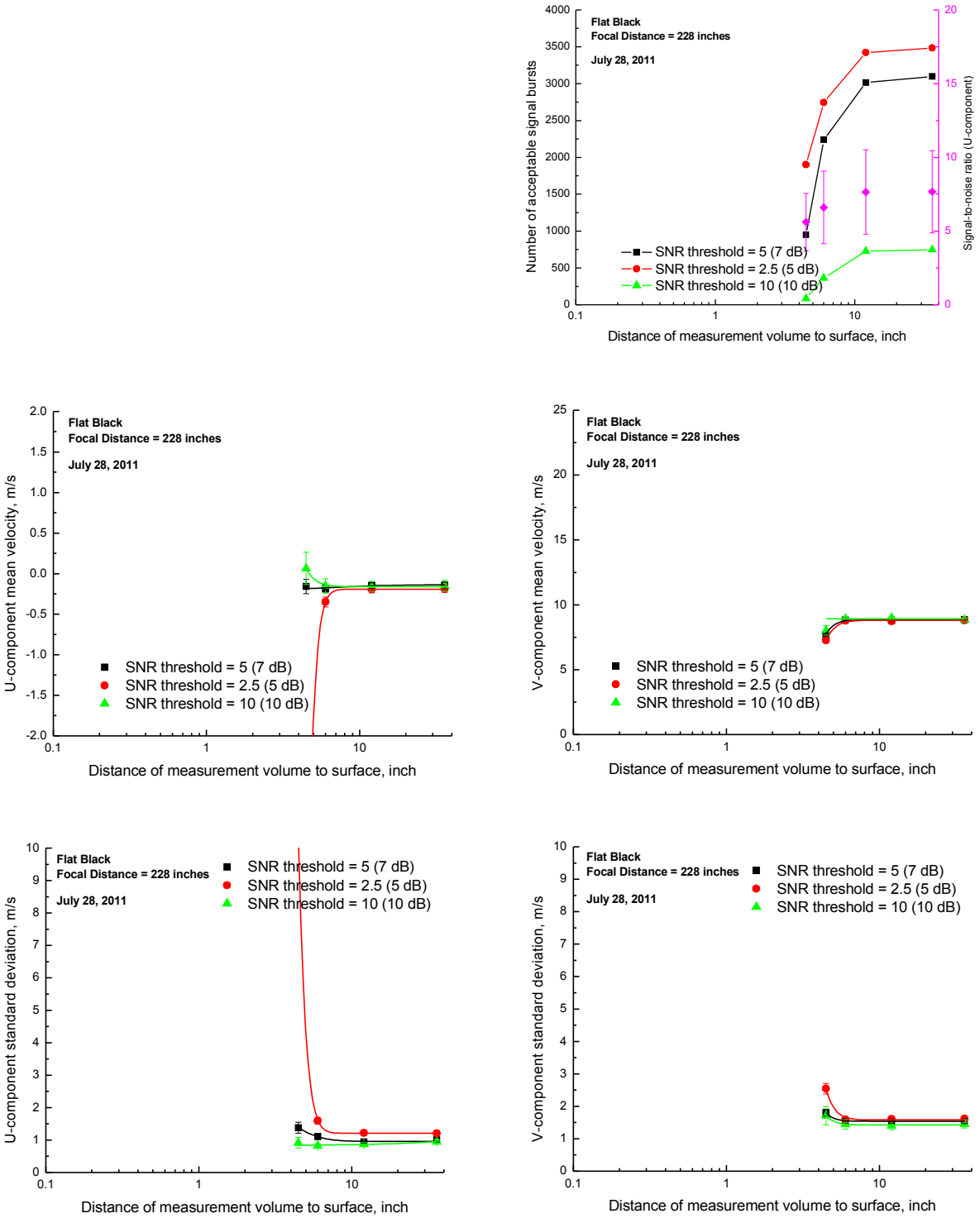

Figure VII.30.c.(1) - Velocity statistics as each surface is moved toward the measurement volume – Flat black sample, Focal distance = 228 inches.

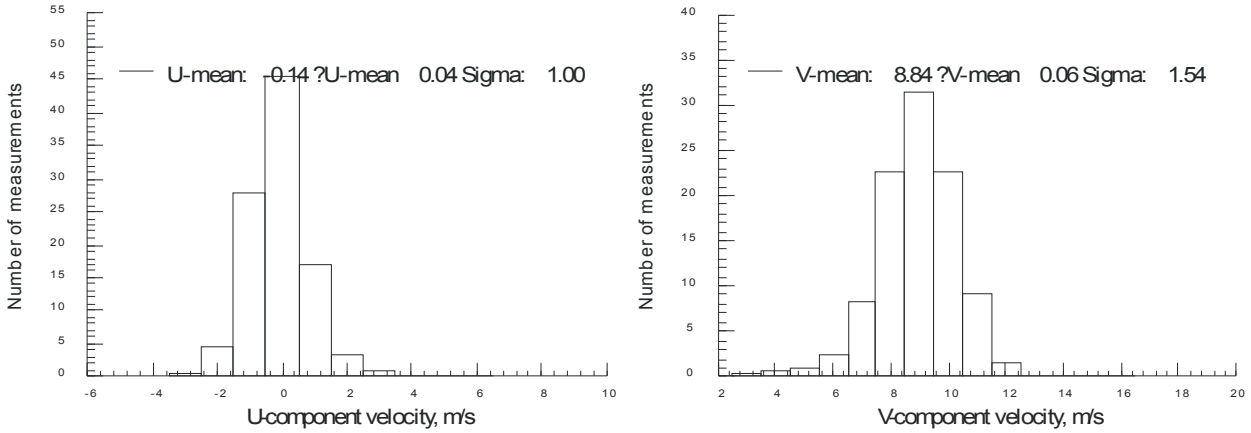

(i) Signal-to-noise ratio threshold = 5 (7 dB)

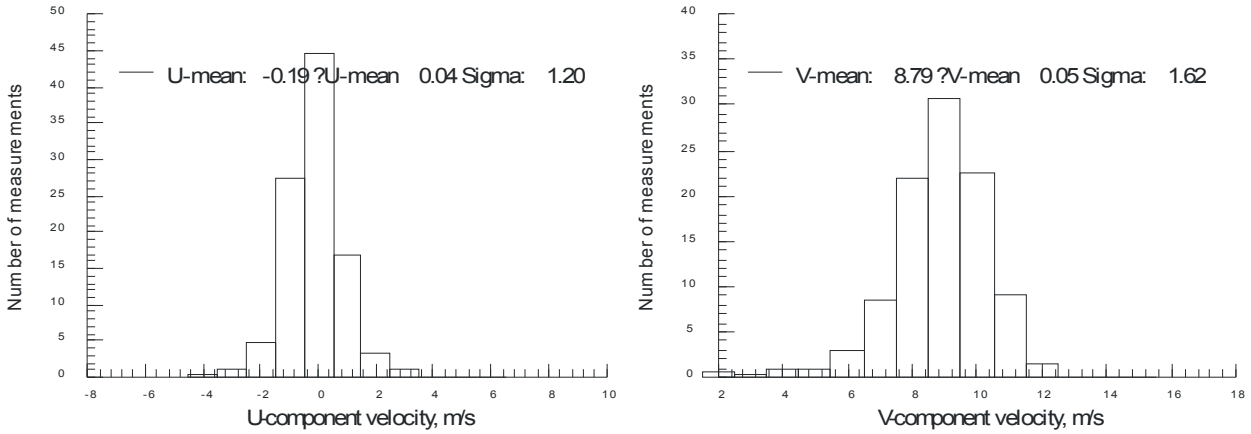

(ii) Signal-to-noise ratio threshold = 2.5 (5 dB)

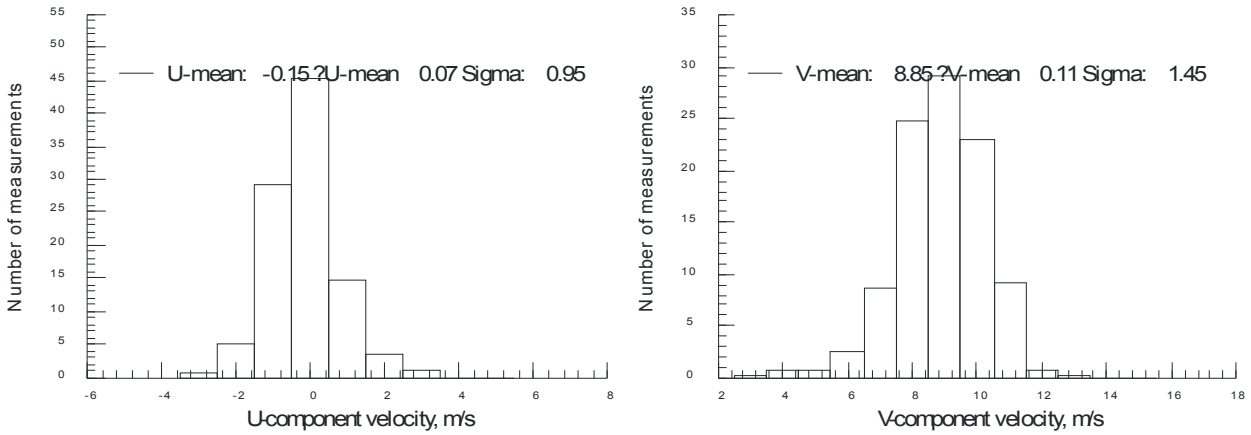

(iii) Signal-to-noise ratio threshold = 10 (10 dB)

Figure VII.30.c.(2)(a) - Velocity histograms obtained at 36-inch separation – Flat black sample, Focal distance = 228 inches.

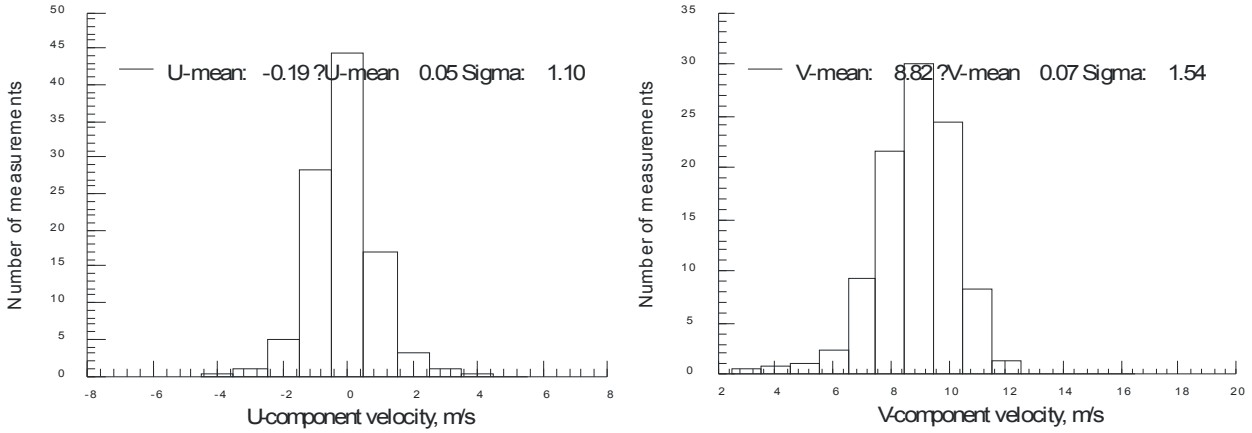

(i) Signal-to-noise ratio threshold = 5 (7 dB)

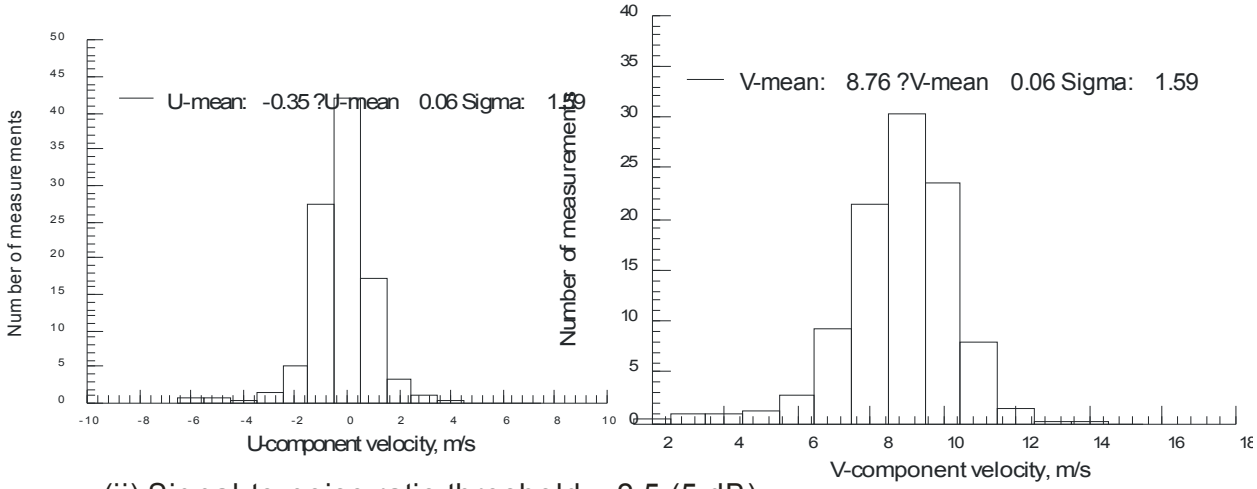

(ii) Signal-to-noise ratio threshold = 2.5 (5 dB)

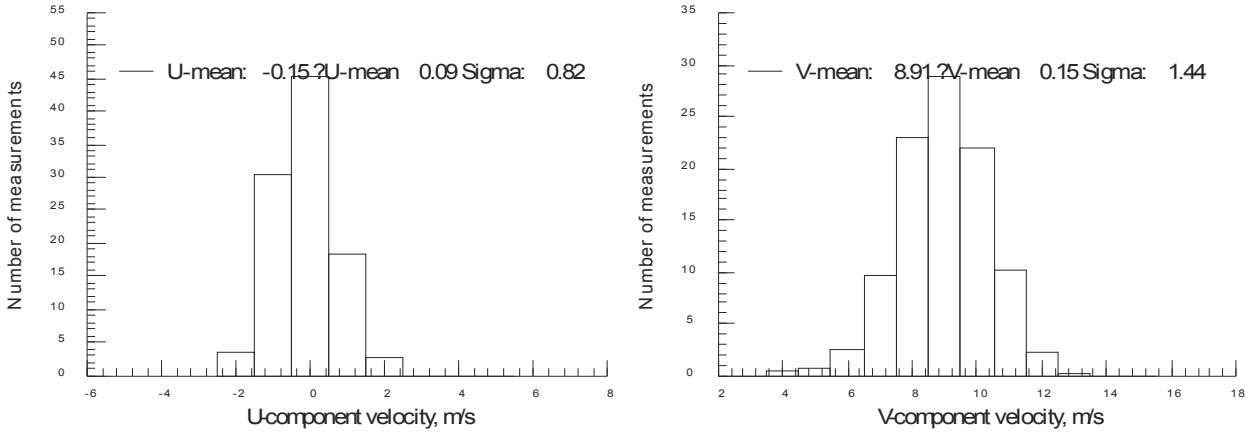

(iii) Signal-to-noise ratio threshold = 10 (10 dB)

Figure VII.30.c.(2)(b) - Velocity histograms obtained at first velocity/sigma deviation – Flat black sample, Focal distance = 228 inches.

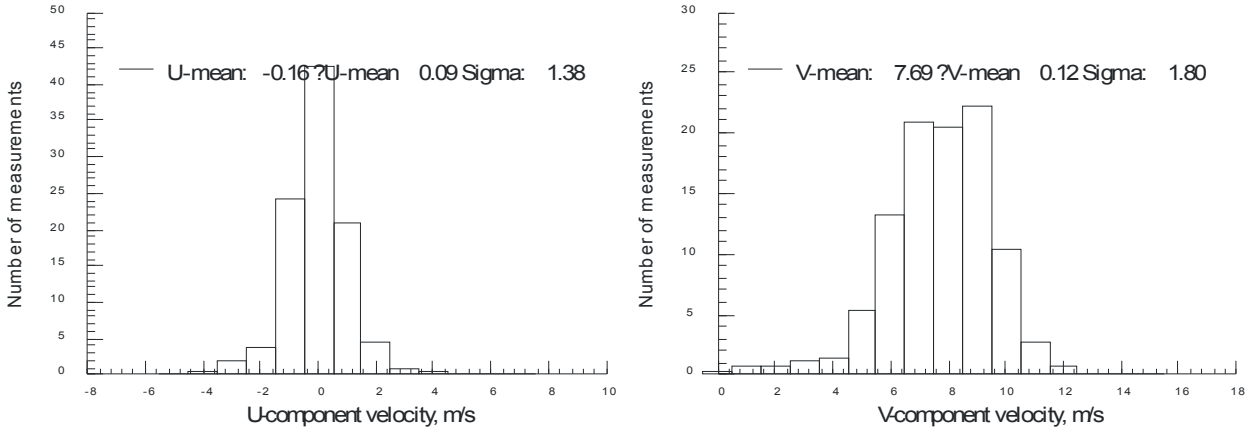

(i) Signal-to-noise ratio threshold = 5 (7 dB)

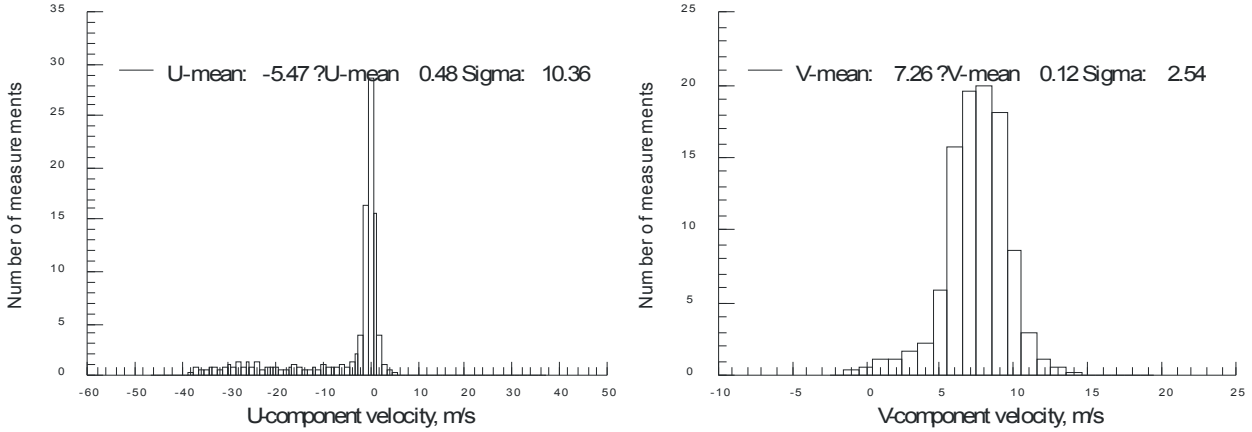

(ii) Signal-to-noise ratio threshold = 2.5 (5 dB)

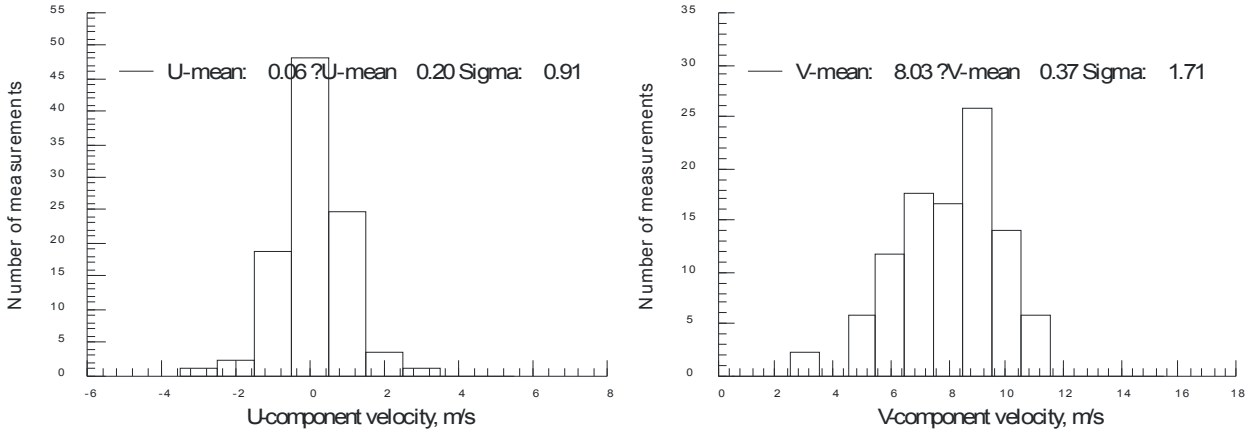

(iii) Signal-to-noise ratio threshold = 10 (10 dB)

Figure VII.30.c.(2)(c) - Velocity histograms obtained at closest approach – Flat black sample, Focal distance = 228 inches.

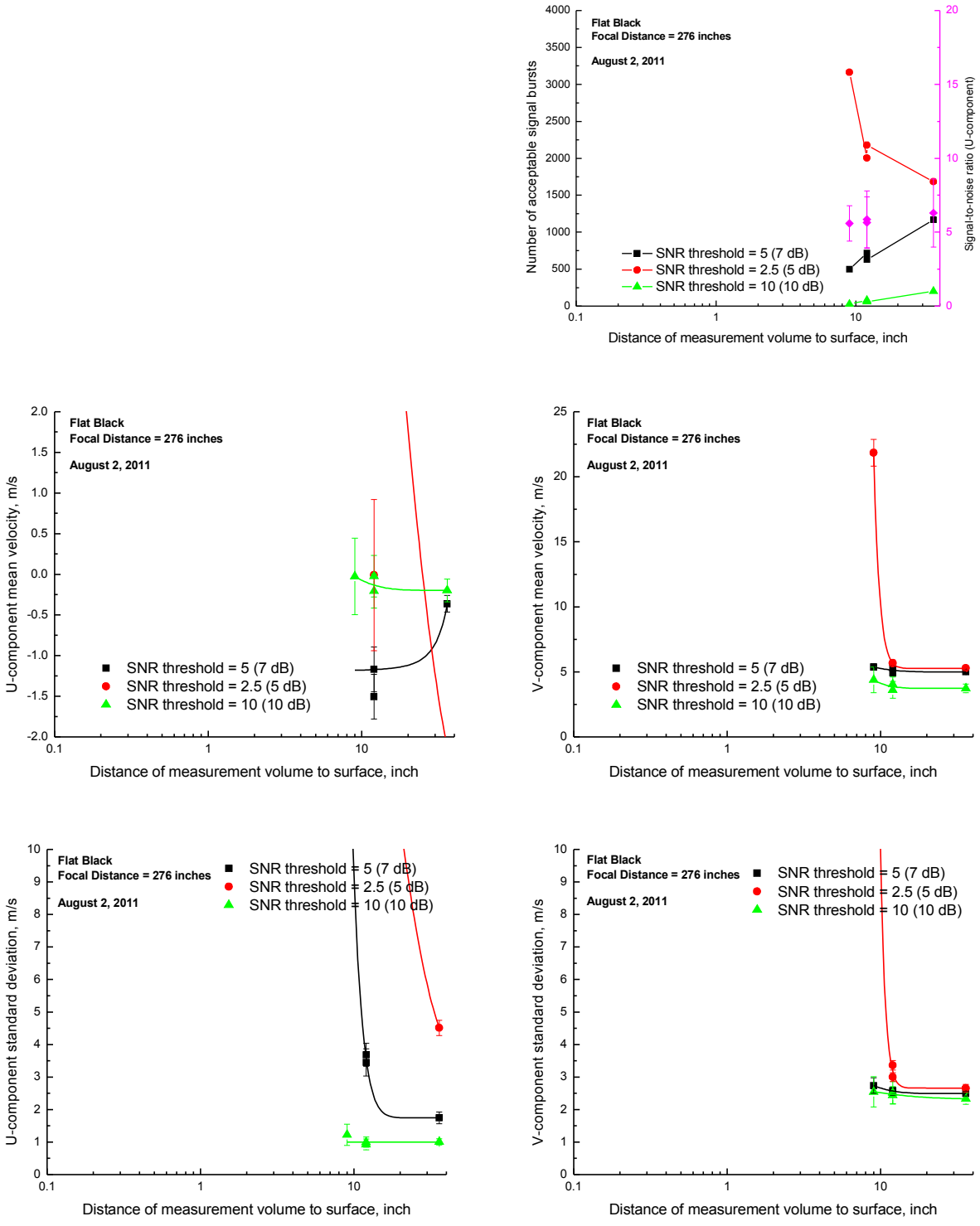

Figure VII.30.d.(1) - Velocity statistics as each surface is moved toward the measurement volume – Flat black sample, Focal distance = 276 inches.

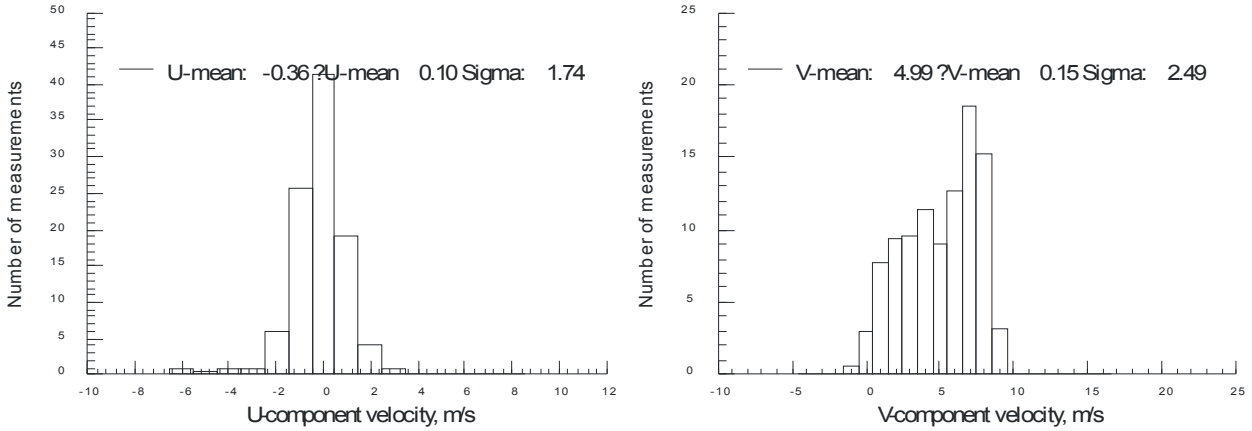

(i) Signal-to-noise ratio threshold = 5 (7 dB)

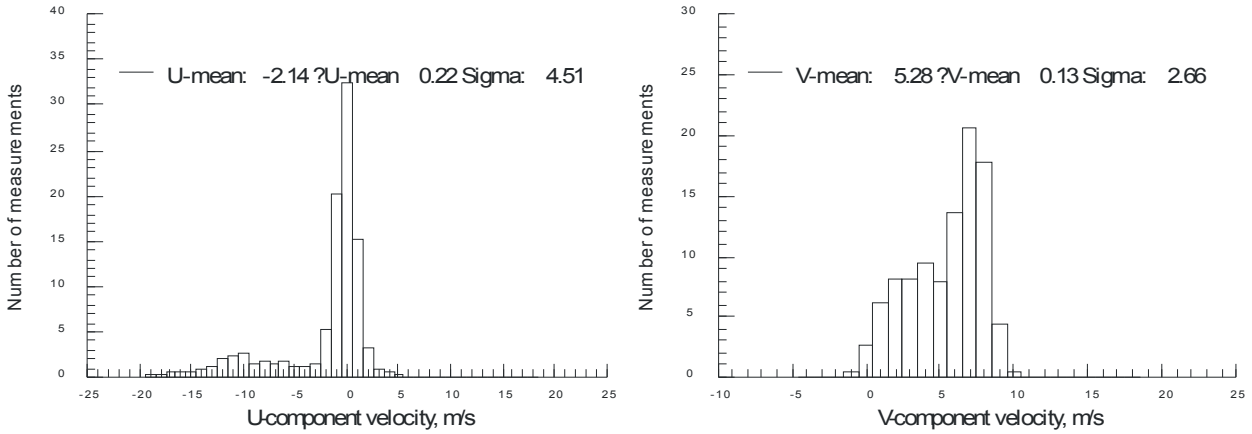

(ii) Signal-to-noise ratio threshold = 2.5 (5 dB)

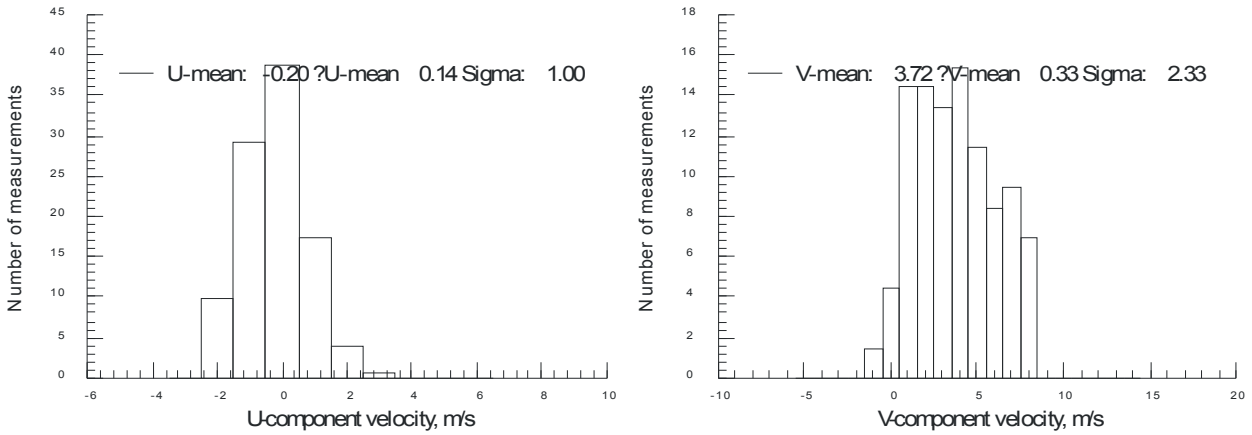

(iii) Signal-to-noise ratio threshold = 10 (10 dB)

Figure VII.30.d.(2)(a) - Velocity histograms obtained at 36-inch separation – Flat black sample, Focal distance = 276 inches.

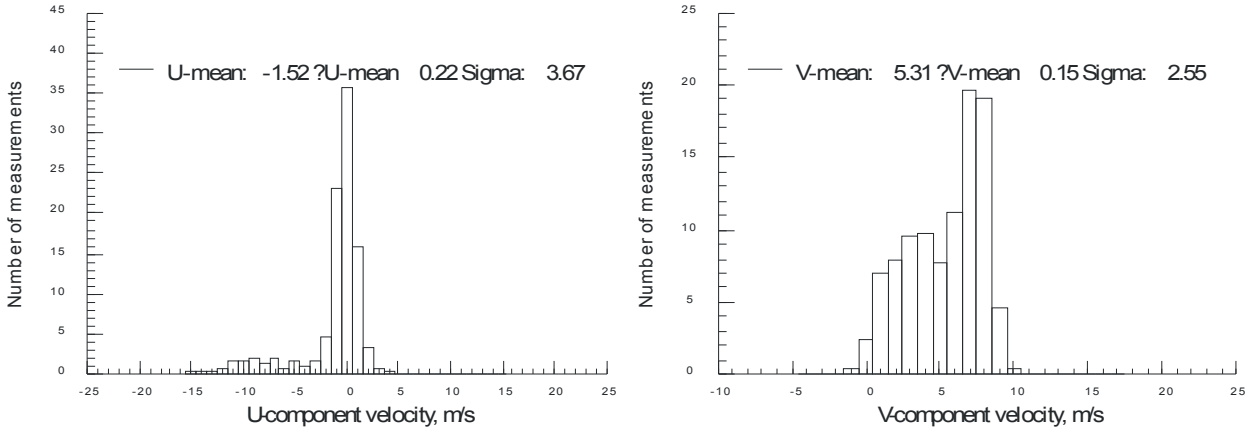

(i) Signal-to-noise ratio threshold = 5 (7 dB)

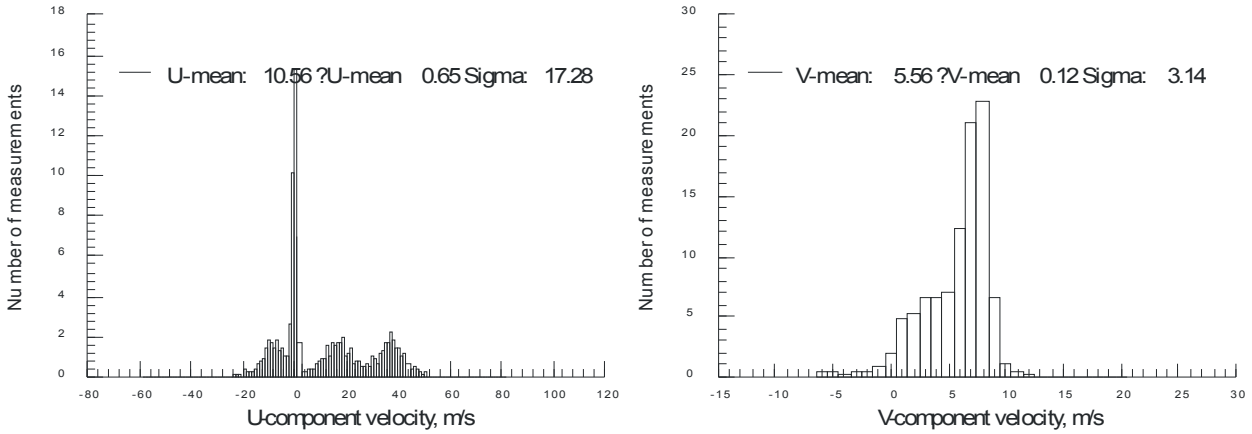

(ii) Signal-to-noise ratio threshold = 2.5 (5 dB)

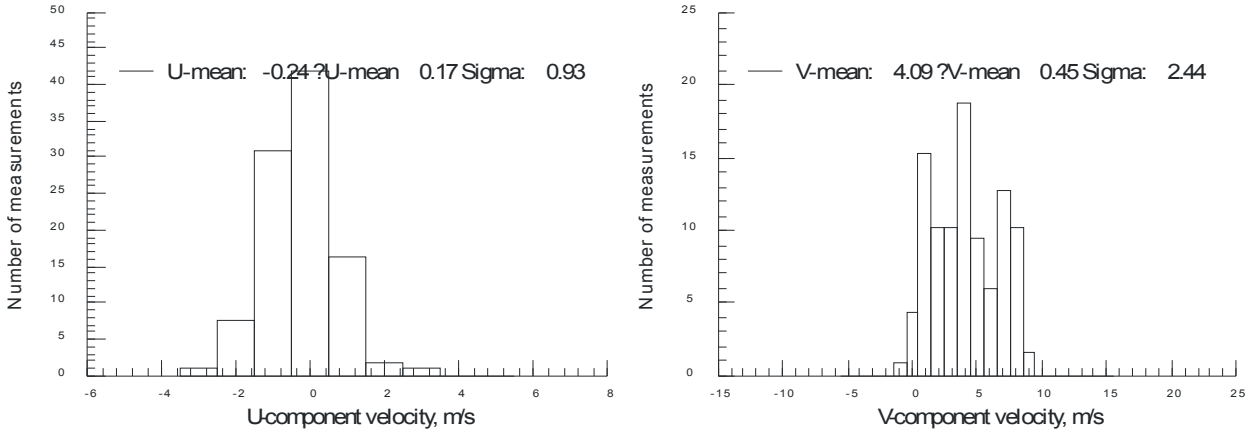

(iii) Signal-to-noise ratio threshold = 10 (10 dB)

Figure VII.30.d.(2)(b) - Velocity histograms obtained at first velocity/sigma deviation – Flat black sample, Focal distance = 276 inches.

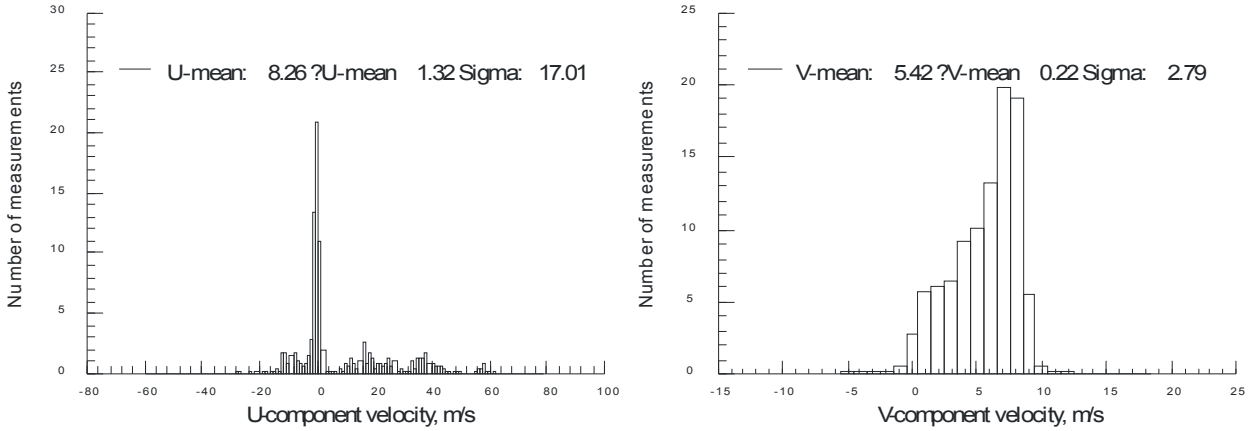

(i) Signal-to-noise ratio threshold = 5 (7 dB)

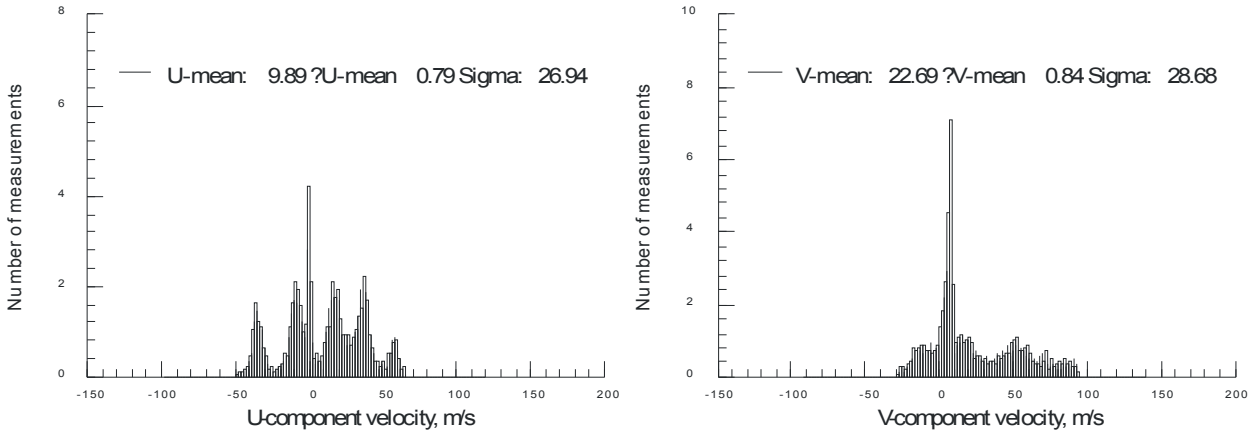

(ii) Signal-to-noise ratio threshold = 2.5 (5 dB)

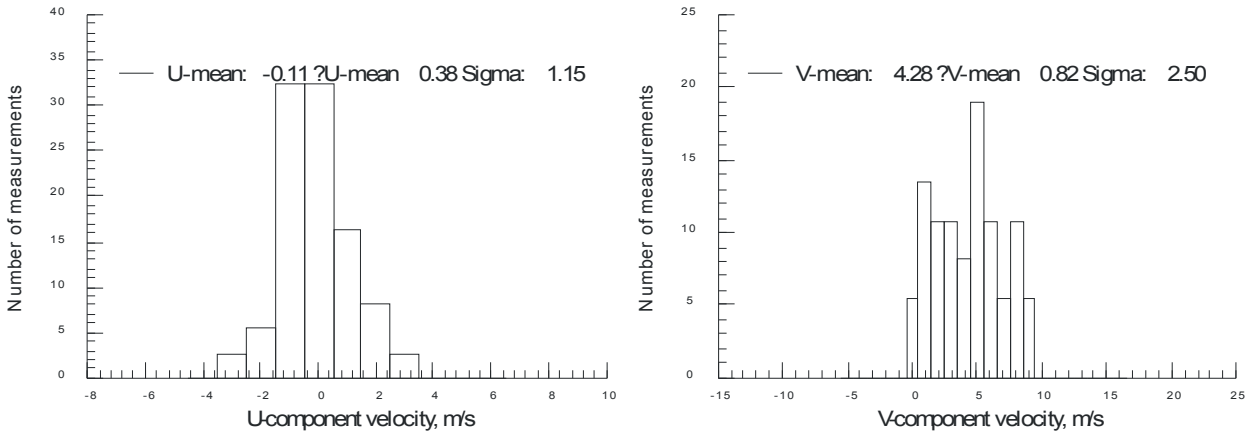

(iii) Signal-to-noise ratio threshold = 10 (10 dB)

Figure VII.30.d.(2)(c) - Velocity histograms obtained at closest approach – Flat black sample, Focal distance = 276 inches.

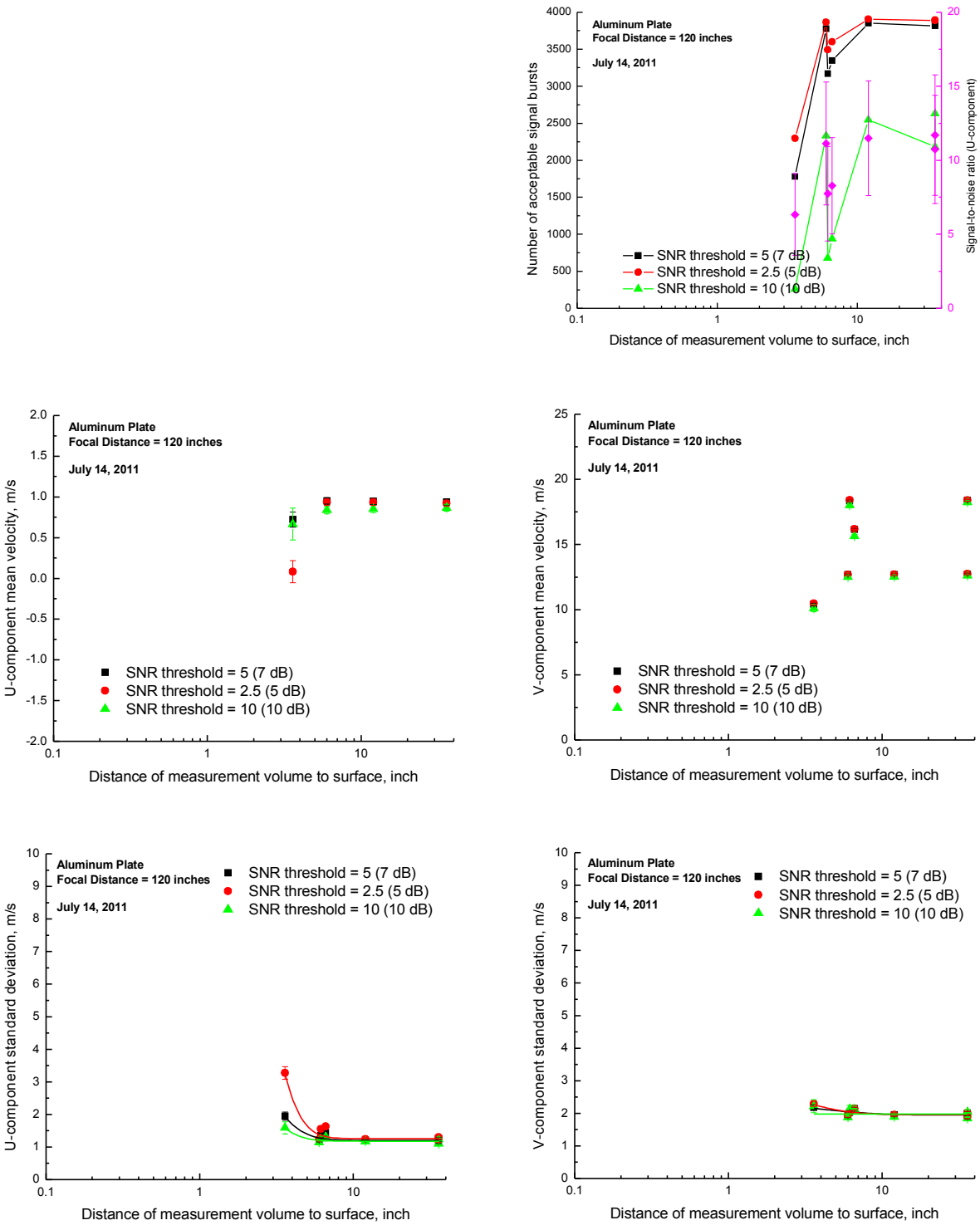

Figure VII.31.a.- Velocity statistics as each surface is moved toward the measurement volume – Unpainted aluminum sample, Focal distance = 120 inches.

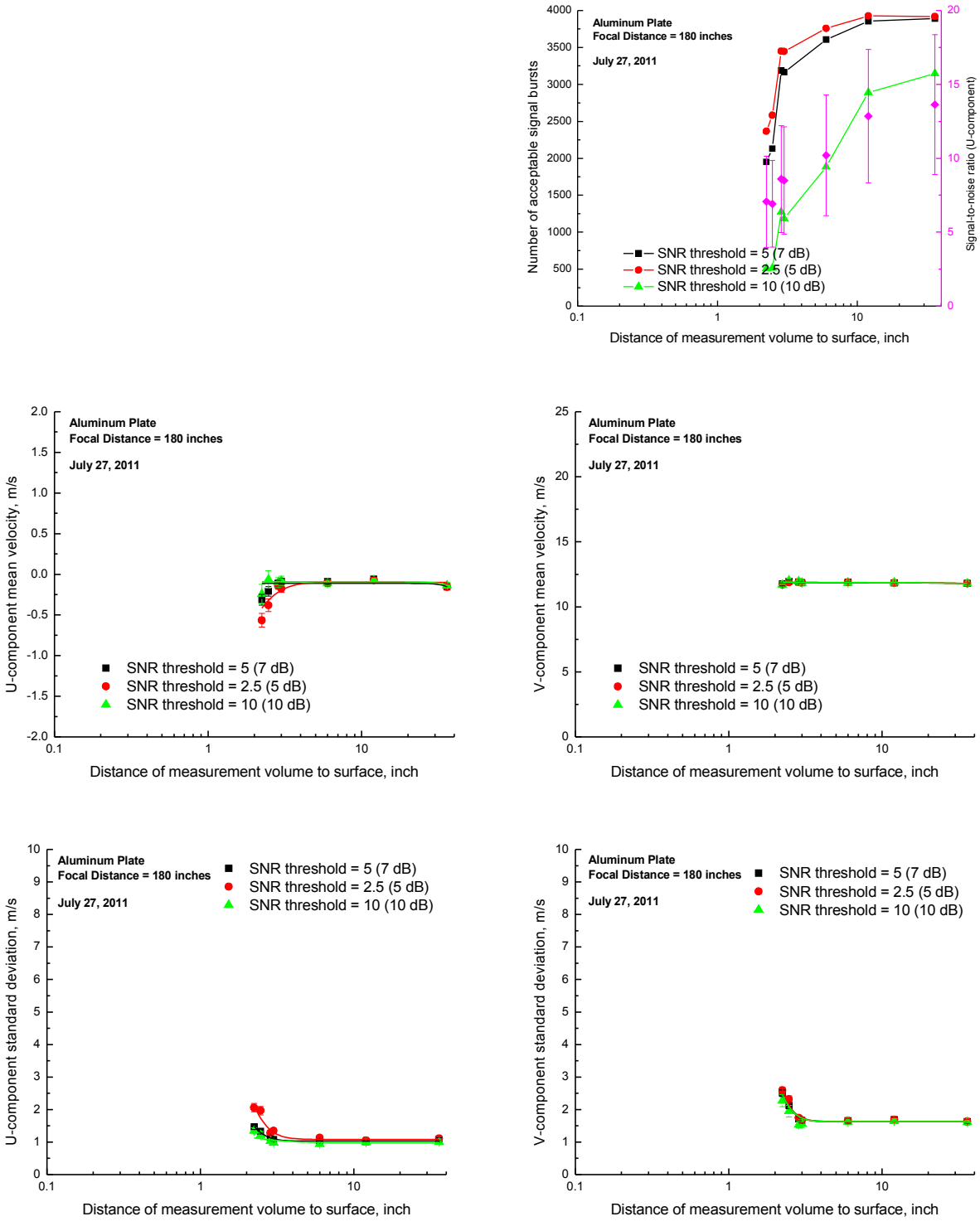

Figure VII.31.b.- Velocity statistics as each surface is moved toward the measurement volume – Unpainted aluminum sample, Focal distance = 180 inches.

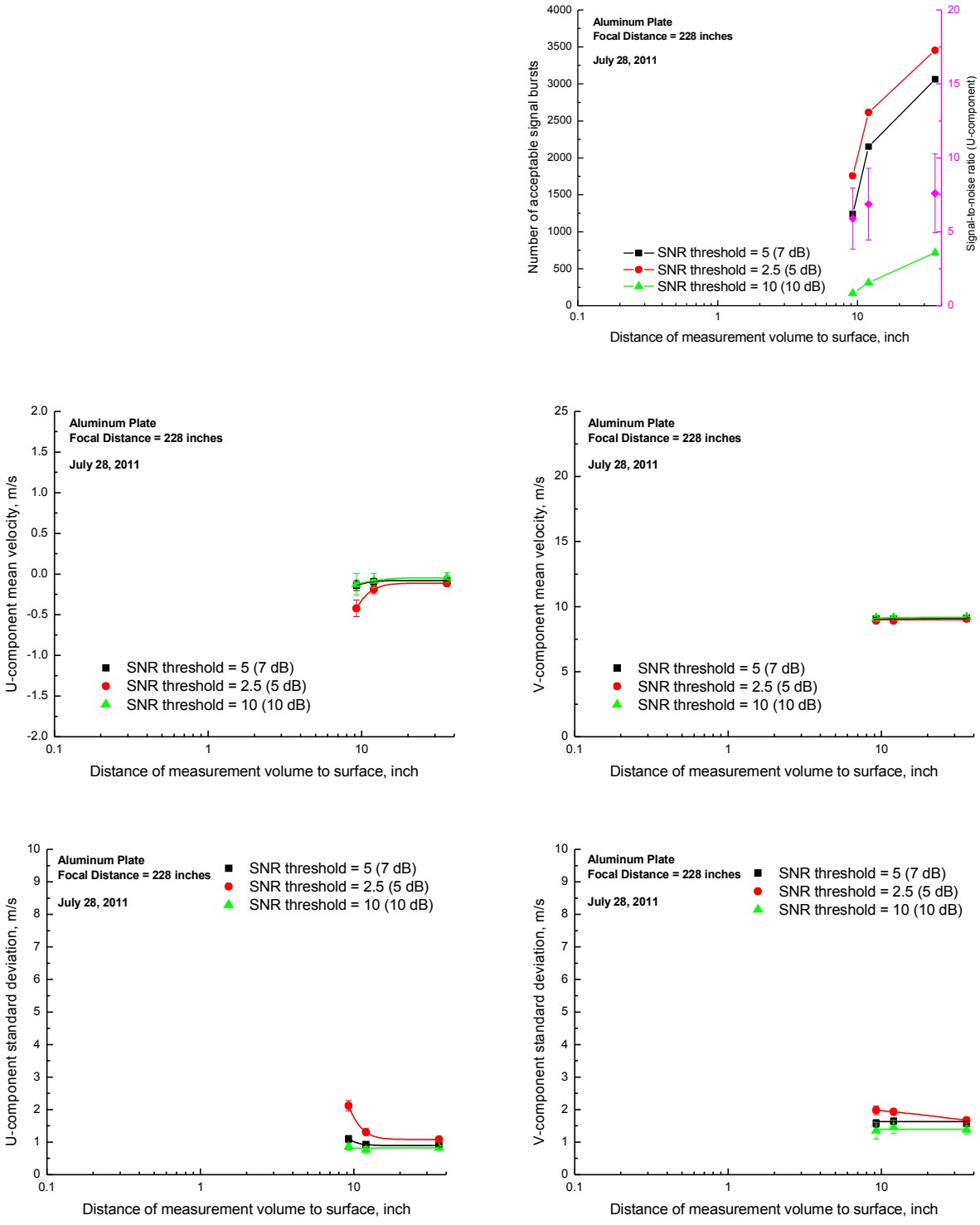

Figure VII.31.c.- Velocity statistics as each surface is moved toward the measurement volume – Unpainted aluminum sample, Focal distance = 228 inches.

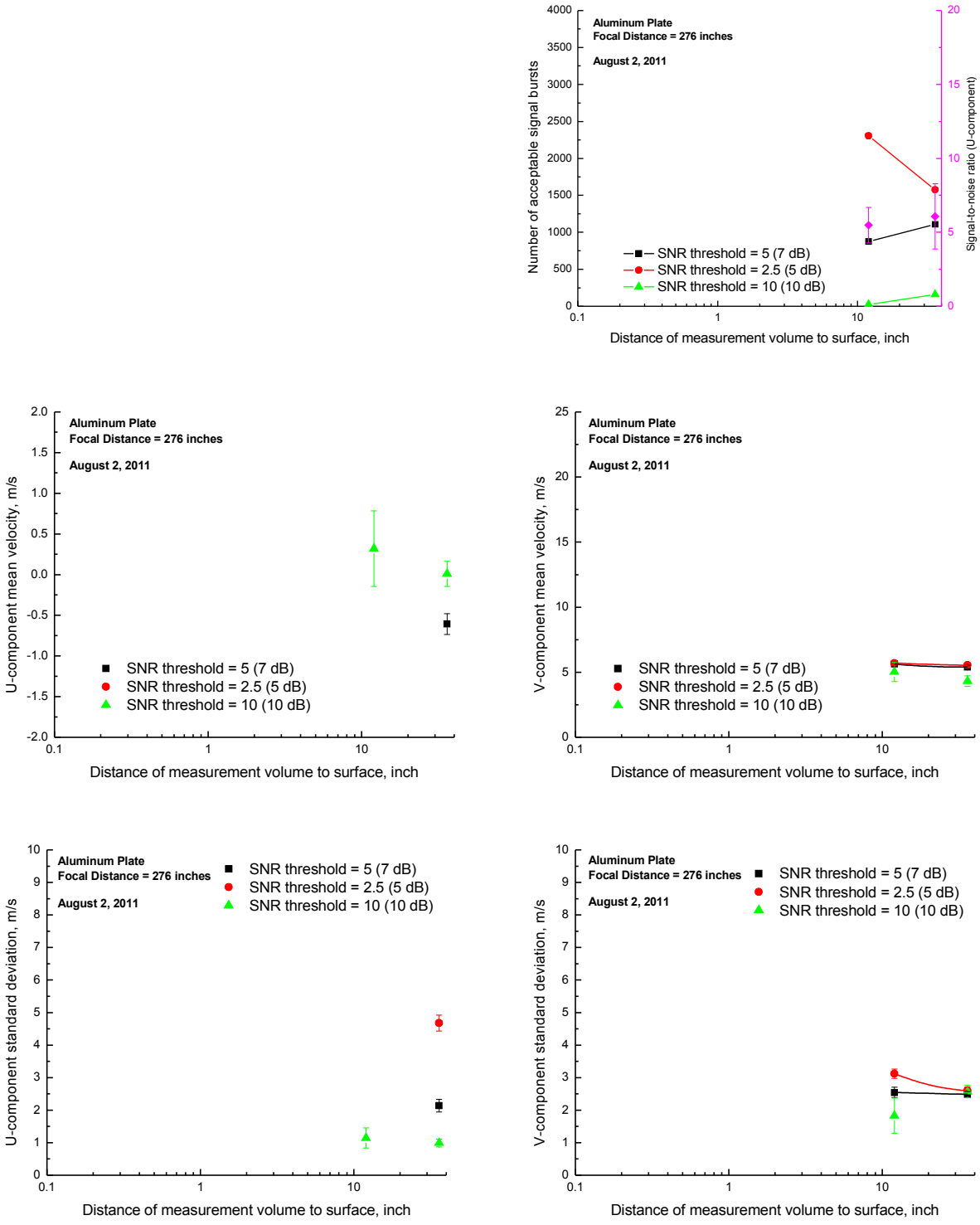

Figure VII.31.d.- Velocity statistics as each surface is moved toward the measurement volume – Unpainted aluminum sample, Focal distance = 276 inches.

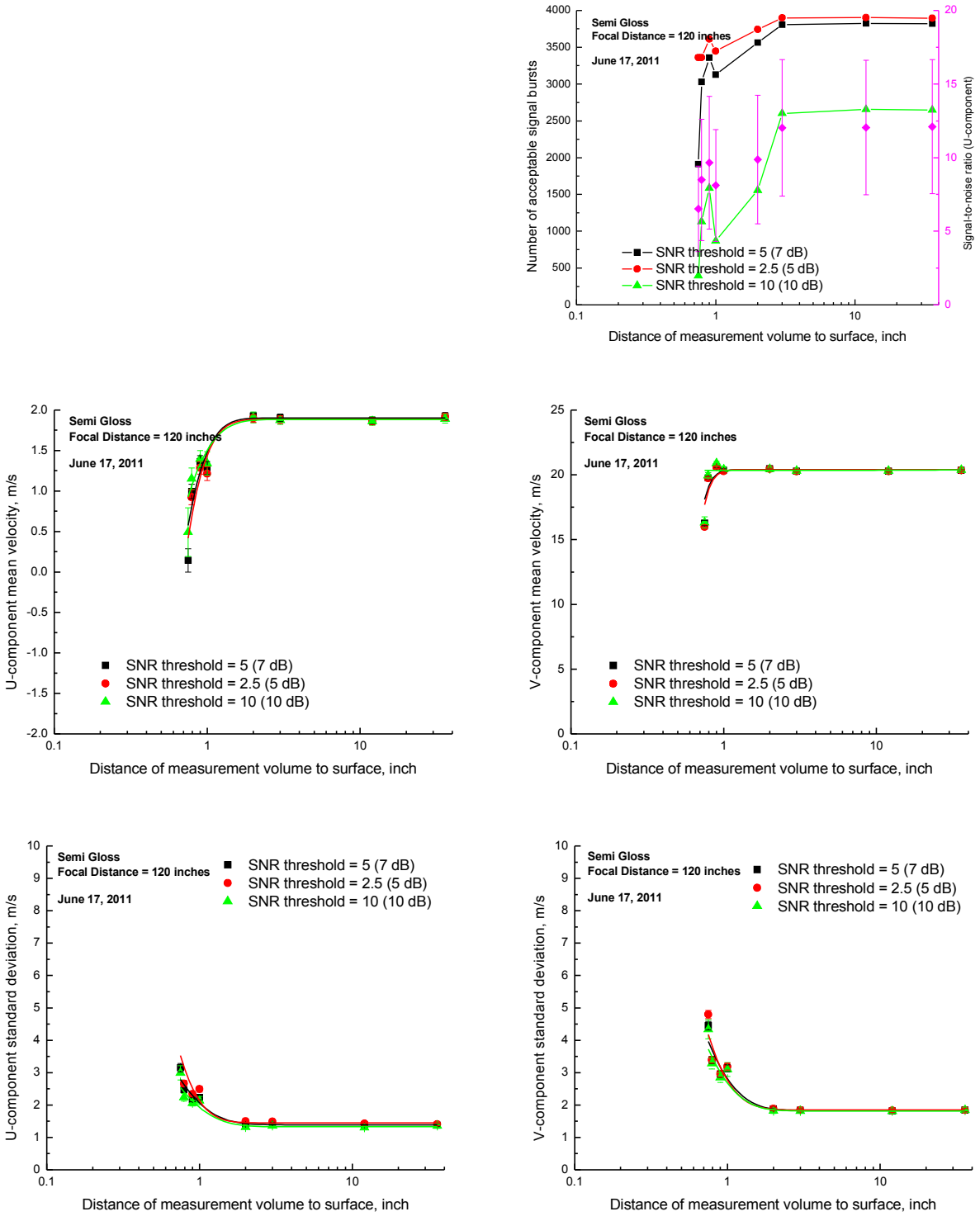

Figure VII.32.- Velocity statistics as each surface is moved toward the measurement volume – Semi gloss black paint sample, Focal distance = 120 inches.

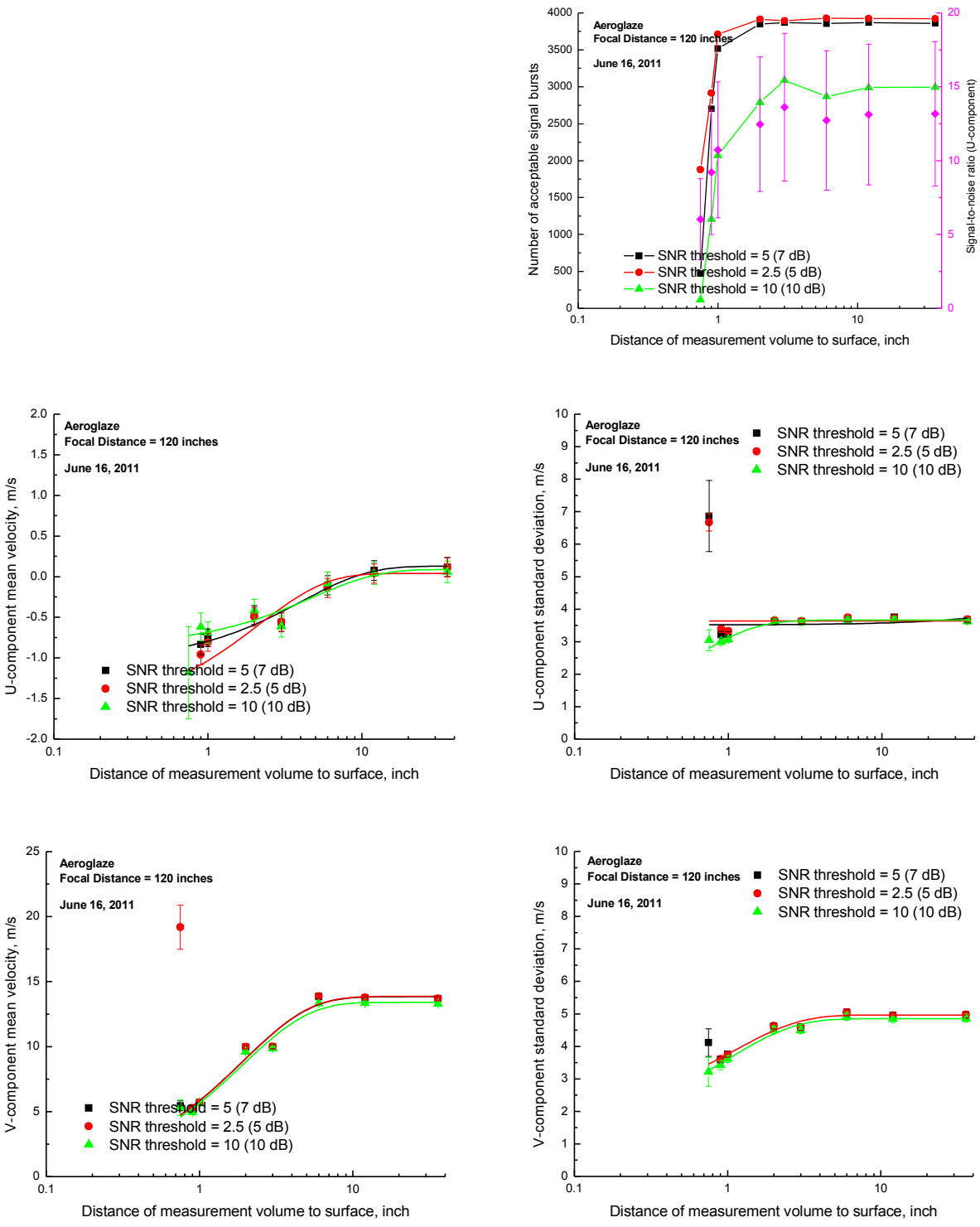

Figure VII.33.a.(1) - Velocity statistics as each surface is moved toward the measurement volume – Aeroglaze, Focal distance = 120 inches.

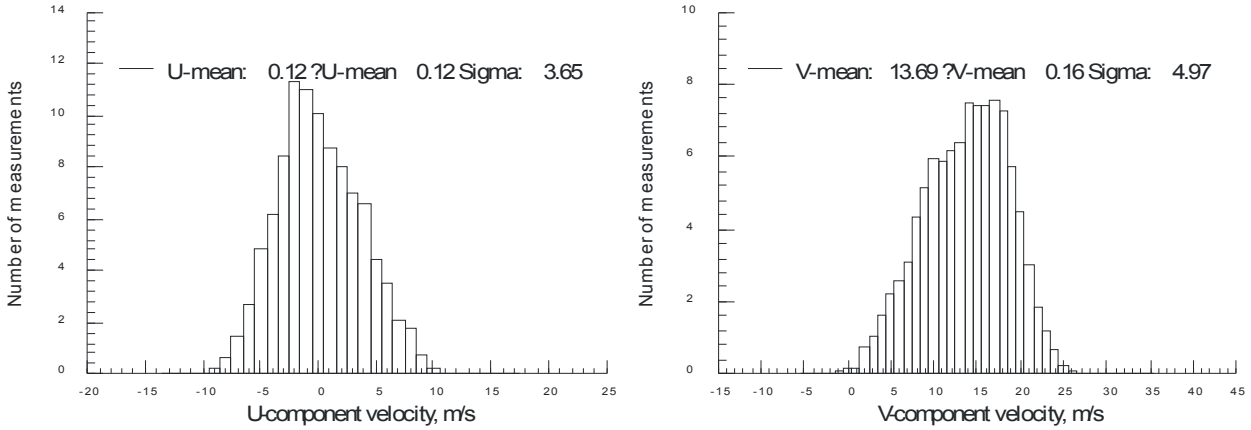

(i) Signal-to-noise ratio threshold = 5 (7 dB)

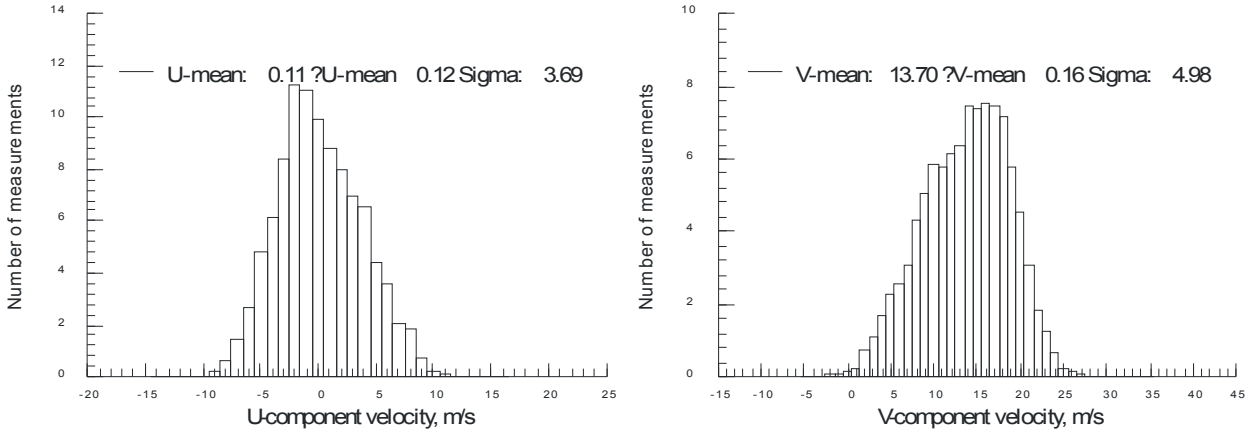

(ii) Signal-to-noise ratio threshold = 2.5 (5 dB)

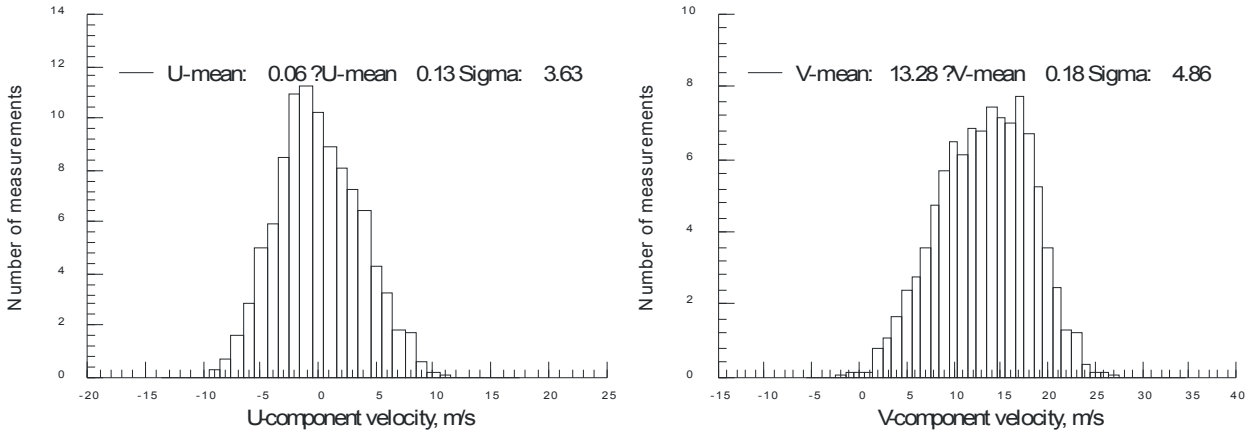

(iii) Signal-to-noise ratio threshold = 10 (10 dB)

Figure VII.33.a.(2)(a) - Velocity histograms obtained at 36-inch separation – Aeroglaze, Focal distance = 120 inches.

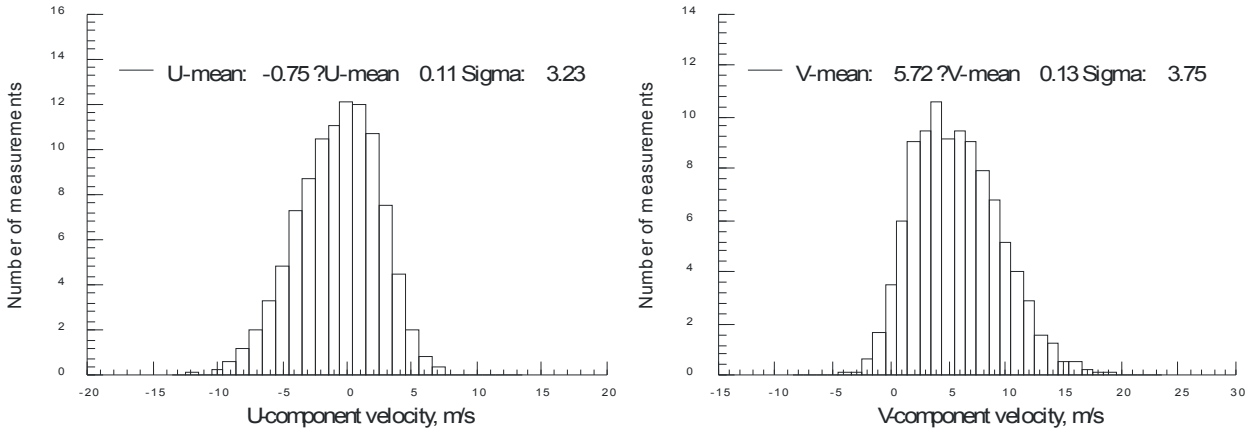

(i) Signal-to-noise ratio threshold = 5 (7 dB)

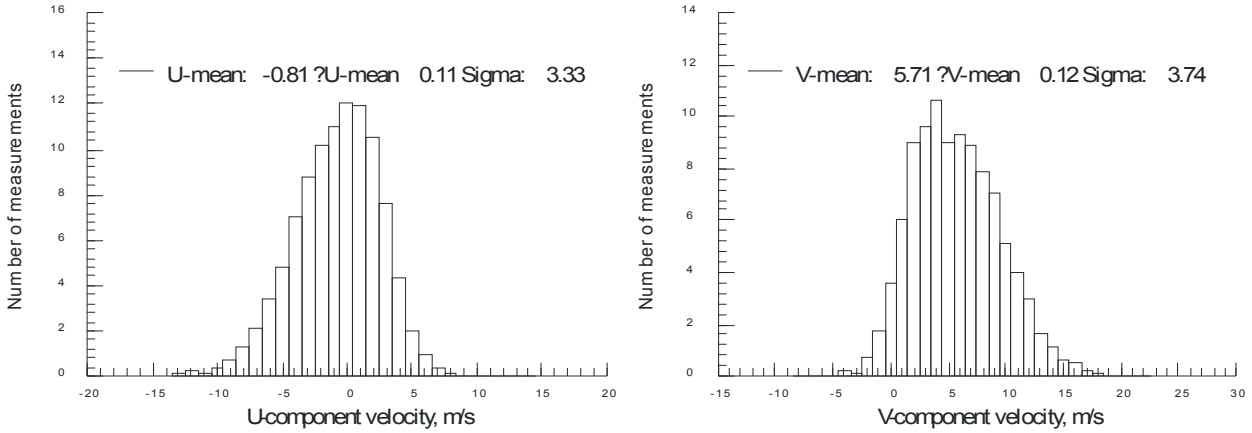

(ii) Signal-to-noise ratio threshold = 2.5 (5 dB)

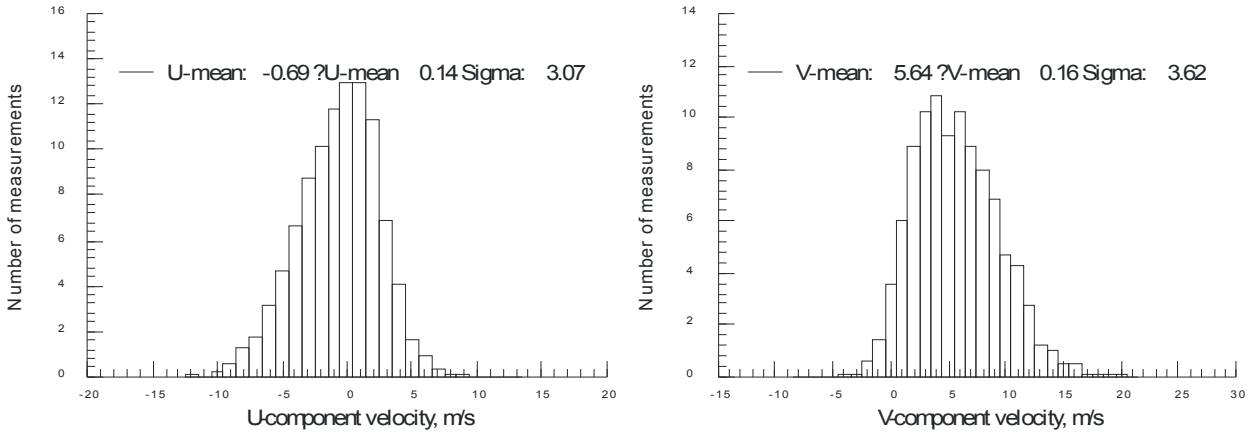

(iii) Signal-to-noise ratio threshold = 10 (10 dB)

Figure VII.33.a.(2)(b) - Velocity histograms obtained at first velocity/sigma deviation – Aeroglaze, Focal distance = 120 inches.

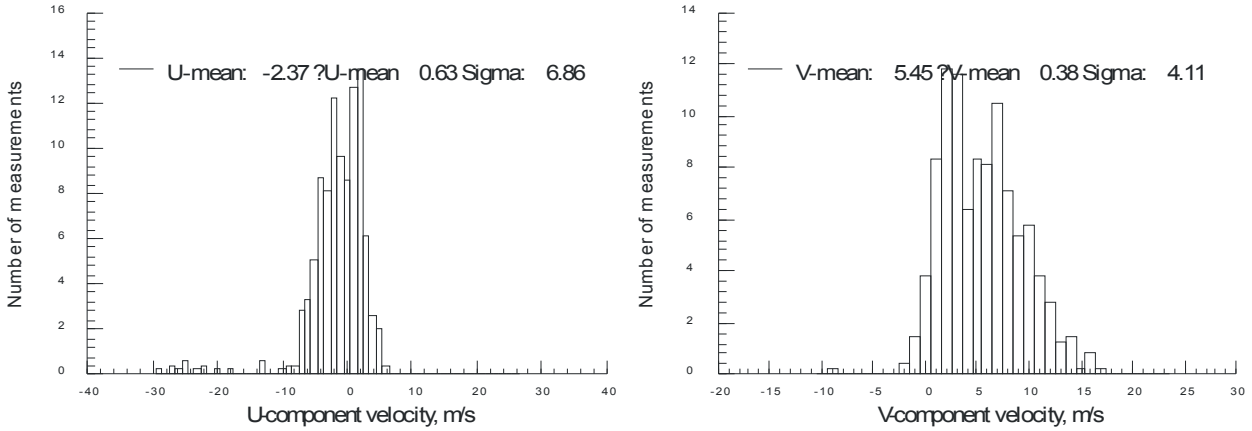

(i) Signal-to-noise ratio threshold = 5 (7 dB)

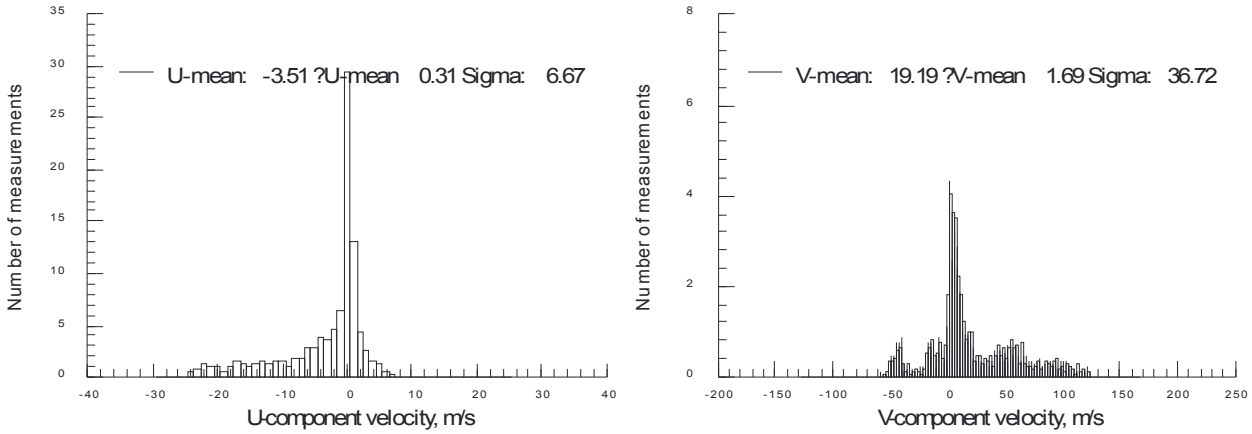

(ii) Signal-to-noise ratio threshold = 2.5 (5 dB)

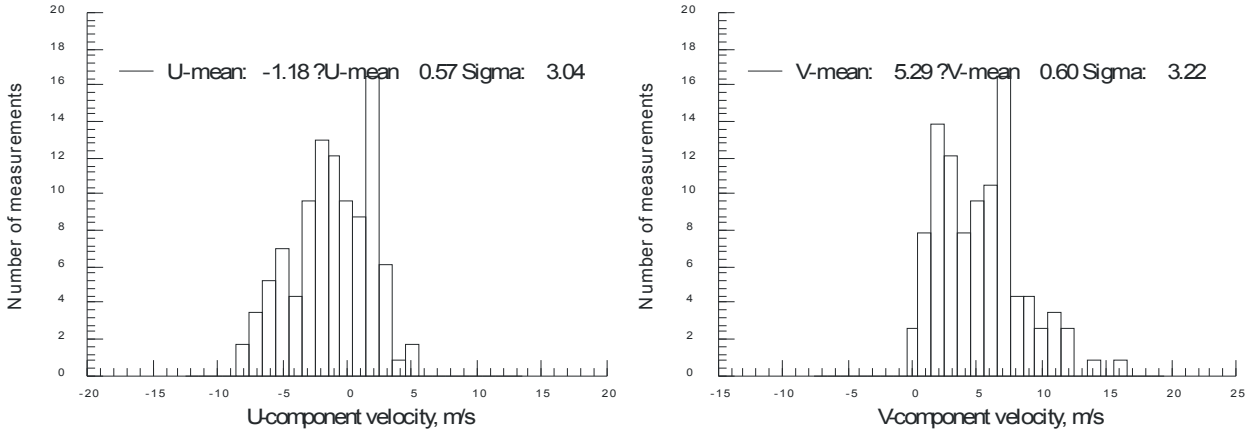

(iii) Signal-to-noise ratio threshold = 10 (10 dB)

Figure VII.33.a.(2)(c) - Velocity histograms obtained at closest approach – Aeroglaze, Focal distance = 120 inches.

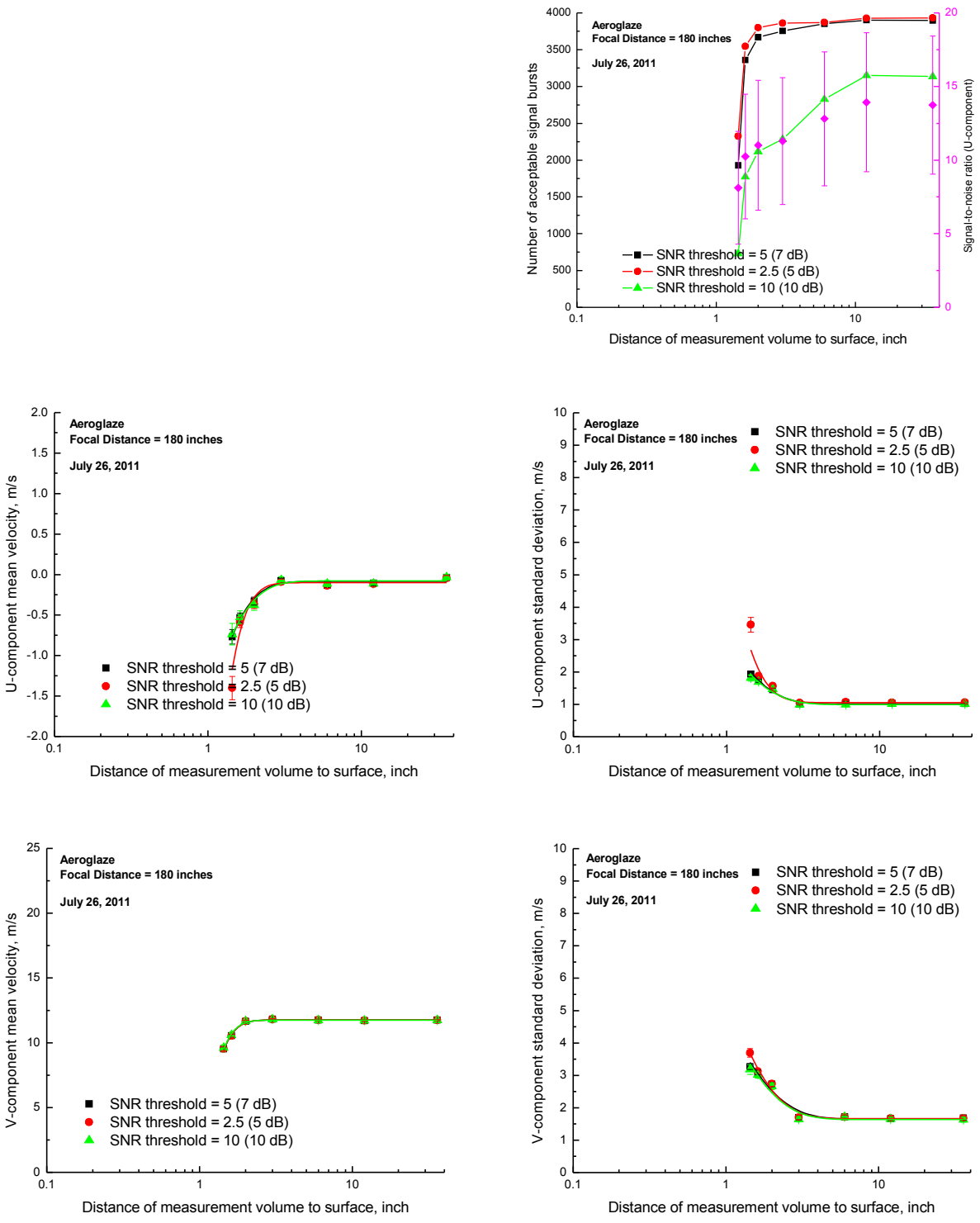

Figure VII.33.b.(1) - Velocity statistics as each surface is moved toward the measurement volume – Aeroglaze, Focal distance = 180 inches.

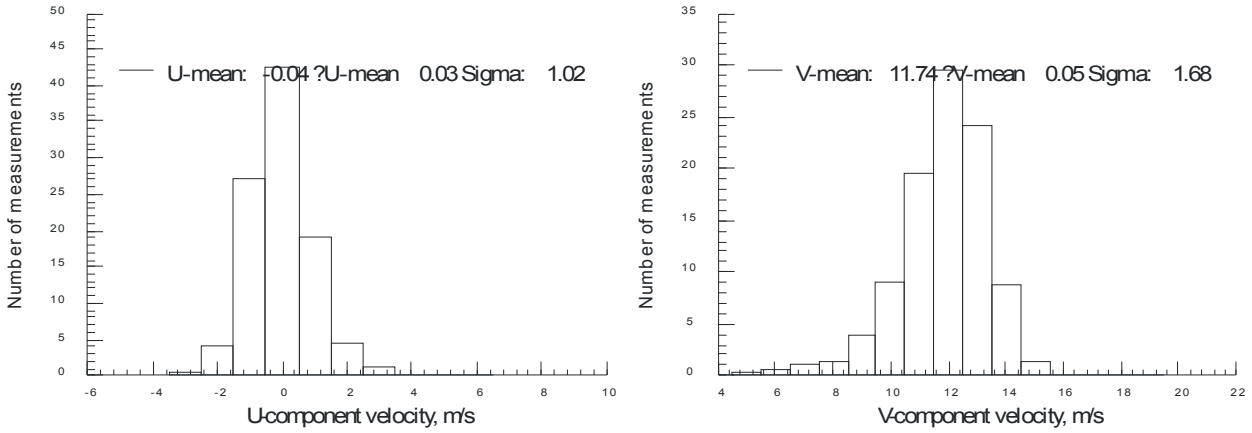

(i) Signal-to-noise ratio threshold = 5 (7 dB)

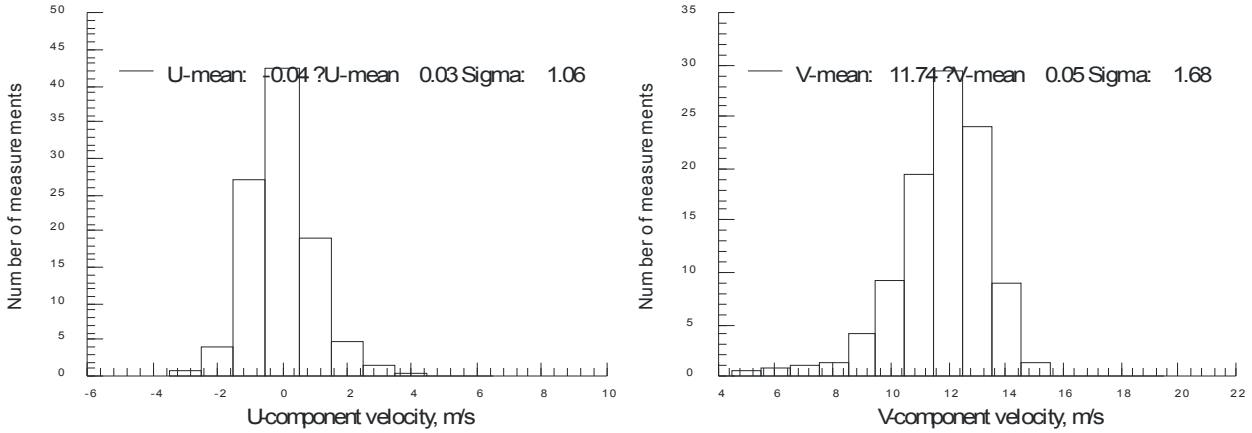

(ii) Signal-to-noise ratio threshold = 2.5 (5 dB)

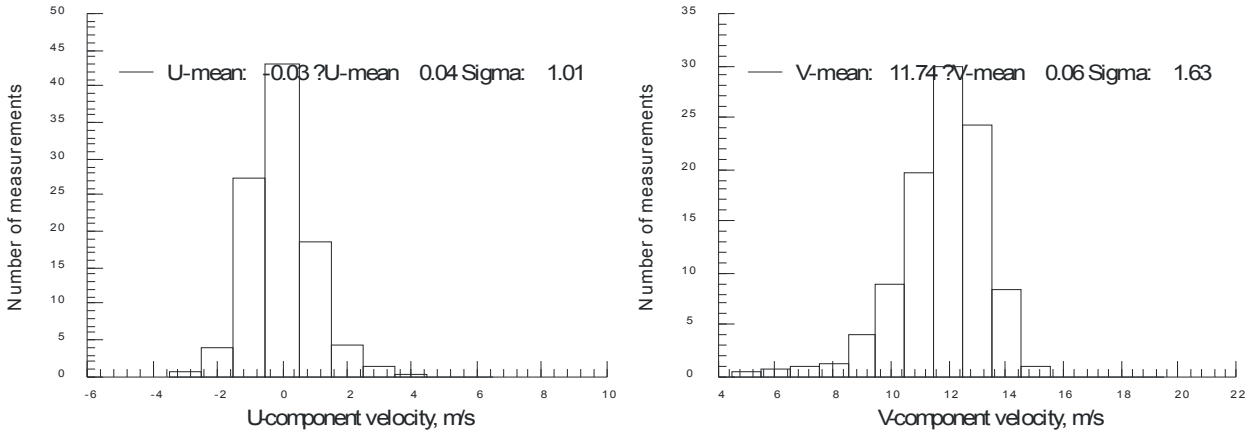

(iii) Signal-to-noise ratio threshold = 10 (10 dB)

Figure VII.33.b.(2)(a) - Velocity histograms obtained at 36-inch separation – Aeroglaze, Focal distance = 180 inches.

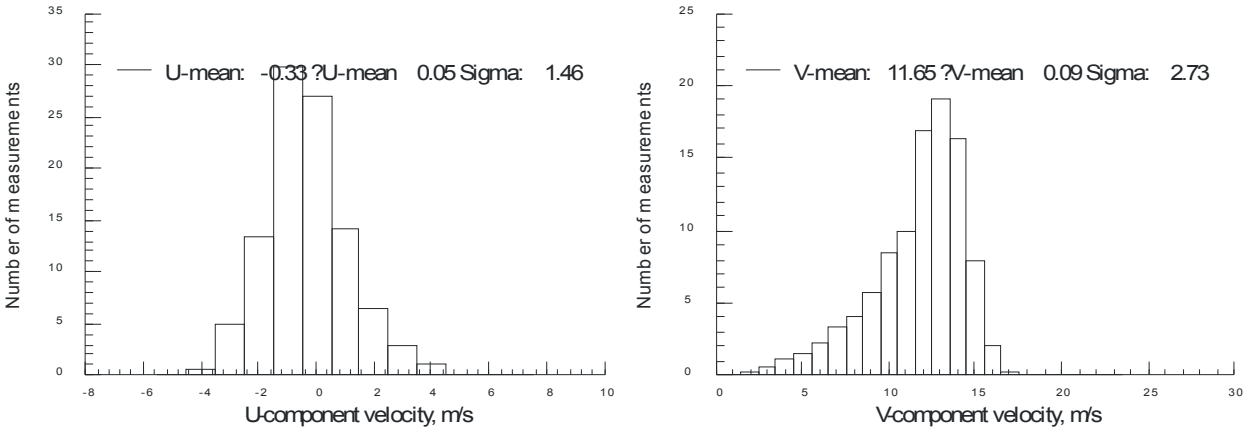

(i) Signal-to-noise ratio threshold = 5 (7 dB)

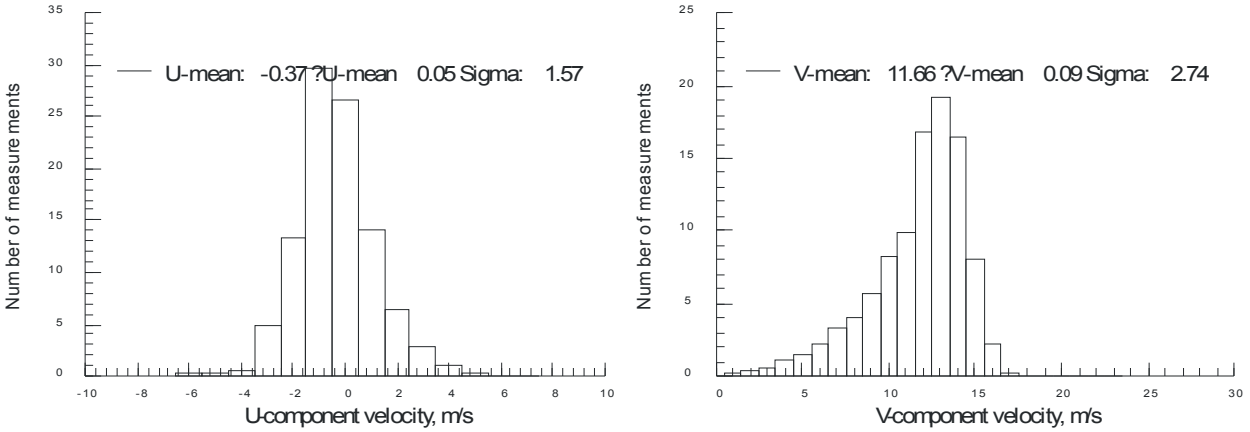

(ii) Signal-to-noise ratio threshold = 2.5 (5 dB)

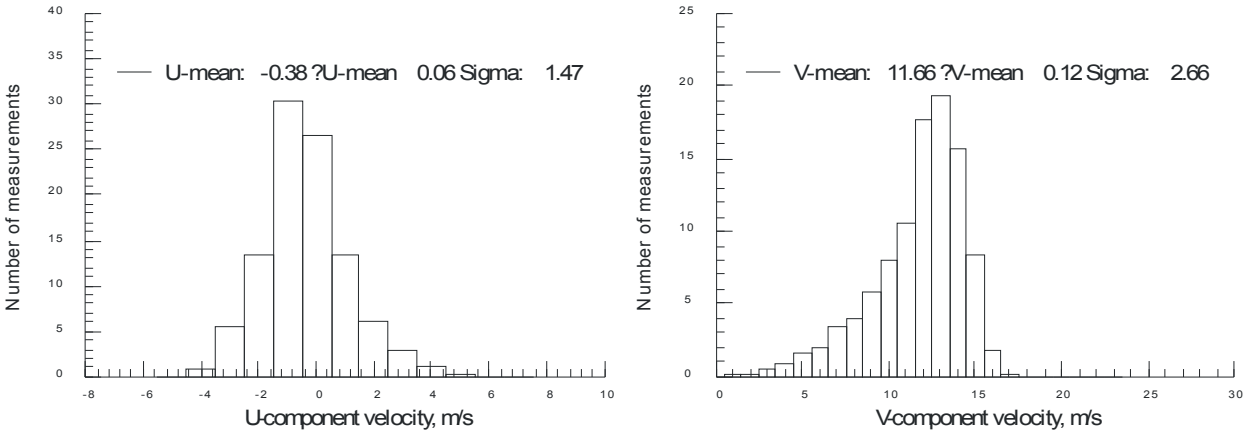

(iii) Signal-to-noise ratio threshold = 10 (10 dB)

Figure VII.33.b.(2)(b) - Velocity histograms obtained at first velocity/sigma deviation – Aeroglaze, Focal distance = 180 inches.

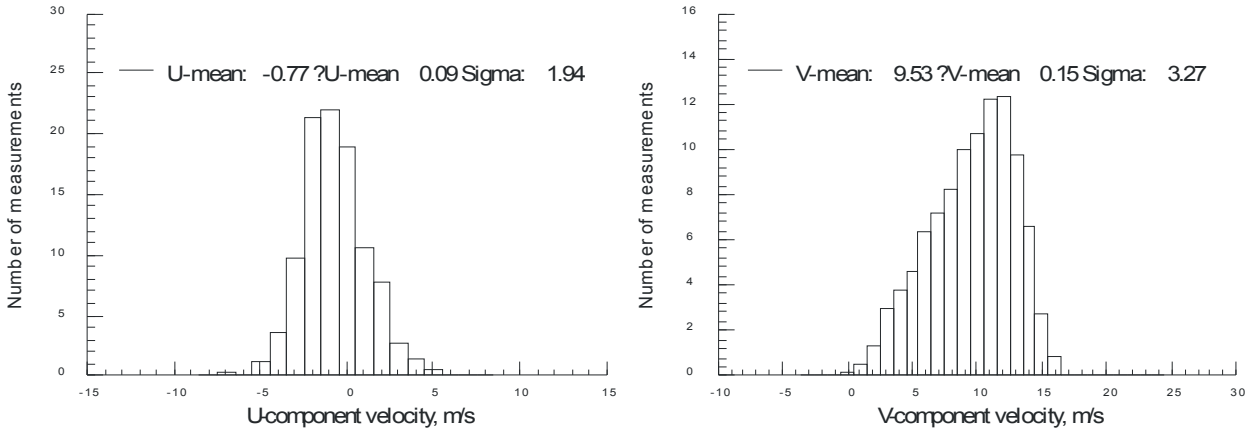

(i) Signal-to-noise ratio threshold = 5 (7 dB)

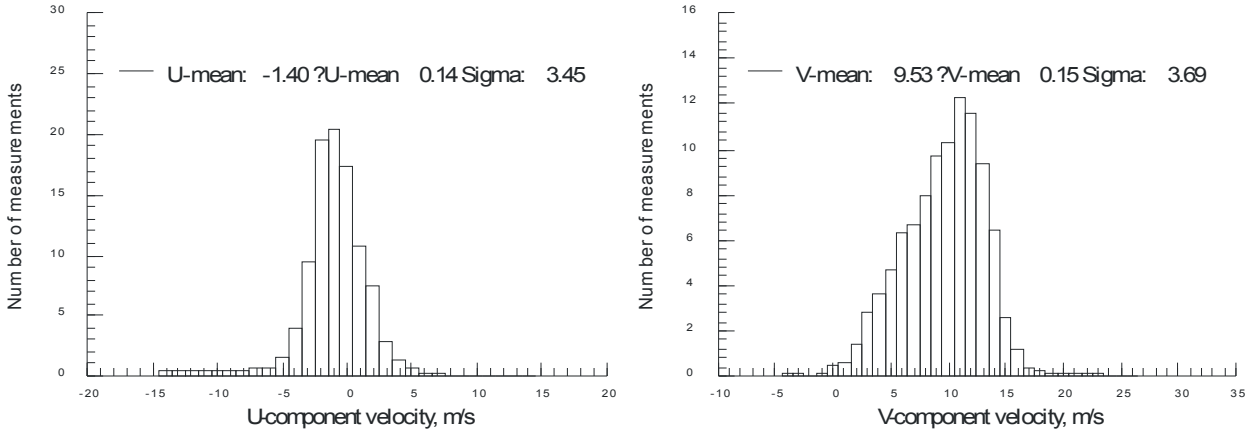

(ii) Signal-to-noise ratio threshold = 2.5 (5 dB)

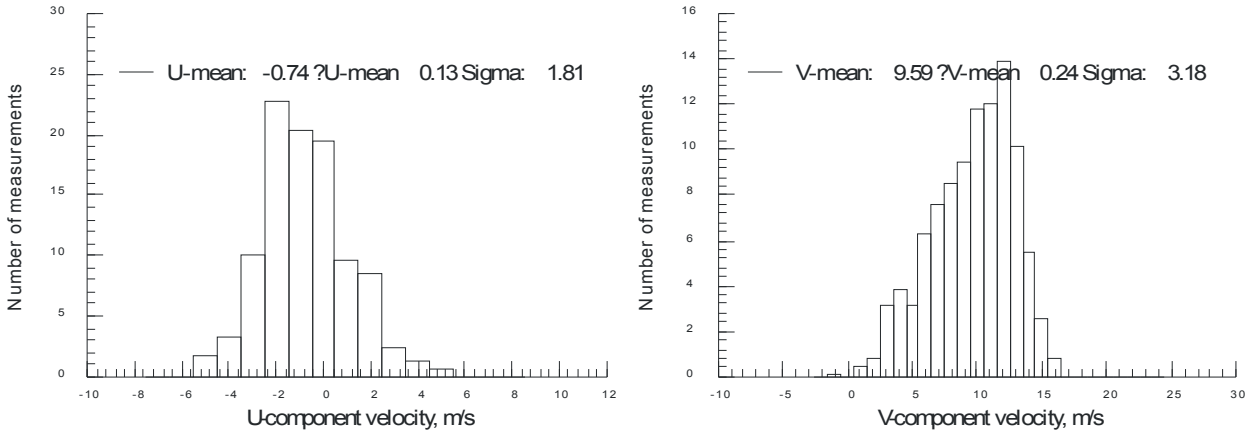

(iii) Signal-to-noise ratio threshold = 10 (10 dB)

Figure VII.33.b.(2)(c) - Velocity histograms obtained at closest approach – Aeroglaze, Focal distance = 180 inches.

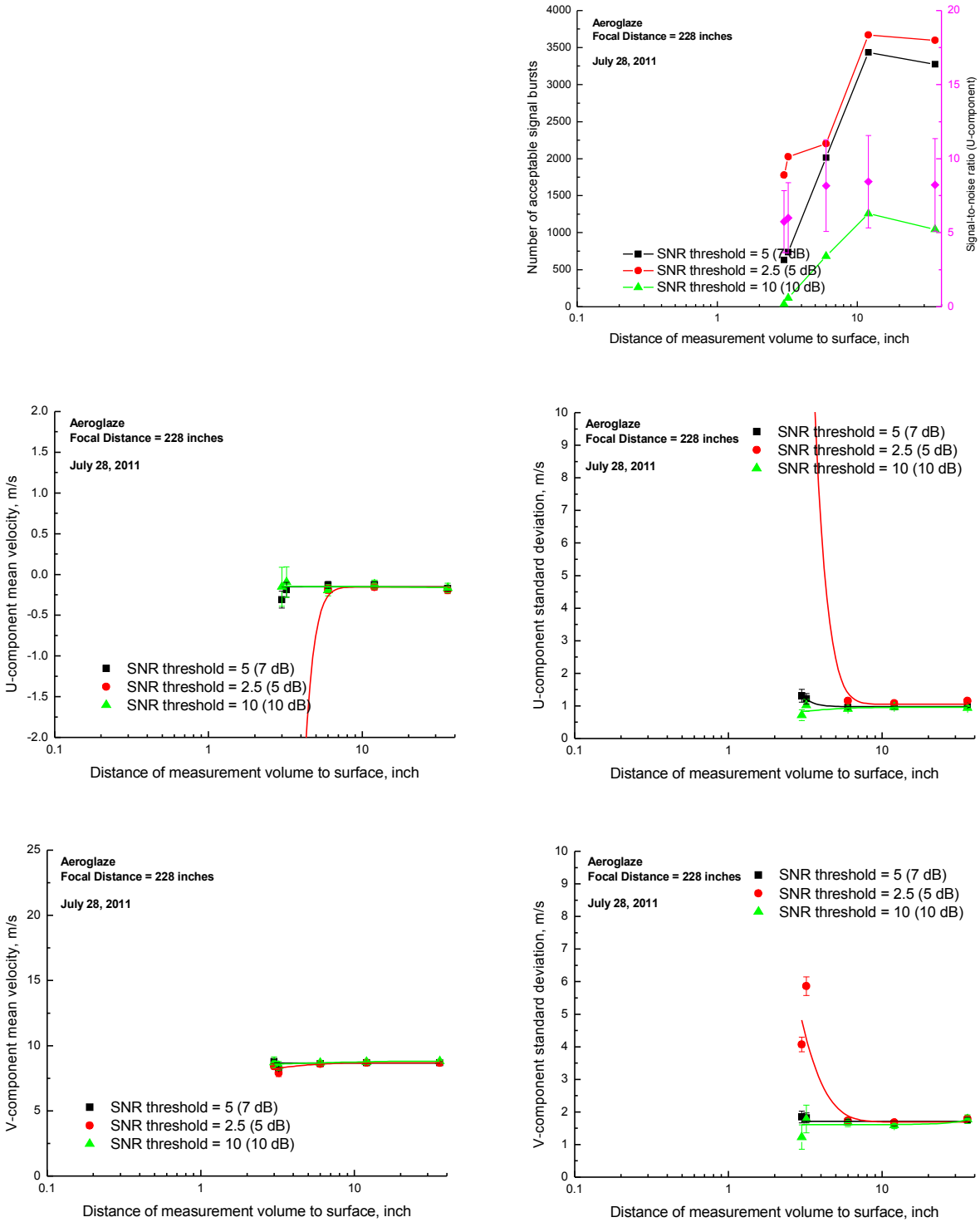

Figure VII.33.c.(1) - Velocity statistics as each surface is moved toward the measurement volume – Aeroglaze, Focal distance = 228 inches.

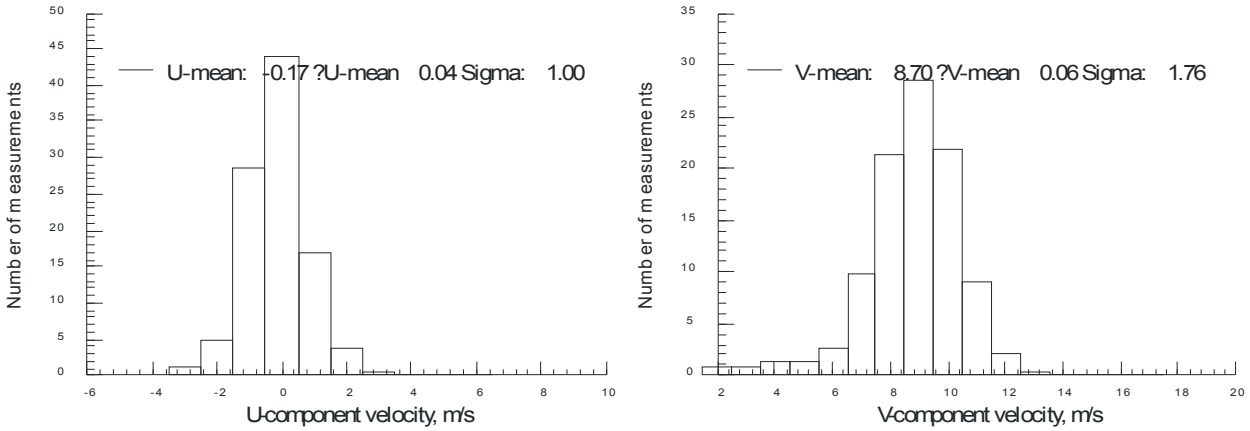

(i) Signal-to-noise ratio threshold = 5 (7 dB)

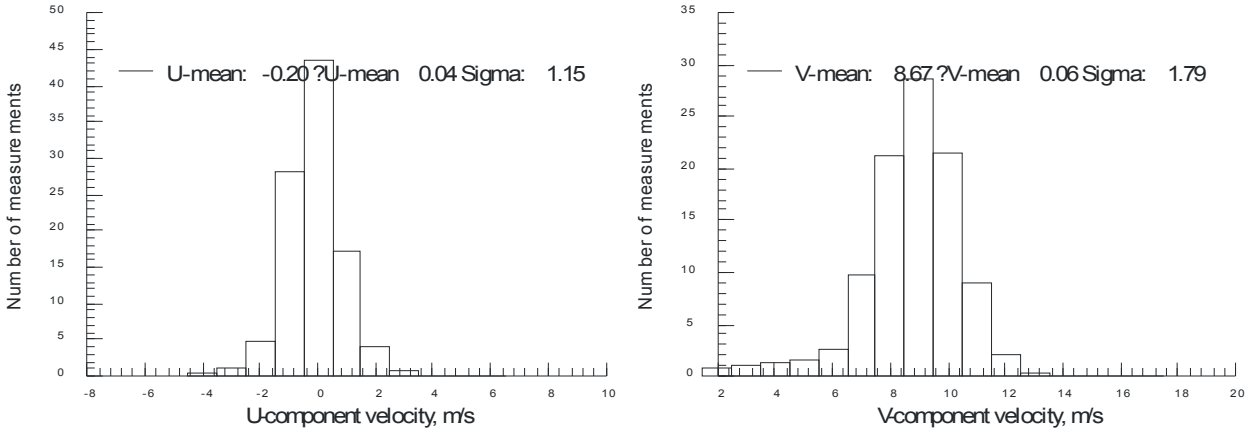

(ii) Signal-to-noise ratio threshold = 2.5 (5 dB)

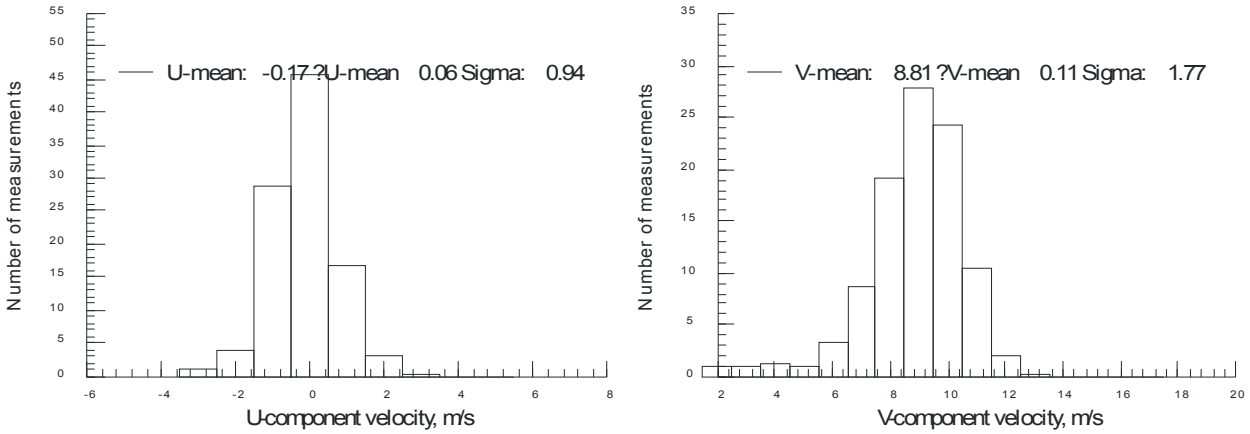

(iii) Signal-to-noise ratio threshold = 10 (10 dB)

Figure VII.33.c.(2)(a) - Velocity histograms obtained at 36-inch separation – Aeroglaze, Focal distance = 228 inches.

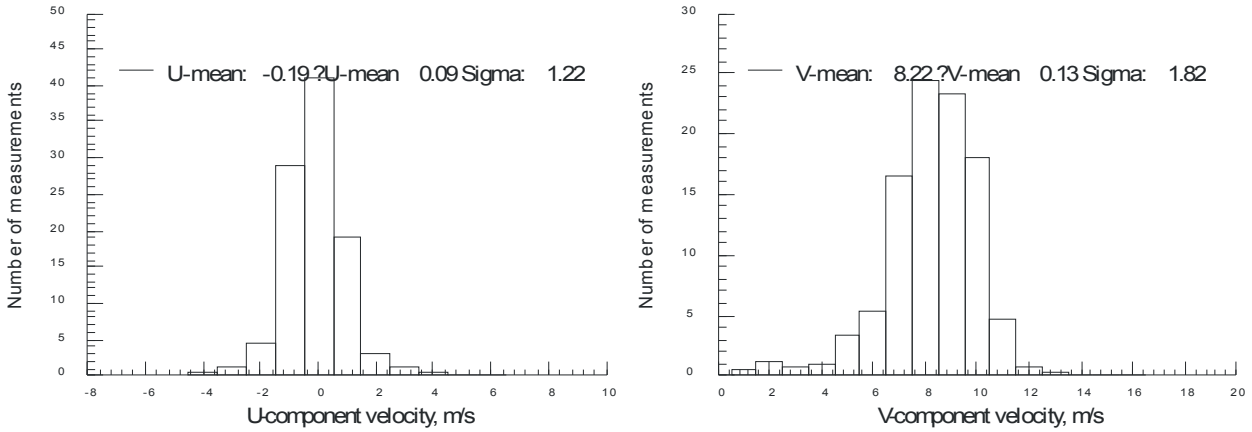

(i) Signal-to-noise ratio threshold = 5 (7 dB)

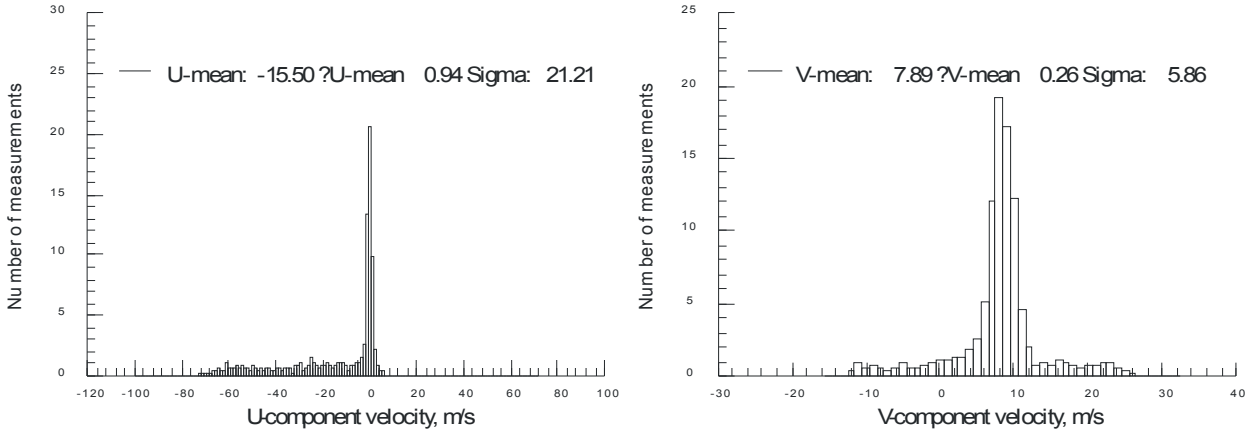

(ii) Signal-to-noise ratio threshold = 2.5 (5 dB)

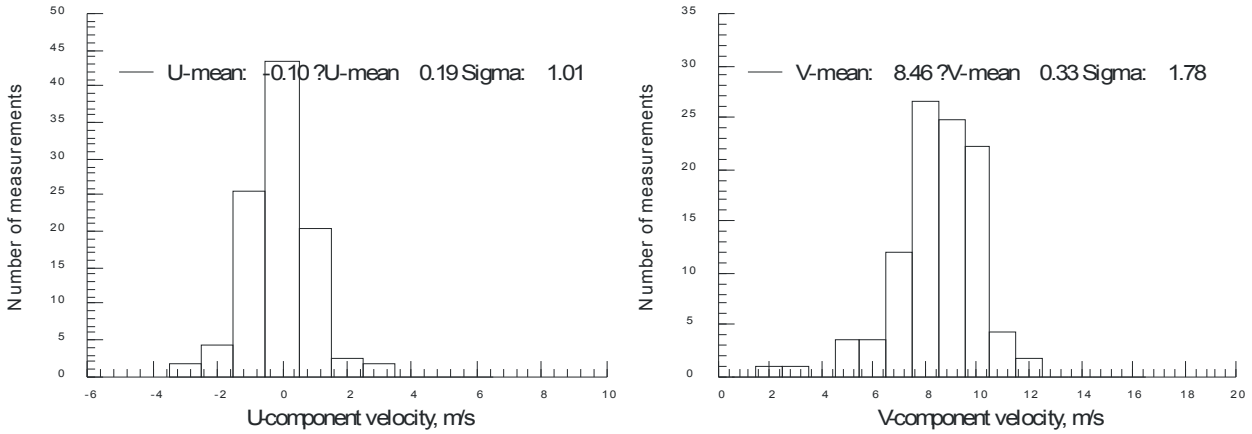

(iii) Signal-to-noise ratio threshold = 10 (10 dB)

Figure VII.33.c.(2)(b) - Velocity histograms obtained at first velocity/sigma deviation – Aeroglaze, Focal distance = 228 inches.

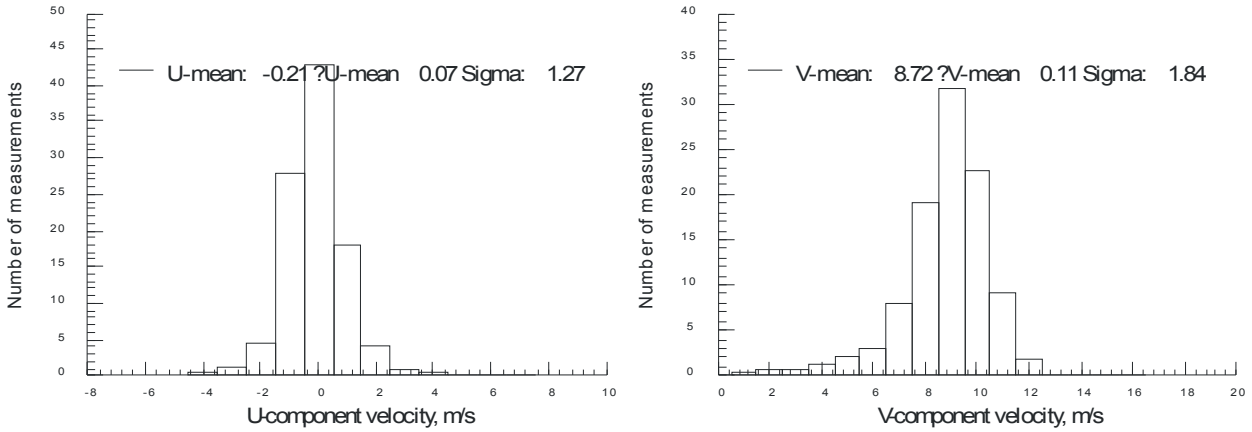

(i) Signal-to-noise ratio threshold = 5 (7 dB)

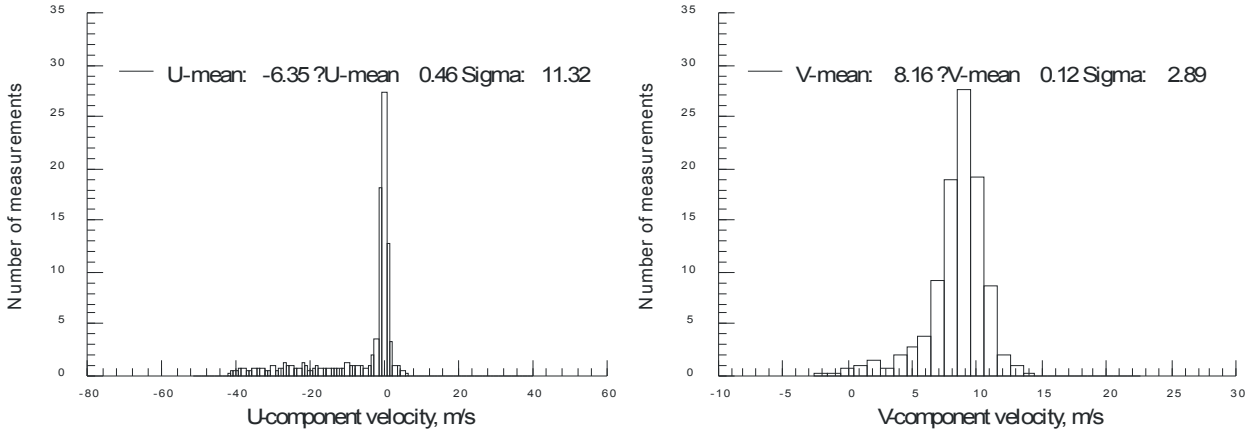

(ii) Signal-to-noise ratio threshold = 2.5 (5 dB)

Figure VII.33.c.(2)(c) - Velocity histograms obtained at closest approach – Aeroglaze, Focal distance = 228 inches.

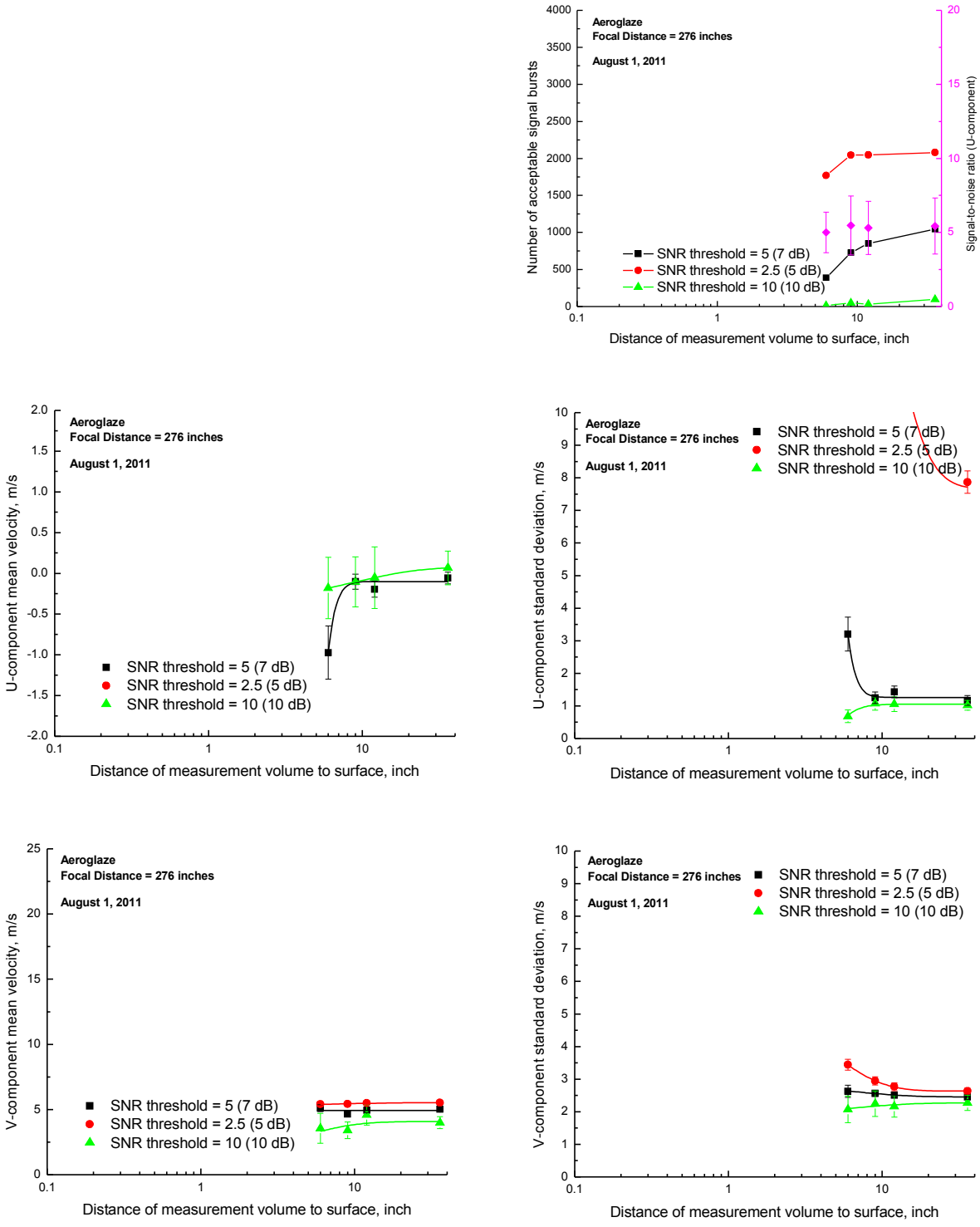

Figure VII.33.d.(1) - Velocity statistics as each surface is moved toward the measurement volume – Aeroglaze, Focal distance = 276 inches.

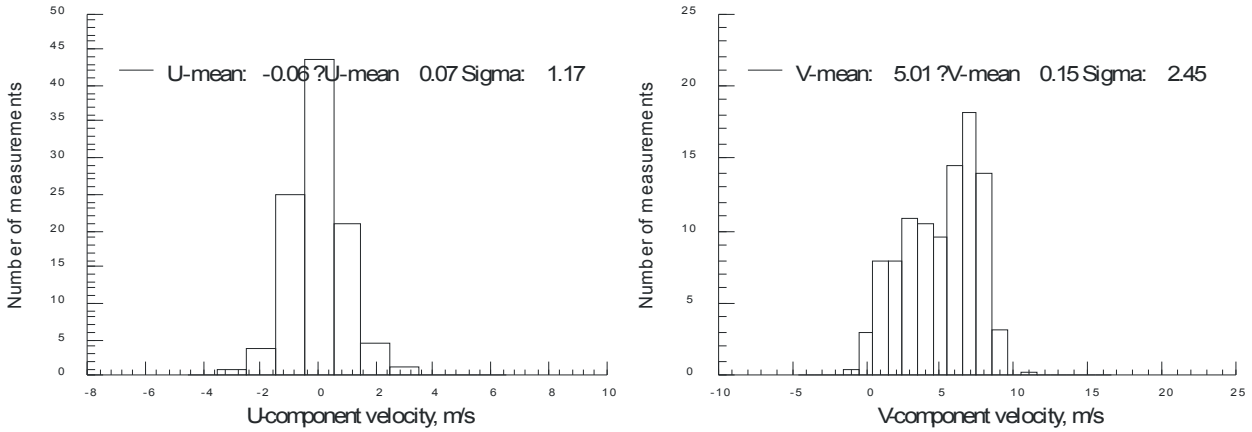

(i) Signal-to-noise ratio threshold = 5 (7 dB)

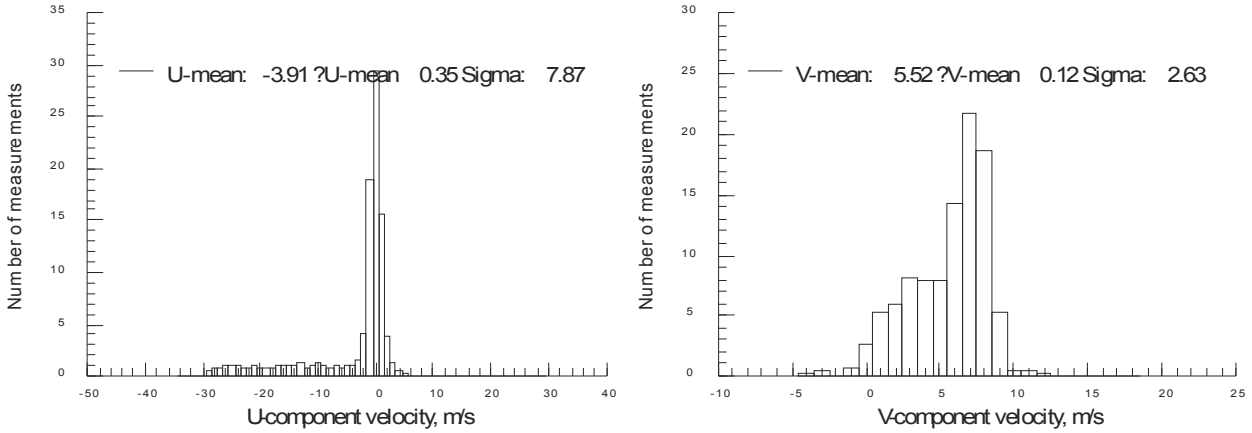

(ii) Signal-to-noise ratio threshold = 2.5 (5 dB)

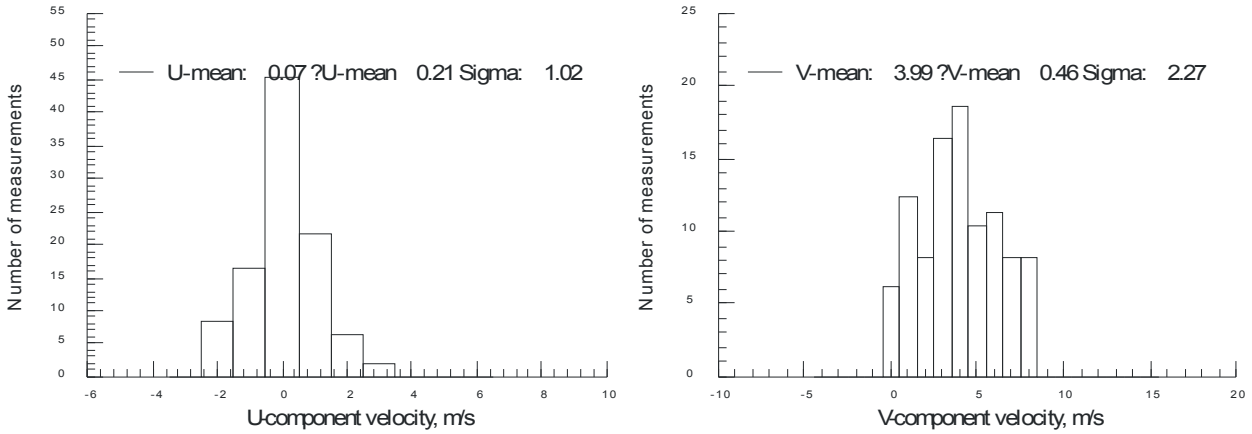

(iii) Signal-to-noise ratio threshold = 10 (10 dB)

Figure VII.33.d.(2)(a) - Velocity histograms obtained at 36-inch separation – Aeroglaze, Focal distance = 276 inches.

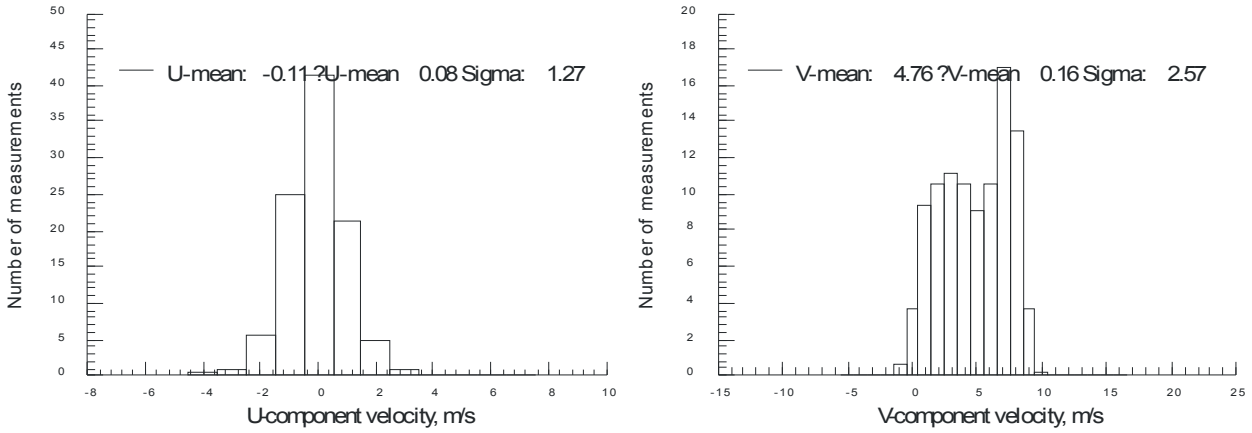

(i) Signal-to-noise ratio threshold = 5 (7 dB)

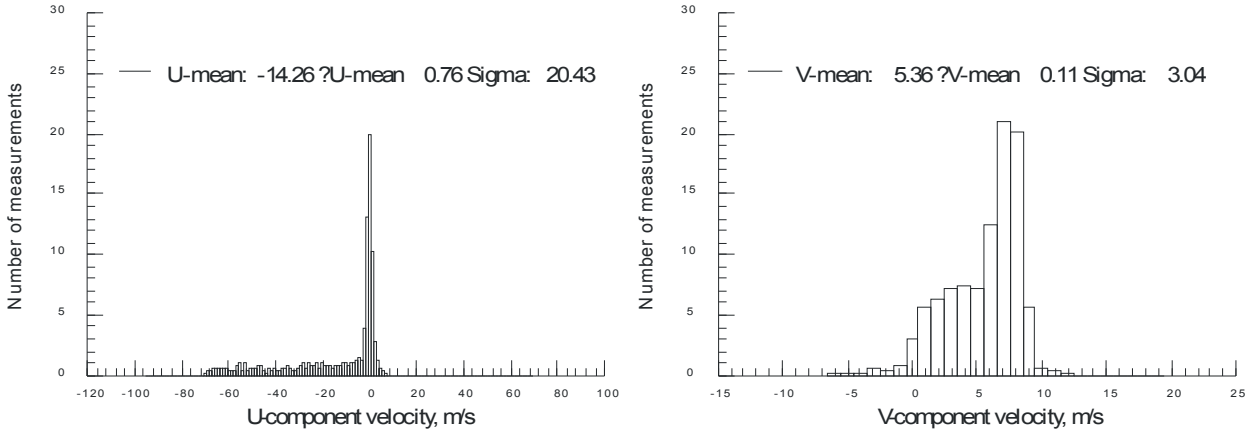

(ii) Signal-to-noise ratio threshold = 2.5 (5 dB)

Figure VII.33.d.(2)(b) - Velocity histograms obtained at first velocity/sigma deviation – Aeroglaze, Focal distance = 276 inches.

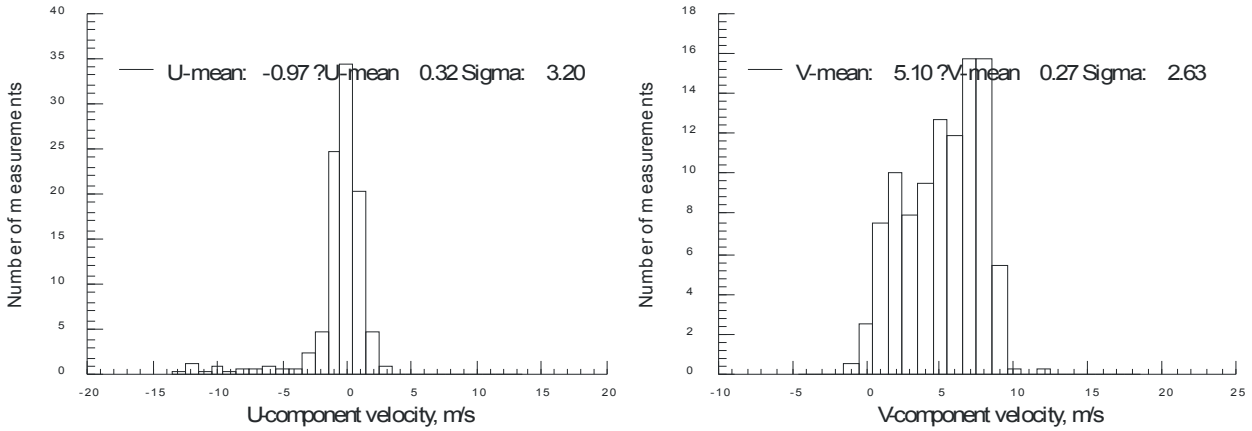

(i) Signal-to-noise ratio threshold = 5 (7 dB)

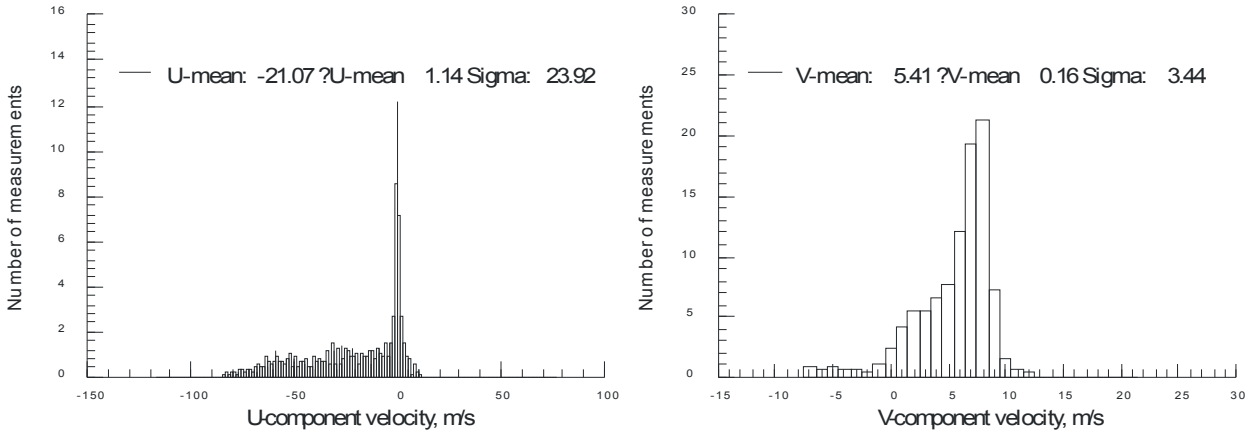

(ii) Signal-to-noise ratio threshold = 2.5 (5 dB)

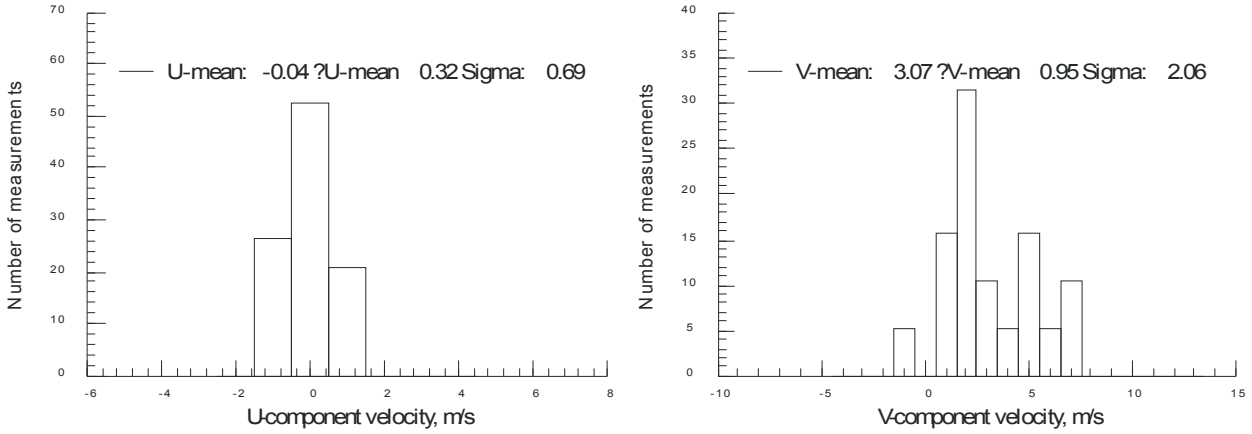

(iii) Signal-to-noise ratio threshold = 10 (10 dB)

Figure VII.33.d.(2)(c) - Velocity histograms obtained at closest approach – Aeroglaze, Focal distance = 276 inches.

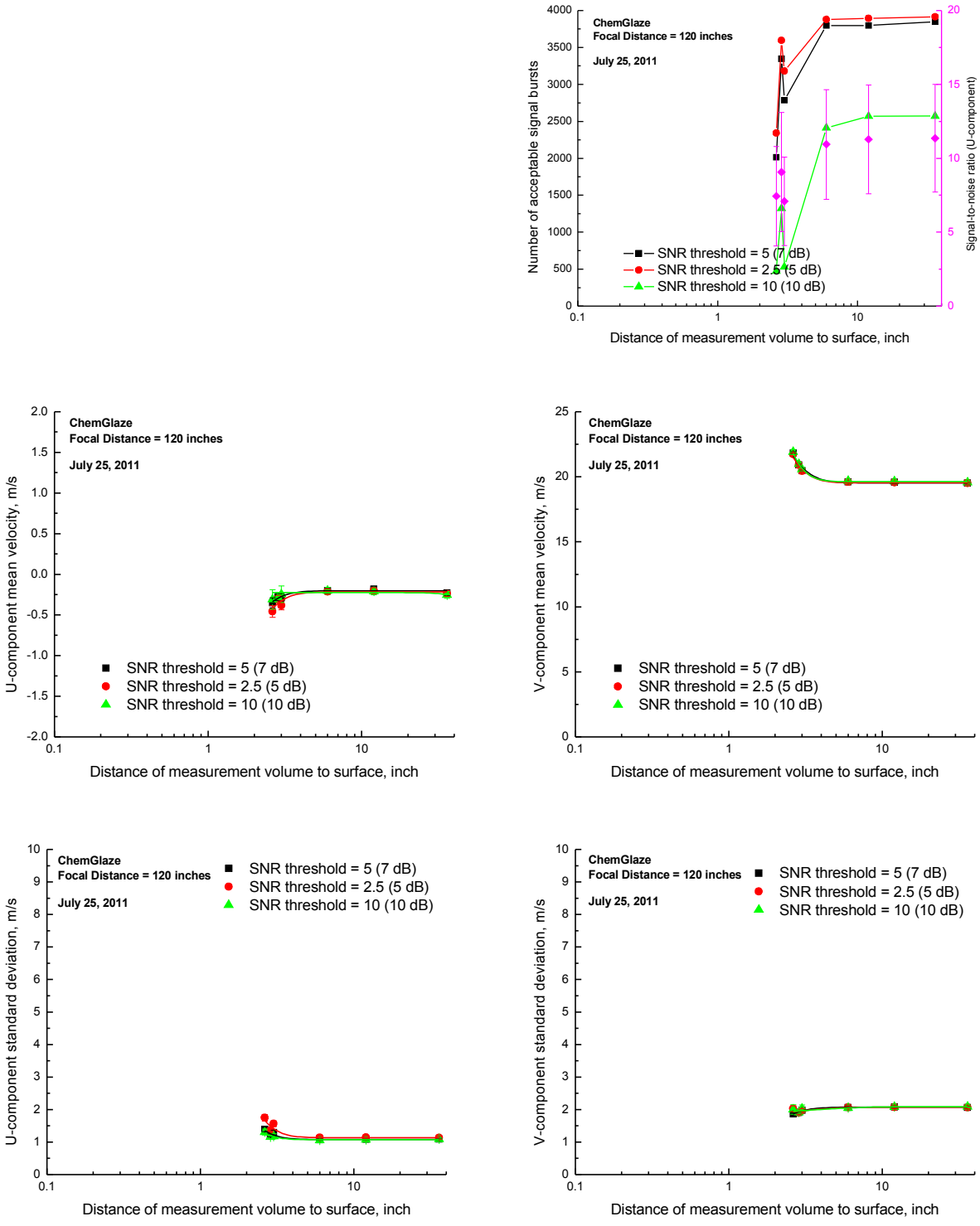

Figure VII.34.a.- Velocity statistics as each surface is moved toward the measurement volume – Chem Glaze sample, Focal distance = 120 inches.

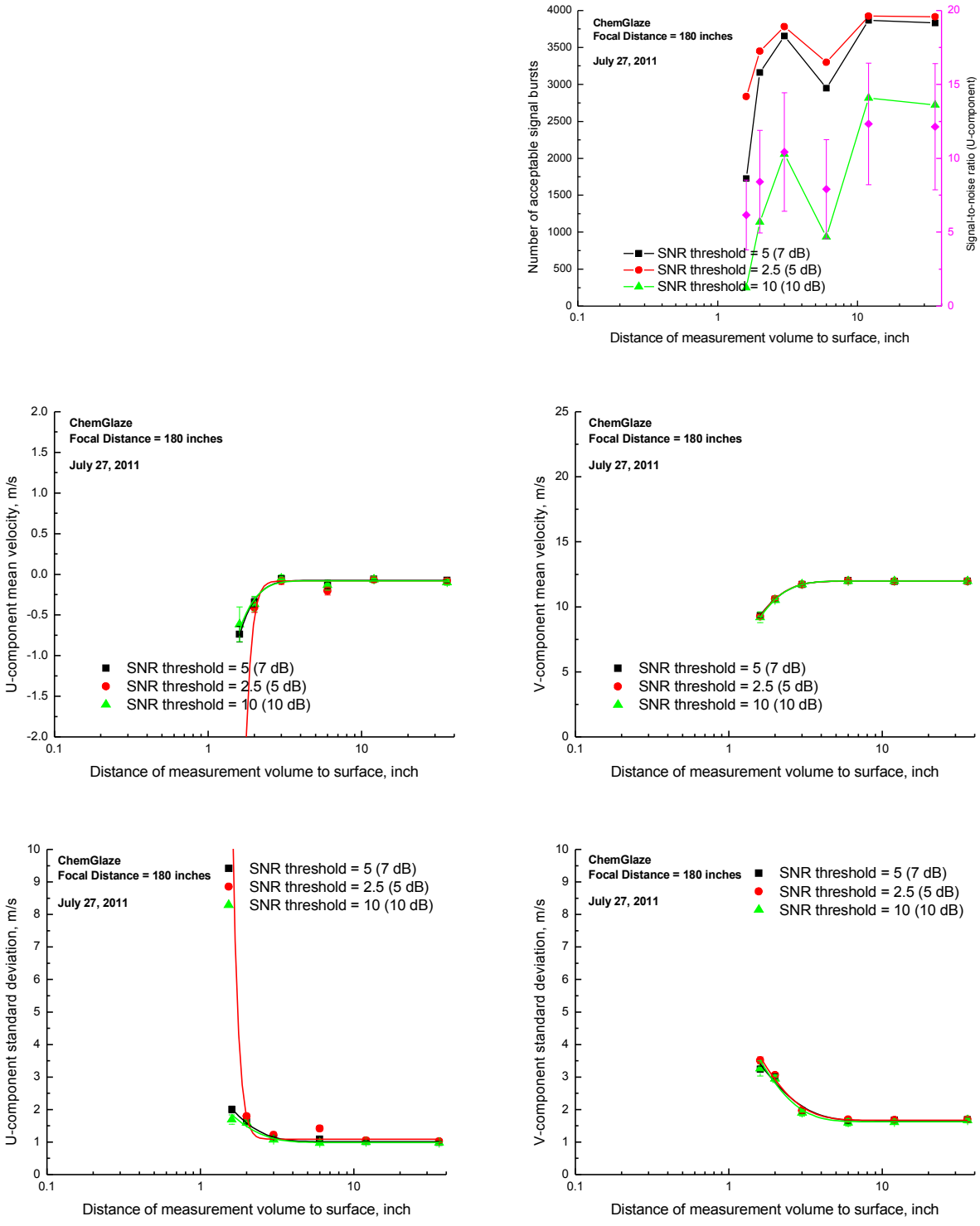

Figure VII.34.b.- Velocity statistics as each surface is moved toward the measurement volume – Chem Glaze sample, Focal distance = 180 inches.

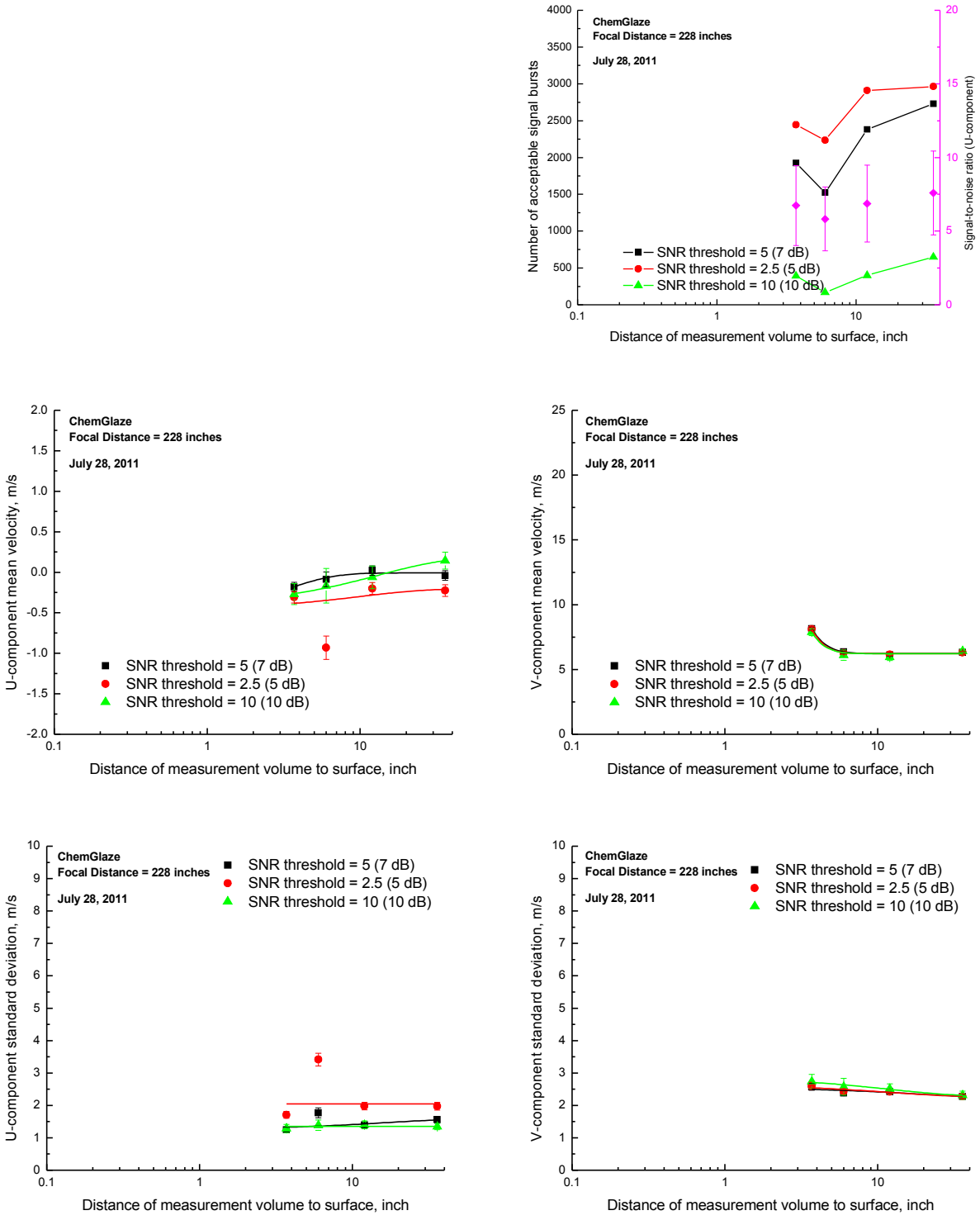

Figure VII.34.c.- Velocity statistics as each surface is moved toward the measurement volume – Chem Glaze sample, Focal distance = 228 inches.

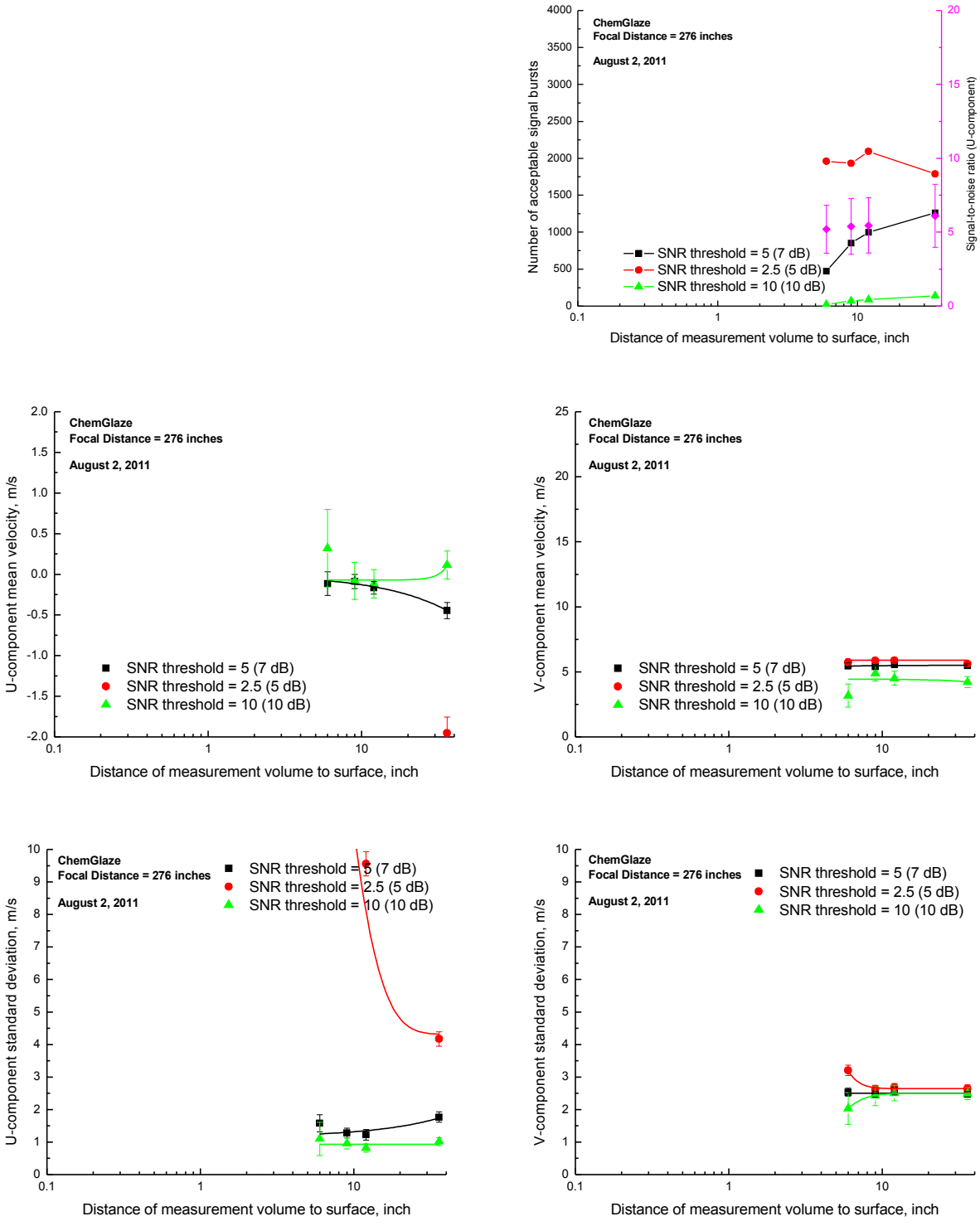

Figure VII.34.d.- Velocity statistics as each surface is moved toward the measurement volume – Chem Glaze sample, Focal distance = 276 inches.

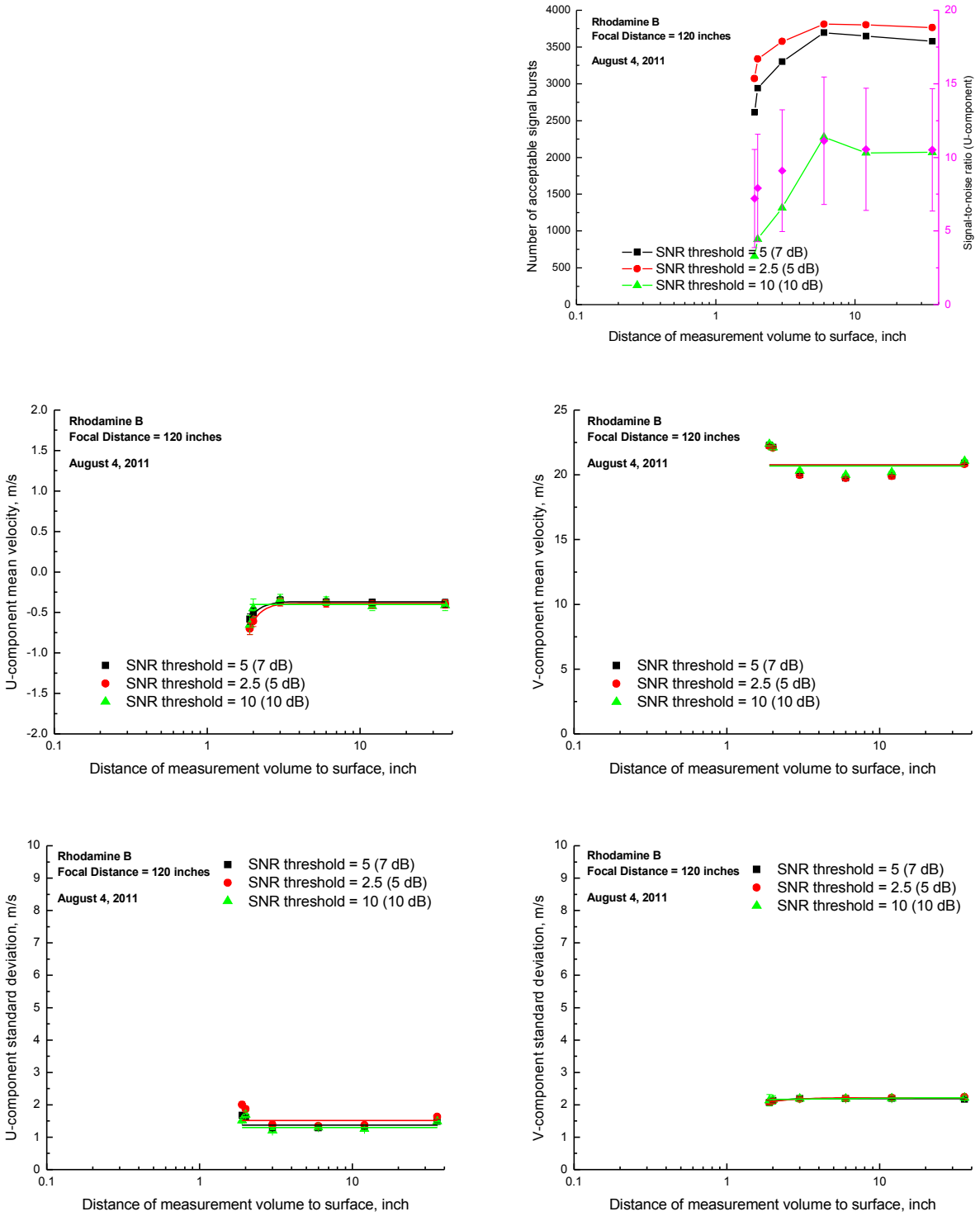

Figure VII.35.a.(1) - Velocity statistics as each surface is moved toward the measurement volume – Semi gloss black paint with Rhodamine B added, Focal distance = 120 inches.

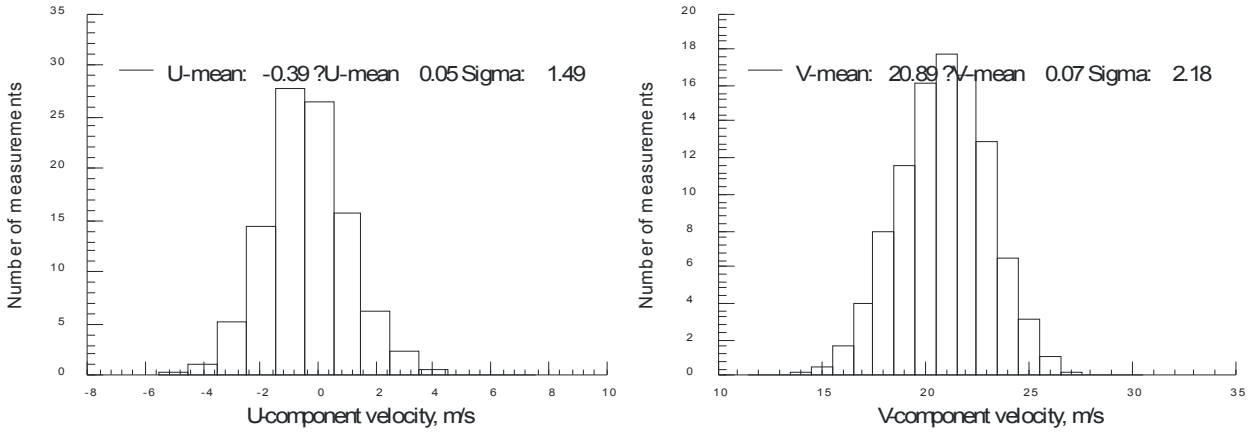

(i) Signal-to-noise ratio threshold = 5 (7 dB)

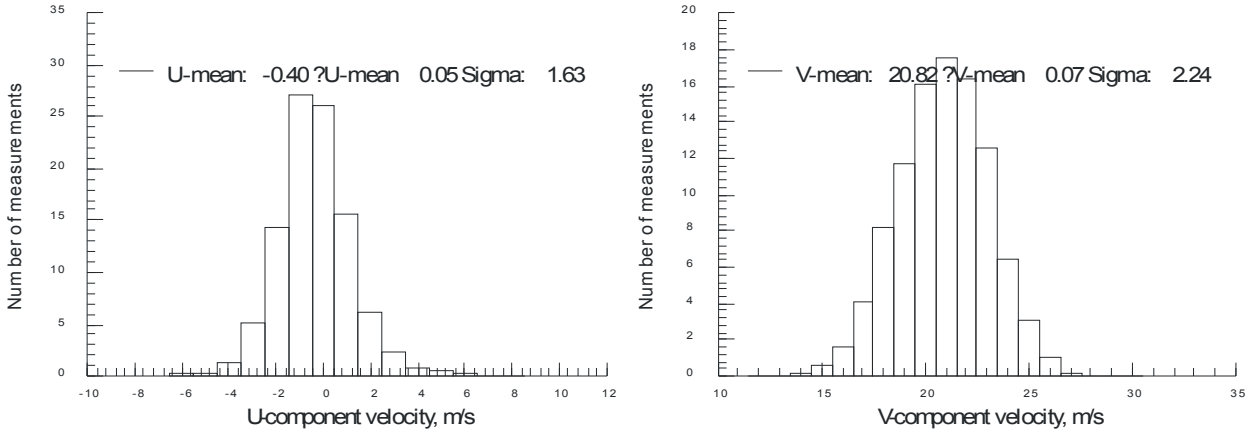

(ii) Signal-to-noise ratio threshold = 2.5 (5 dB)

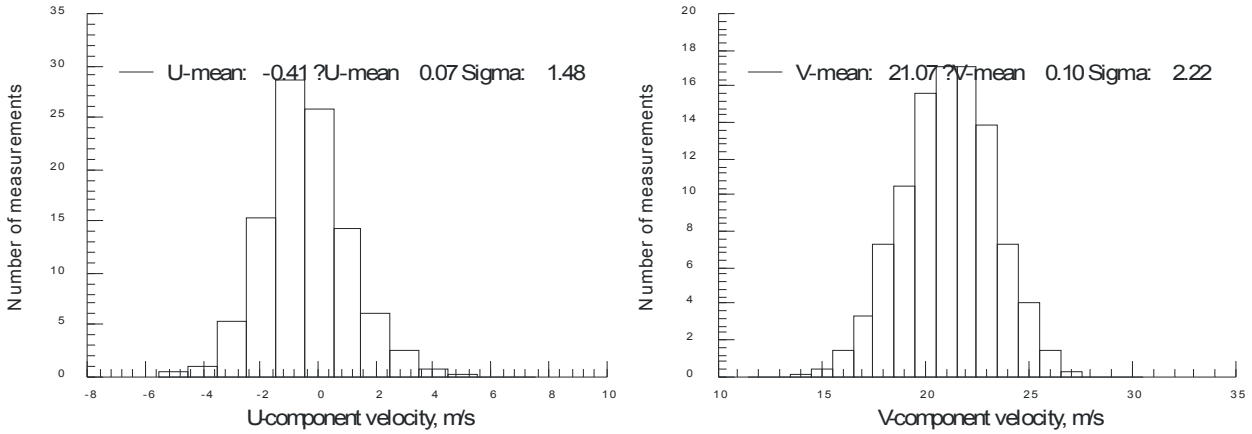

(iii) Signal-to-noise ratio threshold = 10 (10 dB)

Figure VII.35.a.(2)(a) - Velocity histograms obtained at 36-inch separation – Semi gloss black paint with Rhodamine B added, Focal distance = 120 inches.

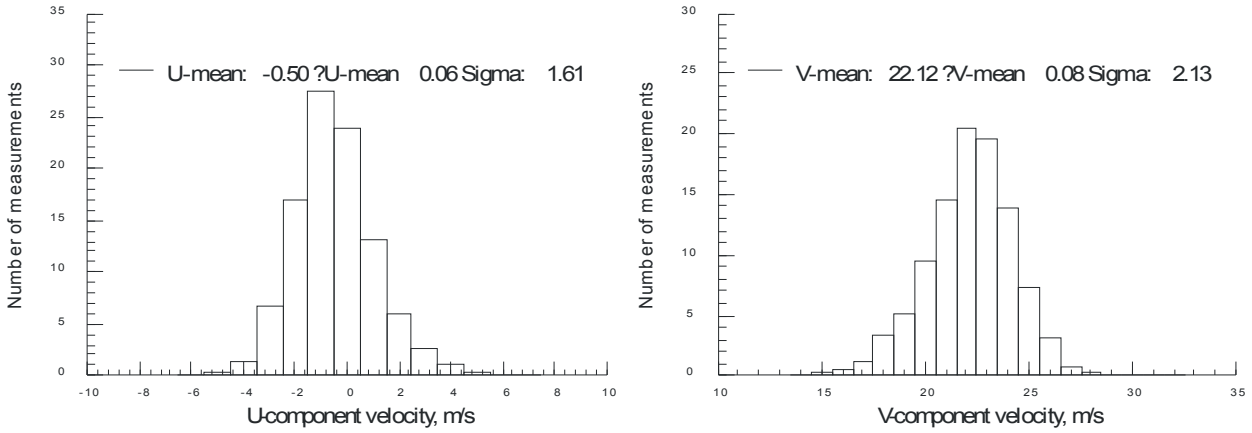

(i) Signal-to-noise ratio threshold = 5 (7 dB)

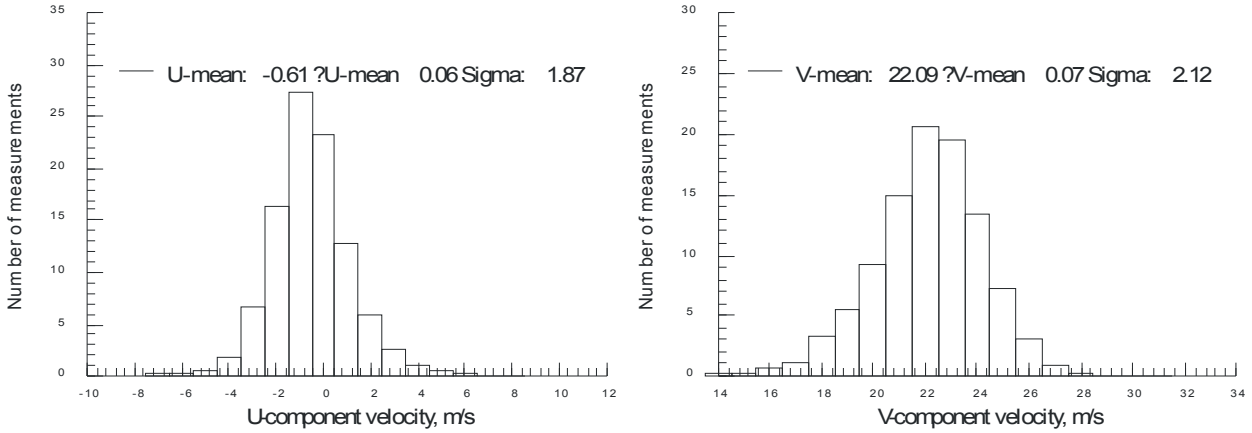

(ii) Signal-to-noise ratio threshold = 2.5 (5 dB)

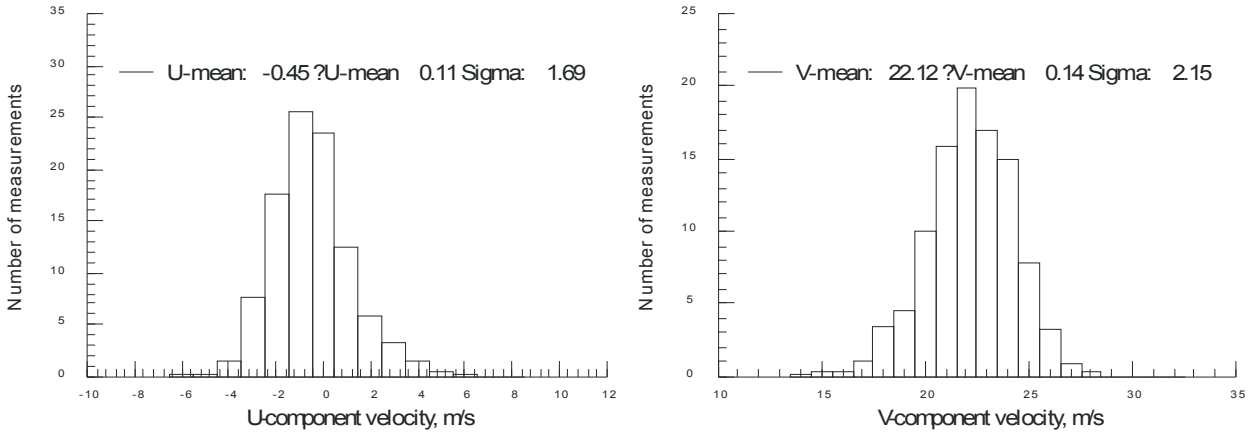

(iii) Signal-to-noise ratio threshold = 10 (10 dB)

Figure VII.35.a.(2)(b) - Velocity histograms obtained at first velocity/sigma deviation – Semi gloss black paint with Rhodamine B added, Focal distance = 120 inches.

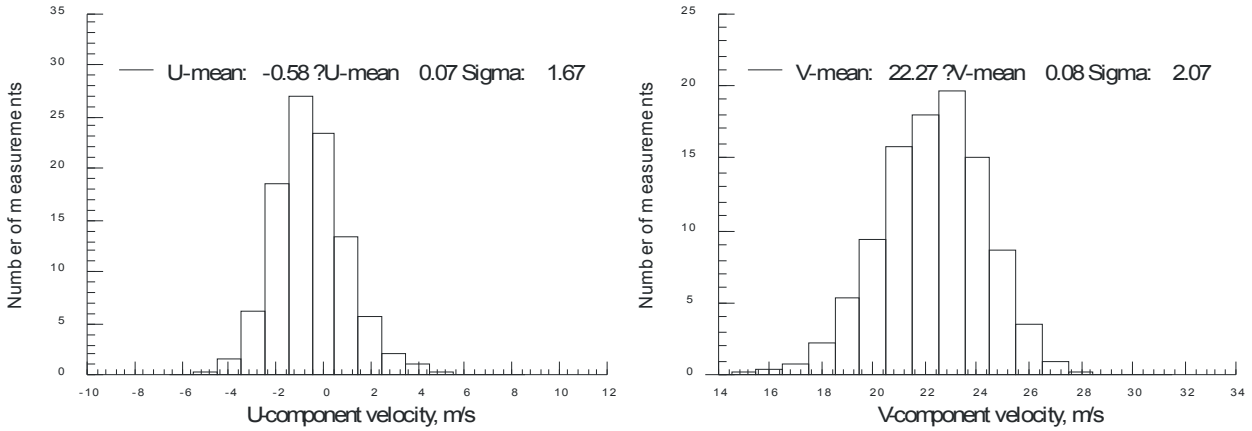

(i) Signal-to-noise ratio threshold = 5 (7 dB)

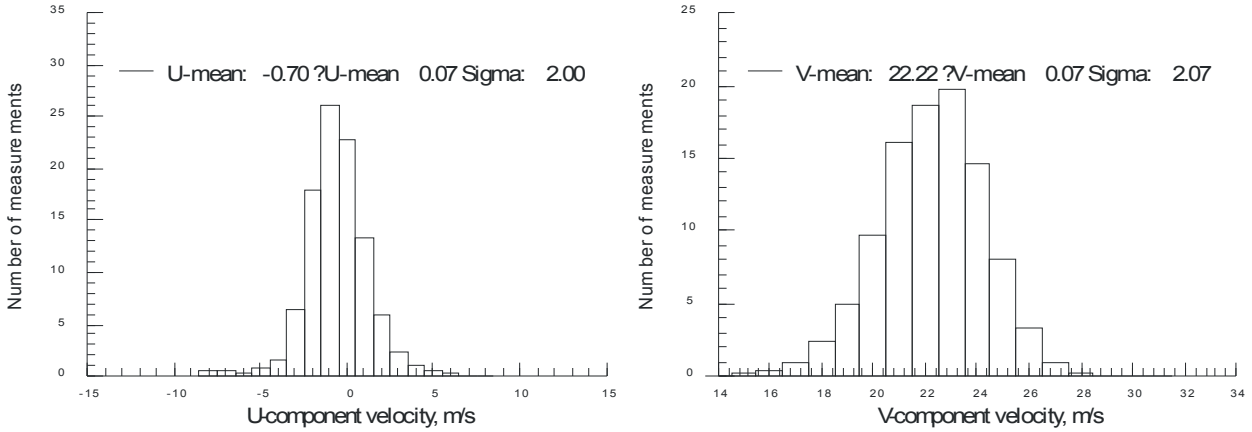

(ii) Signal-to-noise ratio threshold = 2.5 (5 dB)

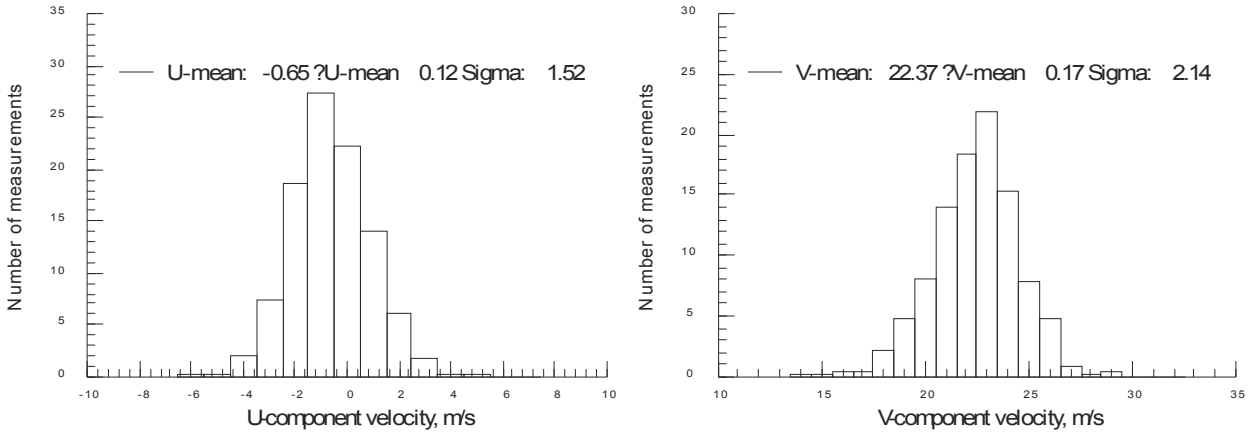

(iii) Signal-to-noise ratio threshold = 10 (10 dB)

Figure VII.35.a.(2)(c) - Velocity histograms obtained at closest approach – Semi gloss black paint with Rhodamine B added, Focal distance = 120 inches.

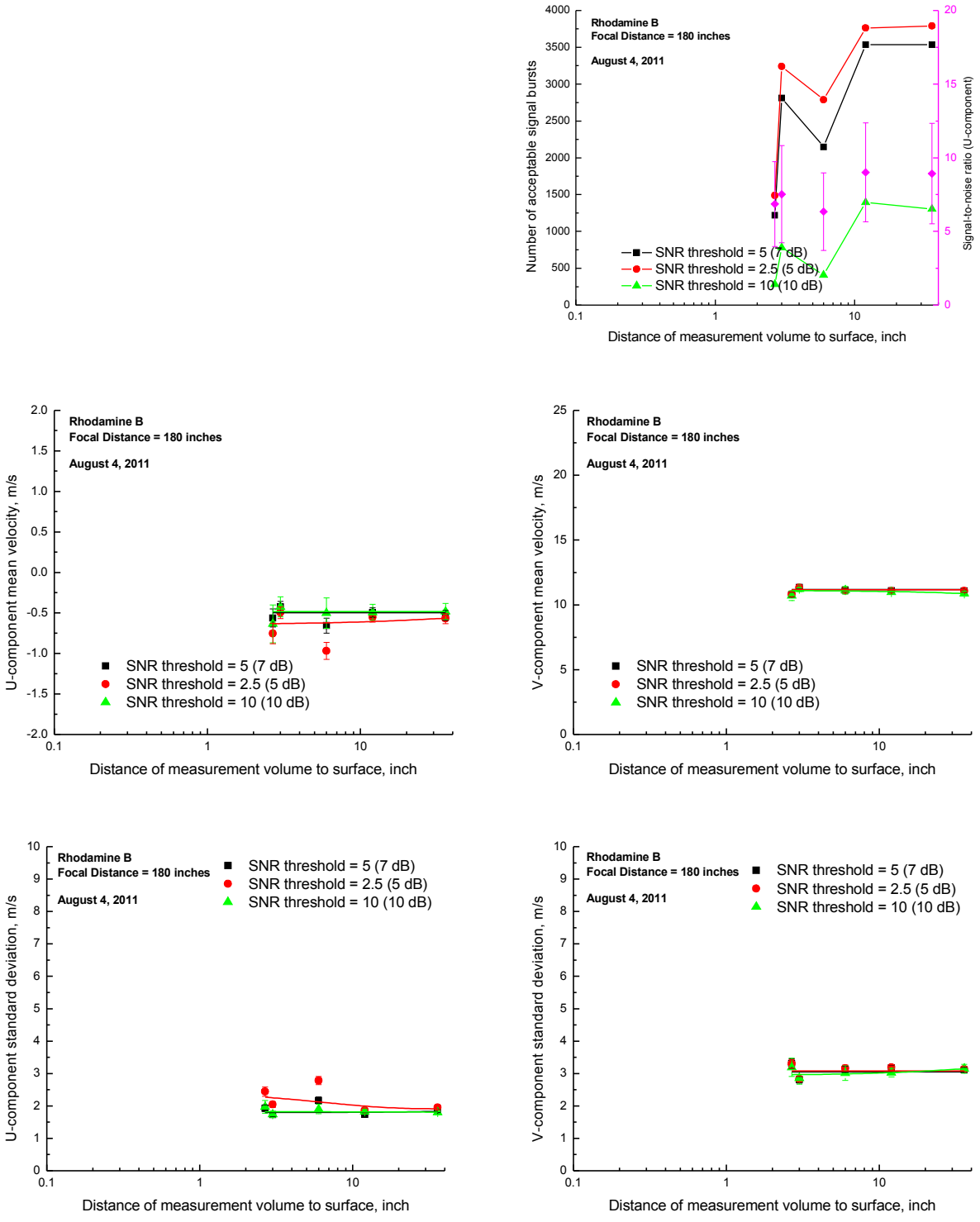

Figure VII.35.b.(1) - Velocity statistics as each surface is moved toward the measurement volume – Semi gloss black paint with Rhodamine B added, Focal distance = 180 inches.

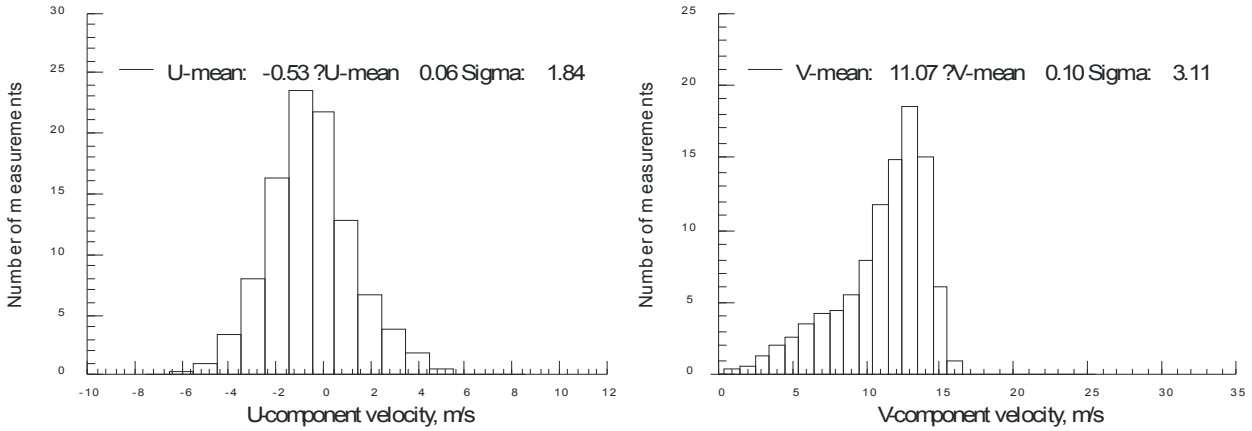

(i) Signal-to-noise ratio threshold = 5 (7 dB)

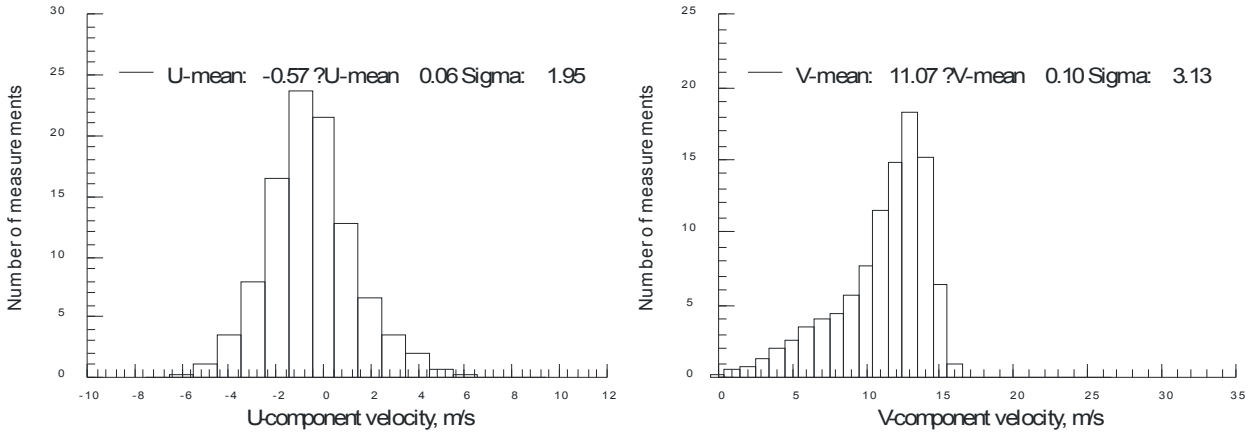

(ii) Signal-to-noise ratio threshold = 2.5 (5 dB)

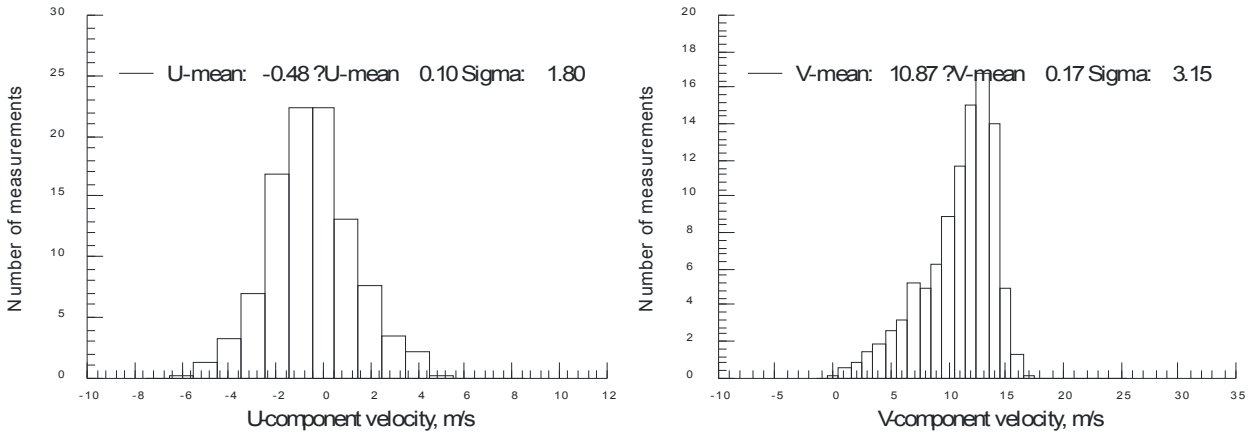

(iii) Signal-to-noise ratio threshold = 10 (10 dB)

Figure VII.35.b.(2)(a) - Velocity histograms obtained at 36-inch separation – Semi gloss black paint with Rhodamine B added, Focal distance = 180 inches.

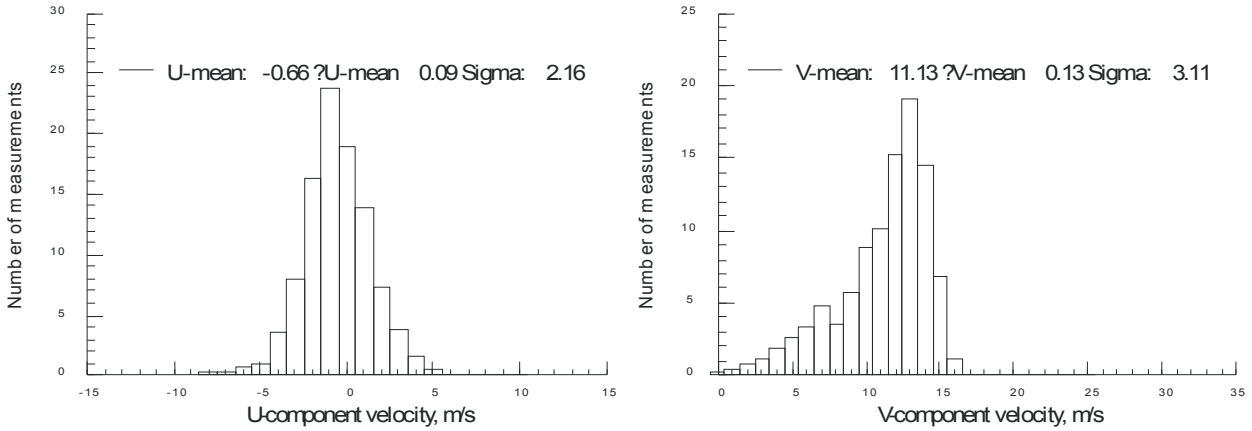

(i) Signal-to-noise ratio threshold = 5 (7 dB)

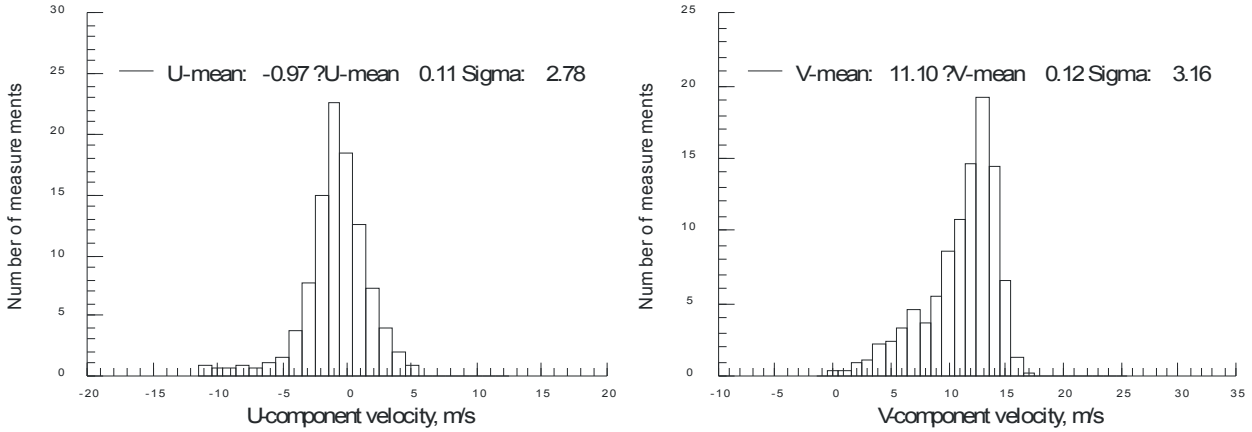

(ii) Signal-to-noise ratio threshold = 2.5 (5 dB)

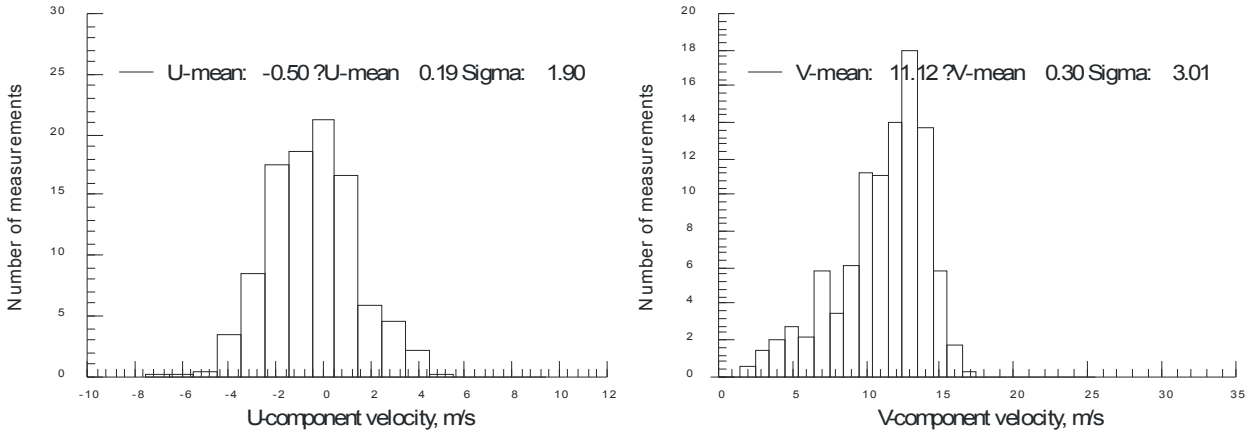

(iii) Signal-to-noise ratio threshold = 10 (10 dB)

Figure VII.35.b.(2)(b) - Velocity histograms obtained at first velocity/sigma deviation – Semi gloss black paint with Rhodamine B added, Focal distance = 180 inches.

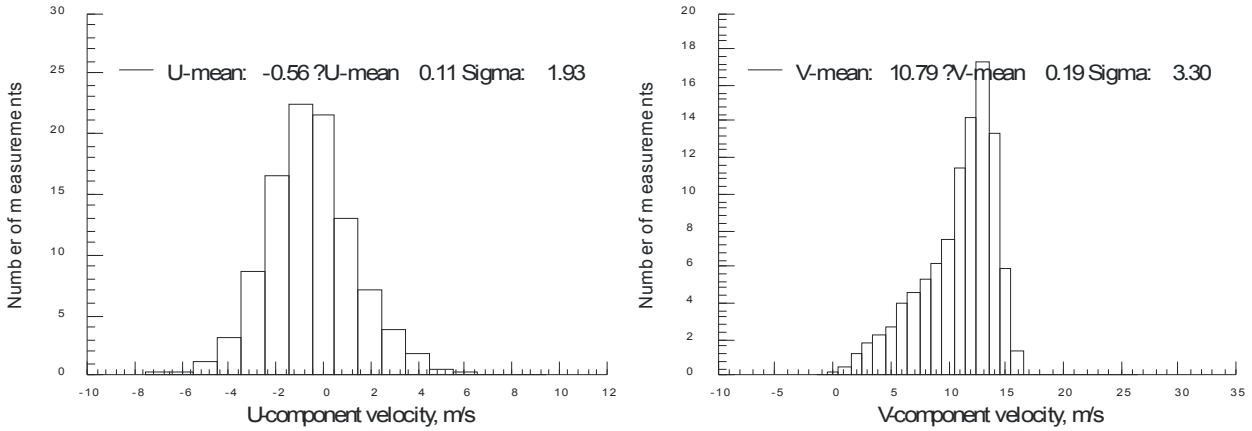

(i) Signal-to-noise ratio threshold = 5 (7 dB)

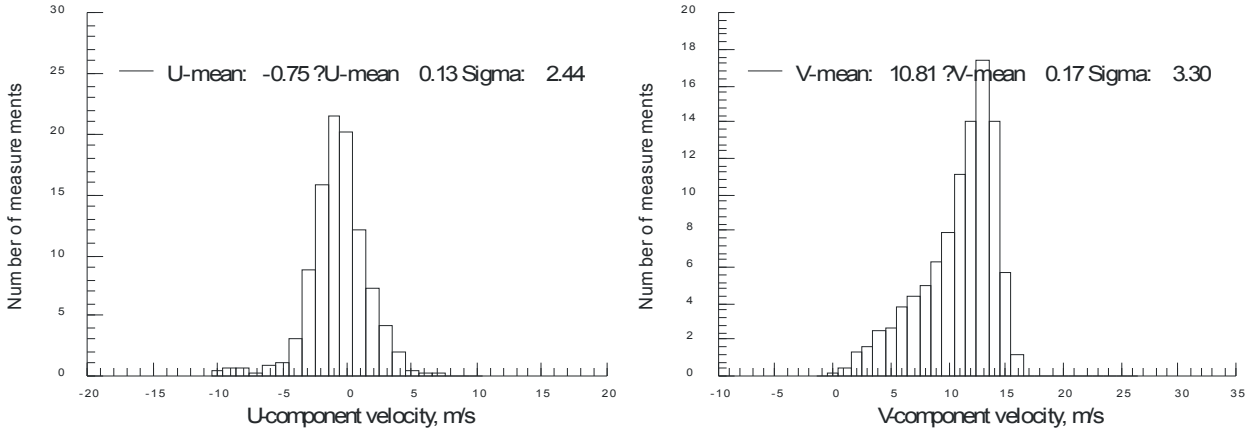

(ii) Signal-to-noise ratio threshold = 2.5 (5 dB)

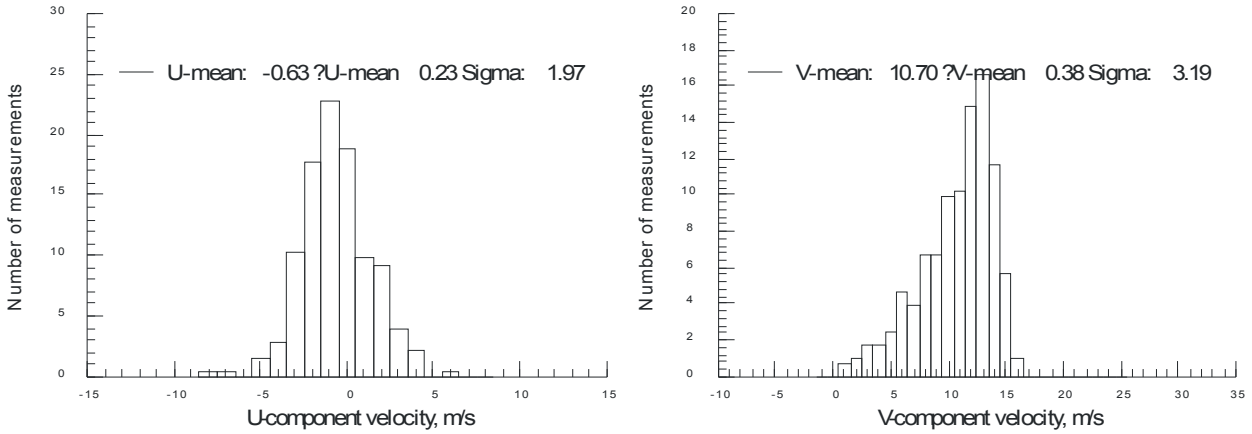

(iii) Signal-to-noise ratio threshold = 10 (10 dB)

Figure VII.35.b.(2)(c) - Velocity histograms obtained at closest approach – Semi gloss black paint with Rhodamine B added, Focal distance = 180 inches.

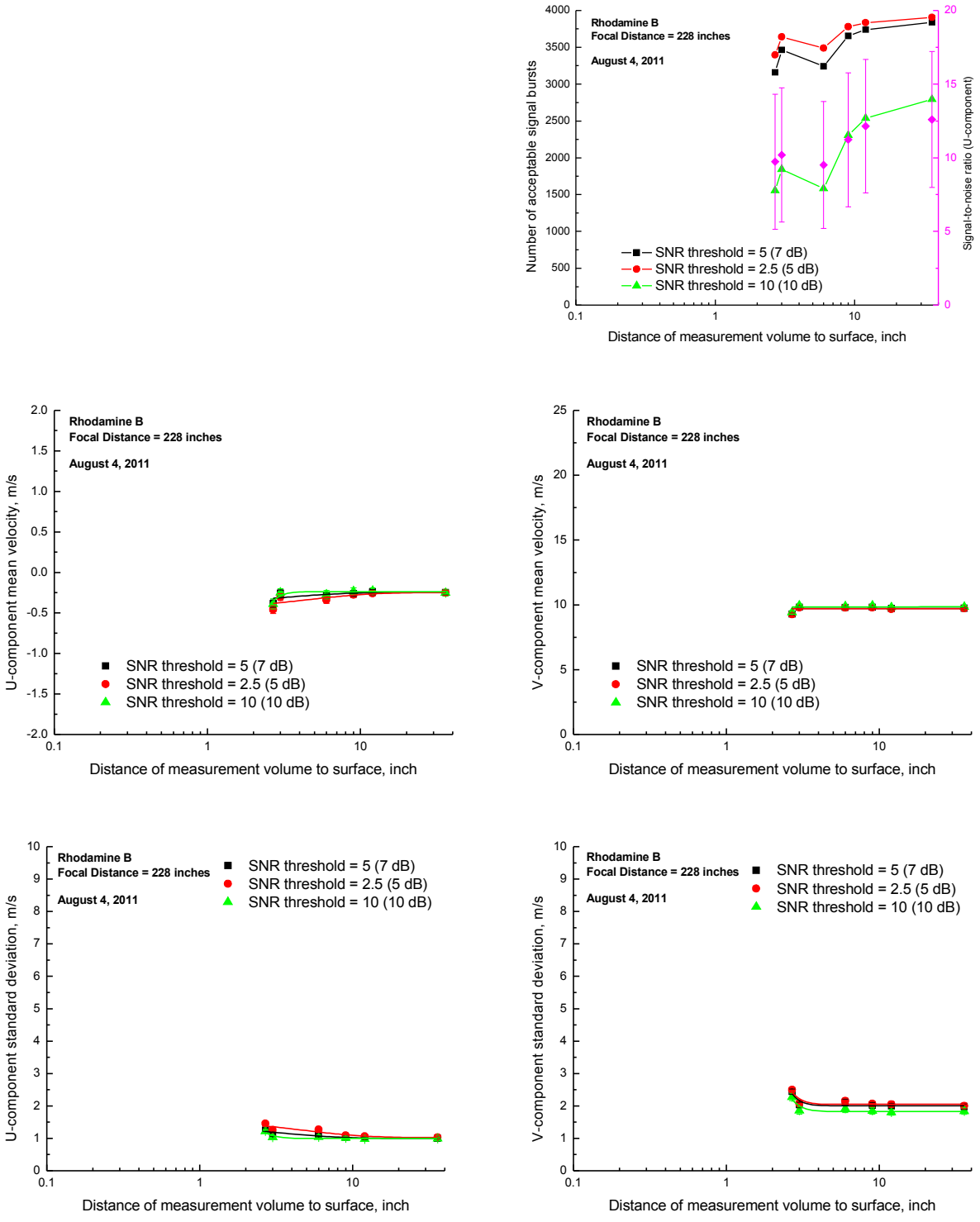

Figure VII.35.c.(1) - Velocity statistics as each surface is moved toward the measurement volume – Semi gloss black paint with Rhodamine B added, Focal distance = 228 inches.

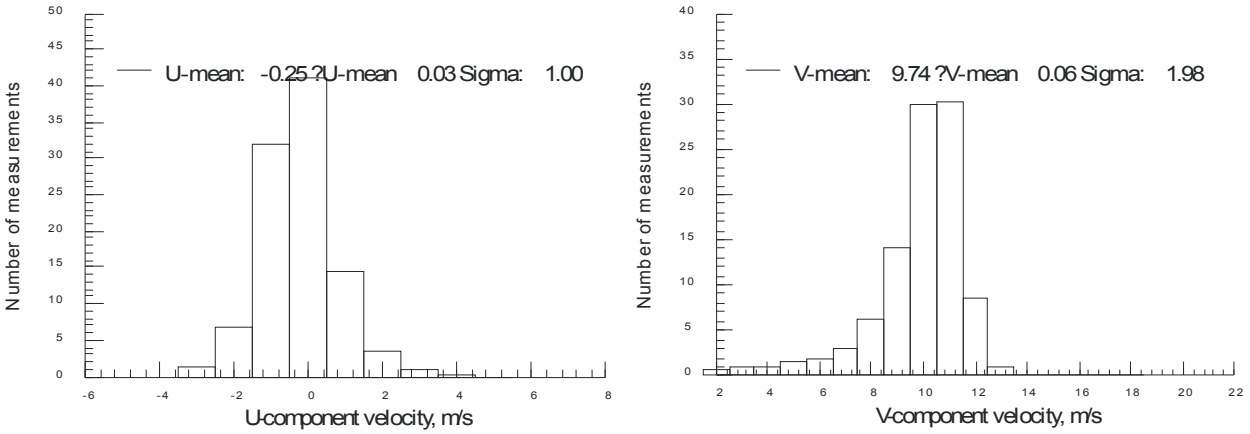

(i) Signal-to-noise ratio threshold = 5 (7 dB)

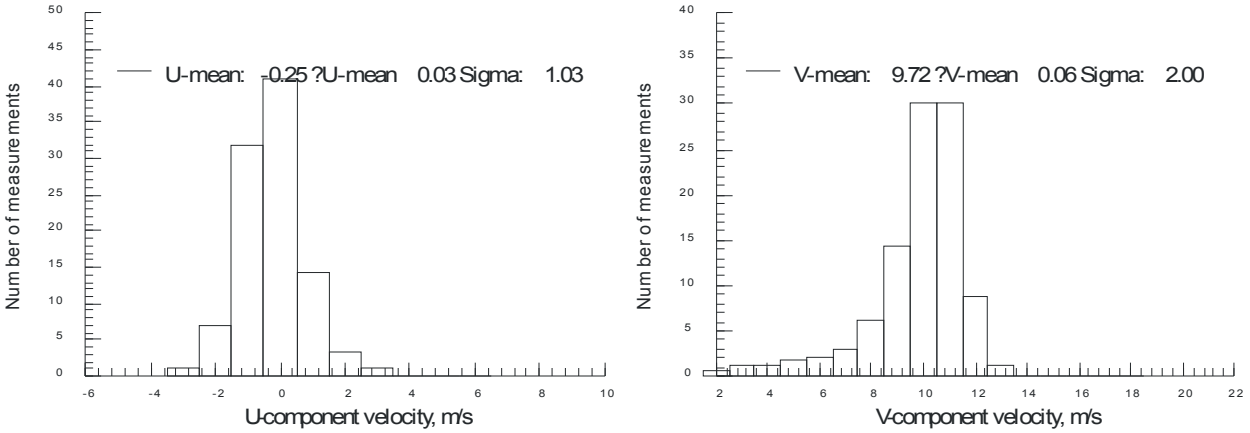

(ii) Signal-to-noise ratio threshold = 2.5 (5 dB)

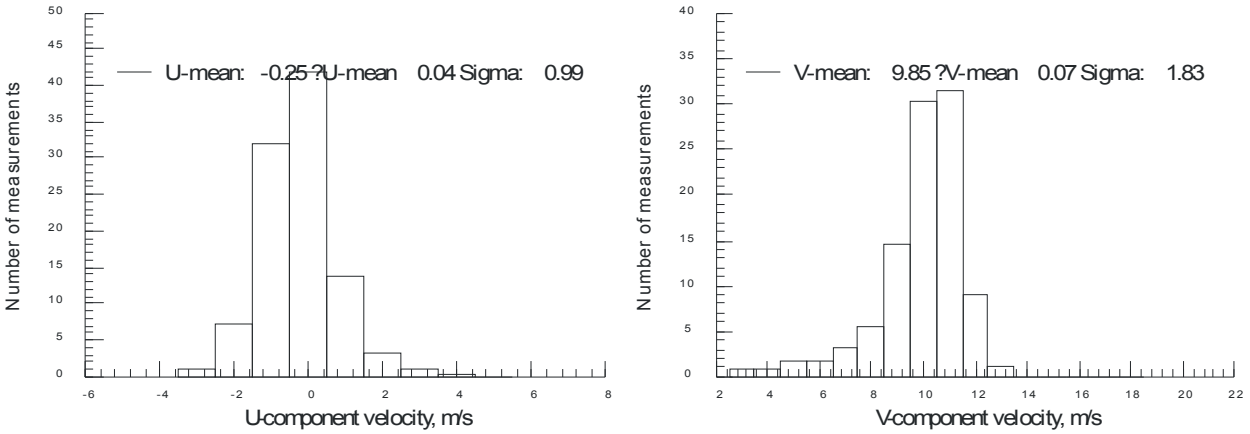

(iii) Signal-to-noise ratio threshold = 10 (10 dB)

Figure VII.35.c.(2)(a) - Velocity histograms obtained at 36-inch separation – Semi gloss black paint with Rhodamine B added, Focal distance = 228 inches.

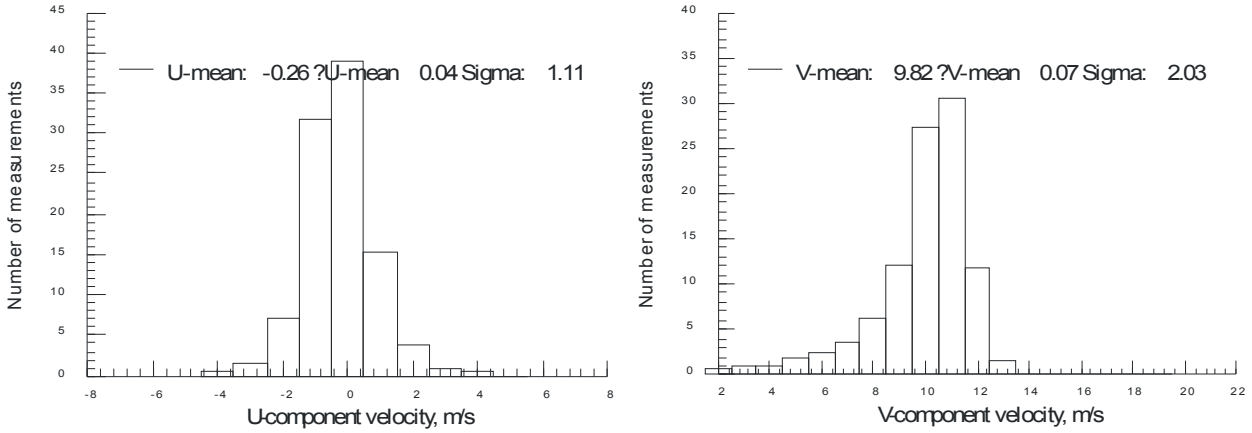

(i) Signal-to-noise ratio threshold = 5 (7 dB)

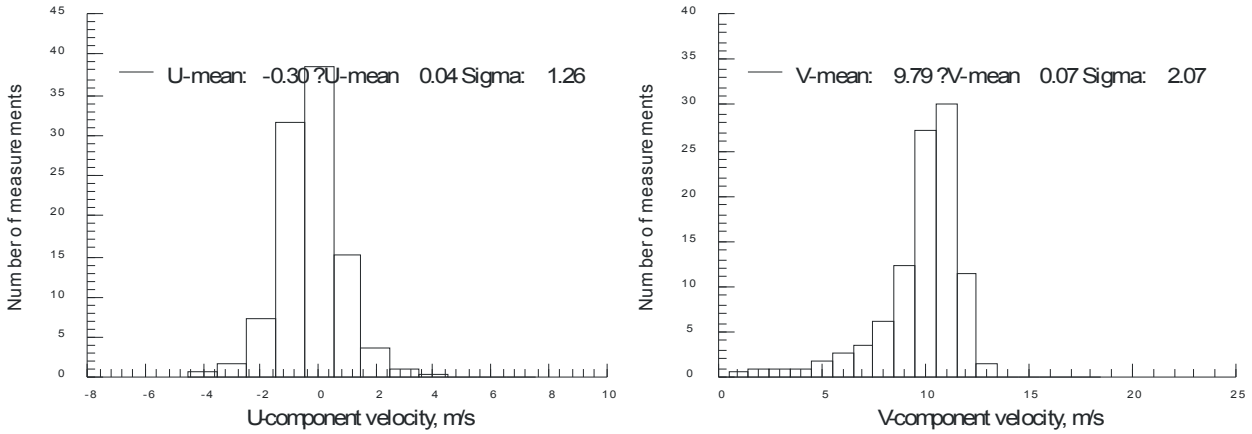

(ii) Signal-to-noise ratio threshold = 2.5 (5 dB)

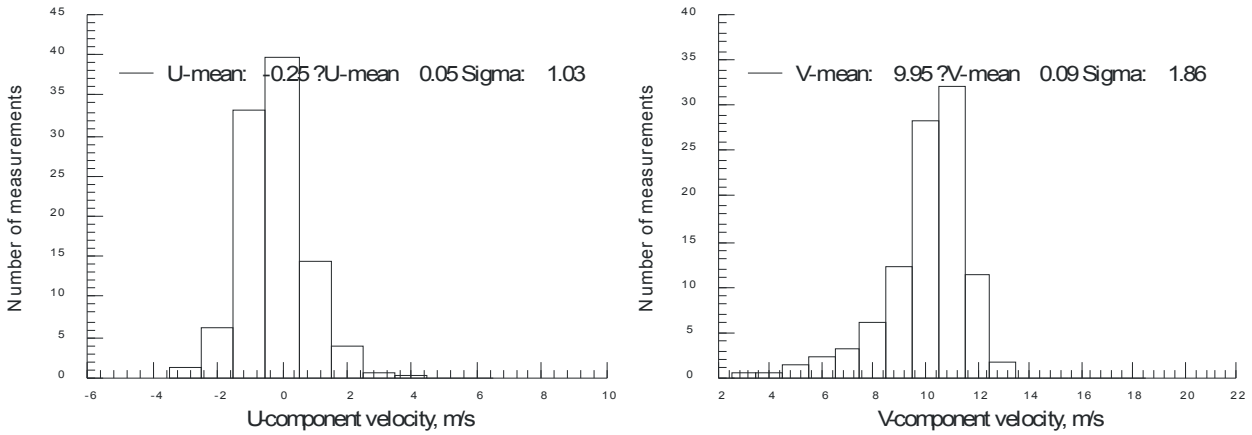

(iii) Signal-to-noise ratio threshold = 10 (10 dB)

Figure VII.35.c.(2)(b) - Velocity histograms obtained at first velocity/sigma deviation – Semi gloss black paint with Rhodamine B added, Focal distance = 228 inches.

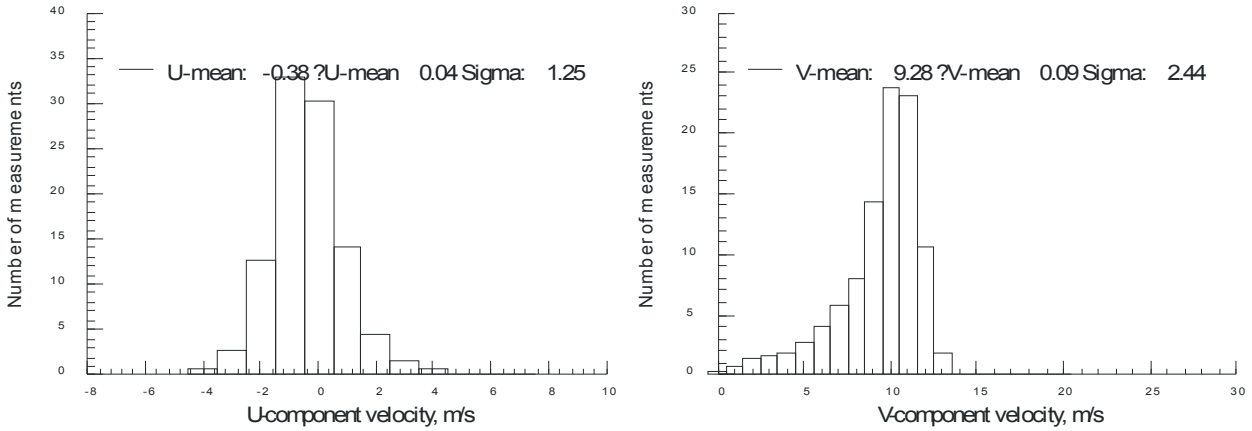

(i) Signal-to-noise ratio threshold = 5 (7 dB)

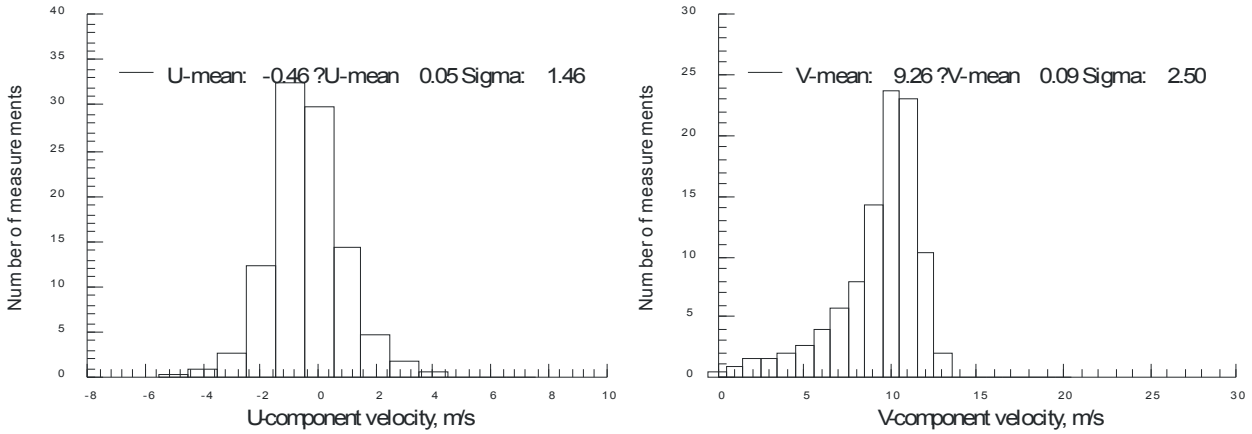

(ii) Signal-to-noise ratio threshold = 2.5 (5 dB)

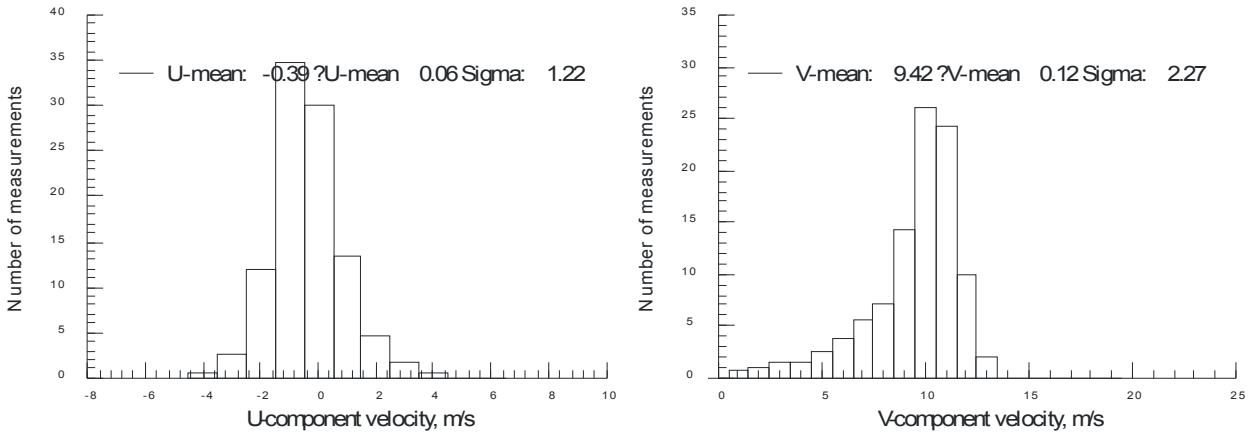

(iii) Signal-to-noise ratio threshold = 10 (10 dB)

Figure VII.35.c.(2)(c) - Velocity histograms obtained at closest approach – Semi gloss black paint with Rhodamine B added, Focal distance = 228 inches.

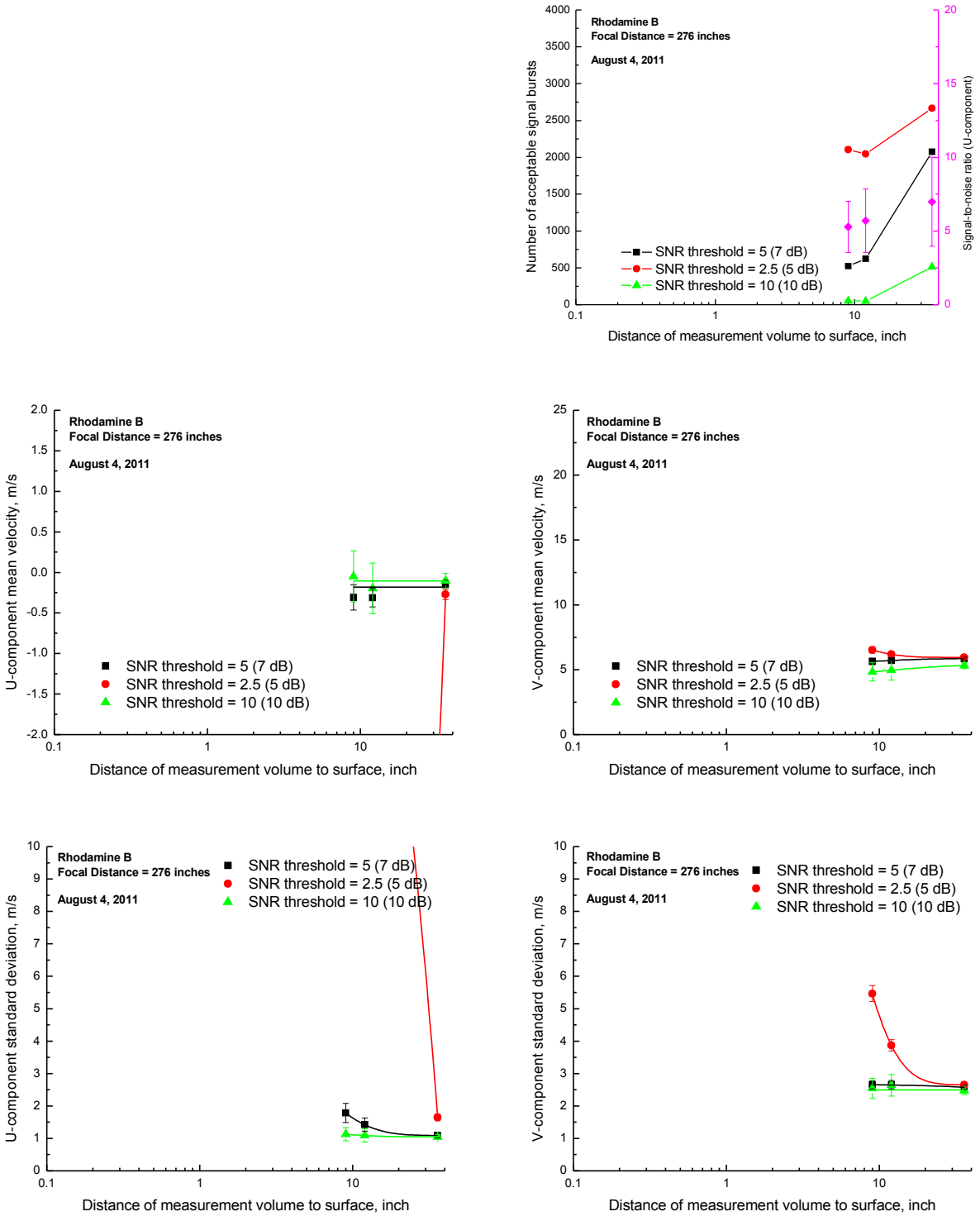

Figure VII.35.d.(1) - Velocity statistics as each surface is moved toward the measurement volume – Semi gloss black paint with Rhodamine B added, Focal distance = 276 inches.

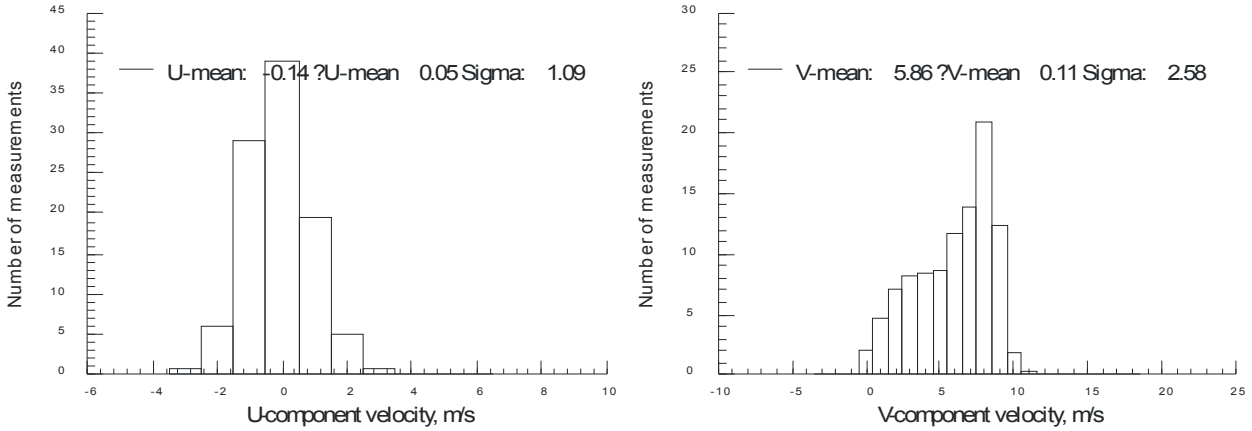

(i) Signal-to-noise ratio threshold = 5 (7 dB)

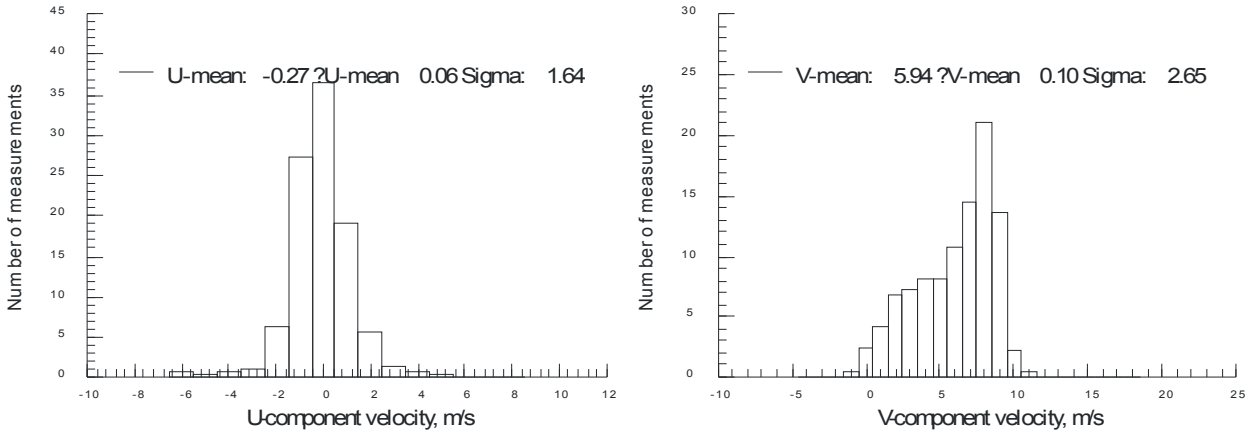

(ii) Signal-to-noise ratio threshold = 2.5 (5 dB)

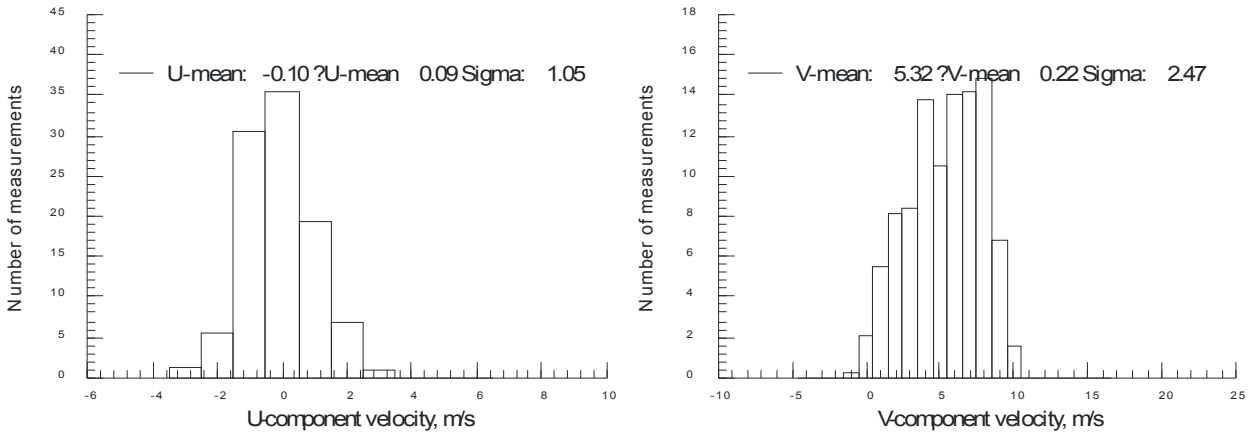

(iii) Signal-to-noise ratio threshold = 10 (10 dB)

Figure VII.35.d.(2)(a) - Velocity histograms obtained at 36-inch separation – Semi gloss black paint with Rhodamine B added, Focal distance = 276 inches.

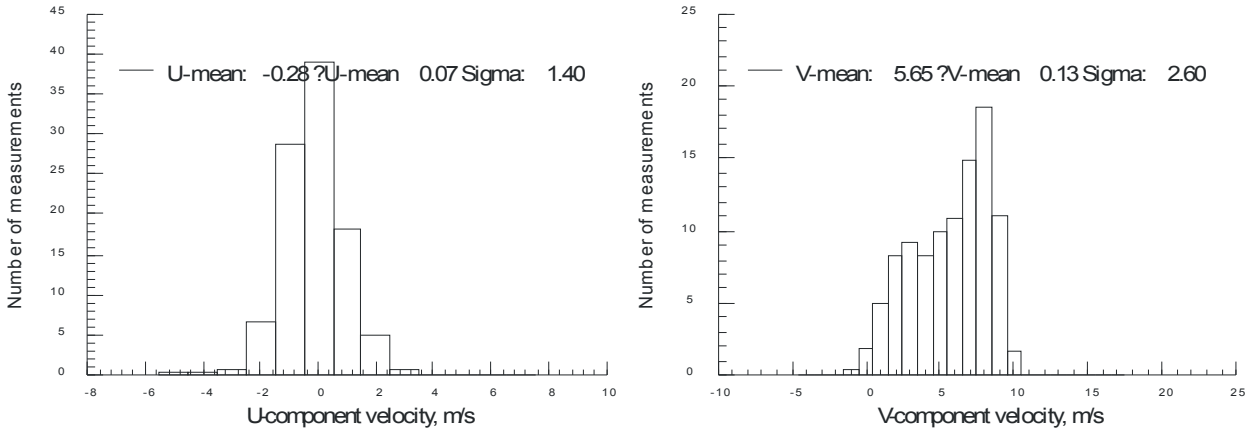

(i) Signal-to-noise ratio threshold = 5 (7 dB)

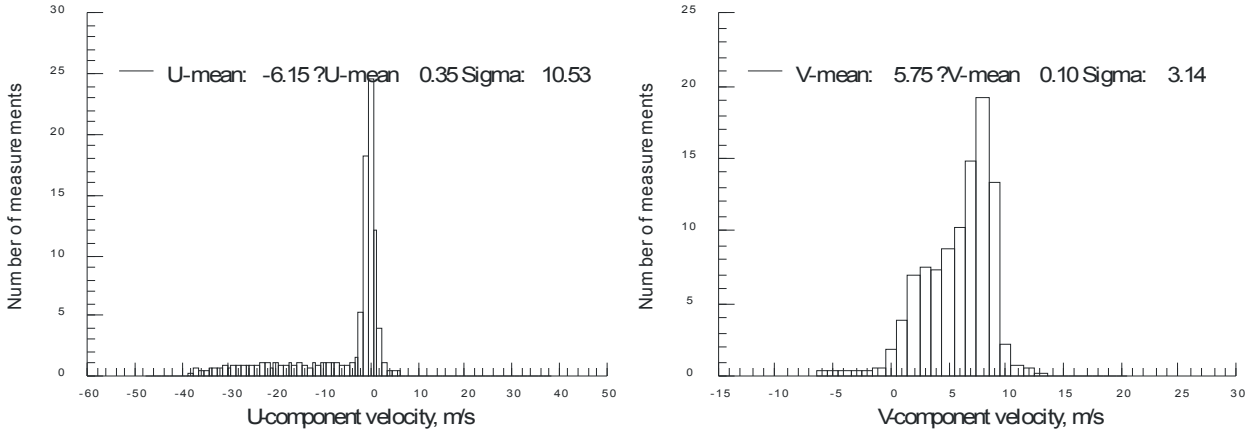

(ii) Signal-to-noise ratio threshold = 2.5 (5 dB)

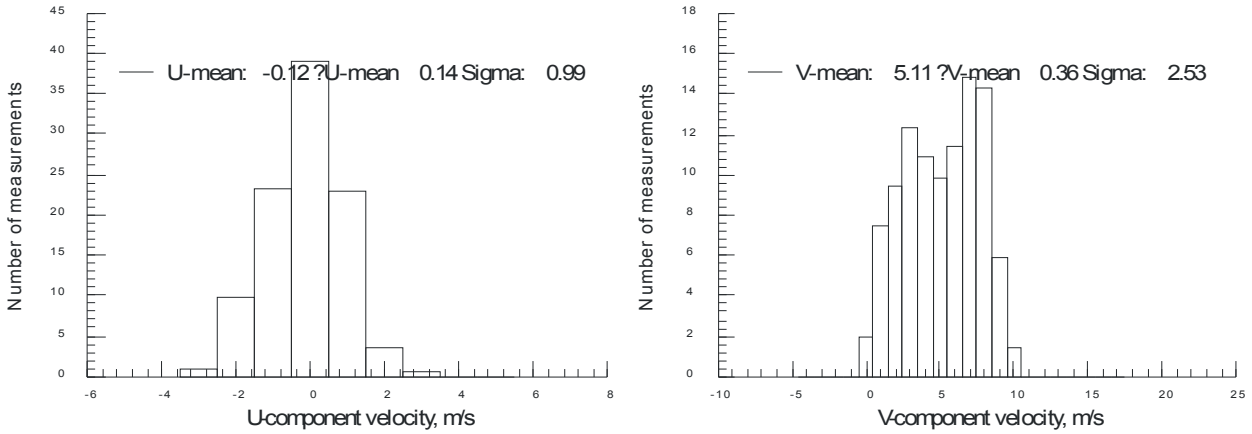

(iii) Signal-to-noise ratio threshold = 10 (10 dB)

Figure VII.35.d.(2)(b) - Velocity histograms obtained at first velocity/sigma deviation – Semi gloss black paint with Rhodamine B added, Focal distance = 276 inches.

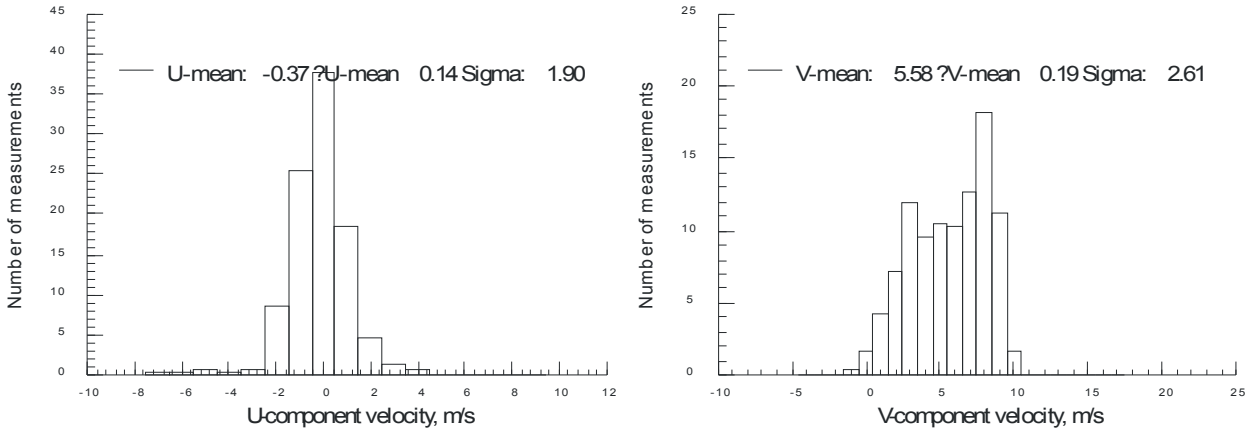

(i) Signal-to-noise ratio threshold = 5 (7 dB)

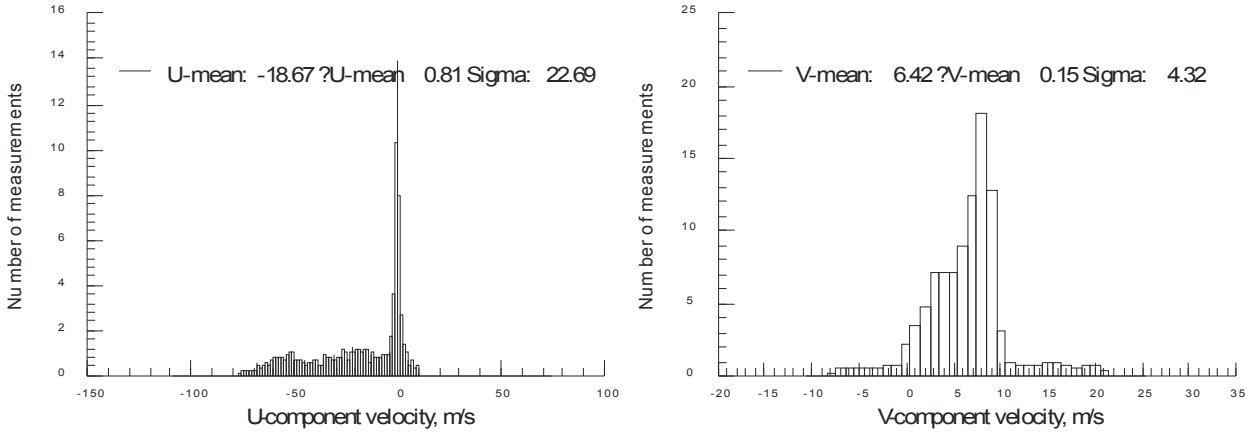

(ii) Signal-to-noise ratio threshold = 2.5 (5 dB)

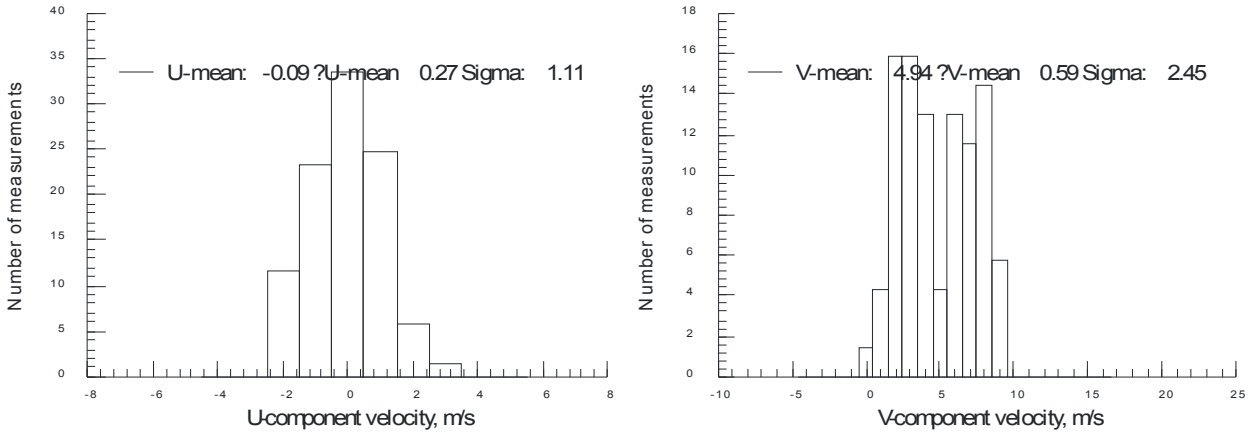

(iii) Signal-to-noise ratio threshold = 10 (10 dB)

Figure VII.35.d.(2)(c) - Velocity histograms obtained at closest approach – Semi gloss black paint with Rhodamine B added, Focal distance = 276 inches.

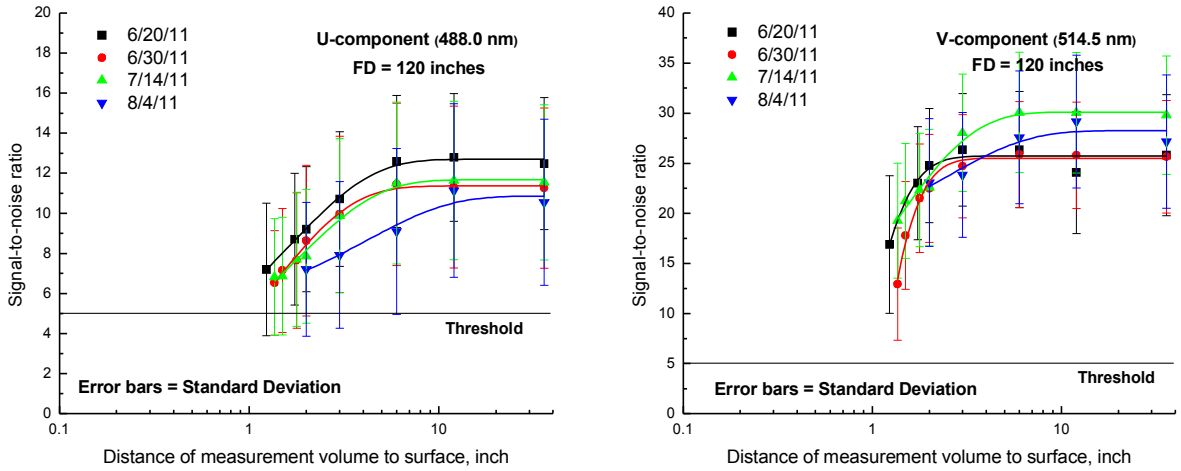

Figure VII.36.- Signal-to-noise statistics as each surface is moved toward the measurement volume – Semi gloss black paint with Rhodamine B added, Focal distance = 120 inches. Comparison to determine effects of Rhodamine B aging.

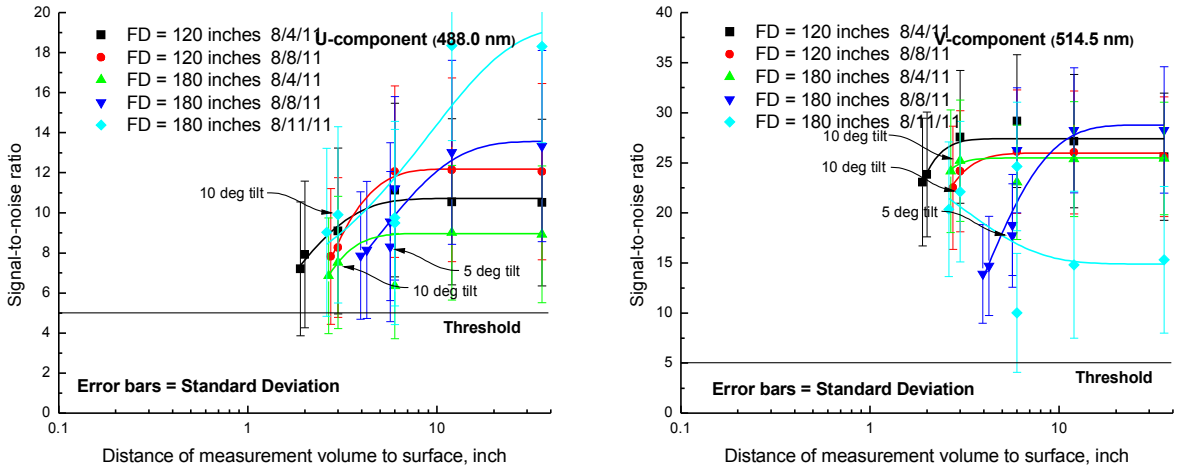

Figure VII.37.- Signal-to-noise statistics as each surface is moved toward the measurement volume – Semi gloss black paint with Rhodamine B added, Focal distance = 120 and 180 inches. Comparison to determine effects of Rhodamine B aging – short interval.

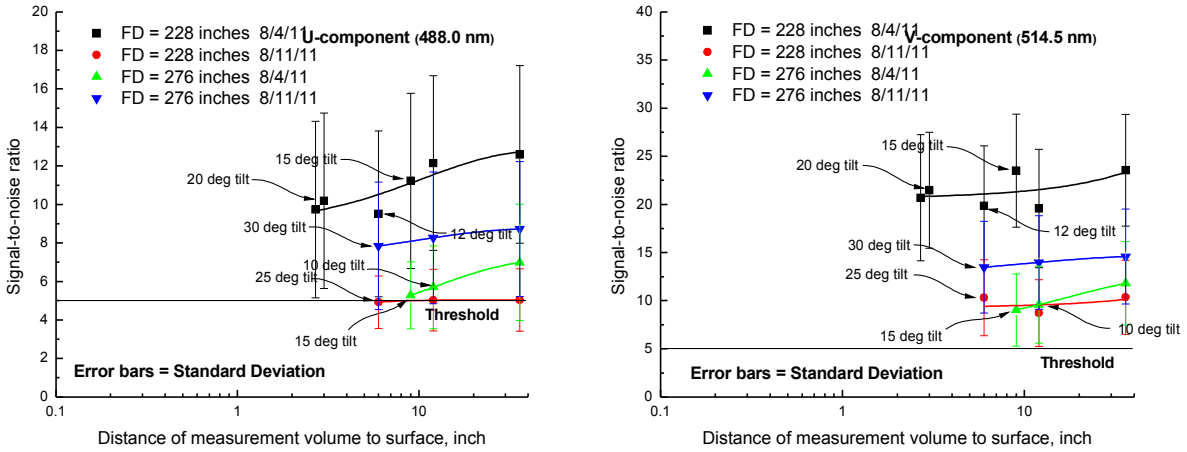

Figure VII.38.- Signal-to-noise statistics as each surface is moved toward the measurement volume – Semi gloss black paint with Rhodamine B added, Focal distance = 228 and 276 inches. Comparison to determine effects of Rhodamine B aging – short interval.

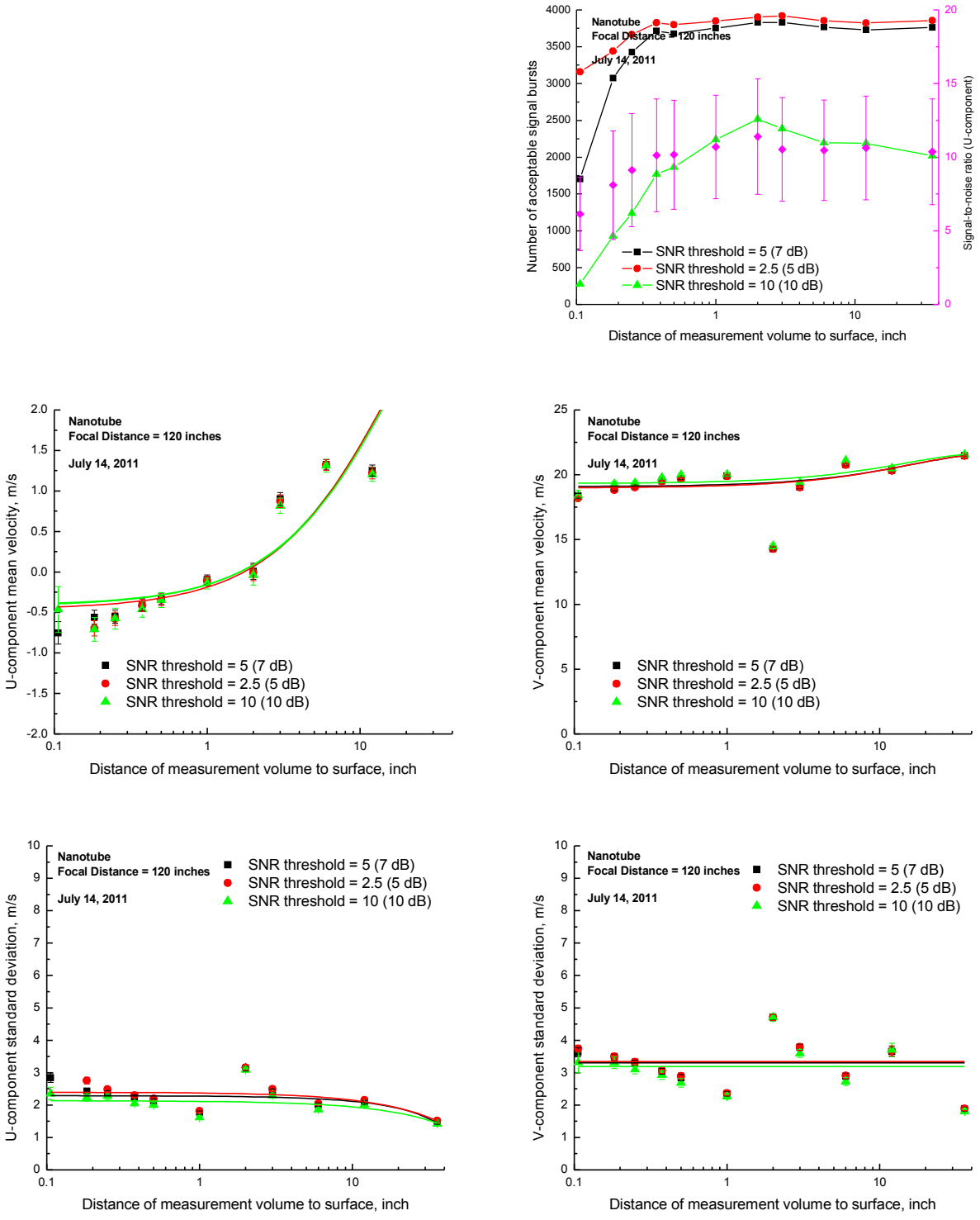

Figure VII.39.a.(1)- Velocity statistics as each surface is moved toward the measurement volume – Nanotube matrix sample, Focal distance = 120 inches.

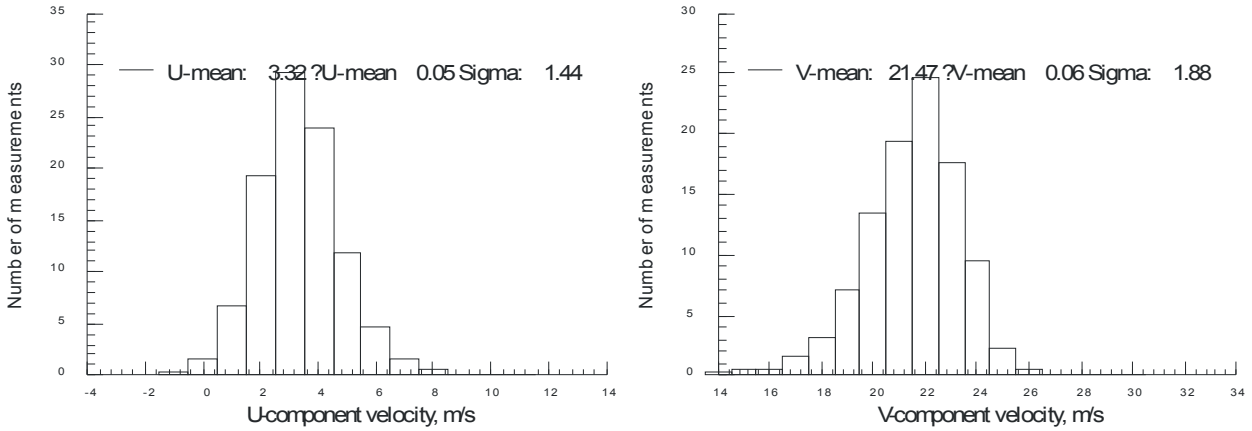

(i) Signal-to-noise ratio threshold = 5 (7 dB)

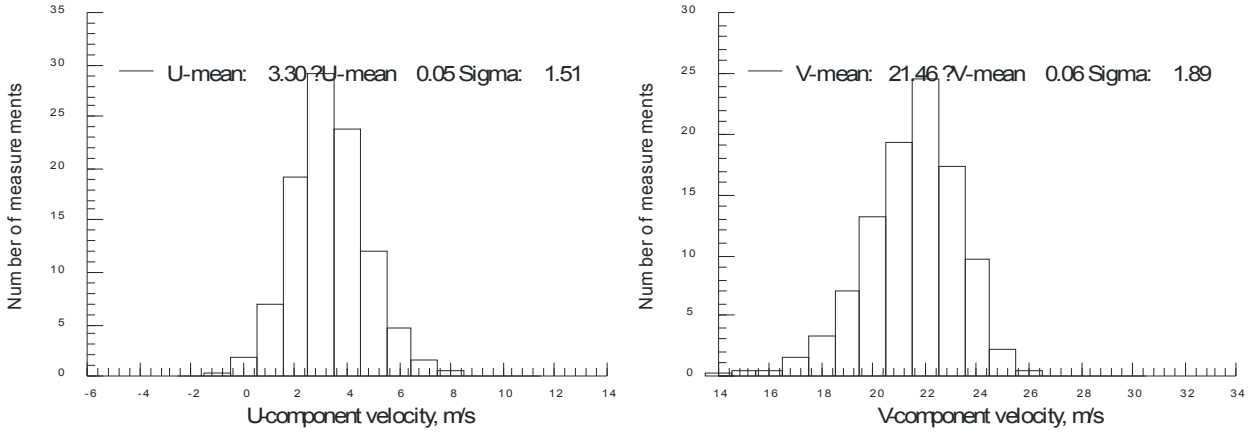

(ii) Signal-to-noise ratio threshold = 2.5 (5 dB)

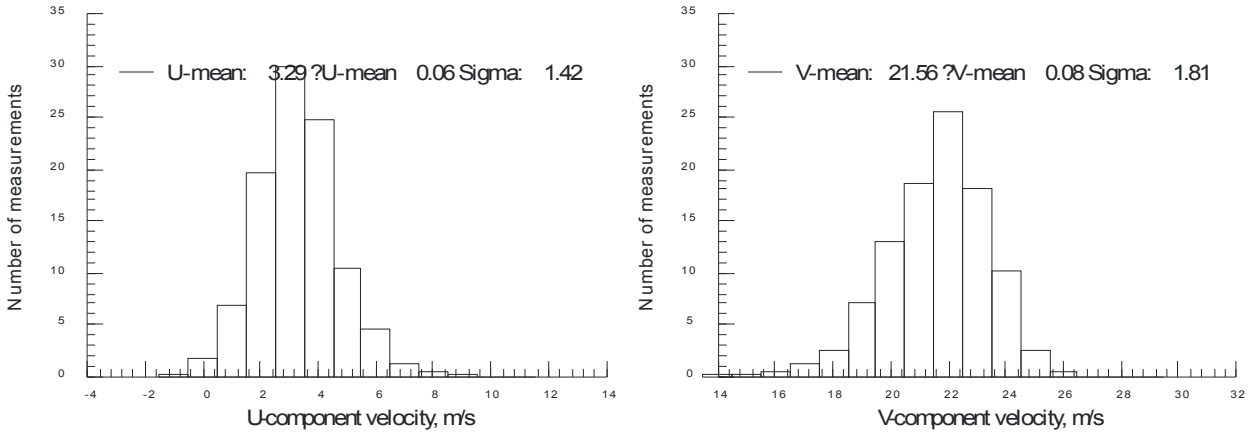

(iii) Signal-to-noise ratio threshold = 10 (10 dB)

Figure VII.39.a.(2)(a) - Velocity histograms obtained at 36-inch separation – Nanotube matrix sample, Focal distance = 120 inches.

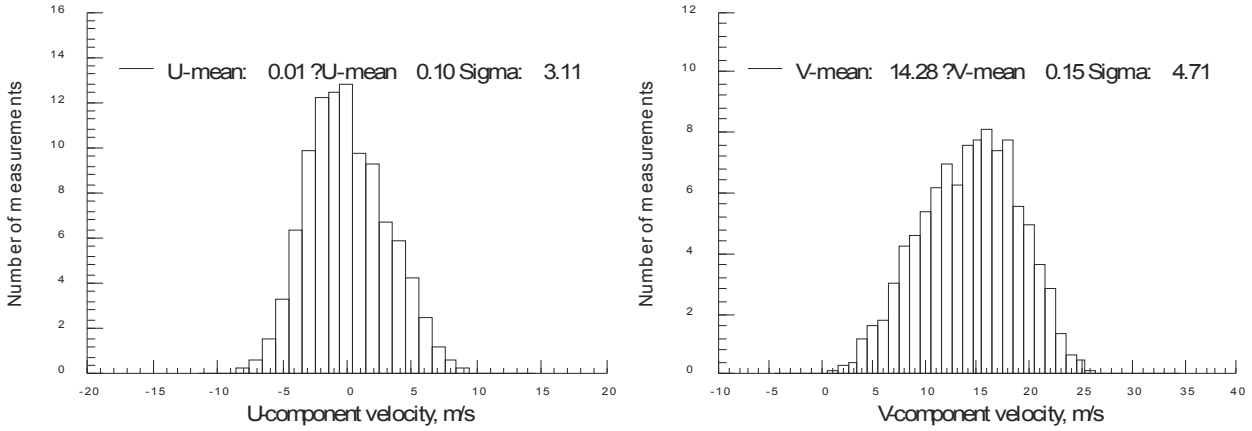

(i) Signal-to-noise ratio threshold = 5 (7 dB)

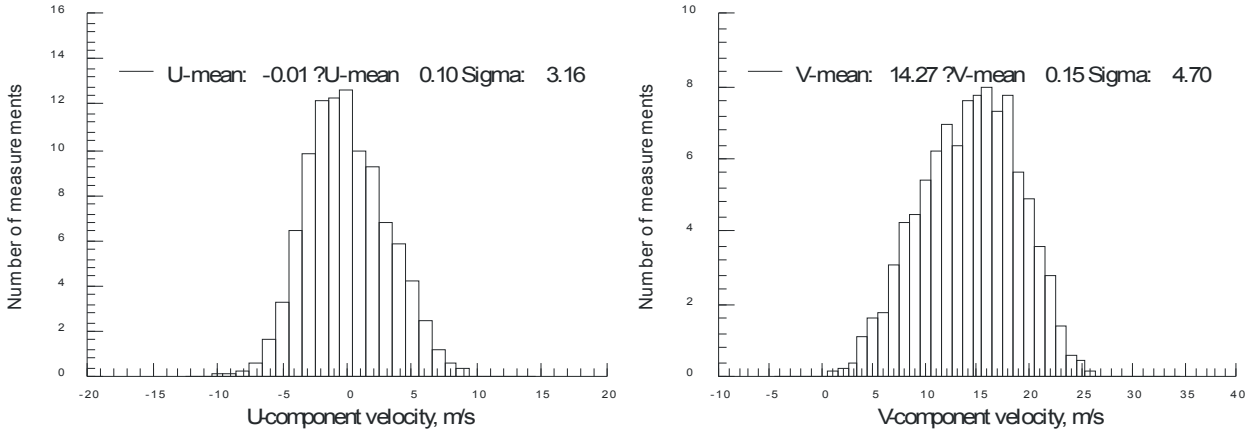

(ii) Signal-to-noise ratio threshold = 2.5 (5 dB)

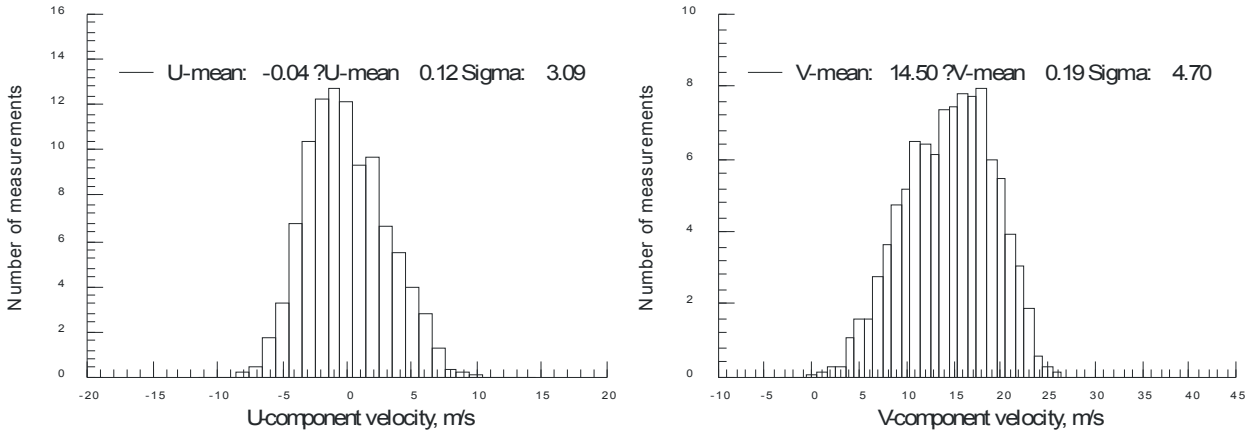

(iii) Signal-to-noise ratio threshold = 10 (10 dB)

Figure VII.39.a.(2)(b) - Velocity histograms obtained at first velocity/sigma deviation – Nanotube matrix sample, Focal distance = 120 inches.

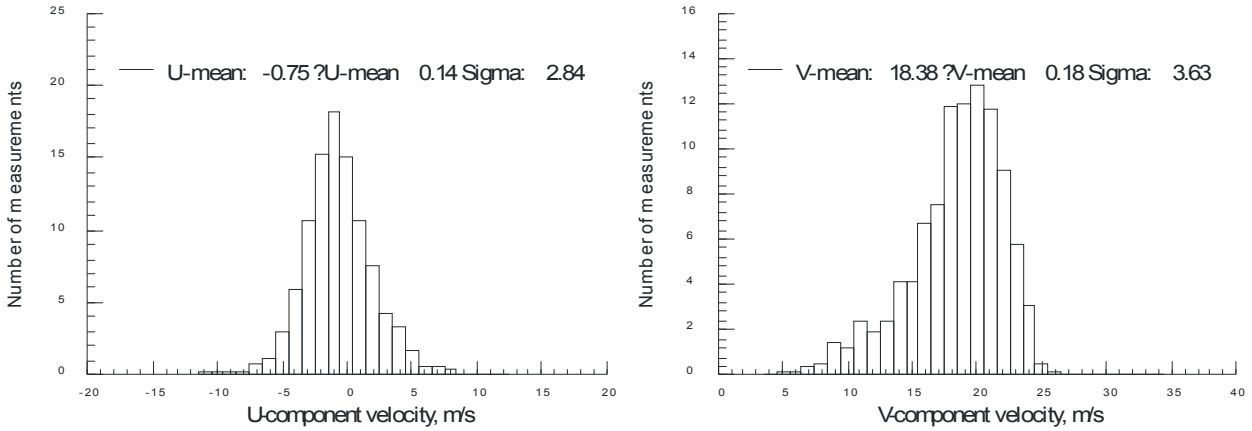

(i) Signal-to-noise ratio threshold = 5 (7 dB)

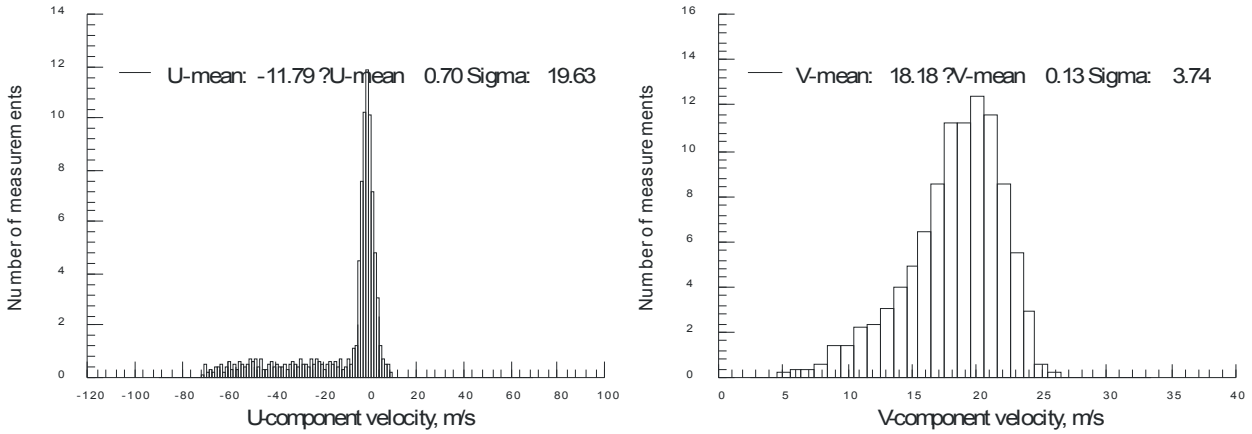

(ii) Signal-to-noise ratio threshold = 2.5 (5 dB)

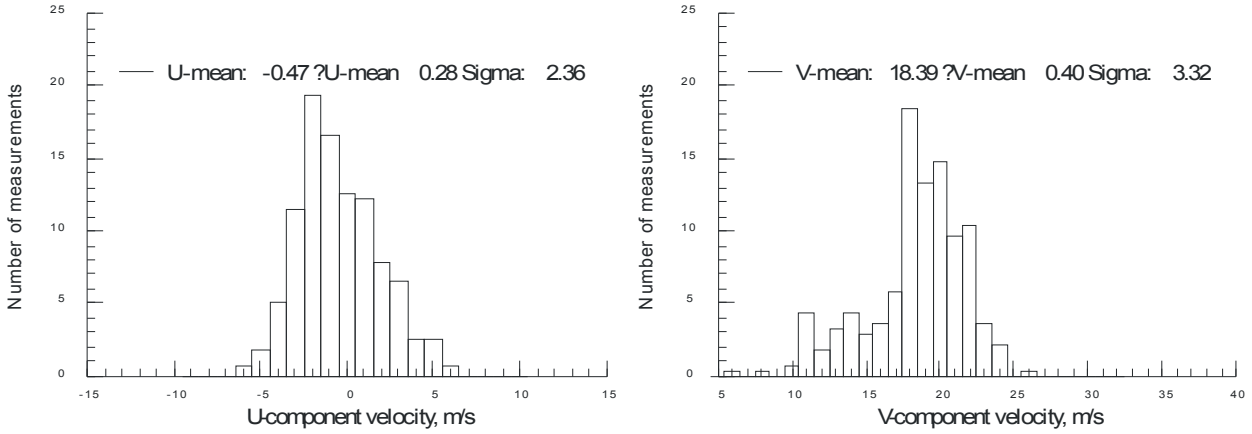

(iii) Signal-to-noise ratio threshold = 10 (10 dB)

Figure VII.39.a.(2)(c) - Velocity histograms obtained at closest approach – Nanotube matrix sample, Focal distance = 120 inches.

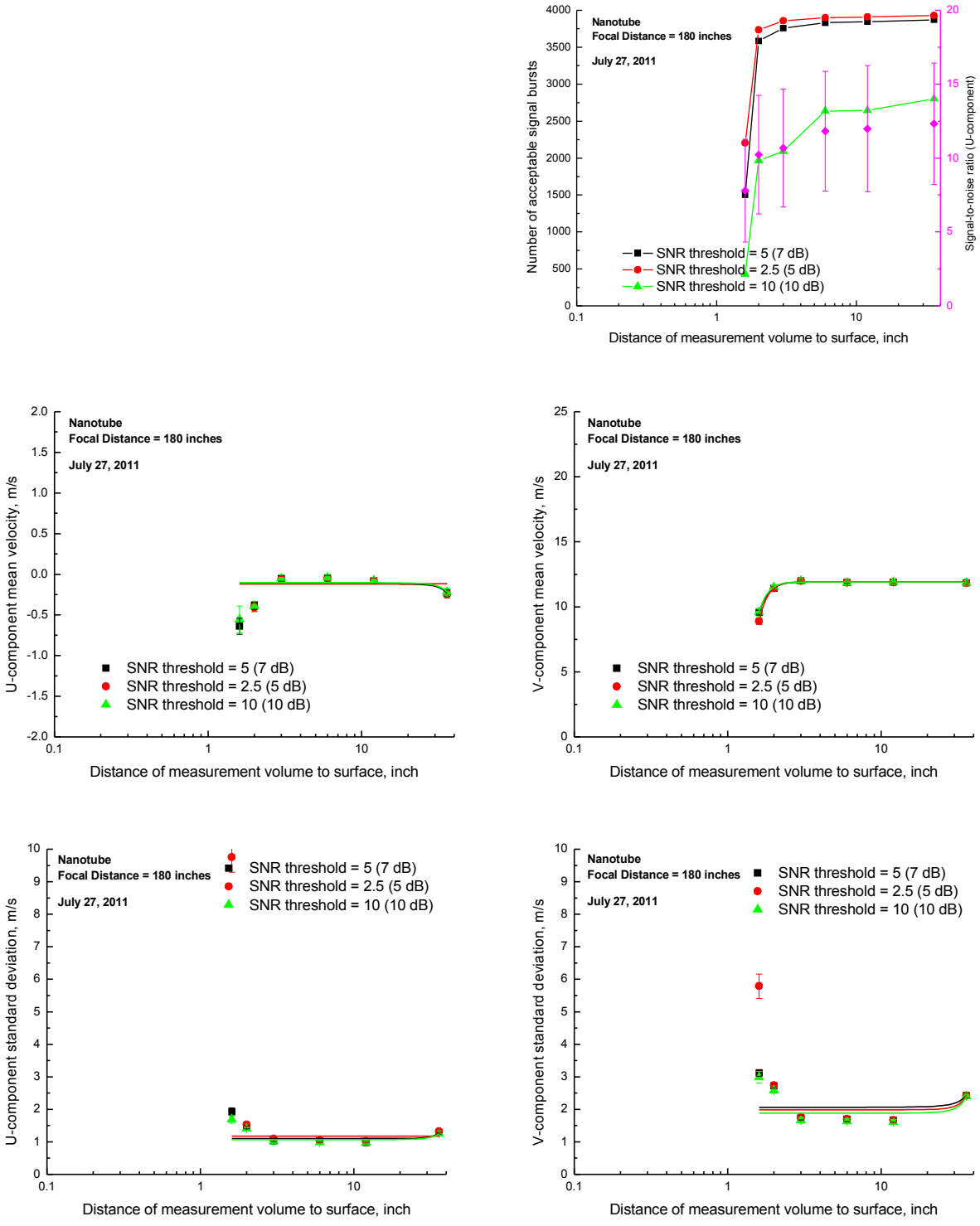

Figure VII.39.b.(1) - Velocity statistics as each surface is moved toward the measurement volume – Nanotube matrix sample, Focal distance = 180 inches.

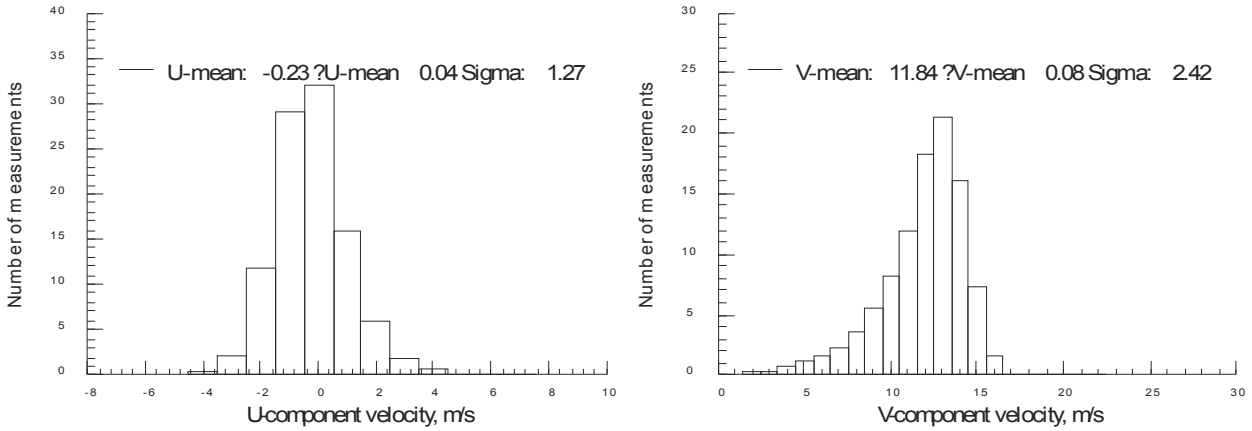

(i) Signal-to-noise ratio threshold = 5 (7 dB)

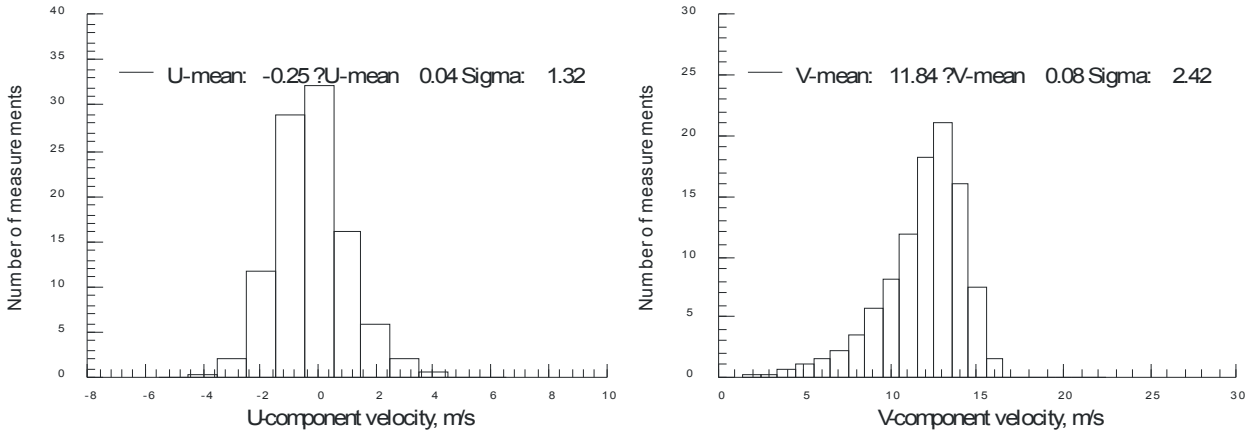

(ii) Signal-to-noise ratio threshold = 2.5 (5 dB)

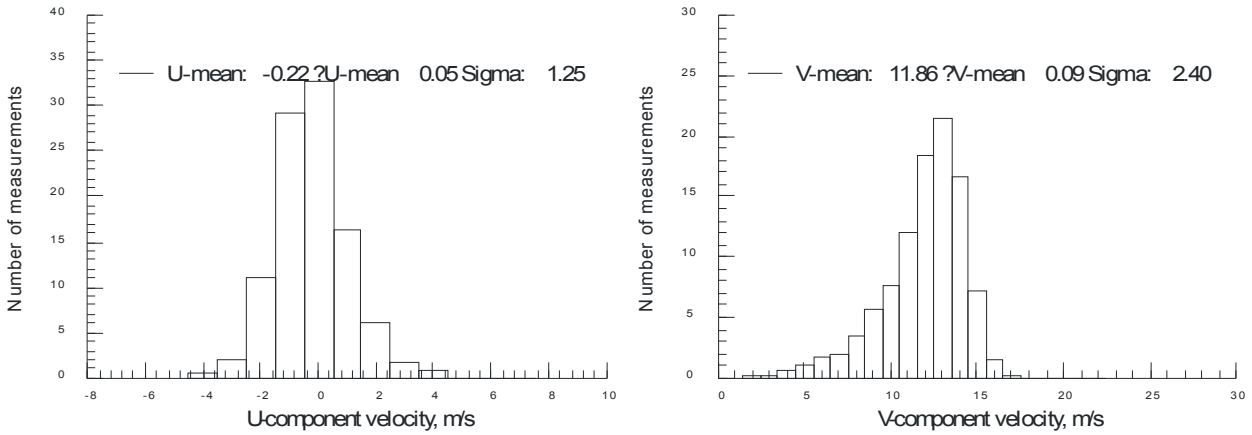

(iii) Signal-to-noise ratio threshold = 10 (10 dB)

Figure VII.39.b.(2)(a) - Velocity histograms obtained at 36-inch separation – Nanotube matrix sample, Focal distance = 180 inches.

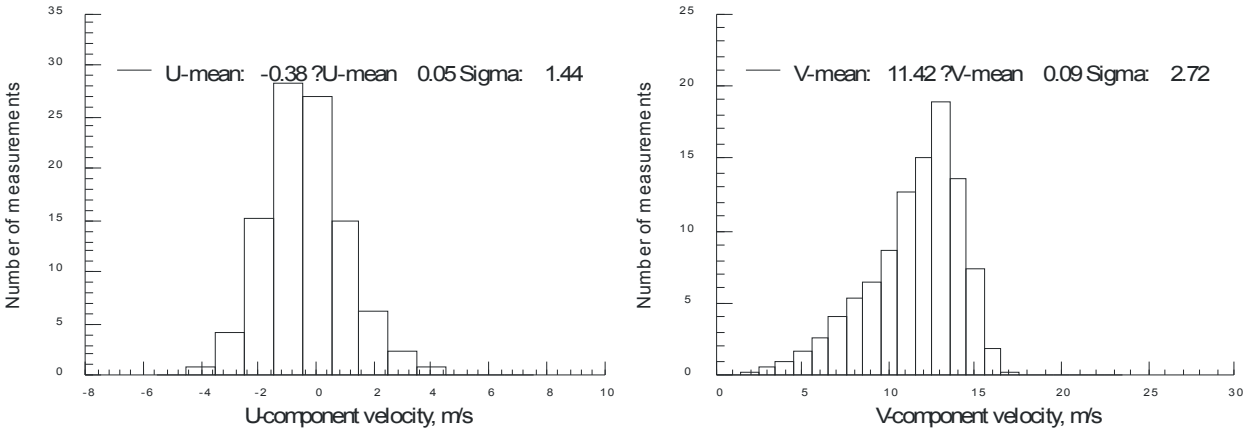

(i) Signal-to-noise ratio threshold = 5 (7 dB)

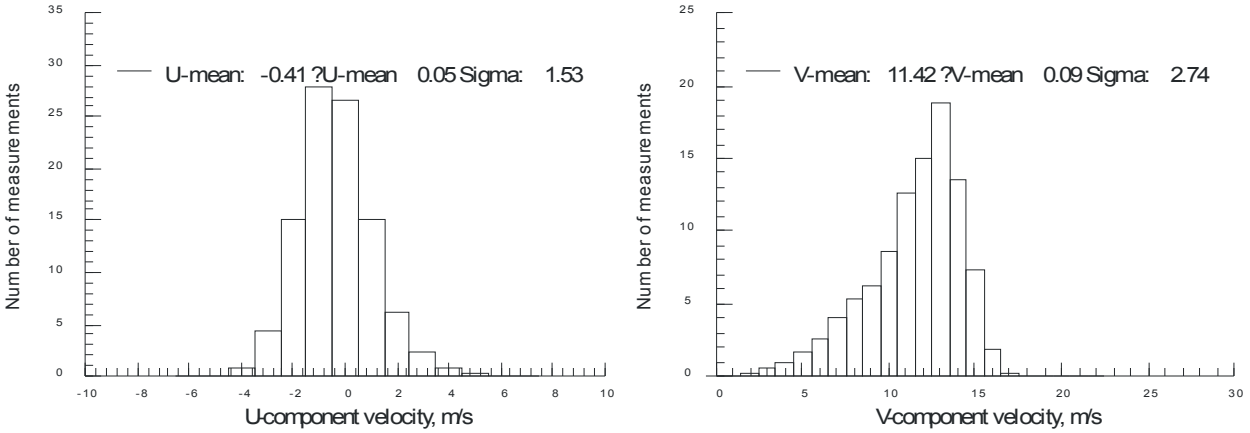

(ii) Signal-to-noise ratio threshold = 2.5 (5 dB)

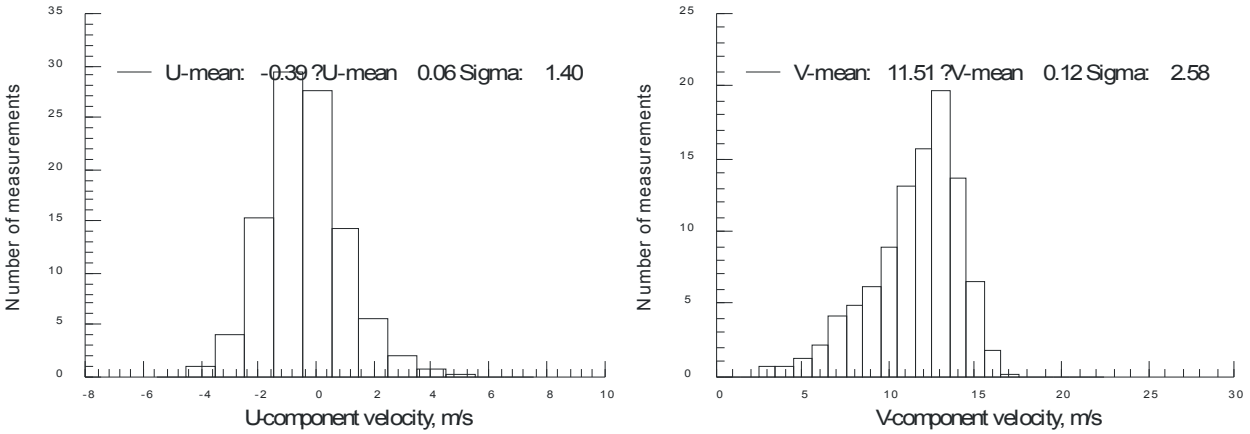

(iii) Signal-to-noise ratio threshold = 10 (10 dB)

Figure VII.39.b.(2)(b) - Velocity histograms obtained at first velocity/sigma deviation – Nanotube matrix sample, Focal distance = 180 inches.

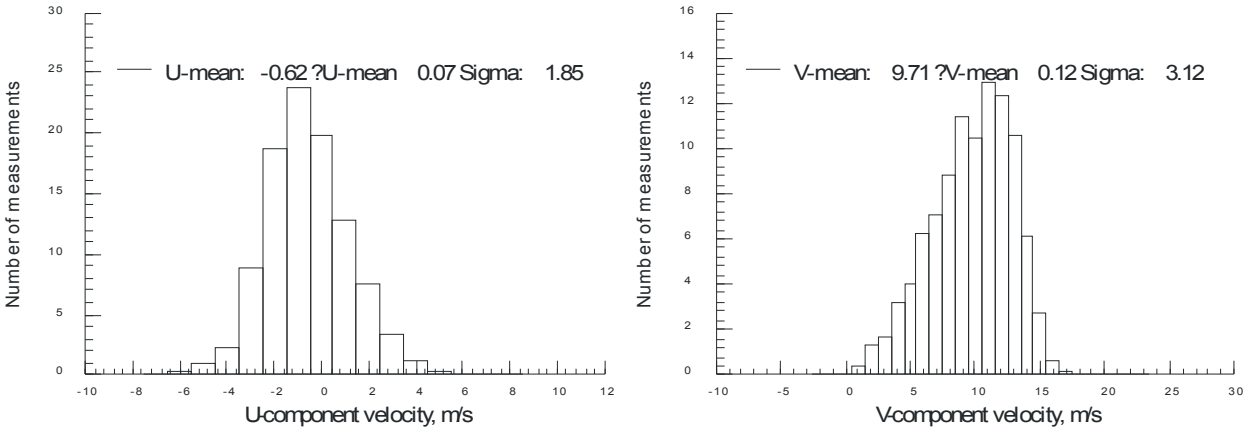

(i) Signal-to-noise ratio threshold = 5 (7 dB)

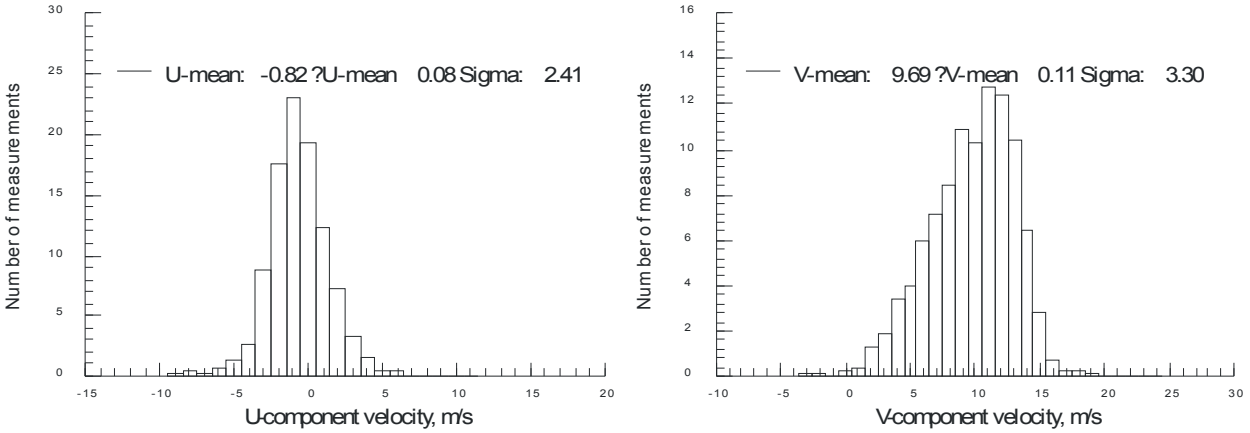

(ii) Signal-to-noise ratio threshold = 2.5 (5 dB)

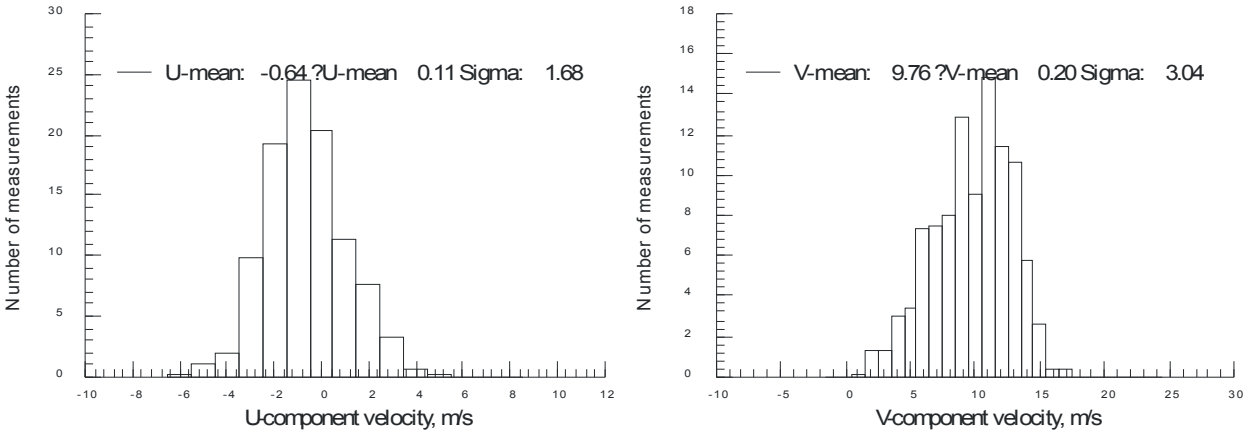

(iii) Signal-to-noise ratio threshold = 10 (10 dB)

Figure VII.39.b.(2)(c) - Velocity histograms obtained at closest approach – Nanotube matrix sample, Focal distance = 180 inches.

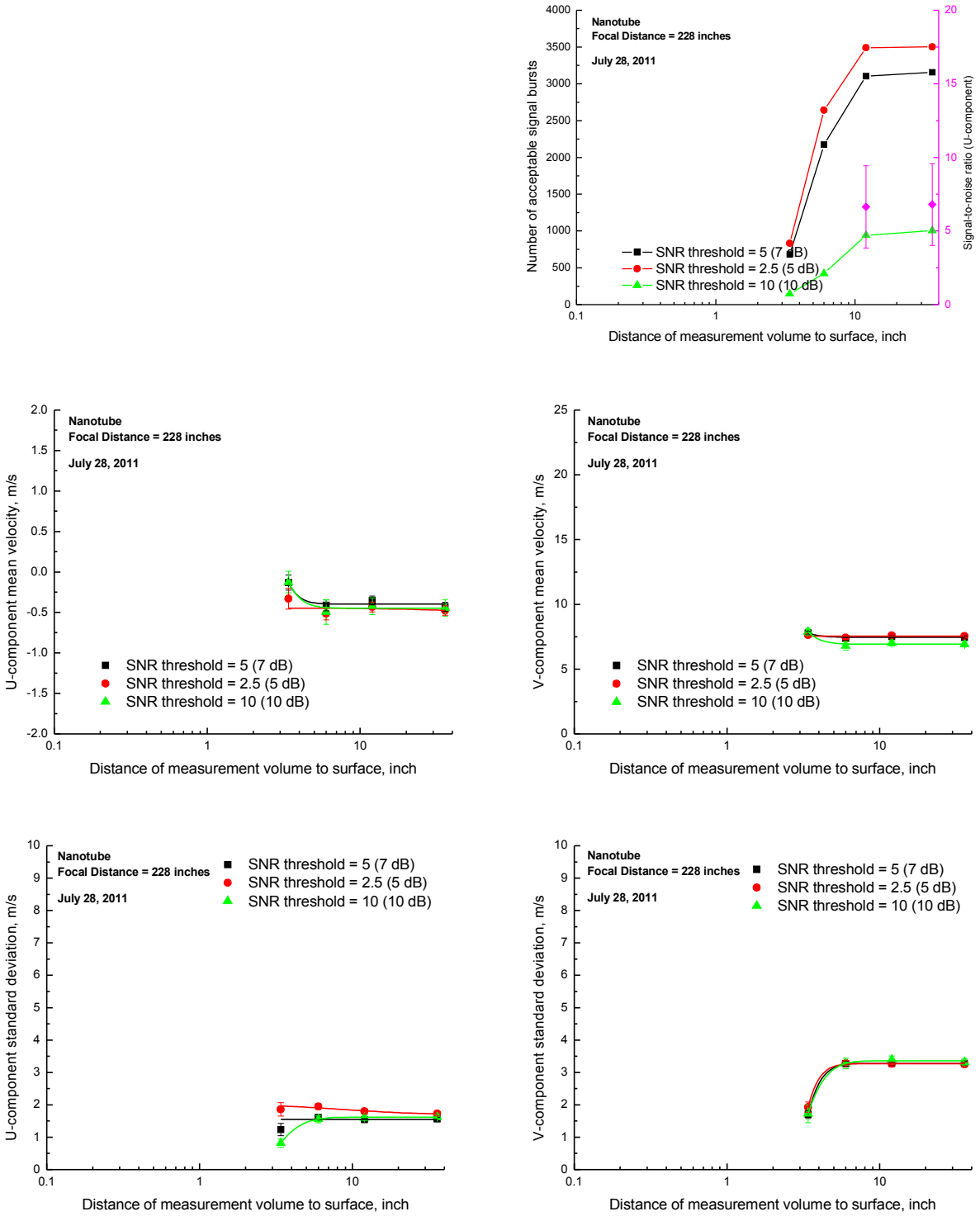

Figure VII.39.c.(1) - Velocity statistics as each surface is moved toward the measurement volume – Nanotube matrix sample, Focal distance = 228 inches.

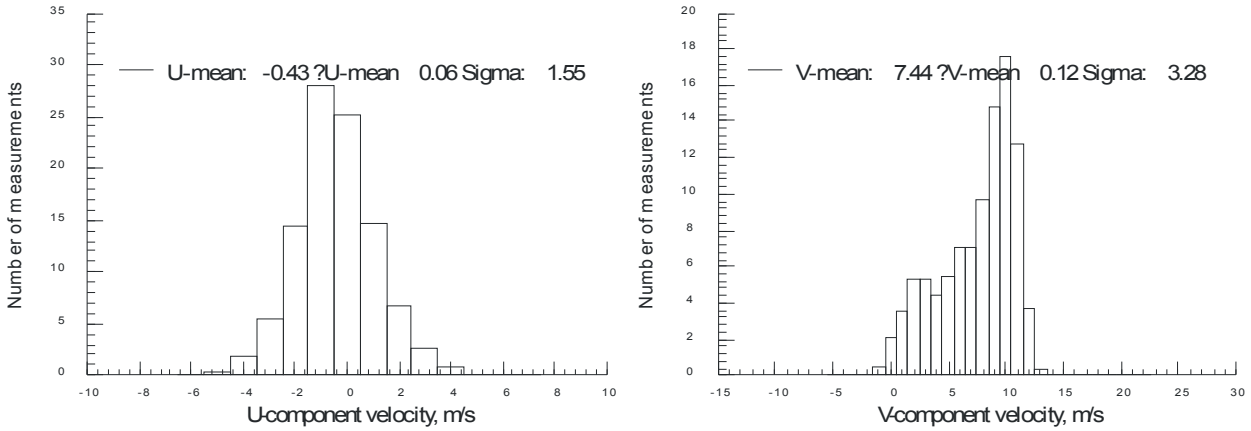

(i) Signal-to-noise ratio threshold = 5 (7 dB)

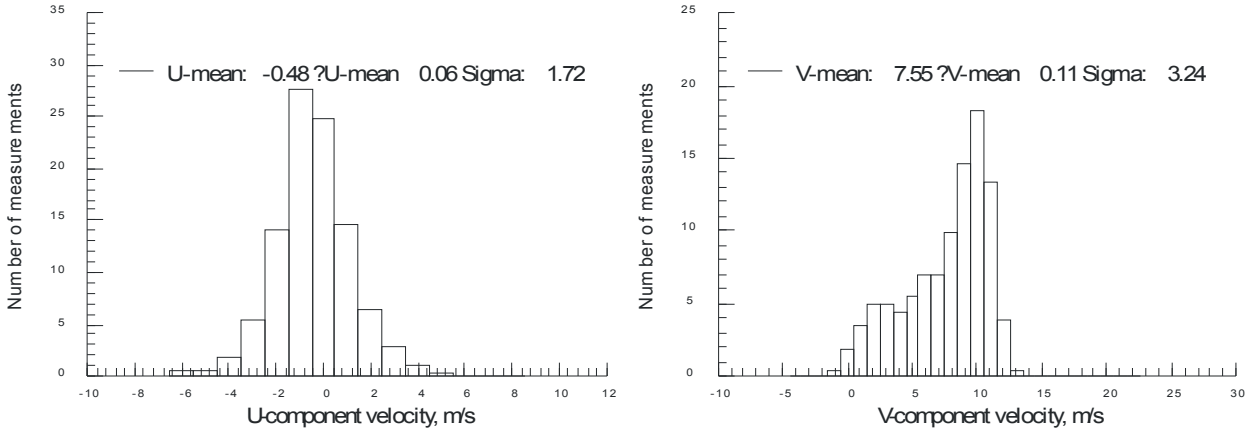

(ii) Signal-to-noise ratio threshold = 2.5 (5 dB)

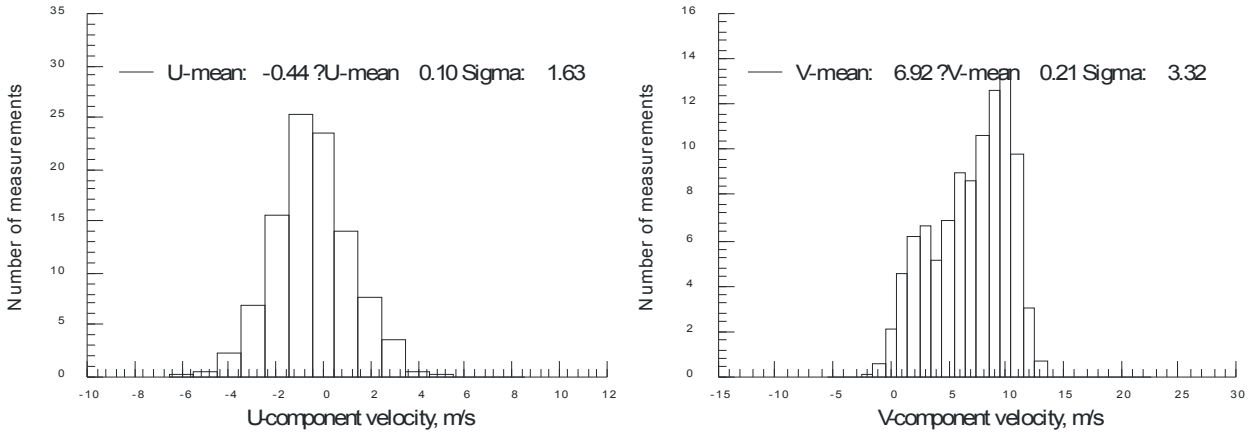

(iii) Signal-to-noise ratio threshold = 10 (10 dB)

Figure VII.39.c.(2)(a) - Velocity histograms obtained at 36-inch separation – Nanotube matrix sample, Focal distance = 228 inches.

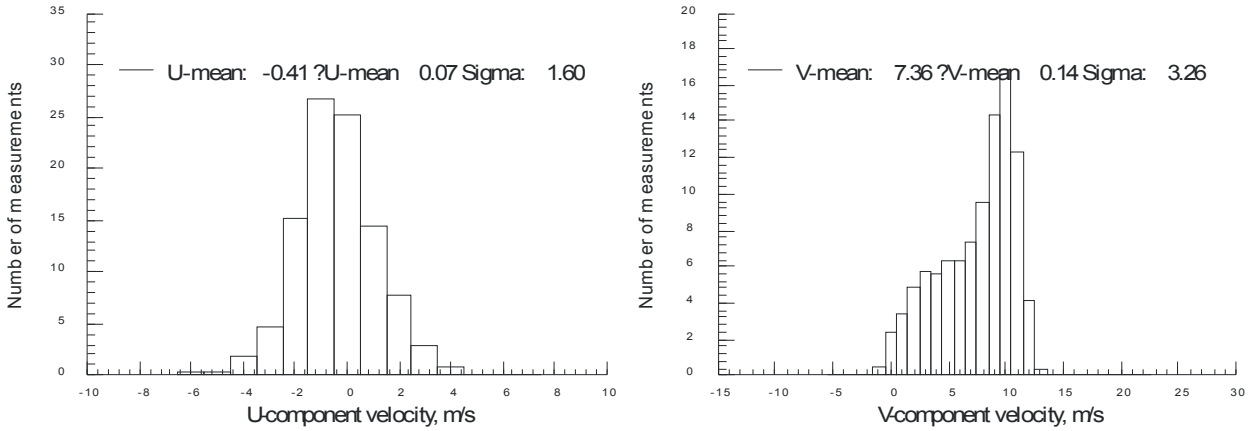

(i) Signal-to-noise ratio threshold = 5 (7 dB)

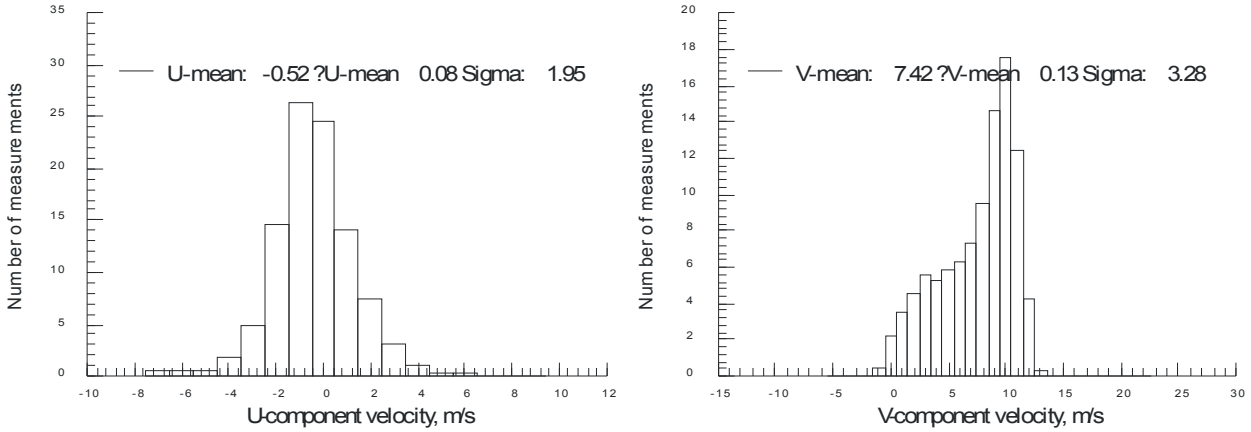

(ii) Signal-to-noise ratio threshold = 2.5 (5 dB)

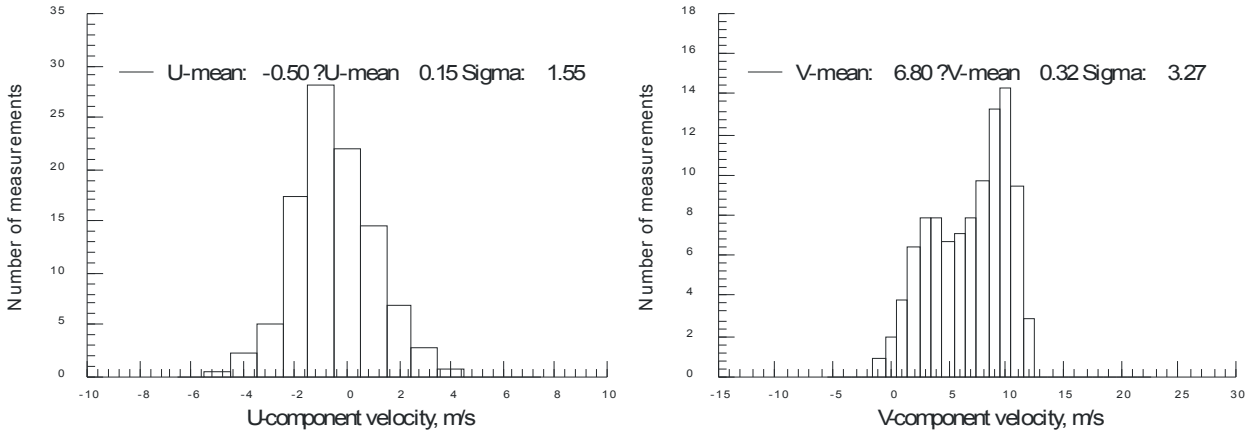

(iii) Signal-to-noise ratio threshold = 10 (10 dB)

Figure VII.39.c.(2)(b) - Velocity histograms obtained at first velocity/sigma deviation – Nanotube matrix sample, Focal distance = 228 inches.

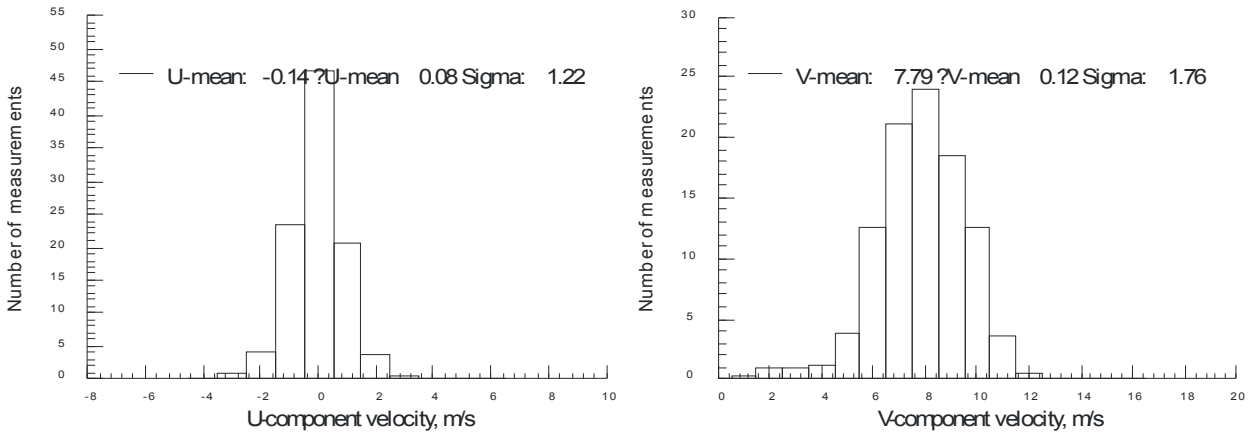

(i) Signal-to-noise ratio threshold = 5 (7 dB)

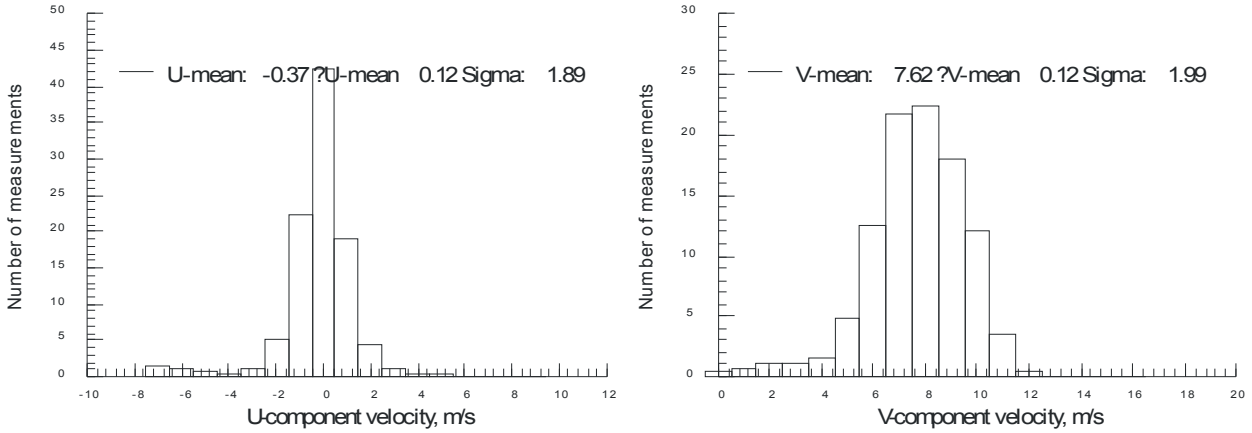

(ii) Signal-to-noise ratio threshold = 2.5 (5 dB)

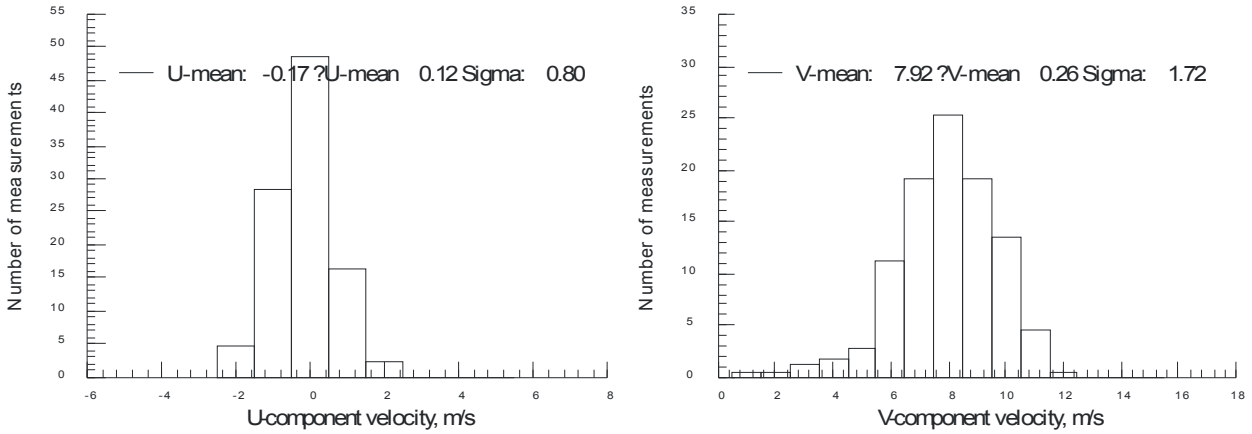

(iii) Signal-to-noise ratio threshold = 10 (10 dB)

Figure VII.39.c.(2)(c) - Velocity histograms obtained at closest approach – Nanotube matrix sample, Focal distance = 228 inches.

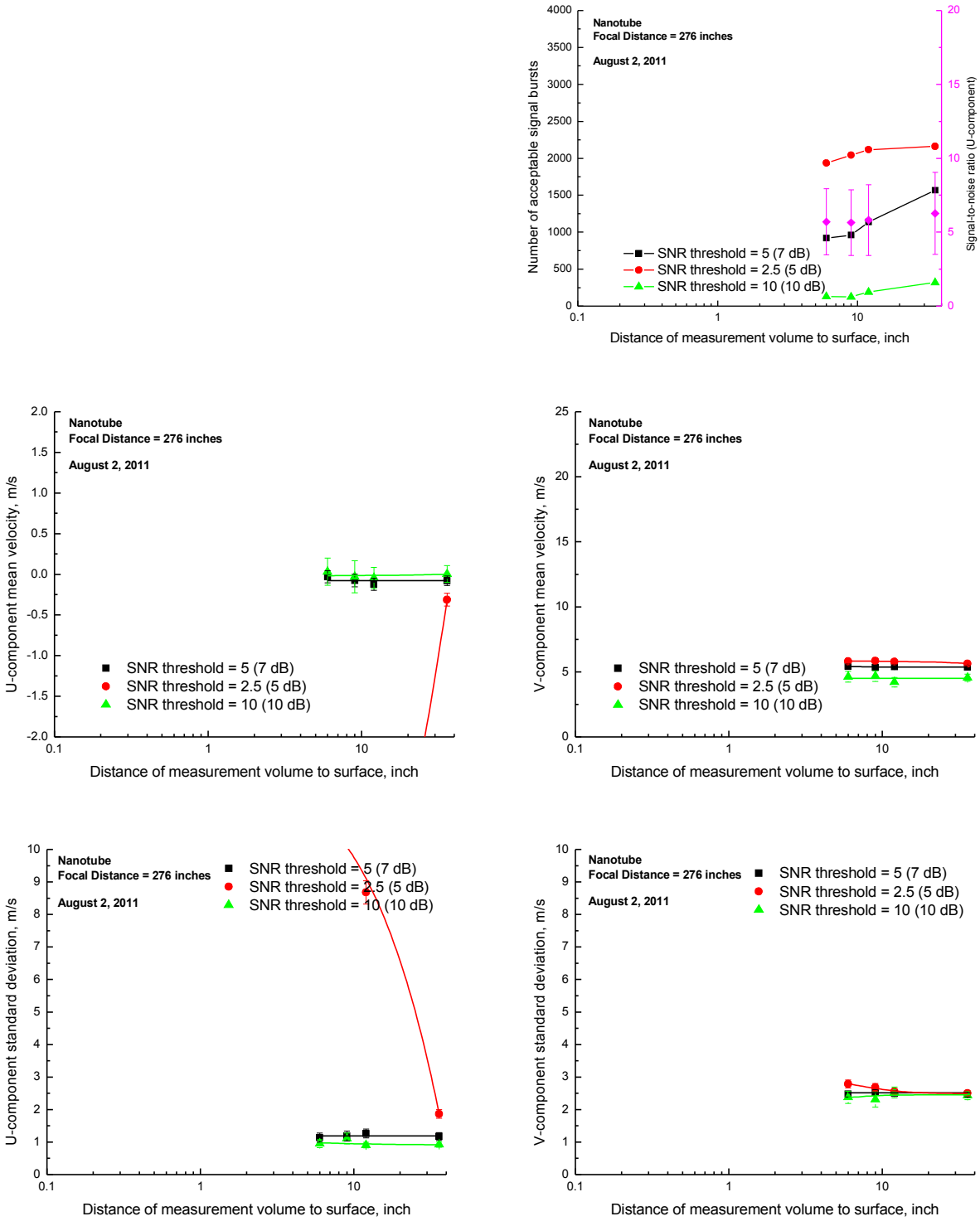

Figure VII.39.d.(1) - Velocity statistics as each surface is moved toward the measurement volume – Nanotube matrix sample, Focal distance = 276 inches.

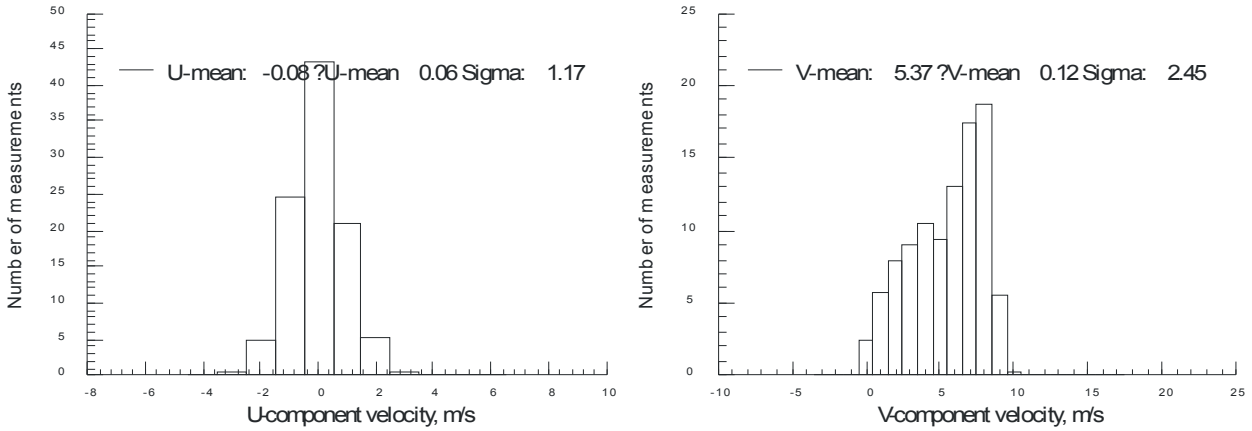

(i) Signal-to-noise ratio threshold = 5 (7 dB)

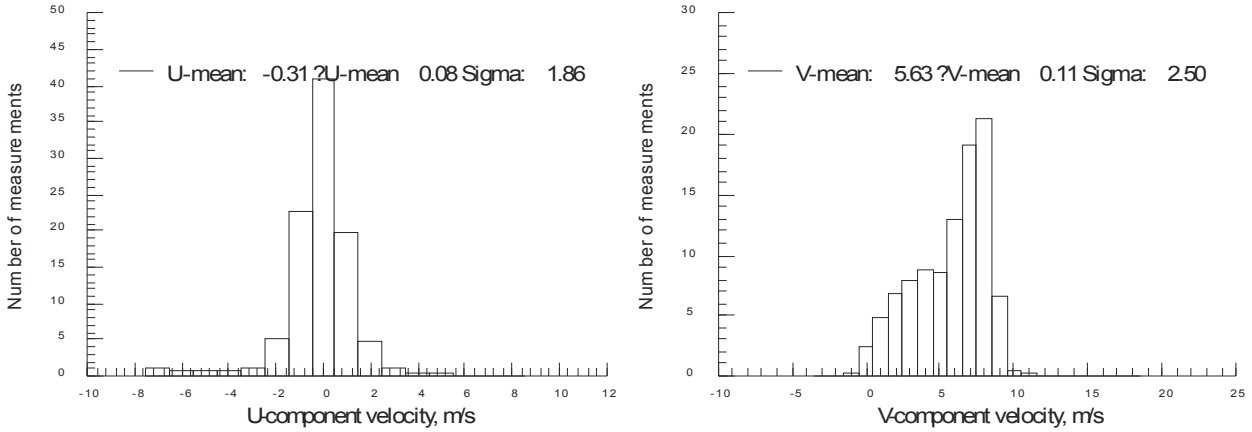

(ii) Signal-to-noise ratio threshold = 2.5 (5 dB)

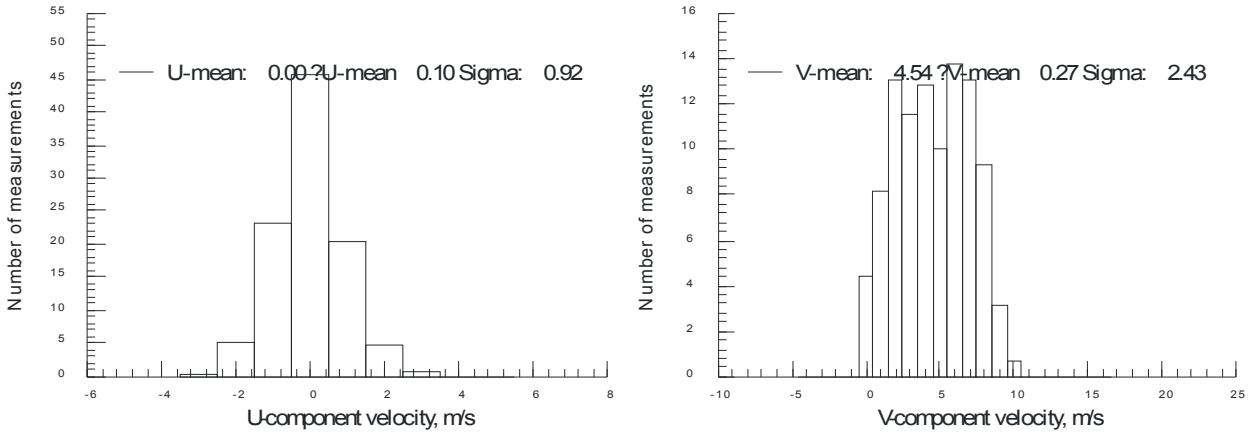

(iii) Signal-to-noise ratio threshold = 10 (10 dB)

Figure VII.39.d.(2)(a) - Velocity histograms obtained at 36-inch separation – Nanotube matrix sample, Focal distance = 276 inches.

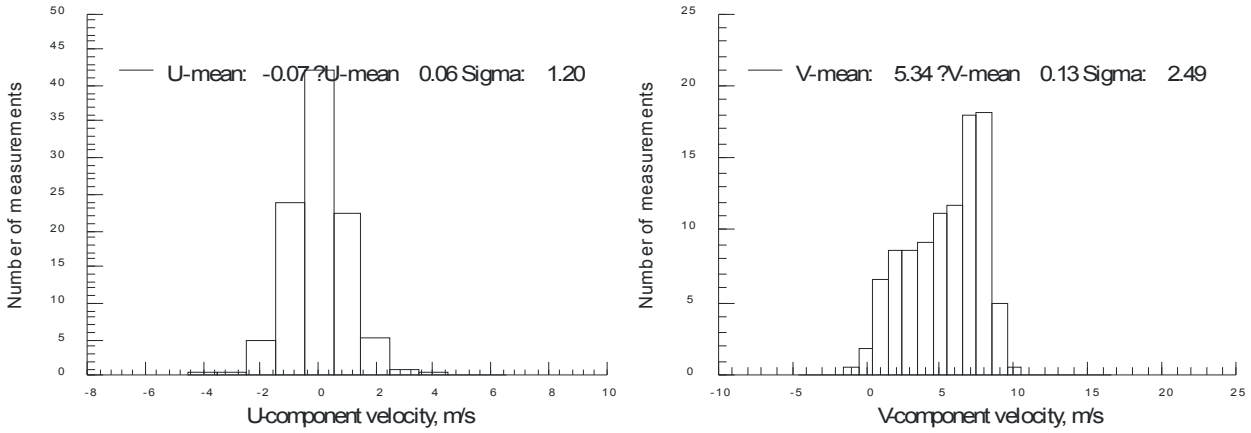

(i) Signal-to-noise ratio threshold = 5 (7 dB)

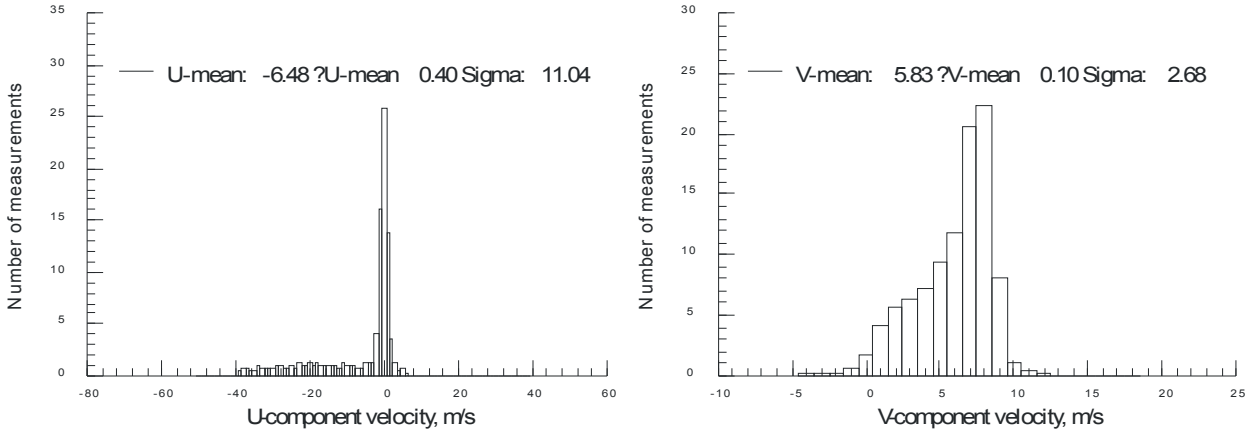

(ii) Signal-to-noise ratio threshold = 2.5 (5 dB)

Figure VII.39.d.(2)(b) - Velocity histograms obtained at first velocity/sigma deviation – Nanotube matrix sample, Focal distance = 276 inches.

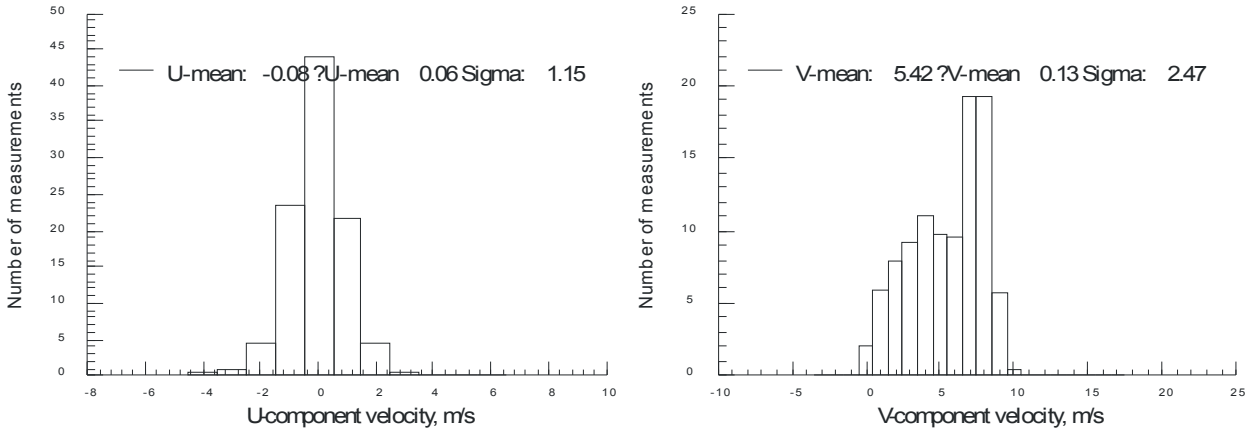

(i) Signal-to-noise ratio threshold = 5 (7 dB)

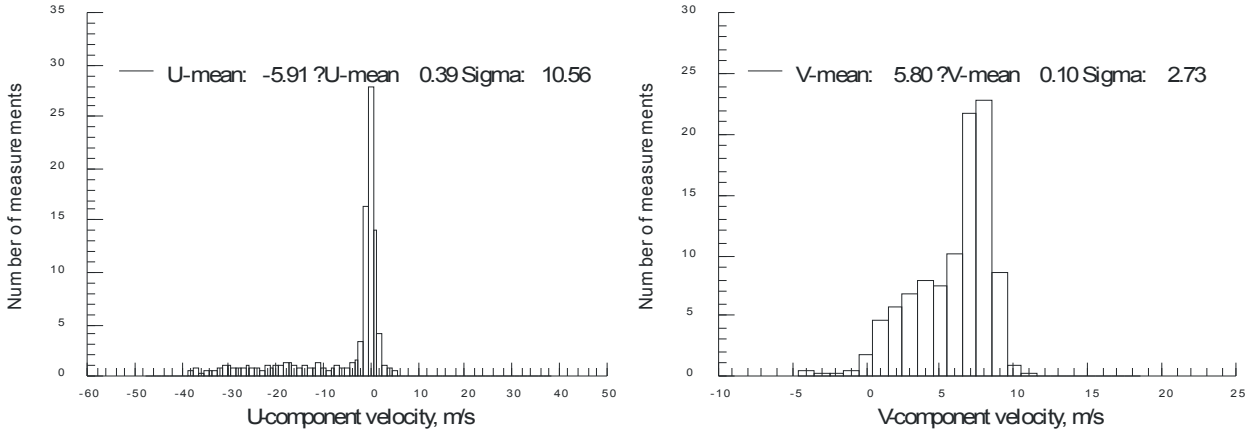

(ii) Signal-to-noise ratio threshold = 2.5 (5 dB)

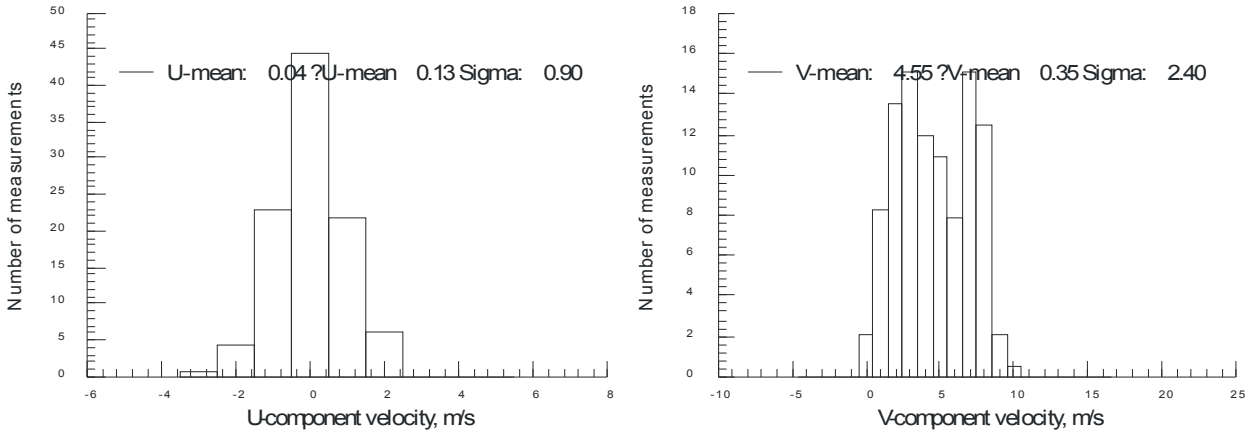

(iii) Signal-to-noise ratio threshold = 10 (10 dB)

Figure VII.39.d.(2)(c) - Velocity histograms obtained at closest approach – Nanotube matrix sample, Focal distance = 276 inches.

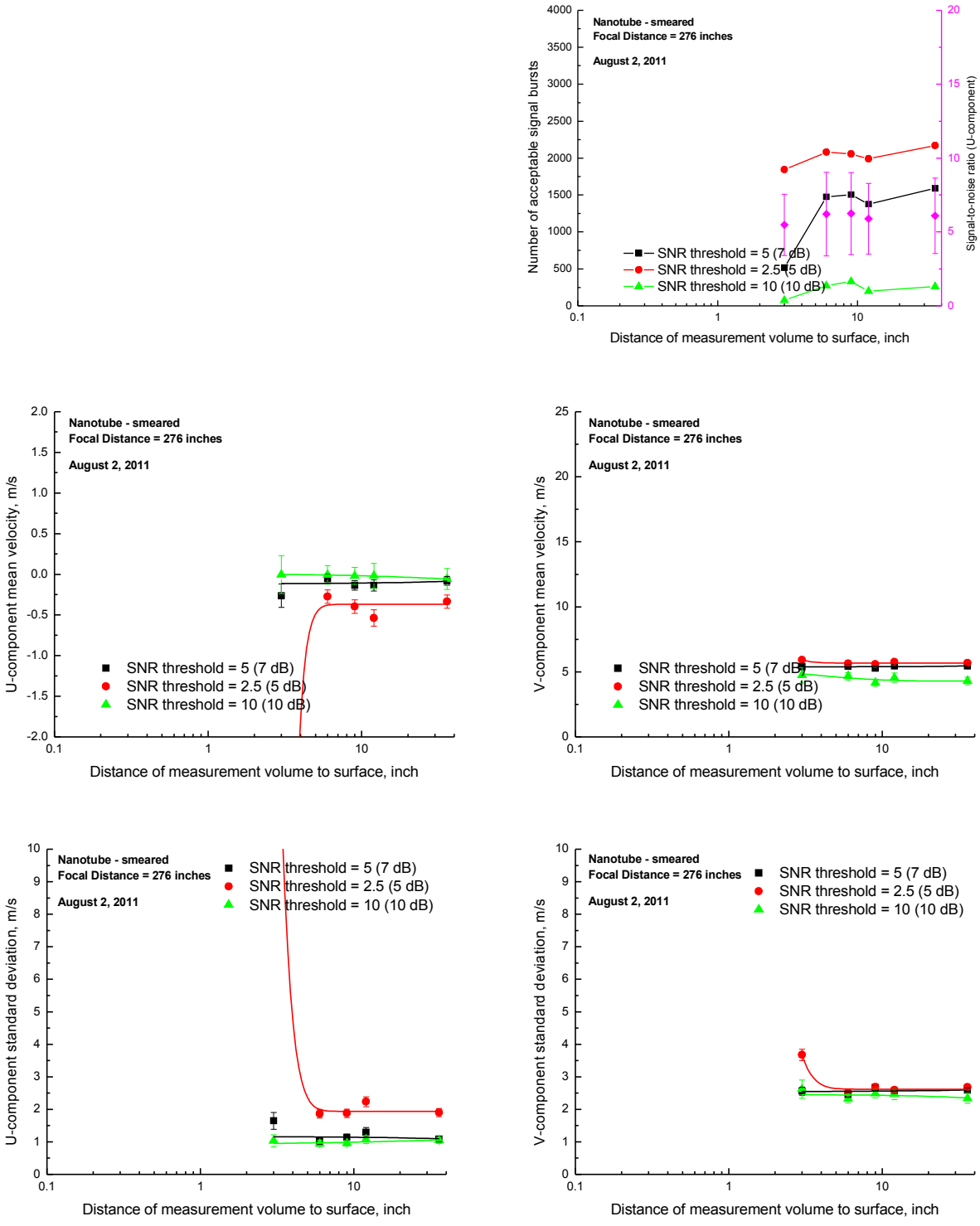

Figure VII.39.e.- Velocity statistics as each surface is moved toward the measurement volume – Nanotube matrix sample, Focal distance = 276 inches – damaged surface.

References

Adrian, R. J.; and Earley, W. L.: *Evaluation of LDV Performance Using Mie Scattering Theory*. Symposium on Laser Anemometry, University of Minnesota, October 22-24, 1975.

Albrecht, H. E.; Borys, M.; Damaschke, N.; and, Tropea, C.: **Laser Doppler and Phase Doppler Measurement Techniques**. Springer, Berlin, 2003.

Asher, J. A.: *LDV Systems Development and Testing*. The Use of the Laser Doppler Velocimeter for Flow Measurements, W. H. Stevenson andH. D. Thompson, eds., ContractN00014-67-A0226-055, Purdue Univ., pp. 338-347, Nov. 1972.

Baker, G. D.; Murphy, R. J.; and Meyers, J. F.: *Database for LDV Signal Processor Performance Analysis*. 13th International Congress on Instrumentation in Aerospace Simulation Facilities, Göttingen, West Germany, September 18-21, 1989.

Brayton, D. B.: *A Simple Laser, Doppler Shift, Velocity Meter with Self-Aligning Optics.* Presented at the Electro-Optical Systems Design Conference, New York, NY, September 16-18, 1969.

Brayton, D. B.; and Goethert, W. H.: *A New Dual Scatter, Laser, Doppler Shift Velocity Measuring Technique.* Instrumentation in the Aerospace Industry, Vol. 16, pp. 14-26, 1970.

Brayton, D. B.; Kalb, H. T.; and Crosswy, F. L.: *A Two- Component, Dual-Scatter Laser Doppler Velocimeter with Frequency Burst Signal Readout.* Presented at the Project Squid Workshop on The Use of the Laser Doppler Velocimeter for Flow Measurements, Purdue University, March 9-10, 1972.

Cavone, A. A.; Sterlina, P. S.; Clemmons, J. I., Jr.; and Meyers, J. F.: *A High-Speed Buffer for LV Data Acquisition*. Proceedings of the International Congress on Instrumentation in Aerospace Simulation Facilities, College of William and Mary, Williamsburg, VA, pp. 113-119, June 22-25, 1987.

Clemmons, J. I., Jr.: *Instrument for determining coincidence and elapse time between independent sources of random sequential events*. United States Patent 4,392,749, July 12, 1983.

Durst, F. and Whitelaw, J. H.: *Optimization of optical anemometers*. Proceedings of the Royal Society of London A, Vol. 324, pp. 157-181, 1971.

Dyott, R. B.: *The fibre-optic Doppler anemometer.* Microwaves, Optics and Acoustics, Vol. 2(1), pp. 13-18, January 1978.

Edwards, R. V.; and Meyers, J. F.: *An Overview of Particle Sampling Bias*. Proceedings of the Second International Symposium on Applications of Laser Anemometry to Fluid Mechanics, Lisbon, Portugal, paper 2.1, July 2-4, 1984.

Report of the Special Panel on Statistical Particle Bias Problems in Laser Anemometry. R. V. Edwards, ed., Journal of Fluid Engineering, Vol. 109, pp. 89-93, June, 1987.

Elliott, J. W.; Althoff, S. L.; and Sailey, R. H.: *Inflow Measurements Made With a Laser Velocimeter on a Helicopter Model in Forward Flight*. Volume III Rectangular Planform Blades at an Advance Ratio of 0.30. NASA TM-100543, 1988.

Foreman, J. W., Jr.; George, E. W.; and Lewis, R. D.: *Measurement of Localized Flow Velocities in Gases With a Laser Doppler Flowmeter*. Applied Physics Letters, Vol. 7, No. 4, pp. 77-78, Aug. 15, 1965.

Fridman, J. D.; Kinnard, K. F.; and Meister, K.: *Laser Doppler Instrumentation for the Measurement of Turbulence in Gas and Fluid Flows*. Electro-Optical Systems Design Conference, New York, NY, September 16-18, 1969.

Gartrell, L. R. and Jordan, F. J.: *Demonstration of a Rapid-ScanTwo-Dimensional Laser Velocimetry in the Langley Vortex Research Facility for Research in Aerial Application*. NASA TM-74081, August, 1977.

Goldstein, R. J.; and Kreid, D. K.: *Measurement of Laminar Flow Developed in a Square Duct Using a Laser Doppler Flowmeter*. Journal of Applied Mechanics, Item 34, Series E, No. 4, pp. 813-818, December 1967.

Grant, G. R.; and Orloff, K. L.: *Two-Color Dual-Beam Backscatter Laser Doppler Velocimeter*. Applied Optics, Vol. 12, No. 12, pp. 2913-2916, December 1973.

Griskey, R. G.; Balmer, R. T.; and Brinkley, J. L.: *An Automatic Scanning LDV System*. Minnesota Symposium on Laser Anemometry - Proceedings, E. R. G. Eckert, ed., Univ. of Minnesota, pp. 217-230, October 22-24, 1975.

Hart, R. C.; Balla, R. J.; Herring, G. C.; and Jenkins, L. N.: *Seedless Laser Velocimetry Using Heterodyne Laser-induced Thermal Acoustics*. Institute for Computer Applications in Science and Engineering, NASA/CR-2001-211021, 2001.

Hepner, T. E.: *State-of-the-art laser Doppler velocimeter signal processors calibration and evaluation*. 32nd Aerospace Sciences Meeting and Exhibit, Reno, NV, paper AIAA-1994-42, January 10-13, 1994.

Hoad, D. R.; Elliott, J. W.; and Althoff, S. L.: *Rotor Inflow Variability with Advance Ratio*. 44th Annual Forum of the American Helicopter Society, Washington, DC, 1988.

Hoad, D. R.; Meyers, J. F.; Young, W. H., Jr.; and Hepner, T. E.: *Laser Velocimeter Survey About a NACA 0012 Wing at Low Angles of Attack*. TM-74040, January 1978.

Hoad, D. R.; Meyers, J. F.; Young, W. H., Jr.; and Hepner, T. E.: *Correlation of Laser Velocimeter Measurements Over a Wing with Results of Two Prediction Techniques*. TP-1168, April 1978.

Hoad, D. R.; Meyers, J. F.; and Young, W. H., Jr.: *Velocity Measurements about a NACA 00l2 Airfoil with Laser Velocimeter.* Army Science Conference, West Point, NY, June 1978.

Hoad, D. R., Rhodes, D. B., and Meyers, J. F.: *Preliminary Rotor Wake Measurements with a Laser Velocimeter.* NASA TM 83246, 1983 .

Huffaker, R. M.; Fuller, C. E.; and Lawrence, T. R.: *Application of Laser Doppler Velocity Instrumentation to the Measurement of Jet Turbulence.* International Automotive Engineering Congress, Detroit, MI, January 13-17, 1969.

Huffaker, R. M.; Fuller, C. E.; and Lawrence, T. R.: *Application of Laser Doppler Velocity Instrumentation to the Measurement of Jet Turbulence*. Paper 690266, Soc. Automotive Engineers, January, 1969.

Huffaker, R.M.: *Laser Doppler Detection Systems for Gas Velocity Measurement.* Applied Optics, Vol. 9, No. 5, pp. 1026-1039, May 1970.

Iten, P. D.; and Mastner, J.: *Laser Doppler Velocimeter Offering High Spatial and Temporal Resolution*. Flow – Its Measurement and Control in Science and Industry, Volume One, Part Two, R. E. Wendt, Jr., ed., Instrument Soc. of America, pp. 1007-1013, 1974.

Junge, C.: *The Size Distribution and Aging of Natural Aerosols as Determined from Electrical and Optical Data on the Atmosphere*. AMS Journal, Vol. 12, Iss. 1, February 1955.

Knuhtsen, J.; Olldag, E.; and, Buchhave, P.: *Fibre-optic laser Doppler anemometer with Bragg frequency shift utilising polarisation-preserving single-mode fibre*. Journal of Physics E: Scientific Instruments, Vol. 15, pp. 1188-1191, 1982.

Lehmann, B.: *Geschwindigkeitsmessung mit Laser-Doppler-Anemometer Verfahren.* Wissenschaftliche Berichte AERG-Telefunken 41, 141-145, 1968. (in German)

Lennert, A. E.; Brayton, D. B.; Goethert, W. H.; and Smith, F. H.: *Laser Applications for Flow Field Diagnostics*. Laser J., vol. 2, no. 2, pp. 19-27, Mar/Apr. 1970.

Lennert, A. E.; Brayton, E. B.; Crosswy, F. L.; *et al*.: *Summary Report of the Development of a Laser Velocimeter To Be Used in AEDC Wind Tunnels*. AEDC-TR-70-101,U. S. Air Force, July 1970.

Lennert, A. E.; Smith, F. H., Jr.; and Kalb, H. T.: *Application of Dual Scatter Laser Doppler Velocimeters for Wind Tunnel Measurements.* 4th International Congress on Instrumentation in Aerospace Simulation Facilities, von Karman Institute for Fluid Dynamics, June 21-23, 1971.

Mazumder, M. K.: *Laser Doppler Velocity Measurement Without Directional Ambiguity by Using Frequency Shifted Incident Beams*. Applied Physics Letters, Vol. 16(11), pp. 462-464, June 1, 1970.

Mayo, W. T., Jr.: *Modeling Laser Velocimeter Signals as Triply Stochastic Poisson Processes*. Symposium on Laser Anemometry, University of Minnesota, October 22-24, 1975.

Meyers, J. F.: *Investigation and Calculations of Basic Parameters for the Application of the Laser Doppler Velocimeter.* TN D-6125, April 1971.

Meyers, J. F.: *Applications of Laser Velocimetry to Large Scale and Specialized Aerodynamic Tests*. TSI Quarterly, Vol. V, Issue 4, pp. 5- 12, November/December 1979.

Meyers, J. F.: *Analysis of the Dedicated Laser Velocimeter Systems at NASA - Langley Research Center.* Proceedings of the Fourth International Symposium on Applications of Laser Anemometry to Fluid Mechanics, Lisbon, Portugal, paper 12.4, July 11-14, 1988.

Meyers, J. F.: *Generation of Particles and Seeding*. von Karman Institute for Fluid Dynamics, Lecture series 1991-08, Laser Velocimetry, Brussels, Belgium, June 10-14, 1991.

Meyers, J. F.: *Biasing Errors and Corrections*. Von Karman Institute for Fluid Dynamics, Lecture series 1991-08, Laser Velocimetry, Brussels, Belgium, June 10-14, 1991.

Meyers, J. F. and Clemmons, J. I., Jr.: *Processing Laser Velocimetry High- Speed Burst Counter Data*. Proceedings of the Third International Workshop on Laser Velocimetry, Purdue University, pp 300-313, July 1978.

Meyers, J. F.; and Clemmons, J. I., Jr.: *Frequency Domain Laser Velocimeter Signal Processor - A New Signal Processing Scheme.* NASA TP-2735, September 1987.

Meyers, J. F.; Clemmons, J. I., Jr.; Stoughton, J. W.; Kanetkar, S. V.; and Savakis, A. E.: *Frequency Domain Laser Velocimeter Signal Processor.* United States Patent 4,786,168, November 22, 1988.

Meyers, J. F.; Couch, L. M.; Feller, W. V.; and Walsh, M. J.: *Laser Velocimeter Measurements in a Large Transonic Wind Tunnel*. Proceedings of the Minnesota Symposium on Laser Anemometry, University of Minnesota, pp. 83-111, October 22-24, 1975.

Meyers, J. F.; and Hepner, T. E.: Velocity Vector Analysis in a Juncture Flow Using a Three Component Laser Velocimeter. The Second International Symposium on Applications of Laser Anemometry to Fluid Mechanics, Lisbon, Portugal, July 2-4, 1984.

Meyers, J. F.; and Hepner, T. E.: *Measurement of Leading Edge Vortices from a Delta Wing Using a Three Component Laser Velocimeter.* AIAA 15th Aerodynamic Testing Conference, San Diego, CA, paper AIAA-88-2024, May 18-20, 1988.

Meyers, J. F. and Hoad, D. R.: *Laser Velocimeter Measurements in the Wake Region Behind a NACA 0012 Wing*. AIAA 14th Thermophysics Conference, Orlando, FL, paper AIAA-79-1087, Orlando, Florida, June 4-6, 1979.

Meyers, J. F.; Kjelgaard, S. O.; and Hepner, T. E.: *Investigation of Particle Sampling Bias in the Shear Flow Field Downstream of a Backward Facing Step*. Proceedings of the Fifth International Symposium on Applications of Laser Anemometry to Fluid Mechanics, Lisbon, Portugal, paper 29.1, July 9-12, 1990.

Meyers, J. F.; and Murphy, R. J.: *Frequency Domain Laser Velocimeter Signal Processor.* Technology 2000, NASA, Washington, DC, November 27-28, 1990.

Meyers, J. F.; and Stoughton, J. W.: *Frequency Domain Laser Velocimeter Signal Processor.* **Laser Anemometry in Fluid Mechanics III - Selected Papers from the Third International Symposium on Applications of Laser Anemometry to Fluid Mechanics**, editors: R. J. Adrian, D. F. G. Durao, F. Durst, H. Mishina and J. H. Whitelaw, LaDoan-Instituto Superior Tecnico, Lisbon, Portugal, pp. 83-102, 1988.

Meyers, J. F.; Usry, J. W.; and Miller, L. S.: Assessing the Capabilities of Doppler Global Velocimetry to Measure Vortical Flow Fields. Journal of Aerospace Engineering, part G, vol 208, pp. 99-105, December 1994.

Meyers, J. F.; and Walsh, M. J.: *Computer Simulation of a Fringe Type Laser Velocimeter.* Proceedings of the Project Squid Workshop on the Use of the Laser Velocimeter for Flow Measurements, Purdue University, pp. 471-509, March 27-29, 1974.

Meyers, J. F.; and Wilkinson, S. P.: *A Comparison of Turbulence Intensity Measurements Using A Laser Velocimeter and A Hot Wire In A Low Speed Jet Flow*. Proceedings of the International Symposium on Applications of Laser- Doppler Anemometry to Fluid Mechanics, Lisbon, Portugal, paper 17.4, July 5-7, 1982.

Mie, G.: *Optics of Turbid Media*. Ann. Phys., vol. 25, no. 3, pp. 377-445, 1908.

Nichols, C.E., Jr.: *Preparation of Polystyrene Microspheres for Laser Velocimetry in Wind Tunnels*. NASA TM-89163, June 1987.

Pike, E. R.: *The Application of Photon-Correlation Spectroscopy to Laser Doppler Velocimetry*. The Use of the Laser Doppler Velocimeter for Flow Measurements, W. H. Stevenson and H. D. Thompson, eds., Contract N00014-67-A0226-055, Purdue Univ., pp. 338-347, Nov. 1972.

Pike, E. R.: *The application of photon correlation spectroscopy to laser Doppler measurements*. Journal of Physics D: Applied Physics, Vol. 5, pp. L23-L25, 1972.

Rudd, M. J.: *A Self Aligning Laser Doppler Velocimeter.* ICO-8, Optical Instruments and Techniques, Oriel Press, 58-166, 1969.

Rhodes, D. B.: *Optical Scanning System for Laser Velocimeter.* SPIE vol. 84, Laser Scanning Components & Techniques, 1976.

Rudd, M. J.: *A New Theoretical Model for the Laser Dopplermeter.* Journal of Scientific Instruments, pp. 55-58, Series 2, Vol. 2, 1969.

Sasaki, O.; Sato, T.; Abe, T.; Mizuguchi, T.; and, Niwayama, M.: *Follow-up-type laser Doppler velocimeter using single-mode optical fibers*. Applied Optics, Vol. 19(8), pp. 1306-1308, April 15, 1980.

Tropea, C.: *Laser Doppler Technique.* **Springer Handbook of Experimental Fluid Mechanics**, Tropea, C.; Yarin, A. L.; and Foss, J. F. (Eds.), Springer, Berlin, chap. 5.3.2., pp. 296-309, 2007.

vom Stein, H. D. and Pfeifer, H. J.: *A Doppler difference method for velocity measurements.* Metrologia 5, 59-61, 1969.

vom Stein, H. D. and Pfeifer, H. J.: An Automatic Data Processing System for Laser Anemometers. The Use of the Laser Doppler Velocimeter for Flow Measurements, W. H. Stevenson andH. D. Thompson, eds., ContractN00014-67-A0226-055, Purdue Univ., pp. 123-132, Nov. 1972.

Young, W. H., Jr.; Meyers, J. F.; and Hepner, T. E.: *A Laser Velocimeter Survey Above a Stalled Wing*. TN D-8408, August 1977.

Yule, G. U.; and Kendall,M. G.: **An Introduction to the Theory of Statistics**. Charles Griffin & Co., Ltd., 1940.

Yeh, Y.; and Cummins, H. Z.: *Localized Fluid Flow Measurements with an He-Ne Laser Spectrometer.* Applied Physics Letters,Vol. 4, pp. 176-178, May 1964.

Young, W. H., Jr.; Meyers, J. F.; and Hoad, D. R.: *Laser Velocimeter Data Interpretation by Histogram and Spectral Analysis*. USACDEC 23rd Conference on the Design of Experiments in Army Research, Development and Testing, Monterey, CA, October 1977.

Young, W. H., Jr.; Meyers, J. F.; and Hoad, D. R.: *A Laser Velocimeter Flow Survey Above a Stalled Wing*. NASA TP-1266, December 1978.

Appendix A
Monte Carlo Simulation of a Laser Velocimeter

The determination of the measurement accuracy for any instrumentation system, including laser velocimetry, requires knowing the actual value being measured. In the real world this is accomplished by comparing one instrument against another – supposedly a trusted measurement, but is it really accurate? This was the question laser velocimetry researchers were asked in the early days. Do you obtain the same mean velocity measurements as a Pitot probe? Then, how did your turbulence measurement compare with hot wire? The counter response was typically, *And how do you know the Pitot probe (or hot wire) measurements were accurate?* No one really knows. In the early days it was not readily accepted that light could be used to measure flow velocities better than the standard time-tested techniques. It seemed to be a no win situation because: 1) if the laser measurements matched the Pitot tube and hot wire results, then why invest in this new technology?, and 2) If it did not match, then what? Recognizing this *Catch 22*, Meyers and Walsh (1974) undertook a different tack: Could the laser velocimeter be theoretically evaluated? And further, could a particle be tracked through a flow field to determine its ability to follow that flow with fidelity? This early work was based on several poor assumptions and a lack of understanding of the physics involved in laser velocimetry. Two major breakthroughs occurred at the 1975 Minnesota Symposium on Laser Anemometry that provided the insight needed. Ron Adrian (Adrian and Earley (1975)) presented the description of the interferometric interactions of two light waves scattered by a particle passing through a laser velocimeter measurement volume. The interaction of the two Mie scattering wavefronts was far more complicated than most realized. Then Bill Mayo (Mayo (1975)) described the entire process of laser velocimetry as a series of random events. A particle arrives at the measurement volume at a random time (Poisson) with a random velocity trajectory (turbulence) and scatters light in the form of photons which arrive at the photomultiplier at random times (Poisson). These two revelations required a major rewrite to the laser velocimeter simulation program to include real interference effects in the scattered light, and the use of Monte Carlo techniques to introduce randomness in the process. Later versions of the simulation program were used in the development of an entirely new signal processor that ultimately displaced the high-speed burst counter as the state-of-the-art laser velocimeter signal processor (Meyers and Clemmons (1987), Meyers *et al* (1988), Meyers and Murphy (1990)).

The Monte Carlo Technique

The Monte Carlo technique is based on the use of random number generators to model some physical phenomenon. The objective is to make use of known physical traits, apply the appropriate random number generator and view the result statistically – much the same way real measurements are made and analyzed. Although this approach is not widely used, it is quite simple in its implementation. It provides a great deal of realism to

the simulation without the assumptions required by most analytical approximations or simulations (or as Meyers did in 1971 – through 1975).

In order to visualize how a Monte Carlo simulation is performed, consider light illuminating the photo-cathode surface of a photomultiplier and its subsequent generation of electric current. The analytic approach would be to determine the power of the light striking the photo-cathode in Watts, multiply by the quantum efficiency, multiply by the gain of the dynode chain, low-pass filter by the bandwidth of the photomultiplier, and the current trace is generated. But wait, there is no noise on the signal leaving the photomultiplier. Just add random Gaussian white noise and a realistic signal is generated. Well almost, seems that the signal contains negative current part of the time – not possible from a photomultiplier.

In the Monte Carlo approach each process is analyzed and modeled, and moving from one small model to the next to the next a signal appears that virtually matches the photomultiplier output seen on an oscilloscope. To begin, when light interacts with a photomultiplier it does not act as a wave, but a series of photons. In this example the light has a constant amplitude of X Watts. In the photon model, x Watts most likely is not a continuum (especially if it is scattered light from a particle) as assumed above, but a train of photons arriving at the photomultiplier with interarrival times that obey Poisson statistics. The average interarrival time is determined by the light power, x Watts, then a Poisson random number generator, based on this interarrival time, is used to determine the arrival time of each photon. Thus a binary train of pulses would be impacting the photo-cathode surface of the photomultiplier. With the binary train defined, how many of these photons actually become photo-electrons?

With the completion of the first model, the photon arrival times, the second model begins. Instead of multiplying the light power by the quantum efficiency (can't multiply a photon train anyway), think of quantum efficiency as a threshold in the range from 0 to 1. Assume the quantum efficiency is 20-percent, so on average 1 photon in five would become a photo-electron, but which one? The answer is provided by using a uniform random number generator to pick a number between 0 and 1 each time a photon arrives. If the random number is 0.2 or less, the photon becomes a photo-electron. The train of photo-electrons, which is now sparser than the photon train, still obeys the random statistics found in the real world.

The third model is actually not a random process, but does rely on the randomness of the train of photo-electrons to yield the signal. The process of converting the photon to a photo-electron requires a bit of time, nominally 5 nsec for an average photomultiplier. This could be approximated by a triangle to model the impulse response of the photomultiplier. If a second photon arrives during the same time as the first, its 5 nsec triangle is just added to the first, only delayed by the difference in the arrival times. This process is referred to as photon pile-up (Mayo (1975)).

The next and final stage of this simulation is the passage of the signal through the dynode chain. Instead of just multiplying the now filtered photo-electron signal by the gain, the signal is amplified by each dynode with a mean and standard deviation attributed to the availability of electrons being present on the dynode. The multiplication factor is not constant, but an average gain with a standard deviation that can be simulated with a Gaussian random number generator operating on the signal in time. Thus the signal exiting the photomultiplier model is all positive and exhibits the noisy characteristics that can be found in the real world. Figure A.1 was a capture of two particles passing through the laser velocimeter measurement volume – the first passed near the center which exhibits the classic signature, while the second, which passed through the edge, was photon resolved. As a comparison consider a simulation of these two particles using Monte Carlo techniques, Figure A.2.

Over time the simulation has become more sophisticated in its continued development since the original Monte Carlo simulation in 1975 (See Figure 4 in Mayo (1975)). Although its development was completed in the mid 1980's, its selection to aid in the development of upgrades to the 14- by 22-Foot Laser Velocimeter, and advances in computer technology provided the stimulus to overhaul the code. The development of a graphical user interface, simulation of two measurement components, replacement of high-speed burst counter processing with signal capture / frequency domain processing, and signal display capabilities increased the utility of the code while keeping the fundamental processes of the original code. Additionally models for the air flow and particle size distributions were strengthened for increased capability. Remember, even with this increased sophistication, Monte Carlo simulation techniques are inherently simple – just breakdown a process into its smallest pieces which can then be modeled without assumptions. By taking a signal from one process to the next, to the next, etc., the real effects a device has on the physics are imposed on the signal. That is why many of the error sources found in laser velocimetry research were also present in the simulation results.

The current Monte Carlo simulation had three purposes during the development of the upgrades for the 14- by 22-Foot Subsonic Tunnel laser velocimeter: 1) determine if the upgraded optical system would yield signals sufficient in strength to measure; 2) provide signals that would serve as benchmarks in the development of an accurate signal processing algorithm; and, 3) provide signals that would drive an arbitrary waveform generator to test and evaluate the upgraded data acquisition/signal processing hardware/software. To help expedite the development of the signal processing algorithm, the processing program was appended to the simulator, with the key algorithm under test added as a subroutine with a common call statement. The simulator was written using Intel Fortran 90, with graphics routines from the GrWin graphics library by Tsuguhiro Tamaribuchi, (http://spdg1.sci.shizuoka.ac.jp/grwinlib/english/). The following is an explanation of the data entry screens for the program.

Simulation Program Data Entry Screens

When the program is started the user will be presented with a series of screens for the entry of the physical characteristics of the laser velocimeter, seeding particles, the test flow, and several program output parameter settings. The program will present the settings from the previous execution, unless this is the first execution on a given computer when a default set of parameters is loaded. Once all the parameters have been set, they will be stored in the program's initialization file to be presented at the next execution of the program. (This program was developed by James F. Meyers while serving as a Distinguished Research Associate at the NASA – Langley Research Center and was copyrighted in 2008. Under the DRA agreement, this program is available for use by NASA – Langley Research Center at no cost.) An overview is given in Chapter III.

Screen 1: Figure A.3. - Laser Velocimeter Simulation

LV Sim INI file: Program start-up file. If a file other than that presented is desired, click on the gray box and a file manager will be presented where the file may be selected. If a new file is to be built, click on the gray box next to **New INI file?**, and then click on the long gray box and the full path and file name can be entered. This new file will be created and the program parameter settings will be stored in it.

Click **Next** when ready to continue, **Exit** to terminate the program.

Screen 2: Figure A.4. - LV Simulation – Transmitter

Laser Wavelenth, μm: (λ_U and λ_V) Click on the box below U-component and V-component and enter the laser wavelength in micrometers for each component.

Laser Power, W: (P_U and P_V) Click on the appropriate box and enter the laser power in Watts, available to each component. This is a carryover from the classic system when a prism was used to separate the laser wavelengths before the splitting optics and the laser power in each color could be measured. With the current system the beam powers leaving the final lens should be measured and the component beam powers added with the results inserted here.

Bragg Frequency, MHz: ($FBragg_U$ and $FBragg_V$) Click on the appropriate box and enter the Bragg cell drive frequency for each component in MegaHertz.

Beam 1 Location (X,Y), m: ($B1X_U$, $B1Y_U$, $B1X_V$, and $B1Y_V$) Click on the appropriate box and enter the X and Y locations of a laser beam at the final lens. The position X = 0, Y = 0 is the center of the lens (optical axis), and X (horizontal) and Y (vertical) are measured looking out from the lens toward the measurement volume in meters.

Beam 2 Location (X,Y), m: ($B2X_U$, $B2Y_U$, $B2X_V$, and $B2Y_V$) Click on the appropriate box and enter the X and Y locations of the other laser beam at the final lens. NOTE: The order of the two beams is immaterial. The position X = 0, Y = 0 is the center of the lens (optical axis), and X (horizontal) and Y (vertical) are measured looking out from the lens toward the measurement volume in meters.

Transmission (Beam 1,2): ($T1_U$, $T2_U$, $T1_V$, and $T2_V$) Click on the appropriate box and enter the decimal fraction of the total power exiting each beam. Measure the output power of each beam comprising a component and determine the fraction of the total power contained within the input beam for that component. Since the output beams are measured in the current system, the fraction would be the power in that beam divided by the sum of both beams.

Polarization (Beam 1,2), degrees: ($\phi 1_U$, $\phi 2_U$, $\phi 1_V$, and $\phi 2_V$) Click on the appropriate box and enter the polarization of each beam. Vertical polarization is 90.0 degrees and horizontal polarization is 0.0. The polarization for each beam should be measured as these parameters are critical in the Mie scattering calculations and the resulting interference at the photomultiplier.

Laser Beam Diameter, m: (d) Click on the appropriate box and enter the diameter of the laser beam at the final lens in meters. It is assumed that all four beams have the same diameter.

Focal Distance, m: (F_T) Click on the appropriate box and enter the distance from the final lens to the measurement volume in meters.

It is assumed that the laser beams are parallel entering the final lens, and that each laser beam is collimated. Thus the beams would cross at the focal length of each beam, i.e., the fringes are parallel. The diameter of the beam focus is assumed to be diffraction limited. It is further assumed that there are no chromatic aberrations in the optics so that both component measurement volumes are at the same location in space.

Click **Next** when ready to continue, **Exit** to terminate the program.

Screen 3: Figure A.5. - LV Simulation – Receiver

Focal Distance, m: (F_R) Click on the appropriate box and enter the distance from the measurement volume to the collecting lens in meters. This would be the same distance as the transmitter focal length for a coaxial backscatter configuration.

Alpha View, deg: (α_R) Click on the appropriate box and enter the vertical angle of the collecting lens above/below the transmitter optical axis in degrees. A coaxial backscatter configuration would have a vertical angle of zero degrees.

Theta View, deg: (θ_R) Click on the appropriate box and enter the horizontal angle of the collecting lens about the transmitter optical axis in degrees. A coaxial backscatter configuration would have a horizontal angle of 180 degrees.

Effective Lens Diameter, m: (d_R) Click on the appropriate box and enter the effective diameter of the collecting lens in meters. The effective diameter is the diameter at the collected lens of the scattered light cone that passes through all lenses, apertures, etc. in the receiver and reaches the photomultiplier.

Sample Rate, MHz (0 = Auto) Click on the appropriate box and enter the sampling rate of the high-speed digitizer in Mega Hertz. Entering a 0 will automatically set the sampling rate to obtain 10 samples per cycle of the Doppler signal based on the Bragg shift input parameter.

Transmission (receiver efficiency): (TR_U and TR_V) Click on the appropriate box and enter the transmission fraction of the receiver optical system for that component. Fraction of the collected scattered light reaching the photomultiplier for the U- and V-component, respectively.

PMT Quantum Efficiency: (η) Click on the appropriate box and enter the photomultiplier quantum efficiency as a decimal fraction.

PMT Gain, M: (G) Click on the appropriate box and enter the photomultiplier gain in millions.

System Gain, dB: (G_S) Click on the appropriate box and enter any extra electronic system gain by amplifiers following the photomultiplier in decibels.

High Pass Filter, MHz: (HPF_U and HPF_V) Click on the appropriate box and enter the high pass filter break point frequency in Mega Hertz. A high pass filter is used primarily to remove the pedestal from the signal burst.

Low Pass Filter, MHz: (LPF_U and LPF_V) Click on the appropriate box and enter the low pass filter break point frequency in Mega Hertz. A low pass filter is used primarily to remove the high frequency noise associated with photon pile-up and the Gaussian noise found in the dynode chain amplification process.

Click **Next** when ready to continue, **Exit** to terminate the program.

Screen 4: Figure A.6. - LV Simulation – Particles and Flow

Refractive Index – Real: (RI_{real}) Click on the appropriate box and enter the real part of the particle index of refraction, e.g., PSL = 1.59, water = 1.33.

Refractive Index – Img: (RI_{img}) Click on the appropriate box and enter the imaginary part of the particle index of refraction, e.g., ploystyrene latex, water, liquids = 0.0, carbon and metals have an imaginary refractive index.

Start/Single Size, micron: (PAR_{Low}) Click on the appropriate box and enter the desired particle size (provided the **Single Size** box is checked), or the smallest particle size in the selected distribution.

End Particle Size, micron: (PAR_{High}) Click on the appropriate box and enter the largest particle size. If the **Single Size** box is checked, this box will not respond.

Data Rate, #/sec: Click on the appropriate box and enter the average number of particles per second to pass through the measurement volume. NOTE: This feature is disabled at this point since it is used as a tool to develop turbulence power spectra algorithms and to simulate other time dependent characteristics of the flow.

Single Size: Click on the appropriate box to select single particle size input – other selections will be turned off by this selection. The desired particle size should be placed in the **Start/Single Size** entry.

Uniform Distribution: Click on the appropriate box to select a uniform particle size distribution – other selections will be turned off by this selection. The smallest desired particle size should be placed in the **Start/Single Size** entry, and the largest desired particle size should be placed in the **End Particle Size** entry.

1/r3 Distribution: Click on the appropriate box to select a Junge (power law) type particle size distribution – other selections will be turned off by this selection. The smallest desired particle size should be placed in the **Start/Single Size** entry and the largest desired particle size should be placed in the **End Particle Size** entry. The Junge distribution describes the distribution of aerosols in the atmosphere and is a power law distribution approximating $1/r^3$ extending from 0.4- to 1.5-micron with a particle number density of 760 particles per cubic centimeter at the ocean shore down to 460 particles per cubic centimeter inland. If this distribution is selected the input particle size limits are mapped to the probabilities of the Junge distribution.

Gaussian Distribution: Click on the appropriate box to select a Gaussian particle size distribution – other selections will be turned off by this selection. The smallest desired particle size should be placed in the **Start/Single Size** entry and the largest desired particle size should be placed in the **End Particle Size** entry. The desired particle sizes will set the lower and higher standard deviations of the distribution. Random particles will be selected from ±3 standard deviations about the mean. Particles less than 0.1-micron will be ignored.

Number of Particles: Click on the appropriate box and enter the number of particles to be passed through the measurement volume.

Mean Velocity, m/s: and Std Deviation, m/s: ($\overline{VEL}_{mag}$ and σ_{mag}) Click on the **Mean Velocity** box and enter the desired average velocity magnitude. Click on the corresponding **Standard Deviation** box and enter the desired standard deviation. The velocity magnitude will obey Gaussian statistics.

Mean Alpha, deg: and Std Deviation, deg: ($\overline{\alpha}$ and σ_{α}) Click on the **Mean Alpha** box and enter the desired average vertical flow angle. Click on the corresponding **Standard Deviation** box and enter the desired standard deviation. The vertical flow angle will obey Gaussian statistics.

Mean Beta, deg: and Std Deviation, deg: ($\overline{\beta}$ and σ_{β}) Click on the **Mean Beta** box and enter the desired average horizontal flow angle. Click on the corresponding **Standard Deviation** box and enter the desired standard deviation. The horizontal flow angle will obey Gaussian statistics.

Signal Threshold, V: ($THRES$) Click on the appropriate box and enter the voltage setting that will trigger a signal capture and the succeeding signal processing.

Full Scale A/D, V: (FS) Click on the appropriate box and enter the full scale voltage for the 8-bit analog-to-digital converter. The full scale voltage follows the 1, 2, 5, 10 sequence and is bi-directional, e.g., an entry of 1.0 will set the A/D converter to measure voltages in the range ± 1.0 V.

Save Histogram Plots? Click on the appropriate box to save the plots of all distributions presented as Extended Windows Metafiles (EMF) in the directory that contains the program setup file (INI – selected in Screen 1).

Auto Display Plots? Click on the appropriate box to automatically display the resultant plots for 15 seconds, then display the next set of plots, etc. If this box is not selected, the user must manually change sets of plots by moving the cursor to the upper left plot where the arrow cursor will change to a +. A left mouse click will display the next set of plots.

Trigger Mid Burst? Click on the appropriate box to configure the signal capture register to pretrigger mode making the trigger occurrence to be at the 40-percent register address in order to capture the entire signal burst. If the box is not selected, the trigger occurrence will be at the beginning register address, e.g., normal oscilloscope triggering.

Downmix Signal? Click on the appropriate box to pass the filtered signal burst through a double-balanced mixer before being digitized by the A/D converter.

U-Downmix Freq, MHz: Click on the appropriate box and enter the reference frequency for the double-balance mixer – U-component signal burst, e.g., an entry of 30 MHz will yield an effective Bragg frequency of 10 MHz from a signal burst shifted by a 40 MHz Bragg cell. The difference frequency is output to the A/D converter. Note: This entry is not available unless the **Downmix Signal** has been selected.

V-Downmix Freq, MHz: Click on the appropriate box and enter the reference frequency for the double-balance mixer – V-component signal burst, e.g., an entry of 30 MHz will yield an effective Bragg frequency of 10 MHz from a signal burst shifted by a 40 MHz Bragg cell. The difference frequency is output to the A/D converter. Note: This entry is not available unless the **Downmix Signal** has been selected.

Save PMT Signals? Click on the appropriate box to save the signal traces from the photomultiplier output. Each signal burst is saved as a three column text file with the name SimSignalsxxxxx.TXT, where xxxxx represents the particle number. The first column is time in microseconds with 0.0 being located at the center of the signal burst. The second column is the U-component signal, and the third column is the V-component signal. The file heading includes the particle's trajectory and velocity magnitude and flow angles along with the U- and V-component velocities. NOTE: Once selected, any other save signal selection will be turned off. If it is desired to turn off signal trace recording, click the selected save option and it will be turned off.

Save High-Pass Signals? Click on the appropriate box to save the signal traces following high-pass filtering of the photomultiplier output. Each signal burst is saved as a three column text file with the name SimSignalxxxxx.TXT, where xxxxx represents the particle number. The first column is time in microseconds with 0.0 being located at the center of the signal burst. The second column is the U-component signal, and the third column is the V-component signal. The file heading includes the particle's trajectory and velocity magnitude and flow angles along with the U-and V-component velocities. NOTE: Once selected, any other save signal selection will be turned off. If it is desired to turn off signal trace recording, click the selected save option and it will be turned off.

Save Triggered Signals? Click on the appropriate box to save the signal traces that triggered the data acquisition system. Each signal burst is saved as a three column text file with the name SimSignalxxxxx.TXT, where xxxxx represents the particle number. The first column is time in microseconds with 0.0 being located at the center of the signal burst. The second column is the U-component signal, and the third column is the V-component signal. The file heading includes the particle's trajectory and velocity magnitude and flow angles along with the U-and V-component velocities. NOTE: Once selected, any other save signal selection will be turned off. If it is desired to turn off signal trace recording, click the selected save option and it will be turned off.

Save A/D Captures? Click on the appropriate box to save the digitized signal trace. This signal is the input to the signal processing software. Each signal burst is saved as a three

column text file with the name SimSignalxxxxx.TXT, where xxxxx represents the particle number. The first column is time in microseconds with 0.0 being located at the center of the signal burst. The second column is the U-component signal, and the third column is the V-component signal. The file heading includes the particle's trajectory and velocity magnitude and flow angles along with the U-and V-component velocities. NOTE: Once selected, any other save signal selection will be turned off. If it is desired to turn off signal trace recording, click the selected save option and it will be turned off.

Click **Run** when ready to run the program, **Exit** to terminate the program. An example set of input data is presented in Table A-1.

The Simulation

As illustrated above a Monte Carlo simulation breaks a large process into small parts which can be simulated using the physical processes involved in that element. The simulation of a laser velocimeter is a mixture of analytical descriptions of the optical system and the Monte Carlo descriptions of the particle trajectories and signal development. The following will address these areas and provide the reader with the methodology involved in the simulation.

The Laser Velocimeter Optical System

The input geometric configuration of the laser velocimeter is used to determine the characteristics of the collected scattered light from particles passing through the measurement volume. There are several assumptions made in the program that should not significantly affect the predictions, but significantly reduce the complications in both the program and the optical system. The assumptions that are the most difficult to obtain in a real optical system are diffraction limited optics with no spherical or chromatic aberrations. The assumptions that all beams are perfectly collimated and parallel as they enter the final lens are obtainable with properly designed systems.

The first task is to compute the cross beam angle for each component. While this may appear to be a simple task, it is complicated by the fact that the simulation is designed to configure not only an orthogonal, two color system, but the three-beam polarization and the four-beam Bragg shifted single color configurations as well. This is followed by the calculation of the receiver location and collecting solid angle of acceptance for each input laser beam. These calculations are needed to determine the Mie scattering characteristics.

Characteristics of the Collected Scattered Light

Now that the geometric optical characteristics have been determined, the characteristics of the collected scattered light must be determined. The complex electro-magnetic field characteristics of light scattering from particles whose diameter is approximately the wavelength of the illuminating radiation was described by Mie (1908). This theory was

enhanced by Adrian and Earley (1975) when they described the interactions of two scattering fields obtained when a particle passes through two crossing coherent laser beams. The current simulation utilizes the theoretical predictions by Adrian and Earley to obtain the complex scattering characteristics by dividing the collecting solid angle into a 1024x1024 grid. The pedestal amplitude from each beam, signal amplitude, and relative phase are determined for each grid point within the collected solid angle and zeroed otherwise. Examples of the Mie scattering characters are shown for the laser velocimeter specifications presented in the data entry screens for 0.5-microns (Figure A.7), 1.0-micron (Figure A.8), 1.7-microns (Figure A.9), 2.0-microns (Figure A.10), and 3.0-microns (Figure A.11). The effects of non-orthogonal polarizations (Figure A.4) can be found at the top and bottom of the U-component grids. These figures also include the distribution of power and signal strength along with the resulting photomultiplier output signal bursts, high-pass filtered signal bursts and frequency spectra of the burst. Once developed, the non-zero elements of the grid are averaged to produce the average pedestal amplitude contribution from each laser beam, the average signal level, and average phase angle.

Instead of performing these time consuming computations for each particle passing through the measurement volume, the particle size distribution is divided into 0.1-micron steps and the Mie scattering characteristics determined once for each particle size. The errors generated by particles passing through the measurement volume with different trajectories, and thus producing slightly different solid angles, are considered negligible based on comparisons of the grid patterns for various trajectories of the same particle. A table is constructed from the results of the computations that contains the average pedestal power for each beam, the average signal level and the average phase angle as a function of particle size.

The Flow Simulator

Once the tables containing the Mie scattering parameters have been developed for the input particle size range, the flow simulator proceeds to determine the size of the measurement volume to lay out the acceptance plane for the particle passages. Assuming diffraction limited optics, the beam waist, length of the measurement volume and cross sectional area of the measurement volume can be determined using the equations below:

$$D_{bw} = \frac{4\lambda F}{\pi d} \tag{A.1}$$

$$L_{mv} = \frac{\sqrt{2}\, D_{bw} \cos\left(\frac{\theta}{2}\right)}{\sin(\theta)} \tag{A.2}$$

$$A_{bw} = \frac{\pi D_{bw}^2}{4} \tag{A.3}$$

where D_{bw} is the beam waist diameter of focused laser beam, and if aligned properly, the diameter of the measurement volume, λ is the laser wavelength, F is the focal distance of

the transmitter, d is the diameter of the laser beam at the final lens, L_{mv} is the length of the measurement volume, θ is the angle between the crossing laser beams, and A_{bw} is the cross sectional area of the focused laser beam at the beam waist.

Random Number Generators:

At this point the program deviates from the analytic development of Mie scattering and laser velocimetry geometry into the world of Monte Carlo. The base of all random number generators is the uniform generator which selects a number from 0 to 1 with equal probability. There are numerous equations that provide this capability and even most computer languages contain a generator in their math library. As an example, consider the following procedure:

Select a 10 digit decimal fraction that contains all digits 0 to 9 in an arbitrary order as a seed, RN_{U0} and apply the equation:

$$RN_{U(n+1)} = RN_{Un} * 29.0 - \mathrm{INT}\left(RN_{Un} * 29.0\right) \qquad \text{(A.4)}$$

where INT is the integer function. As an example, use the seed: 0.2510637948 to obtain the following sequence: 0.28, 0.14, 0.19, 0.65, 0.90, 0.20, 0.85. Since all random number generators will eventually repeat, the more digits available while solving equation A.4 will increase the number of random numbers that will occur before repeating. Therefore double precision is recommended. The current simulator uses the random number generator in the FORTRAN 90 library. It does not appear to repeat and is optimized for speed.

The most commonly used generator based on the Uniform generator is the normal or Gaussian random number generator. Starting with the uniform random number generator, the following equation is applied to convert the uniform random number to a Gaussian random number:

$$RN_G = \sqrt{-2.0 \log(RN_{Un})}\, \cos(2\pi\, RN_{U(n+1)}) \qquad \text{(A.5)}$$

where RN_G is the Gaussian random number and RN_{Un} and $RN_{U(n+1)}$ are two successive uniform random numbers. The generator has a mean of 0.0 with a standard deviation of 1.0, thus an offset must be added to obtain the desired mean and a multiplying factor to obtain the desired standard deviation. This algorithm is used in the simulation program.

While the Gaussian generator provides simulations ranging from grades on a test, to the heights of people in a group, to household incomes, to velocity in a wind tunnel, it can not predict interarrival times of occurrence because time can not be negative. Interarrival times from the passage of cars on a highway to the arrival of photons at a photomultiplier can, however, be modeled with a Poisson distribution. Again using random numbers from the uniform random number generator, a Poisson random number generator can be constructed using the following equation:

$$RN_P = \log\left(\frac{1.0}{RN_{Un}}\right) \tag{A.6}$$

where $X_n > 0.0$. A more robust method that allows for the overall shape variation to fit known characteristics of the random process being modeled is given by the procedure below:

$$\begin{aligned}
&\textbf{Initialization:} \quad Test = e^{-\lambda_P}, \quad \lambda_P = 4.0, \quad k = 0, \quad m = 1 \\
&\textbf{Do:} \quad k = k+1 \\
&\qquad\quad m = m\,RN_{Un} \\
&\textbf{While:} \quad m > Test \\
&\textbf{Return:} \quad k-1
\end{aligned} \tag{A.7}$$

where λ_P is the shape factor, (a value of 4 approximates the statistics for the time between photon arrivals at a photomultiplier, and particle arrivals at the laser velocimeter measurement volume), and RN_{Un} is the uniform random number. Poisson distributions are always positive and the standard deviation is the same as the mean. This algorithm will produce a mean and standard deviation equal to 1.0 and is used in the simulation program.

The final random number generator used in the simulator models the Junge (power law) distribution (Junge (1955)) which approximates the distribution of aerosol particles in the atmosphere. The aerosol distribution extends from 0.4- to 1.5-microns in a $1/r^3$ power form. This distribution also approximates the distribution found in many vaporization/condensation generators, except the particle size limits are different. The procedure used to generate the random number and scale it to the desired particle size range is given below:

$$\begin{aligned}
Y &= 0.81\,RN_{Un} + 0.019 \\
RN_J &= e^{\log(P_{min}) - \frac{\log(Y)}{3.0}} \\
RN_{J-scaled} &= \frac{(RN_J - P_{min}) * (P_{max} - P_{min})}{1.5 - P_{min}} + P_{min}
\end{aligned} \tag{A.8}$$

where RN_{Un} is the uniform random number, RN_J is the random number based on the Junge distribution from 0.4- to 1.5-microns, and $RN_{J\text{-}scaled}$ is the scaled random number for the particle size limits P_{min} to P_{max}. This algorithm is used in the simulation program.

Particle Velocity and Trajectory Through the Measurement Volume:

Once all of the support components are in place, a particle is chosen and assigned a velocity and trajectory, then launched through the measurement volume. The size of the particle is determined using the random number generator configured using settings defined by the user in data entry screen 4 (Figure A.6):

Single Size –	User input the desired particle size (Fixed size);
Uniform Distribution –	Equal probability from the user input smallest size to the largest size (Uniform random number);
$1/r^3$ Distribution –	Junge type distribution from the user input smallest size to the largest size (Junge random number);
Gaussian Distribution –	Gaussian distribution with the input smallest and largest sizes establishing the ±standard deviation about the central size (Gaussian random number obtained within ±3 standard deviations).

The velocity magnitude, vertical flow angle (Alpha), and horizontal flow angle (Beta) are determined using the Gaussian random number generator, each parameter established by the mean and standard deviation settings entered in data entry screen 4. The uniform random number generator is used to determine the vertical (Y) and on-axis (Z) particle entry point into the measurement volume. The limits of 0 to 1 in the uniform random number generator are mapped to the locus of the $1/e^3$ power locations:

$$X = \frac{X_{enter} D_{bwU}}{2.0 \cos\left(\frac{\theta_U}{2.0}\right)}$$

$$Y = \frac{Y_{enter} D_{bwU}}{2.0} \qquad \text{(A.9)}$$

$$Z = \frac{\sqrt{2.0}\, Z_{enter} D_{bwU} \cos\left(\frac{\theta_U}{2.0}\right)}{2.0 \sin\left(\theta_U\right)}$$

where D_{bwU} is the beam waist diameter (equation A.1), θ is the angle between the two crossing laser beams, X_{enter} is -0.75 D_{bwU} to always launch the particle at the $-1/e^3$ power location along the streamwise direction with the exit plane location, X_{exit}, set symmetric at 0.75 D_{bwU}, and Y_{enter} and Z_{enter} are mapped to the uniform random numbers as follows:

$$Y_{\text{enter}} = 3.0\, RN_{Un} - 1.5$$

$$Z_{\text{enter}} = 3.0\, RN_{U(n+1)} - 1.5 \qquad \text{(A.10)}$$

where RN_{Un} and $RN_{U(n+1)}$ are two successive uniform random numbers. This will yield random entrance points within the $1/e^3$ power locations defined as $\pm 0.75\ D_{bwU}$ (equation A.1) in the vertical direction, and $\pm 0.75\ L_{mv}$ (equation A.2) in the on-axis direction.

With the particle's characteristics selected by the random number generators, it is placed in the entrance plane at its random location and launched with the random velocity magnitude along a trajectory established by the random flow angles. As the particle passes through the measurement volume it will scatter laser radiation whose power is dependent on the fringe spacing and Bragg shift of the respective velocity component. The fringe spacing is established using equation (2) and the parameters entered in data entry screen 2 (Figure A.4).

$$l_f = \frac{\lambda}{2\sin(\frac{\theta}{2})} \tag{2}$$

The Bragg shift frequencies are also entered in data entry screen 2 for each component respectively. The ideal U-component signal burst can now be determined based on the particle's characteristics and launch point from the following sequence:

$$\begin{aligned} \Phi_\alpha &= atan\left(\frac{Y_{exit}-Y_{enter}}{X_{exit}-X_{enter}}\right) = atan\left(\frac{Y_{exit}-Y_{enter}}{1.5\,D_{BW}}\right) \\ \Phi_\beta &= atan\left(\frac{Z_{exit}-Z_{enter}}{X_{exit}-X_{enter}}\right) = atan\left(\frac{Y_{exit}-Y_{enter}}{1.5\,D_{BW}}\right) \\ \Phi_\gamma &= atan\left(\frac{Z_{exit}-Z_{enter}}{Y_{exit}-Y_{enter}}\right) \end{aligned} \tag{A.11}$$

where X is streamwise, Y is vertical, Z is along the optical axis (equation A.9), and ϕ_α, ϕ_β, and ϕ_γ are the three trajectory angles: vertical, horizontal, and rotation about the optical axis of the laser velocimeter transmission system, respectively. Next the particle transit time, $T_{transit}$, between the entrance and exit planes is determined along with the effective number of fringes crossed, $N_{fringes}$:

$$\begin{aligned} T_{Transit} &= \frac{1.5\,D_{bw}}{VEL_{mag}} \\ N_{fringes} &= \frac{D_{bw}\cos(\Phi_\alpha)}{l_{fU}} + FBragg_U\,T_{Transit} \end{aligned} \tag{A.10}$$

where VEL_{mag} is the particle velocity magnitude and $FBragg_U$ is the Bragg frequency for the U-component.

The constants needed to determine the ideal signal burst based on the input and randomly selected parameters are then determined:

$$\begin{aligned} PVEL_{XU} &= VEL_{mag}\cos(\phi_\alpha)\cos(\phi_\beta) \\ PVEL_{YU} &= VEL_{mag}\sin(\phi_\alpha)\cos(\phi_\beta) \\ K_U &= 2\pi\left(\frac{PVEL_{XU}}{l_{fU}} + FBragg_U\right) \\ P_{avgU} &= \frac{2P_U\left(T1_U + T2_U\right)}{A_{bw}} \\ k_U &= \frac{2\pi}{\lambda_U} \end{aligned} \tag{A.11}$$

where $PVEL_{XU}$ and $PVEL_{YU}$ are the horizontal and vertical particle velocities, K_U is the U-component signal frequency including the Bragg cell frequency, P_{avgU} is the average U-component laser power illuminating the measurement volume, and k_U is the particle scale factor used in the Mie scattering calculations.

The particle is launched at the entrance plane, location X_{enter}, Y_{enter}, Z_{enter}, with a velocity magnitude, VEL_{mag}, and flow angles ϕ_α and ϕ_β. The particle's trajectory is reduced to components Δx, Δy, and Δz which represent the distance traveled within the time between data samples. This process continues until the exit plane is reached and the particle transit time has been completed. The following procedure generates and then stores the ideal signal burst waveform in the array, S_U:

Initialization:

$$\begin{aligned} \Delta X &= \frac{Vel_{mag}\cos(\alpha)\cos(\beta)}{\Delta T} \\ \Delta Y &= \frac{Vel_{mag}\sin(\alpha)\cos(\beta)}{\Delta T} \\ \Delta Z &= \frac{Vel_{mag}\cos(\alpha)\sin(\beta)}{\Delta T} \\ T &= 0 \end{aligned} \tag{A.12}$$

Do:

$$PED = \frac{-2.0\left(X^2 + Y^2 + \frac{Z^2\theta_U^2}{4.0}\right)}{0.25\,D_{bwU}^2} \tag{A.13}$$

$$PED = e^{PED}$$

$$S_U = \frac{PED * P_{avgU}}{K_U^2}\left(T1_U P_{Mie1U} + T2_U P_{Mie2U}\right)\cosh\left(\frac{2.0\,X\,Z\,\theta}{0.25\,D_{bwU}^2}\right) \tag{A.14}$$

$$+ \sqrt{T1_U T2_U}\,Doppler_{MieU}\cos\left(K_U T - \Phi_{MieU}\right)$$

$$\begin{aligned} X &= X + \Delta X \\ Y &= Y + \Delta Y \\ Z &= Z + \Delta Z \\ T &= T + \Delta T \end{aligned}$$

While:

$$T < T_{Transit}$$

The same process is repeated, using the appropriate characteristics, to create the ideal V-component signal burst waveform which is stored in the array S_V.

The next task is to convert the two ideal signal bursts to a train of photo-electrons leaving the photo-cathode. At each sample of the ideal signal ($P(t)$), given in Watts, the following equation is used to determine the number of photons per second ($R(t)$) that attain that level:

$$R(t) = \frac{\eta\lambda\,T_R\,P(t)}{hc} \tag{A.15}$$

This rate value is then passed to the Poisson routine to determine the time of the photon's arrival at the photo-cathode. The uniform random number generator then generates a number. If the number is less than or equal to the photomultiplier quantum efficiency, the photon becomes a photo-electron. Otherwise, the photon is rejected. When the total time for the photon arrivals exceeds the time for the next sample in the ideal signal, the number of photo-electrons occurring in that time increment is stored as the real signal, the next signal amplitude sample and its occurrence time is then retrieved and the process repeated starting with the arrival of the photon that exceeded the previous sample time and its arrival time. This process is described by the logical description below:

Initialization: $\Sigma TIME = \Delta t \quad T = 0.0$

Do: $N_p = 0$

Do: $T = \frac{\lambda T_R \Delta t S_{Ui}}{hc} RN_P + T$

If: $RN_U < \eta$

Then: $N_P = N_P + 1$ (A.16)

While: $T < \Sigma TIME$

$S_{Ui} = N_P$

$i = i + 1$

$\Sigma TIME = \Sigma TIME + \Delta t$

While: $\Sigma TIME < T_{Transit}$

where:

	ΣTIME	Time defined by the sample time
	Δt	Time between successive digital samples
	T	Time defined by photon arrivals
	N_p	Number of photons acquired within the i^{th} Δt
	λ	Laser wavelength
	T_R	Transmission factor for the LV collecting optics
	h	Planck's constant
	c	Speed of light
	RN_P	Poisson random number
	RN_U	Uniform random number
	η	Photomultiplier quantum efficiency
	$T_{Transit}$	Transit time of the particle through the measurement volume.

It is assumed that the number of photo-electrons acquired within a single sample time (Δt) occurred simultaneously for the 1.0 GHz input data sample rate. If a slower sampling clock is used, the simulation of the photomultiplier impulse response function will be less accurate. A captured photo-electron is shown in Figure A.12 (Baker *et al* (1989)), which shows a pulse with a trailing oscillation. The photomultiplier specifications indicate that the frequency response of the photomultiplier was 200 MHz, which matches the cycle frequency of the captured signal in Figure A.12. The 5.0 nsec cycle time also matches the width of the first and primary pulse. Since a photomultiplier is a unipolar device, the negative voltages in the figure are likely the result of ringing caused by a mismatch in

impedance between the photomultiplier and the oscilloscope. Thus the simulator uses an equilateral triangle with a length of 5.0 nsec to approximate the impulse response of the photomultiplier, illustrated by the first pulse in Figure A.12. If the input data sample rate is greater than 500 MHz, the signal composed of photo-electrons is convolved with the photomultiplier response function, otherwise the signal is untouched.

The signal burst then passes through a high-pass filter to remove the pedestal. This is accomplished by applying a Fast Fourier Transform to the signal burst, then using a Butterworth high-pass filter set to the input filter break point, Screen 3, Figure A.5 (e.g., HPF_U):

$$\begin{aligned} Amp &= \frac{\Delta f^4}{\sqrt{HPF_U^8 + \Delta f^8}} \\ FSignal(real) &= Amp * FSignal(real) \\ FSignal(img) &= Amp * FSignal(img) \end{aligned} \tag{A.17}$$

where Δf is the resolution in the frequency domain, and *FSignal* is the complex Fourier transformed signal burst. The filtered signal is inversely Fourier transformed to yield the filtered burst in the time domain. For examples see the signal traces in Figures A.7 – A.11.

If the signal is to be down-mixed, a model of a double-balance mixer is used to obtain the difference frequency between the signal burst and the reference frequency. For this model, the time domain signal burst is multiplied by a square wave at the reference frequency. The resultant signal is Fast Fourier Transformed and low pass filtered with the break point set to 50-percent of the reference frequency. The filtered frequency spectra is inverse transformed to yield the down-mixed signal burst.

In the next step the signal burst is interrogated to determine if the voltage crosses the triggering threshold (*THRES*, Screen 4, Figure A.6). If the center trigger box was checked, the peak voltage is found and a signal limit threshold is determined to be 10-percent of the peak voltage. Otherwise the value of the trigger threshold, *THRES*, is used as the signal limit threshold. The signal burst is then interrogated from the start, zeroing each sample voltage until the signal limit threshold is crossed. The process is repeated from the end of the burst toward the center. The remaining portion of the signal burst is shifted toward the beginning of the array with the trailing array locations zeroed. The number of samples of the signal burst is then determined and the smallest power of two containing the total signal burst is identified. If the number of samples is less than 128, the signal burst is rejected. Otherwise the signal is digitized based on an 8-bit digitizer set to the input full-scale voltage, *FS* (Screen 4, Figure A.6).

This concludes the simulation portion of the laser velocimeter optical system, triggering system, and data acquisition electronics. Examples of the various stages of signal development are shown in Figures A.13 – A.19. Each example figure includes both the U-

and V-component signals with the U-component signal being used as the triggering burst. The theoretical, photomultiplier output, high-pass filtered, and ADC captured signals are shown. Ten thousand particles were generated and passed through the measurement volume based on a mean velocity magnitude of 100 m/s with a standard deviation of 3.0 m/s, and a vertical flow angle of 0.0-degrees with a standard deviation of 4.0-degrees. The horizontal flow angle was kept at 0.0-degrees. Of these particles, the ones with the closest trajectories to the streamwise direction within the plane established by the two crossing U-component beams at on-axis locations every 0.5 L_{mv} (Equation A.2) from -1.5 L_{mv} to 1.5 L_{mv} were selected for the figures.

Signal and Data Processing

After the filtered signal burst was digitized, the *captured* signal bursts created by the simulator were passed to the signal processing portion of the simulation. Although included as part of the laser velocimeter simulation program, in reality the simulator served as the development platform for the signal processing and data processing algorithms. Further, since the velocity magnitude and trajectory of each particle was known, it also served to determine the precision of the algorithms along with the overall measurement accuracy.

The first step in the signal processing portion of the program was to determine the extent of the signal burst so that a windowing function many be scaled and applied to insure that the burst begins and ends at 0.0 V. A Bartlett (triangular) window was used because of its simplicity and processing speed. Since the signal burst is basically a sinusoid, the characteristics following the frequency break point of the window function are unimportant so more sophisticated windowing functions (Hamming, Hanning, Tukey, etc.) are not necessary. The only requirement was that there was no discontinuity between the beginning and end of the signal burst. This is necessary because the Fast Fourier Transform (FFT) algorithm works as if the signal burst was a continual signal – think of wrapping the signal burst around a cylinder and rotating it. Any discontinuity will add harmonics and noise spikes to the frequency representation of the signal burst that will affect the accuracy of the signal processing algorithms.

Once the windowing function has been scaled in time to match the length of the signal burst, then scaled in amplitude to have an integral area of unity, the signal burst is multiplied by the window. The resulting signal burst is then passed to the signal processing subroutine where the first step is to copy the signal burst waveform into the real portion of a complex array. The imaginary portion of the complex array is set to 0.0. This array is then converted to the frequency domain using a complex FFT utility. The real and imaginary parts of the frequency spectra at each frequency step are squared, summed and the square root computed to obtain the power spectra. To insure that the pedestal has been removed, the first 10 frequency increments are zeroed. The next step is to determine the peak location of the frequency signature that indicates the location of the signal burst frequency. The amplitude of the peak is then used to determine the signal-to-noise threshold of an acceptable signal. If the background spectral level is greater than

10-percent of the amplitude of the peak, the signal burst is rejected and the returned frequency is set to 0.0 to indicate the rejection of the burst. If the signal burst is accepted, one of the following processing schemes selected for testing would then be used to determine the signal frequency:

Peak	The frequency of the peak location is returned.
Gaussian	The peak amplitude and the amplitude of the frequency step (bin) on either side of the peak are fit with a Gaussian curve and the frequency of the peak of the curve fit is returned.
Histogram (3)	The peak amplitude and the amplitude of the frequency bin on either side of the peak are used as the weights of a weighted average of the frequencies for those bins. The weighted average frequency is returned.
Histogram (5)	The peak amplitude and the amplitude of the two frequency bins on either side of the peak are used as the weights of a weighted average of the frequencies for those bins. The weighted average frequency is returned.
Half Power	The peak amplitude is determined and a threshold set to 50-percent of that amplitude. The amplitude of adjacent frequency bins on either side of the peak are interrogated to determine when a bin amplitude falls below the threshold. At this point only those continuous frequency bins with amplitudes greater than the threshold are used as weights of a weighted average of the frequencies for those bins. The weighted average frequency is returned.
True Half Power	This routine is the same as the Half Power routine except the amplitudes of the furthermost bin with an amplitude above the threshold and the adjacent bin with an amplitude below the threshold are interpolated to determine the exact frequency where the threshold is crossed. This process is applied to both sides of the peak. The weights of this fraction of a bin are scaled with the width of the bin fraction. Again these amplitudes along with the amplitudes of the bins with amplitudes above the threshold are used to determine the weighted average of the frequencies for those bins. The weighted average frequency is returned.

This process is repeated for the V-component signal burst. If both components yield a non-zero frequency, a coincident measurement was successful and the processing continues, otherwise this pair of signal bursts are rejected and the next pair of signal bursts are processed.

The Bragg (or equivalent Bragg if downmixing was employed) frequencies are subtracted from the respective two component frequencies to yield the Doppler shift frequency. The frequencies are then converted to velocities using equation (1)

$$V = \frac{\lambda f_D}{2\sin(\frac{\theta}{2})} \quad (1)$$

The resultant U- and V-component velocities are then used to calculate the velocity magnitude and flow angle of the measured particle. These results, along with the time between acceptable signal burst arrivals and its conditionally sampled azimuth angle are stored in their corresponding data arrays, and the next signal burst is then processed. This loop continues until the selected number of particles have been extinguished.

As the signal processing loop continues, the occurrence of every 100th acceptable pair of signal bursts triggers the computation of the ensemble statistics at that point. These results will track the convergence of the statistical results toward statistical stationarity. Once the selected number of particles have been processed, the final statistics are computed, and histograms of velocity and flow angle are developed. The statistical quantities computed include the mean, statistical uncertainty in the mean, standard deviation, the statistical uncertainty in standard deviation, skew, and excess along with the number of signal bursts used in the computations. The histograms are set to bin widths of 1.0 m/s for the velocities and 1.0 degree for the flow angle.

Since the simulation program is used for signal processing and data processing algorithm development, a record of each event is kept in a LOG file. The LOG begins with the listing of the laser velocimeter optical and electronic characteristics along with the particle characteristics and flow parameters and the optional settings placed in the data entry screens. This is followed by the average Mie scattering pedestal levels for both laser beams, the average signal level and average phase angle for the particle size or the range requested (in 0.1 micron steps). The table containing the characteristics of each particle generated is recorded, Table A-2. These characteristics include:

Particle number and size in microns
Velocity magnitude, vertical flow angle and horizontal flow angle
Trajectory starting location (X, Y, and Z)
Trajectory ending location (X, Y, and Z)
U- and V-component velocities
U- and V-component velocities if the signal burst triggers capture
Measured U- and V-component velocities if successfully processed
U- and V-component velocity errors (velocity of the particle – the measured velocity)

Once all particles have been processed, the mean and standard deviation of the velocity magnitude, vertical and horizontal flow angles, U- and V-component velocities, and number of signal bursts included in the ensemble are displayed in the command.com window and the full statistics (including skew and excess) are recorded in the LOG file, Table A-3. The following is displayed and recorded:

Input particle velocity statistics
Selected particle velocity statistics (where the signal bursts triggered capture)
Measured velocity statistics
Measurement errors

Next the program displays the various histograms in the graphics window. The first window contains the input, triggered, and measured histograms for the velocity magnitude and vertical flow angle, Figure A.20. If the auto display option was selected, the histograms are displayed for 15 seconds and the next set is displayed, if not the user must move the cursor to the upper left histogram and left click the mouse to view the next set. The next set contains the input, triggered, and measured histograms for the U- and V-component velocities, Figure A.21. The next set of histograms presents the measurement errors based on a direct particle-by-particle comparison for the velocity magnitude, vertical flow angle and the U- and V-component velocities, Figure A.22.

After the error histograms have cleared, the program then interrogates the measurement histograms searching for outliers. The amplitude of the peak of each histogram is determined and used to establish a minimum amplitude threshold of 5-percent of the peak (or the value of 3, whichever is greater). If the histogram was a Gaussian distribution, the 5-percent threshold would equate to the amplitude at the $1/e^3$ location. Each histogram is then tracked toward the right until the bin amplitude goes below the threshold. If the amplitude remains below the threshold for three consecutive bins, the point where it falls below the threshold becomes the right-hand cutoff. Otherwise the search continues until the condition is met. This process is repeated on the left side of the histogram to establish the left-hand cutoff. The measurement arrays are then interrogated and any values outside their respective cutoffs are eliminated from all arrays. The remaining signal burst results are listed in a table in the LOG file in the form of particle number, particle size, particle velocity magnitude and flow angle, measured velocity magnitude and flow angle and associated measurement errors, U- and V-component particle velocities, U- and V-component measured velocities and their associated measurement errors, Table A-4. Then the statistics are computed and displayed in the command.com window and recorded in the LOG file as:

Measured particle velocity statistics
    Outliers Removed
Measurement Errors

and the outlier removed histograms of measured velocity magnitude, vertical flow angle, U- and V-component velocities and U- and V-component measurement errors are displayed, Figure A.23. Once this display has completed, the computed velocities and flow angle results for each measured signal burst is recorded in the LOG file, Table A-5. The characteristics include the particle velocities and flow angles, measured particle velocities and flow angles, and the measurement errors in a particle-by-particle listing. The LOG file is then closed and the program returns to the second data entry window, **LV Simulation – Transmitter**, Figure A.4. It is noted that if the **Save Histogram Plots?** box in the

fourth data entry window, Figure A.6, is selected, each of the displayed histogram plots will be stored as an independent windows metafile (EMF) in the same directory as the original INI file. Also if one of the record signal files, e.g., **Save PMT signals?**, is selected ASCII text files containing time, U- and V-component signals are stored for all particles in the same directory as the original INI file. During instrument development and verification activities these signal files are used to drive an arbitrary waveform generator to provide realistic electronic signals to the laser velocimeter data acquisition system that are subsequently used to validate signal/data processing procedures. Again, since the answers are known, the actual instrument precision was determined for the hardware/software system used for the upgraded laser velocimeter. The results indicated that the hardware performed exactly as predicted by the simulation, with negligible, if any, electronic noise. Even the captured signals from the PXI high-speed digitizer overlaid exactly on the simulated signal used to drive the waveform generator.

0.5145	Laser wavelength - U component, microns
0.4880	Laser wavelength - V component, microns
1.0000	Laser power - U component, W
1.0000	Laser power - V component, W
40.0000	Bragg frequency - U component, MHz
40.0000	Bragg frequency - V component, MHz
-0.1294	U-component beam 1 X location, m
0.0000	U-component beam 1 Y location, m
0.1294	U-component beam 2 X location, m
0.0000	U-component beam 2 Y location, m
0.0000	V-component beam 1 X location, m
-0.1294	V-component beam 1 Y location, m
0.0000	V-component beam 2 X location, m
0.1294	V-component beam 2 Y location, m
0.3056	Transmission U-component Beam 1
0.2800	Transmission U-component Beam 2
0.3056	Transmission V-component Beam 1
0.2800	Transmission V-component Beam 2
84.0000	Polarization angle U-comp Beam 1, deg
89.0000	Polarization angle U-comp Beam 2, deg
0.0000	Polarization angle V-comp Beam 1, deg
0.0000	Polarization angle V-comp Beam 2, deg
0.0175	Effective diameter of laser beam, m
4.8770	Transmitter focal distance, m
4.8770	Receiver focal distance, m
0.0000	Vertical angle of receiver, deg
180.0000	Horizontal angle of receiver, deg
0.2750	Effective diameter of receiver, m
0.6500	Transmission U-component Rec
0.6500	Transmission V-component Rec
0.1500	PMT quantum efficiency
1.0000	PMT gain, M
10.0000	System gain, dB
2.0000	High Pass filter break U-comp, MHz
100.0000	Low Pass filter break U-comp, MHz
2.0000	High Pass filter break V-comp, MHz
100.0000	Low Pass filter break V-comp, MHz
1000.0	Digitizing sample rate, MHz
1.5900	Particle index of refraction Real
0.0000	Particle index of refraction Img
X	Single particle size
	Uniform particle size distribution
	1/r3 particle size distribution
	Gaussian particle size distribution
1.7000	Starting/Single particle size, microns
0.0000	Ending particle size, microns
1000	Particle data rate, #/sec
10000	Maximum number of particles
100.0000	Mean velocity, input, m/s
3.0000	Velocity standard deviation, input, m/s
0.0000	Mean vertical flow angle, input, deg
4.0000	Flow angle standard deviation, input, deg

Table A-1.- Input parameters for the Monte Carlo simulation program that include the characteristics of the upgraded laser velocimeter optical system, electronics settings, seeding particle characteristics, and flow characteristics.

0.0000	Mean horizontal flow angle, input, deg
0.0000	Flow angle standard deviation, input, deg
0.0500	Signal threshold to trigger capture
X	Trigger at center of burst?
1.0000	+/- Full Scale A/D voltage (1,2,5,10...)
n	Downmix LV signal?
0.0000	U-Reference Frequency for Double-Balanced Mixer, MHz
0.0000	V-Reference Frequency for Double-Balanced Mixer, MHz
y	Save all Histogram Plots?
n	Set all plots to 15 sec view?
	Save PMT signals?
	Save High-Pass Filtered Signals?
	Save Triggered Signals?
	Save A/D Captured Signals?

Particle Size: 1.7

U-component

Pedestal Beam A:	0.080
Pedestal Beam B:	0.079
Average Signal Level:	0.155
Average Phase Angle:	-179.959

V-component

Pedestal Beam A:	0.399
Pedestal Beam B:	0.421
Average Signal Level:	0.818
Average Phase Angle:	-0.063

Table A-1 (cont'd).- Input parameters for the Monte Carlo simulation program that include the characteristics of the upgraded laser velocimeter optical system, electronics settings, seeding particle characteristics, and flow characteristics.

Particle	Size	Vel-mag	Alpha	Beta	X-start	X-end	Y-start	Y-end	Z-start	Z-end	U-in	V-in	U-select	V-select	U-meas	V-meas	Error U	Error V
1	1.70	102.56	7.56	0.00	-1.50	1.50	-1.486	-1.088	-1.473	-1.473	101.671	13.497						
2	1.70	99.11	4.99	0.00	-1.50	1.50	0.340	0.602	1.448	1.448	98.729	8.627	98.73	8.63				
3	1.70	98.85	-8.73	0.00	-1.50	1.50	-1.324	-1.785	-1.281	-1.281	97.707	-15.004						
4	1.70	100.64	3.53	0.00	-1.50	1.50	0.581	0.766	-0.234	-0.234	100.450	6.195	100.45	6.19	100.13	6.13	-0.32	-0.06
5	1.70	101.86	-7.00	0.00	-1.50	1.50	-0.510	-0.878	-0.310	-0.310	101.097	-12.415	101.10	-12.41	101.42	-12.60	0.32	-0.18
6	1.70	94.92	-1.03	0.00	-1.50	1.50	-1.199	-1.254	0.968	0.968	94.903	-1.711						
7	1.70	98.77	-0.59	0.00	-1.50	1.50	0.884	0.853	1.246	1.246	98.767	-1.010						
8	1.70	101.54	4.34	0.00	-1.50	1.50	-0.429	-0.201	-0.062	-0.062	101.246	7.686	101.25	7.69	101.31	7.83	0.06	0.15
9	1.70	99.75	-4.44	0.00	-1.50	1.50	-0.855	-1.088	-0.155	-0.155	99.455	-7.721	99.46	-7.72	99.44	-7.44	-0.02	0.28
10	1.70	101.77	-3.71	0.00	-1.50	1.50	0.473	0.279	-1.369	-1.369	101.554	-6.577	101.55	-6.58				
11	1.70	103.93	-1.48	0.00	-1.50	1.50	0.262	0.185	-0.665	-0.665	103.893	-2.683	103.89	-2.68	104.37	-2.73	0.48	-0.04
12	1.70	101.14	5.32	0.00	-1.50	1.50	-0.815	-0.536	0.352	0.352	100.703	9.375	100.70	9.37	100.21	9.45	-0.49	0.07
13	1.70	102.09	-3.46	0.00	-1.50	1.50	-1.075	-1.256	1.102	1.102	101.904	-6.157						
14	1.70	101.87	-5.06	0.00	-1.50	1.50	-0.657	-0.923	-0.682	-0.682	101.471	-8.986	101.47	-8.99	102.28	-8.80	0.81	0.19
15	1.70	100.43	1.82	0.00	-1.50	1.50	-0.741	-0.646	1.104	1.104	100.382	3.182						
16	1.70	97.95	-6.90	0.00	-1.50	1.50	-1.384	-1.748	1.019	1.019	97.236	-11.771						
17	1.70	100.15	-7.07	0.00	-1.50	1.50	-0.426	-0.798	-1.100	-1.100	99.385	-12.329	99.39	-12.33	100.16	-12.51	0.78	-0.18
18	1.70	98.40	-1.26	0.00	-1.50	1.50	-0.040	-0.106	0.435	0.435	98.377	-2.171	98.38	-2.17	98.40	-2.12	0.02	0.05
19	1.70	101.54	-0.30	0.00	-1.50	1.50	-0.794	-0.810	-0.172	-0.172	101.542	-0.530	101.54	-0.53	101.43	-0.28	-0.11	0.25
20	1.70	96.08	-4.37	0.00	-1.50	1.50	0.482	0.253	0.458	0.458	95.801	-7.318	95.80	-7.32	96.14	-7.35	0.34	-0.03
21	1.70	102.84	-1.59	0.00	-1.50	1.50	-0.536	-0.619	0.768	0.768	102.798	-2.853	102.80	-2.85	102.53	-2.57	-0.27	0.29
22	1.70	99.06	2.93	0.00	-1.50	1.50	0.320	0.473	0.629	0.629	98.934	5.057	98.93	5.06	99.22	5.08	0.29	0.02
23	1.70	104.92	-0.50	0.00	-1.50	1.50	-1.057	-1.084	-1.220	-1.220	104.918	-0.922						
24	1.70	101.83	-3.22	0.00	-1.50	1.50	1.119	0.950	0.493	0.493	101.667	-5.717	101.67	-5.72	101.74	-5.09	0.07	0.63
25	1.70	98.66	-3.19	0.00	-1.50	1.50	-0.673	-0.840	-0.058	-0.058	98.512	-5.487	98.51	-5.49	98.77	-5.42	0.26	0.07
26	1.70	96.13	1.99	0.00	-1.50	1.50	-0.326	-0.221	1.378	1.378	96.074	3.345	96.07	3.34				
27	1.70	95.78	2.19	0.00	-1.50	1.50	-0.659	-0.544	-0.081	-0.081	95.711	3.662	95.71	3.66	96.13	3.78	0.42	0.11
28	1.70	100.14	-6.13	0.00	-1.50	1.50	0.141	-0.181	0.076	0.076	99.570	-10.696	99.57	-10.70	99.64	-10.67	0.07	0.03
29	1.70	103.81	-1.55	0.00	-1.50	1.50	1.286	1.205	0.066	0.066	103.769	-2.805						
30	1.70	96.37	-1.72	0.00	-1.50	1.50	0.309	0.219	-1.293	-1.293	96.327	-2.890	96.33	-2.89	95.42	-2.51	-0.91	0.38
31	1.70	99.35	6.01	0.00	-1.50	1.50	-0.451	-0.136	-0.775	-0.775	98.806	10.396	98.81	10.40	98.96	10.34	0.15	-0.06
32	1.70	100.62	-0.77	0.00	-1.50	1.50	0.948	0.908	1.004	1.004	100.615	-1.348						
33	1.70	98.98	7.04	0.00	-1.50	1.50	-0.622	-0.252	-0.279	-0.279	98.232	12.127	98.23	12.13	98.16	12.04	-0.07	-0.09
34	1.70	101.02	0.11	0.00	-1.50	1.50	0.943	0.948	-0.135	-0.135	101.021	0.187	101.02	0.19	101.39	0.41	0.36	0.22
35	1.70	100.17	-0.43	0.00	-1.50	1.50	-0.122	-0.144	0.930	0.930	100.166	-0.756	100.17	-0.76	99.87	-0.99	-0.30	-0.24
36	1.70	99.15	5.62	0.00	-1.50	1.50	-0.904	-0.608	-0.709	-0.709	98.675	9.712	98.68	9.71	98.92	9.95	0.25	0.24
37	1.70	102.34	0.88	0.00	-1.50	1.50	-0.355	-0.309	-0.545	-0.545	102.333	1.579	102.33	1.58	102.65	1.33	0.32	-0.25
38	1.70	101.43	5.08	0.00	-1.50	1.50	0.326	0.593	-0.941	-0.941	101.030	8.979	101.03	8.98	102.29	9.08	1.26	0.10
39	1.70	100.78	1.45	0.00	-1.50	1.50	-0.847	-0.771	0.089	0.089	100.745	2.555	100.74	2.55	100.73	2.67	-0.02	0.12
40	1.70	98.92	3.65	0.00	-1.50	1.50	-0.665	-0.474	1.484	1.484	98.716	6.299	98.72	6.30				
41	1.70	96.93	-4.69	0.00	-1.50	1.50	0.717	0.471	-0.328	-0.328	96.610	-7.924	96.61	-7.92	96.49	-8.10	-0.12	-0.18
42	1.70	98.13	-0.35	0.00	-1.50	1.50	-1.430	-1.449	1.289	1.289	98.131	-0.596						
43	1.70	107.01	1.83	0.00	-1.50	1.50	0.399	0.495	1.398	1.398	106.955	3.420	106.95	3.42				
44	1.70	100.67	5.03	0.00	-1.50	1.50	0.518	0.782	0.562	0.562	100.286	8.824	100.29	8.82	99.67	9.06	-0.61	0.24
45	1.70	97.42	-0.81	0.00	-1.50	1.50	1.456	1.414	-0.654	-0.654	97.406	-1.372						
46	1.70	103.20	-3.79	0.00	-1.50	1.50	-1.047	-1.246	-0.131	-0.131	102.974	-6.820						
47	1.70	99.47	-3.99	0.00	-1.50	1.50	0.631	0.422	0.474	0.474	99.228	-6.930	99.23	-6.93	99.63	-7.03	0.40	-0.10
48	1.70	95.94	0.95	0.00	-1.50	1.50	0.591	0.641	1.255	1.255	95.926	1.595						
49	1.70	102.79	0.65	0.00	-1.50	1.50	-0.830	-0.796	0.748	0.748	102.785	1.159	102.78	1.16	102.79	0.69	0.01	-0.47

Table A-2.- The input, measured and error characteristics of every particle that was generated in the Monte Carlo simulation.

Input particle velocity statistics

Velocity Magnitude:	100.01	Standard Deviation:	2.97
Alpha:	0.01	Standard Deviation:	4.01
Beta:	0.00	Standard Deviation:	0.00
U-component	99.77	Standard Deviation:	2.97
V-component	0.02	Standard Deviation:	6.99
Number of measurements:		10000.	

Selected particle velocity statistics

Velocity Magnitude:	99.98	Standard Deviation:	2.97
Alpha:	0.03	Standard Deviation:	4.01
U-component	99.74	Standard Deviation:	2.98
V-component	0.05	Standard Deviation:	7.05
Number of measurements:		5707.	

Measured particle velocity statistics

Velocity Magnitude:	101.07	Standard Deviation:	14.00
Alpha:	-0.01	Standard Deviation:	14.37
U-component	97.54	Standard Deviation:	28.89
V-component	0.04	Standard Deviation:	7.86
Number of measurements:		4973.	

Measurement Errors

Velocity Magnitude:	1.09	Standard Deviation:	13.60
Alpha:	-0.04	Standard Deviation:	13.57
U-component	-2.19	Standard Deviation:	28.82
V-component	-0.02	Standard Deviation:	3.60

Table A-3.- Input particle statistics, statistics for particles that triggered the data acquisition system, statistics for particles that were measured along with the statistics for the particle-by-particle errors (instrument precision) based on a flow with a velocity magnitude of 100.0 m/s with a standard deviation of 3.0 m/s, and a mean flow angle of 0.0 degrees with a standard deviation of 4.0 degrees.

Measured particle velocity statistics
Outliers Removed

Velocity Magnitude:	100.02	Standard Deviation:	3.00
Alpha:	0.05	Standard Deviation:	4.02
U-component	99.78	Standard Deviation:	3.01
V-component	0.09	Standard Deviation:	7.00
Number of measurements:		4943.	

Measurement Errors

Velocity Magnitude:	0.05	Standard Deviation:	0.39
Alpha:	0.01	Standard Deviation:	0.13
U-component	0.05	Standard Deviation:	0.39
V-component	0.03	Standard Deviation:	0.22

Table A-4.- Statistics for particles that were measured, outliers removed, along with the statistics for the particle-by-particle errors (final instrument precision) based on a flow with a velocity magnitude of 100.0 m/s with a standard deviation of 3.0 m/s, and a mean flow angle of 0.0 degrees with a standard deviation of 4.0 degrees.

Particle	Size	Vel-mag	Alpha	Mag-meas	Alpha-meas	Error-Mag	Error-Alpha	U-select	V-select	U-meas	V-meas	Error U	Error V
4	1.70	100.641	3.529	100.316	3.504	-0.325	-0.025	100.450	6.195	100.129	6.130	-0.322	-0.065
5	1.70	101.857	-7.001	102.198	-7.081	0.341	-0.081	101.097	-12.415	101.418	-12.599	0.321	-0.184
8	1.70	101.538	4.341	101.611	4.422	0.074	0.081	101.246	7.686	101.309	7.835	0.062	0.149
9	1.70	99.754	-4.439	99.716	-4.281	-0.038	0.158	99.455	-7.721	99.438	-7.443	-0.017	0.278
11	1.70	103.928	-1.480	104.405	-1.497	0.478	-0.017	103.893	-2.683	104.370	-2.727	0.477	-0.043
12	1.70	101.138	5.319	100.654	5.386	-0.484	0.067	100.703	9.375	100.210	9.448	-0.493	0.073
14	1.70	101.868	-5.061	102.662	-4.915	0.794	0.146	101.471	-8.986	102.285	-8.795	0.813	0.191
17	1.70	100.147	-7.072	100.941	-7.117	0.794	-0.045	99.385	-12.329	100.163	-12.506	0.778	-0.177
18	1.70	98.401	-1.264	98.418	-1.237	0.017	0.027	98.377	-2.171	98.395	-2.125	0.018	0.046
19	1.70	101.543	-0.299	101.427	-0.160	-0.116	0.139	101.542	-0.530	101.427	-0.283	-0.115	0.246
20	1.70	96.080	-4.368	96.424	-4.372	0.344	-0.004	95.801	-7.318	96.143	-7.351	0.342	-0.032
21	1.70	102.838	-1.590	102.558	-1.433	-0.280	0.156	102.798	-2.853	102.526	-2.566	-0.272	0.288
22	1.70	99.063	2.926	99.353	2.931	0.289	0.005	98.934	5.057	99.223	5.081	0.288	0.024
24	1.70	101.828	-3.218	101.865	-2.863	0.038	0.355	101.667	-5.717	101.738	-5.089	0.071	0.628
25	1.70	98.665	-3.188	98.918	-3.140	0.254	0.048	98.512	-5.487	98.770	-5.418	0.258	0.069
27	1.70	95.781	2.191	96.209	2.249	0.428	0.059	95.711	3.662	96.135	3.776	0.424	0.115
28	1.70	100.143	-6.131	100.211	-6.112	0.069	0.019	99.570	-10.696	99.642	-10.670	0.072	0.026
30	1.70	96.371	-1.719	95.448	-1.505	-0.923	0.213	96.327	-2.890	95.415	-2.507	-0.912	0.383
31	1.70	99.351	6.007	99.497	5.966	0.146	-0.041	98.806	10.396	98.959	10.341	0.153	-0.055
33	1.70	98.977	7.038	98.895	6.991	-0.083	-0.047	98.232	12.127	98.159	12.037	-0.072	-0.090
34	1.70	101.021	0.106	101.386	0.232	0.365	0.126	101.021	0.187	101.385	0.410	0.364	0.223
35	1.70	100.169	-0.432	99.871	-0.569	-0.299	-0.137	100.166	-0.756	99.866	-0.993	-0.301	-0.237
36	1.70	99.152	5.621	99.423	5.745	0.271	0.124	98.675	9.712	98.924	9.952	0.249	0.240
37	1.70	102.345	0.884	102.661	0.741	0.316	-0.143	102.333	1.579	102.653	1.328	0.320	-0.251
38	1.70	101.428	5.079	102.696	5.070	1.268	-0.009	101.030	8.979	102.294	9.075	1.264	0.096
39	1.70	100.777	1.453	100.764	1.520	-0.013	0.067	100.745	2.555	100.728	2.673	-0.016	0.118
41	1.70	96.934	-4.689	96.825	-4.800	-0.110	-0.111	96.610	-7.924	96.485	-8.101	-0.125	-0.177
44	1.70	100.674	5.029	100.084	5.195	-0.590	0.167	100.286	8.824	99.673	9.063	-0.613	0.238
47	1.70	99.470	-3.995	99.876	-4.037	0.407	-0.042	99.228	-6.930	99.629	-7.031	0.401	-0.101
49	1.70	102.791	0.646	102.795	0.387	0.004	-0.259	102.785	1.159	102.793	0.694	0.008	-0.465
50	1.70	109.355	5.880	109.663	5.813	0.308	-0.067	108.780	11.202	109.099	11.107	0.319	-0.095
51	1.70	98.570	-0.867	98.744	-0.872	0.175	-0.005	98.558	-1.491	98.733	-1.502	0.175	-0.011
53	1.70	103.048	-5.508	103.560	-5.446	0.512	0.062	102.572	-9.892	103.093	-9.828	0.520	0.063
55	1.70	97.654	-1.185	97.593	-0.984	-0.061	0.201	97.633	-2.019	97.578	-1.675	-0.055	0.344
59	1.70	96.339	-0.060	96.602	0.125	0.263	0.185	96.339	-0.101	96.602	0.211	0.263	0.312
61	1.70	100.564	6.086	101.051	6.046	0.487	-0.040	99.998	10.662	100.489	10.644	0.491	-0.018
66	1.70	100.613	0.022	100.195	0.317	-0.419	0.296	100.613	0.038	100.193	0.555	-0.420	0.517
71	1.70	97.334	-1.031	97.121	-1.099	-0.213	-0.068	97.318	-1.752	97.103	-1.863	-0.215	-0.112
72	1.70	101.552	-7.365	101.532	-7.579	-0.020	-0.214	100.714	-13.018	100.645	-13.391	-0.069	-0.373
73	1.70	101.639	-7.759	101.491	-7.852	-0.148	-0.093	100.709	-13.722	100.539	-13.865	-0.169	-0.143
77	1.70	98.721	1.360	98.957	1.399	0.236	0.038	98.693	2.344	98.927	2.416	0.234	0.072
79	1.70	96.089	-1.298	96.256	-1.226	0.166	0.072	96.064	-2.177	96.233	-2.060	0.169	0.117
81	1.70	100.802	0.416	100.879	0.570	0.077	0.155	100.800	0.731	100.874	1.004	0.074	0.273
82	1.70	99.330	2.969	99.404	2.993	0.073	0.023	99.197	5.145	99.268	5.190	0.071	0.044
86	1.70	102.298	0.725	102.387	0.605	0.089	-0.120	102.290	1.295	102.381	1.081	0.091	-0.214
87	1.70	99.973	1.125	100.301	1.054	0.328	-0.071	99.954	1.962	100.284	1.845	0.330	-0.117
88	1.70	99.301	1.268	98.888	1.388	-0.413	0.121	99.277	2.197	98.859	2.396	-0.418	0.199
91	1.70	96.181	-3.003	96.129	-2.946	-0.052	0.057	96.049	-5.040	96.002	-4.941	-0.047	0.099
92	1.70	102.047	3.173	102.341	3.047	0.295	-0.127	101.890	5.649	102.197	5.440	0.307	-0.209

Table A-5.- Input, measured and error characteristics of each particle that had a signal burst level sufficient to trigger the data acquisition system, and was not rejected as an outlier. These particle characteristics were used to calculate the statistical quantities that characterized the flow.

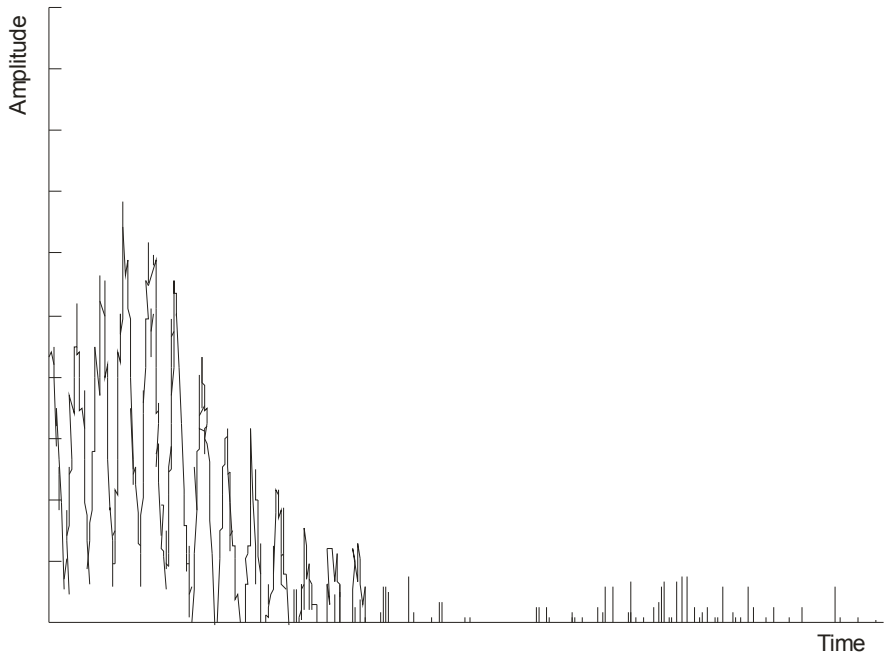

Figure A.1.- Captured signal bursts from particles passing through the center and edge of a laser velocimeter measurement volume.

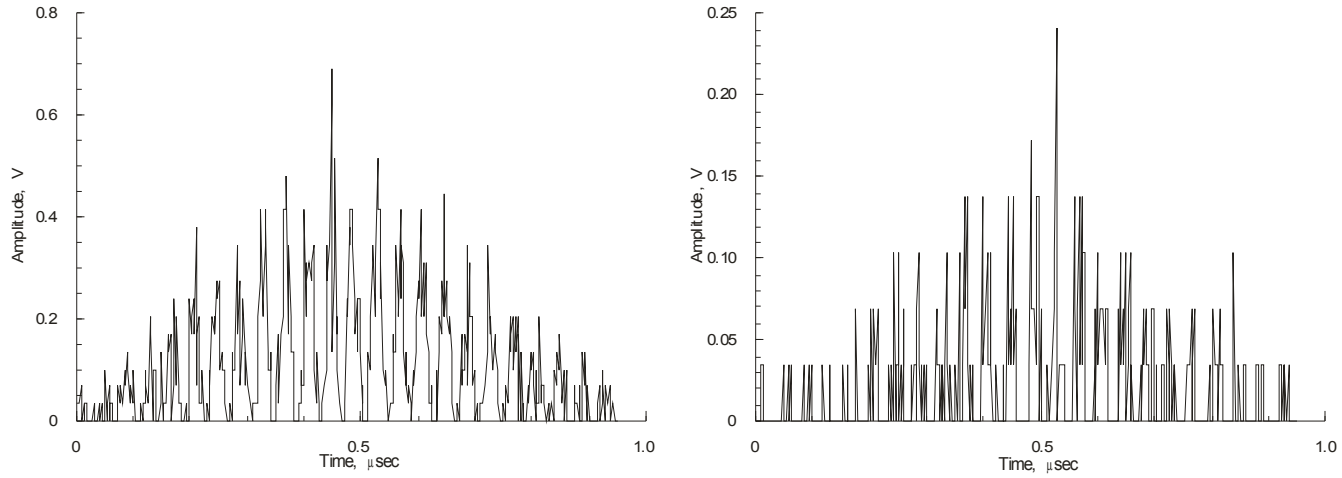

Figure A.2.- Simulated signal bursts from particles passing through the center and edge of a laser velocimeter measurement volume.

Figure A.3.- Opening data entry screen for the Monte Carlo simulation of a two-component, fringe-type laser velocimeter.

Figure A.4.- Data entry screen for the characteristics of the transmission optics for a two-component, fringe-type laser velocimeter.

Figure A.5.- Data entry screen for the characteristics of the receiver optics for a two-component, fringe-type laser velocimeter.

Figure A.6.- Data entry screen for the characteristics of the seeding particles and the flow field along with plotting and storage parameters for the Monte Carlo simulation of a two-component, fringe-type laser velocimeter.

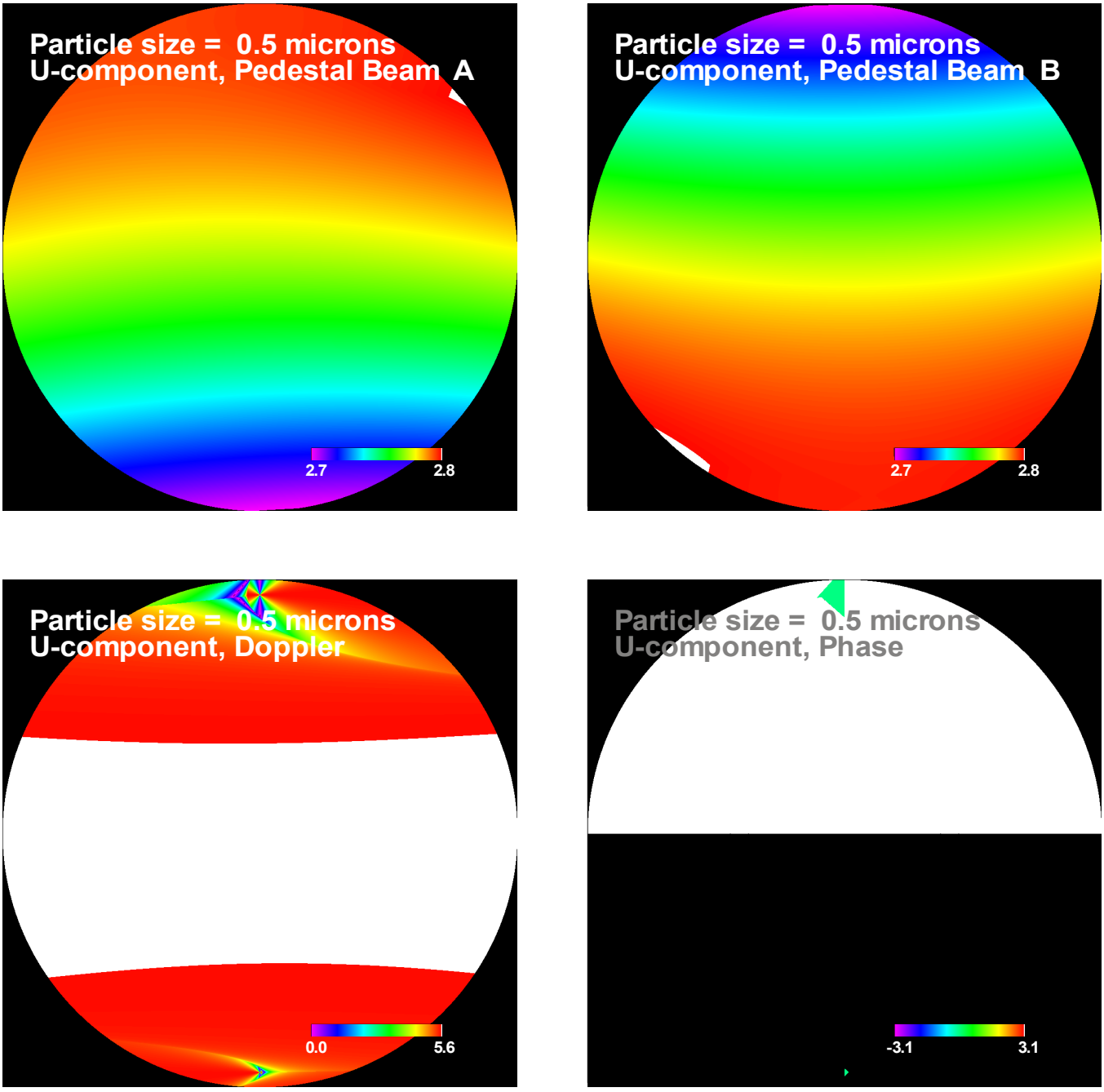

Figure A.7.a.- Mie scattering maps of pedestal amplitude for both laser beams, Doppler signal amplitude, and phase angle for the U-component and a 0.5-micron particle.

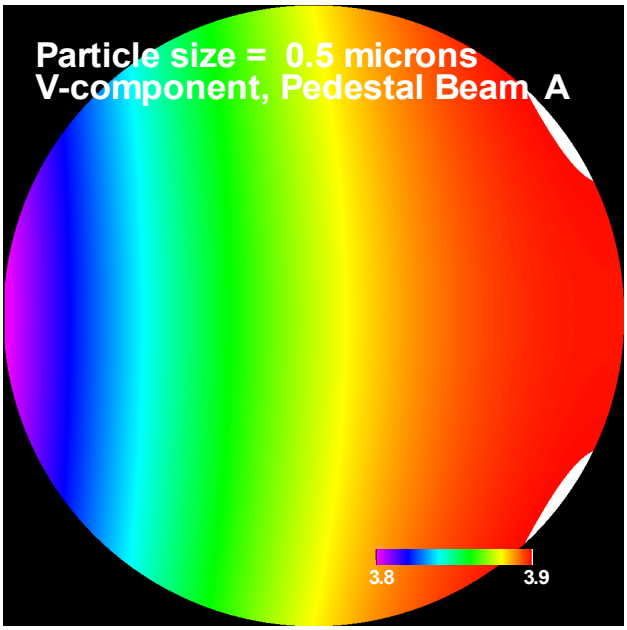

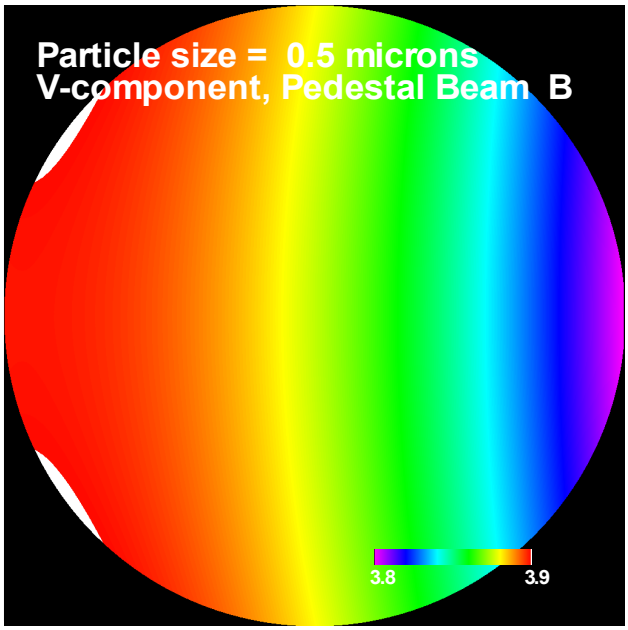

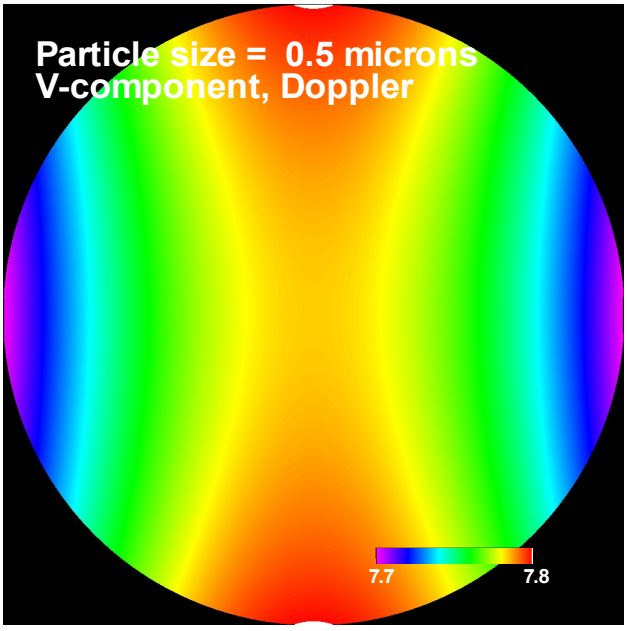

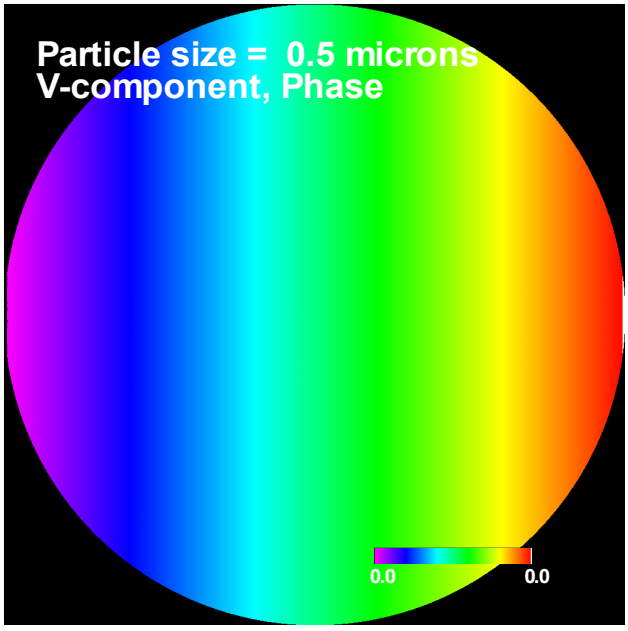

Figure A.7.b.- Mie scattering maps of pedestal amplitude for both laser beams, Doppler signal amplitude, and phase angle for the V-component and a 0.5-micron particle.

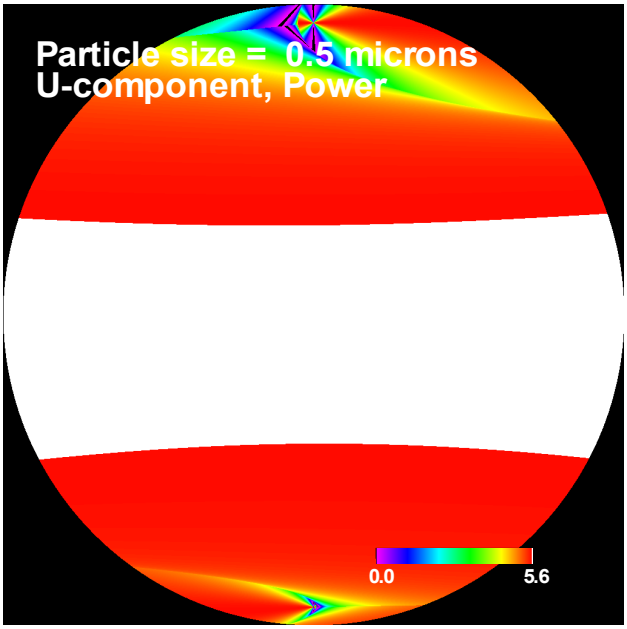

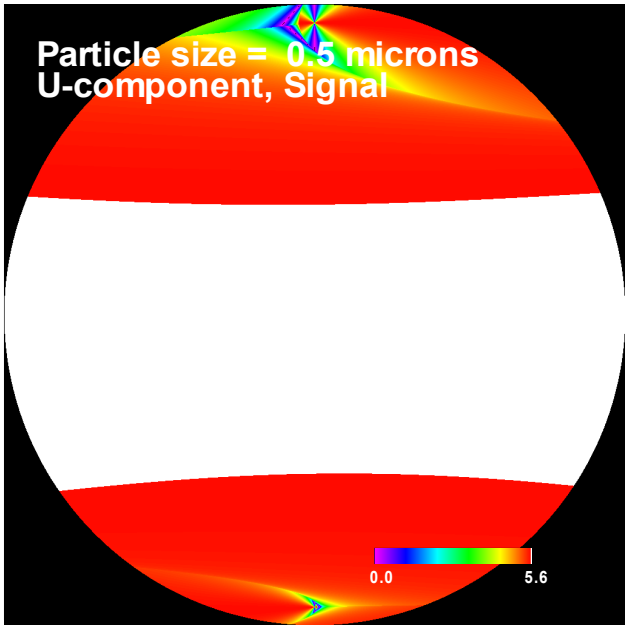

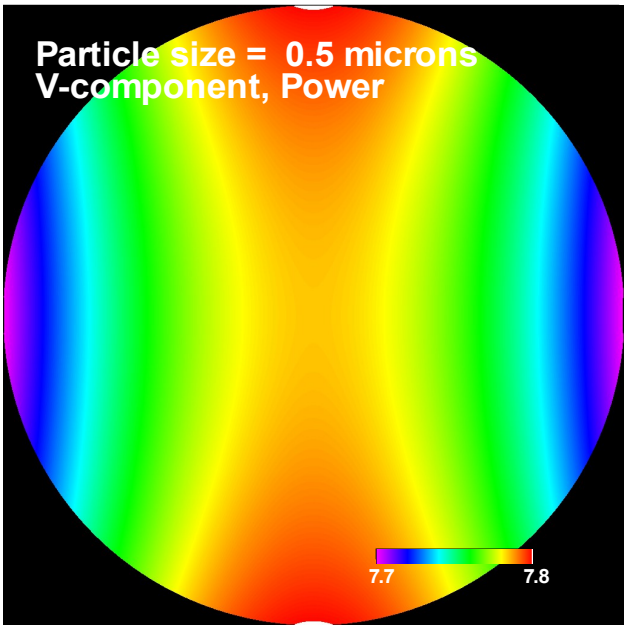

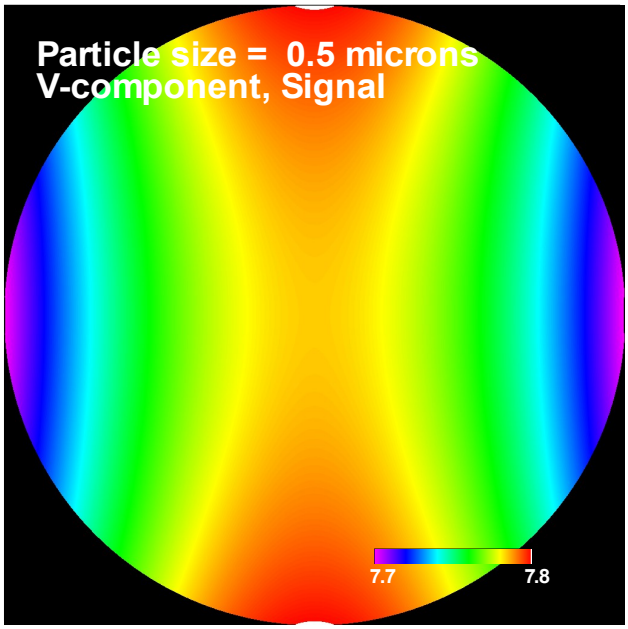

Figure A.7.c.- Mie scattering maps of optical power and signal levels for the U- and V-components from a 0.5-micron particle.

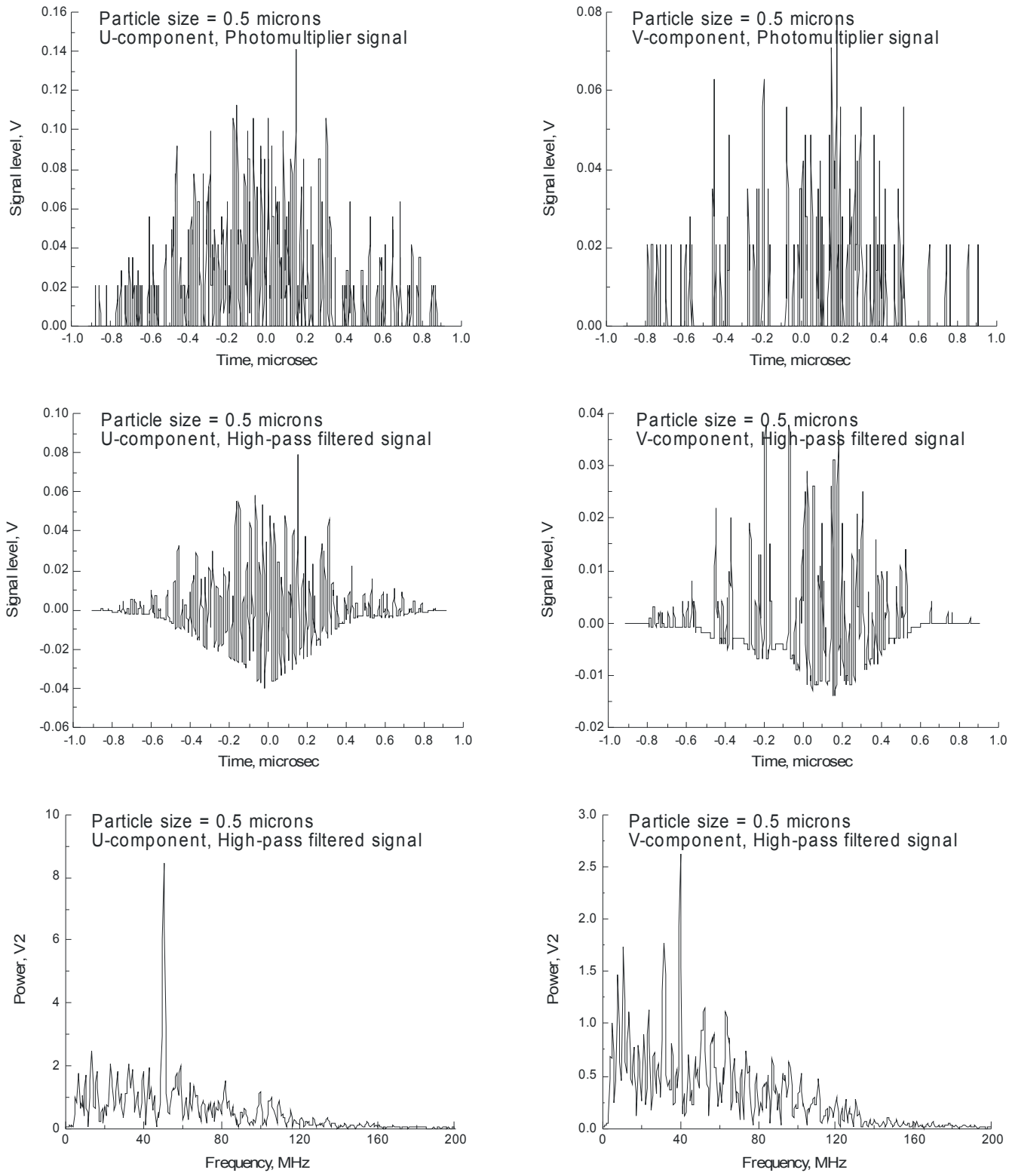

Figure A.7.d.- High-pass filtered U- and V-component signals in the time and frequency domains.

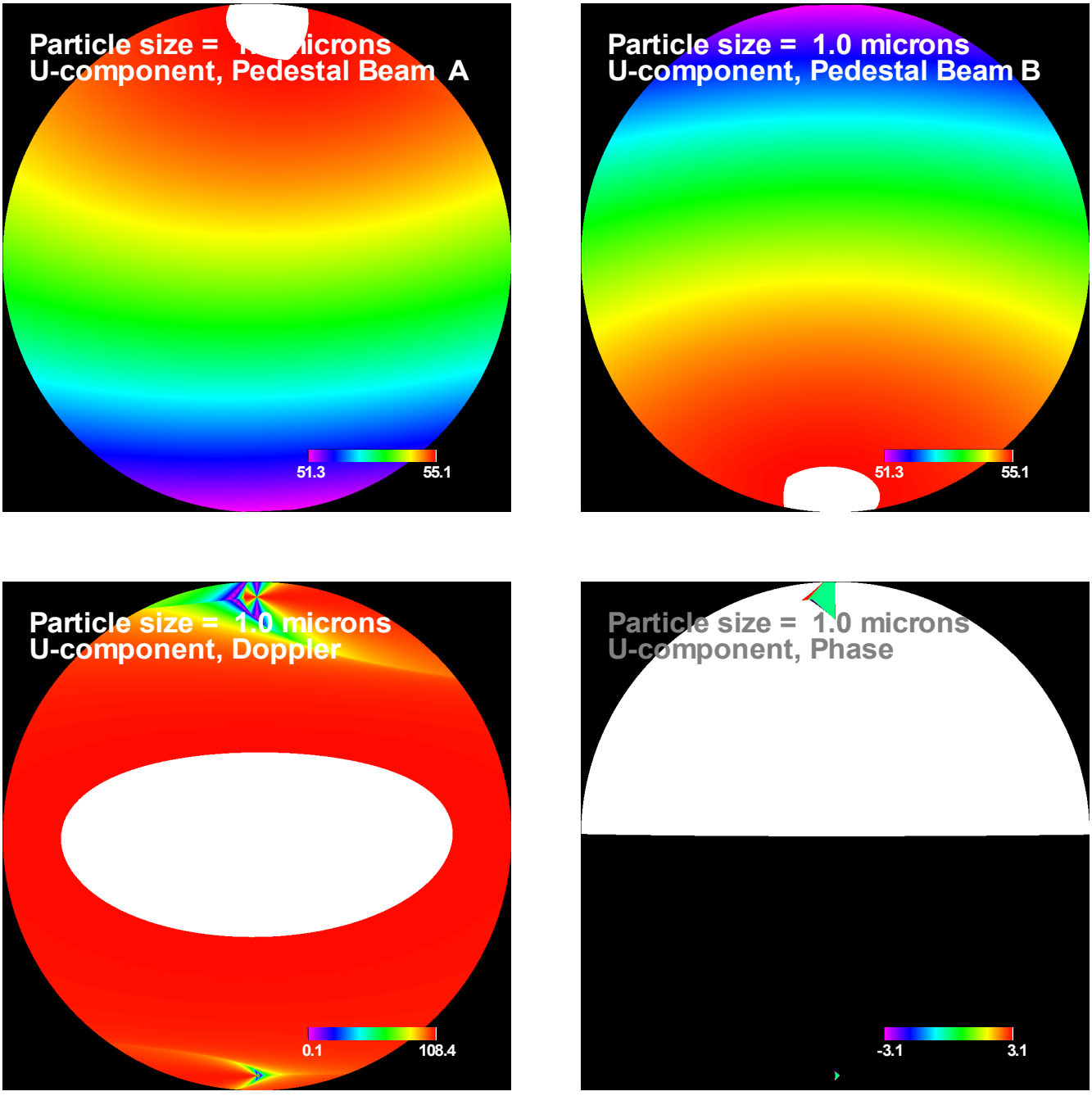

Figure A.8.a.- Mie scattering maps of pedestal amplitude for both laser beams, Doppler signal amplitude, and phase angle for the U-component and a 1.0-micron particle.

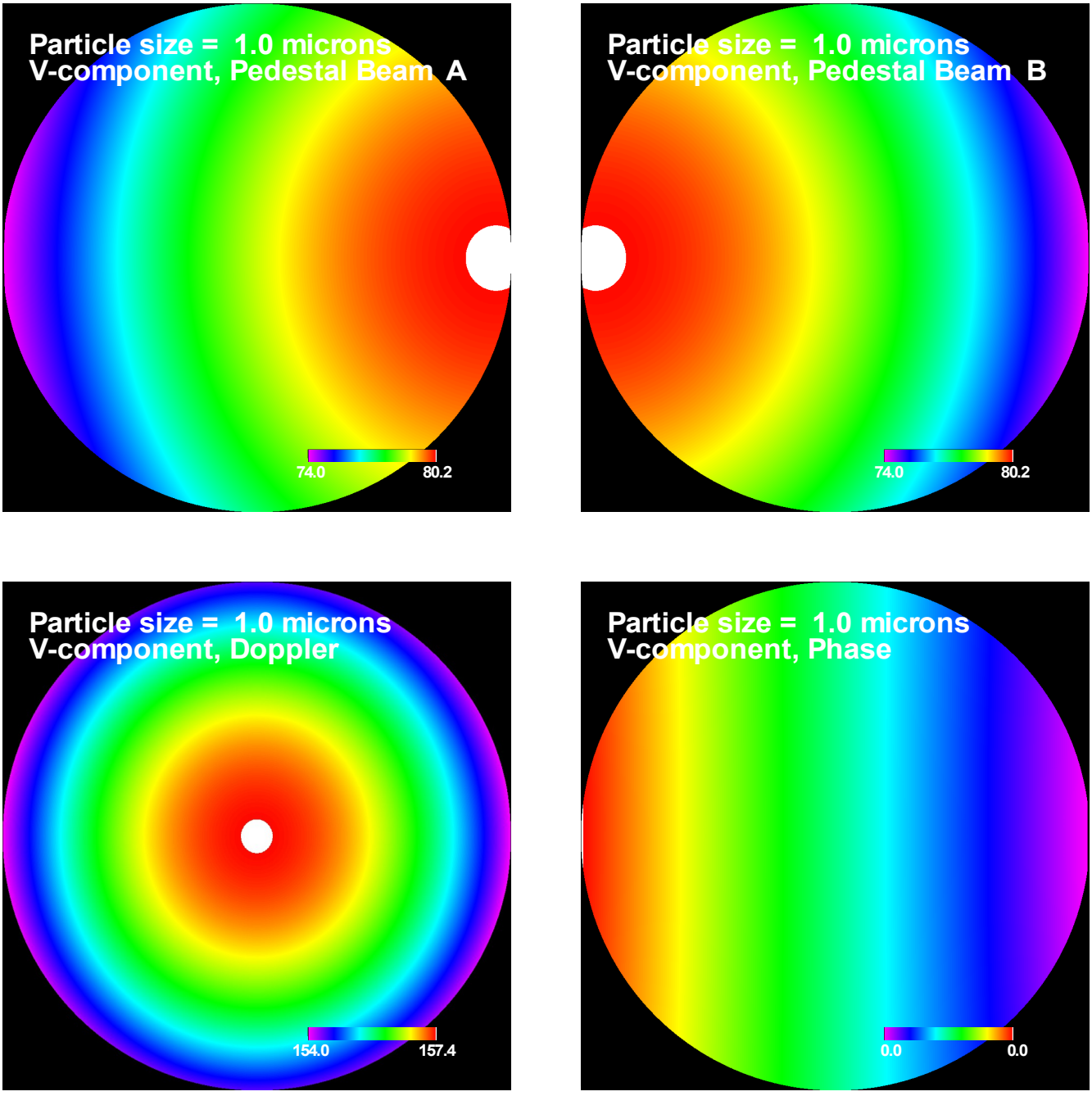

Figure A.8.b.- Mie scattering maps of pedestal amplitude for both laser beams, Doppler signal amplitude, and phase angle for the V-component and a 1.0-micron particle.

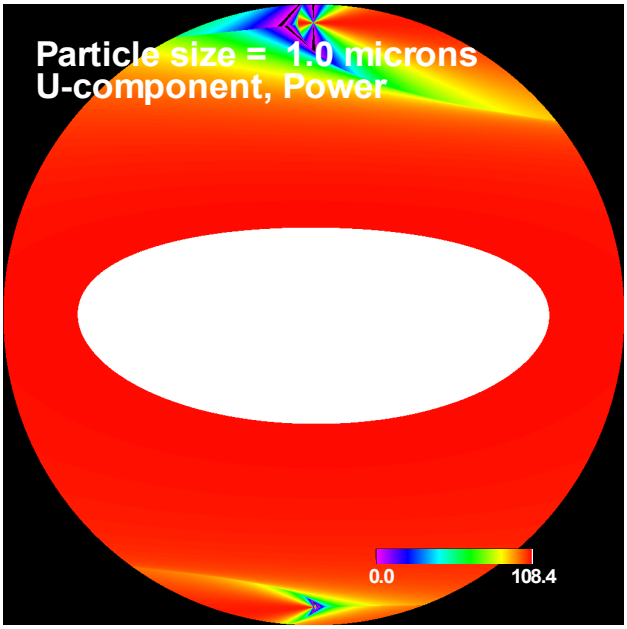

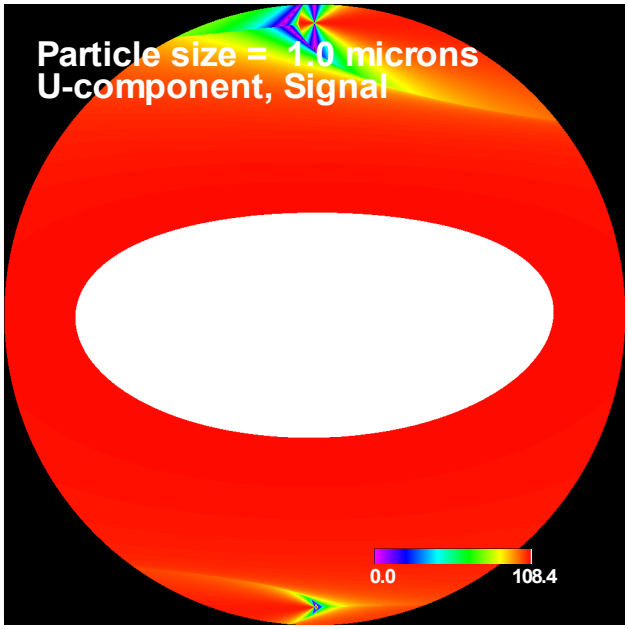

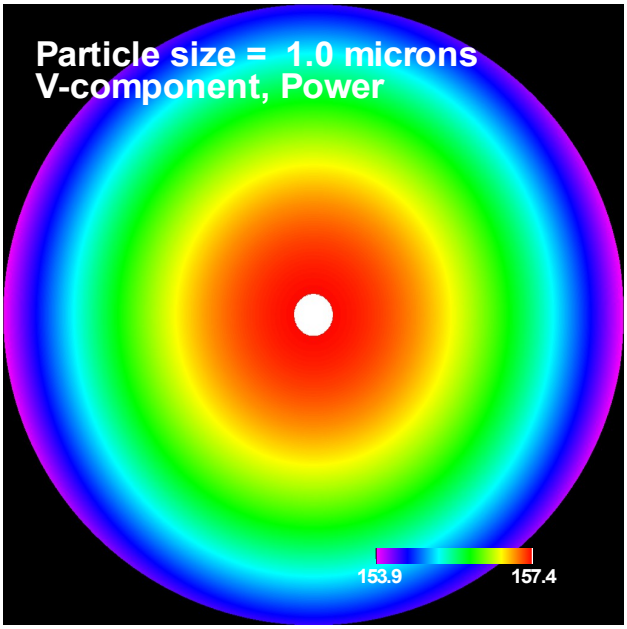

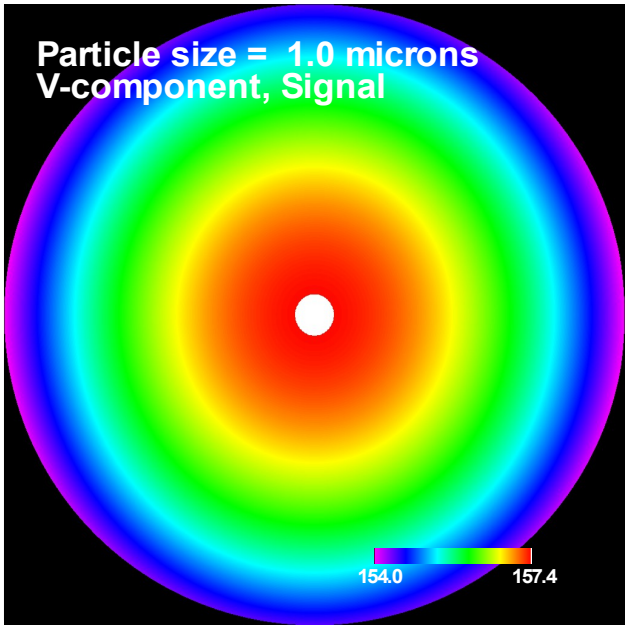

Figure A.8.c.- Mie scattering maps of optical power and signal levels for the U- and V-components from a 1.0-micron particle.

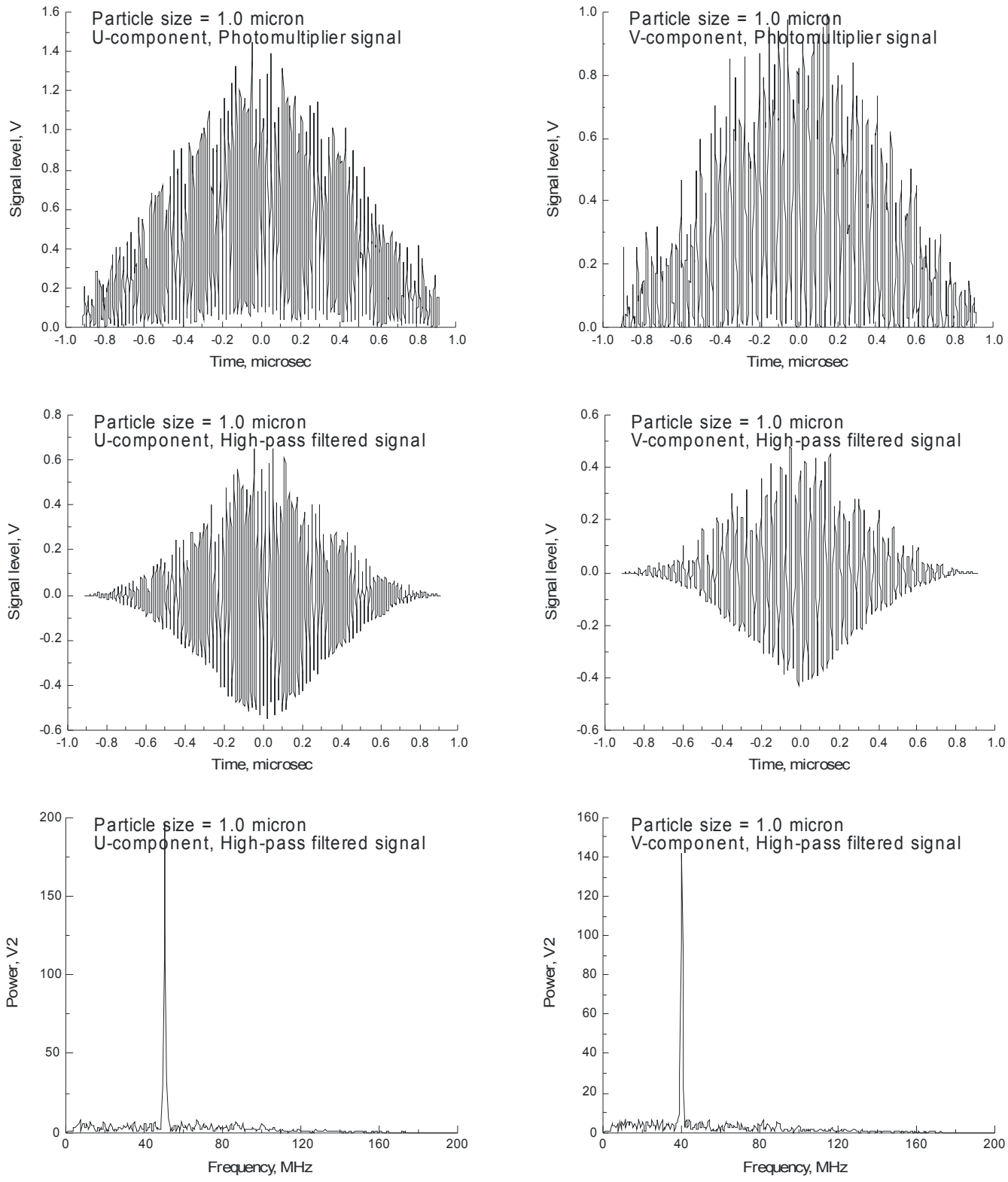

Figure A.8.d.- High-pass filtered U- and V-component signals in the time and frequency domains.

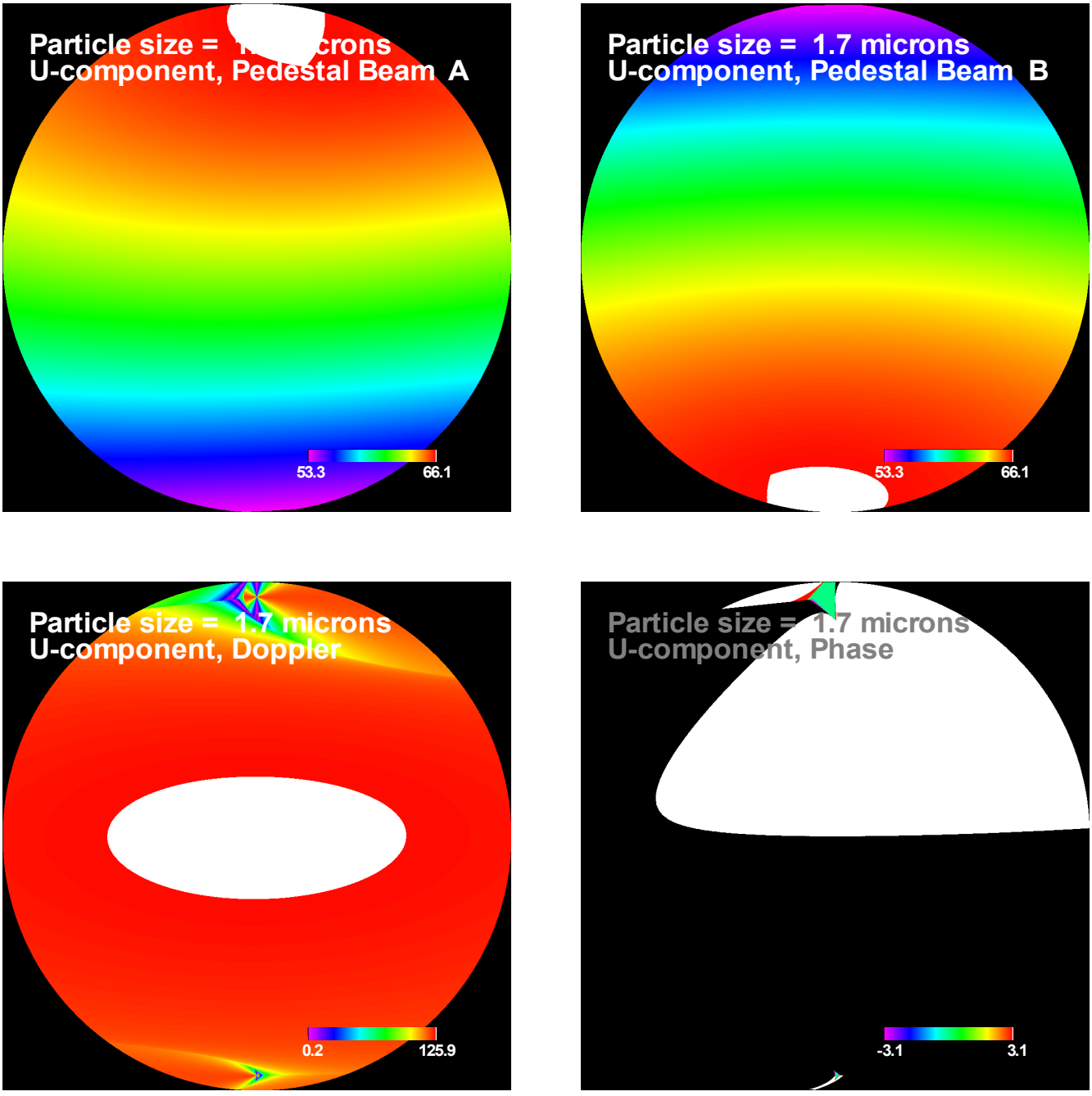

Figure A.9.a.- Mie scattering maps of pedestal amplitude for both laser beams, Doppler signal amplitude, and phase angle for the U-component and a 1.7-micron particle.

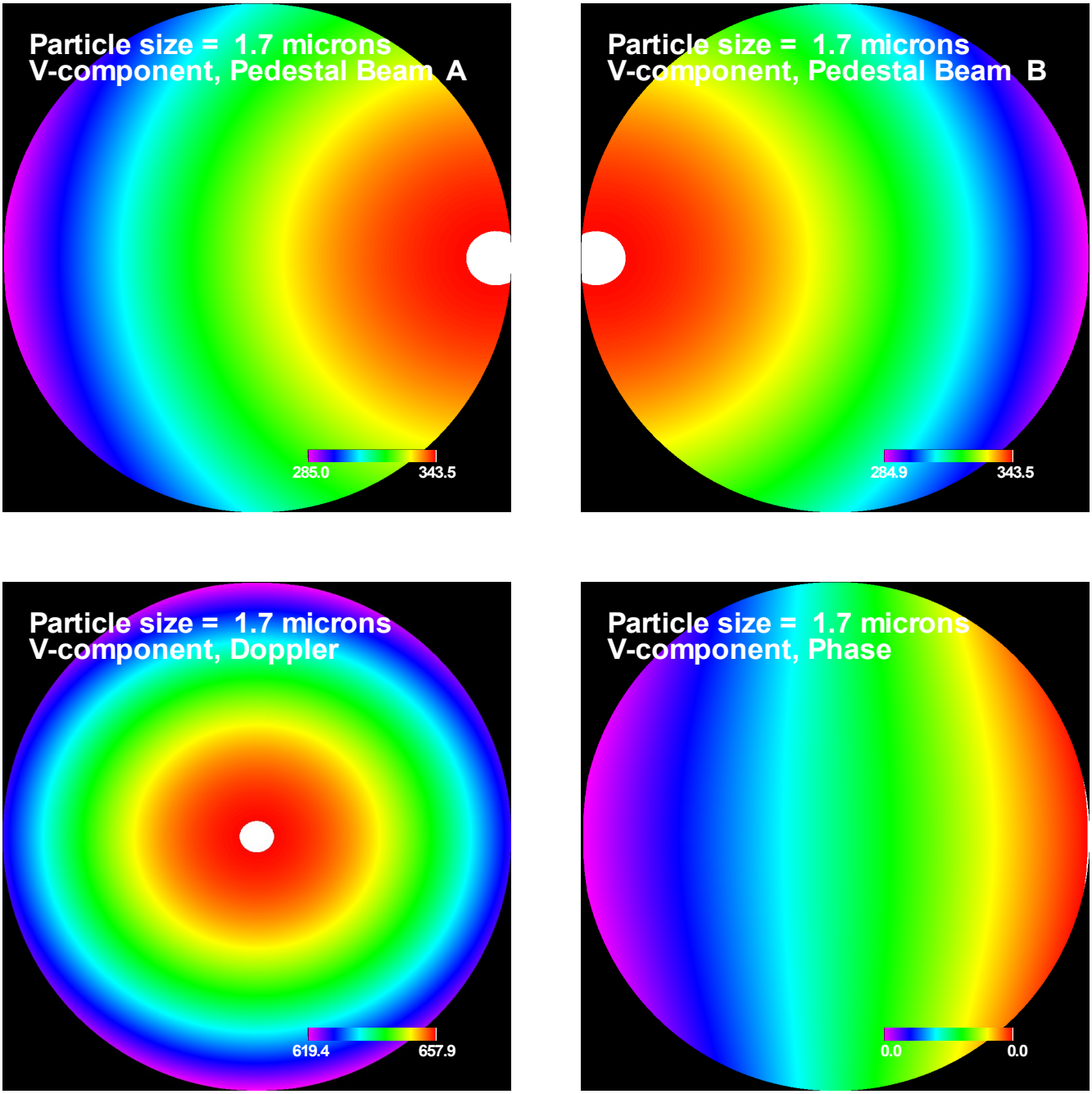

Figure A.9.b.- Mie scattering maps of pedestal amplitude for both laser beams, Doppler signal amplitude, and phase angle for the V-component and a 1.7-micron particle.

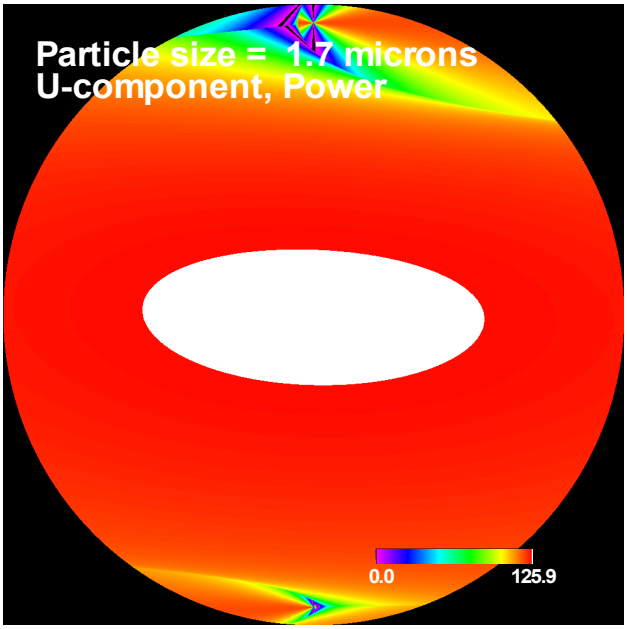

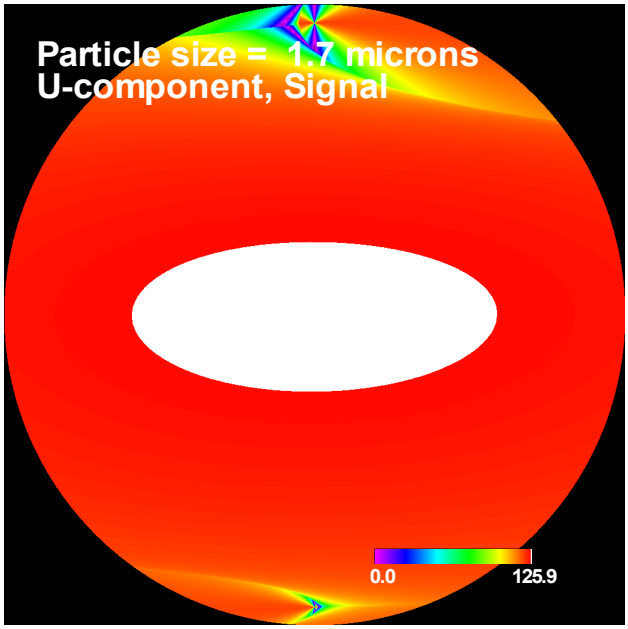

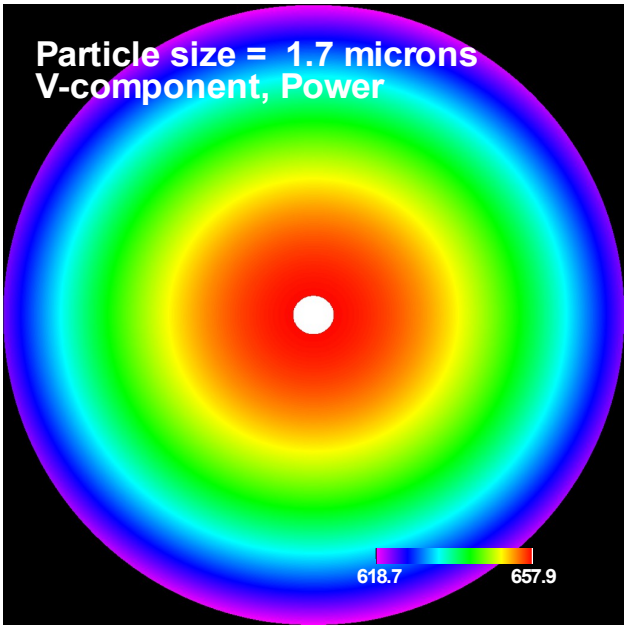

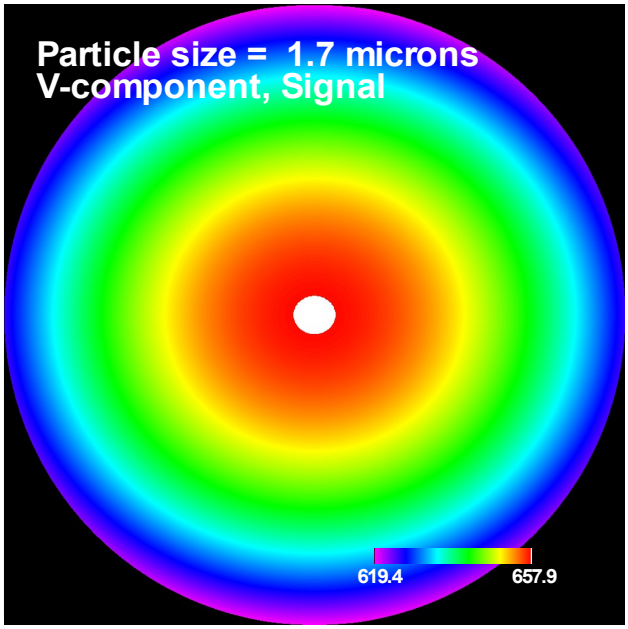

Figure A.9.c.- Mie scattering maps of optical power and signal levels for the U- and V-components from a 1.7-micron particle.

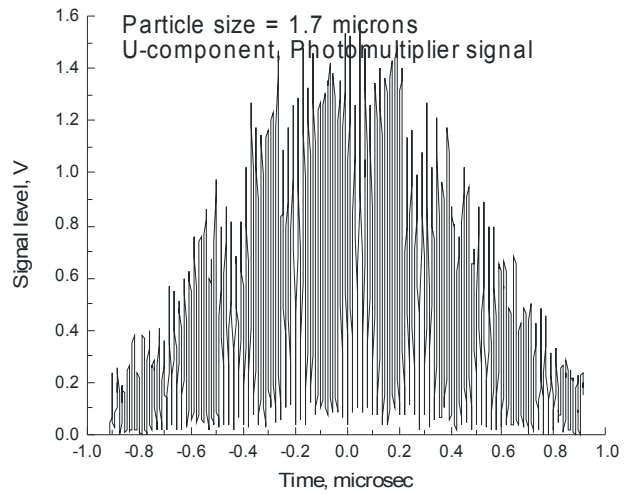

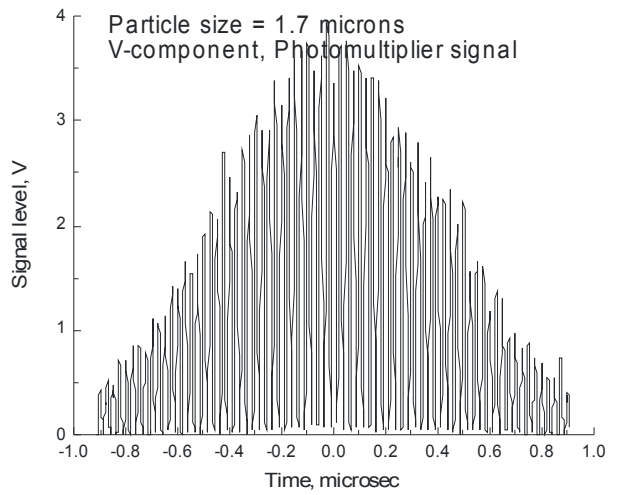

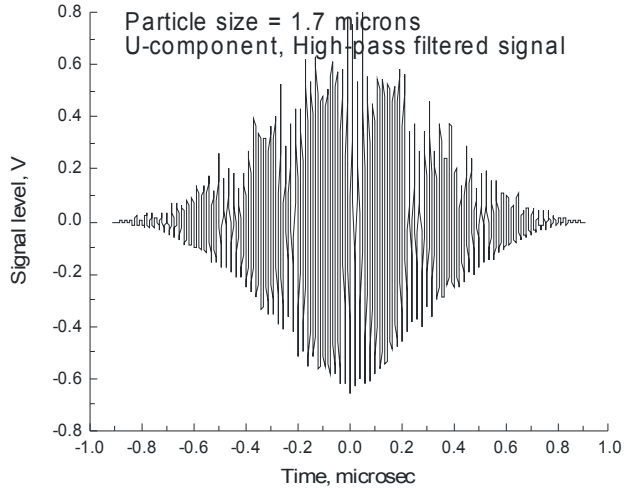

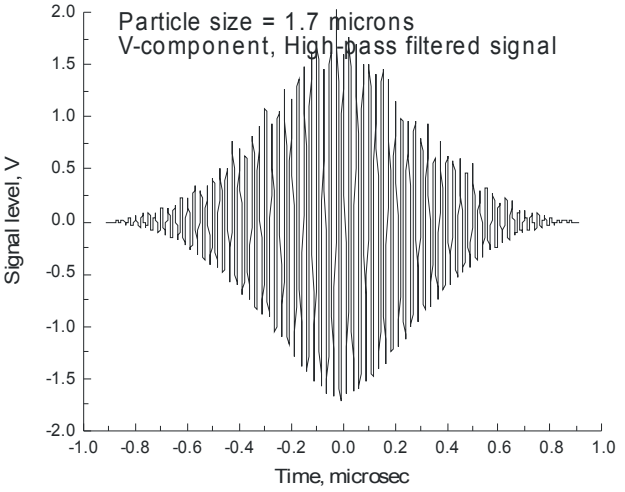

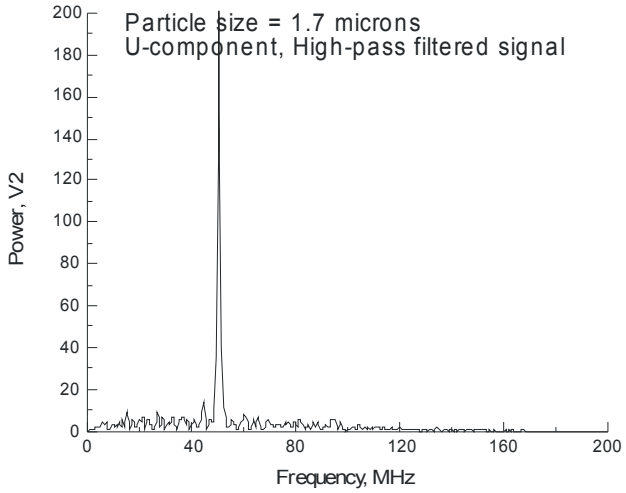

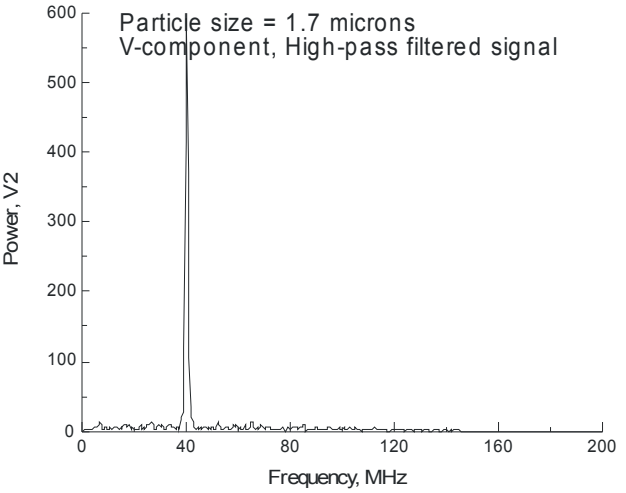

Figure A.9.d.- High-pass filtered U- and V-component signals in the time and frequency domains.

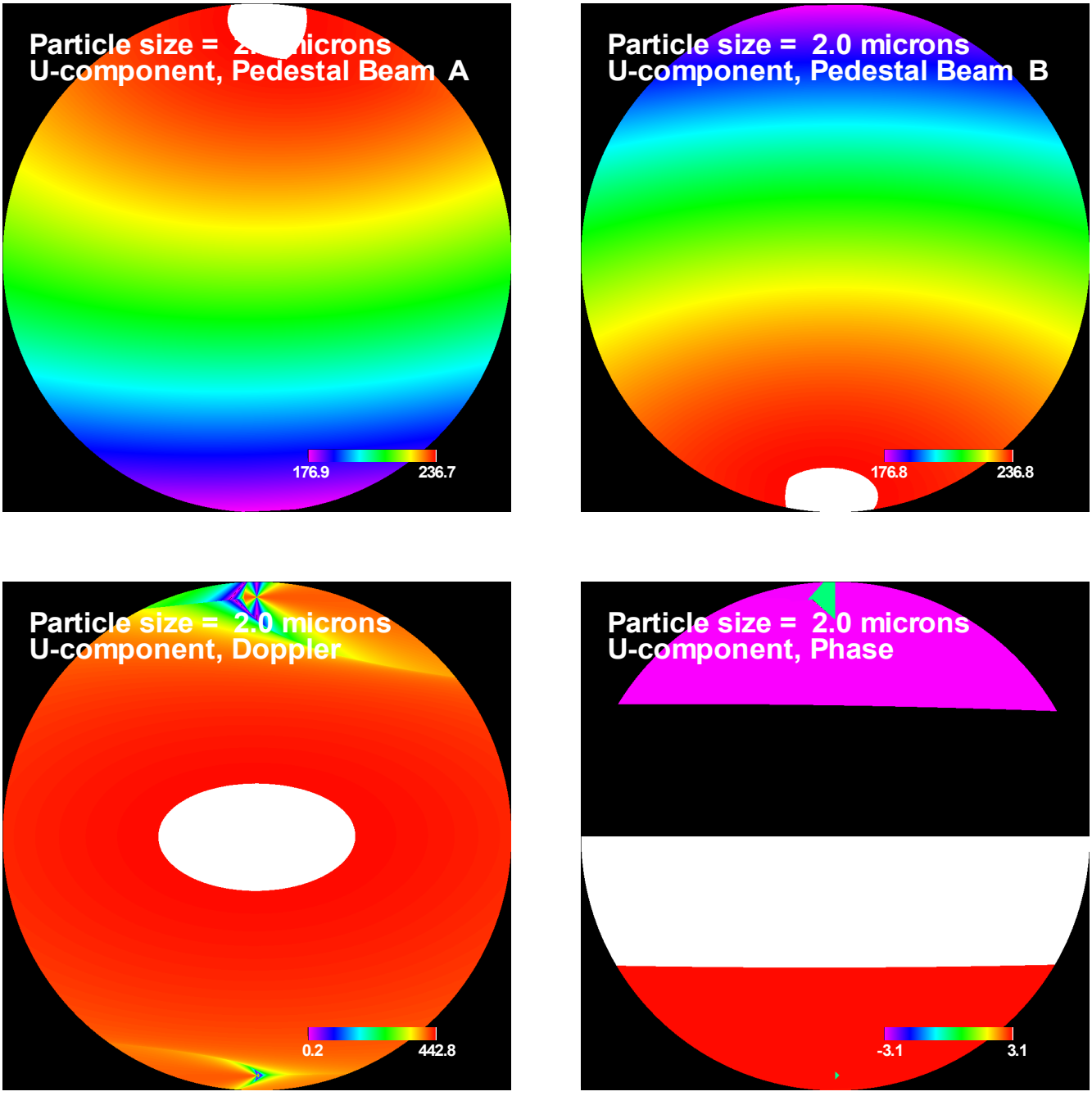

Figure A.10.a.- Mie scattering maps of pedestal amplitude for both laser beams, Doppler signal amplitude, and phase angle for the U-component and a 2.0-micron particle.

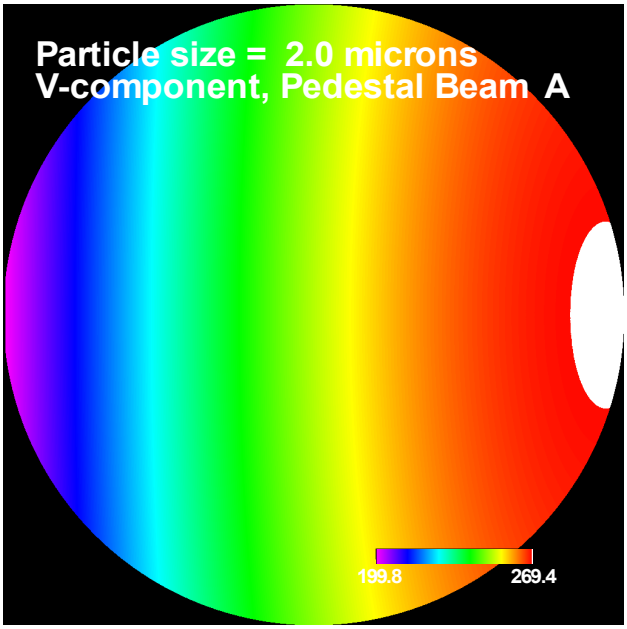

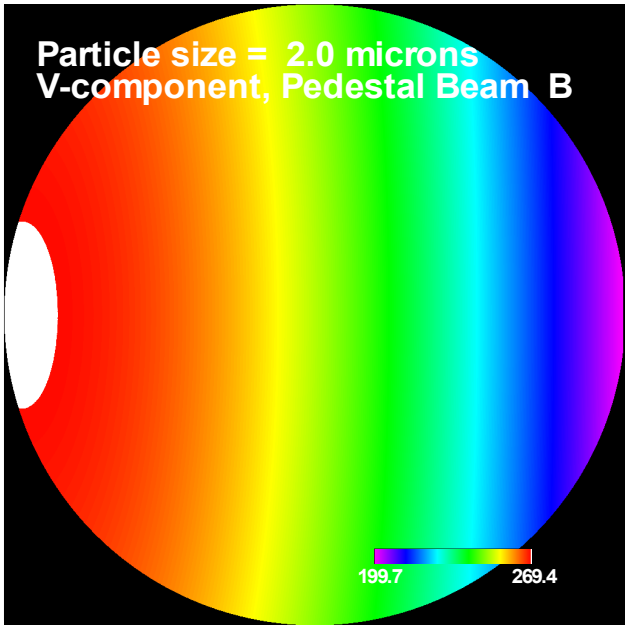

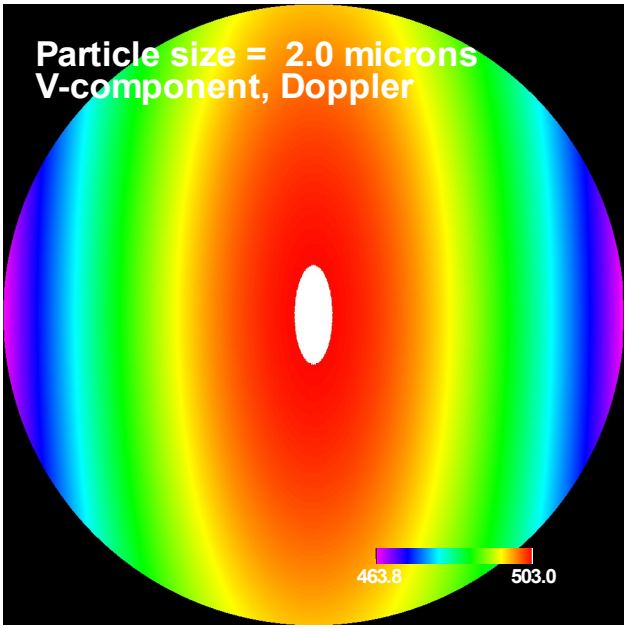

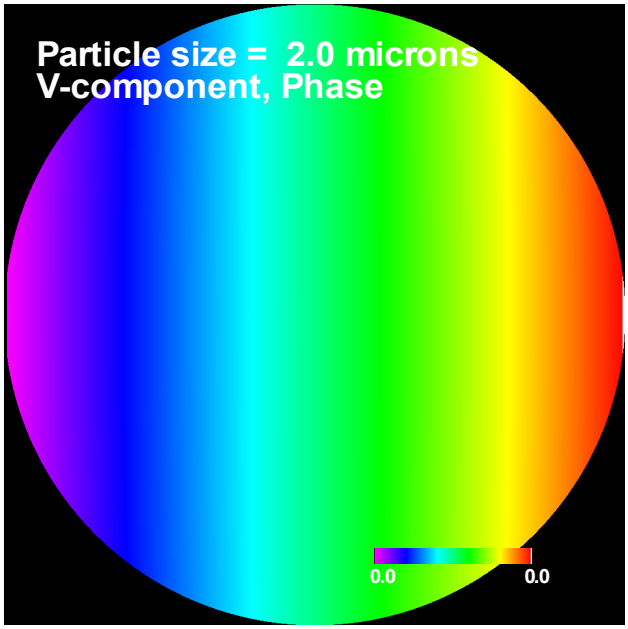

Figure A.10.b.- Mie scattering maps of pedestal amplitude for both laser beams, Doppler signal amplitude, and phase angle for the V-component and a 2.0-micron particle.

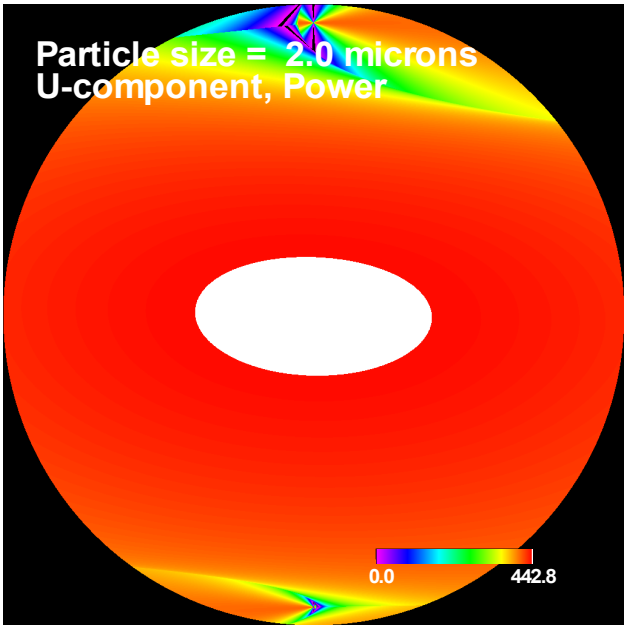

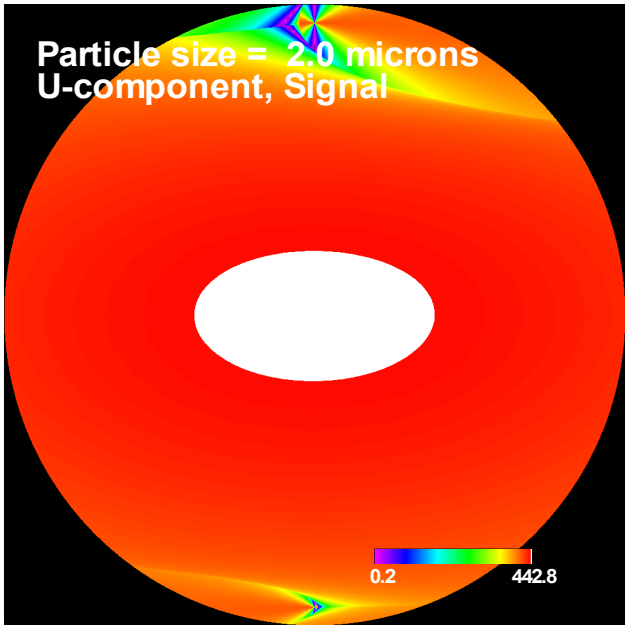

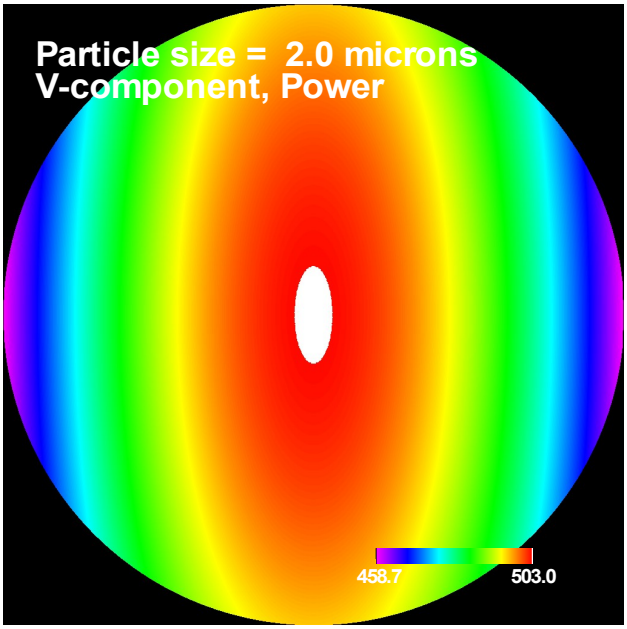

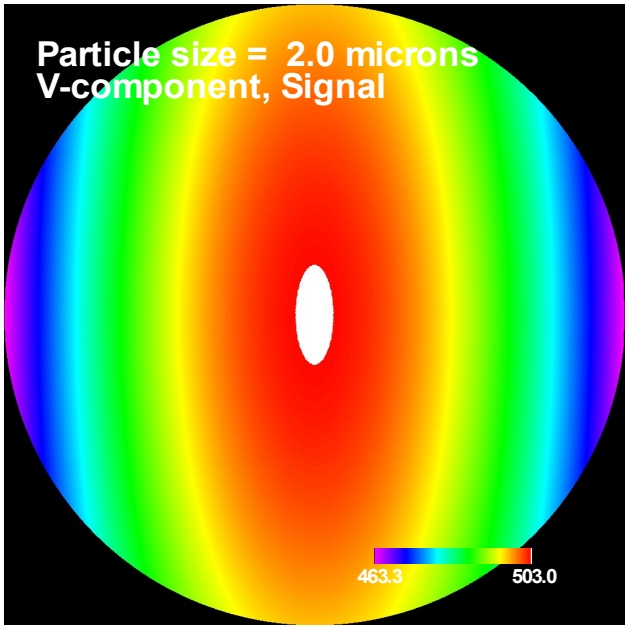

Figure A.10.c.- Mie scattering maps of optical power and signal levels for the U- and V-components from a 2.0-micron particle.

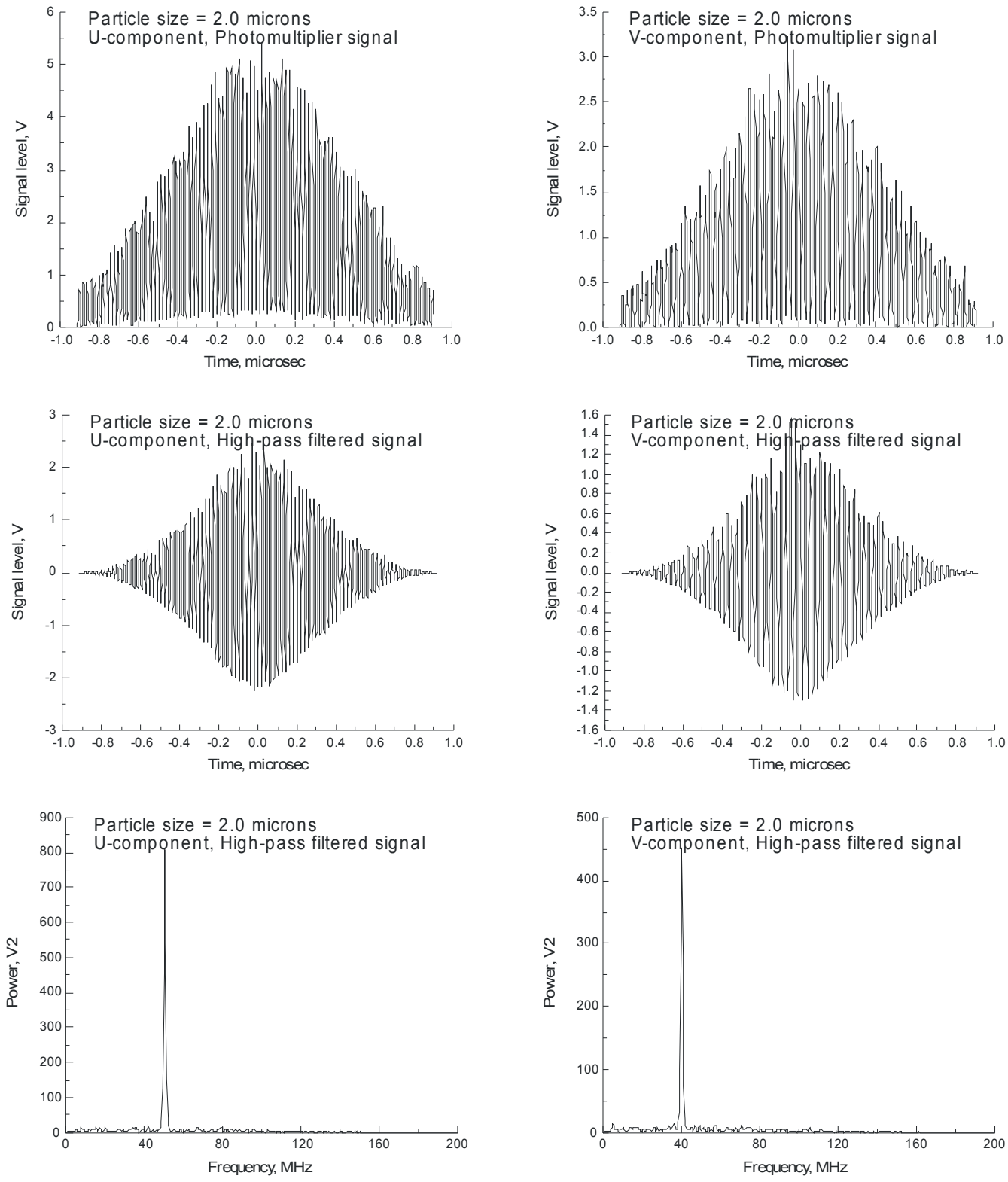

Figure A.10.d.- High-pass filtered U- and V-component signals in the time and frequency domains.

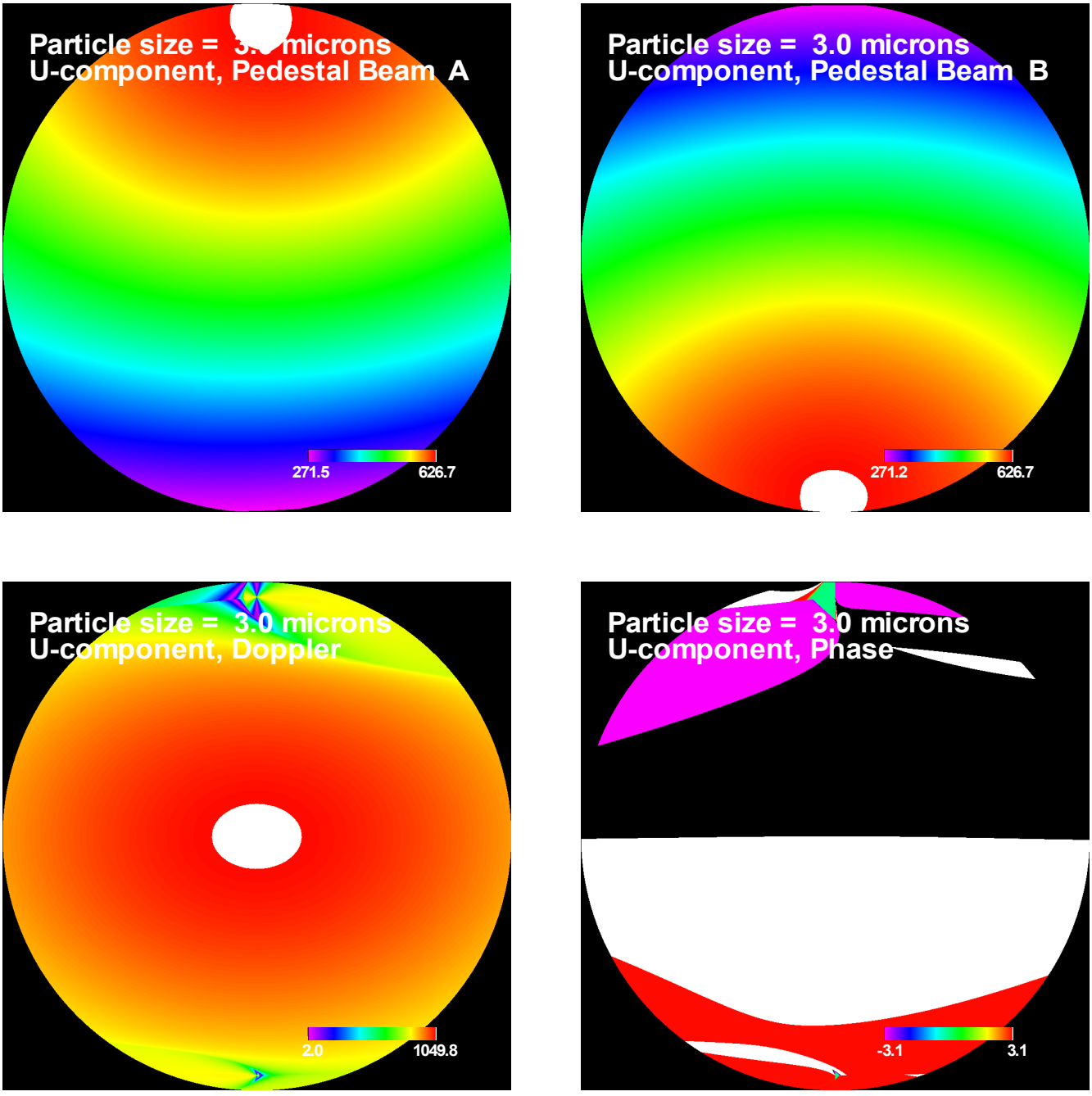

Figure A.11.a.- Mie scattering maps of pedestal amplitude for both laser beams, Doppler signal amplitude, and phase angle for the U-component and a 3.0-micron particle.

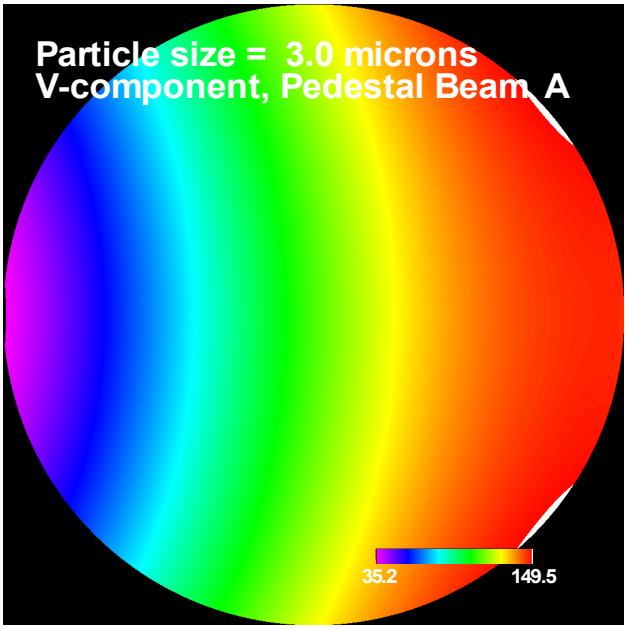

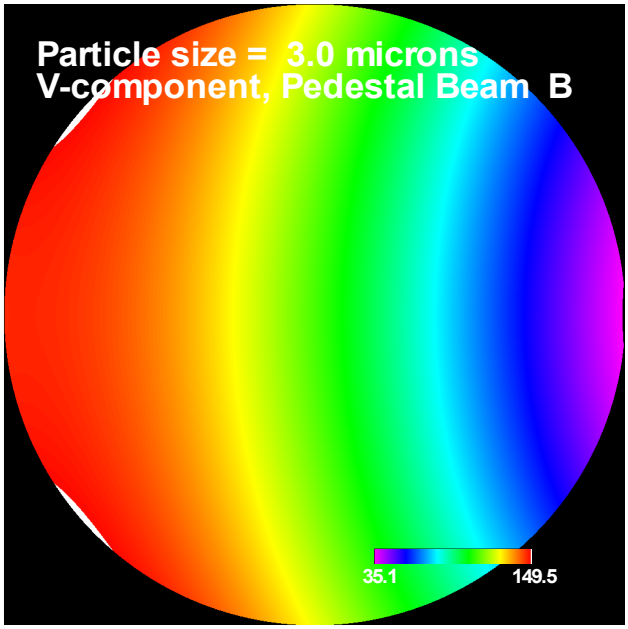

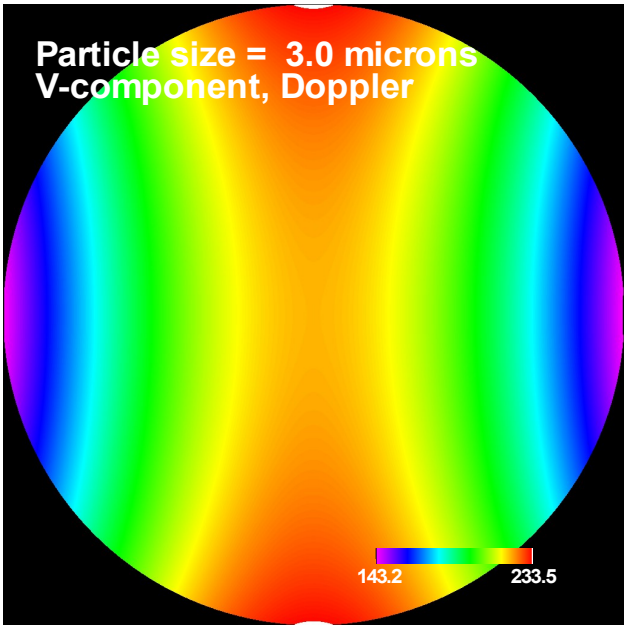

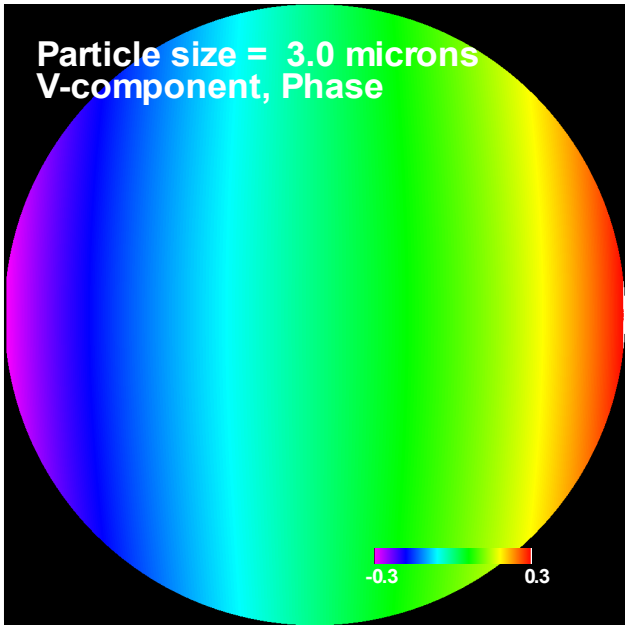

Figure A.11.b.- Mie scattering maps of pedestal amplitude for both laser beams, Doppler signal amplitude, and phase angle for the V-component and a 3.0-micron particle.

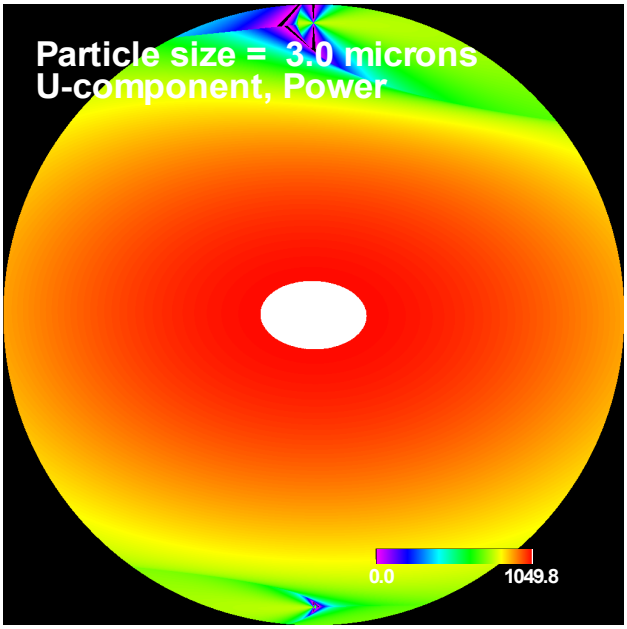

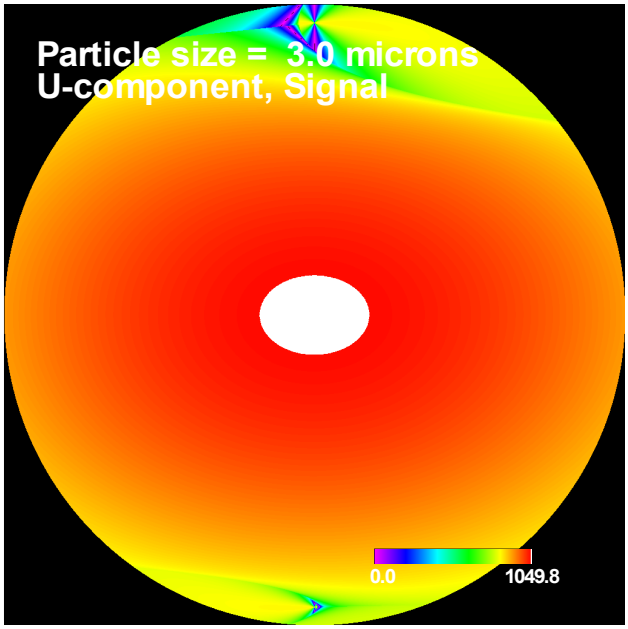

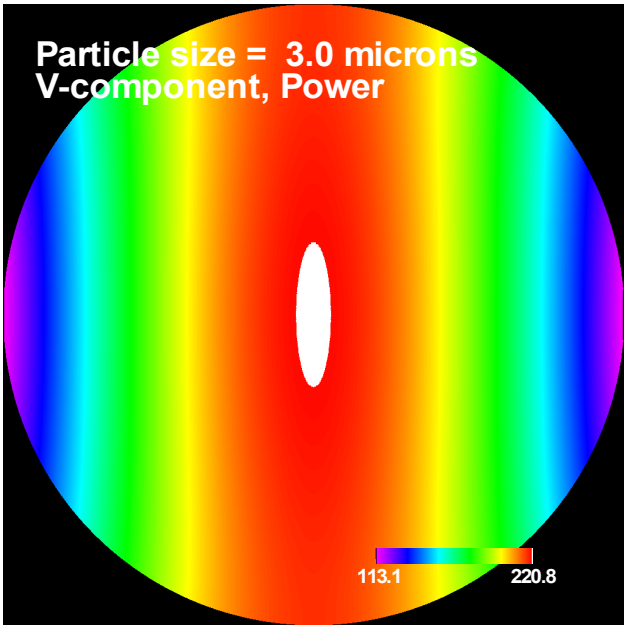

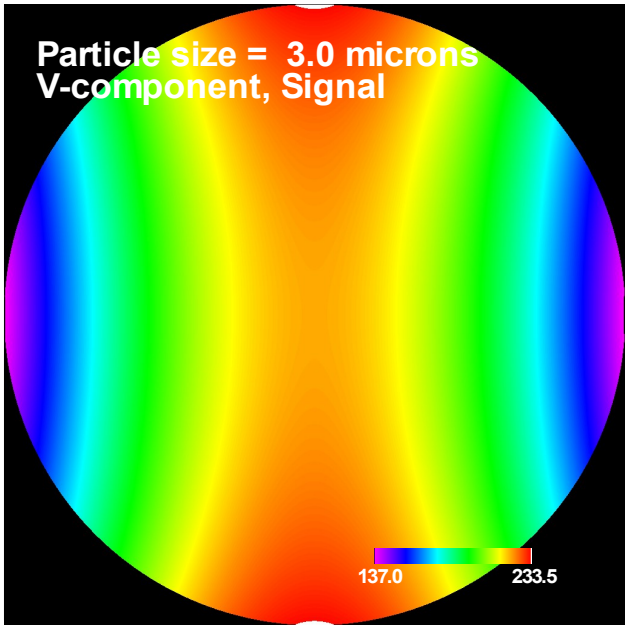

Figure A.11.c.- Mie scattering maps of optical power and signal levels for the U- and V-components from a 3.0-micron particle.

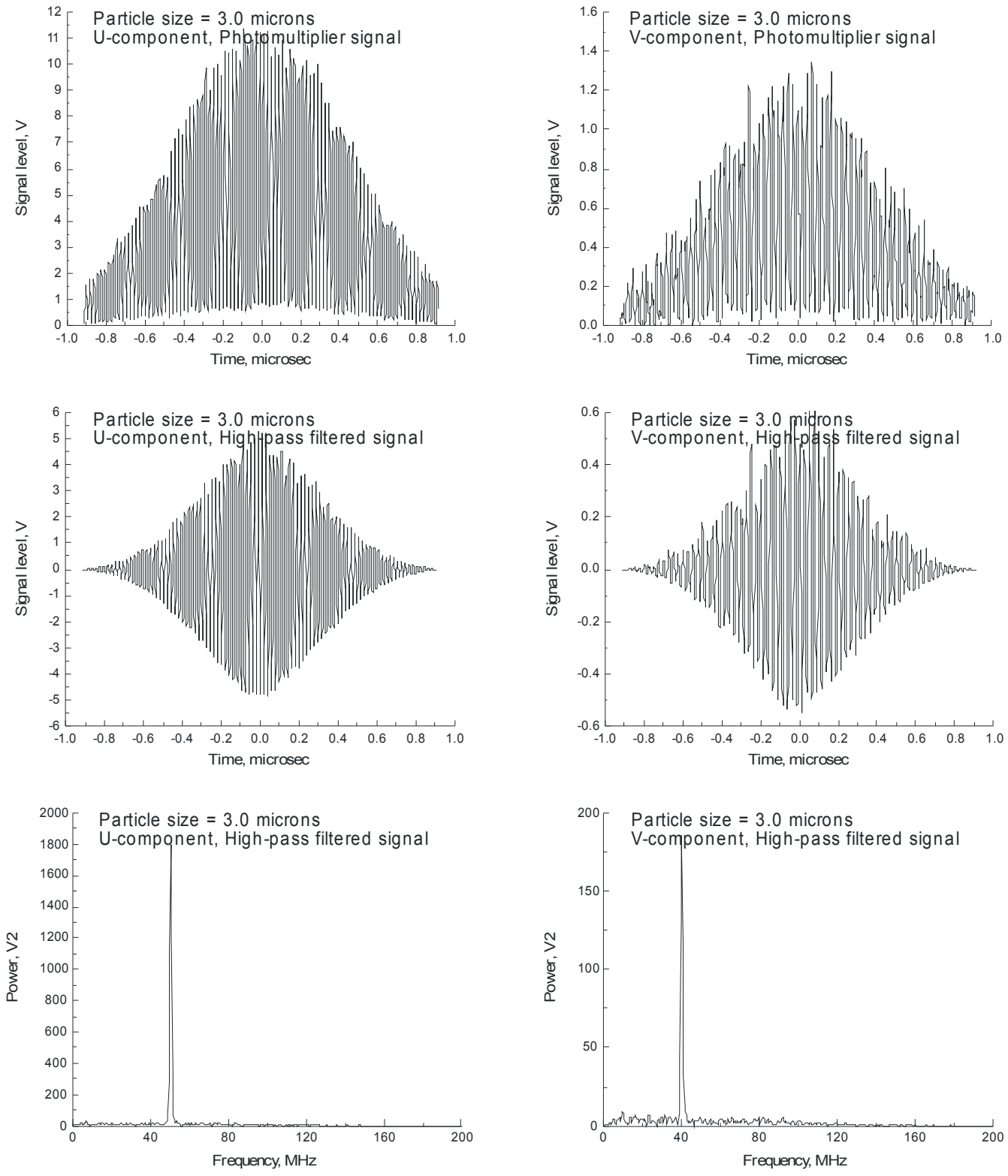

Figure A.11.d.- High-pass filtered U- and V-component signals in the time and frequency domains.

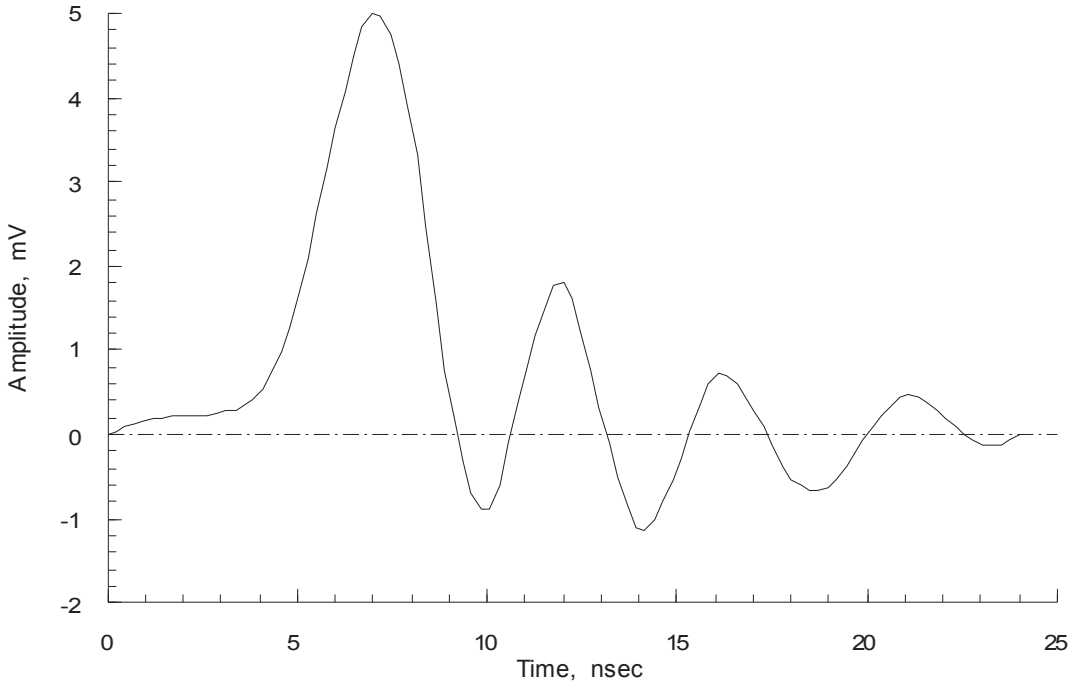

Figure A.12.- Photomultiplier output from a single photon as captured on an analog oscilloscope with 50-ohm termination.

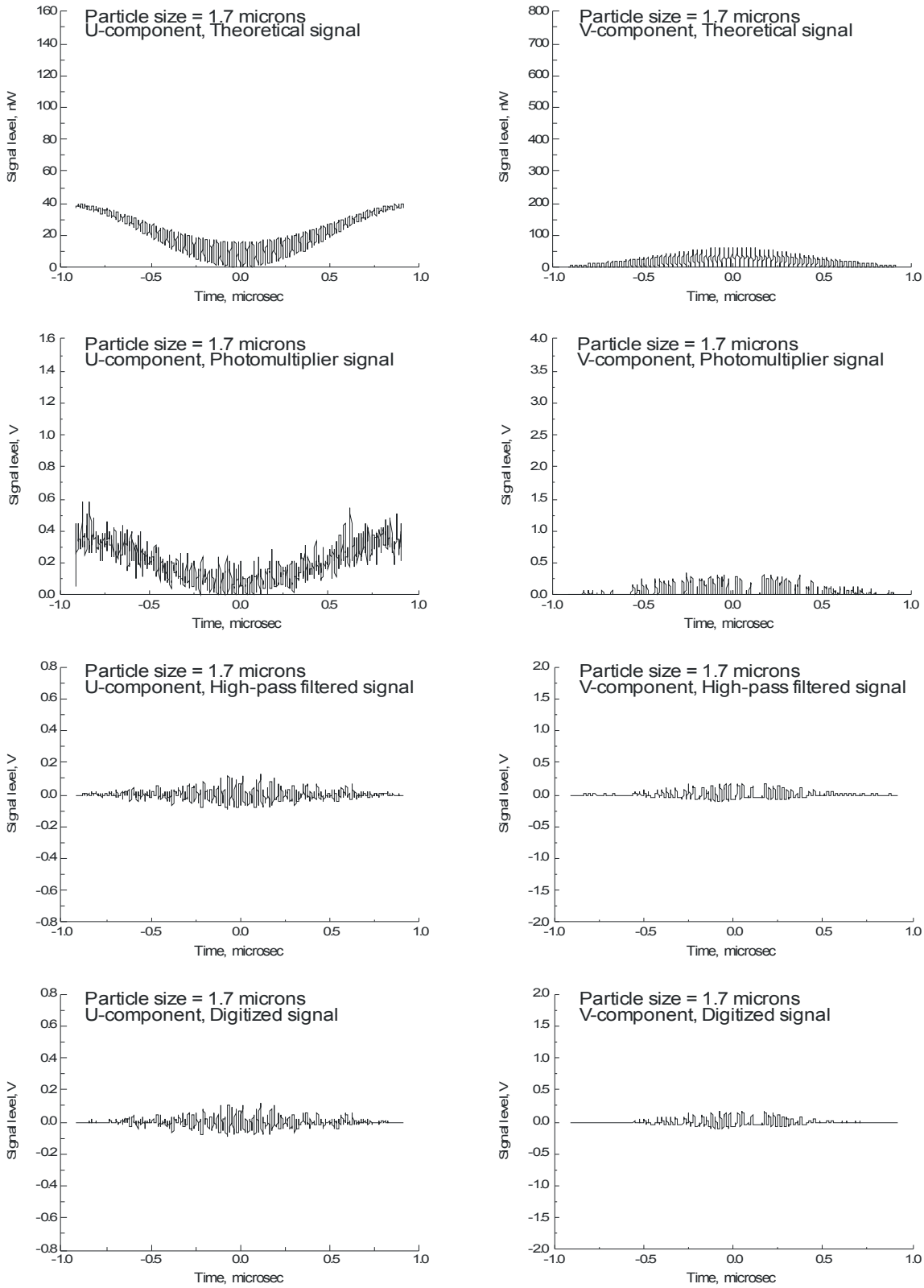

Error U: 0.14 m/s, no measurement

Error V: 0.0 m/s, no measurement

Figure A.13.- Signals obtained at on-axis = -0.75 L_{mv}, Histogram 5, True Half Power processing.

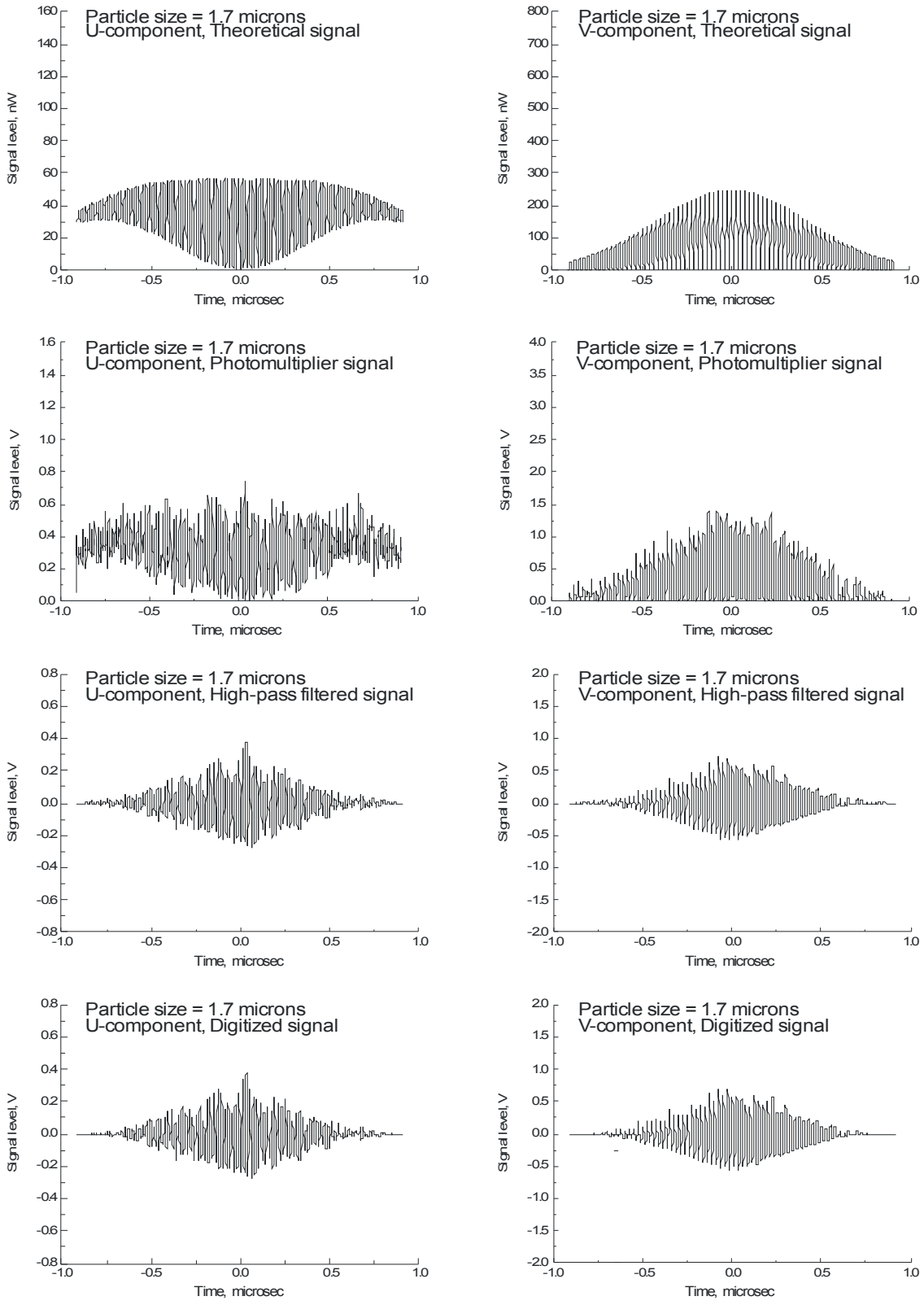

Error U: 0.07 m/s, 0.25 m/s

Error V: 0.16 m/s, 0.22 m/s

Figure A.14.- Signals obtained at on-axis = -0.5 L_{mv}, Histogram 5, True Half Power processing.

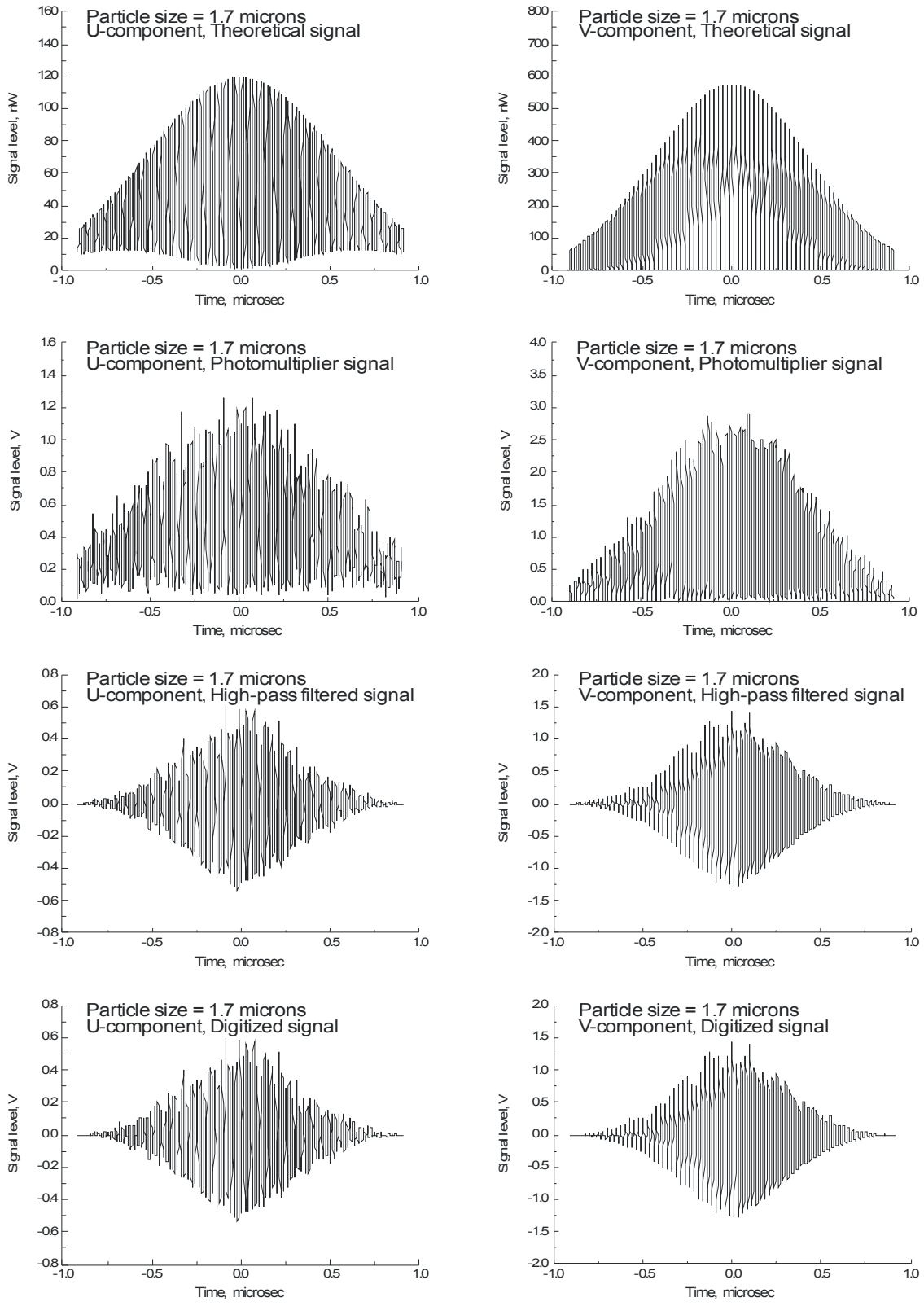

Error U: 0.32 m/s, 0.05 m/s

Error V: -0.07 m/s, 0.25 m/s

Figure A.15.- Signals obtained at on-axis = -0.25 L_{mv}, Histogram 5, True Half Power processing.

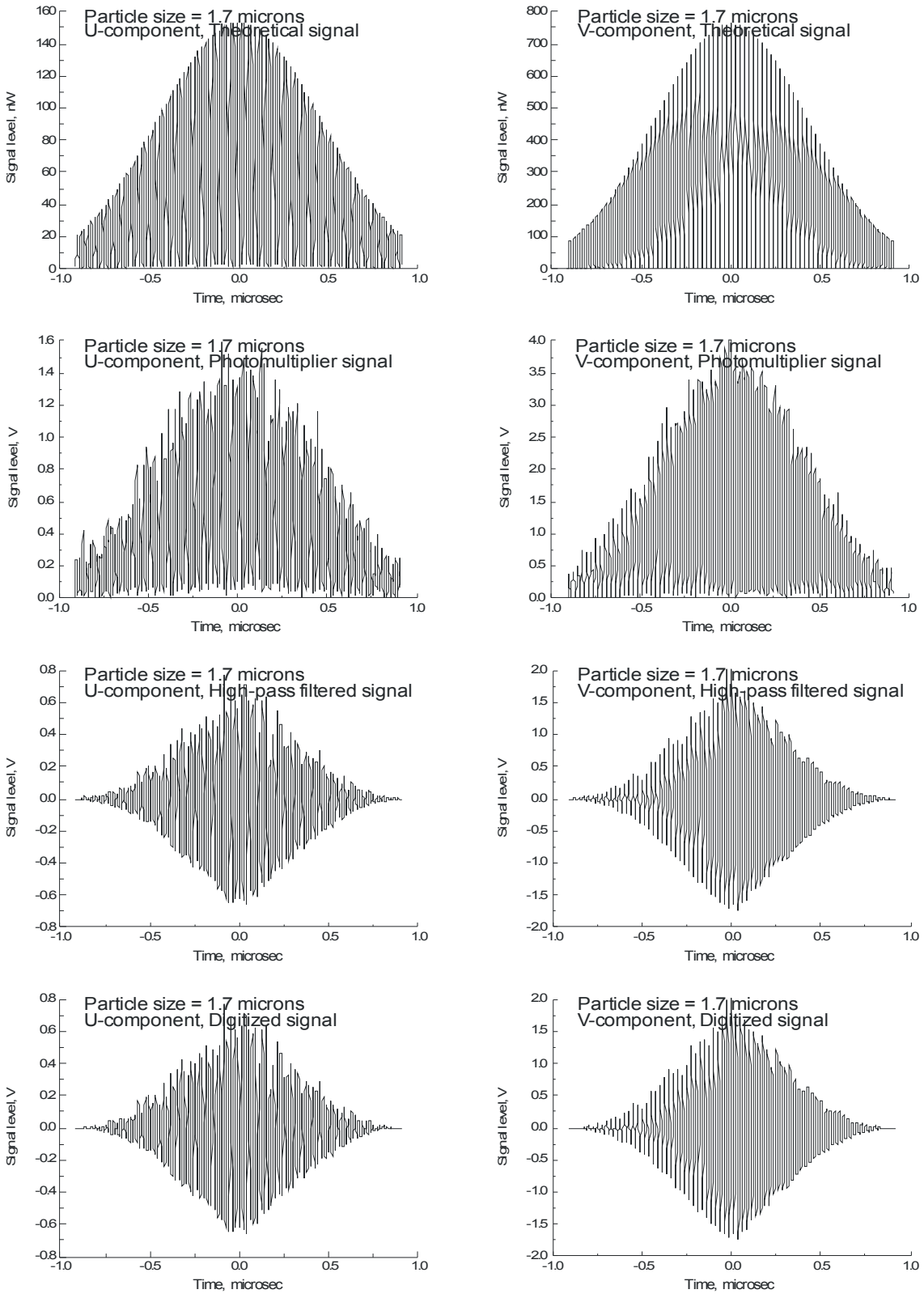

Error U: 0.11 m/s, -0.01 m/s

Error V: -0.02 m/s, -0.05 m/s

Figure A.16.- Signals obtained at on-axis = 0.0, Histogram 5, True Half Power processing.

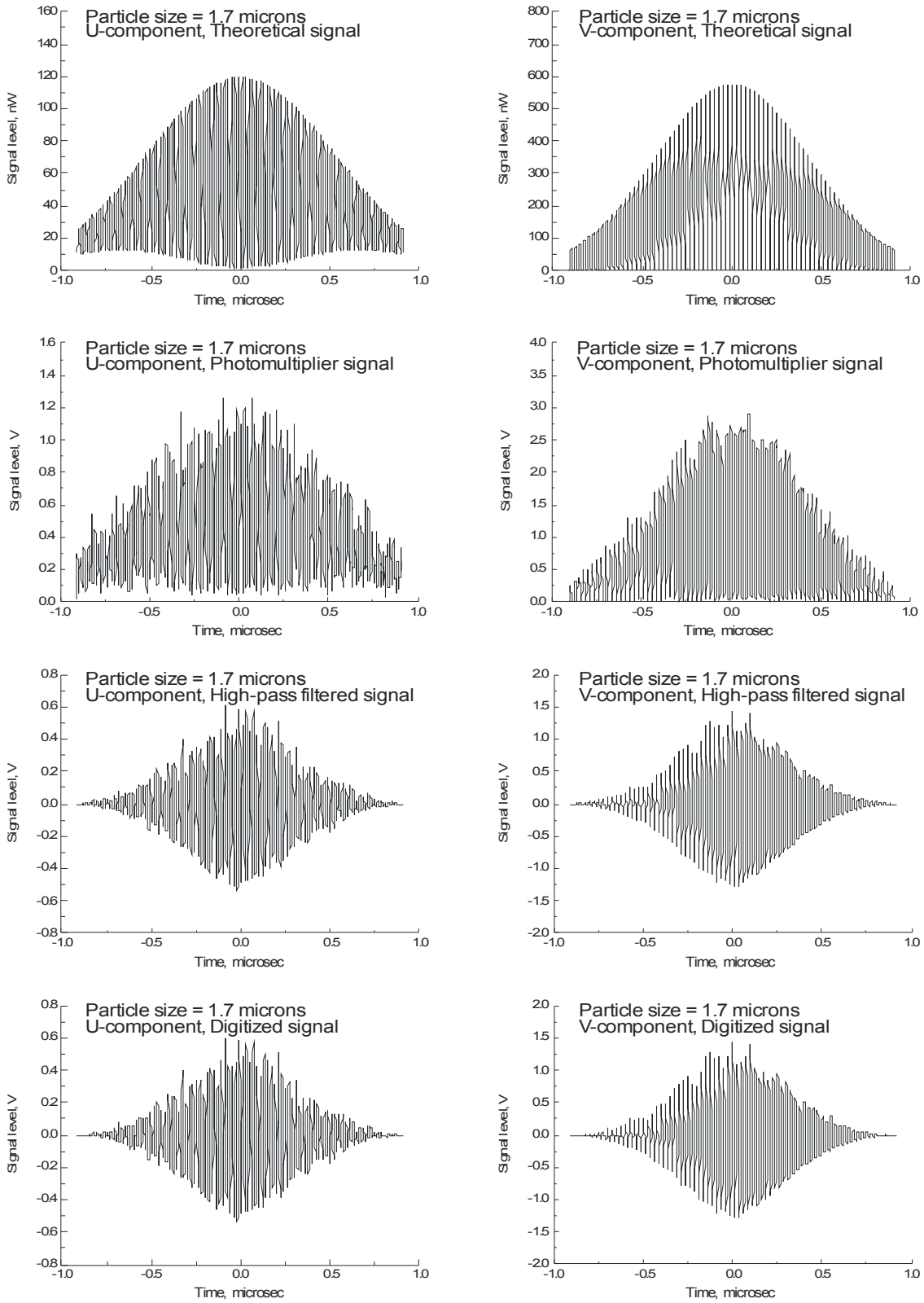

Error U: -0.11 m/s, -0.13 m/s

Error V: 0.13 m/s, 0.19 m/s

Figure A.17.- Signals obtained at on-axis = 0.25 L_{mv}, Histogram 5, True Half Power processing.

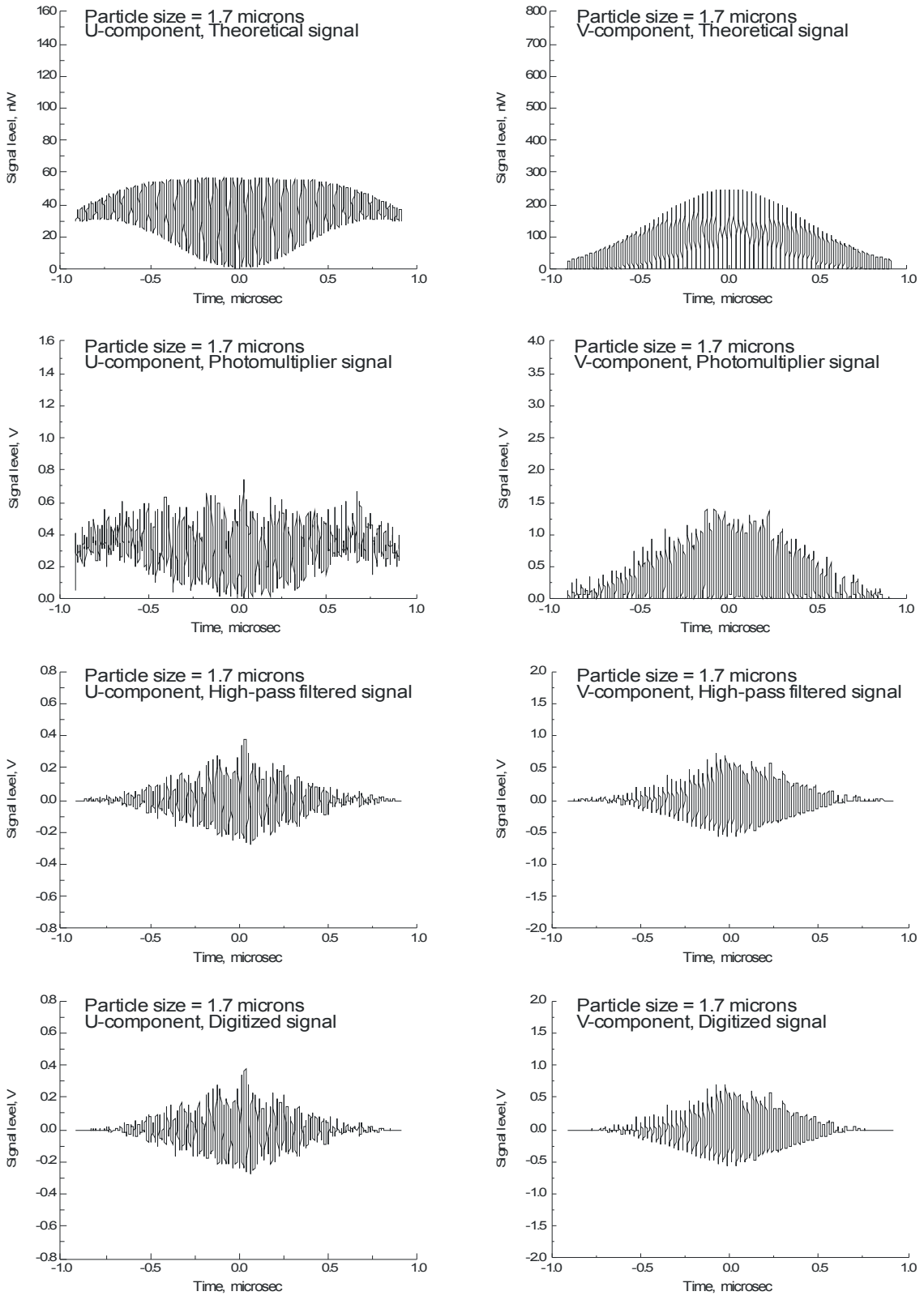

Error U: 0.52 m/s, 0.05 m/s

Error V: -0.02 m/s, -0.18 m/s

Figure A.18.- Signals obtained at on-axis = 0.5 L_{mv}, Histogram 5, True Half Power processing.

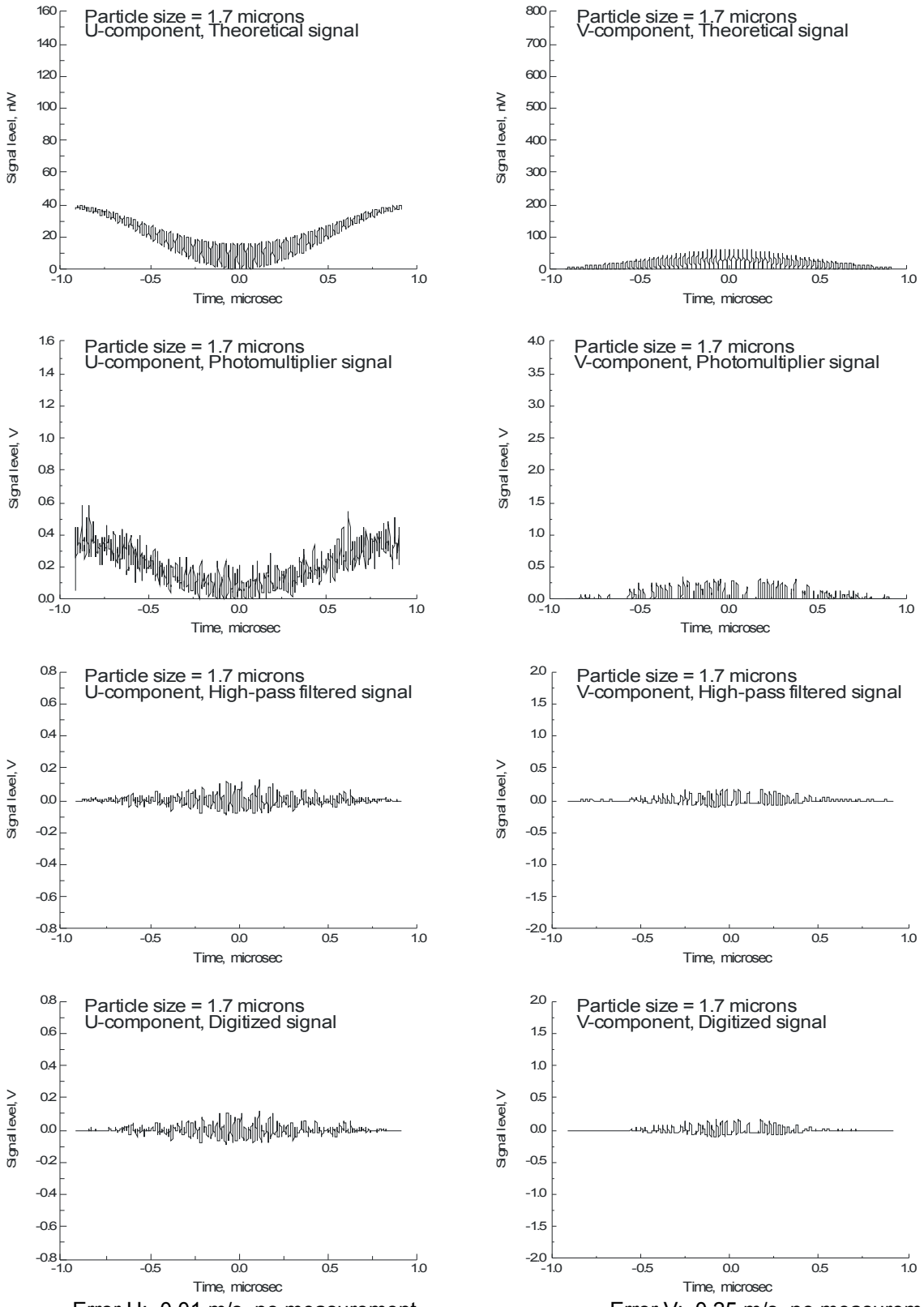

Error U: 0.01 m/s, no measurement

Error V: 0.25 m/s, no measurement

Figure A.19.- Signals obtained at on-axis = 0.75 L_{mv}, Histogram 5, True Half Power processing.

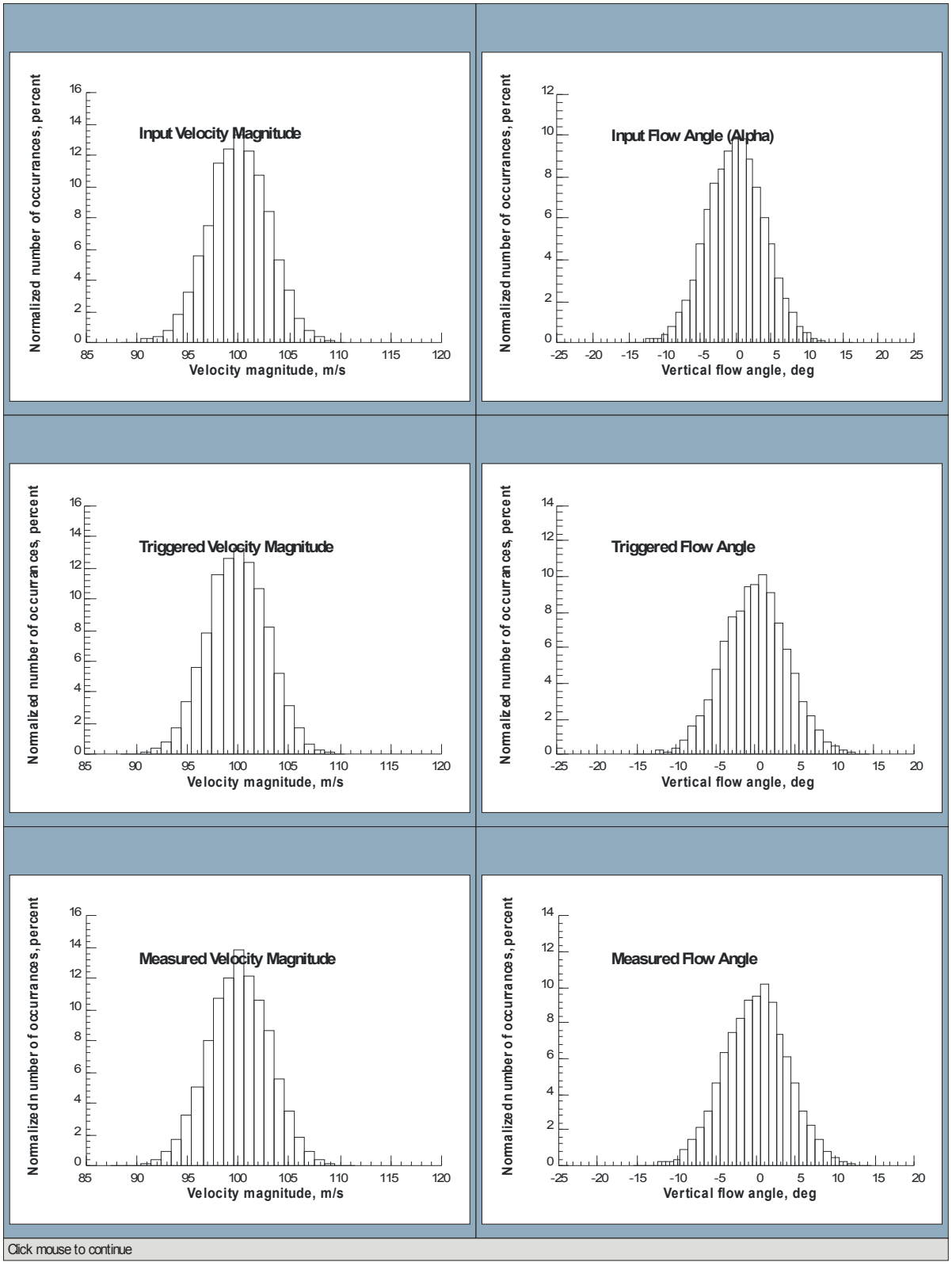

Figure A.20.- Velocity magnitude and flow angle distributions for the input particles selected, particles that triggered acquisition, and particles that were measured.

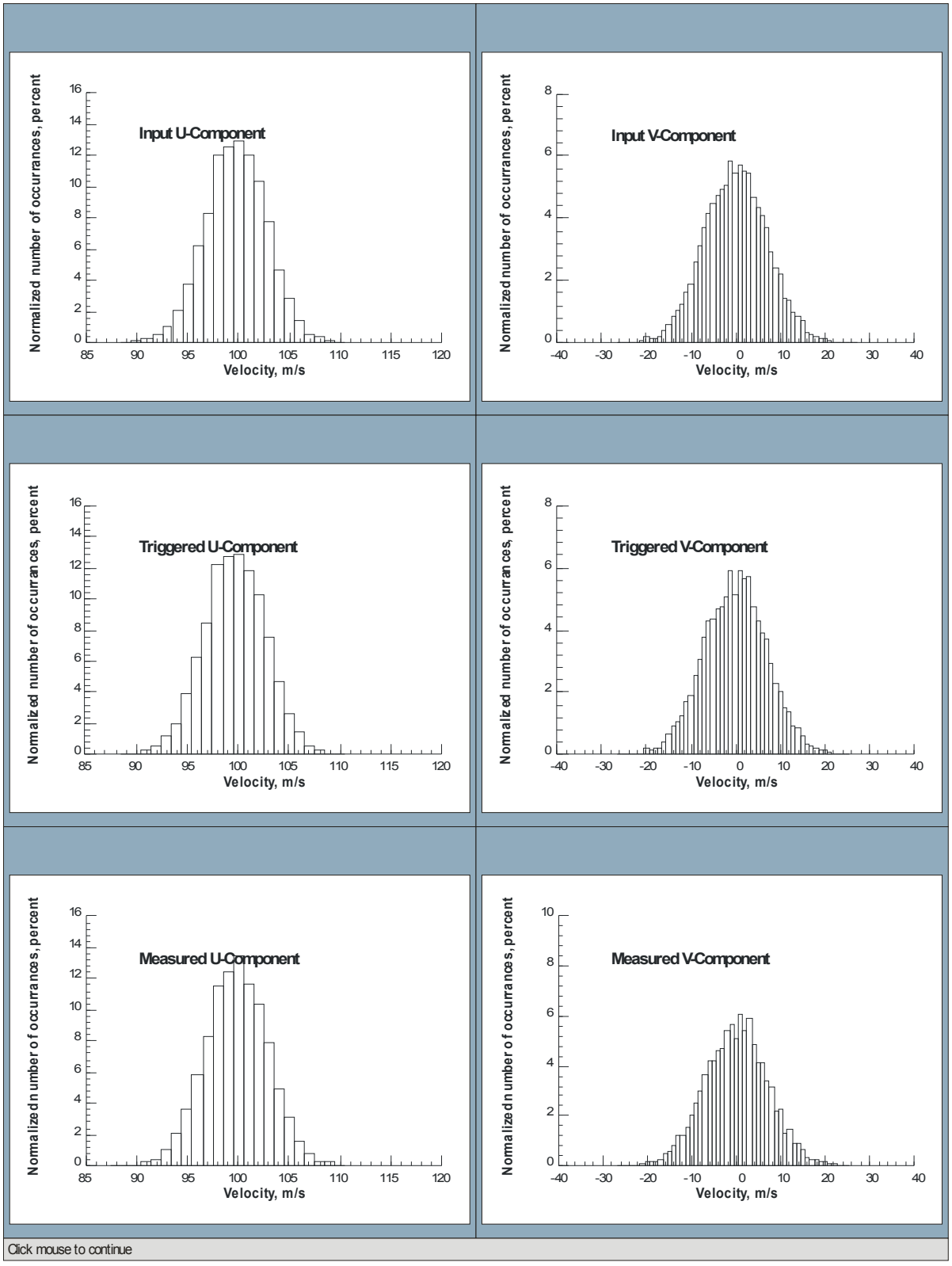

Figure A.21.- U- and V-component velocity distributions for the input particles selected, particles that triggered acquisition, and particles that were measured.

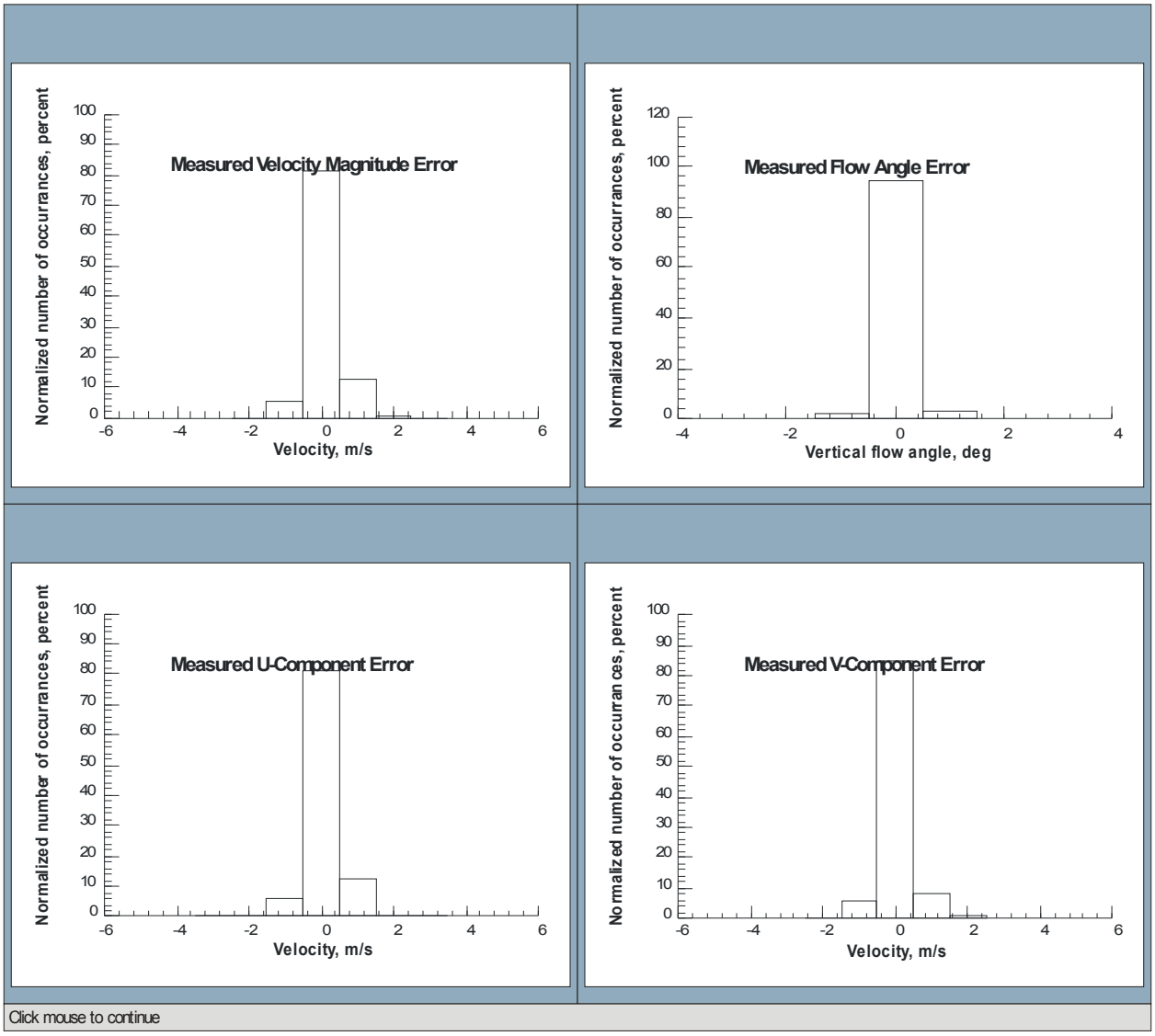

Figure A.22.- Distributions of differences between the particle parameter and the measured parameter for signal bursts that were accepted for processing.

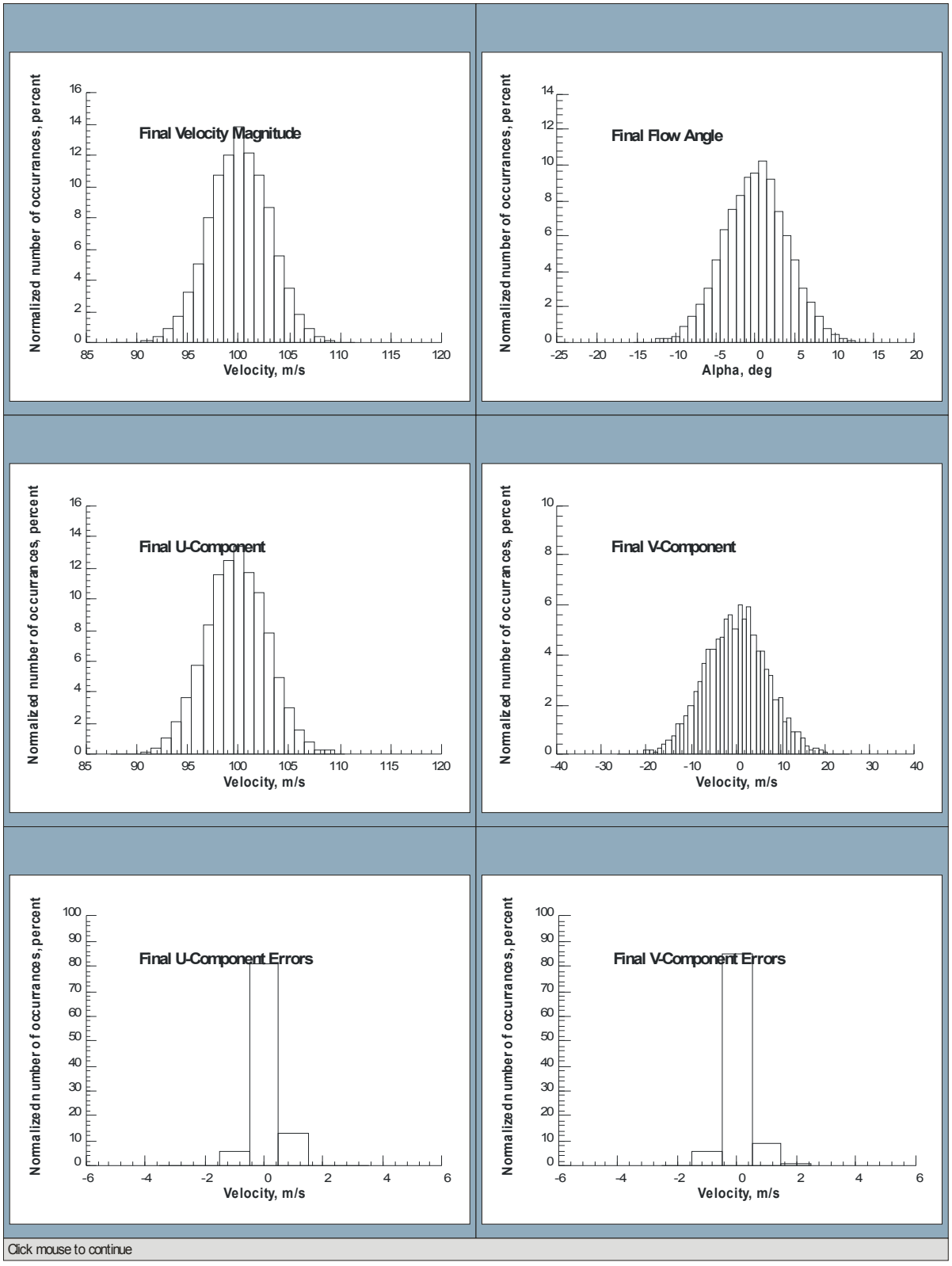

Figure A.23.- Final distributions of velocity and flow angle, along with the final measurement errors (instrument precision) after the outliers were eliminated.

Appendix B
Setup and Alignment of the TSI *Fiberlight* System for the 14- by 22-Foot Subsonic Tunnel Laser Velocimeter System

Laser Safety

Always follow safety procedures outlined in the approved Laser Safety permit for the lab or facility, and the NASA – Langley Non-Ionizing Radiation Safety Manual prior to undertaking any laser related work. Perform all initial alignment procedures with the laser at low power settings.

Laser and *Fiberlight* System Alignment

It is assumed that the optical centerline of the laser and the *Fiberlight* multi-color beam generator are the same and that apertures and mirrors are installed as shown in Figure B.1.

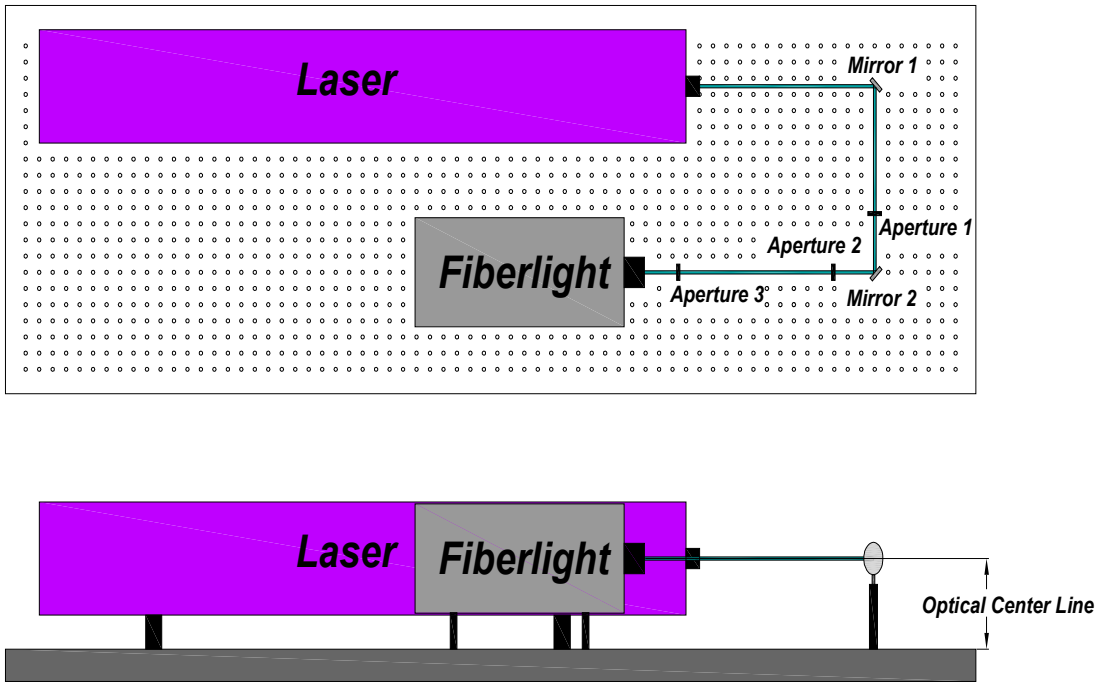

Figure B.1.- Top and front view of the laser – *Fiberlight* setup.

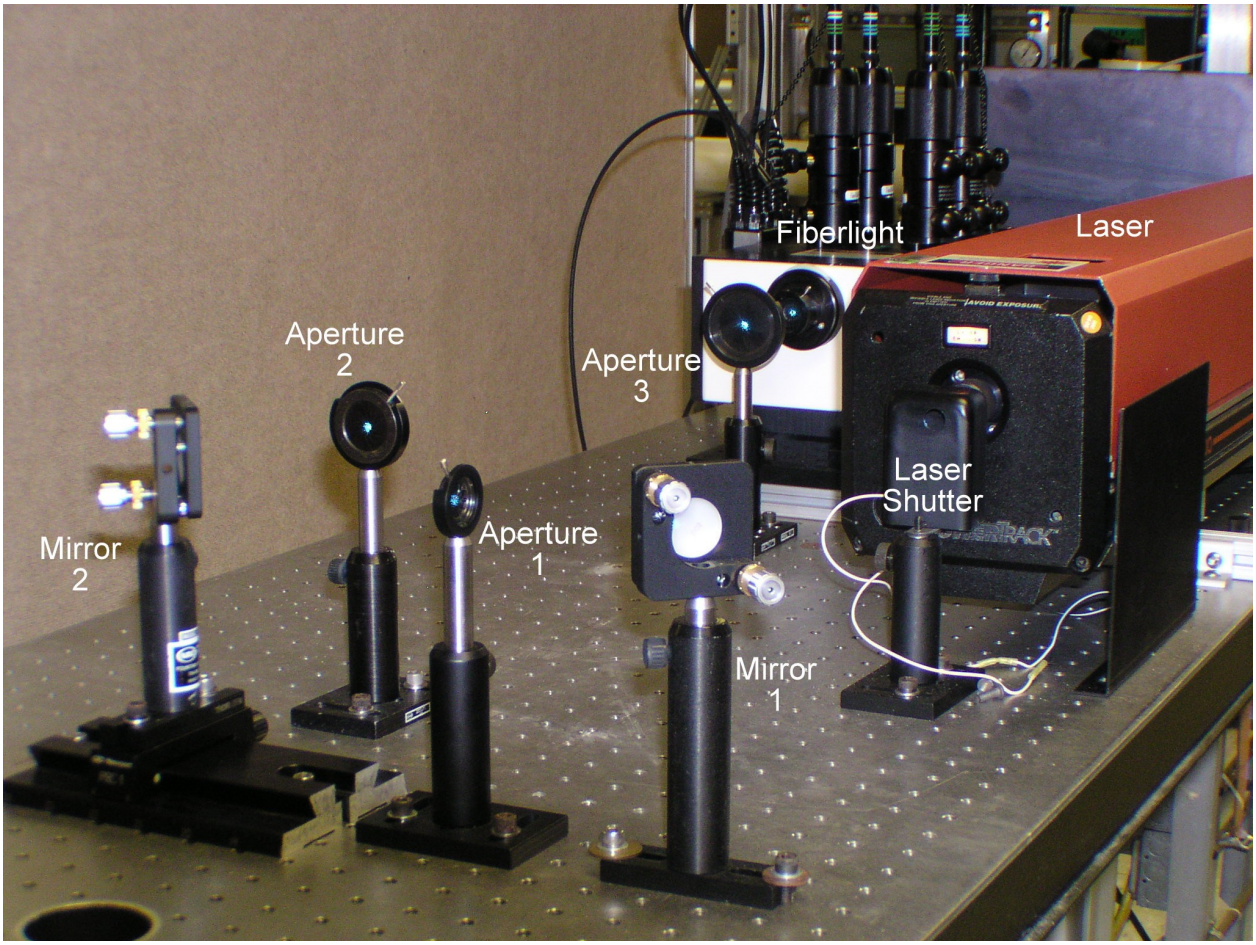

Figure B.2.- Laser and *Fiberlight* with alignment optics.

Initial Alignment Procedures

1) With a beam block in front of the laser, power up the laser and adjust the all-lines output power level to approximately 500 mW and allow it to come up to a stable operating temperature (10 to 20 minutes) before proceeding.

2) Using a power meter, peak the laser power using the adjustments on the high reflector at the rear of the laser.

3) Place a beam block in front of the fiber optic probe head.

4) Verify that the beam path is clear and that the mirrors are in place and appear to be pointed in the correct direction, as shown in Figure B.2.

5) Turn the laser power down to approximately 100 mW for initial alignment.

6) Use Mirror 1 to adjust the beam through the first aperture.

7) Use Mirror 2 to adjust the beam through the second and third aperture and the aperture located in front of the *Fiberlight*.

8) Verify that there is a beam block in front of the fiber optic probe head.

9) Proceed to the section on *Installing the Transmitting Optics* for aligning the *Fiberlight* on page 79 of the TSI Manual titled *LDV/PDPA System Installation Manual*.

10) When aligning the fiber optic couplers, adjust the laser output power level to 500 mW, then peak the output of the fibers using a laser power meter to monitor the output. Peak the output of all four fibers before increasing the laser power into the *Fiberlight*. Increase the input power to the *Fiberlight* to 1 Watt, then re-peak the output of all four fibers. This process should be repeated in approximately 1 Watt increments until the input power to the *Fiberlight* is between 4 and 5 Watts. Table B.1 provides a guide for fiber output power versus laser power input. It is highly recommended that a log similar to the Table be kept every time a fiber alignment is performed.

Date	Power In (w)	515 unshifted Pout	515 shifted Pout	488 unshifted Pout	488 shifted Pout
1/26/2010	0.5	22	21	48	52
	1	60	59	80	90
	2	144	155	151	177
	3	225	255	228	255
	4.3	270	358	300	327

Table B.1.- Laser power versus fiber optic output.

Laser Velocimeter Transmission Optics and Zoom Lens Alignment

1) Decrease the laser input power to the *Fiberlight* to the minimal level where the output is still maintained in both the green (514.5 nm) and blue (488.0 nm) lines. Place the alignment block against the alignment stops between the fiber optic head and Mirror 1 (Figure B.3), and verify that all of the beams pass through the block. The center line height of the package is 9 53/64 inches above the optical table. This is defined by the height of the center of the large zoom lens module. If height adjustment of the fiber optic probe head is necessary, loosen the set screw in the height adjustment knob on the lab jack and rotate the knob. Once the proper height is achieved, tighten the locking set screw.

2) If the beams are rotated with respect to the alignment block, loosen the large brass locking wheel under the probe and rotate the probe head. Once the desired orientation is attained, re-tighten the locking wheel.

3) Once the beams are made parallel, verify that Mirror 1 is in the proper position by placing the alignment block against the alignment stops between Mirror 1 and Mirror 2. Verify that the beams pass through the block. If adjustments are needed, rotate the adjustment knobs on Mirror 1 to adjust the alignment.

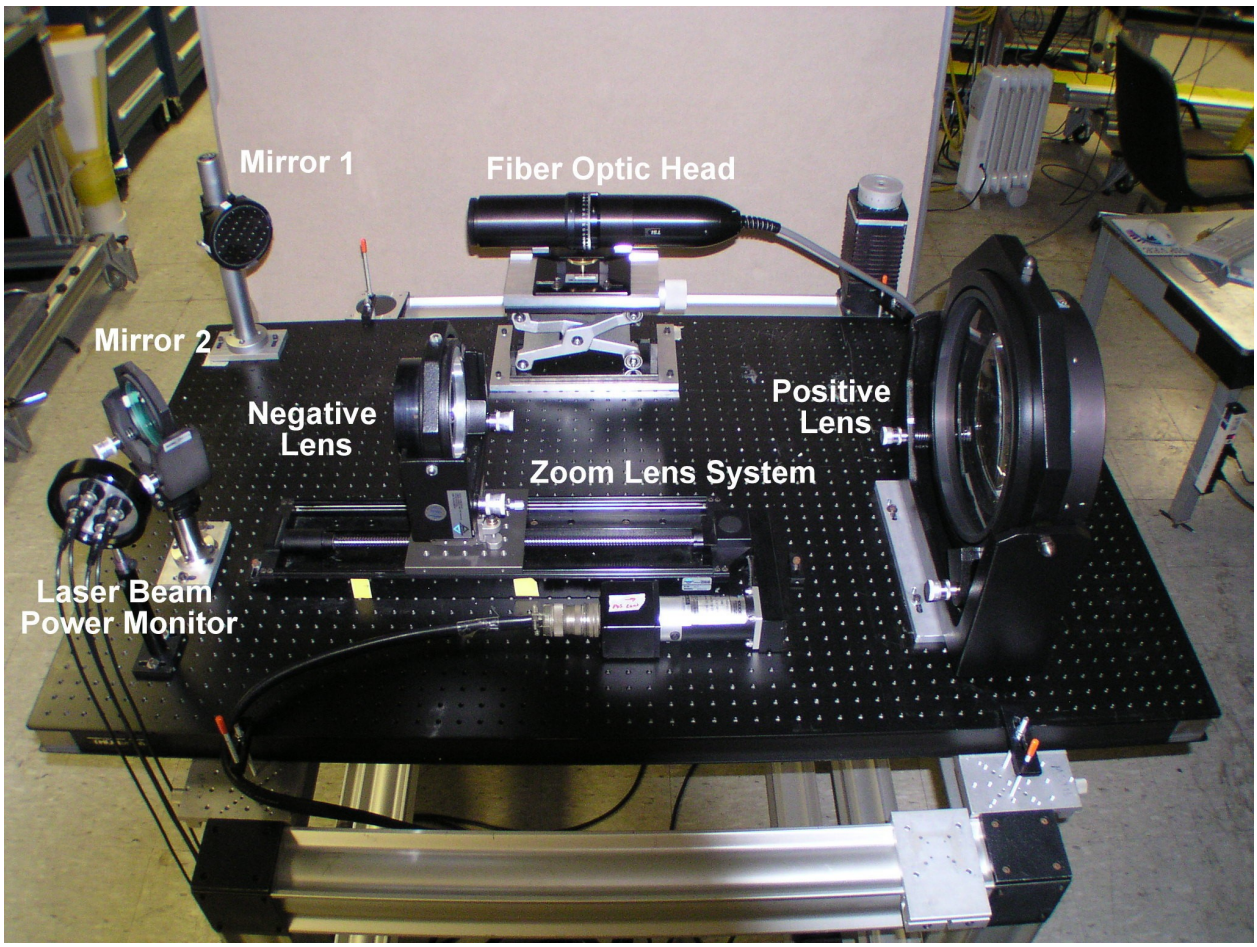

Figure B.3.- Fiber optic head with transmit and receive optics.

4) Verify that Mirror 2 is in the proper position by placing the alignment block against the alignment stops between Mirror 2 and the small zoom (negative) lens module. Verify that the beams pass through the block. If adjustments are needed, then use the adjustment knobs on Mirror 2 to correct the alignment.

5) At this point the beams should be aligned and ready to pass through the zoom lens system. Reflections from the zoom lens are a good indication that the beams are properly aligned. If the alignment is correct, there will be a series of reflections that line up in the same plane as the input laser beams, Figure B.4. If the reflections are not in line, make small adjustments to the small zoom lens module until the reflections are aligned. Begin by making angle adjustments to get the reflections centered in a line in the plane of the laser beams. Follow this by using the left-right adjustments to bring the reflections all in a line. Several iterations may be required in order to obtain satisfactory alignment. Angle adjustments can also be made on the large zoom lens module, however the left-right and up-down positioning is fixed.

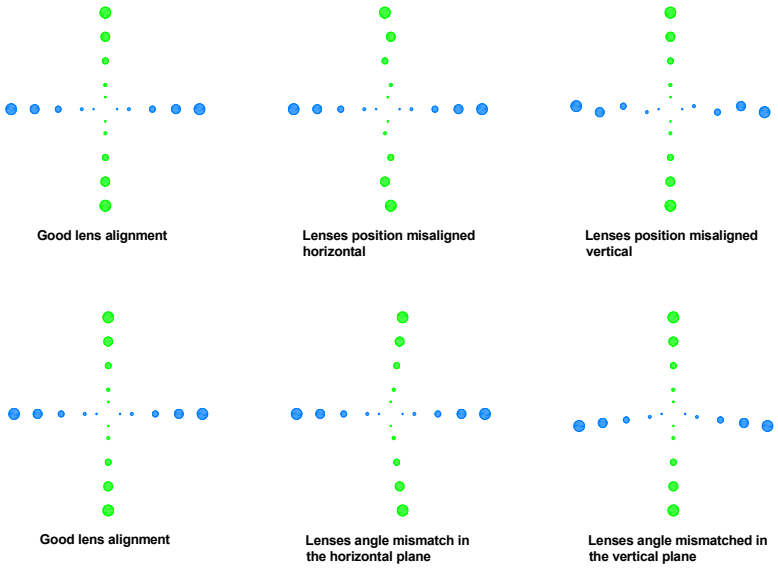

Figure B.4.- Reflection patterns from the zoom lens.

6) Adjust the distance between the zoom lens modules to focus the laser beams close to the area where the measurements are to be made.

7) Check the beam crossing using a microscope objective. Please refer to page 5-5 in the *TR/TM Series Fiberoptic Probes Operations Manual*. If the beams have a good crossover (all beams overlap at the same point) then the initial alignment of the transmit optics is complete. If there are small differences where the laser beams cross, then minor adjustments can be made to the laser beams using the beam steering procedure on page 5-9 of the *TSI Operator's Manual for the TR/TM Series Fiberoptic Probes*. If the crossover is grossly off (>20-percent) then parallelism of the laser beams coming out of the fiber optic probe must be checked as outlined in Step 8. If the alignment is good proceed to Step 9.

8) Check parallelism of the laser beams.
NOTE: This procedure requires two additional 4-inch mirrors and a tripod.

Place the alignment block in front of the fiber optic probe with the beams passing cleanly through the center of the holes. Place one 4-inch mirror between the alignment block and Mirror 1 at approximately 45-degrees to direct the laser beams off the optical table and across the room. Place a tripod and the second 4-inch mirror on the other side of the room to catch the beams and reflect them back on themselves. Examine the beams at the rear of the alignment block and verify that they all come back and overlap – ideally they should pass through the holes in the alignment block. If adjustments are required then refer to the section on *Steering the Beams of TR 60 Probe* on page 5-9 of the *TSI Operator's Manual for the TR/TM Series Fiberoptic Probes*.

9) Recheck zoom lens alignment as described in Step 5 and beam crossing as described in Step 7.

10) The last check in the optical alignment is to determine how well the receiver viewing volume overlaps the laser beam crossing. To verify the overlap refer to the section on *Illuminating the Receiving Fiber* on page 5-6 in the *TR/TM Series Fiberoptic Probes Operations Manual*.

Checking Signal Levels

1) Connect the TSI Photodetector Module (PDM1000) and TSI signal processor (FSA 4000), then run the *FlowSizer* software to enable the photodetectors. Refer to the section *Installing the System Electronics and FlowSizer Software* on page 93 of the *LDV/PDPA System Installation Manual*. **NOTE: This system only uses the TSI Signal Processor (FSA 4000) and *FlowSizer* Software for powering and controlling the high voltage applied to the photomultiplier tubes**.

2) Bring the laser power up gradually just as in the initial alignment procedure and peak the fiber couplers for maximum laser transmission. Do this until a maximum input power of 4 to 5 Watts is achieved. **Do not assume that the alignment has held. Always increase the power in steps and verify the power levels out of the fibers. If the power levels are unbalanced STOP and recheck the initial alignment. This will prevent damage to the optical fibers**.

3) Set up a portable particle generator at the measurement volume and observe the signals at the rear panel output of the TSI PDM-1000 with an oscilloscope. Signal levels should be at least 200 mV p-p with good modulation in the burst. If this is not observed recheck the alignment of the receiver fiber and the beam crossover. With the particles passing through the measurement volume in the horizontal plane, the centers of the signal bursts from the U- and V-components should be tracking together on the oscilloscope. If not, the V-component measurement volume is misaligned left-right. Now align the particle flow in the vertical direction. Again the centers of the signal bursts from the U- and V-components should be tracking together on the oscilloscope. If not, the U-component measurement volume is misaligned up-down.

4) If the measurement volume is to be moved along the optical axis (zoomed), checking the alignment of the measurement volumes, Step 3, should be repeated at several locations along the extent of the planned travel.

Appendix C
Data Acquisition and System Control Software
Installation and Functional Overview

Any software developed for a production environment must be intuitive, easy to use, free from failure, and provide sufficient user feedback to indicate proper functionality or identification of a problem along with instructions on how to correct the issue. In particular the Data Acquisition and System Control Software is designed to provide:

1) An intuitive, easy-to-use interface that enables the researcher to concentrate on the task at hand, and not on the functionality of the software;

2) System management to insure hardware/software configuration and synchronization with uniform and repeatable operation;

3) Control of the discretization of the analog signals obtained from the two photomultipliers, acquisition of auxiliary digital and digitized analog signals including azimuth encoder readings, and interarrival time measurements between signal bursts;

4) Archival management of all data collected so that the acquired measurements are preserved in a standardized manner to facilitate signal and data processing (on- and off-line) with automated real-time backup, provide real-time user feedback, and support for off-line interrogation and analysis;

5) Control of the Signal/Data Processing computer operation including data transmission and storage, program control, and real-time user display of any issues found during processing that may affect data quality; and,

6) Control of the traversing system and remotely controlled turning mirrors used to position and orientate the laser velocimeter measurement volume within the flow field.

Methodology

The Data Acquisition and System Control software is the primary interface between the researcher and the collective system components during the course of a flow field investigation using the laser velocimeter. The software provides a seamless and transparent interface to the data collection subsystems, which include laser and optical system components as well as the signal conditioning, acquisition, and processing hardware, and the measurement volume positioning subsystem. In addition, the software provides the interface and data transfer path to the Signal/Data Processing computer as well as providing all control functions for the processing software.

The Data Acquisition and System Control software was developed using the National Instruments (NI) LabVIEW programming environment (Version 2010, SP1). The software consists of multiple custom program modules with supporting subroutines written in LabVIEW and C/C^{++}. The modules employ NI supplied drivers and LabVIEW subVIs in conjunction with custom C/C^{++} DLLs to interact with the data collection hardware and the networked Signal/Data Processing computer to achieve the necessary functionality for production testing. The Data Acquisition and System Control software supports the following capabilities:

1) Easy to use graphical user interface (GUI);
2) System hardware initialization and control;
3) Data acquisition synchronization and management;
4) Particle interarrival time recording;
5) Conditional sampling of auxiliary inputs, e.g., rotor azimuth;
6) Data retrieval and archival;
7) Traverse mechanism control and management;
8) Signal/Data Processing triggering and control;
9) Processed data validation;
10) System progress logging;
11) Simulation device and signal management; and,
12) System performance monitoring and diagnostics.

Subtasks

In order for the Data Acquisition and System Control program to perform the above tasks, small background programs must be developed to provide the direct control of the external functions, task monitoring, control functions, and housekeeping tasks. Some of these modules are written in the LabVIEW environment while others, especially when execution speed is critical, in C/C++. The selection of tasks to be running at a given time is under the control of the main program as directed by the user and resulting selection of instructions to be executed. Using this methodology, the following benefits are obtained:

Segregation of the optional functionality from the top-level application as certain subtasks are enabled on an *as needed* basis, thus reducing memory/system requirements and resources; and,

Allows for certain software functions or subtasks to be reused, thus reducing duplication along with design, development and debug time.

Subtasks in the LabVIEW Environment

Seven LabVIEW-based subtasks are employed by the Data Acquisition and Control program to support the various operations performed during the course of a typical data acquisition activity:

1) *Storage Path Generator* – This background task is responsible for generating the file storage paths (character strings) where the acquired data records will be stored on both computers. The generation of the data storage paths is a time consuming process and the ability to perform these operations in parallel with the acquisition of new data sets reduces overall acquisition time. The subtask is always launched when the Data Acquisition and Control program is started and it requires no direct user interaction.

2) *One Shot Generator* – This background task is launched at program start-up and is responsible for initializing and controlling the retriggerable one-shot pulse generation circuitry of the PXI-6602 Counter/Timer board (Chapter IV, page IV.3) installed in the PXI chassis. The one shot pulse signal is TTL positive and has a duration of 500 nsec. This pulse is used to control the signal validation hardware.

3) *Log File Manager* – This background task is launched at program start-up and is responsible for saving data acquisition information into a Log file once each data acquisition cycle is completed. The Log file contains information such as data series name, data acquisition rate and duration, number of signal bursts acquired and processed, convergence level, processing code and the location of the measurement volume when the data was acquired.

4) *Traverse Mechanism Manager* – This background task is responsible for the management of the Klinger model MC4 controller used to position the scan rig that in turn locates the measurement volume during a flow field test sequence. The subtask is launched when the user selects the I**nitialize Scan Rig** button on the ***Scan Rig Management*** tab. Once the user has input the desired measurement location in the main program, this subtask will control the traversing mechanism to move the measurement volume to that location, and once completed, return the status to the main program. It is noted that this subtask will be modified as required to manage and control other traversing mechanisms, e.g., original 14-by 22-Foot scan rig, pan/tilt mirror, etc.

5) *Simulation Signal Manager* – This auxiliary program is used to control and operate the Agilent 81150A Pulse Function Arbitrary Waveform generator. This generator is used to convert simulated or previously captured signal bursts into electronic signals that can be used to validate the operation of the data acquisition and Signal/Data Processing systems. This auxiliary program is launched when the user selects the **Enable Test Mode** button on the ***System Configuration*** tab.

6) *1024/Rev Encoder Simulator* – This auxiliary background program is used to produce pulse trains that simulate the operation of a position encoder mounted to a rotating shaft such as those used during rotorcraft investigations. The subtask will generate a pulse train of 1024 pulses (1024/Rev) followed by a single (1/Rev)

pulse signifying the zero azimuth position of the rotor. This 1/Rev is used to reset the pulse train counter signifying the beginning of the next revolution of the rotor.

7) *Processed LV Data Manager* – This background subtask is responsible for the management of statistical velocity measurement results from the most recent data ensemble returned by the Signal/Data Processing program. The subtask retrieves resolved flow-related quantities from output files generated by the Signal/Data Processing program and presents them to the user in both graphical and textural formats. These results duplicate those presented by the Signal/Data Processing program on the Signal/Data Processing computer monitor. Duplication was implemented because the operator needs to ascertain data quality, while the test engineer is more concerned with measurement values. Thus each has their own monitor. This subtask is launched when the user selects the **Enable Online Processing** and **Enable Convergence Validation** buttons on the ***System Configuration*** tab.

Data Management DLL (C-based Subtask)

Since high-speed data transfer of the captured signal burst from the digitizer to the hard drives on both the data acquisition and Signal/Data Processing computers is of the essence, this function is accomplished using a C-based DLL controlled by the LabVIEW-based Data Acquisition and Control program.

Data Acquisition and Control Program Installation and Setup

An installer CD has been developed to facilitate the installation of the Data Acquisition and Control program, its subtasks, and the LabVIEW Run-Time Engine including all necessary drivers, libraries, and other files needed for use on a computer lacking the LabVIEW development environment. The steps outlined below should be followed in combination with the sequence of installation dialogs to install the software:

1) Insert the Data Acquisition and Control program installation CD in the computer's CD or DVD drive.

2) Open a file manager (e.g., Windows Explorer, Free Commander, etc) and navigate to the CD (DVD) drive, e.g., Figure C.1.

3) Move the cursor to the **setup.exe** file (Figure C.1.) and double click the left mouse button to start the setup program. The program welcome screen, Figure C.2., will indicate that the program is ready to begin the installation process. Select the **Next >>** button to proceed.

4) Once the installation files have been loaded, the program destination directory dialog (Figure C.3.) will appear. If the Data Acquisition and Control program and/or the LabVIEW software are to be located in directories other than the default locations, select the appropriate **Browse...** button(s) to the right of the default directory fields to open a file manager where the desired directory can be selected. Once the desired directories have been established, click on the **Next >>** button to proceed.

5) The National Instruments and Microsoft License Agreements are presented in sequence (Figures C.4. and C.5.) for acceptance. If accepted, the installation of the LabVIEW software will commence, otherwise the installation program will terminate. Once each Agreement has been accepted, click the **Next >>** button to continue.

6) An information screen is then presented with a list of modules (Figure C.6.) that will be installed. Selecting the **Next >>** button will begin the installation of those modules.

7) Once the installation begins, a progress meter, Figure C.7., is displayed. If the installation completes without errors, the Completion Screen, Figure C.8., will be displayed. Click the Finish button to exit the installation program.

All modules and components should now be installed and the Data Acquisition and Control program is ready for use.

Data Acquisition and Control Program
Hardware Configuration and Data Acquisition Sequence

An overview of the organization of the hardware and their interactions, both analog and digital, can be found in the layout schematic shown in Figure C.9. The two coaxial cables transmitting the signals from the U- and V-component photomultipliers are electronically Teed with inputs to the monitoring oscilloscope (set to an input impedance of 50 ohms), the Trigger Generator, and the high-speed analog-to-digital converters in the NI PXI Acquisition System. When a signal burst is received that is of sufficient amplitude to trigger the oscilloscope, that trigger is also transmitted to the PXI System. This impulse trigger is modified by the PXI System to a 500 nsec TTL compatible signal which is transmitted to the Trigger Generator indicating that the scope has triggered. Once this pulse has been received, the Trigger Generator monitors the incoming signal burst to determine if 8 cycles are present. If so, the Trigger Generator will output a TTL compatible pulse (Master trigger) that will trigger the high-speed analog-to-digital converters to latch and store the U-and V-component signal bursts. The Master Trigger also latches and stores any auxiliary signals (analog or digital) that have been input to the low-speed analog/digital acquisition module. Although this process requires approximately half of the transit time of the particle through the measurement volume, the pre-triggering

capabilities of the high-speed analog-to-digital converters insure that the entire signal burst is captured by each channel. It is noted that BNC switches are used to select and direct the appropriate signals to each module. **It is mandatory that the same component signal used to trigger the oscilloscope is monitored by the Trigger Generator**. For example, if the U-component signal is used to trigger the oscilloscope, that same signal should be routed through the switches to be input to the Trigger Generator.

Once the preset number of signal bursts have been acquired and stored in the PXI System, a data complete signal is sent to the Data Acquisition computer via the MXI bus to trigger the Data Acquisition and Control program to begin the data retrieval sequence. The program will transfer the two component data ensembles along with the auxiliary data from the PXI System to the hard drive on the Data Acquisition Computer, and via the Ethernet interface, to the hard drive on the Signal/Data Processing Computer. The program then develops the command file for the signal/data acquisition program and stores it on the Signal/Data Processing Computer's hard drive. The update of this file is the trigger for the Signal/Data Processing program to begin processing the data ensembles as instructed in the command file. The Signal/Data Processing program will develop a Log file for that data ensemble containing the velocity statistics for the U- and V-components (both individually and in full coincidence), velocity magnitude and flow angle. The Log file also contains a listing of the individual signal bursts: signal minimum and peak, and signal-to-noise ratio along with the computed particle U- and V-component velocity, velocity magnitude and flow angle, interarrival time, azimuth angle and transit time. In addition the program computes the U- and V-component mean and standard deviation every 100 acceptable signal bursts cumulatively to determine if statistical stationarity has been reached. Plots of these results are displayed followed by histogram plots of the U- and V-component velocities, velocity magnitude and flow angle. These plots are duplicated on the Data Acquisition computer by the Data Acquisition and Control program based on results transmitted by the Signal/Data Processing program. The results file contains data from the statistical stationarity test, the average minimum and maximum voltages, and the average signal-to-noise of the U- and V-component signal bursts. Once received by the Data Acquisition and Control program, these results are compared with user selected levels to determine the quality of the acquired data along with whether additional data ensembles should be acquired to reach statistical stationarity. The data acquisition and processing sequence is outlined in the flow diagram shown in Figure C.10. The green elements signify hardware steps, cyan elements – Data Acquisition and Control program, and red elements – Signal/Data Processing program. A more detailed explanation of each step is given below.

Program Start-Up Sequence

System Power Up

Because the PXI chassis in which the data acquisition hardware resides is an extension of its host computer's PCI bus, **it must be powered on prior to powering the Data Acquisition computer**. After the PXI chassis has been powered up, wait approximately ten seconds before powering the Data Acquisition computer to allow the PXI chassis to initialize its various hardware and software elements.

Once the Data Acquisition hardware and computer have been powered, verify that the networked Signal/Data Processing computer has also been powered on.

System Log On

The default user name on both the Data Acquisition and Signal/Data Processing computers is **lv** and the default password is **lv** (both lower case). At the login prompt, the user should enter the following:

User Name: lv
Password: lv

Mount Network Disk Drive

When a data acquisition cycle is completed, the acquired data resides in the Data Acquisition computer memory after being transferred from the PXI System. This data is then archived on the Data Acquisition computer hard drive and the Signal/Data Processing computer hard drive. In order for the data to be transferred to the Signal/Data Processing computer hard drive, that drive must first be mounted as a local drive on the Data Acquisition computer **before** initialization of the Data Acquisition and Control program. Mounting the remote disk drive as a local drive on the Data Acquisition computer is accomplished by:

1) Open Windows Explorer to display a drive window similar to the one shown in Figure C.11.

   Since during the software installation process (page C.5.) the remote drive was mounted, it should be displayed in the group labeled Network Location(s). If the drive has an **X** over the storage locations available to the Signal/Data Processing computer (as shown in Figure C.11.), the drive did not automatically mount when the two computers were powered on. In order to mount and share a disconnected, but visible drive continue below.

2) Select the desired drive by a left mouse click with the cursor over the drive name (NOTE: Drive E: is the default drive name for the remote drive). This will cause the display of the Log In screen for the network Domain **LVACQ** (Figure C.12.).

   Enter the user name and password below, then select OK:

   User Name: lv
   Password: lv

   Verify that the remote drive has been successfully mounted by the absence of an **X** over drive E:. Now the Data Acquisition and Control program can be launched.

Launching the Data Acquisition and Control Program (Standalone)

To begin, the user should navigate via the file manager to the disk drive where the program was installed (page C.5.), and select the directory named **LV Data Acquisition Application**.

The main program can then be launched by placing the cursor over the executable file: **LV Data Acquisition** and double-clicking the left mouse button. Once the program has been launched, the user is presented with the Opening (Main) Screen shown in Figure C.13. After a few seconds the dialog window shown in Figure C.14. will appear prompting the selection of an Initialization (.INI) file that contains the start-up settings for the Data Acquisition and Control program. The following two options are available:

1) Default.ini – The program settings used during the last execution of the Data Acquisition and Control program as stored stored in the default **.INI** file (**LV_Acq_Setup.ini**) and located in the sub-directory named **Config** in the directory containing the Data Acquisition and Control program. The contents of this file are automatically updated to the settings present when the program is terminated.

2) User.ini – This option allows the user to select an alternative set-up configuration via the file manager, shown in Figure C.15., that opens when this option is selected. The option allows the user to employ previous configurations by copying and renaming the default settings file (**LV_Acq_Setup.ini**) to preserve the current settings for later use.

Once the set-up (.ini) file has been interrogated by the program to configure the program, the Opening (Main) Screen is once again presented, Figure C.13. This screen is divided into two sections: The Program Navigation Bar on the left (Figure C.16.), and the Program Configuration/Management Panel to the right (Figure C.17.).

Mechanisms have been incorporated into the Data Acquisition and Control program to provide the user with a great deal of flexibility in the way it can be used. Controls along with support subroutines, subprograms and simulators have been developed that allow the user to choose signal types, sources and ranges as well as options that enable the functionality of the laser velocimeter system to be verified prior to formal deployment of the instrument in research activities. Additionally it supports the ability to manage devices other than those used in the data collection process from a single interface. The various program controls and options are arranged on the user interface in a manner that affords the user with an easy way to configure and use the system. Access to the system components and settings is obtained via the selection buttons located on the left side of the Opening (Main) Screen, Figures C.13. and C.16.

The intention of this Appendix is to provide an overview of the processes available in the Data Acquisition and Control program. Thus the individual screens will be described as to their general function, with the detailed functions described in Appendix D. The functionality is presented in the order in which the options might be used during the course of a laser velocimeter flow field investigation. It is noted that the user will find that for a majority of applications, the default settings will provide the necessary controls. However, to provide system flexibility and to support various test scenarios where the default settings would not be appropriate, the necessary controls are provided to customize the settings as needed. It is advised that if custom settings are used, the **LV_Acq_Setup.ini** file should be copied and renamed to preserve the original default settings for future use.

Configure System

Selecting the **Configure System** button from the Navigation Bar will open the display shown in Figure C.17., (Figures C.13. (C.16.) [CONFIGURE SYSTEM] → C.17.). Within this display the user is provided with access to controls and options required to configure the data acquisition hardware, data storage, and validation components which ultimately define the manner in which the data ensembles will be collected and archived. Typically the user will adjust the settings, if necessary, at the start of the investigation and utilize them throughout the flow field investigation. An overview of the functions in each group follows:

Select Desired Options – These controls shown in Figure C.18., (Figures C.13. (C.16.) [CONFIGURE SYSTEM] → C.17. (C.18.)), provide the user with the ability to:

1) Enable/Disable signal/data processing in real time;
2) Enable/Disable the measurement of rotor azimuth via the shaft encoder;
3) Enable/Disable communications with the wind tunnel data acquisition hardware;

4) Enable/Disable the input of synthetic signal bursts from the arbitrary waveform generator;

5) Enable/Disable the input of a simulated shaft encoder (only active if the measurement of the shaft encoder is enabled);

6) Enable/Disable warning messages indicating that statistical stationarity of the flow measurements has not been attained based on the user selected threshold; and,

7) Enable/Disable menus containing data acquisition hardware settings.

LV Burst Signal Digitizer Management – The controls found in this sub-panel, Figure C.19., (Figures C.13. (C.16.) [CONFIGURE SYSTEM] → C.17. (C.19.)), define the operation of the high-speed analog-to-digital converters (National Instruments PXI-5152 8-bit, 2.0 GS/s, Chapter IV.2).

Auxiliary Channel Analog Input – The controls found in this sub-panel, Figure C.20., (Figures C.13. (C.16.) [CONFIGURE SYSTEM] → C.17. (C.20.)), define the functionality of the auxiliary channel analog inputs. Auxiliary channels are provided to allow conditional sampling of analog signals produced by instruments external to the laser velocimeter. These instruments would typically be used to coordinate measurements of other flow phenomena or model conditions with the instantaneous velocity measurements. These signals are input to the National Instruments PXI-6120 Multifunction Data Acquisition Module, Chapter IV, page IV.2.

Data Storage Management – The controls found in this sub-panel, Figure C.21., (Figures C.13. (C.16.) [CONFIGURE SYSTEM] → C.17. (C.21.)), define the directory paths for archival storage of the acquired data, the manner in which the file name is configured, and whether the data should be stored in either ASCII or binary form. Also user comments/notes regarding the test can be entered and will be recorded in the ensemble LOG file.

LV Data Acquisition Management – The controls found in this sub-panel, Figure C.22., (Figures C.13. (C.16.) [CONFIGURE SYSTEM] → C.17. (C.22.)), define the characteristics of the acquisition of each data ensemble, convergence threshold, and whether the laser velocimeter traversing mechanism should be automatically moved at the completion of the acquisition of a data ensemble.

Data Acquisition Conditions – The controls found in this sub-panel, Figure C.23., (Figures C.13. (C.16.) [CONFIGURE SYSTEM] → C.17. (C.23.)), provide the user with the ability to record the environmental test conditions and the characteristics of the particles injected in the flow. These inputs will be recorded in the ensemble LOG file.

Control Scan Rig

Laser velocimetry, being a point measurement technique, requires that the measurement volume be moved throughout the flow field in order to develop an understanding of the flow properties. This control button, Figure C.16., will open the display shown in Figure C. 24., (Figures C.13. (C.16.) [CONTROL SCAN RIG] → C.24.). At first this display appears to be cluttered and complicated, but when taken one group at a time, their functions are logical. At the highest level, there are actually three displays as selected by the tabs at the top of the display:

Controls – The primary interface to the scan rig. The display presents current location, automatic scan control options, scan speed and acceleration, and communications information.

Scan File Data – Contains information retrieved from a scan rig position control file selected by the user.

Status/Information – Contains status and related information pertaining to the use of the scan rig.

It is noted that the current control functions are specific to the Klinger MC4 family of traversing mechanisms. If another traversing mechanism is used, the underlying drivers and subroutines must be written to access the capabilities of the rig to place it under the full control of the Data Acquisition and Control program. However, the prime functions and capabilities shown in Figure C.24. will be maintained if possible.

The following sub-panels are found in the **Controls** display:

Scan Rig Functions – The controls found in this sub-panel, Figure C.25., (Figures C.13. (C.16.) [CONTROL SCAN RIG] → C.24. (C.25.)), provide the basic control of the scan rig along with the development of a grid index via a separate dialog, Figure C.26., (Figures C.13. (C.16.) [CONTROL SCAN RIG] → C.24. (C.25.) [Create Scan Grid File] → C.26.), and moving the rig based on positions stored in the index.

Klinger MC4 Scan Rig Status Display – This sub-panel, Figure C.27., (Figures C.13. (C.16.) [CONTROL SCAN RIG] → C.24. (C.27.)), reflects the information presented on the front panel display of the MC4 controller along with communication status information.

Set Scan Rig Index – This sub-panel, Figure C.28., is displayed when the **Scan To Index** control is selected, (Figures C.13. (C.16.) [CONTROL SCAN RIG] → C.24. (C.25.) [Scan To Index...] → C.28)). The control moves the measurement volume to the position obtained at the selected index in the table containing the input grid.

Klinger MC4 Scan Rig Control Panel – This sub-panel, Figure C.29., (Figures C.13. (C.16.) [CONTROL SCAN RIG] → C.24. (C.29.)), contains the controls that give the user additional control of the scan rig and can be used in combination with the capabilities provided by the **Scan Rig Function** controls.

MC4 Scan Rig Position Info – Inches – This indicator, Figure C.30., (Figures C.13. (C.16.) [CONTROL SCAN RIG] → C.24. (C.30.)), displays the current position of the measurement volume for the four scan rig axes in inches.

MC4 Scan Rig Position Info – Meters – This indicator, Figure C.31., (Figures C.13. (C.16.) [CONTROL SCAN RIG] → C.24. (C.31.)), displays the current position of the measurement volume for the four scan rig axes in meters.

Acquire Data

Selection of this control button, Figure C.16., will open the display shown in Figures C.32. and C.33., (Figures C.13. (C.16.) [ACQUIRE DATA] → C.32. [Cumulative Results Tab] → C.33.)). The display presents both controls and indicators to the operator that are typically used during the data acquisition process. Note that the plots indicate the results produced after acquiring 2429 signal burst captures.

The following sub-panels are found in the **Data Acquisition** display (Figure C.32.):

Data Acquisition Controls – This sub-panel, Figure C.34., (Figures C.13. (C.16.) [ACQUIRE DATA] → C.32. (C.34.)), provides the user with the controls and status information applicable to the data acquisition process. The primary control, **Start Data Acquisition**, begins the sequence of events to control the data acquisition hardware, software execution, operation sequencing, file management, progress monitoring, data retrieval, and Log file management. Once started the data acquisition continues until: a) the requested number of data samples have been acquired; b) the specified timeout limit is reached; or, c) the operator activates the **Terminate Data Acquisition** button.

Data Acquisition Information – This sub-panel contains indicators to provide the user with status information regarding the active data acquisition cycle.

System Settings – This sub-panel contains indicators that present the system setting status.

At the conclusion of a given data acquisition cycle, the Data Acquisition and Control program begins interrogating the Return file generated by the Signal/Data Processing program. When this file is updated, indicating that the processing program has completed its task and that the results have been written to the file, the Data Acquisition and Control program retrieves the results and presents them to the user as shown in Figures C.32. and C.33. During the interrogation period, the operator is presented with the dialog shown in

Figure C.35., (Figures C.13. (C.16.) [ACQUIRE DATA] → C.32. (C.34.) [START DATA ACQUISITION] → C.35.). If the retrieved results show that the convergence level is higher than the user specified level (Figure C.22.) a warning message, Figure C.36., (Figures C.13. (C.16.) [ACQUIRE DATA] → C.32. (C.34.) [START DATA ACQUISITION] → C.35. {Convergence Test Failed} → C.36.), is displayed. This message contains the number of processed signal bursts, the resultant convergence level and the specified convergence level along with a recommendation to acquire another ensemble at the current measurement volume location.

It should be noted that selecting the **CONTINUE** button in Figure C.35., will bypass the opportunity for the data processing operation to conclude before the next data ensemble is requested. This prohibits the retrieval of the results needed to evaluate the quality of the previous data ensemble (although this data will still be preserved and presented by the Signal/Data Processing computer). It is recommended that the operator wait until the processing phase is completed and the results reviewed to determine the next course of action.

Since the Signal/Data Processing program was designed with a 10,000 signal burst limit for each component, the Data Acquisition program has an acquisition limit test. If the user requests more than 10,000 signal bursts to be acquired, either as a single ensemble or the sum of multiple ensembles at the same location, the Data Acquisition program will present the warning shown in Figure C.37., (Figures C.13. (C.16.) [ACQUIRE DATA] → C.32. (C.34.) {>10,000 Signal Bursts Requested} → C.37.). Here the user can adjust the requested number of signal bursts to be processed to remain below the limit. If this is disregarded, the Signal/Data Processing program will process the first 10,000 signal bursts and ignore the rest. Thus, if 10,000 signal bursts do not satisfy the convergence test for statistical stationarity, it cannot be satisfied at that location.

System Diagnostics

Selection of this control button, Figure C.16., will present the user with the information panel shown in Figure C.38., (Figures C.13. (C.16.) [SYSTEM DIAGNOSTICS] → C.38.). This panel contains a tab-based interface with settings and feedback/status elements related to the data acquisition process. In most circumstances the operator will not need to interact with this diagnostic information as it is primarily maintained for the purpose of providing feedback to the system developer, although it might answer the question of why doesn't a component yield usable signal bursts. For example, in the U-component signal plot shown in Figure C.38., (***Acquired Data*** tab) only a jitter of the least significant bit in the high-speed analog-to-digital converter is found instead of the typical signal burst shown in the V-component. If this situation occurs, the user should begin searching for the problem because any further acquisitions would not yield usable measurements.

Acquired Data tab – This tab presents the screen shown in Figure C.38., which presents the results from the most recent data ensemble. Activation of the

Plot Data? control (Figure C.39., (Figures C.13. (C.16.) [SYSTEM DIAGNOSTICS] → C.38. (C.39.))), provides the user with a monitoring capability to view the acquired U- and V-component signal bursts. The displayed signal traces are updated at the rate specified by the user via the **Plot Delay (ms)** control. Normally the **Plot Data?** control is turned off unless there is a suspected problem because of the time required to view the signal bursts.

Hardware tab – This tab presents the screen shown in Figure C.40., (Figures C.13. (C.16.) [SYSTEM DIAGNOSTICS] → C.38. [Hardware Tab] → C.40.), which reflects the configuration of the data acquisition hardware as defined by both the operator and settings applied within the control software. At a glance the reader will recognize that there are a myriad of settings and parameters available; thus reflecting both the flexibility of the PXI-based hardware and configuration utilized to realize a system capable of satisfying the requirements of laser velocimetry. Information presented on this tab is grouped according to device or function where possible. Detailed explanations of these settings/information are presented in Appendix D.

Information tab – This tab presents the screen shown in Figure C.41., (Figures C.13. (C.16.) [SYSTEM DIAGNOSTICS] → C.38. [Information Tab] → C.41.), which provides feedback of information reported from the system components rather than user settings. The ability to retrieve and present this information provides confirmation that the system is configured according to the user's specifications.

Sub-Task Info tab – The information presented from this tab, Figure C.42., (Figures C.13. (C.16.) [SYSTEM DIAGNOSTICS] → C.38. [Sub Task Info Tab] → C.42.), pertains to the background tasks conducted in software as activated and controlled by the Data Acquisition and Control program, and *not* the program operator. Some of these sub-tasks are always used while others are used as needed. A discussion of these subtasks along with their functions is presented beginning at Appendix D, page D.31.

Simulation Signal Task Info tab – The information presented by this tab, Figure C.43., (Figures C.13. (C.16.) [SYSTEM DIAGNOSTICS] → C.38. [Simulation Signal Task Info Tab] → C.43.), outlines the location and type of simulated data used to validate the operation of the data acquisition system. The simulation data can originate directly from a file, a file selected to drive the arbitrary waveform generator, or even files captured from a particle generator or flow field measurements.

Log File Info tab – The information presented from this tab, Figure C.44., (Figures C.13. (C.16.) [SYSTEM DIAGNOSTICS] → C.38. [Log File Info Tab] →

C.44.), is related to the Log file that maintains the data acquisition information produced during the course of a flow field investigation. These Log files are uniquely identified by date and measurement time.

Data Management Settings/Info tab – This panel, Figure C.45., (Figures C.13. (C.16.) [SYSTEM DIAGNOSTICS] → C.38. [Data Management Settings/Info Tab] → C.45.), presents information related to the data retrieval and storage operations of the system as well as status information related to the various hardware tasks.

Processed Results tab – This panel, Figure C.46., (Figures C.13. (C.16.) [SYSTEM DIAGNOSTICS] → C.38. [Processed Results Tab] → C.46.), contains information related to the processing of the data ensembles. This information is extracted from a file generated during the signal/data processing phase. Information gleaned from this file, in particular **Convergence Level** is used to determine if another data ensemble should be acquired at the present measurement volume location in an attempt to reach flow statistical stationarity. This test is only performed if the Convergence Validation test has been enabled (**Configuration**: **System Options**).

System Information

Selection of this option, (Figures C.13. (C.16.)), causes a panel containing pdf reader commands that will display information/help files pertaining to the Data Acquisition and Control program and the Signal/Data Processing program. Included in these files are the portions of this document that pertain directly to the hardware/software used in the laser velocimeter.

Quit

Selection of this option, (Figures C.13. (C.16.)), terminates the Data Acquisition and Control and the Signal/Data Processing programs.

Program & System Status

At the bottom of the Navigation Bar, (Figures C.13. (C.16.)), status information is provided in a *quick look* format with a progress monitor indicating the current function being performed during a data acquisition cycle. The number of data ensembles collected during a given test is also displayed.

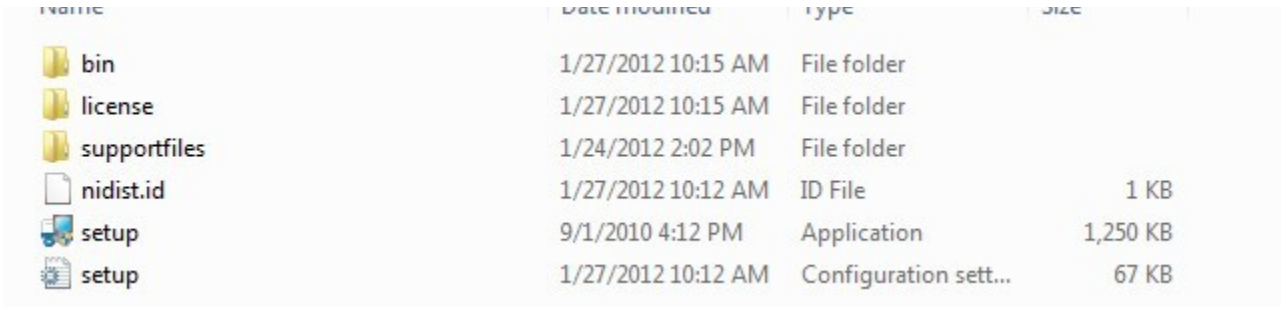

Figure C.1.– Windows Explorer window showing LV Data Acquisition program installation directory.

Figure C.2.– LV Data Acquisition application installation/setup program – Welcome Screen.

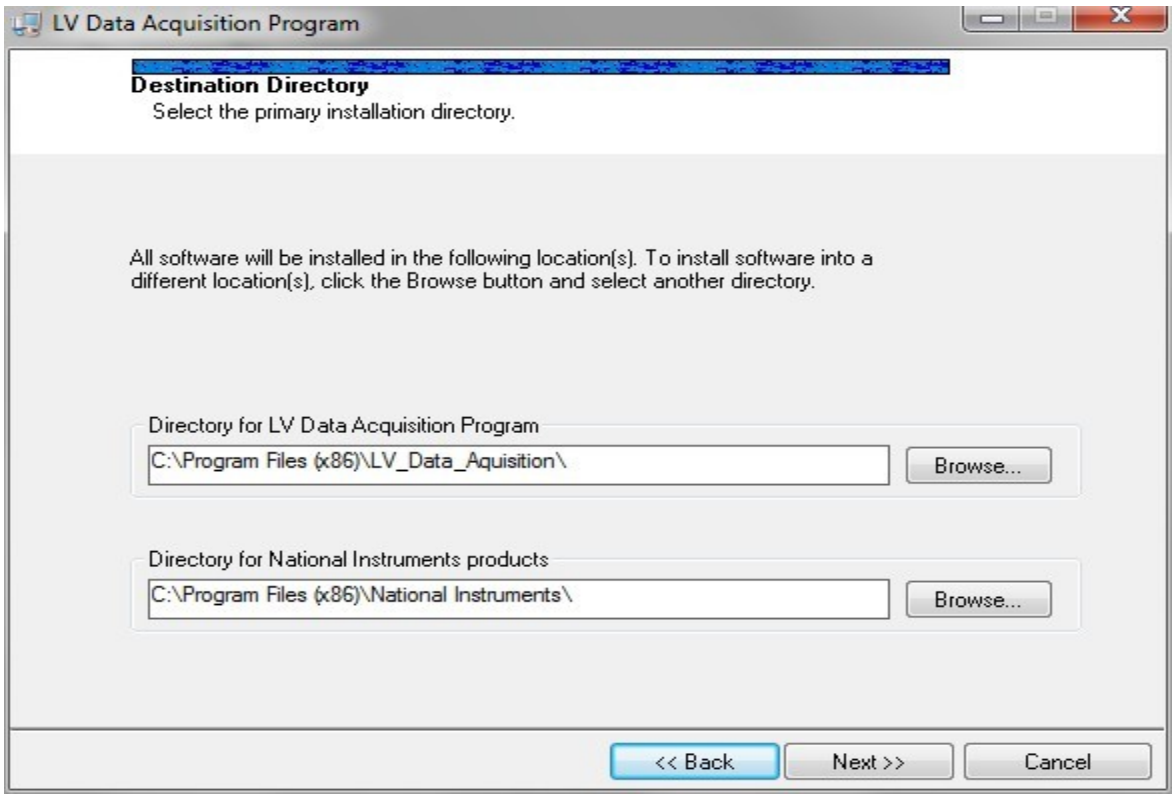

Figure C.3.– LV Data Acquisition application installation/setup program – Program Destination Directory Dialog.

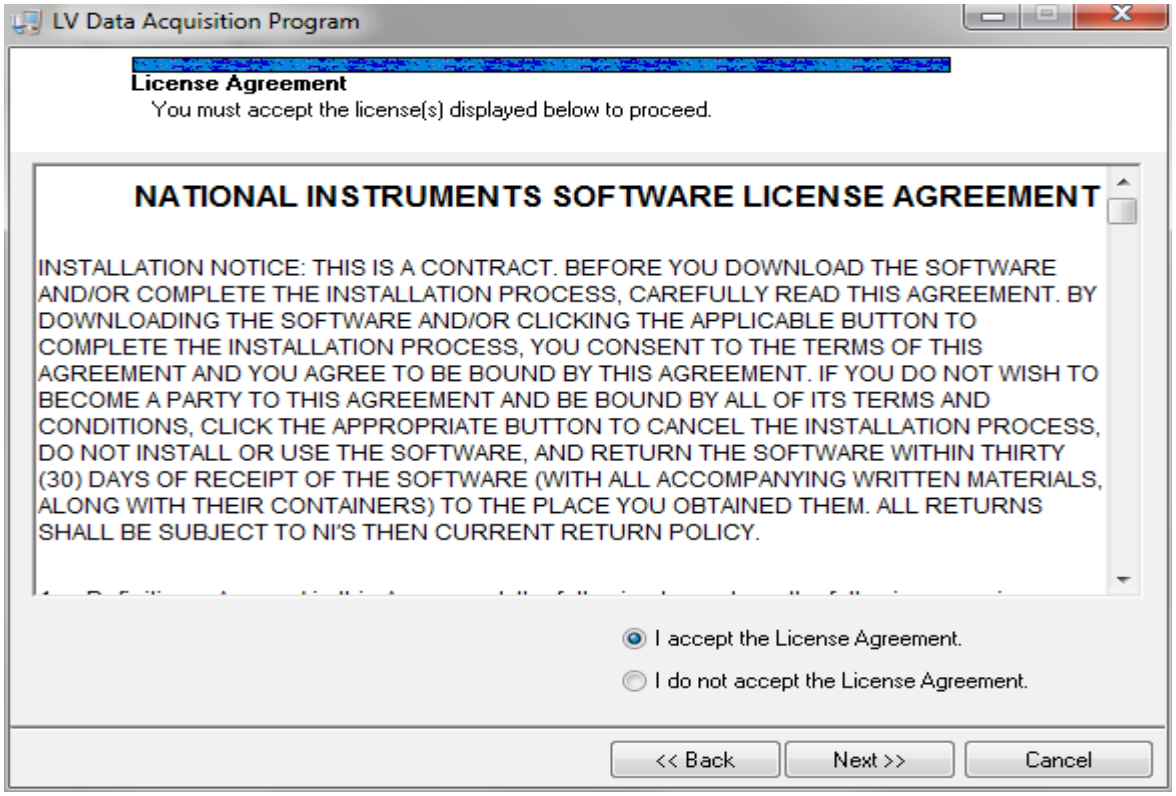

Figure C.4. - LV Data Acquisition program installation/setup program – National Instruments License Agreement.

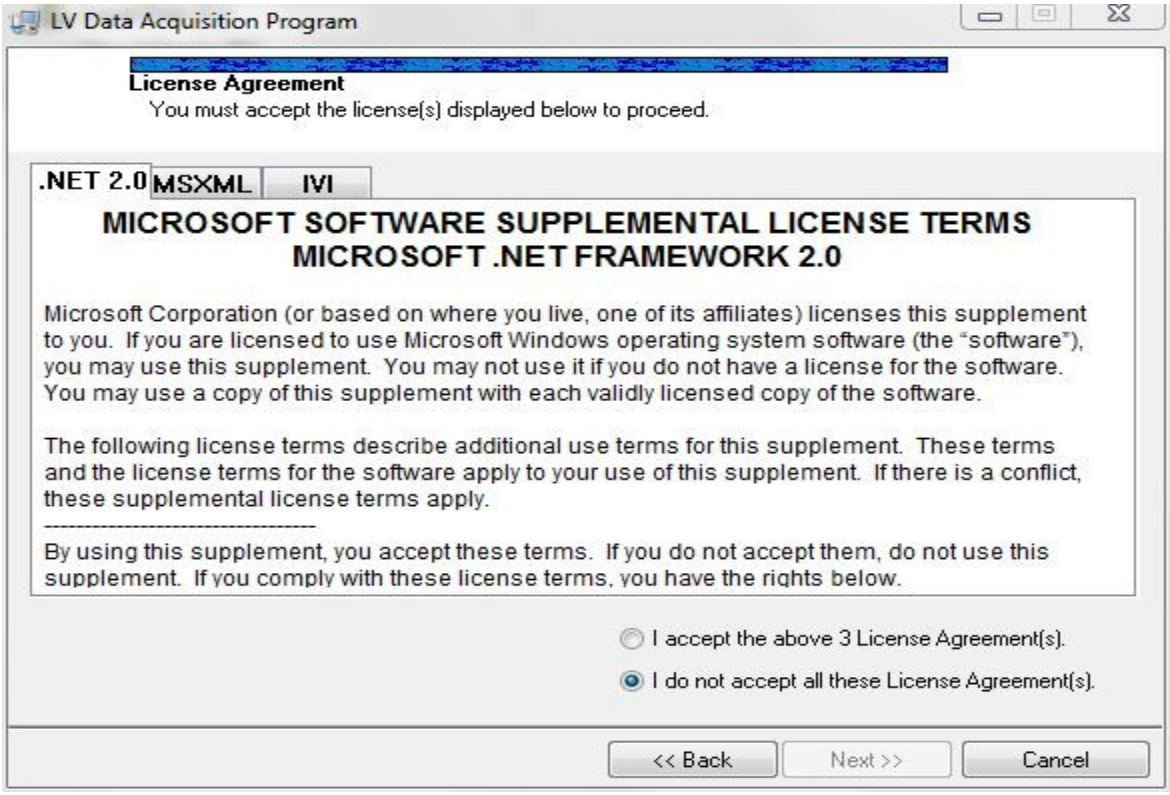

Figure C.5. - LV Data Acquisition program installation/setup program – Microsoft Component License Agreement

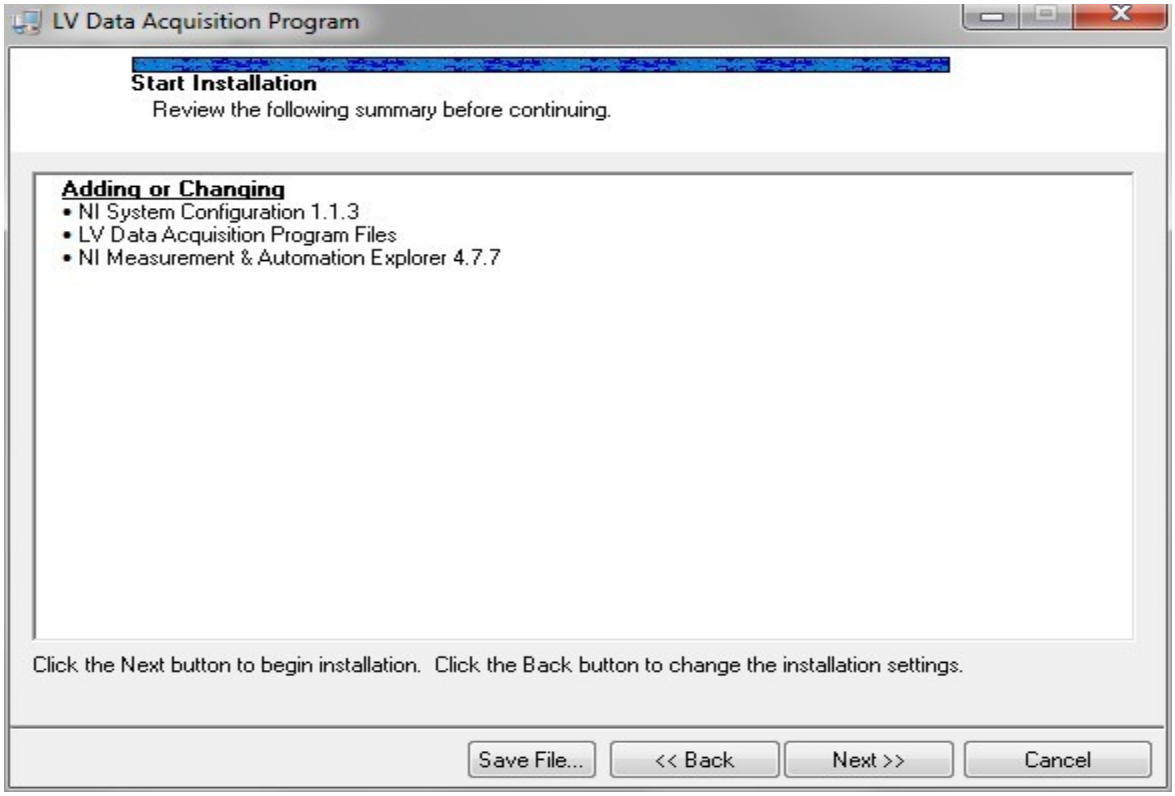

Figure C.6. - LV Data Acquisition program installation/setup program – Installation Review Dialog.

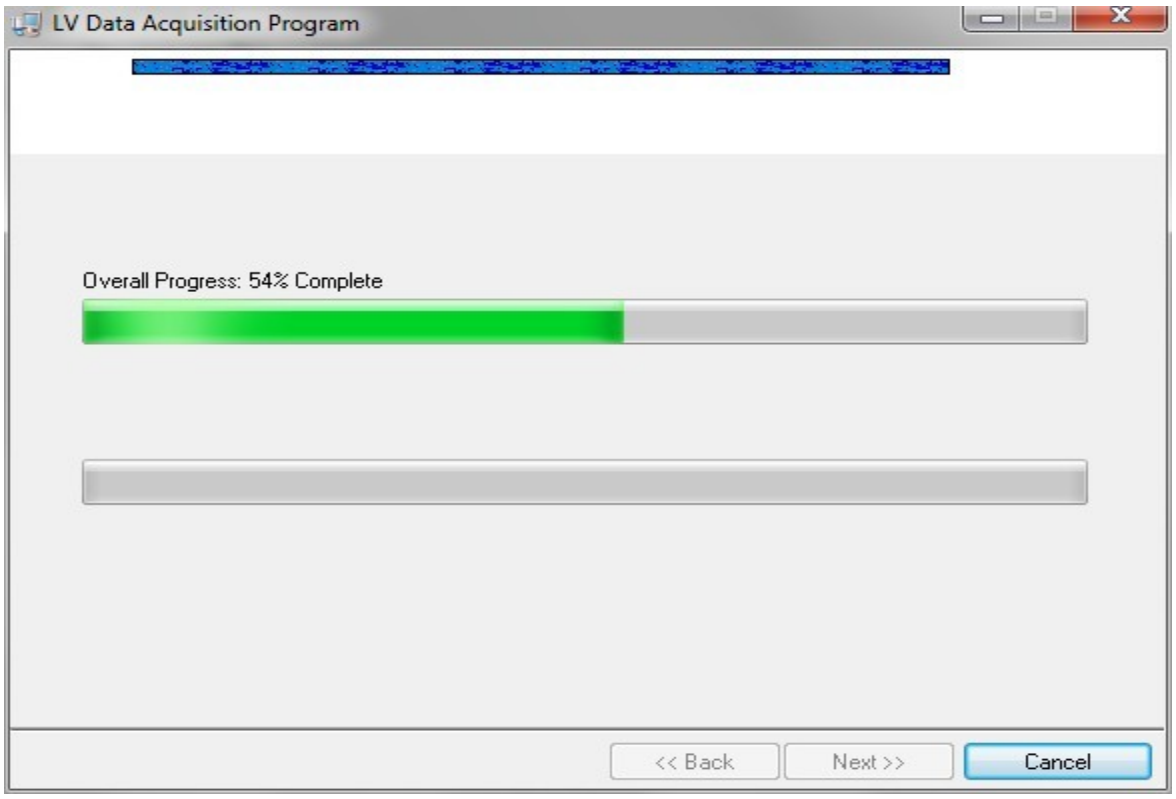

Figure C.7. - LV Data Acquisition program installation/setup program – Installation Progress Dialog.

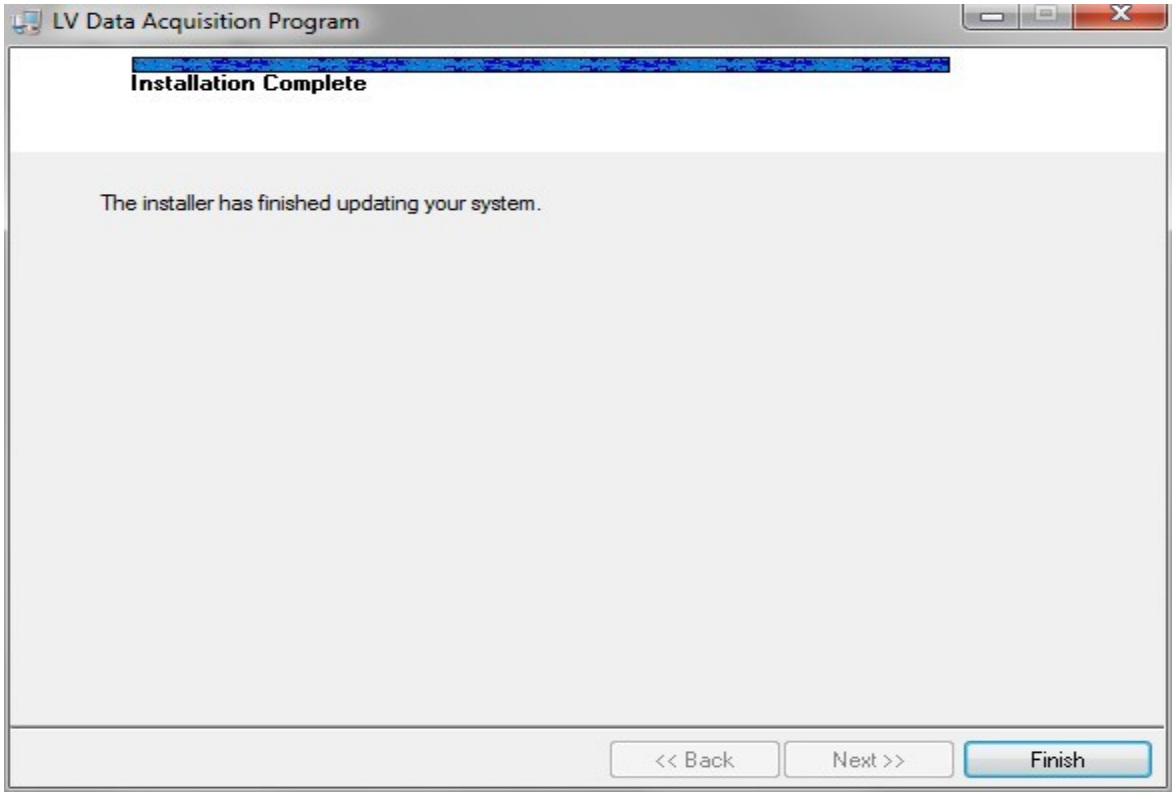

Figure C.8 - LV Data Acquisition program installation/setup program – Installation Complete Dialog.

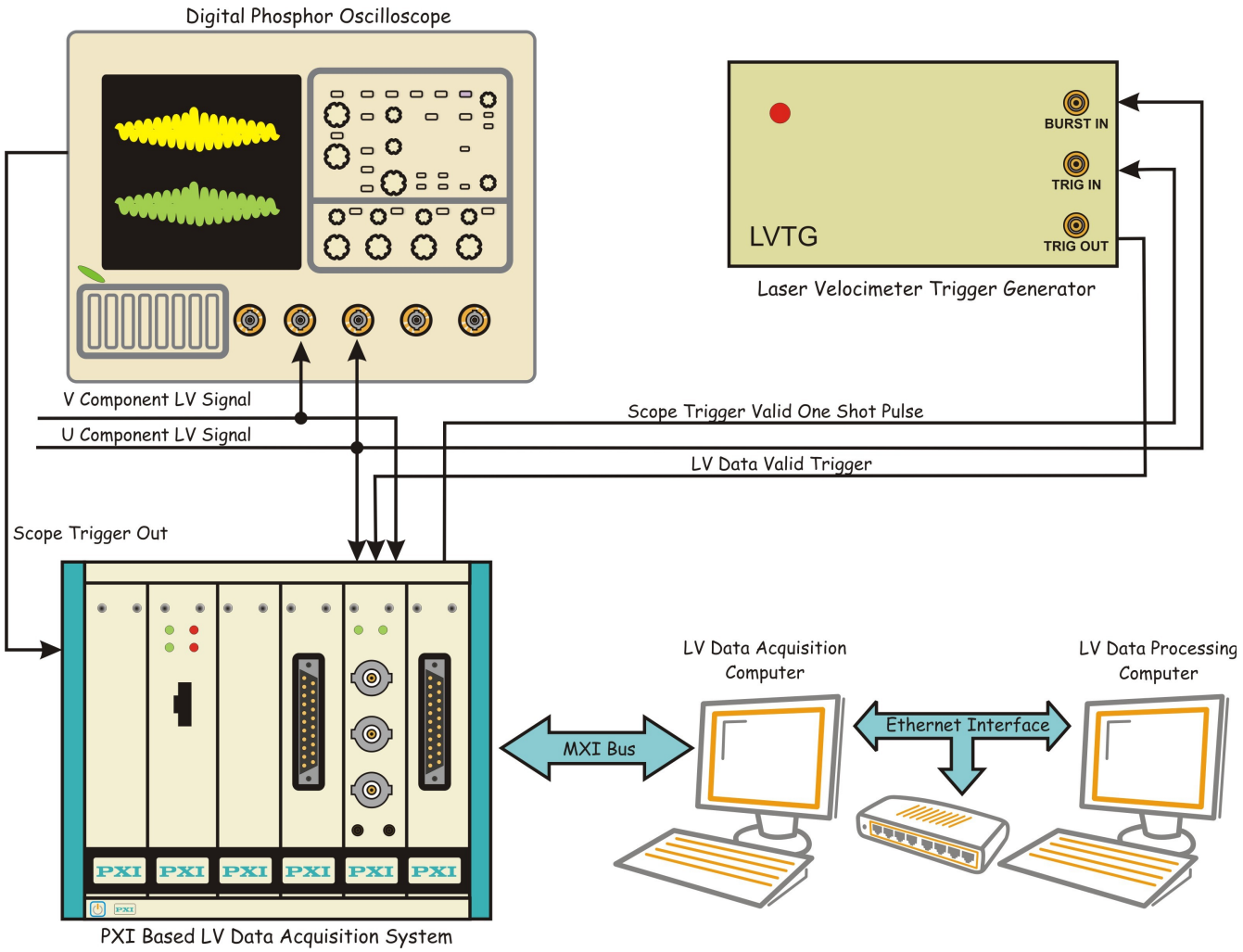

Figure C.9.– Data Acquisition / Signal/Data Processing system hardware interconnection diagram.

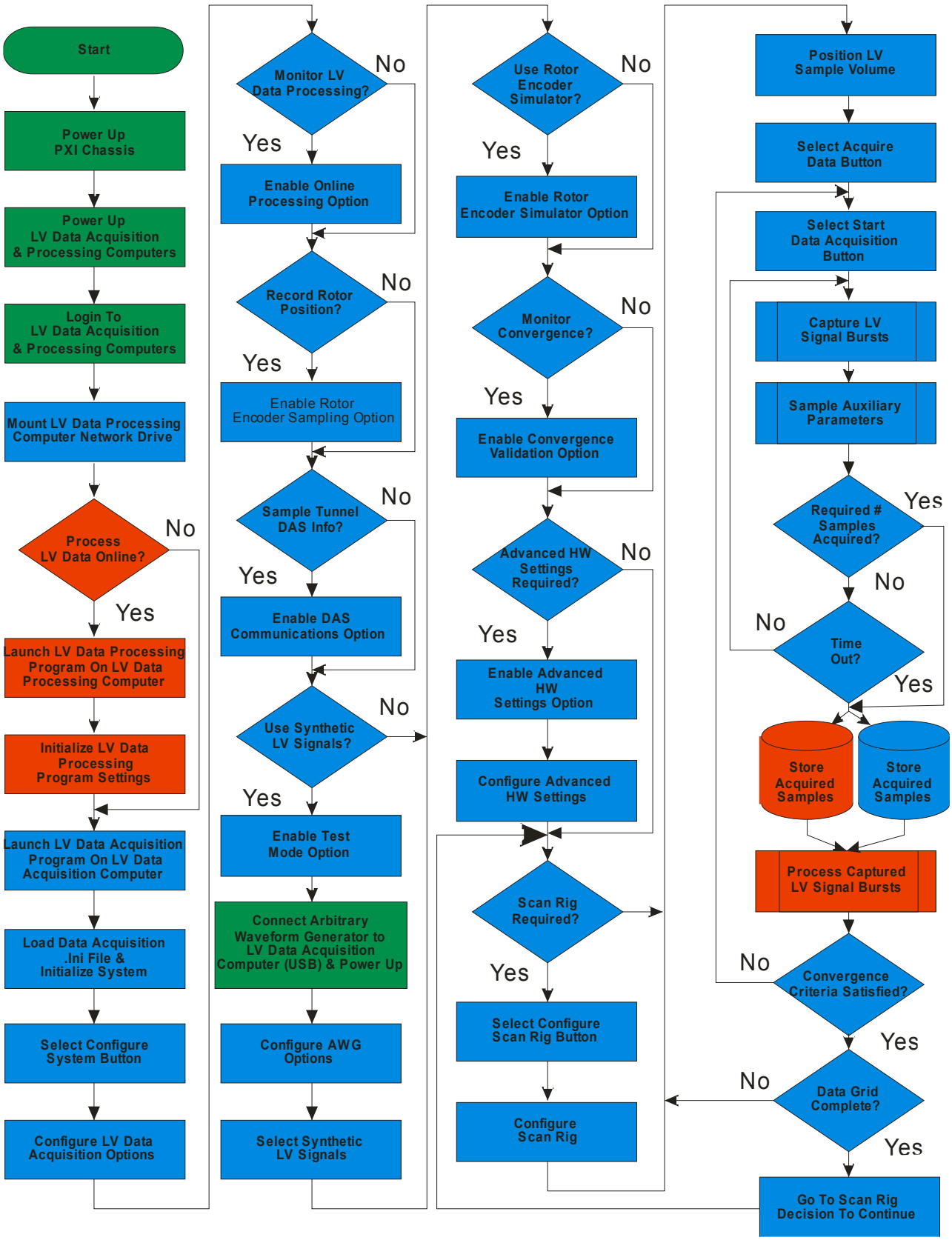

Figure C.10.– Data Acquisition / Signal/Data Processing system operational flow diagram.

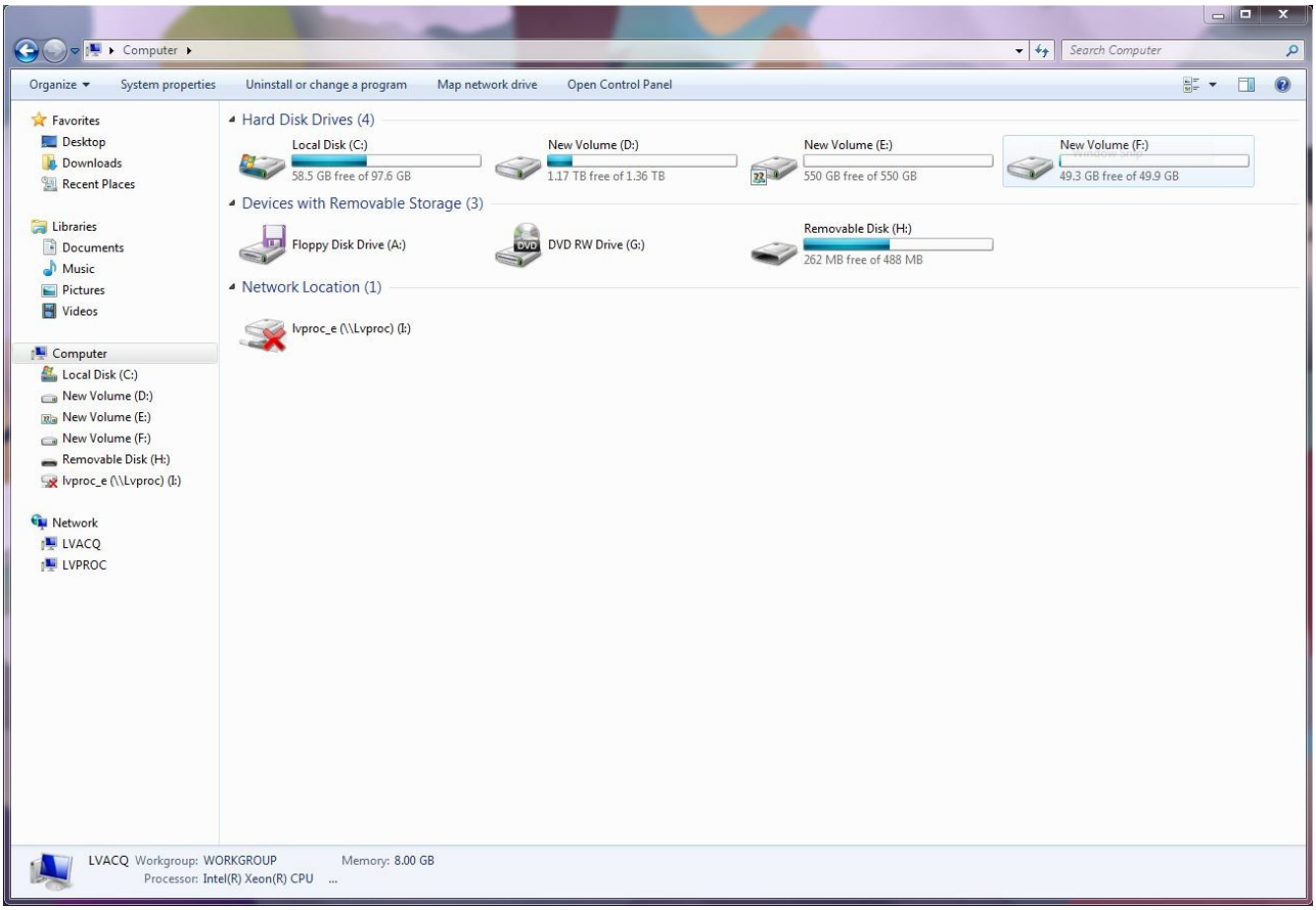

Figure C.11.– Windows Explorer window.

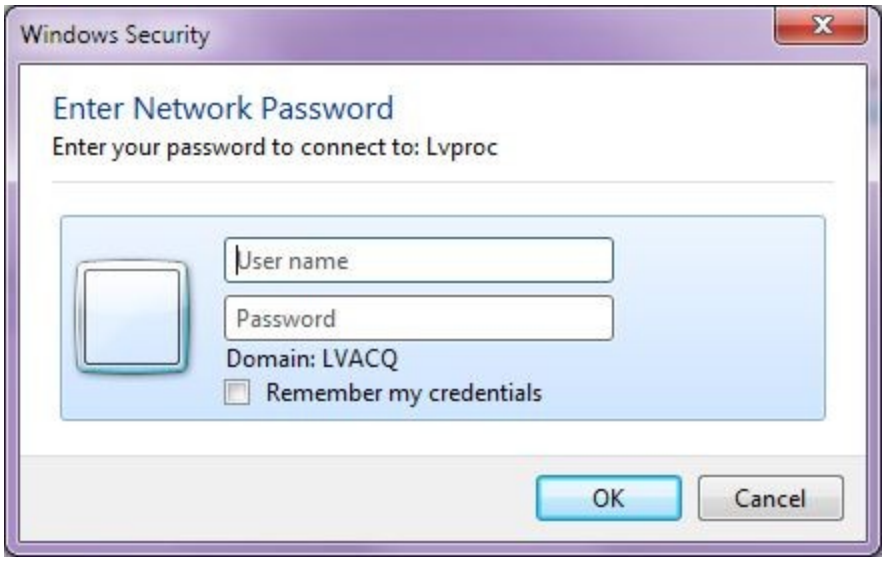

Figure C.12.– Password entry prompt for Network to mount remote disk drive.

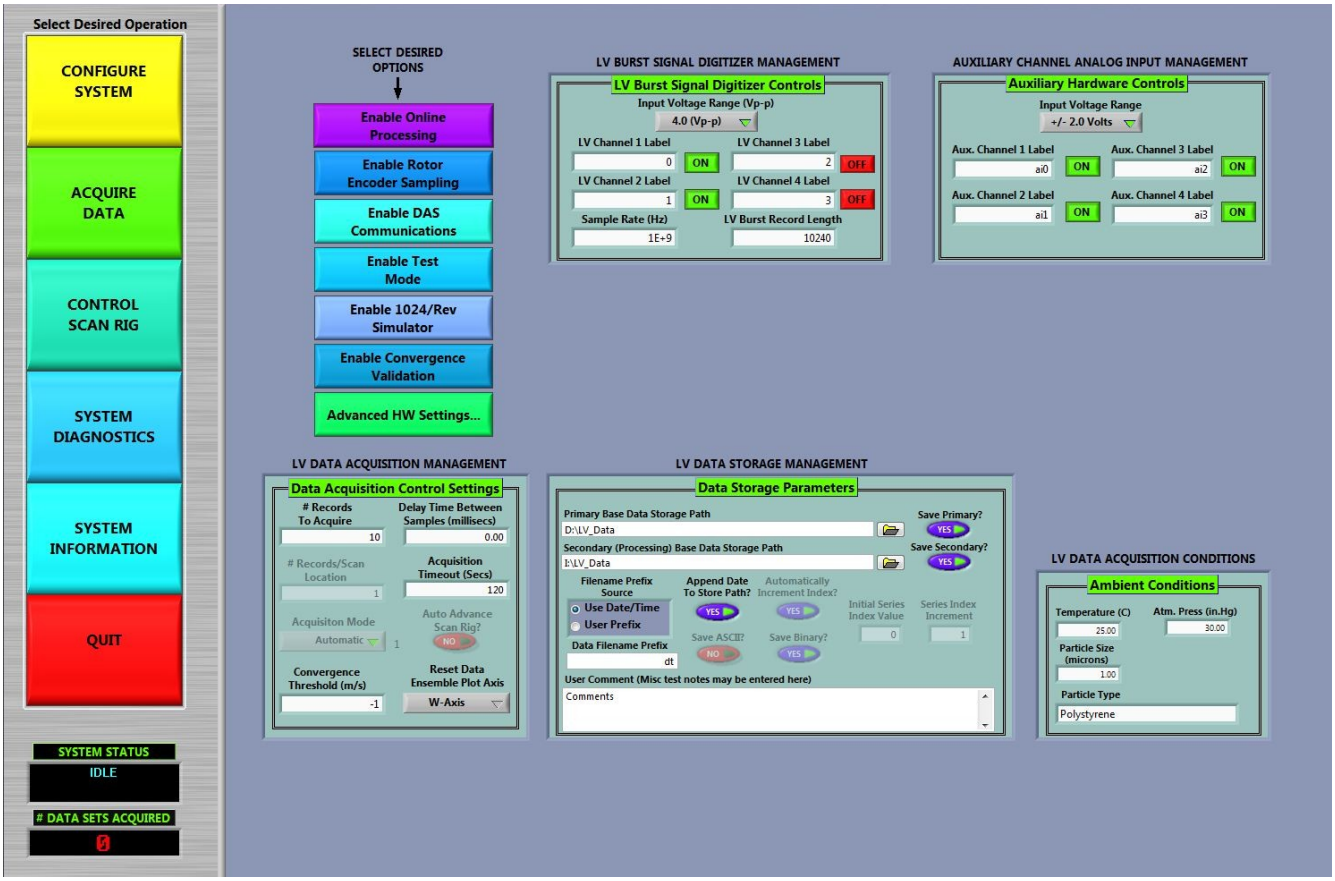

Figure C.13.– Opening (Main) screen for the Data Acquisition and Control program.

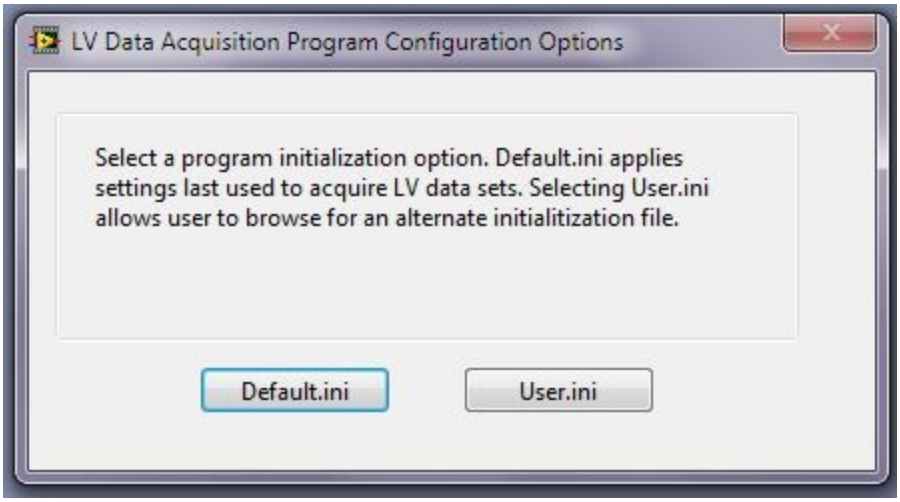

Figure C.14.– Initialization File prompt.

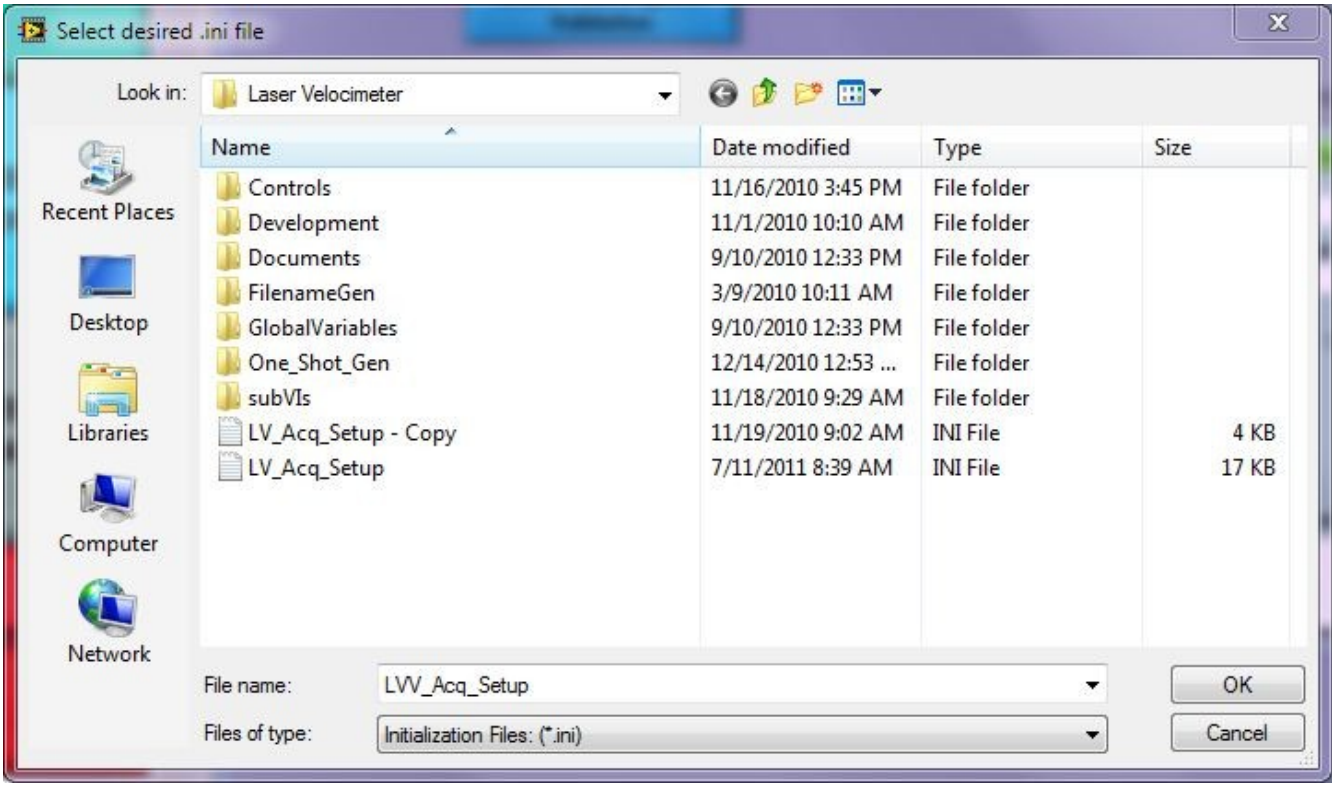

Figure C.15.– File manager window to select User Initialization File.

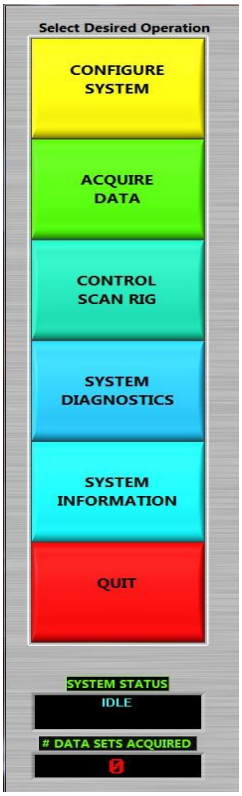

Figure C.16.– Data Acquisition and Control program Navigation Bar.

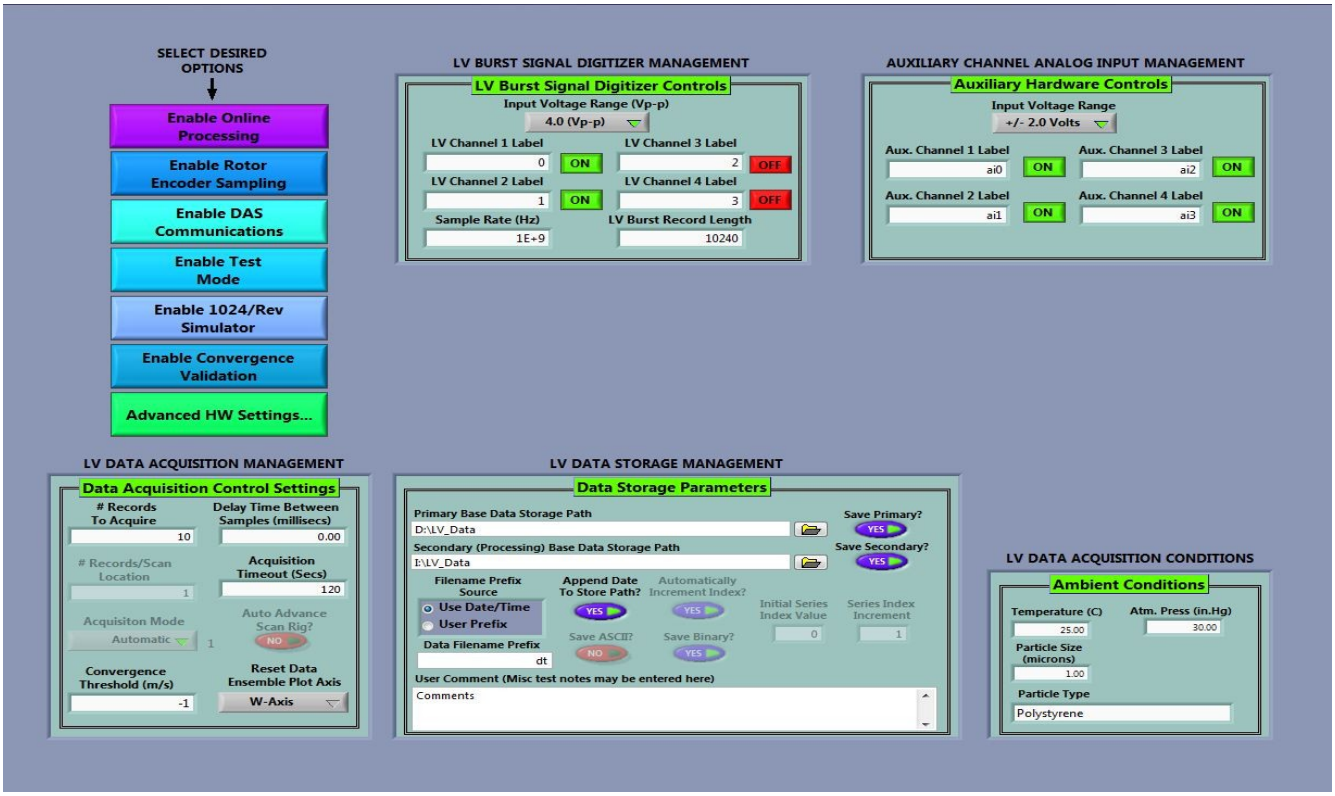

Figure C.17.– Data Acquisition and Control program configuration/management panel (Default configuration).

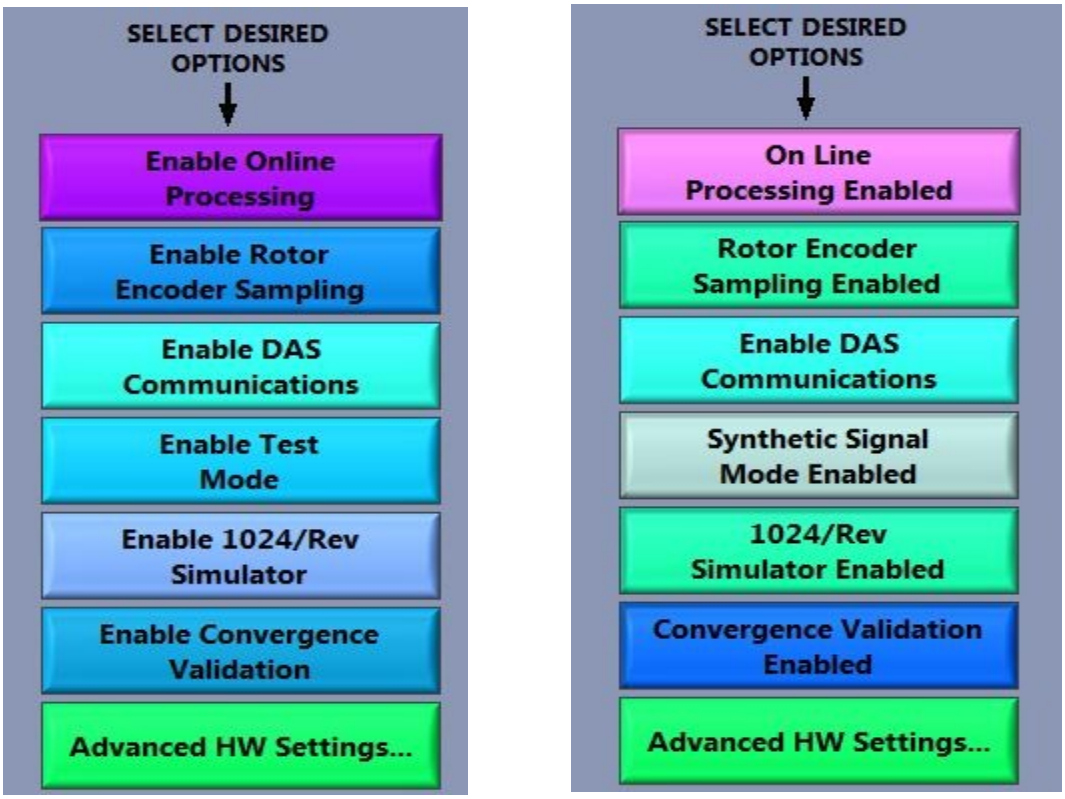

Figure C.18.– Data acquisition options (Disabled &Enabled shown).

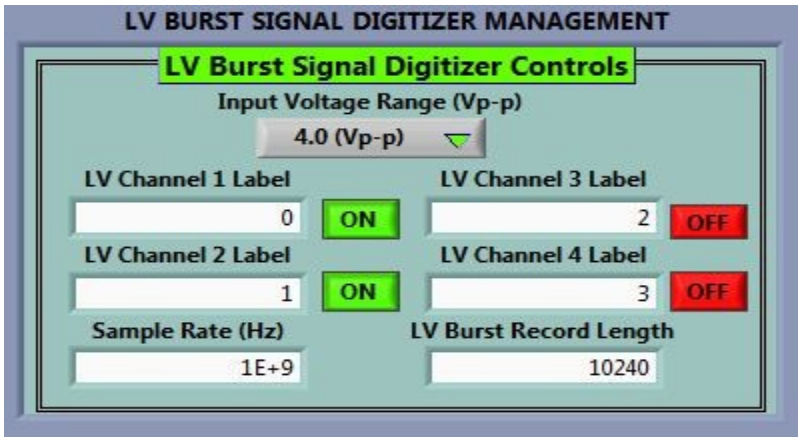

Figure C.19.– LV Burst Signal Digitizer settings.

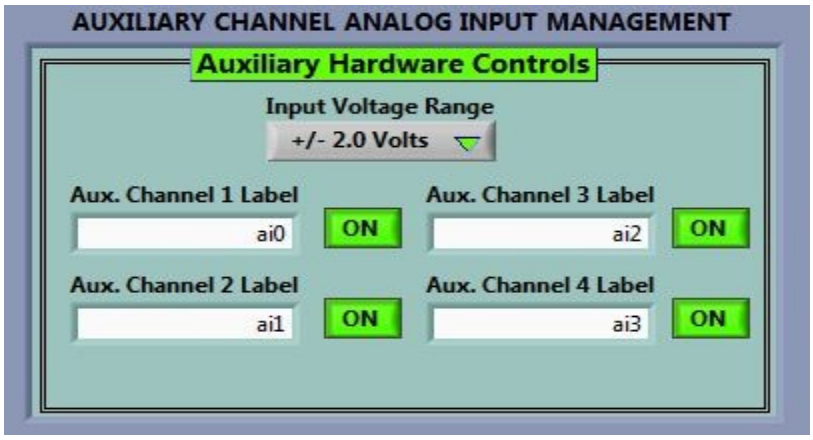

Figure C.20 .– Auxiliary analog input channel management settings.

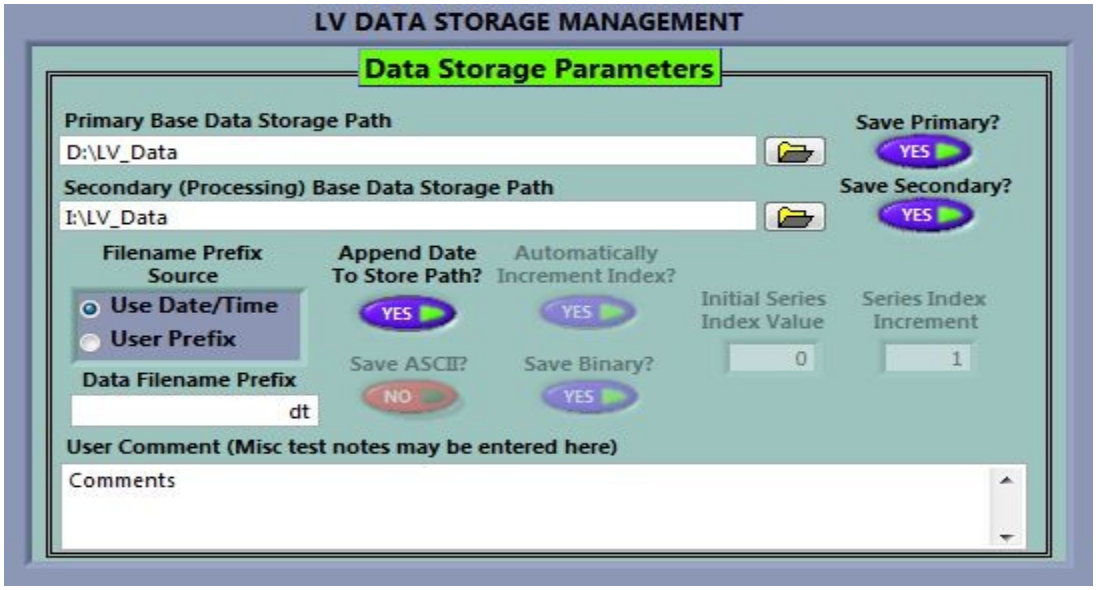

Figure C.21.– Data Storage Management settings

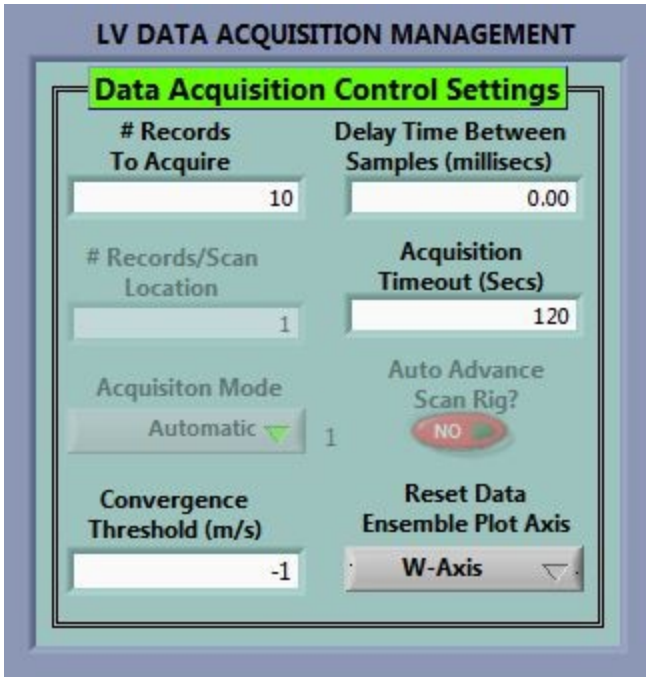

Figure C.22.– LV Data Acquisition Management settings.

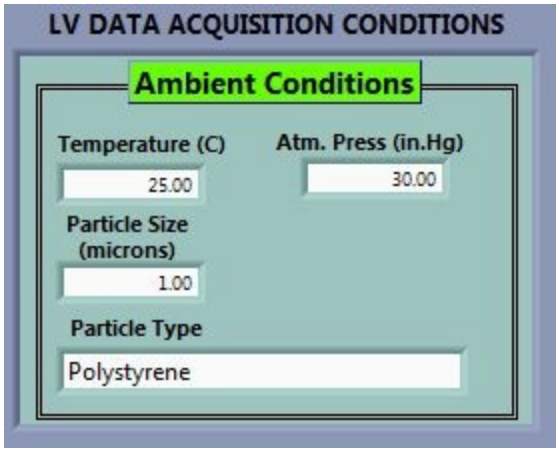

Figure C.23.– Data Acquisition Conditions.

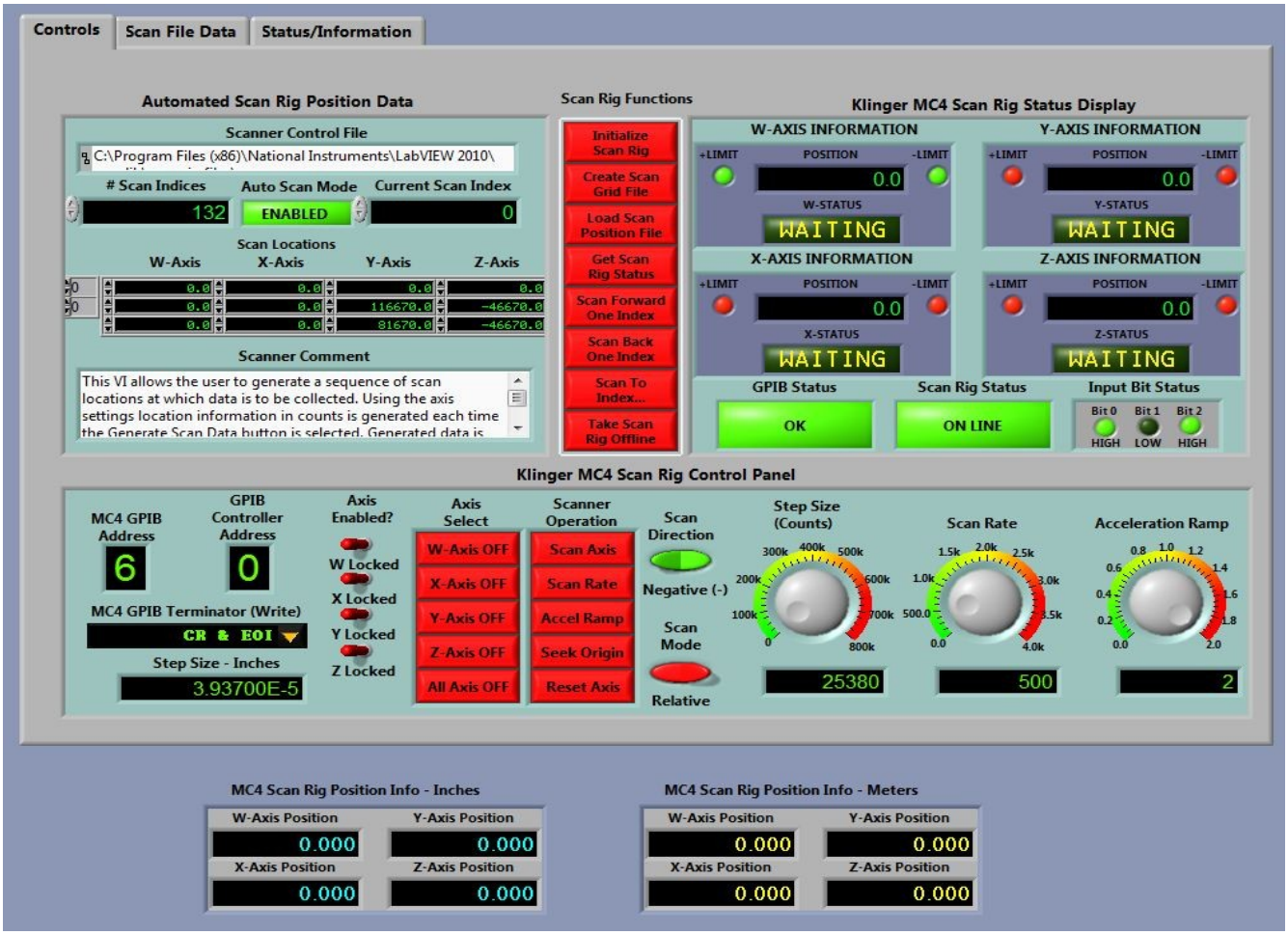

Figure C.24.– Scan Rig Management Interface (System Online).

Figure C.25.– Scan Rig Function controls.

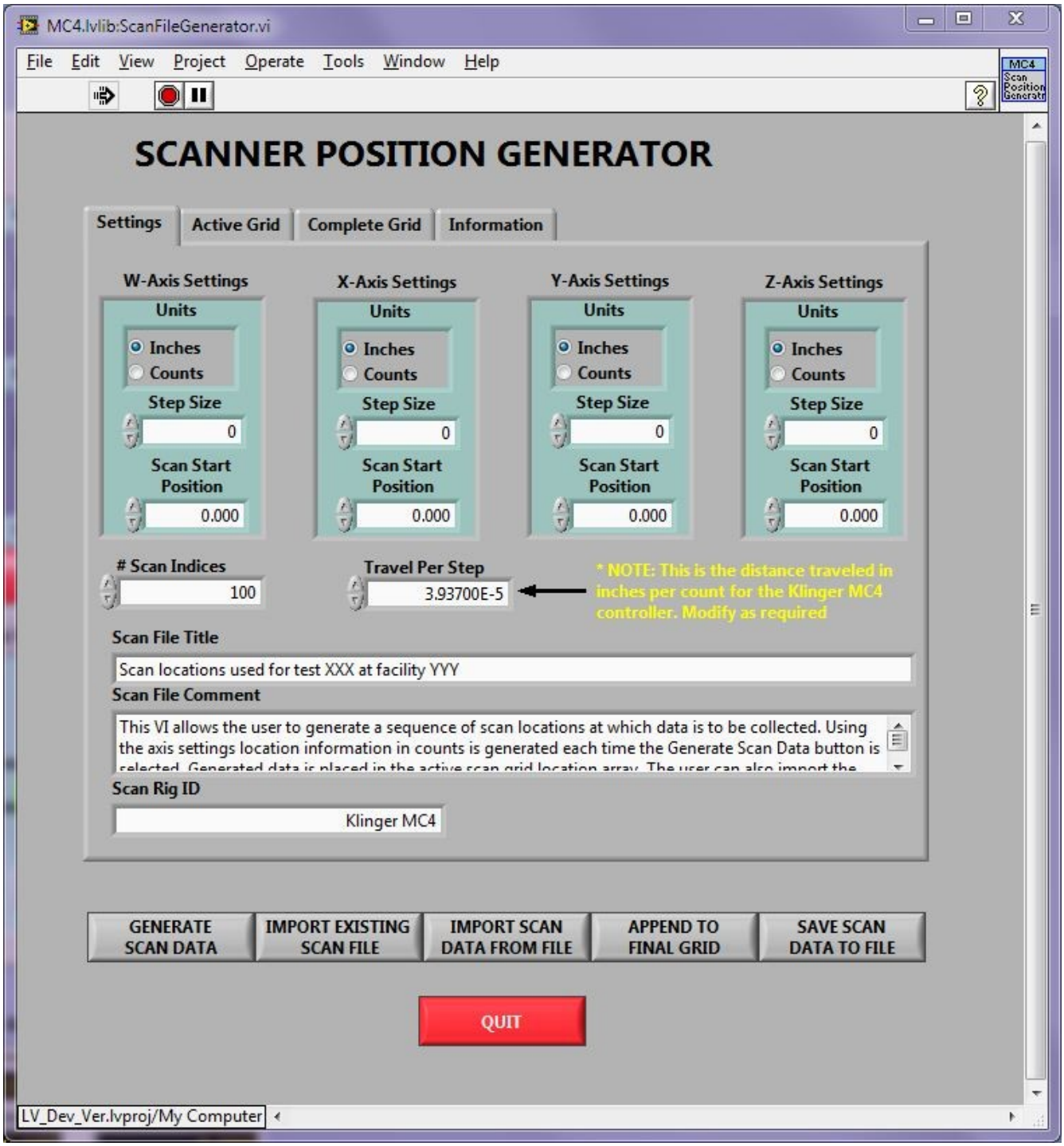

Figure C.26.– Scanner Position Generator dialog.

Figure C.27.– Klinger MC4 Scan Rig Position/Status Display.

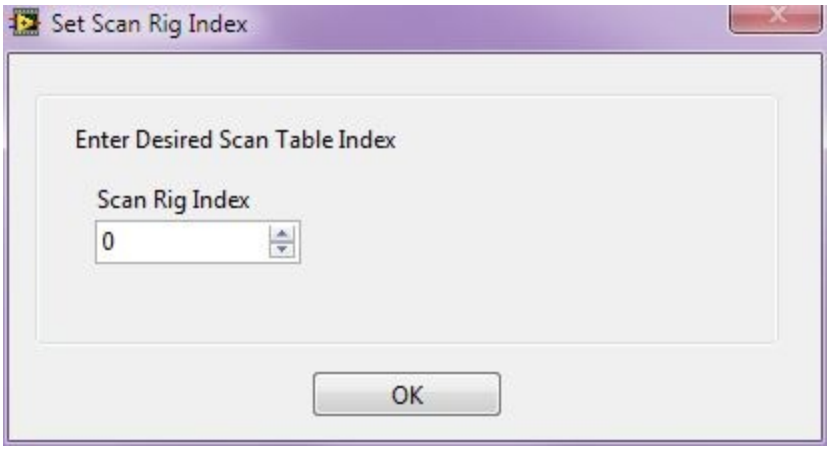

Figure C.28.– Scan rig position manual index selection dialog.

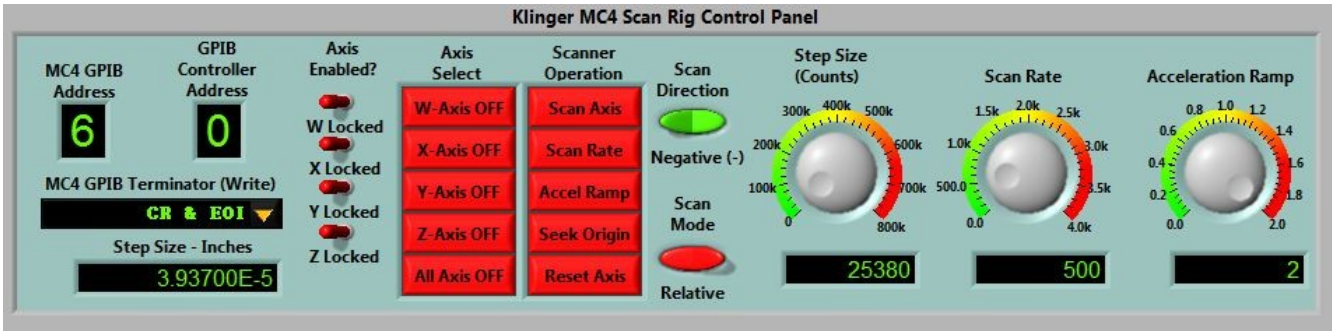

Figure C.29.– Klinger MC4 Scan Rig Control Panel.

Figure C.30.– MC4 Scan Rig Position Info – Inches.

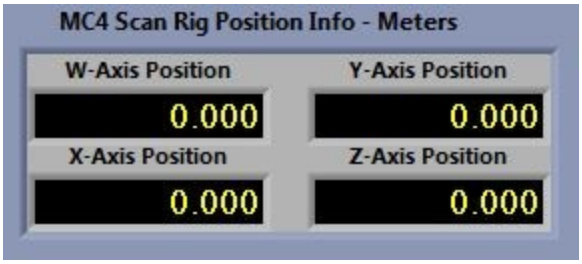

Figure C.31.– MC4 Scan Rig Position Info – Meters.

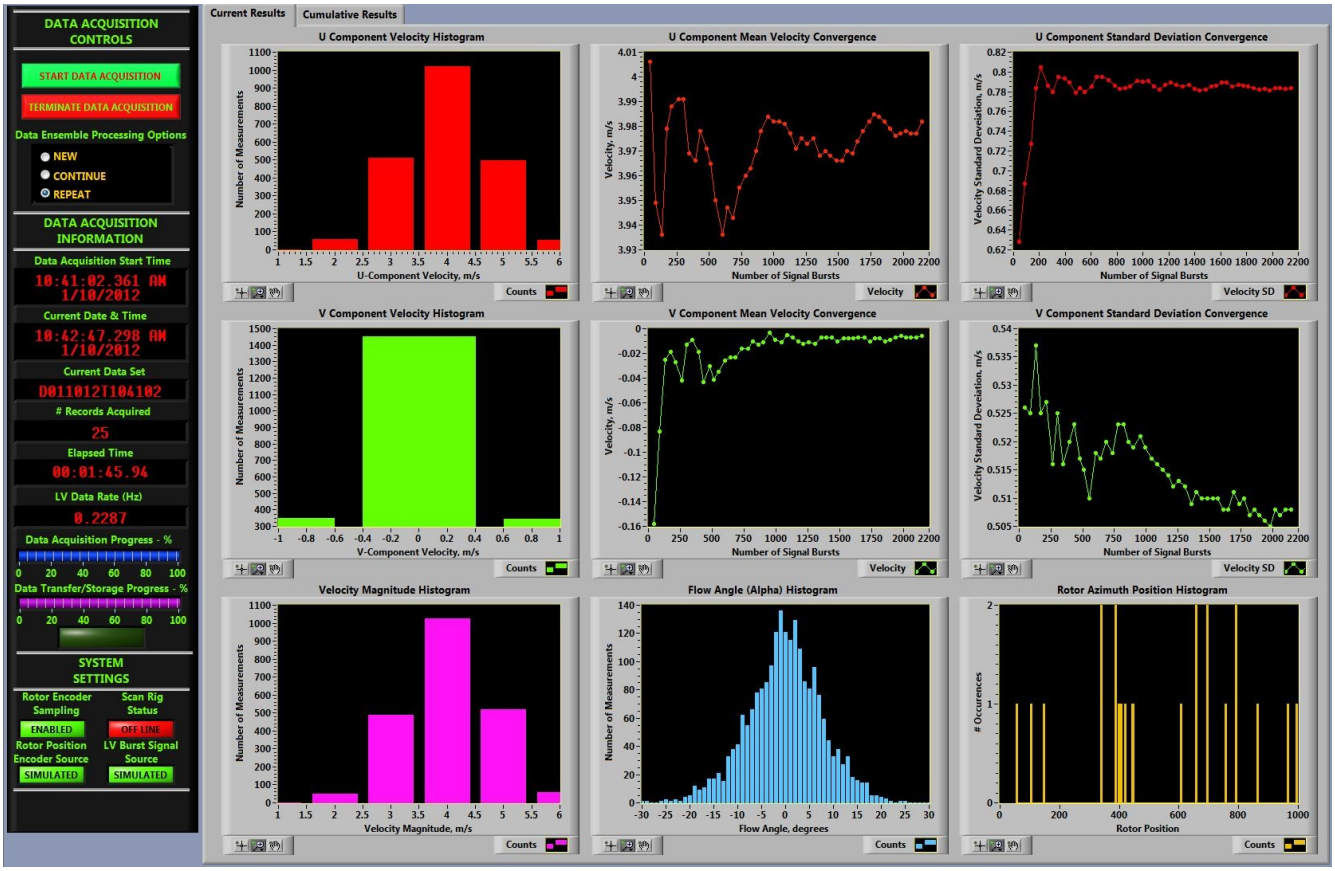

Figure C.32.– Data Acquisition Management Control Interface (Post data acquisition Current Results tab shown).

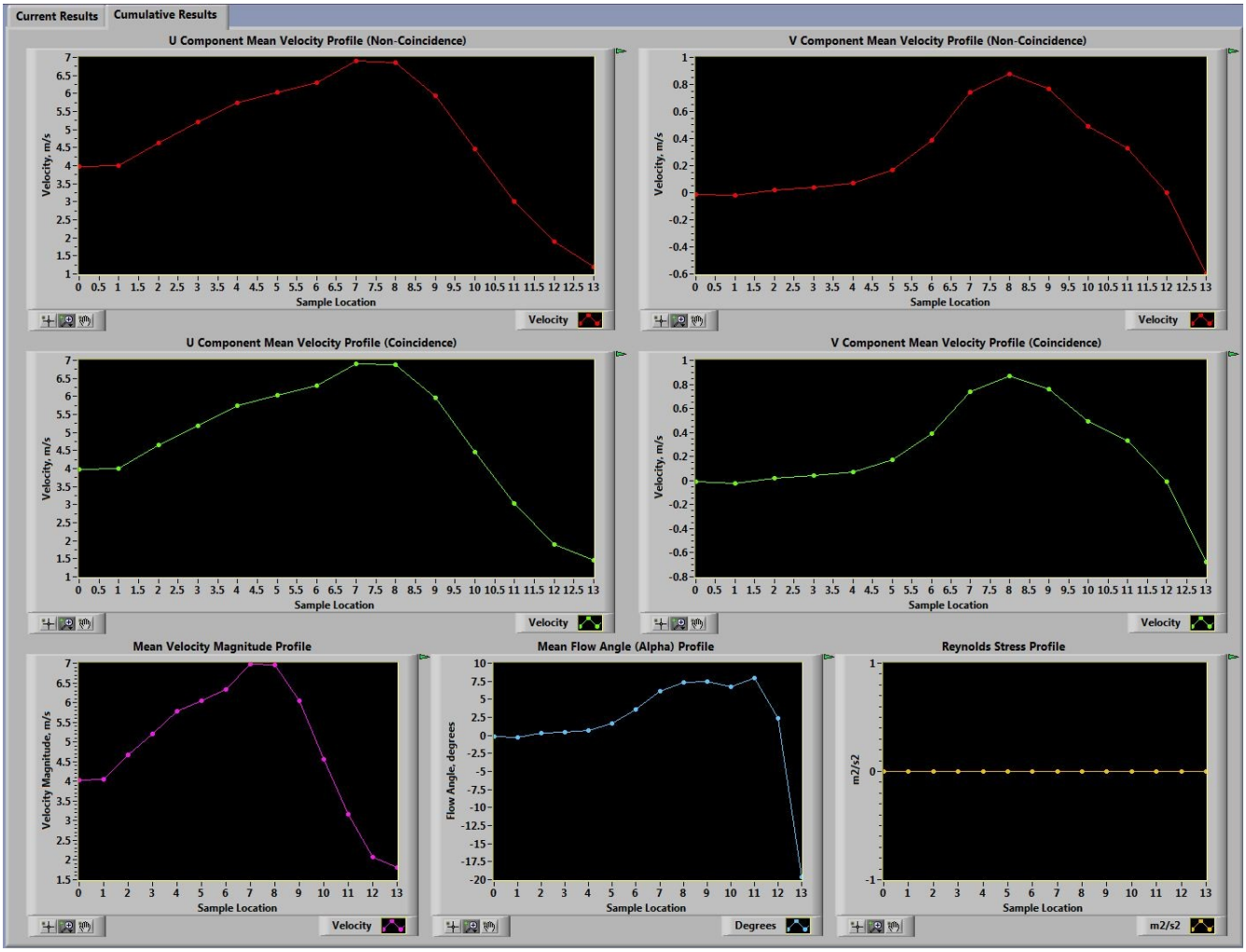

Figure C.33.– Data Acquisition Management Control Interface (Post data acquisition Cumulative Results tab shown).

Figure C.34.– Data acquisition management controls/settings.

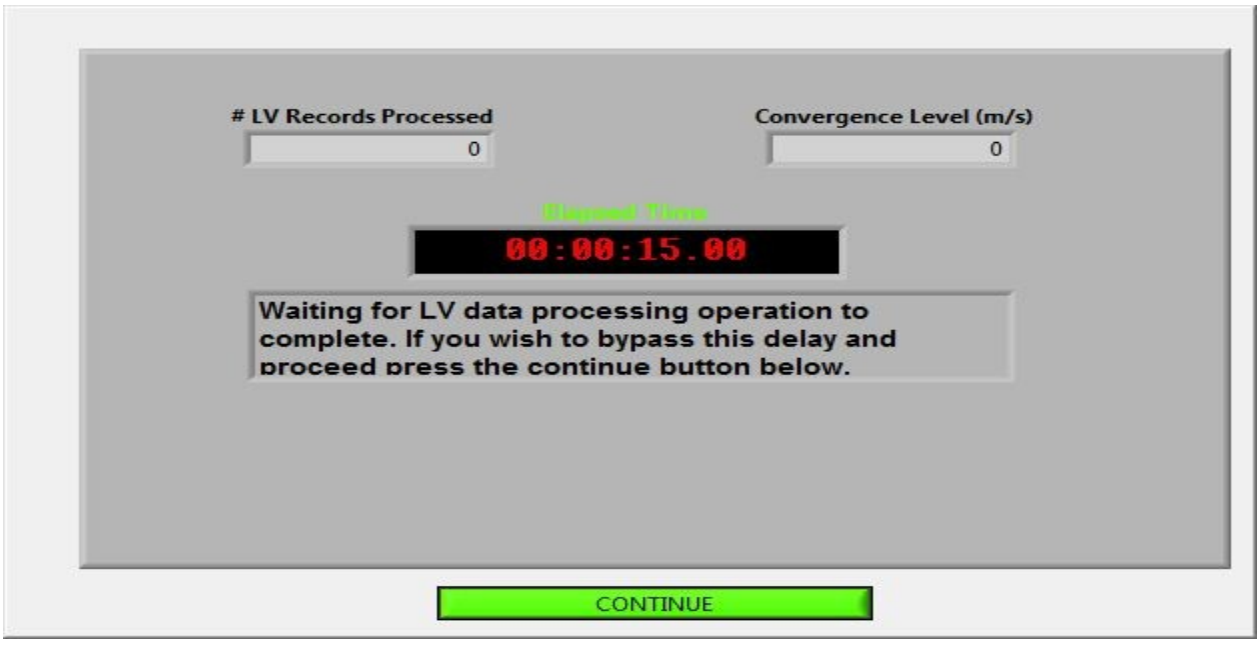

Figure C.35. - LV data processing wait dialog

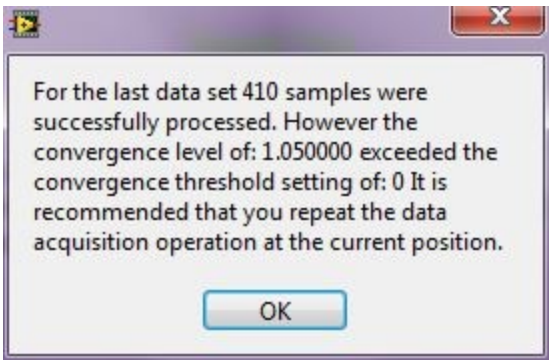

Figure C.36 – Data processing results presentation dialog

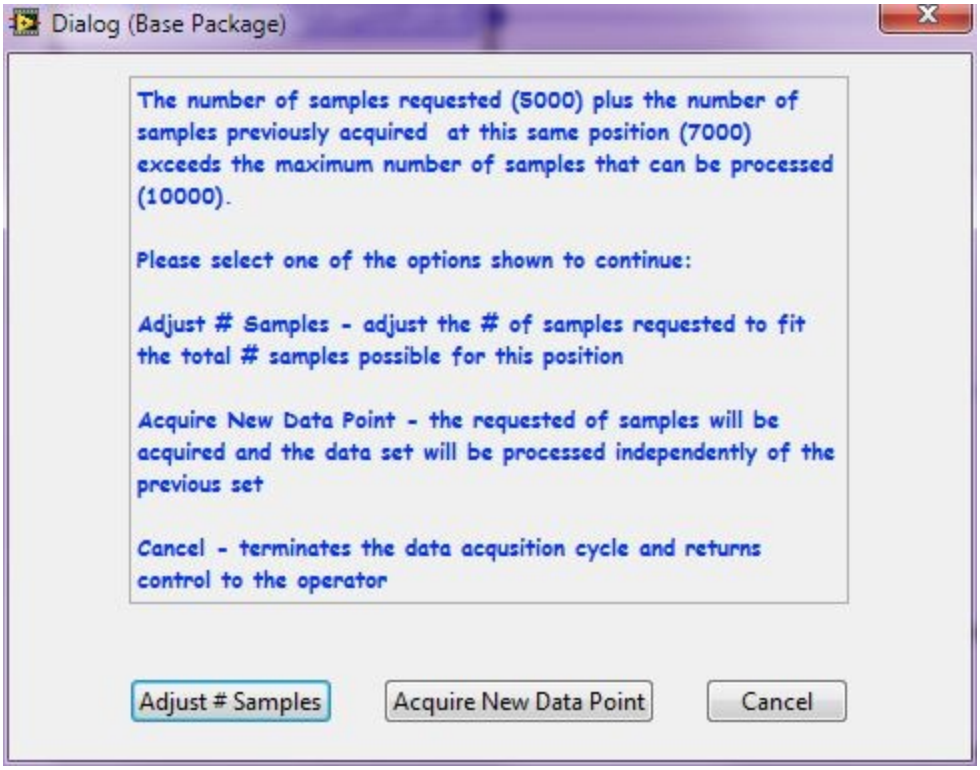

Figure C.37 – Sample quantity adjustment dialog

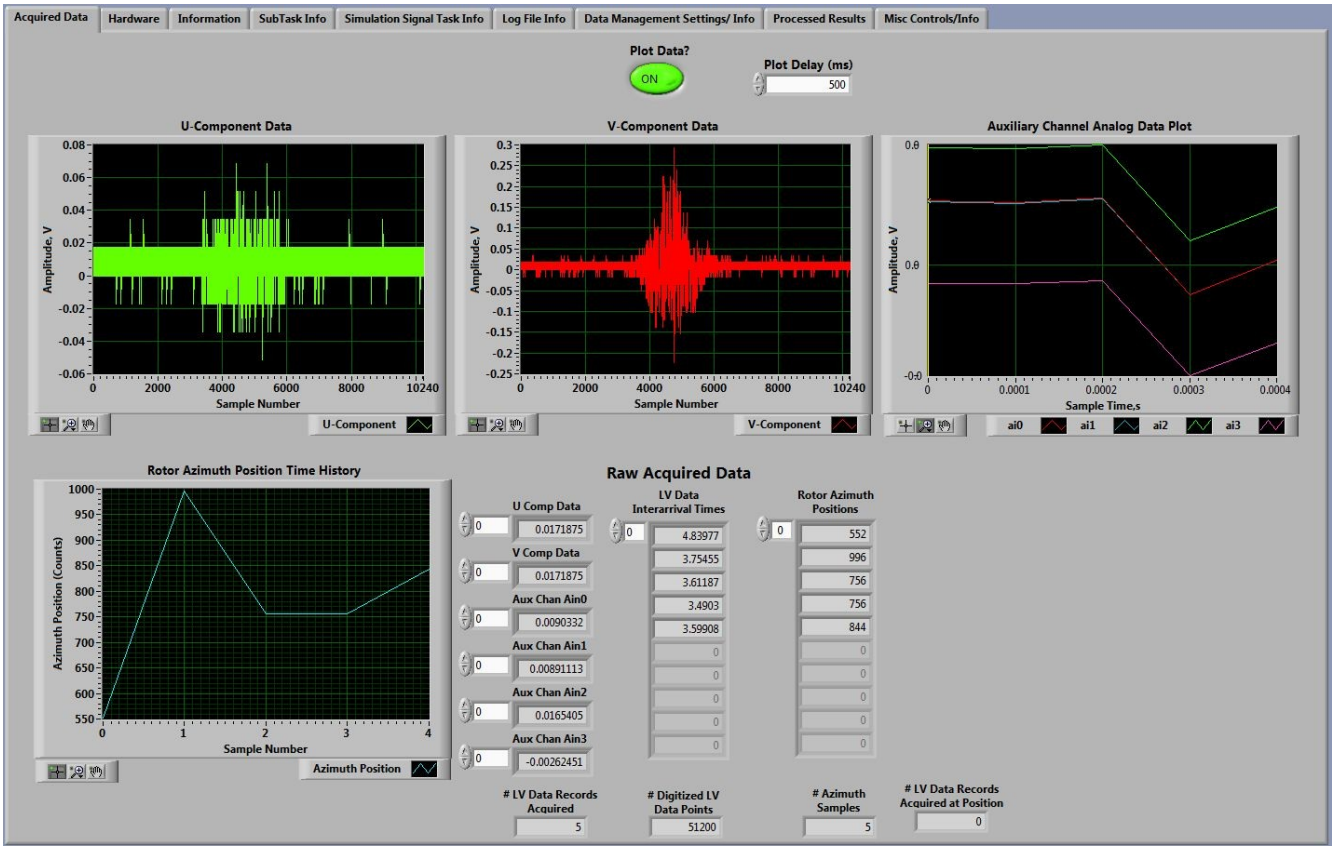

Figure C.38.– Data Acquisition Diagnostics Information Panel (Acquired Data Tab).

Figure C.39.– Data plot options.

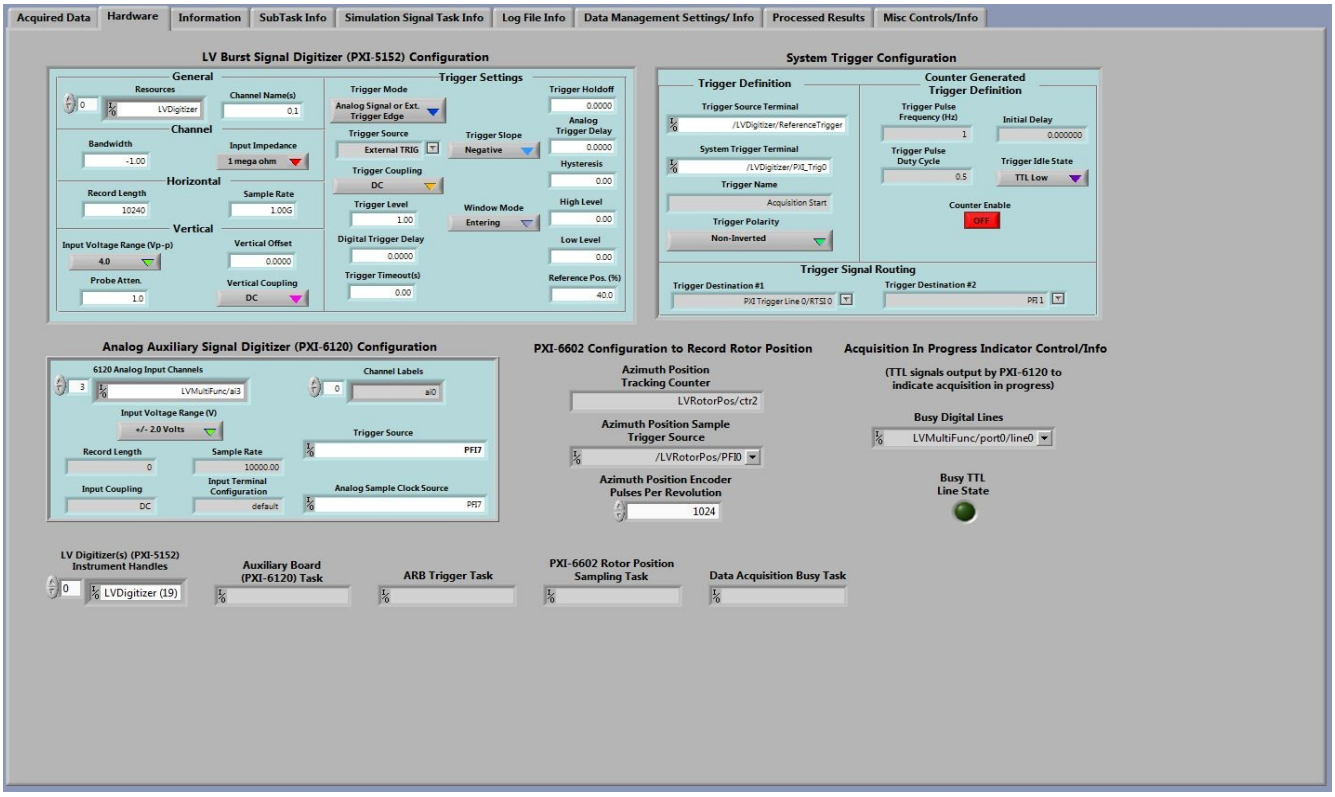

Figure C.40.– Data Acquisition Diagnostics Information Panel (Hardware Tab).

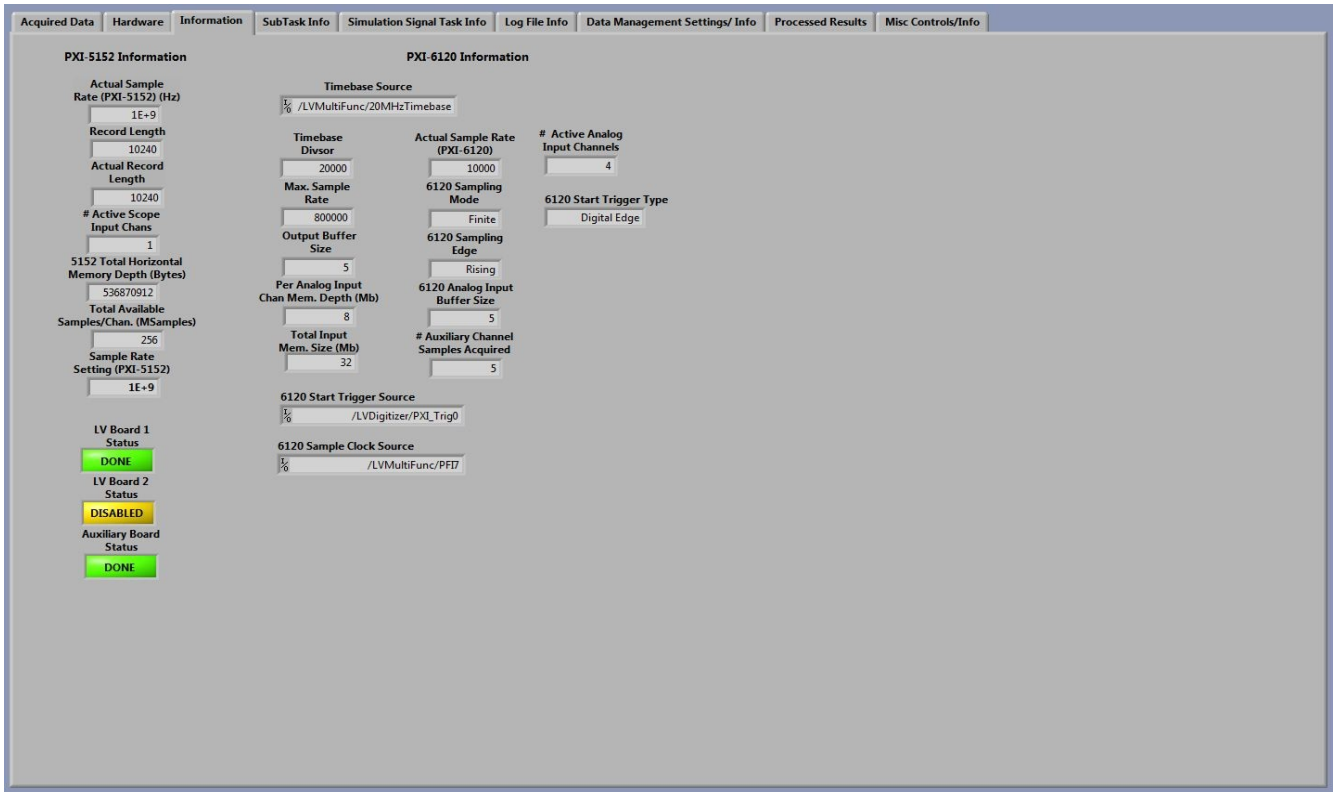

Figure C.41.– Data Acquisition Diagnostics Information Panel (Information Tab).

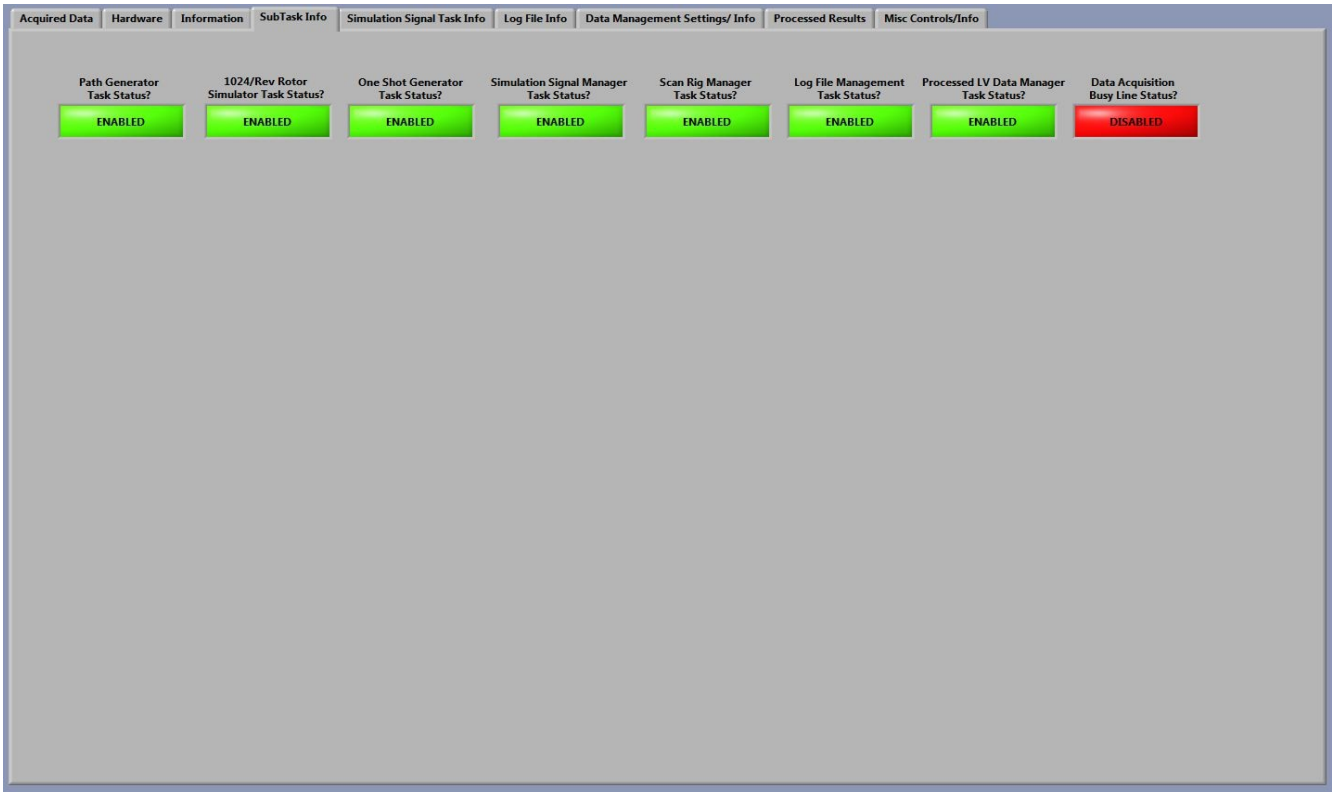

Figure C.42.– Data Acquisition Diagnostics Information Panel (Sub Task Info Tab).

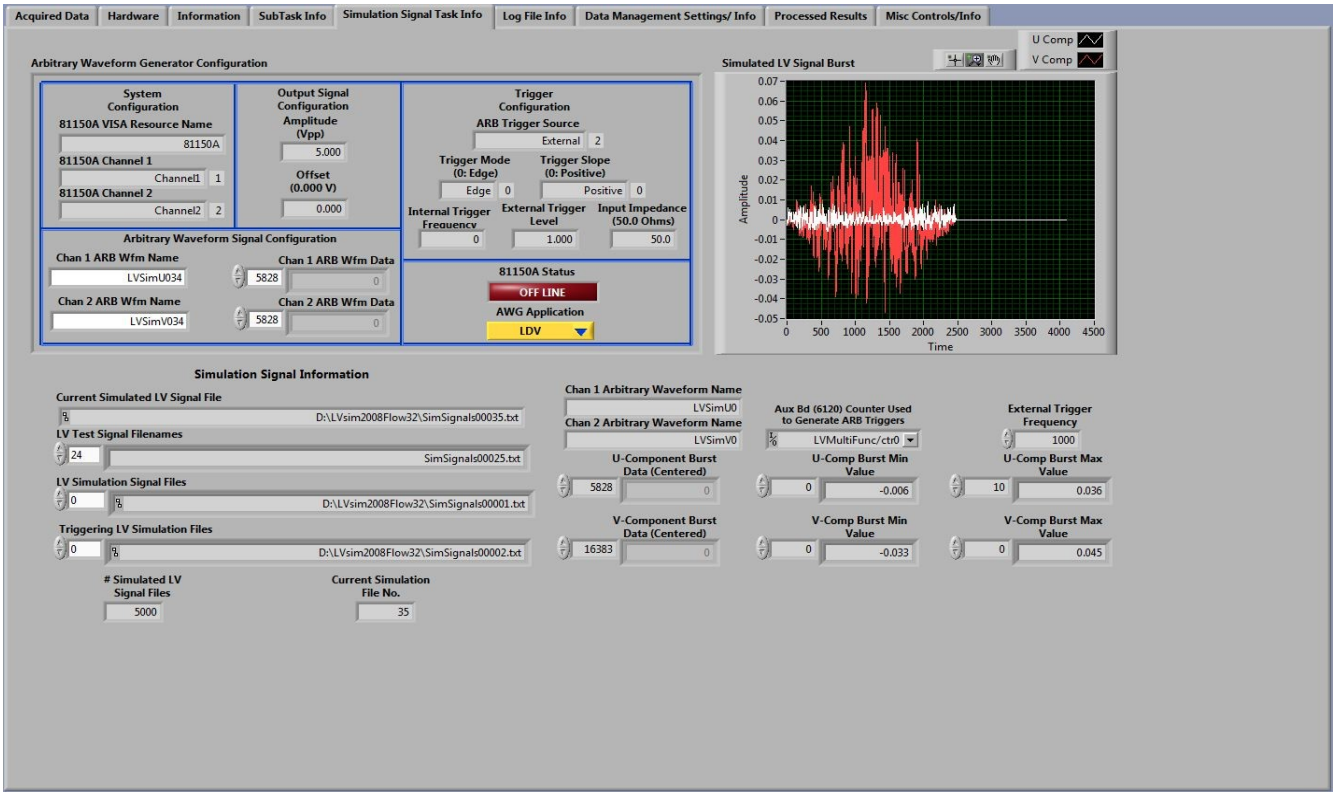

Figure C.43.– Data Acquisition Diagnostics Information Panel (Simulation Signal Task Info Tab).

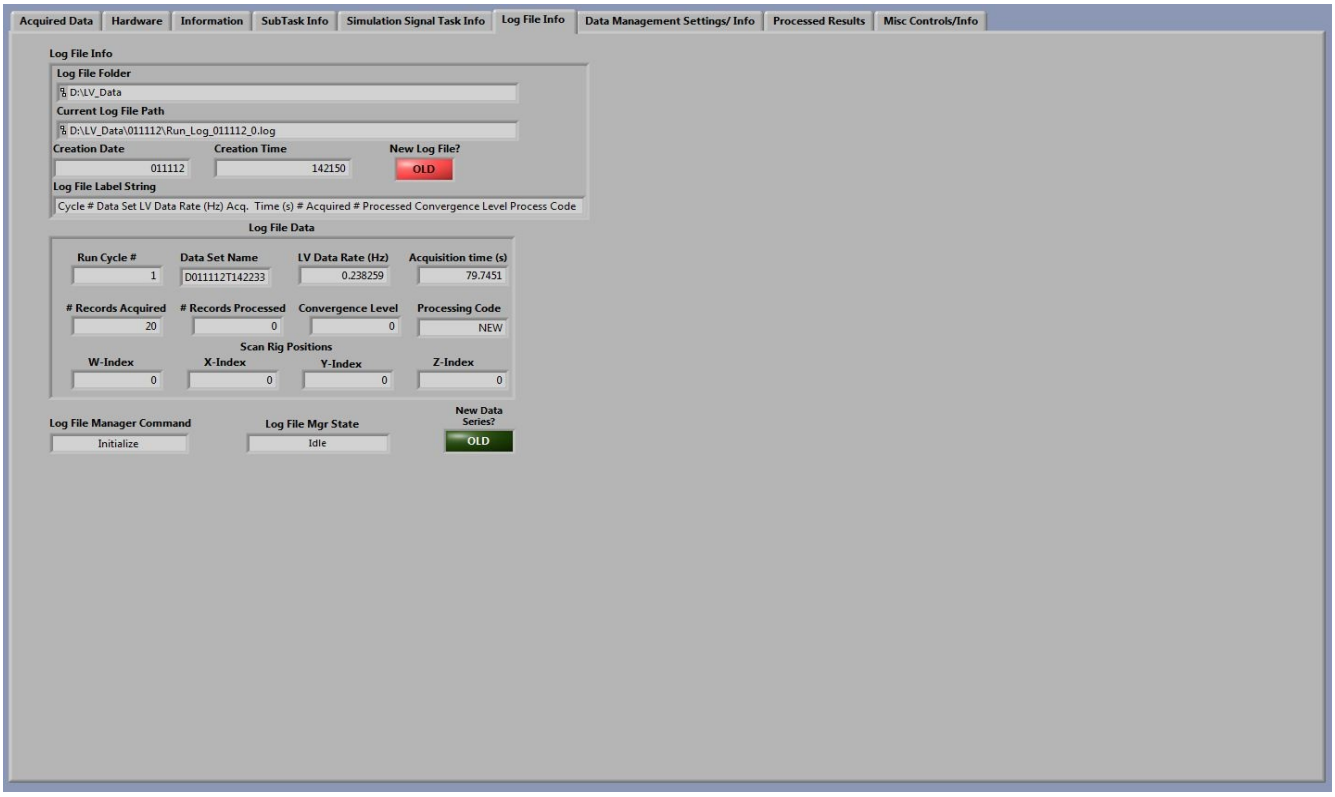

Figure C.44.– Data Acquisition Diagnostics Information Panel (Log File Info Tab).

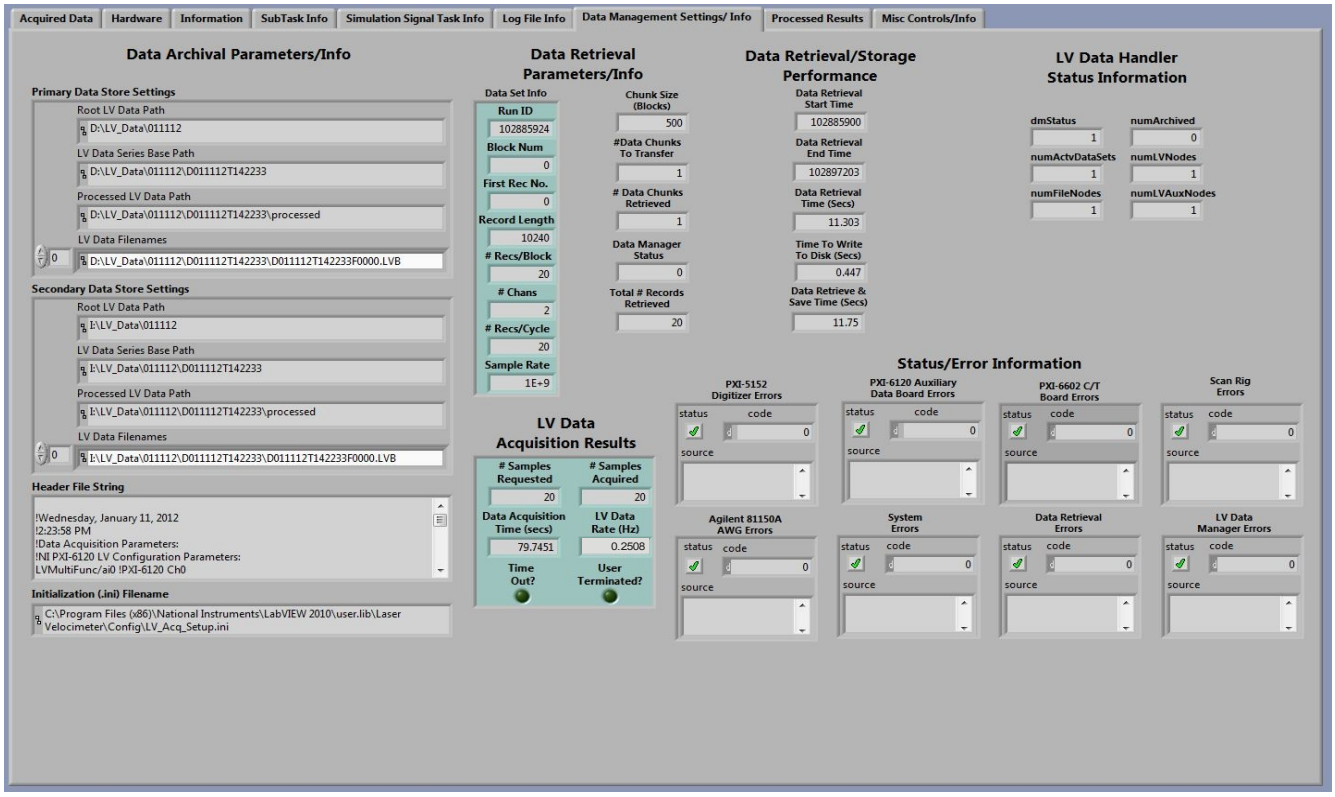

Figure C.45.– Data Acquisition Diagnostics Information Panel (Data Management Settings/ Info Tab).

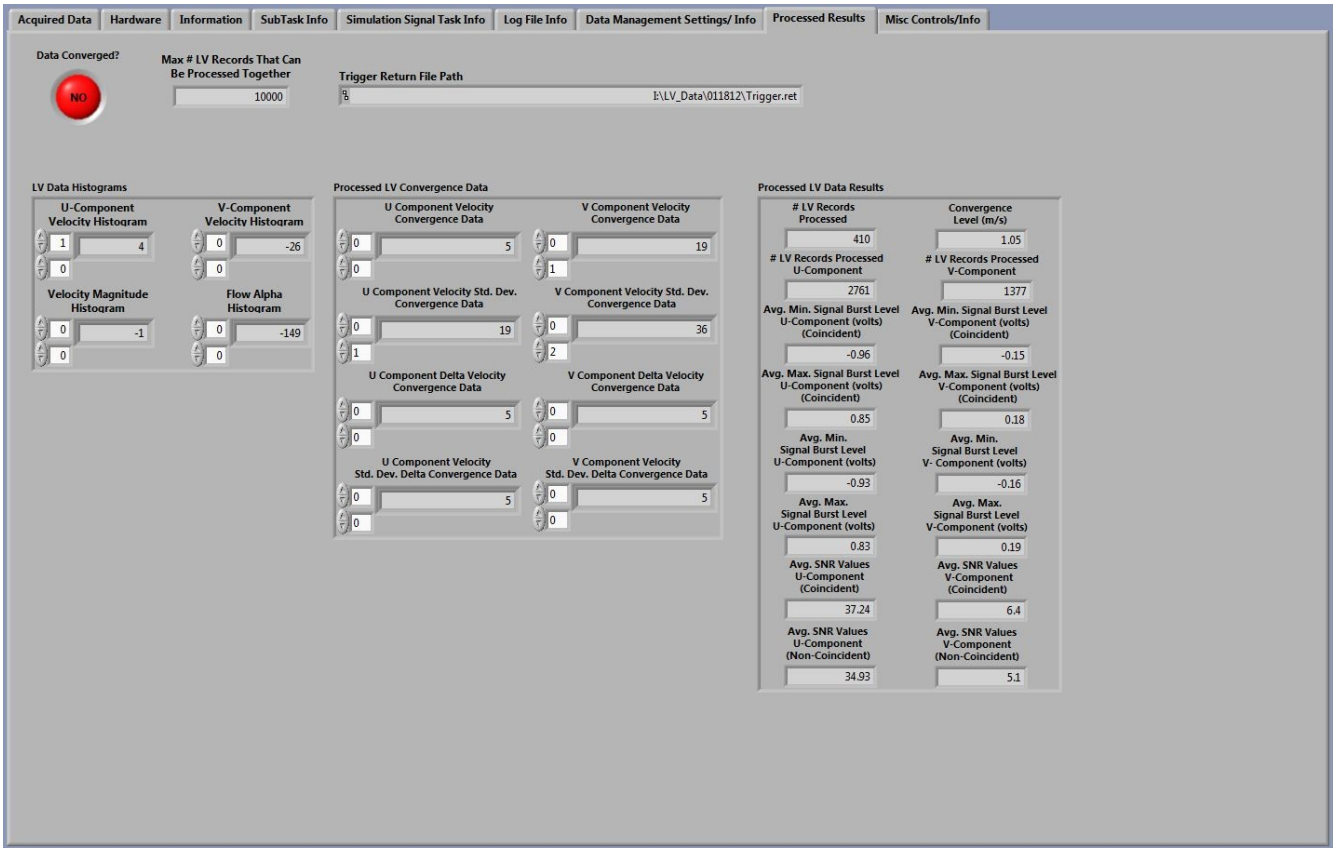

Figure C.46.– Data Acquisition Diagnostics Information Panel (Processed Results Tab).

Appendix D
Data Acquisition and System Control Software
User Input and System Information Definitions

An overview of the operation and display screens of the Data Acquisition and System Control program is given in Appendix C. The specific details and definitions of each user interface and system information display are presented in this Appendix. The descriptions are given in the same order as found in the overview. The major sections are named for the primary program functions found in Figure C.16. Many of the figures referred to are contained in Appendix C. Also the background and auxiliary sub-tasks are defined along with their functions, displays, inputs and results. Figures for the sub-tasks are found in this Appendix.

Nomenclature
Graphical User Interface Inputs/Outputs

Each input/output/display port in the Data Acquisition and Control Program graphical user interface will be classified by the following nomenclature and defined screen by screen in this Appendix.

[Button]	Any field that enables a function/screen by click on, click off operation.
[Display]	Any field where results/settings/graphs, typically color on black, are displayed. Displays can not be changed directly by the user.
[Drop Down Menu]	This field will have a downward pointer on the right side of the field. Clicking on the pointer will drop a menu from which the user may select the desired setting.
[File Manager Entry]	This field will have a folder icon on the right side of the field. Clicking on this folder icon will open a file manager that can be used to select the desired file whose full path/name will be placed in the field.
[Indicator]	Any circle, box, or other shape that lights to show that its monitored condition is enabled. This field can not be changed directly by the user.
[Indicator Button]	Any circle, box, or other shape that lights or turns off to show the state of the parameter identified by the button as it is clicked on/off.

[Switch] A field that appears as a toggle or rocker switch to change the on/off status of the listed parameter.

[Text/Value Entry Field] A field where text and/or values can be entered/changed by the user.

[Value Entry Field] A field where values can be entered/changed by the user.

Equipment / Signals Definitions

(Hardware shown in Figure C.9.)

Arbitrary Waveform Generator (AWG) – Not shown in Figure C.9.

A high-speed waveform generator capable of two channel output at digital-to-analog rates of up to 1.0 GHz. The Agilent 81150A Pulse Function / Arbitrary Waveform Generator is used to convert synthetic or previously captured signal burst waveforms into electronic signals that simulate signal bursts arriving from the laser velocimeter optical system.

Data Acquisition and Control Software (DA/C software)

The LabVIEW based software that controls the acquisition of laser velocimetry and auxiliary sensor data, manages and archives the data on computer hard drives, controls the traversing mechanism holding the laser velocimeter optics, and controls the execution and settings of the Signal/Data Processing Software.

Digital Phosphor Oscilloscope (Scope)

The digital oscilloscope that is used to monitor the signal bursts from the laser velocimeter photomultipliers, and used to generate the source trigger for the LV Data Valid Trigger via the LVTG (Master Trigger).

Ethernet Interface

The electronic hardware that supports communication between the two networked computers using standard 1.0 Gb/sec Ethernet communication protocol mechanisms.

High-Speed Analog-to Digital Converter (High-speed digitizer)

The 2-channel high-speed analog-to-digital converter, PXI-5152, typically operated at 1.0 GHz per channel, digitizes the signal bursts from the U- and V-component photomultipliers.

Laser Velocimeter Trigger Generator (LVTG)

The custom electronics system that, once triggered by the PXI system, performs the validation of the signal burst by insuring that the burst contains

at least eight cycles. If the signal is validated, the LVTG generates the Master Trigger used for all signal burst related data acquisition functions.

LV Data Acquisition Computer (DA/C computer)
: The computer executing the Data Acquisition and Control Software. This computer provides the user interface to the instrumentation.

LV Data Acquisition System (LVDAS)
: The electronics, computers, and communications hardware shown in Figure C.9., along with the Data Acquisition and Control Software.

LV Data Processing Computer (Processing computer)
: The computer executing the Signal/Data Processing Software. This computer is controlled remotely by the Data Acquisition and Control Software.

LV Data Valid Trigger (Master Trigger)
: The trigger pulse generated by the Laser Velocimeter Trigger Generator following receipt of the Scope Trigger Valid One Shot Pulse as modified by the PXI-6602, and validation that eight cycles have occurred in the monitored component signal burst. The Master Trigger is used as the trigger source for all signal burst related data acquisition functions.

Multifunction Analog-to-Digial Converter/Counter/Timer (Multifunction module)
: The multifunction module, PXI-6120, is used to conditionally sample external sensors, shaft encoders, etc. It is also used to generate certain simulation functions to validate proper operation of the Data Acquisition and Control software.

MXI Bus (MXI Bus)
: The electronic communication hardware that provides two way communication between the PXI chassis and enclosed hardware and the LV Data Acquisition Computer.

National Instruments Measurement & Automation Explorer (NI-MAX)
: National Instrument, Inc. instrumentation control microcode accessed and directed by programs operating under the National Instrument, Inc. programming language LabVIEW. NI-MAX provides the driver interface between the control software and the data acquisition hardware. All hardware elements controlled via the system software must be configured through NI-MAX before they can be accessed.

PXI Based LV Data Acquisition System (PXI system)
: The National Instrument PXI chassis that contains the high-speed analog-to-digital converters, analog/digital/timer/counter multifunction device, interface

and communication circuits, and power supplies. This is the primary data acquisition hardware.

Scope Trigger Out (Scope trigger)
The trigger that is generated when the monitored photomultiplier signal crosses the trigger level set by the user. It is normally set to 80-percent of the amplitude from the median signal bursts.

Scope Trigger Valid One Shot Pulse (Trigger One Shot)
The one shot trigger pulse, 500 milliseconds in duration, generated by the counter/timer module (PXI-6602) upon receipt of the trigger signal from the digital oscilloscope.

Signal/Data Processing Software (Processing Software)
The FORTRAN based software that determines the U-and V-component velocities, velocity magnitude, and flow angle of particles passing through the laser velocimeter measurement volume based on the frequency content of the captured signal bursts. The program also computes the full statistics of each data ensemble, and displays the results in the form of histograms and text in real time.

Virtual Instrument Software Architecture (VISA)
Instrument control drivers and status templates used by National Instruments, Inc. NI-MAX microcode to provide instrument control and status capabilities to programs written in the National Instruments, Inc. LabVIEW environment.

Configure System
Data Acquisition and Control Program
Configuration/Management Panel
Figure C.17.
(Figures C.13. (C.16.) [CONFIGURE SYSTEM] → C.17.)

Select Desired Options
Figure C.18.
(Figures C.13. (C.16.) [CONFIGURE SYSTEM] → C.17. (C.18.))

All controls in this sub-panel are click on / click off format.

Enable Online Processing – [Button]: Enables mechanisms that facilitate communication between the DA/C computer and the Processing computer to activate real-time signal/data processing of the data ensembles acquired during a flow field investigation.

Enable Rotor Encoder Sampling – [Button]: Enables conditional sampling of the rotor encoder position to provide velocity versus azimuth angle correlations.

Enable DAS Communications – [Button]: Enables communication with the wind tunnel data acquisition computers (NASA Langley OADAS computer system) to obtain the test parameters for each data ensemble.

Enable Test Mode – [Button]: Enables synthetic signal bursts produced by an Arbitrary Waveform Generator (AWG) to be used to verify the operation of the Data Acquisition System. When the **Test Mode** option is selected, the user will be prompted for additional inputs at the start of the next data acquisition cycle. At that time, the functionality and source of the synthetic signal bursts will be defined. It is noted that origin of these signal bursts may be the Monte Carlo simulation of a laser velocimeter, or previously captured signal bursts from a rotating wheel, Royco particle generation flow, laboratory testing, or flow field investigations. Communication and management of the AWG is performed over a USB 2 interface that is transparent to the user once the data acquisition cycle is initiated. NOTE: The described Data Acquisition System supports the use of the Agilent 8115A Pulse Function Arbitrary Generator only.

Enable 1024/Rev Simulator – [Button]: Generates a simulator that mimics the operation of the rotor position encoder. This would be used during system verification activities. The simulator assumes that a 1024 per revolution encoder with a 1 per revolution reset pulse is used on a shaft rotating at 2800 rpm. Timing is absolute and the selection of encoder count (azimuth angle) is directly related to the acquisition time marker of each captured signal burst.

Enable Convergence Validation – [Button]: Establishes a user feedback that is based on the comparison of the results from the statistical stationarity test, Appendix E.2-3., with the user selected threshold, Figure C.22. If the control is enabled and the statistical stationarity test results are larger than the threshold, a warning message will be displayed suggesting that another data ensemble should be acquired at this location. If another ensemble is acquired, both ensembles will be processed as a single ensemble and the test applied again. This can continue until the ensemble reaches 10,000 signal bursts at which point no further data can be gathered.

Advanced HW Settings – [Button]: Provides the user with additional (advanced) control over the settings used in the data acquisition system (Figure D.1).

LV Burst Signal Digitizer Management
PXI-5152 High-Speed Digitizer
Figure C.19.
(Figures C.13. (C.16.) [CONFIGURE SYSTEM] → C.17. (C.19.))

Input Voltage Range (V p-p) – [Drop Down Menu]: Selects the peak-to-peak voltage range of the high-speed analog-to-digital converters. The range setting should be selected so that

maximum resolution can be realized without saturating the digitizers. Refer to the signal amplitudes displayed on the monitoring oscilloscope that are generated by the passage of seed particles through the measurement volume. It is noted that the range should be set for the larger of the two signals as both channels will have the same range.

LV Channel *n* Label – [Text/Value Entry Field]: Identifies a particular digitizer channel. These are required to be incremental numbers starting with 0. The default settings of 0-3 should never require adjustment.

Channel ON/OFF – [Button]: These control buttons are included for expansion with the intention that they will enable or disable the signal burst digitization of a given channel. NOTE: These controls are intended for future expansion should additional velocity components be added. Thus they should not require adjustment.

Sample Rate (Hz) – [Value Entry Field]: Defines the rate at which the input signal bursts are digitized up to a maximum of 1.0 GHz (default). This setting should be sufficient for most data acquisition applications, especially if a Bragg cell is used (It is recommended that the signals **NOT** be down-mixed).

LV Burst Record Length – [Value Entry Field]: Defines the number of samples to be obtained from a single signal burst. The sample begins when a Master Trigger, Figure C.9., initiates the acquisition of a single record. The use of the pre-triggering capabilities of the high-speed digitizers can insure that the entire signal burst is digitized. This is set using the ***Reference Pos. (%)*** control located on the Advanced HW Settings Panel (Figure D.2.). The default setting of 10240 samples per signal burst has proven to be adequate in both laboratory and wind tunnel testing, and should be sufficient for most scenarios. This record length will allow the Processing software to execute Fast Fourier transforms up to 8192 samples.

Auxiliary Channel Analog Input
PXI-6120 Multifunction Data Acquisition Module
Figures C.20.
(Figures C.13. (C.16.) [CONFIGURE SYSTEM] → C.17. (C.20.))

The controls and settings on this sub-panel define the functionality of the auxiliary channel analog inputs. The auxiliary channels are provided to conditionally sample external sensors based on the acquisition of each randomly arriving signal burst.

Input Voltage Range (V p-p) – [Drop Down Menu]: Defines the peak-to-peak voltage range of the analog-to-digital converters in the multifunction module. The range setting should be selected so that maximum resolution can be realized without saturating the digitizers. It is noted that the range setting applies to all active channels. The default setting is 2.0 volts peak-to-peak.

Channel *n* Label – [Text/Value Entry Field]: Assigns a name to a given auxiliary analog channel. These names should be chosen to reflect the sensor being sampled. The default settings are ai0 – ai3.

Channel ON/OFF – [Button]: These control buttons are used to activate / deactivate the auxiliary channels, and should be activated when sensor voltages are input. The default (recommended) setting is ON.

Data Storage Management
Figures C.21.
(Figures C.13. (C.16.) [CONFIGURE SYSTEM] → C.17. (C.21.))

Primary Base Data Storage Path – [File Manager Entry]: Defines the data storage location on the DA/C computer hard drive. All signal burst ensembles, conditionally sampled data, along with ensemble Log files will be stored in this location. Sub-directories will be created identifying each data ensemble that will contain the Header and Trigger files along with the ensemble of the digitized signal bursts. Alternatively the user can click on the browse icon to the right of the string entry field to access a file manager which can then be used to select the desired drive/directory or type a new directory name using the file manager.

Secondary (Processing) Base Data Storage Path – [File Manager Entry]: Defines the data storage location on the Processing computer hard drive. All signal burst ensembles, conditionally sampled data, along with ensemble Log files will be stored in this location. Sub-directories will be created identifying each data ensemble that will contain the Header and Trigger files along with the ensemble of digitized signal bursts. These sub-directories will have their own sub-directories that will contain the processed results along with Log files of the processing cycle and convergence and histogram plots. It is noted that the hard drive must be mounted as a local drive on the DA/C computer. Even if real time signal/data processing is not used, the use of the Secondary storage location provides an automatic data backup function. The Secondary storage location should be on a different physical drive from the Primary storage location.

Save Primary? Save Secondary? - [Switch]: Enable or disable the storage of the data ensembles on the respective locations. It is recommended that these controls should remain set to the default **YES** state to insure that two copies of the data ensembles are always stored.

Filename Prefix Source – [Indicator Button]: Selects the source used to generate the prefix of the file name that uniquely identifies the acquired digitized signal burst records. The available options are:

> **Use Date/Time** – when selected the file name prefix will be constructed using the date and time at which the data acquisition cycle was initiated, e.g. D100311T132114 represents October 3, 2011 at 1:21:14 pm. This is the default and recommended setting.

User Prefix – when selected the prefix will be constructed using the string defined by the user in the Data Filename Prefix control.

Data Filename Prefix – [Text/Value Entry Field]: Accepts the user defined text that will be the prefix of the files containing the acquired digitized signal burst records.

Initial Series Index Value – [Value Entry Field]: Defines the index of the first file name of a sequence of file names, each containing the acquired digitized signal burst records for the U- and V-components of a particle passing through the measurement volume. The default and recommended setting for this index is 0. (Control disabled – provided for future expansion).

Series Index Increment – [Value Entry Field]: Defines the increment between successive signal burst record file names. The default and recommended setting of this index increment is 1. (Control disabled – provided for future expansion).

Append Date To Store Path? - [Button]: If selected, this control appends the current date, e.g., 100311 as a sub-directory on the data storage paths. The default and recommended setting is **YES**.

Automatically Increment Index? – [Button]: If selected, this control will automatically increment the record file name index by the Series Index Increment setting. The default and recommended setting is **YES**. (Control disabled – provided for future expansion).

Save ASCII? – [Button]: Record the signal burst records in ASCII format. This control was used during the development of the Processing software to allow spreadsheet retrieval of the signal records. The size of the records and the associated lengthy time required to transfer and store the data makes its use impractical in flow field investigations. Thus this control has been disabled, but if necessary it can be reinstated via a recompile of the DA/C program. The conversion of the binary data to ASCII data can also be performed using the auxiliary program ConvertBinary2ASCII (Appendix E.9.) off-line. (Control disabled – provided for future expansion).

Save Binary? - [Button]: Record the signal burst records in binary format. This control is enabled permanently unless the DA/C program is recompiled with the **ASCII storage** option reinstated, thus this Button should always be activated. (Control disabled – provided for future expansion).

User Comment – [Text/Value Entry Field]: Enter notes, comments or other information pertinent to the investigation being conducted. For example: *1.0-micron polystyrene particles in a 50/50 ethanol/water solution used to seed the flow. Ultrasonic generators used*. The comment will be saved within each ensemble Header (.hed) file.

LV Data Acquisition Management
Figures C.22.
(Figures C.13. (C.16.) [CONFIGURE SYSTEM] → C.17. (C.22.))

Records to Acquire – [Value Entry Field]: Defines the number of signal burst records to be contained within an acquisition ensemble.

Delay Time Between Samples (milliseconds) – [Value Entry Field]: Defines a delay that is to be inserted between successive signal burst captures. This control is intended for the implementation of variable instrument reset time to insure flow independence of successive signal bursts. The function would only be implemented in extremely slow flows as the normal reset time of the PXI-5152 digitizer insures independence of successive signal bursts in the velocity ranges of interest. Thus the default and recommended setting is 0.

Records/Scan Location – [Value Entry Field]: When operating with automated scanning of the input measurement volume location grid, this control sets the number of ensembles to be collected at a given spatial location (grid point) before proceeding to the next grid point. This parameter is to support advance future applications and is thus currently disabled. (Control disabled – provided for future expansion).

Acquisition Timeout (Sec) – [Value Entry Field]: Defines the time allocated for the acquisition of a data ensemble. If the specified number of signal bursts have not been captured before the timeout value is reached, a non-fatal **Acquisition Timeout** condition occurs which then closes the data ensemble, stores any acquired samples and returns control for the next command.

Auto Advance Scan Rig? – [Button]: Enables automatic testing where the measurement volume is sequenced through the spatial locations given in the grid file. Once a data ensemble has been acquired at a given location, the program automatically moves the measurement volume to the next spatial location (grid point). This control is currently disabled because the system is not yet set for production testing.

Acquisition Mode – [Drop Down Menu]: Controls the manner in which data records are acquired. The control is currently disabled, but will be activated during future expansion. The control, when activated, will provide the user with a degree of flexibility for verifying system operation and functionality. Three acquisition modes will be possible:

> Continuous – In this mode of operation, signal bursts would be captured, processed and displayed continuously until the user manually stops the sampling activity. This capability is intended to be used for verifying that the system is operating properly. It is noted that no data will be saved to permanent storage.

Automatic – This will be the default mode of operation where the user-defined number of samples is acquired, saved and processed. This mode is the current mode of operation by the Data Acquisition and Control program.

Manual – In this mode of operation, the user will be provided with the ability to arm the data acquisition hardware so that individual signal burst captures can be made as determined by the operator. For example this capability will be useful when the seeding particle plumes arrive at irregular rates.

Convergence Threshold (m/s) – [Value Entry Field]: When convergence validation is enabled, Figure C.8., the value entered in this control establishes the threshold for the statistical stationarity test, Appendix E.2.-3. If the statistical stationarity test results are larger than the threshold, a warning message will be displayed suggesting that another data ensemble be acquired at this location. If another ensemble is acquired, both ensembles will be processed as a single ensemble and the test applied again. This can continue until the ensemble reaches 10,000 signal bursts at which point no further data can be gathered.

Reset Data Ensemble Plot Axis – [Drop Down Menu]: The Running Display program provides profile plots of the mean and standard deviation of the U- and V-component velocities, velocity magnitude, and flow angle as the measurement volume is traversed within the flow field. These plots are updated with each new measurement ensemble obtained at additional locations along the traverse. When a new traverse is begun by moving the measurement volume along a different axis, the plots are cleared and the profile plots begun anew. The axis that is the control to reset the profile plots is selected by the Drop Down Menu activated by the Reset Data Ensemble Plot Axis control.

Data Acquisition Conditions
Figure C.23.
(Figures C.13. (C.16.) [CONFIGURE SYSTEM] → C.17. (C.23.))

Temperature (C) – [Value Entry Field]: Enter the current environmental temperature in degrees C.

Atm. Press (in. Hg) – [Value Entry Field]: Enter the current atmospheric pressure in inches of Mercury.

Particle Size (microns) – [Value Entry Field]: Enter the diameter of the seeding particles in microns. The default particle size is 1.0 micron. Note this control assumes that mono-disperse particles are used.

Particle Type – [Text/Value Entry Field]: Input the type of seeding material used during the flow field investigation. The default is polystyrene.

Control Scan Rig
Data Acquisition and Control Program
Configuration/Management Panel
Figure C.24.
(Figures C.13. (C.16.) [CONTROL SCAN RIG] → C.24.)

Scan Rig Functions
Figure C.25.
(Figures C.13. (C.16.) [CONTROL SCAN RIG] → C.24. (C.25.))

Initialize Scan Rig – [Button]: Establish the GPIB control/data connection with the scan rig. The scan rig is also initialized. This must be the first control executed when the scan rig is to be used during the flow field investigation. Note that upon successful initialization of the GPIB connection and the MC4 scan rig, the GPIB Status Indicator will change its color from red (ERROR) to green (OK), and the Scan Rig Status indicator from red (OFF LINE) to green (ON LINE), Figure C.24.

Create Scan Grid File – [Button]: Display the Scanner Position Generator, Figure C.26. This tabbed screen provides the user with the tools to create a grid map that can be used, either manually or automatically, to move the measurement volume to the desired spatial locations within the flow field. The controls are outlined briefly below, greater detail will be presented in the Sub-Task Section:

Axis Settings – [Button & Value Entry Field]: Spatial units of inches or counts may be selected, number of units per grid increment, and starting location.

Scan Indices – [Value Entry Field]: Number of spatial nodes for each axis.

Travel Per Step – [Value Entry Field]: Distance, in inches, of a single stepping motor increment.

Scan File Title – [Text/Value Entry Field]: File name of the generated grid file.

Scan File Comment – [Text/Value Entry Field]: Descriptive comment regarding the generated grid file, stored as a header in the grid file.

Scan Rig ID – [Text Entry Field]: Name of the scan rig controller.

Tabs:

Active Grid – Displays the grid currently being developed.

Complete Grid – Displays the complete grid that was generated.

Information – Displays information about the Complete Grid.

Control Buttons:

Generate Scan Data – [Button]: Compute the grid based on the parameters as defined on the ***Settings*** tab.

Import Existing Scan File – [Button]: Launches a file manager that can be used to read the grid from an existing file created by the grid generator and previously saved to a file.

Import Scan Data From File – [Button]: Launches a file manager that can be used to read a tab-delimited text file created by a spreadsheet program such as Microsoft Excel.

Append to Final Grid – [Button]: Appends a generated grid (Active Grid) or imported data grid to the data in the Complete Grid.

Save Scan Data to File – [Button]: Store the Complete Grid to a file.

Quit – [Button]: Terminate the Scanner Position Generator.

Load Scan Position File – [Button]: Opens a file manager to allow the user to select an ASCII file containing a table of coordinates that will be used to sequentially move the measurement volume to each spatial location. The coordinates obtained from this file are loaded into the table shown in the indicator labeled Automated Scan Rig Position Data, Figure C.24., along with being stored in the table that is displayed by the ***Scan File Data*** tab.

Get Scan Rig Status – [Button]: Returns the status information from the Klinger MC4 and displays it in the Klinger MC4 Scan Rig Status Display, Figure C.27. This display duplicates the information shown on the front panel display of the MC4 controller. This Control becomes *active* once the scan rig is brought on-line.

Scan Forward One Index – [Button]: Translates the measurement volume to the coordinates listed next in the table presented in the Automated Scan Rig Position Data, (example Scan Locations table shown in Figure C.24.). This Control becomes *active* once a scan position file has been selected and loaded.

Scan Back One Index – [Button]: Translates the measurement volume to the coordinates listed previously in the table presented in the Automated Scan Rig Position Data, Figure C.24. This Control becomes *active* once a scan position file has been selected, loaded, and at least one scan index has been executed.

Scan To Index – [Button]: Moves the measurement volume to the coordinates listed at the selected index as shown in the table presented in the Automated Scan Rig Position Data, (example Scan Locations table shown in Figure C.24.), and maintained in the internal table that can be viewed by selecting the ***Scan File Data*** tab. The Control opens the Set Scan Rig Index dialog [Value Entry Field], Figure C.28., where the user can input the index of the desired spatial location. This Control becomes *active* once a scan position file has been selected and loaded.

Take Scan Rig Offline – [Button]: Disconnects the scan rig from program control by closing the previously established GPIB connection. This Control becomes *active* once the scan rig is on-line.

Klinger MC4 Scan Rig Status Display
Figure C.27.
(Figures C.13. (C.16.) [CONTROL SCAN RIG] → C.24. (C.27.))

Axis Information – [Display]: These four indicators display status information for each of the four axes, W, X, Y, and Z. Each indicator displays the current position of the axis in counts as well as Limit function indicators. These displays are updated after each scan is completed.

GPIB Status – [Indicator]: Indicates the status of the GPIB communications channel. When a successful connection has been established, the display changes color to green and shows the **OK** message. If the connection is uninitialized or has generated an error condition, the indicator becomes red and displays **ERROR**.

Scan Rig Status – [Indicator]: Indicates whether the scan rig is on-line. When the GPIB connection is established and the scan rig has been initialized, this display will be green and shows the **ON LINE** message. When the scan rig is not ready for use, the indicator is red and displays the **OFF LINE** message.

Input Bit Status – [Indicator]: Displays the state of the MC4 input status bits. When TTL low, these lights will be dark green to indicate LOW. When TTL high these lights will be bright green to indicate HIGH. These status bits have not been implemented at present.

Klinger MC4 Scan Rig Control Panel
Figure C.29.
(Figures C.13. (C.16.) [CONTROL SCAN RIG] → C.24. (C.29.))

MC4 GPIB Address – [Value Entry Field]: Displays the GPIB address of the MC4 scan rig controller. The default setting is 6.

GPIB Controller Address – [Value Entry Field]: Displays the address of the GPIB interface used by the DA/C computer. The default setting is 0.

NOTE: Failure to set these two addresses will prohibit connection between the computer and the scan rig controller.

MC4 GPIB Terminator (Write) – [Drop Down Menu]: Defines the character sequence that is used to terminate command strings issued to the MC4 controller through the GPIB interface. The default setting for the MC4 controller is CR & EOI (Carriage Return and End-or-Identify) and should never require adjustment. Additional options are provided to support future devices.

Step Size – Inches – [Value Entry Field]: Displays the distance traveled in inches for each count of the MC4 scan rig. The default setting of 38.37 micro-inches corresponds to the 1-micron slides used in the MC4 system.

Axis Enabled? – [Switch]: The four controls, (W, X, Y, and Z axes), provide a lock on their respective scan axis so that the locked axes cannot be moved during a scan even if the coordinates of the locked axes change in the grid map. For example if the investigation mandates that only the X and Y axes will be used to position the measurement volume, the user should lock out the W and Z axes to prevent them from being accidentally moved should the grid map indicate otherwise or a manual command is attempted through the MC4 front panel.

Axis Select – [Buttons]: Selects the axis to be activated for a given manual operation. The All Axis control applies the next command to all axes. The All Axis control is useful when applying the Scan Rate and Acceleration Ramp commands.

Scanner Operation – [Buttons]: Defines the operation that is to be performed on the selected Axis using the settings found to the right of these buttons. The five available operations are:

a) Scan Axis – Moves the active axis the number of steps defined by the Step Size rotary control or input display;
b) Scan Rate – Sets the rate at which the selected axis is to be moved when active by the Scan Rate rotary control or input display;
c) Acceleration Ramp – Sets the acceleration ramp for the selected axis by the Acceleration Ramp rotary control or input display;
d) Seek Origin – Moves the selected axis to its origin; and,
e) Reset Axis – Resets the count value of the selected axis to 0.

Scan Direction – [Switch]: This switch defines the direction that the selected axis will be scanned.

Scan Mode – [Switch]: Defines the mode that will be used when the selected axis is moved. In *Relative* mode, the move will be in the selected direction and step size counts from the current position. In *Absolute* mode the move will be in the selected direction and step size

counts from the zero count reference position that is defined as the position of a given axis at the time that the MC4 scan rig controller is first power on.

Note: The values set for the following three controls are applied to the active axis or all axes. The value desired by the user can be set either by turning the knob (value will be displayed in the text box) or by manually entering the value in the text box below the knob.

Step Size (Counts) – [Rotary / Value Entry Field]: Defines the number of steps (counts) that the active axis will be moved when the user activates the Scan Axis control.

Scan Rate – [Rotary / Value Entry Field]: Defines the stepping rate for the active axis in steps/second. The range of values is 32 to 4000 steps per second.

Acceleration Ramp – [Rotary / Value Entry field]: Defines the time it takes for the selected ramp to accelerate from 50 Hz to 4000 Hz in seconds. When setting this parameter the user should consider the weight residing on a given axis. The ramp speed should be slower for heavy item moves as attempting to accelerate too fast will cause the axis to bind.

MC4 Scan Rig Position Info – Inches
Figures C.30.
(Figures C.13. (C.16.) [CONTROL SCAN RIG] → C.24. (C.30.))

[Display]: Displays the current position of the four scan rig axes in inches. The position indicated refers to the absolute position of the axis from the MC4 origin which is the position of the axis at the time that power is first applied to the scan rig controller.

MC4 Scan Rig Position Info – Meters
Figures C.31.
(Figures C.13. (C.16.) [CONTROL SCAN RIG] → C.24. (C.31.))

[Display]: Displays the current position of the four scan rig axes in meters. The position indicated refers to the absolute position of the axis from the MC4 origin which is the position of the axis at the time that power is first applied to the scan rig controller.

Acquire Data
Data Acquisition and Control Program
Configuration/Management Panel
Figure C.32.
(Figures C.13. (C.16.) [ACQUIRE DATA] → C.32.)

Selection of the ***Acquire Data*** navigation button presents the user with the display shown in Figure C.32. As can be seen, this panel provides controls for the data acquisition process as well as feedback regarding the data collection activity.

Data Acquisition Controls
Figure C.34.
(Figures C.13. (C.16.) [ACQUIRE DATA] → C.32. (C.34.))

Start Data Acquisition – [Button]: Initiates the data acquisition process, which once started, continues until: a) the requested number of signal bursts have been acquired; b) the specified timeout limit is reached; or, c) the operator activates the Terminate Data Acquisition button. Multiple operations are performed prior to, during and after data acquisition has been initiated:

a) Data acquisition hardware configuration /initialization/management;
b) Software parameter configuration/initialization/management;
c) Operation(s) sequencing;
d) File system management;
e) Synthetic signal management (Rotor Encoder Simulator, Synthetic Signal Burst Generator);
f) System progress monitoring;
g) Status information calculation/presentation;
h) Data retrieval/archival/presentation;
i) Data processing triggering; and,
j) Log file management.

Terminate Data Acquisition – [Button]: Halts the current data acquisition cycle immediately. All of the in-process operations are gracefully halted and all acquired signal bursts are archived to disk prior to returning program control to the user.

Data Ensemble Plot Options – [Button]: Defines data ensemble processing and results display control. All data plots are presented on the Processing computer. The three options are:

New – The current data ensemble marks the start of a new sequence of related data points. The current data ensemble is processed and the statistical stationarity convergence plots, and histogram plots reflect the results of processing the current data ensemble. The running U- and V-component, velocity magnitude and flow angle mean and standard deviation plots are cleared. New running plots will begin when the data ensemble for the next location is acquired and processed.

Continue – The current data ensemble is processed and the statistical stationarity convergence plots, and histogram plots reflect the results of processing the current data ensemble. The running plots are updated with the results.

Repeat – The current data ensemble is combined with the previously acquired ensemble(s) obtained at the current measurement volume location. The combined ensembles are processed as a single ensemble, and the statistical stationarity convergence plots and histogram plots reflect the results from the combined

ensembles. The running plots are updated with the results from the combined ensembles, replacing the previously obtained results for that location.

Data Acquisition Information
Figure C.34.
(Figures C.13. (C.16.) [ACQUIRE DATA] → C.32. (C.34.))

Data Acquisition Start Time – [Display]: Presents the date and time when the current data acquisition cycle was initiated.

Current Date & Time – [Display]: Presents the current date and time-of-day.

Current Data Set – [Display]: Presents the sub-directory name of the current data ensemble (same as the root portion of the digitized signal burst file names), Figures C.17 and C.21.

Records Acquired – [Display]: Presents the real-time count of signal bursts acquired during the current data acquisition cycle.

Elapsed Time – [Display]: Presents the elapsed time of the current data acquisition cycle in Hours:Minutes:Seconds:Hundredths format.

LV Data Rate (Hz) – [Display]: Presents the rate at which signal bursts are being acquired (# Records Acquired / Elapsed Time) for the current data acquisition cycle.

Data Acquisition Progress - % – [Display]: Graphically presents the percentage of the current data acquisition cycle that has been completed based on the number of signal bursts acquired versus the number requested.

Data Transfer/Storage Progress - % – [Display]: Graphically presents the percentage of the number of data records retrieved from the PXI-5152 digitizer versus the total number of signal bursts acquired during the current data acquisition cycle. It is noted that transfer of the data records to the computer hard drives cannot be monitored as this function is executed by the LV Data Manager DLL, which does not provide real-time feedback to the DA/C program.

System Settings
Figure C.34.
(Figures C.13. (C.16.) [ACQUIRE DATA] → C.32. (C.34.))

Rotor Encoder Sampling – [Display]: Presents the status of the conditional sampling of the rotor shaft encoder.

Rotor Position Encoder Source – [Display]: Presents the source of the rotor shaft encoder. The display of **ACTUAL** indicates that the sampled pulse train is from the shaft encoder

attached to the rotor. The display of **SIMULATED** indicates that the sampled pulse train originates from the internal shaft encoder simulator, Figure C.18.

Scan Rig Status – [Display]: Shows whether or not the scan rig has been activated, on-line and ready for use, Figure C.27.

LV Burst Signal Source – [Display]: Presents the source of the signal bursts to be measured. The display of **ACTUAL** indicates that the signal bursts originate from the laser velocimeter photomultipliers. The display of **SIMULATED** indicates that the signal bursts originate from the Arbitrary Waveform Generator. Typically the waveforms being converted to electronic signals by the AWG originate from the Monte Carlo Laser Velocimeter Simulation program. However, the AWG may also be driven by actual signal bursts captured by the laser velocimeter in the laboratory or from a flow field investigation.

Data Acquisition Panel – ***Current Results*** Tab
Figure C.32.
(Figures C.13. (C.16.) [ACQUIRE DATA] → C.32. [Current Results Tab])

When a data acquisition operation has been completed, the acquired data sets are written to hard disk drives located in the Data Acquisition computer and to the networked Signal/Data Processing computer. Once the data ensemble has been written to the networked computer, the Data Acquisition program updates the trigger file on the Signal/Data Processing computer with the parameters needed to process the ensemble. Closing the trigger file alerts the Signal/Data Processing program to read the parameters and begin processing the ensemble. When processing is completed, the program then updates the return file, which when closed, alerts the Data Acquisition program to upload the statistical parameters obtained from the ensemble, and to present them to the user on the ***Current Results*** tab, Figure C.32. That is, if the **Enable Online Processing** and **Enable Convergence Validation** options (Figures C.13 (C.17. (C.18.))) are enabled. This tab contains nine displays presenting the results of the most recent data acquisition/processing sequence, and is automatically updated each data acquisition/processing cycle. The following displays are presented:

U- and V-component Velocity Histograms – [Display]: Presents the histograms of U- and V-component ensemble velocities in meters-per-second.

U- and V-component Mean Velocity Convergence – [Display]: Presents plots of the convergence of the U- and V-component mean velocities for the current data ensemble in meters-per-second as a function of cumulative blocks of 100 measurements, i.e., first 100, first 200, first 300, etc.

U- and V-component Standard Deviation Convergence – [Display]: Presents plots of the convergence of the U- and V-component velocity standard deviations for the current data

ensemble in meters-per-second as a function of cumulative blocks of 100 measurements, i.e., first 100, first 200, first 300, etc.

Velocity Magnitude Histogram – [Display]: Presents the histogram of the resolved velocity magnitude in meters-per-second using the current data ensemble.

Flow Angle (Alpha) Histogram – [Display]: Presents the histogram of the resolved flow angle in the vertical plane in degrees using the current data ensemble.

Rotor Azimuth Position Histogram – [Display]: Presents the histogram of conditionally sampled shaft encoder angles (0-1023 counts) based on the random arrivals of signal bursts contained in the current data ensemble. This histogram plot is displayed when the **Enable Rotor Sampling** option is enabled, Figures C.17. and C.18.

Data Acquisition Panel – ***Cumulative Results*** Tab
Figure C.33.
(Figures C.13. (C.16.) [ACQUIRE DATA] → C.32. [Cumulative Results Tab] → C.33.)

The ***Cumulative Results*** tab, Figure C.33., of the **Data Acquisition Management Control Interface**, Figure C.32., presents resolved flow-related quantities accumulated during a sequence of data acquisition/processing cycles that have occurred as the measurement volume is translated to a series of spatial locations. These plots are updated automatically following each new data acquisition/processing cycle. The **Enable Online Processing** and **Enable Convergence Validation** options, Figures C.17. and C.18., must be enabled to activate these plots. The following plots are presented:

U- and V-component Mean Velocity Profiles (Non-Coincidence) – [Display]: Presents the mean velocity profiles along the measurement volume scan sequence without imposing the requirement of coincident U- and V-component measurements. The velocity profiles, in meters-per-second, are plotted versus either measurement volume position in meters, or sequence number.

U- and V-component Mean Velocity Profiles (Coincidence) – [Display]: Presents the mean velocity profiles along the measurement volume scan sequence with the requirement of coincident U- and V-component measurements. The velocity profiles, in meters-per-second, are plotted versus either measurement volume position in meters, or sequence number.

Mean Velocity Magnitude Profile – [Display]: Presents the mean velocity profile along the measurement volume scan sequence (derived from coincident U- and V-component measurements). The velocity profile, in meters-per-second, is plotted versus either measurement volume position in meters, or sequence number.

Mean Flow Angle (Alpha) Profile – [Display]: Presents the mean vertical flow angle profile along the measurement volume scan sequence (derived from coincident U- and

V-component measurements). The flow angle profile, in degrees, is plotted versus either measurement volume position in meters, or sequence number.

Reynolds Stress Profile – [Display]: Presents the Reynolds stress profile along the measurement volume scan sequence (derived from coincident U- and V-component measurements). The Reynolds stress profile ($\rho\overline{u'v'}$), in kg/m/s^2, is plotted with only the velocity contributions ($\overline{u'v'}$) in m^2/s^2 versus either measurement volume position in meters, or sequence number.

System Diagnostics
Data Acquisition and Control Program
Configuration/Management Panel
Figure C.38.
(Figures C.13. (C.16.) [SYSTEM DIAGNOSTICS] → C.38.)

Selection of the ***System Diagnostics*** navigation button presents the user with the Data Acquisition Diagnostic Information Panel shown in Figure C.38. This panel contains a tab-based interface with settings and feedback/status elements related to the data acquisition process. The information presented in the various tabs provides insight into system operation along with the acquired data, but have no control capabilities.

Data Acquisition Diagnostics Information Panel
Acquired Data Tab
(All Fields Are Display Only)
Figure C.38.
(Figures C.13. (C.16.) [SYSTEM DIAGNOSTICS] → C.38. [Acquired Data Tab])

This sub-panel presents the data obtained during the most recent data acquisition sequence. The data is presented in both graphical and numerical format. This data is in *raw* or unprocessed format and is intended for diagnostics purposes to give the user a degree of confidence that the system is operating properly. It should be noted that graphical data is presented only when the user activates the **Plot Data?** Option, Figure C.38. (C.39.).

Plot Data? - [Button]: When this control is enabled (**ON**), Figure C.39., the acquired digitized signal bursts are presented on the U-Component Data and V-Component Data displays. Typically this operation is used only for diagnostic purposes since the plots greatly increases the time required for a data acquisition cycle. Thus, unless verification of the acquisition of the signal bursts is needed, it is recommended that this control should be disabled (**OFF**) during a flow field investigation.

Plot Delay (ms) – [Value Entry]: This control, Figure C.39., specifies the length of time in milliseconds that each digitized signal burst is displayed when the **Plot Data?** Option is enabled.

U-Component Data & V-Component Data – [Display]: These displays present the digitized signal burst voltage waveforms for these velocity components. The **Plot Data?** Option must be enabled.

Auxiliary Channel Analog Data Plot – [Display]: Presents the time history of the four conditionally sampled analog signals as acquired by the Auxiliary channels, Figure C.17., ((Figures C.13. (C.17. (C.20.))).

Rotor Azimuth Position Time History – [Display]: Presents the time history of the conditionally sampled shaft encoder azimuth (0-1023 counts). The time history is presented following the completion of the current data acquisition cycle. The **Enable Rotor Encoder Sampling** Option must be enabled, Figure C.18., ((Figures C.13. (C.17. (C.18.))).

Raw Acquired Data – [Display]: Displays the diagnostic characteristics of the current data ensemble. These monitors include voltage measurements for the signal burst ensemble and the auxiliary channel analog signals, interarrival times between bursts in seconds, and rotor azimuth position in encoder counts. This information is in raw format, before signal/data processing has been conducted.

Data Acquisition Diagnostics Information Panel
Hardware Tab
(All Fields Are Display Only)
Figure C.40.
(Figures C.13. (C.16.) [SYSTEM DIAGNOSTICS] → C.38. [Hardware Tab] → C.40.)

This sub-panel displays the configuration of the Data Acquisition hardware as defined by the user and internal settings established within the control software. The sub-panels are group characteristics according to the device or function. This panel only displays the information, no settings can be changed.

LV Burst Signal Digitizer (PXI-5152) Configuration
High-Speed Analog-to-Digital Converter
Figure C.40.
(Figures C.13. (C.16.) [SYSTEM DIAGNOSTICS] → C.38. [Hardware Tab] → C.40.)

General Section

Resources – Identifies the device name as it is specified in the NI-MAX microcode.

Channel Name(s) – Lists the names of the digitizer channels available on the PXI-5152 digitizer.

Channel Section

Bandwidth – Presents the bandwidth of the digitizer input channels expressed as the frequency at which the circuitry attenuates the input signal by 3 dB. The value 0 indicates the default value of the PXI-5152 which is 340 MHz at an input impedance of 50 ohms and 300 MHz at an input impedance of 1 Mega ohm.

Input Impedance – Presents the input impedance setting for the PXI-5152. The impedance is set to 1 Mega ohm for laser velocimeter data acquisition applications because the triggering Scope, Figure C.9., is set to 50 ohms to match the impedance of the cable transferring the signals from the current-source photomultipliers.

Horizontal Section

Record Length – Presents the number of samples that will be acquired by the digitizers once triggered by the Scope and validated by the LVTG (Master Trigger), Figure C.19., (Figures C.13. (C.17. (C.19.))).

Sample Rate – Presents the rate in Hertz at which the input signal bursts are digitized. The maximum (default) sample rate for the PXI-5152 digitizer is 1.0 GHz.

Vertical Section

Input Voltage Range (V p-p) – Presents the input voltage range setting in volts. The available settings are 0.1- to 10.0-volts in a 1, 2, 4, 10 sequence.

Vertical Offset – Presents the voltage offset to be applied to the input signal bursts in volts. If the signal bursts originate from the TSI optical system, the pedestal voltage has been removed, thus the offset should be set to 0 volts (default). If the signal bursts originate directly from the photomultipliers, the offset should be set to the peak voltage of the voltage range selected (assuming the negative signals normally produced by current-source photomultipliers) to provide full-scale digitization.

Probe Atten. – Presents the attenuation (scale) factor applied to the input signal burst. This would be set, for example to 10.0 if a 10X probe was used. For laser velocimetry applications, the value would be 1.0 (default) since there is no attenuation by the 50-ohm coaxial cable used to transmit the signal bursts from the photomultiplier to the digitizer.

Vertical Coupling – Presents the coupling setting for the input photomultiplier signals. The available options are **DC**, **AC** and **GND**. **DC** coupling (default) passes both AC and DC signals whereas **AC** blocks offset voltages, thus passing only the AC portion of the signal. **GND** grounds the digitizer inputs.

Trigger Settings Section

Trigger Mode – Presents the manner in which the digitizer (PXI-5152) is to be triggered to initiate the digitization of the input signal. The available options are **Immediate**, **Software**, **Digital**, **Analog Signal** or **External Trigger Edge** (default), or Window.

Trigger Source – Identifies the source of the trigger signal that will initiate signal digitization. The available options are **Channel 0**, **Channel 1**, or **External Trigger**. The display should show Ext. Trigger as the Master Trigger is generated by the LVTG, Figure C.9.

Trigger Slope – Identifies the slope of the trigger signal that will initiate signal digitization. The available options are **Positive** and **Negative**. The display should indicate a Negative slope based on the Master Trigger generated by the LVTG, Figure C.9.

Trigger Coupling – Identifies the coupling applied to the trigger signal. The possible options are **AC**, **DC**, **HF Reject**, **LF Reject**, **AC Plus HF Reject**. The **AC** and **DC** coupling options are identical to the manner that they are applied for the Vertical Coupling setting. The **HF Reject** setting is similar to **DC** coupling except that higher frequencies (typically >20 kHz) are rejected. The **LF Reject** setting is similar to **AC** coupling except the low frequency cutoff is higher (~200 kHz). **AC Plus HF Reject** setting combines the **AC** and **HF Reject** capabilities. Based on the characteristics of the Master Trigger generated by the LVTG, **DC** coupling should be used.

Trigger Level – Presents the triggering threshold, that once exceeded by the trigger pulse, the PXI-5152 will initiate digitization of the input signal. Based on the characteristics of the Master Trigger generated by the LVTG, this is typically 1.0 volt.

Digital Trigger Delay – Presents the delay, 0- to 10.0-seconds, between the acceptance of the trigger and the initiation of signal digitization in the *Digital* and *Software Trigger* modes of operation. The laser velocimeter application does not require a delay, thus the setting should be 0.0 seconds.

Trigger Timeout (s) – Defines the amount of time to wait after the triggering criteria has been satisfied to allow for the data digitizing process to complete before generating an error. The laser velocimeter application does not require a timeout, thus the value should be set to 0.00 so that system control is returned to the application immediately. This places the burden of verifying the completion of the signal burst digitization on the application which uses other mechanisms to verify that the data acquisition criteria has been satisfied. Proceeding in this manner allows the DA/C program to monitor the arrival of signal bursts to the digitizer.

Trigger Holdoff – Defines the amount of time in seconds after the triggering criteria has been satisfied before the digitizer can be triggered again (typically referred to as *dead time* in laser velocimetry applications). The hold-off is set to 0.0 seconds to obtain minimum dead time. The inherent dead time in the electronics typically exceeds the integral time scale of the flow, thus each signal burst measurement is independent, in a flow turbulence sense, from its neighbors.

Analog Trigger Delay – Presents the delay, 0- to 10.0-seconds, between the acceptance of the trigger and the initiation of signal digitization in the *Analog*, *External*, or *Window Trigger* modes of operation. The laser velocimeter application does not require a delay, thus the setting should be 0.0 seconds.

Hysteresis – When the Analog Hysteresis Ref Trigger mode is used, this parameter specifies the size of the hysteresis window on either side of the trigger level in volts. The digitizer triggers when the trigger signal crosses through the hysteresis value specified with this parameter. This parameter is not used for laser velocimetry applications. The default is set to the nominal value of 0.05 volts.

Low Level – When the Window Trigger mode is selected, this parameter specifies the lower voltage threshold of the triggering signal used by the digitizer. This parameter is not used for laser velocimetry applications. The default setting is 0.0 volts.

High Level – When the Window Trigger mode is selected, this parameter specifies the upper voltage threshold of the triggering signal used by the digitizer. This parameter is not used for laser velocimetry applications. The default setting is 0.1 volts.

Reference Pos. (%) – Specifies the number of pre-trigger versus post-trigger points that are stored. The reference position is expressed as a percentage of the complete record, from 0 to 100, as defined by the *Record Length* setting, Figure C.19., (Figures C.13. (C.17. (C.19.))). A value of 40% is the default and recommended setting. This means that 40% of the points saved in the data record occurred prior to the trigger criteria being satisfied. This pre-trigger capability is used in laser velocimetry to allow triggering to be set near the peak of the signal burst, yet the digitizer will capture the entire signal burst. This method effectively shrinks the measurement volume by allowing only particles passing through the center of the measurement volume to be accepted. Also this helps insure that only signal bursts with the highest signal-to-noise ratio will trigger acquisition. This parameter is set in the Advanced HW Settings dialog, Figure D.2., (Figures C.13. (C.17. (C.18. (D.1.))) [Advanced HW Settings] → D.2.).

Window Mode – When window triggering mode is used, this parameter indicates whether the trigger is generated when the incoming signal satisfies the trigger criteria entering or leaving the window.

Analog Auxiliary Signal Digitizer (PXI-6120) Configuration
Multifunction Data Acquisition Module
Figure C.40.
(Figures C.13. (C.16.) [SYSTEM DIAGNOSTICS] → C.38. [Hardware Tab] → C.40.)

6120 Analog Input Channels – Identifies the device names of the input channels as specified in NI-MAX (LVMultiFunc) microcode.

Channel Labels – Displays the unique names of the analog input channels of the PXI-6120. The default names are consecutive labels ai0 – ai3, and are normally not changed for laser velocimeter applications.

Input Voltage Range (V) – Displays the input voltage range settings of the analog input channels. The available ranges are ±0.2-, ±0.5-, ±1.0-, ±2.0-, ±5.0-, ±10.0-, ±20.0- and ±42.0-volts. The default setting is ±2.0 volts.

Record Length – Displays the length of the data acquisition record. Since the analog input channels are used exclusively as conditionally sampled channels in laser velocimetry applications, there is only one measurement taken per Master Trigger event. Thus the record length setting is set to 0.

Sample Rate – Displays the rate at which the analog input channels are sampled. Since the analog input channels are used exclusively as conditionally sampled channels in laser velocimetry applications, there is only one measurement taken per trigger event. Thus sample rate has no meaning for laser velocimetry applications.

Input Coupling – Displays the coupling setting for the input analog signals. The available options are **DC**, **AC** and **GND**. **DC** coupling (default) passes both DC and AC signals into the system while **AC** coupling passes only AC signals (any DC offset is stripped from the signal). **GND** grounds the digitizer inputs.

Input Terminal Configuration – Displays the input signal termination setting for the analog signals. The available settings are default (for the PXI-6120 this is RSE (Reference Single Ended)), Differential, NSRE (Non-Referenced Single Ended) and RSE (Reference Single Ended). Either the default or RSE setting is employed for laser velocimetry applications.

Trigger Source – Displays the source of the signal used to trigger the sampling of the signal applied at the four available analog input channels. The laser velocimeter configuration uses the signal derived from the Master Trigger from the LVTG, Figure C.9., routed to the PXI-6120 via the PXI backplane.

Analog Sample Clock Source – Displays the source of the clock signal used to initiate the digitization of the signals present at the inputs of the analog channels. As described above,

the laser velocimetry application acquires only a single sample of the analog input signals when triggered. Thus the clock source is the same as the Trigger Source.

System Trigger Configuration
Figure C.40.
(Figures C.13. (C.16.) [SYSTEM DIAGNOSTICS] → C.38. [Hardware Tab] → C.40.)

Trigger Definition Section

Trigger Source Terminal – Identifies the source (hardware terminal) of the Start Acquisition Trigger. The laser velocimetry application uses the Reference Trigger derived from the Master Trigger from the LVTG, Figure C.9., routed to the PXI-6120 via the PXI backplane.

System Trigger Terminal – Identifies the terminal where the Start Acquisition Trigger, required by other devices in the PXI chassis, can be obtained.

Trigger Name – Presents the label associated with the System Trigger signal.

Trigger Polarity – Sets the polarity of the System Trigger Signal. The non-inverted version of the trigger signal is employed for laser velocimetry.

Counter Generated Trigger Definition Section – This group of parameters is associated with the use of one of the counters within the PXI-6120 Multifunction module as the source for the trigger signals needed. The counter system can be used to verify system operation when neither signal bursts or synthetic signals produced by an Arbitrary Waveform Generator were available. This capability is maintained for diagnostic purposes only, and is not used during normal laser velocimetry applications.

Trigger Pulse Frequency (Hz) – Presents the rate at which the counter generated trigger pulses are to be generated in Hertz. The default value is 1 Hz.

Initial Delay – Presents the delay in seconds after the counter has been armed before the first trigger signal is generated.

Trigger Pulse Duty Cycle – Defines the duty cycle of the trigger pulse train.

Trigger Idle State – Defines the quiescent state of the trigger signal. Under most conditions this will be TTL Low.

Counter Enable – This button enables the counter circuitry of the PXI-6120 to be used for generating the trigger signals.

Trigger Signal Routing Section

Trigger Destination #1 & Trigger Destination #2 – The flexibility inherent in the PXI system provides the ability to route system signals using software commands to different hardware connectors on the various system devices. These settings reflect the destinations of the Reference trigger generated by the PXI-5152 digitizer. PXI Trigger Line 0/RTSI 0 reflects the routing of the Reference trigger signal to the PXI back plane making it available to other devices residing in the PXI chassis. PFI 1 reflects the routing of the Reference trigger to the PFI 1 connector on the PXI-5152 front panel.

Shaft Encoder Reader (PXI-6602) Configuration
Counter/Timer Module
Figure C.40.
(Figures C.13. (C.16.) [SYSTEM DIAGNOSTICS] → C.38. [Hardware Tab] → C.40.)

The PXI-6602 is a multipurpose counter/timer device capable of performing a number of pulse counting and timing operations. The device has been configured using hardware and software mechanisms for laser velocimetry applications. Specifically the counter/timer was set to perform the following functions:

One counter has been configured to operate in angular shaft encoder mode to record position information generated by a rotatory position encoder such as those installed on a rotorcraft model.

Three counters have been configured to simulate the output signals produced by a rotor shaft encoder mounted at the base of a helicopter shaft rotating at 2800 rpm. The resultant encoder circuitry simulates an encoder producing 1024/rev resolution and 1/rev (signifying the 0 azimuth position) digital pulse trains.

Azimuth Position Tracking Counter – Identifies the counter on the PXI-6602 channel that is configured to operate in angular shaft encoder mode and sample both the 1024/rev and 1/rev pulse trains generated by the rotor shaft encoder.

Azimuth Position Sample Trigger Source – Identifies the hardware connection where the Master Trigger, that causes the Azimuth Position Tracking Counter to store its count value, is located. The Master Trigger, generated by the LVTG, enables the counter to record the rotor position, synchronized with the acquisition of the signal burst.

Azimuth Position Encoder Pulses Per Revolution – Identifies the number of pulses produced per revolution by the rotor shaft encoder.

Acquisition In Progress Indicator Control/Info
Figure C.40.
(Figures C.13. (C.16.) [SYSTEM DIAGNOSTICS] → C.38. [Hardware Tab] → C.40.)

One of the digital lines available on the PXI-6120 module is used as a *System Busy* line to indicate that a data acquisition cycle was currently in progress. The line is raised to a TTL High level at the start of the data acquisition cycle and remains in that state until: a) all of the requested signal bursts have been acquired; b) a timeout condition is reached; or c) the user has chosen to abort the data acquisition operation. At the completion of the data acquisition cycle, the line is returned to a TTL Low state. The *System Busy* line can be used to synchronize laser velocimeter data acquisition activities to external devices/systems.

Busy Digital Lines – Identifies the hardware connection where the *System Busy* signal can be obtained.

Busy TTL Line State – Indicates the state of the *System Busy* signal: lit → Busy.

LV Digitizer(s) (PXI-5152) Instrument Handles – Identifies the device names specified in NI-MAX for digitizers installed in the PXI chassis. NI-MAX provides the driver interface between the control software and the data acquisition hardware.

Auxiliary Board (PXI-6120) Task – Identifies the name of the task associated with the Analog data acquisition operations of the PXI-6120 channel.

ARB Trigger Task – Identifies the name of the task associated with generating a digital trigger pulse that is used to externally trigger the Arbitrary Waveform Generator used to generate synthetic signal bursts.

PXI-6602 Rotor Position Sampling Task – Identifies the name of the task associated with the counter elements of the PXI-6602 used to count encoder pulses produced by a rotor shaft encoder or the simulated shaft encoder.

Data Acquisition Busy Task – Identifies the name of the task associated with the Digital data lines used to generate the *System Busy* signal.

Data Acquisition Diagnostics Information Panel
Information Tab
(All Fields Are Display Only)
Figure C.41.
(Figures C.13. (C.16.) [SYSTEM DIAGNOSTICS] → C.38. [Information Tab] → C.41.)

The ***Information*** tab, Figure C.41., presents a variety of data acquisition information reported back from the system components rather than user settings (as shown on the

Hardware tab of the Data Acquisition Diagnostics Information panel, ((Figures C.13. (C.16.) [SYSTEM DIAGNOSTICS] → C.38. [Hardware Tab] → C.40.)). The ability to retrieve and present this information provides confirmation that the system is configured according to the user's specifications. This panel only displays the information, no settings can be changed.

LV Burst Signal Digitizer (PXI-5152) Information
High-Speed Analog-to-Digital Converter
Figure C.41.
(Figures C.13. (C.16.) [SYSTEM DIAGNOSTICS] → C.38. [Information Tab] → C.41.)

Actual Sample Rate (PXI-5152) (Hz) – Specifies the sample rate used by the PXI-5152 during the last completed data acquisition cycle.

Record Length – Specifies the number of samples requested by the operator for each acquired signal burst, Figure C.19., (Figures C.13. (C.17. (C.19.))).

Actual Record Length – Specifies the number of samples actually contained in each data record acquired during the last completed data acquisition cycle.

Active Scope Input Chans. – Specifies the number of PXI-5152 digitizers available in the Data Acquisition system.

5152 Total Horizontal Memory Depth (Bytes) – Specifies the total on-board memory of the PXI-5152 in bytes. The PXI-5152 used in the Data Acquisition System has 512 Mb of on-board memory.

Total Available Samples/Ch (Mb) – Specifies the total number of samples available on each of the PXI-5152 digitizer's two channels in megabytes (Mb). The PXI-5152 used in the Data Acquisition System has 256 Mega Samples (MSamples) available for each of the two channels.

Sample Rate Setting (PXI-5152) – Specifies the sample rate requested by the user at the start of the data acquisition cycle.

LV Board 1 Status – Identifies the status of the first LV signal digitizer during the data acquisition activity. Note: A two component laser velocimeter only requires a single PXI-5152 digitizer.

LV Board 2 Status – Identifies the status of the second LV signal digitizer during the data acquisition activity. Note: The second PXI-5152 digitizer is utilized for three component laser velocimeters.

Auxiliary Board Status – Identifies the status of the PXI-6120 Multifunction board (Auxiliary Data Channel) during the data acquisition activity.

Analog Auxiliary Signal Digitizer (PXI-6120) Information
Multifunction Data Acquisition Module
Figure C.41.
(Figures C.13. (C.16.) [SYSTEM DIAGNOSTICS] → C.38. [Information Tab] → C.41.)

Timebase Source – Specifies the source of the Master Timebase used on the PXI-6120 Multifunction board.

Timebase Divisor – Specifies the number of Master Timebase pulses required to generate a single sample clock for the PXI-6120. This information is irrelevant for the current Data Acquisition System since the sample clock used is the Master Trigger signal which occurs at a random rate based on the Poisson arrival statistics of the seeding particles.

Max. Sample Rate – Indicates the maximum Sample Clock rate supported by the PXI-6120. This information is irrelevant for the current Data Acquisition System.

Output Buffer Size – Specifies the size of the on-board buffer allocated to store the number of samples requested by the user. The size of the buffer is controlled by the number of LV data samples requested by the user.

Per Analog Input Chan Mem. Depth (Mb) – Specifies the maximum possible number of samples that can be acquired on each of the four Analog Input channels in Mega bytes.

Total Input Mem. Size (Mb) – Specifies the total size of the on-board memory available on the PXI-6120.

Actual Sample Rate (PXI-6120) – Specifies the user setting for the sample rate of the PXI-6120. As the sample rate is dictated by the Master Trigger, this value is irrelevant for the Laser Velocimeter Data Acquisition System.

6120 Sampling Mode – Specifies the sampling mode of the PXI-6120. The mode should be **Finite**.

6120 Sampling Edge – Specifies the edge of the PXI-6120's sample clock on which the input signals are sampled. The edge should be **Rising**.

6120 Analog Input Buffer Size – Specifies the size of the on-board input sample buffer available for the Analog Input sampling task. The size of the buffer is controlled by the number of signal bursts requested by the operator.

Auxiliary Chanel Samples Acquired – Indicates the number of samples acquired during the last completed data acquisition cycle.

6120 Start Trigger Source – Identifies the name of the terminal containing the Start Data Acquisition signal. The signal causes the PXI-6120 to begin performing its data acquisition operations. This signal is the Master Trigger.

6120 Sample Clock Source – Identifies the name of the terminal containing the PXI-6120 Sample Clock Signal. This signal is the Master Trigger.

Active Analog Input Channels – Specifies the number of available Analog Input Channels on the PXI-6120.

6120 Start Trigger Type – Specifies the type of signal that will be used to initiate the data sampling process on the PXI-6120. The type should be **Digital Edge**.

Data Acquisition Diagnostics Information Panel
Sub Task Info Tab
(All Fields Are Display Only)
Figure C.42.
(Figures C.13. (C.16.) [SYSTEM DIAGNOSTICS] → C.38. [Sub Task Info Tab] → C.42.)

The information presented on this tab, Figure C.42., pertains to the Laser Velocimeter Data Acquisition System software background tasks. The activation and use of these tasks is controlled by the underlying Data Acquisition and Control software and *not* the program operator. Some of these tasks are always used while others are used as needed. This panel only displays the information, no settings can be changed.

Data Storage Path Generation Task
Path Generator Task Status?
Figure C.42.
(Figures C.13. (C.16.) [SYSTEM DIAGNOSTICS] → C.38. [Sub Task Info Tab] → C.42.)

This is a background task which generates file paths from the Data Storage Management information entered by the user on the System Configuration panel, Figure C.21., (Figures C.13. (C.17. (C.21.))). The task is always launched at program start up as it facilitates the storage of the acquired data samples during the data acquisition activity.

Path Generator Task Status? – Indicates whether the Data Storage Path Generation task is enabled or disabled.

Shaft Encoder Simulation Task
1024/Rev Rotor Simulator Task Status?
Figure C.42.
(Figures C.13. (C.16.) [SYSTEM DIAGNOSTICS] → C.38. [Sub Task Info Tab] → C.42.)

This background task generates pulse trains that simulate the output signals originating from an azimuth encoder mounted to a rotating shaft. It is launched when the operator

has selected the **Enable 1024/Rev Simulator** option on the System Configuration panel, Figure C.18., (Figures C.13. (C.17. (C.18.))).

1024/Rev Rotor Simulator Task Status? – Indicates whether the 1024/Rev Simulator task is enabled or disabled.

Oscilloscope Trigger Out Pulse Shaping Task
One Shot Generator Task Status?
Figure C.42.
(Figures C.13. (C.16.) [SYSTEM DIAGNOSTICS] → C.38. [Sub Task Info Tab] → C.42.)

This background task serves the purpose of managing the retriggerable one-shot pulse circuit configured on the PXI-6602 Counter/Timer board installed in the PXI chassis. A 500 ns-long one shot pulse signal is generated each time an analog trigger output pulse is received from the signal burst triggering Oscilloscope. The task is always launched at program start up as it facilitates the generation of the Master Trigger by the LVTG.

One Shot Generator Task Status? – Indicates whether the One Shot task is enabled or disabled.

Signal Burst Simulation Manager Task
Simulation Signal Manager Task Status?
Figure C.42.
(Figures C.13. (C.16.) [SYSTEM DIAGNOSTICS] → C.38. [Sub Task Info Tab] → C.42.)

This background task controls and manages the operation of an Agilent 81150A Pulse Function / Arbitrary Waveform Generator used to simulate laser velocimetry signal bursts. This task is launched only when the user has selected the **Enable Test Mode** option on the System Configuration panel, Figure C.18., (Figures C.13. (C.17. (C.18.))).

Simulation Signal Mgr Task Status? – Indicates whether the Simulation Signal Management task is enabled or disabled.

MC4 Scan Rig Management Task
Scan Rig Manager Task Status?
Figure C.42.
(Figures C.13. (C.16.) [SYSTEM DIAGNOSTICS] → C.38. [Sub Task Info Tab] → C.42.)

This background task manages a Klinger MC4 based scan rig used to position the measurement volume during a flow field investigation. This task is launched when the user selects the **Initialize Scan Rig** button on the Scan Rig Management Interface panel, Figure C.25., (Figures C.13. (C.16.) [SYSTEM DIAGNOSTICS] → C.24. (C.25.)).

MC4 Management Task Status? – Indicates whether the MC4 Scan Rig Management task is enabled or disabled.

Log File Management Task
Log File Management Task Status?
Figure C.42.
(Figures C.13. (C.16.) [SYSTEM DIAGNOSTICS] → C.38. [Sub Task Info Tab] → C.42.)

This background task manages a text file containing information related to the data acquisition process. The task is always launched at program start up.

Log File Management Task Status? – Indicates whether the Log File Management task is enabled or disabled.

Processed Data Management Task
Processed LV Data Manager Task Status?
Figure C.42.
(Figures C.13. (C.16.) [SYSTEM DIAGNOSTICS] → C.38. [Sub Task Info Tab] → C.42.)

This background task manages the data returned from the Signal/Data Processing program to the Data Acquisition and Control program. This task is launched when the user selects the **Enable Online Processing** and **Enable Convergence Validation** options on the System Configuration panel, Figure C.18., (Figures C.13 (C.17. (C.18.))).

Processed LV Data Manager Task Status? – Indicates whether the Processed LV Data Manager task is enabled or disabled.

Data Acquisition Monitoring Task
Data Acquisition Busy Line Status?
Figure C.42.
(Figures C.13. (C.16.) [SYSTEM DIAGNOSTICS] → C.38. [Sub Task Info Tab] → C.42.)

This indicator shows the status of the Data Acquisition Line Management signal, enabled or disabled. The signal is enabled (TTL High) at the start of a data acquisition cycle, and is disabled (TTL Low) at the completion of that data acquisition cycle.

Data Acquisition Busy Line Status? – Indicates whether the Data Acquisition Busy Line task is enabled or disabled.

Data Acquisition Diagnostics Information Panel
***Simulation Signal Task Info* Tab**
(All Fields Are Display Only)
Figure C.43.
(Figures C.13. (C.16.) [SYSTEM DIAGNOSTICS] → C.38. [Simulation Signal Task Info Tab] → C.43.)

The information on this tab presents the settings of the controls involved in the operation and use of an Arbitrary Waveform Generator (Agilent 81150A Pulse Function Arbitrary

Generator) to generate electronic signal bursts driven by digital versions. The digital signal bursts can be generated by the Monte Carlo simulation program (Appendix A) or by using the laser velocimeter to digitize actual signal bursts generated in a laboratory or flow field environment. The function of the simulator is to verify the operation and measurement accuracy of the laser velocimeter data acquisition and signal/data processing systems. If simulated signal bursts are used, a direct comparison between simulated statistics and the measured statistics can be made to determine the errors induced by the data acquisition hardware and signal/processing software. This panel only displays the information, no settings can be changed.

The digitized signal bursts are retrieved from an ensemble of files, each containing a single burst – the format expected is the same as used by both the simulation and DA/C programs to store the waveforms. The simulation signal task will format a retrieved signal burst and load it in the arbitrary waveform generator which creates the electronic signal that is input to the data acquisition hardware. Since the arbitrary waveform generator has two output channels that can generate two signals simultaneously, testing of coincident U- and V-component signal bursts is the primary method of operation.

Arbitrary Waveform Generator Configuration
Figure C.43.
(Figures C.13. (C.16.) [SYSTEM DIAGNOSTICS] → C.38. [Simulation Signal Task Info Tab] → C.43.)

This sub-panel presents the configuration of the simulation signal burst hardware when the LVDAS is being used in test mode, Figure C.18., (Figures C.13. (C.17. (C.18.))). The arbitrary waveform generator is configured by the Simulation Signal Manager sub-task, based on user input requested by the sub-task. The sub-task is launched when the **Enable Test Mode** button is enabled, Figure C.18. (Figures C.13. (C.17. (C.18.))).

System Configuration

81150A VISA Resource Name – Indicates the VISA name as defined in NI-MAX for the arbitrary waveform generator. The default value is 81150A.

81150A Channel 1 & 81150A Channel 2 – Displays the labels associated with the two 81150A AWG channels. Channel 1 generates U-component signal bursts, and Channel 2 generates V-component signal bursts.

Output Signal Configuration

Amplitude (V p-p) – Reflects the voltage amplitude setting for the 81150A AWG channels.

Offset (0.000V) – Reflects any offset voltage imposed on the 81150A AWG channels.

Arbitrary Waveform Signal Configuration

Chan 1 ARB Wfm Name & Chan 2 ARB Wfm Name – Identifies the names associated with a given waveform loaded into the 81150A. As each waveform is identified from the list of signal burst files, retrieved from the file and loaded into the 81150A, it is assigned an ascending identification label. Thus the contents of these fields will change during the simulated data acquisition cycle. The names specify the measurement component (U or V) associated with it.

Chan 1 ARB Wfm Data & Chan 2 ARB Wfm Data – Presents the arrays containing the values of the digitized signal bursts retrieved from the disk files. These values will change during the simulated data acquisition cycle as each new signal burst data file is loaded.

Trigger Configuration

ARB Trigger Source – Identifies the trigger source for the 81150A. The External triggering mechanism is used during laser velocimeter applications to: a) maintain the simultaneity required for making valid measurements; and, b) synchronize the operation of the LVDAS hardware and software with the 81150A.

Trigger Mode (0: Edge) – Identifies the manner used to trigger the 81150A.

Trigger Slope (0: Positive) – Indicates the polarity of the pulse signal used to trigger 81150A output signal generation.

Internal Trigger Frequency – Reflects the frequency of the internal 81150A triggering signal when ARB Trigger Source is set to Internal.

External Trigger Level – Reflects the voltage level of the external trigger that, when reached, enables 81150A signal output.

Input Impedance (50.0 Ohms) – Reflects the impedance setting of the 81150A External Trigger input.

81150A Status – Indicates if the 81150A is enabled, on-line and ready for use.

AWG Application – Identifies the operating mode of the 81150A AWG. When used with the LVDAS, the setting will be **LDV**.

Simulated LV Signal Burst
Figure C.43.
(Figures C.13. (C.16.) [SYSTEM DIAGNOSTICS] → C.38. [Simulation Signal Task Info Tab] → C.43.)

Displays a plot of the U- and V-component signal bursts currently being output by the 81150A. The amplitude is presented in volts, and time in nsec.

Simulation Signal Information
Figure C.43.
(Figures C.13. (C.16.) [SYSTEM DIAGNOSTICS] → C.38. [Simulation Signal Task Info Tab] → C.43.)

Current Simulated LV Signal File – Full path and name of the file containing the digitized signal bursts being output.

LV Test Signal Filenames – List of file names containing the digitized signal bursts to be used in the test sequence.

Simulation Data Filenames – Running list of the full path and name of the signal burst files that have been output during the test sequence.

Triggering Simulation Files – Running list of the full path and name of the signal burst files that satisfied the triggering criteria of the Scope and LVTG and created a Master Trigger.

Simulated LV Signal Files – Indicator showing the number of signal bursts that will be used in the current test sequence.

Current Simulation File No. – Indicator showing the current number of the file in the sequence of signal bursts being output.

Chan 1 Arbitrary Waveform Name & Chan 2 Arbitrary Waveform Name – Reflects the base name associated with the waveforms loaded into the 81150A. See Chan 1 ARB Wfm Name & Chan 2 ARB Wfm Name for more information.

U-component Burst Data (Centered) & V-Component Burst Data (Centered) – The voltage levels of the digitized signal bursts retrieved from the disk which have been centered in the AWG buffer memory. These values will change during the simulated data acquisition cycle as each new signal burst is loaded.

Aux Bd. (6120) Counter Used to Generate ARB Triggers – Identifies the PXI-6120 counter employed to generate the External triggering signal used to synchronize the outputs of the 81150A to insure signal simultaneity in the arrival of the U- and V-component signal bursts at the LVDAS.

External Trigger Frequency – Indicates the default frequency setting for the PXI-6120 counter channels listed. This value does not accurately reflect the frequency of the External triggers applied to the 81150A which is controlled by the rate the Master Trigger pulses arrive.

U-Comp Burst Min Value & V-Comp Burst Min Value – Displays the minimum U- and V-component signal burst voltages found in each of the digitized waveforms retrieved from disk. This information is maintained in a Log file.

U-Comp Burst Max Value & V-Comp Burst Max Value – Displays the maximum U- and V-component signal burst voltages found in each of the digitized waveforms retrieved from disk. This information is maintained in a Log file.

Data Acquisition Diagnostics Information Panel
***Log File Info* Tab**
(All Fields Are Display Only)
Figure C.44.
(Figures C.13. (C.16.) [SYSTEM DIAGNOSTICS] → C.38. [Log File Info Tab] → C.44.)

This tab presents information related to the Log file that contains data acquisition information produced during the portion of a flow field investigation conducted during a single day. These Log files are identified by date and stored in the dated sub-directory containing the data ensembles acquired that day. This panel only displays the information, no settings can be changed.

Log File Info – This sub-panel contains information related to the management of the Log file.

Log File Folder – Identifies the root directory where Log files are located.

Current Log File Path – Identifies the current Log file directory path. The sub-directory containing the Log file, along with the sub-directories containing the data ensembles, is the coded name of the date, e.g., 101711 is October 17, 2011.

Creation Date – Identifies the date that the active Log file was created.

Creation Time – Identifies the time-of-day when the active Log file was created.

New Log File? – Indicates if the active Log file is new. The setting is used internally by the DA/C software to determine the actions that must be performed to properly record the current Log data.

Log File Label String – String containing the labels that identify the names of the various columns of data in the Log file.

Log File Data – This sub-panel contains the information pertaining to the current data acquisition cycle that will be written in the Log file.

Run Cycle # – Identifies the number of the current data acquisition cycle (point number)

Data Set Name – Identifies the root name of the files generated during the current data acquisition cycle.

LV Data Rate (Hz) – Presents the average rate signal bursts were captured during the current data acquisition cycle.

Acquisition Time (s) – Duration of the current data acquisition cycle in seconds.

Records Acquired – Number of signal bursts acquired during the current data acquisition cycle.

Records Processed – Indicates the number of signal bursts successfully processed by the Processing program. This number indicates that both the U- and V-component signal bursts were above the signal-to-noise threshold used in the Processing program. Those bursts that do not exceed the threshold represent the difference between Acquired and Processed numbers.

Convergence Level – Specifies the results of the convergence test in the Processing program (Appendix E.2.-E.3.). If the results are higher than the user selected level, Figure C.22., (Figures C.13. (C.17. (C.22.))), a warning would be issued to the user indicating that statistical stationarity had not been reached, Figure C.36, and that another data ensemble should be acquired at the current measurement volume location.

Processing Code – Code used to instruct the Processing program regarding real-time plotting of the mean and standard deviation results, and multiple ensemble processing. The code reflects the setting of the **Data Ensemble Processing Options** control shown in Figure C.34., (Figures C.13. (C.16.) [ACQUIRE DATA] → C.32. (C.34.)).

Scan Rig Positions (W-Index, X-Index, Y-Index, Z-Index) – Identifies the index position of each scan rig axis at the time when the last data acquisition cycle was performed.

Log File Manager Command – Displays the last command issued to the Log file management sub-task.

Log File Manager State – Displays the status of the Log File sub-task.

New Data Series? - Indicator that defines the functionality of the Log File Manager sub-task as set in the **Data Ensemble Processing Options** control shown in Figure C.34., (Figures C.13. (C.16.) [ACQUIRE DATA] → C.32. (C.34.)). **NEW** indicates that a new Log file is to be created such as the case when the DA/C program is first used on a given day, or when a new scan grid has been loaded, thus requiring segregation of the data ensembles. **OLD** indicates that the current data ensemble is a continuation of the previous ensembles and that the existing Log file is being used.

Data Acquisition Diagnostics Information Panel
***Data Management Settings/Info* Tab**
(All Fields Are Display Only)
Figure C.45.
(Figures C.13. (C.16.) [SYSTEM DIAGNOSTICS] → C.38. [Data Management Settings/Info Tab] → C.45.)

This panel presents information regarding data retrieval and storage operations of the system as well as status information related to the various hardware tasks. This panel only displays the information, no settings can be changed.

Data Archival Parameters/Info
Figure C.45.
(Figures C.13. (C.16.) [SYSTEM DIAGNOSTICS] → C.38. [Data Management Settings/Info Tab] → C.45.)

Primary Data Store Settings & Secondary Data Store Settings – Settings used when archiving the acquired data ensembles to both the primary (DA/C) and secondary (Processing) computers.

Root LV Path – Root directory where the data ensembles are archived.

LV Data Series Base Path – Base (root) directory where the data ensembles for the current data acquisition cycle are archived. In most cases this would be the Root LV Path with a unique sub-directory name generated using the date and time, Figure C.21., (Figures C.13. (C.17. (C.21.))), set to the time/date when the current data acquisition cycle initiated.

Processed LV Data Path – Directory path indicating where the results from the Processing program are archived for the current data acquisition cycle. This is typically the LV Data Series Base Path with the added sub-directory, e.g., processed27-OCT-11, where the appended date (in this case October 27, 2011) is the date when the data ensemble was processed.

Header File String – Display of the contents of the Header (.hdr) file that contains the operational characteristics of the LVDAS as they were set for the current data

acquisition cycle. The Header file is stored in the directory whose path is presented in the LV Data Series Base Path.

Initialization (.ini) Filename – Name of the user selected initialization file used to configure the LVDAS at DA/C program start-up.

Data Retrieval Parameters/Info
Figure C.45.
(Figures C.13. (C.16.) [SYSTEM DIAGNOSTICS] → C.38. [Data Management Settings/Info Tab] → C.45.)

Parameters that establish how the digitized signal bursts stored in PXI-5152 digitizer memory are transferred to archival disk storage on the DA/C and Processing computers using the LV Data Manager DLL.

Data Set Info – Listing of the components that uniquely tags a block of data (signal burst ensemble) retrieved from the PXI-5152 digitizer memory.

Run ID – Incrementing value that uniquely identifies the active data acquisition cycle.

Block Num(ber) – Incremental number value that uniquely identifies the current data block in a sequence of data blocks retrieved from the PXI-5152 digitizer memory. These values enable the data to be written to disk in proper order.

First Rec No. – Data retrieved from the PXI-5152 digitizer memory as retrieved in chunks (blocks). The value identifies the number of the first signal burst in the chunk of data being passed to the LV Data Manager.

Record Length – Length of the digitized signal burst data record.

Recs/Block – Number of data records (signal bursts) containing the record length number of samples contained in the data chunk being passed to the LV Data Manager.

Chans – Number of laser velocimeter data channels having data in the data chunk.

Recs/Cycle – Total number of data records (signal bursts) acquired during the active data acquisition cycle.

Sample Rate – Rate that the digitizers sample the signal bursts during the active data acquisition cycle.

In addition to the data retrieval parameters described above, the following parameters are also used for performance monitoring and diagnostics:

Chunk Size (Blocks) – Maximum number of data records (signal bursts) that are contained in a single data chunk. During the data retrieval/transfer process, the chunk size is automatically adjusted (reduced) to accommodate the actual number of records contained in the chunk.

Data Chunks To Transfer – Number of full and partial data chunks that will be transferred/received. This value will vary based on the number of data records (signal bursts) acquired.

Data Chunks Retrieved – Number of data chunks successfully retrieved during the retrieval/archival process.

Data Manager Status – Status code returned by the LV Data Manager DLL describing the status of the last transaction. The value 0 indicates that the last transaction was completed without an error.

Total # Records Retrieved – Total number of data records (signal bursts) that have been retrieved from the PXI-5152 digitizer memory during the current transfer/retrieval process.

Data Retrieval/Storage Performance
Figure C.45.
(Figures C.13. (C.16.) [SYSTEM DIAGNOSTICS] → C.38. [Data Management Settings/Info Tab] → C.45.)

These indicators provide retrieval/archival process performance related feedback information to the operator.

Data Retrieval Start Time – Indicates the time (tick count) in milliseconds when the current data retrieval/archival process was started. Note that this value has no real-world time value. It is the value of a 32-bit counter that counts pulses occurring at a one millisecond interval.

Data Retrieval End Time – The time required to complete the current data retrieval/archival process in milliseconds.

Data Retrieval Time (Secs) – Length of time required to complete the current data retrieval process.

Time To Write To Disk (Secs) – Length of time required to complete archiving the just retrieved data sets to disk files.

Data Retrieval & Save Time (Secs) – Total time duration required to complete the current data retrieval/archival process.

LV Data Handler Status Information
Figure C.45.
(Figures C.13. (C.16.) [SYSTEM DIAGNOSTICS] → C.38. [Data Management Settings/Info Tab] → C.45.)

These indicators relay status information from the LV Data Manager DLL , and are provided for testing and verification purposes.

dmStatus – Provides a status code returned from the LV Data Manager DLL. The value 0 indicates no errors occurred during the last transaction.

numActvDataSets – Number of data sets retrieved from the PXI-5152 digitizers currently being held in the queue that must be permanently archived.

numFileNodes – Number of file info nodes in the file info queue.

numArchived – Number of data ensembles that have been archived since the start of the retrieval/archive process.

numLVNodes – Number of data blocks in the data queue.

numLVAuxNodes – Number of auxiliary data nodes in the auxiliary data queue.

LV Data Acquisition Results
Figure C.45.
(Figures C.13. (C.16.) [SYSTEM DIAGNOSTICS] → C.38. [Data Management Settings/Info Tab] → C.45.)

This structure contains information related to the progress of the current data acquisition cycle. The following parameters are included:

Samples Requested – Number of data records (signal bursts) requested by the user at the start of the data acquisition cycle.

Samples Acquired – Number of data records (signal bursts) actually acquired during the current data acquisition cycle.

Data Acquisition Time (secs) – The elapsed time of the current data acquisition cycle in seconds.

LV Data Rate (Hz) – Rate in Hertz that the current data acquisition cycle acquired the data record (signal burst) ensembles.

Time Out? – Indicates if the current data acquisition cycle terminated because the user-specified timeout limit was reached.

User Terminated? – Indicates if the current data acquisition cycle was terminated by the user before the requested number of records was acquired or timeout was reached.

Status/Error Information
Figure C.45.
(Figures C.13. (C.16.) [SYSTEM DIAGNOSTICS] → C.38. [Data Management Settings/Info Tab] → C.45.)

Eight unique error indicators are available to communicate status and error messages during the data acquisition cycle.

PXI-5152 Digitizer Errors – Displays error and status information related to activities performed by the PXI-5152 digitizer.

PXI-6120 Auxiliary Data Board Errors – Displays error and status information related to activities performed using the PXI-6120 multifunction (auxiliary data) channel.

PXI-6602 C/T Board Errors – Displays error and status information related to activities performed by the PXI-6602 counter/timer channel.

Scan Rig Errors – Displays error and status information related to activities performed by the Klinger (MC4) scan rig management sub-task.

Agilent 81150A AWG Errors – Displays error and status information related to activities performed by the Agilent 81150A Arbitrary Waveform Generator management sub-task.

System Errors – Displays error and status information generated while performing various system management activities during the data acquisition cycle.

Data Retrieval Errors – Displays error and status information generated during the data retrieval/archival phase of the data acquisition cycle.

Data Acquisition Diagnostics Information Panel
***Processed Results* Tab**
(All Fields Are Display Only)
Figure C.46.
(Figures C.13. (C.16.) [SYSTEM DIAGNOSTICS] → C.38. [Processed Results Tab] → C.46.)

This tab contains information transmitted back to the DA/C software from the Processing program following the completion of signal/data processing of the current data ensemble. The parameters include the results of the statistical stationarity test, average minimum and maximum signal burst voltage levels for the U- and V-components, and average signal-

to-noise ratios for the two velocity components. These parameters will help guide the user in assessing the quality of the measurements contained in the ensemble. This panel only displays the information, no settings can be changed.

Data Converged? – Indicates whether or not the convergence level computed for the just processed ensemble of signal bursts is less than the Convergence Threshold (m/s) setting located on the System Configuration panel, Figure C.22., (Figures C.13. (C.17. (C.22.))). When the computed convergence is less than the defined acceptance threshold, this indicator displays **YES**. Conversely, if the computed convergence is greater than the threshold, this indicator displays **NO**.

Max # LV Records That Can Be Processed Together – Indicates the maximum number of signal bursts that can be processed together by the Signal/Data Processing program. The limit applies to a single or the sum of multiple ensembles acquired at the same measurement volume location. This value is hard coded to correspond to the internal limit imposed in the Signal/Data Processing program. If the Signal/Data Processing program is modified to allow the acquisition of a greater number of signal bursts, a Data Acquisition and Control program must also be modified.

Trigger Return File Path – Full path to the Trigger.Ret file generated and updated by the Signal/Data Processing program.

LV Data Histograms
Figure C.46.
(Figures C.13. (C.16.) [SYSTEM DIAGNOSTICS] → C.38. [Processed Results Tab] → C.46.)

At the completion of the signal/data processing cycle, U- and V-component, velocity magnitude, and vertical flow angle histograms and flow statistics developed from the processed data ensembles are stored in a Log file. The contents of the Log file are subsequently retrieved by the Data Acquisition and Control program with the update of the Trigger Return File at the conclusion of the processing cycle. These results and histograms are presented to the operator in numerical (Figure C.46.) and graphical (Figure C.32.) formats. It is noted that all histograms are based on coincident velocity measurements.

U-Component Velocity Histogram – Numeric presentation of the velocity histogram developed from the U-component signal burst ensemble.

V-Component Velocity Histogram – Numeric presentation of the velocity histogram developed from the V-component signal burst ensemble.

Velocity Magnitude Histogram – Numeric presentation of the velocity histogram developed from the velocity magnitude calculations from U- and V-component coincident signal bursts.

Flow Angle Histogram – Numeric presentation of the vertical flow angle histogram developed from the flow angle calculations from U- and V-component coincident signal bursts.

Processed LV Convergence Data
Figure C.46.
(Figures C.13. (C.16.) [SYSTEM DIAGNOSTICS] → C.38. [Processed Results Tab] → C.46.)

The measurement convergence data used as a test of measurement statistical stationarity is preserved in the Log file generated by the Signal/Data Processing program. The contents of the Log file are subsequently retrieved by the Data Acquisition and Control program with the update of the Trigger Return File at the conclusion of the processing cycle. The results from the convergence test are presented to the operator in numerical (Figure C.46.) and graphical (Figure C.32.) formats.

U-Component Velocity Convergence Data – The U-component mean velocity is computed for the first 100 signal bursts, first 200 signal bursts, etc., by the Signal/Data Processing program. The sequence of U-component mean measurements can be stepped through from the convergence trace.

V-Component Velocity Convergence Data – The V-component mean velocity is computed for the first 100 signal bursts, first 200 signal bursts, etc., by the Signal/Data Processing program. The sequence of V-component mean measurements can be stepped through from the convergence trace.

U-Component Velocity Std. Dev. Convergence Data – The U-component standard deviation is computed for the first 100 signal bursts, first 200 signal bursts, etc., by the Signal/Data Processing program. The sequence of U-component standard deviation measurements can be stepped through from the convergence trace.

V-Component Velocity Std. Dev. Convergence Data – The V-component standard deviation is computed for the first 100 signal bursts, first 200 signal bursts, etc., by the Signal/Data Processing program. The sequence of V-component standard deviation measurements can be stepped through from the convergence trace.

U-Component Delta Velocity Convergence Data – The change in U-component mean velocity between each step in the convergence trace is computed by the Data Acquisition and Control program and the resultant trace presented in numeric format.

V-Component Delta Velocity Convergence Data – The change in V-component mean velocity between each step in the convergence trace is computed by the Data Acquisition and Control program and the resultant trace presented in numeric format.

U-Component Velocity Std. Dev. Delta Convergence Data – The change in U-component standard deviation between each step in the convergence trace is computed by the Data Acquisition and Control program and the resultant trace presented in numeric format.

V-Component Velocity Std. Dev. Delta Convergence Data – The change in V-component standard deviation between each step in the convergence trace is computed by the Data Acquisition and Control program and the resultant trace presented in numeric format.

Processed LV Data Results
Figure C.46.
(Figures C.13. (C.16.) [SYSTEM DIAGNOSTICS] → C.38. [Processed Results Tab] → C.46.)

LV Records Processed – Number of data records (signal bursts) within the data ensemble that yielded viable coincident velocity measurements.

Convergence Level (m/s) – Result from the statistical stationarity test. The standard deviation of each of the final five mean and standard deviation entries in the convergence traces (Processed LV Convergence Data) are calculated and then averaged to yield the measured convergence level. This level is then compared by the program with the user input level to determine if additional data is needed at that measurement location to reach statistical stationarity in the data ensemble.

LV Records Processed U-Component – Number of data records (signal bursts) within the data ensemble that yielded viable U-component velocity measurements – coincidence not imposed.

LV Records Processed V-Component – Number of data records (signal bursts) within the data ensemble that yielded viable V-component velocity measurements – coincidence not imposed.

The following parameters are computed from signal bursts where at least one of the two simultaneously acquired signal bursts (U- and V-components) yielded a viable measurement.

Avg Min Signal Burst Level U-Component (volts) (Coincident) – Minimum value for each signal burst is determined and the average for the ensemble calculated – U-component, coincident signal bursts only.

Avg Max Signal Burst Level U-Component (volts) (Coincident) – Maximum value for each signal burst is determined and the average for the ensemble calculated – U-component, coincident signal bursts only.

Avg Min Signal Burst Level U-Component (volts) – Minimum value for each signal burst is determined and the average for the ensemble calculated – U-component, viable signal bursts occurring in either U- or V-components.

Avg Max Signal Burst Level U-Component (volts) – Maximum value for each signal burst is determined and the average for the ensemble calculated – U-component, viable signal bursts occurring in either U- or V-components.

Avg Min Signal Burst Level V-Component (volts) (Coincident) – Minimum value for each signal burst is determined and the average for the ensemble calculated – V-component, coincident signal bursts only.

Avg Max Signal Burst Level V-Component (volts) (Coincident) – Maximum value for each signal burst is determined and the average for the ensemble calculated – V-component, coincident signal bursts only.

Avg Min Signal Burst Level V-Component (volts) – Minimum value for each signal burst is determined and the average for the ensemble calculated – V-component, viable signal bursts occurring in either U- or V-components.

Avg Max Signal Burst Level V-Component (volts) – Maximum value for each signal burst is determined and the average for the ensemble calculated – V-component, viable signal bursts occurring in either U- or V-components.

Avg SNR Values U-Component (Coincident) – Average signal-to-noise ratio of the U-component signal bursts within the ensemble, coincident signal bursts only.

Avg SNR Values U-Component (Non-Coincident) – Average signal-to-noise ratio of the U-component signal bursts within the ensemble, viable signal bursts occurring in either U- or V-components.

Avg SNR Values V-Component (Coincident) – Average signal-to-noise ratio of the V-component signal bursts within the ensemble, coincident signal bursts only.

Avg SNR Values V-Component (Non-Coincident) – Average signal-to-noise ratio of the V-component signal bursts within the ensemble, viable signal bursts occurring in either U- or V-components.

System Information
Data Acquisition and Control Program
Configuration/Management Panel
Figure C.16.
(Figures C.13. (C.16.) [SYSTEM INFORMATION])

Launches a panel containing various system information including Appendices A through E in pdf format. Other hardware and software related documents are also available. Selecting a document will launch a pdf viewer containing the document. To be implemented.

Quit
Data Acquisition and Control Program
Configuration/Management Panel
Figure C.16.
(Figures C.13. (C.16.) [QUIT])

Terminates the Data Acquisition and Control program, which in turn automatically terminates the Signal/Data Processing program. Closes all graphic windows on the Signal/Data Processing computer, however there will be a single command line window remaining that requires manual closing.

Program & System Status
Data Acquisition and Control Program
Configuration/Management Panel
Figure C.16.
(Figures C.13. (C.16.))

At the bottom of the Program Navigation panel, Figure C.16., status information is provided to monitor information relevant to the various system functions.

System Status – Displays the operational state of the DA/C program. Ten possible states are presented.

IDLE – System is in standby, but ready to perform a user selected activity.

INITAILIZING HARDWARE – Launching a data acquisition cycle activates the hardware initialization and configuration sequences to prepare the hardware to acquire data.

DATA ACQUISITION IN PROGRESS – System is actively gathering signal bursts.

RETRIEVING DATA – Requested data ensemble has been acquired and stored in the PXI system. Data ensemble currently being transferred to the DA/C computer memory.

STORING DATA – Data ensemble stored in the DA/C computer memory is being archived in the defined locations on the DA/C and Processing computer hard drives.

ACQUISITION COMPLETE – Data acquisition cycle has been completed and all of the acquired signal bursts and related parameters have been collected and archived successfully.

ACQUISITION TIMEOUT – Data acquisition cycle was terminated because the specified data acquisition timeout was reached prior to acquiring the user specified number of signal bursts.

ACQUISITION TERMINATED – Data acquisition cycle was terminated by the user, **Terminate Data Acquisition** button, Figures C.32. and C.34.

SYSTEM SHUTDOWN IN PROGRESS – System is performing various hardware and software cleanup activities in response to the selection of the **QUIT** button on the Program Navigation panel, Figures C.13. and C.16.

SYSTEM SHUTDOWN COMPLETED – All of the shutdown activities have been completed and the program can gracefully be terminated.

Data Sets Acquired – Number of data ensembles acquired during the current data acquisition activity. This value is incremented at the completion of each data acquisition / processing cycle and preserved in the data acquisition Log file. The value is reset to zero each time the DA/C program is started. However, if a log file exists for a given date, the user is prompted with the choice of whether or not to append to that log file. If the user chooses to continue the existing log file by appending the new information, the program retrieves the last value written to that file in the # Data Sets Acquired field and initializes this parameter with that value.

Data Acquisition and System Control Software Sub-Tasks

There are several small programs that are used during laser velocimetry data acquisition investigations to perform minor, but important functions to relieve the DA/C program from the overhead. Several of these tasks run in parallel with the DA/C program to provide flexibility and/or decrease the data acquisition cycle time. Many of the programs are launched when the DA/C program is started, while others execute only under user control.

LV Data File Name Generation

With thousands of digitized signal bursts needing to be archived with unique file names and placed in directories with names that describe something unique about the data ensemble it contains, this task cannot be performed manually. Thus a sub-task was written to automatically create the directory based on a standard selected by the user, and automatically use this standard to define file names with a file number suffix to store the digitized signal burst data. The sub-task is initiated when the DA/C program starts, and runs in the background executing commands generated by the DA/C program.

The inputs and methods used to develop the directory and file names are selected by the user in the Data Storage Management sub-panel, Figure C.21. (Figures C.13. (C.17. (C.21.))), shown when the **Configuration** button is selected in the DA/C program. The data storage locations must be established before the first data acquisition cycle is initiated by the DA/C program to insure storage of the digitized signal bursts in the desired and known locations. Once established and a data acquisition cycle is initiated, the sub-task will create the directories in the DA/C and Processing computers. As the signal bursts are acquired by the PXI-5152 digitizer, the sub-task is simultaneously creating a list of full path file names to match the number of bursts acquired. When the requested number of signal bursts have been digitized (or time-out or user termination occurred), the sub-task will pass the list of full path file names to the LV Data Management DLL which transfers the acquired data from the DA/C computer memory (following transfer from the PXI-5152 memory to the DA/C computer under NI-MAX control) to the two hard drives at locations specified by the list.

File Path Structure

Options provided in the Data Storage Management sub-panel, Figure C.21., (Figures C.13. (C.17. (C.21.))), allow the user to define how the file names used to archive the acquired digitized signal bursts will be generated. In most cases the default **Use Date/Time** option is preferred. The sub-task will first create directories (if they do not exist) whose paths are entered in the **Primary Base Data Storage Path** (DA/C computer), and **Secondary (Processing) Base Data Storage Path** (Processing computer) [Text/Value Entry Fields], and if activated, create a sub-directory based on the appended date. If the **Use Date/Time** option is selected and the **Append Date To Store Path** is activated, the following file name format will be created (based on the Primary Base path):

D:\LV_Data\mmddyy\DmmddyyThhmmssFXXXX.LVB

where:

a) D: – Disk drive letter where the data records are to be stored;
b) \LV_Data\ – The directory path where the data records are to be stored;
c) mmddyy – Sub-directory based on two number codes representing month, day, and year when the data cycle was initiated. Acquired data records are stored in this subdirectory;
d) D – A fixed letter representing date;
e) mmddyy – two number codes representing month, day, and year when the data acquisition cycle was initiated (leading zeros will be included);
f) T – A fixed letter representing time;
g) hhmmss – two number codes representing hour, minute, and second when the data acquisition cycle was initiated (leading zeros will be included, 24-hour clock used);
h) F – A fixed letter representing File number;

i) XXXX – an ascending index (0000-9999) for each unique archived data record (signal burst); and,
j) .LVB – Fixed file extension signifying that the file contains digitized signal bursts and was archived in binary format (if the **ASCII** option is activated during a recompile of the DA/C program, the extension would be LVA).

The number of file paths generated is defined by the number of records requested by the user. This includes file paths to both the primary and secondary storage paths. If the data acquisition cycle does not obtain the requested number of signal bursts because of time-out or user termination, the LV Data Management DLL will only create paths based on the created list that match the data records. That is, no empty files are created for non-existent data.

LV Data File Structure

Given the fact that hundreds of thousands of signal burst captures can be performed during the course of a flow-field investigation, it is necessary to define and adhere to a standard method for recording the information to permanent storage. In this way the retrieval, manipulation and processing of the data can be standardized and automated. To facilitate the proper processing of the captured data and the accurate presentation of the resultant flow characteristics, a complete description of the manner and conditions in which the data records were acquired is necessary. In addition, each individual data record should possess sufficient information to fully describe the conditions of its origin along with its data content in a single self-contained file.

Although the most user friendly data file format is tab-delimited ASCII, the time required to transmit these large files would be prohibitive in the environment of production wind tunnel testing. Thus the I.E.E.E. Standard binary format was selected to minimize data transmission time for these large data ensembles, along with reducing the number of bytes needed to contain the ensemble information. Since binary files cannot be read / manipulated using standard office or plotting programs, it is necessary to define the structure of these files so that their contents can be properly read by the Signal/Data Processing program and other support programs written to that standard. The structural standard used to construct these binary files is described in Table D.1. As can be seen, the first nine data words describe the acquisition conditions along with the time since the previous signal burst was acquired followed by the conditionally sampled readings of the shaft encoder and auxiliary data channels. This is followed by the captured voltage trace of the U-component signal burst of a length given as the third of nine values in the header, then the captured voltage trace of the V-component. Programs designed to read these files should first read nine 32-bit floating point numbers followed by performing two consecutive 32-bit floating point array reads to retrieve the U- and V-component signal bursts.

Synthetic LV Signal Generation

During the design, development and testing of the LVDAS, synthetic signal bursts were generated by the Monte Carlo Laser Velocimeter Simulation program (Appendix A). The resulting waveforms were stored to disk files so that they could be recalled and used to drive an Arbitrary Waveform Generator which then produced electronic signal bursts that were input to the LVDAS. The process was used for debugging purposes, dynamic range and resolution characterizations, and measurement accuracy investigations. Subsequent to the completion of the LVDAS, the Arbitrary Waveform Generation control program and associated connections were merged into the DA/C program as a sub-task.

The primary component of the synthetic LV signal generation system is an Agilent 81150A arbitrary waveform generator (AWG). The AWG is a two-channel system that can be programmed to generate standard as well as user defined signals as required. The system also provides several triggering modes making it ideal for signal burst generation. The sub-task loads a single pair (U- and V-component) of signal bursts into the AWG memory. The AWG reads the loaded digital signal bursts and outputs them as analog signal bursts when triggered. Upon release of the analog signals, the sub-task loads the next pair of signal bursts based on a file listing the full path/name of the source signal burst files. Thus signals produced by the Simulation program can be the source, or actual signal bursts obtained with the laser velocimeter and captured by the LVDAS can be used as the source by using the auxiliary program ConvertBinary2ASCII, Appendix E, page E.10.

The sequence of operations used to verify system functionality using the synthetic signal bursts follows:

1) Initialize the AWG output signal levels and the trigger source to be external;
2) Retrieve the simulated (or captured) signal bursts for the U- and V-components from the desired file, sequentially selected from the contents of the listing file;
3) Upload the signal bursts (in digital format) to Channels 1 and 2 of the AWG via USB transmission to the AWG from the DA/C computer;
4) Enable the two AWG output channels. (The signal bursts are not generated until a triggering pulse arrives);
5) Initialize, then arm the LVDAS;
6) Generate the external trigger pulse for the AWG using one of the digital output channels available on the PXI-6120 multifunction data acquisition module;
7) Perform a standard data acquisition with the LVDAS; then
8) Repeat steps 1 to 7 until all of the required sample bursts are acquired by the LVDAS.

LV Simulation Signal Management

Since the use of simulated signal bursts by the LVDAS is intended for system verification purposes only, this diagnostic capability must be manually activated and managed by the user. Control and management of the simulated signals is performed by a sub-task

launched via the DA/C program after the user selects the **Enable Test Mode** button on the Configuration/Management panel, Figure D.3. (Figures C.13. (C.17. (C.18. (D.3.)))). Once activated, the sub-task remains activated until the DA/C program is terminated.

Actual selection and management of the synthetic signal bursts is initiated only after the user starts the data acquisition cycle. After the user enters the data acquisition state (Figures C.13. (C.16.) [ACQUIRE DATA] → C.32. (C.34.)), the user is presented with the panel shown in Figure D.4. The 81150A AWG can be configured for synthetic signal burst generation and interaction with the LVDAS from this panel. The settings shown in Figure D.4. are the default configuration which should function correctly for most applications and thus should not require modification. The panel is made available to provide flexibility if needed for future applications.

The parameters shown in Figure D.4. are defined below:

System Configuration

81150A VISA Resource Name – [Drop Down Menu]: Specifies the VISA name as defined in NI-MAX for the arbitrary waveform generator. The default is 81150A.

81150A Channel 1 & 81150A Channel 2 – [Display]: Displays the labels associated with the two 81150A AWG channels. Channel 1 is used to generate the U-component signal bursts, while Channel 2 is used to generate the V-component signal bursts.

Output Signal Configuration

Amplitude (V p-p) – [Value Entry Field]: Voltage amplitude range setting for both of the 81150A AWG channels.

Offset (0.000 V) – [Value Entry Field]: Offset voltage associated with both of the 81150A AWG channels.

Arbitrary Waveform Signal Configuration

Chan 1 ARB Wfm Name & Chan 2 ARB Wfm Name – [Text/Value Entry Field]: Names associated with a given waveform loaded into the 81150A. As each simulated waveform is retrieved from the list of synthetic signal bursts selected by the user and loaded into the 81150A, it is assigned an ascending identification label. Thus the contents of these fields will change during the simulated data acquisition cycle. These names should reflect the measurement component (U or V) associated with that channel.

Trigger Configuration – These settings correspond to the trigger signal generated by the PXI-6120 multifunction data acquisition module installed in the PXI chassis.

ARB Trigger Source – [Drop Down Menu]: Identifies the trigger source for the 81150A. Signal burst generation requires the External triggering mechanism to: a) maintain the simultaneity to simulate a single particle passing through the laser velocimeter measurement volume; and, b) synchronize the operation of the LVDAS with the 81150A.

Trigger Mode (0: Edge) – [Drop Down Menu]: Manner that the 81150A will be triggered.

Trigger Slope (0: Positive) – [Drop Down Menu]: Polarity of the pulse signal that will be used to trigger 81150A output signal burst generation.

Internal Trigger Frequency – [Value Entry Field]: Frequency of the internal triggering signal when used.

External Trigger Level – [Value Entry Field]: Level of the external trigger signal at which the outputs of the 81150A will be enabled.

Input Impedance (50.0 Ohms) – [Drop Down Menu]: Impedance setting of the 81150A External Trigger input.

AWG Application – [Drop Down Menu]: Identifies the operating mode of the 81150A AWG. For use as a signal burst generator, the application would be **LDV**.

Simulation Signal Selection
Figure D.5.
(Figures D.4. [Done] → D.5.)

Once the user exits the Agilent 81150A AWG Configuration panel, the user is prompted to select a directory that contains the signal burst files they wish to use from the file manager that is launched, Figure D.5. Once the desired directory is found, the user should select *Current Folder*.

Having selected the location containing the desired signal bursts, the DA/C program begins loading the AWG and acquiring the resultant electronic signal bursts in the manner of a normal data acquisition cycle. The simulation file manager will retrieve and load the contents of each simulation signal burst file in sequence into the 81150A in succession. There are no differences in the operation of the LVDAS, except for the source of the signal bursts and the control of the AWG by the DA/C program. As with a normal data acquisition cycle, the sequence continues until: a) the requested number of signal bursts is acquired; b) a timeout condition occurs; or c) the user terminates the data acquisition cycle.

Synthetic LV Signal File Format

The simulated signal bursts developed by the Monte Carlo Laser Velocimeter Simulation program are written to disk in tab-delimited ASCII format. The top portion of these files provides the settings used by the simulation program to generate the resulting signal burst file. This is followed by the U- and V-component signal bursts, where time is in microseconds, and the amplitude is in volts. A portion of a typical file is shown in Figure D.6. If captured signal bursts acquired during a laboratory or flow field investigation using the laser velocimeter are to be used, the binary signal burst records must be converted to ASCII data using the auxiliary program ConvertBinary2ASCII, Appendix E, page E.10. The resulting file matches the format shown in Figure D.6.

Advanced Hardware Settings

The PXI hardware platform forms the basis of the data acquisition system. The PXI hardware provides a great deal of flexibility enabling it to be configured to accommodate the needs of the user. Access to the most common settings for the LVDAS application is provided to the user via the user interface in the DA/C program. Access to additional settings of system hardware is available by selecting the **Advanced HW Settings** button, Figure D.1., on the Configuration/Management panel, Figure C.18. (Figures C.13. (C.17. (C.18.))). When the user selects this sub-task, the panel shown in Figure D.2. is presented. The parameters shown in Figure D.2. are defined below:

Laser Velocimeter PXI-Based Data Acquisition Hardware Configuration Dialog
LV Channel (PXI-5152) Settings In Tab
Figure D.2.
(Figures C.13. (C.17. (C.18. (D.1.))) [Advanced HW Settings] → D.2. [LV Channel (PXI-5152) Settings In Tab])

This tab, Figure D.2., provides controls used to configure the PXI-5152 digitizer which is the primary device used to sample and preserve the signal bursts. The controls are very similar to those available in a modern digital storage oscilloscope.

General Section

Resources - [Drop Down Menu]: Links the LabVIEW software to the device name for the PXI-5152 channel specified in NI-MAX which provides the driver interface between the control software and the data acquisition hardware. All of the PXI hardware elements must be configured through NI-MAX before they can be accessed via the system software.

Channel Names(s) - [Text/Value Entry Field]: Name(s) of the digitizer channels available on the PXI-5152 digitizer.

Channel Section

Bandwidth - [Value Entry Field]: Defines the bandwidth of the digitizer input channels expressed as the frequency where the circuitry attenuates the input signal by 3 dB. The value 0 is the default for the PXI-5152 which sets the 3 dB point at 340 MHz for an input impedance of 50 ohms, and 300 MHz for an input impedance of 1 mega ohms.

Input Impedance - [Drop Down Menu]: Sets the PXI-5152 input impedance. The impedance is defaulted to 1 mega ohms since the PXI-5152 is electronically paralleled with the Scope which has a 50 ohm impedance to match the impedance of the coaxial cable connecting it to the current driving photomultipliers.

Horizontal Section

Record Length - [Value Entry Field]: Number of samples that will be digitized each time a signal burst generates a Master Trigger, Figure C.9., that triggers the digitizer. The default value is 10240.

Sample Rate - [Value Entry Field]: Rate in Hertz that the input signal burst is digitized. The default value is 1.0 GHz.

Vertical Section

Input Voltage Range (V p-p) - [Drop Down Menu]: Input signal voltage range in volts. The available options are 0.1 to 10.0 volts p-p in a 1, 2, 4, 10 sequence. The default setting is 4.0 volts p-p, but the signal levels should be checked routinely since the signal burst amplitudes can and do change during the course of the day because of optical alignment drift caused by tunnel vibration, flow buffeting, etc.

Vertical Offset - [Value Entry Field]: Voltage offset applied to the input signal bursts. Since the signal bursts are symmetric about zero volts in the LVDAS configuration, the default of 0 volts should be maintained.

Probe Atten. - [Value Entry Field]: Attenuation (scaling) factor applied to the input signal burst. This setting should match the attenuation of the input cable or probe. For example, a 10X or 10:1 probe would require the setting to be 10.0. In the LVDAS configuration, the input signal is transmitted through a 50-ohm coaxial cable from the photomultiplier. Thus the default value of 1.0 should be used.
Vertical Coupling - [Drop Down Menu]: Coupling setting for the input signal bursts. The available options are **DC**, **AC**, and **GND**. The **DC** setting passes both AC and DC signals, while the **AC** setting blocks any DC offset passing only the AC signals. **GND** grounds the digitizer inputs. The default setting of **DC** should be used.

Trigger Settings Section

Trigger Mode - [Drop Down Menu]: Selects the manner that a trigger signal will initiate the digitization of the input to the PXI-5152. The available options are **Immediate**, **Software**, **Digital**, **Analog Signal or Ext. Trigger Edge** and **Window**. The default setting of **Analog Signal or Ext. Trigger Edge** should be used since the LVDAS controls the hardware with the Master Trigger.

Trigger Source – [Drop Down Menu]: Source of the Trigger signal that will initiate the data sampling process. The available options are **Channel 0**, **Chanel 1**, or **Ext. Trigger**. Since the LVDAS uses the Master Trigger to control the hardware, the **Ext. Trigger** setting is the default and should be used.

Trigger Slope - [Drop Down Menu]: Slope of the trigger signal used to initiate the digitization process. The available options are **Positive** and **Negative**. The Master Trigger is configured to require a **Negative** slope setting to obtain proper timing.

Trigger Coupling - [Drop Down Menu]: Coupling setting applied to the trigger signal. The possible options are **AC**, **DC**, **HF Reject**, **LF Reject**, and **AC Plus HF Reject**. The **AC** and **DC** coupling options are identical to those described in the Vertical Coupling setting. The **HF Reject** setting is similar to **DC** coupling except that higher frequencies (typically >20 kHz) are rejected. The **LF Reject** setting is similar to **AC** coupling except the low frequency cutoff is higher (~200 kHz). The **AC Plus HF Reject** setting combines the **AC** and **HF Reject** capabilities. **DC** coupling should be used with the Master Trigger.

Trigger Level - [Value Entry Field]: Level in volts that initiates digitizing of the input signal. The level should be set to 1.0 volts for the Master Trigger.

Trigger Delay - [Value Entry Field]: Delay in seconds (0.0 to 10.0) that digitization initiates following the receipt of the Master Trigger. The delay should be set to 0.0 seconds for LVDAS operation.

Trigger Timeout(s) - [Value Entry Field]: Amount of time to wait following receipt of the Master Trigger pulse before generating an error. This time is set to 0.00 for immediate return to the DA/C program. This transfers the verification responsibility that the signal burst was acquired normally to the DA/C program. This approach also allows the DA/C program to monitor the number of and rate that signal bursts were acquired.

Trigger Hold off - [Value Entry Field]: Amount of time in seconds after the arrival of the Master Trigger before the digitizers can be rearmed to accept the next trigger pulse. This is often referred to as digitizer “dead time” in laser velocimetry signal processing. The hold off time is set to 0.0 seconds.

Trigger Delay - [Value Entry Field]: Delay in seconds after the arrival of the Master Trigger when signal digitization commences. The delay time is set to 0.0 seconds.

Hysteresis - [Value Entry Field]: Specifies the size of the hysteresis window on either side of the trigger level in volts when the Analog Hysteresis Ref Trigger mode is selected. The digitizer triggers when the trigger pulse passes through the hysteresis value specified, has the slope specified in the trigger slope, and passes through the trigger level. This parameter is not used. The default setting is 0.05 volts.

High Level - [Value Entry Field]: Upper level voltage threshold when the Window Trigger mode is selected. This parameter is not used. The default setting is 0.10 volts.

Low Level - [Value Entry Field]: Lower level voltage threshold when the Window Trigger mode is selected. This parameter is not used. The default setting is 0.0 volts.

Reference Pos. (%) - [Value Entry Field]: Number of pre-trigger versus post-trigger points that are stored. The reference position is expressed as a percent of the record, from 0 to 100. Since it is desired to trigger only on signal bursts generated by particles passing through the measurement volume near the center, the trigger level is set to approximately 80-percent of the peak signal levels. This results in obtaining signal bursts with high signal-to-noise ratios and effectively shrinking the size of the measurement volume. However, this would also result in a non-symmetric signal burst in time if pre-triggering was not used. By setting this parameter to 40, the entire signal burst would be captured at the 80-percent trigger level.

Window Mode - [Drop Down Menu]: Defines whether the trigger is generated when the incoming signal satisfies the triggering criteria entering or leaving the window when the Window triggering mode has been selected. This parameter is not used.

Laser Velocimeter PXI-Based Data Acquisition Hardware Configuration Dialog
Auxiliary Channel (PXI-6120) Settings In Tab
Figure D.7.
(Figures C.13. (C.17. (C.18. (D.1.))) [Advanced HW Settings] → D.2. [Auxiliary Channel (PXI-6120) Settings In Tab] → D.7.)

This panel, shown in Figure D.7., provides controls required to configure the PXI-6120 analog input channels. The PXI-6120 facilitates the capture of analog signals from external sensors (pitot probes, kulites, thermocouples, etc.) that are to be conditionally sampled. The signals input to the analog channels are sampled once every time a signal burst is captured by the PXI-5152 digitizer as controlled by the Master Trigger.

6120 Analog Input Channels – [Drop Down Menu]: Identifies the device names of the input channels as specified in NI-MAX (LVMultiFunc).

Channel Labels – [Drop Down Menu]: Controls the unique names of the analog input channels of the PXI-6120. They are consecutive labels ai0-ai3 (default) and are normally not changed for LVDAS applications.

Input Voltage Range (V) – [Drop Down Menu]: Controls the input voltage range settings of the analog input channels. The available ranges are ±0.2-, ±0.5-, ±1.0-, ±2.0-, ±5.0-, ±10.0-, ±20.0-, and ±42.0-volts. The default setting is ±2.0 volts.

Record Length – [Value Entry Field]: Length of the digitized record of the analog channels. Only a single measurement is obtained during LVDAS conditional sampling applications, thus the default setting is 0.

Sample Rate – [Value Entry Field]: Specifies the rate that the analog channels are digitized. Since the PXI-6120 is externally triggered by the Master Trigger in LVDAS applications, sample rate is not applicable.

Input Coupling – [Text/Value Entry Field]: Coupling setting for the input analog signals. The available options are **DC**, **AC** and **GND**. **DC** coupling passes both AC and DC signals into the system while **AC** coupling only passes AC signals. **GND** grounds the digitizer inputs. The default setting of **DC** should be used for LVDAS applications.

Input Terminal Configuration – [Text/Value Entry Field]: Input signal termination setting for the PXI-6120 analog channels. The available settings are default (RSE (Reference Single Ended) for the PXI-6120), Differential, NSRE (Non-Referenced Single Ended) and RSE (Reference Single Ended). For LVDAS applications, the default (or RSE) setting should be used.

Trigger Source – [Drop Down Menu]: Source of the signal used to trigger sampling of the signals applied to the four available analog input channels. This signal is derived from the Master Trigger and routed to the PXI-6120 via the PXI backplane signal PF17.

Analog Sample Clock Source – [Drop Down Menu]: Source of the clock signal used to initiate the digitization of signals present at the inputs of the analog channels. Since the analog channels are conditionally sampled in the LVDAS application, the clock source is the Master Trigger which produces Poisson random pulses based on the occurrence of seeding particles passing through the measurement volume.

Laser Velocimeter PXI-Based Data Acquisition Hardware Configuration Dialog
LV System Trigger Settings In Tab
Figure D.8.
(Figures C.13. (C.17. (C.18. (D.1.))) [Advanced HW Settings] → D.2. [LV System Trigger Settings In Tab] → D.8.)

Trigger Definition Section

Trigger Source Terminal – [Drop Down Menu]: Sets the source (hardware terminal) of the start acquisition trigger. The source should be set to the default Reference Trigger which is derived from the Master Trigger in LVDAS applications.

System Trigger Terminal – [Drop Down Menu]: Establishes the terminal where the start acquisition trigger required by other devices in the PXI chassis can be obtained. The default setting of PXI_Trig0 should be used for LVDAS applications.

Trigger Name – [Text/Value Entry Field]: Defines the label associated with the System Trigger signal.

Trigger Polarity – [Drop Down Menu]: Sets the polarity of the System Trigger Signal. The default setting of non-inverted should be used for LVDAS applications.

Counter Generated Trigger Definition Section

This group of controls enables one of the counters available on the PXI-6120 Multifunction module to generate trigger signals. The counter system was used during system development to verify system operation when signal bursts were neither available from the laser velocimeter or synthetic signals produced by an Arbitrary Waveform Generator. This capability is not required for LVDAS applications.

Trigger Pulse Frequency (Hz) – [Value Entry Field]: Rate in Hertz that trigger pulses are generated by the counter. The default setting is 1 Hz.

Initial Delay – [Value Entry Field]: Delay time in seconds after the counter has been armed before the first trigger signal is generated.

Trigger Pulse Duty Cycle – [Value Entry Field]: Sets the duty cycle of the trigger pulse train.

Trigger Idle State – [Drop Down Menu]: Sets the quiescent state of the trigger signal. The default setting is TTL Low, which should be used in most applications.

Counter Enable – [Button]: Sets the counter circuitry of the PXI-6120 to be used for generating the trigger signals.

Trigger Signal Routing Section

Trigger Destination #1 & Trigger Destination #2 – [Drop Down Menu]: The flexibility inherent to the PXI system provides the ability to route system signals using software commands to different hardware connectors on the various system devices. These controls define the destinations of the Reference trigger (derived from the Master trigger) generated by the PXI-5152 digitizer. PXI Trigger Line 0/RTSI 0 reflects the routing of the Reference trigger signal to the PXI back plane making it available to other devices residing in the PXI chassis. PFI 1 reflects the routing of the Reference trigger to the PFI 1 connector on the PXI-5152 front panel.

Scan Rig – Grid Generation

During a typical flow field investigation, the user will normally acquire data ensembles throughout a grid of locations in order to develop a better understanding of the flow field. In order to minimize data collection and facility run times, it is often desirable to define the grid of interest prior to initiating data collection so that the laser velocimeter measurement volume can be quickly relocated using a scanning system. To facilitate this capability, mechanisms are included in the DA/C program so that the user can generate, then utilize a data collection grid. Generated grid locations can be preserved in a user-defined disk file so that the grid can be recalled at a later time. The format of this file is detailed in a later section.

Grid generation of the measurement volume spatial locations for the Klinger MC4 based scan rig is initiated by selecting the **Create Scan Grid File** button on the ***Controls*** tab of the Scan Rig Management Interface Panel (Figure C.24.), Figure D.9. (Figures C.13. (C.16.) [CONTROL SCAN RIG] → C.24. (D.9.)). When this button is selected, the Scanner Position Generator panel, Figure D.10. (Figure C.26.), will be displayed. This panel presents the controls and settings to generate the scan position grid. These controls are divided between a tab control and a group of controls that operate independently from the controls on the tab.

Controls provided on the ***Settings*** tab allow the user to generate a range of scan grid locations for the four axes supported by the MC4 system.

Scanner Position Generator Panel
Settings Tab
W-Axis, X-Axis, Y-Axis, & Z-Axis Settings
Figure D.10. (C.26.)
(Figures C.13. (C.16.) [Control Scan Rig] → C.24. (D.9.) [Create Scan Grid File] → D.10. [Settings Tab])

Since the positioning of the measurement volume requires independent movements of one or more axes, it is essential that these locations be defined independently. Thus the Axis specific location generation controls are broken out into individual sub-panels. Each of these sub-panels have controls that provide the user with the tools needed to define the movements on a given axis:

Units – [Button]: Defines the units that will be used when converting the step size and scan start position data into scan rig counts. The available options are **Inches** and **Counts**. If **Inches** is selected, the application will convert the position data to inches. When **Counts** is specified, no conversion is performed and the positions are handled directly.

Step Size – [Value Entry Field]: Size of each successive step (distance between desired measurement volume locations) to be generated in Counts or Inches.

Scan Start Position – [Value Entry Field]: Position of the first measurement volume location in Counts or Inches.

Scan Indices – [Value Entry Field]: Defines the number of scan indices that will be generated automatically when the operator selects the **Generate Scan Data** button at the bottom of the panel.

Travel Per Step – [Value Entry Field]: Travel distance in inches of a single count (1 step of the stepping motor driving the axis). The MC4 scan rig moves 39.37 micro-inches (3.93700E-5 inches) per count (step). This default value should remain unless a different scan rig is used.

Scan File Title – [Text/Value Entry Field]: Title of the measurement volume location grid.

Scan File Comment – [Text/Value Entry Field]: Description of the generated measurement volume location grid.

Scan Rig ID – [Text/Value Entry Field]: Name of the scan rig for which the generated measurement volume location grid was created.

Scanner Position Generator Panel
Active Grid Tab
W-Axis, X-Axis, Y-Axis, & Z-Axis Settings
Figure D.11.
(Figures C.13. (C.16.) → C.24. (D.9.) → D.10. → D.11.)

This tab displays the measurement volume location grid, Figure D.11., generated using the parameter settings contained on the ***Settings*** tab (Figure D.10.) the last time the **Generate Scan Data** button was selected. The display provides the user with the opportunity to verify the grid locations before committing them to the Final Grid.

Clear Data – [Button]: Removes all entries from the measurement volume location grid.

Indices – [Indicator]: Number of grid positions in the active grid.

Scanner Position Generator Panel
Complete Grid Tab
W-Axis, X-Axis, Y-Axis, & Z-Axis Settings
Figure D.12.
(Figures C.13. (C.16.) [Control Scan Rig] → C.24. (D.9.) [Create Scan Grid File] → D.10. [Complete Grid Tab] → D.12.)

This tab displays the entire grid of measurement volume locations, Figure D.12., including those added when the **Append To Final Grid** button has been selected. The presented measurement volume location grid is the data that will be committed to disk file after the user selects the **Save Scan Data To File** button.

Clear Data – [Button]: Removes all entries from the measurement volume location grid.

Indices – [Indicator]: Number of grid positions in the complete grid.

Scanner Position Generator Panel
Information Tab
W-Axis, X-Axis, Y-Axis, & Z-Axis Settings
Figure D.13.
(Figures C.13. (C.16.) [Control Scan Rig] → C.24. (D.9.) [Create Scan Grid File] → D.10. [Information Tab] → D.13.)

This tab displays detailed information about the generated measurement volume location grid, Figure D.13.

W-Axis, X-Axis, Y-Axis, & Z-Axis Indices – [Indicator]: Indicators presenting the most recently generated position indices for each of the W, X, Y, and Z axes after the last selection of the **Generate Scan Data** button.

Counts Per Inch – [Indicator]: Number of scan rig counts per inch of travel (inverse of the **Travel per Step** entry in the ***Settings*** tab).

Import Date – [Indicator]: Date when an imported measurement volume location grid file was created.

Import Time – [Indicator]: Time of day when an imported measurement volume location grid file was created.

New Scan Position File Path – [Indicator]: Displays the path to the measurement volume location grid file that was saved after the **Save Scan Data To Disk** button was selected.

Imported Scan File Path – [Indicator]: Displays the path to the measurement volume location grid file that was last imported into the Scan Position Generator.

Date – [Indicator]: Date when the generated measurement volume location grid was saved to disk.

Time – [Indicator]: Time-of-day when the generated measurement volume location grid was saved to disk.

Error In & Error Out – [Indicator]: Indicators will display information regarding errors that occur while using the Scanner Position Generator.

Scanner Position Generator Panel
Primary Controls
Figure D.14.
(Figures C.13. (C.16.) [Control Scan Rig] → C.24. (D.9.) [Create Scan Grid File] → D.10. (D.14.))

The controls that execute sub-tasks needed to create, edit, and store the measurement volume location grid are presented in a row of buttons at the bottom of the panel, Figure D.14., which apply the settings and selections made within the tabbed sub-panels.

Generate Scan Data – [Button]: Generates the measurement volume location grid based on the values entered in the ***Settings*** tab. Once this button has been selected, the **Append To Final Grid** button changes color to yellow and begins to blink a a reminder that new position data is available and ready to be transferred/appended to the complete grid.

Import Existing Scan Data – [Button]: Presents a file manager panel that allows the user to select a file containing a measurement volume location grid generated previously using the Scan Position Generator. The contents of the file are imported to the Active Grid table so that they may be appended to the Complete Scan Grid (Counts) table. Refer to the Scan

Grid Position File ***Information*** tab for details regarding the contents and format of this custom file.

Import Scan Data From File – [Button]: Presents a file manager panel that allows the user to select a file containing measurement volume locations generated by an external program. The file should be in tab-delimited ASCII format of four columns, one for each of the four supported scan axes. No labels should appear at the top of each column. The contents of the file are imported to the Active Grid table so that they may be appended to the Complete Scan Grid (Counts) table.

Append To Final Grid – [Indicator Button]: Once the **Generate Scan Data** button has been selected, the **Append To Final Grid** button will begin blinking and change color to yellow. When selected the contents of the Active Grid table will be copied to the Complete Scan Grid (Counts) table.

Save Scan Data To File – [Indicator Button]: Stores the contents of the Complete Scan Grid (Counts) table to a custom disk file. The button will present a file manager panel to allow the user to select the directory where the file is to be archived. Refer to the Scan Grid Position File ***Information*** tab for details regarding the contents and format of this custom file.

Quit – [Button]: Terminates the Scanner Position Generation panel and returns control to the DA/C program where the user is prompted by the panel shown in Figure D.15. If the last measurement volume location grid created prior to executing this Button is desired to be used by the DA/C program, the user should select **Yes** in the panel.

Once the user has selected a measurement volume location grid, either when exiting the Scanner Position Generation panel or by selection using the **Load Scan Position File** button, Figure D.9. (Figures C.13. (C.16.) [CONTROL SCAN RIG] → C.24. (D.9.)), the user will be prompted via a panel, Figure D.16., to select the axis that, when scanned will cause the running data plot on the Processing computer to be reset, Appendix E.8.

Scan Grid Position File Information

Measurement volume location information resulting from the operations performed within the Scanner Position Generation panel can be preserved to disk file when the user selects the **Save Scan Data To File** button (Figures D.10. (D.14.)). The file created is a tab-delimited file containing descriptive information at the top followed by scan rig location data in counts for each of the four axes supported by the MC4 scan rig controller. A portion of an example file is shown in Figure D.17. The contents of the file may be manually edited using a text editor or preferably a spreadsheet application such as Microsoft Excel or Libre Office Scalc. Make sure that the resultant file is saved as tab-delimited text and not in Excel or Scalc format.

32-Bit Word Number(s)	Data Value
0	LV Data Record Number
1	Sample Rate
2	Record Length
3	Interarrival Time
4	Rotor Azimuth Position
5	Auxiliary Channel Ain0 Value
6	Auxiliary Channel Ain1 Value
7	Auxiliary Channel Ain2 Value
8	Auxiliary Channel Ain3 Value
9 to (9+RL)	U-Component Digitized LV Burst Signal Data Voltage Samples
(10+RL) to (10+2RL)	V-Component Digitized LV Burst Signal Data Voltage Samples

Table D.1.- Definition of the data record header (first nine 32-bit values) contained in Binary formatted LV data files.

Figure D.1.- Advanced HW Settings button – located on Configuration tab.

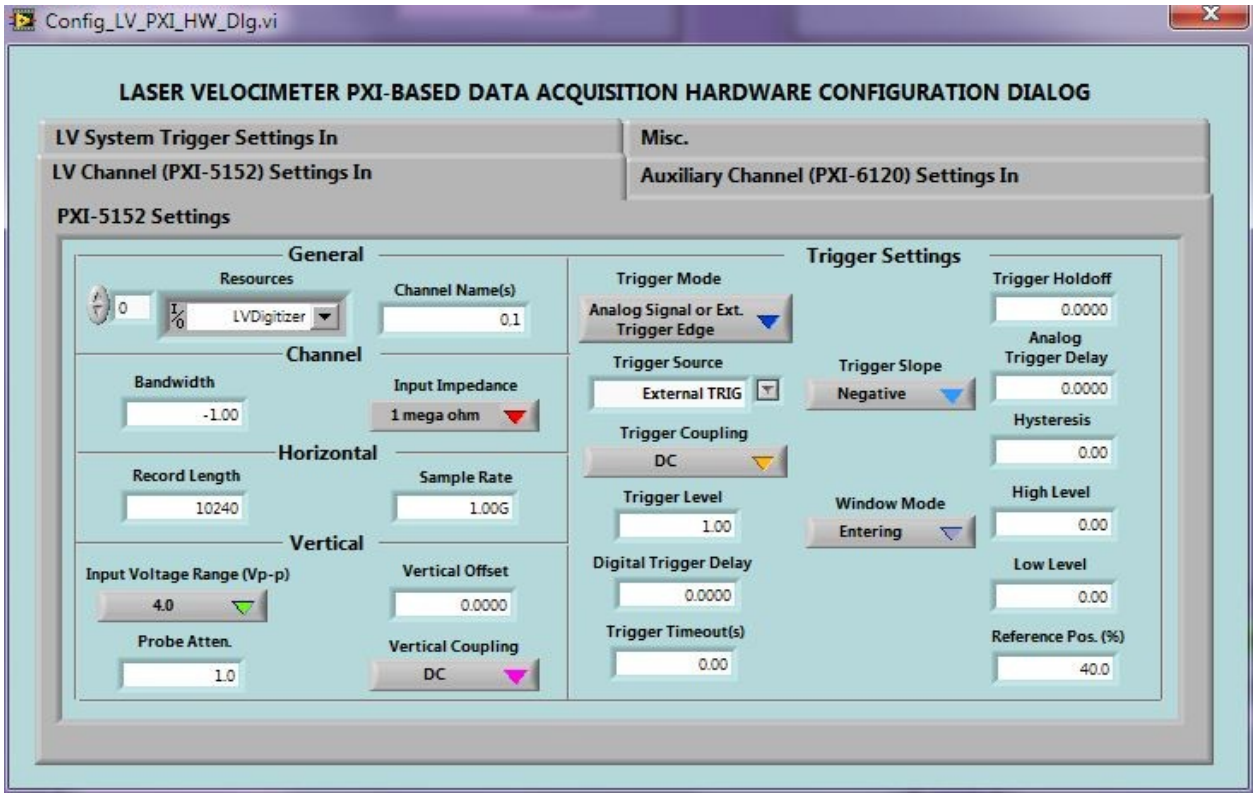

Figure D.2.- Advanced HW Settings – LV Signal Digitizer (PXI-5122) advanced options tab.

Figure D.3.- Test mode / simulation (synthetic) signal operational selection.

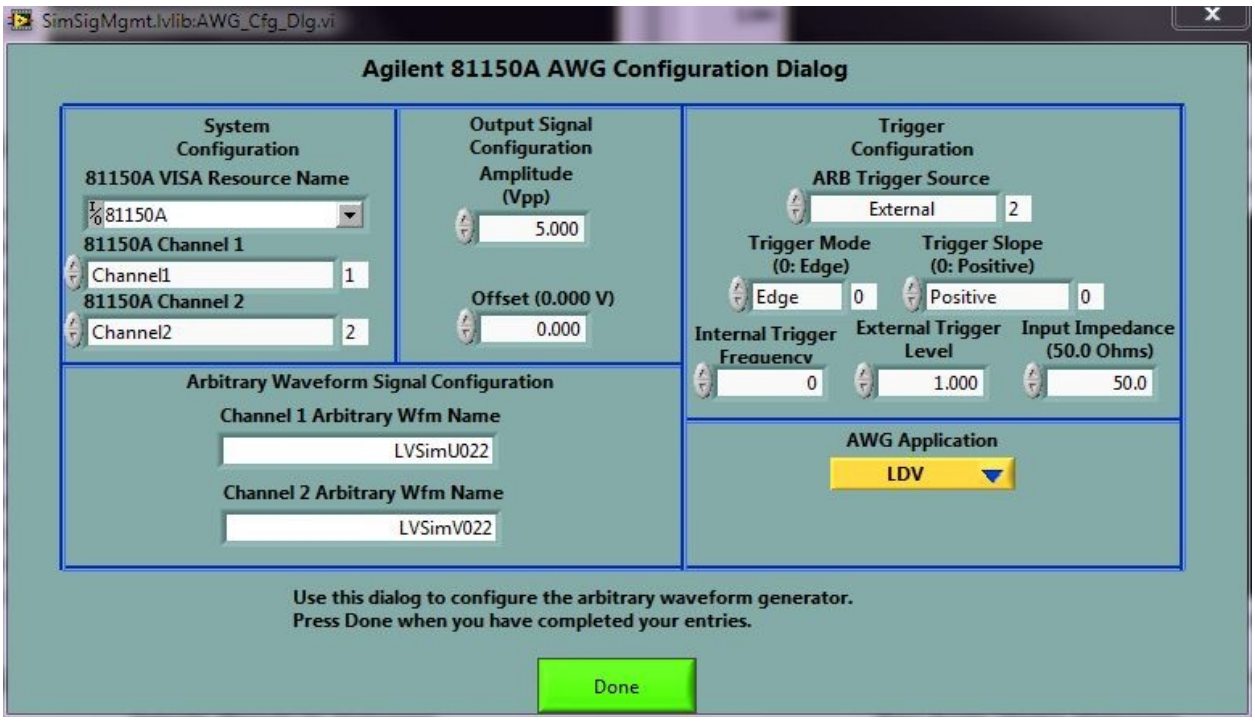

Figure D.4.- LV synthetic signal management – Agilent 81150A AWG Configuration Dialog.

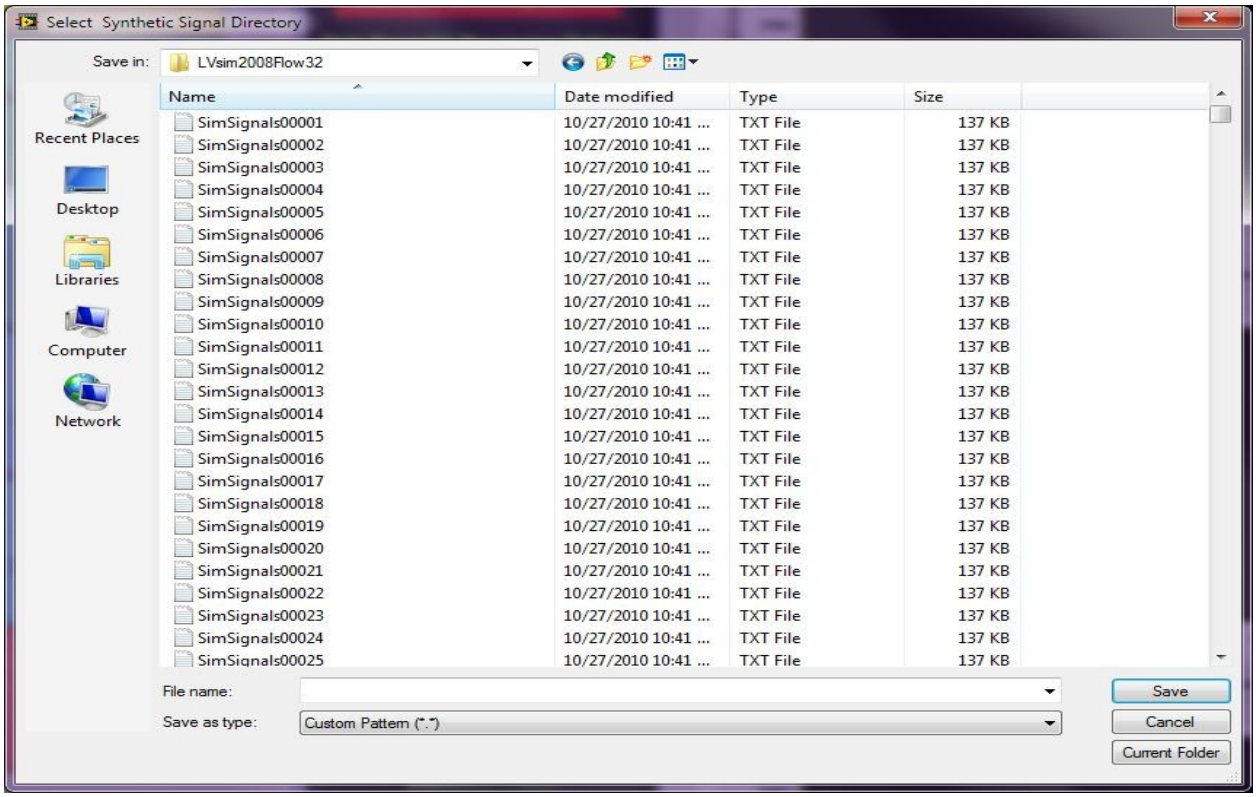

Figure D.5.- Simulated LV signal selection dialog.

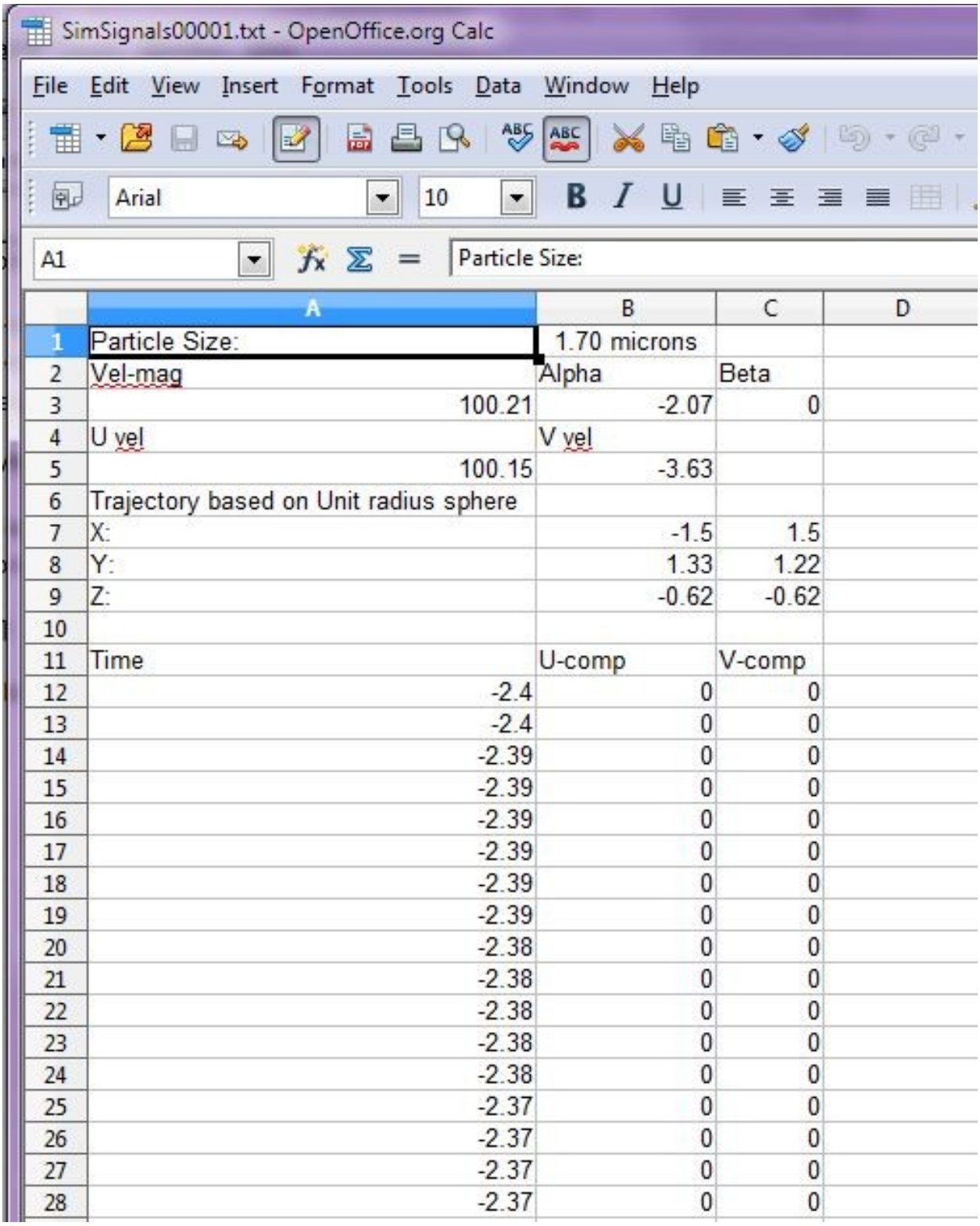

	A	B	C	D
1	Particle Size:	1.70 microns		
2	Vel-mag	Alpha	Beta	
3	100.21	-2.07	0	
4	U vel	V vel		
5	100.15	-3.63		
6	Trajectory based on Unit radius sphere			
7	X:	-1.5	1.5	
8	Y:	1.33	1.22	
9	Z:	-0.62	-0.62	
10				
11	Time	U-comp	V-comp	
12	-2.4	0	0	
13	-2.4	0	0	
14	-2.39	0	0	
15	-2.39	0	0	
16	-2.39	0	0	
17	-2.39	0	0	
18	-2.39	0	0	
19	-2.39	0	0	
20	-2.38	0	0	
21	-2.38	0	0	
22	-2.38	0	0	
23	-2.38	0	0	
24	-2.38	0	0	
25	-2.37	0	0	
26	-2.37	0	0	
27	-2.37	0	0	
28	-2.37	0	0	

Figure D.6.- Simulated LV signal file format.

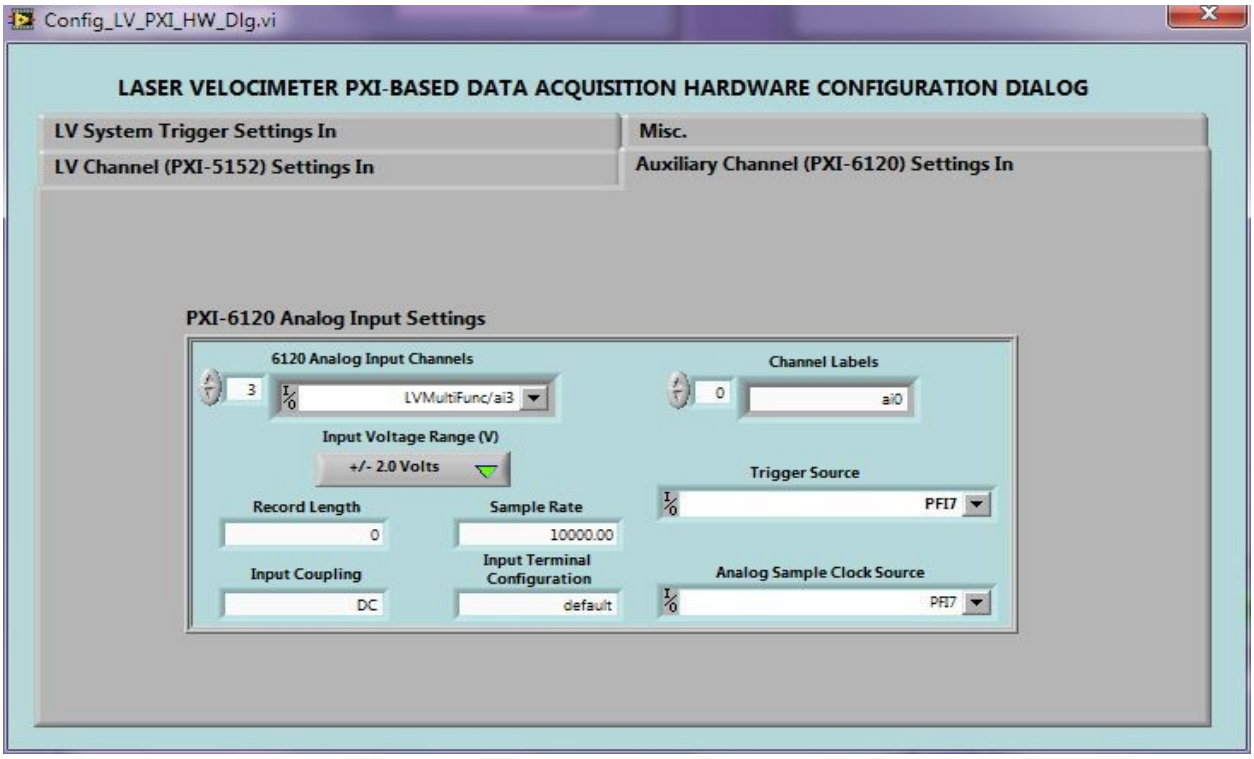

Figure D.7.- Advanced Hardware Configuration – Auxiliary Channel Settings.

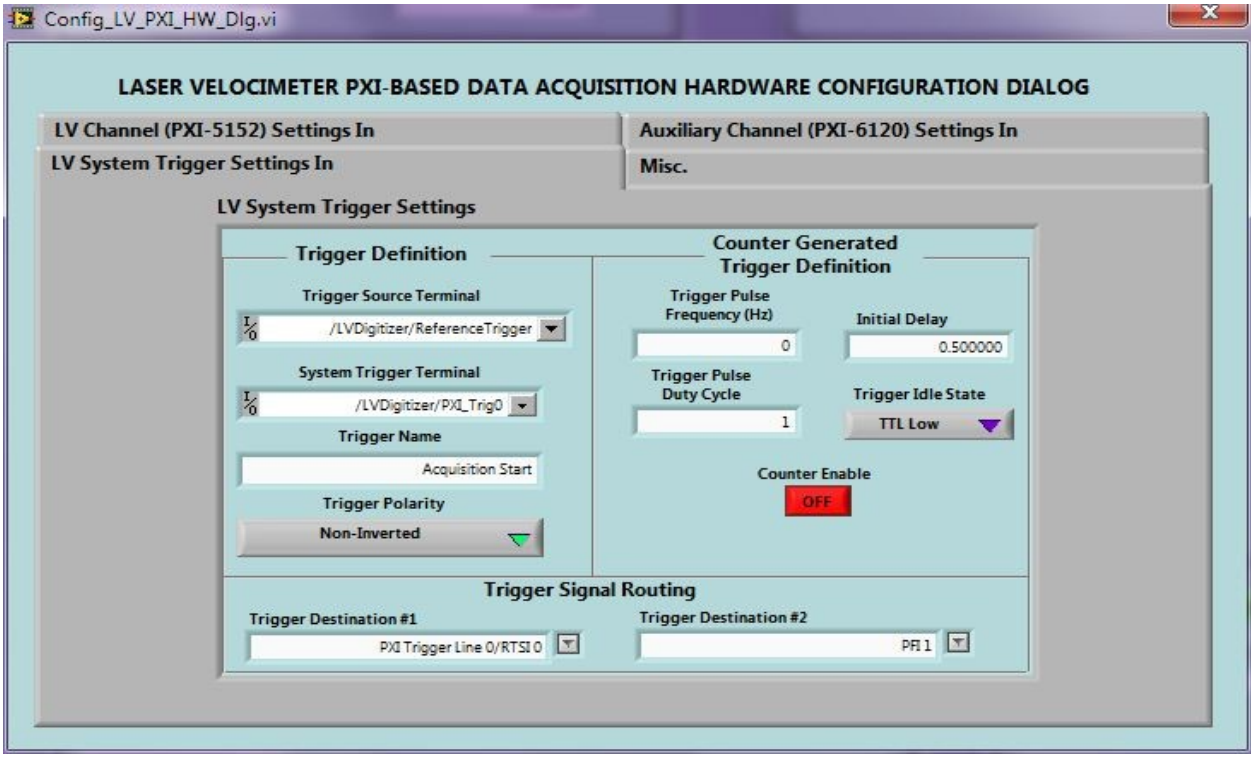

Figure D.8.- Advanced hardware Configuration – LV System Trigger Settings.

Figure D.9.- Create Scan Grid File option.

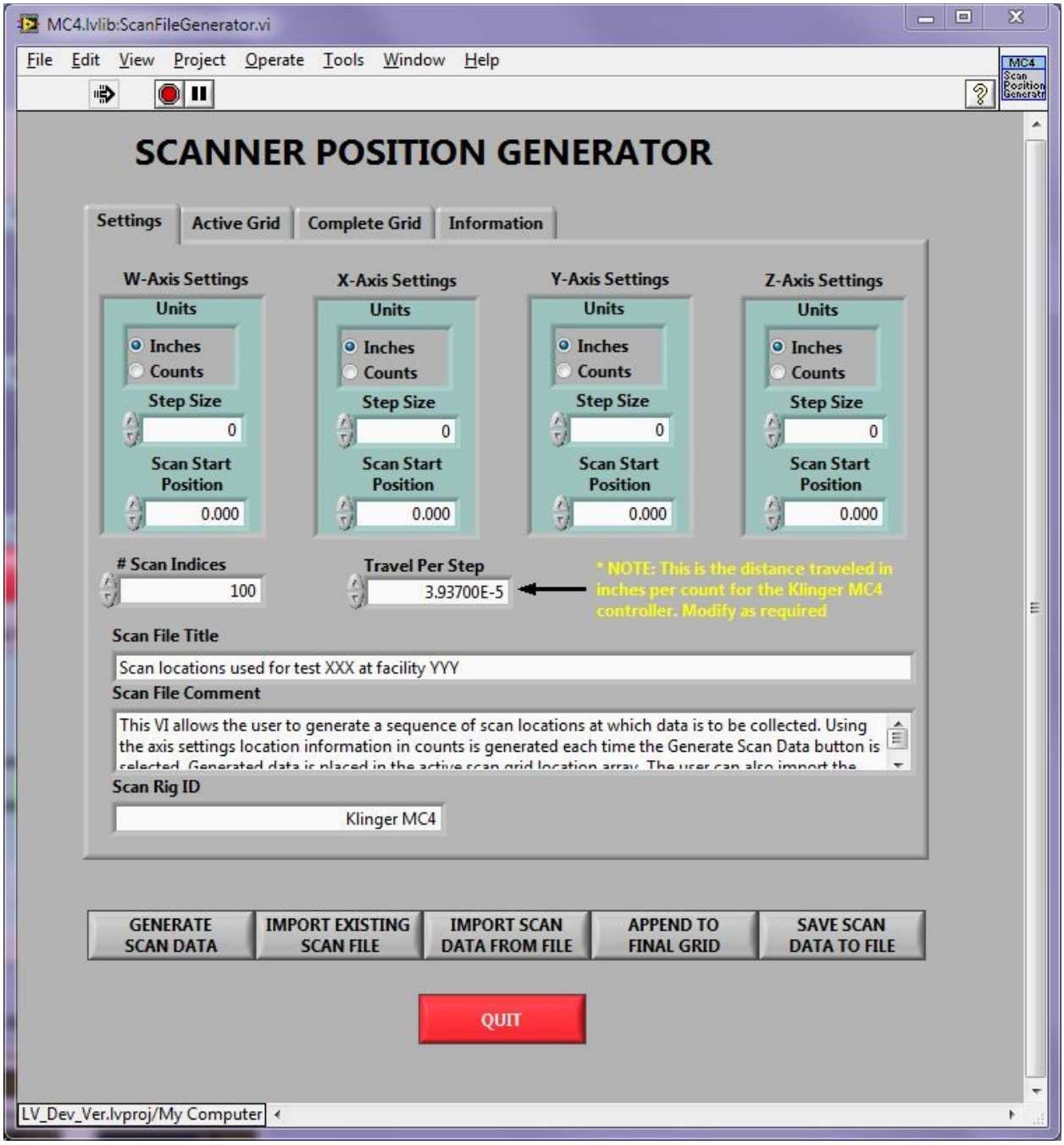

Figure D.10.- Scanner Position Generator dialog.

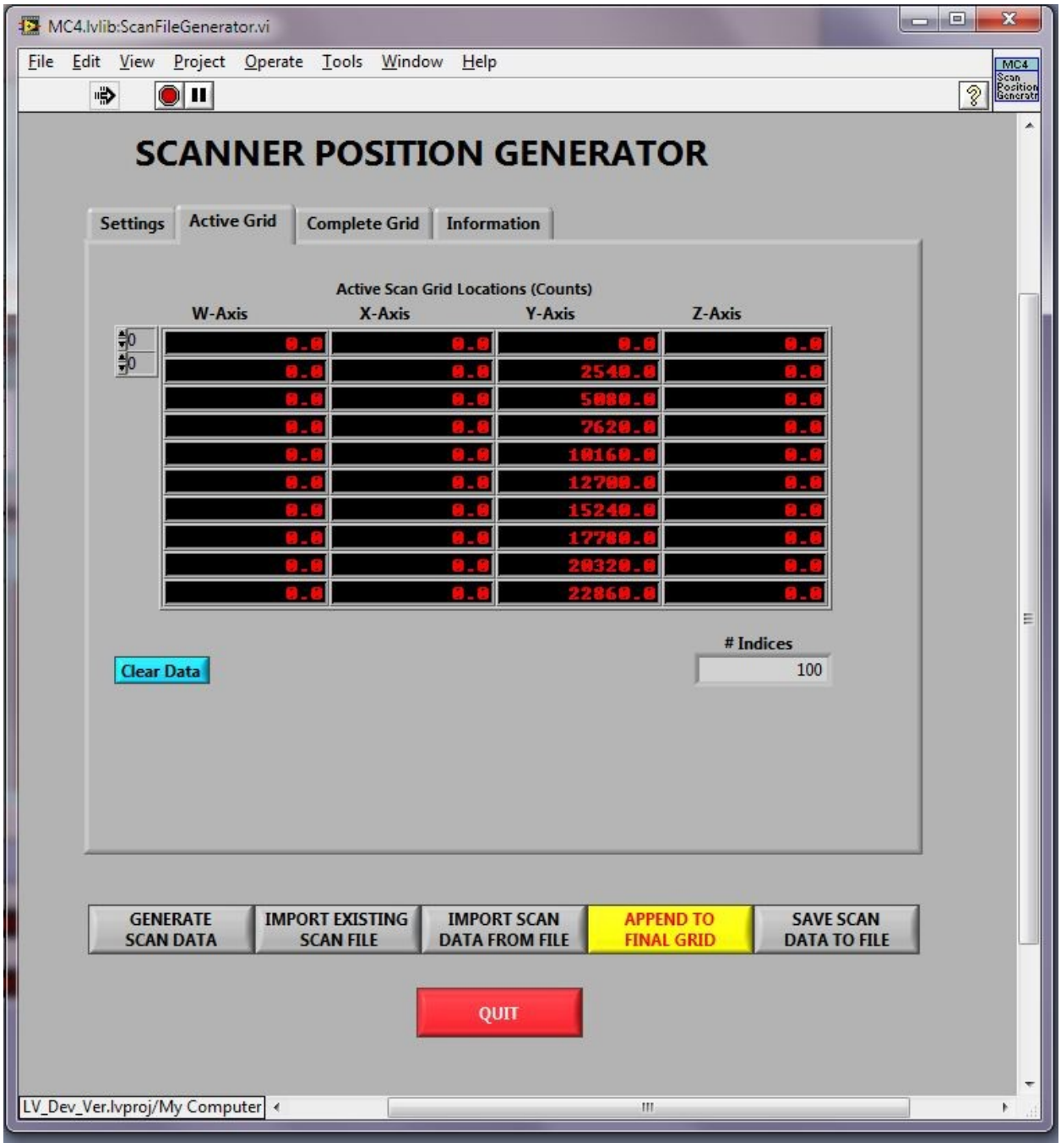

Figure D.11.- Active Grid – Scan Rig Position data tab.

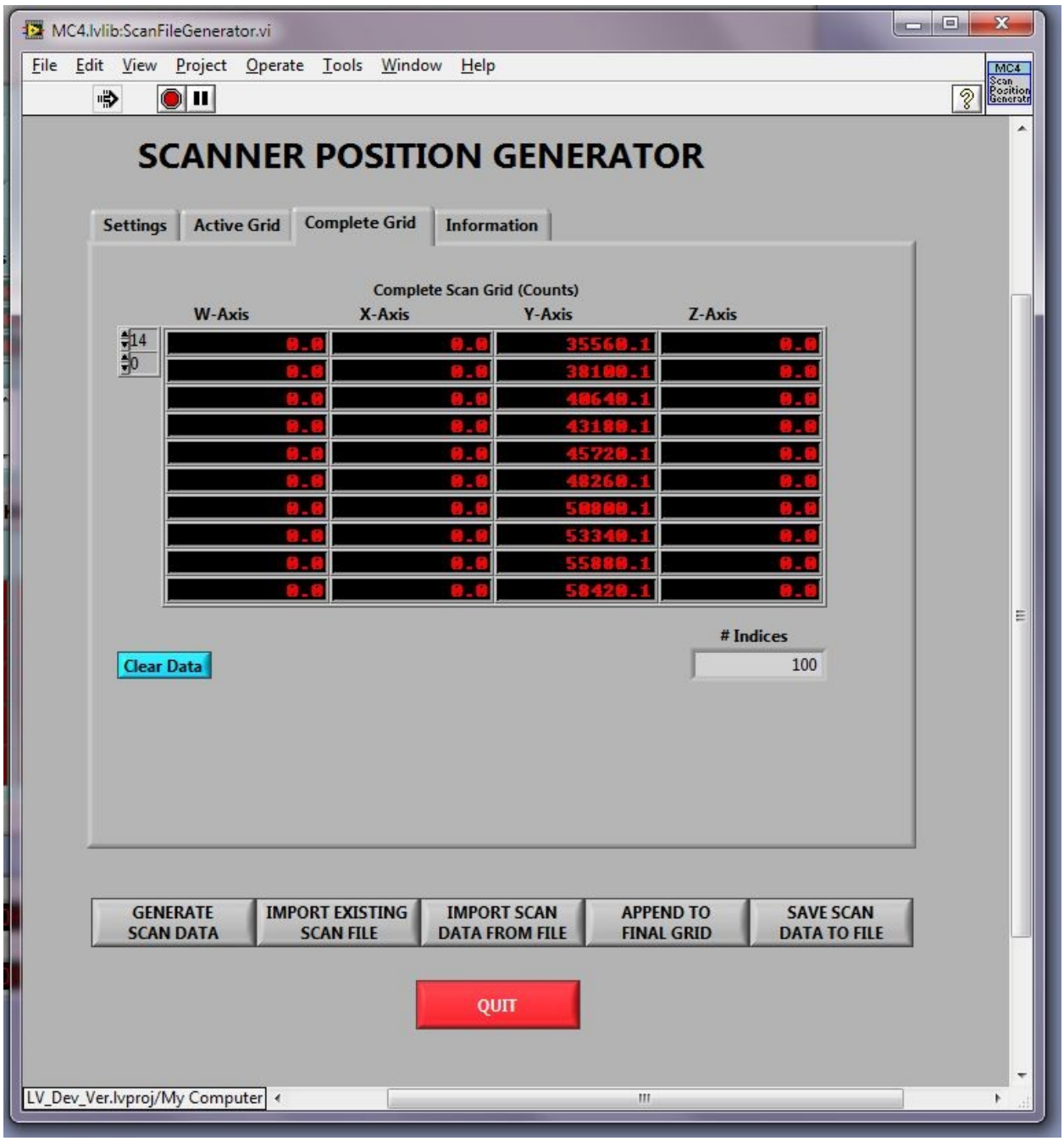

Figure D.12.- Complete Scan Rig Position data tab.

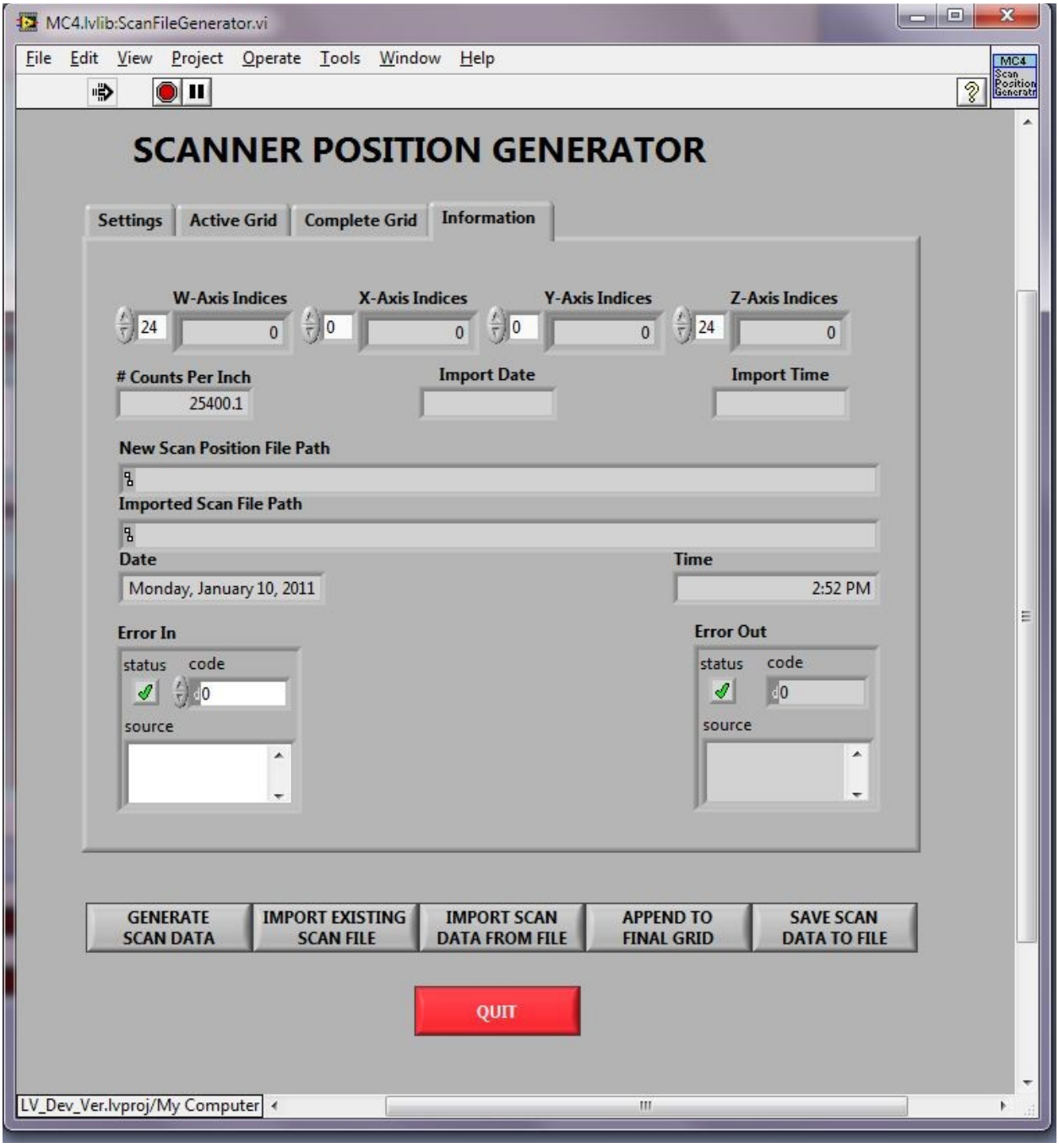

Figure D.13.- Scan Position Generator Information tab.

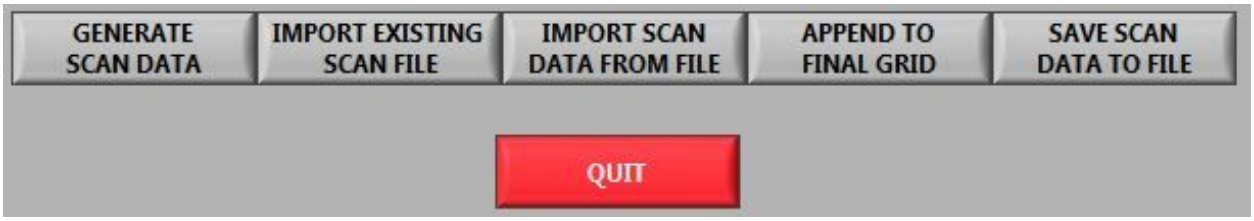

Figure D.14.- Primary Scan Position Generator Controls.

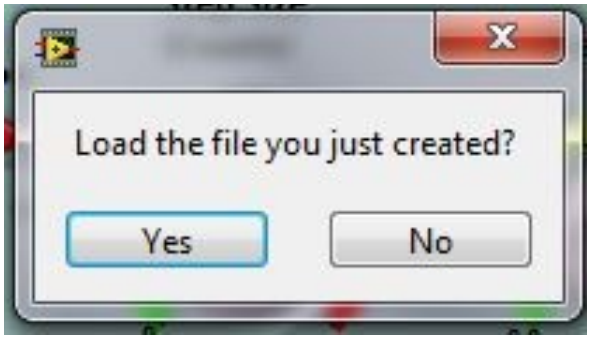

Figure D.15.- Scan grid file use prompt.

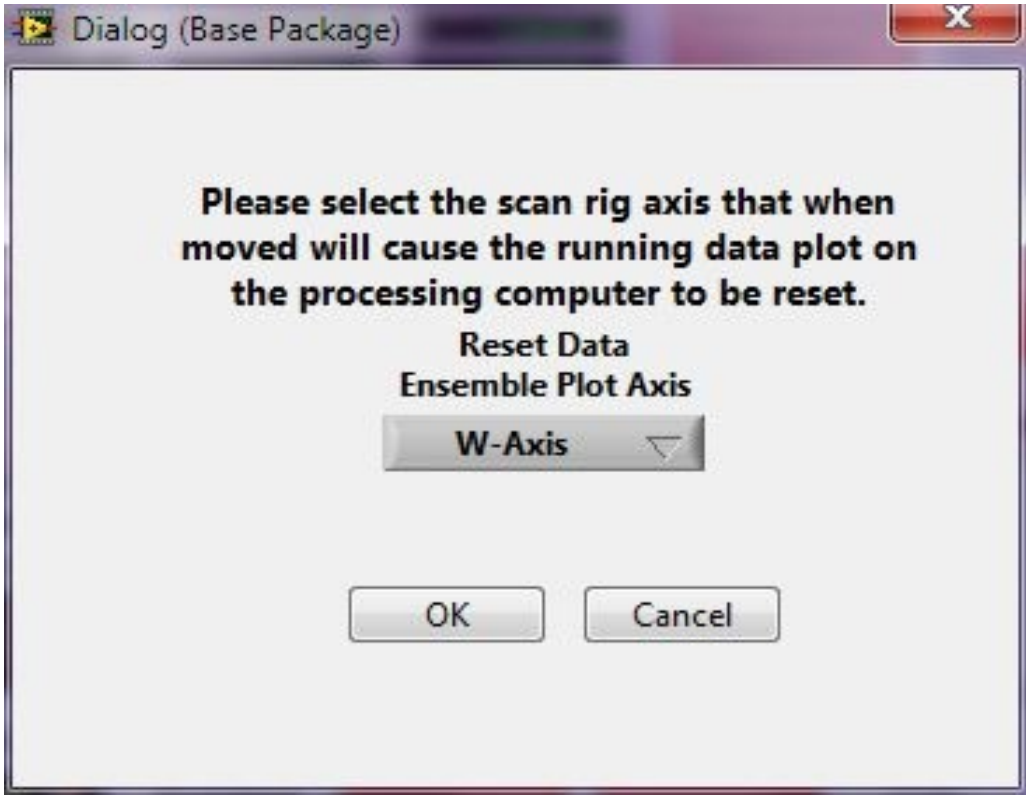

Figure 16.- Scan axis plot reset selection dialog.

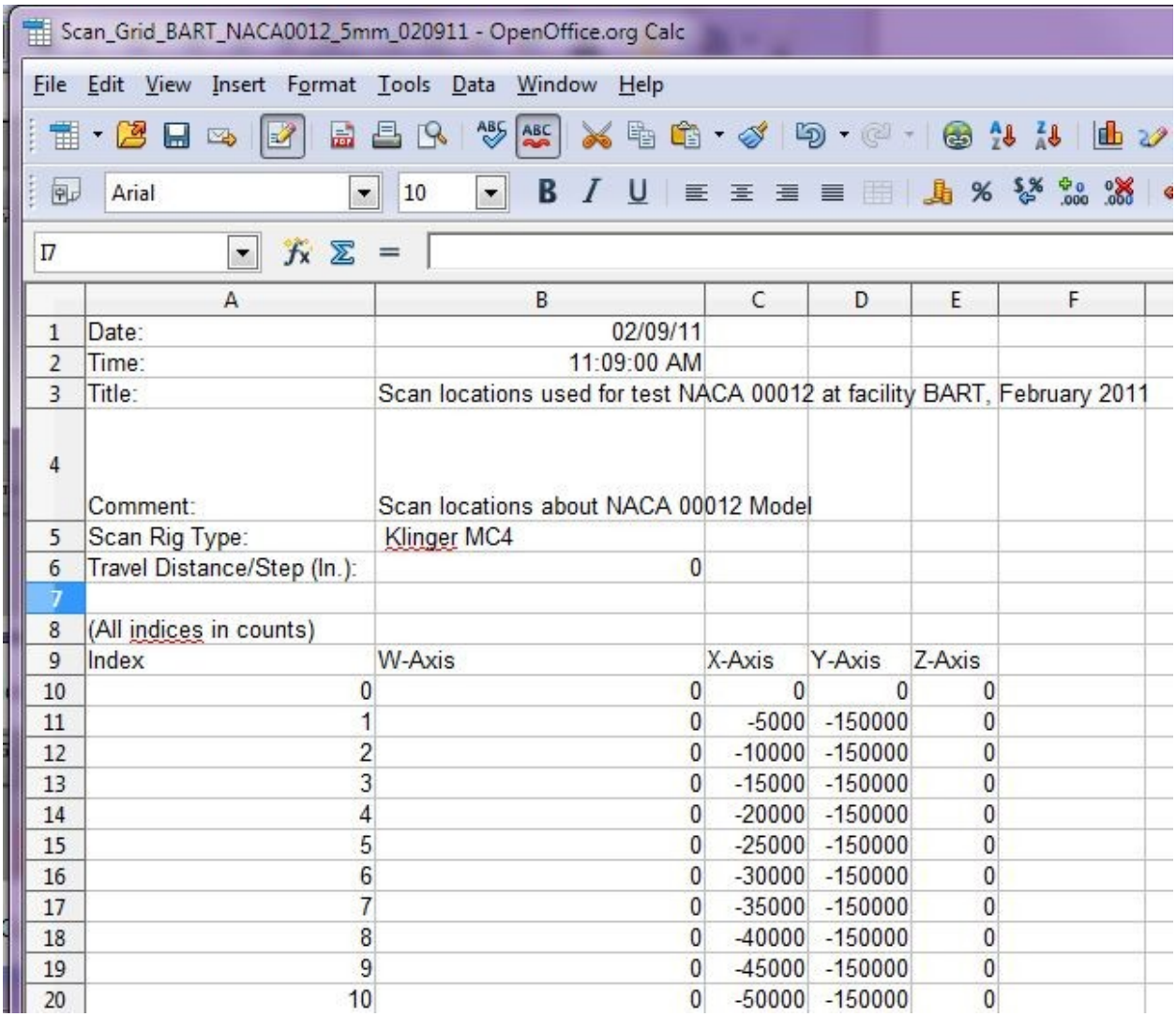

	A	B	C	D	E	F
1	Date:	02/09/11				
2	Time:	11:09:00 AM				
3	Title:	Scan locations used for test NACA 00012 at facility BART, February 2011				
4	Comment:	Scan locations about NACA 00012 Model				
5	Scan Rig Type:	Klinger MC4				
6	Travel Distance/Step (In.):	0				
7						
8	(All indices in counts)					
9	Index	W-Axis	X-Axis	Y-Axis	Z-Axis	
10	0	0	0	0	0	
11	1	0	-5000	-150000	0	
12	2	0	-10000	-150000	0	
13	3	0	-15000	-150000	0	
14	4	0	-20000	-150000	0	
15	5	0	-25000	-150000	0	
16	6	0	-30000	-150000	0	
17	7	0	-35000	-150000	0	
18	8	0	-40000	-150000	0	
19	9	0	-45000	-150000	0	
20	10	0	-50000	-150000	0	

Figure D.17.- Scan Grid Position File – generated using Scanner Position Generator.

Appendix E
Signal Processing / Data Processing Software

Contrary to conventional approaches to laser velocimetry signal processing, the combination of COTS (Commercial Off The Shelf) high-speed digitizers and software signal processing techniques operating on standard PC-type computers was selected. While the concept was first used back in 1975 (Griskey (1975)) it was more a laboratory curiosity than a realistic approach to signal processing. Although it was limited to low velocity liquid flows, it did show far better measurement accuracies than obtainable with the then state-of-the-art high-speed burst counters. The primary concern in its choice for the upgraded laser velocimeter was whether each signal could be processed in a timely manner to provide at least near real time results. However, the potential advantages of capturing and storing the raw signal bursts, and increased measurement accuracy were too intriguing to ignore the challenge.

When contemplating the design of such a system, one realizes that this is not a laboratory exercise but the development of a production based measurement system that will be used by researchers that are not experts in laser velocimetry, electronics or signal/data processing software. In order to reduce the risks, a Monte Carlo based laser velocimetry simulation program (Appendix A) was upgraded for the production of simulated LV signal bursts to be used in data acquisition and data processing simulations. These signal bursts would be used to develop and test signal processing algorithms for instrument precision and measurement accuracy along with processing speed. The results from these studies are outlined in Chapter IV. They show that the instrument precision was far better than specifications required while signal/data processing was conducted at speeds acceptable for real-time processing. The entire upgraded laser velocimeter, including the signal/data processing software were tested under realistic conditions in the laboratory and in the BART, Chapters V and VI, respectively. All expectations were met except that the data transfer time from the data acquisition computer memory to disk storage on the acquisition and processing computers was excessive, and spontaneous impulses generated by the photomultiplier caused false signal captures. These problems have since been corrected and the system is considered operational. Further laboratory and wind tunnel tests were conducted in the laboratory and the BART to assess its performance. The results of these investigations are outlined in Chapter VII.

Computed Statistics and Data Storage

The Laser Velocimeter Signal / Data Processing Program will determine the signal frequencies contained within each captured LV signal burst that comprise an ensemble of measurements obtained by the Laser Velocimeter Data Acquisition system. Each captured signal burst is processed with Fast Fourier Transform (FFT) technology using up to 8192 of the 10,000 digital samples of each burst acquired by the two-channel, 1.0 GHz per channel digitizer. The U- and V-component signals are monitored on a high-speed, digital oscilloscope. One user selected channel is used to trigger both the oscilloscope and the

high-speed digitizer. Normally the trigger level is set to approximately 80-percent of the peak value to limit the size of the measurement volume when using monodisperse particles for seeding. The signal bursts from both components are captured simultaneously in their entirety by utilizing the pre-trigger capabilities of the high-speed digitizer. Once the frequency contained in each signal burst has been determined, the program will use the input system characteristics to calculate the respective particle velocities. The U-and V-component velocity ensembles are then processed using three methods:

1) Standard statistics;
2) Sample-and-Hold techniques in an attempt to reduce/eliminate particle sampling bias (Edwards (1987)); and,
3) Technique used to lessen the effect of particle sampling bias on the statistical results (Edwards and Meyers (1984), Meyers *et al* (1990), Meyers (1991)).

The following statistics are calculated for the three data processing methods:

1) Mean and its statistical uncertainty;
2) Standard deviation and its statistical uncertainty;
3) Skew; and,
4) Excess

These statistics are computed for:

1) U-component velocity;
2) V-component velocity; and since the U- and V-component measurements are coincident,
3) Velocity magnitude; and,
4) Flow angle.

Also the following parameters are determined:

1) Velocity:Data Rate Correlation Coefficient;
2) Average convergence standard deviation among the U- and V-component means and standard deviations based on the last five points of the rolling statistics calculated for the data ensembles as they grow by 100 signal burst increments;
3) Estimated integral time scale;
4) Number of acceptable signal bursts processed;
5) Total measurement time;
6) Estimated number of integral time scales obtained;
7) Reynolds stress;
8) Tables of:
    1. Arrival times for each signal burst,
    2. If a rotor encoder is used, azimuth angle,
    3. U-component velocity,
    4. V-component velocity,

5. Velocity magnitude,
6. Flow angle,
7. Minimum and maximum signal voltages, and,
8. Particle transit time through the measurement volume.

These statistical results and tables are stored in the LOG file accompanying the ensemble of digitized signal bursts in the sub-directory named by the date and time of the ensemble acquisition, e.g., D011911T125816 → January 19, 2011 at 12:58:16 (24-hour clock). This file along with other output files are placed in the **processed** sub-directory created and attached to the ensemble directory by the program, e.g., processed19-JAN-11. If the signals are processed again at a later date, a new processed sub-directory will be created with the date of that processing – the original processing sub-directory is left intact. An example of a LOG file is shown in Table E-1.

The program also plots the U- and V-component mean and standard deviation results as a function of ensemble size. These plots serve as a guide to indicate whether statistical stationarity has been reached by the acquired data ensemble. Along with this visual indicator, the standard deviation of the last five points on each plot is determined, and the average of the four results is returned to the Data Acquisition Program. This data will be compared with the user selected limit that provides the test for statistical stationarity. If the returned value is greater than the selected limit, the Data Acquisition Program will flag the user indicating that statistical stationarity has not been reached, and that another ensemble should be acquired at that measurement location. If a second (or third, etc) ensemble is acquired, the processing program will compute the results and statistics as if all of the ensembles acquired at that location comprised a single ensemble.

The four plots showing the convergence of the U- and V-component mean velocity and their standard deviations will remain displayed on the screen until the user moves the cursor to the upper left plot (U-component mean) and left-clicks the mouse. At this point the program will display the histograms of the U- and V-component velocities, velocity magnitude and flow angle. Again these plots will remain displayed until the user moves the cursor to the upper left plot (U-component) and left-clicks the mouse. The program will then return to the sleep mode awaiting the arrival of the next data ensemble. If the **Auto View Timing?** box was selected on the setup screen and a display time entered in the **Display Time, sec** box, user interaction is not required or accepted. The convergence plots will display for the selected time, the screen will clear and the histogram plots will display for the same amount of time, then the screen will clear and the program returns to the sleep mode. The user may choose to automatically save these plots in the processed sub-directory for that ensemble by activating the **Save Plots?** box in the setup screen. The eight plots are saved as Enhanced Windows Metafiles (EMF).

Finally, an overall log file (*.ALL) is saved in the processed sub-directory for the first ensemble processed after program start-up. The log file contains a table of all of the above mentioned statistical results in a tab-delimited ASCII format. This table will be added to for each new data ensemble processed until the program is terminated. If multiple

ensembles are acquired to obtain statistical stationarity, the results for each stage is recorded, e.g., ensemble 1, ensemble 1 & 2, ensemble 1 & 2 & 3, etc. The processing program also automatically runs the program RUNNINGDISPLAY that presents a running plot of the means and standard deviations for the U- and V-component velocities, velocity magnitudes and flow angles throughout a scan profile. This provides real-time feedback to the user of the velocity profiles as the flow is being interrogated. When a new profile is begun, as controlled by the Data Acquisition Program, the current running plots are erased and plots for the new scan begun. These plots are not saved as they can be regenerated with user settings from the ALL log file using any X-Y plot program.

The results from all three methods are stored in the LOG file, but only the Normal Statistical results are plotted and stored in the cumulative ALL file. The program requires approximately 50 seconds to process 10,000 signal burst pairs (U- and V-components). The statistics calculated include the mean, statistical uncertainty in the mean, standard deviation, statistical uncertainty in the standard deviation, skew, and excess along with the number of measurements included in the calculations. These statistics are determined for each of the three processing methods for the U- and V-component velocities, velocity magnitude and flow angle.

User Input Screen

The data acquisition and signal/data processing functions are performed by two networked server-class PC computers. The data acquisition computer runs the LabView-based data acquisition and hardware control program and serves as the user interface for all functions including the signal/data processing program. The signal/data processing program is started on the second computer during the final checks of the system when the small particle generator is used to validate proper operation of the entire system. The program can be started locally on the signal/data processing computer or remotely by using the program TeamViewer to control the signal/data processing computer including program execution. The program may be started by double clicking on the FringeLVprocessing.exe file. A command (DOS) window will open followed by the graphical user interface shown in Figure E.1. (NOTE: It is recommended that the DOS box should be opened by the RUN command: COMMAND.COM, then navigate to the program location and run the program via the command string **fringelvprocessing**. This is recommended because if the program fails, error messages are presented in the command (DOS) window. Unfortunately a temporary DOS window obtained by double clicking the EXE file, will disappear if the program which opened the window crashes. Any error messages will then be lost. If the DOS window is opened first, it will remain open to display the error messages.) The user inputs to the opening screen, Figure E.1, are described below:

Laser Wavelength, microns:

Click on the desired box and a data entry window will open. Enter the appropriate laser wavelength in microns for that selected component. The new installation setting is 0.0.

Cross Beam Angle, degrees:

Click on the desired box and a data entry window will open. Enter the appropriate cross beam angle (full angle) in degrees for that selected component. The new installation setting is 0.0.

Bragg Frequency, MHz:

Click on the desired box and a data entry window will open. Enter the appropriate Bragg frequency in MHz for that selected component. The new installation setting is 0.0.

IF Frequency, MHz:

Click on the desired box and a data entry window will open. Enter the mixing frequency in MHz that feeds the reference side of a double-balanced mixer, e.g., Bragg = 40 MHz, IF = 30 MHz yields an effective 10 MHz Bragg shift. If the acquired signal is not downmixed, the IF frequencies should be set to 0.0. The new installation setting is 0.0.

Negative Doppler Shift?

Click on the desired box and if the box was blank, an X will show indicating a YES response. Clicking on the box with the X showing will remove the X. Since the TSI optical system uses a Bragg cell to both separate the colors and add the Bragg frequency offset, there is no option as to which of the output beams is shifted. Thus if a positive velocity yields a negative result, click the appropriate box to have the program automatically reverse the sign. The new installation setting is blank.

Delta Azimuth, deg:

Click on the box and a data entry window will open. If a shaft encoder is used, enter the wedge angle in degrees to be used to determine the statistical parameters. For example, a wedge angle (Delta Azimuth) of 3.0 degrees will determine the U- and V-component velocities, velocity magnitude and flow angle statistics for only those measurements that occur within that wedge angle throughout the acquisition time. This wedge angle will yield 120 separate statistical data sets to cover the entire revolution of the shaft (rotor). No convergence, histogram, or real time running plots will be displayed. These must be determined off-line. However, the mean velocity and standard deviations are plotted as a function of azimuth for the U- and V-velocity components, velocity magnitude and flow angle. The new installation setting is 0.0.

Remove Outliers?

Click on the box and if the box was blank an X will show indicating a YES response. Clicking on the box with the X showing will remove the X. This function, if selected, will remove outliers from the distributions. The technique begins by determining the histogram for the U-component velocity with a resolution of 1.0 m/s. The peak of the histogram is then determined and a threshold calculated to be 5.0-percent of the peak value (equivalent to the amplitude at the $1/e^2$ width for a Gaussian

distribution). This histogram is traced from the peak location in the positive velocity direction until the histogram level falls below the threshold. The velocity of the previous bin becomes the upper velocity limit unless the level of one of the next three bins is above threshold which then becomes the new upper limit. The process is repeated in the negative direction to determine the minimum velocity. The technique is then applied to the V-component velocity ensemble. When completed, the U- and V-component ensembles are interrogated and any outlier found removes not only that component measurement, but the other component entry as well as the corresponding velocity magnitude and flow angle entries. It is recommended that this option be selected (and is the new installation setting) unless it is known that the data will be sparse or a shaft encoder is used which could make the histograms sparse.

Save Plots?

Click on the box and if the box was blank, an X will show indicating a YES response. Clicking on the box with the X showing will remove the X. This function, if selected, will save the Convergence and Histogram plots (or Azimuth statistical plots if **Delta Azimuth** is greater than 0.0). The plots are stored in the processed sub-directory of the data ensemble directory in Enhanced Windows Metafile (EMF) format. The new installation setting is a blank box.

Binary Data?

Click on the box and if the box was blank, an X will show indicating a YES response. Clicking on the box with the X showing will remove the X. If selected, this function will inform the program that the data received from the Data Acquisition Program is in standard IEEE binary format. Otherwise the data will be expected to be in ASCII format. It is recommended that binary data be transferred because the much smaller data ensemble size will lower the acquisition turn around time. The new installation setting is an X showing.

Auto View Timing?

Click on the box and if the box was blank, an X will show indicating a YES response. Clicking on the box with the X showing will remove the X. If Selected, the **Display Time, sec** box will become active so the user can select the amount of time the plots will be shown. Otherwise, the plots will stay displayed until the user moves the cursor to the upper left plot and left clicking the mouse which then clears the plots and will display the next set of plots. The new installation setting is a blank box.

Display Time, sec:

Click on the box and a data entry window will open. Enter the time in seconds that the plots are to be displayed. If the entry is less than 3.0 seconds, the program will automatically set the display entry to 3.0. If the display is less than 3.0 seconds, it is possible that internal timing may result in a hung program especially if the BATCHLVPROCESSING program is controlling processing instead of the Data Acquisition Program. For this reason, if a time less than 3.0 seconds is input, the

program will automatically set the time to 3.0 seconds. The new installation setting is a blank box.

Trigger File:

Click on the box and the internal file manager will open. Use the file manager to select the file that will be used to control signal / data processing. This file MUST be the same file selected by the Data Acquisition Program or the Batch Processing Program. If the file does not exist, click on the **New Trigger File?** box to erase any information in the **Trigger File:** box, then click on the **Trigger File:** box. A data entry screen will then open where the user can enter the full path and file name of the new trigger file. This will then create the last subdirectory in the path along with the entered file name for use as the trigger file. The new installation setting is the message "Select Trigger File".

List Velocities?

Click on the box and if the box was blank, an X will show indicating a YES response. Clicking on the box with the X showing will remove the X. If selected, the U- and V-component velocities for each particle will be displayed in the DOS box as they are determined. The new installation setting is a blank box.

Run

Click on the box to start the Signal / Data Processing program. The program now runs hands off under the total control of the Data Acquisition Program or the Batch Processing Program. The data entry screen can not be entered again until the program is terminated by the controlling program and restarted. It is noted that the Signal / Data Processing program must be started before the first data ensemble is acquired by the Data Acquisition Program or the Batch Processing Program is RUN.

Exit

Click on the box to exit the program without doing any signal / data processing.

When all the data has been entered, the **Run** command is selected. The program will overwrite the INI file with the new parameter values/settings so that they are loaded when the Signal / Data Processing Program is started the next time, thus eliminating the need to reenter the values/settings. The program will also read the time signature on the selected Trigger File, and start the real-time display program RunningDisplay.exe. The program will then go into sleep mode for 1.0 second, after which time it will wake up and interrogate the time signature on the Trigger File. If the time signature is the same as recorded previously, the program will go back to sleep for 1.0 second, then wake up and check again. This process continues until the time signature changes indicating that a new data ensemble has been stored on the signal / data processing computer hard drive by the Data Acquisition Program, and that the information needed to process that data ensemble has been stored in the Trigger File. If the program is controlled by the Batch Processing Program, the same sequence will determine when the Trigger File has been overwritten by with the next data ensemble Trigger File indicating that the next ensemble is available for

processing. The new time signature now becomes the reference time and the Trigger File opened, the information read and signal processing begins.

Auxiliary Programs

The following programs provide additional capabilities to the Signal / Data Processing program along with programs to interrogate the original ensembles. All programs and their support INI, BAT, etc., files must be located in the same directory as the Signal / Data Processing program.

Grwnd

This program provides the graphics engine for the data entry screens and the graphics screens presenting the plots. The program is run and controlled from other programs and there is not direct user interaction with the program. The program is described and it, along with supporting routines, can be obtained from:

http://spdg1.sci.shizuoka.ac.jp/grwinlib/english/

It is a general purpose graphics utility library that is available for most 32- and 64-bit Fortran and C/C++ compilers. Along with fundamental graphics controls and commands, the library contains advanced plotting utilities, e.g., graphs with hidden lines and contour diagrams, etc.

RunningDisplay

This program provides the real-time displays of mean and standard deviation profiles with statistical error bars for the U- and V-component velocities, velocity magnitude and flow angle. The program is started, controlled and terminated by the Signal / Data Processing program. There is no user interaction with the program other than following commands generated by the Data Acquisition program:

new	Begin a new velocity/flow angle profile;
run	Plot the statistical results from the process ensemble (along with a re-plot of all the previous data in the current profile;
rep	Current ensemble is a repeat acquisition at the same measurement location as the previous ensemble; and
exit	Terminate the program.

The program automatically scales the plots since there is no a priori knowledge of the velocity/flow angle values or scan distances that will be plotted. If a new scan is started as signified by the command “new”, the data arrays would be cleared and new plots begun. The display program will be terminated by the Signal / Data Processing program as part of its termination procedure that was initiated by the command “exit”. It is noted that this program will not be started if the **Delta Azimuth** setting is not 0.0.

BatchLVprocessing

This program acts as a surrogate for the Data Acquisition and Control program when a series of data ensembles is desired to be processed off-line. It provides a batch processing capability where data from an entire day's run can be automatically processed without user intervention. This program will communicate and control the Signal/Data Processing program in the same manner as the LabVIEW program. It is strongly recommended that this program and the Signal/Data Processing program be run and operated in the following sequence to avoid potential conflicts with the graphics windows:

1) Run the Signal/Data Processing program (preferably in a Command.com window) – Do not go further with this program.
2) Run the BatchLVprocessing program (preferably in a Command.com window) – Do not go further with this program.
3) Adjust the commands/settings/selected files in the data entry screen for the Signal/Data Processing program to match the data ensembles to be processed.
4) In the data entry screen for the BatchLVprocessing program, select the EXACT same Trigger File chosen for the Signal/Data Processing program.
5) Click the **RUN** command button in the Signal/Data Processing program.
6) Click the **RUN** command button in the BatchLVprocessing program.
7) When the entire set of data ensembles have been processed, both programs will automatically terminate with messages to close the graphics windows.

Once the **RUN** command button is selected in the BatchLVprocessing program, the full path to the Trigger File is interrogated to determine the directory tree below its location. The program then builds an ASCII array containing the full path to each subdirectory containing the data ensembles to be processed. Once completed, the program then copies the Trigger File for the first ensemble and overwrites the Trigger File specified in the entry screen. This will in turn trigger the Signal/Data Processing program to begin processing the data ensemble listed within the Trigger File. Once the ensemble is processed, the Signal/Data Processing program will update the Trigger.Ret File which, in turn commands the BatchLVprocessing program to select the Trigger File for the next data ensemble, and the process continues until the final ensemble is processed. At that point, termination commands are issued for both programs.

The data entry screen presented to the user is shown in Figure E-2. Description of the entry is:

Copy Trigger File to:

Click on the box and the program will open its file manager where the trigger file that will be used by the Signal / Data Processing program should be located and selected.

ConvertBinary2ASCII

This program will convert the binary data sent to the Signal / Data Processing program by the Data Acquisition program into ASCII format. The program can be used to generate files that can be used to interrogate, plot, etc. the signals obtained by the laser velocimeter. Once started the program will present an interface screen, Figure E-3, where the user can locate the desired trigger file for the ensemble of interest. Once the trigger file has been selected using the program's file manager (obtained by clicking the Trigger File: box), the **Run** box is clicked to start the conversion. A sub-directory will be created (ASCII) and attached to the directory containing the selected trigger file. This sub-directory will contain all of the ensemble files in ASCII format. When the ensemble has been converted, the program will return to the data entry screen. Another trigger file can then be selected, or the program terminated by clicking the **Exit** box.

```
!Thursday, January 20, 2011
!10:33:03 AM
!Data Acquisition Parameters:
!NI PXI-6120 LV Configuration Parameters:
LVMultiFunc/ai0          !PXI-6120 Ch0
LVMultiFunc/ai1          !PXI-6120 Ch1
LVMultiFunc/ai2          !PXI-6120 Ch2
LVMultiFunc/ai3          !PXI-6120 Ch3
+/-2.0V !Vertical Range
PFI7     !PXI-6120 Trigger Source
PFI7     !PXI-6120 Analog Sample Clock Source
!NI PXI-5152 LV Configuration Parameters:
UComp !PXI-5152 Ch0
VComp !PXI-5152 Ch1
4.00 Vp-p        !Vertical Range
0.000000         !Vertical Offset
10240   !Record Length
1000000000.000000     !Sample Rate
!Trigger Mode: 0(Immediate), 1(Software), 2(Digital), 3(Analog Edge), 4(Analog Window)
3        !Trigger Mode
VAL_EXTERNAL         !Trigger Source:
!Scan Rig Information:
C:\Program Files (x86)\National Instruments\LabVIEW 8.6\user.lib\scan rig files\Scan_Grid_BART_Day2!
        Scanner Control File Path
!Scanner Comment
This VI allows the user to generate a sequence of scan locations at which data is to be collected. Using
        the axis settings location information in counts is generated each time the Generate Scan Data
        button is selected. Generated data is placed in the acti

0.0000390000  !Scan Rig Step Resolution - Inches (Distance/Step)
!Scanner Positions In Counts:
0.000000         !W-Axis
0.000000         !X-Axis
35000.500000  !Y-Axis
-40000.000000 !Z-Axis
!Scanner Positions In Inches:
0.000000         !W-Axis
0.000000         !X-Axis
1.365020         !Y-Axis
-1.560000        !Z-Axis
Scanner Positions In Meters:
0.000000         !W-Axis
0.000000         !X-Axis
0.034671         !Y-Axis
-0.039624        !Z-Axis
!Data Acquisition Conditions::
25.000000        !Temperature (C)
30.000000        !Atm. Pressure (in/Hg)
1.000000         !Particle Size
Polystyrene      !Particle Type
!Data Acquisition Results:
```

Table E.1.- Example LOG file created by the signal/data processing program: Header.

2000 !# LV Data Records Requested
2000 !# LV Data Records Acquired
12.829102 !LV Data Acquistion Cycle Time
152.076121 !LV Data Acquistion Data Rate
0 !Acquisition Cycle Timeout? 0=No, 1=Yes
0 !User Terminated Acquisition? 0=No, 1=Yes
!Running Plots Code
RUN !Code to Control Plotting of Processed Data. NEW = New measurement scan, RUN = Append processed results to existing running plot.

User Comment: Comments

0.4880 Laser wavelength - U-component, microns
0.5145 Laser wavelength - V-component, microns
3.5500 Cross beam angle - U-component, degrees
3.5500 Cross beam angle - V-component, degrees
40.0000 Bragg frequency - U-component, MHz
40.0000 Bragg frequency - V-component, MHz
0.0000 Reference frequency-downmixer - U-component, MHz
0.0000 Reference frequency-downmixer - V-component, MHz

0.0000 Azimuth increment, degrees

2000 Number of particles in data ensemble

NOTE: N or Norm - Standard arithmetic statistics
S/H - Based on Sample and Hold Approach
TS - Based on Time Scale Approach

Velocity & Standard Deviation Convergence

# Bursts	U-mean	U-sigma	V-mean	V-sigma	Delta U	Delta U sigma	Delta V	Delta V sigma
92	17.213	6.852	-1.663	5.672				
186	16.551	7.334	-1.323	5.855	-0.662	0.482	0.340	0.184
281	16.544	7.047	-1.390	6.015	-0.007	-0.288	-0.066	0.160
376	16.210	7.136	-1.307	5.834	-0.334	0.089	0.082	-0.181
475	16.206	7.277	-1.290	5.832	-0.004	0.141	0.018	-0.002
568	16.374	7.452	-1.351	5.816	0.168	0.175	-0.062	-0.016
662	16.598	7.601	-1.540	5.826	0.224	0.149	-0.189	0.011
756	16.567	7.529	-1.603	5.873	-0.031	-0.072	-0.063	0.047
854	16.465	7.493	-1.627	5.802	-0.103	-0.036	-0.024	-0.072
946	16.607	7.490	-1.680	5.847	0.142	-0.003	-0.053	0.045
1044	16.596	7.441	-1.654	5.854	-0.011	-0.048	0.026	0.007
1142	16.639	7.509	-1.622	5.840	0.043	0.067	0.032	-0.014
1235	16.525	7.519	-1.603	5.879	-0.114	0.010	0.019	0.038
1330	16.332	7.459	-1.512	5.859	-0.193	-0.060	0.091	-0.020
1426	16.384	7.413	-1.528	5.882	0.051	-0.046	-0.016	0.023
1520	16.375	7.427	-1.471	5.861	-0.009	0.014	0.058	-0.021

Table E.1. (cont'd) - Example LOG file: Header (cont'd) and statistical stationarity test.

1610	16.330	7.365	-1.390	5.846	-0.045	-0.062	0.081	-0.015
1702	16.359	7.308	-1.404	5.821	0.029	-0.057	-0.015	-0.025
1797	16.403	7.317	-1.404	5.814	0.044	0.009	0.000	-0.007
1894	16.321	7.324	-1.386	5.819	-0.082	0.006	0.018	0.006

Measurement Statistics

Correlation Coefficient 0.003
CorTime, #CorTime, #part: 0.000161 1483 1894

U-component	Mean m/s	? Mean m/s	Sigma m/s	? Sigma m/s	Skew	Excess
Normal Stats	16.321	0.337	7.324	0.235	0.021	-0.050
Sample & Hold	17.216	7.699	17.216	0.002	1.000	-2.000
Time Scale	24.948	12.489	25.374	2.299	1.050	-1.864

V-component	Mean m/s	? Mean m/s	Sigma m/s	? Sigma m/s	Skew	Excess
Normal Stats	-1.386	0.267	5.819	0.181	-0.298	-0.161
Sample & Hold	-0.237	0.106	0.237	NaN	-1.000	-2.000
Time Scale	2.721	1.352	4.061	0.656	0.268	-1.058

Reynolds stress: -22.730665 m2/s2

Magnitude	Mean m/s	? Mean m/s	Sigma m/s	? Sigma m/s	Skew	Excess
Normal Stats	17.529	0.320	6.967	0.210	0.375	-0.279
Sample & Hold	17.218	7.700	17.218	0.001	1.000	-2.000
Time Scale	25.230	12.376	25.621	2.246	1.048	-1.868

Flow Angle	Mean m/s	? Mean m/s	Sigma m/s	? Sigma m/s	Skew	Excess
Normal Stats	0.350	1.228	26.720	1.626	0.960	5.017
Sample & Hold	-0.789	0.353	0.789	0.000	-1.000	-2.000
Time Scale	10.289	6.302	18.566	4.242	1.675	-0.188

Particle Velocity Measurements

Time seconds	Azimuth degrees	U m/s	V m/s	Magnitude m/s	Alpha degrees	V min V	V max V	Transit microsec
0.000000	35.859	10.679	4.436	11.564	22.555	-0.636	0.498	10.236
0.002707	81.211	31.410	-3.995	31.663	-7.248	-0.498	0.464	10.220
0.009842	-158.555	9.428	-5.160	10.747	-28.693	-0.722	0.498	10.239
0.012200	-119.180	14.194	-1.355	14.258	-5.453	-0.516	0.430	10.239
0.016126	-53.086	19.180	-7.975	20.772	-22.576	-0.653	0.498	10.231
0.026127	115.312	23.836	-11.520	26.474	-25.795	-0.292	0.275	10.227
0.041439	12.656	9.017	9.311	12.962	45.920	-0.516	0.413	10.228
0.045880	87.539	19.772	-2.743	19.962	-7.899	-0.464	0.413	10.235
0.053316	-147.305	19.679	5.804	20.517	16.434	-0.481	0.430	10.227
0.064169	35.156	18.150	-14.633	23.314	-38.876	-0.292	0.223	10.234
0.072378	173.320	20.041	0.095	20.041	0.271	-0.464	0.430	10.239

Table E.1. (cont'd) - Example LOG file: statistical stationarity (cont'd), statistical results, individual bursts.

0.073890	-161.367	16.702	-3.682	17.103	-12.431	-0.172	0.155	10.237
0.089708	104.766	22.979	0.176	22.980	0.440	-0.344	0.327	10.239
0.097539	-123.398	20.320	-9.814	22.566	-25.780	-0.464	0.413	10.210
0.115181	173.320	21.094	-2.865	21.288	-7.734	-0.327	0.258	10.217
0.123574	-45.703	18.191	-5.553	19.020	-16.975	-0.584	0.430	10.203
0.125180	-18.633	11.364	7.729	13.744	34.219	-0.584	0.464	10.219
0.125665	-10.547	9.945	0.398	9.953	2.290	-0.584	0.464	10.209
0.131736	91.758	13.326	4.927	14.208	20.292	-0.773	0.533	10.239
0.144099	-60.469	24.716	-6.540	25.567	-14.821	-0.653	0.481	10.234
0.147173	-8.789	19.265	1.795	19.348	5.323	-0.584	0.498	10.228
0.153347	95.273	11.268	4.466	12.120	21.621	-0.773	0.619	10.230
0.170228	19.336	22.153	1.250	22.188	3.229	-0.086	0.103	10.238
0.180542	-167.344	21.453	1.766	21.525	4.705	-0.636	0.464	10.239
0.184755	-96.328	6.347	0.638	6.379	5.739	-0.533	0.430	10.236
0.191441	16.172	19.223	-0.147	19.224	-0.439	-0.842	0.567	10.229
0.193522	50.977	16.098	3.147	16.403	11.062	-0.619	0.464	10.239
0.198097	127.969	14.538	5.271	15.464	19.929	-0.447	0.413	10.183
0.200118	162.070	21.511	-1.019	21.535	-2.712	-0.791	0.550	10.227
0.202304	-161.367	21.347	-2.412	21.483	-6.446	-0.447	0.361	10.237
0.206680	-87.539	4.426	0.400	4.444	5.163	-0.825	0.653	10.224
0.232452	-14.062	6.842	12.740	14.461	61.761	-0.498	0.395	10.208
0.235287	33.398	23.482	-16.144	28.496	-34.508	-0.309	0.258	10.237
0.238675	90.703	20.507	-5.616	21.262	-15.315	-0.344	0.327	10.239
0.250400	-72.070	16.994	-6.644	18.247	-21.353	-0.533	0.481	10.215
0.252874	-30.586	24.380	-8.440	25.800	-19.096	-0.464	0.447	10.239
0.255387	11.602	10.722	-0.095	10.723	-0.507	-0.103	0.103	10.232
0.264485	164.883	9.671	-2.698	10.040	-15.590	-0.516	0.447	10.236
0.266541	-160.664	18.329	-11.740	21.766	-32.641	-0.653	0.567	10.118
0.268400	-129.375	21.034	-6.545	22.028	-17.286	-0.808	0.533	10.239
0.269564	-109.688	11.546	-0.952	11.585	-4.712	-0.172	0.189	10.162
0.269874	-104.766	11.989	7.010	13.888	30.316	-0.705	0.584	10.239
0.271258	-81.211	23.974	-6.028	24.720	-14.114	-0.481	0.430	10.238
0.274293	-30.234	10.205	-2.550	10.519	-14.028	-0.361	0.309	10.239
0.276920	13.711	15.392	-1.678	15.483	-6.221	-0.773	0.533	10.239
0.278635	42.891	5.163	2.768	5.859	28.198	-0.791	0.567	10.239
0.278941	47.812	7.102	-2.465	7.517	-19.144	-0.773	0.550	10.239
0.282666	110.391	22.959	-12.861	26.316	-29.258	-0.705	0.516	10.239
0.285969	165.938	28.508	-2.998	28.666	-6.004	-0.705	0.533	10.239
0.286670	177.891	10.295	9.348	13.906	42.239	-0.550	0.430	10.239
0.291776	-96.328	18.943	-6.307	19.965	-18.414	-0.756	0.602	10.239
0.293937	-59.766	6.579	2.352	6.986	19.670	-0.275	0.258	10.238
0.294682	-47.461	22.451	-2.489	22.589	-6.327	-0.481	0.395	10.228
0.295612	-31.641	32.201	-3.407	32.381	-6.039	-0.653	0.498	10.236
0.299025	25.664	16.718	0.035	16.718	0.120	-0.636	0.498	10.239
0.306843	157.148	15.374	4.522	16.025	16.391	-0.172	0.172	10.236
0.307593	169.805	18.228	-2.764	18.437	-8.623	-0.808	0.584	10.208
0.309756	-153.633	18.022	0.882	18.044	2.800	-0.636	0.481	10.198
0.314294	-77.344	29.679	-6.064	30.292	-11.548	-0.773	0.498	10.239
0.316074	-47.461	6.330	7.140	9.542	48.444	-0.275	0.206	10.235
0.316671	-37.617	19.867	-0.929	19.889	-2.676	-0.825	0.584	10.226
0.318161	-12.305	13.635	0.444	13.642	1.863	-0.378	0.292	10.238

Table E.1. (cont'd) - Example LOG file: individual bursts.

0.319844	15.820	25.302	-7.472	26.382	-16.452	-0.688	0.533	10.226
0.320720	30.586	28.891	-7.061	29.741	-13.733	-0.653	0.567	10.183
0.321352	41.133	16.194	3.424	16.552	11.939	-0.911	0.619	10.239
0.322267	56.602	23.258	-7.045	24.301	-16.851	-0.327	0.275	10.239
0.323941	84.727	12.206	9.461	15.443	37.779	-0.344	0.309	10.239
0.326445	126.914	20.361	-8.780	22.174	-23.326	-0.241	0.223	10.239
0.328154	155.742	20.308	-2.826	20.504	-7.922	-0.688	0.602	10.239
0.328833	166.992	13.258	-1.525	13.345	-6.561	-0.825	0.619	10.227
0.329275	174.375	26.739	-10.398	28.690	-21.249	-0.636	0.464	10.239
0.330742	-160.664	8.383	4.660	9.591	29.066	-0.395	0.361	10.237
0.331777	-143.438	25.623	-3.681	25.886	-8.176	-0.722	0.481	10.239
0.332352	-133.594	15.616	-1.351	15.674	-4.943	-0.773	0.584	10.239
0.332972	-123.398	8.400	1.969	8.628	13.194	-0.670	0.533	10.239
0.335148	-86.484	10.411	2.653	10.743	14.296	-0.533	0.447	10.239
0.337177	-52.383	7.555	1.611	7.725	12.040	-0.705	0.584	10.213
0.338038	-37.969	16.085	1.971	16.206	6.984	-0.430	0.344	10.239
0.338874	-23.906	7.570	2.120	7.861	15.647	-0.739	0.550	10.215
0.339700	-10.195	27.888	-10.433	29.775	-20.511	-0.756	0.567	10.239
0.341405	18.633	20.979	-1.376	21.024	-3.753	-0.653	0.533	10.239
0.346636	106.523	9.088	-1.204	9.167	-7.544	-0.670	0.516	10.229
0.347784	125.859	12.810	-1.604	12.910	-7.136	-0.395	0.327	10.187
0.348777	142.734	18.352	0.407	18.357	1.270	-0.602	0.481	10.237
0.349718	158.555	28.929	-6.249	29.596	-12.190	-0.911	0.584	10.236
0.352575	-153.633	20.711	-6.884	21.825	-18.387	-0.464	0.378	10.226
0.353516	-137.812	24.529	-7.702	25.710	-17.433	-0.739	0.533	10.233
0.354713	-117.422	5.889	7.927	9.875	53.395	-0.859	0.619	10.239
0.355937	-97.031	11.901	-1.056	11.948	-5.071	-0.498	0.413	10.239
0.358337	-56.602	31.513	-10.623	33.255	-18.629	-0.361	0.327	10.239
0.358582	-52.383	17.038	-2.021	17.158	-6.763	-0.756	0.619	10.239
0.359438	-37.969	19.038	0.061	19.038	0.183	-0.447	0.413	10.239
0.005510	-25.664	35.465	-8.043	36.365	-12.778	-0.413	0.344	10.239
0.006784	-4.219	16.119	-8.894	18.410	-28.890	-0.567	0.481	10.202
0.007393	5.977	22.185	4.874	22.714	12.391	-0.842	0.602	10.236
0.008426	23.203	27.913	-4.215	28.229	-8.588	-0.447	0.395	10.239
0.012239	87.539	20.533	-12.151	23.859	-30.615	-0.602	0.498	10.239
0.012494	91.758	12.088	1.160	12.143	5.482	-0.756	0.533	10.239
0.013274	104.766	19.895	-9.965	22.251	-26.607	-0.825	0.584	10.225
0.014399	123.750	17.986	-0.718	18.000	-2.287	-0.722	0.498	10.229
0.015213	137.461	19.647	-5.120	20.303	-14.606	-0.653	0.464	10.209
0.015598	143.789	17.035	-6.387	18.193	-20.552	-0.430	0.413	10.239
0.016387	157.148	6.849	0.042	6.849	0.348	-0.567	0.533	10.234
0.017110	169.453	16.492	-7.550	18.138	-24.599	-0.481	0.447	10.239
0.019514	-150.117	2.384	8.366	8.699	74.097	-0.223	0.189	10.223
0.020239	-138.164	17.760	-2.743	17.971	-8.780	-0.911	0.722	10.228
0.020967	-125.859	4.953	5.449	7.364	47.728	-0.584	0.533	10.219
0.025155	-55.195	14.968	-1.015	15.002	-3.878	-0.842	0.584	10.239
0.030746	38.672	2.291	9.424	9.699	76.336	-0.825	0.670	10.239
0.030993	42.891	0.871	12.352	12.382	85.968	-0.309	0.275	10.227
0.031987	59.414	16.075	-13.458	20.965	-39.937	-0.550	0.430	10.239
0.033295	81.562	0.272	12.569	12.572	88.762	-0.825	0.584	10.238
0.034303	98.438	6.255	2.510	6.740	21.863	-0.361	0.344	10.239

Table E.1. (cont'd) - Example LOG file: individual bursts (cont'd).

0.036857	141.328	11.678	5.831	13.053	26.535	-0.791	0.567	10.239
0.037282	148.711	22.080	-6.935	23.143	-17.437	-0.877	0.636	10.233
0.039281	-177.891	7.500	-6.884	10.180	-42.550	-0.911	0.584	10.239
0.040332	-159.961	20.974	4.173	21.385	11.253	-0.859	0.602	10.239
0.041321	-143.438	15.072	5.332	15.987	19.481	-0.223	0.206	10.216
0.042193	-128.672	4.013	-5.384	6.715	-53.298	-0.378	0.309	10.239
0.046837	-50.625	24.888	-6.361	25.688	-14.337	-0.533	0.447	10.239
0.047304	-42.891	6.071	6.694	9.037	47.794	-0.619	0.498	10.237
0.048449	-23.555	15.319	-6.502	16.642	-23.000	-0.327	0.292	10.239
0.049994	2.461	12.088	1.919	12.240	9.023	-0.705	0.516	10.239
0.050883	17.578	25.665	0.611	25.672	1.363	-0.413	0.395	10.239
0.051721	31.641	16.007	-4.431	16.608	-15.472	-0.361	0.344	10.231
0.055396	93.164	-3.471	7.149	7.947	115.898	-0.859	0.619	10.239
0.059751	166.641	14.484	-6.648	15.937	-24.653	-0.688	0.481	10.238
0.064164	-119.180	18.140	4.839	18.775	14.937	-0.602	0.516	10.218
0.069711	-26.016	20.605	-8.337	22.228	-22.030	-0.894	0.636	10.239
0.073762	42.188	20.429	6.077	21.314	16.567	-0.894	0.670	10.237
0.075015	63.281	14.610	1.319	14.669	5.158	-0.636	0.498	10.239
0.075522	71.719	17.293	-1.167	17.332	-3.859	-0.584	0.481	10.225
0.077697	108.633	2.821	-3.368	4.393	-50.044	-0.361	0.309	10.239
0.078803	126.914	22.814	-5.261	23.413	-12.986	-0.464	0.464	10.221
0.083482	-154.336	9.074	2.418	9.391	14.921	-0.550	0.447	10.239
0.084096	-143.789	7.912	6.713	10.376	40.312	-0.120	0.103	10.235
0.086068	-110.742	3.164	8.394	8.971	69.345	-0.636	0.464	10.239
0.087243	-91.055	11.452	2.340	11.689	11.547	-0.498	0.378	10.239
0.087803	-81.562	6.901	4.809	8.411	34.873	-0.894	0.602	10.237
0.090905	-29.531	9.135	-9.220	12.979	-45.264	-0.550	0.481	10.239
0.091587	-17.930	23.356	-3.590	23.631	-8.737	-0.395	0.395	10.239
0.093072	7.031	12.223	-11.310	16.653	-42.780	-0.705	0.464	10.239
0.093335	11.602	3.959	-1.528	4.244	-21.097	-0.223	0.189	10.229
0.095316	45.000	19.352	7.520	20.761	21.235	-0.739	0.516	10.237
0.096365	62.578	21.560	-14.853	26.181	-34.562	-0.842	0.584	10.239
0.097041	73.828	17.761	6.843	19.033	21.073	-0.550	0.533	10.239
0.099283	111.445	13.966	0.556	13.977	2.280	-0.378	0.378	10.239
0.099856	121.289	24.956	-0.226	24.957	-0.519	-0.344	0.327	10.239
0.100645	134.297	8.992	8.316	12.248	42.764	-0.395	0.344	10.239
0.105973	-136.055	18.554	-0.087	18.554	-0.268	-0.464	0.430	10.222
0.106820	-121.641	8.196	0.908	8.246	6.323	-0.533	0.413	10.235
0.107630	-107.930	31.583	2.647	31.694	4.792	-0.688	0.533	10.239
0.107955	-102.656	26.640	0.259	26.642	0.556	-0.739	0.550	10.239
0.108736	-89.297	26.128	-13.051	29.206	-26.542	-0.498	0.464	10.187
0.111825	-37.617	15.701	0.220	15.703	0.803	-0.292	0.275	10.236
0.112273	-29.883	20.605	-0.732	20.618	-2.034	-0.619	0.464	10.229
0.113378	-11.250	19.364	-4.339	19.844	-12.630	-0.859	0.602	10.239
0.113794	-4.219	16.738	-1.244	16.784	-4.251	-0.430	0.344	10.239
0.114673	10.547	14.511	-2.025	14.652	-7.944	-0.378	0.309	10.239
0.116314	37.969	28.320	-5.779	28.903	-11.534	-0.516	0.481	10.236
0.116814	46.406	26.739	-7.238	27.701	-15.146	-0.481	0.395	10.239
0.117768	62.578	11.782	2.180	11.982	10.484	-0.567	0.498	10.239
0.119004	83.320	19.918	4.337	20.385	12.285	-0.825	0.584	10.239
0.119367	89.297	20.466	-0.639	20.476	-1.789	-0.258	0.241	10.238

Table E.1. (cont'd) - Example LOG file: individual bursts (cont'd).

0.120107	101.953	15.990	5.124	16.791	17.767	-0.550	0.447	10.239
0.121178	119.883	12.432	-0.890	12.463	-4.097	-0.395	0.447	10.231
0.121959	132.891	12.952	2.206	13.139	9.666	-0.791	0.584	10.239
0.123978	166.992	7.712	2.991	8.272	21.197	-0.481	0.430	10.232
0.124556	176.836	30.146	-9.501	31.608	-17.493	-0.619	0.430	10.230
0.125263	-171.562	22.016	-6.181	22.867	-15.682	-0.825	0.584	10.239
0.126000	-158.906	13.449	3.229	13.832	13.502	-0.825	0.653	10.236
0.129089	-107.227	28.392	-12.253	30.923	-23.344	-0.498	0.447	10.237
0.130402	-85.078	20.461	-5.351	21.150	-14.655	-0.808	0.653	10.193
0.131202	-71.367	11.454	1.123	11.509	5.597	-0.808	0.567	10.238
0.133136	-39.023	20.382	-4.213	20.813	-11.678	-0.413	0.361	10.237
0.133657	-30.234	12.072	1.714	12.194	8.079	-0.447	0.430	10.222
0.136513	17.930	18.036	0.050	18.036	0.159	-0.498	0.378	10.233
0.136799	22.500	15.336	-3.264	15.680	-12.016	-0.602	0.447	10.233
0.137854	40.430	11.934	2.532	12.200	11.976	-0.670	0.498	10.239
0.138358	48.867	12.046	-1.701	12.165	-8.035	-0.791	0.584	10.239
0.139057	60.469	18.232	-0.525	18.240	-1.648	-0.773	0.567	10.225
0.140353	82.266	18.182	2.884	18.409	9.014	-0.395	0.395	10.238
0.140932	92.109	13.853	0.984	13.888	4.065	-0.533	0.516	10.239
0.141865	107.930	18.641	1.255	18.683	3.851	-0.241	0.189	10.236
0.142433	117.422	26.559	-6.570	27.360	-13.895	-0.584	0.550	10.236
0.143933	142.734	28.452	-8.550	29.709	-16.725	-0.653	0.516	10.239
0.006439	166.289	22.305	2.606	22.457	6.663	-0.773	0.481	10.238
0.006841	172.969	17.421	-9.357	19.774	-28.240	-0.378	0.327	10.239
0.007895	-169.102	25.926	-3.377	26.145	-7.422	-0.808	0.533	10.239
0.008434	-159.961	15.559	-0.233	15.561	-0.856	-0.808	0.619	10.217
0.009324	-145.195	16.716	2.924	16.970	9.920	-0.756	0.533	10.235
0.010049	-132.891	24.087	-7.446	25.211	-17.178	-0.309	0.292	10.238
0.010655	-122.695	15.484	-0.729	15.501	-2.697	-0.619	0.464	10.238
0.011663	-105.820	32.429	-10.583	34.112	-18.074	-0.464	0.447	10.219
0.012295	-95.273	16.786	-5.835	17.771	-19.167	-0.498	0.430	10.239
0.013230	-79.453	30.876	-8.710	32.081	-15.753	-0.808	0.584	10.236
0.013969	-67.148	21.199	-2.669	21.366	-7.177	-0.619	0.498	10.239
0.014947	-50.625	20.632	2.211	20.750	6.117	-0.894	0.670	10.239
0.015436	-42.188	10.669	4.498	11.578	22.860	-0.413	0.361	10.239
0.016821	-18.984	19.385	-7.389	20.745	-20.866	-0.172	0.189	10.225
0.018966	17.227	21.153	-6.122	22.021	-16.142	-0.722	0.584	10.238
0.019604	27.773	16.658	-5.224	17.458	-17.413	-0.722	0.550	10.235
0.020018	34.805	16.686	-4.516	17.287	-15.144	-0.413	0.430	10.239
0.021300	56.250	9.825	5.929	11.476	31.110	-0.619	0.516	10.237
0.021650	62.227	16.605	-4.425	17.185	-14.922	-0.842	0.567	10.238
0.022980	84.727	16.231	5.862	17.257	19.857	-0.430	0.413	10.239
0.023732	97.383	25.743	-1.680	25.798	-3.734	-0.481	0.447	10.238
0.024193	105.117	18.328	-6.935	19.596	-20.725	-0.378	0.327	10.232
0.024799	115.312	22.917	3.799	23.230	9.412	-0.688	0.567	10.239
0.026374	141.680	13.737	-1.288	13.797	-5.355	-0.481	0.413	10.239
0.027957	168.398	6.808	1.248	6.921	10.389	-0.825	0.533	10.232
0.028950	-175.078	9.750	3.240	10.275	18.384	-0.739	0.567	10.237
0.030347	-151.523	32.099	-5.697	32.601	-10.063	-0.516	0.481	10.239
0.031235	-136.406	13.570	-2.158	13.741	-9.036	-0.138	0.138	10.239
0.032522	-114.961	22.283	-9.403	24.186	-22.879	-0.447	0.413	10.198

Table E.1. (cont'd) - Example LOG file: individual bursts (cont'd).

0.033020	-106.523	22.496	-0.867	22.512	-2.207	-0.516	0.464	10.222
0.034791	-76.641	12.145	-1.904	12.293	-8.910	-0.464	0.378	10.238
0.035836	-59.062	13.898	3.367	14.300	13.617	-0.791	0.584	10.239
0.036794	-42.891	15.396	2.063	15.534	7.632	-0.670	0.498	10.239
0.037204	-36.211	16.764	-1.249	16.811	-4.259	-0.877	0.636	10.232
0.038161	-20.039	8.084	9.484	12.462	49.556	-0.705	0.550	10.238
0.039704	5.977	11.746	8.369	14.422	35.469	-0.498	0.378	10.220
0.040720	22.852	24.640	0.453	24.644	1.054	-0.602	0.567	10.238
0.042373	50.625	15.038	1.953	15.164	7.401	-0.791	0.670	10.239
0.042774	57.656	9.200	9.223	13.027	45.074	-0.172	0.172	10.228
0.044974	94.570	12.923	1.465	13.006	6.467	-0.739	0.550	10.238
0.046027	112.148	12.175	-2.399	12.409	-11.145	-0.533	0.464	10.239
0.048515	153.984	17.770	-3.367	18.086	-10.729	-0.808	0.550	10.239
0.050825	-166.992	14.880	3.548	15.298	13.411	-0.138	0.172	10.222
0.051173	-161.016	8.382	5.952	10.280	35.378	-0.688	0.533	10.231
0.053167	-127.617	5.426	1.762	5.705	17.992	-0.808	0.584	10.239
0.055897	-81.562	5.136	12.100	13.145	66.999	-0.825	0.653	10.235
0.056327	-74.531	19.595	1.345	19.641	3.926	-0.739	0.602	10.239
0.058902	-31.289	14.394	-3.847	14.899	-14.962	-0.842	0.567	10.239
0.059608	-19.336	19.460	-9.540	21.673	-26.114	-0.498	0.447	10.239
0.061472	11.953	7.251	4.294	8.427	30.637	-0.275	0.275	10.239
0.062881	35.859	22.370	-10.646	24.774	-25.449	-0.602	0.516	10.222
0.064656	65.742	15.004	4.375	15.629	16.256	-0.619	0.481	10.239
0.065537	80.508	22.308	-12.438	25.541	-29.142	-0.223	0.189	10.239
0.065973	87.891	26.730	-4.932	27.181	-10.454	-0.825	0.584	10.239
0.066673	99.492	16.572	-6.594	17.835	-21.698	-0.567	0.464	10.229
0.067487	113.203	27.834	-12.919	30.686	-24.898	-0.722	0.550	10.236
0.068499	130.430	17.315	2.930	17.561	9.604	-0.413	0.378	10.239
0.069519	147.305	12.516	-14.053	18.818	-48.312	-0.447	0.378	10.239
0.070635	166.289	-1.500	10.840	10.943	97.879	-0.361	0.309	10.239
0.071917	-172.266	27.738	-1.561	27.782	-3.222	-0.155	0.138	10.239
0.074965	-120.938	15.026	-9.172	17.604	-31.398	-0.653	0.567	10.211
0.075363	-114.258	22.474	-14.096	26.529	-32.097	-0.670	0.533	10.239
0.078123	-67.852	25.990	-13.363	29.224	-27.210	-0.602	0.481	10.239
0.078753	-57.305	13.993	0.402	13.999	1.646	-0.722	0.516	10.239
0.079207	-49.570	12.967	-7.019	14.745	-28.426	-0.550	0.430	10.239
0.080083	-34.805	7.935	5.035	9.397	32.397	-0.705	0.550	10.140
0.081898	-4.219	18.805	-3.387	19.107	-10.212	-0.756	0.533	10.205
0.082107	-0.703	19.197	-13.634	23.546	-35.383	-0.516	0.395	10.238
0.085712	59.766	12.682	2.022	12.843	9.057	-0.825	0.567	10.239
0.086417	71.719	13.058	10.133	16.528	37.813	-0.756	0.602	10.239
0.087501	90.000	12.423	-3.876	13.013	-17.327	-0.584	0.498	10.239
0.088119	100.195	11.150	-1.730	11.284	-8.822	-0.584	0.498	10.239
0.088932	113.906	12.077	-11.747	16.848	-44.207	-0.378	0.344	10.228
0.090109	133.945	21.598	-4.968	22.162	-12.954	-0.670	0.481	10.235
0.091689	160.312	18.237	-6.643	19.409	-20.014	-0.722	0.584	10.239
0.092460	173.320	25.360	-14.319	29.123	-29.450	-0.688	0.516	10.194
0.092976	-177.891	10.457	2.485	10.748	13.369	-0.602	0.481	10.232
0.094101	-158.906	24.931	-2.866	25.095	-6.558	-0.430	0.430	10.238
0.094685	-149.414	24.198	-2.639	24.341	-6.224	-0.481	0.481	10.234
0.097360	-104.414	14.994	-5.784	16.071	-21.093	-0.481	0.430	10.236

Table E.1. (cont'd) - Example LOG file: individual bursts (cont'd).

0.098252	-89.297	21.833	-0.249	21.835	-0.652	-0.292	0.241	10.239
0.100449	-52.383	8.748	5.521	10.345	32.257	-0.447	0.395	10.232
0.101980	-26.367	20.931	-4.743	21.462	-12.769	-0.722	0.516	10.237
0.104333	13.008	19.705	-7.686	21.150	-21.308	-0.430	0.344	10.233
0.105755	36.914	15.606	2.038	15.738	7.441	-0.189	0.155	10.207
0.106922	56.602	11.848	2.674	12.146	12.718	-0.567	0.516	10.239
0.107666	69.258	6.451	5.228	8.303	39.022	-0.619	0.516	10.236
0.108352	80.508	16.045	7.112	17.550	23.905	-0.722	0.516	10.239
0.109006	91.758	20.645	-5.492	21.363	-14.897	-0.464	0.430	10.238
0.109685	103.008	7.687	2.512	8.087	18.093	-0.688	0.516	10.238
0.110907	123.750	14.240	-2.283	14.422	-9.107	-0.705	0.516	10.238
0.111207	128.672	13.011	4.009	13.615	17.126	-0.413	0.413	10.210
0.112533	150.820	10.925	2.352	11.175	12.148	-0.602	0.516	10.237
0.113666	170.156	7.669	7.042	10.412	42.561	-0.550	0.516	10.236
0.114365	-178.242	11.965	6.983	13.853	30.269	-0.722	0.584	10.225
0.006915	-166.289	16.611	-1.130	16.649	-3.893	-0.481	0.413	10.235
0.007746	-152.227	6.717	6.295	9.206	43.145	-0.498	0.413	10.229
0.008996	-131.133	15.812	-4.075	16.328	-14.451	-0.791	0.584	10.077
0.011372	-91.406	17.145	-6.587	18.367	-21.017	-0.842	0.584	10.236
0.012192	-77.695	14.030	8.202	16.252	30.312	-0.447	0.413	10.239
0.014313	-41.836	14.195	-2.851	14.478	-11.356	-0.739	0.516	10.239
0.015298	-25.312	8.476	-2.432	8.818	-16.008	-0.447	0.395	10.236
0.015879	-15.469	21.570	-6.085	22.412	-15.754	-0.567	0.516	10.232
0.016434	-6.328	9.126	10.908	14.222	50.082	-0.550	0.464	10.238
0.018327	25.664	8.817	-0.865	8.859	-5.601	-0.464	0.395	10.238
0.019469	45.000	17.175	-3.311	17.491	-10.913	-0.602	0.430	10.239
0.019801	50.273	12.131	-0.994	12.172	-4.684	-0.498	0.413	10.235
0.021445	78.047	14.617	-3.467	15.022	-13.344	-0.395	0.292	10.238
0.021700	82.266	11.017	-3.336	11.511	-16.845	-0.481	0.378	10.239

Velocity Histograms

U	U-count	V	V-count	Magnitude	Mag-count	Alpha	Alpha-count	
-12.000	0.000	-24.000	0.000	-9.000	0.000	-106.000	0.000	
-11.000	0.000	-23.000	0.000	-8.000	0.000	-105.000	1.000	
-10.000	0.000	-22.000	0.000	-7.000	0.000	-104.000	0.000	
-9.000	0.000	-21.000	2.000	-6.000	0.000	-103.000	0.000	
-8.000	1.000	-20.000	0.000	-5.000	0.000	-102.000	0.000	
-7.000	1.000	-19.000	4.000	-4.000	0.000	-101.000	0.000	
-6.000	0.000	-18.000	3.000	-3.000	0.000	-100.000	1.000	
-5.000	3.000	-17.000	6.000	-2.000	0.000	-99.000	1.000	
-4.000	2.000	-16.000	3.000	-1.000	0.000	-98.000	0.000	
-3.000	8.000	-15.000	12.000	0.000	0.000	-97.000	0.000	
-2.000	2.000	-14.000	16.000	1.000	1.000	-96.000	0.000	
-1.000	8.000	-13.000	22.000	2.000	4.000	-95.000	0.000	
0.000	7.000	-12.000	37.000	3.000	4.000	-94.000	0.000	
1.000	7.000	-11.000	37.000	4.000	14.000	-93.000	0.000	
2.000	13.000	-10.000	46.000	5.000	14.000	-92.000	1.000	

Table E.1. (cont'd) - Example LOG file: individual bursts (cont'd), histograms.

3.000	21.000	-9.000	44.000	6.000	31.000	-91.000	0.000
4.000	17.000	-8.000	61.000	7.000	41.000	-90.000	0.000
5.000	31.000	-7.000	67.000	8.000	62.000	-89.000	0.000
6.000	32.000	-6.000	89.000	9.000	72.000	-88.000	0.000
7.000	42.000	-5.000	94.000	10.000	71.000	-87.000	0.000
8.000	80.000	-4.000	82.000	11.000	79.000	-86.000	0.000
9.000	59.000	-3.000	143.000	12.000	91.000	-85.000	0.000
10.000	75.000	-2.000	121.000	13.000	99.000	-84.000	0.000
11.000	72.000	-1.000	125.000	14.000	103.000	-83.000	0.000
12.000	94.000	0.000	129.000	15.000	102.000	-82.000	0.000
13.000	95.000	1.000	108.000	16.000	108.000	-81.000	0.000
14.000	104.000	2.000	137.000	17.000	108.000	-80.000	1.000
15.000	100.000	3.000	120.000	18.000	102.000	-79.000	0.000
16.000	113.000	4.000	99.000	19.000	88.000	-78.000	0.000
17.000	96.000	5.000	72.000	20.000	101.000	-77.000	0.000
18.000	95.000	6.000	66.000	21.000	87.000	-76.000	0.000
19.000	94.000	7.000	51.000	22.000	72.000	-75.000	0.000
20.000	98.000	8.000	37.000	23.000	62.000	-74.000	0.000
21.000	86.000	9.000	26.000	24.000	55.000	-73.000	0.000
22.000	67.000	10.000	16.000	25.000	57.000	-72.000	0.000
23.000	58.000	11.000	9.000	26.000	52.000	-71.000	0.000
24.000	57.000	12.000	6.000	27.000	40.000	-70.000	0.000
25.000	46.000	13.000	3.000	28.000	28.000	-69.000	2.000
26.000	41.000			29.000	32.000	-68.000	0.000
27.000	38.000			30.000	29.000	-67.000	0.000
28.000	29.000			31.000	17.000	-66.000	1.000
29.000	21.000			32.000	21.000	-65.000	0.000
30.000	21.000			33.000	17.000	-64.000	0.000
31.000	21.000			34.000	9.000	-63.000	0.000
32.000	15.000			35.000	6.000	-62.000	0.000
33.000	8.000			36.000	9.000	-61.000	0.000
34.000	7.000			37.000	3.000	-60.000	1.000
35.000	5.000			38.000	0.000	-59.000	0.000
36.000	2.000			39.000	1.000	-58.000	0.000
37.000	0.000					-57.000	0.000
38.000	1.000					-56.000	0.000
						-55.000	0.000
						-54.000	2.000
						-53.000	3.000
						-52.000	1.000
						-51.000	0.000
						-50.000	2.000
						-49.000	0.000
						-48.000	1.000
						-47.000	0.000
						-46.000	1.000
						-45.000	5.000
						-44.000	1.000
						-43.000	5.000
						-42.000	2.000
						-41.000	5.000

Table E.1. (cont'd) - Example LOG file: histograms (cont'd).

-40.000	5.000
-39.000	6.000
-38.000	3.000
-37.000	5.000
-36.000	4.000
-35.000	9.000
-34.000	8.000
-33.000	8.000
-32.000	9.000
-31.000	15.000
-30.000	12.000
-29.000	21.000
-28.000	12.000
-27.000	17.000
-26.000	16.000
-25.000	20.000
-24.000	21.000
-23.000	26.000
-22.000	29.000
-21.000	37.000
-20.000	19.000
-19.000	29.000
-18.000	28.000
-17.000	33.000
-16.000	30.000
-15.000	36.000
-14.000	42.000
-13.000	37.000
-12.000	38.000
-11.000	38.000
-10.000	44.000
-9.000	49.000
-8.000	46.000
-7.000	35.000
-6.000	41.000
-5.000	42.000
-4.000	41.000
-3.000	37.000
-2.000	33.000
-1.000	39.000
0.000	48.000
1.000	27.000
2.000	28.000
3.000	22.000
4.000	18.000
5.000	35.000
6.000	38.000
7.000	24.000
8.000	22.000
9.000	30.000
10.000	29.000

Table E.1. (cont'd) - Example LOG file: histograms (cont'd).

11.000	20.000
12.000	30.000
13.000	26.000
14.000	19.000
15.000	21.000
16.000	20.000
17.000	19.000
18.000	13.000
19.000	21.000
20.000	18.000
21.000	13.000
22.000	11.000
23.000	11.000
24.000	11.000
25.000	12.000
26.000	9.000
27.000	10.000
28.000	18.000
29.000	6.000
30.000	11.000
31.000	11.000
32.000	9.000
33.000	6.000
34.000	10.000
35.000	7.000
36.000	5.000
37.000	6.000
38.000	10.000
39.000	5.000
40.000	1.000
41.000	5.000
42.000	3.000
43.000	8.000
44.000	3.000
45.000	5.000
46.000	3.000
47.000	3.000
48.000	6.000
49.000	4.000
50.000	5.000
51.000	3.000
52.000	2.000
53.000	4.000
54.000	1.000
55.000	1.000
56.000	0.000
57.000	2.000
58.000	4.000
59.000	1.000
60.000	2.000
61.000	1.000

Table E.1. (cont'd) - Example LOG file: histograms (cont'd).

62.000	1.000
63.000	3.000
64.000	3.000
65.000	0.000
66.000	3.000
67.000	1.000
68.000	2.000
69.000	4.000
70.000	1.000
71.000	0.000
72.000	0.000
73.000	0.000
74.000	1.000
75.000	2.000
76.000	2.000
77.000	3.000
78.000	0.000
79.000	2.000
80.000	1.000
81.000	1.000
82.000	0.000
83.000	0.000
84.000	1.000
85.000	1.000
86.000	1.000
87.000	0.000
88.000	1.000
89.000	1.000
90.000	0.000
91.000	0.000
92.000	1.000
93.000	1.000
94.000	0.000
95.000	1.000
96.000	0.000
97.000	1.000
98.000	2.000
99.000	1.000
100.000	0.000
101.000	0.000
102.000	1.000
103.000	0.000
104.000	1.000
105.000	0.000
106.000	1.000

Convergence:	U-mean,	U-sigma,	V-mean,	V-sigma,	Convergence Avg
	0.0133	0.0196	0.0138	0.0082	0.0137

Table E.1. (cont'd) - Example LOG file: histograms (cont'd), statistical stationarity test convergence.

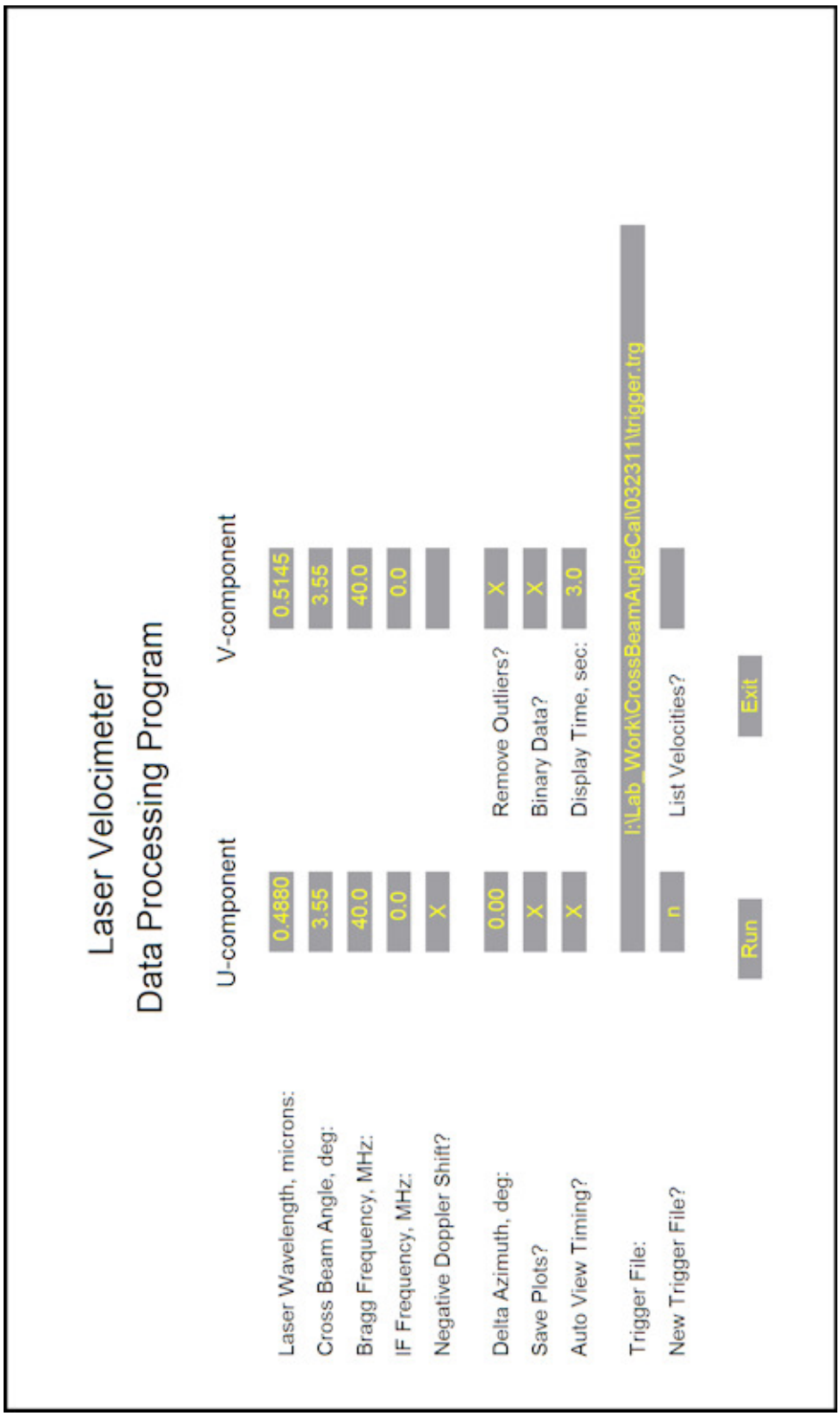

Figure E.1.- Set-up screen for the laser velocimeter signal/data processing program.

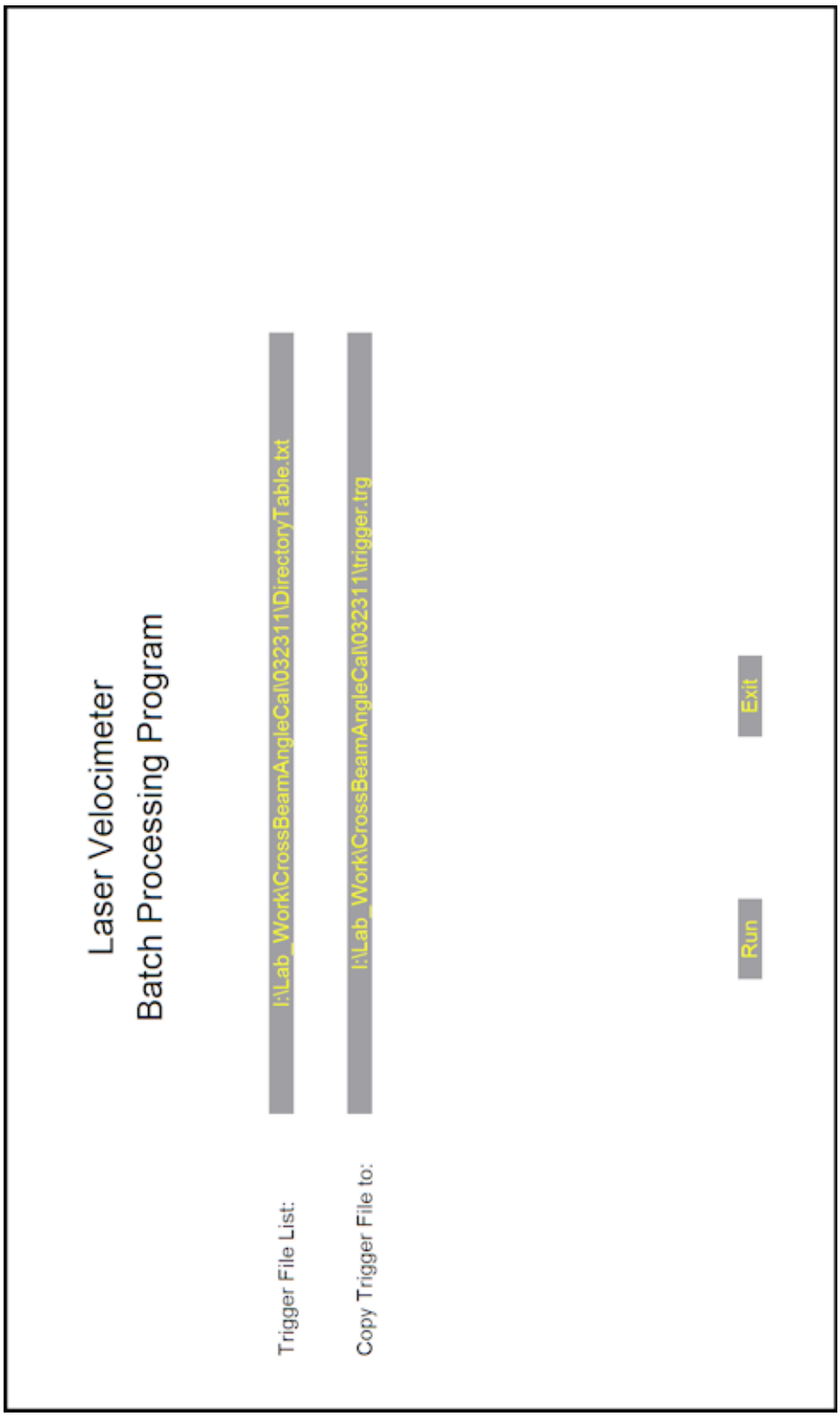

Figure E.2.- Set-up screen for the laser velocimeter batch processing program.

Figure E.3.- Set-up screen for the laser velocimeter binary to ASCII conversion program.

REPORT DOCUMENTATION PAGE

Form Approved
OMB No. 0704-0188

1. REPORT DATE *(DD-MM-YYYY)*	2. REPORT TYPE	3. DATES COVERED *(From - To)*
01- 11 - 2012	Technical Memorandum	October 2009 - July 2012

4. TITLE AND SUBTITLE

14- by 22-Foot Subsonic Tunnel Laser Velocimeter Upgrade

5a. CONTRACT NUMBER

5b. GRANT NUMBER

5c. PROGRAM ELEMENT NUMBER

6. AUTHOR(S)

Meyers, James F.; Lee, Joseph W.; Cavone, Angelo A.; Flecher, Mark T.

5d. PROJECT NUMBER

5e. TASK NUMBER

5f. WORK UNIT NUMBER

380046.02.07.03.03.01

7. PERFORMING ORGANIZATION NAME(S) AND ADDRESS(ES)

NASA Langley Research Center
Hampton, VA 23681-2199

8. PERFORMING ORGANIZATION REPORT NUMBER

L-20201

9. SPONSORING/MONITORING AGENCY NAME(S) AND ADDRESS(ES)

National Aeronautics and Space Administration
Washington, DC 20546-0001

10. SPONSOR/MONITOR'S ACRONYM(S)

NASA

11. SPONSOR/MONITOR'S REPORT NUMBER(S)

NASA/TM-2012-217781

12. DISTRIBUTION/AVAILABILITY STATEMENT

Unclassified - Unlimited
Subject Category 35
Availability: NASA CASI (443) 757-5802

13. SUPPLEMENTARY NOTES

14. ABSTRACT

A long-focal length laser velocimeter constructed in the early 1980's was upgraded using current technology to improve usability, reliability and future serviceability. The original, free-space optics were replaced with a state-of-the-art fiber-optic subsystem which allowed most of the optics, including the laser, to be remote from the harsh tunnel environment. General purpose high-speed digitizers were incorporated in a standard modular data acquisition system, along with custom signal processing software executed on a desktop computer, served as the replacement for the signal processors. The resulting system increased optical sensitivity with real-time signal/data processing that produced measurement precisions exceeding those of the original system. Monte Carlo simulations, along with laboratory and wind tunnel investigations were used to determine system characteristics and measurement precision.

15. SUBJECT TERMS

Analog-to-digital converters; Laser velocimeters; Subsonic tunnel; Velocity measurements; Wind tunnel instrumentation; Wind tunnel tests

16. SECURITY CLASSIFICATION OF:			17. LIMITATION OF ABSTRACT	18. NUMBER OF PAGES	19a. NAME OF RESPONSIBLE PERSON
a. REPORT	b. ABSTRACT	c. THIS PAGE			STI Help Desk (email: help@sti.nasa.gov)
					19b. TELEPHONE NUMBER *(Include area code)*
U	U	U	UU	793	(443) 757-5802